Frontiers in Artificial Intelligence and Applications

FUZZY SYSTEMS AND DATA MINING IX

Proceedings of FSDM 2023

Edited by
Antonio J. Tallón-Ballesteros
Raquel Beltrán-Barba

IOS Press

FUZZY SYSTEMS AND DATA MINING IX

Fuzzy systems and data mining are indispensible aspects of the digital technology on which we now all depend. Fuzzy logic is intrinsic to applications in the electrical, chemical and engineering industries, and also in the fields of management and environmental issues. Data mining is indispensible in dealing with big data, massive data, and scalable, parallel and distributed algorithms.

This book presents the proceedings of FSDM 2023, the 9th International Conference on Fuzzy Systems and Data Mining, held from 10-13 November 2023 as a hybrid event, with some participants attending in Chongqing, China, and others online. The conference focuses on four main areas: fuzzy theory, algorithms and systems; fuzzy application; data mining; and the interdisciplinary field of fuzzy logic and data mining, and provides a forum for experts, researchers, academics and representatives from industry to share the latest advances in the field of fuzzy sets and data mining. This year, topics from two special sessions on granular-ball computing and the application of generative AI, as well as machine learning and neural networks, were also covered. A total of 363 submissions were received, and after careful review by the members of the international program committee, 110 papers were accepted for presentation at the conference and publication here, representing an acceptance rate of just over 30%.

Covering a comprehensive range of current research and developments in fuzzy logic and data mining, the book will be of interest to all those working in the field of data science.

ISBN 978-1-64368-470-3 (print)
ISBN 978-1-64368-471-0 (online)
ISSN 0922-6389 (print)
ISSN 1879-8314 (online)

FUZZY SYSTEMS AND DATA MINING IX

Frontiers in Artificial Intelligence and Applications

The book series Frontiers in Artificial Intelligence and Applications (FAIA) covers all aspects of theoretical and applied Artificial Intelligence research in the form of monographs, selected doctoral dissertations, handbooks and proceedings volumes. The FAIA series contains several sub-series, including 'Information Modelling and Knowledge Bases' and 'Knowledge-Based Intelligent Engineering Systems'. It also includes the biennial European Conference on Artificial Intelligence (ECAI) proceedings volumes, and other EurAI (European Association for Artificial Intelligence, formerly ECCAI) sponsored publications. The series has become a highly visible platform for the publication and dissemination of original research in this field. Volumes are selected for inclusion by an international editorial board of well-known scholars in the field of AI. All contributions to the volumes in the series have been peer reviewed.
The FAIA series is indexed in ACM Digital Library; DBLP; EI Compendex; Google Scholar; Scopus; Web of Science: Conference Proceedings Citation Index – Science (CPCI-S) and Book Citation Index – Science (BKCI-S); Zentralblatt MATH.

Volume 378

Recently published in this series

Vol. 377. N. Aussenac-Gilles, T. Hahmann, A. Galton and M.M. Hedblom (Eds.), Formal Ontology in Information Systems – Proceedings of the 13th International Conference (FOIS 2023)
Vol. 376. R.J. Dwyer (Ed.), Digitalization and Management Innovation II – Proceedings of DMI 2023
Vol. 375. I. Sanz, R. Ros and J. Nin (Eds.), Artificial Intelligence Research and Development – Proceedings of the 25th International Conference of the Catalan Association for Artificial Intelligence
Vol. 374. J.-L. Kim (Ed.), Machine Learning and Artificial Intelligence – Proceedings of MLIS 2023
Vol. 373. G. Grigoras and P. Lorenz (Eds.), Advances in Artificial Intelligence, Big Data and Algorithms – Proceedings of the 3rd International Conference on Artificial Intelligence, Big Data and Algorithms (CAIBDA 2023)
Vol. 372. K. Gal, A. Nowé, G.J. Nalepa, R. Fairstein and R. Rădulescu (Eds.), ECAI 2023 – 26th European Conference on Artificial Intelligence – September 30–October 4, 2023, Kraków, Poland

ISSN 0922-6389 (print)
ISSN 1879-8314 (online)

Fuzzy Systems and Data Mining IX

Proceedings of FSDM 2023

Edited by

Antonio J. Tallón-Ballesteros

Department of Electronic, Computer Systems and Automation Engineering, University of Huelva, Huelva city, Spain

and

Raquel Beltrán-Barba

Department of Integrated Sciences, University of Huelva, Huelva city, Spain

IOS Press

Amsterdam • Berlin • Washington, DC

ISBN 978-1-64368-470-3 (print)
ISBN 978-1-64368-471-0 (online)
Library of Congress Control Number: 2023951646
doi: 10.3233/FAIA378

Publisher
IOS Press BV
Nieuwe Hemweg 6B
1013 BG Amsterdam
Netherlands
e-mail: order@iospress.nl

For book sales in the USA and Canada:
IOS Press, Inc.
6751 Tepper Drive
Clifton, VA 20124
USA
Tel.: +1 703 830 6300
Fax: +1 703 830 2300
sales@iospress.com

Preface

A decade after its inception, the International Conference series on Fuzzy Systems and Data Mining (FSDM) has become established as a mature event. It deals with four main topic groups: a) fuzzy theory, algorithms and systems, b) fuzzy application, c) the interdisciplinary field of fuzzy logic and data mining, and d) data mining. It is a forum for experts, researchers, academics and representatives from industry to share the latest advances in the field of fuzzy sets and data mining. From the outset, the proceedings have formed part of the prestigious book series, Frontiers in Artificial Intelligence and Applications (FAIA), published by IOS Press.

This book contains the papers accepted and presented at the 9th International Conference on Fuzzy Systems and Data Mining (FSDM 2023), held from 10–13 November 2023 in hybrid mode, with most participants gathered in-person in Chongqing, China, and some online. The conference was organized by Chongqing University of Posts and Telecommunications.

All papers were carefully reviewed by members of the international program committee, (listed on http://www.fsdmconf.org/TPC), and peer-reviewers (listed on http://www.academicconf.com/reviewerlist?confname=fsdm2023) taking into consideration the breadth and depth of the research topics that fall within the scope of FSDM, focusing not only on the four main topic groups, but also on the themes of two special sessions on granular-ball computing and the application of generative AI, as well as machine learning and neural networks.

FSDM 2023 received 363 submissions, and after a vibrant and vivid discussion stage, 110 papers were accepted by the committee, representing an acceptance rate of just over 30%.

We would like to thank all the speakers and authors for their effort in preparing a contribution for this leading international conference. Moreover, we are very grateful to all those who devoted their time to the evaluation of the papers, especially the reviewers and the members of the program committee. It is also a great honor to continue with the publication of these proceedings in the prestigious FAIA series from IOS Press.

October 2023

Antonio J. Tallón-Ballesteros[1]
Raquel Beltrán-Barba[2]
[1] *Department of Electronics, Computer Systems and Automation Engineering, University of Huelva, Huelva city, Spain*
[2] *Department of Integrated Sciences, University of Huelva, Huelva city, Spain*

This page intentionally left blank

About the Conference

Organized by Chongqing University of Posts and Telecommunications, the 9th International Conference on Fuzzy Systems and Data Mining (FSDM 2023) was held both onsite in Chongqing, China, and online via MS Teams, from 10–13 November 2023. With an emphasis on fuzzy theory, algorithms and systems, fuzzy application, data mining, and the interdisciplinary field of fuzzy logic and data mining, FSDM2023 also covered the topics from two special sessions on granular-ball computing and the application of generative AI, as well as machine learning and neural networks. The conference agenda consists of keynote speeches, invited speeches, oral presentations and poster presentations. Gathered at the FSDM 2023 conference were 6 remarkable keynote speakers: Prof. Witold Pedrycz from Canada, Prof. Yiyu Yao from Canada, Prof. Hamido Fujita from Japan, Prof. Alfredo Cuzzocrea from France and Italy, and Prof. Hongying Zhang and Prof. Dun Liu both from China.

Organizing Committee

Conference Chairs

Prof. Guoyin Wang, Vice-President, Chongqing University of Posts and Telecommunications, China,
Prof. Witold Pedrycz, University of Alberta, Canada.

Conference Vice-chairs

Prof. Deli Zhang, Vice-President, Changchun Normal University, China,
Prof. Vilem Novak, University of Ostrava, Institute for Research and Applications of Fuzzy Modeling, Ostrava, Czech Republic,
Prof. Mohammed Chadli, University of Paris-Saclay, IBISC Lab., France,
Prof. Jerry Chun-Wei Lin, Western Norway University of Applied Sciences, Bergen, Norway.

Conference Co-chairs

Prof. Jimin Yu, College of Science, Chongqing University of Posts and Telecommunications, China,
Prof. Wei Zhu, College of Science, Chongqing University of Posts and Telecommunications, China,
Prof. Barnabas Bede, Department of Mathematics, DigiPen Institute of Technology, USA,
Assoc. Prof. Dragan Pamucar, Faculty of Organizational Sciences, University of Belgrade, Belgrade, Serbia.

Program Chairs

Prof. Qinghua Zhang, Chongqing University of Posts and Telecommunications, China,
Prof. Zhong Qu, Chongqing University of Posts and Telecommunications, China,
Prof. Fuyuan Xiao, Chongqing University, China,
Prof. Zizhong Chen, University of California, USA.

Steering Committee

Prof. Xizhao Wang, Shenzhen University, China,
Prof. Zengtai Gong, Northwest Normal University, China,
Prof. Degang Chen, North China Electric Power University, China,
Prof. Yong Feng, Chongqing University, China,
Prof. Hao Ying, Wayne State University, Detroit, MI, USA.

Publication Chairs

Prof. Yabin Shao, Chongqing University of Posts and Telecommunications, China,
Prof. Yiming Tang, Hefei University of Technology (HFUT), China,
Dr. Wentao Li, Southwest University, China.

Local-Arrangement Chairs

Prof. Yabin Shao, Chongqing University of Posts and Telecommunications, China,
Prof. Fenglan Sun, Chongqing University of Posts and Telecommunications, China,
Dr. Leilei Tong, Chongqing University of Posts and Telecommunications, China,
Dr. Derong Xie, Chongqing University of Posts and Telecommunications, China.

Contents

This page intentionally left blank

Fuzzy Systems and Data Mining IX
A.J. Tallón-Ballesteros and R. Beltrán-Barba (Eds.)

doi:10.3233/FAIA231000

Advanced Machine Learning Structures over Big Data Repositories: Definitions, Models, Properties, Algorithms

Alfredo CUZZOCREA[a,b, 1]
[a] *Big Data Engineering and Analytics Laboratory* (*iDEA Lab*)*, University of Calabria, Rende, Italy*
[b] *Department of Computer Science, University of Paris City, Paris, France*

Abstract. *Big data repositories* contain great-value data from which actionable knowledge insights can be meaningfully derived in order to support a wide spectrum of modern applications, such as smart cities, social networks, *e*-science, bio-informatics, and so forth. *How to extract these interesting patterns from such large-scale repositories?* The latter is a fundamental research question that is still open. Inspired by the described research challenge, this paper explores the issue of supporting *advanced Machine Learning* (*ML*) *structures over big data repositories*, whose final goal is realizing meaningful knowledge discovery tasks. These "structures" are rather *programs* than *tasks* so that they incorporate ML procedures within high-level (program) controls whose main goal is that of magnifying the expressive power of the whole *big data analytics process* implemented as a collection of singleton *big data analytics tasks*. In turn, each task is implemented in term of a *proper* advanced ML structure. The paper provides introduction and motivations to the investigated problem, analysis of related work, and the proposal of a reference architecture supporting these innovative structures.

Keywords. Big data, Big data analytics, Machine learning over big data.

1. Introduction

Nowadays, *big data repositories* (e.g., [1-3]) contain data of *great value*. *How to extract these interesting patterns from such large-scale repositories?* The latter is a fundamental research question that is still open. Recent approaches that appeared in literature mostly follow the idea of applying classical *Data Mining* (DM) and *Machine Learning* (ML) algorithms to these repositories (e.g., [4-6]), by devising rather-innovative optimizations aimed at coupling with specific characteristics of big data, including *volume*, *velocity*, *variety* and *veracity* [7].

Indeed, even with the modern connexion with emerging paradigms like *Explainable Artificial Intelligence*, which well-couples with ML (e.g., [8]), one of the most relevant limitations of the popular DM and ML approach to *big data analytics* is still represented by the *accuracy* and the *expressive power* of the process itself. This just due to the intrinsic nature of big data repositories, which expose the typical *3V characteristics*.

[1] Corresponding Author, Alfredo CUZZOCREA. E-mail: alfredo.cuzzocrea@unical.it – This research has been made in the context of the Excellence Chair in Big Data Management and Analytics at University of Paris City, Paris, France

Despite the classical approach, thanks to the emerging of *Cloud and high-performance technologies*, nowadays a new paradigm is possible. This paradigm falls under the name of *advanced ML structures over big data repositories*, and its main goal is that of supporting meaningful knowledge discovery over big datasets. These "structures" are rather *programs* than *tasks* so that they incorporate ML procedures within high-level (program) controls whose main goal is that of magnifying the expressive power of the whole *big data analytics process* implemented as a collection of singleton *big data analytics tasks*. In turn, each task is implemented in term of a *proper* advanced ML structure.

While some approaches are starting to follow this novel direction (e.g., [9-13]), the main idea is completely innovative, and also it has direct connexion with the research area predicating to support big data analytics over *commodity hardware* (e.g., [14]). Basically, the advanced ML programs run on top of massive big data repositories to extract actionable knowledge from them, by also realizing *multiple-step iterations*. It should be noted that this model is completely alternative to the classical DM model where the main discovery procedure is *single-step*.

The proposed model also needs to address another relevant problem. Indeed, today's enterprise analytics workloads have became computationally-intensive, with also complex sharing among scientific applications and computing applications, which further makes worse the target scenario. As a consequence, the overall amount of data and processing accessed and processed during the execution of these workloads is prohibitive, and, as a consequence, *parallel executions* are necessary, in order to reduce the whole computational cost. Therefore, *higher-level data-center architectures* and scalable ML programs, with also *parallel cores*, are the most appropriate solution for the setting we are investigating.

The so-depicted scenario opens the door to a plethora of relevant research challenges. First, *granularity of the data processing flow*. When data are partitioned in *chunks* and parallel *pieces* of code are running, supported big data analytics can execute with a time granularity *much higher* than the time granularity of parallel cores. This temporal difference determines relevant practical drawbacks. Second, *failures*. Data/computational failures are always possible in such complex systems. Therefore, *preventing failure events* in big data systems is a very annoying problem to deal with. Third, *openness and standardization*. Big data systems for supporting ML structures are powerful systems. As a consequence, they are usually organized in *sub-systems*. When sub-systems are advocated, then *hardware and software heterogeneities* arise, and the openness and standardization of models, data, systems and tools become a first-class requirement to deal with.

Starting from these considerations, this paper provides introduction and motivations to the investigated problem, analysis of related work, and the proposal of a reference architecture supporting these innovative ML structures over big data. The goal of this paper is to unveil new research opportunities and disruptive technologies in the field, thus opening the door to new milestones to be achieved by the research community.

The remainder of this paper is organized as follows. In Section 2, we provide an overview of research proposals that are relevant to our work. Section 3 focuses the attention on the specific ML algorithms that can be embedded in the target structures. In Section 4, we report a reference architecture for supporting advanced ML structures over big data repositories. Finally, Section 5 contains conclusions and future work.

2. Related Work

In this Section, we provide an overview of research proposals that are related to our work. As we will pinpoint throughout the Section, many proposals deal with framework-oriented aspects of the investigated research area.

In [9], authors present a distributed deep learning framework for *Apache Spark* called *BigDL*. This framework is used by various users to create deep learning applications on *large-scale* data platforms. One of its distinctive features is the ability to process production data as part of an *end-to-end* data analysis flow for deployment and management on an Apache Hadoop/Spark cluster. Furthermore, *BigDL* performs distributed parallel training on data directly over Spark functional computing model, using *copy-on-write* and *coarse-grained* operations.

Authors in [10] tackle the problem of ML applied to big data. The execution of ML algorithms on a vast amount of data involves managing a very high number of parameters. Furthermore, the context requires that ML applications run on distributed cluster systems with a number of machines ranging from tens to thousands. One of the goals is to make such systems efficient by providing support for convergence and scalability. They answer the following questions: (*i*) how an ML program is distributed on a cluster; (*ii*) how communication between machines in the field of ML is managed; (*iii*) how communication is carried out; (*iv*) what should be communicated between the machines. Authors make use of these principles to design and develop *high-performance* distributed ML software.

Today, the generation and collection of data become an activity that involves every aspect of our lives. The use of modern technologies allows for the processing, analysis and understanding of this data. *Cloud computing* is a solution to support the storage and processing of big data and to provide analysis applications that, by utilizing mining structures, offer a fundamental service for data scientists. Based on these considerations, in [11] authors analyze and classify the state of the art of big data analysis frameworks, which are currently primarily available on the cloud and provide various insights into the latest ongoing developments.

In [12], authors examine the latest advancements in optimization under uncertainty from a modern *data-driven* perspective. They also scrutinize the primary research challenges and research opportunities of data-driven optimization, which combines *ML* and *mathematical programming* for *decision-making* under uncertainty. An overview of classical mathematical programming techniques for handling uncertainty is presented initially. Subsequently, they investigate and categorize relevant publications on distributionally-robust data-driven optimization, data-driven *constraint-based* programming, data-driven robust optimization and *scenario-based* data-driven optimization. Finally, by leveraging the potential of deep learning techniques, they present perspectives on data-driven multistage optimization with online learning through a *learning-optimization* approach.

Computing and storing *n-order matrix* in the *Support Vector Machine* (SVM) algorithm, in the case of a large amount of data, may cause issues of slowdown or even memory depletion. In [13], authors argue that using the *Big Data Computing Platform Spark* can address these problems, but not those related to multiclassification. Therefore, authors construct a series of classifiers by combining the Spark framework of the big data programming model and the classification characteristics of SVM to create a parallel *one-to-many* SVM optimization algorithm based on large datasets. The behavior of this framework is superior to the one-to-many SVM in a *single-machine* environment.

3. Advanced Machine Learning Structures over Big Data Repositories: Definitions and Examples

In this Section, we provide an in-depth exploration of *advanced ML techniques and algorithms* applied to the analysis of complex, multidimensional datasets stored within big data repositories. It aims at elucidating these sophisticated techniques by offering clear definitions and demonstrating their practical usage, benefits, and limitations within this investigated context.

Advanced ML structures over big data repositories refer to the application of sophisticated ML algorithms over multidimensional big data in order to extract useful knowledge and valuable insights. Indeed, these advanced structures are playing a pivotal role in harnessing the potential of massive data repositories, they are being applied across various tasks ranging from *image recognition* and *recommendation systems* to *anomaly detection*, *risk assessment*, and *predictive analytics*.

Nevertheless, before applying these algorithms, the ML structure defines the domain on which the ML models are built. Particularly, by specifying (*i*) the data source view, which defines the subset of data that will be used for training and testing; (*ii*) the number and type of columns, which describe the data contained by the data source; (*iii*) partitioning the data into training and testing sets, which allow to specify that a certain percentage of data is held out for testing and the rest is used for training. This particularity admits that it is no longer necessary to separate the raw data in advance. In addition, after defining the domain, the next step consists of choosing the right ML algorithms and training the corresponding model over the training set, as well as evaluating its performance on the testing set.

As an important advanced ML structure that can be used in this context, *Neural Networks* (NN), which are inspired by the structure and functioning of biological neural networks. They are capable of automatically extracting relevant features from data and modeling complex, non-linear relationships, making them particularly well-suited for complex problems. Additionally, neural networks are versatile and can be used for various tasks; as a consequence, they play a significant role in the analysis of multidimensional big data repositories by offering several advantages, such as:

- *Complex Data Structures*: big data repositories often contain diverse and complex data types, such as images, text, and time-series data. Neural networks can process and analyze such data, making them a versatile choice for various data types;
- *Features Extraction:* they can automatically extract relevant features from vast datasets, reducing the need for manual feature engineering. This is especially beneficial when dealing with unstructured or semi-structured data;
- *Pattern Recognition*: they are suitable for recognizing intricate patterns within large datasets. This ability is particularly valuable in big data analytics, where traditional statistical methods may struggle to uncover hidden insights;
- *Predictive Modeling*: neural networks excel at predictive modeling. They can make accurate predictions and classifications, which is crucial in tasks like demand forecasting, fraud detection, and recommendation systems within large datasets;
- *Anomaly Detection*: neural networks can help to identify anomalies or outliers in large datasets, which is essential for various tasks (e.g., fraud detection, network security, quality control, etc.);

- *Real-time Processing*: in some applications, such as real-time monitoring or instant decision-making, neural networks can process data quickly and efficiently. This is crucial when dealing with data streams generated in real-time.

Despite these advantages, neural networks still have some challenges when coupled with big data repositories, such as *computational complexity*, as they can be computationally expensive to be trained especially over very large datasets. As a solution to address these drawbacks, *TensorFlow* has gained a significant focus from researchers in the active literature due to the fact that it supports both large-scale training and inference. *TensorFlow* efficiently uses hundreds of powerful (*GPU-enabled*) servers for fast training and runs models for inference on various platforms, ranging from large distributed clusters, down to running locally on mobile devices [15].

Furthermore, *Logistic Regression* is another popular ML algorithm that can be employed in this situation. It represents a statistical model and a fundamental algorithm in ML used for binary classification tasks. Unlike linear regression, which predicts continuous values, logistic regression predicts the probability of an input belonging to a specific class. Logistic regression is particularly suitable for big data repositories because it can handle large amounts of data and complex relationships between variables. It is also relatively efficient to train and evaluate models on big multidimensional data. Logistic regression is utilized in several applications within the context of multidimensional big data (e.g., risk assessment, marketing, medical diagnosis, and so forth).

Moreover, the usage of logistic regression over big data repositories can lead to various benefits, like (*i*) *scalability and efficiency* for their ability to effectively and efficiently handle very large and complicated datasets; (*ii*) *interpretability*, logistic regression models are relatively easy to interpret and understand. However, although these benefits, there are still several challenges and issues, such as:

- *Features Extraction*: it is important to carefully select and engineer the features that are used to train a logistic regression model. This can be a challenging task, especially when dealing with big multidimensional data;
- *Hyperparameters Tuning:* these models have several hyperparameters that can be tuned to improve their performance. This can be a time-consuming and computationally expensive process;
- *Overfitting*: logistic regression models can overfit the training data, which means that they may not perform well on new data. It is important to use cross-validation and other techniques to avoid this issue.

However, logistic regression is a powerful and simple yet effective algorithm for extracting insights from multidimensional big data repositories and can be used to solve a wide range of problems within this context.

In summary, one significant novelty of this approach consists of coupling *advanced ML structures with multidimensional modeling*, which falls under the recent innovation of *multidimensional big data analytics proposals* (e.g., [16]). This novel idea predicates the marriage between expressive multidimensional models (e.g., [17,18]) and powerful ML algorithms, with the final goal of enhancing the expressive power and accuracy of the whole knowledge discovery process over very-large big data repositories.

As it can be noticed by the contributions of this Section, decades of ML research represent the natural humus for the novel research area we investigate in this paper.

4. A Reference Architecture for Supporting Machine Learning Structures over Big Data Repositories: Anatomy and Main Functionalities

In this Section we introduce the reference architecture for supporting ML structures over big data repositories, where we provide an overview of how ML structures and models can be employed on top of traditional big data processes and big data analytics task in order to extract knowledge from different types of huge and heterogeneous data repositories. The use, management, and combination of such type of structures allows for providing analytical insights and better understanding of these large amounts of data, and, therefore, improve the decision-making process. Figure 1 depicts in detail our proposed architecture.

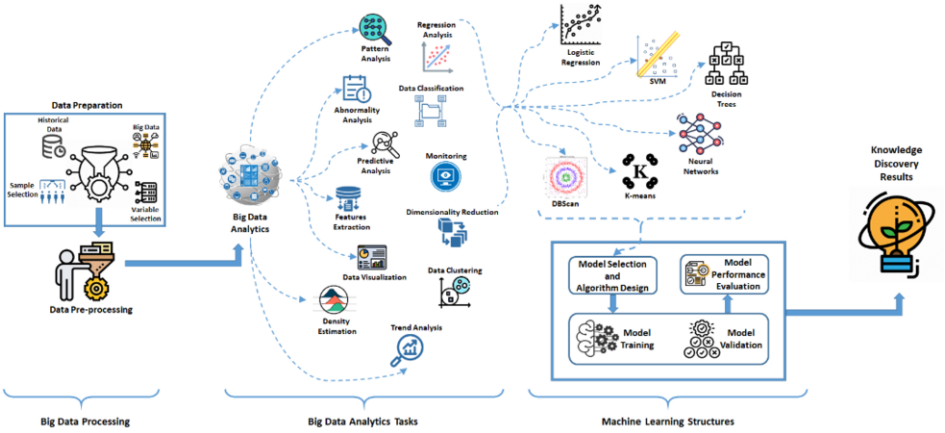

Figure 1. Reference Architecture for Supporting ML Structures over Big Data Repositories.

As shown in Figure 1, our proposed architecture encompasses several functional components that work collaboratively to enable advanced ML structures over big data repositories, which we describe as follows:

- *Big Data Processing Layer*: it is the first phase of the entire process of big data analytics over big data repositories using ML structures, and it is based on two main steps (i.e. *Data Preparation* and *Data Pre-Processing*) where:
    1. The first stage of developing a ML model is data preparation, which selects the best data samples for modeling after obtaining an overview of the data. The main tasks of this step aim to: (*i*) extract the dataset from historical databases and other big data sources, analyze its structure, and select relevant data; (*ii*) guarantee information extraction efficiency and analyze data natures or characteristics, such as non-*Gaussianity*, linear/nonlinear relationships among various attributes, time-series correlations, etc.; (*iii*) select samples and attributes [19]. It is dependent upon the type of model we wish to create and its main task.
    2. Following that, data pre-processing must be done to improve data quality, and some appropriate data transformations may be required to increase efficiency in data modeling. This includes: (*i*) carefully

checking the data and eliminating inconsistencies; (*ii*) removing outliers and gross errors from the modeling dataset, as they will otherwise significantly deteriorate the performance of the ML model [20]; and (*iii*) there may be some missing data in the prepared dataset, this must be addressed by missing value estimation, *Bayesian inference*, etc. [21,22]. Since various models or learning tasks may have requirements on different scales for distinct data properties, data preparation needs to be carefully considered. Various techniques for data transformation and scaling can improve the performance of the data model in this scenario.

- *Big Data Analytics Layer*: in this phase, several big data analytical tasks are carried out such as data clustering, dimensionality reduction, data visualization, trend analysis, monitoring and fault diagnosis, fault classification, prediction, and so on. Some of these examples are described as follows:

    1. Appropriate statistics can be created for online monitoring of various circumstances in order to monitor and diagnose faults. For instance, multivariate statistical monitoring techniques are typically used to create monitoring statistics. It is possible to distinguish between good and poor situations by setting control limits for these statistics. A fault warning indicating abnormal activity is triggered if the statistics values surpass the applicable control limits. Various techniques for fault diagnosis can be used to identify the fault's main causes and produce assessment reports, which will allow for later optimizations or enhancements. Problems with data and fault categorization might arise from a variety of anomalous occurrences or faults that happen but cannot be diagnosed [23]. ML offered several helpful techniques for fault classification modeling which are described in Section 3.
    2. Clustering analysis may be performed in both offline and online phases to investigate data patterns in a dataset (e.g., how many clusters exist within the entire dataset). Several clusters can be identified during the offline phase. Depending on what particular big data analytics can be performed for each cluster, the results of clustering can be used to analyze the pattern or mode of the dataset. As a result, several improvements or decisions can be made. Patterns in new data samples may be found and identified in the online stage. As a result, the corresponding data model may be used to extract information and analyze new data, significantly increasing the effectiveness of online data analytics.
    3. Due to big data characteristics and its highly dimensionality, and as data attributes have a significant correlation with one another, which makes data visualization difficult, carrying out analytics from the original multidimensional data is challenging. For handling such massive volumes of data in an efficient manner, dimensionality reduction is therefore required. By doing so, the computing complexity of the subsequent data analytics methods is reduced and important information may be extracted.
    4. Prediction of key performance indicators, is essential since, unlike normal attributes, it is exceedingly difficult to measure in real-time

online, which cause major delays. Nonetheless, these critical performance metrics may be estimated online through the use of predictive modeling approaches. Predictive data models may be developed and used for online prediction of new data samples, yielding real-time predictions, by identifying the regression correlations between the regular data attributes and those key performance indicators. These regression-based predictive big data analytics models may be used in a variety of scenarios, including estimating quality, energy consumption, assessing environmental performance, calculating economic performance, and more.

- *Machine Learning Structures Layer*: in this layer, ML models are selected trained validated and tested to be used in different analytical tasks using different ML algorithms (e.g., neural networks, logistic regression, etc.), which are described in Section 3.

    1. When the training dataset is ready, we choose a suitable ML algorithm to build the data model. It is possible to evaluate the complexity of the data model by conducting in-depth analysis of the data characteristics [19]; for instance, what sort of ML model ought to be used for the training dataset? to what extent should the data information be described by the model structure in terms of complexity? is a single model structure adequate on its own? or it requires a multiple model structure? and so forth. In regression-based modeling, (*i*) a non-linear learning algorithm, such as a neural network or support vector machine model, is needed for strong non-linear correlations; (*ii*) for linear attribute relationships, a multivariate linear regression learning method can be selected; (*iii*) a multiple regression model structure must be used if numerous conditions have been found in the training dataset. Since there isn't a single, effective technique for selecting models, the ML community offers a number of helpful guidelines or criteria, such the *Akaike Information Criterion*, *Bayesian Information Criterion*, *Hannan-Quinn Criterion*, etc. [19,24].
    2. Using a ML algorithm on the training dataset, model parameters can be determined once the model structure has been selected. The model performance must be evaluated using a variety of techniques, including cross-validation, parameter sensitivity analysis, model stability analysis, and robust analysis, before it is put to use online [19]. An additional separate testing or validation dataset is needed to verify the model and its performance evaluation. On the other hand, there are situations in which we might not be able to gather enough information for independent model validation and performance evaluation. The *Bayesian learning* algorithms and other re-sampling techniques like bagging and boosting can be applied in this situation.

As it can be noticed by the contributions of this Section, just like our ML structures realize multiple-step programs rather than single-step procedures (see Section 1), with a similar analogy, our reference architecture moves the vision towards a *system-oriented point-of-view* rather than a *framework-oriented point-of-view*. Overall, the latter should be intended as a relevant innovation in big data systems research.

5. Conclusions and Future Work

This paper has provided introduction and motivations to the issue of supporting advanced ML structures over big data repositories, whose final goal is realizing meaningful knowledge discovery tasks. The paper has contributed with analysis of related work, and the proposal of a reference architecture supporting these innovative ML structures over big data. The final goal of this paper was to unveil new research opportunities and disruptive technologies in the field, thus opening the door to new milestones to be achieved by the research community.

Future work in the area focuses the attention on dealing with innovative challenges of the proposed framework, namely: (*i*) *performance* (e.g., [25,26]); *explainability* (e.g., [27,28]); (*iii*) *privacy* (e.g., [29,30]).

References

[1] Kang YS, Park IH, Rhee J, Lee YH. MongoDB-based repository design for IoT-generated RFID/sensor big data. *IEEE Sensors Journal, 16(2)*. 2015; p.p. 485–497.
[2] Bellatreche L, Ordonez C, Méry D, Golfarelli M. The central role of data repositories and data models in Data Science and Advanced Analytics. *Future Generation Computer Systems, 129*. 2022; p.p. 13–17.
[3] Ohno-Machado L, Sansone SA, Alter G, Fore I, Grethe J, Xu H, et al. Finding useful data across multiple biomedical data repositories using DataMed. *Nature Genetics, 49(6)*. 2017; p.p. 816–819.
[4] Cuzzocrea A. Analytics over big data: Exploring the convergence of datawarehousing, OLAP and data-intensive cloud infrastructures. In: *IEEE 37th Annual Computer Software and Applications Conference*. 2013: p.p. 481–483.
[5] Zhou L, Pan S, Wang J, Vasilakos AV. Machine learning on big data: Opportunities and challenges. *Neurocomputing, 237*. 2017; p.p. 350–361.
[6] Al-Jarrah OY, Yoo PD, Muhaidat S, Karagiannidis GK, Taha K. Efficient machine learning for big data: A review. *Big Data Research, 2(3)*. 2015; p.p. 87–93.
[7] Laney D. 3D data management: Controlling data volume, velocity and variety. META group research note, 6(70). 2001.
[8] Emmert-Streib F, Yli-Harja O, Dehmer M. Explainable artificial intelligence and machine learning: A reality rooted perspective. *Wiley Interdisciplinary Reviews: Data Mining and Knowledge Discovery, 10(6)*. 2020; art. e1368.
[9] Dai JJ, Wang Y, Qiu X, Ding D, Zhang Y, Wang Y, Jia X, Zhang CL, Wan Y, Li Z, Wang J, Huang S, Wu Z, Wang Y, Yang Y, She B, Shi D, Lu Q, Huang K, Song G. BigDL: A Distributed Deep Learning Framework for Big Data. In: *Proceedings of the ACM Symposium on Cloud Computing*. 2019; p.p. 50–60.
[10] Xing EP, Ho Q, Xie P, Wei D. Strategies and Principles of Distributed Machine Learning on Big Data. *Engineering, Vol. 2, No. 2*. 2016; p.p. 179–195.
[11] Elshawi R, Sakr S, Talia D, Trunfio P. Big Data Systems Meet Machine Learning Challenges: Towards Big Data Science as a Service. *Big Data Research, Vol. 14*. 2018; p.p.1–11.
[12] Ning C, You F. Optimization Under Uncertainty in the Era of Big Data and Deep Learning: When Machine Learning Meets Mathematical Programming. *Computers & Chemical Engineering, Vol. 125*. 2019; p.p. 434–448.
[13] Gong Y, Jia L. Research on SVM Environment Performance of Parallel Computing Based on Large Data Set of Machine Learning. *The Journal of Supercomputing, Vol. 75, No. 9*. 2019; p.p. 5966–5983.
[14] Liu S, Mocanu DC, Matavalam ARR, Pei Y, Pechenizkiy M. Sparse evolutionary deep learning with over one million artificial neurons on commodity hardware. *Neural Computing and Applications, 33*. 2021; p.p. 2589–2604.
[15] Abadi M, Barham P, Chen J, Chen Z, Davis A, Dean J, Devin M, Ghemawat S, Irving G, Isard M, Kudlur M, Levenberg J, Monga R, Moore S, Murray DG, Steiner B, Tucker PA, Vasudevan V, Warden P, Wicke M, Yu Y, Zheng X. TensorFlow: A System for Large-Scale Machine Learning. In: *12th USENIX Symposium on Operating Systems Design and Implementation*. 2016. p.p. 265–283.
[16] Cuzzocrea A. Multidimensional Big Data Analytics over Big Web Knowledge Bases: Models, Issues, Research Trends, and a Reference Architecture. In: *8th IEEE International Conference on Multimedia Big Data*. 2022; p.p. 1–6.

[17] Cuzzocrea A. Providing probabilistically-bounded approximate answers to non-holistic aggregate range queries in OLAP. In: *8th ACM International Workshop on Data Warehousing and OLAP*. 2005; p.p. 97–106.
[18] Cuzzocrea A. Retrieving accurate estimates to OLAP queries over uncertain and imprecise multidimensional data streams. In: *23rd International Conference on Scientific and Statistical Database Management*. 2011; p.p. 575–576.
[19] Bishop CM. *Pattern Recognition and Machine Learning*. New York, NY, USA: Springer-Verlag, 2006.
[20] Liu H, Shah S, Jiang W. On-line outlier detection and data cleaning. *Computers & Chemical Engineering, Vol. 28, No. 9*. 2004; p.p. 1635–1647.
[21] Imtiaz SA, Shah SL. Treatment of missing values in process data analysis. *Canadian Journal of Chemical Engineering, Vol. 85, No. 5*. 2008; p.p. 838–858.
[22] Nelson PRC, Taylor PA, MacGregor JF. Missing data methods in PCA and PLS: Score calculations with incomplete observations. *Chemometrics and Intelligent Laboratory Systems, Vol. 35, No. 1*. 1996; p.p. 45–65.
[23] Kassidas A, Taylor PA, MacGregor JF. Off-line diagnosis of deterministic faults in continuous dynamic multivariable processes using speech recognition methods. *Journal of Process Control, Vol. 8*. 1998, p.p. 381–393.
[24] Mitchell T. *Machine Learning*. New York, NY, USA: McGraw-Hill, 1997.
[25] Yu B, Cuzzocrea A, Jeong D, Maydebura S. On managing very large sensor-network data using bigtable. In: *12th IEEE/ACM International Symposium on Cluster, Cloud and Grid Computing*. 2012; p.p. 918–922.
[26] L'heureux A, Grolinger K, Elyamany HF, Capretz MA. Machine learning with big data: Challenges and approaches. *IEEE Access, 5*. 2017; p.p. 7776–7797.
[27] Belle V, Papantonis I. Principles and practice of explainable machine learning. *Frontiers in Big Data, 39*. 2021; DOI: https://doi.org/10.3389/fdata.2021.688969
[28] Blanco-Justicia A, Domingo-Ferrer J. Machine learning explainability through comprehensible decision trees. 2019; In: *Machine Learning and Knowledge Extraction: Third IFIP TC 5, TC 12, WG 8.4, WG 8.9, WG 12.9 International Cross-Domain Conference*. 2019; p.p. 15–26.
[29] Cuzzocrea A, Saccà D. Balancing accuracy and privacy of OLAP aggregations on data cubes. In: *13th ACM international workshop on Data warehousing and OLAP*. 2010; p.p. 93–98.
[30] Xu K, Yue H, Guo L, Guo Y, Fang Y. Privacy-preserving machine learning algorithms for big data systems. In: *IEEE 35th International Conference on Distributed Computing Systems*. 2015; p.p. 318–327.

Fuzzy Systems and Data Mining IX
A.J. Tallón-Ballesteros and R. Beltrán-Barba (Eds.)

doi:10.3233/FAIA231001

Eye Tracking Data Mining Based on Fuzzy Sets of Fixations

Konstantin RYABININ [a,b,1], Elena EROFEEVA [a,b], and Kira GUSEVA [b]
[a] *Saint Petersburg State University, Saint Petersburg, Russia*
[b] *Perm State University, Perm, Russia*

Abstract. This paper is devoted to the novel method of automated detection of common eye gaze movement patterns by mining the data recorded in eye-tracking-based experiments. For this, a model of aggregated scanpath is proposed that represents a fuzzy set of all possible eye gaze trajectories found in the experimental data. In contrast to the traditional methods of aggregation, no averaging is used to avoid information loss. Instead, the belonging function determines the probability of each particular trajectory. The constructed fuzzy scanpath is then filtered and automatically analyzed by applying methods of network science. For this, the fixations (eye gaze stops) are represented as network nodes and saccades (eye gaze jumps) are mapped to network links. For the network composed, modularity is calculated utilizing the Louvain method of community detection. In the case of eye gaze data, modularity represents saccadic cycles, which can be mapped to the cycles of cognitive processing. Thereby, the common perception structure is retrieved. To support all the analysis steps, we proposed corresponding scalable visualization tools based on our visual analytics platform SciVi. We demonstrate the viability of our approach by analyzing the data obtained from the real-world eye-tracking-based experiment from the Digital Humanities application domain. Preliminary experiment results are discussed along with the efficacy of the proposed methods.

Keywords. Eye Tracking, Aggregated Scanpath, Fuzzy Set, Modularity, Saccadic Cycles, Gaze Movement Patterns, Visual Analytics

1. Introduction

Eye tracking research methodology is widely used to discover information perception peculiarities. It is based on analyzing the eye movement trajectories (also known as scanpaths), which decompose into so-called fixations (moments when the eye gaze is focused on a distinct point) and saccades (rapid jumps of eye gaze between fixations). After more than 100 years long evolution of eye tracking theories, algorithms, software, and hardware, this methodology has grown solid and mature [1]. Nevertheless, when it comes to practical experiments with large numbers of participants, challenges still arise on how to efficiently handle the collected eye tracks, quickly check the hypotheses, and obtain meaningful results [2,3,4].

[1]Corresponding Author: Konstantin Ryabinin, St Petersburg University, 7-9 Universitetskaya Embankment, 199034 St Petersburg, Russia; E-mail: kostya.ryabinin@gmail.com.

Eye tracking data can be classified as Big Data due to their large volume, high sampling velocity, and structural variety [4], which in turn require appropriate data mining tools and machine learning-based methods for efficient and meaningful analysis [5,6]. Traditionally, eye tracks are being analyzed using mathematical statistics [1,2] but recently, the exploratory approach based on visual analytics tends to be an important accompaniment for eye tracking research [7,2,3]. Statistical and exploratory approaches promise a synergy that can increase the value of eye tracking research methodology for various scientific fields, including cognitive science, psychology, medicine, Digital Humanities, etc.

In the present work, we contribute to the development of this synergy by proposing a novel visual data mining approach to analyze the eye tracks leveraged by fuzzy sets of the fixations and modularity of the saccades graph. Thereby we address the challenges of automatic detection of eye movement patterns, scalability of visual analytics tools to a high number of experiment participants (so-called informants), and interactivity of eye tracks spatiotemporal visualizations. These challenges are indicated as belonging to the major ones of state-of-the-art eye tracking research methodology [2]. We implemented the proposed approach within our visual analytics platform SciVi (`https://scivi.tools/`) [8] and tested it in practical use cases within a remit of a research project devoted to studying the peculiarities of multimodal information perception in a virtual reality (VR) environment [9].

The following key contributions of this work can be highlighted:

1. Novel model of an aggregated scanpath of multiple informants based on fuzzy sets of fixations (so-called "fuzzy scanpath").
2. Novel data mining algorithm for revealing the common perception structure of a visual stimulus based on saccades graph modularity within the fuzzy scanpath.
3. Novel interactive visualization tools to display fuzzy scanpath and corresponding graph of saccades.

2. Related Work

Eye tracking data obtained from real-world studies have large volumes and complex structures, which characterize them as Big Data [4]. Thereby, data mining and visual analytics methods are required to efficiently handle them. For example, R. Nava-Martnez et al. successfully utilized Weka, a well-known powerful data mining software, for eye tracking data analysis [5]. The research group that includes M. Burch, T. Blascheck, et al. did a lot of work in applying visual analytics methodology for eye tracking studies starting with a concept published in 2012 [10] and still continuing in 2022 when they presented a very function-rich toolset for the linked and coordinated visual analysis of eye movement data [3]. During their work, this research group also proposed using sequence rule mining and corresponding visual analysis model to detect scanpath patterns [6] and published a very comprehensive survey on visualization of eye tracking data [2]. In this survey, they indicated major challenges of eye tracking as viewed by eye tracking experts. Among other issues, the following are indicated, which are addressed in the present work:

1. "Approaches for automatically detecting patterns are needed".

2. "Visualizations should scale for a high number of participants".
3. "More visualization techniques for eye tracking data are necessary, for example, interactive visualizations or spatiotemporal visualizations".
4. "A way to aggregate and analyze scan paths over a large sample" of informants is required.

Although data mining tasks can often be efficiently tackled by fuzzy systems, the corresponding approaches are underrepresented in eye tracking studies. Only a few authors propose using fuzzy set theory in eye tracking research. For example, D. Zhu et al. propose using fuzzy signatures to detect different eye gaze patterns [11]. T. Opach et al. indicate a possibility to use fuzzy sets for representing areas of interest within the visual stimuli and thereby leveling out the gaze measurement uncertainty [12]. R. A. Naqvi et al. propose a fuzzy system-based approach for improving the eye tracker precision in gaze-based human-computer interaction tasks [13]. In the present work, we apply fuzzy set theory to the scanpath aggregation tasks.

Aggregated scanpaths are traditionally composed as classical sets based on spatial characteristics of fixations and saccades. For example, J. H. Goldberg et al. utilize the so-called "dotplot" method to find sequential matches of scanpaths [14]. V. Peysakhovich et al. propose bundling the saccades and fixations based on geometrical features "to reduce visual clutter" by scanpath rendering "and provide a mathematical base for scanpath comparison" [15]. To the best of our knowledge, no published works address the usage of fuzzy sets for scanpath aggregation.

One of the possible ways to automatically detect eye gaze patterns is fixations and saccades clustering. A. Belardinelli et al. propose a comprehensive mathematical model to estimate fixations neighborhood based on spatiotemporal characteristics and visual saliency of the stimulus in fixations' points [16]. Based on this neighborhood, so-called "saccadic cycles" are retrieved, which represent the cycles of cognitive processing. This method requires no apriori information about the areas of interest (AOIs), which is an advantage in the case of collecting gaze data in natural environments. But this method works on the individual scanpaths of informants, without aggregation. So, for the experiments with predefined semantic AOIs and a large sample of informants, other techniques should be adopted.

Another promising direction of eye gaze patterns detection is "applying network science to eye-movement data" [17]. M. Zhu et al. proposed calculating different network metrics (density, centrality, and clustering measures) for the graph of saccades [18]. Later, this approach was further elaborated by X. Ma et al. [17]. In our work, we take the next step in this direction proposing the approach to retrieving saccadic cycles based on saccades graph modularity calculated for the aggregated scanpath of multiple informants.

There are a lot of community-driven software products designed for eye tracking data analysis (including detection of fixations and saccades, calculating statistical metrics of eye gaze tracks, measuring eye pupil diameter, etc.) [19,20], as well as different tools which help in preprocessing the eye tracking data (for example, an open-source tool for determining the dynamic AOIs created by L. Bonikowski et al. [21]). The novel fuzzy set-based model of representing aggregated scanpaths and the corresponding novel data mining algorithm for revealing common perception patterns proposed in the current paper can be integrated into these software tools in the future. But recently we implemented them within our own software platform SciVi, which distinctive feature is easy extensibility and flexible high-level graphical user interface for declaring data mining

pipelines. The distinctiveness of this platform and its working principles are described in detail in [8].

3. Aggregated Scanpath Model Based on Fuzzy Sets

Traditionally, the eye tracking data aggregation challenge (see item (4) in the list of challenges mentioned in Section 2) is addressed by some kind of data merging, for example, by averaging [17] or intersecting [14] of scanpaths. However, in these cases, some information gets lost. To tackle this problem, we propose a fuzzy set-based model of an aggregated scanpath that bundles all the data sampled from the informants during the particular eye tracking experiment. For a sake of brevity, let us call it a "fuzzy scanpath".

Our implementation of fuzzy scanpath and explanation of the related math can be found in the SciVi platform repository: https://github.com/scivi-tools/scivi.web/tree/master/lib/eye/fuzzyScanpath.

Let $A = \{\alpha_j | j = \overline{1,m}\}$ be a set of m predefined AOIs in a visual stimulus. Let $S = \{\sigma_k | k = \overline{1,p}\}$ be a set of scanpaths recorded for p informants during the experiment. Let the scanpath be a set of fixations, each one belonging to a particular AOI: $\sigma_k = \{\varphi_l^{(k)} | l = \overline{1,r^{(k)}}\}, \forall \varphi_l^{(k)} : \exists j | \varphi_l^{(k)} \in \alpha_j$. Let $n = \max\{r^{(k)}\}$ be a maximal scanpath length in S. Then the fuzzy scanpath is defined as:

$$T = \bigcup_{i=1}^{n} \bigcup_{j=1}^{m} \left(\alpha_j, \omega_j^{(i)}\right), \tag{1}$$

where $\omega_j^{(i)}$ is a fuzzy set's belonging function representing the number of informants who have their i-th fixation in the j-th AOI:

$$\omega_j^{(i)} = \frac{\sum_{k=1}^{p} \begin{cases} 1, & \exists \varphi_i^{(k)} \vee \varphi_i^{(k)} \in \alpha_j \\ 0, & \text{otherwise} \end{cases}}{p}. \tag{2}$$

The fuzzy scanpath T is a sequence of fuzzy sets, which contains all possible eye gaze trajectories from the experimental raw data. The rationale behind the belonging function (2) is that it represents the "popularity" of each AOI in terms of informants' attention at each fixation. This, in turn, allows checking, which AOI attracts more attention at a given moment of time thereby estimating different variants of eye gaze trajectory and revealing the branches, which are more/less common for the informants' sample in question. Each informant has an equal contribution and no information gets lost.

We implemented the assembling of fuzzy scanpaths as a specific data mining step (so-called "operator") in the SciVi visual analytics platform [8]. This platform has a microservice architecture, so each operator is represented as an individual microservice and SciVi can be easily extended with the new data mining capabilities on demand. To compose a particular data mining pipeline, available operators are chained together using a special built-in high-level graphical programming language based on data flow

diagrams (DFDs). A screenshot of the eye gaze data mining algorithm used in this work is presented as a SciVi DFD in Fig. 1. A brief live demo of SciVi functioning is available at https://youtu.be/ItMFmdL1GHY.

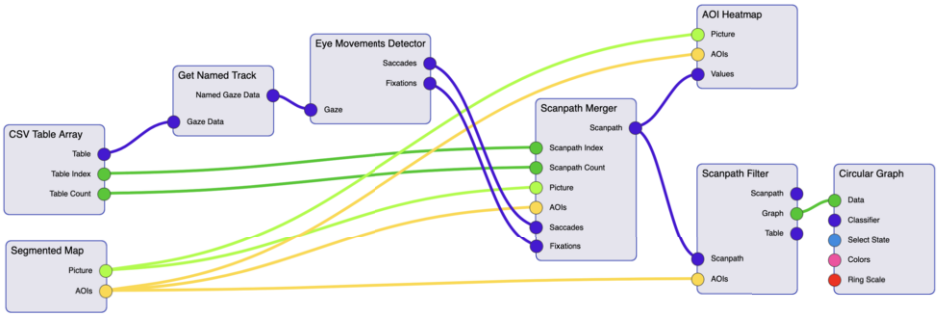

Figure 1. Eye tracking data mining algorithm programmed in SciVi as a data flow diagram.

The "CSV Table Array" operator loads the raw eye tracking data for all informants. These data get filtered by the "Get Named Track" operator to extract the entries belonging to a particular visual stimulus (there are multiple stimuli in our experiment, presented to informants one by one). The "Eye Movement Detector" operator detects saccades and fixations in the set of eye gaze location samples. For this, an algorithm suggested by J. Llanes-Jurado et al. is used [22]. The "Segmented Map" operator loads the descriptions of AOIs for the visual stimulus in question (the segmentation into AOIs is done in the Creative Maps Studio vector graphics editor as described in [9]). The "Scanpath Merger" operator assembles the fuzzy scanpath according to equations (1) and (2). The "AOI Heatmap" operator is used to visualize the fuzzy scanpath as an interactive heatmap. The visualization result is presented in Fig. 2.

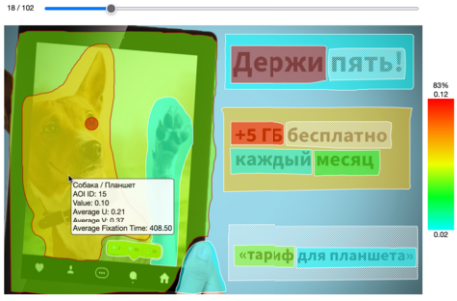

Figure 2. Fuzzy scanpath visualization as interactive heatmap in SciVi (interactive view available online https://scivi.tools/demo/fuzzyScanpath).

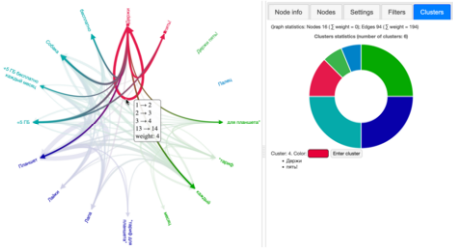

Figure 3. Saccades graph and its modularity visualization in SciVi (interactive view available online https://scivi.tools/demo/saccadicCycles).

The slider on the top allows choosing the fixation. The heatmap represents the values of $\omega_j^{(i)}$ for the chosen fixation. The percentage on top of the color scale represents the ratio of informants who have the chosen fixation. Mouse hover triggers the tooltip with context information about AOIs: name and identifier of AOI, value of $\omega_j^{(i)}$ for this AOI, average fixation time, and average fixation coordinates (called U and V, as they are

normalized in image space; at this point, the red circle is drawn for the hovered AOI; the radius of this circle is proportional to the average fixation time). This visualization helps the analyst to explore the fuzzy scanpath and discover its peculiarities.

4. Retrieval of Common Perception Structure

We propose using the fuzzy scanpath to automatically detect eye movement patterns addressing challenge (1) from the list of challenges mentioned in Section 2. We follow the assumption of A. Belardinelli et al. that "... saccades and fixations can be clustered, considering them related to a single cycle of cognitive processing" [16], combining this idea of clustering with the idea of M. Zhu et al. and X. Ma et al. on using a network representation of saccades and fixations [18,17]. Fixations and saccades are mapped to the network's nodes and links, respectively, and network science methods are applied to analyze this network. In particular, we propose retrieving the saccadic cycles (described by A. Belardinelli et al. [16]) by using the Louvain method for community detection [23]. This method calculates the graph modularity by finding so-called "cliques" – graph components of high connectivity. In the case of the saccades graph, modularity can be interpreted as the saccadic cycles. Since the saccades graph is built on top of the aggregated scanpath, the retrieved saccadic cycles reveal the common perception structure of the informants.

In the case of a large sample of informants, threshold filtering of the fuzzy scanpath is reasonable to extract the mainstream eye gaze trajectory. This can be done by rejecting all the outlier elements of T (see equation (1)), which do not meet the following condition for each i-th fixation:

$$\omega_j^{(i)} \geq \max\{\omega_j^{(i)}\} - \tau \vee \vartheta^{(i)} > \theta, j = \overline{1,m}, \tag{3}$$

$$\vartheta^{(i)} = \frac{\sum_{k=1}^{p} \begin{cases} 1, & \exists \varphi_i^{(k)} \\ 0, & \text{otherwise} \end{cases}}{p}, \tag{4}$$

where τ and θ are given threshold values, p is a number of informants, $\varphi_i^{(k)}$ is a fixation of k-th informant.

In the pipeline shown in Fig. 1, the "Scanpath Filter" operator performs this filtering. After that, the "Circular Graph" operator visualizes the saccades graph. This operator provides a rich toolset for comprehensive analytics of graphs, including the calculation of modularity based on the Louvain method [24]. The visualization result is shown in Fig. 3 (in this example, $\tau = 0.03$, $\theta = 0.33$, $p = 41$). The nodes of the graph represent fixations in the AOIs; the edges represent the bundled saccades. The edge thickness represents the number of saccades in a bundle. The saccadic cycles are color-coded and their size is reflected by a pie chart on the right. Mouse hover on the edge triggers a tooltip showing individual saccades in a bundle, ordered chronologically.

5. Discussion and Conclusion

We applied the proposed data mining algorithm to analyze the eye tracking data recorded in the following experiment (see the schema in Fig. 4). 14 visual stimuli were demonstrated to 41 informants (sample balanced by age and gender) in VR. The visual stimuli were the posters with an image and a short text (taken from the different commercial advertisements and normalized to look uniformly) [25]. 7 posters presented a story with a single interpretation and 7 had an ambiguous sense. Each "ambiguous" poster presents some idiomatic expression that is represented in a text and is supported by a picture, whereby its literal meaning is used in an advertising context. One of the "ambiguous" posters is shown in Fig. 2 overlaid with a gaze heatmap. In this poster, there is a slogan "High five!", followed by an explanation "+5 Gb free each month" and "tablet plan" (advertising a service of a mobile telecommunications provider). The picture shows a dog with a raised paw inside a tablet frame.

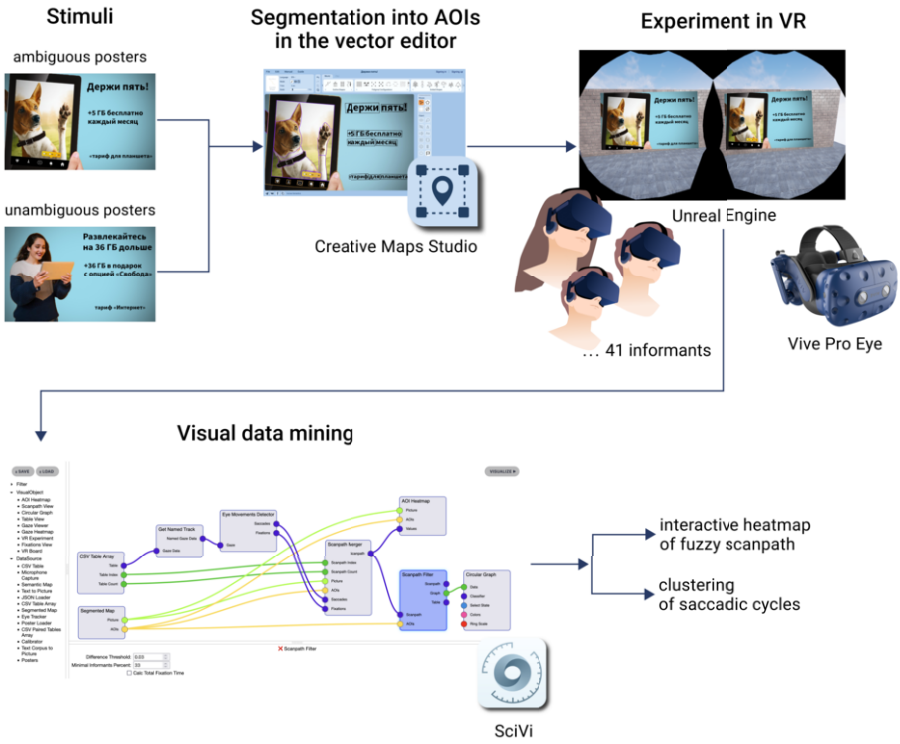

Figure 4. Schema of the experiment conducted.

The posters were shown one by one in a VR environment rendered by the Unreal Engine and demonstrated to the informants via the Vive Pro Eye VR station. The informants' eye gaze tracks were recorded by an embedded Tobii eye tracker. Each poster was manually segmented into AOIs in the Creative Maps Studio vector editor [9]. Then, the experimental data were analyzed in the SciVi platform using the data mining algorithm shown in Fig. 1. The average processing time of this data mining algorithm for the single

poster (41 eye gaze tracks; 42324 eye gaze samples in total) is 538 ms (on a MacBook Pro, 2.3 GHz 8-Core Intel Core i9 CPU, 16 Gb RAM), which is nearly a real-time speed in terms of fine-tuning the data mining parameters and checking hypotheses about the data.

The following preliminary results were obtained by exploratory and statistical analysis of the fuzzy scanpath constructed from the collected data (see Fig. 2 and Fig. 3 which represent the visualizations related to the analysis of fuzzy scanpath and saccadic cycles for the single poster). The gaze trajectory follows the general pattern: "the text viewed first, then the image". It seems, that informants are able to catch the ambiguity from the text by the first 3 fixations, and then start searching for the explanation of ambiguity in the image. While the reading time for "ambiguous" and "unambiguous" posters is approximately equal, image inspection time for "ambiguous" posters is significantly longer, including more saccadic cycles. As a result, the total dwell time for "ambiguous" posters is longer. Saccadic cycles reveal groups of AOIs. For "unambiguous" posters, these groups are rather morphological (text and image are separated into different groups), and for "ambiguous" posters, groups are semantical (text and image are mixed; semantically connected parts of text and image are grouped).

In the example of an "ambiguous" poster analysis shown in Fig. 3, the following saccadic cycles have been found through the graph modularity:

1. "tablet", "plan", "each", "month".
2. "tablet plan", tablet picture, dog's paw picture, picture with likes on a tablet.
3. "+5 Gb", "free", "+5 Gb free each month", dog picture.
4. "High", "five!".

These saccadic cycles (especially (2) and (3)) clearly show the process of comprehension whereby the informants reveal the story represented by a poster.

We can state that these preliminary results prove the viability and efficacy of the approach proposed.

The proposed fuzzy scanpath model, data mining algorithm built on top of that model, and corresponding visualization tools address altogether the 4 challenges mentioned in Section 2. The developed software solution allows for aggregating the scanpaths over the large sample of informants, automatic detection of their common eye gaze movement patterns, and provides scalable interactive spatiotemporal visualization via heatmaps and graphs. This software solution is open source and freely available on GitHub under GPL3 license: https://github.com/scivi-tools/scivi.web.

Acknowledgments

Supported by the research grant No. ID92566385 from Saint Petersburg State University.

References

[1] Holmqvist K, Andersson R. Eye-tracking: A Comprehensive Guide to Methods, Paradigms and Measures. Lund; 2017.

[2] Blascheck T, Kurzhals K, Raschke M, Burch M, Weiskopf D, Ertl T. Visualization of Eye Tracking Data: A Taxonomy and Survey. Computer Graphics Forum. 2017;36(8):260–284.

[3] Burch M, Wallner G, Fürst V, Lungu TC, Boelhouwers D, Rajasekaran D, et al. Linked and Coordinated Visual Analysis of Eye Movement Data. In: 2022 Symposium on Eye Tracking Research and Applications; 2022.
[4] Blascheck T, Burch M, Raschke M, Weiskopf D. Challenges and Perspectives in Big Eye-Movement Data Visual Analytics. In: 2015 Big Data Visual Analytics (BDVA); 2015. p. 1–8.
[5] Nava-Martnez R, Gmez-Velzquez FR, Mendizabal-Ruiz G, Gonzlez-Garrido AA, Vlez-Prez H, Vergara-Basulto I. Data Mining for the Analysis of Eye Tracking Records. In: 2018 15th International Conference on Electrical Engineering, Computing Science and Automatic Control (CCE); 2018. p. 1–6.
[6] Burch M. Mining and Visualizing Eye Movement Data. In: SIGGRAPH Asia 2017 Symposium on Visualization; 2017.
[7] Kurzhals K, Fisher B, Burch M, Weiskopf D. Eye Tracking Evaluation of Visual Analytics. Information Visualization. 2016;15(4):340–358.
[8] Ryabinin K, Chumakov R, Belousov K, Kolesnik M. Ontology-Driven Visual Analytics Platform for Semantic Data Mining and Fuzzy Classification. Frontiers in Artificial Intelligence and Applications. 2022;358:1–7.
[9] Ryabinin K, Belousov K, Chumakov R. Visual Analytics Tools for Polycode Stimuli Eye Gaze Tracking in Virtual Reality. In: Proceedings of the 31st International Conference on Computer Graphics and Vision (GraphiCon 2021); 2021. p. 211–222.
[10] Andrienko G, Andrienko N, Burch M, Weiskopf D. Visual Analytics Methodology for Eye Movement Studies. IEEE Transactions on Visualization and Computer Graphics. 2012;18(12):2889–2898.
[11] Zhu D, Mendis BSU, Gedeon T, Asthana A, Goecke R. A Hybrid Fuzzy Approach for Human Eye Gaze Pattern Recognition. In: Advances in Neuro-Information Processing; 2009. p. 655–662.
[12] Opach T, Nossum AS. Evaluating the Usability of Cartographic Animations with Eye-Movement Analysis. In: Proceedings of the 25th International Cartographic Conference; 2011.
[13] Naqvi RA, Arsalan M, Park KR. Fuzzy System-Based Target Selection for a NIR Camera-Based Gaze Tracker. Sensors. 2017;17(4).
[14] Goldberg JH, Helfman JI. Identifying Aggregate Scanning Strategies to Improve Usability Evaluations. Proceedings of the Human Factors and Ergonomics Society Annual Meeting. 2010;54(6):590–594.
[15] Peysakhovich V, Hurter C. Scanpath Visualization and Comparison Using Visual Aggregation Techniques; 2018.
[16] Belardinelli A, Pirri F, Carbone A. Gaze Motion Clustering in Scan-Path Estimation. Cognitive Processing. 2008;9:269–282.
[17] Ma X, Liu Y, Clariana R, Gu C, Li P. From Eye Movements to Scanpath Networks: A Method for Studying Individual Differences in Expository Text Reading. Behavior Research Methods. 2022.
[18] Zhu M, Feng G. An Exploratory Study Using Social Network Analysis to Model Eye Movements in Mathematics Problem Solving. In: Proceedings of the Fifth International Conference on Learning Analytics And Knowledge; 2015. p. 383–387.
[19] Farnsworth B. 10 Free Eye Tracking Software Programs [Pros and Cons]. iMotions; 2021. Available from: https://imotions.com/blog/free-eye-tracking-software/.
[20] Sharafi Z, Sharif B, Guhneuc YG, Begel A, Bednarik R, Crosby M. A Practical Guide on Conducting Eye Tracking Studies in Software Engineering; 2020.
[21] Bonikowski L, Gruszczyski D, Matulewski J. Open-Source Software for Determining the Dynamic Areas of Interest for Eye Tracking Data Analysis. Procedia Computer Science. 2021;192:2568–2575.
[22] Llanes-Jurado J, Marn-Morales J, Guixeres J, Alcaiz M. Development and Calibration of an Eye-Tracking Fixation Identification Algorithm for Immersive Virtual Reality. Sensors. 2020;20(17).
[23] Blondel VD, Guillaume JL, Lambiotte R, Lefebvre E. Fast Unfolding of Communities in Large Networks. Journal of Statistical Mechanics: Theory and Experiment. 2008;2008(10).
[24] Ryabinin K, Belousov K, Chuprina S. Novel Circular Graph Capabilities for Comprehensive Visual Analytics of Interconnected Data in Digital Humanities. Scientific Visualization. 2020;12(4):56–70.
[25] Konovalova A, Petrova T. Image and Text in Ambiguous Advertising Posters. In: Proceedings of Seventh International Congress on Information and Communication Technology; 2023. p. 109–119.

Fuzzy Systems and Data Mining IX
A.J. Tallón-Ballesteros and R. Beltrán-Barba (Eds.)

doi:10.3233/FAIA231002

Towards a Universal Understanding of Color Harmony: Fuzzy Approach

Pakizar SHAMOI [a,1], Muragul MURATBEKOVA [a], Assylzhan IZBASSAR [a], Atsushi INOUE [b] and Hiroharu KAWANAKA [c]

[a] *School of Information Technology and Engineering, Kazakh-British Technical University, Almaty, Kazakhstan*
[b] *Kyushu Institute of Technology, Kitakyushu, Japan*
[c] *Graduate School of Engineering, Mie University, Tsu, Japan*

Abstract. Harmony level prediction is receiving increasing attention nowadays. Color plays a crucial role in affecting human aesthetic responses. In this paper, we explore color harmony using a fuzzy-based color model and address the question of its universality. For our experiments, we utilize a dataset containing attractive images from five domains: fashion, art, nature, interior design, and brand logos. Using a fuzzy approach, we aim to identify harmony patterns and dominant color palettes within these images. It is well-suited for this task because it can handle the inherent subjectivity and contextual variability associated with aesthetics and color harmony evaluation. Our experimental results suggest that color harmony is largely universal. Additionally, our findings reveal that color harmony is not solely influenced by hue relationships on the color wheel but also by the saturation and intensity of colors. In palettes with high harmony levels, we observed a prevalent adherence to color wheel principles while maintaining moderate levels of saturation and intensity. These findings contribute to ongoing research on color harmony and its underlying principles, offering valuable insights for designers, artists, and researchers in the field of aesthetics.

Keywords. color harmony, image analysis, fuzzy sets, aesthetics, color wheel

1. Introduction

The human brain tends to seek a visually harmonious experience. With an increase of digital affective information, automatic prediction of image harmony value is receiving more attention [1], however, still, there is no well-constructed theory to use as a guidance for practical purposes [2], [3], [4]. One reason for this is that aesthetic levels can vary across different domains [5]. Moreover, human perception is subjective by nature [6].

Color harmony is the primary driver of aesthetic preference for color schemes [7]. Several researches have shown that color harmonies can be universal [8]. Such combinations as monochromatic, complementary, analogous, etc. are widely used in art, fashion, and interior design. However, most of them only use hue as a parameter, whereas color should be described by several parameters (e.g., hue, saturation, and intensity). On the

[1] Corresponding Author: Pakizar Shamoi; E-mail: p.shamoi@kbtu.kz

other hand, some studies [9], [10] show that the aesthetics level is highly context-specific. So, further research is required in order to resolve these contradictions.

This paper aims to comprehend the extent of color harmony universality. Our study goes beyond traditional approaches by considering the role of saturation and intensity alongside hue in color harmony assessment. In our earlier studies, we introduced the fuzzy color model (FHSI) [3,11,12,13] that can be used to address visual uncertainty. This study employs FHSI to investigate color harmony universality. Whether color palettes that are considered harmonious in one context are likewise considered harmonious in other contexts? Most studies focus on harmonies within 2 or 3-color palettes, but in real-world scenarios, we often deal with much more complex palettes. In our research, we analyze 8-color palettes in five domains (nature, fashion, art, logo and interior design) to better reflect the complexity found in practical applications.

The paper is structured as follows. Section I is this introduction. Section II provides an overview of studies on color harmony. Next, we recall basic ideas from our previous works on fuzzy color space in Section III. Section IV describes the methods we use in this study. Section V presents experimental results. The next Section is Discussion. Finally, Section VII concludes the paper and provides ideas for future improvements.

2. Related Work

The harmony of the color scheme is very important in color aesthetics [14,3,4]. The study of color harmony has a long history. None of the methods, however, were found to be appropriate [14]. The most common method of creating harmony is likely a selection of colors from a color wheel as recommended by Goethe [15] and Itten [16]. Other approaches proposed by Moon and Spencer [17] and Chevreul [18], are based on the examination of color relationships. Typically, these studies operate on the premise that colors achieve harmony when they are either complementary or analogous. Other methods include Matsuda's color coordination [19], and deep learning approaches [20].

The other important question is color harmony universality. Many researchers concluded that it is highly context-dependent [21]. This specificity varies from the application field we observe to the viewer's personal condition and subjective judgments. Color preference can also be influenced by different factors, such as gender, age, sex, and geographical region [22]. At the same time, some studies obtained in their experiments certain rules of color aesthetic universality [23], [4]. Specifically, some color combinations tend to arouse similar human responses in whatever context is given.

From the studies mentioned above, we can see that the mechanisms underlying the color harmonies remain controversial. As aesthetic-level prediction receives more attention, it is crucial to understand the patterns that form the basis of this area of interest.

3. Research Background: Fuzzy Color Modelling

In our earlier works [3,13,12,24,11], we presented a novel fuzzy sets based color space, FHSI, which is consistent with human perception. Our method relies on fuzzifying the well-known HSI color space (see Table 1 and Figure 1). We also provided objective measures for finding the image similarity to match human evaluation. So, fuzzy color is

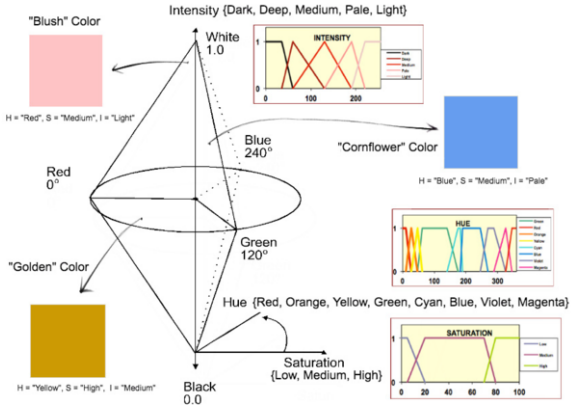

Figure 1. FHSI Color Space. Hue, Saturation, and Intensity attributes are represented as fuzzy sets.

a fuzzy subset of points of some crisp color space[25], which is the HSI space in our case [26,3]. Let D_H, D_S, D_I be domains of the H, S, I attributes respectively.

Definition 1 ***FHSI (fuzzy HSI) color*** *C is a linguistic label whose semantic is represented in HSI color space by a normalized fuzzy subset of $D_H \times D_S \times D_I$.*

From Definition 1 it is obvious that for each fuzzy color C there exists at least one representative crisp color whose membership to C is 1.

Definition 2 ***FHSI (fuzzy HSI) color space*** *is a set of fuzzy colors that define a partition of $D_H \times D_S \times D_I$.*

In other words, a fuzzy color space is a collection of fuzzy sets that provides a conceptual quantization (with soft boundaries) of crisp color space [25].

Definition 3 ***FHSI (fuzzy HSI) color palette*** *is a combination of several fuzzy colors.*

In a fuzzy color palette, each color is not crisp (point), but a fuzzy color (region). Let us take *Blush* color as an example. For the fuzzification, we take crisp inputs and transform them into fuzzy sets. For instance, if the color is in RGB format (*Blush*: R=241, G=171, B=185), we first convert it into HSI model (H = 349, S = 14%, I = 78%), then to the FHSI model (H = *Red*, S = *Medium*, I = *Light*, see Figure 1). Hue, in this case, is partially 'Red' and 'Magenta', while Saturation is partially 'Low' and partially 'Medium'.

Table 1. Description of fuzzy attributes of the fuzzy color space we proposed in earlier works [26], [13], [27].

Fuzzy variable	Term set	Domain
Hue	T = { Red, Orange, Yellow, Green, Cyan, Blue, Violet, Magenta }	X = [0, 360]
Saturation	T = { Low, Medium, High }	X = [0, 100]
Intensity	T = { Dark, Deep, Medium, Pale, Light }	X = [0, 255]

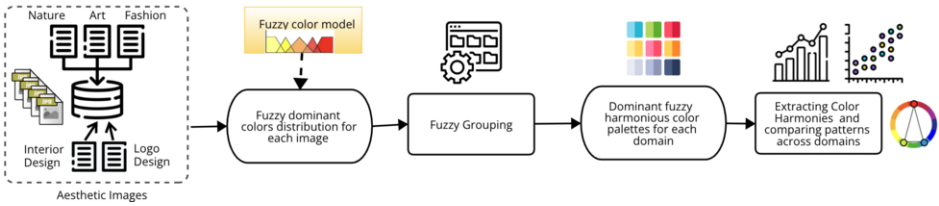

Figure 2. Proposed fuzzy approach for color harmony universality estimation

4. Methods

The proposed approach is schematically shown in Figure 2. First, we collect a dataset comprising aesthetically appealing images from five distinct domains. Then, we extract fuzzy dominant colors in each image and group the images, forming fuzzy color palettes for each domain. Finally, we extract color harmony patterns and compare them.

4.1. Data Collection and Description

- ***Fashion.*** The dataset and fuzzy color-based palettes presented in [3] were utilized. The dataset comprises looks from various sources, including prominent fashion websites like lookbook.nu, instyle.com, and dailylook.com, as well as different style communities on social networking sites (e.g., Instagram, VK, etc.).
- ***Art.*** The experiment utilized a total of 1276 artworks from the 'Best Artworks of All Time' dataset [28]. This dataset comprises famous pieces of art created by various artists representing diverse movements and eras.
- ***Nature.*** We used a dataset of pictures of natural landscapes [29]. This dataset includes real-world photos from Flickr, consisting of 100 desert pictures and 184 pictures for each of the following categories: landscapes, mountains, seas, beaches, islands, and Japan. In total, we collected 1204 images.
- ***Interior Design.*** We utilized a dataset of Modern Architecture [30]. Specifically, we focused on the Private Apartments section (U-W) and excluded images containing keywords like 'Garden,' 'Exterior,' 'Facade,' etc., as our interest was solely in interior design. This led to a total collection of 1250 interior design images.
- ***Brand Logos.*** For dominant harmonious palettes in marketing, we used the Popular Brand Logos image dataset [31], which comprises vector images of numerous well-known brand logos. A total of 1250 logos were utilized in the experiment.

4.2. Color Wheel

Johannes Itten proposed a color wheel and described graphical schemes for constructing harmonious color combinations (Figure 3) [16]. For instance, using a monochromatic color scheme means selecting one hue and its darker or lighter variations. Diametrically opposed colors are called complementary and produce the highest possible contrast. A split complementary color scheme involves one base color and two secondary colors. The triad scheme employs three colors that form a triangle on the color wheel, the square and rectangular harmonies follow the same logic. The analogous scheme entails selecting from 3 to 5 adjacent colors. Balancing saturation and lightness is vital for color harmony, especially with more colors. Our experiment explores *Monochromatic, Complementary, Split Complementary, Triad, Square, Rectangular, Analogous* harmonies.

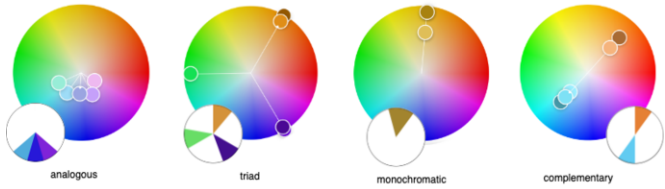

Figure 3. Color harmony rules

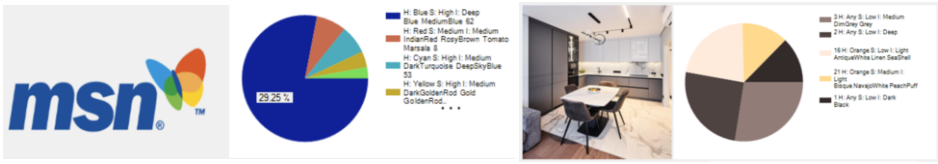

(a) Logo design (b) Interior design

Figure 4. Examples of extracted fuzzy color palettes

4.3. Fuzzy Palettes Extraction

Harmonious fuzzy color palettes were generated from the dataset by grouping images with similar color compositions. Examples of fuzzy dominant color detection are in Figure 4. We used the fuzzy color model with formulas for color difference and palette similarity, as detailed in [13], [12], [3]. Algorithm 1 (outlined below) identifies dominant fuzzy color palettes $P_1, ..., P_k$ within a domain D, employing a method for assessing image similarity using FHSI, as defined in M_1 and M_2 [26]. For a more detailed explanation, see [26]. We averaged the number of images per group for each domain, then selected dominant palettes with more images than this average for each group.

Data: dataset of images $M_1, ..., M_n$ in some domain D
Result: list of fuzzy dominant color palettes $P_1, ..., P_k$ in D
$FuzzyPalettes \leftarrow$ an empty list;
while *not at end of dataset* **do**
  read current image M_i;
  $FP_i \leftarrow$ FindFuzzyDomColors (M_i);
  $Dp_{avg} \leftarrow$ FindAvgPercDif (M_i);
  ... `/* the perceptual difference` Dp_{avg} `is found between` FP_i
    `and members of each fetched harmonious group. See`
    `Algorithm 1 in [3]. */`
  if *minimal* $Dp_{avg} \geq diffThreshold$ **then**
    form a new Palette and add M_i to it. Add Palette to $FuzzyPalettes$
  else
    add M_i to a palette in $FuzzyPalettes$ with which M_i has minimal Dp_{avg}.
  end
end
return $FuzzyPalettes$;

Algorithm 1: Extracting fuzzy dominant palettes

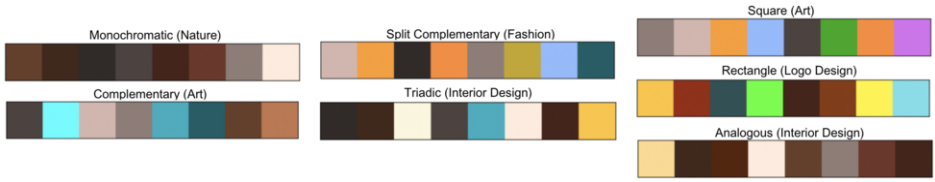

Figure 5. Examples of color palettes associated with certain harmonies

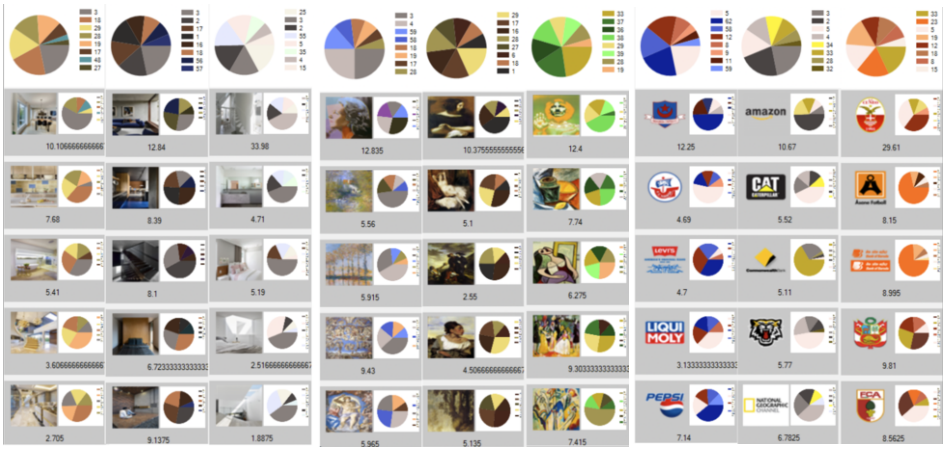

(a) Interior (b) Art (c) Logo

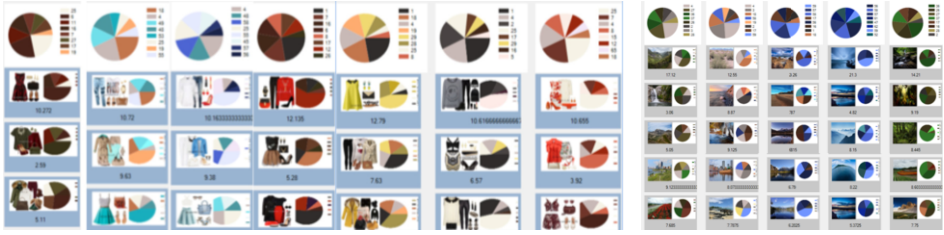

(d) Fashion (e) Nature

Figure 6. Examples of fuzzy dominant palettes and representative images extracted from considered domains

5. Experimental Results

We processed datasets with Algorithm 1 to obtain fuzzy color palettes for each context. In the *Art* domain, we found 46 groups of similar palettes. See Figure 5 for specific harmony-related color palettes, and Figure 6 for dominant palettes from various domains with accompanying images.

We identified colors on the RGB wheel, examined tertiary hues (12-split), and computed harmonies. The comparative results are in Table 2 and Figure 7. Most schemes adhered to color wheel relationships, but some fell into the *'Other'* category, deviating from these norms. Some rules like 'Triad,' 'Square,' and 'Rectangle' were less frequent, while 'Analogous' and 'Complementary' harmonies prevailed in all domains. Note that

Table 2. Summary of harmonious dominant fuzzy palettes from considered domains

Context	#Palettes	Top harmony	Other, %	Mean I	Mean S	Top Fuzzy Colors
Fashion	59	Analogous	6.8	0.50	0.40	
Nature	62	Complimentary	6.5	0.53	0.46	
Logo Design	34	Analogous	2.9	0.49	0.48	
Interior Design	37	Analogous	0	0.47	0.36	
Art Images	46	Analogous	0	0.46	0.40	

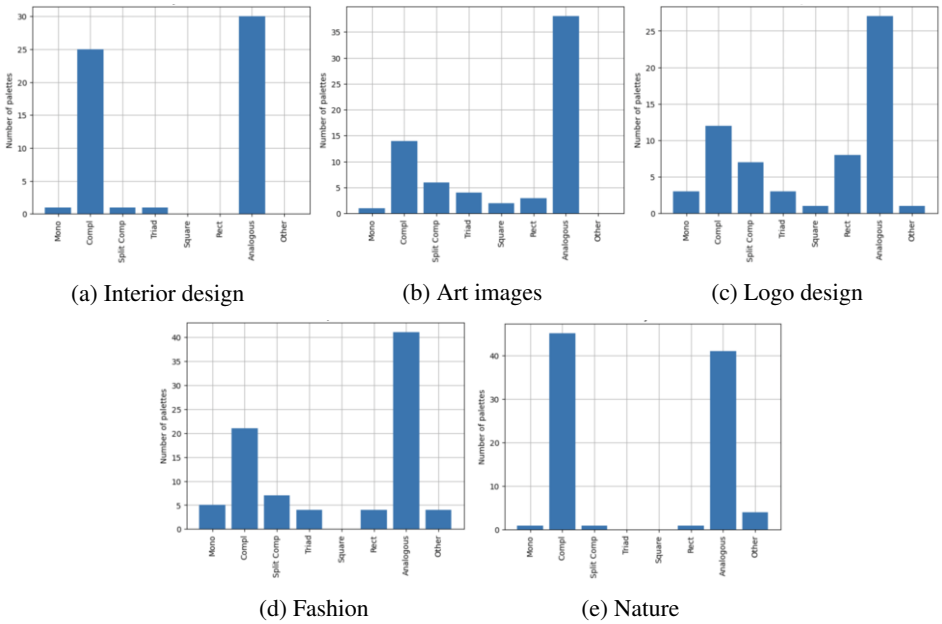

(a) Interior design (b) Art images (c) Logo design

(d) Fashion (e) Nature

Figure 7. Distribution of Color Harmonies among considered domains

one palette could have multiple harmony schemes, like 'Analogous' and 'Triadic,' due to our use of eight-color palettes.

Figures 8b and 8a show that color harmony based on the color wheel relates to specific *Intensity* and *Saturation* levels. Even when following color wheel relationships like 'Triadic,' variations in saturation and intensity impact harmony. In the majority of harmonious schemes, consistency in adhering to color wheel rules aligns with 'medium' *Saturation* and *Intensity*. This holds across all contexts. Overall, the experimental results suggest that while color harmony is largely universal, some context influence remains.

The current paper explores universal harmony patterns using fuzzification across diverse contexts. The future phase will formalize these patterns as fuzzy rules for predicting image harmony. We'll illustrate with a simple example, evaluating 'Color Harmony' using three fuzzy variables: Color Wheel Correspondence (C), Saturation (S), and Intensity (I), each with terms like 'low,' 'medium,' and 'high.' We then apply fuzzy rules connecting these variables to 'Color Harmony.' For instance: *"IF (C is 'high') AND (S is 'medium') AND (I is 'medium'), THEN Color Harmony is 'very High."* This process concludes with defuzzification, yielding the crisp color harmony value.

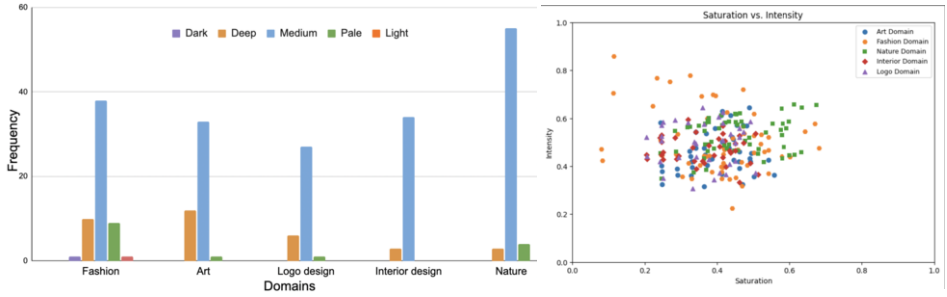

(a) Distibution of fuzzy intensities across domains (b) Trends in *Intensity* and *Saturation*

Figure 8. Distribution of intensities. Fuzzy partition *(Dark, Deep, Medium, Pale, Light)* is shown in Figure 1.

6. Discussion

Compared to Itten's focus on balanced color combinations [16], favoring analogous or complementary pairs for harmony, our experiments affirm the prevalence of these pairs. Yet, our results diverge from Itten's view, showing a tendency for mid-range S and I values in harmonious images. Our findings align with Granger's work [32], emphasizing the significance of consistent saturation and intensity levels for harmony. Across five domains, we observed saturation and intensity clustering around mid-ranges, confirming their consistency. Overall, our study confirms the idea that color harmony often relates to color wheel schemes, as discussed by Itten, Munsell, and Ostwald [33].

The obtained results support the idea of the universal nature of color harmony while also highlighting its sensitivity to context. Our results are consistent with those reported in [14] regarding general patterns of color harmony. Some works, however, suggest that color harmony exhibits both universal and domain-specific characteristics [5].

7. Conclusion

This paper explores the context-dependency of color harmony using a fuzzy approach. We analyzed harmony in art, fashion, nature, interior design, and branding. Our results highlight the importance of color wheel principles and the critical role of saturation and intensity. Most harmonious schemes follow 'Analogous' and 'Complementary' color wheel rules, balancing medium saturation and intensity.

The study has limitations, with datasets potentially not fully representative of real-world diversity. Expanding dataset variety and size can enhance generalizability. In future work, we aim to introduce a fuzzy inference system using rules based on color wheel correspondence, saturation, and intensity. We also plan to include user evaluations for deeper insights into color harmony.

References

[1] Rodriguez-Fernandez N, Alvarez-Gonzalez S, Santos I, Torrente-Patiño A, Carballal A, Romero J. Validation of an Aesthetic Assessment System for Commercial Tasks. Entropy. 2022;24(1).

[2] Hayn-Leichsenring GU, Lehmann T, Redies C. Subjective Ratings of Beauty and Aesthetics: Correlations With Statistical Image Properties in Western Oil Paintings. i-Perception. 2017;8(3).
[3] Shamoi P, Inoue A, Kawanaka H. Modeling aesthetic preferences: Color coordination and fuzzy sets. Fuzzy Sets and Systems. 2020;395:217-34.
[4] Shamoi P, Inoue A, Kawanaka H. Color Aesthetics and Context-Dependency. In: Joint 12th Int. Conf. on Soft Computing and Intel. Systems and 23rd Int. Symposium on Adv. Intel. Systems; 2022. p. 1-7.
[5] Markovic S. Object Domains and the Experience of Beauty. Art and Perception. 2014;2(1-2):140-19.
[6] Singh S. Impact of color on marketing. Management Decision. 2006 07;44:783-9.
[7] Schloss K, Palmer S. Aesthetic response to color combinations: Preference, harmony, and similarity. Attention, perception, psychophysics. 2011 02;73:551-71.
[8] Aslam M. Are You Selling the Right Colour? A Cross-cultural Review of Colour as a Marketing Cue. Journal of Marketing Communications. 2006 03;12:15-30.
[9] Jacobs LW, Keown CF, Worthley R. Cross-cultural Colour Comparisons: Global Marketers Beware! Int Mark Review. 1991;8.
[10] Amsteus M, Al-shaaban S, Wallin E. Colors in Marketing : A Study of Color Associations and Context (in) Dependence. Int Journal of Business and Soc Science. 2015;6(3):32-45.
[11] Shamoi P, Inoue A, Kawanaka H. Deep Color Semantics for E-Commerce Content-Based Image Retrieval. In: Int. Conf. on Fuzzy Logic in Artificial. Int. - Volume 1424. CEUR-WS.org; 2015. p. 14–20.
[12] Shamoi P, Inoue A, Kawanaka H. Fuzzy Model for Human Color Perception and Its Application in E-Commerce. Int-l Journal of Unc, Fuzziness and Knowledge-Based Systems. 2016;24:47-70.
[13] Shamoi P, Inoue A, , Kawanaka H. FHSI: Toward More Human-Consistent Color Representation. Journal of Advanced Computational Intelligence and Intelligent Informatics. 2016;20(3).
[14] Ou LC, Luo MR, Cui G. A Colour Design Tool Based on Empirical Studies. Und Des Res Society Conf. 2009:175.
[15] von Goethe JW, Eastlake CL. Goethe's Theory of Colours; 1840.
[16] Briggs D, Westland S. In: Itten, Johannes; 2014. p. 1-3.
[17] Moon P, Spencer D. Geometric Formulation of Classical Color Harmony. J Opt Soc Am. 1944;34:46-59.
[18] Chevreul M. The Principles of Harmony and Contrast of Colours, and Their App. to the Arts; 1860.
[19] Tokumaru M, Muranaka N, Imanishi S. Color design support system considering color harmony. In: IEEE World Congr. on Comput. Intel. IEEE Intern. Conf. on Fuzzy Syst.. vol. 1; 2002. p. 378-83 vol.1.
[20] Cetinic E, Lipic T, Grgic S. A Deep Learning Perspective on Beauty, Sentiment, and Remembrance of Art. IEEE Access. 2019;7:73694-710.
[21] Elliot A, Maier M. Color and Psychological Functioning. Cur Dir in Psychol Sc. 2007 10;16:250 -254.
[22] Saito M. Comparative studies on color preference in Japan and other Asian regions, with special emphasis on the preference for white. Color Research & Application. 1996;21(1):35-49.
[23] Nakauchi S, Kondo T, Kinzuka Y, Taniyama Y, Tamura H, Higashi H, et al. Universality and superiority in preference for chromatic composition of art paintings. Scientific Reports. 2022 03;12.
[24] Shamoi P, Inoue A, Kawanaka H. Fuzzy Color Space for Apparel Coordination. Open Journal of Information Systems (OJIS). 2014:20-8.
[25] Chamorro-Martínez J, Sánchez D, Soto-Hidalgo JM, Martínez-Jiménez P. Histograms for Fuzzy Color Spaces. In: Eurofuse 2011. Berlin, Heidelberg: Springer Berlin Heidelberg; 2012. p. 339-50.
[26] Shamoi P. Fuzzy Model For Human Color Perception and its Application in E-commerce - Apparel Color Coordination; 2019. PhD thesis.
[27] Shamoi P, Inoue A, Kawanaka H. Perceptual Color Space: Motivations, Methodology, Applications. SCIS-ISIS14. 2014.
[28] Icaro. Best Artworks of All Time - Collection of Paintings of the 50 Most Influential Artists of All Time(Kaggle);. `www.kaggle.com/datasets/ikarus777/best-artworks-of-all-time.`.
[29] Rougetet A. Landscape Pictures - Datasets of pictures of natural landscapes (Kaggle);.
[30] Modern Architecture (100k Images)(Kaggle) CtS, of Modern Buildings P;. `www.kaggle.com/datasets/ikarus777/best-artworks-of-all-time.`.
[31] Koustubhk. Popular brand Logos - Image Dataset (Kaggle);. www.kaggle.com/datasets/kkhandekar/popular-brand-logos-image-dataset.
[32] Granger GW. An Experimental Study of Colour Harmony, The Journal of General Psychology. General Psychology. 1955;52:1:21 -35.
[33] Schloss K, Palmer S. Aesthetic response to color combinations: Preference, harmony, and similarity. Attention, perception & psychophysics. 2011 02;73:551-71.

Fuzzy Systems and Data Mining IX
A.J. Tallón-Ballesteros and R. Beltrán-Barba (Eds.)

doi:10.3233/FAIA231003

The Level Cardinality of Fuzzy Module Under $\mathbb{Z}$-Module Homomorphism on $\mathbb{Z}_n$ into $\mathbb{Z}_m$ Where $gcd(n,m)$ Is Product of Primes

Manju VARGHESE[b, a], Shery FERNANDEZ [c,1]
[a] *Research Scholar, Cochin University of Science and Techonology*
[b] *Assistant Professor, Mar Thoma College for Women, Perumbavoor*
[c] *Professor, Cochin University of Science and Techonology*

Abstract. The homomorphic image of a fuzzy module of an R-module is a fuzzy module[1]. In one of our papers [2] we have proved that if $f : \mathbb{Z}_n \to \mathbb{Z}_m$ is a $\mathbb{Z}$-module homomorphism with $gcd(n,m) = p$, a prime and λ is any fuzzy module on $\mathbb{Z}_n$ with any level cardinality then the fuzzy module $f(\lambda)$ on $\mathbb{Z}_m$ has level cardinality atmost 3. In this paper, we are considering the fuzzy module homomorphism between the $\mathbb{Z}$-modules $\mathbb{Z}_n$ and $\mathbb{Z}_m$ where $n,m \in \mathbb{Z}^+$ with $gcd(n,m) = pq$, where p and q are primes and trying to find the level cardinality of the fuzzy module $f(\lambda)$ on $\mathbb{Z}_m$ when λ is a fuzzy module on $\mathbb{Z}_n$.

Keywords. Fuzzy module, level submodule, Fuzzy module homomorphism

1. Introduction

The idea of fuzzy set on a nonempty set was first introduced by L A Zadeh [3] in 1965. He defined the fuzzy subset of a nonempty set X as a membership function $\lambda : X \to [0,1]$. In 1971 a milestone in the development of fuzzy group was laid by Rosenfeld [4]. The level set or a-cut [1] of a fuzzy set λ for $a \in [0,1]$ is defined as $\lambda_a = \{x/x \in X, \lambda(x) \geq a\}$. In 1975 Negoita and Ralescu [5] came up with the concept of fuzzy module. The module homomorphism is a mapping between modules which preserves the module structure. The image of a fuzzy module of an R-module is a fuzzy module under module homomorphism [1]. In our previous paper [2] we have studied the level cardinalities of image of fuzzy modules of $\mathbb{Z}$-module $\mathbb{Z}_n$, $n \in \mathbb{Z}$. Also the level cardinalites of image of fuzzy module under $\mathbb{Z}$-module homomorphism of $\mathbb{Z}_n$ into $\mathbb{Z}_m$ when $gcd(n,m) = p$, a prime and when $gcd(n,m) = 1$. Now we are checking the level cardinality of the image of the fuzzy module on $\mathbb{Z}_n$ where f is a homomorphism of $\mathbb{Z}_n$ into $\mathbb{Z}_m$ when $gcd(n,m) = pq$, p,q are primes.

[1]Corresponding Author: Shery Fernandez, Professor, Cochin University of Science and Techonology; E-mail: sheryfernandezaok@gmail.com.

2. Preliminaries

Definition 2.1. [6] Let R be a ring. A left R-module is a set M together with

1. a binary operation $+$ on M under which M is an abelian group, and
2. an action of R on M (that is, a map $R \times M \to M$) denoted by ax, for all $a \in R$ and for all $x \in M$ which satisfies

   (a) $(a+b)x = ax+bx$, for all $a,b \in R, x \in M$
   (b) $(ab)x = a(bx)$, for all $a,b \in R, x \in M$ and
   (c) $a(x+y) = ax+ay$, for all $a \in R, x,y \in M$
   If the ring R has a unity $'1'$ we impose the additional axiom:
   (d) $1.x = x$, for all $x \in M$

Definition 2.2. [7] Let R be a ring, M and N be R-modules. An R-module homomorphism from M to N is a map $f : M \to N$ which respects addition and scalar multiplication of these modules and satisfies the following axioms

1. $f(m+n) = f(m)+f(n)$ for all $m,n \in M$
2. $f(rm) = rf(m)$ for all $m \in M$ and $r \in R$

Definition 2.3. [8] Let R be a ring and let M be an R-module, then a fuzzy module on M is a map $\lambda : M \to [0,1]$ satisfying the following conditions

1. $\lambda(m_1+m_2) \geq \min\{\lambda(m_1), \lambda(m_2)\}, \ \ \forall m_1, m_2 \in M$
2. $\lambda(-m_1) = \lambda(m_1) \ \ \forall m_1 \in M$
3. $\lambda(rm_1) \geq \lambda(m_1) \ \ \forall m_1 \in M, \ \ r \in R$
4. $\lambda(0) = 1$

Definition 2.4. [9] Let μ and λ be two fuzzy modules of an R-module M, then λ is called a fuzzy submodule of μ if $\lambda \subseteq \mu$ (i.e $\lambda(m) \leq \mu(m) \ \ \forall m \in M$)

Definition 2.5. [1] Let f be a mapping from X into Y and let λ be a fuzzy subset on X then the fuzzy subset $f(\lambda)$ on Y is defined by $\forall y \in Y$,

$$f(\lambda)(y) = \begin{cases} \vee\{\lambda(x)/x \in M, f(x) = y\} & \text{if } f^{-1}(y) \neq \emptyset \\ 0 & \text{otherwise} \end{cases}$$

is called the image of λ under f, where $\vee$ denotes the maximum or supremum.

Theorem 2.6. *Let f be an $\mathbb{Z}$-module homomorphism of $\mathbb{Z}_n$ into $\mathbb{Z}_m$ where $n,m \in \mathbb{Z}$ then*

1. $f(0) = 0$.
2. *$f(h) = hf(1)$ for all $h \in \mathbb{Z}$ i.e, The module homomorphism is determined by the value of $f(1) \in \mathbb{Z}_m$.*
3. *order of $f(h) \in \mathbb{Z}_m$ divides order of h for all $h \in \mathbb{Z}_n$.*
4. *If H be a submodule of $\mathbb{Z}_n$ then $f(H)$ is a submodule of $\mathbb{Z}_m$.*

Theorem 2.7. *[2] The level cardinality of any fuzzy module of an $\mathbb{Z}$-module $\mathbb{Z}_n$ where $n = p_1^{r_1}.p_2^{r_2}\ldots p_k^{r_k}$, $p_i's$ are distinct primes and $r = r_1+r_2+\cdots+r_k$ is less than or equal to $r+1$.*

Theorem 2.8. *[10] Let $gcd(n,m) = d$ and suppose that d divides l, then the linear congruence $na \equiv l \pmod m$ has exactly d solutions modulo m and the solutions are $t, t+\frac{m}{d}, t+\frac{2m}{d}, \ldots, t+\frac{(d-1)m}{d}$ where t is the solution, unique modulo $\frac{m}{d}$, of the linear congruence $\frac{a}{d}x \equiv \frac{b}{d} \pmod{\frac{m}{d}}$.*

Remark 2.9. From (2) of theorem 2.6, we have the $\mathbb{Z}$-module homomorphism is determined by the value of $f(1) = a \in \mathbb{Z}_m$ and also we have $na \equiv 0 \pmod m$. So the number of homomorphisms from $\mathbb{Z}_n \to \mathbb{Z}_m$ is equal to the possible values of a. By theorem 2.8 there are $gcd(n,m) = d$ possible values for a and they are $0, \frac{m}{d}, 2\frac{m}{d}, \ldots, (d-1)\frac{m}{d}$. So there are $'d'$ $\mathbb{Z}$-module homomorphisms from $\mathbb{Z}_n \to \mathbb{Z}_m$, where $gcd(n,m) = d$ and the module homomorphisms are $f_k(x) = \frac{m}{d}kx \pmod m$, $k = 0, 1, \ldots, d-1$.

Theorem 2.10. *[2] Let M_1 and M_2 be R-modules and f be an R-module homomorphism of M_1 into M_2. If λ is a fuzzy module on M_1 then $f(\lambda)$ is a fuzzy module on M_2.*

Theorem 2.11. *[2] Let $f : \mathbb{Z}_n \to \mathbb{Z}_m$ be an $\mathbb{Z}$-module homomorphism with $gcd(n,m) = p$, a prime and let λ be any fuzzy module on $\mathbb{Z}_n$ then the level cardinality of $f(\lambda)$ is atmost* 3.

3. Fuzzy module homomorphism

Theorem 3.1. *Let $f : \mathbb{Z}_n \to \mathbb{Z}_m$ be an $\mathbb{Z}$-module homomorphism with $gcd(n,m) = pq$, product of primes p and q and let λ be any fuzzy module on $\mathbb{Z}_n$ then the level cardinality of $f(\lambda)$ is atmost* 4.

Proof. By remark 2.9 the only $\mathbb{Z}$-module homomorphisms of $\mathbb{Z}_n$ into $\mathbb{Z}_m$ are $f_k(x) = \frac{m}{pq}kx \pmod m$ where $k = 0, 1, 2, \ldots, pq-1$, as $gcd(n,m) = pq$. There are pq homomorphisms. By theorem 2.10 $f_k(\lambda)$ is a fuzzy module on $\mathbb{Z}_m$. Now the $\mathbb{Z}$-module homomorphisms are divided into 4 according to the value of $k = 0$ and values of $gcd(pq,k)$. Let in the prime factorisation of n, the highest power of p is r_1 and q is r_2. Without loss of generality we can assume that $p < q$.

I $k = 0$. It is the trivial homomorphism, $f_0(x) = 0$ for all $x \in \mathbb{Z}_n$, then only $0 \in \mathbb{Z}_m$ has preimage in $\mathbb{Z}_n$ under f_0. Let λ be any fuzzy module on $\mathbb{Z}_n$ then the fuzzy module $f_0(\lambda)$ is defined by,

$$f_0(\lambda)(y) = \begin{cases} 1 & \text{if } y \in <0> \\ 0 & \text{if } y \in <1> \setminus <0> \end{cases}$$

Hence the level cardinality of $f_0(\lambda)$ on $\mathbb{Z}_m$ is 2.

II $gcd(k, pq) = p$.
When $gcd(k, pq) = p$ we can write the homomorphisms $f_k(x) = \frac{m}{pq}kx \pmod m$ as $f_k(x) = \frac{m}{q}k'x \pmod m$ where $k = k'p$ and $gcd(k', q) = 1$. So there are $\phi(q) = q-1$ such k' and hence $q-1$ homomorphisms. In these homomorphisms $f_k(x) = 0$ if x is a multiple q or 0. Hence the submodule $<q> = \{0, q, 2q, \ldots, (\frac{n}{q}-1)q\}$ of $\mathbb{Z}_n$ of order $\frac{n}{q}$ is mapped

to 0 in $\mathbb{Z}_m$ under these f_ks. So the elements in $\mathbb{Z}_n$ having non zero images under these f_ks has orders which are not factors of $\frac{n}{q}$. The possible orders of elements in $\mathbb{Z}_n$ with non zero images under these f_k are lq^{r_2} where $l \mid (\frac{n}{q^{r_2}})$. Also by theorem 2.6 order of $f_k(h)$ divides both order of h and m for all $h \in \mathbb{Z}_n$, hence $|f(h)| \mid gcd(n,m) = pq$. But in the $\mathbb{Z}$-module homomorphisms $f_k(x) = \frac{m}{q}k'x(\bmod m)$ where $k = k'p$ and $gcd(k',q) = 1$, the order of $\frac{m}{q}k'x(\bmod m)$ is 1 or q for all $x \in \mathbb{Z}_n$. So if $x \in < q > i.e$ order of x, $|x| = \frac{n}{q}$ or its divisor then $\frac{m}{q}k'x(\bmod m) = 0 \in \mathbb{Z}_m$ and if $x \in < 1 > \setminus < q > \subset \mathbb{Z}_n$ or $|x| = lq^{r_2}$ such that $l \mid (\frac{n}{q^{r_2}})$ then $\frac{m}{q}k'x(\bmod m) = a \in < \frac{m}{q} > \setminus < 0 >$ in $\mathbb{Z}_m$ and the submodule $< \frac{m}{q} > = \{0, \frac{m}{q}, 2\frac{m}{q}, \ldots, (q-1)\frac{m}{q}\}$ of $\mathbb{Z}_m$ of order q has only preimage under these f_k's.

$$f_k(x) = \begin{cases} 0 & \text{if } |x| = \frac{n}{q} \text{ or its divisors} \\ a & \text{if } |x| = lq^{r_2} \text{ such that } l \mid (\frac{n}{q^{r_2}}) \text{ and } a \text{ is any element in } < \frac{m}{q} > \setminus < 0 > \subset \mathbb{Z}_m \end{cases}$$

Now let λ be a fuzzy module on $\mathbb{Z}_n$ then $f_k(\lambda)(y) = 0$ for all $y \in < 1 > \setminus < \frac{m}{q} > \subset \mathbb{Z}_m$.

1. If $\lambda(0) = t \neq 0$ where $t = \vee\{\lambda(x) \,/\, x \in \mathbb{Z}_n, |x| = lq^{r_2}, l \mid (\frac{n}{q^{r_2}})\}$ then $f_k(\lambda)$ have level submodule of order q, Also $f_k(\lambda)$ on $\mathbb{Z}_m$ is

$$f_k(\lambda)(y) = \begin{cases} 1 & \text{if } y \in < \frac{m}{q} > \\ 0 & \text{if } y \in < 1 > \setminus < \frac{m}{q} > \end{cases}$$

   Hence the level cardinality of $f_k(\lambda)$ is 2.
2. If $\lambda(0) \neq t \neq 0$ where $t = \vee\{\lambda(x) \,/\, x \in \mathbb{Z}_n, |x| = q^{r_2}, l \mid (\frac{n}{q^{r_2}})\}$ then $f_k(\lambda)$ have level submodules of order 1 and q, Also $f_k(\lambda)$ on $\mathbb{Z}_m$ is

$$f_k(\lambda)(y) = \begin{cases} 1 & \text{if } y \in < 0 > \\ t & \text{if } y \in < \frac{m}{q} > \setminus < 0 > \\ 0 & \text{if } y \in < 1 > \setminus < \frac{m}{q} > \end{cases}$$

   Hence the level cardinality of $f_k(\lambda)$ is 3.

So the level cardinality of $f_k(\lambda)$ is either 2 or 3 when $gcd(k, pq) = p$.

III $gcd(k, pq) = q$. This is similar to **II** $gcd(k, pq) = p$, as the homomorphisms $f_k(x) = \frac{m}{pq}kx$ (mod m) can be written as $f_k(x) = \frac{m}{p}k'x$ (mod m) where $k = k'q$ and $gcd(k', p) = 1$ and the submodule $< \frac{m}{p} > = \{0, \frac{m}{p}, 2\frac{m}{p}, \ldots, (p-1)\frac{m}{p}\}$ of $\mathbb{Z}_m$ of order p has only preimage under these f_k's. So the level cardinality of $f_k(\lambda)$ is either 2 or 3 when $gcd(k, pq) = q$.

IV $gcd(k, pq) = 1$. There are $\phi(pq) = (p-1)(q-1)$ such k and hence $(p-1)(q-1)$ homomorphisms. The $\mathbb{Z}$-module homomorphisms are $f_k(x) = \frac{m}{pq}kx$ (mod m) with $gcd(k, pq) = 1$. So $f_k(x) = 0$ if and only if x is a multiple of pq or 0 and hence the submodule of $\mathbb{Z}_n$, $< pq > = \{0, pq, 2pq, \ldots, (\frac{n}{pq} - 1)pq\}$ of order $\frac{n}{pq}$ is mapped to 0 in $\mathbb{Z}_m$ under these f_k. So the elements of $\mathbb{Z}_n$ under f_k having non zero images will have order either lp^{r_1} with $l \mid (\frac{n}{p^{r_1}})$ or lq^{r_2} with $l \mid (\frac{n}{q^{r_2}})$. Also by theorem 2.6 order of $f_k(h)$ divides both order of h and m for all $h \in \mathbb{Z}_n$, hence $|f(h)| \mid gcd(n,m) = pq$. So the possible values

of order of $f(h)$ are $1, p, q, pq$. Hence the elements in $\mathbb{Z}_m$ of order $1, p, q, pq$ can only have preimages *i.e* the submodule $< \frac{m}{pq} >= \{0, \frac{m}{pq}, 2\frac{m}{pq}, \ldots, (pq-1)\frac{m}{pq}\}$ of $\mathbb{Z}_m$ of order pq only have preimage in $\mathbb{Z}_n$ under these f_k and $f_k(\lambda)(y) = 0$ for all $y \in < 1 > \setminus < \frac{m}{pq} >$ for every fuzzy module λ on $\mathbb{Z}_n$, if $m \neq pq$. When $m = pq$, the $\mathbb{Z}$-module homomorphism is ONTO. If $x \in < pq >$ *i.e* $|x| = \frac{n}{pq}$ or its divisors then $\frac{m}{pq}kx = 0 \in \mathbb{Z}_m$, if $x \in < p > \setminus < pq >$ or $|x| = lq^{r_2}$ with $l \mid (\frac{n}{pq^{r_2}})$ then $\frac{m}{pq}kx \pmod m = a_1$ is any element in $< \frac{m}{q} > \setminus < 0 >$, if $x \in < q > \setminus < pq >$ or $|x| = lp^{r_1}$ with $l \mid (\frac{n}{p^{r_1}q})$ then $\frac{m}{pq}kx \pmod m = a_2$ is any element in $< \frac{m}{p} > \setminus < 0 >$ and if $x \in < 1 > \setminus (< p > \cup < q >)$ or $|x| = lp^{r_1}q^{r_2}$ with $l \mid (\frac{n}{p^{r_1}q^{r_2}})$ then $\frac{m}{pq}kx \pmod m = a_3$ is any element in $< \frac{m}{pq} > \setminus (< \frac{m}{p} > \cup < \frac{m}{q} >)$. Then

$$f_k(x) = \begin{cases} 0 & \text{if } |x| = \frac{n}{pq} \text{ or its divisor} \\ a_1 & \text{if } |x| = lq^{r_2} \text{ with } l \mid (\frac{n}{pq^{r_2}}) \\ a_2 & \text{if } |x| = lp^{r_1} \text{ with } l \mid (\frac{n}{p^{r_1}q}) \\ a_3 & \text{if } |x| = lp^{r_1}q^{r_2} \text{ with } l \mid (\frac{n}{p^{r_1}q^{r_2}}) \end{cases}$$

Now let λ be a fuzzy module on $\mathbb{Z}_n$, then the fuzzy module $f_k(\lambda)$ on $\mathbb{Z}_m$ is defined as follows

1. If $\lambda(0) = t_1 = t_2 \neq 0$ where $t_1 = \vee\{\lambda(x_1) \,/\, x_1 \in \mathbb{Z}_n, |x_1| = lq^{r_2}, l \mid (\frac{n}{pq^{r_2}})\}$ or $t_1 = \vee\{\lambda(x_1) / x_1 \in \mathbb{Z}_n, |x_1| = lp^{r_1}, l \mid (\frac{n}{p^{r_1}q})\}$ and $t_2 = \vee\{\lambda(x_2) / x_2 \in \mathbb{Z}_n, |x_2| = lp^{r_1}q^{r_2}, l \mid (\frac{n}{p^{r_1}q^{r_2}})\}$ then $f_k(\lambda)$ have level submodule of order pq, Also $f_k(\lambda)$ on $\mathbb{Z}_m$ is

$$f_k(\lambda)(y) = \begin{cases} 1 & \text{if } y \in < \frac{m}{pq} > \\ 0 & \text{if } y \in < 1 > \setminus < \frac{m}{pq} > \end{cases}$$

   Hence the level cardinality of $f_k(\lambda)$ is 2 if $m \neq pq$ and has level cardinality 1 if $m = pq$.
2. If $\lambda(0) \neq t_1 = t_2 \neq 0$ where $t_1 = \vee\{\lambda(x_1) \,/\, x_1 \in \mathbb{Z}_n, |x_1| = lq^{r_2}, l \mid (\frac{n}{pq^{r_2}})\}$ or $t_1 = \vee\{\lambda(x_1) / x_1 \in \mathbb{Z}_n, |x_1| = lp^{r_1}, l \mid (\frac{n}{p^{r_1}q})\}$ and $t_2 = \vee\{\lambda(x_2) / x_2 \in \mathbb{Z}_n, |x_2| = lp^{r_1}q^{r_2}, l \mid (\frac{n}{p^{r_1}q^{r_2}})\}$ then $f_k(\lambda)$ have level submodules of orders 1 and pq, Also $f_k(\lambda)$ on $\mathbb{Z}_m$ is

$$f_k(\lambda)(y) = \begin{cases} 1 & \text{if } y \in < 0 > \\ t_1 & \text{if } y \in < \frac{m}{pq} > \setminus < 0 > \\ 0 & \text{if } y \in < 1 > \setminus < \frac{m}{pq} > \end{cases}$$

   Hence the level cardinality of $f_k(\lambda)$ is 3 if $m \neq pq$ and has level cardinality 2 if $m = pq$.
3. If $\lambda(0) = t_1 \neq t_2 \neq 0$ where $t_1 = \vee\{\lambda(x_1) \,/\, x_1 \in \mathbb{Z}_n, |x_1| = lq^{r_2}, l \mid (\frac{n}{pq^{r_2}})\}$ or $t_1 = \vee\{\lambda(x_1) / x_1 \in \mathbb{Z}_n, |x_1| = lp^{r_1}, l \mid (\frac{n}{p^{r_1}q})\}$ and $t_2 = \vee\{\lambda(x_2) / x_2 \in \mathbb{Z}_n, |x_2| = lp^{r_1}q^{r_2}, l \mid (\frac{n}{p^{r_1}q^{r_2}})\}$ then $f_k(\lambda)$ have level submodules of orders p or q and pq, Also $f_k(\lambda)$ on $\mathbb{Z}_m$ is

$$f_k(\lambda)(y) = \begin{cases} 1 & \text{if } y \in <\frac{m}{p}> \text{ or } y \in <\frac{m}{q}> \\ t_2 & \text{if } y \in <\frac{m}{pq}> \setminus <\frac{m}{p}> \text{ or } y \in <\frac{m}{pq}> \setminus <\frac{m}{q}> \\ 0 & \text{if } y \in <1> \setminus <\frac{m}{pq}> \end{cases}$$

Hence the level cardinality of $f_k(\lambda)$ is 3 if $m \neq pq$ and has level cardinality 2 if $m = pq$.

4. If $\lambda(0) \neq t_1 \neq t_2 \neq 0$ where $t_1 = \vee\{\lambda(x_1) \,/\, x_1 \in \mathbb{Z}_n, |x_1| = lq^{r_2}, l \mid (\frac{n}{pq^{r_2}})\}$ or $t_1 = \vee\{\lambda(x_1) \,/\, x_1 \in \mathbb{Z}_n, |x_1| = lp^{r_1}, l \mid (\frac{n}{p^{r_1}q})\}$ and $t_2 = \vee\{\lambda(x_2) \,/\, x_2 \in \mathbb{Z}_n, |x_2| = lp^{r_1}q^{r_2}, l \mid (\frac{n}{p^{r_1}q^{r_2}})\}$ then $f_k(\lambda)$ have level submodules of orders 1, p or q and pq, Also $f_k(\lambda)$ on $\mathbb{Z}_m$ is

$$f_k(\lambda)(y) = \begin{cases} 1 & \text{if } y \in <0> \\ t_1 & \text{if } y \in <\frac{m}{p}> \setminus <0> \text{ or } y \in <\frac{m}{q}> \setminus <0> \\ t_2 & \text{if } y \in <\frac{m}{pq}> \setminus <\frac{m}{p}> \text{ or } y \in <\frac{m}{pq}> \setminus <\frac{m}{q}> \\ 0 & \text{if } y \in <1> \setminus <\frac{m}{pq}> \end{cases}$$

Hence the level cardinality of $f_k(\lambda)$ is 4 if $m \neq pq$ and has level cardinality 3 if $m = pq$.

Hence the level cardinality of the fuzzy module $f(\lambda)$ on $\mathbb{Z}_m$ is atmost 4 where f is an $\mathbb{Z}$-module homomorphism of $\mathbb{Z}_n$ into $\mathbb{Z}_m$.

□

Example 3.2. The $\mathbb{Z}$-module homomorphisms of $\mathbb{Z}_{315}$ into $\mathbb{Z}_{150}$ are $f_k(x) = 10kx$ (mod 150) $\forall x \in \mathbb{Z}_{105}$ $k = 0,1,2,\ldots,14$, by remark 2.9 and since $gcd(315,150) = 15$. By theorem 2.7 the maximum level cardinality of fuzzy module on $\mathbb{Z}_{315}$ is 5. Consider a fuzzy module on $\mathbb{Z}_{315}$ with level cardinality 5 and for the $\mathbb{Z}$-module homomorphisms f_k, where $k = 0,1,2,\ldots 14$.

$$Let \;\; \lambda(x) = \begin{cases} 1 & \text{if } x \in <0> \\ 1/2 & \text{if } x \in <63> \setminus <0> \\ 1/3 & \text{if } x \in <21> \setminus <63> \\ 1/4 & \text{if } x \in <7> \setminus <21> \\ 1/5 & \text{if } x \in <1> \setminus <7> \end{cases}$$

then

Cases	$k=0$	$gcd(k,15)=3$	$gcd(k,15)=5$	$gcd(k,15)=1$
Number of homomorphisms	1	$\phi(5)=4$	$\phi(3)=2$	$\phi(15)=8$
Homomorphisms	f_0	f_3, f_6, f_9, f_{12}	f_5, f_{10}	$f_1, f_2, f_4, f_7, f_8, f_{11}, f_{13}, f_{14}$
Fuzzy module	$f_0(\lambda)(y) = \begin{cases} 1 & \text{if } y \in <0> \\ 0 & \text{if } y \in <1> \setminus <0> \end{cases}$	$f_3(\lambda)(y) = \begin{cases} 1 & \text{if } y \in <0> \\ 1/2 & \text{if } y \in <30> \setminus <0> \\ 0 & \text{if } y \in <1> \setminus <30> \end{cases}$	$f_5(\lambda)(y) = \begin{cases} 1 & \text{if } y \in <0> \\ 1/4 & \text{if } y \in <50> \setminus <0> \\ 0 & \text{if } y \in <1> \setminus <50> \end{cases}$	$f_1(\lambda)(y) = \begin{cases} 1 & \text{if } y \in <0> \\ 1/2 & \text{if } y \in <30> \setminus <0> \\ 1/4 & \text{if } y \in <10> \setminus <30> \\ 0 & \text{if } y \in <1> \setminus <10> \end{cases}$

4. Conclusion

In this paper, We have proved that the level cardinalities of fuzzy module $f(\lambda)$ is atmost 4, where f is an $\mathbb{Z}$- module homomorphism of fuzzy modules of the $\mathbb{Z}$-module $\mathbb{Z}_n$ into the $\mathbb{Z}$-module $\mathbb{Z}_m$ where $n,m \in \mathbb{Z}^+$, $gcd(n,m) = pq$, p and q are primes. In our future work, we are trying to extend this result in the case of fuzzy module homomorphism from $\mathbb{Z}_n$ into $\mathbb{Z}_m$ $n,m \in \mathbb{Z}$, $gcd(n,m) = p^r q^s$

References

[1] John N Mordeson and D S Malik, Fuzzy Commutative Algebra, World Scientific Publishing Co. Pte. Ltd.(1998)

[2] Manju Varghese, Shery Fernandez, The level cardinality of fuzzy module under $\mathbb{Z}$-module homomorphism on $\mathbb{Z}_n$, International conference on Recent Trends in Science, Engineering and Technology ICRTSET-2022 (Presented)

[3] Zadeh L. A., Fuzzy Sets, Information and Control, 8 (1965) 338-353

[4] Rosenfeld A, Fuzzy Groups; J.Math. Anal. Appl., 35(1971) 512-517

[5] Negoiţă, C. V.; Ralescu, D. A. âit Applications of fuzzy sets to systems analysis. Translated from the Romanian. ISR Interdisciplinary Systems Research, Vol. 11. Birkhäuser Verlag, Basel-Stuttgart, (1975).

[6] David M Dummit , Richard M Foote, Abstract Algebra,III Edition John Wiley & Sons, INC(2004).

[7] M E Keating, A First Course in Module Theory. Imperial College Press.(1998)

[8] Pan, F. Fuzzy Finitely Generated Modules. *Fuzzy Sets and Systems* **21** (1987) 105-113.

[9] Shukur Neamah Al-aeashi. Completely semi essential fuzzy submodule. *J. Kufa Math. Comput.* Vol.2, no.2,(2014)1-7.

[10] Tom M Apostol, Introduction to Analytic Number Theory , Springer-Verlag New York Inc. ,(1976).

Fuzzy Systems and Data Mining IX
A.J. Tallón-Ballesteros and R. Beltrán-Barba (Eds.)

doi:10.3233/FAIA231004

NEO: Neural Demand Prediction and Evolutionary Optimization of EV Network Charging Infrastructure

Chia E. Tungom[a,b], Ben Niu[a] and Hong Wang[a]
[a] *Shenzhen University, Shenzhen 518060, China*
[b] *Onewo Space-Tech Service Co., Ltd., Shenzhen, 518049, China*

Abstract. Electric vehicles (EVs) are becoming increasingly popular as a cleaner alternative to traditional gasoline-powered vehicles due to advances in battery technology, climate change impacts, and a host of other factors. However, one of the major challenges to the widespread adoption of EVs is the lack of sufficient charging infrastructure. In this study, we explore the use of predictive and optimization algorithms to estimate future demand and find the optimal placement and allocation of EV charging stations in a given charging network. For demand forecasting, we develop a neural network model that takes into account the location of charging stations and historical demand data to predict future EV charging demand. These predicted demands are then used to optimize the infrastructure. Specifically, we use the CMA-ES algorithm to optimize the placement and allocation of charging stations based on factors such as predicted demand, infrastructure costs, driving distance to charging stations, and available space. We compare the results of this approach to a baseline approach that allocates charging stations based on simple heuristics. Our results show that our proposed optimization algorithm effectively handles uncertainty, which can lead to significant improvements in the efficiency and effectiveness of EV infrastructure planning and help accelerate EV adoption.

Keywords. Demand Prediction, Evolutionary Computing, Electric Vehicle, Network Optimization, Infrastructure Allocation

1. Introduction

Optimization problems are ubiquitous in theory, and many real-world problems can be formulated as such. The problem of EV infrastructure network optimization is one such problem that involves the allocation of charging stations to different supply points to meet demand. In recent years, there has been growing interest in using optimization algorithms to improve the efficiency and effectiveness of EV infrastructure planning.

Previous studies have approached this topic from various angles, based on their focus and methodology. Some studies focus on classical location models for recharging EVs. These models consider factors such as the need to revisit charging facilities and the concept of range limitations. For instance, [1] specifically evaluate optimal charging station locations, while [2] optimize a system for dynamic charging in multiple-route environments.

Another category of studies focusses on the impact of demand uncertainty and proposes robust optimization models to address this challenge. The studies [3 and 4] respectively are examples of studies in this category. They introduce robust optimization

models that can handle uncertain in EV demands and minimize the total infrastructure cost under different scenarios.

Data-driven approaches utilizing machine learning and data analytics techniques to predict EV demand and optimize charging infrastructure allocation. Almaghrebi et al. in [5] and Hafeez et al. in [6] achieve high accuracy in demand forecasting and infrastructure allocation; however, scalability issues may arise, and significant data and computation resources may be required. A comprehensive overview of the research on EV infrastructure network optimization in [7] is a notable and summarizes the key findings and contributions of previous studies while highlighting future research directions in this field.

Research focused on optimizing the EV infrastructure network has played a crucial role in designing and implementing charging infrastructure. However, there are still areas that require improvement, particularly in addressing demand uncertainties and dynamic changes in urban design, while simultaneously reducing costs and quality of service (QoS). This study aims to fill an important gap by introducing an end-to-end framework for predicting demand and allocating infrastructure.

This study proposes a demand prediction and optimization framework that can efficiently and effectively optimize EV infrastructure dynamically under uncertainty, with a specific focus on infrastructure cost and driver satisfaction (Quality of Service). We propose a robust prediction and optimization solution framework adaptable to any given EV charging network layout and charging demand using state-of-the-art algorithms in Artificial Intelligence, particularly neural networks for prediction and Evolutionary strategy for optimization.

The rest of this study is structured as follows: Section 2 provides a detailed description of the problem we aim to solve, including data preparation and problem formulation, demand predictive modeling, and optimization framework modeling. In section 3, the predictive and optimization approach are combined into an end-to-end optimization framework. Section 4 evaluates the algorithm and provides numerical results. Finally, section 5 concludes the study.

2. Problem Formulation

This section provides a detailed explanation of the problem, data, problem formulation and design objective and constraints.

2.1. Problem Description

The challenge is optimizing charging infrastructure for an electric vehicle (EV) network. The goal is to minimize costs, reduce carbon emissions, and enhance driver satisfaction by efficiently allocating charging resources based on uncertain and varying demand.

2.2. Data Preparation

The dataset from the shell.ai EV Charging Network Challenge [8], which is specifically designed to closely resemble real-world practical scenarios. The dataset is as follows:

Demand history: A time-series of charging demand over a 64x64 region, spanning from 2010 to 2020. It includes the index, x-coordinate, and y-coordinate of each demand point. To create a more realistic scenario, an augmented dataset was created by randomly multiplying the x and y coordinates of each demand point by a sampled uniform random number between 0.8 and 1.2 (The range was chosen to ensure reasonable variation in the dataset).

Existing EV infrastructure: The dataset provides information on the existing EV infrastructure in 2018, including the index, x-coordinate, and y-coordinate of each of the 100 parking locations (supply points). Additionally, it includes the maximum number of parking slots available at each location, as well as the number of slow charging stations (SCS) and fast charging stations (FCS) already in place as of 2018. In the augmented dataset we randomly added 5 supply points with parking slots where chargers have not been installed. We determine the number of parking slots for an added supply point by taking the mean of parking slots of its 5 nearest neighboring supplying points.

2.3. Problem modelling and formulation

Notations used are introduce as follows:

Notations for Demand Point: We use the notation i to represent an individual demand point among n demand points in a network, while D_i refers to the EV charging demand at that specific demand point.

Notations for Supply point: In a network with m supply points, we represent a supply point with index j. Each supply point j has a total of PS_j parking slots, with SCS_j slow charging stations and FCS_j fast charging stations. The maximum supply capacity $Smax_j$ of a supply point is the sum of the total capacity of its SCS_j slow charging stations and FCS_j fast charging stations, which is given by $(Cap_{SCS} * SCS_j + Cap_{FCS} * FCS_j)$. In this study the Cap_{FCS} and Cap_{SCS} are constants equal to 400 and 200 respectively.

Network Notation: These includes two matrices, a distance matrix $Dist_{ij}$ which represents the distance between demand points and supply points and demand supply matrix DS_{ij} which represents how much demand of the i^{th} supply point is satisfied by the j^{th} supply point.

Demand prediction evaluation metric: We evaluate the accuracy of our prediction model using the square root of demand mismatch DM where demand mismatch is the error derived from incorrect demand forecast and is formulated in Eq.1. To quantify uncertainty at every demand point, we compute an uncertainty vector DU_i (demand uncertainty) at every demand point i as shown in Eq.2. DU_i is utilized in the optimization loop to deal with uncertainty in demand.

$$DM = \sqrt{\sum_i abs\left(D_{forecaast,i} - D_{true,i}\right)} \tag{1}$$

$$DU_i = abs\ \frac{\left(D_{forecaast,i} - D_{true,i}\right)}{D_{true,i}} \tag{2}$$

$D_{forecaast,i}$ is the demand estimated by the model or forecasted demand and $D_{true,i}$ is the true demand. DU_i is the demand uncertainty at demand point i for the given model.

Infrastructure Optimization Objective: The objective is to minimize the cost of EV maintenance and driver range anxiety while maximizing infrastructure utility. The cost of infrastructure operation and maintenance at any given supply point depends on the number of SCS and FCS because the cost of maintenance of these chargers are difference with our formulation assuming a 1.5 to 1 ration of FCS to SCS maintenance cost as shown in the study [3]. The network infrastructure cost (IC) is computed using Eq.3 which gives us an estimate of how much it cost to run the built infrastructure. We also aim to ensure EV drivers have a good experience which we formulate as the cost of finding the nearest charging station computed as the distance travelled by a driver from a demand point to a supply point to satisfy charging demand called dissatisfaction cost (DC) as shown in Eq.4.

$$IC = \sum_{j} SCS_j + \left(1.5 * FCS_j\right) \tag{3}$$

$$DC = \sum_{i,j} Dist_{ij} * DS_{ij} \tag{4}$$

$$Cost = a * IC + b * DC \tag{5}$$

The two objectives are combined by weighting with parameters a and b determined empirically based on the network as shown in Eq 5. Therefore, our objective is to minimize the infrastructure cost and driver anxiety as summed up in Eq 5. a and b are set to 1 and 600 respectively.

The weighting parameters a and b are chosen such that scale of measurement for both IC and DC are balanced, this is because the units are different but the total cost has no units. The conversion depends on the network problem and in our case, we adopt [8] approach because we use the dataset for our study. The final cost informs us how well the network is balances both IC and DC and has no units.

The above optimization objective is subject to the following constraints:

1. All values of the demand supply matrix DS_{ij} must be non-negative
2. Number of SCS and FCS at a supply point must be a positive integer
3. The sum of FCS and SCS at a supply point must be less than the number of parking slots
4. SCS and FCS can only be added or remain constant but not removed
5. $\sum_i DS_{ij} \leq Smax_j$. Demand satisfied by a supply point must be less than or equal to the maximum supply available.
6. $\sum_j DS_{ij} \leq D_{forecast,i}$. forecast demand must exactly be satisfied

3. Methodology

In this section, the proposed optimization solution is introduced. The proposed framework consists of interconnected components to achieve the optimization objective. The components include input data, demand prediction, infrastructure optimization, demand supply allocation, and objective function evaluation as shown in Figure 1. and discussed in subsequent sections.

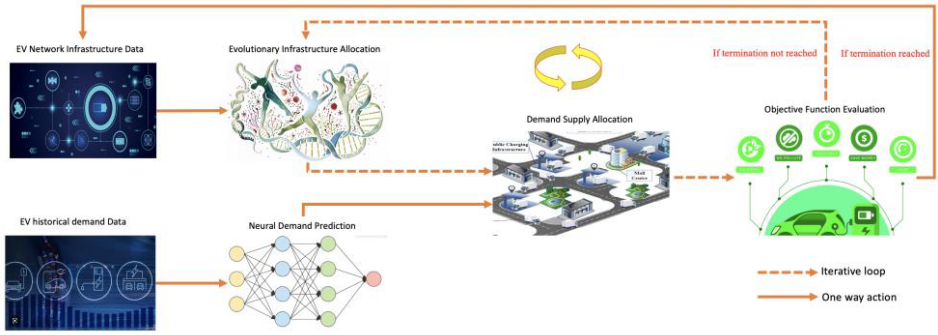

Figure 1. EV Neural Demand Prediction and Infrastructure Optimization Framework.

3.1. Neural Demand Prediction

In predicting future demand of EV charging at demand points, we train a deep neural network on historical demand data and geolocation coordinates. The network input includes the demand values and geolocation coordinates of the target demand point, as well as the demand values of neighboring demand points (this captures spatial relationship between demand points and demand in same neighborhood). The input is processed through two hidden layers, each performing computations and passing outputs to the next layer. The output layer predicts the future demand value for the target demand point. The network is trained using supervised learning to minimize the difference between predicted and actual demand values. The trained network is then used to predict future demand.

The neural network architecture is shown in Figure 2(a) and consists of an input layer with neurons corresponding to input features which are the historical demand data and geolocation data. These neurons are connected to multiple hidden layers. The first hidden layer has 128 neurons, the second hidden layer has 64 neurons, and the third hidden layer has 8 neurons. Each hidden layer performs a weighted sum of inputs from the previous layer and applies a ReLU activation function. Finally, the output layer, consisting of a single neuron, takes the weighted sum of inputs from the last hidden layer and applies a softmax activation function to predict the future demand for EV charging at the given demand point.

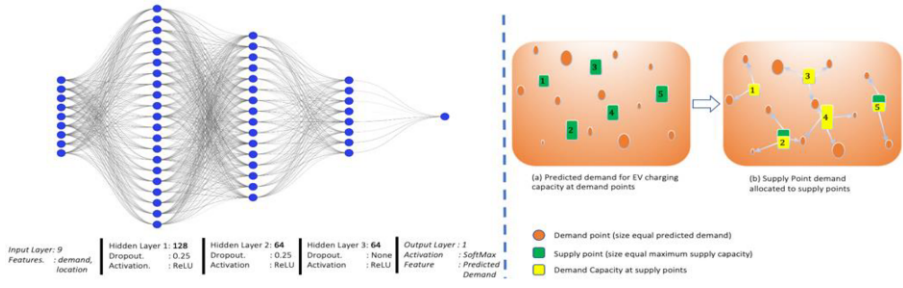

Figure 2. (a) left is a Neural Network Architecture for demand prediction and (b) right is a Demand Supply Allocation illustration

3.2. Evolutionary infrastructure allocation

First, the number of SCS and FCS to build at each demand point is determined. This is done using an evolutionary strategy algorithm that aims to minimize the total IC of the network. The infrastructure is built and the next step is to model the demand supply allocation problem in the network. A linear programming approach to allocate the EV charging demand from demand points to supply points, considering travel costs.

The travel cost serves as a measure of driver anxiety, representing the distance a driver needs to travel to find a charging station. The objective of the evolutionary infrastructure allocation algorithm is to minimize both the IC and DC. This is achieved through an iterative process of building, evaluating, and evolving the infrastructure in the network. The subsequent subsections discuss the design and modeling of the solution, specifically focusing on determining the number of SCS and FCS to build for each charging station.

Infrastructure building: In a charging network with n supply points, for each supply point, we want to build additional charging stations where there are parking slots without charging stations so as to meet projected demand. We will denote the number of parking slots without chargers in supply point j as FS_j standing for free slots. This means our upper bound for the number of charging stations we can build at a supply point is equal to FS_j. Therefore, for every supply point, the lower bound which is the smallest number of chargers to be added is zero and the upper bound is the number of parking slots without chargers. Additionally, for every supply point we need to decided how many SCS and how many FCS should be built, where the sum of the SCSs and FCSs should be less than the upper bound.

We model the allocation of infrastructure as a discrete optimization problem with $2 * n$ dimensions. Where the first n dimensions represent the number of FCSs in supply points one and the n+1 to 2n dimension represents the number of SCS in supply points as shown in Figure 3. The lower bound and upper bound for each dimension is set to zero and number of parking slots without chargers in that station respectively. The constraint for optimization is that the sum of FCS and SCS for every station should be less than or equal to the number of parking slots without chargers in that station.

Dimension	1	...	n	$n+1$	...	$2n$
Charging Stations	FCS_1	...	FCS_n	SCS_1	...	SCS_n
Upper Bound	FS_1	...	FS_n	FS_1	...	FS_n

Figure 3. Discrete Modelling of Infrastructure Allocation at supply points.

With this modelling, we can now use our evolutionary strategy algorithm to find the optimal number of chargers to be allocated for each charging station and compute the infrastructure cost using Eq 3. After the construction a demand supply balancing network model is used to allocate and evaluate network charging supply using predicted demand which we discuss next.

3.3. Demand Supply Allocation

In a network with m demand points with projected demands for EV charging and n supply points with supply capacity determined by its charging stations and where demand and supply points are a distance $Dist_{ij}$ apart. We want to allocate projected demand to supply points such that drivers travel the shortest distance to get their EVs

charged. To achieve this, demand at demand point is allocated to supply point or points across the network where the supply points can only accept demand up to its capacity determined by its infrastructure as illustrated in Figure 2(b). This approach deals with uncertainty and empirically proves to be more efficient. This can be formulated as the classic transportation problem [9] and solved to optimality using linear programming [10]. Note that our aim here is not to solve the transportation problem but to find an allocation of demand to supply that informs us of how well our infrastructure meets demand by computing the distance cost using the built infrastructure. With this formulation we find an allocation using linear programming solved using the PuLP library in python.

To deal with uncertainty in demand prediction, we multiply the predicted demand at every demand point by a random uniform in the range $(1-\alpha_i, 1+\alpha_i)$ where α_i is error rate at a demand point estimated after every iteration.

3.4. Infrastructure optimization with Evolutionary Strategy

In this study, we adopt the Covariance Matrix Adaptation Evolution Strategy (CMA-ES), a variant of evolutionary algorithms for discrete optimization problems. ES for discrete optimization has been extensively studied. We choose the CMA-ES variant due to its efficient treatment of constraints and integer values, making it well-suited for our infrastructure allocation problem. By adjusting the search bounds in certain dimensions, we demonstrate the suitability of CMA-ES for the EV network optimization problem. We adopt CMA-ES with margin whose main features, particularly the lower-bounding marginal probability, are discussed in relation to their application in our problem.

We describe CMA-ES and how we scale down solutions to a smaller search space. Given an objective function $f: R^N \rightarrow R$ in a search space, the CMA-ES samples an N-dimensional candidate solution $x \in R^N$ from a multivariate gaussian distribution (MGD) with mean $m \in R^N$, covariance matrix $C \in R^{NxN}$ and a step size $\sigma \in R_{>0}$. The MGD is in the form $\mathcal{N}(m, \sigma^2 C)$ and the parameters are updated based on the objective function value $f(x)$. The solution is evolved from one generation to the next until a stopping criterion is met. In every generation the Algorithm updates candidate solutions by doing the following.

1. Sample and Evaluate Candidate Solutions: Candidate solutions are generated in the t^{th} generation by independently sampling from the MGD distribution as $y_i = \xi_i\sqrt{C^t}$ and $x_i = m^t + \sigma^t y_i$

where $\xi_i \sim N(0, I)$ is a zero mean random vector with a covariance matrix of the identity matrix I. The candidate solutions generated are evaluated on the objective function and ranked. y_i is a random vector corresponding to x_i.

2. Update Mean Vector: This uses the weighted sum of the of the best μ candidates where μ is a parameter less the number of candidates in the given generation and is calculated as follows.

$$m^{t+1} = m^t + c_m \sum_{i=1}^{\mu} w_i (x_i - m^t) \quad (8)$$

where c_m is the mean vector learning rate and w_i is the weight in the range [0,1], whose value depends on the rank of the candidate solution with highly ranked solutions having higher weights. Additionally, the sum of all the μ weights must sum to 1.

The weight of each individual candidate solution w_i is computed by first sorting the individuals in the population based on their fitness values. The best individual (highest

fitness) receives the highest rank, and the worst individual (lowest fitness) receives the lowest rank. The weight of each solution is then calculated using a linear interpolation formula as follows

$$w_i = \frac{\sum_{j=1}^{\mu} ln(\mu + 0.5) - ln(j)}{ln(\mu + 0.5) - ln(j)} \tag{9}$$

3. Compute Evolution Paths: Evolutionary paths are used for adaptation of step size and rank-one update of the covariance matrix. They accumulate for a sequence of generations a mean vector of an exponential fading pathway. The step size adaptation p_σ and rank-one update p_c are updated as follows

$$p_\sigma^{t+1} = (1 + c_\sigma)p_\sigma^t + \sqrt{c_\sigma(2 - c_\sigma)\mu_w}\,\frac{1}{\sqrt{C^t}}\sum_{i=1}^{\mu} w_i y_i \tag{10}$$

$$p_c^{t+1} = (1 + c_c)p_c^t + h_\sigma\sqrt{c_c(2 - c_c)\mu_w}\,\sum_{i=1}^{\mu} w_i y_i \tag{11}$$

where c_c and $c_\sigma$are cumulative rates and h_σ is an indicator function used to suppress a rapid increase in p_c and is computed as $1\left\{||p_\sigma^{t+1}|| < \sqrt{1 - (1 - c_\sigma)^{2(t+1)}}\left(1.4 + \frac{2}{N+1}\right)E[||N(0,N)||]\right\}$. μ_w *is the weignt of the lowest rank candidate solution.*

4. Update step-size and Covariance Matrix: The step size is updated using the evolutionary step size adaptation path as follows

$$\sigma^{t+1} = \sigma^t \exp\left(\frac{c_\sigma}{d_\sigma}\left(\frac{||p_\sigma^{t+1}||}{E[||N(0,I)||]} - 1\right)\right) \tag{12}$$

where d_σ is a step-size adaptation parameter and $E[||N(0,I)||]$ is the expected Euclidean norm sampled from a standard gaussian distribution and is computed as $\sqrt{N}(1 - \frac{1}{N} + \frac{1}{21N^2})$. The covariance matrix is updated using the rank-one update as follows

$$C^{t+1} = \left(1 - c_1 - c_\mu\sum_{i=1}^{\lambda} w_i + (1 - h_\sigma)c_1c_2(2 - c_c)\right)C^t + c_1 p_c^{t+1}p_c^{(t+1)T} + c_\mu\sum_{i=1}^{\lambda} w_i^o y_i y_i^T \tag{13}$$

where c_1 and c_μ are the learning rates for the rank-one and rank- μ *update.* $w_i^o = w_i.\left(1\ if\ w_i \geq 0\ else\ \frac{N}{y_i C^{(t)-\frac{1}{2}}}\right)$

The CMA-ES algorithm is efficient for high dimensional search problems but is shown to struggle with dimensions where the search domain is large which is the case with our problem. To handle this, we scale down the upper bound of each dimension to 1 so that the algorithm searches for parameters in the range 0 to 1 which is best suited for the algorithm. After obtaining a solution, the solution is rescaled to a value in the range of the standard search range and rounded to the nearest integer. This helps the algorithm converge faster and is able to efficiently search the problem space.

4. Experiments, Results and Discussion

In this section, we present numerical results for our proposed NEO framework algorithms on the shell.ai dataset [8] and an augmented dataset. The algorithm is compared with two naive baseline allocation algorithms, a state-of-the-art discrete evolutionary strategy algorithm and a heuristic for EV allocation. We also study the effect of uncertainty quantification by comparing the performance of our ES algorithm

with and without uncertainty quantified. Additionally, we experiment on using other optimization methods in the infrastructure optimization section which is possible because on our design.

Hyperparameters are an influential factor to the behavior of an algorithm and the choice of parameters to use varies with application. It is important to note that these parameters are not universally optimal and may need to be adjusted based on the specific problem being solved. Additionally, tuning hyperparameters can be a time-consuming and computationally expensive process, so it is important to carefully consider which parameters to test and use. With extensive testing, the best parameters worked well for us were those proposed in [12]. Our implementation followed that defined in [12] which proved to be robust and stable.

4.1. Simulation results

We run our experiments with and without uncertainty in-cooperated into our algorithm and compare its performances as listed in the Table 1. In the comparison method we use the algorithms as shown in the references and ALL and NONE strategies. In the ALL strategy, we build charging stations at all parking slots without chargers at each supply points. This builds each supply point to maximum capacity by building FCS to the remaining slots. The NONE strategy simply means we do not build any charging stations. With the ALL and NONE strategies, we can effectively compare the gains losses incurred by an allocation algorithm from doing nothing and from over supplying infrastructure. The results are shown in Table 1.

Table 1. Performance of algorithms

	Shell.ai Dataset			Augmented Dataset		
	IC	DC	Cost	IC	DC	Cost
ALL	4447	964982	578,993,647	4447	965348	386,143,647
NONE	1499	2422144	968,859,099	1499	2423847	969,540,299
Heuristic [13]	2293	1904248	761,701,493	2363	1938746	775,500,763
GA [14]	2370	1884401	753,762,770	2382	1897630	759,054,382
ES [11]	2819	1748134	699,256,419	2912	1749367	699,749,712
CMA-ES [12]	2958	1667258	666,906,158	2947	1668347	667,341,747
CMA-ES (Ours)	3019	1484934	593,976,619	3004	1492834	597,136,604
CMA-ES (Ours + Uncertainty)	2956	1336748	534,702,156	2943	1349237	539,697,743

Table 2. Performance of Algorithms with uncertainty consideration

	Shell.ai Dataset			Augmented Dataset		
	IC	DC	Cost	IC	DC	Cost
Heuristic	2311	1892380	756,954,311	2344	1894389	757,757,944
GA	2420	1881286	752,516,820	2489	1891284	756,516,089
ES	2991	1713826	685,533,391	2999	1718374	687,352,599
CMA-ES	3123	1584057	633,625,923	3133	1584498	633,802,333
CMA-ES (Ours)	2956	1336748	534,702,156	2943	1349237	539,697,743

4.2. Discussions

The performance evaluation of optimization algorithms in terms of Infrastructure Cost (IC), Dissatisfaction Cost (DC), and their combined measure (referred to as Cost)

modeled in equations 3, 4, and 5, respectively, is depicted in Table 1 and Table 2. Table 1 presents the outcomes obtained using five distinct optimization algorithms. Notably, lower IC values in Table 1 indicate superior efficiency in optimizing infrastructure cost. Upon careful examination of Tables 1 and 2, it is evident that NONE, Heuristic, and GA algorithms exhibit significantly improved performance in IC compared to the remaining algorithms. This indicates their remarkable capability to identify the most optimal configuration of infrastructure while minimizing costs.

On the other hand, when evaluating DC, ALL and CMA-ES (Ours + Uncertainty) algorithms demonstrate noteworthy advancements. The heightened performance of NONE and ALL algorithms, particularly in IC and DC, can be attributed to their simplistic approach, involving the allocation of either no infrastructure or full infrastructure without due consideration. However, it is essential to strike a balance between IC and DC simultaneously, as this is the primary objective. In this regard, CMA-ES and CMA-ES (Ours + Uncertainty) algorithms exhibit remarkable competence, effectively managing both objectives.

The superior performance of CMA-ES (Ours + Uncertainty) algorithm can be attributed to the incorporation of uncertainty, which significantly influences the decision-making process concerning the location and extent of infrastructure development. This inclusion of uncertainty enhances the algorithm's ability to optimize infrastructure allocation and maintain a balance between IC and DC, ultimately resulting in its superior performance.

5. Conclusion

We have presented an approach for infrastructure allocation and demand-supply balancing in EV charging networks. Our approach combines neural networks, evolutionary strategy, and linear programming techniques to optimize the allocation of charging stations. By iteratively building and evaluating the infrastructure while considering uncertainty in demand, we aim to minimize infrastructure cost and dissatisfaction cost. Our approach provides a framework that can be easily adapted to any EV network type, meeting the requirements of real-world charging network infrastructure. It allows for the utilization of any efficient discrete optimizer for high-dimensional problems. Moreover, by dealing with uncertainty in demand prediction, we ensure a dynamic balance between infrastructure cost and driver satisfaction. Overall, our approach offers a promising solution to the challenge of infrastructure allocation and demand-supply balancing in EV charging networks. It can reduce driver anxiety, optimize resource utilization, and support long-term planning horizons. While our work focuses on existing supply points, future research will explore the placement of new supply points to further enhance the charging network's capabilities.

Acknowledgments. This work is supported by the National Natural Science Foundation of China (Grants Nos. 71901152, 71971143), Guangdong Basic and Applied Basic Research Foundation (2023A1515010919, 2020A1515010752), Guangdong Innovation Team Project of Intelligent Management and Cross Innovation (2021WCXTD002), Shenzhen Stable Support Grant (Grant No. 20220810100952001), and the Shenzhen University - Lingnan University Joint Research Programme.

References

[1] Fadda, E., Manerba, D., Cabodi, G., Camurati, P., & Tadei, R. (2021). Evaluation of optimal charging station location for electric vehicles: An italian case study. In Recent Advances in Computational Optimization: Results of the Workshop on Computational
Optimization WCO 2019 (pp. 71–87). Springer.
[2] Huang, K., Kanaroglou, P., & Zhang, X. (2016). The design of electric vehicle charging network. Transportation Research Part D: Transport and Environment, 49, 1–17.
[3] Quddus, M. A., Yavuz, M., Usher, J. M., & Marufuzzaman, M. (2019). Managing load congestion in electric vehicle charging stations under power demand uncertainty. Expert Systems with Applications, 125, 195–220.
[4] Pourgholamali, M., Homem de Almeida Correia, G., Tarighati Tabesh, M., Esmaeilzadeh Seilabi, S., Miralinaghi, M., & Labi, S. (2023). Robust design of electric charging infrastructure locations under travel demand uncertainty and driving range heterogeneity. Journal of Infrastructure Systems, 29, 04023016.
[5] Almaghrebi, A., Aljuheshi, F., Rafaie, M., James, K., & Alahmad, M. (2020). Data-driven charging demand prediction at public charging stations using supervised machine learning regression methods. Energies,13, 4231.
[6] Hafeez, A., Alammari, R., & Iqbal, A. (2023). Utilization of EV charging station in demand side management using deep learning method. IEEE Access, 11, 8747–8760.
[7] Reddy, A. K. V. K., & Narayana, K. V. L. (2022). Metaheuristics optimization in electric vehicles-an extensive review. Renewable and Sustainable Energy Reviews, 160, 112285.
[8] Shell. (n.d.). Digital and AI Competitions. Retrieved April 17, 2023, from https://www.shell.com/energy-and-innovation/digitalisation/digital-and-ai-competitions.html
[9] Ford Jr, L. R., & Fulkerson, D. R. (1956). Solving the transportation problem. Management Science, 3(1), 24-32.
[10] Luderer, B., Nollau, V., & Vetters, K. (2007). Linear Programming. Transportation Problem. Mathematical Formulas for Economists, 129-138.
[11] Sawada, J., Ono, I., & Kobayashi, S. (2020). Discrete optimization by evolutionary strategies with a diversity-inducing mechanism. IEEE Transactions on Evolutionary Computation, 24(4), 688-699.
[12] Hansen, N., & Akimoto, Y. (2021). CMA-ES: Covariance Matrix Adaptation Evolution Strategy. CyberAgent, Inc. Github repository. Retrieved April 29, 2023, from https://github.com/CyberAgentAILab/cmaes.
[13] A Heuristic Algorithm for Placement of Electric Vehicle Charging Stations" by A. M. Al-Saggaf, in the Journal "IEEE Transactions on Smart Grid" (2016)
[14] A genetic algorithm-based optimization approach for planning electric vehicle charging station locations" by J.A. Roa-Garcia, R.V. Sanz-Bobi, R.J. Gómez-García, in the journal "Applied Energy" (2021)

Fuzzy Systems and Data Mining IX
A.J. Tallón-Ballesteros and R. Beltrán-Barba (Eds.)

doi:10.3233/FAIA231005

The Role of Data Stream Mining in Improving Self-Medication Practices in the Syrian Arab Republic

Labeb Abood [1]
Belgorod State University, Belgorod 308007, Russian Federation

Abstract. Self-medication is a widespread practice throughout the world, especially in the Syrian Arab Republic. However, if done incorrectly, this method might be harmful. Data stream mining, which involves analyzing vast amounts of data from multiple sources, has proven to be an effective technique for enhancing self-medication practices. The role of data stream mining, and how it may evaluate information from various sources like social media, electronic health records, pharmacy sales data, sensor-based medical devices, etc. have been explored for the research. Healthcare professionals in Syria can improve patient outcomes and safety related to self medication by employing data stream mining to uncover important information about patient behaviors, drug effectiveness, and adverse events. In this paper, a strategy for generating evidence-based medical data utilizing data stream mining techniques is suggested. Here, methods including association rule mining, categorization, and data clustering have been described. For future progression of this research, the information gap and other data collection-related problems need to be resolved. The implementation demonstrates that healthcare professionals can use a variety of data stream mining techniques to better understand drug usage patterns and spot opportunities while also learning about the prevalence of self-medication in different parts of the Syrian Arab Republic.

Keywords. Self-medication, data stream mining, Syria, data mining in healthcare, data clustering.

1. Introduction

By providing real-time analysis of health data that can spot changes and patterns in a person's health, mining data streams can enhance self-medication. The term “self-medication” is a common term in the medical field. People engage in daily self-care of their health, and practice self-medication in the form of personal care. [1] Self-medication has traditionally been defined as “the taking of drugs, herbs or home remedies on one's own initiative, or on the advice of another person, without consulting a doctor.” [2]

There are no accurate statistics about self-medication specifically for those countries where the medical sector lacks many basic facilities to fulfill the demand of the people. The Syrian Arab Republic is one of them. It’s difficult to identify how many people

[1] Corresponding Author, Labeb Abood, Belgorod State University, Belgorod 308007, Russian Federation; E-mail: marcabood028@gmail.com.

exercise self-medication and the consequences related to this practice. The lack of access to the information necessary to improve "self-medication" in Syria, make it more difficult to implement the proposed approach. For this reason, a unique method has been created to gather the data in a continuous flow. Memory errors can be decreased and dynamic elements of health phenomena can be better understood by combining self-reported data with other reality mining data streams [3]. In the areas of disease risk assessment and clinical decision support, the use of big data mining in clinical care has been examined [4].

The use of data stream mining in self-medication practices has several benefits. Firstly, it can help identify the most commonly used drugs and their indications, which can aid in the development of evidence-based treatment guidelines. Secondly, it can help healthcare providers identify potential drug interactions and side effects, which can reduce the risk of adverse events. It also can assist healthcare professionals in identifying individuals who are more susceptible to prescription misuse or abuse, allowing them to take early action and minimize harm. Taking into account all of these, an effort has been made through this research to improve the practice of self-medication in Syria.

Overall, data stream mining has the potential to revolutionize self-medication practices in Syria and other parts of the world. By leveraging this technique, healthcare providers can improve patient outcomes, reduce healthcare costs, and enhance the overall quality of care.

2. Problem Statement

In Syria, the need for improved self-medication practices is particularly acute due to the ongoing conflict and resulting healthcare system challenges. According to a study conducted at Damascus Hospital in Syria, 67.3% of 453 adult inpatients practiced self-medication, with analgesics, antipyretics, and antibiotics being the most commonly used drugs [5].

Another study found that the 7-day prevalence of medicine use among Syrian adults was 34.9%, indicating a significant percentage of individuals practicing self-medication [6]. However, it is essential to note that self-medication with antibiotics as prophylactics against COVID-19 has also been observed, with an estimated 19.5% of participants engaging in this practice [7]. These findings suggest that self-medication is widespread in Syria and highlight the need for further investigation to control its risks, such as antibiotic resistance and misdiagnosis.

Therefore, the use of data stream mining could be particularly beneficial in this context. By analyzing data from multiple sources, healthcare providers can gain a more comprehensive understanding of drug usage patterns and identify opportunities for intervention.

3. Research Methodology

The information from numerous medical devices and search engines was used to construct the dataset for this research. While different search engines are used to gather data on self-medication activities, medical devices are utilized to collect data on vital signs like heart rate, blood pressure, and others. Using data stream mining techniques,

the data is gathered in real-time. The process of dataset creation and stream mining is defined in figure 1.

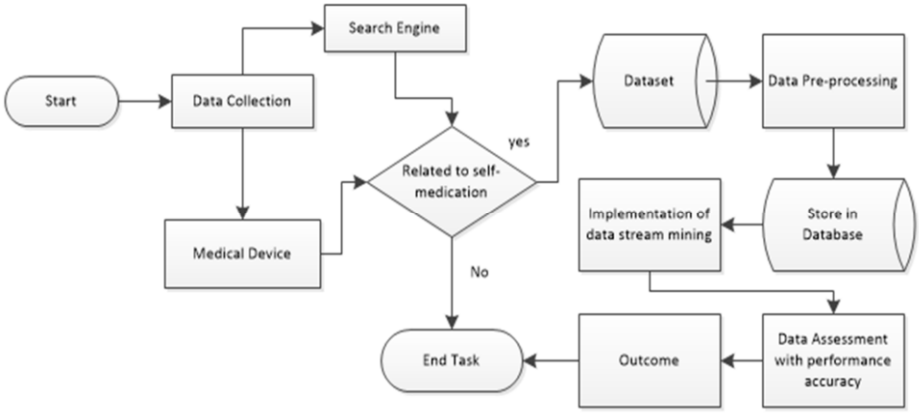

Figure 1. The process of data collection and implementation of stream mining techniques.

The collected data is preprocessed to remove any noise and outliers. This involves data cleaning, data transformation, and data reduction techniques. We then stored the cleaned data in a database for further analysis.

The cleaned data is analyzed using three data stream mining techniques:

- Clustering,
- Classification, and
- Association rule mining.

While classification is used to forecast the likelihood of self-medication activities based on specific criteria, clustering is used to group similar data points together. To find patterns and connections between self-medication practices and other factors, association rule mining is performed.

The analysis's findings are assessed using measures for performance accuracy. By contrasting the outcomes of the data stream mining techniques with the source data, the evaluation will be carried out.

4. Implementation

Collected data related to self medication from various regions of Syria has been prepared for implementing different data steaming techniques. Various search engines, such as Google, Yandex, Yahoo, Bing, and YouTube, have been utilized for data collection. Health-related trending topics in the Syrian Arab Republic have been examined. Then, the topics that had the highest percentage of exploration were chosen using data stream mining techniques described below -

4.1 Data stream Clustering

The pre-processed data is used for applying stream clustering. It is one of the most suitable methods for real-time data stream processing, because it can be applied with less prior information about the data and it does not need labeled instances. [8]

A Python implementation of the data stream clustering algorithm named "DenStream" is applied for the collected data. [9] Where micro clusters have been used. Micro-clusters are a popular technique in stream clustering, which maintain the compact representation of the clustering. [10]

For clustering text documents, a spherical k-means clustering algorithm is generally used. [11] This multivariate numerical data clustering is done using a traditional clustering method. Documents d_i, are represented by feature vectors x_i, clustering this data into k groups is to minimize the function:

$$\sum_i d(x_i, p_{c(i)}) \quad (1)$$

Where, $p_{c(i)}$ is the function of centroid representing an assignment of c of objects i to cluster ids $c(i) \in \{1,\ldots, k\}$ for a suitable similarity measured. [11]

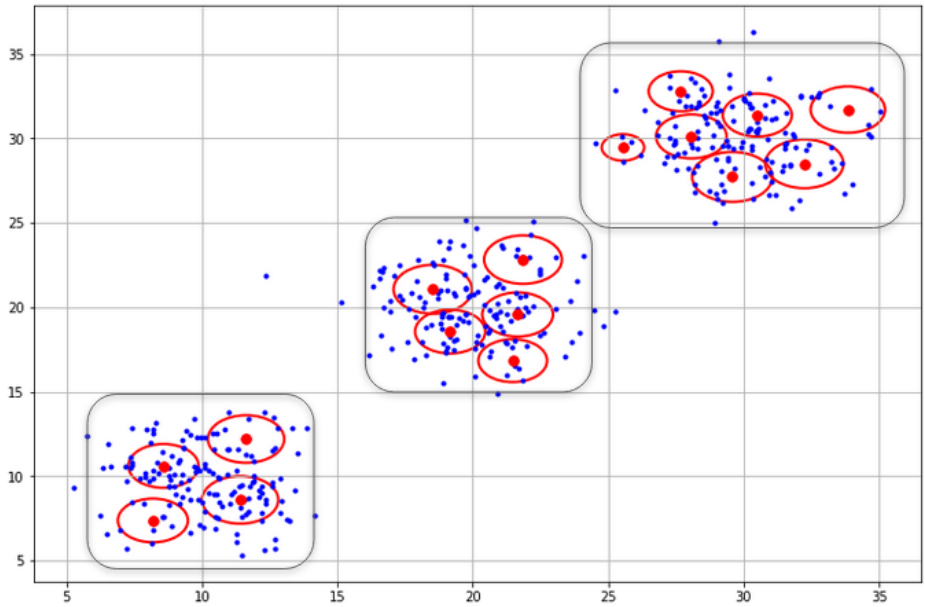

Figure 2. Random sample of potential micro-cluster using DenStream. [9]

4.2 Data classification

Data classification is the process of classifying data into appropriate groupings (or "classes") based on shared traits, such as their degree of sensitivity, the dangers they pose, and the compliance laws that protect them. [12]

4.3 Association rule mining

Association rule mining (ARM) is used to define the relation between a large number of data objects. [13]

5. Results and Analysis

The result shows Cholera has been a health related most discussed topic for the last 12 months in the Syrian Arab Republic.

Table 1. Keywords categorization using search queries in search engines for the Damascus region in the Syrian Arab Republic.

Keywords	Total Search (Damascus)
cholera	4384
cholera symptoms	662
cholera treatments	41
cholera home remedies	33
how to treat cholera at home	67
cholera medicine	987
cholera complications	598
cholera side effects	521

Having this in mind, these topics and questions were selected for the categorization of the keywords of the dataset. The information is gathered for various locations of Syria using different search engines, and then it is integrated to use data stream techniques.

The data reveals that searches for self-medication are more prevalent in the Damascus area. Given that medical equipment was only examined from there, a variety of data mining approaches were used. The percentage of keyword searches in figure 3 is significantly consistent across all of Syria.

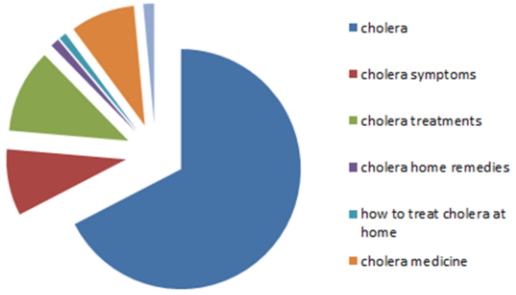

Figure 3. An average percentage for various cholera-related keywords in the Syrian Arab Republic.

While other strategies also had an average accuracy of over 80%, the data classification technique demonstrated an accuracy of over 85%.

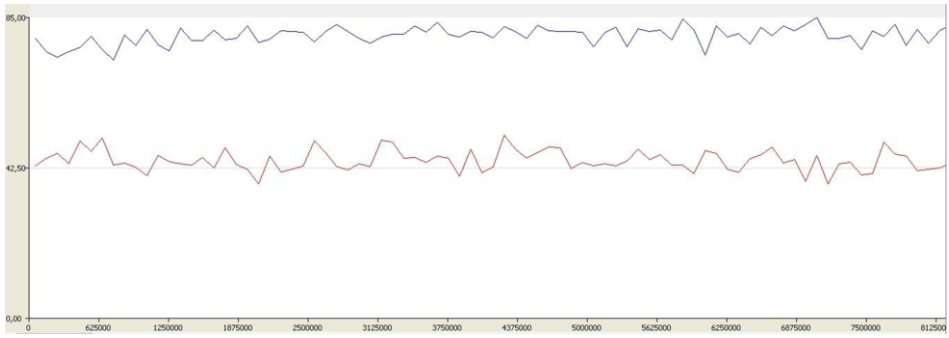

Figure 4. Average accuracy, and loss of the training and test set.

MOA (Massive online Analysis) framework has been used to evaluate methods for mining tasks on evolving data streams over the full space only. [14] With the assistance of around 4,000 participants over the course of 30 days, a second individual study was conducted in the Damascus region, and the sample data was gathered while taking the findings of the earlier studies into consideration. To assess the situation relating to cholera self-medication, data has been gathered from various medical devices and surveys.

The analysis of the result shows the following findings -

- Women look for self-medication more than men.
- Patients have a true sign of eagerness in order to improve the practice.
- Proper information, guidelines, and awareness can improve this practice rapidly among both men and women.
- It is necessary to look for the data which are not only written in English but also in Arabic.
- A high-quality dataset with an approach for collecting data can make the result more accurate.

6. Conclusion

Data stream mining has become a potent tool for enhancing self-medication practices and unearthing insightful information from a variety of healthcare data sources. The study has shown the method's potential for detecting self-medication-related patient behaviors, pharmacological efficacy, and adverse events in the Syrian Arab Republic. Healthcare practitioners can create evidence-based medical data to improve patient outcomes and safety by using techniques including association rule mining, classification, and data clustering. To assure the efficacy and dependability of data stream mining in healthcare, more research is necessary to address the knowledge gap and data collection-related issues. Overall, the application of data stream mining techniques can give healthcare practitioners a plethora of knowledge and enable them to make informed decisions.

References

[1] Vizhi SK, Senapathi R. Evaluation of the perception, attitude and practice of self-medication among business students in 3 select Cities, South India. International Journal of Enterprise and Innovation Management Studies (IJEIMS) July-December. 2010;1(3):40–4.

[2] Hernandez-Juyol M, Job-Quesada JR. Dentistry and self-medication: A current challenge. Med Oral. 2002;7:344–7.

[3] Pentland A, Lazer D, Brewer D, Heibeck T. Using reality mining to improve public health and medicine. Stud Health Technol Inform. 2009;149:93-102. PMID: 19745474.

[4] Zhang Y, Guo SL, Han LN, Li TL. Application and Exploration of Big Data Mining in Clinical Medicine. Chin Med J (Engl). 2016 Mar 20;129(6):731-8. doi: 10.4103/0366-6999.178019. PMID: 26960378; PMCID: PMC4804421.

[5] Abdelwahed RNK, Jassem M, Alyousbashi A. Self-Medication Practices, Prevalence, and Associated Factors among Syrian Adult Patients: A Cross-Sectional Study. J Environ Public Health. 2022 Jun 28;2022:9274610. doi: 10.1155/2022/9274610. PMID: 35800339; PMCID: PMC9256391.

[6] Aljadeeah S, Wirtz VJ, Nagel Cross-sectional survey to describe medicine use among Syrian asylum seekers and refugees in a German federal state: looking beyond infectious diseases BMJ Open 2021;11:e053044. doi: 10.1136/bmjopen-2021-053044

[7] Marcel Alied, Antimicrobial resistance, COVID-19 and self-medication in Syria: a potential boost for an already escalating problem, JAC-Antimicrobial Resistance, Volume 3, Issue 3, September 2021, dlab100, https://doi.org/10.1093/jacamr/dlab100

[8] Alaettin Z., Volkan A., Data Stream Clustering: A Review, CoRR, 28 Jul 2020, https://doi.org/10.48550/arXiv.2007.10781.

[9] Feng Cao, Martin Ester, Weining Qian, Aoying Zhou, Density-Based Clustering over an Evolving Data Stream with Noise, Conference: Proceedings of the Sixth SIAM International Conference on Data Mining, April 20-22, 2006, Bethesda, MD, USA, 2006, DOI: 10.1137/1.9781611972764.29.

[10] Amineh Amini, Teh Ying Wah, Density Micro-Clustering Algorithms on Data Streams: A Review, Proceedings of the international MultiConference of Engineer and Computer Scientists 2011, Vol I, IMECS 2011, March 16-18, 2011, Hong Kong.

[11] Kokate, U.; Deshpande, A.; Mahalle, P.; Patil, P. Data Stream Clustering Techniques, Applications, and Models: Comparative Analysis and Discussion. Big Data Cogn. Comput. 2018, 2, 32. https://doi.org/10.3390/bdcc2040032

[12] Data Classification Guide, URL: https://www.spirion.com/data-classification

[13] Akash S., Vikram R., A Comparative Analysis of Association Rule Mining Algorithms, 2021 IOP Conf. Ser.: Mater. Sci. Eng. 1099 012032, DOI 10.1088/1757-899X/1099/1/012032.

[14] Hassani M., Kim Y., Seidl T. (2013). Subspace MOA: Subspace Stream Clustering Evaluation Using the MOA Framework. 7826. 10.1007/978-3-642-37450-0_33.

Fuzzy Systems and Data Mining IX
A.J. Tallón-Ballesteros and R. Beltrán-Barba (Eds.)

doi:10.3233/FAIA231006

An End-to-End Solution for Net Promoter Score Estimation and Explanation from Social Media Using Natural Language Processing

Xinghua LIANG [a,1], Yingwei YU [a], Diego SOCOLINSKY [a], Tianyi MAO [a], Carlos ROJAS [a], Alex GORYAINOV [a], Fang WANG [a] and Xin CHEN [a]
[a] *Machine Learning Solutions Lab, Amazon Web Services, WA, USA*

Abstract. The Net Promoter Score (NPS) is often used in customer experience programs for measuring customer loyalty. Increasingly more companies seek to automatically process millions of pieces of customer feedback from social media per month in order to estimate their NPS, leveraging advanced analytics like machine learning (ML) and natural language processing (NLP). Discovering trends and themes in customer interactions helps explain the NPS, empowering companies to improve products and customer experience. In this paper, we describe an end-to-end solution for NPS estimation and explanation from social media. The process includes sentiment analysis on user comments, estimating product information based on text semantics, grouping and tagging user comments for text discovery, and NPS explanation. The solution gives companies the capability to identify overall customer sentiment and common topics in a unified platform, allowing faster analysis and insights on NPS based on customer feedback.

Keywords. Business insights, net promoter score, social media, sentiment analysis, product prediction

1. Introduction

1.1. Motivation

The Net Promoter Score (NPS) [1, 2, 3, 4] is widely used as a measure of customer loyalty, customer satisfaction and potential for growth, and is obtained by aggregating the single-digit answers of a closed question survey. However, for rapidly growing businesses, the number of people answering surveys generally represents a small portion of the overall customer base. Additionally, the NPS provides only a coarse measure and does not capture the reasons behind customer opinions. On the other hand, people often spontaneously voice their opinions via social networks and customer-centric forums, providing insight into how they feel about a product and why. These large and heterogeneous text datasets may include the answers to open questions that are part of the survey used to calculate the NPS. Systematically analyzing customer comments at

[1] Corresponding Author, Xinghua Liang, 227 W Monroe St #1400, Chicago, IL 60606, United States; E-mail: lxinghua@amazon.com.

scale, we can enable businesses to listen to more customer voices and understand the root causes behind trends in NPS.

In this paper we outline a solution realizing that vision, along with a case study using a subset of the Amazon Customer Reviews Dataset (ACR dataset) [5]. We show how we can apply natural language processing and machine learning techniques in a unified platform that enables fast analysis and insights into changes in NPS over time, based on customer feedback.

1.2. Net Promoter Score Computation

The NPS is usually computed from answers to a single survey question with a 0-10 scale: "How likely is it that you would recommend [company X] to a friend or colleague?". The answers are mapped into three classes: promoters (score of 9-10), the passively satisfied (score of 7-8), and detractors (score of 0-6). The NPS is defined as the percentage of promoters minus the percentage of detractors. An additional open question asking to explain the rated answer is also included as part of the survey [1].

1.3. NPS Explanation

Despite being widely adopted, the NPS does not provide any insight into the contributing factors leading to the score. Analysis of the replies to the associated open-ended question may provide such insights. In particular, this may be achieved by identifying specific products people discuss, how they feel about them and any recurring themes connected with them. These goals may be mapped directly into standard NLP and ML problems, namely text categorization, sentiment analysis and topic modeling, respectively. This high-level breakdown facilitates reuse of a solution for similar datasets, such as tweets or customer comments, providing the means to aggregate and handle disparate sources in a unified manner.

1.4. Related Work

The NPS is discussed in [1, 2, 3, 4]. A critical view which addresses overreliance on the score, is presented in [6]. A use case of the application of NLP to extract insights from comments from NPS surveys is presented in [7].

Details of NLP and ML problems and techniques are outside the scope of this work. Sentiment analysis has been a topic of research for over two decades – [8] presents a survey of approaches based on deep learning, and [9] covers earlier techniques in detail. Text classification is also a well-studied problem; in particular, the advantages of the approach we use, fine tuning from embeddings, is discussed in [10]. The survey in [11] covers topic modeling, including approaches that leverage embeddings, as ours does.

Extracting business insights from customers opinions has been studied over the years. It was advised in [12], that the original NPS survey include at least one open question: "What is the primary reason for your score?". Including the correct open question is critical to understanding customer motivations, as studied in [13]. Since many customers are reluctant to complete surveys, one possible mechanism to augment survey data is to include posts and comments spontaneously voiced by the customers. Because the manual analysis of large numbers of comments is infeasible, it has been common to apply machine learning and natural language processing techniques. For instance, the reviews on [14] and [15] focus on healthcare and food delivery services scenarios. Our

work extends this line of work by proposing a mechanism to estimate an analog of the NPS using sentiment analysis. For simplicity, we refer to the original NPS and our proposed method by the same name.

2. Methodology

2.1. Solution Overview

We aim to accomplish the following goals:

- Estimate the NPS for each relevant product via sentiment analysis of customer comments from multiple sources
- Group user comments into clusters to aid in root cause analysis
- Create a unified dashboard to facilitate data exploration

The proposed workflow is shown in Figure 1 and includes four separate modules.

- **Module 1 – Sentiment Analysis:** We use Amazon Comprehend to estimate customer sentiment for all comments.
- **Module 2 – Product Alignment:** We train a supervised deep learning model to predict the most likely relevant product given the comment text. We use a pre-trained multilingual Sentence-BERT model [16] for comment encoding.
- **Module 3 – Comment Clustering:** We develop an unsupervised topic clustering model to group and rank comments for each dataset.
- **Module 4 – Comment Tagging:** We apply part-of-speech tagging to extract keywords from comments. The tags can be used as a filter for comment clusters.

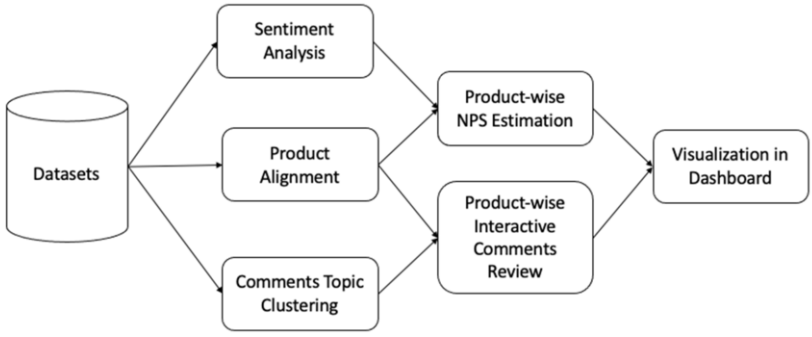

Figure 1. Solution Overview.

2.2. Exploratory Data Analysis

We use online customer feedback datasets to build the solution. Data from social media, review sites and customer service interactions can also be used. Some of the datasets may only contain parts of the relevant information needed for NPS estimation and explanation. Two primary components are needed to build the desired solution. First, we need a tool to estimate the dominant sentiment for millions of customer comments across multiple datasets. Second, in order to identify common trends and customer sentiment about specific products, we need to know which product is being discussed in each

comment. Consequently, at least one dataset must have ground truth product names associated with customer comments. This dataset is used for training a supervised learning model (see Section 2.3 Product Alignment). Other datasets may have no explicit product labels at all. The trained model is used to predict products for any comments missing product information.

2.3. Product-wise NPS Estimation with Sentiment Analysis

2.3.1. Module 1: Sentiment Analysis of User Comments

We estimate comment sentiment using Amazon Comprehend, which is a machine learning service with many NLP features, including sentiment analysis. It has been pre-trained and supports multiple languages including English, making it a good fit for all relevant datasets in our case study.

The sentiment analysis is treated as a classification task. For each comment, Amazon Comprehend will classify the input into one of the following four sentiment classes with confidence scores [17]:

- Positive: The text expresses an overall positive sentiment
- Negative: The text expresses an overall negative sentiment
- Mixed: The text expresses both positive and negative sentiments
- Neutral: The text does not express either positive or negative sentiments

2.3.2. ***Module 2: Product Alignment***

We are interested in estimating NPS for a specific product or product category. Since some relevant datasets may not include such product information, we developed a machine learning model to predict the product based on the text in the comments.

We use a dataset with both user comments and product labels for training a supervised learning model, where the input is the comment text and the output is one out of several product labels. The workflow for training the product alignment model includes comment cleaning, comment embedding, and model training. We start by extracting input comments from the training dataset and cleaning them by removing special characters such as emojis. We then embed comments into a high-dimensional vector space using Sentence-BERT. Finally, we use AutoGluon Tabular [18] to train a classifier that predicts product labels from the embedding vector corresponding to each user comment.

2.3.3. Net Promoter Score Estimation

We estimate the net promoter score using the predicted comments' sentiment for each product in a rolling time window via the Eq. (1) as defined below:

$$NPS_p = \frac{C_p^+ - C_p^-}{T_p} \times 100 \quad (1)$$

where p is the product, C_p^+ is the number of positive comments for product p and C_p^- is the number of negative comments of the same product. The normalizing factor T_p is the total number of comments for product p in the given time window, which can be refreshed daily, weekly, or monthly as a user input. The resulting statistic ranges between

-100 and 100. This is an analog of the original NPS definition, where comments with positive sentiment are taken as promoters and those with negative sentiment as detractors.

2.4. Explaining NPS Changes

*2.4.1. **Module 3: Unsupervised Topic Clustering***

We group comments into topics for ease of browsing. The workflow for topic clustering is illustrated in Figure 2. We encode comments in each dataset using Sentence-BERT and then apply the UMAP algorithm [19] to project the resulting embedding vectors onto a 2-dimensional feature space. Finally, we use the HDBScan algorithm [20], a density-based hierarchical clustering method, to cluster vectors on the feature space.

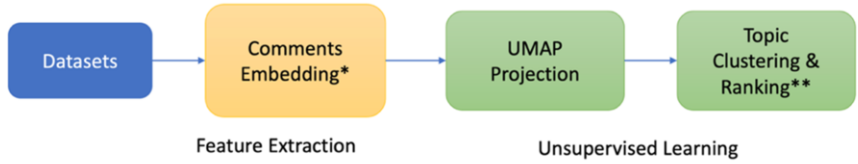

Figure 2. Workflow for Topic Clustering. (*) Comments are embedded with Sentence-BERT; (**) HDBScan is the clustering algorithm.

For example, Figure 3 shows the UMAP projection of comment embeddings for the Electronics product in the ACR dataset described below. Each point in the figure represents the UMAP projection of a single comment. Points are subsequently aggregated into clusters, ranked by size and color-coded. We extract the top five most frequent tags from comments in each cluster and use them to represent the cluster, as discussed in the following section.

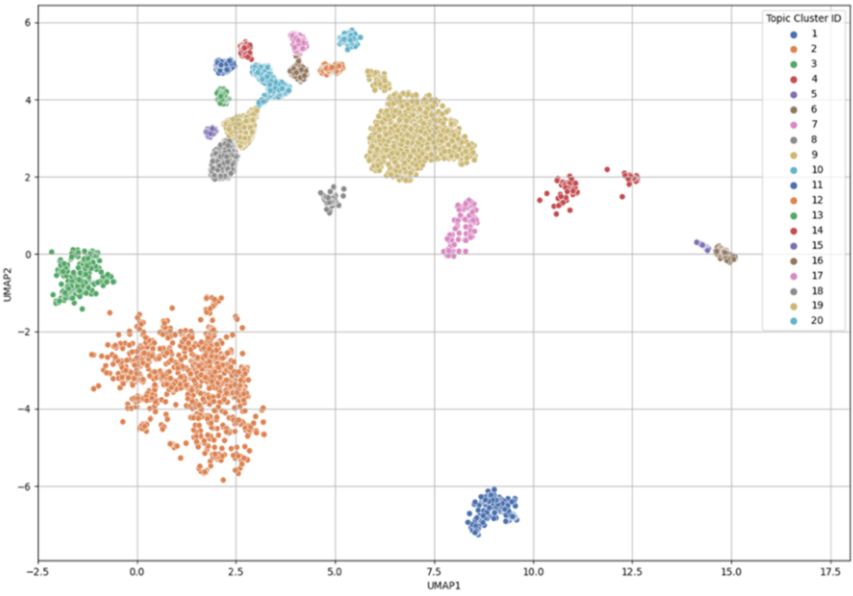

Figure 3. Example comment UMAP projections and clustering results with HDBScan for a single product category. Clusters are color-coded by ID.

2.4.2. Module 4: Comment Tagging

We assign tags to each comment to allow search and facilitate business insights. Tags are words extracted from comments through a three-step process:

- **Lemmatization:** for each word in the comment, we extract the root of the word to minimize variation due to word forms. For example, the word "shirts" is lemmatized to its base form "shirt".
- **Part of Speech (POS) analysis:** we keep only nouns, verbs and adjectives, and discard all other words.
- **Tagging deduplication:** we remove duplicate words and combine the remaining ones into a tag list.

Table 1 below shows the process of extracting tags for the comment "Shirts are too long, with heavy hem".

Table 1. Example of lemmatization and POS analysis. The input is "Shirts are too long, with heavy hem.". The final tag set for this input comment is [shirt, long, heavy, hem].

Input:	Shirts are too long, with heavy hem.	
Word	**Lemma**	**POS**
Shirts	shirt	NOUN
are	be	AUX
too	too	ADV
long	long	ADJ
,	,	PUNCT
with	with	ADP
heavy	heavy	ADJ
hem	hem	NOUN
.	.	PUNCT
Final tags list:	[shirt, long, heavy, hem]	

The survey paper "The Evolution of Topic Modeling" [11] extensively discusses the evolution and challenges of topic modeling methods. It highlights that many newer topic models still suffer from noise pollution in topics and are not scalable to the size of modern data sets. There are very few topic models designed to model on a temporal aspect, which is a significant issue given the speed with which topics on a platform can change. In addition, unsupervised topic models have limitations and that semi-supervised models may be an important future direction that balances the computational cost and the cost of labeling training data.

In contrast, our approach to topic modeling, uses an end-to-end solution for Net Promoter Score (NPS) estimation and explanation from social media. Our solution includes sentiment analysis on user comments, estimating product information based on text semantics, grouping and tagging user comments for text discovery, and NPS explanation. We use Sentence-BERT for comment encoding and apply the UMAP algorithm to project the resulting embedding vectors onto a 2-dimensional feature space. We then use the HDBScan algorithm, a density-based hierarchical clustering method, to cluster vectors on the feature space. The advantages of our approach are as follows:

- **Handling Noise**: our approach uses Sentence-BERT for encoding and HDBScan for clustering, which can handle noise in the data more effectively.
- **Scalability**: our approach is designed to handle large-scale social media data, making it more scalable for modern data sets.
- **Temporal Aspect**: our approach is designed to work with real-time social media data, implicitly taking into account the temporal nature of the data.
- **Supervised Learning**: our approach uses supervised deep learning for product alignment, which can potentially provide more accurate results than unsupervised models.
- **Practical Application**: our approach is designed with a specific application in mind (NPS estimation and explanation), making it more practical and directly useful for businesses.

3. Case Study

We used the ACR dataset to demonstrate the proposed solution for NPS estimation and explanation. This dataset contains over 130+ million customer reviews and 40+ products from 1995 through 2015. For simplicity, we restrict our case study to the ten most popular product categories: automotive, beauty, books, digital software, electronics, gift card, grocery, jewelry, kitchen and music. We sample 1,000 data points per category for each month from January to December, 2014.

3.1. Sentiment Analysis

Figure 4 shows the estimated sentiment for the top ten product categories in the ACR dataset. Positive sentiment comprises the largest percentage. Gift cards have the least negative sentiment, which is understandable since buying and redeeming a gift card is simple and straightforward. In contrast, products in the digital software category have the most negative sentiment. We will show below how the proposed solution can identify the source of this negative sentiment and how it can be addressed.

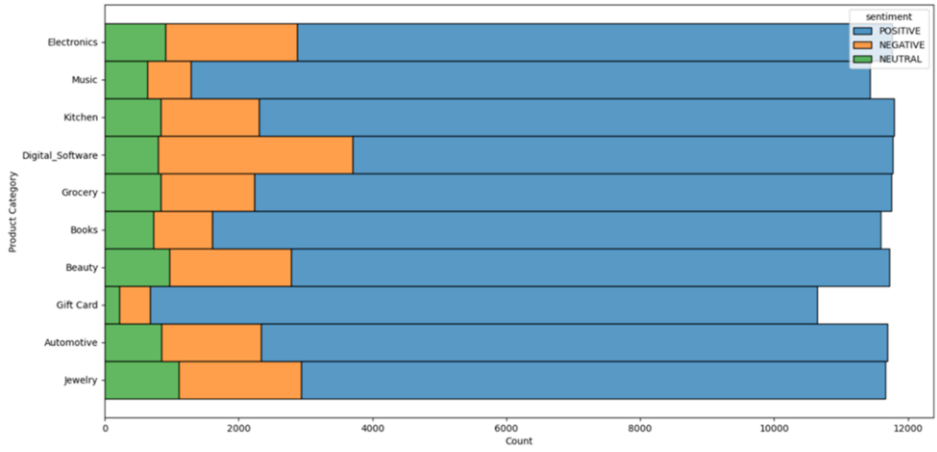

Figure 4. Sentiment result for the Amazon dataset.

3.2. Product Alignment

As described above, in many relevant cases such as social media posts there is no explicit product information. Since the ACR dataset has product information for all user comments, we simulated this situation by using separate sets for product prediction training and inference. We split the ACR dataset into training, validation and testing sets with a ratio of 70:10:20 across all product categories, encoded comments in the ACR dataset into vectors using Sentence-BERT, and trained a multi-class classifier acting on those vectors to predict product categories, achieving 79.5% accuracy for product estimation from the comment text. The confusion matrix is shown in Figure 5(a). Among the ten product categories, the "books" has the highest prediction accuracy, while kitchen is the most difficult one to predict. The model also achieved high ROC-AUC scores, ranging from 95% to 99% for each of the ten product categories. The ROC-AUC scores are shown in Figure 5(b).

3.3. Interactive Dashboard

Amazon QuickSight is a business analytics platform that powers data-driven organizations with unified business intelligence. We created a QuickSight Dashboard to visualize all insights extracted from the ACR dataset (see Figure 6). This dashboard includes 120,000 comments from January through December of 2014. In the Overview panel, besides showing sentiment and product distribution, the bottom left chart presents the NPS trend for 2014, with the score remaining around 70 throughout the year. The bottom right chart shows product-level NPS trends. We see that gift card has the highest NPS and digital software has the lowest NPS, with significant temporal fluctuation.

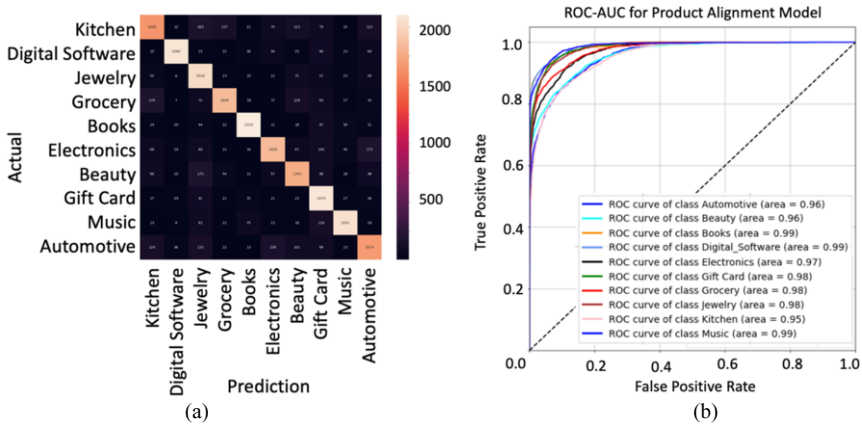

(a) (b)

Figure 5. (a) Confusion matrix for product category prediction. (b) ROC-AUC curve for product category prediction.

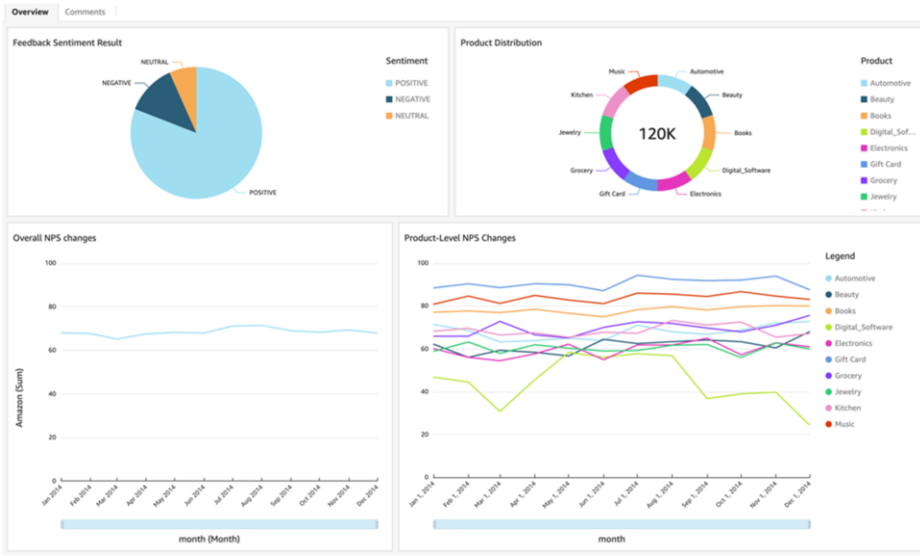

Figure 6. QuickSight dashboard overview.

The dashboard also includes a comments panel which allows business analysts to review individual user comments. By clicking on the interactive sentiment chart and product chart, users can access a filtered view showing only comments about a particular product with a particular sentiment (see Figure 7).

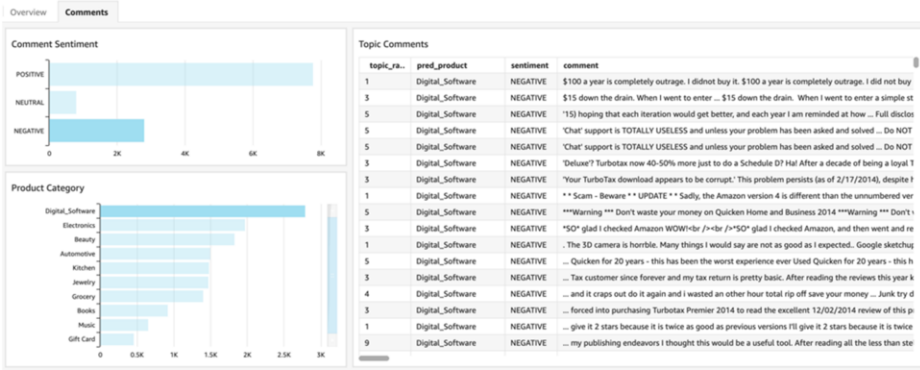

Figure 7. Topic ranking panel in the QuickSight dashboard.

Other visualizations provide insight on the primary themes for each comment cluster. An interactive chart shows topic clusters ordered by number of comments and tags extracted as described above (see Figure 8). By clicking on a particular topic cluster and a particular keyword, users can access a filtered view showing only comments of that cluster which contain the selected keyword. This helps uncover reasons underlying customer sentiment for a particular product and topic, enabling business intelligence and improving customer satisfaction. For example, looking at Figure 8, we see that the main complain about digital software is that it is difficult to download and/or install the software, which makes it unusable for many consumers.

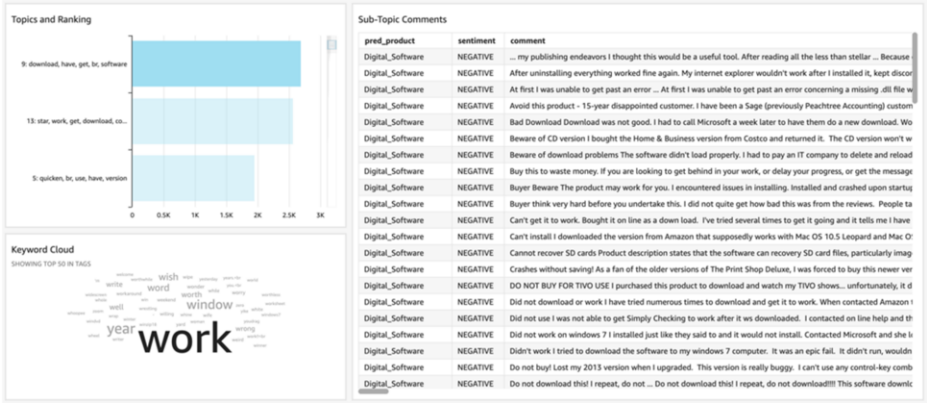

Figure 8. Topic ranking and keyword cloud panel in the dashboard.

4. Deployment

We developed an automated end-to-end pipeline implementing the solution on Amazon Web Services (AWS). We use multiple services including Amazon SageMaker (a machine learning platform), Amazon Simple Storage Service (a cloud storage service), AWS Lambda (an event-driven compute service), Amazon Simple Queue Service (a message queuing service), Amazon Elastic Container Registry (a container storage service) and Amazon QuickSight. The solution architecture is illustrated in Figure 9.

The architecture is designed to have low-overhead, be cost-effective, user-friendly and robust. It can initialize models with historical data, train and perform inference on new incremental data and update insights on a daily basis. It can also allocate computing resources dynamically, either using idle time on existing compute instances or creating dedicated instances and releasing them once processing is complete.

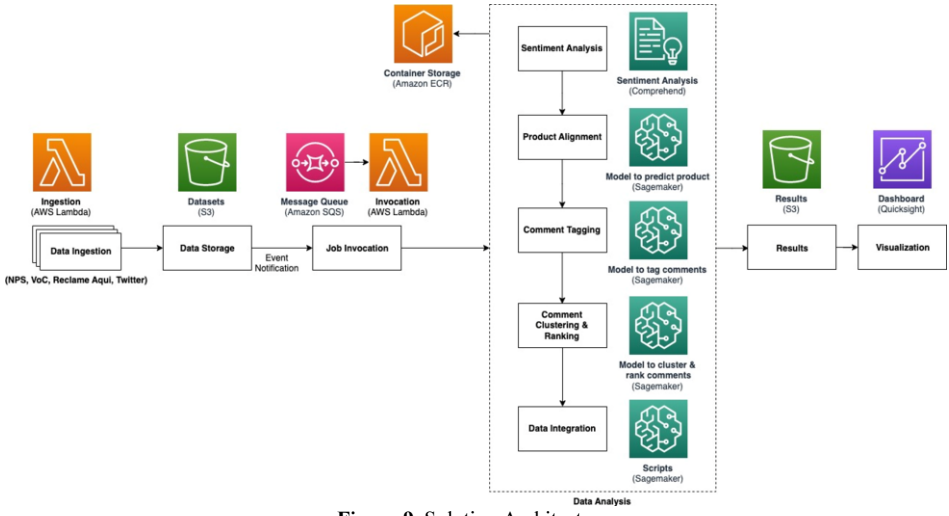

Figure 9. Solution Architecture.

Our pipeline sequentially runs through the following modules:

- A data ingestion module that fetches new daily data and saves it to a designated Amazon S3 bucket.
- An invoking module that receives data update events from a message queue and kickstarts the inference.
- A processing module that retrieves a prebuilt Docker image from Amazon ECR containing all custom models and processes new incremental data, saving the result to another designated Amazon S3 bucket.
- A trigger to refresh the QuickSight dashboard and display the updated results.

Our architecture can be extended to incorporate new models in the processing module, supporting parallelized inference based on different types of data feeds and more frequent update of the insights at additional computation cost.

5. Opportunities for Improvement

One strength of the proposed solution is the ability to seamlessly incorporate additional modules. Emerging large language models (LLMs) present an opportunity to improve this solution, given their wide-ranging capabilities in natural language processing and generation. We performed a simple experiment incorporating the Flan-T5 [21] (flan-t5-xl) language model to offer insights into customers' comments. Since the model supports a limited number of tokens as input, it is not possible to use it for summarization of all comments in a cluster. Only some of the most relevant comments can be included into the prompt template shown in Figure 10a.

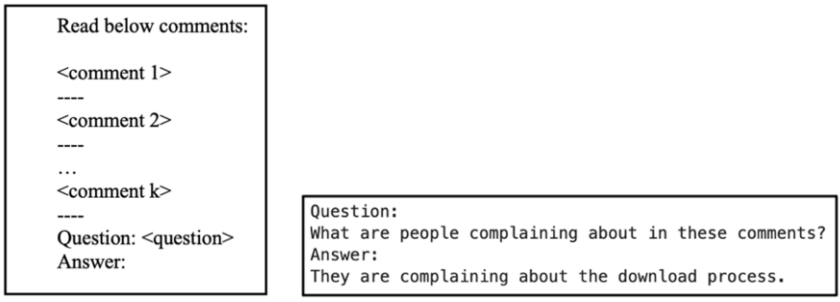

(a) Prompt Template (b) Using LLM to gain Insights

Figure 10. Improving Customer Experience with LLM

Fortunately, our solution already provides topic clustering and ranking. We can include the top-k comments for a particular topic cluster into the prompt template. For example, Figure 8 shows comments with negative sentiment for the 9th topic cluster for digital software. As a test, we included the top 27 comments in the prompt template, with the question “What are people complaining about in these comments?”. Using this prompt, Flan-T5 generates the answer “They are complaining about the download process.”, as shown in Figure 10b. The model’s answer matches our own conclusion based on manual review. This experiment suggests that our solution can easily incorporate a LLM to automatically identify valuable insights from customers' feedback

and better understand their concerns. Our future work includes studying mechanisms to use LLMs in other modules and to identify the best way to integrate them with the solution.

6. Conclusion

In this study, we developed a comprehensive customer comment analytics platform that integrates sentiment analysis, product category prediction, common topic clustering, and keyword extraction, along with an interactive dashboard. Our solution enables business analysts to identify overall customer sentiment, feedback trends, and themes in a unified environment, thereby facilitating faster insights into why net promoter scores (NPS) rise and fall. This, in turn, empowers companies to adjust their strategies for specific product categories in a timely manner.

Our approach is unique in its application of natural language processing and machine learning techniques in a unified platform to analyze changes in NPS over time, based on customer feedback. We validated our methodology using the Amazon Customer Reviews Dataset, which provided us with a rich source of customer feedback across a wide range of product categories.

One of the key findings of our study is the potential of our solution to incorporate large language models (LLMs) to automatically identify valuable insights from customers' feedback and better understand their concerns. This was demonstrated through a test case where the LLM's answer matched our own conclusion based on manual review. Looking ahead, our future work includes studying mechanisms to use LLMs in other modules and identifying the best way to integrate them with our solution. We believe that by scaling our solution, we can enable businesses to listen to more customer voices and understand the root causes behind trends in NPS.

In conclusion, our study contributes to the field by providing a robust and scalable solution for NPS estimation and explanation from social media. We believe that our work will be valuable for businesses seeking to leverage advanced analytics to improve their products and customer experience.

Acknowledgement

The authors would like to thanks to Aldo Arizmendi and Hellen Rosa for many helpful discussions.

References

[1] Reichheld F. The one number you need to grow. Harvard Business Review. 2003; 81(12): 46–124
[2] Reichheld F. The Ultimate Question: Driving Good Profits and True Growth. Harvard Business School Press. 2006
[3] Reichheld F. Darnell D. and B. Maureen, Net Promoter 3.0. Harvard Business Review. Nov – Dec 2021.
[4] Reichheld F. and B. Markey, The Ultimate Question 2.0: How Net Promoter Companies Thrive in a Customer-Driven World. Harvard Business School Press. 2011

[5] Amazon Customer Reviews Dataset. https://s3.amazonaws.com/amazon-reviews-pds/readme.html
[6] Safdar K, Pacheco I: CEOs Embrace a Dubious Metric. The Wall Street Journal (May 16, 2019). Print edition. Online as "The Dubious Management Fad Sweeping Corporate America" at https://www.wsj.com/articles/the-dubious-management-fad-sweeping-corporate-america-11557932084
[7] Zaki M, McColl-Kennedy JR, Neely A. Using AI to Track How Customers Feel — In Real Time. Harvard Business Review. 2021. Available online at https://hbr.org/2021/05/using-ai-to-track-how-customers-feel-in-real-time
[8] Zhang L, Wang S, Liu B. Deep Learning for Sentiment Analysis: A Survey. Preprint arXiv:1801.07883. Wiley Interdisciplinary Reviews - Data Mining and Knowledge Discovery. 2018; 8(4). DOI: 10.1002/widm.1253, (invited paper).
[9] Liu B. Sentiment Analysis: Mining Opinions, Sentiments, and Emotions. Cambridge University Press. June 2015 June.
[10] Howard J, Ruder S. Universal language model fine-tuning for text classification. Association for Computational Linguistics. 2018.
[11] Churchill R, Singh L. The Evolution of Topic Modeling. ACM Comput. Surv. 2022 Jan; 54, 10s, Article 215. DOI: https://doi.org/10.1145/3507900
[12] Reichheld F, Markey R. The Ultimate Question 2.0: How Net Promoter Companies Thrive in a Customer-Driven. Harvard Business Review Press. 2020.
[13] Bone SA, Lemon KN, Voorhees CM, Liljenquist KA, Fombelle PW, Detienne KB, Money RB. "Mere Measurement Plus": How Solicitation of Open-Ended Positive Feedback Influences Customer Purchase Behavior. Journal of Marketing Research. 2017; 54(1):156–170. https://doi.org/10.1509/jmr.14.0232
[14] Khanbhai M, Anyadi P, Symons J, Flott K, Darzi A, Mayer E. Applying natural language processing and machine learning techniques to patient experience feedback: a systematic review. BMJ health & care informatics. 2021; 28(1), e100262. https://doi.org/10.1136/bmjhci-2020-100262
[15] Adak A, Pradhan B, Shukla N. Sentiment Analysis of Customer Reviews of Food Delivery Services Using Deep Learning and Explainable Artificial Intelligence: Systematic Review. Foods. 2022 Nov; 1500. https://doi.org/10.3390/foods11101500
[16] Reimers N, Gurevych I. Sentence-BERT: Sentence Embeddings using Siamese BET-Networks. In 2019 Conference on Empirical Methods in Natural Language Processing and 9th International Joint Conference on Natural Language Processing, Hong Kong, China. 2019. DOI: https://doi.org/10.48550/arXiv.1908.10084
[17] Amazon Comprehend Documentation, URL: https://docs.aws.amazon.com/comprehend/latest/dg/how-sentiment.html
[18] Erickson N, Mueller J, Shirkov A, Zhang H, Larroy , Li M, Smola A. Autogluon-tabular: Robust and accurate automl for structured data. 2020. https://doi.org/10.48550/arXiv.2003.06505.
[19] McInnes L, Healy J, Melville J. UMAP: Uniform Manifold Approximation and Projection for Dimension Reduction. 2018. DOI: https://doi.org/10.48550/arXiv.1802.03426
[20] Campello RJGB, Moulavi D, Sander J. Density-Based Clustering Based on Hierarchical Density Estimates. In: Pei J, Tseng VS, Cao L, Motoda H, Xu G. (eds) Advances in Knowledge Discovery and Data Mining. PAKDD 2013. Lecture Notes in Computer Science. 2013; vol 7819. Springer, Berlin, Heidelberg. https://doi.org/10.1007/978-3-642-37456-2_14
[21] Chung HW, Hou L, Longpre S, et al. Scaling Instruction-Finetuned Language Models. DOI: https://doi.org/10.48550/arXiv.2210.11416

Fuzzy Systems and Data Mining IX
A.J. Tallón-Ballesteros and R. Beltrán-Barba (Eds.)

doi:10.3233/FAIA231007

Robust Convolutional Neural Network for Image Classification with Gaussian Noise

Sugiyarto Surono[a,1], Dyiyah Kresna Eni Arofah[a] and Aris Thobirin[a]
[a]*Department of Mathematic, FAST Universitas Ahmad Dahlan Yogyakarta, Indonesia*

Abstract. A Convolutional Neural Network (CNN) is one branch of Deep Learning widely used for image classification. CNN have complex architectures and capable of achieving high accuracy and producing good results. However, CNN have limitations, especially when dealing with noisy images. Image noise can decrease classification performance and increase network training time. This research was tested the robustness of two CNN methods, namely VGG16 and ResNet50, in processing images with added Gaussian noise at various levels, without any preprocessing. The dataset used is the Rice Image Dataset, which consists of images of 5 different types of rice. The data is divided into three parts: 70% for training, 20% for testing, and 10% for validation. The results of this study show that as the variability in generating Gaussian noise in the images increases, the loss function value consistently increases, and the accuracy decreases. However, the increase in the loss function value and the decrease in accuracy are not significantly different among the different levels of noise variability.

Keywords. Convolution Neural Network (CNN), VGG16, ResNet 50, Noise Gaussian

1. Introduction

Deep Learning is a branch of Artificial Intelligence that revolves around machine learning methods, particularly focused on neural network modeling. Recognized for its exceptional precision [1], Deep Learning has witnessed a substantial surge in popularity recently, exhibiting mastery across diverse domains such as image, video, audio, and text recognition [2]. A prominent tool within Deep Learning for image classification is Convolutional Neural Network (CNN) [3].

Classification, a pivotal technique in data analysis, employs models to categorize data into distinct classes based on predefined criteria [4]. Its objective is to predict the class of an object in each data, thereby unveiling characteristic traits of classes and data types [5]. The criteria for classification should be predetermined prior to segregating data into identifiable classes. Various factors, including the quantity and types of features, influence classification studies. These criteria continue to evolve as data goes through manipulation, a process that endures until logical data grouping is achieved from both structural and practical perspectives.

CNN possesses the capability to directly process images and yield definitive classification output, regardless of whether preprocessing is applied [6]. Harnessing an

[1] Corresponding Author, Sugiyarto Surono, FAST Universitas Ahmad Dahlan Yogyakarta, Indonesia; Email: sugiyarto@math.uad.ac.id

intricate architecture, CNN finds widespread utility in tasks involving image pattern recognition, consistently attaining heightened accuracy levels and favorable results [7]. However, in specific scenarios where this model is employed, image data quality may not be consistently high, potentially introducing degradations that manifest as image noise [7]. This noise embedded within images can trigger a decline in image quality [8]. In the context of image processing, noise refers to disturbances or impairments arising during the storage of digital image data within receiving devices [9].

CNN is typically susceptible to noise, in such a way that even slight noise in an image can lead to a significant performance drop and alter the accuracy of the output [10]. The presence of noise in images frequently presents a major challenge in image data processing, where the primary objective is to preserve the inherent structure of the image and the information it contains while avoiding a reduction in quality [11]. The mitigation of this phenomenon can be accomplished through the preprocessing of noisy images, effectively eradicating unwanted disturbances [12]. However, this preprocessing procedure demands a substantial allocation of computational resources and time, resulting in elevated computational expenses [13].

Previous studies conducted by Mohammad Momeny (2021), titled "A noise-robust convolutional neural network for image classification" [14], elucidates the process of noise reduction in image data without relying on preprocessing. Similarly, another study by Adel Akbarimajd (2022), titled "Learning-to-augment incorporated noise-robust deep CNN for detection of COVID-19 in noisy X-ray images" [15], shares a parallel focus and employs the same approach by utilizing a Noise-Robust Convolutional Neural Network. Building upon the foundation laid by these prior investigations, this study employs CNN architectures, specifically VGG16 and ResNet 50, to assess the resilience of both architectures in classifying images degraded by Gaussian noise.

2. Method

This section described several essential methods that served as foundational support for subsequent discussions regarding the rigidity of CNN architecture.

2.1 Gaussian Noise

Gaussian Noise, a term from signal processing theory, denoted a type of signal interference characterized by a probability density function (PDF) that conformed to a Gaussian distribution, also known as a normal distribution. In simpler terms, the potential values of the noise followed a normal distribution pattern, and the probability density function was formulated as follows:

$$P(x) = \frac{1}{\sigma\sqrt{2\pi}} e^{-\frac{(x-\mu)^2}{2\sigma^2}} \quad (1)$$

Where x represented a normal random variable with parameters μ and σ^2. The probability density function p pertained to the Gaussian random variable x. μ denoted the mean and σ indicated the standard deviation of the distribution. The square of σ, labeled as σ^2, referred to the variance of x [16][17].

2.2 Convolutional Neural Networks

CNN had currently gained immense popularity as deep learning models for image processing and classification [18]. Additionally, it functioned as feedforward networks, facilitating unidirectional information processing, from input to output. Similar to the Artificial Neural Network (ANN), inspired by the intricate neural network of the brain, CNN architecture comprised several integral components, including the convolution layer, Non-linearity (ReLU), and pooling, all grouped within the model. The final element of the model was the Fully connected layer, which served for classification [19].

2.3 MaxPooling

The pooling layer employed a function that operated on a feature map (derived from convolution) as input and applied statistical operations based on the nearest pixel values. This pooling operation aimed to diminish the output size, leading to a reduction in parameters and computations within the network [20].

2.4 Activation Function

The activation function played a pivotal role in determining the "activity" of a neuron based on the weighted sum of inputs. Broadly, two activation functions were employed in this study.

a. Rectified Linear Unit (ReLU)

ReLU referred to an activation function designed to transform negative values into zeros while retaining positive values intact. Utilizing ReLU offered a performance enhancement for neural networks, as it effectively disregarded values below zero [21]. The mathematical definition was as follows:

$$f(x) = \begin{cases} x, & for\ x \geq 0 \\ 0, & for\ x < 0 \end{cases} \qquad range = \{0, \infty) \tag{2}$$

b. Softmax

The softmax referred to an activation function that scaled numbers (logits) into probabilities. Additionally, its output formed a vector comprising probabilities for all potential outcomes. The probabilities in this vector are collectively summed up to one for all classes or outcomes [22]. Softmax was commonly deployed in the final layer of classification-oriented neural networks. This network was typically trained using the log loss (cross-entropy) function, presenting a nonlinear version of multinomial logistic regression. The softmax layer played a pivotal role by facilitating the calculation of the loss function, which aided in optimizing neural network parameters [23]. The mathematical representation of the function was as follows:

$$f(x_i) = \frac{e^{x_i}}{\sum_{j=1}^{n} e^{x_j}} \qquad range = [0,1] \tag{3}$$

The Softmax activation function exclusively found application in the final network layer.

2.5 Loss Function

The choice of the loss function in a neural network was influenced by both the activation function and the output layer of a network. When the output layer assumed the form of discrete values, there would be a need to employ the softmax activation function along with the cross-entropy loss function [24]. The cross-entropy loss function took the following form, with L_CE representing the cross-entropy loss, y_j denoting the target, O_j signifying the output values of the model, and k denoting the length of the output and target vectors.

$$L_{CE} = -\left(\sum_{j=1}^{k} y_j \log(O_j)\right) \tag{4}$$

3. Material and Methods

The final results encompassed the accuracy rate and loss function of two CNN architectures, namely VGG16 and ResNet50. These architectures were exposed to a dataset of degraded Gaussian images. The utilized dataset was the Rice Image Dataset (https://www.kaggle.com/datasets/muratkokludataset/rice-image-dataset), consisting of 75,000 images categorized into five types (a) Arborio, (b) Basmati, (c) Ipsala, (d) Jasmine, and (e) Karacadag, with each class comprising 15,000 data.

The VGG16 and ResNet50 architectures used in this study consisted of several layers as shown in Tables 1 and Table 2.

Table 1. VGG16 architecture

Layer	Output Size	Filter Size / Stride	Activation Function
Input	$224 \times 224 \times 3$	-	-
Convolution 1-1	$224 \times 224 \times 64$	$3 \times 3 \,/\, 1$	ReLU
Convolution 1-2	$224 \times 224 \times 64$	$3 \times 3 \,/\, 1$	ReLU
Max Pooling 1	$112 \times 112 \times 64$	$2 \times 2 \,/\, 2$	-
Convolution 2-1	$112 \times 112 \times 128$	$3 \times 3 \,/\, 1$	ReLU
Convolution 2-2	$112 \times 112 \times 128$	$3 \times 3 \,/\, 1$	ReLU
Max Pooling 2	$56 \times 56 \times 128$	$2 \times 2 \,/\, 2$	-
Convolution 3-1	$56 \times 56 \times 256$	$3 \times 3 \,/\, 1$	ReLU
Convolution 3-2	$56 \times 56 \times 256$	$3 \times 3 \,/\, 1$	ReLU
Convolution 3-3	$56 \times 56 \times 256$	$3 \times 3 \,/\, 1$	ReLU
Max Pooling 3	$28 \times 28 \times 256$	$2 \times 2 \,/\, 2$	-
Convolution 4-1	$28 \times 28 \times 512$	$3 \times 3 \,/\, 1$	ReLU

Convolution 4-2	$28 \times 28 \times 512$	$3 \times 3 / 1$	ReLU
Convolution 4-3	$28 \times 28 \times 512$	$3 \times 3 / 1$	ReLU
Max Pooling 4	$14 \times 14 \times 512$	$2 \times 2 / 2$	-
Convolution 5-1	$14 \times 14 \times 512$	$3 \times 3 / 1$	ReLU
Convolution 5-2	$14 \times 14 \times 512$	$3 \times 3 / 1$	ReLU
Convolution 5-3	$14 \times 14 \times 512$	$3 \times 3 / 1$	ReLU
Max Pooling 5	$7 \times 7 \times 512$	$2 \times 2 / 2$	-
Fully Connected 6	4096	-	-
Flatten	25088	-	-
Dense	5	-	Softmax

Table 1 presents the network structure found in the VGG16 architecture, consisting of a total of 16 layers. Each layer consists of a convolutional layer and a pooling layer, followed by three fully connected layers used for the final classification process. Each convolutional layer in VGG16 employs a 3x3 kernel, and each pooling layer uses a 2x2 filter with a stride of 2. Max pooling is used to reduce the output size, which leads to a reduction in the number of parameters and calculations in the network.

Table 2. ResNet 50 Architecture

Layer	Output Size	Kernel Size/ Stride	Activation Function
Input	$224 \times 224 \times 3$	-	-
Convolutional	$112 \times 112 \times 64$	$7 \times 7. stride\ 2$	-
Batch Normalization	$112 \times 112 \times 64$	-	-
Activation	$112 \times 112 \times 64$	-	ReLU
Max Pooling	$56 \times 56 \times 64$	$3 \times 3, stride\ 2$	-
Residual Block 1	$56 \times 56 \times 256$	-	-
Convolutional	$56 \times 56 \times 64$	1×1	-
Batch Normalization	$56 \times 56 \times 64$	-	-
Activation	$56 \times 56 \times 64$	-	ReLU
Convolutional	$56 \times 56 \times 64$	3×3	-
Batch Normalization	$56 \times 56 \times 64$	-	-
Activation	$56 \times 56 \times 64$	-	ReLU
Convolutional	$56 \times 56 \times 256$	1×1	-
Batch Normalization	$56 \times 56 \times 256$	-	-
Shortcut Connection	$56 \times 56 \times 256$	-	-
Activation	$56 \times 56 \times 256$	-	ReLU

⋮	⋮	⋮	⋮
Residual Block 3	$28 \times 28 \times 512$	-	-
Convolutional	$28 \times 28 \times 128$	$1 \times 1, stride\ 2$	-
Batch Normalization	$28 \times 28 \times 128$	-	-
Activation	$28 \times 28 \times 128$	-	ReLU
Convolutional	$28 \times 28 \times 128$	3×3	-
Batch Normalization	$28 \times 28 \times 128$	-	-
Activation	$28 \times 28 \times 128$	-	ReLU
Convolutional	$28 \times 28 \times 512$	1×1	-
Batch Normalization	$28 \times 28 \times 512$	-	-
Shortcut Connection	$28 \times 28 \times 512$	-	-
Activation	$28 \times 28 \times 512$	-	ReLU

Table 2 displays the network structure of the ResNet 50 architecture, comprising a total of 50 layers, including 49 convolutional layers and 1 final fully connected layer. This architecture is distinct from other CNN architectures because ResNet 50 employs shortcut connections that aid in mitigating the vanishing gradient problem and accelerate network training.

4. Experiment and Discussion

4.1 Data split process

The Rice Image Dataset was divided into three segments, namely training, testing, and validation. This division allocated 70% for training, 20% for testing, and 10% for validation. Consequently, the dataset comprised 52,500 training data, 15,000 testing, and 7,500 validations. Both the VGG16 and ResNet50 architecture models were trained using the training and validation data. Gaussian noise was introduced to each image in the testing dataset, serving as a means of evaluating the model.

4.2 The process of adding Gaussian noise to the image

Gaussian noise referred to the noise characterized by an intensity that adhered to a normal distribution, defined by a specific mean and variance. The procedure of adding Gaussian noise could be executed using the following formula.

$$g(x, y) = f(x, y) + n(x, y) \tag{5}$$

Where $g(x, y)$ represented the noise-degraded input image, $f(x, y)$ denoted the original image, and $n(x, y)$ signified Gaussian noise. Here is an illustration of the process of adding Gaussian noise to one of the data classes (d) Jasmine:

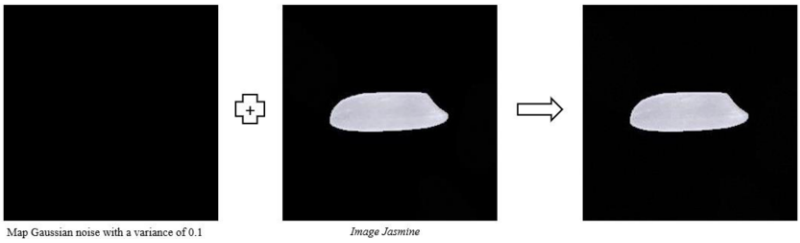

Figure 1. Illustration of the Noise Addition Process

In Figure 1 above, it illustrates the process of adding Gaussian noise with a variance of 0.1 to an image of Jasmine rice, resulting in an image degraded by Gaussian noise (on the right side of Figure 1). The image appears almost identical to the original one due to the use of a variance of 0.1 as the generator of Gaussian noise, which produces very subtle noise.

4.3 Results and Discussion

The VGG16 and ResNet 50 architectures are pre-trained. The parameters used in both architectures are batch size 128 and the number of epochs for each architecture is 30 epochs. The activation functions used are ReLU and softmax which are located on each architecture and the loss fnction used is categorical crossentropy because there is more than 1 class in the dataset used. In testing the VGG16 and ResNet50 architectures before adding Gaussian noise, the accuracy results for VGG16 were 99% with a loss of 0.0193, while for ResNet50 the accuracy results were 97% and a loss of 0.0692. Below is a table of test results for both architectures using 11 variants of the Gaussian noise generator taken at random. Variance in a Gaussian noise generator refers to the parameters that control the variation or distribution of the noise produced.

Table 3. Accuracy and Loss Function Results after Adding Gaussian Noise

variant	Test Loss		Test Accuracy	
	VGG16	ResNet50	VGG16	ResNet50
0.1	0.019315265	0.069177568	0.994400024	0.977599978
0.2	0.01951633	0.069170088	0.994400024	0.977466643
0.3	0.019556299	0.069170088	0.994266689	0.977466643
0.4	0.019678228	0.069189705	0.994266689	0.977333307
0.6	0.019830426	0.069132991	0.994000018	0.977333307
0.8	0.019966107	0.069164671	0.994000018	0.977333307
1	0.020005373	0.06918934	0.994133353	0.977466643
3	0.021122711	0.06918864	0.993200004	0.977466643
5	0.022036267	0.069290794	0.992933333	0.977599978
7	0.023722436	0.069510028	0.991999984	0.977066696
9	0.025188256	0.069510028	0.99119997	0.977066696

Table 3 shows the loss function and accuracy results of VGG16 and ResNet 50 with 11 variance Gaussian noise generators. In the table, it can be seen that the greater the variance in generating Gaussian noise in the image, the loss function increases for both architectures, while the accuracy value for each architecture decreases. The following graphic is presented to explain the increase in the loss function value and the decrease in the accuracy value.

The following is a graph of the accuracy and loss function of VGG16 and ResNet50

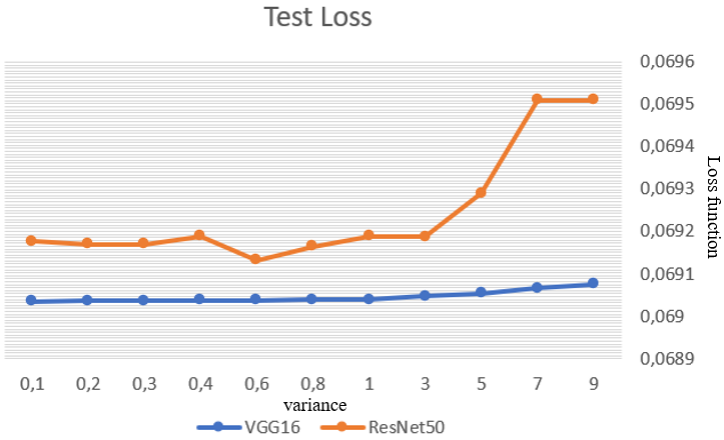

Figure 2. Loss Function of VGG16 and ResNet 50

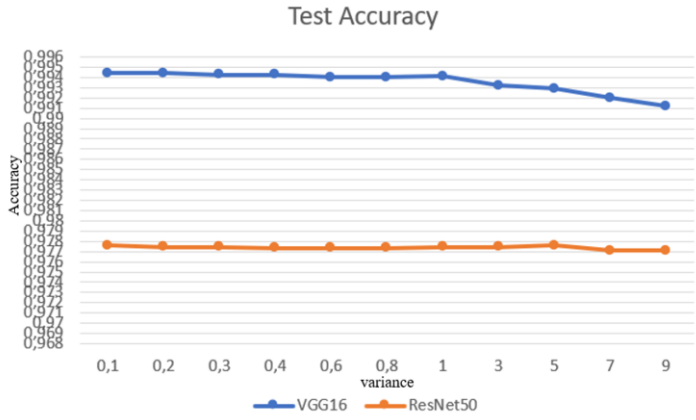

Figure 3. Accuracy values of VGG16 and ResNet 50

The results of testing 11 noise generator variants for VGG16 and ResNet 50 are shown in Figure 2, where the loss function values of the two architectures have increased. The most visible increase occurred in the loss function value on ResNet 50. It can be seen that the increase in the loss function value was not too large for each variance in the Gaussian noise generator. Likewise, Figure 3 the accuracy of the two architectures decreased with each variant, but the decrease was not too big between variants, this is shown in table 3 which shows the value of the Loss Function and accuracy of the two architectures, both VGG16 and ResNet 50.

5. Conclusion

In conclusion, this study outlined the performance evaluation of the VGG16 and ResNet50 architectures when processing images subjected to varying degrees of Gaussian noise degradation. The analyzed images pertained to diverse rice varieties classified into five distinct classes. The test results of VGG16 examination, encompassing 11 different noise variance levels, were shown in Table 3. This graph described an elevation in the loss function and a corresponding decline in accuracy for the test data. For ResNet50, the results revealed an upward trend in the loss function for tested noise variance levels, as shown in Figure 2. Interestingly, the accuracy of the test data showed a minor enhancement. Based on the values derived from the testing data, it was evident that the influence of noise on both architectures remained relatively moderate. Consequently, it was deduced that both VGG16 and ResNet50 architectures exhibited effectiveness in processing images subjected to Gaussian noise degradation, even in the absence of prior pre-processing. In the future, it was highly recommended to explore a diverse array of noise types.

Acknowledgements

This study was funded by the Ministry of Education and Culture for the fiscal year 2023 with the contract number: 075/E5/PG.02.00.PL/2023,0254.8/LL5-INT/AL.04./2023, 007/PDUPT/LPPM UAD/IV/2023. The authors are grateful to the Ministry of Education and Culture for funding the PUDPT research for fiscal year 2023 with contract number 075/E5/PG.02.00.PL/2023.

References

[1] J. D. Kelleher, *The Deep Learning*. 2019.

[2] D. X. Zhou, "Universality of deep convolutional neural networks," *Appl. Comput. Harmon. Anal.*, vol. 48, no. 2, pp. 787–794, 2020, doi: 10.1016/j.acha.2019.06.004.

[3] J. Gu *et al.*, "Recent advances in convolutional neural networks," *Pattern Recognit.*, vol. 77, pp. 354–377, 2018, doi: 10.1016/j.patcog.2017.10.013.

[4] J. Wen *et al.*, "Convolutional neural networks for classification of Alzheimer's disease: Overview and reproducible evaluation," *Med. Image Anal.*, vol. 63, p. 101694, 2020, doi: 10.1016/j.media.2020.101694.

[5] T. J. Brinker *et al.*, "Skin cancer classification using convolutional neural networks: Systematic review," *J. Med. Internet Res.*, vol. 20, no. 10, pp. 1–8, 2018, doi: 10.2196/11936.

[6] F. Sultana, A. Sufian, and P. Dutta, "Advancements in image classification using convolutional neural network," *Proc. - 2018 4th IEEE Int. Conf. Res. Comput. Intell. Commun. Networks, ICRCICN 2018*, pp. 122–129, 2018, doi: 10.1109/ICRCICN.2018.8718718.

[7] M. R. Alwanda, R. P. K. Ramadhan, and D. Alamsyah, "Implementasi Metode Convolutional Neural Network Menggunakan Arsitektur LeNet-5 untuk Pengenalan Doodle," *J. Algoritm.*, vol. 1, no. 1, pp. 45–56, 2020, doi: 10.35957/algoritme.v1i1.434.

[8] I. G. A. Gunadi, "Analisis Perbandingan Metode Filter Mean, Median, Maximum, Minimum, Dan Gaussian Terhadap Reduksi Noise Gaussian, Salt&Papper , Speckle, Poisson, Dan Localvar," *J. Ilm. SINUS*, vol. 17, no. 1, p. 15, 2019, doi: 10.30646/sinus.v17i1.392.

[9] B. Fachri, "Aplikasi Perbaikan Citra Efek Noise Salt Papper Menggunakan Metode Contraharmonic Mean Filter," vol. 9986, no. September, 2018.

[10] Q. Li, L. Shen, S. Guo, and Z. Lai, "Wavelet Integrated CNNs for Noise-Robust Image Classification," *Proc. IEEE Comput. Soc. Conf. Comput. Vis. Pattern Recognit.*, pp. 7243–7252, 2020, doi: 10.1109/CVPR42600.2020.00727.

[11] M. Elhoseny and K. Shankar, "Optimal bilateral filter and Convolutional Neural Network based

denoising method of medical image measurements," *Meas. J. Int. Meas. Confed.*, vol. 143, pp. 125–135, 2019, doi: 10.1016/j.measurement.2019.04.072.

[12] S. Karamizadeh and S. M. Abdullah, "Race classification using Gaussian-based weight K-nn algorithm for face recognition," *J. Eng. Res.*, vol. 6, no. 2, pp. 103–121, 2018.

[13] A. E. Ilesanmi and T. O. Ilesanmi, "Methods for image denoising using convolutional neural network: a review," *Complex Intell. Syst.*, vol. 7, no. 5, pp. 2179–2198, 2021, doi: 10.1007/s40747-021-00428-4.

[14] M. Momeny, A. M. Latif, M. Agha Sarram, R. Sheikhpour, and Y. D. Zhang, "A noise robust convolutional neural network for image classification," *Results Eng.*, vol. 10, no. March, p. 100225, 2021, doi: 10.1016/j.rineng.2021.100225.

[15] A. Akbarimajd *et al.*, "Learning-to-augment incorporated noise-robust deep CNN for detection of COVID-19 in noisy X-ray images," *J. Comput. Sci.*, vol. 63, no. July, p. 101763, 2022, doi: 10.1016/j.jocs.2022.101763.

[16] D. Sundararajan, *Digital image processing: A signal processing and algorithmic approach*. 2017. doi: 10.1007/978-981-10-6113-4.

[17] W. Xu, Y. Liang, W. Chen, and F. Wang, "Recent advances of stretched Gaussian distribution underlying Hausdorff fractal distance and its applications in fitting stretched Gaussian noise," *Phys. A Stat. Mech. its Appl.*, vol. 539, p. 122996, 2020, doi: 10.1016/j.physa.2019.122996.

[18] H. Ling, J. Wu, J. Huang, J. Chen, and P. Li, "Attention-based convolutional neural network for deep face recognition," *Multimed. Tools Appl.*, vol. 79, no. 9–10, pp. 5595–5616, 2020, doi: 10.1007/s11042-019-08422-2.

[19] H. Salman, J. Grover, and T. Shankar, "Hierarchical Reinforcement Learning for Sequencing Behaviors," vol. 2733, no. March, pp. 2709–2733, 2018, doi: 10.1162/NECO.

[20] A. Kholik, "Klasifikasi Menggunakan Convolutional Neural Network (Cnn) Pada Tangkapan Layar Halaman Instagram," *Jdmsi*, vol. 2, no. 2, pp. 10–20, 2021.

[21] Y. Wang, Y. Li, Y. Song, and X. Rong, "The influence of the activation function in a convolution neural network model of facial expression recognition," *Appl. Sci.*, vol. 10, no. 5, 2020, doi: 10.3390/app10051897.

[22] A. Kholik, A. Harjoko, and W. Wahyono, "Classification of Traffic Vehicle Density Using Deep Learning," *IJCCS (Indonesian J. Comput. Cybern. Syst.*, vol. 14, no. 1, p. 69, 2020, doi: 10.22146/ijccs.50376.

[23] R. Hu, B. Tian, S. Yin, and S. Wei, "Efficient Hardware Architecture of Softmax Layer in Deep Neural Network," *Int. Conf. Digit. Signal Process. DSP*, vol. 2018-Novem, pp. 1–5, 2019, doi: 10.1109/ICDSP.2018.8631588.

[24] S. Jadon, "A survey of loss functions for semantic segmentation," *2020 IEEE Conf. Comput. Intell. Bioinforma. Comput. Biol. CIBCB 2020*, 2020, doi: 10.1109/CIBCB48159.2020.9277638.

Fuzzy Systems and Data Mining IX
A.J. Tallón-Ballesteros and R. Beltrán-Barba (Eds.)

doi:10.3233/FAIA231008

Development of a Fuzzy Approach for Consistency Determination of ATC Students' Opinions During Aircraft Flight Norms Violation Hazard Identification

Oleksii REVA[a], Serhii BORSUK[b,1], Volodymyr KAMYSHYN[b], Andrii NEVYNITSYN[a]
[a] *National Aviation University, Kyiv, Ukraine*
[b] *Ukrainian Institute of Scientific and Technical Expertise and Information, Kyiv, Ukraine*

Abstract. This paper underscores the significance of employing fuzzy methods for monitoring the risk attitudes of air traffic controllers. It offers an account of the implementation of such a method within a student group. The development of membership functions is elaborated upon, including their alignment with the ICAO recommended scale. Additionally, the paper outlines the calculation of personal opinions for membership function of fuzzy variable term set. It also presents the integral alignment comparison of personal opinions with the group opinion for the entire set of fuzzy variable terms. The distribution of survey participants along a competence scale and future research directions are discussed.

Keywords. Air traffic control, flight safety, opinions consistency, competence level

1. Introduction

"Forecasting hazards related to flight norms violations by air traffic controllers (ATC) is a challenge that can be addressed using qualimetric methods and means [1]. These tools encompass intricate measurements, tests, and surveys that reflect the ATC's attitude towards risk factors [2, 3]. Considered circumstances can be of various types and nature including horizontal distances between aircraft under simultaneous control. Among the totality of available methods, fuzzy methods hold a special significance as they are best suited to capture the uncertain nature of human behavior and reasoning [4, 5]. Such fuzzy measures should be represented in corresponding models, as illustrated in Fig.1.

It includes empirical membership function that were adjusted for research purpose with help of Cooper-Harper scale and supplementary matrix [5].

[1] Corresponding Author, Serhii BORSUK, Ukrainian Institute of Scientific and Technical Expertise and Information, Kyiv, Ukraine; Email: greyone.ff@gmail.com

2. Research description

This research presents the case study results of ATC students' attitude to risk. Each participant was suggested to express his opinion toward hazard on certain distance range fuzzy terms representing hazard levels: "very high", "high", "above the average", "average", "low", "very low". There were 131 participants, all students of 4th and 5th grades of National Aviation University (Kyiv, Ukraine) and Kropyvnytsky Flight Academy (Kropynvytsky, Ukraine). Each participant had at least 150 hours of air traffic management simulation experience. Same curriculum was mastered by them all. Given these circumstances nothing can be inferred from the results in regard to difference in education level, country/region, training methods, etc.

ICAO recommendations that can be considered important in such case include 5 terms per variable [6] but this can be easily achieved with fuzzy operations over terms with modifier "very".

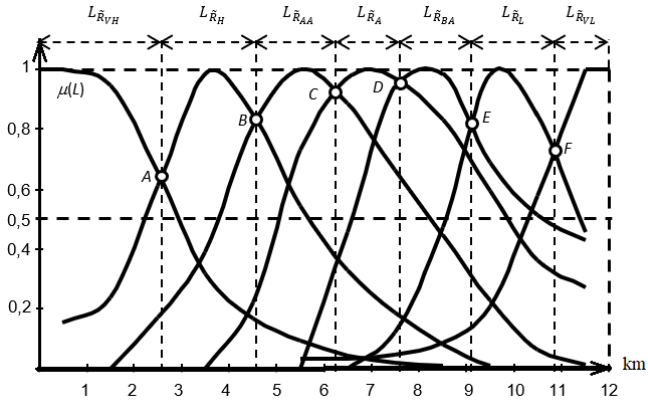

Figure 1. Membership function of fuzzy variable hazard level for aircraft flight norm of 12 km.

Let' s consider example with three students from our sample and compare their answers (which values are represented with ATC_A, ATC_B and ATC_C) with membership function built from the sample as a whole (Fig.2). Let's consider "average" term membership function. We consider that generalized group opinion about membership level as an opinion of "common expert" that is valid one for this group. This means that any deviation from this generalized group opinion represents particular expert lack of competence relative to the group. In our particular case $\mu_{\tilde{R}_C}(L = 6.9\ km) = 1$ is a top value of membership function and can be considered as a referential.

Then we can state that every particular value of membership function received from distance claimed by a single student defines his competence expressed by his opinion consistency with group integral opinion.

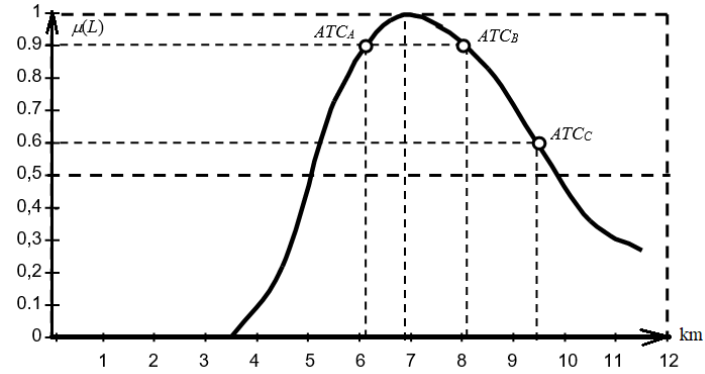

Figure 2. membership function of fuzzy variable hazard level for aircraft flight norm of 12 km.

3. Discussion

Let the meaning of membership function $\mu_{\tilde{R}_{ij}}(L)$ establish a correspondence in mind of the *j*-th ATC student between a certain flight norm distance L and the *i*-th score of the linguistic scale variable "hazard level" described in figure 1. Then, considering that this scale is formed by seven terms, it is not difficult, using the research experience [2, 7, 8], to obtain such an integral indicator of their opinion correspondence regarding the overall group opinion within the *q*-th flight norm:

$$K^{q}_{ATC_j} = \sqrt[n=7]{\prod_{i=1}^{n=7} \mu_{\tilde{R}_{ij}}(L)}, \quad L = \overline{0, L_q} \tag{1}$$

The distribution (histogram) of the integral indicators, obtained using the expression 1 for the researched flight norm $L_q = 12\ km$, is presented in Figure 3.

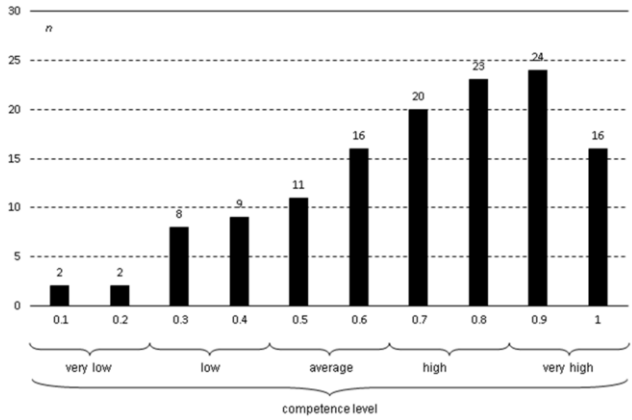

Figure 3. Histograms depicting the integral indicators distribution for the alignment of individual opinions among polled ATC student, compared to the overall group opinion concerning the risk of violating flight norm *L=12*.

Let's introduce a linguistic variable for opinions consistency level (OCL) for the polled ATC students as an indicator of their opinions alignment with the overall group opinion regarding the hazard of flight norm $L = 12\ km$ violation:

$$T(CL) = \underset{\tilde{R}_{VL}^{OCL}}{vey\ low} + \underset{\tilde{R}_{L}^{OCL}}{low} + \underset{\tilde{R}_{A}^{OCL}}{average} + \underset{\tilde{R}_{H}^{OCL}}{high} + \underset{\tilde{R}_{VH}^{OCL}}{very\ high} \quad (2)$$

After further dividing the range of the sample in Figure 3 into five equal intervals corresponding to the terms of the linguistic variable "OCL" (Figure 3), we obtain the statistics of the qualitative characteristics of the OCL of ATC students being polled (Table 1). As we can see from Table 1, an absolute majority of the participants (63.35%) shows high and very high alignment of opinions with the overall group opinion. Meanwhile, a minority (16.03%) is represented by participants who show low and very low alignment of opinions with the overall group opinion. Therefore, the developed methodology for assessing the competence of ATS students through their opinions' consistency may be considered refined.

Table 1. Opinions consistency levels statistics among the polled ATS students in relation to alignment with the overall group opinion.

OCL	$\tilde{R}_{VL}^{OCL}$	$\tilde{R}_{L}^{OCL}$	$\tilde{R}_{A}^{OCL}$	$\tilde{R}_{H}^{OCL}$	$\tilde{R}_{VH}^{OCL}$
Respondents number	4	17	27	43	40
Respondents share	3.05%	12.98%	20.61%	32.82%	30.53%

Furthermore, when considering the spectrum of q flight norms, expression (2) transforms into the following:

$$K_{ATC_j}^{*} = \sqrt[q]{\prod_{q=1}^{q} K_{ATC_j}^{q}} = \sqrt[q]{\prod_{q=1}^{q} \sqrt[n=7]{\prod_{i=1}^{n=7} \mu_{\tilde{R}_{ij}}(L)}}, \quad L = \overrightarrow{0, L_q} \quad (3)$$

4. Conclusion

To conclude, it should be noted that our considerations (and therefore the corresponding results) were based on the equivalence of deviations in opinions from the overall group opinion when they correspond to the same values of membership function.

However, from the perspective of ensuring an adequate level of flight safety, preference should be given to the opinion of student with ATC_B pattern, as they believe that a "typical (average) flight situation" should correspond to a greater distance between aircraft than what is indicated by the overall group opinion. In other words, they are less prone to risk both in comparison to ATC_A student pattern and the overall group opinion.

It is also worth noting that it would be advisable to establish the opinions consistency levels of ATC students not based on their overall group opinion but by taking into account the opinions of professional ATC controllers. Moreover, as inferred from our research [2, 3, 4], the ratio of risk-prone and risk-averse ATC students is inversely proportional compared to professional ATC controllers.

That said, opinions deviation calculated over distances deviations would be reasonable method development intended to substitute membership function indicators. This is expected to be valid for all participants and every fuzzy variable term. Such research should discover ATC students risk attitude in more detailed fashion.

References

[1] Bartulović, D., Steiner, S. Predictive Safety Risk Assessment Methods Applicable in Aviation Ergonomics. In: Salopek Čubrić, I., Čubrić, G., Jambrošić, K., Jurčević Lulić, T., Sumpor, D. (eds) Proceedings of the 9th International Ergonomics Conference. ERGONOMICS 2022. Lecture Notes in Networks and Systems, 2023, vol 701. Springer, Cham.

[2] Reva, O., Borsuk S. Distributions of air traffic control students' attitudes towards workload, Aviation, 2021, 25(4), pp. 241–251

[3] Reva, O., Borsuk S. Air traffic controllers attitude to the aircraft flight level norms violation. Materials of the 2014 International Conference on Industrial Electronics and Engineering (ICIEE 2014), held in Hong Kong, 1-2 May 2014, - 2015. – WIT Transactions on Engineering Sciences, Vol. 93 . – pp. 575-582.

[4] Reva, O. Borsuk, S. Fuzzy Model of Air Traffic Controller Attitude to the Risk During Decision Making, Proceedings of the 5th International Conference on Applied Human Factors and Ergonomics AHFE 2014, Kraków, Poland 19-23 July 2014, ISBN 978-1-4951-1572-1, pp. 6229 – 6238.

[5] Mazdak Khodadadi-Karimvand and Sara TaheriFar, Safety Risk Assessment; Using Fuzzy Failure Mode and EffectAnalysis and Fault Tree Analysis, Trans. Fuzzy Sets Syst., 2022, 1(2), pp. 90-98

[6] ICAO. Safety Management Manual, Fourth Edition – 2018: Doc. ICAO 9859-AN/474. Montreal, Canada, 2018. 182 p.

[7] Kudrytska, N. Simulation of the assessment of the competitiveness of sea ports of Ukraine using the Harrington function. University Economic Bulletin, 2021, 48, pp. 92-97

[8] Vasylevych L., Yurtin I. Decision making under conflict circumstances and environment uncertainty: manual. Kyiv, 2013. 128 p.

Fuzzy Systems and Data Mining IX
A.J. Tallón-Ballesteros and R. Beltrán-Barba (Eds.)

doi:10.3233/FAIA231009

Noncommunicable Diseases (NCDs) Classification by the Radius Local *k*-Point Radial Basis Function (RLRBF) Neural Networks

Pichapop PAEWPOLSONG[a], Narongdech DUNGKRATOKE[a], Niwatchai NAMVICHAISIRIKUL[c], and Sayan KAENNAKHAM[b,1]
[a] *Department of Interdisciplinary Science and Internationalization, Institute of Science, Suranaree University of Technology, Nakhon Ratchasima, 30000, Thailand*
[b] *School of Mathematics, Institute of Science, Suranaree University of Technology, Nakhon Ratchasima, 30000, Thailand*
[c] *School of Family and Community Medicine, Institute of Medicine, Suranaree University of Technology, Nakhon Ratchasima, 30000, Thailand*

Abstract. Chronic illnesses like cancer and diabetes are a big deal worldwide, especially in poorer countries. They're tough on healthcare systems and people's wallets. Various strategies, like early detection and better management, can help. Machine learning (ML) is getting really good at helping us understand and manage these diseases. Within ML, something called classification algorithms are super useful in figuring out who's at higher risk for these diseases by sifting through things like medical records and lab results. One standout technique within these algorithms is neural networks, particularly a type called 'shallow neural networks' or RBF-NNs. In this investigation, a tweaked version of RBF-NNs namely 'Radius Local k-Point Radial Basis Function (RLRBF) Neural Networks' is paid attention to, to see how good they are at classifying people based on their risk of getting a chronic illness. Generally, the two objectives are firstly, to test out how effective this specific type of neural network is, and secondly, to provide useful insights into identifying chronic diseases. Our findings could be a big help for doctors and patients in the future.

Keywords. Noncommunicable Diseases (NCDs), Radial Basis Function (RBF), Classification, Neural Networks (NN).

1. Introduction

NCDs (Noncommunicable Diseases) do more than just make people sick; they also hit hard economically and mess with public health. They lower the quality of life, make work harder, and are a big drain on money and healthcare resources. Understanding the root causes is key to creating better ways to prevent, spot, and manage these diseases. Recent developments in machine learning (ML) techniques and the expanding availability of health data have created new opportunities for handling NCD-related

[1] Sayan Kaennakham, Corresponding author; E-mail: sayan_kk@g.sut.ac.th

problems. By utilizing complex patterns and connections found in large data sets, ML techniques have the potential to improve the ability to predict, diagnose, and manage NCDs. These methods have shown promise in a number of medical fields, including image processing [1], genomics, clinical diagnosis, and prognosis. Support vector machines [2], random forests, neural networks, and ensemble approaches are some of the technologies being proposed and developed. An RBF (Radial Basis Function) neural network is a type of artificial neural network that uses radial basis functions as activation functions. It's particularly good at handling complex problems where the relationship between input and output isn't straightforward. Imagine it as a smart filter that can make sense of messy, non-linear data, often used for things like classification and prediction. It's considered a "shallow" network, meaning it typically doesn't have many layers between the input and output, but it's still pretty powerful for various tasks.

In this work, we present the Radius Local *k*-Point Radial Basis Function (RLRBF) Neural Networks, a novel approach for predicting NCDs that combines the advantages of radial basis function networks with local *k*-point techniques. We compare the performance of RLRBF to other methods of in-depth testing, evaluating its potential to improve the precision and understandability of NCD prediction models.

2. Methodology

2.1. Classification with RLRBFNN

Forming a sample set of real-value functions $\left\{g\left(\mathbf{x}_j\right)\right\}_{j=1}^{M}$ on a finite and discrete centre set $\mathrm{X}=\left\{\mathbf{x}_j\right\}_{j=1}^{M} \subset \Xi$, a multivariate function $g: \Xi \rightarrow \mathbb{R}$ can be formulated and is the starting point of this study. This can be done by relying on the linear combination of interpolation functions using the popular Euclidean norm $\|\cdot\|_2$. Mathematically, such functions are known as 'Radial Basis Function (RBF)' with those centre $\left\{\mathbf{x}_j\right\}_{j=1}^{M}$. Interpolants G of g can be constructed as $G(\mathbf{x})=\sum_{j=1}^{M} a_j \phi\left(\|\mathbf{x}-\mathbf{x}_j\|_2\right)$ with real coefficients, $\left\{a_j\right\}_{j=1}^{M}$, determined using the interpolating condition $G(\mathbf{x}_i)=g(\mathbf{x}_i)$, for all ($i=1, 2, ..., M$) leading to the following form.

$$g(\mathbf{x}_i)=G(\mathbf{x}_i)=\sum_{j=1}^{M} a_j \phi\left(\|\mathbf{x}_i-\mathbf{x}_j\|\right) \tag{1}$$

Hence, what comes next is a system of linear equations with $\left\{a_j\right\}_{j=1}^{M}$ being the unknowns, expressed as $\mathbf{\Phi \alpha}=\mathbf{g}$, where $\boldsymbol{\alpha}=\left[a_1,\ldots,a_M\right]^T$ and $\mathbf{g}=\left[g\left(\mathbf{x}_1\right),\ldots,g\left(\mathbf{x}_M\right)\right]^T$, and $\mathbf{\Phi}=\left[\phi_{ij}\right]_{M\times M}$. After obtaining the coefficient matrix $\boldsymbol{\alpha}$, the solution calculation procedure can then get started. For unknown locations $\hat{\mathrm{X}}=\left\{\hat{\mathbf{x}}_j\right\}_{j=1}^{\hat{M}} \subset \Xi$ and $\mathrm{X} \cap \hat{\mathrm{X}}=[\ ]$,

the approximate values of the corresponding function $\hat{g}\left(\hat{\mathbf{x}}_j\right)$ is obtained for all $j = 1, 2, ..., \hat{M}$, by.

$$\hat{g}(\hat{\mathbf{x}}_j) \approx G(\hat{\mathbf{x}}_j) = \sum_{i=1}^{M} a_i \phi\left(\| \hat{\mathbf{x}}_j - \hat{\mathbf{x}}_i \|_2, c\right) \tag{2}$$

2.2. The Radius Local Radial Basis Function Scheme (RLRBF)

The study can be seen as a more comprehensive adaptation of the research presented in [3]. It starts by considering $\{x_i\}_{i=1}^{N}$ as a vast collection of dispersed data points (referred to as Interpolation points) and uses $\left\{\mathbf{z}_j\right\}_{j=1}^{N_t}$ to represent a group of assessment points, as depicted in Figure 1. Given the function values $\{f(\mathbf{x}_i)\}_{i=1}^{N}$ at specific interpolation points, our goal is to use these values to estimate the values of $\left\{f(\mathbf{z}_j)\right\}_{j=1}^{N_t}$. If ϕ represents a radial basis function, then every interpolation point within the local domain Ω_j is selected as the center for these basis functions. When we apply RBF interpolation within Ω_j, it results in a corresponding linear system.

$$\begin{bmatrix} \hat{f}(\mathbf{x}_1^{[i]}) \\ \hat{f}(\mathbf{x}_2^{[i]}) \\ \vdots \\ \hat{f}(\mathbf{x}_k^{[i]}) \end{bmatrix} = \begin{bmatrix} \phi(\left\|\mathbf{x}_1^{[i]} - \mathbf{x}_1^{[i]}\right\|) & \phi(\left\|\mathbf{x}_1^{[i]} - \mathbf{x}_2^{[i]}\right\|) & \cdots & \phi(\left\|\mathbf{x}_1^{[i]} - \mathbf{x}_k^{[i]}\right\|) \\ \phi(\left\|\mathbf{x}_2^{[i]} - \mathbf{x}_1^{[i]}\right\|) & \phi(\left\|\mathbf{x}_2^{[i]} - \mathbf{x}_2^{[i]}\right\|) & \cdots & \phi(\left\|\mathbf{x}_2^{[i]} - \mathbf{x}_k^{[i]}\right\|) \\ \vdots & \vdots & \vdots & \vdots \\ \phi(\left\|\mathbf{x}_k^{[i]} - \mathbf{x}_1^{[i]}\right\|) & \phi(\left\|\mathbf{x}_k^{[i]} - \mathbf{x}_2^{[i]}\right\|) & \cdots & \phi(\left\|\mathbf{x}_k^{[i]} - \mathbf{x}_k^{[i]}\right\|) \end{bmatrix} \begin{bmatrix} \alpha_1^{[i]} \\ \alpha_2^{[i]} \\ \vdots \\ \alpha_k^{[i]} \end{bmatrix}. \tag{3}$$

This can be rewritten as shown below.

$$\hat{\mathbf{f}}_k = \mathbf{\Phi}_{k\times k} \boldsymbol{\alpha}^{[i]} \tag{4}$$

As a result, it will receive the coefficient matrix as follows.

$$\boldsymbol{\alpha}^{[i]} = \mathbf{\Phi}_{k\times k}^{-1} \hat{\mathbf{f}}_k \tag{5}$$

Therefore,

$$\begin{aligned} f(\mathbf{z}_i) &= \sum_{j=1}^{k} \alpha_j^{[i]} \phi(\left\|\mathbf{z}_i - \mathbf{x}_j^{[i]}\right\|) \\ &= \left[\phi(\left\|\mathbf{z}_i - \mathbf{x}_1^{[i]}\right\|), \phi(\left\|\mathbf{z}_i - \mathbf{x}_2^{[i]}\right\|), ..., \phi(\left\|\mathbf{z}_i - \mathbf{x}_k^{[i]}\right\|)\right] \boldsymbol{\alpha}^{[i]} \\ &= \left[\phi(\left\|\mathbf{z}_i - \mathbf{x}_1^{[i]}\right\|), \phi(\left\|\mathbf{z}_i - \mathbf{x}_2^{[i]}\right\|), ..., \phi(\left\|\mathbf{z}_i - \mathbf{x}_k^{[i]}\right\|)\right] \mathbf{\Phi}_{k\times k}^{-1} \hat{\mathbf{f}}_k. \end{aligned} \tag{6}$$

The values of $\left\{f(\mathbf{z}_j)\right\}_{j=1}^{N_t}$ can now be numerically approximated.

Starting from here, the primary concept merges with the sliding technique from a local influential domain as previously described by [4]. This results in the creation of the local interpolation method used in this study.

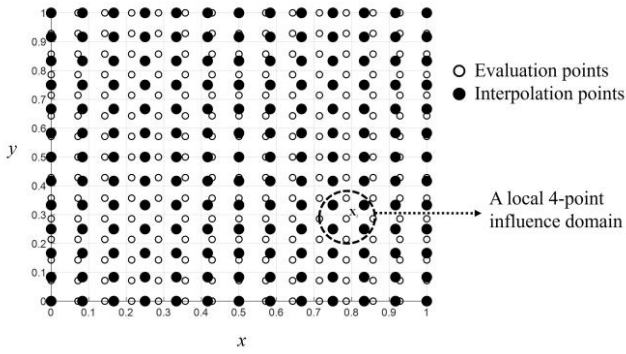

Figure 1. An example of a local domain with the interpolation and evaluation points.

For each local domain Ω_j , the proposed method generates a radius r_j around $\mathbf{z}_j$. The number of K nearest interpolation points from $\mathbf{z}_j$ are now chosen. The distance to the furthest point from $\mathbf{z}_j$ denotes the radius from each local domain. Any interpolation points inside this radius serves as central points for the RBF to approximate $f(\mathbf{z}_j)$'s values. The process of approximation for these values can now be carried out. This technique is beneficial; as data becomes denser, interpolation accuracy tends to increase. The method excels especially in detailing intricate or ambiguous zones, providing enhanced predictions in these areas.

3. Data preparation

3.1. Data source

The Pima Indian Diabetes Dataset (PIDD) originates from the National Institute of Diabetes and Digestive and Kidney Diseases. It comprises data related to 768 women from a population residing near Phoenix, Arizona, USA. All individuals in the dataset are female and belong to the Pima Indian heritage, with a minimum age of 21.

The primary purpose of this dataset is to predict, through diagnostic measurements, whether a patient is likely to have diabetes or not. The dataset's focus is on diagnosing diabetes. Out of the patients tested, 258 were positively diagnosed with diabetes, while 500 tested negative. The dataset encompasses various medical predictor variables and a target variable named “Outcome”. These predictor variables include the number of pregnancies, BMI, insulin levels, age, and more.

The Pima population has been under the observation of the National Institute of Diabetes and Digestive and Kidney Diseases since 1965, with regular intervals of 2 years. Given that type 2 diabetes mellitus (T2DM) emerges from the interplay of genetic and environmental factors, the Pima Indian Diabetes Dataset contains information about attributes that could be linked to the onset of diabetes and its potential complications.

3.2. Description of attributes

The Pima Indian Diabetes Dataset (PIDD) comprises several attributes that provide valuable insights into the diagnostic measurements and characteristics of the patients. Each attribute contributes to the understanding of factors potentially associated with diabetes prediction. Table 1 contains comprehensive list of attributes present in the dataset along with a brief description of each.

Table 1. Attributes description in the PIDD.

No.	Attributes	Description
1	Pregnancies	Number of times pregnant
2	Glucose	Plasma glucose concentration 2 hours in an oral glucose tolerance test
3	BloodPressure	Diastolic blood pressure (mm Hg)
4	SkinThickness	Triceps skin fold thickness (mm)
5	Insulin	2-Hour serum insulin (μIU/ml)
6	BMI	Body mass index (kg / (height in m)^2)
7	DiabetesPedigreeFunction	Diabetes pedigree function, which assesses the likelihood of diabetes based on family history
8	Age	Age in years
9	Outcome	Class variable indicating whether a patient has diabetes or not (0: No, 1: Yes)

We used the same features as in reference [5], selected via correlation coefficient: Glucose, BMI, Insulin, Pregnancy (Preg), and Age, following their methodology.

3.3. Normalization

The data is normalized between 0 and 1. The normalization equation was applied to achieve this rescaling. The equation for normalization is as follows.

$$X_{norm} = \frac{X - X_{\min}}{X_{\max} - X_{\min}} \tag{7}$$

where $X_{norm} = i-$ th normalized data, $X = (X_1, X_2, ..., X_n)$, min and max represents the minimum and maximum value of the range respectively.

3.4. Evaluation metrics

To ascertain various performance measurement metrics, the confusion matrix of each classifier model is utilized to calculate TP (True Positive), FP (False Positive), TN (True Negative), and FN (False Negative), as shown in Table 2.

Table 2. Calculation of Performance Measurement Metrics.

Measures	Formulas	Measures	Formulas
Accuracy	$\frac{TP+TN}{TP+TN+FP+FN}$	Recall	$\frac{TP}{TP+FN}$
Precision	$\frac{TP}{TP+FP}$	F1-Score	$\frac{2\times Precision\times Recall}{Precision+Recall}$

Using these measurements, the following section presents the scheme's performance for the given dataset.

4. Numerical experiments and results

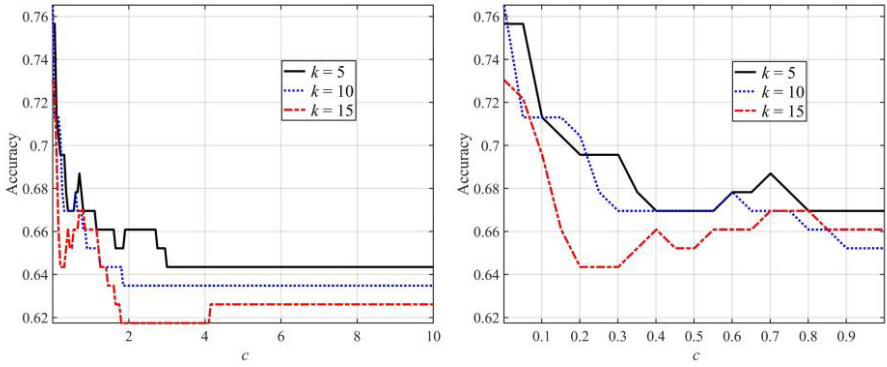

Figure 2. Accuracy of RLRBF for each value of k 's ($k = 5$, 10 and 15) on Diabetes dataset.

Figure 2 depicts the accuracy trend within the range of parameter c . There is a noticeable and consistent decline in accuracy as the shape parameter c increases for all three sizes of k . The accuracy values for all three k sizes rapidly decrease within the range of 0.001 to less than 2 of c . Although there is a slight uptick in accuracy within the range of 0.3 to 1 for some values of c , additionally, for c values greater than 4, the accuracy levels for each k remain relatively constant. Overall, the highest accuracy is achieved at $k = 5$, followed by $k = 10$, and the lowest accuracy is observed at $k = 15$.

Table 3. The performance comparisons of parameter values on the PIDD.

Classification	Shape parameters	Precision	Recall	F-measure	Accuracy
DT	-	0.735	0.731	0.733	73.14%
RF	-	0.779	0.771	0.774	77.14%
NB	-	0.787	0.783	0.785	78.28%
LR	-	0.788	0.789	0.788	78.85%
KNN	-	0.804	0.794	0.798	79.42%
SVM	-	0.774	0.777	0.775	77.71%
RLRBF ($k = 5$)	$c = 0.001$	0.575	0.676	0.622	75.65%
	$c = 0.01$	0.575	0.697	0.630	76.52%
	$c = 0.1$	0.525	0.600	0.560	71.30%
RLRBF ($k = 10$)	$c = 0.001$	0.575	0.697	0.630	76.52%
	$c = 0.01$	0.575	0.697	0.630	76.52%
	$c = 0.1$	0.525	0.600	0.560	71.30%
RLRBF ($k = 15$)	$c = 0.001$	0.550	0.628	0.587	73.04%
	$c = 0.01$	0.550	0.628	0.587	73.04%
	$c = 0.1$	0.500	0.571	0.533	69.57%

We performed comparisons using the parameters (DT, RF, NB, LR, KNN, SVM) listed in [5] in order to assess the parameter performance of the suggested The Radius Local Radial Basis Function Scheme (RLRBF) for classification. The KNN provided in [5] has the maximum accuracy of 79.42% when compared to the other parameters, as shown in Table 3.

This table provides information about the trends in accuracy values in relation to the shape parameter (c), similar to the findings presented in Figure 2. Specifically, as the

value of c increases, it leads to a decrease in accuracy. For the RLRBF model, the highest accuracy is recorded at 76.52% for the cases where (k , c) = (5, 0.01), (10, 0.001), and (10, 0.01).

5. Conclusions

In summary, the classification of noncommunicable diseases (NCDs), particularly diabetes, has far-reaching implications for healthcare. Accurate classification supports timely interventions and personalized treatments, ultimately improving patient well-being. The characteristic of the proposed Radius Local *k*-Point Radial Basis Function (RLRBF) Neural Networks method offers a significant advancement in NCD classification by enabling the model to capture intricate local patterns within the data.

Our results underscore the importance of the shape parameter, c , and k size in influencing accuracy trends. Increasing c values impact accuracy, while distinct k sizes lead to varied performance outcomes. Comparison with established models validates RLRBF's effectiveness, reaching a peak accuracy of 76.52% for specific settings. This aligns with trends seen in Figure 2 and Table 3, reinforcing c 's impact on accuracy.

Moving forward, refining RLRBF through parameter optimization and hybrid approaches holds promise. Exploring broader datasets and diverse NCDs can extend its applicability. Integrating domain knowledge and advanced features may further enhance performance.

Acknowledgement

This work was supported by (i) Suranaree University of Technology (SUT, http://www.sut.ac.th), (ii) Thailand Science Research Innovation (TSRI, https://www.tsri.or.th), and (iii) National Science, Research and Innovation Fund (NSRF) (NRIIS number 179338). The grant recipient is S. Kaennakham who would like to express his sincere gratitude for their support.

References

[1] Allugunti VR. Breast cancer detection based on thermographic images using machine learning and deep learning algorithms. International Journal of Engineering in Computer Science, 2022. 4(1): p. 49-56.
[2] Pethunachiyar G. Classification of diabetes patients using kernel based support vector machines. in 2020 International Conference on Computer Communication and Informatics (ICCCI). 2020. IEEE.
[3] Yao G, Duo J, Chen CS, Shen LH. Implicit local radial basis function interpolations based on function values. Applied Mathematics and Computation, 2015. 265: p. 91-102.
[4] Paewpolsong P, Chanthawara K, Dungkratoke N, Kaennakham S. Numerical Investigation on Three Local-Adaptive *k*-Point Multiquadric Neural Networks. Machine Learning and Artificial Intelligence: Proceedings of MLIS 2022, 2022. 360: p. 84.
[5] Khanam JJ, Foo SY. A comparison of machine learning algorithms for diabetes prediction. Ict Express, 2021. 7(4): p. 432-439.

Fuzzy Systems and Data Mining IX
A.J. Tallón-Ballesteros and R. Beltrán-Barba (Eds.)

doi:10.3233/FAIA231010

On the Wavelet Convolution Neural Networks for Ultra-Sound Based Breast Cancer Detection

Kittikorn SRIWICHAI[a], Chantana SIMTRAKANKUL[a], Ratapong ONJUN[a], Pichapop PAEWPOLSONG[a], and Sayan KAENNAKHAM[b,1]
[a] *Department of Interdisciplinary Science and Internationalization, Institute of Science, Suranaree University of Technology, Nakhon Ratchasima, 30000, Thailand*
[b] *School of Mathematics, Institute of Science, Suranaree University of Technology, Nakhon Ratchasima, 30000, Thailand*

Abstract. Breast cancer is one of the deadliest types of cancer, and it comes in a wide variety of forms, resulting in a wide variety of detection methods. Several deep learning techniques have been applied to decrease unnecessary biopsies and lessen the burden on radiologists. One of the most popular architectures for this task is the Convolutional Neural Networks (CNNs). This paper aims to explore the integration of convolutional neural networks (CNN) and wavelet transform (WT) to identify the optimal combination and architecture of these methods for efficient detection of breast cancer in ultrasound images. To accomplish this task, the wavelet convolutional neural network (WCNN) structures are proposed and trained for the mission of screening breast cancer abnormalities embedded in ultrasound type of images. Compared with other two popular networks, ResNet50 and MobileNetV2, it has been found that the proposed WCNN has produced a satisfactory solution, with an accuracy of 98.24 %, precision of 97.29%, recall of 100%, and F measure of 98.24%.

Keywords. Convolution neural network, Wavelet transformation, Breast cancer.

1. Introduction

Breast cancer remains a paramount global concern for women, being the most widespread cancer among them and resulting in countless deaths. Numerous factors can lead to its development, and alarmingly, almost a million cases remain unidentified each year. Many women face barriers in accessing diagnostic tools, causing late detections, delayed treatments, and exacerbated symptoms. Thankfully, a variety of screening methods like mammograms, needle breast biopsies, breast ultrasound (BUS), and MRI are available. Incorporating machine learning into these diagnostic processes offers a promising avenue for earlier and more accurate detection, enhancing the potential for successful treatment outcomes. [1].

Over the past decades, a large number of machine learning tools have been proposed, developed, and applied for this task. Yassi et al. [2] proposed a Fuzzy system combined

[1] Corresponding Author, Sayan Kaennakham, Suranaree University of Technology, Nakhon Ratchasima, 30000, Thailand; E-mail: sayan_kk@g.sut.ac.th

with optimization for distinguishing breast cancer types in 2014. Amrane et al. [3] compared Naive Bayes and k-nearest neighbor classifiers in 2018, with KNN achieving 97.51% accuracy. Deep learning, like Convolutional Neural Networks (CNNs), has also made strides. Haq et al. [4] used Relief and Autoencoder PCA for feature selection, achieving 99.91% accuracy. Nawaz et al. [5] achieved 95.4% accuracy using DenseNet CNNs on histopathological images. Onjun et al. [6] enhanced CNNs with wavelet transformation, reaching 96.49% accuracy. Sriwichai et al. [7] proposed WT-CNN hybrids for improved breast cancer detection. T. Saba et al. [8] obtained 92.8% accuracy with CNNs on breast ultrasound images (only mention a few).

While many well-documented studies have been highlighted, it's worth noting that ultrasound images have not been extensively addressed by CNN-based deep learning to the best of our understanding. Additionally, the CNN can benefit from integration with other robust mathematical techniques to enhance its efficiency. To address this deficiency, our research emphasizes the use of wavelet transformation in tandem with CNN to identify breast cancer in ultrasound images.

2. Mathematical components

As noted earlier, the objective of this study is to integrate two primary components: the traditional neural network (CNN) and the wavelet transformation. In this section, we provide a concise overview of these two elements.

2.1. Convolution Neural Networks (CNN)

A typical CNN comprises input, output, and hidden layers, divided into convolution, pooling, and fully connected (FC) stages. The convolution layer identifies correlations between larger input images and lighter counterparts. Meanwhile, the pooling layer reduces computational load and the network's sensitivity to variations, aiding subsequent pattern recognition. It replaces input blocks with singular values, either through peak aggregation or averaging. The FC layer synthesizes information for final decisions. Various CNN architectures exist, differing in layer structure and count.

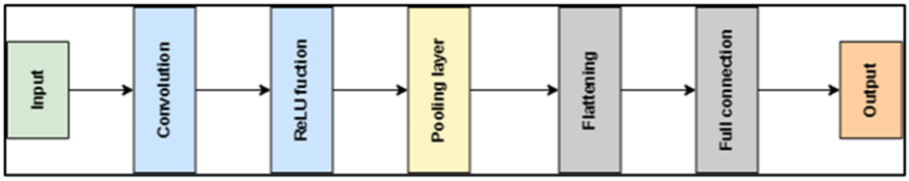

Figure 1. Typical architecture of a convolution neural network.

2.2. Heading Wavelet transformation (WT)

Wavelet Transformation is a mathematical technique used for analyzing intricate signal systems, which include different signals. It primarily works by transitioning signals from the time domain to the frequency domain. There are two main kinds of wavelet transformations: Continuous Wavelet Transform (CWT) and Discrete Wavelet Transform (DWT). In this study, we employ DWT. Through this transformation, a signal is depicted as a combination of low-frequency signals, where wavelet coefficients act as

their respective magnitudes. These coefficients are computed using low-pass and high-pass filters to derive the low-frequency and high-frequency components. Specifically, for a time-dependent signal, the low-frequency component signal at a certain resolution level and position is calculated using Eq. (1).

$$A_j(k) = \sum_{l=0}^{n} h(l) A_{j-1}(k + 2^j l) \tag{1}$$

Where h(l) is a low-pass filter, and the high-frequency component signal at j- level resolution at the k- position (i.e. $D_j(k)$) can be calculated from the difference between the two low-pass component signals at next to each other as in Eq. (2)

$$D_j(k) = A_{j-1}(k) - A_j(k) \tag{2}$$

Therefore, we can deduce that the desired $x(k)$ signal is produced by combining the high-frequency and low-frequency component signals as described below.

$$x(k) = A_n(k) + \sum_{j-1}^{n} D_j(k) \tag{3}$$

Where n denotes the resolution level and we chose seven varieties of DWT, specifically Daubechies namely Daubechies (db2).

3. Experiment preparation

3.1. Data preparation

A subset of ultrasound from Ultrasound Breast Images for Breast Cancer (UBIBC) is used to train and evaluate the proposed approach. UBIBC consists of 9,016 images as 8,116 training set, 900 testing set detailed in Table 1. The examples of ultrasound used in the work shown in the Figure 2. The preprocessing phase involves resizing the ultrasound images to meet the specifications of the suggested pretrained models. All models require images of dimensions 224×224×3. Every image is presented in a 700×460 pixel resolution, saved in PNG format, and has a 3-channel RGB with an 8-bit depth per channel.

Table 1. Details of Ultrasound Breast Images for Breast Cancer (UBIBC).

Type of dataset	Classes	Total
Training set	Benign	4,074
	Malignant	4,042
Testing set	Benign	500
	Malignant	400

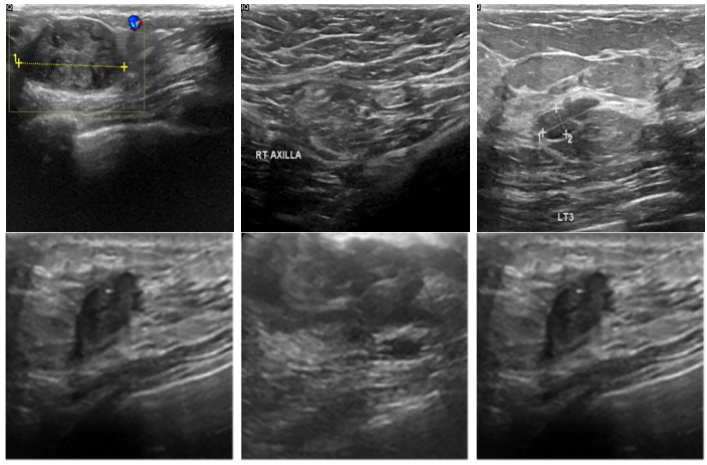

Figure 2. The example ultrasound images of benign (top) and malignant (bottom).

3.2. Experiment Design

In our research, we utilized the Python3 programming language for our experiments. We developed a neural network model by integrating wavelet transformation with a convolutional neural network, termed as wavelet convolution neural network (WCNN). Figure 3 presents the comprehensive layout of this model.

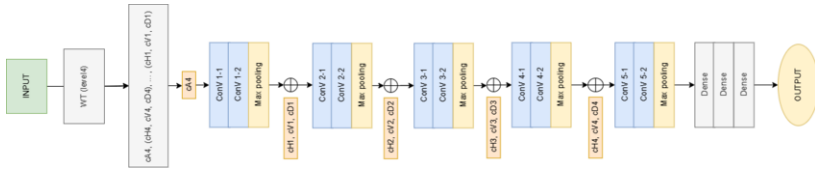

Figure 3. The detailed structure of WCNN.

Every neural network design is processed using Adamax Optimization from start to finish. We initiate with a learning rate of 0.01, followed by decay steps set at 10,000 and a decay rate of 0.9. The batch size chosen is 32, and the Categorical Cross entropy loss serves as the loss function. These neural network structures underwent training from the ground up for a total of 1000 epochs.

3.3. Evaluation metrics

In machine learning, the confusion matrix is a widely embraced tool for evaluating classification model performance. It tallies correct and incorrect outcomes, gauging the model against real data. Accuracy, precision, recall, and F1-score are prevalent metrics. Moreover, in medical contexts, the receiver operating characteristic curve (ROC) holds significance. Thus, in our study's final phase, we compared WCNN, ResNet50, and MobileNetV2 using accuracy, precision, recall, F1-score, and the ROC curve.

4. Experiments and results

The proposed model (WCNN model) and the other two neural networks, ResNet50 and MobileNetV2, were evaluated using UBIBC images. The three CNN architectures were trained on 8,116 UBIBC images and tested on 900 UBIBC images. In the training process of the three neural network architectures, a total of 1000 epochs were conducted. After completing the training process, WCNN achieved the highest accuracy of 98.25% in epoch 412, as shown in Figure 4(a). The best accuracy for ResNet50 and MobileNetV2 was 97.98% in epoch 686 and 95.00% in epoch 403, as shown in Figures 4(b) and 4(c), respectively. Importantly, WCNN's accuracy displayed greater consistency compared to the other models, an essential characteristic in the field of diagnostics. Figure 5 showcases the ROC curve for all models, with WCNN being the frontrunner in accuracy. Its 99.21% area under the ROC curve (AUC) further underscores WCNN's dominance in breast cancer detection compared to the other models. Additionally, the system's effectiveness in accurately identifying benign and malignant cases through random selection is emphasized. Their performance metrics are presented in Table 2. Notably, the WCNN model demonstrated outstanding classification capabilities, achieving impressive metrics: accuracy (98.24%), precision (97.29%), recall (100%), and F1-score (98.24%). In comparison, the ResNet50 model posted a solid performance with an accuracy of 95.61%, precision of 95.77%, recall of 97.14%, and F1-score of 96.45%. The MobileNetV2 model also exhibited commendable results with an accuracy of 93.86%, precision of 93.15%, recall of 97.14%, and F1-score of 95.10%. Significantly, WCNN outperformed both ResNet50 and MobileNetV2 in various metrics.

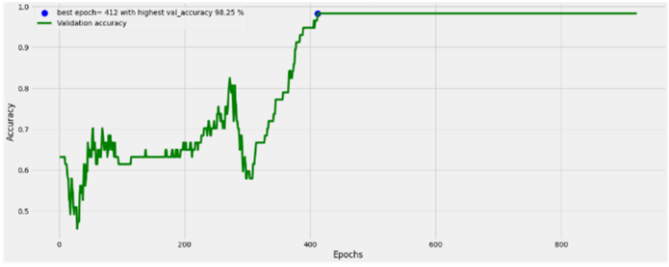

(a) Validation of accuracy of WCNN

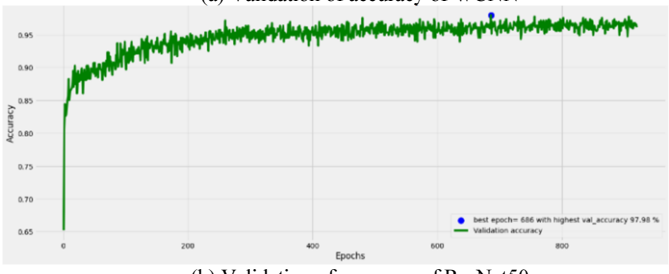

(b) Validation of accuracy of ResNet50

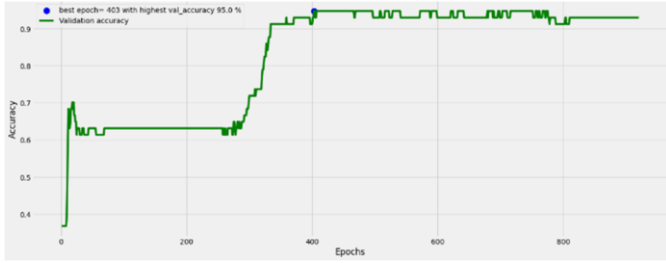

(c) Validation of accuracy of MobileNetV2

Figure 4. Validation of accuracy of all models.

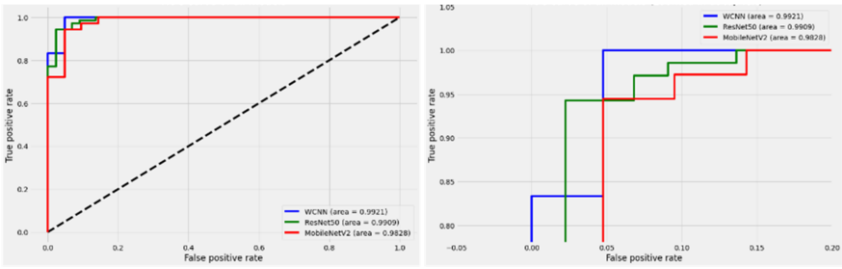

Figure 5. ROC curve of all models, with an inset zooming in on the top-left portion for more detail.

Table 2. The evaluation metrics computed from best result of WCNN, ResNet50 and MobileNetV2.

Model	Accuracy (%)	Precision (%)	Recall (%)	F-Measure (%)
WCNN	**98.24**	**97.29**	**100**	**98.24**
ResNet50	95.61	95.77	97.14	96.45
MobileNetV2	93.86	93.15	97.14	95.10

5. Conclusions

By considering the desirable features provided by the wavelet transformation (WT), this work attempts to improve the performance of the convolutional neural network (CNN) for detecting breast cancer using an ultrasound dataset. This new combination is named a 'wavelet neural network (WCNN)'. For the sake of comparison, two other popular architectures, ResNet50 and MobileNetV2, are parallelly executed on the same dataset. It has been found in this work that WCNN has produced a satisfactory solution, with an accuracy of 98.24 %, precision of 97.29%, recall of 100%, and F measure of 98.24%. With this promising aspect of the new architecture, it is truly worth investing further as to what extent this will work for more complex problems and it is set as our future work.

Acknowledgements

This work was supported by (i) Suranaree University of Technology (SUT, http://www.sut.ac.th), (ii) Thailand Science Research Innovation (TSRI, https://www.tsri.or.th), and (iii) National Science, Research and Innovation Fund (NSRF) (NRIIS number 179338). The grant recipient is S. Kaennakham who would like to express his sincere gratitude for their support.

References

[1] Abbas N, Saba T, Mohamad D, Rehman A, Almazyad AS, Al-Ghamdi JS. Machine aided malaria parasitemia detection in Giemsa-stained thin blood smears. Neural Computing and Applications, 2018. 29(3):803-818.

[2] Yassi M, Yassi A, Yaghoobi M. Distinguishing and clustering breast cancer according to hierarchical structures based on chaotic multispecies particle swarm optimization. in 2014 Iranian Conference on Intelligent Systems (ICIS). 2014.

[3] Amrane M, Oukid S, Gagaoua I, Ensari T. Breast cancer classification using machine learning. in 2018 Electric Electronics, Computer Science, Biomedical Engineerings Meeting (EBBT). 2018.

[4] Haq AU, Li JP, Saboor A, Khan J, Wali S, Ahmad S, Zhou W. Detection of Breast Cancer Through Clinical Data Using Supervised and Unsupervised Feature Selection Techniques. IEEE Access, 2021. 9: 22090-22105.

[5] Nawaz M, Sewissy AA, Soliman THA. Multi-class breast cancer classification using deep learning convolutional neural network. Int. J. Adv. Comput. Sci. Appl, 2018. 9(6): 316-332.

[6] Onjun R, Sriwichai K, Dungkratoke N, Kaennakham S. Wavelet Pooling Scheme in the Convolution Neural Network (CNN) for Breast Cancer Detection. 2022.

[7] Sriwichai K, Onjun R, Simtrakankul C, Kaennakham S. On the Wavelet Convolution Neural Network for Breast Cancer Image Analysis. 2022.

[8] Saba T, Abunadi I, Sadad T, Khan AR, Bahaj SA. Optimizing the transfer-learning with pretrained deep convolutional neural networks for first stage breast tumor diagnosis using breast ultrasound visual images. Microscopy Research and Technique, 2022. 85(4):1444-1453.

Fuzzy Systems and Data Mining IX
A.J. Tallón-Ballesteros and R. Beltrán-Barba (Eds.)

doi:10.3233/FAIA231011

Enhanced Multi-Target Tracking with Combination of Position, Power and Ambiguous Doppler Measurements

Tran Thi THANH[a,1], Tran Trung KIEN[a], Nguyen Van KHUONG[a], Pham Duong NAM[a], Tran Vu HOP[a] and Nguyen Van LOI[a]
[a] *Radar Center, Viettel High Technology and Industries Corporation, Viet Nam*

Abstract. Multiple Target Tracking (MTT) is one of the most challenging topics in radar target tracking. In addition to conventional position measurements, the integration of target Doppler and power information can offer valuable insights into a target's kinematic state, thereby improving tracking performance. This article discusses a tracking approach that incorporates those components into the measurement enhancement process and assesses the advantages of the proposed strategy. Firstly, we investigated an improved data association scheme that exploits statistical features of position, Doppler and power. The estimated Doppler value calculated from the target range and timestamp will be compared with the measured Doppler to deal with the Doppler ambiguity situation. Secondly, we studied an augmented unscented Kalman filter (UKF) algorithm using position, Doppler measures, and the indirect measure of radial velocity in the linear domain. The experimental results show that the proposed solution has good performance in terms of reduced number of false tracks and improving the accuracy of the target state estimation.

Keywords. MTT, data association, position, power, Doppler ambiguity, UKF

1. Introduction

In the MTT system, sensors generate multiple detections from many targets in a scan. To track these targets, the conventional methods only use the position information of the detections in the data assignment algorithms. However, those methods lead to outstanding problems if the number of targets or detections is large. Especially, when the target moves in the noise area, the noise detections appear around the target detection, so the targets may choose the wrong detections. In a pulse-Doppler radar system, beyond conventional position measurements, Doppler and power measurements can offer additional information about the target state, which would improve tracking performance. Literature [1] discussed an adjusted JPDA (Joint Probabilistic Data Association) algorithm which combines range rate measurements with position measurements to enhance the tracking operation. A better data association scheme, which utilizes range rate measurements to reduce the number of false tracks [2]. Literature [3] recommended an enhanced Doppler data association approach which utilizes target range and target

[1] Corresponding Author: Tran Thi Thanh, Radar Center, Viettel High Technology and Industries Corporation, Ha Noi, Viet Nam; E-mail: tranthithanhbg1995@gmail.com.

velocity measurements for linear multi-target tracking. The target velocity measurements are applied to the observation likelihood estimation, which is an essential part of differentiating true measurements from false targets. Reference [4] recommended the Doppler information of the target based on multiple models generalized labeled multi-Bernoulli (MM-GLMB) in the high clutter environment and the processing of the measurements using the adaptive tracking gate can improve the tracking performance.

Most traditional tracking filters consider only position measurements to estimate the moving state of the target. However, the operation principle of the track filters shows that a filter using both position and Doppler measurements is more efficient than a filter using only position. Reference [2] developed a scheme by using an interacting multiple model estimator containing several extended Kalman filter (EKF) elements to handle Doppler measurements. Various recursive nonlinear filtering approaches are used to process Doppler measurements [5-6]. A linear denoising filter is presented in [7] to reduce the converted Doppler measurement errors is investigated. A sequential converted measurement Kalman filter with Doppler measurements when there is a correlation between Doppler and slant range was proposed in [8]. Motion models in the range-Doppler plane and state estimation technique using Doppler and range measurements were also investigated in [9]. Literature [10] proposed a sequential linear filtering algorithm to process the position-Doppler information. The proposed method was combined with the IMM algorithm to enhance the maneuvering target tracking.

Conversely, the aforementioned methods only integrate the measurement of Doppler without any ambiguity. Because of the spectral aliasing, an elementary problem is Doppler ambiguity, particularly at low pulse repetition frequencies (PRF) [11]. Reference [12] discussed a target tracking method in ambiguous Doppler situations using Gaussian Mixture. A Track-Before-Resolving approach for resolving the ambiguity in Doppler measurements was proposed in [13]. This new method considers the maximum probability computed in the multiple model estimation. Literature [14] proposed a scheme that is based on the modified multiple hypothesis tracking and the probabilistic data association to resolve the ambiguous Doppler problem.

In this study, a new approach for Multi-Target Tracking with a combination of position, ambiguous Doppler and power measurements is presented. Firstly, we investigated an improved data association scheme that exploits statistical features of position, Doppler and power. The estimated Doppler value calculated from the target range and timestamp will be compared with the measured Doppler to deal with the Doppler ambiguity situation. Secondly, we studied an augmented unscented Kalman filter algorithm using position, Doppler measures, and the indirect measure of radial velocity in the linear domain.

2. Methodology

2.1. Data Association

The proposed data association method uses position, Doppler and power measurements to calculate the score value of each detection in the target gate. The radial velocity value is indirectly calculated from the range and the timestamp of the detection. After that it will be converted to the estimated Doppler. If the detection comes from the target, the difference between the measured Doppler and estimated Doppler will be small. This is a new and effective solution when applying information directly in the Doppler ambiguity

situation. Similarly, if a detection belongs to the target, the difference between the measured power value and the average power value of the target will also be small.

Detailed algorithm is done through the following steps:

Step 1: Calculate the radial velocity

Determine the value of the radial velocity using the range and timestamp in the following formula:

$$rr_i = \frac{1}{N}\left(\frac{r_{i-N+1}-r_{i-N+2}}{t_{i-N+2}-t_{i-N+1}} + \frac{r_{i-N+2}-r_{i-N+3}}{t_{i-N+3}-t_{i-N+2}} + \cdots + \frac{r_{i-1}-r_i}{t_i-t_{i-1}}\right) \quad (1)$$

where rr_i, r_i and t_i denote the radial velocity, range and timestamp at the scan i, respectively.

N is the integer selected depending on the maneuverability of the target and the data update cycle of the radar. The less maneuver the target or the faster the target data update, the greater N can choose. In common situations, we propose to use N in the range of 2-4. The timestamp is taken directly from the Analog-to-Digital module of the hardware device to increase the accuracy of calculating the value of the radial velocity.

Step 2: Calculate the estimated Doppler from the radial velocity

The estimated Doppler $\widehat{F_D}$ is calculated from the radial velocity according to the following formula:

$$DopplerAbs = mod\left(\frac{rr}{v_d}, M\right) \quad (2)$$

where $DopplerAbs$ denotes the absolute estimated Doppler value, v_d is the Doppler resolution and M is the total number of Doppler banks processed.

If the Doppler increases clockwise with the original bank F_0,

$$\widehat{F_D} = mod(F_0 + DopplerAbs, M) \quad (3)$$

If the Doppler increases counter-clockwise with the original bank F_0,

$$\widehat{F_D} = \begin{cases} F_0 - DopplerAbs & if\ F_0 \geq DopplerAbs \\ F_0 + M - DopplerAbs & if\ F_0 < DopplerAbs \end{cases} \quad (4)$$

Step 3: Determine Doppler difference and power difference

The main idea of using Doppler information is that assuming y_i is the detection of the target at the time i, the value of the estimated Doppler from the radial velocity will be approximately equal to the measured Doppler at the time i.

The Doppler difference ΔF_D is calculated as follows:

$$\Delta F_D = \left|F_D - \widehat{F_D}\right| \quad (5)$$

If $\Delta F_D >$ M/2:

$$\Delta F_D = M - \Delta F_D \quad (6)$$

where F_D is the measured Doppler of the detection.

The use of the Doppler difference is completely unwavering by the Doppler ambiguity problem.

Similarly, the main idea of using power information is that assuming y_i is the detection of the target at the time i, the value of the measured power at the time i will be

approximately equal to the mean power of the target. In particular, the power value used to calculate is the normalized value regardless of the range.

The power difference ΔP is described by:

$$\Delta P = |P - \bar{P}| \tag{7}$$

where P is the measured power and $\bar{P}$ is the mean power.

Step 4: Determine Doppler difference distance, power difference distance and position distance

The Doppler difference distance $d_{\Delta F_D}$ is calculated according to the following formula:

$$d_{\Delta F_D} = \sqrt{(\Delta F_D - \mu_{\Delta F_D})(S^2_{\Delta F_D})^{-1}(\Delta F_D - \mu_{\Delta F_D})^{-1}} \tag{8}$$

where $\mu_{\Delta F_D}$ and $S^2_{\Delta F_D}$ are the mean and variance of Doppler difference values, respectively.

The power difference distance $d_{\Delta P}$ is given by:

$$d_{\Delta P} = \sqrt{(\Delta P - \mu_{\Delta P})(S^2_{\Delta P})^{-1}(\Delta P - \mu_{\Delta P})^{-1}} \tag{9}$$

where $\mu_{\Delta P}$ and $S^2_{\Delta P}$ are the mean and variance of power difference values, respectively.

The position distance d_p is expressed as following:

$$d_p = \sqrt{(\boldsymbol{p} - \boldsymbol{\mu}_p)\sum^{-1}(\boldsymbol{p} - \boldsymbol{\mu}_p)^{-1}} \tag{10}$$

where p is the measured position vector, $\boldsymbol{\mu}_p$ and $\sum$ are the predicted position vector and covariance matrix of the tracking filter used, respectively.

Step 5: Calculate the score for each distance value

The score value $score_{\Delta F_D}$ for the Doppler difference distance is calculated using the following form:

$$score_{\Delta F_D} = \begin{cases} (thres_{F_D} - d_{\Delta F_D}) & if\ d_{\Delta F_D} < thres_{F_D} \\ 0 & if\ d_{\Delta F_D} > thres_{F_D} \end{cases} \tag{11}$$

where $thres_{F_D}$ is the cut threshold of the Doppler difference distance which is determined by:

$$thres_{F_D} = F^{-1}(95\%) \tag{12}$$

where F is the cumulative distribution function of the Doppler difference distance distribution.

The score value $score_{\Delta P}$ for the power difference distance can be derived as:

$$score_{\Delta P} = \begin{cases} (thres_{\Delta P} - d_{\Delta P}) & if\ d_{\Delta P} < thres_{\Delta P} \\ 0 & if\ d_{\Delta P} > thres_{\Delta P} \end{cases} \tag{13}$$

The score value $score_p$ for the position distance is calculated according to the following formula:

$$score_p = \begin{cases} (thres_p - d_p) & if\ d_p < thres_p \\ 0 & if\ d_p > thres_p \end{cases} \tag{14}$$

where $thres_{\Delta P}$ and $thres_p$ are the cut thresholds of the power difference distance and position distance, respectively. The method of determining these two values is similar to the way of determining $thres_{F_D}$.

Step 6: Normalize the score

Because Doppler and power are used to complement the position information to enhance the efficiency of the detection score calculation function, the score values must be normalized in the range of [0 q], where $q = q_{max}/3$ and q_{max} is the maximum value of the position distance scores.

$$score_{\Delta F_D norm} = \frac{score_{\Delta F_D} * q}{thres_{F_D}} \tag{15}$$

$$score_{\Delta P norm} = \frac{score_{\Delta P} * q}{thres_{\Delta P}} \tag{16}$$

Step 7: Calculate the total score for the detection

The total score value *TScore* of the detection in the target gate shows the appropriate level of that detection for the target. The higher the value of this score, the more suitable the detection to assign the target.

$$TScore = score_p + W_{Doppler} * score_{\Delta F_D norm} + W_{Power} * score_{\Delta P norm} \tag{17}$$

where $W_{Doppler}$ and W_{Power} are weights of $score_{\Delta F_D norm}$ and $score_{\Delta P norm}$, respectively.

$$W_{Doppler} + W_{Power} = 1 \tag{18}$$

The value of the weights depends on the measurement accuracy of each quantity in the radar system. The total score value of the detection in the gate of all tracks is put into auction algorithm to select the most appropriate track-to-detection.

2.2. Tracking Filter

Firstly, the position measurements, including azimuth, range and elevation in sphere coordinates, will be transformed into linear forms in Cartesian coordinates using the method presented in [15]. The completed UKF algorithm is used as follows [16]. In this study, a linear time-invariant system with constant velocity model is considered for simplicity. Accordingly, the state estimate $\widehat{\boldsymbol{X}}$ and the state covariance matrix $\widehat{\boldsymbol{P}}$ of the proposed augmented-state UKF filter are written as the following equation:

$$\widehat{\boldsymbol{X}} = \begin{bmatrix} x & v_x & y & v_y & z & v_z & v_h & F_D \end{bmatrix}^T \tag{19}$$

$$\widehat{\boldsymbol{P}} = \begin{bmatrix} \sigma^{xx} & 0 & \sigma^{xy} & 0 & \sigma^{xz} & 0 & 0 & 0 \\ 0 & \sigma^{v_x v_x} & 0 & 0 & 0 & 0 & 0 & 0 \\ \sigma^{yx} & 0 & \sigma^{yy} & 0 & \sigma^{yz} & 0 & 0 & 0 \\ 0 & 0 & 0 & \sigma^{v_y v_y} & 0 & 0 & 0 & 0 \\ \sigma^{zx} & 0 & \sigma^{zy} & 0 & \sigma^{zz} & 0 & 0 & 0 \\ 0 & 0 & 0 & 0 & 0 & \sigma^{v_z v_z} & 0 & 0 \\ 0 & 0 & 0 & 0 & 0 & 0 & \sigma^{v_h v_h} & 0 \\ 0 & 0 & 0 & 0 & 0 & 0 & 0 & \sigma^{F_D F_D} \end{bmatrix} \tag{20}$$

where *x, y, z,* v_x, v_y, v_z are the position and velocity components of target in the 3-D Cartesian space, v_h which is the augmented element of the state estimate is the radial velocity or range rate, F_D is the Doppler bank, σ is the standard deviation.

Measurement vector $\boldsymbol{z}$ can be written as:

$$\boldsymbol{z} = \left[z_p \;\; rr \;\; F_D\right]^T \tag{21}$$

where $z_p = [r, a, e]$ is the position measurement of range, azimuth and elevation, respectively; *rr* is the indirect radial velocity measurement calculated based on equation (1); F_D is the Doppler measurement.

State transition equations of the filter are used:

$$v_x^k = v_x^{k-1} \tag{22}$$

$$v_y^k = v_y^{k-1} \tag{23}$$

$$v_z^k = v_z^{k-1} \tag{24}$$

$$x^k = x^{k-1} + v_x^k * \Delta T \tag{25}$$

$$y^k = y^{k-1} + v_y^k * \Delta T \tag{26}$$

$$z^k = z^{k-1} + v_z^k * \Delta T \tag{27}$$

$$v_h^k = \frac{-(x^k * v_x^k + y^k * v_y^k + z^k * v_z^k)}{\sqrt{x^k * x^k + y^k * y^k + z^k * z^k}} \tag{28}$$

If Doppler increases clockwise:

$$F_D^k = mod\left(F_0 + mod\left(\frac{v_h^k}{v_d}, M\right), M\right) \tag{29}$$

Otherwise,

$$F_D^k = F_0 - mod\left(\frac{v_h^k}{v_d}, M\right) \; if \; F_0 \geq mod\left(\frac{v_h^k}{v_d}, M\right) \tag{30}$$

$$F_D^k = F_0 + M - mod\left(\frac{v_h^k}{v_d}, M\right) \; if \; F_0 < mod\left(\frac{v_h^k}{v_d}, M\right) \tag{31}$$

3. Result and discussion

3.1. Single target case

We now consider tracking a single target in a clean environment using the constant velocity model with the following set of parameters. For the target, the initial state is $\widehat{X_0} = \left[950\ m,\ 10\frac{m}{s},\ 310\ m,\ 10\frac{\mathrm{m}}{\mathrm{s}},\ 0\ m,\ 0\frac{\mathrm{m}}{\mathrm{s}},\ 0\frac{m}{s}, 0\right]^T$. The radar is located at Cartesian coordinates (0 km, 0 km, 0 km) and sampling interval of T = 1 s. The process noises are presumed to be zero-mean white Gaussian with standard deviations of azimuth, range, and Doppler measurements are σ_a = 2 deg, σ_r = 90 m, and σ_D = 1 bank Doppler, respectively. The Doppler resolution is 0.5 m/s and the total number of Doppler banks processed is 24. The tracking result is compared with the traditional method which only used the position measurement and the modified UKF presented in [14] in two different groups of measurements: 1) position and ambiguous Doppler, 2) position and unambiguous Doppler. The position and velocity root-mean-squared error (RMSE) errors are utilized to estimate the tracking performance.

In most cases, both modified UKF in [14] and proposed method can effectively resolve the Doppler ambiguity and obtain the same track performance as with unambiguous Doppler situation as indicated in Figure 1(a). Both methods also present the better tracking result than the position-only method. However, in some instances, the modified UKF [14] uses an inaccurate estimate of mean and covariance or an erroneous innovation, which would lead to divergence as illustrated in Figure 1(b). On the other hand, the proposed method shows the same result as the unambiguous Doppler case.

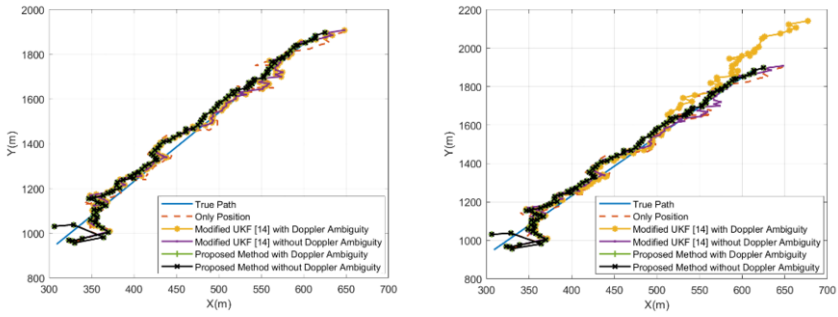

(a) (b)

Figure 1. Tracking results in convergent case (a) and divergent case of modified UKF [14] (b)

As can be seen from Figure 2, the proposed method obtains the velocity and position RMSE values of the Doppler ambiguity situation almost overlie with those of the unambiguous situation. Moreover, the enhancements in position and velocity RMSEs are approximately 18% and 55%, respectively, compared with RMSE when using the position-only method, about 8% and 10% compared with RMSE when using the modified UKF [14] method.

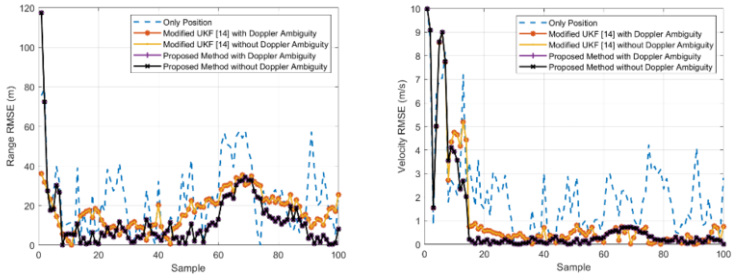

(a) (b)

Figure 2. RMSE for modified UKF [14] and Proposed method, (a) Range RMSE, (b) Velocity RMSE

3.2. Multitarget case

A multi-target tracking scenario with three targets using the constant velocity model is illustrated. The starting time for each target is zero seconds. The radar is located at Cartesian coordinates (0 km, 0 km, 0 km) and sampling interval of T = 1 s. The process noises are assumed to be zero-mean white Gaussian with standard deviations of range, azimuth, Doppler and power measurements are σ_r = 15 m, σ_a = 0.3 deg, σ_D = 1 bank Doppler, and σ_p = 15 dB, respectively. The Doppler resolution is 0.5 m/s and the total number of Doppler banks processed is 24. The trajectory of each target is shown in

Figure 4(a). The high clutter region is generated around the target. The Doppler and power measurements for clutter points have uniform distributions over the regions (0, 12) and (0, 100), respectively.

Figure 3 shows the distributions of three parameters: position distance, power difference distance and Doppler difference distance. The cut threshold value for each of those parameters is determined based on the corresponding distribution. Accordingly, the cut thresholds of position distance, power difference distance and Doppler difference distance are 5.3, 2.8 and 8, respectively.

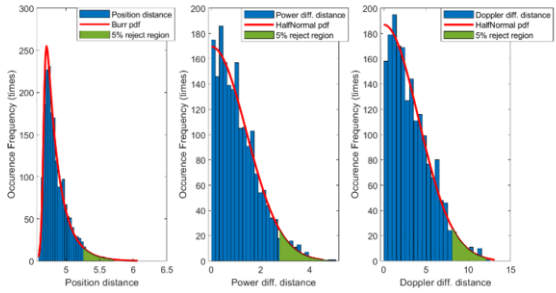

Figure 3. Histogram with distribution fit of position, power difference and Doppler difference distance

Figure 4(b) presents the tracking results with three methods: 1) Position only, 2) joint integrated probabilistic data association (JIPDA) method [14] and 3) the proposed method. The performances are compared in terms of RMSE and false detection rate. The false detection rate is defined as the number of false detections per time scan, determined by

$$R_f = \frac{1}{T_{sim}} \sum_{i=1}^{T_{sim}} N_f(i)$$

where T_{sim} is the total simulation time and $N_f(i)$ is the total number of false detections at the time i.

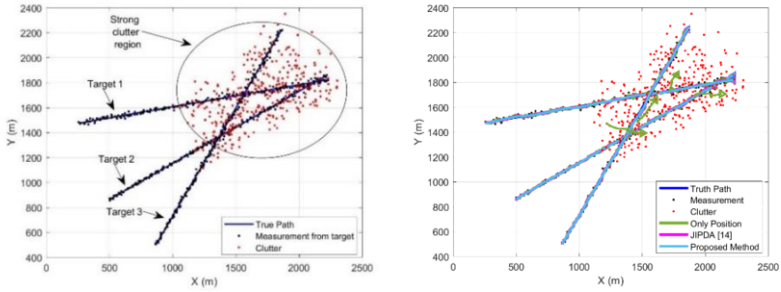

(a) (b)

Figure 4. Simulated targets and surrounded clutter (left) and Estimated tracks (right)

It can be seen that the relative position RMSE of the proposed method becomes smaller than those of the position-only method and JIPDA [14] method (shown in Figure 4b). It means the estimated tracks are close to the true paths. Meanwhile, the position-only method generates a lot of false tracks. Numerically, from Table 1, the improvements in the position and velocity RMSEs are about 21% and 40% with respect to those of the

JIPDA [14] method. With the presence of power measurement, the proposed method also obtains the lower false detection rate than the JIPDA [14] method in the high clutter situation. Specifically, the false detection rate has decreased up to 95% compared with the JIPDA [14] method.

Table 1. The performance comparison of the proposed method and the peer method JIPDA

	Position Only	**JIPDA [14]**	**Proposed Method**
RMSE Position (m)	11.5	8.8	6.9
RMSE Velocity (m/s)	0.63	0.41	0.25
False detection rate	35	5.6	0.3

The proposed method is also applied to a coastal surveillance radar station for our test. We are interested in "Track 1" area (inside the blue circle) in which there are usually sea and weather clutters. The results are shown in Figure 5. The position-only method which only used position in MTT system leading the target chose wrong detection from clutter and move incorrect direction (left figure). The proposed method shows that the target choose correct detection and move right direction (right figure).

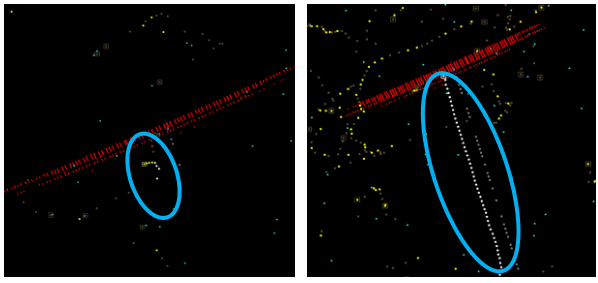

Figure 5. Target tracking result with position-only method (left) and proposed method (right)

4. Conclusion

In this paper, a new approach for Multi-Target Tracking with combination of position, power and ambiguous Doppler measurements is presented. Firstly, we investigated an improved data association scheme that utilizes statistical features of position, Doppler and power. The estimated Doppler value calculated from the target range and timestamp will be compared with the measured Doppler to deal with the Doppler ambiguity situation. Secondly, we studied an augmented UKF algorithm using position, Doppler measures, and the indirect measure of radial velocity in the linear domain. Based on the simulated and real data, it was shown that our proposed method has good performance in terms of reduced number of false track-to-detection association and improving the accuracy of the target state estimation. The improvements in the position and velocity RMSEs are about 21% and 40% with respect to the JIPDA [14] method. The false detection rate has decreased up to 95% compared with the reference method.

References

[1] H. Kameda, S. Tsujimichi and Y. Kosuge, "Target tracking under dense environments using range rate measurements," *Proceedings of the 37th SICE Annual Conference. International Session Papers*, Chiba, Japan, 1998, pp. 927-932, doi: 10.1109/SICE.1998.742946.

[2] S-W. Yeom, T. Kirubarajan and Y. Bar-Shalom, "Track segment association, fine-step IMM and initialization with Doppler for improved track performance," in *IEEE Transactions on Aerospace and Electronic Systems*, vol. 40, no. 1, pp. 293-309, Jan. 2004, doi: 10.1109/TAES.2004.1292161.

[3] Y. Yao, J. Zhao and L. Wu, "Doppler Data Association Scheme for Multi-Target Tracking in an Active Sonar System," *Sensors*, vol. 19, no. 9, pp. 2003, 2019, doi: https://doi.org/10.3390/s19092003.

[4] H. Wang, T. Zhao, W. Wu, M. Lu and L. Xiong, "The Multi-target Tracking Algorithm Based on the MM-GLMB Filter with Doppler Information," *4th International Conference on Robotics, Control and Automation Engineering (RCAE),* Wuhan, China, 2021, pp. 326-332, doi: 10.1109/RCAE53607.2021.9638957.

[5] M. Lei and C. Han, "Sequential nonlinear tracking using UKF and raw range-rate measurements," in *IEEE Transactions on Aerospace and Electronic Systems*, vol. 43, no. 1, pp. 239-250, January 2007, doi: 10.1109/TAES.2007.357130.

[6] Jianguo Wang, Peikun He and Teng Long, "Use of the radial velocity measurement in target tracking," in *IEEE Transactions on Aerospace and Electronic Systems*, vol. 39, no. 2, pp. 401-413, April 2003, doi: 10.1109/TAES.2003.1207253.

[7] G. Zhou, N. Zhao, T. Fu, T. Quan and T. Kirubarajan, "Enhanced sequential nonlinear tracking filter with denoised pseudo measurements," *14th International Conference on Information Fusion*, Chicago, IL, USA, 2011, pp. 1-7.

[8] W. Wu, J. Jiang, W. Liu, X. Qin and W. Zhang, "A sequential converted measurement Kalman filter in the ECEF coordinate system for airborne Doppler radar," in *Aerospace Science and Technology*, vol. 25, no. 1, pp. 11-17, Jan. 2016, doi: 10.1016/j.ast.2016.01.008.

[9] G. Zhou, Z. Guo, K. Li and L. Wu, "Motion modeling and state estimation in range-Doppler plane," in *Aerospace Science and Technology*, vol. 115, Aug. 2021, doi: 10.1016/j.ast.2021.106792.

[10] T. Cheng, L. Li, "Sequential linear filtering with non-linear position and Doppler measurements for target tracking", IET Radar Sonar Navigation, 16 (4), pp. 646–658, 2021, doi: 10.1049/rsn2.12209.

[11] C. M. Alabaster, E. J. Hughes and J. H. Matthew, "Medium PRF radar PRF selection using evolutionary algorithms," in *IEEE Transactions on Aerospace and Electronic Systems*, vol. 39, no. 3, pp. 990-1001, July 2003, doi: 10.1109/TAES.2003.1238751.

[12] G. Zhou, M. Pelletier, T. Kirubarajan, and T. Quan, "A Gaussian mixture filter for target tracking with Doppler ambiguity", Proc. SPIE 8392, Signal Processing, Sensor Fusion, and Target Recognition XXI, 839206, May 2012, doi: 10.1117/12.921298.

[13] S.-J. Shin, E.H. Kim, "Track-Before-Resolving: Doppler ambiguity resolution at low SNR", IET Radar Sonar Navig, 17(1), pp. 117–127, 2023, doi: 10.1049/rsn2.12328.

[14] K. Li, B. Habtemariam, R. Tharmarasa, M. Pelletier and T. Kirubarjan, "Multitarget Tracking with Doppler Ambiguity," in *IEEE Transactions on Aerospace and Electronic Systems*, vol. 49, no. 4, pp. 2640-2656, October 2013, doi: 10.1109/TAES.2013.6621842.

[15] S. Blackman and R. Popoli, *Design and Analysis of Modern Tracking systems*, Artech House Publisher, Boston, 1999.

[16] E. A. Wan and R. Van Der Merwe, "The unscented Kalman filter for nonlinear estimation," *Proceedings of the IEEE 2000 Adaptive Systems for Signal Processing, Communications, and Control Symposium (Cat. No.00EX373)*, Lake Louise, AB, Canada, 2000, pp. 153-158, doi: 10.1109/ASSPCC.2000.882463.

Fuzzy Systems and Data Mining IX
A.J. Tallón-Ballesteros and R. Beltrán-Barba (Eds.)

doi:10.3233/FAIA231012

Wind Loads on Structures: A Finite Element-Based Computational Fluid Dynamics Analysis in Evaluating the Wind Tunnel Effects on Low-Rise Structures

Benjamin D. FLORES [a,1], Dante L. SILVA [b]
[a] *School of Graduate Studies, Mapua University, Manila, Philippines*
[b] *School of Civil, Environmental, and Geotechnical Engineering, Mapua University, Manila, Philippines*

Abstract. This research paper evaluates the effects of wind tunnel testing on low-rise buildings using a Finite Element-based computational fluid dynamics (CFD) model in order to compare the results of the traditional Directional Procedure (Building of All Heights Method) to the results of the CFD analysis. This study utilized all necessary parameters for the Wind Tunnel Procedure in accordance with the National Structural Code of the Philippines section 207F together with the guidelines prescribed in ASCE 7-16. The mathematical prototype of 3 different buildings with the same dimensions were created using midas NFX, and the necessary boundary conditions for CFD analysis were set up. The pressure caused by wind load on these buildings were evaluated and compared with the Directional procedure in Section 207B of the NSCP (Buildings of all heights method). Atmospheric turbulence was also modelled using Kinetic Energy and Length Scale method utilizing 2-equation k-ε turbulence model. The results show significant differences in pressure effects on walls with considerable number of openings and unique façade features. CFD results also show accurate internal pressure and velocity profile in areas near the wall openings and building edges. This research is particularly relevant for the design and construction of buildings in areas prone to strong winds, such as the Philippines, where accurate wind load calculations are crucial to ensuring structural safety and integrity. While numerous studies in other countries have explored the impact of wind on low-rise structures through mathematical simulations, there remains a substantial gap in the Philippines regarding research concerning wind tunnel effects on structures using mathematical and numerical approaches. This study aims to fill this gap by connecting the existing National Structural Code of the Philippines with contemporary trends in mathematical simulations.

Keywords. Wind load, Wind Tunnel, Computational Fluid Dynamics (CFD), Finite Element Method, Main Wind Force Resisting System (MWFRS)

1. Introduction

Wind loads on buildings can cause major damage, especially in areas with frequent strong winds like the Philippines. It is crucial to accurately calculate these loads to ensure

[1] Corresponding Author: Benjamin D. Flores, School of Graduate Studies, Mapua University, Manila, Philippines, E-mail: bdflores@mymail.mapua.edu.ph

buildings can withstand them. The National Structural Code of the Philippines, which serves as the main design code in the Philippines, offers different methods for calculating wind loads, with the Wind Tunnel Procedure being the most precise.

Wind tunnel testing is a highly popular method in wind engineering due to its cost-effectiveness compared to field measurements[1]. Over the years, numerous wind tunnel tests have been carried out to evaluate the wind pressures on models of tall buildings [2]. In their study in 2022,[3] conducted wind tunnel experiments for three commonly utilized shapes of storm shelters at Ryerson University. The objective of the investigation is to contrast North American standards for designing wind shelters with an extensive experimental wind simulation using boundary layer wind tunnel testing under synoptic wind conditions.

An emerging technology that is being utilized in structural engineering is the use of CFD. CFD is an integrable technology that can be used to estimate important information about the outdoor environment, such as wind flow patterns, air temperature distributions, relative humidity, and even contaminant concentrations if necessary[4]. In recent times, computational fluid dynamics (CFD) has emerged as a useful tool to address many similar problems[5]. Additionally, CFD can provide information on environmental variables over the entire computational domain, under precise set conditions, without worrying about incomplete and inaccurate observation data caused by factors like oversimplification or obstruction of laser by complex models[6]. Traditional observational approaches such as wind tunnel experiments are limited in their ability to compute such information. CFD is becoming more popular, especially for creating natural ventilation systems in buildings with opened-roof structures such as atria, because it can provide a detailed analysis of the flow and temperature, avoiding the need for empirical correlations regarding flow and heat transfer rates [7].

This research centers on developing a mathematical model of the wind tunnel procedure in compliance with Section 207F of the National Structural Code of the Philippines 2015 through FE-based CFD analysis. This research compared the results of the Wind Tunnel procedure and the Directional Procedure (Building of All Heights Method). Although there are many existing studies conducted in other countries relating to the effects of wind on low-rise structures using mathematical simulations, the Philippines still has a huge gap in terms of related studies prior to mathematical and numerical simulations of wind tunnel effects on structures. This study aims to bridge the gap between the current National Structural Code of the Philippines and the modern trends in mathematical simulations. The results of this study can be used to propose a new methodology for calculating wind loads on partially enclosed buildings based on the analysis results of the wind tunnel procedure. This research is particularly relevant for those involved in the design and construction of buildings in the Philippines, as it provides valuable insights into the effects of wind loads on structures, and proposes potential solutions for mitigating these effects.

2. Related Studies

To evaluate the impact of wind on such structures, wind tunnel testing is often employed. However, the results obtained from wind tunnel testing are influenced by various factors such as the size and shape of the model, the type of wind tunnel used, and the instrumentation used for measuring the wind loads. In recent years, Finite Element-based

computational fluid dynamics (CFD) analysis has emerged as a powerful tool for predicting fluid flow using a mathematical model[8].

Several literatures were presented in this paper which greatly contributes to the development of this research. [9] analyzed the wind load characteristics of low-rise structures subjected to the effects of high-rise structures. The results of this investigation reveal that modifying the height and spacing ratios can significantly impact the wind pressure distribution of a specific low-rise building. [10]The design coefficients for wind load on the main wind-force resisting systems (MWFRSs) should be established based on the highest load effect [11]. [12] conducted smaller-sized experiments to measure turbulent flow patterns in three dimensions around a cluster of buildings in a wind tunnel located at the Niigata Institute of Technology, Japan. In 2022, [3] studied storm shelter shapes at Ryerson University via wind tunnel experiments. They aimed to compare North American design standards with boundary layer wind tunnel tests simulating synoptic wind conditions. Wind tunnel results were compared with codes for structural forces and cladding pressures. [11] used wind tunnel tests to examine design wind force coefficients for main wind forces in open and semi-open framed membrane structures. They determined varied load effects for each structure and proposed design coefficients using the load response correlation (LRC) approach. CFD numerical simulation technique was employed to examine how multi-story or high-rise structures affect the surface wind loads of low-rise buildings by [9]. [10] utilized the ASCE 7-16 provisions for Main Wind-Force Resisting System (MWFRS) for comparison in order to validate the results of their study. In 2022, [12]comprehensively assessed the accuracy of computational fluid dynamics (CFD) models in predicting average and turbulent wind patterns around a tall skyscraper within a context of short buildings and narrow streets.

In 2022, [13] created machine learning models to predict real-time vertical displacement of a structure using temperature field data. They tested these models on a virtual steel roof (8m x 8m x 0.6m), evaluating their performance across 1200 simulated fire scenarios.

3. Methodology

3.1. Identifying necessary parameters based on NSCP 2015 section 207A

Phase 1 of the wind tunnel procedure involves collecting all the necessary parameters in accordance with the NSCP 2015. Section 207A of the National Structural Code of the Philippines will be the primary source of data in this phase. These data include the building risk category, basic wind speed, wind directionality factor, exposure category, gust effect factor, enclosure classification, and internal pressure coefficient.

3.2. Creating a mathematical prototype of the Wind Tunnel procedure using midas NFX

In this phase, a 3D model of the structures is created using AutoCAD 3D. The model includes dimensions, roof and wall openings. It is treated as a solid object without significant stiffness values (*Rigid Pressure model, PM*). The completed AutoCAD model is saved as a DXF file and imported into midas NFX software for Computational Fluid Dynamics (CFD) analysis. Three different models are made based on enclosure classifications (Enclosed, Partially Enclosed, Open). All structures have dimensions of

28m length, 15m width, 6m eave height, and 12m roof peak height. The test section size is 150m x 75m x 300m.

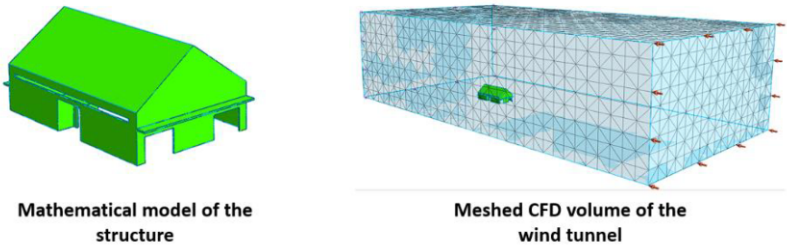

Figure 1. Mathematical model of the partially enclosed structure with the wind tunnel

3.3. Setting up boundary and testing conditions in accordance to the provisions of Section 207F.2 of the NSCP 2015 and running the analysis

In midas NFX, the CFD analysis consists of several steps: meshing, applying loads and boundary conditions, defining material and air properties, performing the analysis, and interpreting the results.

Atmospheric turbulence was also modelled using Kinetic Energy and Length Scale method. The turbulence model used in this study was the 2-Equation k-ε model. The air was assumed to be dry and at constant temperature of 25°C with a constant velocity of 270 kph as per the basic wind speed provision of NSCP 2015

3.4. Evaluating the results and comparing it to NSCP Section 207B procedure

Once the analysis for various wind directions is complete in midas NFX, the researcher will save the graphical and tabular results in a specific file location. However, these raw data require an additional step outlined in Section 207F of the NSCP. According to the code, the highest wind speeds are expected in directions where the building's design has fewer form or pressure coefficients at their maximum values. To maintain safety, the code limits the reduction allowed from wind tunnel testing to 80% of the results obtained from Section 207B.

4. Results and Discussion

4.1. Results of Manual calculation using the Directional Procedure

The manual calculations provided results that focused on the effects of wind pressure on different parts of the building. The sidewalls and leeward walls, as well as the windward wall up to a height of 4.5m, had specific pressure values. This division was due to consistent coefficients for wall pressure. Enclosed and Partially Enclosed structures showed similar wind behavior. Tables 1 and 2 present the specific wind pressure values on the walls and roof when the wind direction aligns with the ridge of the gable roof in an enclosed building.

Table 1. Wall pressure values in an Enclosed building with 80% reduction factor applied at each meter above ground level (Wind parallel to ridge)

Height above ground (m)	Windward pressure (N/m^2)	Sidewall pressure (N/m^2)	Leeward pressure (N/m^2)
4	1203.64	-1255.66	-713.97
5	1229.63	-1255.66	-713.97
6	1281.77	-1255.66	-713.97

Table 2. Roof pressure values in an Enclosed building with 80% reduction factor applied at each meter above ground level (Wind parallel to ridge)

Distance from the Windward wall	Positive windward (N/m^2)	Negative windward (N/m^2)
0 to 9	-1913.87	54.68
9 to 18	-1225.28	54.68
18 to 28	-880.99	54.68

4.2. Results from CFD

Results obtained from the CFD analysis were shown in Figures 2 to 4. It can be seen that the actual velocity and pressure profile were reflected in the analysis. The effects of wall openings also contributed to the overall behavior of the wind.

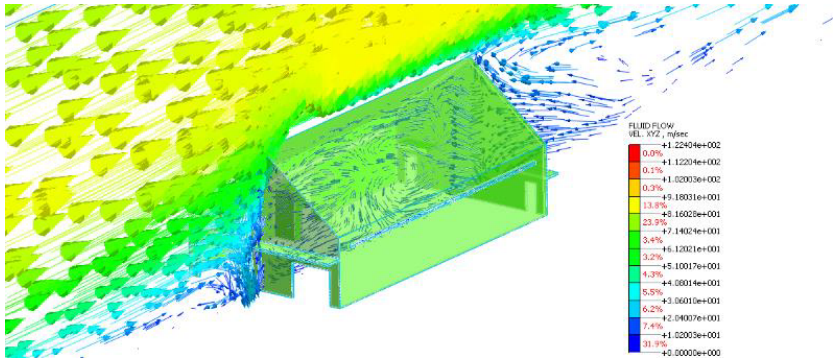

Figure 2. Velocity vector profile at midpoint of the windward wall

The maximum effects of wind pressure on walls and roofs are tabulated in figures 3 and 4. It is noticeable that wind pressure gradually increases as the height increases with the exception of the windward wall. Due to the ground effect on the velocity of the wind, there is an abrupt increase in wall pressure up to 2m above ground level.

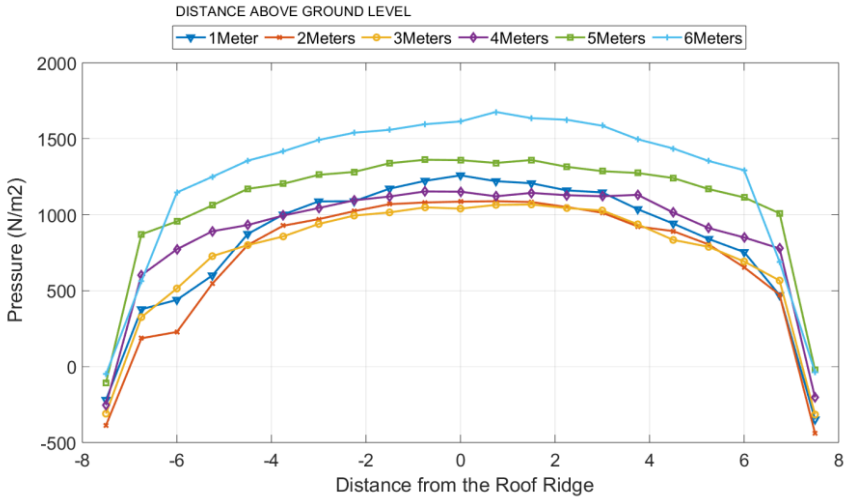

Figure 3. Pressure at Windward wall in an Enclosed building

It can be seen that the maximum positive wind pressure occurs near mid-section of the windward wall. Negative pressure also develops near the edges of the windward wall. On the other hand, the leeward wall receives pure negative wind pressure with a considerable variation from edges to the middle of the leeward wall.

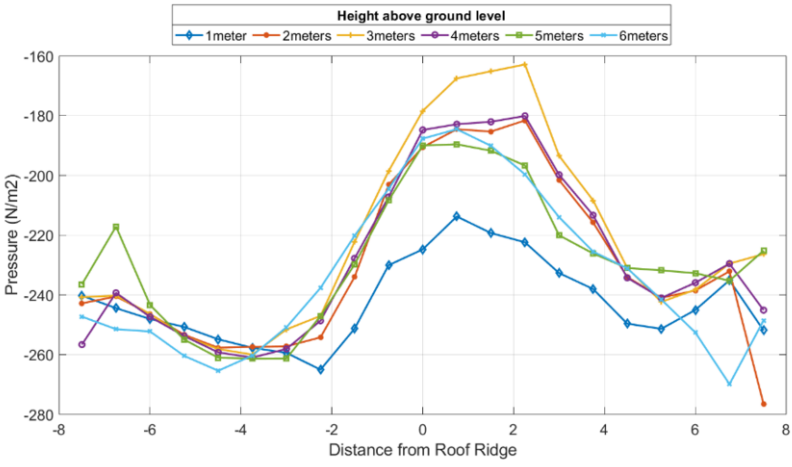

Figure 4. Pressure at Leeward wall in an Enclosed building

4.3. Comparison between the Directional Procedure and CFD

It can be seen that the values obtained from the Directional procedure generally is greater than what is obtained from the wind tunnel testing. This corresponds to the user notes in section 207F which states that wind tunnel tests frequently measure wind loads that are significantly lower than required by the directional procedure[14].

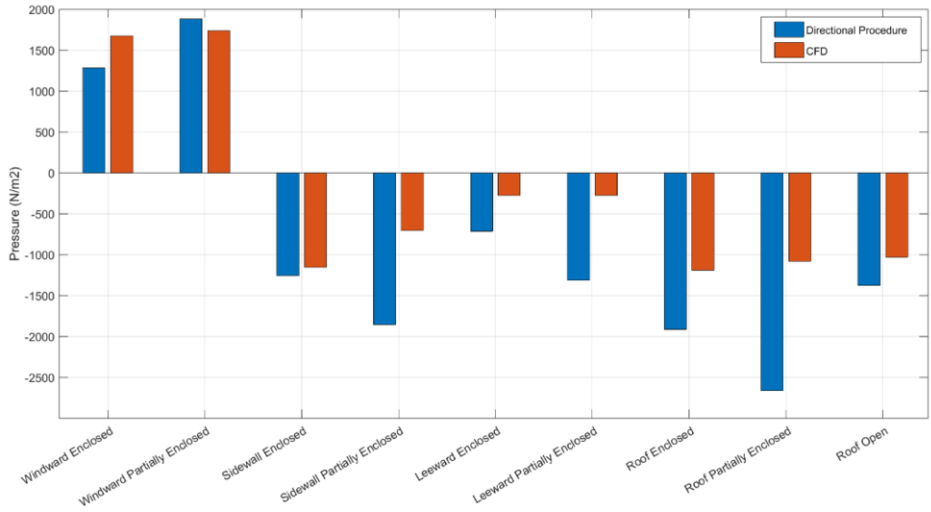

Figure 5. Maximum wind pressure at each wall and roof faces using Directional procedure and CFD

5. Conclusion

The purpose of this study is to compare the results of the Directional procedure and the CFD Wind tunnel procedure for different types of low-rise structures. Results obtained from the Directional procedure shows great approximation and overestimation in the side walls and leeward walls of the structures. Additionally, it can also be noticed that pressure values at the windward wall from ground level up to 4.5 meters above ground has the same values regardless of the geometry of the windward face.

On the other hand, CFD wind tunnel procedure calculates wind pressure values which are significantly lower than that obtained from the Directional procedure. CFD wind tunnel results show the exact wind behavior, the location of pressure concentration, and internal pressure effects due to vortex shedding at wall openings.

As of now, even with the use of modern structural analysis software (STAAD, ETABS, midas Gen) wind load calculation for low-rise structures still has to be done manually using the directional procedure. This study aims to utilize the available tools that we have in the industry like solid modelling and CFD analysis in order to offer an alternative and faster solution to complex problems.

This research focused only on structures with simple geometry with a limited height in order to have a clear comparison to the Directional procedure. Additionally, terrains, obstructions, and ground elevation were not considered in this paper. A more detailed study comparing other complex building shapes and environment is recommended by the researcher.

References

[1] K. C. A. Lat, D. L. Silva, and K. L. M. De Jesus, “Neural Network-based Approach for Identifying the Influence of Factors affecting the Green Building Rating of a

Rural Housing Construction," Proceedings - 2022 International Conference on Management Engineering, Software Engineering and Service Sciences, ICMSS 2022, pp. 36–43, 2022, doi: 10.1109/ICMSS55574.2022.00013.

[2] X. L. Han, Q. S. Li, K. Zhou, and X. Li, "Comparative study between field measurements of wind pressures on a 600-m-high skyscraper during Super Typhoon Mangkhut and wind tunnel test," Eng Struct, vol. 272, Dec. 2022, doi: 10.1016/j.engstruct.2022.114958.

[3] T. Ghazal, A. Elshaer, and H. Aboshosha, "Wind load evaluation on storm shelters using wind tunnel testing and North American design codes," Eng Struct, vol. 254, Mar. 2022, doi: 10.1016/j.engstruct.2021.113821.

[4] L. Zheng, W. Lu, L. Wu, and Q. Zhou, "A review of integration between BIM and CFD for building outdoor environment simulation," Building and Environment, vol. 228. Elsevier Ltd, Jan. 15, 2023. doi: 10.1016/j.buildenv.2022.109862.

[5] Y. Tominaga and M. Shirzadi, "Influence of detailed air flow distribution on corrosion damage due to airborne sea salt adhesion in a large sports stadium: A CFD analysis," Journal of Building Engineering, vol. 64, Apr. 2023, doi: 10.1016/j.jobe.2022.105690.

[6] D. Silva et al., "Post-pandemic Project Change Management Model: An Adaptable Framework Utilizing Levenberg–Marquardt Algorithm and Dynamic Causal Loop Diagram for Construction Innovation," Lecture Notes in Civil Engineering, vol. 201, pp. 587–600, 2022, doi: 10.1007/978-981-16-6932-3_51.

[7] C. Chen and C. Gorlé, "Full-scale validation of CFD simulations of buoyancy-driven ventilation in a three-story office building," Build Environ, vol. 221, Aug. 2022, doi: 10.1016/j.buildenv.2022.109240.

[8] D. Silva et al., "Backpropagation Neural Network in Flexural Members: Prediction of Capacity Reduction of Beams with Cold Joints using the Angle of Inclination and Discontinuity Location," ACM International Conference Proceeding Series, pp. 60–67, Nov. 2021, doi: 10.1145/3507524.3507535.

[9] L. Zhao and Y. Li, "The influence of multi/high-rise building on the surface wind load of low-rise building," Alexandria Engineering Journal, vol. 61, no. 12, pp. 11979–11991, Dec. 2022, doi: 10.1016/j.aej.2022.05.053.

[10] Y. Liu, G. A. Kopp, and S. fu Chen, "Effects of plan dimensions on gust wind loads for high-rise buildings," Journal of Wind Engineering and Industrial Aerodynamics, vol. 194, Nov. 2019, doi: 10.1016/j.jweia.2019.103980.

[11] Y. Takadate and Y. Uematsu, "Design wind force coefficients for the main wind force resisting systems of open- and semi-open-type framed membrane structures with gable roofs," Journal of Wind Engineering and Industrial Aerodynamics, vol. 184, pp. 265–276, Jan. 2019, doi: 10.1016/j.jweia.2018.11.023.

[12] M. Shirzadi and Y. Tominaga, "CFD evaluation of mean and turbulent wind characteristics around a high-rise building affected by its surroundings," Build Environ, vol. 225, Nov. 2022, doi: 10.1016/j.buildenv.2022.109637.

[13] Z. Ye and S. C. Hsu, "Predicting real-time deformation of structure in fire using machine learning with CFD and FEM," Autom Constr, vol. 143, Nov. 2022, doi: 10.1016/j.autcon.2022.104574.

[14] D. L. Silva, K. L. M. D. Jesus, E. M. Adina, D. V. Mangrobang, M. D. Escalante, and N. A. M. Susi, "Prediction of Tensile Strength and Erosional Effectiveness of Natural Geotextiles Using Artificial Neural Network," 2021 13th International Conference on Computer and Automation Engineering, ICCAE 2021, pp. 121–127, Mar. 2021, doi: 10.1109/ICCAE51876.2021.9426170.

Fuzzy Systems and Data Mining IX
A.J. Tallón-Ballesteros and R. Beltrán-Barba (Eds.)

doi:10.3233/FAIA231013

The Processing Method of Wrist Radial Artery Ultrasonic Signal Based on CORDIC Algorithm

Chaohong Zhang[a,b], Xingguang Geng[a,b] ,Jun Zhang[a,b],Yunfeng Wang[a,b] and Yitao Zhang[a,b,1]
[a] *Institute of Microelectronics of Chinese Academy of Sciences, China*
[b] *University of Chinese Academy of Sciences, China*

Abstract. The human wrist radial artery is rich in important physiological and pathological information. The rapid dynamic detection of radial artery can be realized by ultrasonic imaging method. Because of the small amplitude fluctuation and narrow vessel width of the wrist radial artery, it is difficult to detect the vessels by ultrasound. In ultrasonic nondestructive testing system, CORDIC algorithm can realize complex operation only through simple addition, subtraction and shift transformation. It has obvious advantages in high-speed operation, especially suitable for optimizing ultrasonic signal processing algorithm. Based on CORDIC algorithm, this paper proposes a phased array ultrasonic signal processing method for wrist radial artery. The dynamic filtering, orthogonal demodulation and logarithmic compression techniques using CORDIC algorithm are mainly studied. FPGA simulation results show that CORDIC algorithm can realize the rapid reproduction of the wrist radial artery ultrasonic echo signal, which lays the foundation for the next step of the interpretation of the physiological and pathological information on the radial artery.

Keywords. wrist radial artery, ultrasonic phased array, CORDIC algorithm, dynamic filtering, quadrature demodulation, logarithmic compression, FPGA simulation

1. Introduction

Traditional Chinese medicine (TCM) can judge the patient's physical state by interpreting the basic information such as pulse width and pulse length[1]. However, TCM doctor mainly interprets the information related to the wrist radial artery through finger perception, which has subjective factors and lacks objective quantitative standards. With the development of pressure sensor technology, pulse diagnosis equipment used to detect radial artery information provides a basis for the objectification of pulse diagnosis[2]. Its acquisition probe is also transformed from the original single pressure sensor probe to the array pressure sensor probe. And its detection range is gradually transformed from the original single pulse wave detection to the measurement of pulse width and pulse length. At present, most of the detection methods are passive detection.

[1] Corresponding Author, Yitao Zhang (Institute of Microelectronics of the Chinese Academy of Sciences, Beijing 100029, China; University of Chinese Academy of Sciences, Beijing 100049, China) and E-mail: zhangyitao@ime.ac.cn.

The pulse width and pulse length are estimated according to the three-dimensional topographic map of array signal, which lacks certain accuracy.

Ultrasonic phased array system, which is an important nondestructive testing method, can ensure the high precision real-time processing of data signals, so as to effectively improve the stability of the system. With the rapid development of modern IC integrated circuits, high-end FPGA chip resources are now quite rich, with sufficient high-speed I/O pin resources, and even embedded DSP hardware resources, which can provide fast signal communication processing capabilities, especially for ultrasonic phased array system design[3].

CORDIC is the abbreviation of coordinate rotation numerical calculation method. The essence is to approximate the desired rotation Angle by constantly adding and subtracting the positive and negative directions through a fixed angle [4,5]. It can make proper rotation and orientation operations without complex mathematical operations, such as trigonometric function table, multiplication, square root, and inverse trigonometric function, and reduce the difficulty of hardware implementation [6]. CORDIC algorithm has developed rapidly, and is improving towards the trend of high base, high precision and high throughput [7]. In view of its own characteristics, it is especially suitable for the practice of complex function algorithm design based on FPGA and other programmable hardware. It provides a new idea for ultrasonic signal processing and has practical significance for ultrasonic nondestructive testing technology and its development.

The structure of the paper is arranged as follows. The system architecture is briefly outlined in Section 2 firstly. In Section 3, this paper focuses on the application of CORDIC algorithm in the detection of wrist radial artery ultrasonic signals. The echo signal dynamic filtering is completed based on the radix-4 CORDIC algorithm. The digital signal envelope quadrature demodulation is completed based on the Mixed Coarse Fine Tuning CORDIC Algorithm. And based on the improved SF-CORDIC algorithm, the logarithmic compression of the signal is completed. Finally, the preprocessing of radial artery ultrasound signal is realized. and the performance of the algorithm is simulated on FPGA. Then, FPGA simulation results are displayed in Section 4. Finally, in Section 5, we draw the conclusions that CORDIC algorithm can realize the rapid reproduction of the ultrasonic echo signal of the radial artery, laying the foundation for the next step of the interpretation of the physiological and pathological information of the radial artery.

2. System architecture

Ultrasonic phased array system, which is mainly composed of four parts, includes ultrasonic sensor, transmit-receive module, radial artery ultrasonic echo signal processing and upper computer main control module. The ultrasonic sensor is a transducer which realizes the conversion of electrical signal and acoustic signal. The transmit-receive module outputs the transmitting array element excitation signal according to the required delay, generates the corresponding sequential logic control signal when scanning the array, and receives the ultrasonic echo signal with the acquisition array. In the whole radial artery ultrasonic phased system, signal processing is the key part, which can realize dynamic filtering, orthogonal demodulation, dynamic range compression and other functions[8].The upper computer is responsible for the reconstruction and evaluation of the high-fidelity image Fig.1 shows the overall

architecture of the system used to process the radial artery of the wrist. Fig.2 shows the experimental system for processing the radial artery of the wrist.

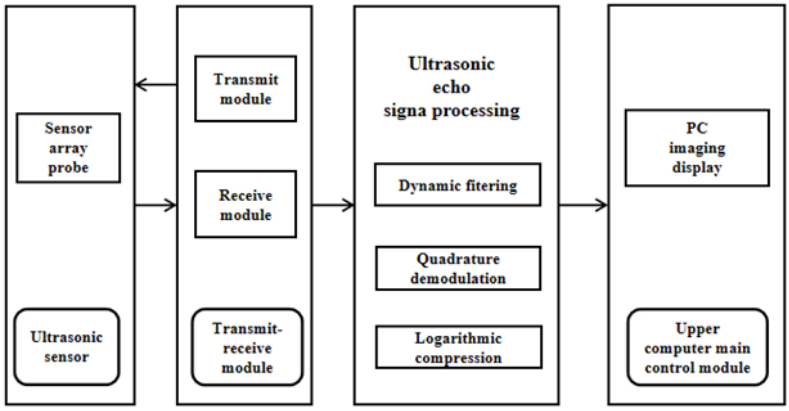

Figure 1. Overall architecture of the system used to process the radial artery of the wrist

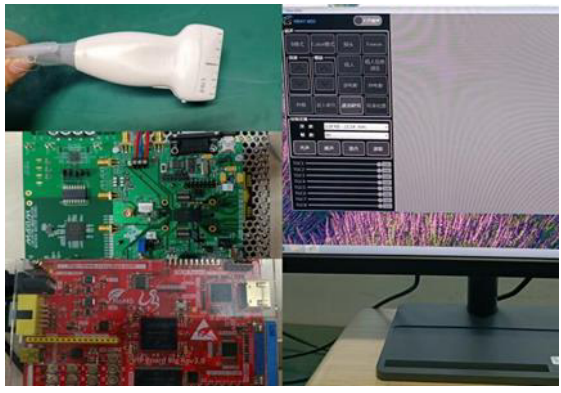

Figure 2. Experimental system for processing the radial artery of the wrist

3. Radial artery ultrasonic phased array signal processing

Radial artery ultrasonic phased array signal processing can be divided into the following modules: dynamic filtering to remove the interference and noise in the signal, orthogonal demodulation to extract the useful amplitude signal, and logarithmic compression is responsible for the dynamic range of the signal compression within 30dB.The block diagram of echo signal pre-processing system is shown in Fig.3.

3.1. Dynamic filtering based on radix-4 CORDIC algorithm

In order to solve the problem that human tissues attenuate different ultrasonic energy at different frequencies, it is necessary to dynamically filter the echo signal after beam synthesis. The implementation of dynamic filtering technology is directly related to the imaging resolution of digital ultrasonic imaging system. By dynamically receiving useful

ultrasonic echo signals of different frequency bands at different depths, the near-field echo receives its high-frequency components with better resolution, and the far-field echo receives its low-frequency components to ensure the depth of detection[9].

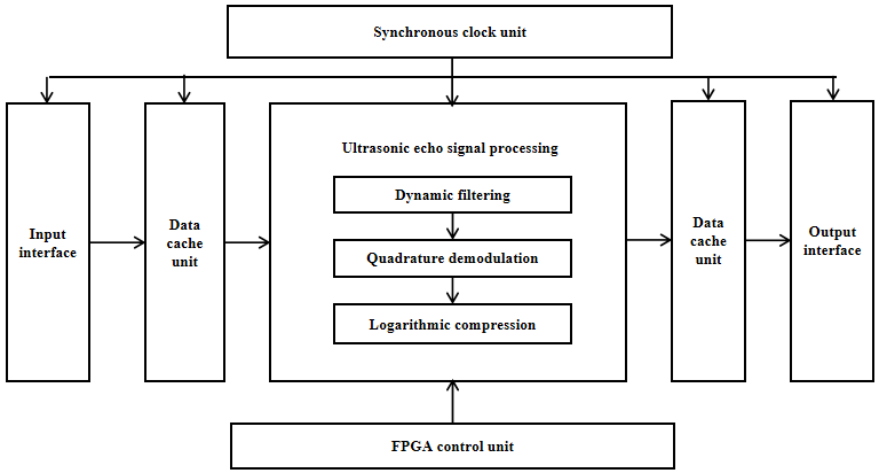

Figure 3. Logic block diagram of ultrasonic echo signal preprocessing system

In this paper, FIR filter based on distributed algorithm is used to transform multiplication into addition based on looking up RAM table, which saves multiplier resources and is faster than multiplier structure. Since the ultrasonic probe used in this paper is an 8-channel probe, and the center frequency is 3.5MHz, 64 groups of band-pass filters with order of 32 and Blackman window are used to complete dynamic filtering. To achieve the purpose of dynamic real-time calculation of filter coefficients, the radix-4 CORDIC algorithm is used[10]. Under the control of the system clock, the filter coefficients are dynamically loaded into the filter distributed RAM to achieve the purpose of dynamic filtering. The schematic diagram of dynamic filtering implemented by FPGA is shown in Fig.4.

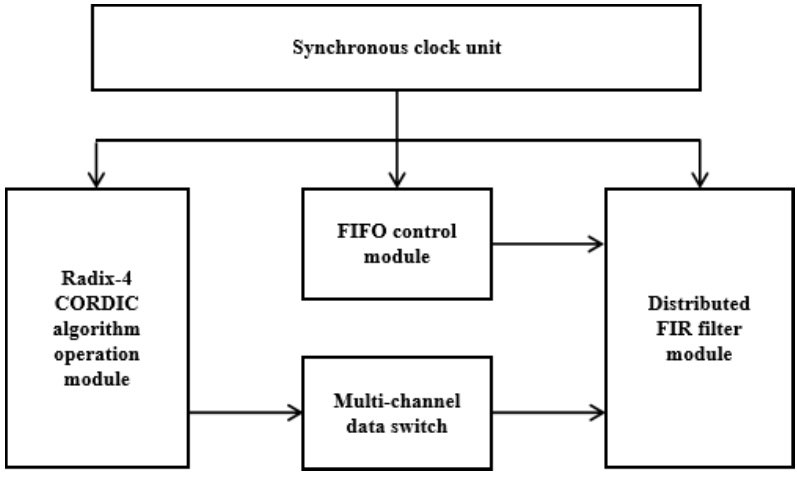

Figure 4. Schematic diagram of dynamic filtering

3.2. Quadrature demodulation based on hybrid coarse fine tuning CORDIC algorithm

In order to obtain the filtered digital signal envelope and use envelope amplitude imaging, envelope detection must be carried out[11]. The common methods of detection include low-pass filtering, Hilbert transform and quadrature demodulation. The ultrasonic echo quadrature demodulation module has excellent anti-interference performance, but it involves a large number of data operations, including square root operations, which will greatly affect the working efficiency of the ultrasonic phased array echo quadrature module.

Since the key operation of this module is square root operation, it needs to meet the requirements of operation accuracy and speed. In this paper, the mixed coarse fine-tuning CORDIC algorithm is adopted. By introducing a hierarchical pipeline, the CORDIC algorithm is divided into two levels: the input value is obtained through the rough operation module, and then as the input of the fine operation module, the final result is obtained by further calculation[12].While ensuring the calculation accuracy, both coarse and fine operations can be performed simultaneously to improve the efficiency of the algorithm and reduce the resource overhead in FPGA. Fig.5 shows the schematic diagram of CORDIC algorithm with mixed coarse fine-tuning.

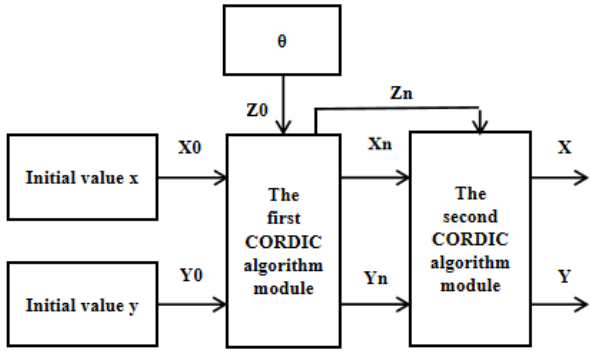

Figure 5. Schematic diagram of CORDIC algorithm with mixed coarse fine-tuning

3.3. Logarithmic compression based on improved SF-CORDIC algorithm

In this paper, an improved SF-CORDIC algorithm is used to realize logarithmic operation. By selecting the appropriate order of the McLaughlin expansion of hyperbolic sine cosine function, the algorithm completely eliminates the calculation of expansion factor and z path and does not need to do area mapping for rotation angle in advance, which greatly reduces the area cost. The figure shows the flow chart of SF CORDIC algorithm for calculating logarithmic function in vector mode, which is mainly divided into two modules: angle accumulation and iterative processing. The objective function is lnk. Initialize, x_0=k+1, y_0=k-1, z_0=0. If the i-th rotation is positive, then the i-th bit of z_1 is 1, otherwise z_2 is 1. The rotation Angle at the end of the rotation is

$$z = z_1 - z_2 \tag{1}$$

Fig.6 is shown the schematic diagram of improved SF-CORDIC algorithm implemented by FPGA in vector mode.

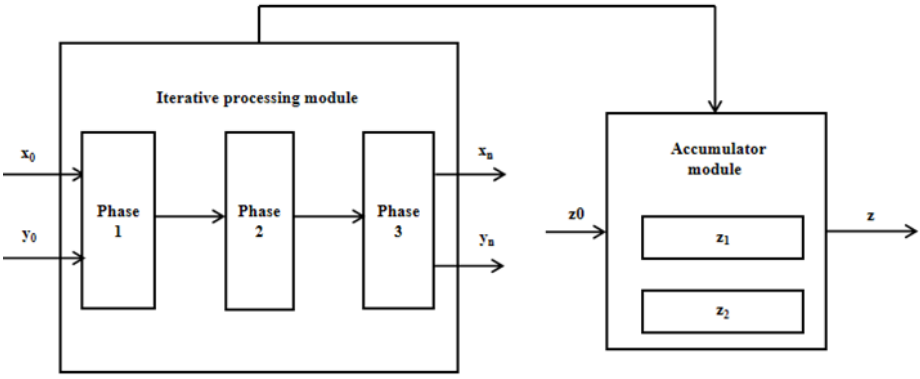

Figure 6. Schematic diagram of improved SF-CORDIC algorithm implemented by FPGA in vector mode

4. Simulation verification

In this paper, Altera's Quartus II 13.0 software is used to design the above three signal processing modules, and Mentor's ModelSim10.1d is used for simulation verification.Fig.7 is the simulation diagram of the dynamic filtering. The results show that the distributed FIR dynamic filtering can achieve better filtering effect. Fig.8 is the simulation diagram of the open square root operation of the mixed coarse fine-tuning CORDIC algorithm. It can be seen from the analysis of the waveform that both meet the design requirements.

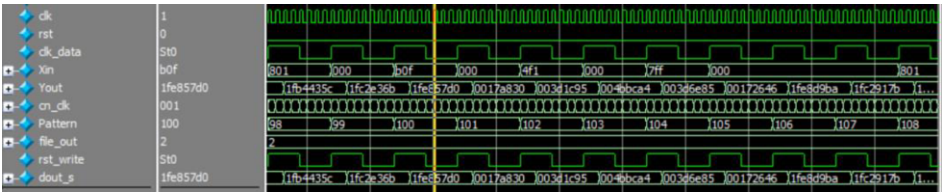

Figure 7. Simulation diagram of dynamic filtering

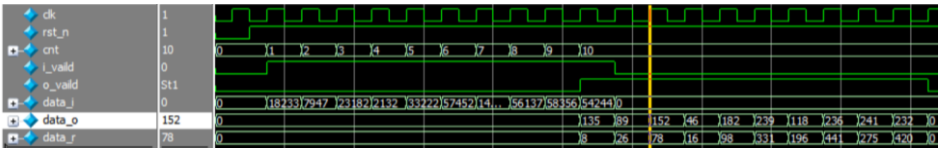

Figure8. Simulation diagram of open square root operation of mixed coarse fine-tuning CORDIC algorithm

5. Conclusion

The radial artery contains important physiological and pathological information. The ultrasonic phased array signal processing implemented by CORDIC algorithm can realize the active dynamic detection of the radial artery. In order to achieve real-time, fast and high-precision processing of radial artery ultrasonic echo signal, and reduce the design requirements of resource consumption, this paper deeply studies the application

of CORDIC algorithm in the detection of wrist radial artery ultrasonic signals based on FPGA platform. In the dynamic filter module, the radix-4 CORDIC algorithm, which can effectively filter the burr, and has achieved an ideal filtering effect. Combined with the characteristics of ultrasonic echo signal quadrature demodulation and hybrid coarse fine adjustment CORDIC algorithm, the real-time signal processing is guaranteed and the hardware complexity is reduced through modeling and simulation. Finally, the improved SF-CORDIC algorithm is used to compress the dynamic range from 60dB to 30dB. CORDIC algorithm can realize the rapid reproduction of the ultrasonic echo signal of the radial artery of the wrist, and lay a foundation for the next interpretation of the physiological and pathological information of the radial artery. This paper only studies three key technologies of radial artery ultrasonic phased array signal processing module, but the applicability of CORDIC algorithm is not limited to these modules, and other improved CORDIC algorithms also need to be further studied. In the future work, the application value of the improved CORDIC algorithm in other modules of ultrasonic phased array will be studied, and to fully utilize the performance advantages of CORDIC algorithm in the field of medical ultrasound.

6. Funding and patents

Sichuan Major Science and Technology Projects (NO. 2022ZDZX0033) provides necessary financial support for data acquisition and algorithm verification.

References

[1] Lui T H, Chan S K. Endoscopic ganglionectomy of the tarsal tunnel: A medial approach[J]. Arthroscopy Techniques, 2021, 10(6): e1615-e1619.
[2] Wang S, Zhang Z, Chen Z, et al. Development of Pressure Sensor Based Wearable Pulse Detection Device for Radial Pulse Monitoring[J]. Micromachines, 2022, 13(10): 1699.
[3] Zhu K, Wen C, Aljarb A A, et al. The development of integrated circuits based on two-dimensional materials[J]. Nature Electronics, 2021, 4(11): 775-785.
[4] Shin K Y, Jeon S C, Nam K C, et al. Implementation of array sensor module for a radial artery tonometry[C]//2010 Annual International Conference of the IEEE Engineering in Medicine and Biology. IEEE, 2010: 6397-6400.
[5] Shi Z, He Q, Liu Y. Accelerating parallel Jacobi method for matrix eigenvalue computation in DOA estimation algorithm[J]. IEEE Transactions on Vehicular Technology, 2020, 69(6): 6275-6285.
[6] Zhu Z, Quan H, Tian L, et al. The Design of NCO Built in Ultra High-Speed Data Converter[C]//2020 IEEE 3rd International Conference on Electronics Technology (ICET). IEEE, 2020: 319-323.
[7] Lopez S, Vladimirova T, Gonzalez C, et al. The promise of reconfigurable computing for hyperspectral imaging onboard systems: A review and trends[J]. Proceedings of the IEEE, 2013, 101(3): 698-722.
[8] Boekhoven R W. Mechanical characterisation of healthy and diseased carotid arteries using ultrasound[J]. 2015.
[9] Gupta A K, Chowdhury V, Khandelwal N. Diagnostic radiology: recent advances and applied physics in imaging[J]. 2013.
[10] Shiri A. A Novel Implementation of CORDIC Algorithm Based on Dynamic Microrotation Generation[J]. International Journal of Electrical and Computer Sciences (IJECS), 2021, 3(1): 17-27.
[11] Wachinger C, Klein T, Navab N. The 2D analytic signal for envelope detection and feature extraction on ultrasound images[J]. Medical image analysis, 2012, 16(6): 1073-1084.
[12] Choi Y C, Yoo S S, Yoo H J. A fully digital polar transmitter using a digital-to-time converter for high data rate system[C]//2009 IEEE International Symposium on Radio-Frequency Integration Technology (RFIT). IEEE, 2009: 56-59.

Fuzzy Systems and Data Mining IX
A.J. Tallón-Ballesteros and R. Beltrán-Barba (Eds.)

doi:10.3233/FAIA231014

Ecosystem Stability Analysis and Numerical Simulation via Three Improved Lotka-Volterra Models

Xueying Wang[1], Tingyue Zhou and Yuanshen Wang
School of Mathematics and Big Data, Chongqing University of Arts and Sciences, Chongqing, China

Abstract. This study analyzed the stability of predator-prey ecosystem (including the sensitivity of the initial value and coefficient) via the original Lotka-Volterra model and three improved models. The first improved model considered the impact of hunting and internal competition on the ecosystem, the second introduced the second prey to the original model, while the third added the second-type predator and the second-type prey to the original system. The performed numerical simulation of the original and three improved models proved instability of the ecosystem represented by the original Lotka-Volterra model and the stability of those represented by all three improved models.

Keywords. Lotka-Volterra model, predator-prey ecosystem, dynamic system, stability analysis

1. INTRODUCTION

The Lotka-Volterra (LV) model, introduced by Lotka in 1925 and later refined by Volterra, has been originally focused on simulating the predator-prey relationship between species [1]. This model was found applicable to enterprise competition, coexistence, and competition among marine organisms, etc. Therefore, it found application in competition analysis research, such as species competition research in ecosystems and competition between enterprises or industries [2-3].

While the original LV model comprised one type of prey and one type of predator, it also has some drawbacks that do not consider the inhibitory effect of limited resources and environment on population growth, its applicability to multiprey-single predator, single prey-multipredator, and multiprey-multipredator systems is problematic due to a lack of accurate theoretical systems and numerical simulations of application scenarios. Thus, the theoretical data and the real data are far from different. Therefore, the LV model needs to be adapted to the above ecosystems, which typically have more than two species and feature some diversity [4-5].

[1] Corresponding Author, Xueying Wang, Chongqing University of Arts and Sciences, China; Email: Wxy17322@163.com

This study introduces three improved LV models simulating (i) multiprey-predator, (ii) prey-multipredator, and (iii) multiprey-multipredator ecosystems.

2. RELATED WORKS

The LV model can simulate scenarios involving predation and competition. Regarding predation, Liu et al. conducted a dynamic analysis of a stage-structured predator-prey model with harvesting power and multiple time delays. They assumed that multiple time delays were introduced into the model system due to the delayed maturation of the prey population and the delayed pregnancy of the predator population [6].

Many researchers have applied the LV model to competitive analysis. Thus, Han et al. used the LV model to study the cooperation between enterprises to resist market competition, simulating various situations, including the market equilibrium obtained through control conditions [7]. Zhang applied a recurrent neural network (RNN) to realize the competitive layer model (CLM) and proposed implementing the LV RNN. The contributions of this paper included establishing the necessary and sufficient conditions for the minimum point of the CLM energy function, verifying the convergence of the LV RNN model, and proving that the stable attractor subset of the LV RNN was precisely equal to the minimum point set of the CLM energy function in the nonnegative direction [8]. Guharay and Chang used a Bayesian simulation algorithm to study whether competition between living species can be detected statistically. Their study (mainly aimed at mammals, plants, birds, marine organisms, and reptiles) proved that birds valued habitats more than marine organisms and assessed the competitive process in detail [9]. Chen and Lin established a mathematical model of the interaction and coexistence mechanisms of two competitive ecosystems with nonlinear intraspecific regulation. They discussed the joint dynamic effects of ripening delay and harvesting effort on population dynamics and the local stability of the model near the internal balance by analyzing the relevant characteristic equations [10].

Several researchers have attempted to improve the LV model. Liu et al. proposed an improved model with a logistic blocking effect. Based on the analysis of the positive equilibrium point's local stability, the improved system's global stability criterion was proposed for predator-prey systems [11]. Hung et al. developed a sales forecasting model to analyze the interaction between convenience and budget retail formats. This improved model mitigated the impact of self-growth, internal competition, and external competition among species neglected in the traditional LV model, making the model more consistent with the actual conditions of the sales market [12]. Mao et al. established the Grey LV model to quantitatively analyse and predict the impact of online payment systems of Chinese commercial banks on the development of third-party online payment systems. In the modeling process, the continuous model is discretized using gray theory, and the model parameters are estimated using the least squares method [13]. Ray and Chaudhuri studied the system by considering the changes in biological parameters and the time cycle of the harvesting effort [14]. Ma et al. used the LV model to perform voltage stability analysis of power systems based on bifurcation theory [15]. Chiang et al. discussed the innovative growth of Taiwan's personal computer (PC) shipments, analyzing the dynamic competitive relationship between PC categories using the LV model to explain the actual diffusion phenomenon in the competitive market [16]. Luo et al. studied the collinear competition between

urban rail and bus public transport based on the population competition model. They used the ecological theory and methods to assess the collinear competition various between public transport modes [17]. Manjunath and Raina performed the stability and bifurcation analysis of the Lotka-Volterra time-delayed system [18]. Gao considered the LV model of three species with discrete delay, studied the stability of positive equilibrium and the existence of Hopf bifurcation, and then obtained the direction and stability criteria of the periodic bifurcation solution using the normal form theory and the central manifold theorem [19]. Wang and Gui studied the existence of periodic solutions for a class of three-species periodic LV predator-prey systems with impulsive perturbations and obtained sufficient and realistic conditions by using the Mawhin extension theorem of the degree of coincidence [20]. El Arabi et al. performed the numerical simulation of the SIR and the Lotka-Volterra models used to describe the dynamics of predator-prey biological systems, the evolution of an infectious disease in any population, and bacterial growth in a given environment. These models formed a system of non-linear and coupled equations, which required special numerical processing [21]. Bouaine and Rachik established an improved spatiotemporal discrete LV model, including different species occupying a three-dimensional area and obeying any complex marine food chain. The method's effectiveness was validated by numerical simulation [22].

3. ORIGINAL MODEL

Before establishing the model, it was assumed that the resources in this ecosystem were infinite and could accommodate an unlimited number of living creatures. According to the above assumptions, it was concluded that the growth rate of prey continuously increased and was affected by its number. With the increased number of prey, the growth rate gradually accelerated, and the prey growth model could be expressed as follows:

$$\frac{dx}{dt} = \alpha x, \alpha > 0 \tag{1}$$

After the introduction of predators, the number of prey will decrease with the number of predators, which will slow down the growth rate of predators. Therefore, the growth rate model of predators can be described as

$$\frac{dy}{dt} = -\beta y, \beta > 0 \tag{2}$$

The growth rate of prey will be affected by the number of predators. It will slow down with increasing predation intensity, and the growth rate of predators will increase with increasing predation intensity. Combining Eqs. (1) and (2) yields the original LV prey-predator model:

$$\begin{cases} \frac{dx}{dt} = \alpha x - \lambda xy = (\alpha - \lambda y)x \\ \frac{dy}{dt} = -\beta y + \gamma xy = (-\beta + \gamma x)y \end{cases} \tag{3}$$

The notations involved in the original LV model are listed in Table 1.

Table 1. Notations in the original LV model.

Notations	Meaning
$x(t)$	number of the first-type predators
$y(t)$	number of the first-type preys
α	growth rate of preys without predators
β	Mortality of predators without preys
λ	predation parameter
γ	γ/λ is the conversion factor

4. IMPROVED MODELS

4.1 The First Improved Model

The first improved model considers artificial fishing, hunting, and internal competition on the original LV model. In the ecosystem, the internal competition between hunting species will cause the growth rate of this species to decrease. This improved model can be adapted to the above conditions as follows:

$$\begin{cases} \frac{dx}{dt} = \alpha x - \lambda xy - r_1 x - r_3 x^2 \\ \frac{dy}{dt} = -\beta y + \gamma xy - r_2 y - r_4 y^2 \end{cases} \tag{4}$$

The notations in the first improved model are listed in Table 2.

Table 2. Notations in the first improved LV model.

Parameter	Meaning
r_1	hunting coefficient of prey
r_2	hunting coefficient of predator
r_3	internal competition coefficient of prey
r_4	internal competition coefficient of predator

4.2 The Second Improved Model

The second improved model considers that there is one predator and two types of prey in an ecosystem, and competition exists between the two types of prey, assuming that there is no fishing in this model. The competition between two types of prey will slow down their growth. According to the above conditions, an improved model of two types of prey and one type of predator can be obtained, as shown in the following equation set:

$$\begin{cases} \frac{dx}{dt} = \alpha x - \lambda xy - \lambda_2 xp - r_3 x^2 \\ \frac{dp}{dt} = \mu p - \lambda_3 px - \lambda_1 py - r_5 p^2 \\ \frac{dy}{dt} = -\beta y + \gamma xy + \gamma_1 py - r_4 y^2 \end{cases} \tag{5}$$

The notations in the second improved model are listed in Table 3.

Table 3. Notations in the second improved LV model.

Parameter	Meaning
p(t)	number of the second-type prey
λ_1	predation parameter
λ_2	competition coefficient between prey
λ_3	internal competition coefficient of prey
γ_1	γ_1/λ_3 is the conversion factor
r_5	internal competition coefficient of prey

4.3 The Third Improved Model

The third improved model covers a system of two types of predators and two types of prey. Compared to the second improved model, one more type of predator is introduced. Both types of predators will hunt on both types of prey, so there will be competition between predators, reducing the growth of predators' population. At the same time, the internal competition between the two types of predators will also inhibit their population growth. A model can be established according to the above conditions, as follows:

$$\begin{cases} \frac{dx}{dt} = \alpha x - \lambda xy - \lambda_2 xp - \lambda_4 xq - r_3 x^2 \\ \frac{dp}{dt} = \mu p - \lambda_3 px - \lambda_1 py - \lambda_5 pq - r_5 p^2 \\ \frac{dy}{dt} = -\beta y + \gamma xy + \gamma_1 py - \gamma_4 yq - r_4 y^2 \\ \frac{dq}{dt} = -\delta q + \gamma_2 xq + \gamma_3 pq - \gamma_5 yq - r_6 q^2 \end{cases} \tag{6}$$

The notations in the third improved model are listed in Table 4.

Table 4. Notations in the third improved LV model.

Parameter	Meaning
q(t)	number of the second-type predators
λ_4 , λ_5	predation parameter
γ_2	γ_2/λ_4 is the conversion factor
γ_3	γ_3/λ_5 is the conversion factor
γ_4 ,γ_5	competition coefficients between predators
r_6	internal competition coefficient of predator

5 NUMERICAL SIMULATION

The numerical simulation via the original and three proposed improved LV models was performed by choosing appropriate coefficients to verify the respective ecosystems' stability.

5.1 Original LV Model

Only one predator and one prey are considered in the original model, and there is no internal fishing competition. For $\alpha = 2, \beta = 1.5, \lambda = 0.02, \gamma = 0.02$, the following set is obtained.

$$\begin{cases} \frac{dx}{dt} = 2x - 0.02xy \\ \frac{dy}{dt} = -1.5y + 0.02xy \end{cases} \tag{7}$$

To test whether the model is sensitive to the initial values of predators and prey, we set two groups of initial values, $(x_0, y_0) = (20,200)$ and $(x_0, y_0) = (200,20)$, respectively. According to the model and initial values, we can obtain the quantitative change of predators and prey, as shown in Fig. 1 (a) and (b).

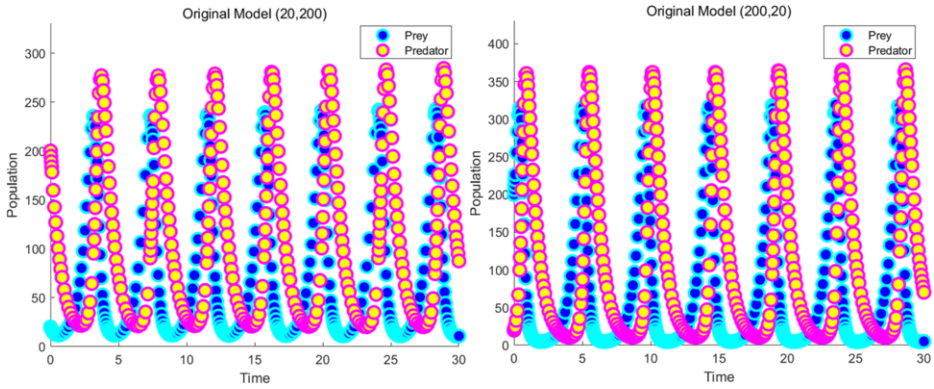

(a) (b)

Fig. 1. The original LV model: (a) x=20; y=200; (b) x=200; y=20.

According to the results in Fig. 1, under the two initial conditions of $x_0 > y_0$ and $x_0 < y_0$, the changes in the populations of prey and predators present an oscillating state, indicating that the ecosystem represented by the original model is unstable.

5.2 The First Improved LV Model

For the first improved model, only one type of predator and one type of prey are considered, and internal competition and hunting (fishing) coexist. For $\alpha = 2, \beta = 1.5, \lambda = 0.02, \gamma = 0.02, r_1 = 0.05, r_2 = 0.03, r_3 = 0.02, r_4 = 0.01$, the following set is obtained.

$$\begin{cases} \frac{dx}{dt} = 2x - 0.02xy - 0.05x - 0.02x^2 \\ \frac{dy}{dt} = -1.5y + 0.02xy - 0.03y - 0.01y^2 \end{cases} \tag{8}$$

The initial values are selected as $(x_0, y_0) = (20,200)$ and $(x_0, y_0) = (200,20)$. The numerical simulation results are shown in Fig. 2.

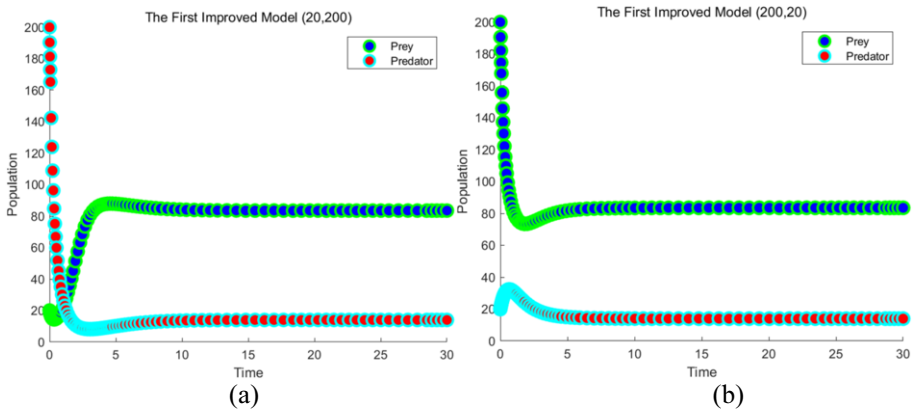

(a) (b)

Fig. 2. The first improved LV model: (a) x=20; y=200; (b) x=200; y=20.

According to the results in Fig. 2, for the first improved model considering hunting and internal competition, under the two initial conditions of $x_0 > y_0$ and $x_0 < y_0$, the population of predator and prey gradually tends to be stable without oscillation, indicating that the ecosystem represented by the first improved model is stable.

5.3 The Second Improved LV Model

One type of predator and two types of prey are considered for the second improved model, and internal competition exists. Taking the parameters $\alpha = 2, \beta = 1.5, \mu = 3, \lambda = 0.02, \lambda_1 = 0.01, \lambda_2 = 0.01, \lambda_3 = 0.02, \gamma = 0.02, \gamma_1 = 0.02, r_3 = 0.02, r_4 = 0.01$, and $r_5 = 0.02$, the following equation set can be obtained.

$$\begin{cases} \frac{dx}{dt} = 2x - 0.02xy - 0.01xp - 0.02x^2 \\ \frac{dp}{dt} = 3p - 0.01px - 0.02py - 0.02p^2 \\ \frac{dy}{dt} = -1.5y + 0.02xy + 0.02py - 0.01y^2 \end{cases} \tag{9}$$

In the numerical simulation of the second improved model, $(x_0, y_0, p_0) = (30,200,20)$ and $(x_0, y_0, p_0) = (300,20,200)$ are selected for the initial value sensitivity test. The numerical simulation results are shown in Fig. 3.

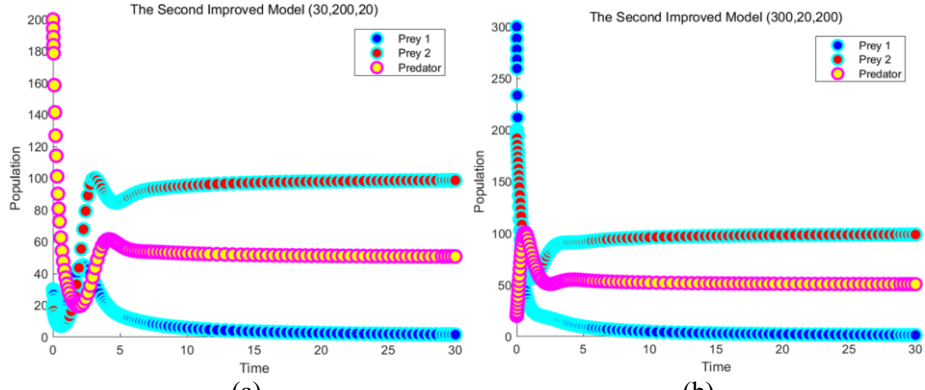

(a) (b)

Fig. 3. The second improved LV model: (a) x=30; y=200; p=20; (b) x=300; y=20; p=200.

According to the results in Fig. 3, for the second improved model considering hunting (fishing) and internal competition, under the two initial conditions of $x_0 > y_0, p_0 > y_0$ and $x_0 < y_0, p_0 < y_0$, the population of predators and two types of prey gradually tend to be stable without oscillation, indicating that the ecosystem represented by the second improved model is stable.

5.4 The Third Improved LV Model

Two types of predators and two types of prey are considered in the third model, and internal competition exists. Take $\alpha = 2, \beta = 1.5, \mu = 3, \lambda = 0.02, \lambda_1 = 0.01, \lambda_2 = 0.01, \lambda_3 = 0.02,\ \gamma = 0.02,\ \gamma_1 = 0.02, r_3 = 0.02,\ \gamma_4 = 0.01, \gamma_5 = 0.01,\ r_4 = 0.01, r_5 = 0.02, r_6 = 0.01$. The equation set (10) can be obtained.

$$\begin{cases} \frac{dx}{dt} = 2x - 0.02xy - 0.01xp - 0.03xq - 0.02x^2 \\ \frac{dp}{dt} = 3p - 0.02px - 0.02py - 0.03pq - 0.02p^2 \\ \frac{dy}{dt} = -1.5y + 0.02xy + 0.02py - 0.01yq - 0.01y^2 \\ \frac{dq}{dt} = -2q + 0.03xq + 0.03pq - 0.01yq - 0.01q^2 \end{cases} \tag{10}$$

The initial values $(x_0, y_0, p_0, q_0) = (30,300,20,200)$, and $(x_0, y_0, p_0, q_0) = (300,30,20,200)$ were selected for the initial value sensitivity test. The numerical simulation results are shown in Fig. 4.

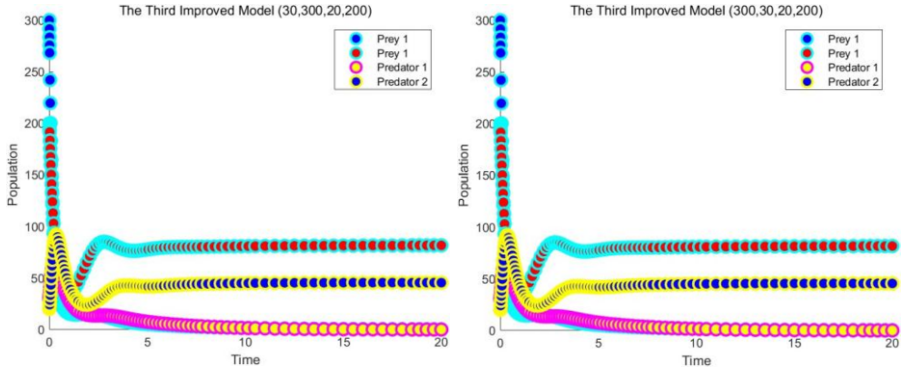

(a) (b)

Fig. 4. The third improved LV model: (a) x=30; y=300; p=20; q =200; (b) x=300; y=30; p=20; q =20.

According to the results in Fig. 4, for the third improved LV model considering hunting and internal competition, under the two initial conditions of $x_0 > y_0, p_0 > y_0, x_0 > q_0, y_0 > q_0$ and $x_0 < y_0, p_0 < y_0, x_0 < q_0, y_0 < q_0$, the population of two types of predators and two types of prey gradually tends to be stable without oscillation, indicating that the respective ecosystem is stable.

6 Equilibrium Points and Stability Analysis

After the model's establishment, the system's equilibrium point can be obtained according to the model, and the stability of the equilibrium point can be judged [21]. In

solving the equilibrium point, we must set each equation to zero. Taking the original model as an example, the calculation process is expressed as follows:

$$\begin{cases} \frac{dx}{dt} = \alpha x - \lambda xy = (\alpha - \lambda y)x = 0 \\ \frac{dy}{dt} = -\beta y + \gamma xy = (-\beta + \gamma x)y = 0 \end{cases} \tag{11}$$

According to formula (7), two equilibrium points $(0,0)$ and $(\frac{\beta}{\gamma}, \frac{\alpha}{\lambda})$ can be obtained.

Then, let $U = \frac{dx}{dt}, V = \frac{dy}{dt}$ and calculate the Jacobian row matrix of the system, via Eq. (12).

$$\mathcal{F} = \begin{pmatrix} \frac{\partial U}{\partial x} & \frac{\partial U}{\partial y} \\ \frac{\partial V}{\partial x} & \frac{\partial V}{\partial y} \end{pmatrix} = \begin{pmatrix} \alpha - \lambda y & -\lambda x \\ \gamma y & -\beta + \gamma x \end{pmatrix} \tag{12}$$

After obtaining the Jacobian matrix, it is necessary to check whether the equilibrium solution is stable. The value of ω can be used as the judgment basis (see [22]). The characteristic equation has the following form:

$$|\omega I - \mathcal{F}| = \begin{vmatrix} \omega - \alpha + \lambda y & \lambda x \\ -\gamma y & \omega + \beta - \gamma x \end{vmatrix} \tag{13}$$

6.1 Equilibrium Points

The equilibrium points of the original model are $(0,0)$ and $(75,100)$. The equilibrium points of the first improved model are $(0,0), (0,-153), (83.5,14)$, and $(97.5,0)$. The equilibrium points of the original model are $(0,0,0), (100,0,0), (0,-150,0), (0,0,150), (0,50,100), (25,0,150)$ and $\left(\frac{3375}{43}, \frac{800}{43}, \frac{250}{43}\right)$. The equilibrium points of the third improved LV model are listed in Table 5 (all negative equilibrium points are meaningless in the present work) [18].

Table 5. Equilibrium Points of the Third Improved Model

variable	E_1	E_2	E_3	E_4	E_5	E_6	E_7
x	0	100	0	0	0	25	0
y	0	0	-150	0	50	0	0
p	0	0	0	150	100	150	0
q	0	0	0	0	0	0	-200
variable	E_8	E_9	E_{10}	E_{11}	E_{12}	E_{13}	E_{14}
x	0	800/11	0	1375/19	-200/30	$30\sqrt{6}+70$	$70-30\sqrt{6}$
y	-350	0	0	400/19	0	$30\sqrt{6}-230$	$-30\sqrt{6}-230$
p	50	0	900/11	250/19	2700/31	$-30\sqrt{6}-20$	$30\sqrt{6}-20$
q	300	200/11	500/11	0	1300/31	$180-30\sqrt{6}$	$30\sqrt{6}+180$

6.2 Stability Analysis

This paper mainly analyses the stability about the two equilibrium points of the original LV model and $\left(\frac{3375}{43}, \frac{800}{43}, \frac{250}{43}\right)$ of the second improved LV model. The calculation process of the equilibrium point $(0,0)$ is expressed in Eqs. (14) and (15):

$$\mathcal{F}(0,0) = \begin{pmatrix} \alpha & 0 \\ 0 & -\beta \end{pmatrix} = \begin{pmatrix} 2 & 0 \\ 0 & -1.5 \end{pmatrix} \tag{14}$$

$$|\omega \mathrm{I} - \mathcal{F}(0,0)| = \begin{vmatrix} \omega - 2 & 0 \\ 0 & \omega + 1.5 \end{vmatrix} = 0 \tag{15}$$

According to formula (15), we can obtain $\omega_1 = -1.5, \omega_2 = 2$. Therefore, $(0,0)$ is a saddle point and not a stable equilibrium point.

The calculation process of the equilibrium point $(75,100)$ is given in Eqs. (16) and (17).

$$\mathcal{F}(75,100) = \begin{pmatrix} \alpha - 100\lambda & -75\lambda \\ 100\gamma & -\beta + 75\gamma \end{pmatrix} = \begin{pmatrix} 0 & -1.5 \\ 2 & 0 \end{pmatrix} \tag{16}$$

$$|\omega \mathrm{I} - \mathcal{F}(75,100)| = \begin{vmatrix} \omega & 1.5 \\ -2 & \omega \end{vmatrix} = 0 \tag{17}$$

According to formula (17), we can obtain $\omega_1 = -\sqrt{3}\mathrm{i}, \omega_2 = \sqrt{3}\mathrm{i}$. Therefore, $(75,100)$ is a central point and not a stable equilibrium point.

The equilibrium point $\left(\frac{3375}{43}, \frac{250}{43}, \frac{800}{43}\right)$ is calculated in Eq. (18) and Eq. (19).

$$\mathcal{F}\left(\frac{3375}{43}, \frac{250}{43}, \frac{800}{43}\right) = \begin{pmatrix} -1.57 & -0.78 & -1.57 \\ -0.06 & 1.61 & 0.12 \\ 0.37 & 0.37 & -0.19 \end{pmatrix} \tag{18}$$

$$\left|\omega \mathrm{I} - \mathcal{F}\left(\frac{3375}{43}, \frac{250}{43}, \frac{800}{43}\right)\right| = \begin{vmatrix} \omega + 1.57 & 0.78 & 1.57 \\ 0.06 & \omega - 1.61 & -0.12 \\ -0.37 & -0.37 & \omega + 0.19 \end{vmatrix} = \omega^3 + 0.15\omega^2 - 2.0456\omega - 1.494 \tag{19}$$

According to formulas (18) and (19), we get $\omega_1 = 1.65, \omega_2 = -0.90 - 0.31\mathrm{i}, \omega_3 = -0.90 + 0.31\mathrm{i}$.

Therefore, $\left(\frac{3375}{43}, \frac{250}{43}, \frac{800}{43}\right)$ is a stable equilibrium point.

7 CONCLUSIONS

This study aimed to extend the Lotka-Volterra model to ecosystems containing more than one type of predator and prey, as well as internal competition. The first improved model considered hunting and internal competition, the second one considered two types of prey and one type of predator, and the third one covered two types of prey and two types of predators. The performed numerical computation proved that appropriate human activities play a role in maintaining the stability of the ecosystem, while biological diversity is conducive to improving this stability. From Fig. 2 to 4 and numerical simulations, the three improved LV models tend to stabilize their respective ecosystems. In future research, the LV model will be further modified to consider

climate and terrain images in the stability analysis of biological systems. At the same time, in model verification and solution, actual data will be collected for their numerical simulation.

REFERENCES

[1] A. J. Lotka. Elements of Physical Biology, Williams and Wilkins, Baltimore, 1925: 168-177.

[2] J. Chattopadhyay and O. Arino (1999). A predator-prey model with disease in the prey. Nonlinear Analysis: Theory, Methods & Application, 36(6), 747-766.

[3] L.Yu and S. Bin (2022). Research on the competition between high-speed rail and air express transportation based on the Lotka-Volterra model. Railway Transportation and Economy, 2022, 44 (03): 73-78+91. (in Chinese).

[4] N. L. Christensen, A.M. Bartuska, J. H. Brown, et al. (1996). The report of the Ecological Society of America Committee on the scientific basis for ecosystem management. Ecological Applications, 6(3), 665-691.

[5] D. Qiu, X. Ma, J. Yan, et al. (2020). Biogeomorphological processes and structures facilitate seedling establishment and distribution of annual plants: implications for coastal restoration. Science of The Total Environment, 143842.

[6] C. Liu, Q. Zhang, Y. Li, and W. Yue (2014). Dynamical analysis of a stage-structured prey-predator model with harvest effort and multiple time delays. Proc. 33rd Chinese Control Conference.

[7] R. W. Han et al. (2021). Research on the cooperation between large and medium-sized enterprises based on the Lotka-Volterra model. Science and Technology Economic Market, 2021 (07): 99-102. (in Chinese).

[8] Z. Yi, (2010). Foundations of implementing the competitive layer model by the Lotka-Volterra Recurrent Neural Networks, in IEEE Transactions on Neural Networks, vol. 21, no. 3, pp. 494-507, March 2010.

[9] S. Guharay and K. Chang (2015). Application of Bayesian simulation framework in quantitatively measuring presence of competition in living species, In Proc. 2015 Winter Simulation Conference (WSC), 2015, pp. 4033-4044.

[10] L. L. Chen and Z. Z. Lin (2008). The effect of habitat destruction on the multispecies competition system with allee effects, In Proc. 2008 Fourth International Conference on Natural Computation, 2008, pp. 628-632, doi: 10.1109/ICNC.2008.740.

[11] W. Liu, C. Fu, F. Zeng, and T. Xuan (2014). Stability analysis for an improved Volterra predator-prey model, Proc. 4th IEEE International Conference on Information Science and Technology, 2014, pp. 345-348.

[12] H. C. Hung, Y.C. Chiu, H.C. Huang, M. C. Wu (2017). An enhanced application of Lotka-Volterra model to forecast the sales of two competing retail formats. Computers & Industrial Engineering, 109(), 325-334.

[13] S. Mao, M. Zhu, X. Wang, and X. Xiao (2020). Grey Lotka-Volterra model for the competition and cooperation between third-party online payment systems and online banking in China. Applied Soft Computing, 106501.

[14] S. Saha Ray and K. S. Chaudhuri (1989). Lotka-Volterra prey-predator model with harvesting and environmental perturbations. Ecological Modelling, 47(3-4), 283-290. doi:10.1016/0304-3800(89)90006-9.

[15] Y. Ma, S. Lv, X. Zhou, and Z. Gao (2018). Voltage stability analysis of power system based on bifurcation theory. 2018 IEEE International Conference on Mechatronics and Automation (ICMA).

[16] S. Y. Chiang, G. G. Wong, Y. Li, and H. C. Yu (2008). A dynamic competition analysis on the personal computer shipments in Taiwan using the Lotka-Volterra model. 2008 IEEE Asia-Pacific Services Computing Conference, Yilan, Taiwan, 2008, pp. 1412-1417, doi: 10.1109/APSCC.2008.296.

[17] Q. Y. Luo, B. F. Sun, and Y. P. Zhong (2010). Collinear competition between rail transit and bus transit based on population competition model, 2010 WASE International Conference on Information Engineering, Beidai, China, 2010, pp. 313-315, doi: 10.1109/ICIE.2010.251.

[18] S. Manjunath and G. Raina (2014) Stability and bifurcation analysis of the Lotka–Volterra time delayed system, The 26th Chinese Control and Decision Conference (2014 CCDC), Changsha, China, 2014, pp. 2056-2063, doi: 10.1109/CCDC.2014.6852506.

[19] Q. Gao (2009). Stability and Hopf bifurcations of a three-species symbiosis model with delays, 2009 International Workshop on Chaos-Fractals Theories and Applications, Shenyang, China, 2009, pp. 272-276, doi: 10.1109/IWCFTA.2009.63.

[20] K. Wang and Z. Gui (2012). Existence and simulations of periodic solution of a three-species the Lotka-Volterra predator-prey system with impulsive perturbations, 2012 IEEE International Conference on Computer Science and Automation Engineering (CSAE), Zhangjiajie, China, 2012, pp. 179-183, doi: 10.1109/CSAE.2012.6272934.

[21] I. El Arabi, A. Chafi, and S. K. Alami (2019). Numerical simulation of the SIR and the Lotka-Volterra models used in biology, 2019 International Conference on Intelligent Systems and Advanced Computing Sciences (ISACS), Taza, Morocco, 2019, pp. 1-4, doi: 10.1109/ISACS48493.2019.9068876.

[22] A. Bouaine and M. Rachik (2017). Adjustment submersible cages for optimal fish farming: improved spatiotemporal Lotka-Volterra model for *n* species in partitioned area. International Journal of Dynamics and Control, 6(3), 919-928. doi:10.1007/s40435-017-0329-3.

Fuzzy Systems and Data Mining IX
A.J. Tallón-Ballesteros and R. Beltrán-Barba (Eds.)

doi:10.3233/FAIA231015

Bayesian Matrix Completion for Ranking COVID-19 Cases

Yushu Cao and Lei Zhang[1]
School of Economics and Management, Beijing Jiaotong University, Beijing, 100044, China

Abstract. Due to the surge in COVID-19 cases, hospitals have had to receive many more patients than before, which has brought unprecedented pressure to the hospital system. Therefore, the emphasis of medical decision-making has shifted from reaching the best treatment effect to prioritizing the treatment of COVID-19 patients by hospitals, which is key to relieving the pressure on the hospital system and reducing the overall mortality rate of COVID-19. There is no doubt that establishing the prioritization of COVID-19 cases is fundamental and pivotal for hospitals to achieve the shift in medical decision-making. Prioritization of COVID-19 cases in previous studies was mostly based on one patient characteristic, mainly including age, health conditions, and gender. This paper focuses on two patient characteristics at the same time. The probability that a COVID-19 patient who died had a given health condition in a given age group is calculated using the matrix completion technique based on the high-rank assumption of Bayesian matrices and the properties of Markov matrices. The calculated results show that doctors should give patients over 55 with respiratory diseases, patients over 65 with circulatory diseases, and patients over 65 with diabetes a higher prioritization in COVID-19 treatment.

Keywords. COVID-19, matrix completion, high-rank assumption, Bayesian matrices, Markov matrices, treatment prioritization

1. Introduction

Since the outbreak of the COVID-19 epidemic, it has seriously influenced people's daily lives and affected various industries and sectors around the world, including healthcare, economy, and society, to varying degrees [1]. According to the World Health Organization, the number of COVID-19 related deaths has reached 744,175 as of January 2, 2023 [2]. However, having COVID-19 is not the only factor that contributes to COVID-19 related deaths. These deaths are also influenced by other factors, including the age and health condition of patients. Specifically, the mortality rate of patients with underlying diseases is four times that of patients without underlying diseases, and patients older than 41 years are considered to be at higher risk [3]. In addition, due to the surge in COVID-19 cases, hospital systems are under unprecedented pressure. In this case, the focus of medical decision-making shifts from achieving the best treatment outcome for individual patients to providing treatment for a larger patient population to ensure the maximum overall benefit of all patients [4]. Therefore, determining the prioritization of COVID-19 cases and maximizing the use of hospital resources to reduce

[1] Corresponding Author: Lei Zhang, School of Economics and Management, Beijing Jiaotong University, Beijing, 100044, China. Email: zhlei@bjtu.edu.cn.

the overall mortality rate of patients with COVID-19 has become the top priority of hospital management. Due to the relatively crude nature of relevant data, previous related research was limited to a single-factor statistical analysis of age and health condition, so the prioritization of patient treatment was also relatively rough, limited to a single-factor priority [3]. Hence, this paper focuses on combining age and health conditions to determine more precise treatment priorities and provide more accurate recommendations to hospital systems.

Low-rank matrix completion techniques are currently being studied in the literature on missing value completion. Trever Hastie et al. developed a brand-new algorithm that can handle data from the Netflix challenge by applying low-rank singular value decomposition (SVD) to improve previous matrix completion algorithms [5]. Xiaofeng Liu et al. took advantage of the high spatial correlation and consistency of the air pollutant spatial matrix and used the low-rank matrix completion algorithm to fill in the missing values of the environmental station data [6]. Xuelong Li et al. introduced a new method for fusing HS and MS images using nonlocal low-rank tensor approximation and sparse representation [7]. Feiping Nie et al. introduced a non-convex regularizer and used it to develop two models for matrix completion based on the low-rank assumption [8].

However, since there is a causal relationship between patient age and health condition, age and health condition form a high-rank Bayesian matrix. Therefore, low-rank matrix completion is no longer applicable. This paper performs Bayesian matrix completion under the assumption of high-rank matrices [9] to provide hospitals with more accurate treatment prioritization of COVID-19 cases during the pandemic.

2. Data and Bayesian Matrix

The data comes from the official website of the US government, and the dataset displays health conditions by age group and jurisdiction of occurrence that were reported in connection with deaths from COVID-19. This paper selects data recorded for the entire United States from January 1, 2020, to January 29, 2023, and properly cleans the data to remove very few records of unknown age. Health conditions recorded in the dataset include respiratory diseases, circulatory diseases, sepsis, malignant neoplasms, diabetes, obesity, Alzheimer's disease, vascular and unspecified dementia, renal failure, intentional and unintentional injury, poisoning, and other adverse events, as well as all other conditions and causes (residual), and COVID-19 (COVID-19 is the only health condition that leads to COVID-19 deaths). There are eight different age groups in the dataset, including 0-24, 25-34, 35-44, 45-54, 55-64, 65-74, 75-84, and 85+. Figure 1 shows the proportion of various health conditions, while Figure 2 shows the proportion of various age groups.

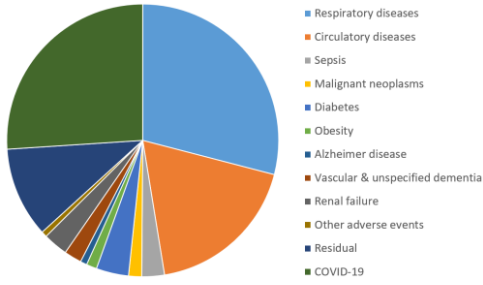

Figure 1. The proportion of various health conditions.

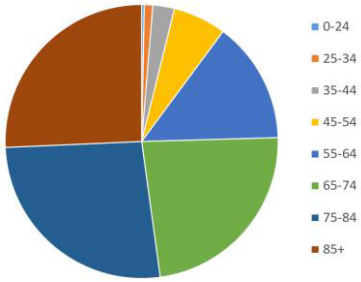

Figure 2. The proportion of various age groups.

Let the health conditions be written as $C = (c_1, c_2, c_3, \cdots, c_n)$, and the age groups be written as $A = (a_1, a_2, a_3, \cdots, a_m)$. The concrete Bayesian matrix B $\big((n+m) \times (n+m)\big)$ can be written as follows, and it is divided into four main parts:

$$B = \begin{pmatrix} b_1 & b_2 \\ b_3 & b_4 \end{pmatrix} = \begin{pmatrix} 0 & P(A|C) \\ P(C|A) & 0 \end{pmatrix} \tag{1}$$

b_1 refers to the association between each age group. It can be seen as 0 since there is no association between different age groups. b_2 refers to the probability of a COVID-19 patient dying due to an i age group, based on a given health condition. b_3 refers to the association between each health condition. It can be seen as 0 since there is almost no association between different health conditions because the dataset has categorized different health conditions. b_4 refers to the probability of a COVID-19 patient dying due to a j health condition, based on a given age group.

3. Bayesian Matrix Learning

In the Bayesian matrix B, b_1 and b_4 are equal to 0, and b_2 and b_3 represent conditional probabilities. Thus, all elements in the matrix are in the closed interval from 0 to 1. Additionally, since $(c_1, c_2, c_3, \cdots, c_n)$ and $(a_1, a_2, a_3, \cdots, a_m)$ are collectively exhaustive events for the entire dataset, the sum of all elements in each column in the matrix is 1. Therefore, according to the characteristics of the Markov matrix, it can be determined that the Bayesian matrix B is a Markov matrix. From the properties of Markov matrices, the Bayesian matrix B has an eigenvalue of 1 [10]. The next task is to find the eigenvector with eigenvalue 1 and find the Bayesian matrix B according to the eigenvector and high-rank assumption.

$$\begin{pmatrix} 0 & P(A|C) \\ P(C|A) & 0 \end{pmatrix} \begin{pmatrix} P(A) \\ P(C) \end{pmatrix} = \begin{pmatrix} P(A) \\ P(C) \end{pmatrix} \tag{2}$$

i.e.

$$\begin{pmatrix} \begin{pmatrix} 0 & \cdots & 0 \\ \vdots & \ddots & \vdots \\ 0 & \cdots & 0 \end{pmatrix} & \begin{pmatrix} P(a_1|c_1) & \cdots & P(a_1|c_n) \\ \vdots & \ddots & \vdots \\ P(a_m|c_1) & \cdots & P(a_m|c_n) \end{pmatrix} \\ \begin{pmatrix} P(c_1|a_1) & \cdots & P(c_1|a_m) \\ \vdots & \ddots & \vdots \\ P(c_n|a_1) & \cdots & P(c_n|a_m) \end{pmatrix} & \begin{pmatrix} 0 & \cdots & 0 \\ \vdots & \ddots & \vdots \\ 0 & \cdots & 0 \end{pmatrix} \end{pmatrix} \begin{pmatrix} P(a_1) \\ \vdots \\ P(a_m) \\ P(c_1) \\ \vdots \\ P(c_n) \end{pmatrix} = \begin{pmatrix} P(a_1) \\ \vdots \\ P(a_m) \\ P(c_1) \\ \vdots \\ P(c_n) \end{pmatrix} \quad (3)$$

It is crystal clear that $s = \begin{pmatrix} P(A) \\ P(C) \end{pmatrix}$ is the eigenvector with eigenvalue 1, which is also the principal eigenvector of the Bayesian matrix B. Since B is a Markov matrix, it becomes a stable state after limiting self-multiplication. Therefore, there is:

$$\lim_{n\to\infty} B^n = S = (s, s, \cdots, s) \quad (4)$$

i.e.

$$BS = SB = S \quad (5)$$

And because the principal eigenvector s is known, the task of finding the Bayesian matrix B can be transformed into finding the maximum eigenvalue of the Bayesian matrix B. For eigenvalue λ, there is:

$$Bs = \lambda s \quad (6)$$

$$SBs = \lambda Ss \quad (7)$$

$$s^T SBs = \lambda s^T Ss = 2\lambda s^T s \quad (8)$$

$$\lambda = \frac{s^T SBs}{2s^T s} = \frac{s^T Ss}{2s^T s} \quad (9)$$

Utilizing the characteristics of the Markov matrix as a constraint on the solution, after maximizing the eigenvalue λ, the Bayesian matrix B can be solved, and a more accurate prioritization of COVID-19 case treatment can be obtained.

4. Experiment and Result

The data from the official website of the US government demonstrates the frequencies of each age group and each health condition. Treating frequencies as probabilities, the probability for each age group is: 0-24 (0.31%), 25-34 (1.00%), 35-44 (2.56%), 45-54 (6.30%), 55-64 (14.39%), 65-74 (23.27%), 75-84 (26.48%), 85+ (25.69%). The probability for each health condition is: respiratory diseases (29.04%), circulatory diseases (18.39%), sepsis (2.69%), malignant neoplasms (1.56%), diabetes (3.86%), obesity (1.24%), Alzheimer's disease (0.79%), vascular and unspecified dementia (2.08%), renal failure (2.94%), intentional and unintentional injury, poisoning, and other adverse events (0.67%), all other conditions and causes (residual) (10.71%), and COVID-19 (26.03%). Therefore, the principal eigenvector of the Bayesian matrix B is

$s^T = (0.0031,\ 0.0100,\ 0.0256,\ 0.0630,\ 0.1439,\ 0.2327,\ 0.2648,\ 0.2569,\ 0.2904,\ 0.1839,\ 0.0269,\ 0.0156,\ 0.0386,\ 0.0124,\ 0.0079,\ 0.0208,\ 0.0294,\ 0.0067,\ 0.1071,\ 0.2603)$.

After identifying the principal eigenvector s, use the fmincon function from Matlab to find the minimum value of the constrained nonlinear multivariable function and solve the Bayesian matrix B. The first constraint condition, based on the characteristic of probability, is that all elements in the Bayesian matrix B must be in the interval [0, 1]. Therefore, all elements in the lb vector of the fmincon function are 0, and all elements in ub are 1. Additionally, the second constraint condition, based on the characteristic of collectively exhaustive events, is that the sum of each column in the matrix B is 1. Thus, the task is to construct the matrix Aeq and the vector beq. The third constraint condition, based on the properties of Markov matrices, is that $BS = SB$. Hence, it is vital to build another matrix Aeq and another vector beq. Lastly, based on the model from section 3, it is obvious that the $f(x)$ of the fmincon function is the maximization of the eigenvalue λ, which needs to be converted into the minimum problem by taking the negative value of λ.

The calculated Bayesian matrix B based on the above is shown below, and the specific value of each element in the matrix is presented in Figure 3. Figure 3 contains 192 values from left to right, and the Bayesian matrix B is filled column by column from left to right, top to bottom.

$$B = \begin{pmatrix} \begin{pmatrix} 0 & \cdots & 0 \\ \vdots & \ddots & \vdots \\ 0 & \cdots & 0 \end{pmatrix} & \begin{pmatrix} 0.0007 & \cdots & 0.0008 \\ \vdots & \ddots & \vdots \\ 0.2840 & \cdots & 0.2802 \end{pmatrix} \\ \begin{pmatrix} 0.0697 & \cdots & 0.3210 \\ \vdots & \ddots & \vdots \\ 0.0696 & \cdots & 0.2839 \end{pmatrix} & \begin{pmatrix} 0 & \cdots & 0 \\ \vdots & \ddots & \vdots \\ 0 & \cdots & 0 \end{pmatrix} \end{pmatrix} \tag{10}$$

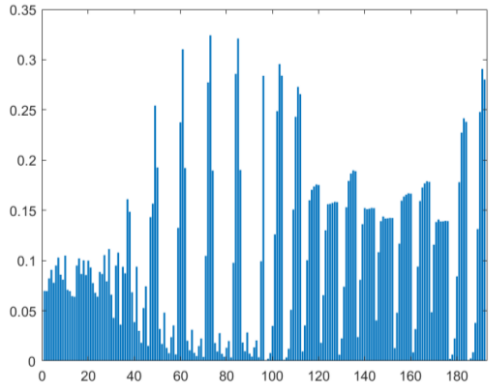

Figure 3. The value of 192 elements in B.

Based on the conditional probability given by B, $P(a_i|c_j)$ and $P(c_j|a_i)$ can be obtained. Therefore, the probability that a COVID-19 death patient had a health condition j in an age group i can be calculated through the following way:

$$P(a_i \cap c_j) = P(a_i|c_j) \times P(c_j) = P(c_j|a_i) \times P(a_i) \quad (11)$$

Sort the probabilities in descending order, the top 10 probabilities that a COVID-19 dead patients had a j health condition in an i age group are shown in Table 1:

Table 1. Hits for TOP 10 of the Results

COVID-19 dead patients had a j health condition in an i age group	Probability
85+ years old with respiratory diseases	0.0932
75-84 years old with respiratory diseases	0.0858
85+ years old with COVID only	0.0825
75-84 years old with COVID only	0.0757
65-74 years old with respiratory diseases	0.0722
65-74 years old with COVID only	0.0645
85+ years old with circulatory diseases	0.0552
75-84 years old with circulatory diseases	0.0502
65-74 years old with circulatory diseases	0.0447
55-64 years old with respiratory diseases	0.0366

5. Discussion and Conclusion

In this paper, according to the high-rank assumptions different from the previous low-rank assumptions, and using the characteristics of the Markov matrices, in the case of known principal eigenvectors, the Bayesian matrix B is completed, and 192 conditional probability values related to age groups and health conditions are obtained. Based on these conditional probabilities, it is easy to calculate the probability that a COVID-19 dead patients had a health condition j in an age group i. From the results, it should be noticed that there is a high probability that dead patients aged 85+ with respiratory diseases, followed by patients aged 75 to 84 with respiratory diseases. Besides, among the COVID-19 deaths, people aged 65+ who had circulatory diseases and those aged 55 to 74 who had respiratory diseases also accounted for a large proportion. Except for the top 10, patients over 65 with diabetes also have a high percentage of deaths. These findings can help hospitals to realize new medical decision-making and ensure the maximum overall benefit for all patients. In daily hospital management, doctors should give these patients a higher prioritization in the treatment of COVID-19.

Since COVID-19 is an RNA virus that mutates quickly, there are certain stability issues with this conclusion. In the future, experimental data could be limited to a period of time when the virus is relatively stable, and health conditions and age groups could be described in more detail to provide more stable and precise prioritization.

Acknowledgment

The work was supported by the National Natural Science Foundation of China (No.72271017).

References

[1] Haleem A, Javaid M, Vaishya R. Effects of covid-19 pandemic in Daily Life. Current Medicine Research and Practice. 2020;10(2):78–9.
[2] Who coronavirus (COVID-19) dashboard [Internet]. World Health Organization. World Health Organization; [cited 2023Feb24]. Available from: https://covid19.who.int/
[3] Choi W-Y. Mortality rate of patients with covid-19 based on underlying health conditions. Disaster Medicine and Public Health Preparedness. 2021;16(6):2480–5.
[4] John L. Hick DH. Crisis standards of care and covid-19: What did we learn? how do we ensure equity? what should we do? [Internet]. National Academy of Medicine. 2021 [cited 2023Feb24]. Available from: https://nam.edu/crisis-standards-of-care-and-covid-19-what-did-we-learn-how-do-we-ensure-equity-what-should-we-do/
[5] Hastie T, Friedman J, Tisbshirani R. The elements of Statistical Learning: Data Mining, Inference, and prediction. New York: Springer; 2017.
[6] Liu X, Wang X, Zou L, Xia J, Pang W. Spatial imputation for air pollutants data sets via low rank matrix completion algorithm. Environment International. 2020;139:105713.
[7] Li X, Yuan Y, Wang Q. Hyperspectral and multispectral image fusion via nonlocal low-rank tensor approximation and sparse representation. IEEE Transactions on Geoscience and Remote Sensing. 2021;59(1):550–62.
[8] Nie F, Hu Z, Li X. Matrix completion based on non-convex low-rank approximation. IEEE Transactions on Image Processing. 2019;28(5):2378–88.
[9] Hang Wu, Chihwen Cheng, Xiaoning Han, Yong Huo, Wenhui Ding, Wang MD. Post-surgical complication prediction in the presence of low-rank missing data. 2015 37th Annual International Conference of the IEEE Engineering in Medicine and Biology Society (EMBC). 2015;
[10] Gilks WR, Richardson S, Spiegelhalter DJ. Markov chain Monte Carlo in practice. Boca Raton etc.: Chapman and Hall; 1998.

Fuzzy Systems and Data Mining IX
A.J. Tallón-Ballesteros and R. Beltrán-Barba (Eds.)

doi:10.3233/FAIA231016

A Method for Measuring Node Similarity in Heterogeneous Information Networks

Liudi Zhan [a], Hongmei Chen [a,b,1], Lihua Zhou [a,b] and Qing Xiao [a]
[a] *School of Information Science and Engineering, Yunnan University, Kunming, China*
[b] *Yunnan Key Laboratory of Intelligent Systems and Computing, Yunnan University, Kunming, China*

Abstract. Meta-path-based methods for measuring the similarities between nodes in Heterogeneous Information Networks (HINs) have attracted attention from researchers due to excellent performance. However, these methods suffer from some issues: (1) it is difficult for users to provide effective meta-paths of complex HINs; (2) it is inefficient to enumerate all instances of meta-paths. In order to solve the above issues, this paper proposes a novel method, K-order Neighbors based Heterogeneous Graph Neural Network (KN-HGNN), for measuring node similarity. Firstly, KN-HGNN generates meta-paths based on network schema. Then, KN-HGNN obtains the features of nodes by aggregating itself type feature and its k-order neighbors' type features under the constraints of meta-paths. Finally, KN-HGNN calculates the similarities between nodes based on the features of nodes. The experimental results on real datasets show that KN-HGNN outperforms the baselines.

Keywords. Heterogeneous Information Network, Node Similarity, Meta-path, Heterogeneous Graph Neural Network

1. Introduction

Unlike homogeneous information networks which have only one node type and one edge type, Heterogeneous Information Networks (HINs) [1] have multiple node types and various types of edges connecting nodes. In complex network analysis [2], measuring node similarity [3] is a research focus, which can be used in many applications. For example, users can discover the authors who share similar characteristics with a specific author based on specific relationships in a literature information network. Another example is searching for users with similar location preferences on a location-based social network.

The methods used to measure node similarity in homogeneous information networks rely on link-based information, such as SimRank [4] and P-PageRank [5]. While these methods have achieved great success in measuring node similarity in homogeneous information networks, they are often challenging to apply to HINs. Sun et al. [6] introduced the concept of meta-paths and proposed a method called PathSim to measure node similarity in HINs using meta-paths. However, meta-path-based methods typically

[1] Corresponding Author: Email: hmchen@ynu.edu.cn.

require user-specified meta-paths which is difficult to users, and counting instances of meta-paths which is computationally expensive. To address the above issues, this paper proposes a novel method called K-order Neighbors based Heterogeneous Graph Neural Network (KN-HGNN). The main contributions of this paper are as follows:

- Firstly, meta-paths are generated effectively based on the network schema, rather than relying on user-specified meta-paths, which is more suitable for HINs.
- Secondly, a novel method called KN-HGNN is proposed to obtain node type feature by aggregating the features of its own type and its k-order neighbors' type under the constraints of meta-paths, which improves efficiency due to avoiding enumerating all instances of meta-paths.
- Finally, node similarities are calculated based on the node features obtained by utilizing the proposed KN-HGNN. The experimental results on real datasets demonstrate that KN-HGNN outperforms the baseline methods.

2. Related Work

Sun et al. [6] introduced the concept of meta-path and the method PathSim for measuring node similarity in HINs based on meta-paths. PathSim utilizes meta-paths to represent the semantic relationship between nodes and calculates node similarity based on the number of meta-path instances. PathSim has limited ability to measure node similarity because it only can use symmetric meta-paths. To overcome this limitation and evaluate the similarities of different node types, Shi et al. [7] drew inspiration from SimRank and introduced HeteSim. HeteSim utilizes bidirectional random walks to calculate the encounter probability between two nodes and measure similarity between the two nodes under any meta-path. To alleviate the high computational complexity of HeteSim, Meng et al. [8] introduced AvgSim. AvgSim calculates the mean of the arrival probabilities between two nodes on given meta-paths. However, these methods require pre-defined meta-paths and are suffered from low efficiency. Further, node similarity can be evaluated from alternative perspectives, such as node neighbors and node features. Zhang et al. [9] developed LRE, a node similarity measurement that utilizes relative entropy and node local structure. Junfang et al. [10] introduced DDRE, a method that utilizes relative entropy and distance distribution to measure node similarity.

3. Related Concept

This section describes some basic concepts regarding HINs, and Table 1 summarizes the main notations utilized throughout this paper.

Definition 1. Heterogeneous Information Network (HIN). A HIN is defined as a directed graph $G = (V, E, T, R)$ that contains the mapping relationship of nodes $\phi : V \to T$ and the mapping relationship of edges $\varphi : E \to R$. HINs have the following properties.

1. For any node $v \in V$ in the graph G, existing a specific node type $t \in T$.
2. For any edge $e \in E$ in the graph G, existing a specific edge type $r \in R$.
3. In the graph G, existing $|T| + |R| > 2$.

Definition 2. Network Schema. Given a HIN $G = (V, E, T, R)$, $\phi : V \to T$, $\varphi : E \to R$, the network schema $H_G = (T, R)$ can be defined as a directed graph of node types T and edge types R.

Table 1. Main Notations.

Notations	Descriptions
G, H_G	Heterogeneous information network and network schema
V, E, T, R	Node set, edge set, node type set, edge type set
ϕ, φ	Node type mapping and edge type mapping
$(N_t)_k$	K-order neighbors of node type t
F^t	Initial feature of node type t
$Y^{(N_t)_k \to t}$	K-order aggregation feature of node type t
$W^{t_i \to t_j}$	Adjacency matrix between node type t_i and node type t_j

Definition 3. Meta-path. The meta-path p is defined on the network schema $H_G = (T, R)$ and expressed as $p = t_1 \xrightarrow{r_1} t_2 \xrightarrow{r_2} \cdots \xrightarrow{r_l} t_{l+1}$, where $t_i, t_{i+1} \in T$, $r_i \in R$ and r_i is the edge between nodes t_i and t_{i+1}. The length of the meta-path p is the number of edges in p, i.e. l.

4. KN-HGNN

4.1. Meta-path Generation

When specifying a node type, a set of meta-paths with limited length can be obtained based on the network schema. We begin by taking the user-specified node type as the start node type of meta-paths. At each step, we extend meta-paths by adding the neighbor node type of the current node type based on network schema. For instance, on the network schema of DBLP, if the start node type is A (Author), we first get AP (Author-Paper) with length of 1 in which P is the first-order neighbor of A. Then we get APA (Author-Paper-Author), APT (Author-Paper-Term), APC (Author-Paper-Conference) with length of 2 in which T and C are the second-order neighbor of A. Iteratively, we can obtain a set of meta-paths with limited length. In fact, when the meta-path length is l, we can infer that the neighbor order of node types is at least $l/2$. As shown in Section 5.2.3, the limited length of meta-paths is set 4 which can capture sufficient high-order neighbor information in KN-HGNN.

4.2. Node Type Feature Aggregation

In KN-HGNN, the features of nodes are learned by aggregating itself type feature and its k-order neighbors' type features under the constraints of meta-paths. Firstly, we initialize the feature of each node type by concatenating the features of all nodes belonging to this node type, which extracted utilizing the Bag-of-Words model. Then, we iteratively learn the feature of each node by aggregating itself type feature and its k-order neighbors' type features based on meta-paths. This can be described as $W^{t' \to t} \cdot F^{t'}$, where t represents the target node type and t' represents the neighbor node type of t, $W^{t' \to t}$ is the adjacency matrix between the two types of nodes belonging to the neighbor node type and the target node type, respectively. The procedure of aggregating itself type feature and its first-order neighbors' type features can be expressed as Eq. (1):

$$Y^{(N_t)_1 \to t} = \sigma\left(\underset{t' \in (N_t)_1}{||} W^{t' \to t} \cdot F^{t'} + \beta \right) \tag{1}$$

Table 2. Dataset Statistics.

Dataset	Node Type	Number	Edge Type	Some Meta-paths Obtained in Dataset
DBLP	$A(Author)$	4057	$P \leftrightarrows A$	APA
	$P(Paper)$	14328	$P \leftrightarrows C$	$APCPA$
	$C(Conference)$	20	$P \leftrightarrows T$	$APTPA$
	$T(Term)$	8898	$P \leftrightarrows P$	$APAPA$
ACM	$P(Paper)$	4025	$P \leftrightarrows A$	PAP
	$A(Author)$	7167	$P \leftrightarrows S$	PSP
	$S(Subject)$	60	$P \leftrightarrows P$	$PAPAP$
IMDB	$M(Movie)$	3328	$M \leftrightarrows A$	MAM
	$A(Actor)$	42553	$M \leftrightarrows U$	MUM
	$U(User)$	2103	$M \leftrightarrows D$	MDM
	$D(Director)$	2016	$M \leftrightarrows M$	$MAMAM$

where σ represents the activation function and β represents the bias term. By iterating the procedure of Eq. (1) k times, we can learn the node feature by aggregating k-order neighbors' type features. As shown in Section 5.2.3, it is a good choice that k is set 2.

4.3. Node Similarity Measurement

As previously mentioned, KN-HGNN does not enumerate instances of meta-paths to measure node similarity. Instead, it calculates the Euclidean distance between nodes based on their features learned. The smaller the Euclidean distance between two nodes, the more similar they should be. The similarity between two nodes is defined as Eq. (2):

$$S(x,y) = \frac{1}{1+D} \tag{2}$$

Where D represents the Euclidean distance between two nodes in the feature space. The range of $S(x,y)$ is $(0,1]$. If the two nodes are identical, then $S(x,y) = 1$.

5. Experiments

5.1. Experimental Setup

To evaluate the performance of the proposed KN-HGNN, we compare KN-HGNN with three baselines PathSim [6], HeteSim [7], and AvgSim [8] on 3 real datasets provided by the literature [11]. Table 2 shows the statistics of the datasets. Firstly, we compare the AUC of KN-HGNN with that of the baselines by similarity query. Then, we compare the running time of KN-HGNN with that of the baselines. Finally, we analyse the effect of parameter on KN-HGNN.

5.2. Experimental Results

5.2.1. Similarity Query

In this subsection, we compare the AUC of methods about similarity query. Specifically, we measure the similarities between the query node and other nodes, and select the top

Table 3. Similarity Query Based on Symmetric Meta-path.

Dataset	PathSim	AvgSim	HeteSim	KN-HGNN
DBLP(*APCPA*)	0.7446	0.7579	**0.7968**	0.7726
ACM(*PAP*)	0.7249	0.7151	0.7667	**0.7811**
IMDB(*MAMAM*)	0.7245	0.7522	0.7694	**0.7872**

Table 4. Similarity Query Based on Asymmetric Meta-path.

Conference(*APC*)	AvgSim	HeteSim	KN-HGNN
KDD	0.8117	0.8111	**0.8290**
ICDM	0.6753	0.6752	**0.7363**
SDM	0.6072	0.6132	**0.7089**
SIGMOD	0.7668	0.7662	**0.7872**
VLDB	**0.8274**	0.8262	0.7095

100 nodes with the highest similarities to calculate the AUC. Table 3 shows the average AUC of all four methods based on some symmetric meta-paths on three real datasets. Table 4 shows the average AUC of three methods except for the method PathSim, which is unable for asymmetric meta-paths, based on some asymmetric meta-paths on the conference subsets of the dataset DBLP.

From Table 3 and Table 4, the proposed KN-HGNN outperforms the baselines in most cases. The reason is that KN-HGNN can better capture the semantic similarity between nodes by exploiting meta-paths and aggregating neighbor node types' features.

5.2.2. Efficiency Analysis

In this subsection, we compare the running time of KN-HGNN with that of PathSim and AvgSim when using different meta-paths on three real datasets. For each dataset, we select specific meta-paths as follows:

- DBLP: (1) *APA* (2) *APAPA* (3) *APCPA* (4) *APTPA*
- ACM: (1) *PAPAPAP* (2) *PAPAPAPAP* (3) *PSP* (4) *PSPSP*
- IMDB: (1) *MUM* (2) *MAMAM* (3) *MDMDMDM* (4) *MDMDMDMDM*

Here, the numbers in front of meta-paths are their No.. In the experiment, the training times of the proposed KN-HGNN are controlled to 150. The experimental results are shown in Figure 1. It can be seen from Figure 1 that the running time of KN-HGNN is stable as meta-path is becoming longer, while that of the baselines grows rapidly, especially AvgSim. In both ACM and IMDB, the length of the No.4 meta-path is slightly longer than the No.3 meta-path. However, the baselines exhibit rapid growth in running time, whereas KN-HGNN is almost unaffected. Additionally, the running time of KN-HGNN remains stable across different meta-paths with the same length. For example, in DBLP, although the No.2, No.3, and No.4 meta-paths have the same length, the running time of the baselines increases rapidly. These experimental results can be attributed to the fact that the baselines measure node similarity based on the number of meta-path instances. The number of instances of different meta-paths can vary greatly in HINs. For instance, in IMDB, even though the length of the No.3 meta-path is longer than the No.2 meta-path, the baselines exhibit smaller running time on the No.3 meta-path.

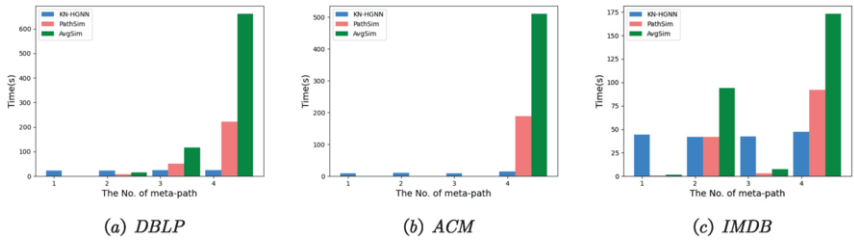

Figure 1. Running time comparison under different meta-paths.

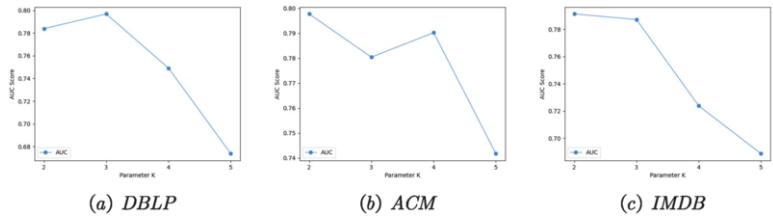

Figure 2. Similarity query performance of KN-HGNN w.r.t. the parameter k of aggregated feature.

5.2.3. Effect of Parameter k

In this subsection, we analyse the effect of the parameter k on the proposed KN-HGNN. For DBLP, ACM, and IMDB, we select Author (A), Paper (P), and Movie(M) as the query node types, respectively. We gradually increase k from 2 to 5 with fixing other hyper-parameters, and report the average AUC about similarity query in Figure 2. We observe that the average AUC generally decreases with increasing k. The possible reason is that the specificity of different node features is weakened as k is becoming larger. Thus, we set $k = 2$ for KN-HGNN.

6. Conclusion

The paper proposes a method for measuring node similarity called KN-HGNN based on heterogeneous graph neural network. The proposed method can not only generate meta-paths based on the network schema, but also learn the features of nodes by aggregating itself type feature and its k-order neighbors' type features under the constraints of meta-paths. The learned features of nodes can be used effectively to measure the similarities between nodes and support similarity query in HINs.

Acknowledgements

This work is supported by the National Natural Science Foundation of China (62266050, 62062066), the Program for Young and Middle-aged Academic and Technical Reserve Leaders of Yunnan Province (202205AC160033), Yunnan Fundamental Research Projects (202201AS070015), the Open Project Program of Yunnan Key Laboratory of Intelligent Systems and Computing (ISC22Z02).

References

[1] Bo-Wei Zhao, Lun Hu, Zhu-Hong You, Lei Wang, and Xiao-Rui Su. Hingrl: predicting drug–disease associations with graph representation learning on heterogeneous information networks. *Briefings in bioinformatics*, 23(1):bbab515, 2022.

[2] Chuan Shi, Yitong Li, Jiawei Zhang, Yizhou Sun, and S Yu Philip. A survey of heterogeneous information network analysis. *IEEE Transactions on Knowledge and Data Engineering*, 29(1):17–37, 2016.

[3] Tao Wen, Shuyu Duan, and Wen Jiang. Node similarity measuring in complex networks with relative entropy. *Communications in Nonlinear Science and Numerical Simulation*, 78:104867, 2019.

[4] Glen Jeh and Jennifer Widom. Simrank: a measure of structural-context similarity. In *Proceedings of the eighth ACM SIGKDD international conference on Knowledge discovery and data mining*, pages 538–543, 2002.

[5] Glen Jeh and Jennifer Widom. Scaling personalized web search. In *Proceedings of the 12th international conference on World Wide Web*, pages 271–279, 2003.

[6] Yizhou Sun, Jiawei Han, Xifeng Yan, Philip S Yu, and Tianyi Wu. Pathsim: Meta path-based top-k similarity search in heterogeneous information networks. *Proceedings of the VLDB Endowment*, 4(11):992–1003, 2011.

[7] Chuan Shi, Xiangnan Kong, Yue Huang, S Yu Philip, and Bin Wu. Hetesim: A general framework for relevance measure in heterogeneous networks. *IEEE Transactions on Knowledge and Data Engineering*, 26(10):2479–2492, 2014.

[8] Xiaofeng Meng, Chuan Shi, Yitong Li, Lei Zhang, and Bin Wu. Relevance measure in large-scale heterogeneous networks. In *Web Technologies and Applications: 16th Asia-Pacific Web Conference, APWeb 2014, Changsha, China, September 5-7, 2014. Proceedings 16*, pages 636–643. Springer, 2014.

[9] Qi Zhang, Meizhu Li, and Yong Deng. Measure the structure similarity of nodes in complex networks based on relative entropy. *Physica A: Statistical Mechanics and its Applications*, 491:749–763, 2018.

[10] MU Junfang, LIANG Jiye, ZHENG Wenping, LIU Shaoqian, and WANG Jie. Node similarity measure for complex networks. *Journal of Frontiers of Computer Science & Technology*, 14(5):749, 2020.

[11] Yaming Yang, Ziyu Guan, Jianxin Li, Wei Zhao, Jiangtao Cui, and Quan Wang. Interpretable and efficient heterogeneous graph convolutional network. *IEEE Transactions on Knowledge and Data Engineering*, 2021.

Fuzzy Systems and Data Mining IX
A.J. Tallón-Ballesteros and R. Beltrán-Barba (Eds.)

doi:10.3233/FAIA231017

A Portfolio Adjusting Model with Triangular Intuitionistic Fuzzy Return

Qiansheng Zhang[1] and Jinyun Li
School of Mathematics and Statistics, Guangdong University of Foreign Studies, Guangzhou 510006

Abstract. To fit the changes in the investment process, a portfolio adjusting method with triangular intuitionistic fuzzy return is put forward. The expected return rate and risk of the portfolio are characterized by mean value and variance of triangular intuitionistic fuzzy number. Then, an intuitionistic fuzzy portfolio adjusting model is established by minimizing the variance risk of portfolio and ensuring the expected return greater than some aspired return levels. Finally, an application example of stock portfolio is given to demonstrate the practicability of intuitionistic fuzzy portfolio adjusting model.

Keywords. Intuitionistic fuzzy portfolio, weighted mean, variance

1. Introduction

Due to the incomplete disclosure of company's financial information, there is a large amount of fuzzy uncertainty in the expected return of the stock asset. To deal with the asset portfolio problem involved fuzzy returns, a lot of scholars have put forward many optimization models [1-5]. However, in the uncertain scenario the expected return of invested asset can be more conveniently estimated by triangular intuitionistic fuzzy number (TrIFN) than fuzzy numbers. Since TrIFN is more powerful and flexible for representing uncertain return data than ordinary fuzzy number because TrIFN can comprehensively consider both membership and nonmembership of return. In fact, the existing fuzzy portfolio decision models only consider the true membership or satisfaction degree of uncertain return without considering the nonmembership of uncertain return. So, it is more valuable to investigate intuitionistic fuzzy portfolio problem than ordinary fuzzy portfolio.

Till now, there are few studies on intuitionistic fuzzy portfolio decision problem. Although some intuitionistic fuzzy optimization methods [6-9] of portfolio selection problem have been investigated, the existing intuitionistic fuzzy portfolio models (IFPMs) only transform fuzzy portfolio objectives to intuitionistic fuzzy objectives. The existing IFPMs are generally constructed by maximizing the membership and

[1] Corresponding Author, Qiansheng Zhang, Department of Statistics,Guangdong University of Foreign Studies, Guangzhou 510006, P.R.China; E-mail: zhqiansh01@126.com.

minimizing nonmembership or hesitation degree of all the portfolio objectives. Recently, Zhou [10] proposed an IFPM based on score-hesitation of IFN. Deng [11] investigated portfolio programming model based on distance measure of IFN. However, the existing IFPM are still unable to directly handle the asset selection problems with TrIFN returns.

Motivated by the above limitations, we try to establish a new IFPM involved with TrIFN returns of the assets and transaction costs. Since TrIFN is widely used in real-world application fields [12-15], we employ TrIFN to assess uncertain return of each security and construct an intuitionistic fuzzy portfolio adjusting model.

2. The weighted possibility mean and variance of TrIFN

A TrIFN $\widetilde{a}=(a_1',a_1,a_2,a_3,a_3')$ is a special kind of intuitionistic fuzzy set on R, whose membership and nonmembership functions are as the following forms [16].

$$\mu_{\widetilde{a}}(x)=\begin{cases}(x-a_1)/(a_2-a_1), & if \quad a_1\le x<a_2,\\ 1\ , & if \quad x=a_2,\\ (a_3-x)/(a_3-a_2), & if \quad a_2<x\le a_3,\\ 0\ , & otherwise.\end{cases}\qquad \nu_{\widetilde{a}}(x)=\begin{cases}(a_2-x)/(a_2-a_1'), & if \quad a_1'\le x<a_2,\\ 0\ , & if \quad x=a_2,\\ (x-a_2)/(a_3'-a_2), & if \quad a_2<x\le a_3',\\ 1\ , & otherwise.\end{cases}$$

where $-\infty<a_1'\le a_1\le a_2\le a_3\le a_3'<+\infty.$

Definition 1[16]**.** Let $\widetilde{a}=(a_1',a_1,a_2,a_3,a_3')$ and $\widetilde{b}=(b_1',b_1,b_2,b_3,b_3')$ be two TrIFNs, some basic operations of them are defined by

(1) $\widetilde{a}+\widetilde{b}=(a_1'+b_1',a_1+b_1,a_2+b_2,a_3+b_3,a_3'+b_3')$.

(2) $\widetilde{a}-\widetilde{b}=(a_1'-b_3',a_1-b_3,a_2-b_2,a_3-b_1,a_3'-b_1')$

(3) $x\widetilde{a}=(xa_1',xa_1,xa_2,xa_3,xa_3'),\forall x\ge 0;\ x\widetilde{a}=(xa_3',xa_3,xa_2,xa_1,xa_1'),\forall x<0.$

Definition 2[17]. Let $\widetilde{a}=(a_1',a_1,a_2,a_3,a_3')$ be a TrIFN, the λ -cut set of membership and γ -cut set of nonmembership function of $\widetilde{a}$ are respectively defined as

$$\widetilde{a}^{[\lambda]}=[a^-(\lambda),a^+(\lambda)]=[a_2-(a_2-a_1)(1-\lambda),a_2+(a_3-a_2)(1-\lambda)];$$

$$\widetilde{a}_{[\gamma]}=[a^-(\gamma),a^+(\gamma)]=[a_2-(a_2-a_1')\gamma,a_2+(a_3'-a_2)\gamma];\qquad \forall\lambda,\gamma\in(0,1).$$

Definition 3[17]. The expected mean of membership and nonmembership of TrIFN $\widetilde{a}$ are respectively defined as

$$M_\mu(\widetilde{a})=\int_0^1[a^-(\lambda)+a^+(\lambda)]\lambda d\lambda=\tfrac{4a_2+(a_1+a_3)}{6};$$

$$M_\nu(\widetilde{a})=\int_0^1[a^-(\gamma)+a^+(\gamma)](1-\gamma)d\gamma=\tfrac{4a_2+(a_1'+a_3')}{6}.$$

Definition 4. Let $\widetilde{a}=(a_1',a_1,a_2,a_3,a_3')$ be a TrIFN, the weighted expected mean value of $\widetilde{a}$ is defined as

$$M(\tilde{a}) = (1-t)M_{\mu}(\tilde{a}) + tM_{\nu}(\tilde{a}) = \frac{4a_2}{6} + \frac{(1-t)(a_1+a_3)+t(a_1'+a_3')}{6} \quad , \quad \forall t \in [0,1]. \quad (1)$$

Definition 5. Assume $\tilde{a} = (a_1', a_1, a_2, a_3, a_3')$ is a TrIFN, the variance of membership and nonmembership of $\tilde{a}$ are, respectively, defined as

$$Var_{\mu}(\tilde{a}) = \frac{1}{2}\int_0^1 \lambda[a^+(\lambda) - a^-(\lambda)]^2 d\lambda = \frac{1}{24}(a_3 - a_1)^2.$$

$$Var_{\nu}(\tilde{a}) = \frac{1}{2}\int_0^1 (1-\gamma)[a^+(\gamma) - a^-(\gamma)]^2 d\gamma = \frac{1}{24}(a_3' - a_1')^2.$$

Definition 6. Let $\tilde{a} = (a_1', a_1, a_2, a_3, a_3')$ be a TrIFN, the variance of $\tilde{a}$ is defined as

$$\mathrm{var}(\tilde{a}) = \frac{1}{2}[\mathrm{var}_{\mu}(\tilde{a}) + \mathrm{var}_{\nu}(\tilde{a})] = \frac{1}{48}[(a_3 - a_1)^2 + (a_3' - a_1')^2]. \quad (2)$$

Definition 7. Let $\tilde{a} = (a_1', a_1, a_2, a_3, a_3')$, $\tilde{b} = (b_1', b_1, b_2, b_3, b_3')$ be two TrIFNs, the covariance of membership and nonmembership of $\tilde{a}, \tilde{b}$ are, respectively, defined as

$$\mathrm{cov}_{\mu}(\tilde{a}, \tilde{b}) = \frac{1}{2}\int_0^1 [a^-(\lambda) - a^+(\lambda)][b^-(\lambda) - b^+(\lambda)]\lambda d\lambda \ ;$$

$$\mathrm{cov}_{\nu}(\tilde{a}, \tilde{b}) = \frac{1}{2}\int_0^1 [a^-(\gamma) - a^+(\gamma)][b^-(\gamma) - b^+(\gamma)](1-\gamma) d\gamma \ .$$

Definition 8. Let $\tilde{a} = (a_1', a_1, a_2, a_3, a_3')$, $\tilde{b} = (b_1', b_1, b_2, b_3, b_3')$ be two TrIFNs, the covariance of $\tilde{a}, \tilde{b}$ is defined as

$$\mathrm{cov}(\tilde{a}, \tilde{b}) = \frac{1}{2}[\mathrm{cov}_{\mu}(\tilde{a}, \tilde{b}) + \mathrm{cov}_{\nu}(\tilde{a}, \tilde{b})] = \frac{(a_1 - a_3)(b_1 - b_3) + (a_1' - a_3')(b_1' - b_3')}{48}. \quad (3)$$

Property 1. Assume $\tilde{a} = (a_1', a_1, a_2, a_3, a_3')$, $\tilde{b} = (b_1', b_1, b_2, b_3, b_3')$ are two TrIFNs, for any x, y, we have

$$M(x\tilde{a} + y\tilde{b}) = xM(\tilde{a}) + yM(\tilde{b}). \quad (4)$$

It can be easily verified by Definition 1, 4 and formula (1). (Omitted)

Property 2. Let $\tilde{a} = (a_1', a_1, a_2, a_3, a_3')$, $\tilde{b} = (b_1', b_1, b_2, b_3, b_3')$ be two TrIFNs. Then for any $x, y \geq 0$, we have

$$\mathrm{var}(x\tilde{a} + y\tilde{b}) = x^2\,\mathrm{var}(\tilde{a}) + 2xy\,\mathrm{cov}(\tilde{a}, \tilde{b}) + y^2\,\mathrm{var}(\tilde{b}).$$

It can be easily proved with Definition 1,5,7 and formulas (2), (3) .

3. Intuitionistic fuzzy portfolio adjusting model

3.1 Intuitionistic fuzzy return mean and risk of portfolio

Let us consider a portfolio includes n risky securities $\{S_1, \Lambda, S_n\}$. Since the expected returns of assets $\{S_i\}(i = 1,2,\Lambda\ n)$ are imprecise, we use the historical return data of financial assets and extend Vercher's method [18] to evaluate the intuitionistic

fuzzy return of S_i as a TrIFN $\widetilde{r}_i = (r'_{i1}, r_{i1}, r_{i2}, r_{i3}, r'_{i3})$, where $r'_{i1}, r_{i1}, r_{i2}, r_{i3}, r'_{i3}$ are the 3-th percentile, 5-th percentile, 50-th percentile, 95-th percentile, 97-th percentile of the historical return rates of security S_i, respectively.

Assume the investor holds an existing portfolio $X^0 = (x_1^0, x_2^0, \Lambda\ , x_n^0)$ and plans to adjust his capital on each asset. Suppose the whole investment process is self-financing and the cost rate of buying or selling security i is $c_i, (1 \le i \le n)$. After adjusting capital the optimal portfolio changes to $x = (x_1, x_2, \Lambda\ , x_n)$, and the IFP return is $\sum_{i=1}^n x_i \widetilde{r}_i = (\sum_{i=1}^n x_i r'_{i1}, \sum_{i=1}^n x_i r_{i1}, \sum_{i=1}^n x_i r_{i2}, \sum_{i=1}^n x_i r_{i3}, \sum_{i=1}^n x_i r'_{i3})$.
Then, with formula (4) we calculate the weighted return mean of the portfolio as

$$r_p = M(\sum_{i=1}^n x_i \widetilde{r}_i) = \sum_{i=1}^n x_i [\frac{4r_{i2}}{6} + \frac{(1-t)(r_{i1}+r_{i3})+t(r'_{i1}+r'_{i3})}{6}].$$

By utilizing formula (2) we compute the variance risk of portfolio as

$$\mathrm{var}(\sum_{i=1}^n x_i \widetilde{R}_i) = \frac{1}{48}\{[\sum_{i=1}^n x_i (r_{i3} - r_{i1})]^2 + [\sum_{i=1}^n x_i (r'_{i3} - r'_{i1})]^2\}. \quad (5)$$

The total transaction cost of portfolio in the adjusting process is calculated by

$$Cost(X) = \sum_{i=1}^n c_i \left| x_i - x_i^0 \right|.$$

And the net return of this portfolio is

$$r_{p,N} = \sum_{i=1}^n x_i [\frac{4r_{i2}}{6} + \frac{(1-t)(r_{i1}+r_{i3})+t(r'_{i1}+r'_{i3})}{6}] - \sum_{i=1}^n c_i \left| x_i - x_i^0 \right|. \quad (6)$$

3.2 Construction of intuitionistic fuzzy portfolio model

Assume an investor now holds the existing portfolio $X^0 = (x_1^0, x_2^0, \Lambda\ , x_n^0)$ and he/she try to reallocate n assets by minimizing the risk of portfolio under some uncertain constraints. Thus, the intuitionistic fuzzy portfolio adjusting method is formulated as programming model (P1) by minimizing variance risk formula (5) and ensuring net return formula (6) of portfolio greater than a given aspiration level.

$$\text{(P1)}\quad \min\ \frac{1}{48}\{[\sum_{i=1}^n x_i (r_{i3} - r_{i1})]^2 + [\sum_{i=1}^n x_i (r'_{i3} - r'_{i1})]^2\}$$

$$\text{s.t.}\ \begin{cases} \sum_{i=1}^n [\frac{2r_{i2}}{3} + \frac{(1-t)(r_{i1}+r_{i3})+t(r'_{i1}+r'_{i3})}{6}] x_i - \sum_{i=1}^n c_i \left| x_i - x_i^0 \right| \ge \eta \\ \sum_{i=1}^n x_i + \sum_{i=1}^n c_i \left| x_i - x_i^0 \right| = 1 \\ l_i \le x_i \le u_i, i = 1,2\Lambda\ , n; \end{cases}$$

where η denotes the minimum aspired net return level determined by the risky investor. $l_i, u_i \in [0,1]$ denote lower bound and upper bound of capital invested on security i.

Note that there is an absolute value function in the constraint of the above portfolio model, it results in complexity of solving this model. In order to simplify the optimization model, we let $d_i^+ = \frac{\left| x_i - x_i^0 \right| + (x_i - x_i^0)}{2}, d_i^- = \frac{\left| x_i - x_i^0 \right| - (x_i - x_i^0)}{2}$, then the above

complex portfolio adjusting model (P1) can be transformed to the following simple quadratic programming model.

$$\text{(P2)}\quad \min \tfrac{1}{48}\{[\sum_{i=1}^{n} x_i(r_{i3}-r_{i1})]^2+[\sum_{i=1}^{n} x_i(r'_{i3}-r'_{i1})]^2\}$$

$$\text{s.t.}\begin{cases}\sum_{i=1}^{n}[\frac{2r_{i2}}{3}+\frac{(1-t)(r_{i1}+r_{i3})+t(r'_{i1}+r'_{i3})}{6}]x_i-\sum_{i=1}^{n} c_i(d_i^+ + d_i^-)\geq \eta\\ \sum_{i=1}^{n} x_i+\sum_{i=1}^{n} c_i(d_i^+ + d_i^-)=1\\ l_i\leq x_i\leq u_i,\\ d_i^+, d_i^-\geq 0, \forall i=1,2\Lambda\ ,n;\end{cases}$$

Thus, one can easily solve the optimal strategy of model (P2) by taking different return aspiration η and using Lingo nonlinear optimization software. The portfolio solutions of model (P2) vary according to the different aspired return value η .

4. Application example

Suppose an investor already holds an existing portfolio comprising of the following five stocks: S_1 (code 600192), S_2 (code 600537), S_3 (code 603256), S_4 (code 603223), S_5 (code 603628), which are selected from Shanghai Stock Exchange in China. And the adjusting investment process is self-financing.

We collect the alternative corporations' financial statement information and the assets' monthly prices from September 2018 to September 2022. By utilizing the historical monthly return data and Vercher's percentile method [18] we estimate the uncertain return of each stock Si as a TrIFN $\tilde{r}_i=(r'_{i1},r_{i1},r_{i2},r_{i3},r'_{i3})$. The distribution parameters of the evaluated TrIFN return rates of Stock i are listed in Table 1. Some coefficients of the proposed adjusting model are listed in Table 2.

Table 1. TrIFN return assessment of the five stocks

Parameter of TrIFN	S1	S2	S3	S4	S5
r'_{i1}	-0.215	-0.156	-0.193	-0.151	-0.231
r_{i1}	-0.165	-0.134	-0.186	-0.131	-0.21
r_{i2}	0.030	0 .022	0.004	0.049	0.0264
r_{i3}	0.249	0.282	0.275	0.286	0.2976
r'_{i3}	0.271 0.3314	0.339	0.411	0.301	
Variance risk	0.0085	0.0087	0.012	0.0079	0.012

Table 2. Some coefficients of the portfolio adjusting model

Coefficients	S1	S2	S3	S4	S5
$r_{i3}-r_{i1}$	0.4140	0.4160	0.4610	0.4170	0.5076
$r'_{i3}-r'_{i1}$	0.4860	0.4950	0.6040	0.4520	0.5624
$r'_{i1}+r'_{i3}$	0.0560	0.1830	0.2180	0.150	0.1004

$r_{i1}+r_{i3}$	0.0840	0.1480	0.0890	0.1550	0.0876
$\frac{4r_{i2}+(1-t)(r_{i1}+r_{i3})+t(r'_{i1}+r'_{i3})}{6}$	0.034-0.0047t	0.039+0.0058t	0.0175+0.0215t	0.0585-0.0008t	0.0322+0.002t

Let the existing portfolio be $x^0=(x_1^0,x_2^0,x_3^0,x_4^0,x_5^0)=(0.15,0.2,0.25,0.2,0.2)$.

If taking t=1, $M(r_{x^0})=0.0416;\quad \mathrm{var}(r_{x^0})=0.4099.$

If taking t=0, $M(r_{x^0})=0.0355;\quad \mathrm{var}(r_{x^0})=0.4099.$

Now we use the portfolio adjusting model to reallocate the assets. Assume the capital upper bounds of five stocks is $(u_1,\Lambda\ ,u_5)=(0.3,\ 0.3,\ 0.4,\ 0.4,\ 0.5)$ and the cost rates of purchasing and selling stocks are the same as $c_i=0.001,\forall i=1,2,\Lambda\ ,5.$

In order to obtain the optimal adjusting strategy, we substitute the return mean, variance and coefficients of each stock into the constructed portfolio model (P2) and reformulate the IFP adjusting problem as the following programming model (P3).

$$\text{(P3)}\ \min\ \tfrac{1}{48}\{[\textstyle\sum_{i=1}^{5}x_i(r_{i3}-r_{i1})]^2+[\sum_{i=1}^{5}x_i(r'_{i3}-r'_{i1})]^2\}$$

$$\text{s.t.}\quad\begin{cases}\displaystyle\sum_{i=1}^{5}[\frac{4r_{i2}+(1-t)(r_{i1}+r_{i3})+t(r'_{i1}+r'_{i3})}{6}]x_i-\sum_{i=1}^{5}c_i(d_i^+ + d_i^-)\ge\eta\\ \displaystyle\sum_{i=1}^{5}x_i+\sum_{i=1}^{5}0.001(d_i^+ + d_i^-)=1\\ 0\le x_1,x_2\le 0.3,\\ 0\le x_3,x_4\le 0.4,\\ 0\le x_5\le 0.5,\\ d_i^+,d_i^-\ge 0,i=1,2,\Lambda\ ,5.\end{cases}$$

By solving the above model (P3), some optimal portfolio results are listed in Table 3 when the investor is optimistic and take t=1. If the investor is pessimistic and take t=0, then the solved optimal portfolio strategies are displayed in Table 4. If the investor is neutral and take t= 0.5, then he can obtain the optimal portfolio adjusting strategies in Table 5 by taking different aspired return level η.

Table 3. Some optimal portfolios when taking t=1

η	**0.01**	**0.02**	**0.03**
Min var	0.008	0.0082	0.0083
X1	0.3	0.3	0.3
X2	0.2	0.229	0.2991
X3	0	0	0
X4	0.38	0.39	0.4
X5	0	0	0

Table 4. Some optimal portfolios when taking t=0

η	**0.015**	**0.025**	**0.04**
Min var	0.0006	0.0017	0.0062
X1	0	0	0.16394

X2	0.0012	0.0645	0.3
X3	0	0	0
X4	0.2713	0.4	0.4
X5	0	0	0

Table 5. Some optimal portfolios when taking t=0.5

η	**0.031**	**0.042**	**0.045**
Min var	0.00296	0.00696	0.00874
X1	0	0.21824	0.1639
X2	0.2029	0.3	0.3
X3	0	0	0
X4	0.4	0.4	0.4
X5	0	0	0.1361

Table 6. Some optimal portfolios when taking t=1 with the proportion lower bound

η	**0.01**	**0.02**	**0.03**
Min var	0.0084	0.00848	0.0085
X1	0.3	0.3	0.3
X2	0.22	0.228	0.23
X3	0.03	0.03	0.03
X4	0.4	0.4	0.4
X5	0.04	0.04	0.04

From Table 3, 4, 5 one can see that the investor should adjust the existing portfolio to obtain the optimal portfolios. Especially in Table 3, for $\eta = 1\%$, the investor should buy 0.15 of stock 1, sell 0.25 of stock 3, buy 0.18 of stock 4, and sell 0.2 of stock 5 to get the optimal portfolio $x^* = (0.3, 0.2, 0, 0.38, 0)$. If the investor is optimistic and plans to hold five assets in the portfolio, he need set the lower bound constraints such as l_1=0.02, $l_2 = 0.02$, l_3=0.03, l_4=0.03, l_5=0.04. Then by solving the portfolio adjusting model (P3) he can get some optimal portfolios as shown in Table 6. Comparing Table 3 and Table 6, we find that the optimal portfolio in Table 3 is more efficient than the corresponding one in Table 6.

5. Comparative analysis

In this section, we will compare our proposed intuitionistic fuzzy adjusting portfolio model with the existing fuzzy adjusting portfolio model.

When $r'_{i1} = r_{i1}, r'_{i3} = r_{i3}$, the estimated TrIFN return $\widetilde{r_i} = (r'_{i1}, r_{i1}, r_{i2}, r_{i3}, r'_{i3})$ of asset i in this paper is degenerated into triangular fuzzy return $\widetilde{r_i} = (r_{i1}, r_{i2}, r_{i3})$, which is fuzzy possibility distribution $\widetilde{r_i} = (r_{i2}; \alpha, \beta)$, where $\alpha = r_{i2} - r_{i1}, \beta = (r_{i3} - r_{i2})$ are respectively the left width and right width of TrFN in literature [1]. The proposed IFPM is reduced to the corresponding FPM. So, the existing FPM [1] is a special case of our proposed IFPM. Hence, our presented intuitionistic fuzzy portfolio adjusting model is more extensive than the existing fuzzy adjusting portfolio method [1, 19].

Moreover, if $r'_{i1} = r_{i1}, r'_{i3} = r_{i3}$, the presented intuitionistic fuzzy adjusting model is transformed into the following fuzzy portfolio form.

$$\min \ \tfrac{1}{24}\{[\sum_{i=1}^{n} x_i(r_{i3} - r_{i1})]^2\}$$

s.t.

$$\sum_{i=1}^{n}[\tfrac{2r_{i2}}{3} + \tfrac{(r_{i1}+r_{i3}))}{6}]x_i - \sum_{i=1}^{n} c_i\left|x_i - x_i^0\right| \geq \eta$$

$$\sum_{i=1}^{n} x_i + \sum_{i=1}^{n} c_i\left|x_i - x_i^0\right| = 1$$

$$l_i \leq x_i \leq u_i, i = 1,2\Lambda\ ,n;$$

We compare our portfolio adjusting model with the following known fuzzy portfolio adjusting model proposed in Zhang's work [1].

$$\min \ \ \tfrac{1}{24}[\sum_{i=1}^{n} x_i(\alpha_i + \beta_i)]^2 + \tfrac{1}{72}[\sum_{i=1}^{n} x_i(\alpha_i - \beta_i)]^2$$

$$\text{s.t.} \begin{cases} \sum_{i=1}^{n}[\tfrac{2r_{i2}}{3} + \tfrac{(r_{i1}+r_{i3}))}{6}]x_i - \sum_{i=1}^{n} c_i\left|x_i - x_i^0\right| \geq \eta \\ \sum_{i=1}^{n} x_i + \sum_{i=1}^{n} c_i\left|x_i - x_i^0\right| = 1 \\ l_i \leq x_i \leq u_i, i = 1,2\Lambda\ ,n; \end{cases}$$

In the above-mentioned two adjusting portfolio models, the objective function is different but the constraints are setting same for comparing the portfolio efficiency.

Here, we set the lower bound and upper bound vector on holding five assets as $(l_1, l_2, l_3, l_4, l_5) = (0.02, 0.02, 0.03, 0.03, 0.04), (u_1, u_2, u_3, u_4, u_5) = (0.3, 0.3, 0.4, 0.4, 0.5)$. By utilizing optimization software, we get the portfolio strategy results as in Table 7, 8.

Table 7. The optimal portfolio result obtained from our model

η	**0.01**	**0.02**	**0.03**
Min var	**0.00736**	**0.007364**	**0.007365**
X1	0.3	0.3	0.3
X2	0.3	0.29	0.292
X3	0.03	0.028	0.029
X4	0.3292	0.393	0.394
X5	0.04	0.041	0.0415

Table 8. The optimal portfolio result obtained from Zhang's fuzzy model [1]

η	**0.01**	**0.02**	**0.03**
Min var	**0.00741**	**0.007416**	**0.00742**
X1	0.3	0.3	0.3
X2	0.3	0.3	0.3
X3	0.03	0.03	0.03
X4	0.32924	0.32925	0.32926
X5	0.04	0.0415	0.042

From the above optimal strategy Tables 7, 8 one can see that the risk objective of our intuitionistic fuzzy adjusting portfolio model is smaller than that obtained from zhang's adjusting portfolio model [1] under the same aspired return level η . So, our proposed intuitionistic fuzzy portfolio adjusting model is better than the known fuzzy portfolio adjusting model of Zhang [1].

6. Conclusion

We study the portfolio adjusting problem when transaction cost is considered. The presented portfolio adjusting model can deal with the TrIFN returns of stocks and the bounded holding proportions of assets. With the portfolio adjusting model, the investors can obtain the appropriate portfolio according to their risk preference.

Acknowledgment

This paper is supported by the Guangdong Basic and Applied Basic Research Foundation (Nos. 2021A1515011974, 2023A1515011354 , 2018A030313996).

References

[1] Zhang W. G., Xiao W. L., Xu W.J., A possibilistic portfolio adjusting model with new added assets, Economic Modelling, 2010, 27(1): 208-213.
[2] Deng X., Chen J., Wang X., & Geng F. , Non-dominated sorting genetic algorithm-II for possibilistic mean-semiabsolute deviation-Yager entropy portfolio model with complex real-world constraints, Mathematics and Computers in Simulation, 2022, 202, 59-78.
[3] Pahade J. K., & Jha M. , A hybrid fuzzy-scoot algorithm to optimize possibilistic mean semi-absolute deviation model for optimal portfolio selection, International Journal of Fuzzy Systems, 2022, 24(4), 1958-1973.
[4] Yang X. Y., Chen S. D., Liu W. L., & Zhang Y. , A Multi-period fuzzy portfolio optimization model with short selling constraints, International Journal of Fuzzy Systems, 2022, 24(6), 2798-2812.
[5] Jalota H., Mandal P. K., Thakur M., & Mittal, G., A novel approach to incorporate investor's preference in fuzzy multi-objective portfolio selection problem using credibility measure, Expert Systems with Applications, 2023, 212, 118583.
[6] Chen G.H., Luo Z.J. , Liao X. L. , Yu X. , Yang L., Mean-variance-skewness fuzzy portfolio selection model based on intuitionistic fuzzy optimization, Procedia Engineering, 2011,15(2), 2062-2066.
[7] Deng X., Pan X.Q.,The research and comparison of multi-objective portfolio based on intuitionistic fuzzy optimization, Computers and Industrial Engineering, 2018,124(10), 411-421.
[8] Gupta P., Mehlawat M.K., Yadav S., Kumar A., A polynomial goal programming approach for intuitionistic fuzzy portfolio optimization using entropy and higher moments, Applied Soft Computing, 2019, 85, 105781.
[9] Yu G. F., Li D. F., Liang D.C., Li G. X., An intuitionistic fuzzy multi-objective goal programming approach to portfolio selection, International Journal of Information Technology & Decision Making, 2021, 20(5), 1477-1497.
[10] Zhou W., Xu Z. S., Score-hesitation trade-off and portfolio selection under intuitionistic fuzzy Environment, International Journal of Intelligent Systems 2019, 34(2), 325-341.
[11] Deng X., Chen C., Novel linear programming models based on distance measure of IFSs and modified TOPSIS method for portfolio selection. Egyptian Informatics Journal, 2022, 23(4), 13-31
[12] Zhang S., Li X., & Meng F., A distance measure based intuitionistic triangular fuzzy multi-criteria group decision making method and its application. Applied Intelligence, 2022,1-20.
[13] Wang Z., Xiao F., & Ding W., Interval-valued intuitionistic fuzzy Jenson-Shannon divergence and its application in multi-attribute decision making, 2022, Applied Intelligence, 1-17.
[14] Jiang Q., Jin X., Lee S. J., Yao, S. , A new similarity/distance measure between intuitionistic fuzzy sets based on the transformed isosceles triangles and its applications to pattern recognition. Expert Systems with Applications, 2019,116, 439-453.
[15] Dhiman N., Gupta M. M., Singh D. P., Mishra V. N., Sharma M. K. On Z-Intuitionistic Fuzzy Fractional Valuations for Medical Diagnosis: An Intuitionistic Fuzzy Knowledge-Based Expert System, Fractal and Fractional, 2022,6(3), 151.
[16] Garai T., Chakraborty D., Roy T. K., Possibility-necessity-credibility measures on generalized intuitionistic fuzzy number and their applications to multi-product manufacturing system, Granular

Computing, 2018, 3, 285-299.

[17] Li D. F., A ratio ranking method of triangular intuitionistic fuzzy numbers and its application to MADM problems, Computers and Mathematics with Applications, 2010, 60(6), 1557-1570.

[18] Vercher E., Bermúdez J.D., Segura J.V., Fuzzy portfolio optimization under downside risk measures, Fuzzy Sets and Systems, 2007,158, 769-782.

[19] Fang Y., Lai K. K., Wang S.Y., Portfolio rebalancing model with transaction costs based on fuzzy decision theory, European Journal of Operational Research, 2006,175, 879-893.

Fuzzy Systems and Data Mining IX
A.J. Tallón-Ballesteros and R. Beltrán-Barba (Eds.)

doi:10.3233/FAIA231018

A Novel Nonferrous Metals Price Prediction Model Based on BiLSTM-ResNet with Grey Wolf Optimization and Wavelet Transform

ZHANGLONG LI [a], YUNLEI YANG [a,1], JIACHUN ZHENG [a], YANG WU [a] and YINGHAO CHEN [b]

[a] *School of Mathematics and Statistics, Guizhou University, Guiyang, Guizhou 550025, China*

[b] *School of Mathematics and Statistics, Central South University, Changsha, 410083, China; Eastern Institute for Advanced Study, Yongriver Institute of Technology, Ningbo, Zhejiang 315201, China*

Abstract. Nonferrous metals are important commodities, and it is of great significance for policy makers and investors to accurately predict their price changes. Nevertheless, because the price of nonferrous metals present drastic fluctuations, developing a robust price prediction method is a tricky task. In this research, a hybrid model based on discrete wavelet transform (DWT), bidirectional long short-term memory (BiLSTM) and residual network (ResNet) is constructed for nonferrous metals price prediction. The hyper-parameters of the hybrid neural network are searched by grey wolf optimization (GWO) algorithm. Configuring reasonable parameters, which enhances the final prediction effect. Additionally, behind the second hidden layer, the low and high dimensional features are fused to prevent the degradation of the model. The original sequence is processed by DWT technology, then the sequence is reconstructed, which is beneficial to capture the essential trend. The experimental results show that the proposed BiLSTM-ResNet-GWO-DWT model is more accurate compared with the other benchmark models, which provides an effective reference significance.

Keywords. Nonferrous metals price prediction, BiLSTM, ResNet, Discrete wavelet transform, Grey wolf optimization

1. Introduction

Nonferrous metals, as the bulk commodity, have a vital role in the global economy. For instance, aluminum, copper and zinc are closely related to aviation, construction and other industries. Unique material characteristics make them more widely use. Meanwhile, the fluctuation of these nonferrous metals price is a barometer of economic action,

[1]Corresponding Author: Yunlei Yang, School of Mathematics and Statistics in Guizhou University, ylyang5@gzu.edu.cn

which offers a risk reference for the financial participants [1,2,3]. There is no denying that it is a meaningful work to carry out the relevant price prediction research.

In the past, some traditional statistical models had been proposed for the metals price prediction. For example, Thomas Kriechbaumer et al. proposed the improved wavelet-ARIMA approach, and demonstrated its usefulness in predicting monthly prices for aluminum, copper, lead and zinc [4]. Nevertheless, the ARIMA-type forecast models require that temporal data is stable and essentially only capture linear relationships. Lasheras et al. tested that the prediction performance of both neural network models (multilayer perceptron and Elman), using copper spot price data released on the New York Mercantile Exchange, was better than ARIMA [5]. What's more, the ARIMA model has an error assumption, namely, the constant variance. But generally for highly fluctuating data, the variance of the error is nonconstant. Consequently, the ARIMA model is basically not applicable to gold prices. On account of the above considerations, Yaziz et al. combined ARIMA and Symmetric GARCH-type Models to forecast Malaysian gold price [6]. However, these equations are based on the hypothesis of independence of local laws, that is why they are only suitable for short-term forecast.

In the advance of artificial intelligence (AI), many excellent data prediction models have been published based on extreme learning machine (ELM), support vector machine (SVM), decision tree and so on [7,8,9]. For instance, Kumar Chandar Sivalingam et al. taken full advantage of ELM method to focus on predicting the future gold prices of four commodities to predict business trend[10]. Results proved that ELM model was better than other feed-forward networks. Moreover, Shao Bilin et al. used the reformative particle swarm optimization (PSO) to optimize LSTM network and then predicted the nickel price [11]. Contrasted with the traditional LSTM and ARIMA model, the prediction error of this model was reduced by 9% and 13%, respectively, which had high reliability. Notwithstanding, the generalization ability of the single model is limited. Hou Muzhou et al. proposed the hybrid constructive neural network method (HCNNM) to fix the impact values in the raw data [12,13]. Through a series of numerical experiments, compared with the machine learning algorithms (including ELM, SVM and deep learning), they fully verify the correctness and effectiveness of the proposed theory. Chengshi Tian and Yan Hao proposed a newly designed hybrid optimization algorithm and applied to train adaptive neuro-fuzzy inference system, which provides more reliable information for decisions according to the point and interval prediction of carbon price sequence [14]. Dania Batool et al. Designed a tea yield prediction model based on combining different data sources through a crop simulation model and machine learning algorithms, which offers guidance for improving management practice [15].

At present, it is a consensus that fusion model is more generalized than single model. The hybrid stochastic-grey model with the singular spectrum analysis is proposed by Zoran Gligoric et al. to predict the behavior of metal price, as a result, it has better prediction accuracy than the traditional grey model [16]. Moreover, Ni Jian et al. combined LSTM-ANN with GARCH model to forecast the copper price volatility and significantly promote the forecast precision [17]. In 2022, a hybrid neural network combining Bayesian optimization and wavelet transform was applied to copper price prediction by Liu Kailei et al [18]. According to the advantage of each model, the hybrid model was fully utilized to capture the fluctuation characteristics of the historical data, whereas the optimal configuration of the hyperparameters was insufficient.

Undoubtedly, a majority of efforts have been made to heighten the effectiveness of predicting non-ferrous metals price, but a more stable benchmark model should be proposed. In the light of the consideration of the network degradation phenomenon, the purpose of this study is to establish a novel model based on the ResNet and BiLSTM neural network. At the same time, optimizing the hyper-parameters is a time-consuming process, but it is very imperative for the stability of the model. Previously, the optimization of hyperparameters can be performed by grid search or random search, but neither method was satisfactory. On the one hand, grid search solutions will consume a lot of computing resources. On the other hand, although random search will generally be faster than grid search, the global optimal value is not guaranteed. In addition, due to the complexity of the raw sequence, it is essential to make the data preprocessing. In view of the above problems, we construct the hybrid BiLSTM-ResNet model with GWO algorithm and discrete wavelet transform to forecast the non-ferrous metals price. Here, the wavelet transform is selected to remove noise and then the processed data input to the mentioned hybrid network.

The arrangement of this paper is presented as follows. The methodology including the wavelet transform, grey wolf optimization and normalization are introduced in section 2. We describe the basic theories of the related BiLSTM and ResNet model in section 3. Experiment results and its analyses are presented in section 4. Section 5 summarizes the entire paper, puts forward conclusions. The direction of the future work is given in the final section.

2. Methodology

2.1. Wavelet transform

The wavelet transform algorithm has been widely used in the fields of science, engineering and so on [19]. It is a significant time-scale and time-frequency localization analysis method that both time window and frequency window can be changed. There are two forms of wavelet transform including continuous wavelet transform (CWT) as well as discrete wavelet transform (DWT) [18,20].

The CWT is defined as shown in Eq. (1).

$$CWT_h(m,\tau) = \frac{1}{\sqrt{|m|}} \int_R h(t)\phi(\frac{t-\tau}{m})dt \tag{1}$$

where m, τ, ϕ and h(t) indicate the scaling factor, translating factor, the mother wavelet and the raw signal, respectively.

The DWT is defined as shown in Eq. (2).

$$DWT_h(p,q) = (\frac{1}{\sqrt{2}})^p \int_R h(t)\phi(2^{-p}t-q)dt \tag{2}$$

where p called scale is a parameter characterizing the frequency; q is a parameter characterizing the temporal or spatial location.

The DWT is applied to remove noise Gaussian interference from the raw sequence, with the aim to reduce the adverse effects of complex nonlinear signal. To make the reconstructed signal not distorted, the Daubechies of order 2 (db2) is choosen as the

benchmark wavelet. Then, the key step is the wavelet inversion reconstruction to return the denoised data to the time-frequency domain. Ultimately, a threshold function should be selected to filter the Gaussian noise coefficient, such as the soft threshold or the hard threshold method.

The hard threshold method is shown as follows:

$$\overline{\mu}_{i,j} = \begin{cases} \mu_{i,j} & if \quad |\mu_{i,j}| \geq \alpha, \\ 0 & if \quad |\mu_{i,j}| < \alpha. \end{cases} \tag{3}$$

The soft threshold method is shown as follows:

$$\overline{\mu}_{i,j} = \begin{cases} sgn(\mu_{i,j})|\mu_{i,j} - \alpha| & if \quad |\mu_{i,j}| \geq \alpha, \\ 0 & if \quad |\mu_{i,j}| < \alpha. \end{cases} \tag{4}$$

where $\mu_{i,j}$, α is the wavelet coefficient after multi-layer decomposition and threshold, respectively. In this research, the soft threshold method is used.

2.2. *Grey wolf optimizer*

The grey wolf optimizer (GWO) inspired by the prey hunting activity of grey wolves, is a group intelligent optimization algorithm developed by scholar Mirjalili et al. of Griffith University in Australia [21].

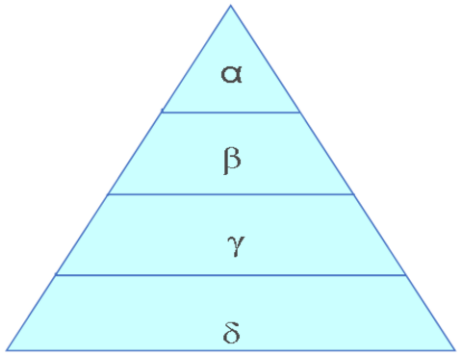

Fig. 1. The top-down dominance hierarchy from grey wolf.

The grey wolf belongs to social canids. They strictly adhere to a top-down social dominance hierarchy, as shown in Fig.1. Where the head wolf in the wolf pack is recorded as α, and α wolf is mainly responsible for making decisions on predation, habitat, work and rest time and other activities. Moreover, β wolf, it obeys and assists α wolf in making decisions, but at the same time β wolf can control wolves at other social levels. After α wolf dies or aging, β wolf will be the best candidate for α wolf. The γ wolf generally consists of juvenile, sentinel, hunting, aged and nursing wolves. It obeys α and β wolf, while dominating the remaining hierarchy of wolves. The δ wolf, it usually needs to obey other social levels of wolves. Although it seems that δ wolf plays little role in wolves, δ wolf exists for reasonable team building, such as avoiding infighting problems.

The algorithm considers the optimal solution as a prey which is constantly approached by the grey wolf pack, as follows: (a)The hunting space of the grey wolf pack is set to $m \times n$ Euclidean space, where m is the number of grey wolves and n is the dimension of the prey. The location of each wolf can be expressed as $Z_i = (z_1, z_1, ..., z_n)(i = 1, 2, ..., m)$. Nextly, the distance between each grey wolf and its prey was judged according to the hyperparameters of the location. Assuming α, β and γ wolf have stronger ability to identify potential prey location, the rest is the δ wolf. (b)Under the guidance of the three strongest wolves, the search activity is updated according to the location information of the four wolves. The mathematical model is represented by Eqs. (5)-(7) as follows:

$$\begin{cases} \overrightarrow{d}_\alpha = |\overrightarrow{c}_1 \bullet \overrightarrow{Z}_\alpha - \overrightarrow{Z}_t|, \\ \overrightarrow{d}_\beta = |\overrightarrow{c}_2 \bullet \overrightarrow{Z}_\beta - \overrightarrow{Z}_t|, \\ \overrightarrow{d}_\gamma = |\overrightarrow{c}_3 \bullet \overrightarrow{Z}_\gamma - \overrightarrow{Z}_t|. \end{cases} \tag{5}$$

$$\begin{cases} \overrightarrow{Z}_1 = \overrightarrow{Z}_\alpha - \overrightarrow{A}_1 \bullet d_\alpha, \\ \overrightarrow{Z}_2 = \overrightarrow{Z}_\beta - \overrightarrow{A}_2 \bullet d_\beta, \\ \overrightarrow{Z}_3 = \overrightarrow{Z}_\gamma - \overrightarrow{A}_3 \bullet d_\gamma. \end{cases} \tag{6}$$

$$\begin{cases} \overrightarrow{C} = 2\overrightarrow{r}_2, \\ \overrightarrow{A} = 2\overrightarrow{a} \bullet \overrightarrow{r}_1 - \overrightarrow{a}, \\ \overrightarrow{Z}_{t+1} = \frac{\overrightarrow{Z}_1 + \overrightarrow{Z}_2 + \overrightarrow{Z}_3}{3}. \end{cases} \tag{7}$$

where $\overrightarrow{d}_\alpha$, $\overrightarrow{d}_\beta$ and $\overrightarrow{d}_\gamma$ indicate the distance between the current candidate wolf and the optimal three wolves, respectively. Z_α, Z_β, and Z_γ indicate the positional vectors of α, β and γ wolf in the current population, respectively. Z_t represents the location vector of the grey wolf in the t iterations, $\overrightarrow{a}$ drops linearly from 2 to 0 throughout the iteration; r_1 and r_2 are random vectors in the range [0,1], and '•' represents the Hadamard product.

When $|A| < 1$, then the next moment position of search agent can be at any position between the current grey wolf and the prey. For the establishment of the dispersion model with $|A| > 1$, the search method enables the GWO to make a global search. Besides, the vector $\overrightarrow{C}$ composed of random values over the interval range [0,2], which is a nonlinear decreasing search coefficient that provides random weights to the prey [22].

2.3. Data normalization

It is significant that a standardization processing can improve training efficiency, which makes gradient descent almost along the same direction. We select MinMaxScaler method to normalize the original price data, calculated as in Eq. (8). Finally, all test results need to make inverse normalization so that we can be easily able to observe the proximity to the original data.

$$\widehat{x}_t = \frac{x_t - x_{\min}}{x_{\max} - x_{\min}} \tag{8}$$

Where, $\widehat{x}_t \in [0, 1]$, x_t is the normalized and the actual value at time t, severally; $x_{\min}$, $x_{\max}$ is minimum and maximum value of the original sequence, respectively.

3. Deep model

3.1. BiLSTM

Recurrent neural network (RNN) plays an important role in the processing of a time-series. However, it tends to appear gradient disappearance or gradient burst [13,20]. LSTM coming into being, it was proposed by Schmidhuber et al, seen in literature [23]. General structure of deep LSTM can be seen in Fig.2.

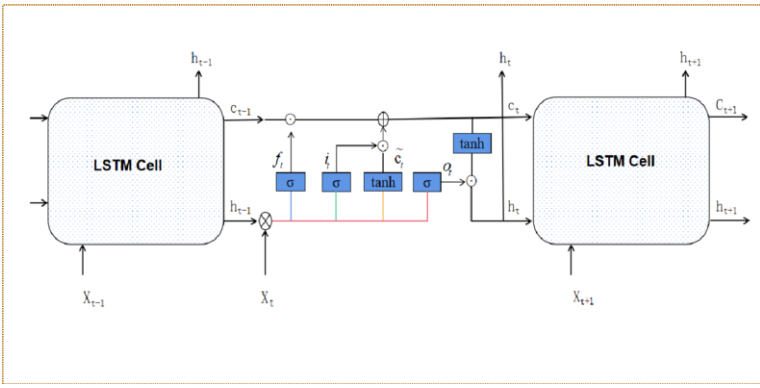

Fig. 2. The overall framework of LSTM neural networks.

As a forward network, LSTM can only excavate the characteristic of forward historical price data [24]. Notwithstanding, price data is not only dependent on information from the past, but also related to future financial conditions. BiLSTM is the expansion of LSTM that combines the forward and backward processing to capture useful information [25,26]. Hence, it can be performed to make the forecast more precise. The framewok of BiLSTM is shown as in Fig.3:

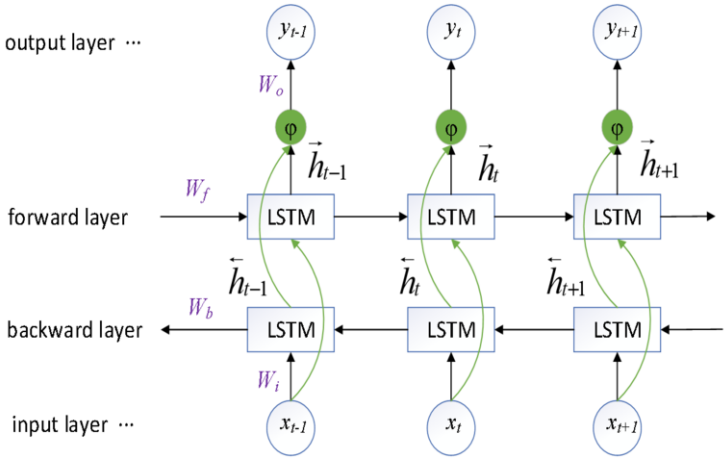

Fig. 3. The overall framework of deep BiLSTM network.

Concretely, the forward hidden layer state $\overrightarrow{h_t}$ is received via the forward network unit where the historical price series $X = [x_1, x_2, ..., x_T]$ is input. Historical price series X, as input to the LSTM is employed to forecast future price series $X' = [x'_1, x'_2, ..., x'_T]$ as an input to the reverse network unit, it obtains the reverse hidden-layer state $\overleftarrow{h}_t$. The output y_t of the network can be obtained through $\overrightarrow{h}_t$ and $\overleftarrow{h}_t$, and BiLSTM of the cells are calculated as follows:

$$\overleftarrow{h}_t = W_{x\overleftarrow{h}} x_t + W_{\overleftarrow{h}\overleftarrow{h}} \overleftarrow{h}_{t-1} + \overleftarrow{b}_h \tag{9}$$

$$\overrightarrow{h}_t = W_{x\overrightarrow{h}} x_t + W_{\overrightarrow{h}\overrightarrow{h}} \overrightarrow{h}_{t-1} + \overrightarrow{b}_h \tag{10}$$

$$y_t = \varphi(W_{\overrightarrow{h}y} \overrightarrow{h}_t + W_{\overleftarrow{h}y} \overleftarrow{h}_t + b_y) \tag{11}$$

Where, φ represents nonlinear activation function. $W_{x\overleftarrow{h}}$ represents the weight from the input x of the current neuron to $\overleftarrow{h}$ at this moment, $W_{\overleftarrow{h}\overleftarrow{h}}$ represents the weight from the state at the previous moment to the current state, and $\overleftarrow{b}_h$ represents the threshold value. Each of $W_{x\overrightarrow{h}}$, $W_{\overrightarrow{h}\overrightarrow{h}}$ and $\overrightarrow{b_h}$ has a similar meaning to the above specific representation. Additionally, b_y denotes the offset value, $W_{\overrightarrow{h}y}$ denotes the weight from $\overrightarrow{h}_t$ to the output, and $W_{\overleftarrow{h}y}$ denotes the weight from $\overleftarrow{h}_t$ to the output.

3.2. ResNet

Usually, neural network demonstrate a powerful learning ability to various features. However, the deeper networks trend to appear overfitting or underfitting and lead to low accuracy. Although we can take a regularization approach to handle it, network degradation phenomenon is along. In 2015, He et al. proposed a deep residual network through making innovative works to the traditional convolutional neural network that appended the shortcut connection [27], which greatly eliminates the thorny problem of too deep network for training. Assuming $f(x)$ is a nonlinear unit, and $h(x)$ is an objective function. When the dimensions of $f(x)$ and input vetor x are consistent, the raw mapping $h(x)$ can be directly represented as $f(x) = h(x) - x$. Otherwise, we need to expand through the autoencoder matrix $\overline{v}$ and then convert to shortcut connection form [28,29], which is represented mathematically as follows:

$$h(x) = f(x) + \overline{v}x \tag{12}$$

where $\overline{v}$ is required to satisfy the following condition:

$$\overline{v}, z = \underset{\overline{v}\in R^{m\times n}, z\in R^{n\times m}}{\arg\min} \|x - z(v(x))\|_2^2 \tag{13}$$

In this work, we employ a special residual connection, as is depicted in Fig.4(a). It can be expressed as:

$$H_i = F_i(G_{i-1}) \otimes ReLU(T(G_{i-1})) \otimes x \tag{14}$$

where $T(r)$ denotes the output of 1D CNN input for r, F_i is a mapping of hideeen layer i. Concretely, the range of filters for 1D CNN is [16,32], the kernel size of 1D CNN is 2, the stride is 1. For the concatenation compution, it means if $\eta^{(1)} = (\eta_1, .., \eta_s)$, $\eta^{(2)} = (\theta_1, ..., \theta_t)$, then $\eta^{(1)} \otimes \eta^{(2)} = (\eta_1, .., \eta_s, \theta_1, ..., \theta_t)$. Particularly, the rectified linear unit (ReLU) is defined:

$$ReLU(t) = \begin{cases} t \ if & t \geq 0, \\ 0 \ if & t < 0. \end{cases} \tag{15}$$

3.3. BiLSTM-ResNet model

In contrast, the hybrid networks have greater generalization ability than single networks. Regarding time-series prediction, the LSTM is one of the most widely used models. In this work, we construct the BiLSTM-ResNet network, considering BiLSTM as a benchmark framework. As shown in Fig.4(b), behind the second hidden layer, the low and high dimensional features are fused to prevent the degradation of the model.

The historical price series is as input, and the data transmitting for each hidden layer is as follows. After a mapping F, feature information is passed to the first hidden layer. There is a residual connection behind the first hidden layer to prevent the disappearance of the gradient during the back-propagation, and its output is

$$H_1 = F_1(\bar{v}_1 x + B_1) \tag{16}$$

where B_1, $\bar{v}_1$ denote bias and weight factors, severally.

The network continues to learn, and the next one is mathematically expressed as

$$H_2 = F_2(\bar{v}_2 H_1 + B_2) \tag{17}$$

$$H_3 = F_3(\bar{v}_3 H_2 \otimes ReLU(T(H_1)) \otimes (v_3 x) + B_3) \tag{18}$$

where the low and high dimensional features are fused to prevent the degradation of the model, the concatenation is same as the second hidden layer.

Particularly, in the every hidden layer, the Kaiming-uniform is used to initialize the weights and thresholds. At the same time, we employ the L_2 regularization which adds an item to the objective function to reduce the feature weight, producing a smooth effect [30]. Concretely, the mathematical expression is as follows:

$$G(\bar{v}) = \frac{1}{L} \sum_{l=1}^{L} (\bar{v}^T x_j - y_j)^2 + c\|\bar{v}\|_2^2 \tag{19}$$

where $G(\bar{v})$ is the objective function, c is a smaller attenuation factor, L is the number of layers.

Lastly, the scaled exponential linear unit (SeLU) is choosen to be output activation function of the dense layer [26]. The formula is expressed as in Eq. (20). The predicted value is calculated as shown in Eq. (21).

$$SeLU(t) = \begin{cases} \kappa t & if \quad t > 0, \\ \kappa\mu(e^t - 1) & if \quad t \leq 0. \end{cases} \tag{20}$$

$$y_p = SeLU(\bar{v}_4 H_3 + B_4) \tag{21}$$

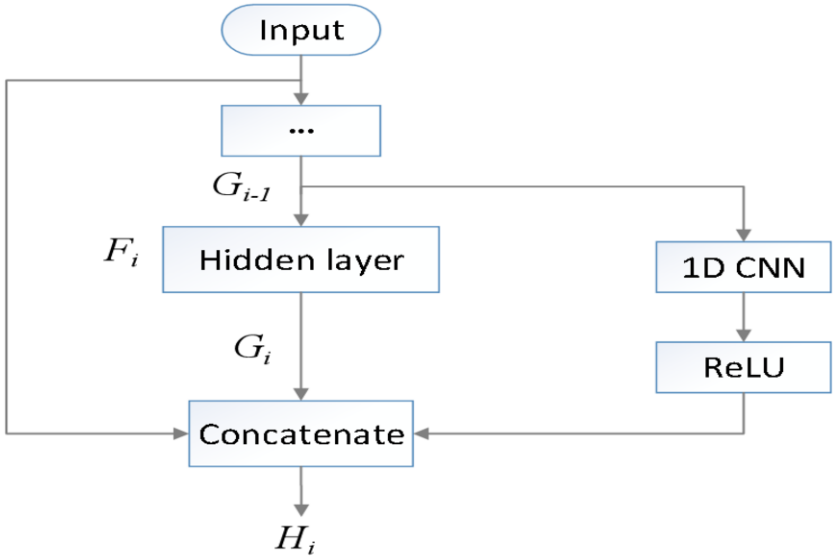

(a) The structure of ResNet network

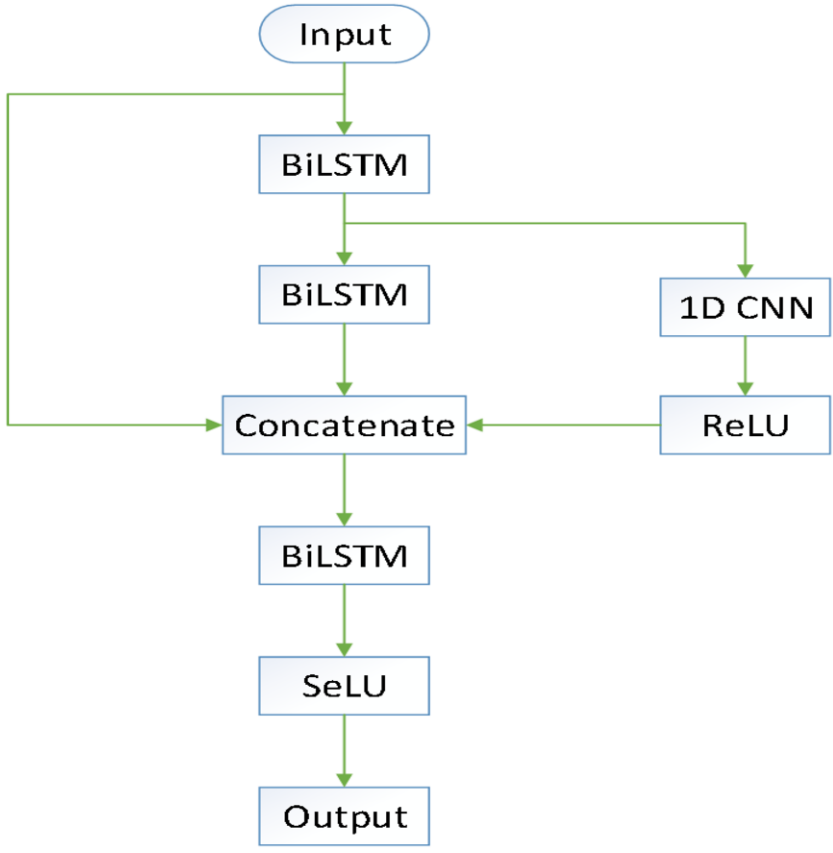

(b) The overall structure of BiLSTM-ResNet model

Fig. 4. The general framework of the hybrid model.

4. Experiment and analysis

4.1. Problem description

In the financial market, the time series cannot be considered as absolutely continuous due to a certain time interval in the trading range [31,32]. If a discrete stock index price sequence is recorded as: $y_1, y_2, \ldots, y_n$, the nonlinear fluctuation process f can be simulated by building a appropriate prediction model in the light of the observed historical data and selecting the optimal parameters. The final goal of predicting the y_t is reached, as shown in formula (22).

$$y_t = f(y_{t-d}, y_{t-d-1}, \ldots, y_{t-d-m+1}) + p(t) \tag{22}$$

where, d, m and $p(t)$ is the delay duration, the time span to be considered and the noise in the observed data at time t, severally.

In this study, we select three price datasets of nonferrous metals(including aluminum, copper and zinc) on Shanghai Futures Exchange (SHFE) to validate the stability of the established model. The data are obtained from the website https://al.iyunhui.com/market/analysis/, as shown Fig.5. For a more ideal fitting effect, all data are normalized. The data set is divided according to ratio 9:1, and transaction data for the first 21 days corresponds to a price on the next day. We carry out all the experiments via employing TensorFlow 2.1.0 under the running environment of Windows 10.

4.2. Evaluation indicators of the forecast results

The common Root Mean Square Error (RMSE), Mean Absolute Error (MAE) and Mean Absolute Percentage Error (MAPE) are employed to estimate the effectiveness of proposed model [13]. They are calculated by the following formula:

$$RMSE = \sqrt{\frac{1}{N_{test}} \sum_{n=1}^{N_{test}} (\widehat{y}_n - y_n)^2} \tag{23}$$

$$MAE = \frac{1}{N_{test}} \sum_{n=1}^{N_{test}} |\widehat{y}_n - y_n| \tag{24}$$

$$MAPE = \frac{1}{N_{test}} \sum_{n=1}^{N_{test}} \left|\frac{\widehat{y}_n - y_n}{\widehat{y}_n}\right| \times 100\% \tag{25}$$

Where y_n, $\widehat{y}_n$ are the raw data and the predicted value, respectively; N_{tset} indicates the size of the test set.

4.3. The determination of parameters

In the experiment, we make the initialization of weights and bias through Kaiming uniform distribution. In addition, the batch size is firstly determined to be 16, the initial

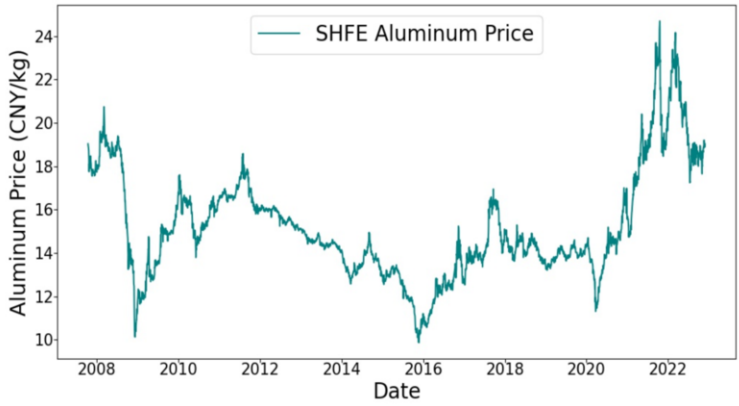

(a) The change of aluminum price

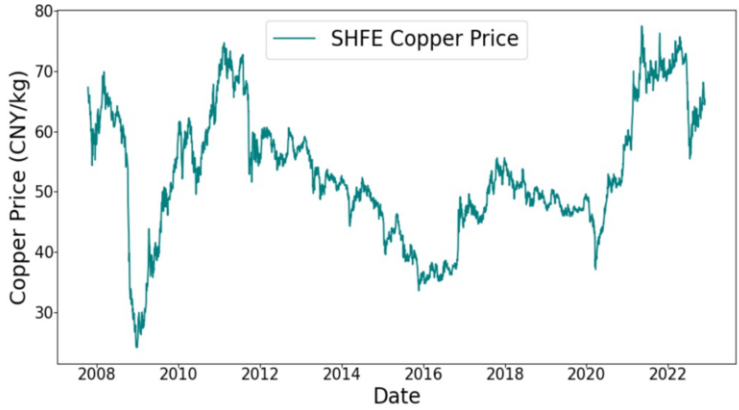

(b) The change of copper price

(c) The change of zinc price

Fig. 5. The nonferrous metals price on SHFE from 16th October 2007 to 25th November 2022.

epochs is 100, the initial attenuation factor of L_2 regularization is 0.01. While the range of hyperparameters is given in Table 1.

Reference to the relevant literature, the number of hidden neurons for the BiLSTM in hybrid model is assumed to be N_1-N_2-N_3. In the beginning, N_1=N_2=N_3=32 and the learning rate is 1×10^{-3}. The iterative search trial is performed based on the GWO algorithm. Take aluminum price as example, we can see that the mentioned model achieves the convergence point after 4 iterations in Fig.6. Furthermore, it is very friendly to judge that the gray wolf optimization model works well. In the end, the optimal parameter combination is $N_1 = 16$, $N_2 = 22$, $N_3 = 19$, learning rate $= 2.74 \times 10^{-3}$, decay rate $= 6.07 \times 10^{-3}$, shown in Table 2.

Table 1. The range of hyperparameters in GWO algorithm

Specific parameter	Range
neurons in each hidden layer	16-32
L_2 regularization	0.01-0.1
learning rate	0.001-0.01
Nadam decay	0.0001-0.01

Table 2. Related parameters of the proposed model

Parameters	Value
neurons in the hidden layer	16-22-19
Nadam learning rate	2.74×10^{-3}
Nadam decay rate	6.07×10^{-3}
L_2 regularization factor	0.01
wavelet base	db2
epochs	100
time-step	21
batch-size	16

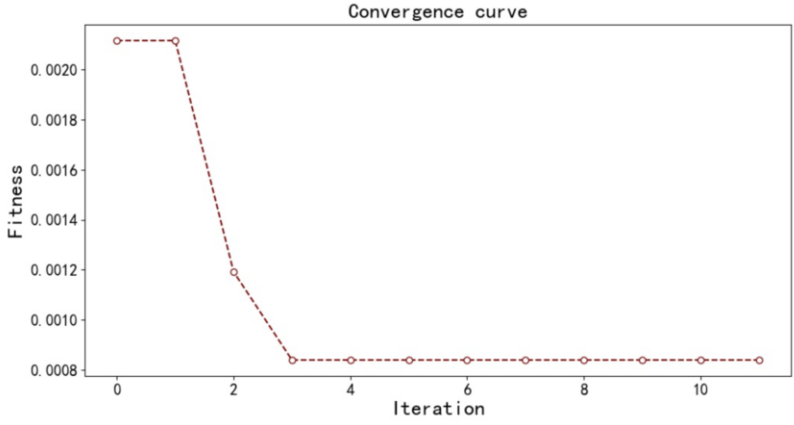

Fig. 6. Convergence diagram of gray wolf optimization model.

4.4. Data preprocessing

Take aluminum price as example, we use the wavelet transform to remove outliers in the original data, as shown in Fig.7. The original sequence is decomposed into three parts: one trend component and two detail components. Obviously, the denoising data curve is exceedingly smooth better than the original data curve. Here, the detail parts are still high frequency signal containing the details or differences of the signal.

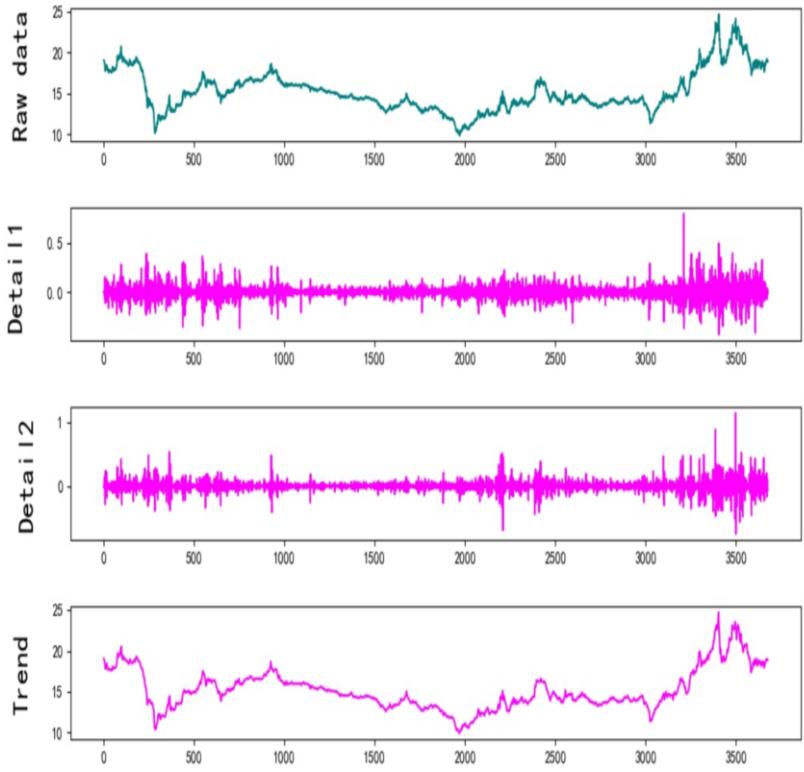

Fig. 7. The wavelet transform result of aluminum price.

4.5. Empirical results and analysis

To demonstrate the validity of the proposed model, we performed a series of experiments, with the forecast schemes as follows: LSTM, BiLSTM, BiLSTM-ResNet, BiLSTM-ResNet-DWT and BiLSTM-ResNet-GWO-DWT.

The Fig.8 illustrate the comparison graph and bar graph of error, which visually show the forecast accuracy. In the case of aluminum price, the single model BiLSTM

performs better than LSTM. However, the hybrid model BiLSTM-ResNet outperforms all single models in RMSE, MAE and MAPE. While the wavelet transform is used to decompose the complex nonlinear price sequence into multiple subsequences, it presents more obvious trend and fluctuation characteristic. Further, if the hyperparameters are optimized, the prediction accuracy is improved again.

Quantitative analyses are performed, and the RMSE, MAE, and MAPE for each method on the three datasets are shown in Table 3-5. Take aluminum as an example, the RMSE, MAE and MAPE of BiLSTM-ResNet are 0.3458, 0.2469 and 1.2133%, which is significantly better than BiLSTM and LSTM. This means that BiLSTM-ResNet improves the generalization ability by constructing the residual blocks. The RMSE, MAE and MAPE of BiLSTM-ResNet-DWT are 0.3320, 0.2404 and 1.1681%, respectively. Additionally, the RMSE, MAE and MAPE of BiLSTM-ResNet-GWO-DWT are 0.2672, 0.1935 and 0.9434%, concretely. This is ascribed to the fact that GWO algorithm has optimized the model by searching the optimal parameters for the neural network. Being compared with four other methods, a series of experiments results fully demonstrate the effectiveness of the BiLSTM-ResNet-GWO-DWT method.

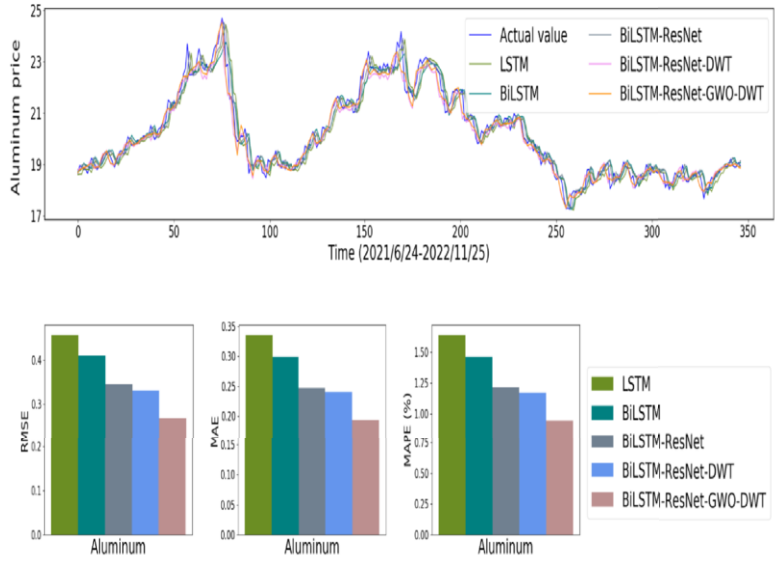

Fig. 8. The prediction result of aluminum price.

Table 3. The metrics of aluminum price prediction with various model.

Models	epochs=100		
	RMSE	MAE	MAPE
LSTM	0.4574	0.3354	1.6413%
BiLSTM	0.4105	0.2989	1.4653%
BiLSTM-ResNet	0.3458	0.2469	1.2133%
BiLSTM-ResNet-DWT	0.3320	0.2404	1.1681%
BiLSTM-ResNet-GWO-DWT	0.2672	0.1935	0.9434%

Table 4. The metrics of copper price prediction with various model.

Models	epochs=100		
	RMSE	MAE	MAPE
LSTM	1.2919	0.9881	1.4632%
BiLSTM	0.9363	0.7246	1.0793%
BiLSTM-ResNet	0.8461	0.6452	0.9598%
BiLSTM-ResNet-DWT	0.6347	0.4670	0.6950%
BiLSTM-ResNet-GWO-DWT	0.5780	0.4209	0.6254%

Table 5. The metrics of zinc price prediction with various model.

Models	epochs=100		
	RMSE	MAE	MAPE
LSTM	0.5326	0.3796	1.5428%
BiLSTM	0.5061	0.3690	1.4972%
BiLSTM-ResNet	0.4399	0.3050	1.2414%
BiLSTM-ResNet-DWT	0.4073	0.2809	1.1392%
BiLSTM-ResNet-GWO-DWT	0.3092	0.2171	0.8839%

5. Conclusion

For the industry, the price forecast of nonferrous metals is a meaningful work. In this work, a deep learning framework based on BiLSTM-ResNet-GWO-DWT is proposed. The qualitative and quantitative analysis results demonstrate that BiLSTM-ResNet-GWO-DWT model is better than other benchmark models. Moreover, because the proposed method takes the irregularities of price sequence into account, it further illustrates the validity of the model.

6. Future works

These prediction methods perform well in nonferrous metals price forecast, but at the same time, we also need to consider some shortcomings of this hyperparameter search

and data preprocessing. Firstly, applying GWO algorithm can reduce falling into the local optimum, while it also faces the trouble of high computational cost. It is believed that with the continuous advancement of research, there will be more new optimization algorithms in the future, and this problem will be improved. Secondly, in spite of the wavelet transform can remove the noise interference from the original data, it pays the cost of losing part of the real information. Hence, we will focus on the preprocessing of original data to fully mine the essential feature and enhance the prediction performance as for the future work.

Acknowledgements

This work was supported by Guizhou Provincial Science and Technology Projects(No. QKHJC-ZK[2023]YB036), Guizhou Provincial Science and Technology Projects (No. QKHJC-ZK[2021]YB017), Guizhou Provincial Education Department Higher Education Institution Youth Science Research Projects (QJJ[2022]098).

Declaration of interest statement

No conflict of interest.

Availability of data

Data available if required.

References

[1] Diego Garcła, Werner Kristjanpoller. An adaptive forecasting approach for copper price volatility through hybrid and non-hybrid models. Applied Soft Computing. 2019, 74:466-478.
[2] Alquist, Ron, Saroj Bhattarai, Olivier Coibion. Commodity-price comovement and global economic activity. Journal of Monetary Economics. 2020, 112:41-56.
[3] Cohen Gil. Algorithmic Strategies for Precious Metals Price Forecasting. Mathematics. 2022, 10(7):1134.
[4] Kriechbaumer, Thomas, et al. An improved wavelet–ARIMA approach for forecasting metal prices. Resources Policy. 2014, 39:32-41.
[5] Lasheras, Fernando Sánchez, et al. Forecasting the COMEX copper spot price by means of neural networks and ARIMA models. Resources Policy. 2015, 45:37-43.
[6] Yaziz Siti Roslindar,Zakaria Roslinazairimah,Suhartono. ARIMA and Symmetric GARCH-type Models in Forecasting Malaysia Gold Price. Journal of Physics: Conference Series. 2019, 1366(1):012126.
[7] Yang Y, Hou M, Luo J, et al. Numerical solution of several kinds of differential equations using block neural network method with improved extreme learning machine algorithm. Journal of Intelligent and Fuzzy Systems. 2020, 38(3):3445-3461.
[8] Carrasco, R., Astudillo, G., Soto, I., Chacon, M., Fuentealba, D.,Forecast of copper price series using vector support machines. In: 2018 7th Int. Conf. Ind. Technol. Manag. 2018, 380-384.
[9] Shaukat K, Luo S, Abbas N, et al. An analysis of blessed Friday sale at a retail store using classification models. The 4th International Conference on Software Engineering and Information Management. 2021, 193-198.

[10] Kumar Chandar Sivalingam,Sumathi Mahendran, Sivanandam Natarajan. Forecasting Gold Prices Based on Extreme Learning Machine. International Journal of Computers Communications and Control. 2016, 11(3).
[11] Shao Bilin, Li Maolin, Zhao Yu, Bian Genqing. Nickel Price Forecast Based on the LSTM Neural Network Optimized by the Improved PSO Algorithm. Mathematical Problems in Engineering, 2019.
[12] Hou Muzhou, Liu Taohua, Yang Yunlei, et al. A new hybrid constructive neural network method for impacting and its application on tungsten price prediction. Applied Intelligence. 2017, 47(1).
[13] Zhanglong Li, Yunlei Yang, Yinghao Chen, et al. A Novel Non-Ferrous Metals Price Forecast Model Based on LSTM and Multivariate Mode Decomposition. Axioms, 2023, 12(7):670.
[14] Chengshi Tian, Yan Hao. Point and interval forecasting for carbon price based on an improved analysis-forecast system. Applied Mathematical Modelling. (2019).
[15] Batool D, Shahbaz M, Shahzad Asif H, et al. A Hybrid Approach to Tea Crop Yield Prediction Using Simulation Models and Machine Learning. Plants. 2022, 11(15):1925.
[16] Gligoric Z, Gligoric M, Halilovic D, et al. Hybrid stochastic-grey model to forecast the behavior of metal price in the mining industry. Sustainability. 2020, 12(16):6533.
[17] Yan Hu,Jian Ni,Liu Wen. A hybrid deep learning approach by integrating LSTM-ANN networks with GARCH model for copper price volatility prediction. Physica A: Statistical Mechanics and its Applications. 2020, 557.
[18] Liu Kailei,Cheng Jinhua,Yi Jiahui. Copper price forecasted by hybrid neural network with Bayesian Optimization and wavelet transform. Resources Policy. 2022, 75.
[19] Zhang Chu,Hua Lei,Ji Chunlei,Shahzad Nazir Muhammad,Peng Tian. An evolutionary robust solar radiation prediction model based on WT-CEEMDAN and IASO-optimized outlier robust extreme learning machine. Applied Energy, 2022, 322.
[20] Zhongyu Li , Hongxia Ge , Rongjun Cheng. Traffic flow prediction based on BILSTM model and data denoising scheme. Chinese Physics B. 2022, 31:040502.
[21] Seyedali Mirjalili, Seyed Mohammad Mirjalili, Andrew Lewis. Grey Wolf Optimizer. Advances in Engineering Software, 2014, 69.
[22] Jinxin Pan, Bo Jing, Xiaoxuan Jiao, Shenglong Wang. Analysis and Application of Grey Wolf Optimizer-Long Short-Term Memory. IEEE Access. 2020, 8.
[23] Sepp Hochreiter, Jürgen Schmidhuber. Long short-term memory. Neural computation. 1997, 9(8):1735-1780.
[24] Wei, Wangyang, Honghai Wu, Huadong Ma. An autoencoder and LSTM-based traffic flow prediction method. Sensors. 2019, 19(13):2946.
[25] Yi Peng et al. Meteorological Satellite Operation Prediction Using a BiLSTM Deep Learning Model. Security and Communication Networks. 2021, 1-9.
[26] Min-seung Ko, Kwangsuk Lee, Chang Woo Hong, et al. Deep Concatenated Residual Network with Bidirectional LSTM for One-Hour-Ahead Wind Power Forecasting. IEEE Transactions on Sustainable Energy. 2020, 12(2):1321-1335.
[27] He Kaiming, Sun Jian, et al. Deep Residual Learning for Image Recognition. In: 2016 IEEE Conference on Computer Vision and Pattern Recognition (CVPR). 2016, 770-778.
[28] Chen Yinghao, Wang Dongdong, Hou Muzhou, et al. Prediction of safety parameters of pressurized water reactor based on feature fusion neural network. Annals of Nuclear Energy. 2022, 166:108803.
[29] Krizhevsky, Alex, Ilya Sutskever, Geoffrey E., Hinton. Imagenet classification with deep convolutional neural networks. Communications of the ACM. 2017, 60(6):84-90.
[30] Xue Yan, Wang Weihan, Miao Chang. Research on financial assets transaction prediction model based on LSTM neural network. Neural Computing and Applications. 2020, 33(1):257-270.
[31] Liu, Huilan, Junjie Ma, Changgen Peng. Shrinkage estimation for identification of linear components in composite quantile additive models. Communications in Statistics-Simulation and Computation. 2020, 49(10):2678-2692.
[32] Pengfei Yu, Xuesong Yan. Stock price prediction based on deep neural networks. Neural Computing and Applications. 2020, 32(6):1609-1628.

Fuzzy Systems and Data Mining IX
A.J. Tallón-Ballesteros and R. Beltrán-Barba (Eds.)

doi:10.3233/FAIA231019

Scalable Interactive Keyword Query Interface over Knowledge Graph

Xin Hu, Jiangli Duan*, Sulan Zhang
Yangtze Normal University, Chongqing, China

Abstract. Abstract goes here. Existing keyword query systems over knowledge graph can produce interesting results and are easy to use. However, they cannot handle the ambiguities that have matches in the knowledge graph, namely, multiple interpretations may be correct so that they cannot determine which interpretation is what the user expects. And they cannot scale to handle the knowledge graphs with more than billions of triples or thousands of types/predicates. On the one hand, we construct an interactive interface in which the above ambiguities will resort to the user. To enhance the user experience, we formalize the interaction problem and then propose an algorithm to find a best scheme of interaction (i.e., a verifying sequence with lowest interaction times and candidates) based on the dependency relations between mappings. On the other hand, we propose a new schema graph, i.e., type-predicate graph, which has good scalability while containing complete information for building query graph. No matter how large the knowledge graph is, the size of type-predicate graph is always very small because its size depends on the number of types and predicates whose number are far less than that of triples in knowledge graph. Finally, we have demonstrated our contributions with several well-directed experiments over real datasets (DBpedia and Yago).

Keywords. Artificial intelligence; knowledge graph; keyword query; interactive interface; type-predicate graph

1. Introduction

Keyword query is a useful tool for exploring large knowledge graphs, as it is user-friendly. Without requiring users to master the domain knowledge of the data schema and syntax of SPARQL, the keyword query technique can easily return satisfactory query results by only specifying a few enquiry keywords, e.g., "China capital". Existing keyword query systems over knowledge graph can produce interesting results, but they suffer from limitations as follows.

Existing keyword query systems [1-12] enable users to query information in knowledge graph by returning the subgraph containing the keywords, but they may return unwanted answers because there are too many possible interpretations. For query "Feng_xiaogang films", it is not easy to answer this query since there are too many paths between the entity "Feng_xiaogang" and the instances of the type "Film" (e.g., the paths "-direct/starringIn-,""-direct-," "-starringIn-," "-award-," "-FilmDirector," "-spouse-x-starringIn-" as shown in Figure 6). Existing techniques can filter out some false and valueless interpretations, but for valuable interpretations matching knowledge graph,

* Corresponding author. Jiangli Duan, Yangtze Normal University, Chongqing, China; E-mail addresses: duanjl@yznu.edu.cn

they could do no more. For instance, the entity recognition technique can recognize the entity "Feng_xiaogang", the phrase mapping technique can map "films" to the type "Film", and the backward search technique can filter out the interpretation "Feng_xiaogang-FilmDirector" and "Feng_xiaogang-spouse-x-starringIn-film" by score and so on. However, the 4 interpretations in Figure 1 cannot be filtered out by existing techniques because each interpretation has at least one matching subgraph in the knowledge graph, that is, any one may be users' expectation.

Keyword Query: *Feng_xiaogang films*
Interpretation 1:
All films that are directed and acted by Feng_xiaogang.
Interpretation 2:
All films that are directed by Feng_xiaogang.
Interpretation 3:
All films that are acted by Feng_xiaogang.
Interpretation 4:
All filmaward which Feng_xiaogang was awarded.

Figure 1. Possible interpretations

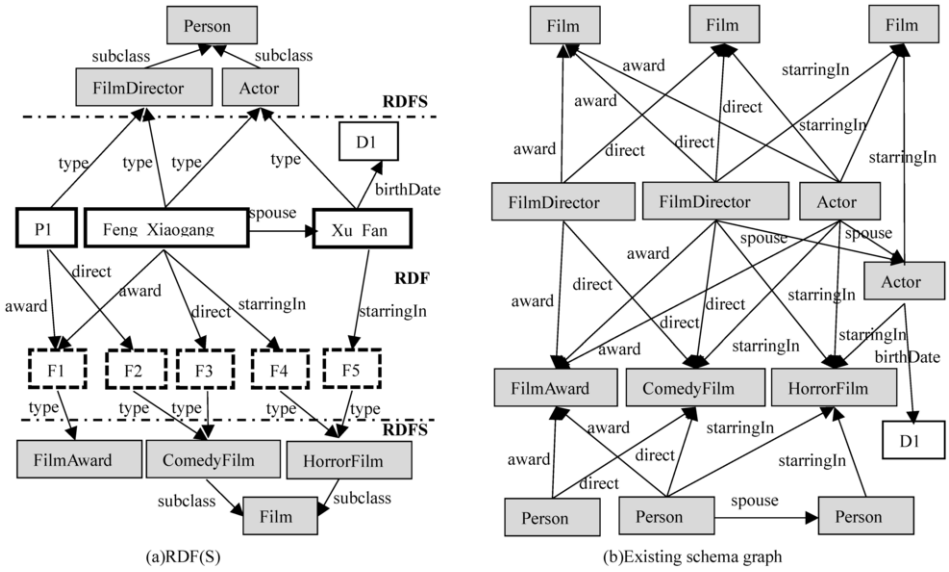

Figure 2. RDF(S) and existing schema graph

Existing keyword query systems cannot scale to handle the knowledge graphs with more than billions of triples or thousands of types/predicates. They can be divided into two categories: **1)** ***data index*****.** The prevalent approaches [1-8] building on dedicated indexing techniques aim at finding substructures that connect the data elements which match the keywords. With the explosive growth of knowledge graph, it is obvious that the dedicated data index will be faced with bottleneck, especially knowledge graph with billions of triples. **2)** ***schema graph*****.** Some systems [9-12] build schema graph to capture the "schema" information in knowledge graph and then automatically generate query graphs (which is used to produce SPARQL statements) by schema graph. However, these systems capture all relations without standardizing them, so that each type/predicate will appear many times in schema graph as **Figure 2**(b), which will lead to that the volume of

schema graph will increase exponentially. Moreover, the schema-free nature of RDFS enables knowledge graph has great power of expression, while it also makes RDFS more complex, as shown in **Figure 2**(a): 1) The types have multiple levels in RDFS; 2) One entity may have multiple types; 3) The RDFS contains a large amount of data.

In our daily communication, if we are not sure of the meaning of a question, we will make the question clear by asking some related questions back to the asker. Inspired by the daily communication habits [13,14], we propose an interactive keyword query interface, which filters out the query graphs (i.e., query interpretations) that has matches in knowledge graph but don't correspond to expectation of the user. Different from existing interactive query methods [15-17] that has a bad user experience because they build query almost entirely depended on user, in our framework, most of the process of building query is resorted to computer, and the ambiguousness that existing techniques cannot filter out are resorted to user, which can improve user experience. Moreover, we propose a scalable schema graph (i.e., a type-predicate graph) to support the process of producing query graph, where query graph is the bridge between keyword query and SPARQL statement. We make the following contributions in this paper:

1) In the offline phase, we propose a scalable schema graph (i.e., a type-predicate graph) over knowledge graph, which contains complete information for building query graph and has good scalability because its size depends on the types and predicates.

2) To handle the ambiguities that have matches in knowledge graph, we construct an interactive interface, in which part of the process of building query be resorted to computer, and the ambiguities that existing method cannot handle will resort to the user by presenting user with the ambiguous candidates and letting user make choice.

3) To enhancing the user experience during the verification of the ambiguities, we formalize the interaction problem and propose an algorithm to find a best scheme of interaction (i.e., a verifying sequence with lowest interaction times and candidates) based on dependency relations between mappings.

2. Type-Predicate Graph

As mentioned in the motivating example, existing methods concerning schema graph cannot scale to handle the knowledge graph with more than thousands of types or predicates. In contrast, we construct a type-predicate graph consisting of relationships between types and predicates, which has a smaller amount of data and contains complete information for building query graph. With the type-predicate graph, adjacent predicates and types for any type or predicate can be efficiently retrieved from small amounts of data rather than knowledge graph with billions of triples.

2.1 Extracting Relationship Subgraph

Relationship subgraph consists of types and predicates from the triples. For instance, as shown in Figure 2(a), the entity "Feng_Xiaogang" has three types, i.e., "Person," "FilmDirector" and "Actor". Except for "type", "Feng_Xiaogang" has four predicates (i.e., "spouse," "direct," "starringIn" and "award") corresponding to four entities (i.e., "F1," "F3," "F4" and "Xu_Fan"), and these entities also have their own type set, i.e., "Person,Actor," "Film,ComedyFilm," "Film, HorrorFilm" and "FilmAward". From these, we can obtain the first adjacent relationships subgraph between types and

predicates as shown in Figure 3. In the same way, for entities P1/Xu_Fan, two other relationship subgraphs in Figure 3 can be obtained.

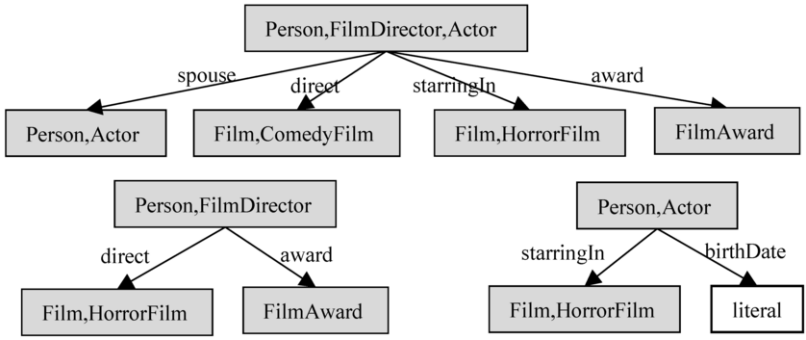

Figure 3. Extracted Relationship Subgraph

2.2 Standardization

The number of types is far less than that of triples in knowledge graph, so the amount of data in the relationship subgraphs will be small if any type only has one corresponding relationship subgraph. For the relationship subgraphs with same type, by combining all outgoing adjacent predicates and counting the number of repeat times for each outgoing edge, we can obtain one standardized relationship subgraph, e.g., Figure 4.

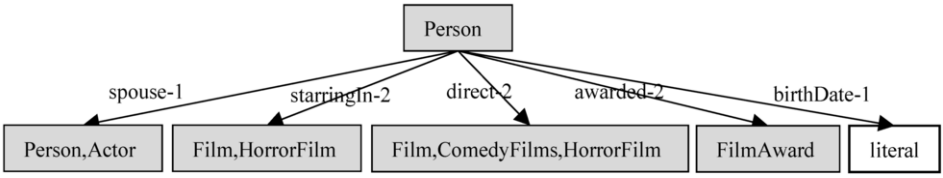

Figure 4. Standardized Relationship Subgraph

2.3 Type-Predicate Graph

All standardized relationship subgraphs form the type-predicate graph, where these subgraphs link to each other by the same types, but we do not actually connect them, as shown in Figure 5. From the type-predicate graph, for any type or predicate, all its adjacent types or predicates can be found easily.

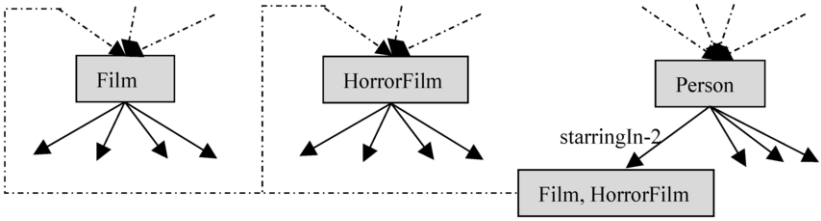

Figure 5. Type-Predicate Graph

3. Interactive Keyword Query Interface

As mentioned in motivating example, although existing methods concerning keyword query can filter out false interpretations, they cannot handle the ambiguities that have matches in knowledge graph. In contrast, we will construct an interactive interface in which the ambiguities will resort to the user by presenting the ambiguous candidates and letting user make choice. Furthermore, to enhance the user experience, we formalize the interaction problem and then propose an algorithm to find a best scheme of interaction. In this section, we first introduce the general process of keyword query in existing methods and then propose the scheme of interaction.

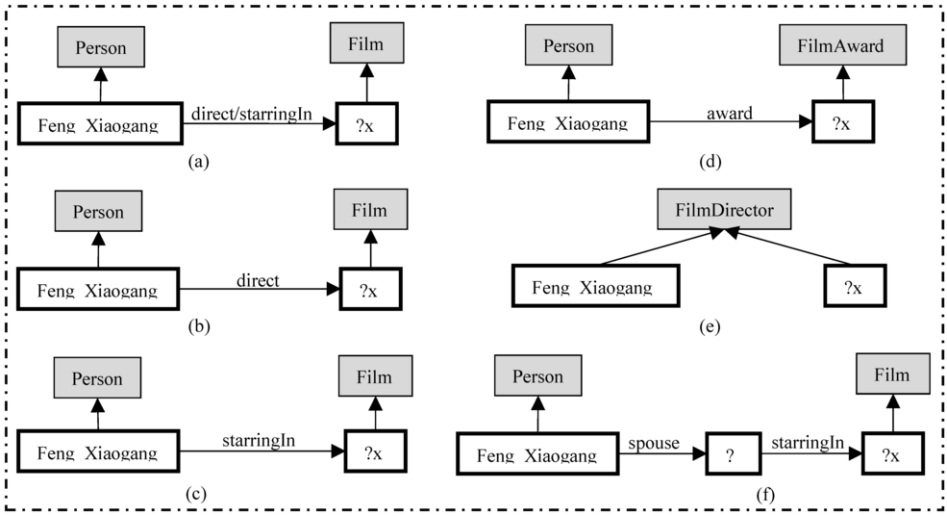

Figure 6. Query graphs for sample query

3.1 The General Process of Keyword Query

Existing methods first find all candidate mappings for each keyword in keyword query, then construct query graphs by schema graph and finally translate query graphs into SPARQL statements [18].

Example 1. For sample query "Feng_xiaogang films", firstly, existing methods obtain candidate entities (e.g., "Feng_Xiaogang" and "Feng_xiaogangX") and their corresponding types (e.g., "FilmDirector," "Actor" and "Person" for the former, and "Book" for the latter) for the keyword "Feng_xiaogang", and candidate types (e.g., "FilmDirector," "FilmAward," "ComedyFilm," "HorrorFilm" and "Film") for the keyword "films". Secondly, they combine candidate mappings of all keywords to obtain a set of query graphs by schema graph. During combination, the ambiguities without matches in knowledge graph and some query graphs with low value are deleted, e.g., Figure 6(e) and Figure 6(f). Thirdly, they translate remained query graphs, e.g., Figure 6(a)/(b)/(c)/(d), to SPARQL statements and then return answers.

3.2 Scheme of Interaction

Existing methods can delete valueless candidates, i.e., ambiguities that has no matches in knowledge graph and query graph with low value (Example 1). However, if multiple

query graphs match the subgraphs in the knowledge graph, they cannot recognize which one is user's expectation. This paper will resort to user by presenting the ambiguous candidates and letting user make choice. To enhance the user experience, we formalize the interaction problem and propose an algorithm to find a best scheme of interaction.

Definition 1. (Interaction Diagram) An interaction diagram is a tuple G=(V, E, N). 1) Each vertex $v \in V$ represents an object that needs to be verified. 2) E includes directed edges and undirected edges. Directed edge $<v_1, v_2> \in E$ means we don't need to verify v_2 if v_1 is verified to be true. Undirected edge $<v_1, v_2> \in E$ represents that v_1 and v_2 are adjacent in query graph, which will be omitted if there is a directed edge. 3) $c(v) \in N$ represents the number of candidate mappings of vertex v.

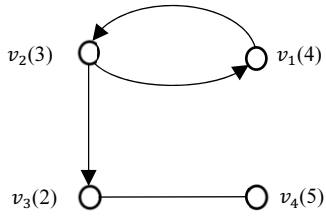

Figure 7. An interaction diagram

Example 2. Figure 7 presents an example of interaction diagram, where $v_3(2)$ represents that vertex v_3 has 2 candidate mappings (e.g., keyword "films" has two mappings "Film" and "FilmAward" in retained valuable query graphs in Figure 6, where Figure 6(e) and Figure 6(f) were deleted in Example 1).

Since each vertex $v \in V$ represents an object that needs the user to verify which candidate mapping is correct. For a set of vertices V= $\{v_1, v_2, \ldots, v_n\}$, in general, there are n! possible verifying sequences.

Definition 2. (Possible/Verifying Sequence, *ps*/*vs*). *ps* is a set of all vertices in an interaction diagram G, and these vertices have a deterministic order. All vertices that need to be verified form a verifying sequence *vs*.

Definition 3. (Calls/Candidates of a verifying sequence, *Calls*/*Cans*). Given a verifying sequence *vs*, we count the interaction times, denoted as *Calls*(*vs*), and the number of candidates of necessary interaction, denoted as *Cans*(*vs*).

Example 3. Table 1 presents all verifying sequences for the interaction diagram in Figure 7. From Figure 7, verifying v_4 doesn't affect other vertex (i.e., undirected edge (v_3, v_4)) so that we only consider the order for other three vertices $v_1/v_2/v_3$ in Table 1. For the possible sequence *ps*= $\{v_1, v_2, v_3, v_4\}$, there are two directed edges (i.e., $<v_1, v_2>$ and $<v_2, v_3>$) so that both v_2 and v_3 don't need to be verified after verifying v_1. Thus, we obtain the verifying sequence *vs*= $\{v_1, v_4\}$, and then *Calls*(*s*)=2 and *Cans*(*s*)=9 (i.e., v_1 and v_4 have 4 and 5 candidate mappings, respectively). Moreover, to find a best verifying sequence, we first find the verifying sequences that have lowest *Calls* (i.e., *Calls*(*vs*)=2), and then we select one of them with lowest *Cans* (i.e., *Cans*(*vs*)=8), so verifying sequence with lowest *Calls*/*Cans* is *vs*= $\{v_2, v_4\}$.

Table 1. A set of verifying sequences

ps	*vs*	*Calls*	*Cans*
$v_1, v_2, v_3, (v_4)$	v_1, v_4	2	9
$v_1, v_3, v_2, (v_4)$	v_1, v_4	2	9
$v_2, v_1, v_3, (v_4)$	v_2, v_4	2	8
$v_2, v_3, v_1, (v_4)$	v_2, v_4	2	8
$v_3, v_1, v_2, (v_4)$	v_3, v_1, v_4	3	11
$v_3, v_2, v_1, (v_4)$	v_3, v_2, v_4	3	12

Definition 4. (Interaction Problem). Given an interaction diagram, interaction problem is to find a verifying sequence with lowest *Calls*/*Cans*.

During solving interaction problem, several issues are worthy of considering: 1) different from topological graph, in interaction diagram or its subgraph, the loop may exist, and the vertex whose indegree is zero may not exist; 2) to obtain a verifying sequence, we should delete the vertices that doesn't need to be verified from the possible sequences; 3) it is necessary to obtain all verifying sequences with lowest *Calls*, because *Cans* needs to be contrasted when several verifying sequences has same lowest *Calls*.

Therefore, we divide the process of solving interaction problem into two stages that correspond to two sub-algorithms, i.e., Algorithm FPS and Algorithm FVS. Algorithm FPS outlines the process of finding all possible sequences from interaction diagram. Based on recursive function *FPS*(), if there is a vertex whose indegree is zero, adding it to *ps* should be a top priority. Otherwise, we select suboptimal scheme, namely, adding the vertex whose outdegree is not zero to *ps*, which lead to that we can delete one vertex at least in the process from *ps* to *vs*. Moreover, if there is no directed edge in *G*, we add all vertices to *ps* and stop the recursion of this branch.

Algorithm FPS (Finding all possible sequences)

Input: *G*: the interaction diagram
Output: *PS*: the set of all possible sequences
Values: *ps*: a possible sequence; *n*: the number of vertices in *G*; v_i: the *i*-th vertex in *G*.

```
1:  ps={};n=Get_count_vertices(G);
2:  FPS(n, G, ps);
3:    If (n>0)
4:      If (there is no directed edge in G)
5:          For (i=0; i<n; i++)
6:              ps=ps+v_i;
7:          Adding ps to PS;
8:      Else For (flag=0, i=0; i<n; i++)
9:              If (indegree of v_i is zero) FPS(n-1, G-v_i, ps+v_i); flag=1;
10:         If (flag == 0)
11:             For (i=0; i<n; i++)
12:                 If (outdegree of v_i is not zero) FPS(n-1, G-v_i, ps+v_i);
13:   Else Adding ps to PS;
```

Algorithm FVS outlines the process of finding the verifying sequences with lowest *Calls*/*Cans*: 1) obtaining the verifying sequences by deleting the vertices that doesn't need to be verified from possible sequences; 2) retaining the verifying sequences with lowest *Calls*; 3) for the verifying sequences with same lowest *Calls*, calculating their *Cans* and then retaining the verifying sequence with lowest *Cans*.

Algorithm FVS (Finding Verifying Sequence with lowest Calls)

Input: *E*: the set of directed edges
PS: the set of all possible sequences
Output: *BVS:* the set of verifying sequences with lowest *Calls/Cans*
Values: *count_min*: currently minimum; *VS*: a set of verifying sequences; *count_ps*: the number of possible sequences; *ps*: the *i*-th possible sequence in *PS*; *count_v*: the number of vertices in *ps*; v_i,v_j: a vertex in *ps*.

```
1:  count_min=∞; VS={}
2:  count_ps=Get_count_ps(PS)
3:  For (i=0; i<count_ps; i++)
4:      ps=PS[i]; count_v=Get_count_vertices(ps);
5:      For (i=count_v-1; i>0; i--)
6:          For (j=count_v-2; j>0; j--)
7:              If(directed edge <v_j, v_i>∈E) Delete v_i from ps; count_v--; Break;
8:      If(count_v<count_min) count_min=count_v; Deleting all ps in VS; Adding ps to VS;
9:      Else if (Count_v==Count_min) Adding ps to VS;
10: Calculating Cans of all ps in VS
11: Selecting the ps with lowest Cans as BVS
```

4. Experimental Evaluation

We have demonstrated our contributions with several well-directed experiments over real datasets (DBpedia and Yago). First, we propose the type-predicate graph that has good scalability and was used to build query graph, so we explain the scalability and the filtering capability of the type-predicate graph. Second, we construct an interactive interface to handle the ambiguities that have matches in the knowledge graph, so we contrast keyword query with or without interaction to demonstrate the interaction capability. Third, we propose an algorithm to find a best verifying sequence, so we show the optimization capability of the algorithm.

4.1 The Scalability of The Type-Predicate Graph

Type-predicate graph has good scalability because its size depends on the number of types and predicates. Table 2 shows the sizes of Yago (core) dataset, DBpedia (infobox) dataset and the type-predicate graph. From triples ratio, the number of triples in type-predicate graph is far less than that in Yago and DBpedia. Moreover, the number of relationship subgraphs is equal to the number of types because the relationship subgraph is dominated by the types, and the size of graph triples depends on the number of types and predicates because graph triples are the combinations of types and predicates. Since the number of types and predicates is far less than the number of triples in a knowledge graph, the size of type-predicate graph is far smaller than that of knowledge graph.

Table 2. Data size

		YAGO (core)	DBpedia (infobox)
knowledge graph	Data triples	45453166	64813068
	Types	347868	418
	Predicates	70	46510
Type-predicate graph	Relationship Subgraphs	347868	418
	Graph triples	1978891	126637
	Triples Ratio	4.35%	0.19%

4.2 The Filtering Capability of The Type-Predicate Graph

During building query graph, type-predicate graph can filter out some inappropriate candidate mappings as shown in Table 3. For instance, for the mappings of keyword "produce" in query "feng_xiaogang, produce, film", there are 182 predicates containing the string "produce" in DBpedia (infobox) dataset. Among of them, in the relationship subgraph whose main type is "Film", there are 73 predicates containing the string "produce" so that we can delete 109 (182-73) predicates. Furthermore, between type "Film" and "Person", there are only 24 predicates containing string "produce". And then, we use existing techniques (e.g., similarity scores, interaction and so on) to select candidate mappings. In conclusion, type-predicate graph has filtering capability so that we can obtain more suitable candidate predicates than existing methods.

Table 3. The filtering capability of type-predicate graph

triples whose predicate contains string "*produce*" in DBpedia	number
?*subject*, ****produce***, ?*object*	182
?*subject*(whose type is "*Film*"), ****produce***, ?*object*	73
?*subject*(whose type is "*Film*"), ****produce***, ?object(whose type is "*Person*")	24

Table 4. The sample queries

Keyword queries	Query intention
Feng Xiaogang, film	*All film whose actor (or director) is Feng xiaogang.*
Free University, Amsterdam, students	*The number of students in the Free University, Amsterdam.*
car, Germany	*All cars that are produced in Germany.*
people, born, Vienna, die, Berlin	*All people that were born in Vienna and died in Berlin.*
actor, movie, direct, starring, William Shatner	*All actors starring in movies directed by and starring William Shatner.*

4.3 The Interaction Capability

With interaction, users can fully express their expectations. Existing keyword query methods (i.e., keyword query method without interaction) always return top-k results for one keyword query, and if the top-k set contains the correct one, it is considered to be able to answer this keyword query. In contrast, during the process from query to result, our method enable user to select query graph that satisfies their expectations by interaction, so the correct one can be always selected. As shown in Figure 8, we show the rank number of correct query graph in top-k set by existing methods (i.e., without interaction) and our method (i.e., with interaction), where the keyword queries come from Table 4.

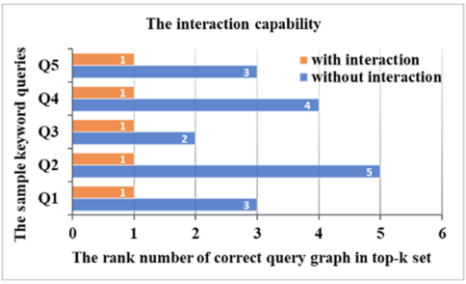

Figure 8. The interaction capability

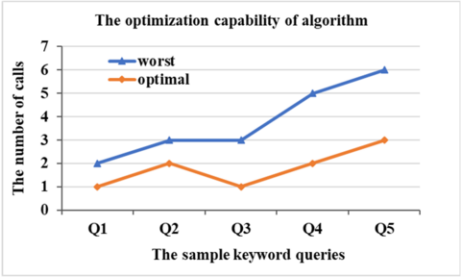

Figure 9. The optimization capability of algorithm

4.4 The Optimization Capability of Algorithm

To enhance the user experience, we formalize the interaction problem and then propose an algorithm to find a verifying sequence with lowest *Calls*/*Cans*. For an interaction diagram, there are multiple possible verifying sequences. We show the number of *calls* (i.e., interaction times) in worst/optimal case as shown in Figure 9, and the algorithm always can obtain the optimal verifying sequence for the keyword queries come from Table 4. Moreover, the increasing number of keywords in queries leads to increase number of possible candidate combinations, so interaction times (i.e., *calls*) will increase, but it is not absolute (e.g., $Q2$ and $Q4$ have 3 and 5 keywords, respectively. However, they have same number of *calls*.).

5. Conclusions

Although existing keyword query systems over knowledge graph can produce interesting results and are easy to use, they cannot handle the ambiguities that have matches in knowledge graph and cannot scale to handle the knowledge graph with more than billions of triples or thousands of types/predicates. So, we propose an interactive keyword query

interface with type-predicate graph, which handle above ambiguities by a best scheme of interaction, and type-predicate graph enables keyword query can scale to handle various huge knowledge graphs. At last, we have demonstrated our contributions with several well-directed experiments over real datasets (DBpedia and Yago).

Acknowledgments

This work is supported by the National Natural Science Foundation of China (No. 62106024, No. 62006029), the China Postdoctoral Science Foundation (No. 2022M711458), the Natural Science Foundation of Chongqing (No. CSTB2022NSCQ-BHX0018), the Chongqing Language Research Project (No. yyk22105), and the youth project of Chongqing Education Commission of China (No. KJQN202201410, No. KJQN202201413, KJQN202001434).

References

[1] Cheng G, Li S, Zhang K, Li C. Generating compact and relaxable answers to keyword queries over knowledge graphs. Proceedings of the 19th International Semantic Web Conference; 2020. p.110-127.
[2] Hu X, Duan J, Dang D. Natural language question answering over knowledge graph: The marriage of SPARQL query and keyword search. Knowledge and Information Systems. 2021; 63(4): 819-844.
[3] Nikas C, Fafalios P, Tzitzikas Y. Open domain question answering over knowledge graphs using keyword search, answer type prediction, sparql and pre-trained neural models. Proceedings of the International Semantic Web Conference; 2021. p.235-251.
[4] Shan Y, Li M, Chen Y, Constructing target-aware results for keyword search on knowledge graphs. Data & Knowledge Engineering. 2017; 110:1-23.
[5] Shi Y, Cheng G, Kharlamov E. Keyword search over knowledge graphs via static and dynamic hub labelings. Proceedings of the International World Wide Web Conference; 2020. p.235-245.
[6] Shi Y, Cheng G, Tran TK, Tang J, Kharlamov E. Keyword-based knowledge graph exploration based on quadratic group steiner trees. Proceedings of the Thirtieth International Joint Conference on Artificial Intelligence; 2021. p.1555-1562.
[7] Shi Y, Cheng G, Tran TK, Tang J, Kharlamov E, Shen Y. Efficient computation of semantically cohesive subgraphs for keyword-based knowledge graph exploration. Proceedings of the International World Wide Web Conference; 2021. p.1410-1421.
[8] Yang Y, Agrawal D, Jagadish HV, Tung KH, Wu S. An efficient parallel keyword search engine on knowledge graphs. Proceedings of the 35th IEEE International Conference on Data Engineering; 2019. p.338-349.
[9] Feddoul L. Semantics-driven keyword search over knowledge graphs. Proceedings of the 19th International Semantic Web Conference; 2020. p.17-24.
[10] Lin X, Ma Z, Yan L. RDF keyword search using a type-based summary. Journal of Information Science and Engineering. 2018; 34(2):489-504.
[11] Sinha SB, Lu X, Theodoratos D. Personalized keyword search on large RDF graphs based on pattern graph similarity. Proceedings of the 22nd International Database Engineering & Applications Symposium; 2018. p.12-21.
[12] Yan W, Ding Y. RDF knowledge graph keyword type search using frequent patterns. Journal of Intelligent & Fuzzy Systems. 2021; 41(1):2239-2253.
[13] Gupta S, Pandey K, Yadav J, Sharma R. Keystroke dynamics based authentication system with unrestricted data collection. Proceedings of the 10th International Conference on Contemporary Computing; 2017. p.1-6.
[14] Yadav J, Pandey K, Gupta S, Sharma R. Keystroke dynamics based authentication using fuzzy logic. Proceedings of the 10th International Conference on Contemporary Computing; 2017. p.1-6.
[15] Ferré S. Analytical queries on vanilla RDF graphs with a guided query builder approach. Proceedings of the 14th International Conference on Flexible Query Answering Systems; 2021. p.41-53
[16] Zafar H, Dubey M, Lehmann J, Demidova E. IQA: Interactive query construction in semantic question answering systems. Journal of Web Semantics. 2020; 64:100586.
[17] Papadaki ME, Spyratos N, Tzitzikas Y. Towards interactive analytics over RDF graphs. Algorithms. 2021;14(2):1-22.
[18] Hu X, Duan J, Dang D. Scalable aggregate keyword query over knowledge graph. Future Generation Computer Systems. 2020; 107:588-600.

Fuzzy Systems and Data Mining IX
A.J. Tallón-Ballesteros and R. Beltrán-Barba (Eds.)

doi:10.3233/FAIA231020

An Efficient Matching Algorithm for Question Answering System

Jing ZHANG [a], XinYue ZHAO [a], Jianing HUANG [a], and Yunsheng SONG [a,1]
[a] *School of Information Science and Engineering, Shandong Agricultural University, Taian 271018, China*

Abstract. Wheat and corn are the two most important grain crops in northern China, and at this stage, it is difficult to obtain professional information in the field of wheat and corn, the acquisition efficiency is low, and the accuracy is poor, which seriously restricts the production efficiency. The intelligent question answering system can efficiently and accurately automatically screen out professional information, to effectively solve the above problems. However, the existing intelligent question answering system for wheat and maize has too low matching accuracy and slow retrieval speed to be widely promoted. Therefore, an efficient and accurate two-stage matching algorithm is designed, which uses the BM25 algorithm to recall the candidate set, and then uses the BERT model to screen out the optimal solution based on the candidate set. Experimental results show that the algorithm has high retrieval accuracy and retrieval efficiency.

Keywords. Question Answering System, Pre-trained models, Information Retrieval, Agriculture

1. Introduction

In the past, the acquisition of expertise in the agricultural field mainly relied on expert consultation, but with the spread of the Internet, farmers are more likely to use search engines to find the information they need from the Internet. However, the results returned by search engines are often very redundant and complex, containing a lot of inaccurate information, and users need to sift through this information themselves, which takes a lot of time and effort. And many farmers don't know enough about the Internet, making it difficult for them to use the Internet to get the knowledge they need. The emergence of an intelligent question answering system can effectively solve this problem, users only need to enter the questions they want to query through voice or text [1], intelligent question answering system can efficiently screen out the most accurate answer for users, simplifying the process of users to obtain knowledge [2]. The existing intelligent question answering system for wheat and corn has problems such as slow retrieval speed and low retrieval efficiency, and this paper constructs an efficient and accurate two-stage matching algorithm to help users solve problems in the planting process [3].

TF-IDF[4], BM25, LDA[5] and other traditional information retrieval algorithms to match text similarity, and the matching speed is fast. However, the semantic similarity of

[1]Corresponding Author: Yunsheng Song ; E-mail: songys@sdau.edu.cn

the text cannot be fully captured, and the matching accuracy rate is low. BERT[6] model can capture the semantic similarity of text, matching accuracy is high, but the matching speed of these models is very slow, can not be well applied in practical problems, so this paper designs a two-step retrieval algorithm, first with a faster traditional information retrieval method to screen out a candidate set containing the target question and answer, and then on this candidate set with slow but high accuracy deep matching method for accurate matching, to ensure the speed and accuracy of retrieval at the same time.

2. Main Content

To meet the needs of users for retrieval speed and retrieval accuracy, this paper designs a two-stage retrieval-style question answering algorithm based on BM25 algorithm and BERT model, which is described in detail in this section.

2.1. The overall architecture of the searchable question answering algorithm

Figure 1 shows the overall architecture of the search-style algorithm. The retrieval algorithm is generally divided into two stages, the first stage is recalled, using the BM25 algorithm to quickly recall several questions most similar to the user query problem from the database as a candidate set, and the second stage is rearrangement, training the BERT model to judge the semantic similarity of the two texts, scoring the questions in the candidate set, and returning the question with the highest score in the candidate set and its reply. The algorithm combines the advantages of the fast retrieval speed of BM25 algorithm and the high matching accuracy of BERT model, and can efficiently and accurately retrieve the target question and answer.

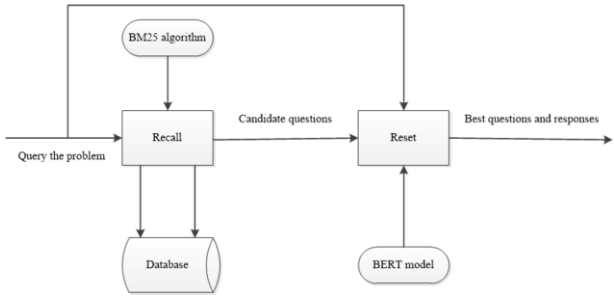

Figure 1. The overall architecture of the search-based algorithm

2.2. Recall module based on BM25 algorithm

The purpose of the recall module is to quickly screen out a candidate set that contains the target problem. The algorithm for selecting the recall module needs to consider two factors at the same time, the accuracy of retrieval and the speed of retrieval, and this paper uses the BM25 algorithm for recall .

2.2.1. Inverted indexing technique

Before using the BM25 algorithm to recall, this paper first uses the inverted index technique to improve the speed and accuracy of the recall. An inverted index is a vocabulary-document index that can quickly retrieve all documents containing that term based on a term. First, build an inverted table of all issues in the database according to the steps in algorithm 1. Break the user query question into words, and for each word in the query question, you can get a list of questions containing the word through the inverted table. Put the problem list corresponding to all the words in the user query problem into a collection, and then use this collection to recall, which can effectively improve the speed and accuracy of the recall stage.

Algorithm 1 Inverted index building process

Input: A list of all issues in the Q database.

Output: inverted table, dictionary form, the key is a word, value is a list of documents containing the word .

1: OInitialize the inverted table as a dictionary table;
2: Iterate through the list Q, taking out each issue q and its index id:
3: Use the jieba participle to turn the question q into a list of words q_L;
4: Traverse the q_L and take out each word w:

$$table[w] = table.get(w, id) + [id]$$

5: **return** Inverted table.

2.2.2. Inverted indexing technique

BM25 algorithm is a method to calculate the similarity between a query and a document, the specific steps of using the BM25 algorithm to calculate the similarity score between the query problem and the problem in the database are shown in algorithm 2, and the obtained similarity score is sorted from largest to smallest, and the top k questions with the highest score are returned, and the recall process is completed. For convenience, this article uses the BM25 module packaged in the Gensim library to complete this process.

2.3. BERT model design and implementation

At the heart of the rearrangement module is the matching model, which should accurately determine how similar two sentences are. The BERT model is the most powerful text-matching model at present, and this paper fine-tunes the trained BERT model on the constructed problem-problem similarity matching dataset, predicts whether two sentences are similar, and uses the trained model to score the recalled candidate question set to return the highest scoring questions and replies.

2.3.1. BERT matches the overall architecture of the model

In this paper, a linear layer is superimposed on the BERT model[7], which maps the BERT-encoded information to the output probability distribution, and uses the softmax function to normalize the output probability to a value between 0 and 1. The dimension

Algorithm 2 The BM25 algorithm calculates similarity

Input: Document set D consisting of all questions in the database, with each problem represented by d_i, The user queries Q.

Output: A list of scores containing the similarity scores of Q to all questions d_i.

1: Calculate the inverse document frequency idf for each word in D according to Equations , saved in the dictionary idf, $idf[w]$ represents the idf value of the word w;
2: Calculate the frequency of occurrence of each word in each question d_i, saved in list f,$f[i][w]$ indicates the number of occurrences of the word w in the ith question;
3: Calculate the average length $avgdl$ for all problems in D;
4: Use jieba to query the user for q word segmentation, each word is represented by q_i, and $TF(q_i)$ and $IDF(q_i)$ are obtained according to steps 1, 2;
5: Calculate the similarity score of Q to each question d_i according to Equations and save it to the list scores;
6: **return** Returns a list of similarity score scores.

of the output probability distribution is 2, which represents the probability of similarity and the probability of dissimilarity between two texts. The training phase uses this distribution to predict the similarity labels of the two texts, and the inference stage uses this distribution to score the similarity of the two texts and complete the rearrangement.

2.3.2. Pre-training and fine-tuning of BERT matching models

This paper uses the Bert-Chinese model officially released by Google as a pre-training model, retrains on the dataset built by itself, fine-tunes the parameters of the model, and predicts whether the two texts are similar, with a similar label of 1 and a non-similar label of 0, which can be regarded as a text binary classification problem. Each piece of data in the training set is converted into the format required by the fine-tuning task [8], fed into the BERT model, the output probability distribution is obtained, and the loss value of the predicted label and the real label is calculated using the cross-entropy function. Use the AdamW optimizer to optimize the loss value, and use the warm-up strategy to adjust the learning rate. After each training iteration is completed, the validation set is used to evaluate the model effect, and the accuracy rate is used as the evaluation index of the validation set, the accuracy is defined as the probability that the prediction result is correct, and the model with the highest accuracy is saved.

2.3.3. Rearrange the process

Use the trained BERT model to rearrange the questions in the recalled candidate set. Firstly, the user query problem is spliced with each question in the candidate set into the required input format, the text is converted into a text embedding vector according to the vocabulary, and the output probability distribution is obtained by feeding the trained BERT model, that is, the similar probability and the dissimilar probability of the two texts. The candidate questions are reordered according to the size of the similarity probability, and the candidate questions with the highest probability of similarity to the user query question and their corresponding replies are returned.

3. Experimental Result

To better illustrate the effect of each stage, this paper tests the recall stage, rearrangement stage, and the entire algorithm separately.

3.1. Experiment setup

This paper needs to use two datasets: the question-answer dataset and the question-question dataset[9], which use crawler technology to capture the data of wheat and corn on agricultural forums such as the Agricultural Science and Technology Online Book House and the China Agricultural Technology Extension Information Platform.

This paper uses the parameter settings of BERT-BASE, the constructed BERT model has a total of 12 layers, the number of heads of multi-head self-attention is also 12, the dimension of the coding vector is 768, and the parameters that the model can train have a total of 110,000. The model uses words as input units, and the size of the vocabulary is 21128. The maximum length of the model input vector is 512, and vectors smaller than this length are filled and vectors larger than this length are truncated. The rearrangement stage uses the trained BERT model to rearrange the candidate set. Using Sia-GRU, ESIM [10] models as comparison models. The hidden size of both models is set to 300, and the training data, training process, and training parameters are consistent with the settings of the BERT model.

3.2. Experimental testing during the recall phase

Use the TOP-K recall accuracy Recall@k as an evaluation metric. For each query question, the first k questions are retrieved using the above algorithm, and if the target question is included in the k, the query question is successfully recalled, Recall@k represents the ratio of the number of successfully recalled query questions to the total number of questions. Table 1shows the results of the experimental tests.

Table 1. Recall algorithm test results

	Recall@1	Recall@5	Recall@10	Recall@20
TF-IDF algorithm	88.30%	94.00%	97.50%	98.8%
LDA algorithm	68.30%	72.80%	76.50%	81.80%
BM25 algorithm	90.50%	95.50%	98.30%	99.50%

From the experimental results, the BM25 algorithm has a higher accuracy rate than the other two algorithms for the dataset constructed in this paper, so the BM25 algorithm is used to recall the set of candidate questions. At the same time, it can be seen that when the value of k is small, the recall accuracy is poor, and as the value of k increases, the recall accuracy continues to rise, but the increase of k slows down the speed of the subsequent matching stage.

The speed of recall of the BM25 algorithm is fast, and through the recall step, a candidate set containing the target problem can be quickly obtained, but the target problem cannot be accurately obtained, so the candidate problem needs to be further rearranged using the deep matching model.

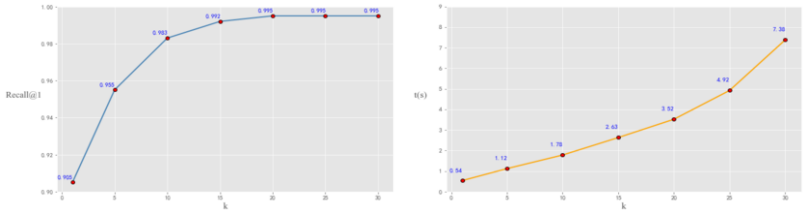

(a) The retrieval accuracy varies with k (b) The retrieval time varies with k

Figure 2. The performance of the proposed algorithm with k

3.3. Rearrange phase experimental testing

Table 2 shows the results of the text-matching experiment test, it can be seen that the performance of the BERT model in the text matching task is much better than that of the commonly used deep text-matching models such as Sia-GRU and ESIM, so this paper uses the BERT model to rearrange the candidate set problem. The matching speed of the BERT model is very slow, and it is not realistic to directly use the BERT model to match all the problems in the database, and the recall step must be performed first to narrow the matching scope.

Table 2. Rearrange model test results

	Accuracy	Recall	F1
SiamGRU	82.60%	82.40%	82.40%
ESIM	83.80%	84.20%	83.90%
BERT	89.50%	90.40%	89.90%

3.4. Overall experimental test of the algorithm

The BM25 algorithm was used to recall the first k similar problems as the candidate set, and then the BERT model was used to select the most similar problems from the candidate set. Figures 2 show the relationship between the retrieval accuracy Recall@1 and the average retrieval time t of the algorithm and the number of candidate set questions k, respectively, Recall@1 indicates that the retrieved top-1 problem is equal to the probability of the target problem. It mainly verifies the retrieval accuracy and retrieval efficiency of the entire algorithm, verifies the impact of the number of recall questions k on the retrieval time and retrieval accuracy, and selects the most suitable k.

Comparing the results of Figure 2(a) with the results of Table 1, it is found that the rearrangement module based on the BERT model can accurately retrieve the target problem from the recalled candidate set, which verifies the necessity of the rearrangement stage and the effectiveness of the entire algorithm. At the same time, it can be found that the selection of k value will affect the retrieval accuracy and retrieval efficiency of the algorithm, the k value is too small, the retrieval accuracy is low, the k value is too large, and the retrieval speed is slow. This paper prioritizes the accuracy of the algorithm, and then considers the retrieval speed of the algorithm under the premise that the accuracy

rate is as high as possible. Therefore, this paper finally sets the number of recall questions k to 20, which has high search accuracy and relatively fast retrieval speed, which is within the acceptable range of users.

4. Conclusions

In this paper, a two-stage retrieval algorithm is designed, which uses BM25 algorithm to recall candidate problem sets and uses BERT model to rearrange candidate question sets, which combines the advantages of fast matching speed and high matching accuracy of BM25 algorithm. Experimental results show that the algorithm designed in this paper can obtain high accuracy while ensuring accuracy.

In addition, based on the retrieval algorithm designed in this paper, a web-based intelligent question answering system is developed by using Flask back-end framework and front-end technology. More features can be introduced, such as the introduction of login and registration modules to save user information, and it can also introduce users with various permissions, such as experts and administrators, to improve the scalability and reliability of the system.

Acknowledgement

This research was supported by Shandong Provincial Natural Science Foundation, China, grant number ZR2020MF146, and Open Project Foundation of Intelligent Information Processing Key Laboratory of Shanxi Province, grant number CICIP2021002.

References

[1] Fehri H, Dardour S, Haddar K. ARmed question answering system. CONCURRENCY AND COMPUTATION-PRACTICE & EXPERIENCE. 2022;34(21):1-13.
[2] Shum HY, He X, Li D. From Eliza to XiaoIce: challenges and opportunities with social chatbots. Frontiers of Information Technology & Electronic Engineering. 2018;19:10-26.
[3] Aithal SG, Rao AB, Singh S. Automatic question-answer pairs generation and question similarity mechanism in question answering system. Applied Intelligence. 2021;51(11):8484-97.
[4] Qaiser S, Ali R. Text mining: use of TF-IDF to examine the relevance of words to documents. International Journal of Computer Applications. 2018;181(1):25-9.
[5] Jelodar H, Wang Y, Yuan C, Feng X, Jiang X, Li Y, et al. Latent Dirichlet allocation (LDA) and topic modeling: models, applications, a survey. Multimedia Tools and Applications. 2019;78:15169-211.
[6] Elsadig M, Ibrahim AO, Basheer S, Alohali MA, Alshunaifi S, Alqahtani H, et al. Intelligent Deep Machine Learning Cyber Phishing URL Detection Based on BERT Features Extraction. Electronics. 2022;11(22):3647.
[7] Geetha M, Renuka DK. Improving the performance of aspect based sentiment analysis using fine-tuned Bert Base Uncased model. International Journal of Intelligent Networks. 2021;2:64-9.
[8] Zhang J, Chang WC, Yu HF, Dhillon I. Fast multi-resolution transformer fine-tuning for extreme multi-label text classification. Advances in Neural Information Processing Systems. 2021;34:7267-80.
[9] Zou Y, He Y, Liu Y. Research and implementation of intelligent question answering system based on knowledge Graph of traditional Chinese medicine. In: 2020 39th Chinese Control Conference (CCC). IEEE; 2020. p. 4266-72.
[10] Rebecq H, Gehrig D, Scaramuzza D. ESIM: an open event camera simulator. In: Conference on robot learning. PMLR; 2018. p. 969-82.

Fuzzy Systems and Data Mining IX
A.J. Tallón-Ballesteros and R. Beltrán-Barba (Eds.)

doi:10.3233/FAIA231021

Scalable Semi-Supervised Support Vector Machine Based on Adaptive Sampling

XinYue ZHAO [a], Xiaoyang SUN [a], and Jing ZHANG [a] Yunsheng SONG [a,1]
[a] *School of Information Science and Engineering, Shandong Agricultural University, Taian 271018, China*

Abstract. Semi-supervised support vector machine (S3VM) algorithms can effectively deal with the problem of a few labeled instance and a large number of unlabeled instances due to its good performance. The solution of the existing semi-supervised support vector machine algorithms requires the use of many types of optimization strategies because it takes all the training data as parameters to participate in iterative optimization, which makes it difficult to efficiently process large-scale data. Although simple random sampling is an effective means to consider efficient modeling from the perspective of data preprocessing, the problem that it determines the sample size in advance is difficult to process for the existence of sampling randomness and sample difference. To fully characterize the original unlabeled data and ensure the robustness of the model, we have proposed an adaptive sampling to train the model on the labeled set and the sampled unlabeled set. The fixed size unlabeled instances are continually sampled from the original unlabeled set until the proposed statistics on the obtained sample meet the stopping condition, where the statistics and stopping condition are generated by the density estimation. This method solves the problem of subjectively determining the sample size in advance, the robustness of the proposed algorithm has been proved with the probably approximately correct learning theory.

Keywords. Semi-supervised classification, support vector machine, sample size, random sampling, large-scale unlabeled data

1. Introduction

Semi-supervised learning is a paradigm that incorporates both labeled and unlabeled data during the learning process. Semi-supervised support vector machines (S3VMs) extend the SVM framework by incorporating both labeled and unlabeled data during the training process. The idea is that the unlabeled data can provide additional information about the underlying structure of the data, potentially improving the classifier's performance [1,2,3,4,3]. In recent years, advances in hardware and software have enabled researchers to develop scalable algorithms for large-scale semi-supervised SVMs. There exist popular algorithms for large-scale semi-supervised SVMs, including transductive SVMs (TSVMs)[5], Laplacian SVMs (LapSVMs)[6], and online SVMs (OS^{3}VMs)[7].

Transductive support vector machines (TSVMs) were introduced by Vapnik as a semi-supervised extension of SVMs. The core idea of TSVMs is to find a decision bound-

[1]Corresponding Author: Yunsheng Song ; E-mail: songys@sdau.edu.cn

ary that separates not only the labeled data but also the unlabeled data. This can be achieved by minimizing a cost function that accounts for both labeled and unlabeled data. The most popular TSVM algorithm is the S3VM by Joachims [5], which scales well to large datasets. Laplacian support vector machines (LapSVMs) were introduced by Belkin et al. [6] as another approach to semi-supervised SVMs. LapSVMs utilize a graph-based representation of the data to incorporate unlabeled data into the training process. The algorithm minimizes a cost function that includes a regularization term based on the graph Laplacian, which encourages the smoothness of the decision function over the data manifold. Facing large-scale stream data, Liu et al. [7] propose an online least squares support vector machine based on flow pattern regularization, which uses some key samples to construct regularization factors to achieve the decomposition of higher-order matrices, thereby greatly improving the solving efficiency of the algorithm.

Moreover, several optimization techniques have been proposed to improve the scalability of semi-supervised SVM algorithms. Some of the most popular techniques include the decomposition method [8], stochastic gradient descent [9], and parallelization [10]. These techniques have been shown to significantly improve the computational efficiency of semi-supervised SVMs, making them more suitable for large-scale applications. Large-scale semi-supervised SVMs have been applied in various domains, including text classification, image recognition, bioinformatics, and speech recognition. These applications have demonstrated the potential of semi-supervised SVMs to effectively handle large datasets and improve classification performance when labeled data are scarce.

The current research work simply considers the efficient approximation solution of discriminant semi-supervised classification algorithm from the perspective of optimization, but it is difficult to efficiently process massive data because it requires multiple alternating iterative optimizations and all data as parameters to participate in optimization. In addition, label-free data not only provides parametric optimization information, but also contains rich feature information, and how to use this information to consider efficient modeling from the perspective of data granulation is the key means to solve large-scale complex problems. In this paper, we have proposed a scalable learning dreamwork for semi-supervised SVM. The proposed method can efficiently deal with large-scale data with comparable classification performance.

2. Main Content

2.1. Basic Description

For the given training set T which is the union of the labeled instance set $L = \{x_1, x_2, \cdots, x_l\}$ and the unlabeled instance set $U = \{x_{l+1}, x_{l+2}, \cdots, x_{l+u}\}$, where each instance $x_i = \{x_{i1}, x_{i2}, \cdots, x_{im}\}^\top$ is expressed by a m-dimension vector, l and u are the number of labeled instances and unlabeled instances, and $i = 1, 2, \cdots, l+u$. Semi-supervised classification algorithms simultaneously use the labeled instance set L and unlabeled instance set U to train a classifier $f(x)$ with good performance.

2.2. Learning Curve

Traditional learning curve mainly is widely used for supervised classification problem, it describes the relationship between the classification performance of the learner and the training set size. Generally speaking, the classification performance of the learner gradually improves as the increasing training set at the beginning stage, and it then reaches the top and then no longer increases significantly. Tradition SVM algorithm is fit for the learning curve, while the adaptability of semi-supervised SVM for it needs to be verified. Different from supervised methods, we use the labeled set L and the sampled labeled instances from U to construct the increasing training set. Therefore, we have used a real dataset with LapSVM algorithm to study this problem.

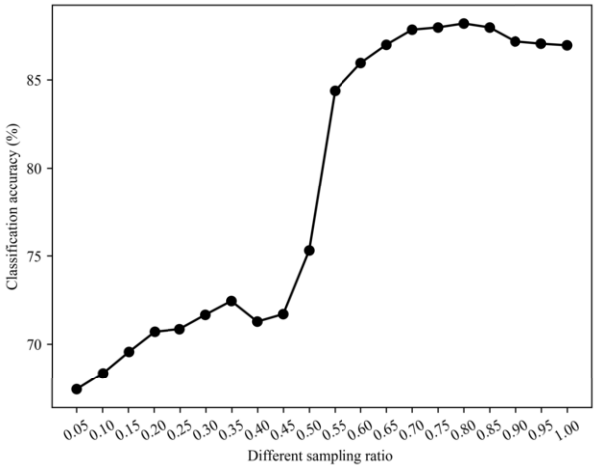

Figure 1. The learning curve under different sampling ratio

Fig. 1 shows the classification accuracy of LapSVM algorithm under the fixed labeled set and different sampled ratio of unlabeled instances on the real dataset. It can be found that classification accuracy increases until the sampled ratio is 0.7, and then it tends to stabilize. This phenomenon can be also verified for other kinds of semi-supervised SVM algorithms, because they have the same assumption that the hyperplane passes through a low-density region in the input space, where the instances close to the decision surface contribute more than instances farther from the decision boundary. This validates the feasibility of sampling several unlabeled instances with the labeled instances to obtain an SVM classifier with good performance.

Therefore, we have proposed a scalable learning framework for semi-supervised SVM to deal with large-scale unlabeled instances. In this framework, the subset S of the original unlabeled instance set U combined with the labeled set L are used to train the classifier. Owning to the fact that the execution efficiency is positively correlated to the size of the training set, then the obtained classifier with a smaller training set has high execution efficiency. On the other hand, the learning curve has confirmed that the obtained classifier can achieve a similar classification performance as the one trained on the original set as long as the sample is enough. The pseudocode of the proposed framework is listed in Algorithm 1.

Algorithm 1 Scalable learning framework under sampling for semi-supervised SVM

Input: The training set T which is the union of the labeled instance set $L = \{x_1, x_2, \cdots, x_l\}$ and the unlabeled instance set $U = \{x_{l+1}, x_{l+2}, \cdots, x_{l+u}\}$, semi-supervised SVM algorithm A.

Output: The classifier f.

1: Obtain a subset S form the set U using sampling, where S keeps the most distribution information of U;
2: Train the classifier f on the union of L and S using algorithm A ;
3: **return** f.

2.3. Adaptive Sampling

The sample size is critical for the random sampling method, and it decides the equality of the sample. As random sampling exists randomness, the obtained sample of the fixed size has significantly different instances. Moreover, different unlabeled instances take different degrees of contribution to the classifier and the randomness of sampling, then the same amount of sampled unlabeled instances also have larger differences. So the sample size cannot be pre-determined before sampling, it should be chosen by the features of the data and task.

For semi-supervised classification task, there exists a hypothesis that the probability distribution $P(x)$ of the input instance x takes valuable information to the posterior probability distribution $P(y|x)$. If we want to reduce the unlabeled instance set U to be a smaller S while keeping the information, the difference in probability distribution between U and S is smaller. Therefore, it needs a measurement to evaluate the difference. The kernel function is widely used to estimate the density function, where the density estimation is the average value of the kernel function on the given set. Therefore, we use the difference in the density estimation between U and S to obtain the subset S of high quality.

Let $K(x)$ be the kernel function. Then $\overline{g} = \sum_{x_i \in U} K(x_i)/u$ and $\widehat{g} = \sum_{x_i \in S} K(x_i)/s$ are the density estimation for the set U and its subset $S \subseteq U$ using simple random sampling without replacement, where s is the size of the set S. In this way, the difference in density estimation between the set U and its subset S can be measured by $|\overline{g} - \widehat{g}|$. If the sample S is a good subset of U with high equality, the difference is small. The absolute difference is difficult to be used because its value always changes greatly for different data. Therefore, the condition $|\overline{g} - \widehat{g}| \leq \gamma|\overline{g}|$ to judge, where $\gamma \in (0,1)$. Owning to the fact that $\overline{g}$ cannot be efficiently computed for large-scale data. On other hand, the stability of $\overline{g}$ on the sample S under fixed size is also difficult to be guaranteed due to the presence of randomness. To solve this problem, we have proposed an adaptive sampling algorithm which is one kind of multiphase sampling. In this method, the unlabeled instances are continuously sampled from the set U to form the subset S until the estimation $\overline{g}$ on the obtained subset S satisfies the stopping condition. The stooping condition is related to the number of iterations and the range of the kernel function on the set U. Moreover, fixed-volume unlabeled instances are drawn during each iteration to accelerate the satisfaction of the termination condition. Though the estimation is continuously computed in the process of iteration, it can be efficiently calculated using the by linearly weighting of the results of the previous iteration and but the current results. The pseudocode of adaptive sampling algorithm is listed in algorithm 2.

Algorithm 2 Adaptive Sampling algorithm

Input: The unlabel set $U = \{x_{l+1}, x_{l+2} \cdots, x_{l+u}\}$, the batch size b.
Output: The subset S.

```
Initialization: S = ∅, r = 0, ĝ = 1, β_r = −∞;
while ĝ > β_r(1 + 1/ε) do
    r = r + 1, β_r = λ √(ln(r(r+1)/δ)/(2r ∗ b));
    Sampling b unlabeled instance without replacement from the set U to be S_r ;
    S = S ⋃ S_r, and compute ĝ on the set S ;
end while
return S
```

2.4. Robustness

Supposed that the unlabeled instance set U is the population, then S is one sample set of U. Obviously, the expectation of $\widehat{g}$ is that $E(\widehat{g}) = \overline{g}$. According to the Hoeffding inequality, we can get the following lemma.

Lemma 1 *Let $S \subseteq U$ be the set of the fixed size s instances independently sampled from the set U. For any real number $\varepsilon > 0$, it has $P(|\widehat{g} - \overline{g}| \leq \varepsilon) \leq 2exp(-2s\varepsilon^2/\lambda^2)$, where $\lambda = \max_{x_i \in U} K(x_i,) - \min_{x_i \in U} K(x_i)$.*

Proof *Let $z_i = K(x_i)$ be the random variable on the sample space $\{x_{l+1}, x_{l+2}, \cdots, x_{l+u}\}$, $\widehat{g}$ is the mean of z_i value on the sample S, and $E(\widehat{g}) = \overline{g}$. According to the Hoeffding inequality, $P(\widehat{g} - \overline{g} \leq \varepsilon) \leq exp(-2s\varepsilon^2/\lambda^2)$ and $P(\overline{g} - \widehat{g} \leq \varepsilon) \leq exp(-2s\varepsilon^2/\lambda^2)$, then the lemma can be obtained by combining these two inequations.*

The final number of iterations r of algorithm 2 depends on the randomness of the sampled instances, and it is a random variable. Two number r_0 and r_1 are defined, $r_0 = \min_r\{\beta_r \leq \varepsilon|\overline{g}|\}$, and $r_1 = \min_r\{\beta_r \leq \varepsilon|\overline{g}|/(1+2\varepsilon)\}$. Because $\beta(r)$ is a strictly decreasing function, then r_0 and r_1 are uniquely determined. Similar to the result of the paper [11], we can get these two lemmas.

Lemma 2 *[11] For any $\varepsilon > 0$, the probability that adaptive sampling algorithm 2 stops before $t_0 - th$ iteration is smaller than $\delta(1 - 1/r_0)$.*

Lemma 3 *[11] For any $\varepsilon > 0$ and $\delta \in (0,1)$, the probability that adaptive sampling algorithm 2 stops after $t_1 - th$ iteration is smaller than $\delta/(2r_0)$.*

Combining Lemma 2 and Lemma 3, we have the following lemma.

Lemma 4 *For any $\varepsilon > 0$ and $\delta \in (0,1)$, the probability that adaptive sampling algorithm 2 stops between $t_0 - th$ iteration and $t_1 - th$ iteration is larger than $1 - 1 - \delta + \delta/(2r_0)$.*

Proof $P(r_0 \leq t \leq r_1) = 1 - P(r < r_0) - P(r > r_1) \geq 1 - \delta/(2r_0) - \delta(1 - 1/r_0) = 1 - \delta + \delta/(2r_0)$

Lemma 5 *[11] For any $\varepsilon > 0$ and $\delta \in (0,1)$, the output of adaptive sampling output $\widehat{g}$ satisfies $P(|\overline{g} - \widehat{g}| \leq \varepsilon\overline{g}|r_0 \leq t \leq r_1) > 1 - 2\delta/r_0$.*

Theorem *For any* $\varepsilon > 0$ *and* $\delta \in (0,1)$*, the output of adaptive sampling output* $\widehat{g}$ *satisfies* $P(|\overline{g} - \widehat{g}| \leq \varepsilon\overline{g}) > 1 - \delta$.

Proof *Combining the lemma 5 and lemma 4, we have* $P(|\overline{g} - \widehat{g}| \leq \varepsilon\overline{g}) \geq P(|\overline{g} - \widehat{g}| \leq \varepsilon\overline{g}, r_0 \leq t \leq r_1) = P(|\overline{g} - \widehat{g}| \leq \varepsilon\overline{g} | r_0 \leq t \leq r_1) * P(r_0 \leq t \leq r_1) > (1 - 2\delta/r_0) * (1 - 2\delta/r_0) = 1 - \delta + \delta^2/(2r_0) - \delta^2/(4r_0^2) > 1 - \delta$.

3. Experiments

To test the effectiveness and efficiency of the proposed algorithm, the comparison in the performance between the classifier trained using the original unlabeled instance set and the classifier using the unlabeled instance subset obtained by adaptive sampling is made. LapSVM algorithm [6] and HGSVM algorithm [12] are selected for their representativeness to be the basic classifier, where the classifiers trained on the sampled subset denotes LapSVM-AS and HGSVM-AS. Meanwhile, a large dataset named phonme size of 5404 is also used, it is divided into the training set and test set in a ratio of 7 to 3, where the labeled instances account for 10% of the training set. The parameters of adaptive sampling algorithm $\varepsilon = 0.5, \delta = 0.2$, and other parameters of LapSVM algorithm and HGSVM algorithm are set as default parameters. All the codes of the adopted algorithms are written by Python3.10, and they are executed on a server of Intel(R) Xeon(R) Silver 4208 CPU @ 2.10GHz and 160GB RAM. Classification accuracy (Acc) and execution time (ET) in seconds of two kinds of algorithms are listed in Table 1.

Table 1. Performance comparison of the two algorithms

LapSVM VS LapSVM-AS				HGSVM VS HGSVM-AS			
LapSVM		LapSVM-AS		HGSVM-AS		HGSVM-AS	
Acc	ET	Acc	ET	Acc	ET	Acc	ET
81.36	2650.32	80.51	1527.95	87.19	2740.33	86.51	1583.58

Table 1 shows that LapSVM-AS algorithm has a slightly lower classification accuracy than LapSVM algorithm, and the difference between them is 0.85% which is tiny compared with the original classification accuracy. Meanwhile, HGSVM-AS algorithm gets a very similar classification accuracy to HGSVM algorithm, and the difference between them is 0.68%. The experience result indicates two representative algorithms trained on the sampled subset obtained by adaptive sampling achieve very similar classification accuracy, and it also validates that the proposed sampling method can get enough distribution information as the original unlabeled instances.

Besides classification performance, execution time is also an important performance evaluation metric. The less execution time, the much higher efficiency. The execution time of LapSVM algorithm and LapSVM-AS algorithm are 2650.32 and 1527.95, where LapSVM-AS algorithm obtains nearly half the time savings compared to algorithm LapSVM algorithm. Meanwhile, HGSVM-AS algorithm also obtains nearly half the time savings compared to algorithm HGSVM algorithm. So the proposed sampling method has high execution efficiency.

4. Conclusions

For the problem that massive unlabeled instances bring a great challenge to efficiently train semi-supervised semi-supervised support vector machine algorithms, this paper has developed an adaptive sampling algorithm. Different from the previous approaches from the view of algorithm optimization, it takes advantage of data reduction to avoid the difficulty of using domain knowledge to improve the efficiency of algorithms. The proposed method continually samples the fixed number of unlabeled instance from the unlabeled set until the estimation on the obtained subset meets the stopping condition, and its robustness has been proved by related lemmas. Moreover, its effectiveness and efficiency have been validated by the experience results on the real dataset. In the future, the proposed algorithm will be popularized and applied to many pattern recognition fields such as question classification, sentiment classification and face recognition in intelligent question answering.

Acknowledgement

This research was supported by Shandong Provincial Natural Science Foundation, China, grant number ZR2020MF146.

References

[1] Zhu X, Goldberg AB. Introduction to semi-supervised learning. Synthesis Lectures on Artificial Intelligence and Machine Learning. 2009;3(1):1-130.
[2] Li Z, Kang Y, Feng D, Wang XM, Lv W, Chang J, et al. Semi-supervised learning for lithology identification using laplacian support vector machine. Journal of Petroleum Science and Engineering. 2020;195:107510.
[3] Bai L, Chen X, Wang Z, Shao YH. Safe intuitionistic fuzzy twin support vector machine for semi-supervised learning. Applied Soft Computing. 2022;123:108906.
[4] Tao J, Zhang N, Chang J, Chen L, Zhang H, Chi Y. Unlabeled sample selection for mineral prospectivity mapping by semi-supervised support vector machine. Natural Resources Research. 2022;31(5):2247-69.
[5] Joachims T, et al. Transductive inference for text classification using support vector machines. In: Proceedings of The Sixteenth International Conference on Machine Learning. vol. 99; 1999. p. 200-9.
[6] Belkin M, Niyogi P, Sindhwani V. Manifold regularization: a geometric framework for learning from labeled and unlabeled examples. Journal of Machine Learning Research. 2006;7(11).
[7] Liu Y, Xu Z, Li C. Online semi-supervised support vector machine. Information Sciences. 2018;439:125-41.
[8] Zeng ZQ, Yu HB, Xu HR, Xie YQ, Gao J. Fast training support vector machines using parallel sequential minimal optimization. In: Proceedings of 3rd International Conference on Intelligent System and Knowledge Engineering. vol. 1. IEEE; 2008. p. 997-1001.
[9] Bottou L. Large-scale machine learning with stochastic gradient descent. In: Proceedings of 19th International Conference on Computational Statistics. Springer; 2010. p. 177-86.
[10] Zinkevich M, Weimer M, Li L, Smola A. Parallelized stochastic gradient descent. In: Advances in Neural Information Processing Systems. vol. 23; 2010. p. 2595-603.
[11] Watanabe O. Sequential sampling techniques for algorithmic learning theory. Theoretical Computer Science. 2005;348(1):3-14.
[12] Sun Y, Ding S, Guo L, Zhang Z. Hypergraph regularized semi-supervised support vector machine. Information Sciences. 2022;591:400-21.

Fuzzy Systems and Data Mining IX
A.J. Tallón-Ballesteros and R. Beltrán-Barba (Eds.)

doi:10.3233/FAIA231022

Research on the Application of Fuzzy Control in Braking of Gasoline-Electric Hybrid Vehicles

Yuanbo Wang [a,1] , Yang LI[b] and Junhong Meng [a]
[a] *Shenyang City College, China*
[b] *China Northeast Architectural Design and Research Institute Co., Ltd, China*

Abstract. Fuzzy control has great advantages in dealing with imprecision and uncertainty in inference systems and control systems. At present, an important area of the development of new energy vehicle vehicles, the purpose is to save non-renewable resources and reduce air pollution, good control methods can improve the energy efficiency of new energy vehicles. This paper focuses on the recovery and utilization of braking energy in gasoline-electric hybrid vehicles, which increases the energy reuse of gasoline-electric hybrid vehicles, so that the energy consumption of the whole vehicle is lower and the pollution is less. In this paper, fuzzy control theory is used to reasonably allocate the ratio of mechanical braking and regenerative braking according to vehicle speed and braking requirements, so as to achieve a reasonable balance between braking reliability and braking energy recovery when braking..

Keywords. New energy vehicles, regenerative braking, fuzzy control

1. Introduction

As the most practical control method in the field of intelligence, fuzzy control has solved many problems in the field of industrial control, power system, household appliance automation and other fields.

With the intensification of the energy crisis and the deterioration of the global environment, the production and penetration rate of automobiles, which are major energy consumers, have increased greatly in recent years, and the production of more energy-efficient electric vehicles has become a trend in the development of the automobile industry[1]. On the one hand, electric vehicles can be driven by electricity, without the consumption of gasoline and the pollution generated by traditional cars, on the other hand, it can realize the diversified recovery of energy flow and realize the reuse of energy[2].

This paper will use fuzzy control theory to focus on the scheme of braking energy recuperation in the context of electric vehicles, including how to distribute electric braking and mechanical braking.

[1] Corresponding Author, Yuanbo Wang, Shenyang City College, China; E-mail:45073697@qq.com.

2. Introduction to braking schemes

An important aspect of automobile energy saving and consumption reduction is the recovery of braking energy, and braking plays a vital role in the safety of the whole vehicle, and how to balance the two is an important topic in vehicle control research.

The braking device in the traditional fuel vehicle is mainly divided into drum brake and disc brake, using friction for mechanical braking, the heat energy generated cannot be recovered, and the loss is very large[3]. The braking system of electric vehicles is the same as the ordinary car braking system, in terms of structure, it is only a kinetic energy recovery device more than ordinary cars, when the electric vehicle completely releases the accelerator, the motor will receive instructions from the control system, it will judge how much braking force should be applied according to the accelerator pedal position and wheel speed and other signals, so that the motor provides a reverse torque, this reverse torque is transmitted to the wheels, which can achieve the effect of traditional vehicles pressing brakes, and slow down or stop the vehicle. Therefore, electric vehicles braking both mechanically and electrically when braking. One of the reasons why electric vehicles can save energy is that they use regenerative braking in electric braking, and the electrical energy generated by regenerative braking can be stored and reused for the driving energy of the car. This method is adopted because of the reversibility of the motor, that is, the motor can be used as a motor to convert electrical energy into mechanical energy, and can be used as a generator to convert mechanical energy into electrical energy. In particular, the DC motor is better for dragging electric vehicles, but because the advantages in other aspects are not outstanding, the current electric vehicle will use other motors, of course, other types of motors are also reversible when braking[4].

An important aspect of the efficiency of electric vehicles is the recovery and reuse of braking energy, and braking plays a vital role in the safety of the whole vehicle, how to balance the two is an important field of electric vehicle control research.

3. Braking scheme determined

Electric vehicles use motors to replace traditional internal combustion engines, drag motors also have the ability to provide acceleration and deceleration torque to the vehicle, and this ability can also be applied in the vehicle braking process, that is, braking energy recovery technology, which is also the biggest difference between electric vehicles and fuel vehicle braking systems. According to relevant research, the theoretical recoverable inertia energy of vehicles in urban highways is about 48% when braking, considering that the recovered energy passes through a component, there is a certain amount of energy loss, without damaging the battery, only 5% of the braking energy at the tire can be fed back to the battery, so improve the ability to recover energy, reduce energy transmission loss, and become a hot spot in the current research on energy conservation of electric vehicles[5].

Considering the reliability of automobile braking, gasoline-electric hybrid vehicles should adopt a composite braking method - a combination of regenerative braking and friction braking. The two brakes should be reasonably distributed throughout the braking process, and the entire braking system can consist of three parts:

1. Input part: The stroke signal of the brake pedal;

2. Control part: the core part of the power transmission and control system to realize the feedback braking;

3. Actuator: friction brake system and regenerative braking system.

4. Brake control method

4.1. The principle of energy recovery

A very important feature of electric vehicles is that the motor enters the generator state in some cases, which can convert kinetic energy into electrical energy, more typically brush DC motor, this basic principle also applies to all types of motors, as long as the speed is greater than the ideal no-load speed can be regarded as a generator.

Taking the pure electric driven by the four-wheel hub motor as an example, the structure and principle of the automobile brake energy recovery system are shown in Figure 1. The braking of electric vehicles works in harmony between the frictional braking generated by the hydraulic system and the regenerative braking of the motor in the electric brake. The regenerative braking system of the motor is mainly composed of five parts: hub motor, motor controller, inverter, brake controller and power battery pack[6]. When the car brakes, the brake controller issues different commands according to different braking conditions, controls the hub motor through the motor controller, and performs regenerative braking in addition to friction brake, that is, energy recovery.

The advantage of fuzzy control is that it adopts linguistic control rules, has experienced people to provide experience, and does not need to accurately calculate the mathematical model in the design - this also greatly reduces the difficulty and inaccuracy of modeling, especially the model of car braking varies from car to car, and it is difficult to determine, so the use of fuzzy control is a very feasible control method.[7]

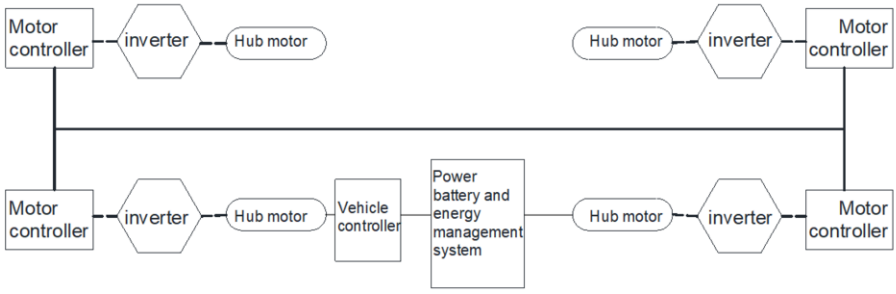

Figure 1. Structural schematic diagram of automobile brake energy recovery system

When braking, if the energy management system sends the power battery SOC value, that is, the remaining battery power value, to the brake controller, when the SOC > 0.8, no energy recovery is performed; When $0.7 \leq SOC \leq 0.8$, the braking energy recovery is lower than the maximum charging current allowed by the power battery; when the SOC < 0.7, the brake energy recovery is not limited by the maximum charging current allowed by the power battery[8]. The brake controller receives the master cylinder pressure signal transmitted by the pressure sensor and calculates the upper limit of the required motor regenerative braking strength. The brake controller calculates the braking strength that the hub motor can actually provide based on the encoder signal connected to the in-wheel motor speed. Measure the upper limit of the motor's regenerative braking strength and the braking strength that the in-wheel motor can actually provide, and send

the result as an electrical signal to the motor controller. When the hub motor works in the generator state, it can provide DC current, charge the electric energy to the power battery pack, and then generate the voltage frequency in line with the motor operation and boost the voltage through the inverter.

4.2. Brake control method

Considering the operating characteristics of frequent braking and low braking degree of the car under urban working conditions, it is set that when braking at lower intensity, regenerative braking is preferred; When braking at medium strength, compound braking is used; When braking at higher intensity, all other brakes after saturation of regenerative braking are borne by friction brakes.

How to reasonably arrange these braking situations to achieve energy recovery during braking can be controlled by fuzzy logic. The essence of fuzzy control is a non-linear control, which is an intelligent control method developed in the 70s of the last century, which belongs to the category of intelligent control and is widely used in the control of modern intelligent appliances. For example, fuzzy control theory has been adopted in many aspects such as intelligent washing machines, sweepers, and robots.

4.3. Implementation of the method

The input amount of fuzzy control is the vehicle speed and the stroke change rate of the brake pedal, and the so-called stroke change rate of the brake pedal is the speed at which the brake pedal is pressed, which reflects the user's demand for the braking strength of the car[9]. Set the fuzzy subset to:

$$E\ (\text{speed}) = \{\text{high, medium, low}\} \quad (1)$$

$$E\ (\text{pedal stroke rate of change}) = \{\text{fast, medium, slow}\} \quad (2)$$

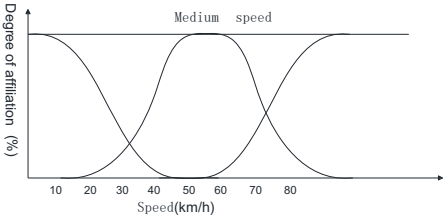

Figure 2: Vehicle speed membership function

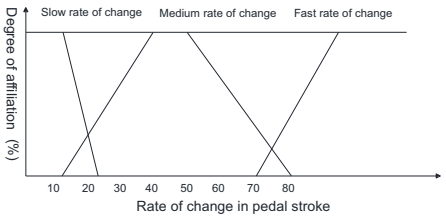

Figure 3: Brake pedal stroke rate change membership function

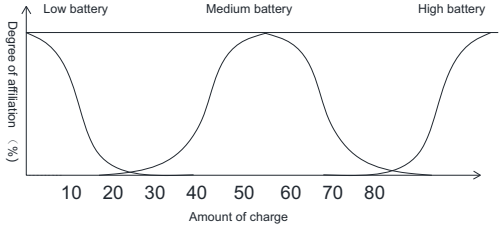

Figure 4: Charge quantity membership degree function

According to experimental data and theoretical analysis, the membership function set for the rate of change of vehicle speed and brake pedal stroke [10].

The membership function of the velocity is shown in Figure 2, and the membership function of the rate of change of the stroke of the brake pedal is shown in Figure 3.

The amount of battery charge indicates the current charge of the battery. The ratio between the amount and the maximum capacity of the battery. The amount of battery charge directly determines whether the motor can brake or not. As shown in Figure 4, the battery charge is divided into high, medium and low to establish a fuzzy model. Combined with the discussion of SOC in Part 4.2, the membership function of the battery charge can be determined.

$$E(\text{The amount of battery charge}) = \{\text{high, medium, low}\} \tag{3}$$

Regardless of the amount of battery charge, the fuzzy controller adopts Sugeno fuzzy inference when gliding, and the fuzzy subset and domain of discourse of the two-dimensional output are:

$$Mf=\{T1,T2,T3,T4,T5\}=(0.2,0.4,0.6,0.75,1) \tag{4}$$

In order to achieve the safety and comfort of the whole vehicle and recover as much energy as possible, the following table of fuzzy rules is summarized.

Table 1. Fuzzy rules table.

velocity / pedal Rate of change in stroke	High speed	Medium speed	Low speed
fast	T5	T4	T1
middle	T5	T3	T2
slow	T2	T2	T1

Since the previous output control quantity is a fuzzy quantity, and the actual control quantity is an exact quantity, the following formula can be used to convert the fuzzy control quantity into the exact amount of torque T generated by the applied motor:

$$T = \frac{\sum_{i=1}^{9} \beta_i i_i}{\sum_{i=1}^{9} \beta_i} \tag{5}$$

The battery charge factor is also taken into account during the braking process, and the motor braking should be preferred when the vehicle brakes to maximize the recovered energy. When the braking force is large, friction brakes are used to stabilize the vehicle. When the vehicle is driving normally, try to choose motor braking to recover braking energy. When the vehicle is driving at low speeds, try to choose mechanical braking to avoid low motor torque and insufficient power. Based on the above principles, a fuzzy relationship model between vehicle driving speed V, braking force F and battery charge amount SOC and regenerative braking ratio K can be established. The three-dimensional surface diagram of the relationship between the four is shown in Figure 5. It can be seen from Figure 3 that under normal circumstances, the ratio of regenerative braking is inversely proportional to the amount of battery charge and braking force, and the

relationship between it and the speed of the vehicle is directly proportional, that is, the higher the battery charge and the greater the braking force, the smaller the proportion of regenerative braking; The higher the speed of the vehicle, the greater the proportion of regenerative braking.

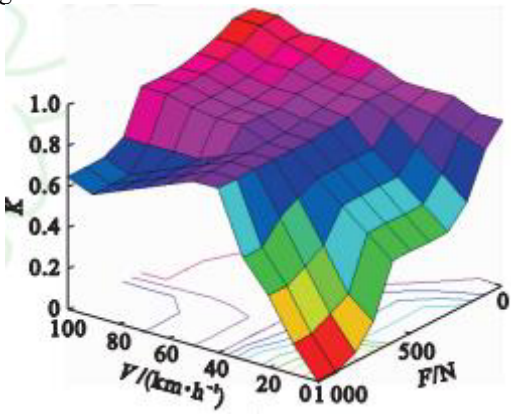

Figure 5. Fuzzy relationship among various factors and regenerative braking ratios

5. Conclusion

This paper discusses the process of regenerative braking in the process of frequent braking under urban conditions, which can reduce the wear of brake pads by mechanical braking and realize the reuse of braking energy. In this paper, an optimized braking energy recovery strategy is formulated by using empirical method and fuzzy control theory as a means, which reasonably considers the distribution of mechanical braking and regenerative braking, which has certain feasibility.The limitation of this design is that there is no individual analysis of specific vehicle types, specific motor types and powers. Considering the battery power and as a constraint condition for energy recovery, a three-dimensional energy recovery model is established. The disadvantage of this method is that according to different models and motor types, power, the membership function will change accordingly, and the solution is to use adaptive theory combined with fuzzy control for further research. In the further use of this method, different empirical membership functions can be formulated according to the model model.

References

[1] Caineng Zou a b, Qun Zhao.Energy revolution: From a fossil energy era to a new energy era.Natural Gas Industry B. 2016,Jan;3(1):1-11.

[2] A.G. Olabi a b, Mohammad Ali Abdelkareem.Battery electric vehicles: Progress, power electronic converters, strength (S), weakness (W), opportunity (O), and threats (T).International Journal of Thermofluids.2022, Nov;16:100212.

[3] Lingfei Qi a, Xiaoping Wu.An electro-mechanical braking energy recovery system based on coil springs for energy saving applications in electric vehicles.Energy.2020,June;200(1):117472.

[4] Sreedhar Madichetty, Sukumar Mishra, Malabika Basu.New trends in electric motors and selection for electric vehicle propulsion systems.2021,Sep;11(3):186-199.

[5] Guoqing Xu,Kun Xu.Fully Electrified Regenerative Braking Control for Deep Energy Recovery and Safety Maintaining of Electric Vehicles.EEE Transactions on Vehicular Technology. 2015,Jan;65(3):1-1.

[6] Bo Guo; Hui Wang; Tao Zhang; Yifei Wang.Electrical Topology and Control of Four-wheel Hub Motor Pure Electric Vehicle.2022 IEEE 5th International Electrical and Energy Conference.2022,Aug.
[7] Ahmed T. Hamada, Mehmet F. Orhan.An overview of regenerative braking systems.Journal of Energy Storage. 2022,Aug;52, Part C, 25 : 105033.
[8] Zhai Yu ,ORCID logo, Haibo Feng,Yanmei Meng.Braking energy management strategy for electric vehicles based on working condition prediction.AIP advances .2022,Jan;12(1):94-96.
[9] Hongwen He.An intelligent braking system composed single-pedal and multi-objective optimization neural network braking control strategies for electric vehicle.Applied Energy. 2020, Feb ;259,(1):114172.
[10] Jiang Biao, Zhang Xiangwen.Regenerative Braking Control Strategy of Electric Vehicles Based on Braking Stability Requirements.International Journal of Automotive Technology.2021,Nov;22:465–473.

Fuzzy Systems and Data Mining IX
A.J. Tallón-Ballesteros and R. Beltrán-Barba (Eds.)

doi:10.3233/FAIA231023

A Method to Explore the Synchronous Changes of High-Traffic Events Based on Dynamic Networks

Yu-Wen HUANG[a], Li-Na WANG[a,b,1] and Chen-Rui ZANG[c]
[a]*College of Sciences, Inner Mongolia University of Technology, Hohhot, 010051, China*
[b]*Inner Mongolia Key Laboratory of Statistical Analysis Theory for Life Data and Neural Network Modeling, Hohhot, 010051, China*
[c]*Inner Mongolia Branch, China Unicom, Hohhot, 010050, China*

Abstract. With the rapid development of mobile communication technologies, the mobile network has evolved into a highly heterogeneous network structure. Based on dynamic networks, we mainly investigated a method to explore the synchronous changes of high-traffic events. Event coincidence analysis is used to quantify the concurrency of high-traffic events. A variety of network measures are used to analyze the dynamic spatio-temporal characteristics of high-traffic. The static network is constructed to analyze the synchronous influence area and the temporal and spatial characteristics of high-traffic of base station. Taking hour as the time window, the dynamic network is constructed to study the dynamic spatio-temporal variation rule of high-traffic and the interactive relationship of traffic between base stations. It is found that static network is a small-world network. The spatial connectivity of high-traffic events at the base station is high, and the spatial connectivity is not sensitive to temporal changes. The traffic of different base stations has interactive relation at the same time in different days.

Keywords. Complex networks; Event coincidence analysis; Dynamic networks; Communication system

1. Introduction

With the rapid development of mobile communication and sensor technology, a large amount of spatiotemporal data emerges. Spatiotemporal data is spatial data that has a temporal element and changes with time. This information has important application value for urban traffic planning, cellular network management, air forecasting, disaster prediction, and other fields. Observe the spatial distribution of spatio-temporal data through visualization methods, and intuitively analyze requirements.

Event coincidence analysis (ECA) is often applied to analyze the statistical relation between event sequences in spatiotemporal data to study the spatiotemporal

[1] Corresponding Author, Li-Na WANG, Mathematics Department, Inner Mongolia University of Technology, AiMin Road #49, Hohhot, China; E-mail: wanglina@imut.edu.cn.
This work was supported by the Natural Science Foundation of Inner Mongolia (Grant Number 2022LHMS01005); and the Fundamental Research Funds for the Directly Affiliated Universities of Inner Mongolia (Grant Number JY20220095).

characteristics of event occurrence. ECA was originally used to study possible statistical correlations between mechanisms of paleoclimate variability in Africa and human evolution[1]. Until 2016, Donges et al.[2] described in detail the specific algorithmic process of event coincidence analysis, and provided a framework for quantifying the statistical correlation strength and the directional time lag between event sequences. At present, event coincidence analysis has been successfully applied in earthquake science, climatology, neuroscience, social science, epidemiology and other fields.

ECA is often used to study the temporal and spatial evolution of events. Frederik et al.[3] used the ECA to explored the temporal evolution of heavy precipitation patterns during the monsoon season. Sun et al.[4] studied the dynamic spatiotemporal covariation patterns of soil moisture and precipitation in India in four seasons. Ashish et al.[5] studied the dynamic relationship between soil moisture and precipitation in India from 2004 to 2020. Marc et al.[6] evaluated the dynamic changes in the possibility of synchronous occurrence of seasonal extreme precipitation on the global surface and El Niño and La Niña in different seasons. Fan et al.[7] quantified the probability of extreme temperature events under precipitation in different months and their comprehensive impact on crops. We use ECA to construct complex networks to study the dynamic characteristics of high traffic in mobile communication systems.

With the development of mobile Internet and mobile communication, traffic data of mobile communication services has attracted more attention. Using complex networks to study mobile communication complex systems and analyzing the time and space requirements of mobile users for data services will help operators plan base stations. Wang et al.[8] used the event synchronization method to study the similarity between high traffic base stations to visualize the system congestion. To optimize network resource allocation Zhang et al.[9] proposed an optimization algorithm for complex network communication resource allocation based on an improved neural network. Zhao et al.[10] studied the spatio-temporal similarity of cellular traffic between base stations, and conducted a detailed spatial study of traffic and base station deployment. Mining the spatio-temporal data of mobile communication analyzed the evolution law of communication data so that the utilization rate of network resources improved.

The ECA method is used to identify high-traffic event synchronization and construct a complex network, which is used to study the spatio-temporal characteristics of high-traffic dynamic changes. A static network is constructed to analyze the spatial connectivity of high-traffic events and the synchronous influence area of high-traffic occurrence in base stations. The dynamic network is constructed by dividing the time window by an hour to explore the dynamic changes of high-traffic synchronization spatio-temporal characteristics. Excavate the interactive relationship between base stations and the law of dynamic synchronization of high-traffic base stations.

2. Data and Methods

2.1 Data

The data comes from hourly traffic data automatically collected by a certain operator's base station in a certain city. From 0:00 on February 22, 2017, to 23:00 on February 27, 2017, a total of nearly 90,000 pieces of spatio-temporal data (including time, longitude,

latitude, and traffic) were collected. The study area contains a total of 171 base stations, and the length of the time series at each base station is 144 hours.

The research steps include identifying high traffic events, extracting events, quantifying the similarity between event sequences, and constructing complex networks. The threshold method is applied to identify high-traffic events. The 90th percentile of global spatio-temporal data is taken as the threshold[2], and events above the threshold are considered as high-traffic events.

2.2 Event Coincidence Analysis

Event coincidence analysis (ECA) is used to quantify the statistical correlation between event sequences. ECA defines a coincidence interval $\triangle T$ to identify event synchronization. If the time interval of event occurrence is within the coincidence interval $\triangle T$, the event is considered to occur synchronously, i.e., $0 <= |t_i^l - t_j^m| <= \triangle T$. where $t_i^l - t_j^m$ is the time interval between the l-th occurrence of the event at geographic location i and the m-th occurrence of the event at geographic location j. In order to be statistically significant, the coincidence interval $\triangle T$ needs to be smaller than T/N_{max} [2]. N_{max} is the maximum value of the length of the event sequence, which means that the event sequence has N_{max} times of high-traffic events. In order to quantify the synchronicity between two event sequences, the event coincidence rate is defined as [3]

$$r(i \mid j;\Delta T) = \frac{1}{N_i}\sum_{l=1}^{N_i}\Theta\{\sum_{m=1}^{N_j} 1_{[0,\Delta T]}(t_i^l - t_j^m)\}, \tag{1}$$

where r($i|j;\triangle T$) represents the fraction of events in event sequence i which are preceded by at least one event in event sequence j within $\triangle T$. l = 1, 2, ⋯, N_i, m = 1,2, ⋯, N_j indicates that N_i and N_j high-traffic events occurred at geographic location i and geographic location j respectively. $\Theta(\blacksquare)$ is the Heaviside function ($\Theta(x)$ = 0 when x <= 0, $\Theta(x)$ = 1 when x is other). The Heaviside function prevents double counting [3], enabling subsequent calculations to be properly normalized. $1_I(\blacksquare)$ indicates the indicator function ($1_I(x)$ = 1 when $x \in I$, $1_I(x)$ = 0 when x is other).

Similarly, $r(j|i; \triangle T)$ represents the fraction of events in event sequence j which are preceded by at least one event in event sequence i within $\triangle T$. ECA is used toconstruct the adjacency matrix $A = (a_{ij})_{n\times n}$. $a_{ij} = [r(i|j; \triangle T) + r(j|i; \triangle T)] / 2$, n is the total number of geographical locations in the study area. Adjacency matrix A is a symmetrical matrix, i.e., $a_{ij} = a_{ji}$.

3. Results

3.1 Static Networks

The purpose of this study is to explore the dynamic characteristics of high-traffic events. Firstly, the static network across the study area is analyzed to explore the spatiotemporal characteristics of high-traffic events. All locations share one threshold (determined by the 90th percentile for all sequences). The maximum event sequence

length is N_{max} = 109. The coincidence interval $\triangle T$ must be less than T / N_{max}, so the $\triangle T$ is taken as one hour. Treat the base station as a node and build an undirected and unweighted network. The existence of edges between nodes indicates that there are events occurring synchronously between nodes. Build static networks with high-traffic event sequences. The network has 104 nodes and 3839 edges. The average degree is 73.827, the average clustering coefficient is 0.864 and the average path length is 1.283. A static network is a small-world network. According to Clauset, Shalizi and Newman method, the cumulative degree distribution is Weibull distribution, and the parameters are alpha = 4.000 and scale = 81.715.

The degree represents the synchronous influence area of high-traffic events occurring in the base station. The degree of a node is defined as the number of edges linked with it. The existence of an edge between two nodes indicates that there is an event synchronously occurring between the two base stations. The base stations are distributed in different geographical locations. Therefore, base stations with high degrees have synchronized events with a wide area of base stations, that is, base stations with a high degree have a large area of synchronous influence. The base station with a high degree in the southwestern region and some northern regions are large, as shown in Figure 1(a). High-traffic events in these regions exhibit a wide synchronous influence area. Base stations with high degrees exhibit high synchronization and a wide area of synchronization influence.

The clustering coefficient reflects the spatial connectivity of high-traffic e vents at the base station. The node clustering coefficient can be used to measure the possibility of synchronous events occurring among neighboring base stations. A base station with a high clustering coefficient indicates that there is a high probability of connecting edges between neighboring base stations. That is, the possibility of event synchronization between neighboring base stations is high. Therefore, the clustering coefficient can reflect the spatial connectivity of high-traffic in the base station. The base stations all exhibit high clustering coefficients, as shown in Figure 1(b). The high-traffic events of the base stations in the study area exhibit high spatial connectivity.

Average link distance (LD) is the average geographical distance between a node and its connected neighbor nodes, which is normalized by node degree centrality. A base station with a high-valued LD indicates that the base station has high synchronization with the base station at a long distance. The base stations in the southwestern region have a low-valued LD, which shows that the synchronization between the base stations in this region and the nearby base stations is high, as shown in Figure 1(c). With the southwest region as the center, the LD of base stations increases from south to north, and the base stations in the northern region show the characteristics of high synchronization with long-distance base stations.

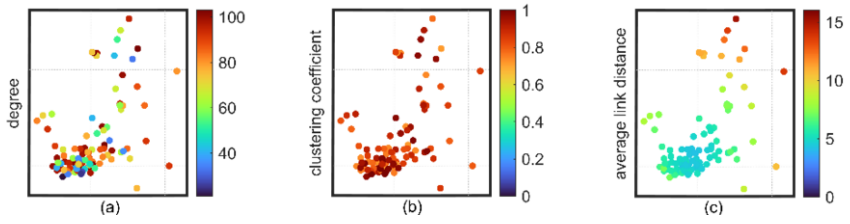

Figure 1. The geographic distribution of (a) node degree, (b) node clustering coefficient, (c) node average link distance in the static network.

3.2 Dynamic Network

The fluctuation of the hourly data flow of the base station is constantly changing with the usage of the users. The time series data (the length is 6 hours) of six days at the same hour were used to construct 24 dynamic networks, which are undirected and unweighted. The maximum value of the event sequences length is 6, and the conformance interval is still one hour. If there is a connection between nodes, it means that event synchronization occurs between base stations at the same time on different days. There are obvious changes in the number of dynamic network nodes, the number of connected edges, and the degree at different times, as shown in Figure 2(a)(b)(c). Excluding points 2am to 7am (rest time), the clustering coefficient and the average link distance fluctuated similarly in the dynamic network, as shown in Figure 2(d)(e). The high-traffic event synchronization of the base station presents regular fluctuations at different hours.

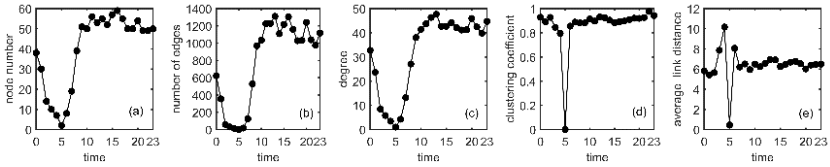

Figure 2. The topology characteristics of dynamic network, (a) number of nodes, (b) number of edges, (c) degree, (d) clustering coefficient, (e) average link distance.

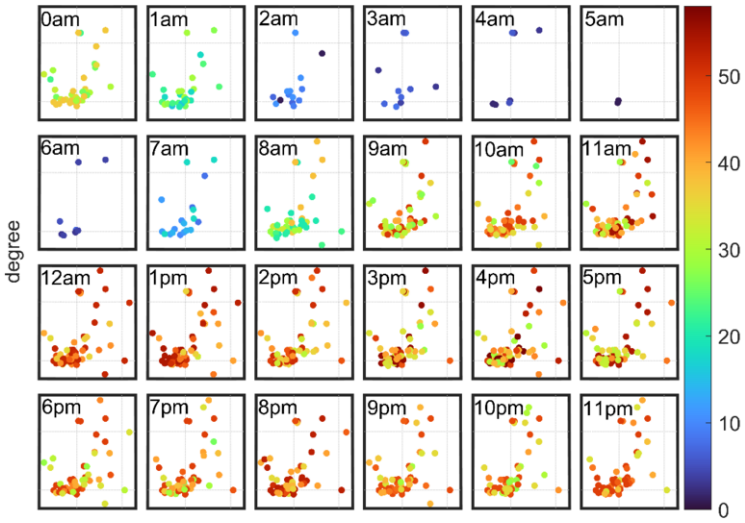

Figure 3. Geographic distribution of node degrees in dynamic network.

The synchronous influence area of high-traffic events in base stations is affected by time and geographical location. The synchronization of high-traffic events at a large number of base stations at 9am to 11pm has a wide synchronous influence area, as shown in Figure 3. From 2am to 7am, there are few base stations where event synchronization occurs, and the synchronous influence area of high-traffic event

synchronization of base stations is narrow. It shows the dynamic spatio-temporal changes of user traffic demands. The location of high-traffic events varies during different time periods.

The node degree of dynamic network reflects the interaction of the traffic of the base station at the same time on different days. The event synchronization between base stations includes the synchronization of high traffic events between base stations at the same time on different days. The traffic between a base station with a high degree and other base stations has a high number of interactions.

High-traffic events have high spatial connectivity and are insensitive to temporal changes, as shown in Figure 4. Although, the number of base stations with high-traffic events at 4am and 5am is small. Most of the nodes in the dynamic network show the characteristics of high clustering coefficients and are less affected by time.

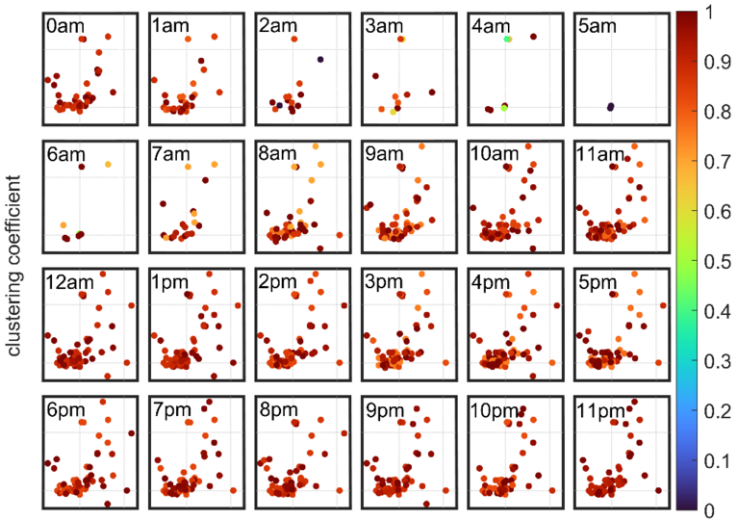

Figure 4. Geographic distribution of node clustering coefficient in dynamic network.

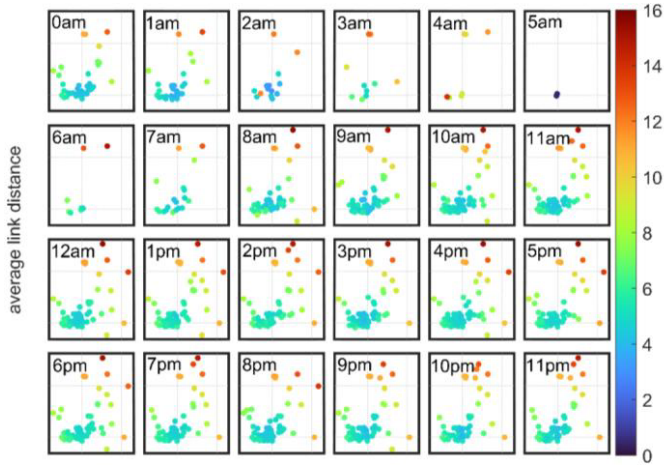

Figure 5. Geographic distribution of node average link distance in dynamic network.

The geographical distribution of the LD of base stations at different times shows a similar pattern. The color division of scatter points in different areas at different times is similar, as shown in Figure 5. The pattern of LD is insensitive to temporal and geographic changes.

4. Conclusions

We identify high-traffic events in base station traffic data. ECA is used to quantify the statistical correlation between high traffic event sequences and construct complex networks to analyze network topology characteristics. Visualize dynamic changes in high-traffic features. Mining the rules of high-traffic changes can help prevent problems such as network congestion and communication delays caused by traffic surges.

High traffic has high spatial connectivity, and it changes regularly. There is an interaction of high traffic between base stations. The high traffic synchronization distance mode of the base station is relatively fixed. The concurrency of high-traffic events is often related to the flow of people and economic development. In future research, crowd activity information can be combined to mine and predict traffic.

References

[1] Donges JF, Donner RV, Trauth MH, et al. Nonlinear detection of paleoclimate-variability transitions possibly related to human evolution. PNAS, 2011, 108(51): 20422-20427.
[2] Donges JF,Schleussner CF, Siegmund JF,et al. Event coincidence analysis for quantifying statistical interrelationships between event time series. EPJ ST, 2016, 225(3): 471-487.
[3] Wolf F, Ozturk U, Cheung K, et al. Spatiotemporal patterns of synchronous heavy rainfall events in East Asia during the Baiu season. Earth System Dynamics, 2021, 12(1): 295–312.
[4] Sun AY, Xia Y, Todd GC, et al. Patterns of precipitation and soil moisture extremes in Texas, US: a complex network analysis. Advances in Water Resources, 2018, 112(2): 203-213.
[5] Ashish MJ, Ravi KG, Ankit A. Spatiotemporal dependence of soil moisture and precipitation over India. Journal of Hydrology, 2022, 610(7): 127898.
[6] Wiedermann M, Siegmund JF, Donges JF, et al. Differential imprints of distinct ENSO flavors in global patterns of very low and high seasonal precipitation. Frontiers in Climate, 2021, 3(1): 618548.
[7] Fan X, Zhu D, Sun X, et al. Impacts of extreme temperature and precipitation on crops during the growing season in South Asia. Remote Sensing, 2022, 14(23): 6093.
[8] Wang LN, Tan GM, Zang CR. Identifying the spatiotemporal organization of high-traffic events in a mobile communication system using event synchronization and complex networks. Chaos, 2022, 32(9): 093122.
[9] Zhang H, Liu Q. Optimization algorithm of communication resource allocation in a complex network based on an improved neural network. Journal of Function Spaces, 2022, 2022(7): 7309612.
[10] Zhao Z, Li M, Li R, et al. Temporal-spatial distribution nature of traffic and base stations in cellular networks. IET Communications, 2017, 11(16): 2410-2416.

Fuzzy Systems and Data Mining IX
A.J. Tallón-Ballesteros and R. Beltrán-Barba (Eds.)

doi:10.3233/FAIA231024

Algorithms of Time Series Network: Approaches Reproduction and Networks Topology

Li-Na WANG[a,b,1], Yuan-Yuan CHENG[a] and Gui-Min TAN[a]
[a]*Science College, Inner Mongolia University of Technology, Hohhot, 010051, China*
[b]*Inner Mongolian Key Laboratory of Statistical Analysis Theory for Life Data and Neural Network Modeling, Hohhot, 010051, China*

Abstract. Network analysis methods of time series provide a new analytical framework on describing complex behaviors using sample data. Reproducibility is one of the important principles in scientific research. This work focuses on the algorithm review and reproduction of time series network. We paid special attention to the applicability and data characteristics of the five typical algorithms: visibility graph, phase space reconstruction, fluctuation mode, symbolic representation and coarsened multidimensional time series. It provides a reference and inspiration for future analysis of time series with various characteristics. Although two pioneer methods are widely applicable, while the directed weighted network established by coarsening thoughts contains more information about time series. In addition, coarseness process makes these approaches perform better for massive data analysis. It should be noted that: the process of data coarsening needs to ensure that the data characteristics of the original time series are inherited.

Keywords. Time series, network science, complex system, scale free, small world, visibility graph, phase space reconstruction

1. Introduction

In statistics, economics, sociology, physics and other fields, time series analysis is an important research direction. With the increase of time series length and system complexity, some methods are no longer applicable, and a series of new methods have being proposed constantly. Among them, time series analysis based on network science has become a hot research topic.

The construction process of the network is to abstract the components and dynamic relationships between components into the node set V and edge set E, forming the graph G = (V, E). The characteristics of time series can be analyzed by the topological features of network, which makes the time series analysis methods based on networks applied to various fields. Literatures on the time series analysis methods based on networks is growing rapidly. In 2016, Gao et al[1] wrote a short review article on network approaches to time series analysis, which briefly summarized the methods and applications. They divided the time series analysis methods based on networks into two

[1] Corresponding Author, Li-Na WANG, Mathematics Department, Inner Mongolia University of Technology, AiMin Road #49, Hohhot, China; E-mail: wanglina@imut.edu.cn.

categories, single-variant time series analysis and multivariate time series analysis. In 2019, Zou et al[2] wrote a long review article on complex network approaches to nonlinear time series analysis. They reviewed the existing approaches of time series networks and mainly explored three approaches: phase space based recurrence networks, visibility graphs and Markova chain based transition networks.

Reproducibility is one of the important principles in scientific research. We believe that it is not only suitable for experimental sciences such as biology and medicine, but also suitable for algorithm studies. The reproducibility of scientific results is also an important principle for algorithm. The focus of this article is on the algorithm reproduction of classical time series network. 1) Pay attention to the algorithm itself, including the characteristics of the data. 2) Reproduce the algorithm to realize the time series network. 3) Study the topological characteristics of the network. We choose five classical models of time series network, including visibility graph[3], phase space reconstruction method[4], fluctuation mode approach[5], symbolic representation method[6] and the method of coarsened multidimensional time series[7]. The visibility graph[3] and phase space reconstruction method[4] are the pioneer achievements of time series network. The fluctuation mode approach[5], symbolic representation method[6] and coarsened multidimensional sequences[7], based on coarse-grained thought, are newly proposed in recent years.

2. Data

Visibility graph[3] is an efficient method and suitable for various types of data. Phase space reconstruction[4] method can be used to analyze chaotic time series to mining the characteristics of chaotic systems. The fluctuation mode[5] approach is based on a class of data with change rate and it can reflect the changes of time series. Symbolic representation method[6] is effective for analyzing the jumping data. The method of coarsened multidimensional[7] time series can be used to assess the evolutions of the correlations between multi-variable time series. When reproducing the above five classical approaches, we choose random numbers with normal distribution as experiment data. The length of time series is 1000. Due to uncertainties in the process to generating the random numbers, it can be considered that the time series has characteristics of randomness, fluctuation and jumping. The initial time series is denoted as $\{ x_t, t = 1, 2, \ldots, n \}$, where n is the length of the time series.

3. Approaches reproduction and networks topology

Classical network-based time series analysis includes visibility graph analysis and phase space reconstruction method. Furthermore, network construction approaches based on symbolized time series have become a new research hotspot in recent years. We reproduce three approaches include fluctuation mode approach, symbolic representation method, and network based on coarsened multidimensional time series. On the one hand, these networks have directed edges and weighted edges. Thus, the constructed network can reflect the reality better. On the other hand, these approaches perform better for massive data, because the scale of the network can be effectively controlled.

Table 1. The topological characteristics of the five typical time series networks. N, |E|, <k>, <s>, C, L denotes the number of nodes, number of edges, average degree, average strength, average clustering coefficient and average link distance. p(k), P(k), P(s) denotes the degree distribution, cumulative degree distribution, and cumulative strength distribution.

Methods	Topological characteristics of the networks							
	N	|E|	<k>	<s>	C	L	p(k) or P(k)	P(s)
Visibility graph	1000	4365	8.730	—	0.707	4.608	log-normal	—
Phase space reconstruction	200	519	5.216	—	0.052	3.481	Gaussian	—
Fluctuation mode	99	238	2.404	2.475	0.088	4.130	power law	power law
Symbolic representation	320	586	1.831	3.075	0.008	7.103	exponential	power law
Coarsened multi-dimensional time series	23	59	2.565	6.913	0.211	3.164	exponential	exponential

3.1. Visibility graph analysis

Visibility graph[3, 8], proposed in 2008, is a simple and faster method for analyzing time series by network methods. The properties of time series are inherited in the process of network construction. In recent years, the extended models of the visibility graph brought into sharp focus, for instance, horizontal visibility graph[9], horizontal visibility graph with limited traversing[10], limited penetrable visibility graph[11] and multivariate horizontally visibility graph[12]. Where, limited traversing visibility graph with distance one is equivalent to visibility graph and multivariate horizontally visibility graph is the extension of horizontal visibility graph, which can be applied to analyze nonlinear time series.

Visibility graph and its extension have been successfully applied to many fields, for example analyzing problems on earthquake[13, 14], finance[15, 16], or medical science[17, 18]. In addition, on dynamics of two-phase flow, the additional information on the dynamical properties of hemispheric asymmetry is obtained by using visibility graph[19].

The principle of visibility graph[3] is: the time series is presented as a histogram. Each bar in the histogram is treated as a node in the network and a connection exists when two bars can "see" each other unobstructedly. In this way, a time series can be transformed into an undirected and unweighted network. Mathematically, if two data bars (x_a, y_a) and (x_b, y_b) can "see" each other unobstructedly, then any data point (x_c, y_c) between them satisfies: $y_c < y_b + (y_a - y_b)(x_b - x_c)/(x_b - x_a)$.

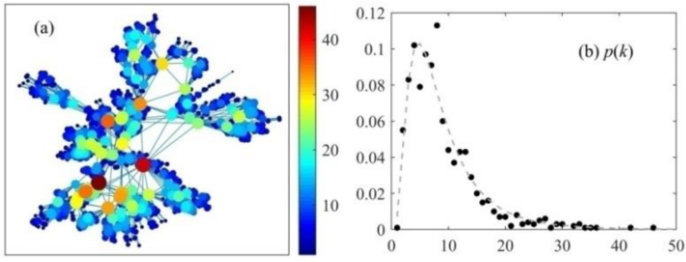

Figure 1. (a) The time series network based on visibility graph; (b) The degree distribution of the network.

According to the classical visibility graph method mentioned above, we reproduce the network from random numbers of standard normal distribution. An unweighted and undirected network is obtained, as shown in Figure 1(a). The basic topological characteristics of the network are shown in Table 1. Obvious, it is small-world network.

The degree distribution is lognormal distribution $p(k) = 0.1e^{-((\ln k-1.6)/0.9)^2}$, and goodness of fit $R^2 = 0.9386$. As shown in Figure 1 (b), about ten percent nodes have degree value around 8, and the proportion of large degree nodes is small.

3.2. Phase space reconstruction method

In order to mining the characteristics of chaotic systems, some scientists have analyzed chaotic time series in phase space. Since the phase space reconstruction method[4] was proposed in 2008, it has been further developed. Gao et al[20] analyzed the dynamic characteristics of chaotic time series according to the network constructed by phase space reconstruction method. Wang et al[21] proposed a coarse-grained phase space reconstruction to map the time series into a directed weighted network. Furthermore, the phase space reconstruction method is applied to analyze specific practical problems.[22-25] For instance, the phase space reconstruction method was used to study the nonlinear characteristics and cognitive functions of the patient's brains[24], and to study the air quality in Beijing based on PM2.5 data[25].

When modeling chaotic time series to network by the phase space reconstruction method, the key part of network construction is to reconstruct vectors, using delay time and embedding dimension. Then, vectors are taken as nodes, and relations between vectors are taken as edges. The process of network construction based on phase space reconstruction[4] is as follows:

Step 1: Vector reconstruction. A new vector is constructed based on the delay coordinate embedding method. The equation is $Y_i = (x_i, x_{i+\tau}, \ldots, x_{i+(m-1)\tau})$, where i = 1, 2, ..., n-(m-1)τ, m is the embedding dimension, τ is the delay time and Yi is the recombined vector.

Step 2: Parameter determination. Parameter determination includes determination of the delay time τ and determination of the embedding dimension m.

Step 3: Network construction. Vectors are regarded as nodes and edges are determined by the correlation of vectors. When $|r| \geq r_c$, $e_{ij} = 1$ indicates that nodes i and j are connected; When $|r| < r_c$, $e_{ij} = 0$ indicates that there is no connection between nodes i and j. Where r is Pearson correlation coefficient of two different vectors, r_c is the threshold, and e_{ij} is the element of adjacency matrix. Then, an unweighted and undirected network can be obtained.

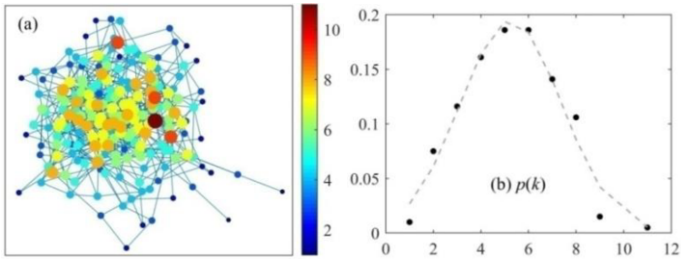

Figure 2. (a) The time series network based on phase space reconstruction; (b) The degree distribution of the network.

Using random numbers of standard normal distribution as the experimental data, we reproduce the network by the classical phase space reconstruction method. The time series data with length of 1000 is reconstructed into two hundred vectors with length of

50. The vectors are mapped as nodes. If the correlation coefficient of two vectors is greater than 0.9 ($r_c = 0.9$), the corresponding nodes will be connected. The unweighted undirected network is obtained, as shown in Figure 2(a). The topological characteristics are shown in Table 1. The degree distribution of the network follows the Gauss distribution $p(k) = 0.2e^{-((k-5.3)/3.0)^2}$ ($R^2 = 0.9624$). As shown in Figure 2(b), the degree values are relatively centralized, and near the value of five and six.

3.3. Fluctuation mode approach

The fluctuation mode approach can reflect the change rate of time series intuitively. Yao et al.[5] studies the exchange rate of RMB based on the fluctuation mode approach. Liu et al.[26] analyzed the changes of six stock indexes in Shanghai according to the characteristics of the network.

According to the extent of fluctuation, the time series are divided into intervals and represented as symbols. The approach details[5] are as follows:

Step 1: Change rate. In order to reflect the fluctuation of data, the initial data is transformed into the change rate data. The change rate is defined as $y_i = (x_i - x_{i-1})/x_{i-1}$.

Step 2: Symbolization. The change rate data is converted into symbolic data. If the change rate is more than 1%, it is considered that the data increase greatly, and denoted as symbol "a". If the change rate is between 0.1% and 1% (or -1% and -0.1%), it is considered that the range of changes is moderate, and denoted as symbol "b" (or "d"). If the change rate is between -0.1% and 0.1%, it is indicates that the data is almost unchanged, and denoted as symbol "c". If the change rate is less than -1%, it is considered that the data decreases significantly, and then denoted as symbol "e".

Step3: Mode. The symbolized data will be transformed into the mode data in this step. Taking four as the time window, the symbolized time series is divided into the mode time series $g(y)_1g(y)_2g(y)_3g(y)_4$, $g(y)_5g(y)_6g(y)_7g(y)_8$, …. Where, $g(y)_i$ belongs to the set {a, b, c, d, e}.

Step 4: Network. A directed weighted network will be obtained. Different modes are treated as nodes. Mode conversion relationship is treated as edge. The direction and the frequency of conversion are treated as the direction and the weight of edge respectively.

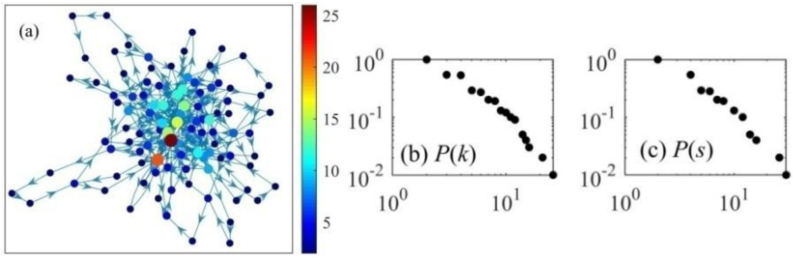

Figure 3. (a) The time series network based on fluctuation mode approach; (b) The cumulative degree distribution of the network; (c) The cumulative strength distribution of the network

Here, we reproduce the fluctuation mode approach by using random number from the standard normal distribution. Firstly, the time series with length of 1000 is transformed into change rate data. According to intervals (–∞, –1], (-1, 0], (0, 1] and (1,

∞), the change rate data is transformed into symbolic data. Then, taking four as the time window, the symbolic data is transformed into the mode data. Taking different modes as nodes, there will be an edge linked with two nodes if the former mode is different from the latter. The direction of the edge is from the former mode to the latter. The weight of the edge is the total number of the modes transformation. The directed weighted network is shown in Figure 3(a). The cumulative degree distribution is power law $P(k) = 2.5k^{-1.3}$ ($R^2 = 0.9761$), which indicates that there is large number of small degree nodes (blue color in Figure 3(a)) and a few nodes with large degree (warm color in Figure 3(a)). The cumulative strength distribution is power law $P(s) = 2.4s^{-1.2}$ and $R^2 = 0.9781$. As shown in Figure 3(b) and Figure 3(c), the scatter points are straight lines in log-log coordinates.

3.4. Symbolic representation method

The symbolic representation method was proposed by Zeng et al.[6]. This method is fit for a class of jumping data and by the topological characteristics of the network, the periodic time series and chaotic time series can be distinguished. Furthermore, Zhang et al. [27] studied air quality index by using symbolic representation method.

The symbolic representation method is a combination of coarsening technology and slide-window technology. This method can map time series into a directed weighted network and the details are as follows:

Step 1: Coarsening. By standardizing the initial time series, the standardized time series $\{y_i, i = 1, 2, \ldots, n\}$ can be obtained, where $y_i = (x_i - \bar{x})/s$, $\bar{x}$ is the mean and s is standard deviation. Using equal probability partition, the standardized time series are coarsened and then the coarsened time series $\{s_1, s_2, ..., s_n\}$ is obtained. Where s_i is the coarse-grained data and can be represented by symbols a, b, c, d, etc.

Step 2: Network. Set the slide-window with a certain length ω and slide along the time series. Then, the time series composed of patterns is obtained. Different pattern fragments are taken as nodes, and the transformation between patterns are defined as edges. The direction of the transformation is defined as the direction of the edge, and the frequency of the transformation is defined as the weight of the edge. A directed weighted network can be obtained.

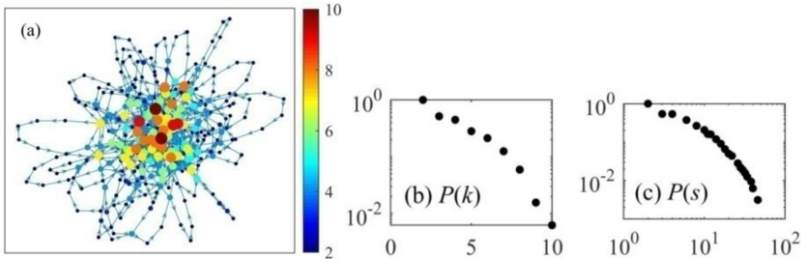

Figure 4. (a) The time series network based on symbolic representation method; (b) The cumulative degree distribution of the network; (c) The cumulative strength distribution of the network.

The random jump data are used as experimental data to reproduce the method. After normalization and equal probability division, the symbolized time series is obtained. Here we use symbols with six levels: a, b, c, d, e, f. Then the slide-window of length 4 is moved along the symbolized time series, and a series of mode segments are obtained. Since the slide-window with length 4 is used when building the network, the

state of the node in the network reflects the state of the four adjacent moments in the time series. And the directed edge reflects the transition between the moments of the time series. The obtained directed weighted network is shown in Figure 4(a). The cumulative degree distribution is exponential $P(k) = 2.3e^{-0.4k}$ ($R^2 = 0.9769$). As shown in Figure 4(b), the scatter points are straight line in semi-log coordinates. The cumulative strength distribution is power law $P(s) = 2.1s^{-1.1}$ ($R^2 = 0.9723$), as shown in Figure 4(c).

3.5. Coarsened multidimensional sequence

Reconstructing a time series into a network can help uncover the dynamic information hidden in the time series.[7] Based on coarsened multidimensional sequence, Fang et al.[7] assess the evolution dynamics of the correlations among energy prices.

For multidimensional time series, the algorithm of coarsened multidimensional sequence is to construct a network combined with Pearson correlation coefficient. The extent of linear correlation between variables can be measured by Pearson correlation coefficient. There is a strong correlation between the variables if the absolute value of Pearson correlation coefficient is close to 1. The correlation between variables is considered as weak when the absolute value of Pearson correlation coefficient is close to zero. By coarsening, the nodes are determined. By the movement of slide-window, the edges are determined. The network modeling method based on coarsened multidimensional time series[7] is as follows:

Step 1: Reconstruction. The multidimensional time series are reconstructed. Three time series are recorded as X_1, X_2 and X_3 respectively. The slide-window with length ω slides along with the time series and then the time series are transformed into a series of time series fragments. In each slide-window, the length of time series is ω. The i-th slide-window of X_1, X_2 and X_3 is denoted as (x_{1i}, x_{1i+1}, x_{1i+2}, …, $x_{1i+\omega}$), (x_{2i}, x_{2i+1}, x_{2i+2}, …, $x_{2i+\omega}$) and (x_{3i}, x_{3i+1}, x_{3i+2}, …, $x_{3i+\omega}$), respectively.

Step 2: Symbolization. Calculate Pearson correlation coefficient between the pairs of three time series fragments (x_{1i}, x_{1i+1}, x_{1i+2}, …, $x_{1i+\omega}$), (x_{2i}, x_{2i+1}, x_{2i+2}, …, $x_{2i+\omega}$) and (x_{3i}, x_{3i+1}, x_{3i+2}, …, $x_{3i+\omega}$), and recorded as r_{12i}, r_{13i}, r_{23i} respectively. That is, the correlation is (r_{12i}, r_{13i}, r_{23i}) in the i-th slide-window. Then, the symbolized mode $mode_i$ = ($g(r_{12i})$, $g(r_{13i})$, $g(r_{23i})$) is obtained according to the correlation values and the following principles: g(r) = a, if $r \in (0.6, 1]$; g(r) = b, if $r \in (0.2, 0.6]$; g(r) = c, if $r \in (-0.2, 0.2]$; g(r) = d, if $r \in (-0.6, -0.2]$; g(r) = e, if $r \in (-1, -0.6]$. Where r is the value of Pearson correlation coefficient.

Step 3: Network. The symbolized modes are taken as nodes and the edge is defined by the conversion between symbolized modes. The frequency of conversions is defined as the weight of the edge, and the transformation direction is taken as the direction of the edge. A directed weighted network can be obtained.

The method on coarsened multidimensional time series is reproduced in this subsection. Firstly, three time series, which are random numbers satisfying the standard normal distribution, are generated. Secondly, a slide-window with a length of 50 is set up, and a series of 50×3 time series fragments can be obtained. According to the above approach, a directed and weighted network is established, as shown in Figure 5(a). The adjacency matrix of the network is non-symmetrical, shown in Figure 5 (b). The cumulative degree distribution is exponential $P(k) = 1.5e^{-0.2k}$ ($R^2 = 0.9352$), shown in

Figure 5(c). The cumulative strength distribution is exponential $P(s) = 1.0e^{-0.1s}$ (R^2 = 0.9531), shown in Figure 5(d).

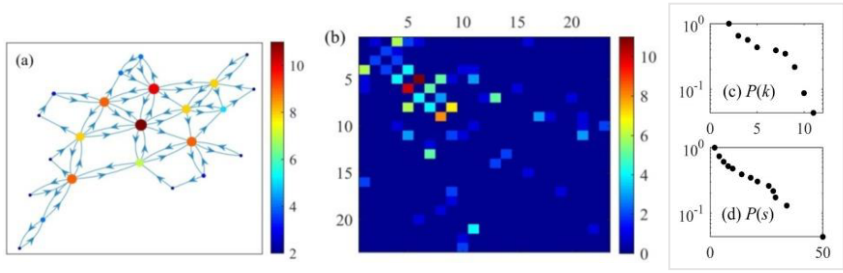

Figure 5. (a) The time series network based on coarsened multidimensional sequence; (b) The graphical representation of adjacency matrix; (c) The cumulative degree distribution; (d) The cumulative strength distribution.

4. Conclusion and discussion

In reference 3, the degree distribution of the network constructed by uniformly distributed numbers obeys the exponential distribution, and the degree distribution of the network constructed by fractal time series obeys power-law distribution. In this paper, we reproduced the visibility graph network constructed by normal distributed random numbers, and the degree distribution obeys lognormal. In addition, the network has a small world feature, which is consistent with the results of the original literature. In reference 4, the degree distribution of the network constructed by stock price time series obeys Gaussian distribution. In this paper, we reproduced the phase space reconstruction network with normal distributed random numbers, and the degree distribution obeys Gaussian distribution.

The networks based on visibility graph and phase space reconstruction are unweighted and undirected. In visibility graph network, nodes with large degree are corresponding to big value data of the time series, which can "see" many others unobstructedly. In time series network based on phase space reconstruction, nodes with large degree are corresponding to reconstructed vectors strong correlated with many other vectors. In visibility graph network, the higher the node clustering coefficient is, the stronger the visibility is among its neighbors. In time series network based on phase space reconstruction, the higher the node clustering coefficient is, the stronger the correlation is among its neighbors.

When make other three coarseness method[5-7] to model the network, the directed weighted networks are obtained. We analyzed the strength distributions of the three time series networks. In these networks, nodes with large strength are corresponding to symbolic modes with high frequency. This kind of nodes converts to other nodes more frequently. Furthermore, nodes with large clustering coefficient are corresponding to symbolic modes, among neighbors of which mode conversion occurs frequently.

The above three time series networks, proposed in recent years, have one thing in common: they all use symbolic mode, the essence of which is coarsening. Coarseness process leads to less number of nodes in the network, which can make the computational complexity of time series analysis reduced. Thus these approaches perform better for massive data analysis. It should be noted that: the process of data coarsening needs to ensure that the data characteristics of the original time series are

inherited. In addition, the directed weighted network established by the latter three algorithms contains more information from time series. For example, the data of time series are related to the time order, and the edge direction in directed weighted network just contains this time order information.

Network analysis methods of time series provide a new analytical framework on describing complex behaviors using sample data. Nowadays, there are abundant data in many fields. Analyzing these data by appropriate methods will promote the development of science.

Acknowledgments

This work was supported by the Natural Science Foundation of Inner Mongolia (Grant Number 2022LHMS01005); and the Fundamental Research Funds for the Directly Affiliated Universities of Inner Mongolia (Grant Number JY20220095).

References

[1] Gao ZK, Small M, Kurths J. Euro phys Lett, 2016, 116, 50001. doi: 10.1209/0295-5075/116/50001
[2] Zou Y, Conner RV, Marwan N, et al. Phys Rep, 2019, 787, 1–97. doi: 10.1016/j.physrep.2018.10.005
[3] Lucas L, Bartolo L, Fernando B, et al. Proc Natl Acad Sci U S A, 2008, 105, 4972-4975. doi: 10.1073/pnas.0709247105
[4] Yang Y, Yang H. Physica A, 2008, 387, 1381-1386. doi: 10.1016/j.physa.2007.10.055
[5] Yao CZ, Lin JN, Zheng XZ, et al. Physica A, 2015, 436, 359-376. doi: 10.1016/j.physa.2015.05.025
[6] Zeng M, Wang EH, Zhao MY, et al. Acta Phys Sin, 2017, 66, 210502. doi: 10.7498/aps.66.210502
[7] Fang W, Gao X, Huang S, et al. Open Phys, 2018, 16, 346-354. doi: 10.1515/phys-2018-0047
[8] Lucas L, Raul T. Phys Rev E, 2010, 82, 036120. doi: 10.1103/PhysRevE.82.036120
[9] Luque B, Lacasa L, Ballesteros F, et al. Phys Rev E, 2009, 80, 046103. doi: 10.1103/PhysRevE.80.046103
[10] Zhou TT, Jin ND, Gao ZK, et al. Acta Phys Sin, 2012, 61, 030506. doi: 10.7498/aps.61.030506
[11] Gap Z, Hu L, Zhou T, et al. Acta Phys Sin, 2013, 62, 110507. doi: 10.7498/aps.62.110507
[12] Gao ZK, Cai Q, Yang YX, et al. Sci Rep, 2016, 6, 35622. doi: 10.1038/srep35622
[13] Juan BA, Vargas LG. Eur Phys J B, 2013, 86, 454. doi: 10.1140/epjb/e2013-40762-2
[14] George H. Commun Nonlinear Sci Numer Simul, 2017, 51, 13-22. doi: 10.1016/j.cnsns.2017.03.015
[15] Wang N, Li D, Wang Q. Physica A, 2012, 391, 6543-6555. doi: 10.1016/j.physa.2012.07.054
[16] Zhuang E, Small M, Feng G. Physica A, 2014, 410, 483-495. doi: 10.1016/j.physa.2014.05.058
[17] Wang L, Long X, Arends JBAMA, et al. J Neurosci Methods, 2017, 290, 85-94. doi: 10.1016/j.jneumeth.2017.07.013
[18] Anirban B, Susmita B, Dipak G. Physica A, 2017, 482, 786–795. doi: 10.1016/j.physa.2017.04.091
[19] Zou Y, Donner RV, Marwan N, et al. Nonlinear Process Geophys, 2014, 21, 1113-1126. doi: 10.5194/npg-21-1113-2014
[20] Gao ZK, Jin ND. Nonlinear Anal Real World Appl, 2012, 13, 947-952. doi: 10.1016/j.nonrwa.2011.08.029
[21] Wang M, Tian L. Physica A, 2016, 461, 456-468. doi: 10.1016/j.physa.2016.06.028
[22] Wang RX, Gao JM, Gao ZY, et al. Sci China Technol Sci, 2016, 59, 604-617. doi: 10.1007/s11431-16-6025-2
[23] Tang J, Liu F, Zhang W, et al. Physica A, 2016, 450, 635-648. doi: 10.1016/j.physa.2016.01.012
[24] Wang J, Yang C, Wang R, et al. Physica A, 2016, 460,174-187. doi: 10. 1016/j.physa.2016.05.012
[25] Fan X, Wang L, Xu H, et al. Environ Sci Pollut Res, 2016, 23, 3621–3631. doi: 10.1007/s11356-015-5596-y
[26] Liu S, Gao X, Fang W, et al. IEEE Access, 2018, 6, 29088-29097. doi: 10.1109/ACCESS.2018.2842069
[27] Zhang Y, Na S. Sustainability, 2018, 10, 1073. doi: 10.3390/su10041073

Fuzzy Systems and Data Mining IX
A.J. Tallón-Ballesteros and R. Beltrán-Barba (Eds.)

doi:10.3233/FAIA231025

Identifying Key Nodes Based on TS Distance in Time-Varying Social Networks

Yayun LIU[a], Zhijian ZHANG[a,1], Lin JIANG[a], Hui ZHONG[a], and Xinyang LI[a]
[a]*Faculty of Science, Kunming University of Science and Technology, China*

Abstract. Key nodes are important for analyzing the evolution of time-varying networks. Persistent homology can calculate topological information of the network in different dimensions and encode it into a persistence diagram. This paper first defines the Topological Similarity (TS) distance based on the theory of persistent homology to describe the topological similarity of the networks. The smaller the TS distance, the more similar the network is. Secondly, an algorithm for identifying key nodes based on TS distance (KITS) is proposed to obtain the sequence of key nodes in time-varying network. Finally, the paper analyses the TS distance on two real time-varying social networks and compares it with the degree centrality. The experimental results show that the TS distance can effectively characterize the topological similarity between two networks and that the KITS algorithm accurately and comprehensively identifies key nodes.

Keywords. Time-varying social networks, Persistent homology, Topological Similarity (TS) distance, KITS algorithm

1. Introduction

In social networks, Key nodes have an important position in the network, and their removal or destruction may lead to the collapse of the network structure or the disruption of information diffusion [1]. However, traditional key node identification methods focus on a single piece of local information, sometimes ignoring key nodes with obvious global topology information but not obvious local information. To solve this problem, we consider the application of persistent homology to identify key nodes. Persistent homology is an algebraic tool for measuring topological features of shapes and functions [2]. It can calculate the topological features of a dataset in different dimensions to extract its topological information and structure [3]. Finally, it can obtain stable topological features, represented as persistence diagrams [4] or persistence barcodes. Topological similarity between persistence diagrams can be measured in terms of Wasserstein distance [5], with smaller distances indicating that the two persistence diagrams are more similar.

Based on persistent homology theory and network topology, this paper first defines the Topological Similarity (TS) distance to describe the topological similarity of networks, and the smaller the TS distance, the more similar the networks. Secondly, a

[1] Corresponding Author: Zhijian ZHANG, E-mail: zhijian@kust.edu.cn.

This work is supported by the National Natural Science Foundation of China (11461037), the Scientific Research Foundation of Yunnan Provincial Department of Education(2017ZZX133), and the Introduction of talent scientific research start-up Foundation Kunming University of Science (KKZ3202207025).

key node identification algorithm based on TS distance is proposed. Finally, the top k key node sequences are obtained on two real time-varying social networks based on the TS distance.

2. Related works

Key nodes are important in the study of social networks. Ren Z M et al. [6] proposed a new method to measure the importance of nodes by combining neighborhood and clustering coefficient information. Bo S et al. [7] combined the PageRank algorithm with the discovery of key nodes in social networks and proposed a PageRank algorithm to discover key nodes in social networks with each linked page as a premise. However, none of the above authors have taken into account the influence of topology.

Persistent homology as a major tool for topological data analysis has been widely used to analyze various networks, such as brain networks [8,9,10,11], social networks [12,13,14,15], financial networks [16,17,18], etc. Using simplex in persistent homology, Hui Zhong et al. [12] defined a node importance description metric for online social networks, which provides an effective new method for describing node importance in online social networks, but the authors do not involve the study of time-varying networks. Hajij M et al. [14] detected structural changes in time-varying graphs using persistent homology, providing a new idea for studying time-varying graphs, However, the authors do not study the identification of key nodes in the paper. Based on the above studies, this paper considers the identification of key nodes in time-varying networks based on persistent homology theory. To our knowledge, this paper is the first to identify key nodes in time-varying social networks based on persistent homology.

In this paper, time is discretized by dividing a continuous period into several discrete periods, each corresponding to a small data set. This has the advantage that the data can be better processed and analyzed.

3. Key node identification based on TS distance in time-varying social networks

Current methods for evaluating key nodes in time-varying social networks are mainly based on centrality metrics (like degree centrality [19]), mostly without considering the influence of topology. In this paper, we propose a method for identifying key nodes with reference to the Wasserstein distance in persistent homology theory.

3.1. Research objectives

This paper aims to define a distance that can describe the topological differences between two networks and identify key nodes in time-varying social networks considering topological global information.

3.2. Definition of TS distance

The similarity between persistence diagrams can be measured by the Wasserstein distance to indicate the similarity between two networks. Therefore, this paper defines the TS distance based on the Wasserstein distance and calculates the TS distance between

the persistence diagram of the network after removing nodes at each time period and the original network persistence diagram, The smaller the TS distance, the more similar the topology between networks.

Assuming that d_1 and d_2 are two persistence diagrams and that η is a bijection between the two persistence diagrams, where η maps each point in d_1 to a point in d_2. Let $p \in (1,\infty)$, The p-th Wasserstein distance between X and Y is defined:

$$W_p(d_1,d_2) = \left(\inf_{\eta:d_1\to d_2}\sum_{d\in d_1}\left\|d-\eta(d)\right\|^p\right)^{\frac{1}{p}} \tag{3.1}$$

The TS distance is defined as follow:

$$TS(d_t, d_t s(i)) = \log_2\sqrt{(W_0)^2+(W_1)^2} \tag{3.2}$$

W_0 and W_1 are the Wasserstein distances of the 0-dimensional and the 1-dimensional persistence diagrams, and d_t is the persistence diagram of the tth time period in the original network. $d_t s(i)$ is the persistence diagram after removing node number i under the tth time period. TS distance combines 0,1-dimensional topology information, which means that the topology of the network is captured more accurately. A larger TS distance indicates that the network obtained after removing the node at tth time period is less similar to the original network.

3.3. Key nodes identification algorithm based on TS distance

The distances in the input distance matrix are social distances, which are the degree of closeness or acceptance of an individual or group to another person or group in the social network [20]. The first three steps of the algorithm are to calculate the Rips complex using the distance matrix, and then to encode the persistence diagram d_t of the original network for each time period and the persistence diagram $d_t s(i)$ of the removed node i for each time period. Steps 4 to 8 calculate the TS distance between the persistence diagram of the network after the removal of node i and the original network persistence diagram for each time period. Steps 9 and 10 are to rank the node i removed in each time period by the size of the TS distance and output the sequence of key nodes in each time period.

Algorithm 1 Key node identification algorithm based on TS distance

Input:

The original network distance matrix at c time periods

Distance matrix after removing nodes one by one under c time periods

Output:

The sequence L_t of key nodes for each time period // t=1…c

1. Use the distance matrix to calculate the Rips complex flirtation
2. encode the original persistence diagram d_t for each time period
3. encode the persistence diagram $d_t s(i)$ after removing node i for each time period // $s(i)$ indicating the removal of node i
4. **for** each d_t in d_c
5. **for** each $d_t s(i)$ in $d_c s(i)$ do

6. Calculate $TS(d_t, d_t s(i)) = \log_2 \sqrt{(W_0)^2 + (W_1)^2}$

7. **end for**

8. **end for**

9. Add node i to the sequence L according to the TS distance from largest to smallest

10. Return the sequence L_t of key nodes for each time period

With c time periods, the upper bound on the time complexity of outputting a persistent diagram is $O(n^2)$, and the upper bound on the time complexity of outputting a persistent diagram after removing nodes one by one is $O(n^3)$, so the time complexity of this algorithm is $O(n^3)$.

4. Numerical experiments

4.1. Experimental data

In order to demonstrate the validity of the work presented in this paper, this paper selects the CollegeMsg temporal network and the Math Overflow temporal network datasets from SNAP [21]. The CollegeMsg temporal network consists of private messages sent on online social networks and the Math Overflow temporal network represents user u commented on user v's answer at time t, both datasets provide a list of edges and a column of timestamped information. and the dataset is shown in Table 1.

Table 1 Composition of the data

Name of the network	Nodes	Temporal Edges	Time span
CollegeMsg temporal network	1899	59835	193 days
Math Overflow temporal network	16836	203639	2349 days

In this paper, we treat the data in the following way. In the CollegeMsg temporal network, we used data from the first 19 time periods in a 10-day time period. In the Math Overflow temporal network, we used the data for the first 30 days in a period of 5 days.

4.2. Experimental steps

In this paper, social distance is defined as follows. In the first time period, there is a connection of 1 and no connection of 0. The social distance of the later time period is updated according to the previous time period, if there is a connection in the latter time period but no connection in the previous time period, the distance is 1. If there is no connection in the latter time period but a connection in the previous time period, the distance is added by 1.

First, the distance matrix of the original network and the distance matrix of the network after removing the nodes are obtained separately by using social distance. Then, the flirtation of the Rips complex is calculated by applying the persistence homology, and finally, the corresponding persistence diagrams are obtained respectively.

4.3. Experimental results and comparisons

The identification of key nodes in this paper is based on TS distance, which measures the topological difference between the persistence diagrams of two networks, so we

present the persistence diagrams first. Persistence diagrams can describe topological features in different dimensions, each topological feature corresponding to a persistence feature point. Figure 1 shows the persistence diagram for the CollegeMsg temporal network in the time periods 0-10, 10-20,180-190.

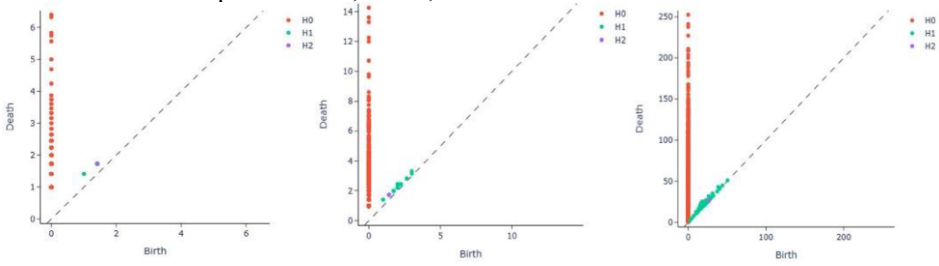

(a) (b) (c)

Figure 1 Original persistence diagrams of the CollegeMsg temporal network for different time periods

The red H0 in the diagram is a 0-dimensional feature point, the green H1 is a 1-dimensional feature point and the purple H2 is a 2-dimensional feature point. The b in each feature point (b, d) indicates the birth of the topological feature, the d indicates death, and the $d-b$ indicates the persistence of the topological feature, with further away from the diagonal indicating a longer topological feature persistence. The 0-dimensional topological features in (a) are all born at b = 0 and continue to generate new features, some of which die out quickly and some of which are retained indefinitely to form the largest connected component when d is infinite (the infinitely retained portion is not shown in the continuum diagram). 1-dimensional features are born at b = 1 and generate 2-dimensional features at t = 1.41. (b) and (c) are similarly analyzed.

4.3.1. Key node sequence based on TS distance in the CollegeMsg temporal network

The TS distance between the original network's persistence diagram and the network's persistence diagram after the removal of node i was calculated, and the symbol is TS (d, di). The top 4 key nodes were found in descending order of TS distance and compared with the degree centrality ranking, as shown in Table 2.

Table 2 Key ranking of nodes in the CollegeMsg temporal network based on TS distance

Node numbering in 0-10	TS (d, di)	Ranked by degree centrality	Node numbering in 50-60	TS (d, di)	Ranked by degree centrality	Node numbering in 70-80	TS (d, di)	Ranked by degree centrality
41	3.74025714	1	103	7.38210745	1	103	7.93573728	1
9	3.50767608	2	9	7.24174099	7	9	7.81849904	6
176	3.48570250	3	400	7.13277841	2	400	7.70597712	2
32	3.33623287	4	42	6.25821125	3	32	7.35622930	3
Node numbering in 160-170	TS (d, di)	Ranked by degree centrality	Node numbering in 170-180	TS (d, di)	Ranked by degree centrality	Node numbering in 180-190	TS (d, di)	Ranked by degree centrality
103	9.18565666	1	103	9.28262694	1	103	9.37789180	1
9	9.16288618	5	9	9.25619254	5	9	9.35151969	5
400	9.05032495	4	400	9.14595687	4	400	9.22805282	4
32	8.74528326	2	32	8.84885056	2	32	8.93529709	2

The following conclusions can be drawn from Table 2.

1. The key nodes obtained using TS distance and using degree centrality at different

time periods are very close to each other, indicating that the identification of key nodes based on TS distance proposed in this paper is feasible, only the ranking order is different, which is due to the fact that the TS distance in this paper combines 0-dimensional and 1-dimensional topological features and considers global information, while degree centrality considers local information, so key node sequences identified based on TS distance are more accurate and comprehensive.

2. The key nodes identified when the network is gradually stabilized are relatively stable and change less compared to the initial stage, this is because their structure and the relationship between the nodes do not change significantly when the network is gradually stabilized.

4.3.2. Key node sequence based on TS distance in the Math Overflow temporal network

From Table 3, it can be observed that the key nodes identified based on TS distance are very close to those identified based on degree centrality in the Math Overflow temporal network, with only a slightly different order, proving that the key node identification based on TS distance proposed in this paper is effective.

Table 3 Key ranking of nodes in the Math Overflow temporal network based on TS distance

Node numbering in 0-5	TS (d, di)	Ranked by degree centrality	Node numbering in 5-10	TS (d, di)	Ranked by degree centrality
1	1.36737107	1	1	2.82660471	1
3	1.08406427	4	2	2.14110799	4
2	0.77399632	2	3	1.92610433	2
Node numbering in 10-15	TS (d, di)	Ranked by degree centrality	Node numbering in 25-30	TS (d, di)	Ranked by degree centrality
1	3.59877469	1	1	5.13332215	2
3	2.85577400	6	3	4.66141767	4
2	2.77263603	9	65	4.49693461	1

5. Conclusion and Future work

This paper identifies key nodes in time-varying networks based on TS distances. Based on persistent homology theory, the TS distance is defined and the KITS algorithm is proposed, which eventually identifies the top k key nodes on real time-varying social networks. Through the experimental results of this paper, it is found that the key node identification based on TS distance takes into account the global topological features of the network. Since the TS distance in this paper combines the topological features of 0 and 1 dimensions, it ensures that the identified key nodes are more accurate and comprehensive, so it is better compared with the degree centrality. However, the efficiency of identifying key nodes in this paper is not very high. So, the combination of persistent homology and machine learning to identify key nodes is considered in the future. As multilayer networks are at the forefront of research and hotspots, in the future we consider identifying key nodes on multilayer networks based on TS distance. It is set up in this way. 1. Create a user interaction layer [22]: Mapping common user interactions in social networks to a separate layer. 2. Add a time layer. On top of the user interaction layer, introduce a time layer to represent the time information of the interaction. 3. Connecting user interactions and temporal layers: Temporal relationships are established by connecting the user interaction layer to the temporal layer. We then use TS distance

to identify key nodes in a multi-layered network.

References

[1] Liu J, Xiong Q, Shi W, et al. Evaluating the importance of nodes in complex networks. Physica A: Statistical Mechanics and its Applications. 2016 Jun; 452: 209-219.

[2] Edelsbrunner H, Harer J. Persistent homology-a survey. Contemporary mathematics. 2008 Jan; 453(26): 257-282.

[3] Edelsbrunner and Morozov D. Persistent homology: theory and practice. Proceedings of the European Congress of Mathematics; 2012 Jul 2-7; Berlin, Germany. Berlin: Springer; 2012. p. 31-50.

[4] Oner D, Garin A, Koziński M, et al. Persistent homology with improved locality information for more effective delineation. IEEE Transactions on Pattern Analysis and Machine Intelligence. 2023 Mar:1-8.

[5] Bhatia S, Chatterjee B, Nathani D, et al. A persistent homology perspective to the link prediction problem. Complex Networks and Their Applications VIII: Volume 1 Proceedings of the Eighth International Conference on Complex Networks and Their Applications COMPLEX NETWORKS 2019; 2019 Dec 10–12; Lisbon, Portugal. Cham: Springer International Publishing; 2019. P. 27-39.

[6] Ren Z M, et al. Node importance measurement based on the degree and clustering coefficient information. Acta Phys. 2013 Jun; 62:128901.

[7] Bo S, Wenfeng G, Yan L. Discovery of Key Nodes in Social Networks Premised on PageRank Algorithm. 2020 Asia-Pacific Conference on Image Processing, Electronics and Computers (IPEC); 2020 Apr 14-16; Dalian, China. IEEE; 2020. p. 26-28.

[8] Lee H, Chung M K, Kang H, et al. Discriminative persistent homology of brain networks. 2011 IEEE international symposium on biomedical imaging: from nano to macro; 2011 Mar 30- Apr 02; Chicago, IL, USA. IEEE; 2011. p. 841-844.

[9] Jafadideh A T, Asl B M. Topological analysis of brain dynamics in autism based on graph and persistent homology. Computers in Biology and Medicine. 2022 Nov; 150: 106202.

[10] Kim H, Hahm J, Lee H, et al. Brain networks engaged in audiovisual integration during speech perception revealed by persistent homology-based network filtration. Brain connectivity. 2015 May; 5(4): 245-258.

[11] El Yaagoubi A, Ombao H. Topological Data Analysis for Directed Dependence Networks of Multivariate Time Series Data. Research Papers in Statistical Inference for Time Series and Related Models: Essays in Honor of Masanobu Taniguchi. Singapore: Springer Nature Singapore. 2023 Jun: 403-417.

[12] Hui Z, Lvlin Q, Zhijian Z et al. The Discovery Method of Key Nodes in Online Social Networks Based on Persistent Homology. Journal of Systems Science and Mathematical Sciences. 2022 Jan; 42(8): 2157-2179.

[13] Hui Z, Lvlin Q, Zhijian Z et al. Community Division Metric Based on Persistent Homology. The 8th International Conference on Fuzzy Systems and Data Minin; 2022 Nov 04-07; Xiamen, China. IOS Press; 2022. p. 58-65.

[14] Hajij M, Wang B, Scheidegger C, et al. Visual detection of structural changes in time-varying graphs using persistent homology. 2018 IEEE pacific visualization symposium (PacificVis); 2018 Apr 10-13; Kobe, Japan. IEEE; 2018. p. 125-134.

[15] Nguyen M, Aktas M, Akbas E. Bot detection on social networks using persistent homology. Mathematical and Computational Applications. 2020 Sep; 25(3): 58.

[16] Ismail M S, Noorani M S M, Ismail M, et al. Predicting next day direction of stock price movement using machine learning methods with persistent homology: Evidence from Kuala Lumpur Stock Exchange. Applied Soft Computing. 2020 Aug; 93: 106422.

[17] Ismail M S, Noorani M S M, Ismail M, et al. Early warning signals of financial crises using persistent homology. Physica A: Statistical Mechanics and Its Applications. 2022 Jan; 586: 126459.

[18] Baitinger E, Flegel S. The better turbulence index? Forecasting adverse financial markets regimes with persistent homology. Financial Markets and Portfolio Management. 2021 Feb; 35(3): 277-308.

[19] Zhang J, Luo Y. Degree centrality, betweenness centrality, and closeness centrality in social network. 2017 2nd international conference on modelling, simulation and applied mathematics (MSAM2017); 2017 Mar 26 – 27; Bangkok, Thailand. Atlantis press; 2017. p. 300-303.

[20] Boguná M, Pastor-Satorras R, Díaz-Guilera A, et al. Models of social networks based on social distance attachment. Physical review E. 2004 Dec; 70(5): 056122.

[21] Jure Leskovec L, Krevl A. SNAP Graph Library: Stanford Large Network Dataset Collection. http://snap.stanford.edu/data. June 2014.

[22] Bonifazi, Gianluca et al. Investigating the COVID-19 vaccine discussions on Twitter through a multilayer network-based approach. Information Processing & Management. 2022 Sep; 59: 103095 - 103095.

Fuzzy Systems and Data Mining IX
A.J. Tallón-Ballesteros and R. Beltrán-Barba (Eds.)

doi:10.3233/FAIA231026

AMF-RetinaNet: Improved RetinaNet for Transmission Line Fittings Detection Based on Attention Mechanism and Multi-Scale Feature Fusion

Xudong CHEN[a,1], Lili HAN[a], Yinghao XIAO[a], Baoguo XUE[a], Liuyang MA[a] and Sheng DING[a]
[a] *Guangzhou Nansha Power Supply Bureau of Guangdong Power Grid Co., Ltd.*

Abstract. The detection of transmission line fittings is extremly significant for keeping the operation of the power grid safe and stable. In order to avoid the occurrence of poor detection results caused by the complicated background environment and different shapes and sizes of the detected targets in aerial photographs of transmission lines, an enhanced RetinaNet method for detecting transmission line fittings is proposed. The proposed approach incorporates an attention mechanism and multi-scale feature fusion,called AMF- RetinaNet. First, a RetinaNet detection network has been built. To enhance the significance of the detected fittings, a spatial and channel convolutional attention model is introduced to suppress complicated background interference. Then, the FPN structure of the original RetinaNet detection structure Neck is changed to the FPN+PAN structure, thereby obtaining more comprehensive multi-scale features. Finally, experiments on the self-built fittings dataset verified the feasibility of AMF-RetinaNet. Experimental results demonstrate that AMF-RetinaNet can effectively detect multi-scale fitting targets on transmission lines, even in challengin environment. Compared with standard RetinaNet, its average detection accuracy mAP has increased by 4.81%.

Keywords. fittings detection; attention mechanism; multi-scale feature fusion; RetinaNet

1. Introduction

Transmission lines play a crucial role in constructing the Energy Internet and line failures are the primary cause of widespread power outages [1]. Fittings are metal accessories that support, fix, and connect bare wires and conductors on transmission lines, such as grading rings, shielding rings, shock hammers, spacers, and various plate fittings. Various types of fittings exhibit a wide range of shapes. Since the fittings are exposed to the outdoors throughout the year, It is highly susceptible to rust, deformation, damage, and other occurrences. The flaws in fittings pose a significant threat to the safe and stable operation of the power grid, so that achieving high-precision automatic detection of fittings can anticipate their failures ahead of time, which is crucial for keeping the operation of the power grid safe[2].

[1] Corresponding Author, Xudong CHEN, Guangzhou Nansha Power Supply Bureau of Guangdong Power Grid Co., Ltd., Guangzhou, China; Email: 578647513@qq.com.

For the past few years, the development of drone technology [3-6] has made the detection of transmission line fittings using drone inspections and computer vision techniques a hot research topic. Detection on fittings can be classified into two main kinds. The first kind utilizes classical machine learning algorithms, combining artificial features with linear classifiers for fittings detection [7]. This approach is typically used for simple background object detection. The second one utilizes deep learning algorithms for the detection of transmission line components. This approach works best in images with a single target and simple backgrounds. However, aerial images of transmission lines often have complex backgrounds and diverse objects, making accurate detection of targets a key research challenge. In reference [8], An enhanced SSD model is proposed for detecting targets of transmission line fittings using aerial inspection images. Reference [9] leverages the fittings features in transmission line images, utilizing depth separable convolutions and multiscale feature fusion methods for the recognition and detection of insulators, suspension clamps, and seismic dampers.

Although the aforementioned research has made great progress in detecting transmission line fittings targets, it still falls short of meeting the actual production requirements. In order to efficiently and precisely identify various types of fittings in aerial images that have complex backgrounds, we employ the RetinaNet [10] model to detect. We further enhance and optimize the model by considering the specific characteristics of the fittings dataset. The RetinaNet network model is a regression-based target detection network proposed by Lin et al. The network proposes a Focal loss function, which alleviates the issue of poor detection accuracy due to the imbalance of sample categories. Aiming at the problems existing in the existing fitting detection methods for transmission lines, this paper proposes an improved RetinaNet transmission line fitting detection method incorporating attention mechanism and multi-scale feature fusion. The attention mechanism allows for a focus on key information, leading to improved network accuracy. This feature extraction ability has resulted in high detection accuracy on the test dataset.

2. RetinaNet

2.1. Network structure

The structure of RetinaNet is displayed in Figure 1. The network primarily comprises three modules: (a) A backbone network based on ResNet [11], utilized for extracting features from input images; (b) Feature pyramid networks (FPN) [12], which employ the feature maps from various stages of the feature extraction network to build a Multi-scale feature pyramid;(c) detection head, including two convolutional subnetworks: classification subnetwork and regression subnetwork. The classification subnetwork extracts information about object categories from FPN to solve classification problems; the regression subnetwork extracts information about object coordinates in images from FPN to solve regression problems.

As the depth of the neural network increases, a simple linear transformation cannot be achieved due to the introduction of too many nonlinear transformations in the deeper neural network. The residual network ResNet directly outputs part of the original data to the next layer through the shortcut connection in the residual block, which balances the contradiction between linear conversion and nonlinear conversion. Without adding additional network parameters, it solves the problems of network gradient descent and

accuracy saturation. The low-level features of the image include less semantic information, but still provide accurate target position. On the other hand, the high-level features include more semantic information, but usually offer rough position information. To address this issue, FPN incorporates top-down operations and horizontal connections to combine high-level semantic features with low-level positional features. This integration enhances the feature extraction capabilities of neural networks.

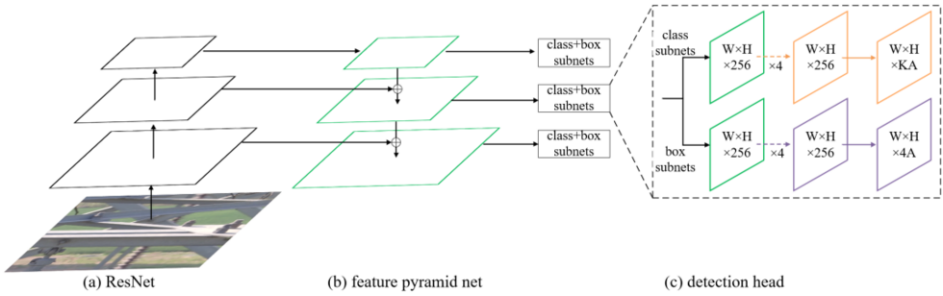

Figure 1. The structure of RetinaNet

2.2. Focal loss

RetinaNet adopts the optimized cross entropy loss function focal loss, which improves the cross entropy function by adding an adjustment factor before the cross entropy function, reduces the weight of loss for samples during the training procedure, and makes the algorithm focus more on the learning of difficult samples. It is of great benefit to feature learning of difficult detection targets, and the expression is:

$$FL(p_t) = -\alpha_t (1 - p_t)^{\gamma} \ln(p_t) \tag{1}$$

where αt represents the balance parameter, which controls the weighting of borh positive and negative samples in the overall loss. A lower value of αt decreases the importance of negative samples. γ is the modulation coefficient, which aims to decrease the weight of easily classifiable samples, enabling our model training to prioritize challenging samples.

3. AMF-RetinaNet

The quality of images of transmission lines is affected by many factors. The resolution of images containing fittings is not high, the shapes and sizes of fittings are different, and the background of aerial images in high-altitude environments is complex. The feature extraction capability of RetinaNet cannot be applied to this complex situation. Therefore, when the original RetinaNet is used for detecting transmission line fittings with complex backgrounds,issues of poor detection accuracy still exist, even some detections are missed or falsed. This paper presents AMF-RetinaNet, an enhanced RetinaNet detection model that addresses these issues. Its structure is shown in Figure 2. AMF-RetinaNet mainly improves in two aspects: 1) The network is enhanced with an attention mechanism module that enables the detection network to pay more attention to the target

features of the feature map, leading to an improved accuracy in network detection. 2) Change the FPN structure in the original RetinaNet detection framework Neck to the FPN+PAN (Path Aggregation Network) [13] structure to efficiently fuse target features at various scales.

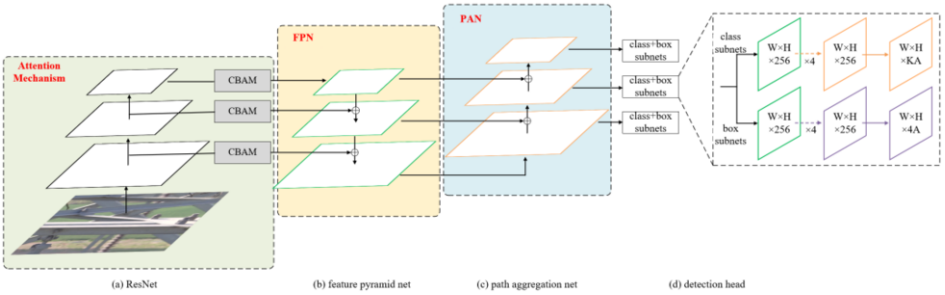

Figure 2. The structure of AMF-RetinaNet

3.1. Attention mechanism

To strengthen the feature expression ability of fault targets in complicated backgrounds and enhance their prominence, we have incorporated the Convolutional Block Attention Module (CBAM) [14] into RetinaNet. The detailed structure of CBAM is illustrated in Figure 3. The CBAM module utilizes a channel attention mechanism to boost the feature information of the desired region via global average pooling and max pooling. However, this mechanism may result in the loss of positional information in the image. To mitigate this issue, a spatial attention model is incorporated. After bringing CBAM into the Backbone, the target detection can be enhanced in terms of salient features in complicated backgrounds, established a solid foundation to detect the subsequent fitting targets accurately.

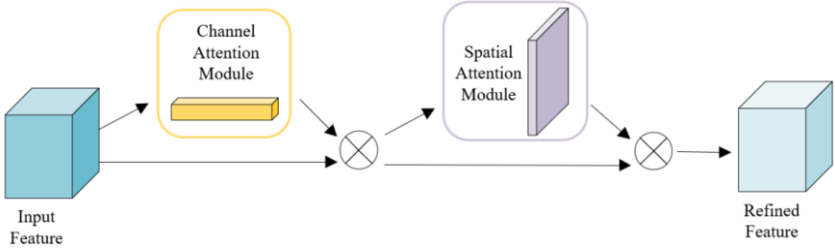

Figure 3. The structure of CBAM

CBAM model in Backbone are depicted in Figure 4. The red space in this figure signifies regions of high significance, with darker colors indicating higher levels of significance. Figure 4 demonstrates that the red box represents the target object to be detected, and and the saliency of this target in complicated backgrounds can be enhanced through the introduction of CBAM.

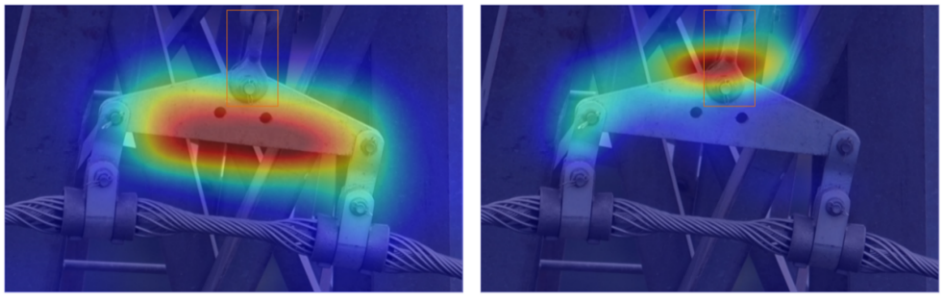

(a) Without CBAM (b) With CBAM

Figure 4. Comparison results before and after adding CBAM

3.2. Multi-scale Feature Fusion

Effectively processing multi-scale features is one of the difficulties in target detection. The original RetinaNet utilizes a top-down feature pyramid network FPN to merge features of various scales. However, this fusion approach converts the feature maps to the same size and cascades them, which limits the utilization of features across different scales. Consequently, the detection accuracy is compromised. To solve this issue, an efficient FPN+PAN feature fusion strategy is introduced into the Neck of RetinaNet, as depicted in Figure 2 (b) and (c).

When multi-scale feature fusion is performed on images, the upper layer feature map network has deeper layers and contains stronger image semantic information; the lower layer feature map has fewer convolution layers and less loss of image position information. The FPN structure is up-sampled from top to bottom, enhancing the image's semantic information in the underlying feature map. Conversely, the PAN structure is down-sampled from the bottom, ensuring that the top-level features retain image position information. We further add a bottom-up branch to the structure of FPN (Figure 2 (b)), adopting the structure of FPN+PAN (Figure 2 (b) and (c)). Integrating the powerful semantic information conveyed from the top with the strong positional information conveyed from the bottom up, the aggregation ability of the network is enhanced, and the accurate prediction of pictures of different sizes is guaranteed.

4. AMF-RetinaNet

4.1. Dataset

This paper constructs a dataset of aerial transmission line fittings detection images for professional use. The dataset contains 1034 images and 2282 labeled objects. There are 12 types of fittings including shielding rings, grading ring, anti-vibration hammers, etc. and the dataset is divided into training and testing sets in an 8:2 quantity. The details are displayed in Table 1.

Table 1. Transmission Line Fitting Image Dataset

Fittings	Nums	Fittings	Nums
shielding ring	70	pre-twisted suspension clamp	102
grading ring	367	bag-type suspension clamp	287
shock hammers	211	u-type hanging ring	336

yoke plate	253	adjusting plate	98
hanging board	214	weight	185
strain clamp	73	spacers	86

4.2. Experimental Results and Analysis

In the experimental part, this paper selects the evaluation indicators mAP, recall rate Recall and detection time t/s, which are commonly used in target detection, as the basis for fairly measuring the performance of this method. To demonstrate the superiority of our method, we make comparisons with various popular models using the same dataset. Parameters used during training are the same, and the experimental results are in Table 2.

Table 2. Experimental comparison of different algorithms

Method	mAP(%)	FLOPs(G)	Time(s)
SSD[15]	74.37	31.75	0.048
Faster RCNN[16]	78.28	181.12	3.082
YOLOv4[17]	77.15	6.96	0.006
YOLOX[18]	79.34	6.45	0.005
RetinaNet[10]	75.62	91.35	0.057
AMF-RetinaNET(ours)	**80.43**	101.50	0.313

Compared with Faster RCNN, our model AMF-RetinaNET not only has faster detection speed, but also obtain higher detection accuracy. Furthermore, the model complexity of different methods influences the accuracy and speed of detection. Compared with several other classes of single-stage models, the mAP of AMF-RetinaNET is the highest. Although the detection speed is the slowest and the FlOPs is larger, it is acceptable. Compared with its basic model RetinaNet, AMF-RetinaNET has an increase of mAP by 4.81%. But it also brings a FlOPs increase of 10.15G in model complexity. The introduction of CBAM and the feature pyramid FPN+PAN has increased the amount of calculation and complexity but in exchange for a substantial performance improvement. Overall, AMF-RetinaNET has the best performance in fittings detection.

To further validate the efficacy of each module in the AMF-RetinaNET network, ablation experiments were conducted, as presented in Table 3. From Table 3 we can konw that after introducing the self-attention mechanism CBAM in the baseline, the mAP increased by 2.76%; after using the FPN+PAN feature fusion in the baseline, the mAP increased by 3.33%; AMF-RetinaNET introduced two improvements to achieve the optimal performance, mAP increased by 4.81%, and recall increased by 1.47%, which demonstrated the effectiveness of the method. Although the introduction of each module increases the computational complexity of the model, it is acceptable for performance improvement.

Table 3. Experimental comparison of different algorithms

Method	mAP(%)	FLOPs(G)	Recall(%)
RetinaNet（baseline）	75.62	91.35	88.21
+CBAM	78.38	95.28	88.67
+PAN	78.95	98.39	88.84
AMF-RetinaNET(ours)	**80.43**	101.50	**89.68**

Finally, we also detect and display the image of the transmission line fittings to show the superiority of the method we proposed. The results are presented in Figure 5. Figure 5(a) shows the outcome of baseline model RetinaNet, while Figure 5(b) displays the result of the proposed method AMF -RetinaNet. The detection result diagram reveals that RetinaNet fails to identify a U-shaped hanging ring in the image, some detection frames are not standardized enough, and the accuracy of fitting detection is lower. The detection effect of AMF-RetinaNet surpasses the baseline model in all aspects. Although the detection accuracy of the U-shaped hanging ring is only 63%, it is still a significant improvement. This demonstrates that the improved method we presented performs notably greater than the baseline model in fittings detection.

5.Conclusion

Object detection algorithms for detecting defects have long been a topic of interest for scientific research teams and researchers. This paper presents an enhanced RetinaNet transmission line fitting detection method called AMF-RetinaNet. This method incorporates attention mechanisms and multi-scale feature fusion. When using CBAM, the salience of the metal fittings in complicated backgrounds is enhanced, thereby improving the accuracy of their detection. Additionally, the original structure in RetinaNet detection framework has been replaced from FPN to FPN+PAN structure. Through experimental verification, AMF-RetinaNet can accurately detect multi-scale fittings targets on transmission lines in complicated environments, and its average detection accuracy mAP has increased by 4.81%. This method is extremely crucial for keeping operation of the power grid safe and stable.

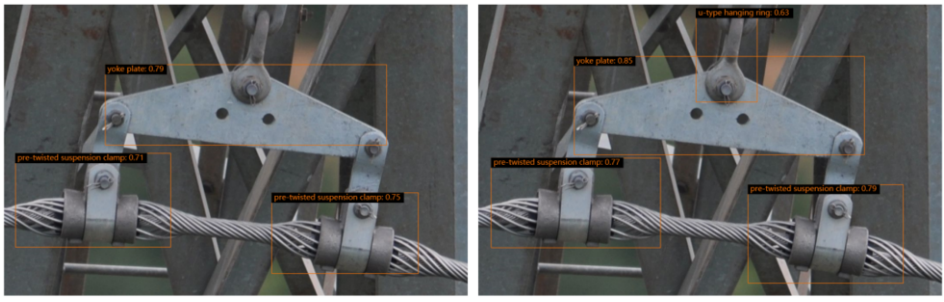

(a) RetinaNet (b) AMF-RetinaNet

Figure 5. Comparison of detection results between RetinaNet and AMF-RetinaNet fittings

References

[1] DONG Zhaoyang, ZHAO Junhua, WEN Fushuan, et al. From smart grid to energy internet: basic concept and research framework[J]. Automation of Electric Power Systems, 2014, 38(15): 1-11.

[2] ZHAO Zhenbing, JIANG Zhigang, LI Yanxu, et al. Overview of visual defect detection of transmission line components[J]. Journal of Image and Graphics, 2021, 26(11): 2545-2560.

[3] Hao S, An B, Ma X, et al. PKAMNet: A Transmission Line Insulator Parallel-Gap Fault Detection Network Based on Prior Knowledge Transfer and Attention Mechanism[J]. IEEE Transactions on Power Delivery, 2023.

[4] Cao Y, Xu H, Su C, et al. Accurate Glass Insulators Defect Detection in Power Transmission Grids using Aerial Image Augmentation[J]. IEEE Transactions on Power Delivery, 2022.
[5] Zhai Y, Wang Q, Yang X, et al. Multi-fitting Detection on Transmission Line based on Cascade Reasoning Graph Network[J]. IEEE Transactions on Power Delivery, 2022, 37(6): 4858-4868.
[6] Hao S, Yang L, Ma X, et al. YOLOv5 Transmission Line Fault Detection Based on Attention Mechanism and Cross-Scale Feature Fusion[J]. Chinese Journal of Electrical Engineering,2023,43(06):2319-2331.
[7] Tang Yong, Han Jun, Wei Wenli, et al. Research on part recognition and defect detection of transmission line in deep learning[J]. Electronic Measurement Technology, 2018, 41(6): 60-65.
[8] Qi Yincheng, Jiang Aixue, Zhao Zhenbing, et al. Detection method of transmission line inspection image fittings based on improved SSD model [J]. Electrical Measurement & Instrumentation, 2019, 56(22): 7-12.
[9] Yang Gang, Sun Changwen, Zhang Na, et al. Detection of key compo- nents of transmission lines based on multi-scale feature fusion [J]. E- lectrical Measurement & Instrumentation, 2020, 57(3): 54-59.
[10] Lin T Y, Goyal P, Girshick R, et al. Focal loss for dense object detection[C]//Proceedings of the IEEE international conference on computer vision. 2017: 2980-2988.
[11] He K, Zhang X, Ren S, et al. Deep residual learning for image recognition[C]//Proceedings of the IEEE conference on computer vision and pattern recognition. 2016: 770-778.
[12] Lin T Y, Dollár P, Girshick R, et al. Feature pyramid networks for object detection[C]//Proceedings of the IEEE conference on computer vision and pattern recognition. 2017: 2117-2125.
[13] Liu S, Qi L, Qin H, et al. Path aggregation network for instance segmentation[C]//Proceedings of the IEEE conference on computer vision and pattern recognition. 2018: 8759-8768.
[14] Woo S, Park J, Lee J Y, et al. Cbam: Convolutional block attention module[C]//Proceedings of the European conference on computer vision (ECCV). 2018: 3-19.
[15] Liu W, Anguelov D, Erhan D, et al. Ssd: Single shot multibox detector[C]//Computer Vision–ECCV 2016: 14th European Conference, Amsterdam, The Netherlands, October 11–14, 2016, Proceedings, Part I 14. Springer International Publishing, 2016: 21-37.
[16] Ren S, He K, Girshick R, et al. Faster r-cnn: Towards real-time object detection with region proposal networks[J]. Advances in neural information processing systems, 2015, 28.
[17] Bochkovskiy A, Wang C Y, Liao H Y M. Yolov4: Optimal speed and accuracy of object detection[J]. arXiv preprint arXiv:2004.10934, 2020.
[18] Ge Z, Liu S, Wang F, et al. Yolox: Exceeding yolo series in 2021[J]. arXiv preprint arXiv:2107.08430, 2021.

Fuzzy Systems and Data Mining IX
A.J. Tallón-Ballesteros and R. Beltrán-Barba (Eds.)

doi:10.3233/FAIA231027

Changes of Consumer Purchase Behavior Under Data Mining Technology

Zijie Chen[1] , Rosita Binti Mohd Tajuddin, Benhui Ren and Jing Deng
College of Creative Arts, Universiti Teknologi MARA (UiTM), 40450 Shah Alam, Malaysia

Abstract. In the era of rapid development of data mining technology, diversified consumption channels have led to changes in consumer online shopping behavior. In the face of changes in consumer purchasing behavior and driven by resources, demand and data, enterprises need to innovate business models. This article aims to summarize and summarize the connotation of data mining technology, analyze the changes in consumer purchasing behavior under data mining technology, identify the dilemma of business innovation, and propose business model innovation strategies to provide management decision-making reference for enterprise e-commerce platforms. The main changes of consumers' purchasing behavior: more rational choice of brands, more emphasis on personalized services and contract spirit, more self-directed consciousness, but the supporting policies, marketing ability, cooperation ability and risk management ability in the business model fail to keep pace with the times. Therefore, this paper gives relevant targeted strategies: create a 'government+society' policy support environment, pay attention to the value of user experience, upgrade business cooperation, and strengthen risk management, so as to keep up with the pace of consumer purchase behavior changes under the data mining technology.

Keywords. Data mining, Purchasing behavior, Business model

1. Introduction

Data mining technology is deeply integrated into the e-commerce industry. In the process of online shopping, businesses use the data left by users in online shopping to mine and analyze users' behavior information and guess preferences and concerns [1]. Driven by the development of data mining technology, the change of demand, intention and perceptual behavior affect the change of consumer behavior [2]. The business model of businesses needs to be adjusted in time according to the change of consumer behavior. Consumers also put forward higher requirements for the brand, contract spirit and service safety of consumer products [3]. How to use data mining technology combined with the change of consumer purchase behavior to drive the effective innovation of business model, so as to ensure that consumption has become a positive driving force for economic development is a topic worthy of in-depth study. This paper first summarizes the relevant literature review, then finds new difficulties and analyzes problems, and finally puts forward suggestions and countermeasures. Through analysis and summary, it is concluded that in the era of data mining, business model innovation should be based

[1] Corresponding author, Zijie Chen, College of Creative Arts, Universiti Teknologi MARA (UiTM), 40450 Shah Alam, Malaysia. E-mail: huang87956673@163.com.

on changes in consumer behavior, understand consumers' feelings for brands, form a top-level policy pattern of "government+society", comprehensively improve the brand market, and fully meet consumers' perceptual needs. Tap the maximum demand of consumers, improve the ability to discover new businesses and new markets in time through data, consolidate the underlying logic of enterprise profits, timely innovate the business model and scientifically carry out the future strategic layout of the enterprise. It is found that the idea of consumer contract has changed, and the resource integration has been realized through the efficient service platform system, which makes the business cooperation more flexible and convenient. Optimize the risk management system. Respect consumers' choice of goods, establish a risk case database based on consumer choice factors, reduce the occurrence of similar risks, so as to more effectively control the risk of business model innovation in the context of data mining in advance.

2. Literature review on Data Mining

Data mining is the basis of artificial intelligence or machine learning. At present, it is mainly to mine all kinds of useful information from complex and changeable data for industry use. Data mining is usually divided into three steps: data preparation, data discovery and data representation [4]. Because data mining technology involves a wide range of fields, scholars from different research directions use different classification methods for research. What is mentioned here is the data mining classification methods that have been learned in professional knowledge textbooks at this stage, which can be roughly divided into the following four categories: statistical learning methods, machine learning methods, neural networks and database methods [5].

In the context of big data, 'data mining' technology has been widely used in all aspects of life. No matter in health care or app development, or in finance, education and other fields, you can see the traces left by data mining technology everywhere. The application of data mining technology in all walks of life shows the importance of big data in society [6]. For example, in the financial sector, most banks provide customers with a variety of savings services, insurance services or investment services [7]. In sales, data mining technology plays an important role in accumulating sales customers, dividing sales groups, and counting sales data [8]. In scientific research, the application of data mining, such as observation satellites, remote sensors, DNA molecular technology and so on, is very important [9].

With the wider application of data mining technology in the e-commerce industry, businesses can develop precise marketing strategies to conduct more in-depth analysis of existing data, such as customer segmentation and customer churn analysis [10]. Enterprises can use data mining technology to analyze sales data, identifying important customers, valuable customers, and new customers. Based on the attributes of different customers, they can infer which customers may be lost, which may have an impact on the sales of some products. This technology can also be used for time series analysis from the perspective of customer value. [11].

Data mining technology is based on customers' purchase behavior, as well as customers' own characteristics and attributes, and uses data mining to infer customers' future purchase behavior through comprehensive analysis of different dimensions [12]. That is to say, further management based on customer value can also realize store cross sales analysis, collaborative filtering recommendation, deepening customer purchase and mining customer value [13]. At the same time, the big data visualization technology can

also be used to analyze and infer the influence of customers in society, so that stores can carry out one-to-one precise sales, such as giving different discounts and preferences to customers with different influence [14]. In particular, the technology can also be used to provide personalized service mode based on customer characteristics, which not only improves the service quality, but also increases the sales profit of stores [15].

3. Research Process of Consumer Behavior Data Mining

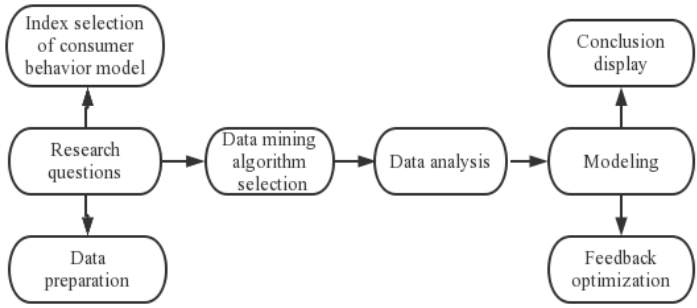

Figure 1. Consumer behavior flow chart of data mining

4. Comparative analysis of data mining algorithms

Table 1. The advantages and disadvantages comparative analysis of data mining algorithm

Algorithm name	Advantage	Disadvantage	Role
clustering algorithm	Solve numerical data	Unable to process text data, the algorithm sometimes needs to be improved	Mainly used for classification
Decision tree algorithm	The model has high efficiency and small amount of calculation	Difficult to handle continuous data	Used for forecasting and rule exploration, such as consumer churn early warning analysis
Association algorithm	Clear results, time-consuming and controllable	It is easy to ignore rare data, and the amount of calculation increases rapidly	Used for correlation analysis to find the correlation between things
Regression analysis	Clarify the relationship between variables and determine the degree of correlation	Interactions and non-linear relationships maybe ignored	For correlation analysis and hypothesis testing

5. Consumer behavior change and business innovation dilemma under data mining

Under the background of data mining, consumers choose brands more rationally, pay attention to personalized service and contract spirit, and enhance their safety awareness, but the supporting policies, marketing ability, cooperation ability and risk management ability required by the business model have not been improved in time.

5.1. Consumers pay more attention to brand rationality

Consumers' choice of brand is more rational, but the business strategy is insufficient. In the era of big data, Consumers no longer rely solely on advertising to judge the quality of a brand, and their decision-making behavior is becoming more and more rational [16]. Data mining technology makes information transparent, so that consumers are willing to spend more time and cognition to determine the final product choice, and rationally analyze the differences between brands in the form of data, so as to select the product that best meets the needs of consumers [17]. When a brand's products are far away from its needs, consumer loyalty will decline. Even in the context involvement stage, consumers will be affected by the online platform evaluation results and social media product purchase evaluation and turn to other brands [18]. It can be seen that at this stage, consumers' attention to brand rationality hides the problem of choice anxiety, which is largely due to the lack of brand management and the corresponding strategies are not in place.

5.2. Consumers pay more attention to personalized services

Personalized service is also the new demand of today's consumers, but the enterprise's exclusive big data capability is insufficient. The young consumer group's outlook on career, life and consumption is more personalized, and many middle-aged and elderly people have joined the Internet consumer group, showing diversified characteristics such as focusing on experience and giving priority to interest [19]. The overall consumption demand of consumers has been upgraded from meeting the basic needs of life to the refinement of all aspects of life, and the personalization and complexity have been continuously improved [20]. At this stage, most enterprises lack the ability of big data, lack the ability to obtain data mining resources, and lack data mining professionals, resulting in inaccurate grasp of the development trend of big data, lack of ability to use big data to locate consumer groups, and a large number of data resources are in a wasteful state.

5.3. Consumers pay more attention to the spirit of re contract

The new contract spirit has become a trend, but the enterprise industry barriers have not been broken through. The unremitting efforts of the state in the field of network security and the in-depth response of enterprises based on the consumer information have, to a large extent, prompted consumers to re-examine the spirit of contract, and it has gradually become a trend to buy 'owned' items to buy 'shared' items [21]. However, the ability to share data between different enterprises has not been improved in time, and consumer data may be cross cutting . In the face of this situation, enterprises are affected by traditional trade barriers and trade barriers in the era of big data. The insufficient and

low quality of consumer data directly affects the establishment of a close relationship between enterprises and consumers. The gap between the spirit of contract held by consumers and the connotation of enterprise business model continues to widen, which is not conducive to the breakthrough of industrial barriers.

5.4. Consumers pay more attention to self leading

Enhanced consumer subjectivity is easy to change the result of purchase choice, but the commercial risk is large. Consumers are faced with more choices of content and methods, which are affected by more objective factors, and the subjective dominance of consumption is stronger [22]. In many cases, it is easy for consumers to change their choice results through virtual purchase, or their consumption behavior has occurred and may change their choice again, bringing some unpredictable risks to the operation of enterprises [23]. The fundamental reason is that consumers' choice cost is low, but it has a great negative impact on enterprises. If the enterprise does not have certain anti risk ability, the existing business model may collapse at a faster speed, and it is too late to improve the corresponding risk management mechanism. This is a practical problem faced by many enterprises at this stage. Enterprises are likely to fail in their innovative business model due to the lack of this aspect.

6. Conclusions and Countermeasures

In the era of data mining, business model innovation should be based on the change of consumer behavior, actively create a business environment supported by the government and society, respect the value of consumer experience, reshape the cooperative relationship, and optimize the risk management system.

6.1. Understand consumers' brand feelings

Understand consumers' brand feelings and create a ‘government+society’ policy support environment. Under the influence of data mining technology, the environment created by the 'government+society' policy support can enhance the connotation and mode of brand, play a macro-control and even decisive role in brand management. The layout of government policies represents a system, which can guide the brand management and application of relevant departments and social enterprises in the general direction, broaden the development path of society and enterprises. As a stakeholder of business model innovation, the government should formulate an open policy in line with the development of commercial brands in the era of big data, and at the same time, with the assistance of special support policies [24], invest in the development of a big data commercial brand promotion platform, build a bridge between different enterprises, and promote the interconnection of different brands. On this solid basis, the government should further strengthen legislation and supervision in the face of the characteristics of prominent consumer information property rights in the era of big data, weak personal controllability, wider scope, easy disclosure, and both public and private. To this end, the government can improve the technical specifications for information security, personal information security specifications and other policy documents, specify the scope of personal data and enterprise data, and clearly define the legal, personality and

public attributes of consumer personal information, so as to enhance the attention of all sectors of society to data security [25].

6.2. Tap the biggest demand of consumers

Tap the maximum demand of consumers and strengthen the marketing operation ability. Enterprises should continue to expand the source of data resources, accurately locate consumer groups, and obtain accurate data. As a specific resource required by enterprises and even different departments, enterprises should combine their business scope with consumer data, make effective use of data analysis functions, adjust the direction of data processing and integration, realize the demand of extracting value from consumer data information, promote resource reorganization and integration, improve the ability of personal data analysis and problem solving, and accelerate the process of digitalization of individuals and enterprises. At the same time, enterprises also need to regularly organize employees to carry out data analysis reports, grasp the regions and platforms where consumers are mainly concentrated, realize user sinking, improve the ability to discover new businesses and new markets in time through data, consolidate the underlying logic of enterprise profits, timely innovate business models, and scientifically carry out the future strategic layout of enterprises [26].

6.3. Comply with the change of consumer contract concept

Comply with the change of consumer contract concept and upgrade business cooperation. In the data age, consumers' concept has changed from passive to active. They not only have a single understanding of the contract between themselves and enterprises, but also can understand the needs of enterprises to collect information. Enterprises should recognize the significant changes in consumer concepts, upgrade the business cooperation relationship in the business model, and enhance the sharing ability of 'partner+customer relationship' exchange. In the innovation of business model, the cooperation relationship is more subtle. We should not continue to rely on the so-called experience to perceive the market, but should use the big data platform to establish online cooperation relationship [27]. Enterprises should also make good use of the large-scale platform mode, use the effective service system and transaction space, and promote the formation of extensive cooperative relations between two or more enterprises to form a value-added effect. Therefore, the platform model can become a business model innovation, help enterprises accurately expand their business scope, form a new relationship of comprehensive perception and wisdom exchange between people, people and machines, people and things, promote enterprises and industries to break through barriers by using big data, realize resource integration through efficient service platform system, and make business cooperation more flexible and convenient [28].

6.4. Respect consumers' choice

Respect consumers' choices and strengthen risk management. In the process of business model innovation, the increase of uncertain factors in enterprise activities, the increase of the probability of uncertain consumer behavior and some unpredictable and uncontrollable factors jointly lead to the increase of enterprise risk [29]. It is urgent to build a risk identification framework for business model innovation, and subdivide environmental analysis, model design, organizational planning and model

implementation as macro modules. Environmental analysis should comprehensively analyze the external environment and consider customers, partners, suppliers, governments and social organizations. The risk management system should integrate and analyze the environmental subjects involved by using big data in combination with relevant theories, enterprise conditions and network environment. The pattern design module should identify the most attractive value proposition of the enterprise, analyze the potential and potential risks of value creation and innovation by using the use value and customer perception. The organization planning module comprehensively analyzes the enterprise infrastructure, the organization and coordination ability of personnel at all levels, personnel quality, employee recognition, consumer recognition and other factors, and obtains the possible risk categories of human resources using data technology software and hardware resources. The mode implementation module focuses on the recent stakeholders around the interests of the enterprise, as well as the macro risks posed by the economy, laws and policies. For the former, the risk analysis index can be refined to supplier bargaining power, competitor price strategy, partner information sharing and enterprise technology cooperation ability. For the latter, the analysis of risk indicators can be specific to social and economic stability, legal improvement and government policy support. Therefore, enterprises should further improve the risk early warning system, preset risk emergency plans, and establish a risk case database based on consumer selection factors to reduce the occurrence of similar risks, so as to more effectively control the risk of business model innovation in the context of data mining in advance [30].

References

[1] Cai Yifan. Research on online purchase behavior prediction based on user clustering and feature selection [Internet] [Master]. Huazhong University of science and technology; 2019 [see cited on August 3, 2023] Contained in: https://kns.cnki.net/kcms2/article/abstract?v=3uoqIhG8C475KOm_zrgu4lQARvep2SAkEcTGK3Qt5VuzQzk0e7M1z2ILn4Bf5QXfCulhjTtp3xBVts0tFEBI4-7QWFag4Bir&uniplatform=NZKPT

[2] Yang Dan. Research on Consumer Behavior and Precision Marketing in the Era of Big Data[Internet] [Master]. Shanghai University of Engineering and Technology; 2015 [see cited on September 15, 2023]. Contained in: https://kns.cnki.net/kcms2/article/abstract?v=3uoqIhG8C475KOm_zrgu4lQARvep2SAkVNKPvpjdBoadmPoNwLRuZyjMsvzbWum03obSQGa7rDqAkT6tMGrqlXMHKTJ2K83O&uniplatform=NZKPT

[3] Chen Kun. Research on consumer behavior changes and business model innovation in the era of big data. Journal of Shenyang Agricultural University (Social Sciences Edition). 2022;24(6):678–82.

[4] Niu Jiahui. Analysis of the Application of Data Mining in Human Resource Informationization Management. Digital Communication World. 2022;(3):94–6.

[5] Zhang Liyi, Li Yiran, Wen Xuan. Research on Predicting New Consumers' Repetitive Purchase Intention. Data Analysis and Knowledge Discovery. 2018;2(11):10–8.

[6] Sunhare P, Chowdhary RR, Chattopadhyay MK. Internet of things and data mining: An application oriented survey. Journal of King Saud University-Computer and Information Sciences. 2022;34(6):3569–90.

[7] Regin R, Rajest SS, Shynu T. A Review of Secure Neural Networks and Big Data Mining Applications in Financial Risk Assessment. Central Asian Journal of Innovations on Tourism Management and Finance. 2023;4(2):73–90.

[8] Ramageri BM, Desai BL. Role of data mining in retail sector. International Journal on Computer Science and Engineering. 2013;5(1):47.

[9] Liu Kui. Application of data mining method based on digital neural network in CRM [Internet] [Master]. Sichuan University; 2004 [see cited on 3 August 2023]. Contained in: https://kns.cnki.net/kcms2/article/abstract?v=3uoqIhG8C475KOm_zrgu4h_jQYuCnj_co8vp4jCXSivDpWurecxFtJTF2MS6zd8B5vrJyrheHOFTzAnMT4Fi6dRaD4n_r2Wk&uniplatform=NZKPT

[10] Çelik O, Osmanoglu UO. Comparing to techniques used in customer churn analysis. Journal of Multidisciplinary Developments. 2019;4(1):30–8.

[11] Zhao Tingting, Han Yajie, Yang Mengnan, Ren Dehua, Chen Yarui, Wang Yuan, Liu Jianzheng. A survey of time series data prediction methods based on machine learning. Journal of Tianjin University of science and technology. 2021;36(5):1–9.

[12] Alghanam OA, Al-Khatib SN, Hiari MO. Data mining model for predicting customer purchase behavior in e-commerce context. International Journal of Advanced Computer Science and Applications. 2022;13(2).

[13] Sumathi S, Sivanandam SN. Data mining in customer value and customer relationship management. Introduction to Data Mining and its Applications. 2006;321–86.

[14] Zhang Guangkai. The application of big data technology in enterprise strategic management. China's collective economy. 2021;(3):160–2.

[15] Cheng X, Liu H. Personalized services research based on web data mining technology. Included in: 2009 Second International Symposium on Computational Intelligence and Design. IEEE; 2009. 177–80.

[16] Yu J, Zhao J, Zhou C, Ren Y. Strategic business mode choices for e-commerce platforms under brand competition. Journal of Theoretical and Applied Electronic Commerce Research. 2022;17(4):1769–90.

[17] Pina R, Dias Á. The influence of brand experiences on consumer-based brand equity. Journal of brand Management. 2021;28:99–115.

[18] Yang Jie, Wang Lu. Influencing factors of consumers' repurchase intention under the mode of 'live+e-commerce'. China's circulation economy. 2021;35(11):56–66.

[19] Vullam N, Vellela SS, Reddy V, Rao MV, SK KB, Roja D. Multi-Agent Personalized Recommendation System in E-Commerce based on User. Included in: 2023 2nd International Conference on Applied Artificial Intelligence and Computing (ICAAIC). IEEE; 2023.1194–9.

[20] Li T, Ye X, Ryzhikh A. Consumer behavior in China and Russia: Comparative analysis. BRICS Journal of Economics. 2021;2(1):74–90.

[21] Redine A, Deshpande S, Jebarajakirthy C, Surachartkumtonkun J. Impulse buying: A systematic literature review and future research directions. International Journal of Consumer Studies. 2023;47(1):3–41.

[22] Haider M, Shannon R, Moschis GP. Sustainable consumption research and the role of marketing: A review of the literature (1976–2021). Sustainability. 2022;14(7):3999.

[23] Wang RJH, Malthouse EC, Krishnamurthi L. On the go: How mobile shopping affects customer purchase behavior. Journal of retailing. 2015;91(2):217–34.

[24] Chen CL, Lin YC, Chen WH, Chao CF, Pandia H. Role of government to enhance digital transformation in small service business. Sustainability. 2021;13(3):1028.

[25] Ikenwe IJ, Igbinovia OM, Elogie AA. Information security in the digital age: The case of developing countries. Chinese Librarianship: An International Electronic Journal. 2016;42:16–24.

[26] Lin R, Xie Z, Hao Y, Wang J. Improving high-tech enterprise innovation in big data environment: a combinative view of internal and external governance. International Journal of Information Management. 2020;50:575–85.

[27] Chen Jianxin, Zhao Xiaoke. Reconstruction of retail business model under the background of big data: factor perspective. Business economics research. 2021;(16):21–4.

[28] Ciampi F, Demi S, Magrini A, Marzi G, Papa A. Exploring the impact of big data analytics capabilities on business model innovation: The mediating role of entrepreneurial orientation. Journal of Business Research. 2021;123:1–13.

[29] Horvath J, Gavurova B, Bacik R, Fedorko R. Identification of Uncertainty Factors in the Consumer Behaviour of the New Generation of Customers at the E-commerce Level. Journal of Tourism and Services. 2021;12(22):168–83.

[30] Tohănean D, Buzatu AI, Baba CA, Georgescu B. Business model innovation through the use of digital technologies: Managing risks and creating sustainability. Amfiteatru Economic. 2020;22(55):758–74.

Fuzzy Systems and Data Mining IX
A.J. Tallón-Ballesteros and R. Beltrán-Barba (Eds.)

doi:10.3233/FAIA231028

Fully 2D Convolutional Network for Continuous Sign Language Recognition

Qidan ZHU [a] Jing LI [a,1] Fei YUAN [b] and Quan GAN [a]
[a] *College of Intelligent Systems Science and Engineering, Harbin Engineering University, Harbin, 150001, China*
[b] *Northwest Institute of Mechanical and Electrical Engineering, Xianyang, 712099, China*

Abstract. In continuous sign language recognition(CSLR) models based on deep learning, hierarchical models are more favored by researchers compared to non-hierarchical models due to their simple model, fewer parameters, and clear hierarchy. In the hierarchical model, spatial feature extraction and temporal feature extraction are separated and there is a sequential order. This paper proposes an end-to-end fully 2D convolutional network (F2DCNet) for CSLR to explore a novel spatial-temporal feature extraction method in hierarchical models. The network consists of 2D-CNN only. After extracting frame level features from sign language videos, the frame level features are concatenated by temporal dimension to form new 2D features, which are later fed into a custom 2D-CNN for spatial-temporal feature extraction, and finally the network is trained using the multi-level connectionist temporal classification(CTC) loss proposed in our previous study. We conduct experiments on two large-scale publicly available continuous sign language datasets, and the experimental results demonstrate the effectiveness of the F2DCNet, achieving highly competitive results against other advanced methods. And the proposed F2DCNet feature extraction method can be applied to other video feature extraction to extract spatial-temporal features.

Keywords. continuous sign language recognition, sequence learning, 2D spatial-temporal features, spatial-temporal feature extraction

1. Introduction

As a basic means of communication with hearing-impaired individuals, accurate sign language recognition and understanding are crucial for real life. Therefore, video based CSLR has become a research hotspot [1-4]. Its purpose is to translate a continuous sign language video into several glosses (basic units of sign language), and finally into a complete written language [5].

In recent years, with the development of deep learning, methods using deep learning for continuous sign language video recognition have taken the mainstream. As can be seen from [6], CSLR based on deep learning can be divided into hierarchical and non-hierarchical models. Compared to non-hierarchical models, hierarchical models are more favored by researchers due to their simplicity of models, small number of parameters, and

[1]Corresponding Author: Jing Li; E-mail: ljing@hrbeu.edu.cn.

hierarchy. In hierarchical models, the spatial feature extraction part generally uses classical CNN as the backbone, while the temporal feature extraction part usually uses methods such as temporal convolutional network(TCN) [7], long short-term memory(LSTM) [8] ,Transformer[9] or a combination of them for temporal feature extraction. Cheng et al. [7] proposed a new fully convolutional network that does not require pre-training, which extracts features layer by layer for CSLR. Min et al. [10] also used a hierarchical model to predict more alignment supervision through a new visual alignment constraint method, and combined 1D-CNN and Bi-directional long short-term memory(BiLSTM) to process temporal features. Gao et al. [11] proposed a Chinese sign language processing method based on RNN converters and designed a multi-level visual hierarchical transcription network to explore multi-scale visual semantic features, which also belongs to a hierarchical model.

To obtain more feature information and improve model accuracy, multimodal multicue models are applied to CSLR. Researchers in [1] combined RGB images with optical flow images to obtain continuous sign language features for recognition using a multimodal approach. In [12], researchers used graph convolution and graph Transformer to encode sign language video data in different modalities, followed by temporal feature extraction using LSTM. Parelli et al. [13] also used spatial-temporal graph convolutional networks to collect multiple feature streams, capture gesture, shape, appearance, and motion information of sign language presenters, and used BiLSTM to process temporal features to form a new deep learning framework. It can be seen that there are endless feature extraction methods for continuous sign language videos.

In this paper, we explore the spatial-temporal feature extraction approach from a new perspective, propose an end-to-end F2DCNet for CSLR, consisting of 2D-CNN solely. The network is divided into three parts: the first part uses the classic classification network ResNet[14] as the backbone, to extract frame level features from video frames; the second part is the spatial-temporal stitching module, which stitches the extracted frame-level features according to the temporal dimension to form a new 2D spatial-temporal feature; the third part is a custom 2D-CNN, which feeds 2D spatial-temporal features into the custom 2D-CNN for spatial-temporal feature extraction. Finally, we trained the network using the multi-level CTC loss proposed in our previous research [15]. We conduct experiments on two large-scale publicly available continuous sign language datasets, and the experimental results demonstrate the effectiveness of the F2DCNet, achieving highly competitive results compared to other advanced methods.

The main contributions of this paper are as follows:

1. In this paper, we propose a new end-to-end CSLR network F2DCNet, consisting of 2D-CNN only, which provides a new method for continuous sign language feature extraction.
2. The CSLR model F2DCNet proposed in this paper has been experimented on two publicly available continuous sign language datasets, both of which have achieved highly competitive results.
3. The F2DCNet feature extraction method proposed in this paper can be applied to other video feature extraction to extract spatial-temporal features.

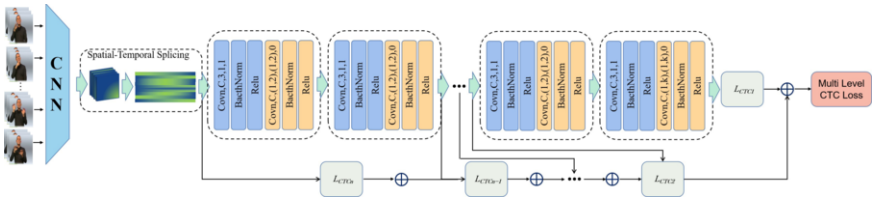

Figure 1. The overall architecture of the F2DCNet.

2. Methodology

The overall architecture of the proposed F2DCNet in this paper is shown in Figure 1. The model mainly consists of three parts: a frame-level feature extractor, a spatial-temporal stitching module and a spatial-temporal feature extractor. For the continuous sign language video, the first step is to use the frame level feature extractor composed of a classic classification network Resnet as backbone. The obtained frame level features are then expanded and concatenated according to temporal dimension through the spatial-temporal stitching module. Then, the spatial-temporal feature extractor composed of the custom 2D-CNN is used for spatial-temporal feature extraction. Finally, the network is trained using multi-level CTC loss.

2.1. Fully 2D convolutional network

The fully 2D convolutional network F2DCNet consists of three main components: a frame-level feature extractor, a spatial-temporal stitching module, and a spatial-temporal feature extractor. In this paper, we use ResNet50 as the backbone to form a frame-level feature extractor. For a continuous sign language video $V = (x_1, x_2, ..., x_T) = \{x_t|_1^T \in \mathbf{R}^{T\times c\times h\times w}\}$. with T frame as the input, where x_t is the t-th frame image in the video, $h \times w$ is the size of x_t, and c is the number of channels. First, the video is split into mutually non-overlapping segments every l frames and combined, then the continuous sign language video is $V^{'} = (x_1^{'}, x_2^{'}, ..., x_T^{'}) = \{x_t^{'}|_1^{T^{'}} \in \mathbf{R}^{T^{'}\times c^{'}\times h\times w}\}$, where $x_t^{'}$ is the t-th video segment in the video, $h \times w$ is the image size in $x_t^{'}$, $c^{'} = c \times l$ is the number of channels, and $T^{'} = \frac{T}{l}$ is the temporal length of the video after cutting. The $F_{backbone}$ is the frame-level feature extractor and obtain the feature expression as follows:

$$f_{spatial} = F_{backbone}(V^{'}) \in \mathbf{R}^{T^{'}\times c^{''}\times h^{'}\times w^{'}} \tag{1}$$

where $f_{spatial}$ is the extracted frame-level feature, $c^{''}$ is the number of channels after frame-level feature extraction, and $h^{'} \times w^{'}$ is the size of the frame-level feature map.

Then the frame-level features $f_{spatial}$ are input into the spatial-temporal stitching module F_s to obtain:

$$f_{spatial-temporal} = F_s(f_{spatial}) \in \mathbf{R}^{C\times H\times W} \tag{2}$$

where $f_{spatial-temporal}$ is the spatial-temporal feature after stitching, and the number of frame level feature channels is consistent, i.e., $C = c^{''}$, $H = T^{'}$ is the temporal length after video segmentation, and $W = h^{'} \times w^{'}$ is the length after frame level feature expansion.

Take the concatenated spatial-temporal feature $f_{spatial-temporal}$ as the input of spatial-temporal feature extractor $F_{spatial-temporal}$ for feature extraction, whose results exchange the dimensionality of channels and heights, finally classify through a fully connected layer:

$$f_{classification} = F_{Linear}(F_{spatial-temporal}(f_{spatial-temporal})) \in \mathbf{R}^{T' \times m} \tag{3}$$

where $f_{classification}$ is the final classification result and m is the number of classifications.

2.2. Multi-level CTC loss function

CTC introduced the blank label - to mark the unclassified label during decoding. For the input video V of T frames, the label of each frame is represented by $\pi = (\pi_1, \pi_2, ..., \pi_T)$, where $\pi_t \in v \cup \{-\}$, v are sign language glossary, so the posterior probability of the label is:

$$p(\pi|V) = \prod_{t=1}^{T} p(\pi_t|V) = \prod_{t=1}^{T} Y_{t,\pi_t} \tag{4}$$

For a given sentence-level label $s = (s_1, s_2, ..., s_L)$, where L is the number of words in the sentence. Then the conditional probability of label s is the sum of the occurrence probabilities of all corresponding paths:

$$p(s|V) = \sum_{\pi \in B^{-1}(s)} p(\pi|V) \tag{5}$$

where $B^{-1}(s) = \{\pi|B(\pi) = s\}$ is the inverse mapping of B and B is a many-to-one mapping defined by CTC. The CTC loss is defined as the negative log likelihood of the conditional probability of the label s:

$$L_{CTC} = -\ln p(s|V) \tag{6}$$

Then the multi-level CTC loss can be expressed as follows, where n is the number of CTCs.

$$L_{sum} = -\ln \prod_{i=1}^{n} p(s|V_i) = -\ln(p(s|V_1)p(s|V_2)...p(s|V_{n-1})p(s|V_n)) \tag{7}$$

In this paper, the 6-level loss function obtained from the 5-level downsampling layer and the 1-level frame level feature output is summed up as the final loss for training.

$$L_{sum} = -\ln \prod_{i=1}^{6} p(s|V_i) = -\ln(p(s|V_1)p(s|V_2)p(s|V_3)p(s|V_4)p(s|V_5)p(s|V_6)) \tag{8}$$

2.3. Model parameters

In this section, we show the parameter settings of the overall architecture of the fully 2D convolutional network, as shown in Table 1. We set some base conditions with an input video length of 201 frames and a resolution of $224 \times 224 \times 3$. The F2DCNet con-

sists of three main components: a frame-level feature extractor, a spatial-temporal stitching module, and a spatial-temporal feature extractor. However, only the frame level feature extractor and the spatial-temporal feature extractor exist among them with weight parameters that need to be trained.

In the frame-level feature extractor, we use the classical classification network ResNet50 as the backbone for feature extraction of video frames. In the spatial-temporal feature extractor, we use only 2D convolution as the basic unit, and still use 2D convolution to down-sample the last dimension of the data after each 2D convolution. Batch normalization and ReLu activation function operations are used sequentially after each convolution operation for the whole network.

Table 1. Parameters of the main architecture of the fully 2D convolutional network

Layer	Input Size	Input Channels	Output Channels	Kernel Size	Stride
Cat	$201 \times 3 \times 224 \times 224$	3	9	-	-
Backbone	$67 \times 9 \times 224 \times 224$	9	2048	-	-
Splicing	$67 \times 2048 \times 7 \times 7$	2048	2048	-	-
Conv	$2048 \times 67 \times 49$	2048	2048	3	1
Conv	$2048 \times 67 \times 49$	2048	2048	1×2	1×2
Conv	$2048 \times 67 \times 24$	2048	2048	3	1
Conv	$2048 \times 67 \times 24$	2048	2048	1×2	1×2
Conv	$2048 \times 67 \times 12$	2048	2048	3	1
Conv	$2048 \times 67 \times 12$	2048	2048	1×2	1×2
Conv	$2048 \times 67 \times 6$	2048	2048	3	1
Conv	$2048 \times 67 \times 6$	2048	2048	1×2	1×2
Conv	$2048 \times 67 \times 3$	2048	2048	3	1
Conv	$2048 \times 67 \times 3$	2048	2048	1×3	1×3
FC	$67 \times 2048 \times 1$	2048	1296	-	-
Softmax	67×1296	1296	1296	-	-

3. Experiment

In this section, we conduct comprehensive experiments on two widely used CSLR datasets to validate the effectiveness of the F2DCNet proposed in this paper. A series of ablation experiments are also conducted to demonstrate the usefulness of each component of the F2DCNet.

3.1. Dataset and Judgment Criteria

In this paper, we conduct experiments using two large-scale publicly available datasets, the RWTH dataset [16] and the RWTH-T dataset [17].The RWTH dataset is a sign language video recorded by the German weather broadcasting and television station. The information corresponding to the sign language video is mostly weather-related, and the recording staff are all broadcasting and television staff. A total of 9 people, wearing dark jackets, perform sign language demonstrations in front of a solid color background. After processing the recorded sign language videos, each video corresponds to a sign lan-

guage sentence, totaling 6841 different videos. The official has divided 5672 videos into training sets, 540 videos into validation sets, and 629 videos into test sets. The RWTH-T dataset is an extension of the RWTH dataset, with the demonstrators being completely consistent and only expanding on the dataset scale. There are a total of 8257 different videos, of which 7096 are divided into training sets, 519 into validation sets, and 642 into test sets. This paper is an experimental study on the first approach. We use the Word Error Rate (WER) [16] as a criterion for judging, which is defined as shown below:

$$WER = 100\% \times \frac{ins + del + sub}{sum} \tag{9}$$

where *ins* represents the number of words to be inserted, *del* represents the number of words to be deleted, *sub* represents the number of words to be replaced, and sum represents the total number of words in the label.

3.2. Implementation Rules

In the experimental implementation of the overall model in this paper, the Adam optimizer [18] is used for training, the initial learning rate and weight factor are set to 10^{-4}, and the batch size used is 4. The graphics card used in the experiments is RTX3090Ti, with a GPU-specific memory size of 24 G. The execution details of the training model on both the RWTH and RWTH-T datasets are consistent. During training, the data augmentation methods used is randomly cropped and flipped to increase the generalization of the model. The flipping and cropping process is performed for video sequences. The input data of size 256×256 is randomly cropped to 224×224, and a random flip operation is performed with a flip probability of 0.5. In addition, the length of the video sequence is also randomly grown or shortened within $\pm 20\%$. For specific training, the model is trained using 6-level of CTC loss. During model testing, only center cropping is used for data augmentation, and the beam search algorithm is used for decoding in the final CTC decoding stage, with a beam width of 10. There are a total of 85 epochs in the training phase, and the learning rate decreased by 90% in the 45th and 65th epochs.

3.3. Experimental results

In this paper, the proposed model F2DCNet is experimented on two publicly available datasets, the RWTH dataset and the RWTH-T dataset, respectively. The model recognition accuracy obtained is shown in Table 2, and the tow curves generated by WER respectively in Table 2 are shown in Figures 2 and 3.

As shown in Table 2, we compare the RWTH dataset with other advanced models and achieve highly competitive results, with WERs of 20.1% and 20.0% on the validation and test sets, respectively. As can be seen in Table 2, the F2DCNet also achieves competitive results on the RWTH-T dataset with WER of 20.0% and 20.6% on the validation and test sets, respectively. In the curves plotted in Figures 2 and 3, it can be seen that the WER decreases as the epoch increases, and there is a significant decrease in WER at the first lr change. On the RWTH dataset, WER reaches its minimum value of 20.1% at the 69th epoch in the validation set, and 20.0% at the 81st epoch in the test set; On the RWTH-T dataset, the validation set reached a minimum WER value of 20.0% at the 46th epoch, and the test set reached a minimum WER value of 20.6% at the 47th epoch.

Table 2. We compare the performance with different CSLR models on the RWTH dataset and the RWTH-T dataset, using WER as a metric (lower is better)

Methods	Backbone	RWTH		RWTH-T	
		Dev	Test	Dev	Test
Re-Sign[19]	GoogLeNet	27.1	26.8	25.7	26.6
CNN+LSTM+HMM[20]	GoogLeNet	26.0	26.0	24.5	26.5
Bi-ST-LSTM-A[21]	Custom	-	23.9	-	24.7
BiLSTM-CTC[22]	BN-Inception	23.9	24.0	24.1	24.3
VAC[10]	ResNet18	21.2	22.3	-	-
TLP[8]	ResNet18	19.7	20.8	19.4	21.2
STMC[23]	VGG11	21.1	20.7	19.6	21.0
HST-GNN[12]	ResNet-152	19.5	19.8	20.1	20.3
H-GAN[24]	Custom	18.8	20.7	-	-
F2DCNet	ResNet50	20.1	20.0	20.0	20.6

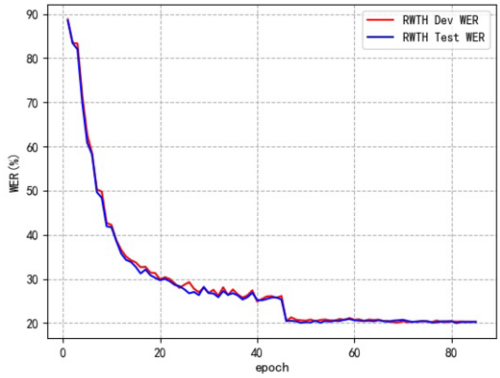

Figure 2. WER variation curves of the RWTH validation and test set.

3.4. Ablation experiment

In this section, we perform ablation experiments on the RWTH dataset to further validate the effectiveness of each component of the model, using WER as the metric, where a smaller WER represents better performance.

Ablation of the backbone depth. The ablation effect of backbone depth is shown in Table 3. This paper uses ResNet network as the backbone of the F2DCNet, but there is an impact of different depths of ResNet network on the accuracy of the model. Therefore, ablation experiments are conducted on ResNet networks of different depths. From Table 3, it can be seen that we only used ResNet18, ResNet30, and ResNet50 for experiments, while deeper ResNet networks could not be used due to GPU memory limitation. The results of the ablation experiment show that as the depth of the ResNet network deepens, the model recognition accuracy improves. At ResNet50, the validation set and test set WER reach the minimum.

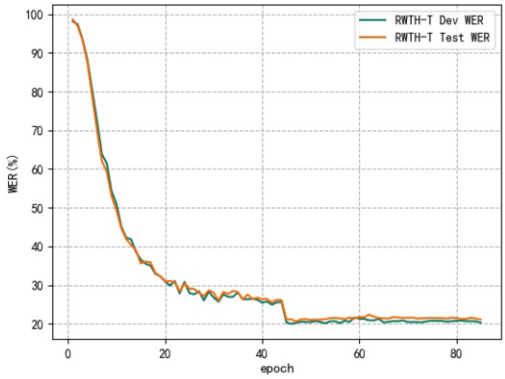

Figure 3. WER variation curves of the RWTH-T validation and test set.

Table 3. Ablation study of backbone depth

Model	ResNet18	ResNet32	ResNet50
dev	21.6	21.5	20.1
test	21.5	21.3	20.0

Ablation of the number of multi-level CTC loss function. The ablation effect of the number of multi-level CTC loss function is shown in Table 4. The multi-level CTC loss function can update the shallow network parameters and decoding time features well, and can effectively train the network model to further improve the recognition performance. The series of multi-level CTC loss function is calculated from backward to forward, and the last CTC loss function used in the network is called the level 1 CTC loss function, the penultimate CTC loss function is called the level 2 CTC loss function, and so on. From Table 4, we can see that as the number of CTC levels increases, the WER of the validation and testing sets decreases. When the CTC loss reaches to level 6, the WER reaches its minimum, at which point the validation and testing sets are 20.1% and 20.0%, respectively. At this point, compared to the Level 1 CTC loss, the validation set WER decreases by 6.3% and the test set WER decreases by 6.2%.

Table 4. Ablation study of the number of multi-level CTC loss functions

The number of multi-level CTC loss functions	1	2	3	4	5	6
dev	26.4	23.3	21.5	21.2	20.8	20.1
test	26.2	23.3	21.7	21.1	20.8	20.0

Ablation of down-sampling layers. The ablation effect of down-sampling layers is shown in Table 5. The number of down-sampling layers here refers to the number of layers in the spatial-temporal feature extractor using 2D convolution to down-sampling the last dimension. Because the last dimension of the spatial-temporal feature needs to be eliminated eventually, the change of the number of layers will affect the change in the convolution kernel corresponding to the down-sampling 2D convolution. In this paper, we input an image with a resolution of $3 \times 224 \times 224$ into the ResNet50 network, and

the final frame level feature size is $2048 \times 7 \times 7$. We pass the frame-level feature through the spatial-temporal stitching module and get the final dimensional size of the spatial-temporal feature as 49. Then when there is only 1 layer of down-sampling, the 2D convolution kernel in down-sampling is kernel=(1,49) and stride=(1,49) at this time; When there is only 2 down-sampling, the first 2D convolutional kernel in down-sampling at this time is kernel=(1,2), stride=(1,2), the second 2D convolutional kernel is kernel=(1,24), stride=(1,24), and so on. From Table 5, we can see that the 2D convolutional kernels in each down-sampling layer decreases as the number of layers increases, and the accuracy reaches the optimum when the number of down-sampling layers is 5, at which time the WERs of the validation and test sets are 20.1% and 20.0%, respectively.

Table 5. Ablation study of the number of multi-level CTC loss functions

The number of down-sampling layers	1(49)	2(2,24)	3(2,2,12)	4(2,2,2,6)	5(2,2,2,2,3)
dev	23.6	21.4	20.7	20.4	20.1
test	24.2	21.3	20.3	20.1	20.0

Ablation of the number of overlapping frames between adjacent frames. The ablation effect of overlapping frames of adjacent frames is shown in Table 6. In this paper, we divide the video into non-overlapping segments every other frame and combine them, where is the number of frames overlapped by adjacent frames. Superimposing adjacent frames and inputting them into the network for calculation can greatly reduce the computational workload of the network and also reduce the GPU memory occupied by the network during training. Due to GPU memory limitation, the number of adjacent frames superimposed starts from 3 frames for ablation. It can be seen from Table 6 that when the number of adjacent frames stacked is 3, the accuracy reaches its optimal level. As the number of stacked frames increases, the accuracy decreases. Therefore, although an increase in the number of stacked frames can reduce network computation, it also has an impact on recognition accuracy. When the number of frames is too many, it will affect the feature extraction effect and reduce recognition accuracy.

Table 6. Ablation study of the number of multi-level CTC loss functions

Number of overlapping frames of adjacent frames	3	4	5
dev	20.1	21.5	24.4
test	20.0	21.2	24.2

4. Conclusion

In this paper, we propose a novel end-to-end fully 2D convolutional network for CSLR. Different from the current spatial-temporal feature processing methods, we explore a new spatial-temporal feature extraction approach in CSLR by using only 2D-CNN network. First, the frame-level features are obtained by classical classification network as the backbone. After that, the extracted frame-level features are stitched by temporal dimension to form new 2D features. Then, the features are fed into a custom 2D-CNN for spatial-temporal feature extraction. Finally, the network is trained using the multi-level CTC loss proposed in our previous study. We perform experimental validation on two

large-scale sign language datasets, and the experimental results demonstrate the effectiveness of the proposed model in this paper, achieving highly competitive results. And our proposed F2DCNet feature extraction method can be applied to other video feature extraction to extract spatial-temporal features.

References

[1] Cui R, Liu H, Zhang C. A deep neural framework for continuous sign language recognition by iterative training[J]. IEEE Transactions on Multimedia, 2019, 21(7): 1880-1891.

[2] Huang S, Ye Z. Boundary-adaptive encoder with attention method for Chinese sign language recognition[J]. IEEE Access, 2021, 9: 70948-70960.

[3] Duarte A, Palaskar S, Ventura L, et al. How2sign: a large-scale multimodal dataset for continuous american sign language[C]. Proceedings of the IEEE/CVF conference on computer vision and pattern recognition, 2021: 2735-2744.

[4] Hao A, Min Y, Chen X. Self-mutual distillation learning for continuous sign language recognition[C]. Proceedings of the IEEE/CVF International Conference on Computer Vision, 2021: 11303-11312.

[5] Ong S C, Ranganath S. Automatic sign language analysis: A survey and the future beyond lexical meaning[J]. IEEE Transactions on Pattern Analysis & Machine Intelligence, 2005, 27(06): 873-891.

[6] Zhu Q, Li J, Yuan F, et al. Continuous Sign Language Recognition Via Temporal Super-Resolution Network[J]. Arabian Journal for Science and Engineering, 2023: 1-15.

[7] Cheng K L, Yang Z, Chen Q, et al. Fully convolutional networks for continuous sign language recognition[C]. Computer Vision–ECCV 2020: 16th European Conference, Glasgow, UK, August 23–28, 2020, Proceedings, Part XXIV 16, 2020: 697-714.

[8] Hu L, Gao L, Liu Z, et al. Temporal lift pooling for continuous sign language recognition[C]. Computer Vision–ECCV 2022: 17th European Conference, Tel Aviv, Israel, October 23–27, 2022, Proceedings, Part XXXV, 2022: 511-527.

[9] Hu J, Ni L. Transformer with sequence relative position for continuous sign language translation[C]. International Conference on Advanced Algorithms and Neural Networks (AANN 2022), 2022: 170-176.

[10] Min Y, Hao A, Chai X, et al. Visual alignment constraint for continuous sign language recognition[C]. Proceedings of the IEEE/CVF International Conference on Computer Vision, 2021: 11542-11551.

[11] Gao L, Li H, Liu Z, et al. RNN-transducer based Chinese sign language recognition[J]. Neurocomputing, 2021, 434: 45-54.

[12] Kan J, Hu K, Hagenbuchner M, et al. Sign language translation with hierarchical spatio-temporal graph neural network[C]. Proceedings of the IEEE/CVF Winter Conference on Applications of Computer Vision, 2022: 3367-3376.

[13] Parelli M, Papadimitriou K, Potamianos G, et al. Spatio-temporal graph convolutional networks for continuous sign language recognition[C]. ICASSP 2022-2022 IEEE International Conference on Acoustics, Speech and Signal Processing (ICASSP), 2022: 8457-8461.

[14] He K, Zhang X, Ren S, et al. Deep residual learning for image recognition[C]. Proceedings of the IEEE conference on computer vision and pattern recognition, 2016: 770-778.

[15] Zhu Q, Li J, Yuan F, et al. Multi-scale temporal network for continuous sign language recognition[J]. arXiv preprint arXiv:2204.03864, 2022.

[16] Koller O, Forster J, Ney H. Continuous sign language recognition: Towards large vocabulary statistical recognition systems handling multiple signers[J]. Computer Vision and Image Understanding, 2015, 141: 108-125.

[17] Camgoz N C, Hadfield S, Koller O, et al. Neural sign language translation[C]. Proceedings of the IEEE conference on computer vision and pattern recognition, 2018: 7784-7793.

[18] Kingma D P, Ba J. Adam: A method for stochastic optimization[J]. arXiv preprint arXiv:1412.6980, 2014.

[19] Koller O, Zargaran S, Ney H. Re-sign: Re-aligned end-to-end sequence modelling with deep recurrent CNN-HMMs[C]. Proceedings of the IEEE conference on computer vision and pattern recognition, 2017: 4297-4305.

[20] Koller O, Camgoz N C, Ney H, et al. Weakly supervised learning with multi-stream CNN-LSTM-HMMs to discover sequential parallelism in sign language videos[J]. IEEE transactions on pattern analysis and machine intelligence, 2019, 42(9): 2306-2320.

[21] Xiao Q, Chang X, Zhang X, et al. Multi-information spatial–temporal LSTM fusion continuous sign language neural machine translation[J]. IEEE Access, 2020, 8: 216718-216728.

[22] Papastratis I, Dimitropoulos K, Konstantinidis D, et al. Continuous sign language recognition through cross-modal alignment of video and text embeddings in a joint-latent space[J]. IEEE Access, 2020, 8: 91170-91180.

[23] Zhou H, Zhou W, Zhou Y, et al. Spatial-temporal multi-cue network for continuous sign language recognition[C]. Proceedings of the AAAI Conference on Artificial Intelligence, 2020: 13009-13016.

[24] Elakkiya R, Vijayakumar P, Kumar N. An optimized Generative Adversarial Network based continuous sign language classification[J]. Expert Systems with Applications, 2021, 182: 115276.

Fuzzy Systems and Data Mining IX
A.J. Tallón-Ballesteros and R. Beltrán-Barba (Eds.)

doi:10.3233/FAIA231029

A New Entropy–Based Uncertainty Measure for Rough Set

Luyuan CHEN [a], Yong DENG [a,1]
[a] *Institute of Fundamental and Frontier Sciences, University of Electronic Science and Technology of China, Chengdu, China.*

Abstract. Rough set (RS) theory is an efficient technique for handling uncertain information, and one of the primary tasks in RS is to measure the uncertainty of knowledge. Considering that some existing information measures may not accurately quantify the uncertainty in certain situations. In addition, Such methods seem to be less explored for describing the physical meaning behind the functions. To address such issues, we defined a new entropy-based uncertainty measure named DE(X) in this paper. Some properties of the proposed DE(X) include the performance under the coarsest and finest division are investigated and numerical examples are illustrated to show the efficiency. The result shows that DE(X) more accurately measures the uncertainty under the roughest and finest division. The comprehensive advantages of the proposed DE(X) have been stated over the existing methods.

Keywords. Entropy, Rough set theory, Uncertainty measure

1. Introduction

Rough set (RS) theory is a generalization of the classical set theory for modeling uncertainty or incomplete information [1,2]. Uncertainty measure plays a pivotal role in knowledge discovery and data mining, which is an important direction in RS theory [3,4]. The entropy of a system as defined by Shannon gives a measure of uncertainty about its actual structure [5]. Inspired by Shannon entropy, various scholars have defined information measure to calculate the uncertainty in rough set. For example, in 1998, Düntsch and Günther [6] first defined the concept of information entropy H(X) and three conditional entropy functions for the prediction of a decision attribute under a rough set environment. Liang *et. al* [7] developed a complementary entropy E(X) under RS information. Qian and Liang [8] formed a combination entropy CE(X) to measure the knowledge content. Zhu and Wen [9] suggested an information-theoretic entropy IE(X) by considering the approximate space. Tang et al. [10] constructed an uncertain entropy UE(X) to calculate the uncertainty of knowledge.

The above-listed literature suggests that several studies define the entropy measure and hence compute the degree of uncertainties of the object by using uncertain and vague

[1]Corresponding Author: Yong Deng, Institute of Fundamental and Frontier Sciences, University of Electronic Science and Technology of China, Chengdu, China; E-mail: dengentropy@uestc.edu.cn, prof.deng@hotmail.com

information. Although several entropy-based methods exist for the various problems, they fail to accurately measure the uncertainty in certain situations. For example, certain existing techniques give the value zero for the "most unsophisticated" element present in the universal set U, which implies that uncertainty does not exist in that set. However, it is evident that all objects belong to the same partition; thus, they are uncertain due to their Indistinguishability. In addition, many of the existing entropy-based methods differ due to their mathematical behavior. As a result, such approaches seem to be less explored for describing the physical meaning behind the functions.

In this paper, we introduced a concept of novel entropy, named DE(X), to overcome the hindrances of existing studies. The proposed DE(X) considers the inner-class and out-class information and thus delivers a potential physical meaning for the uncertainty. The study also notes that the proposed DE(X) meets the monotonicity property, i.e., the rougher the knowledge is, the larger the value of DE(X). To illustrate the relevance of the stated DE(X), we have assessed several numerical examples in the study and compared their results with other existing measures such as H(X), E(X), CE(X), IE(X) and UE(X). The experimental outcome reveals that the suggested entropy has an extensive advantage compared with existing methods.

The organization of this paper is presented as follows: Section 2 briefly lists basic concepts related to RS theory and uncertainty measurement. Section 3 introduces the idea of entropy measure DE(X) with RS information. Section 4 summarizes the work and advantages of the proposed DE(X) over the existing measures. Concluding remarks are given in Section 5.

2. Preliminaries

Let $\Phi = (U,R)$ be a Pawlak approximation space, and let $X = \{X_1, X_2, \ldots, X_m\}$ be a partition of U. $X = U/R = \{X_1, X_2, \ldots, X_m\}$ symbolizes the set of all equivalence classes induced by R, and called a knowledge. If $X = U$, it is the roughest division on U, while when $X = \{[u_1], [u_2], \ldots, [u_n]\}$, then it is the "most exemplary (finest)" division on U.

2.1. Pawlak rough set

Given an arbitrary set $P \subseteq U$, which is characterized by a pair of lower and upper approximations as follows [1]:

$$\underline{R}(P) = \{u \in U \mid [u] \subseteq P\} \tag{1}$$

and

$$\overline{R}(P) = \{u \in U \mid [u] \cap P \neq \varnothing\} \tag{2}$$

Here, $[u]$ represents the equivalence class regarding u. The pair $(\underline{R}(P), \overline{R}(P))$ is the representation of P in the approximation space (U,R).

2.2. Existing entropy measures

Some of existing entropy measures are listed in Table 1.

$|X_i|$ represents the cardinality of X_i, $m = |X|$ and n is the total number of objects in U. In Eq. (4) $X_i^C = U - X_i$ represent the complementary objects of X_i in U. In Eq. (5),

Table 1. Existing entropy measures

- Information measure $H(X)$ [6]

$$H(X) = -\sum_{i=1}^{m} \frac{|X_i|}{n} \log \frac{|X_i|}{n} \tag{3}$$

- Complementary entropy $E(X)$ [7]

$$E(X) = \frac{1}{n^2} \sum_{i=1}^{m} |X_i||X_i^C| \tag{4}$$

- Combination entropy $CE(X)$ [8]

$$CE(X) = \sum_{i=1}^{m} \left(1 - \frac{D^2_{|X_i|}}{D^2_n}\right) \frac{|X_i|}{n} \tag{5}$$

- Information-theoretic entropy $IE(X)$ [9]

$$IE(X) = -\sum_{i=1}^{m} \frac{r_i}{2^n} \log \frac{r_i}{2^n} \tag{6}$$

- Uncertainty entropy $UE(X)$ [10]

$$UE(X) = -\log\left(\frac{2}{n} \sum_{i=1}^{m} \frac{|X_i|}{2^{|X_i|}}\right) \tag{7}$$

$D^2_{|X_i|} = \frac{|X_i|(|X_i|-1)}{2}$, $D^2_n = \frac{n(n-1)}{2}$. In Eq. (6), r_i is the number of subsets of U that have the same lower and upper approximations with the constraint that $\sum_{i=1}^{m} r_i = 2^n$.

3. Proposed entropy

In this section, we defined a new entropy measure that comprehensively measures the uncertainty from inside and outside the knowledge.

Definition 1 *For the approximation space (U,R) and in which $X = U/R = \{X_1, X_2, \ldots, X_m\}$ symbolizes the set of all equivalence classes induced by R, referred to as a knowledge. We define a new entropy, denoted by DE(X), to measure the uncertainty of knowledge as follows:*

$$DE(X) = -\sum_{i=1}^{m} p_i \log \frac{p_i}{2^{|X_i|} - 1} \tag{8}$$

where $p_i = \frac{|X_i|}{n}$ represents the probability of equivalence class X_i within U.

The proposed entropy $DE(X)$ can be rewritten as

$$DE(X) = \sum_{i=1}^{m} p_i \log\left(2^{|X_i|} - 1\right) - \sum_{i=1}^{m} p_i \log p_i \tag{9}$$

Here, the term $\sum_{i=1}^{m} p_i \log\left(2^{|X_i|}-1\right)$ refers to the total vagueness in partition U/R, which assesses the number of segments in each division. The term $-\sum_{i=1}^{m} p_i \log p_i$ is the total measure of the nonconsensus among different divisions. Therefore, the proposed entropy has an explicit physical meaning toward the uncertainty of knowledge.

Before examining the proposed entropy properties, we state the partial order on U. Let X and Y be two different partitions on U. X is coarser than Y, which is denoted as $X \succeq Y$, if it satisfies the following equation [8]

$$\forall\ Y_i \in Y, \exists\ X_i \in X,\ \ Y_i \subseteq X_i \tag{10}$$

Proposition 1 *For the approximation space (U,R), if we consider the partition as $X = \{U\}$, that is, the coarsest division on U, we have $|X_i| = n$, which subsequently yields $p_i = 1$. Therefore, from Eq.* (8)*, we obtain $DE(X) = \log(2^n - 1)$.*

Proposition 2 *For $\Phi = (U,R)$, if we consider the finest partition on U as $X = \{[u_1],[u_2],\ldots,[u_n]\}$, then from Eq.* (8)*, we obtain $DE(X) = \log(n)$.*

Proposition 3 *For two different partitions X and Y on U such that $X \succeq Y$, then we have $DE(X) \geq DE(Y)$. DE(X) satisfies the monotonic property.*

4. Numerical examples

In this section, we have considered several numerical examples to demonstrate the effectiveness of the new proposed entropy and compared their results with the other existing measures.

Example 4.1. Consider the universal set $U = \{x_1, x_2, x_3, x_4\}$ and its division is $X = \{U\}$, i.e., the coarsest division. By using this information, Table 2 represents the obtained results for the given division with all the existing and proposed entropy measures.

Table 2. Different entropy measures regarding Example 4.1

H(X)	E(X)	CE(X)	IE(X)	UE(X)	DE(X)
0	**0**	**0**	0.67	0.875	3.91

This table shows that the computed measurement values corresponding to the entropies H(X), E(X) and CE(X) are 0, while the proposed measure and the existing measures IE(X) and UE(X) give values greater than 0. Hence, we conclude that the measures IE(X), UE(X) and DE(X) obtain good results in this situation.

Example 4.2. For an approximation space (U,R), consider the "most satisfactory" (finest) division $X = U/R = \{[x_1],[x_2],[x_3],[x_4]\}$ of the universal set $U = \{x_1, x_2, x_3, x_4\}$, which represents the knowledge. By applying the existing and proposed entropy measures on this set, we obtain the associated results listed in Table 3.

This table shows that excluding UE(X), all other entropies deliver nonzero values. This example extrapolates that the measures DE(X), H(X), E(X), CE(X), and IE(X) are sufficient for measuring the uncertainty of knowledge associated with the finest division.

Table 3. Different entropy measures regarding Example 4.2

H(X)	E(X)	CE(X)	IE(X)	UE(X)	DE(X)
2	0.75	1	4	**0**	2

From the above two examples, we determined that only IE(X) and the proposed DE(X) measures will simultaneously give the desired results under the coarsest and "most satisfactory" division.

Example 4.3 Consider the six different partitions or divisions $X1, X2, X3, X4, X5, X6$ regarding the universal set $U = \{x_1, x_2, x_3, \ldots, x_9, x_{10}\}$, as shown below.

$$X1 = \{[x_1, x_2, x_3, x_4, x_5, x_6, x_7, x_8, x_9, x_{10}]\}$$
$$X2 = \{[x_1, x_2, x_4, x_5, x_7, x_9, x_{10}], [x_3, x_6, x_8]\}$$
$$X3 = \{[x_1, x_4, x_7, x_{10}], [x_2, x_9], [x_3, x_6], [x_5], [x_8]\}$$
$$X4 = \{[x_1, x_7, x_{10}], [x_2], [x_3], [x_4], [x_5], [x_6], [x_8], [x_9]\}$$
$$X5 = \{[x_1, x_{10}], [x_2], [x_3], [x_4], [x_5], [x_6], [x_7], [x_8], [x_9]\}$$
$$X6 = \{[x_1], [x_2], [x_3], [x_4], [x_5], [x_6], [x_7], [x_8], [x_9], [x_{10}]\}$$

According to such partitions, X1 is the coarsest partition, while X6 is the finest division. From the perspective of entropy, if the rougher (coarsest) knowledge is in a particular set, more information is required to distinguish the objects, and hence, the more extensive the value of uncertainty of knowledge, i.e., entropy. Thus, the entropy values must satisfy the following requirement:

$$Ent(X1) > Ent(X2) > Ent(X3) > Ent(X4) > Ent(X5) > Ent(X6) \tag{11}$$

where $Ent(X)$ represents the entropy value of X.

For each division, we apply the proposed DE(X) and existing entropy measures such as H(X), E(X), CE(X), IE(X) and UE(X), and list their associated results in Fig. 1, show that all measures follow the monotonous property. However, we encountered that the existing measures H(X), E(X), CE(X) and IE(X) do not meet the requirement given in Eq. (11), while the proposed DE(X) and UE(X) satisfy the requirement.

Furthermore, as for the complexity, the measure IE(X) is $O(2^n)$ which needs 2^n subsets when calculating the lower and upper approximations r_i and is very high as n increases. The computational complexity of the proposed DE(X) measure is $O(1)$, the same as H(X), E(X), CE(X) and UE(X).

In summary, we conclude from all these examples that the proposed measure DE(X) efficiently works in all cases compared with H(X), E(X), CE(X), IE(X) and UE(X). In addition, the characteristic comparison of the proposed DE(X) with that in existing studies is summarized in Table 4. This analysis concludes that the proposed DE(X) measure is comprehensively superior to the other measures.

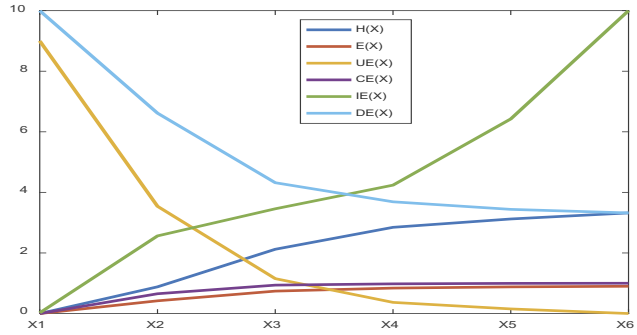

Figure 1. Different entropy measures regarding Example 4.3

Table 4. Characteristic comparison between the proposed entropy and other entropies

	Features		
Entropy	The coarsest division	The finest division	Easy calculation
H(X)	×	✓	✓
E(X)	×	✓	✓
CE(X)	×	✓	✓
IE(X)	✓	✓	×
UE(X)	✓	×	✓
DE(X)	✓	✓	✓

5. Conclusion

The main contribution of this paper is that a new entropy-based definition for measuring the uncertainty of knowledge in RS theory is presented, which is abbreviated as DE(X). The proposed DE(X) measures the uncertainty from the vagueness in each partition and the nonconsensus among different divisions, which considers inner- and outer-partition information, thus delivering a potential physical meaning for the uncertainty. The properties including the performance under the coarsest and the finest division are explored, which proofs that the proposed DE(X) measures the uncertainty more accurately compared to existing methods like H(X), E(X), CE(X), IE(X) and UE(X). DE(X) has a comprehensive advantage compared with existing methods. The new entropy provides a novel perspective to understand the uncertainty, and also gives a promising way to measure the uncertainty in rough set.

References

[1] Zdzislaw Pawlak, Lech Polkowski, and Andrzej Skowron. Rough set theory. *KI*, 15(3):38–39, 2001.

[2] Qinghua Zhang, Shuaihua Yang, and Guoyin Wang. Measuring uncertainty of probabilistic rough set model from its three regions. *IEEE Transactions on Systems, Man, and Cybernetics: Systems*, 47(12):3299–3309, 2016.

[3] Zhaohao Wang, Huifang Yue, and Jianping Deng. An uncertainty measure based on lower and upper approximations for generalized rough set models. *Fundamenta Informaticae*, 166(3):273–296, 2019.

[4] Shengjun Liao, Xianyong Zhang, and Zhiwen Mo. Three-level and three-way uncertainty measurements for interval-valued decision systems. *International Journal of Machine Learning and Cybernetics*, 12(5):1459–1481, 2021.

[5] Claude E Shannon. A mathematical theory of communication. *The Bell system technical journal*, 27(3):379–423, 1948.

[6] Ivo Düntsch and Günther Gediga. Uncertainty measures of rough set prediction. *Artificial intelligence*, 106(1):109–137, 1998.

[7] Jiye Liang, Kwai-Sang Chin, Chuangyin Dang, and Richard CM Yam. A new method for measuring uncertainty and fuzziness in rough set theory. *International Journal of General Systems*, 31(4):331–342, 2002.

[8] Yuhua Qian and Jiye Liang. Combination entropy and combination granulation in rough set theory. *International Journal of Uncertainty, Fuzziness and Knowledge-Based Systems*, 16:179–193, 04 2008.

[9] Ping Zhu and Qiaoyan Wen. Information-theoretic measures associated with rough set approximations. *Information Sciences*, 212:33–43, 2012.

[10] Jianguo Tang, Jianghua Wang, Chunling Wu, and Guojian Ou. On uncertainty measure issues in rough set theory. *IEEE Access*, 8:91089–91102, 2020.

Fuzzy Systems and Data Mining IX
A.J. Tallón-Ballesteros and R. Beltrán-Barba (Eds.)

doi:10.3233/FAIA231030

Application of AI Technology in Online Platforms Based on Cognitive Emotion Regulation

Qian ZHOU [a,1]
[a] *School of Foreign Language Studies, Anhui Sanlian University, Hefei, Anhui, China*

Abstract. In order to cater to the reform of online platforms and improve online users' learning efficiency, this study conducted a design and readjustment of the function of online platforms through application of AI Technology based on cognitive emotion regulation. The results show that AI Facial Recognition Technology can not only identify and regulate users' emotional states, but also improve the learning states in the online learning process. It is effective in cultivating online users' planning and adjusting the content of online platforms. The research put forward improving strategies of online platforms. The results mark a new direction for the improvement of learning state and lay a theoretical foundation for the design of online platforms.

Keywords. Online platform, AI Facial Recognition Technology, Learning states, Cognitive Emotion Regulation

1. Introduction

Due to the COVID-19 outbreak and the development of era, the number of active users of online platform applications is increasing. More and more users choose to use online platforms to improve themselves and make up for their shortcomings in professional knowledge and skills[1]. Meanwhile, Online platforms hope to take advantage of the period of rapid growth and enhance platform functions[2]. In view of such a market demand, people gradually realize that obvious manifestation of individual differences of user groups in online platforms and the differences in individual users' learning status will lead to inefficient learning and low-quality education[3]. Therefore, how to solve the problems of online learning inefficiency and low education quality has become the core of online platform development[4]. With the continuous development of artificial intelligence, more and more online platforms hope that AI technology can become a dynamic engine to help online education platforms solve the problem of individual learning status differences[5]. The author takes AI Facial Recognition Technology as a technical tool and takes cognitive emotion regulation of cognitive linguistics as the theoretical basis to explore the adjustment of individual learning state, with an aim to improve the learning efficiency and teaching quality of online platform.

[1] Qian ZHOU (1984-), female, Jiang Su, School of Foreign Studies, Anhui Sanlian University, Associate Professor, Research Interests: Foreign Linguistics and Applied Linguistics; E-mail: 114954052@qq.com.
Funding Resources: The paper is one of the results of the Anhui Provincial Humanities & Social Sciences Project (Code: 2022jyxm482)&(Code:SK2021A0794)& (2023AH051676).

2. Literature Review

2.1. Researches on SRL

It is known that current educational research shows individual cognitive state and learning state become important factors which affect learning. Cognitive state refers to different individual receptivity or understanding of the same knowledge and the same teaching method such as the influence of personal state, education level, learning background and other factors. Studies on self-regulated learning (SRL) show that excellent students can recognize their individual differences in self-regulated learning, and they often use self-regulated learning (SRL), an effective learning method to improve their learning efficiency[6]. Therefore, learners must set goals and make plans before starting to learn. Individuals who involved in certain learning need to monitor and adjust their own cognition, motivation and behavior, and reflect on the learning process, which should be repeated as a cycle. Moreover, learning state is also a very important factor in the teaching process which affects teaching quality and learning efficiency. Professor Wilson, Prosser and Trigwell conducted an empirical analysis of the relationship between learning environment and learning style. Learners have two learning styles: shallow and deep[7]. According to their findings, the better the students' cognitive and perceptual abilities, the more willing the students are to use the deep learning style; Otherwise, students learn at a shallow level. In online platform learning, students' cognitive state may be weakened due to the disappearance of classroom and school. According to the latest research by The National Engineering Research Center for Electronic Learning of Central China Normal University, students' facial expressions identifies students' different cognitive emotions and students' different motions will also have a great positive or negative interference effect on learning cognitive state[8]. Learners learn best when they are focused and in a positive mood. In addition, according to the study, when faced with science or math class, positive emotions can help learners to build confidence and a sense of accomplishment, and too difficult subject can cause the learner to escape because of the psychological fear. These emotions will significantly reduce the learner's cognitive level and learning speed. Therefore, in order to improve the quality and efficiency of the online platform, personalized teaching method must be carried out according to the individual cognition and learning state of different students.

2.2. AI Recognition of Facial Expressions

The study of intelligent perception and identification of facial expressions began in the 19th century. In 1872, Darwin first proposed a theory of the consistency of expressions. He pointed out that the meaning of facial expressions does not change with gender or race. In 1970, Ekman and Friesen made a pioneering and important work in facial expression recognition. They studied and determined seven basic types of human expressions: happy, sad, afraid, disgusted, surprised, angry and neutral. Having developed seven basic expressions, Ekman and Friesen developed a specific Coding System for facial expressions based on human facial features: the Face Action Coding System (FACS) [9]. In this system, a total of 44 independent but related monomers are used to describe human face motion. According to this basic coding system, researchers in various countries have established a number of different facial expression libraries [10]. These libraries provide key resources and important learning

basis for the development of AI facial expression recognition[11]. The commonly used methods of artificial intelligence identification can be roughly divided into feature extraction method and classification of learning. Feature extraction method is to determine individual expression by extracting the available features during recognition. For example, Kunar Chanda in India used optical flow method to extract facial expression features, and applied facial expression recognition to human-computer interaction design[12]. The classification of learning is an intelligent facial expression recognition technology that classifies the facial expressions in the facial expression library and generates deep learning through artificial intelligence[13]. Its recognition rate is relatively high and its application is more extensive. CNN, an artificial neural network for image processing, is composed of different layers, namely convolution layer, convergence layer and complete connection layer. There are many expansion studies on deep learning network expression recognition technology based on CNN, and the recognition rate can be improved[14]. The recognition rate in current studies can reach 93%-95%. In addition, present artificial intelligence is more mature in the recognition of individual attention than facial expression recognition[15]. The main research method is to determine through sight capture. When the user's line of sight deviates from the core target area, the intelligent technology will judge the user as an unfocused state. Facial expression recognition and eye line recognition of integrated artificial intelligence can basically determine individual emotion and attention, and studies showed that the success rate of intelligence recognition was more than 80%. Therefore, it is feasible to apply AI facial recognition technology to online platforms[16].

Artificial intelligence will change future teaching in three aspects: the first is to change the method of online and offline education, embedding artificial intelligence technology into tangible physical spaces and intangible virtual data spaces, thereby filling online education with warmer feeling of knowledge ocean. The second is to change the teaching skills of teachers. Through the intervention of AI recognition technology, the teacher can provide personalized development paths for students in online education applications, and design improvement plans to improve the quality of online education. The third is to change students' ways of learning and provide personalized and customized learning content methods to stimulate their deep-seated learning desire. After AI empowers education, immersive perceptual interaction is designed through scene optimization to improve students' learning enthusiasm, achievement, thereby improving the quality of online products.

Through literature review of online platform application, the author found that most of the former research was focused on specific groups of people who participate in online platform. For example, for primary school and preschool children, and the study often aimed to help students understand the curriculum through game-assisted teaching and narrative role-playing teaching[17]. In addition, research and analysis were mainly conducted from the perspective of teaching methods. Some studies found teaching could be carried out through online platforms for specific courses, such as the education of music courses by using acoustic wave[18]. Therefore, based on the above findings, in the design of online platform, it is necessary to consider the basic needs of users and the nature of the course. These studies demonstrate that there are certain differences among individual learners and courses. The advantage of offline traditional education over online education lies in efficient interaction. To improve the quality and learning efficiency of online platforms, the interaction between teachers and students also needs to be taken into consideration[19].

3. Research Tools

Cognitive psychology has given the basic definition of emotion in related disciplines: emotion is the attitude experience of an organism reflecting the relationship between objective things and subjective needs. According to its definition, when the needs of the individual are satisfied, there will be positive emotions, otherwise there will be negative emotions[20]. The emotional subject at this time not only refers to human beings, but is a common feature of animals. Different objects will have different emotional impact on the same person, and different subjects will have different emotions on the same object[21]. After analyzing and disassembling emotions, researchers evaluated and observed emotions from two perspectives: basic emotions and emotional dimensions. The basic emotion theory orientation is the seven basic human emotion expressions defined by Ekman and Friesen above, which forms all human expressions through the combination of different basic expressions. The orientation of the emotion dimension theory is to form the emotion coordinate system through the three basic dimensions, and carry on the emotion evaluation and evaluation through the coordinate system. The three basic dimensions are valence, dominance and arousal. Valence refers to the positive and negative degree of emotion and experience, arousal refers to the influence of emotion on physical behavior, and dominance refers to the control of individuals emotions. Although facial expression is not only reflected by facial change, facial change is the most important expression of emotion, so it lays a theoretical foundation for artificial intelligence facial recognition to recognize individual emotion[22].

According to the above research, it is known that individual cognition and learning state are affected by objectives, thus arousing certain differences. Firstly, from the study of individual group attributes, it is found that individual cognitive intelligence and cognitive ability are closely related to age group. After analyzing the relationship between age group and cognitive ability, this paper finds that young people aged 18-27 are in a relatively mature state of cognitive ability and have the desire for professional skill improvement and interest in learning, furthermore, this group has the ability of autonomous learning. The research investigates the tendency of individuals to adjust their consciousness when they are affected by negative emotional states. The tendency varies in different age groups. This paper advocates regulating users' emotional states in the online learning process through recognition of individual learning states, formulating emotion regulation strategies according to different learning states, and adjusting the content of online platforms, with an aim to improve the learning efficiency and teaching quality of the platform.

4. Research Design

4.1. AI Attention and Facial Information Recognition

Artificial Intelligence Application is used as a tool in this research. It is found that students' learning state is composed of attention state and emotional state, and the change of learning state will have a significant impact on students' learning efficiency and education quality. The change of learning states has obvious influence on students' learning efficiency and education quality. Although artificial intelligence is poor in direct recognition of learning state, it can help with the recognition of learning state

through recognition of individual attention and recognition of facial expressions and emotions. AI attention recognition can be divided into two parts, head posture recognition and sight recognition respectively. The combination of these two parts together constitutes the body's attention recognition. Head pose recognition is accomplished through a process from face recognition to pose feature recognition and then to pose datum recognition. This technical process is the same as facial expression recognition in the first half of the technical process. Facial expression recognition also determines facial recognition by features first, and then obtains individual facial expressions of users by feature and classification. Therefore, individual head posture recognition and facial expression recognition can be technically combined, and their sensing terminals are similar. At present, users' facial information can also be obtained through camera sensors, and it is feasible to apply it to mobile terminals.

4.2. AI Learning State Recognition

Technically, the AI facial recognition technology can be combined with head posture to speculate the user's attention and estimate the emotional state of the user. The attention state and emotional state can tell the users' learning state. In addition, although eye-motion processing technology cannot be carried out by means of facial recognition yet, its technical feasibility can also help the machine recognize the user's head posture and improve the accuracy of identifying the user's attention state[23].

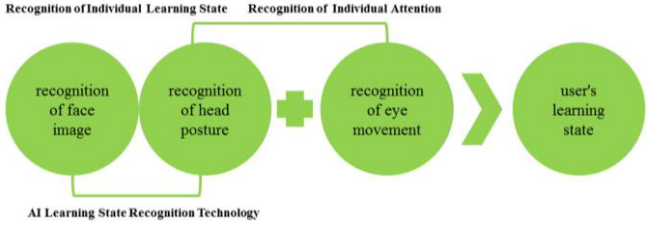

Figure 1. AI Learning State Recognition Technology Diagram

Since the excellent performance of the AlexNet model in image classification competitions, a new convolutional network model is constructed based on the structure of the AlexNet network model and referring to the parameter configuration of the VGG model, and name it the Continuous Net model. At the same time, in order to demonstrate the effectiveness of the improved model, the AlexNet model was compared and modified. The process is as follows: change the single convolutional structure of the first two layers of the AlexNet model to two continuous convolutional structures similar to the VGG model, while keeping the subsequent structure and fully connected layers unchanged, thus forming a new Continuous Net model. Compared with the AlexNet model, the new model has a 10-layer structure and two more convolution operations than the 8-layer AlexNet model, which uses two more nonlinear activation function. The specific network model is shown in Figure 2.

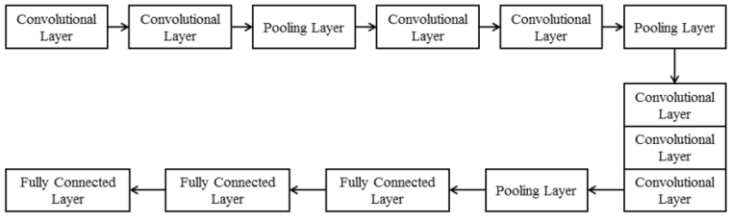

Figure 2. Structure diagram of Continuous Net model

The input data of the improved Continuous Net model are 48*48 black and white emoticon images. The convolutional kernel size of the first convolutional layer is 4*4, the sliding step size is 2, and 64 convolutional kernels are set. Then use the ReLU function as the Activation function, and the size of the pooled operation window is 2*2, with a step size of 2. The second convolutional layer is connected to the first convolutional layer, connecting 4*4 convolutions concatenated together, equivalent to an effect of convolution7*7, but the number of parameters is only half of the previous one. This method of concatenating multiple small convolutions for continuous convolution also increases the usage times of ReLU nonlinear activation, thereby enhancing the model's ability to survey image features.

4.3. The Identification of Three-level Learning States

This study focuses on the research and formulation of adjustment strategy for individual learning state. Therefore, in terms of intelligent recognition of individual learning state, mature research conclusions are used as a technical tool to determine the technical basis, and design practice is completed on this basis. This paper adopts conclusion of individual learning state recognition in the research document *'Towards emotion-sensitive learning cognitive state analysis of big data in education: deep learning based facial expression analysis using ordinal information'* published in 2020 by researchers from The National Engineering Research Center for Electronic Learning of Central China Normal University in Wuhan, China. Through the procedure of AI recognition of face image, head posture and eye movement, the user's learning state is further divided into two aspects, namely, emotional state and learning state. According to the recognition results, the user's learning state is divided into three grades: poor, medium and good. Based on the identification of the three levels, this study puts forward that the formulation and design of AI learning state adjustment can be applied for online platform users to improve their online efficiency.

5. Data Collection and Analysis

The purpose of this experiment is to verify the performance of the improved CNN model - Continuous Net model, and compare it with the Alex Net model. Divide the images from the CK+ emoticon library into training and testing sets in an 8:2 ratio, among which, there are 1084 training images. Set Batch size to 16, requires 68 attempts to complete all training samples. The FER2013 emoticon database training set has 28708 images and among which 64 images are randomly selected with the batch size set or one training batch. Input two types of database images into the above two models for training, and take the first 600 iterations of the training process to obtain the correct

recognition rate change curve images of the two image training sets, as shown in Figure 3.

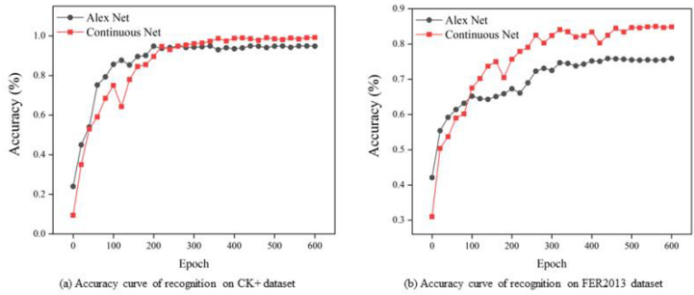

Figure 3. Accuracy curves of recognition of the models on two training datasets

From the accuracy curve of the CK+ training dataset, it can be seen that the recognition rates of both models improve rapidly in the first 200 epochs, while the recognition rate curve of the Alex Net model tends to be stable, but the recognition rate of the Continuous Net model is still increasing, reaching a plateau after 400 epochs. Therefore, the Continuous Net model shows better recognition performance than the Alex Net model on the CK+ training set. On the FER2013 training set, the Continuous Net model also shows better recognition performance compared to the Alex Net model. The Continuous Net model proposed in this study has an accuracy of nearly 100% on the CK+ training set and over 80% on the FER2013 training set. However, because the Continuous Net model is slightly more complex than the Alex Net model, more images are needed to complete the training process of parameter optimization, making the Rate of convergence of the Continuous Net model lower than that of the Alex Net model.

When specific artificial intelligence recognition technology is applied to online education applications, whenever the intelligent technology determines that the user's learning state is low or high, corresponding functions and strategies need to be used to help users adjust their learning state, in order to avoid the low learning efficiency of users affecting the learning of course content. In addition, from the perspective of feedback, real-time recognition of the attention and emotional states of all users of the same course can help evaluate and analyze the structure and state of the course content. Such accurate and efficient feedback can effectively assist teachers or course creators in adjusting and improving course content. From the above, research on the application of AI recognition in online education, there is still relatively wider possibility on the technical feasibility, and lack of specific functional design research in the application.

This study will utilize the specific artificial intelligence recognition technology mentioned earlier to supplement the practical application scenarios of emotion regulation strategies in online education. A cognitive emotion regulation questionnaire was used to conduct a survey on the emotional regulation methods and strategy preferences of users. The survey focused on young users who focus on self-directed learning and career improvement. Research on this group of users can provide more accurate perception of strategic tendencies based on potential users, providing a reference for the practical application of artificial intelligence technology in online education content settings.

The Cognitive Emotional Regulation Questionnaire was designed by N.Garnefski. The revised version of the Cognitive Emotion Regulation Questionnaire (CERQ-C) will be used in this project. The revised CERQ has a total of 32 question options, including 8 dimensions: self-blame, tolerance, contemplation, positive adjustment,

positive imagination, self-comfort, disaster, and blaming others. The questionnaire of this study is distributed to young people aged 18-27, who are in line with online user groups with independent professional skills and knowledge upgrading requirement. The author used the questionnaire as the distribution channel and conducted descriptive statistics on the results to obtain the regulatory strategy preferences of this user group. AI technical methods were used in research to form strategy and help design test. Through questionnaire for the core users of career promotion in online platforms, users' tendency of emotion regulation was found to be 3 aspects, namely, positive assumption, positive adjustment and tolerance. The three tendencies were expanded and transformed into 5 behavior adjustment methods, which are designed into a five sub-scale questionnaire, and the author made these five ways of emotional state regulation in the process of online education into a questionnaire and sent it to the user groups who had participated in the previous questionnaire survey for research.

Questionnaire1 was designed and a survey was conducted on the same experimented users. By comparing the results of consistency and similarity, the recognition degree of cognitive adjustment in the online platform was investigated and the user's demand tendency was obtained. The questionnaire was distributed online with a total of 110 questionnaires, including 2 invalid and 108 valid.

Questionnaire 1

Table 1. Results of the questionnaire on behavioral adjustment of online learning

Adjustment dimension	Subjects	N	M	SD	D (X)
Positive assumption T1/T2/T4/T5	I think we should reduce the difficulty of learning content to improve learning status?	108	3.78	1.213	1.471
Positive assumption T3/T6	I should review the courses I just learned to improve the parts I didn't learn well before?	108	3.21	0.956	0.914
Tolerance	I can't change the emotions I have got. I need to keep learning?	108	2.43	1.103	1.217
Positive adjustment	I think the current state is not suitable for the current study. I should learn other contents to adjust?	108	3.63	1.311	1.719
Positive assumption T7/T8	I want to overcome the negative state and deal with the more difficult content with a positive attitude.	108	3.54	1.323	1.750

From the perspective of design, users need to have a certain degree of cognitive recognition of individual needs in order to have a certain degree of acceptance of the relevant improved functions of mobile applications. Therefore, it is necessary to observe the needs and recognition of users through the investigation of the cognitive degree of the impact of users' learning state and learning efficiency and the recognition degree of adjusting learning state through learning strategies. The author uses the software Questionnaire Star and the main form of the topic is 5-subscale, which is distributed online with a total of 281 valid data. The results are shown below.

Questionnaire 2

Table 2. Research results of the recognition of learning state regulation

Subjects	N	M	SD	D (X)
Do you agree that personal learning efficiency will be affected by emotion or attention?	281	3.87	0.865	0.748
Do you agree that inattention will affect memory, comprehension and learning efficiency?	281	4.21	0.952	0.906
Do you agree that concentration can improve memory, understanding and learning efficiency?	281	4.13	0.803	0.645

Do you agree that negative emotions can make people tired of studying and courses?	281	4.23	0.841	0.707
Do you agree that positive emotions will improve learning efficiency?	281	4.35	0.765	0.585
Do you agree that your attention and mood will be affected by the course content?	281	3.92	0.847	0.717

It shows that emotional state and attention state will affect learning efficiency. In addition, the average score of the questions is 3.87, and its user recognition is relatively high. Therefore, the function of relevant online education applications can be improved through course adjustment.

In the survey of online learning state adjustment, the author also conducted a 5 sub-scale. Questionnaire 3 is based on teachers who have been engaged in education. The main topic is to investigate teachers' recognition of adjusting students' learning state through curriculum content or curriculum process changes, as well as their recognition of strategies to adjust curriculum content through students' learning state feedback. A total of 63 teachers' questionnaires were collected and the results are shown below.

Questionnaire3

Table 3. Research results of teachers' attitude towards learning state adjustment

Subjects	N	M	SD	D (X)
Do you agree that the teacher can adjust the course content or course progress at any time according to the students' state?	63	4.33	0.614	0.377
Do you agree that teachers should adjust the course content according to students' state feedback?	63	4.1	0.781	0.610

Teachers have a supportive attitude towards the adjustment of learning curriculum content through the perception of students' state, and they agree to adjust the curriculum according to the feedback of students' state. Therefore, it is feasible to adjust and improve the online education application function of teachers' direction.

Through market research on online platforms such as Chaoxing, Tencent Conference and other similar products, this paper finds that core users of online platforms for autonomous skills-improving learning is more inclined to regulate emotions by reducing the difficulty of the course, reviewing the course with low emotion and adjusting the content of the online courses. According to the emotion regulation data obtained from the questionnaire survey of cognitive emotion regulation theory, the improvement strategy of online platform is proposed.

6. Conclusion

Based on the application of AI recognition technology and theory of cognitive emotion regulation, this paper explores the functions and strategies for improving learning state in online platforms. In view of the learning tendency of online core users, the emotion regulation strategy is transformed into course regulation. The research was conducted from emotion regulation to individual learning state and to improve learning efficiency. In the research, AI technology such as facial expression, head posture and eye movement state were applied to the study of learning state recognition. The improvement strategy of online platform is put forward. The research results mark a new direction for the improvement of learning state and lay a theoretical foundation for the design of online platforms.

References

[1] Peng Q. The Interaction Design of Mobile Apps for Chinese Early Education. Design, User Experience, and Usability: Designing Pleasurable Experiences. 2017, 10289: 288-289.

[2] Chen MP, Wang LC. The Effects of Type of Interactivity in Experiential Game-Based Learning. Learning by Playing. Game-based Education System Design and Development. 2009, 5670: 273-282.

[3] Tsai CW. Improving Undergraduates' Experience of Online Learning: An Approach of Web-Mediated Self-Regulated Learning and Collaborative Learning. Advances in Computer Science and Education Applications. 2011, 202: 346-349.

[4] Yimeng Xu, Linong Dai. Research on the Influence of Situational Teaching Mode on Online Learning Experience. Design, User Experience, and Usability. Application Domains. 2019, 11585: 514-527.

[5] Bernardo P D, Bains A, Westwood S, et al. Mood Induction Using Virtual Reality: a Systematic Review of Recent Findings. Journal of Technology in Behavioral Science, 2021, 6(1): 3-24.

[6] Yang Y, Van Aalst J, Chan C. Dynamics of reflective assessment and knowledge building for academically low-achieving students. American Educational Research Journal, 2020, 57(3): 1241-1289.

[7] Xu Y, Dai L. Research on the influence of situational teaching mode on online learning experience. Design, User Experience, and Usability. Application Domains, 2019, 11585: 514-527.

[8] Chen J, Lv Y, Xu R, et al. Automatic social signal analysis: Facial expression recognition using difference convolution neural network. Journal of Parallel and Distributed Computing, 2019, 131: 97-102.

[9] Ekman P, Friesen W V. Constants across cultures in the face and emotion. Journal of personality and social psychology, 1971, 17(2): 124-129.

[10] WuDan, LinXue-yin. The design and realization of avideo database for facial expression analysis. Computer Engineering and Applications. 2004, 40(5): 177-180.

[11] Gunnar Schmidtmann,Ben J. Jennings,Dasha A. Sandra,Jordan Pollock, Ian Gold. The McGill Face Database: Validation and Insights Into the Recognition of Facial Expressions of Complex Mental States. Perception. 2020, 49(3): 310-329.

[12] Kunal Chanda, Washef Ahmed, Soma Mitra,Debasis Mazumdar. Improvement and Estimation of Intensity of Facial Expression Recognition for Human-Computer Interaction. Advanced Computing, Networking and Informatics. 2014, 1(27): 629-636.

[13] Xu R, Chen J, Han J, et al. Towards emotion-sensitive learning cognitive state analysis of big data in education: deep learning-based facial expression analysis using ordinal information. Computing, 2020, 102(10): 765-780.

[14] Li K, Jin Y, Akram M W, et al. Facial expression recognition with convolutional neural networks via a new face cropping and rotation strategy. The Visual Computer. 2020, 36(2): 391-404.

[15] Javier Marín-Morales, Higuera-Trujillo J L, Greco A, et al. Affective computing in virtual reality: emotion recognition from brain and heartbeat dynamics using wearable sensors. Scientific Reports, 2018, 8(1): 13657.

[16] Ray A, Chakrabarti A. Design and implementation of technology enabled affective learning using fusion of bio -physical and facial expression. Journal of educational technology & society, 2016, 19(4): 112-125.

[17] Lim M.Y. et al. Towards Intelligent Computer Assisted Educational Role-Play. Learning by Playing. Game-based Education System Design and Development. 2009, 5670: 208-219.

[18] Muis K R, Sinatra G M, Pekrun R, et al. Main and moderator effects of refutation on value， epistemic emotions and learning processes during knowledge revision. Contemporary educational psychology, 2018, 55(1): 155-165.

[19] Lin L, Ginns P, Wang T, et al. Using a pedagogical agent to deliver conversational style instruction: What benefits can you obtain?. Computers & Education, 2020, 143:103658.

[20] Garnefski N, Kraaij V, Spinhoven P. Negative life events, cognitive emotion regulation and emotional problems. Personality and Individual Differences, 2001, 30(8): 1311-1327.

[21] Buchanan T W. Retrieval of emotional memories. Psychol Bull, 2007, 133: 761-779.

[22] Black M J, Yacoob Y. Recognizing facial expressions in image sequences using local parameterized models of image motion. International Journal of Computer Vision, 1997, 25(1): 23-48.

[23] Wang X, Zhao X, Zhang Y. Deep-learning-based reading eye-movement analysis for aiding biometric recognition. Neurocomputing, 2020, 444: 390-398.

Fuzzy Systems and Data Mining IX
A.J. Tallón-Ballesteros and R. Beltrán-Barba (Eds.)

doi:10.3233/FAIA231031

Birth Rate Prediction System Based on Grey Prediction and Gradient Boosting Regression Tree Ensemble Model

Weibo Huang[1], Fei Lin, Yijia Qin and Li Ling
Guangdong University of Foreign Studies, Guangzhou, China.

Abstract. We selected several factors affecting the Birth Rate in Guangdong Province. Then we saw the contribution of each characteristic to the Birth Rate by the gradient boosting regression tree model. The grey prediction algorithm used each characteristic to predict its value in a certain year. Using variance ratio and small residual probability, we evaluated the prediction accuracy. We used the gradient boosting regression tree for predicting the Birth Rate in the next two years. This was done under the premise of knowing the data of each characteristic. The thinking of the factors affecting the Birth Rate and the prediction of the Birth Rate prompt us to think about the relevant realistic factors. They also assist the government in focusing on the adjustment of fertility policy. The aim is to promote population development and social progress to the greatest extent possible.

Keywords. Grey prediction, gradient boosting regression tree, combination model, birth rate prediction

1. Introduction

The development mode of different regions is different, different time stages will have different effects, and the change trend of Birth Rate is also different. At present, the research on the Birth Rate is mainly based on national theoretical and practical analysis. But the research on the analysis and prediction of the Birth Rate of each province need to be further studied. This paper takes the relevant data of Guangdong Province as an example to explore and analyze from a more microscopic perspective. Secondly, the current research on the Birth Rate mostly focuses on fertility desire and fertility behavior. It lacks a comprehensive analysis of more dimensions such as economy and education level.[1][2] While realizing the Birth Rate prediction, this work also demonstrates the contribution of each feature to the birth rate. It further analyzes the main factors that cause the birth rate change in multiple dimensions.

This paper analyzes data from the Guangdong Statistical Yearbook. To forecast the birth rate, we first identify the key factors that may influence the birth rate in Guangdong Province. We select these influencing factors and screen out nine factors that have a significant impact on the birth rate. Next, we employ the grey prediction algorithm to forecast the values of these nine indicators for the next two years. Finally, we use the

[1] Corresponding Author, Huang Weibo, Modern Education Technology Center, Experimental Teaching Center, Guangdong University of Foreign Studies, China; This study is financially supported by the 2021 Guangdong Higher Education Teaching Research and Reform Project. Email: hwb444@163.com

gradient boosting regression tree model with the parameter values to predict the birth rate of Guangdong Province for the next two years. However, we observed that the predictions provided by the random forest model, KNN, and SVR were inaccurate in forecasting the birth rate.[3]

2. Method design

Firstly, the system used gradient boosting regression tree for feature selection.[4] We screened out nine influencing factors that made a greater contribution to the birth rate. Secondly, we used the combination model of grey prediction and gradient boosting regression tree to predict the birth rate. The following will show the data indicators selected by the study and the required algorithms.

2.1. Indicator description

This paper selected the Birth Rate from 2000 to 2021 and 13 representative factors that may affect the Birth Rate in Guangdong Province. It included the Proportion of urban population, the Proportion of education level, the Average Household Size, the total Population of Household Registration at the end of the year, the total burden coefficient, the Consumer Price Index, the Retail Price Index, the Per Capita Disposable Income of all residents, the Local Fiscal Tax Revenue, the Sex Ratio, the Household Consumption Expenditure, the Medical Bed and the Medical and Health Institutions.

2.2. Gradient boosting regression tree feature selection

Feature selection is a process that involves selecting a subset of features from the original data. This selection aims to improve the model's performance and efficiency. The gradient boosting regression tree is an ensemble learning algorithm that is based on decision trees. This algorithm utilizes specific principles for feature selection, primarily focusing on two aspects. Feature selection is highly significant in gradient boosting regression tree. It helps improve the generalization ability and interpretability of the model. Additionally, it reduces the time and resource consumption during model training. The feature selection steps in the gradient boosting regression tree algorithm are as follows.

- To determine the importance of each feature to the target variable, there are two measurement approaches. One approach is to count the number of feature splits across all trees. The other approach involves calculating the average error reduction achieved through feature splitting.
- The model selects the first N features as input features, based on the order of feature importance.

The following is the derivation of the principle equation of feature selection.

In the t-th tree, the goal is to minimize the loss function $\mathrm{L}(y, f_{\mathrm{t}}(x))$. The target variable y and the input feature x are involved in the process. To compute the loss function, the predicted $f_t(x)$ of the previous t-1 tree is added to the predicted value of the t-th tree. The training process of the gradient boosting tree utilizes the addition model, specifically described by Equation (1).

$$f_t(x) = f_{t-1}(x) + h_t(x) \tag{1}$$

$f_{t-1}(x)$ is the predicted value of the first t-1 tree and is the predicted value of the t-th tree. In order to minimize the loss function, we need to find the best. The model selects the first N features as input features, based on the order of feature importance.

2.3. Grey prediction algorithm

Grey prediction algorithm is a method to predict the system with uncertain factors. It is generally applicable to time series occasions.[5] We employed the Grey Prediction Algorithm GM(1,1) to predict the values of various indicators for the years 2022 and 2023. The following is the elaboration of prediction principle.

We Assumed that the feature $X^{(0)} = \{X^{(0)}(i), i = 1,2,\cdots,n\}$ was a non-negative original data sequence. Below, we showed the process of constructing the Grey Prediction Model.[6]

- First, we accumulated $< math >$ and obtained an accumulation sequence.
- We established the following first-order differential equation for $< math >$. That was GM (1,1) model, such as Equation (2).

$$\frac{dX^{(1)}}{dt} + aX^{(1)} = \mu \tag{2}$$

- By solving differential equations, we obtained the predictive model, as in Equation (3).

$$\hat{X}^{(1)}(k+1) = [X^{(0)}(1) - \frac{\mu}{a}]e^{-ak} + \frac{\mu}{a} \tag{3}$$

- The GM (1,1) model was a cumulative amount. We simplified the data obtained from the GM (1,1) model as $\hat{X}^{(0)}(k+1)$. That was the grey prediction of $\hat{X}^{(0)}(k+1)$, as in Equation (4).

$$\hat{X}^{(0)}(k+1) = (e^{-\hat{a}} - 1)[X^{(0)}(n) - \frac{\hat{\mu}}{\hat{a}}]e^{-\hat{a}k} \tag{4}$$

2.4. Gradient boosting regression tree algorithm

The gradient boosting regression tree algorithm was an ensemble learning method based on decision trees. It performed model fitting by gradually learning residuals through a gradual process. The algorithm combined multiple decision trees, with each decision tree optimizing the error of the previous tree. Eventually, it obtained an integrated model with a reduced prediction error.[7][8]

The training process of the gradient boosting regression tree model proceeded as follows.

We denoted the number of decision trees as M. And we designated the gradient boosting regression tree model for the final output as $f_{(M)}(x_i)$.

- Initialization

We created the first regression tree $f_{(1)}(x_i)$, as Equation (5).

$$f_{(1)}(x) = arg_c min \sum_{i=1}^{N} L(y_i, c) \tag{5}$$

- Iteration

For the second to the m-th regression tree, we used the residual of the previous result, as shown in Equation (6).

$$r_{mi} = -[\frac{\partial L(y_i, f(x_i))}{\partial f(x_i)}] f(x) = f_{m-1}(x) \tag{6}$$

For the current m-th subtree, we traversed its feasible cut points and thresholds. We found the parameters corresponding to the optimal predicted value c. So it approached the residual as much as possible, as shown in Equation (7).

$$c_{mj} = arg_c min \sum_{x_i \in R_{mj}} L(y_i, f_{m\_1}(x_i) + c \tag{7}$$

R_{mj} referred to the collection of predicted values of the leaf nodes in the m-th subtree. It was obtained using all the partitioning methods. The collection represented the predicted values of the leaf nodes in the m-th subtree. The range of j was $\{1,2,\cdots,J\}$.

We renewed the m-th regression tree according to the following Equation (8).

$$f_m(x) = f_{m-1}(x) + \sum_{j=1}^{J} c_{mj} I(x \in R_{mj}) \tag{8}$$

I was a function. We set I to 1 if the sample fell on the node; otherwise, we set I to 0.

- Finally, we obtained the regression tree, such as Equation (9).

$$F(x) = f_M(x) = \sum_{m=1}^{M} f_m(x) = \sum_{m=1}^{M} \sum_{j=1}^{J} c_{mj} I(x \in R_{mj}) \tag{9}$$

The advantages of this algorithm were its ability to handle high-dimensional, nonlinear, and non-stationary data. It could also adaptively add new decision trees.

3. Results and discussion

In the implementation process of the system, we designed and adopted a combination model of grey prediction and gradient boosting regression tree. Feature selection model based on gradient boosting regression tree had a strong selection effect. It could select nine features with the highest correlation with the birth rate. Grey prediction demonstrates excellent performance in predicting small amounts of data. We have established a grey prediction model for the selected individual factor. We used this model to obtain the forecast values for the years 2022 and 2023.[9] Gradient boosting regression tree has the strong applicability and fault tolerance. We established a training model for historical data. This model was developed based on its robustness and versatility.[10] We substituted the data results of grey prediction into the trained model. By obtaining

more accurate prediction results, we indicated a higher level of prediction accuracy. This provided further evidence of the model's feasibility in delivering precise predictions. The following is a step-by-step description of the combination model of grey prediction and gradient boosting regression tree.

3.1. Data preprocessing results

Feature selection aimed to select the most representative feature subset from the original data. This improved the performance and efficiency of the model by enhancing its discriminative ability. Feature selection can reduce irrelevant features. It can also enhance the generalization ability and interpretability of the model. Moreover, it can also decrease the complexity and training time of the model. We initially employed the gradient boosting regression tree to train the 13 features gathered for the collected data. This training aimed to assess their potential impact on the birth rate. Subsequently, we utilized an interface to assess the contribution of each feature to the birth rate. Based on our observations, we could clearly see that the total population at the end of the year and the education level had a significant impact on the birth rate. These features played a crucial role in influencing birth rates. On the other hand, we found many features have a relatively small influence on the birth rate. We ranked the importance scores of each feature from high to low. And we selected the top 9 features for further analysis.

3.2. Model construction and evaluation

3.2.1. Construction and evaluation of grey prediction model

We based the prediction of the birth rate on 9 selected features through feature selection. The data for 2022 and 2023 were unknown. We needed to first predict the values of these 9 features that affected the birth rate. Here, we could use the gray prediction algorithm GM (1,1) model.

Finally, we predicted that the birth rate in Guangdong Province in 2022 would be 8.904‰ and in 2023 would be 8.741‰, as shown in **Figure 1**.

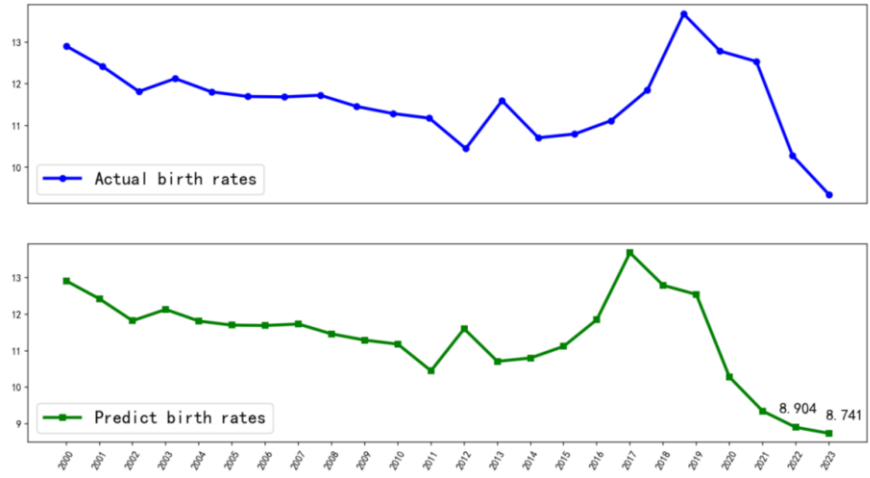

Figure 1. Actual birth rates and predict birth rates.

Calculate the root-mean-square error of the model, the mean absolute error, R^2, as Equation (10) to Equation (12).

$$\mathrm{MAE} = \frac{1}{\mathrm{m}}\sum_{\mathrm{i}=1}^{\mathrm{n}}\left|\mathrm{y_i} - \mathrm{y'_i}\right| \tag{10}$$

$$\mathrm{RMSE} = \sqrt{\frac{1}{\mathrm{m}}\sum_{\mathrm{i}=1}^{\mathrm{n}}\left((\mathrm{y_i} - \mathrm{y'_i})^2\right)} \tag{11}$$

$$\mathrm{R}^2 = 1 - \frac{\sum_{\mathrm{i}=1}^{\mathrm{n}}(\mathrm{y_i} - \hat{\mathrm{y}}_\mathrm{i})^2}{\sum_{\mathrm{i}=1}^{\mathrm{n}}(\mathrm{y_i} - \bar{\mathrm{y}})^2} \tag{12}$$

Table 1. Precision index of Gradient boosting regression tree prediction algorithm

Mean Absolute Error (MAE)	Mean Square Error(MSE)	Root Mean Squared Error(RMSE)	R^2
0.001	4.279	0.001	0.99

From **Figure 1**, we can see that the predicted birth rate values and actual birth rate values have shown a decreasing trend over the past 20 years. The birth rate in Guangdong Province increased in 2016 and reached its highest value in 2017. This was due to the "two-child" policy implemented by the government in 2016. From 2019 to 2021, the birth rate in Guangdong Province has significantly declined, largely due to the impact of COVID-19. Assuming that there are no major social upheavals in the coming year, we can estimate that the birth rate. **Table 1** also reflects that the model has a good fit, and can explain more variability.

3.3. Results and discussion

We wrote the code in the Python language and mainly utilized the pandas and sklearn libraries, making it highly portable. We used all of the data in this paper from the Guangdong Statistical Yearbook, ensuring its reliability and validity. The entire testing program ran smoothly. We used a combination of mathematical models and machine learning algorithms for prediction. We integrated the Grey Prediction Algorithm with the Gradient Boosting Regression Tree Algorithm. By doing so, we obtained an improved data prediction model, thereby enhancing the experimental accuracy. At the same time, this solution also optimized the complexity of the algorithm. And it reduced unnecessary function parameters. The combination of the grey prediction and gradient boosting regression tree models played a mutually corrective role. Both models themselves are suitable for short-term forecasting with small sample sizes. They could effectively predict the birth rate. This model has high prediction accuracy and stability, and is reliable and effective.

Table 2. Comparison of prediction accuracy metrics among different models.

Model	Prediction accuracy metrics R^2
Random Forest Model	0.89
K-Nearest Neighbors	0.36
Support Vector Regression	0.77
Gradient boosting regression tree	0.99

In addition, we selected R^2 as the measure of the regression model's goodness of fit. It measured the percentage of variability in the dependent variable explained by the model. We compared the R^2 of other regression models, such as random forest regression. And we supported vector machine regression and K-Nearest neighbor regression. **Table 2** showed the comparison results. This once again demonstrated the accuracy of using gradient boosting trees.

This work utilizes a combination of the grey prediction and gradient boosting regression tree models. So it is more effective in data prediction than other similar products. This model is suitable for short-term forecasting with small sample sizes, and can effectively predict the birth rate. The model also improves the accuracy and stability of prediction values, and is reliable and effective. At the same time, these two algorithms correct each other, greatly improving the accuracy of the data. Based on this, we obtained the predicted birth rate of Guangdong Province. The birth rate in Guangdong Province in 2022 is predicted to be 8.904‰, and the birth rate in 2023 is predicted to be 8.741‰.

4. Conclusion

In this paper, we combined the Grey Prediction model with gradient boosting regression tree. We used mathematical models and machine learning algorithms to predict future birth rates. This process prompts us to consider the factors that influence birth rates and improve relevant factors. Based on our findings, we could propose recommendations to the Guangdong provincial government. This could assist them in adjusting their birth policies. They could focus on household registration population, disposable income of residents, and educational level of residents.

The mathematical model designed and optimized in this study achieved good data prediction results. It improved the accuracy of the experiment. It can be applied to the analysis of birth rates and influencing factors in provinces across the country and even in other countries.

References

[1] Kearney Melissa S.,Levine Phillip B.,Pardue Luke. The Puzzle of Falling US Birth Rates since the Great Recession. Journal of Economic Perspectives.2022 Feb; 36(1): 151-76.
[2] Furtunov S.,Ruseva J.,Madjova V.. Analysis of some indicators and trends related to birth rates and optional abortions in Bulgaria and Europe and possibilities for their optimizing. General Medicine.2021 Nov;23(2):20-4.
[3] Yun Jungha,Kim Chae Young,Son SeHyung,Bae ChongWoo,Choi YongSung,Chung SungHoon. Birth Rate Transition in the Republic of Korea: Trends and Prospects. Journal of Korean medical science.2022 Oct; 37 (42): 304.
[4] Wang Wen Bao,Hu Yi Chung. Multivariate Grey Prediction Models for Pattern Classification Irrespective of Time Series. JOURNAL OF GREY SYSTEM.2019 Jan;31(2):135-42.
[5] Jiang Peng,Hu Yi Chung. Constructing interval models using neural networks with non-additive combinations of grey prediction models in tourism demand. Grey Systems: Theory and Application.2023 Jan;13 (1):58-77.
[6] Qiuping Wang,Subing Liu,Haixia Yan. The application of trigonometric grey prediction model to average per capita natural gas consumption of households in China. Grey Systems: Theory and Application.2019 Feb; 9 (1):19-30.
[7] Di Persio Luca,Fraccarolo Nicola. Energy Consumption Forecasts by Gradient Boosting Regression Trees. Mathematics.2023 Feb; 11 (5):1068.
[8] Park Soyoung,Jung Solyoung,Lee Jaegul,Hur Jin. A Short-Term Forecasting of Wind Power Outputs Based on Gradient Boosting Regression Tree Algorithms. Energies.2023 Jan; 16(3):1132.
[9] Xuejun Shen,Minghui Yue,Pengfei Duan,Guihai Wu,Xuerui Tan. Application of grey prediction model to the prediction of medical consumables consumption. Grey Systems: Theory and Application.2019 Apr;9(2):213-23.
[10] Shatnawi Amjed,Alkassar Hana Mahmood,AlAbdaly Nadia Moneem,AlHamdany Emadaldeen A.,Bernardo Luís Filipe Almeida,Imran Hamza. Shear Strength Prediction of Slender Steel Fiber Reinforced Concrete Beams Using a Gradient Boosting Regression Tree Method. Buildings.2022 Apr; 12 (5):550.

Fuzzy Systems and Data Mining IX
A.J. Tallón-Ballesteros and R. Beltrán-Barba (Eds.)

doi:10.3233/FAIA231032

A Multimodal Multi-Objective Evolutionary Particle Swarm Algorithm Based on Grey Prediction Selection Strategy

Renyun Liu [a], Ruihong Wang [a,1], Yifei Yao [b] and Fanhua Yu [c]
[a] *Department of Mathematics, Changchun Normal University, Jilin 130000, China*
[b] *Department of Computer Science, Changchun Normal University, Jilin 130032, China*
[c] *Department of Computer Science, Beihua University, Jilin 132013, China*

Abstract. In view of the fact that the diversity of the objective space of multimodal multi-objective optimization will decrease with the increase of the diversity of the decision space, and it is unable to identify all pareto optimal solution sets, this paper proposes an evolutionary particle swarm optimization algorithm based on the gray prediction selection strategy to solve this problem. First, the historical optimal individuals and the neighborhood optimal individuals are selected by using multivariable gray prediction to improve the diversity of the target space; Secondly, the index based ring topology is used to update the neighborhood optimal archive, induce a stable ecological niche, and identify more pareto optimal solution sets; Finally, the non dominated special crowding distance is used as a density measure in the decision space and objective space to identify more pareto optimal solutions. In the experimental stage, 11 MMO test functions are selected and compared with four classic multimodal optimization algorithms. The results show that the proposed algorithm can identify all pareto optimal solution sets in the decision space and maintain good convergence and diversity in the objective space.

Keywords. Multimodal multi-objective optimization, particle swarm algorithm, decision space, multivariate gray prediction

1. Introduction

In multi-objective optimization problems, there are often cases where a solution in the objective space corresponds to multiple optimal solutions in the decision space, which are called multimodal multi-objective optimization problems (MMOPs)[1]. For example, site selection problems, feature selection problems, etc. For the decision maker, on the one hand, obtaining more equivalent optimal solutions provides a clear understanding of the intrinsic properties of the problem, and on the other hand, there are more options to choose from when realistic conditions change.

In the study of diversity of solutions to multimodal multi-objective optimization problems, Liu et al[2] proposed a dual-file and recombination strategy (named TriMOEA-TA&R). Among them, two files are used to maintain population diversity, and

[1]Corresponding Author. E-mail:w1353965525@126.com

the recombination strategy is used to obtain multiple Pareto optimal sets (PS). Based on this, a penalized density method is proposed for unbalanced MMOPs[3], which uses a weight-based fitness metric to evaluate individual density and a convergent first criterion in environmental selection for progeny selection. The algorithm improves the decision space diversity. Fan[4] et al. proposed a method based on partition search: the solution space is divided into a number of subspaces, and the number of evolutions in each subspace is adjusted according to the quality of the solution in each subspace The algorithm can reduce the difficulty of MMOPs, but the number of subspaces is challenging to set. Although all the above algorithms improve the diversity of the decision space, they reduce the diversity of the objective space.

In identifying more pareto-optimal solution sets, Li et al[5], inspired by the literature[6], designed a weighted indicator (MMEA-WI) that can accelerate population convergence by employing convergence archiving while maintaining population diversity. Wang et al.[7] proposed the Modified Maximum Extension Distance (MMED) as a distance indicator, using different mutation strategies to improve diversity in different evolution stages in two stages. Li et al.[8] used a reference point strategy to generate multiple uniformly distributed solutions and a local solution preservation strategy to independently evolve in each neighborhood, searching for more PSs in the decision space. Luo et al.[9] used density based clustering methods in the local detection mechanism to find multiple equivalent solutions. The above study considered the problem of optimal solution set distribution in decision space, but as the decision space diversity increases, the diversity of the objective space always decreases, instead of identifying all PSs.Therefore, the above algorithm is limited by the decision space diversity in identifying more PSs.

To address the above problems, this paper proposes a selection strategy based on multivariate gray prediction, and adopts an evolutionary particle swarm algorithm to solve the multimodal multi-objective problem. The algorithm can not only balance the convergence and diversity of the objective space and decision space, but also improve the quality of the solution.

2. Related work

2.1. Multi-objective optimization problem

In optimization problems, if there are multiple objective functions and there are conflicting or correlated objective functions, such problems are called multi-objective optimization problems [1]. It is expressed by the following equation:

$$MinF(x) = (f_1(x), f_2(x), \cdots, f_M(x)) \tag{1}$$

$$s.t.g_j(x) \leq 0(j = 1, 2, \cdots, \mu) \tag{2}$$

where, M is the number of optimization objectives, x is a set of n-dimensional solutions in this optimization problem, called the decision space (DS). $f_i(x)$ is a set of solutions in the M-dimensional space corresponding to x, called the objective space (OS). $g_j(x) \leq 0$ is the constraint of this optimization problem.

2.2. Multimodal multi-objective optimization problem

In a multi-objective optimization problem, if there are multiple PSs corresponding to the same point in the objective space, the problem is said to be a multimodal multi-objective optimization problem[1].

As shown in Figure 1. Figure (a) represents the decision space, and Figure (b) represents the objective space. The two curves ps_1 and ps_2 in the decision space are equivalent Pareto optimal solution sets, which correspond to the same pareto front (PF) curve in the objective space.

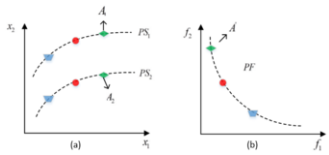

Figure 1. Schematic diagram of multimodal and multi-objective optimization

2.3. Multivariate gray prediction

Gray prediction[10] is a method for predicting systems with uncertainty factors. The factors extracted from the original data are processed by correlation analysis to generate a series of data with strong regularity, and then the corresponding differential equation model is established to predict the future trend of the data. In this paper, the multivariate gray prediction model MGM$(1,n)$[11] is used to predict the particles with better convergence and diversity in the objective space and decision space by using the population chain of evolutionary algorithm as the time series of the prediction model.

MGM$(1,n)$ involves the following three processes: the first-order cumulative generation operation (1-AGO), the average series and its underlying model.

Suppose$X^{(0)} = (X_1^{(0)}, X_2^{(0)}, \cdot, X_n^{(0)})$is the initial non-negative series, where $X_j^0 = (X_j^{(0)}(1), X_j^{(0)}(2), \cdot, X_j^{(0)}(m))$,$X_i^{(0)}(j)$ are the jth dimensional variables at the i-th moment of the initial sequence $X^{(0)}$, and the predicted values of $X^{(0)}$ are obtained by the first-order cumulative generation operation (1-AGO), the average generation operation and the establishment of the basic model as shown in equation (3).

$$\hat{\chi}^{(0)}(i) = e^{-(i-1)*A}\left(X^{(0)}(1) - A^{-1}B\right) - e^{-(i-2)*A}\left(X^{(0)}(1) - A^{-1}B\right) \tag{3}$$

where$(A,B)^T = (L^T L)^{-1} L^T M$, A is the development gray matrix, B is the control gray matrix, L is the matrix generated by the average sequence obtained by the average generation operation, and M is the matrix generated by the initial sequence. This equation will be used in the next section to construct the selection strategy for the proposed algorithm.

2.4. Particle swarm algorithm

The particle swarm optimization method[12] is an early intelligent algorithm that has the advantages of requiring few tuning parameters, simple principle and easy

implementation[13]. Each particle in the population updates its location by individual best extreme (pbest) and neighborhood best extreme (nbest) to guide the particle to fly to a better area and get a better location. Let $x_i(t)$ and $v_i(t)$ be the position and velocity of the ith particle at the tth iteration, respectively, and each particle updates its position and velocity according to the following equation:

$$x_i(t) = x_i(t-1) + v_i(t) \tag{4}$$

$$v_i(t) = W v_i(t-1) + C_1 r_1 \left(x_{\text{pbest}\,i} - x_i(t)\right) + C_2 r_2 \left(x_{\text{nbest}\,i} - x_i(t)\right) \tag{5}$$

Here, W is the weighting coefficient (usually taken as 0.7298), $C_1$and C_2 is a constant, satisfying $C_1 + C_2 = 4.1$, and r_1 and r_2 are the random values within [0,1].

3. The algorithm of this paper

In order to solve the problem of difficult balance between the diversity of decision space solutions and the diversity of objective space in multimodal multi-objective optimization, this paper proposes a multimodal multi-objective particle swarm optimization algorithm (MGP_MMPSO) based on multivariate gray prediction, which guides the positions of $pbest_i$ and $nbest_i$ through the selection strategy of multivariate gray prediction to lead the population to evolve in the direction of better diversity. The algorithm is divided into four steps: initialization of the population, selection of $pbest_i$ and $nbest_i$, updating each particle position, i.e., evolving offspring, and updating the PBA, NBA archive, i.e., environmental selection.

3.1. Algorithm framework

The basic flow of the MGP_MMPSO algorithm is shown in Algorithm 1.

A new selection strategy (Algorithm 2) is designed for the selection of $pbest_i$, $nbest_i$. The velocity and position of each particle in the population are updated. Two archives PBA and NBA are updated simultaneously, the individual optimal position of the i-th particle is stored in $PBA\{i\}$, and the neighborhood optimal position of the i-th particle is stored in $NBA\{i\}$. The particles of the generated offspring are put into PBA, and the PBA archive is updated based on the non-dominated special crowding distance ranking, keeping the N particles with higher ranking and removing the particles with lower ranking. The NBA archive is updated, and the PBA forms a ring topology based on the metrics to generate the NBA (as in Figure 2), where each particle exchanges information with two neighboring particles to find the equivalent optimal solution more accurately. The closed-loop topology is used to generate stable ecological sites and locate multiple PSs. When i is the first particle, $NBA\{i\} = \{PBA\{N\}, PBA\{1\}, PBA\{2\}\}$; when i is the last particle, $NBA\{i\} = \{PBA\{N-1\}, PBA\{N\}, PBA\{1\}\}$; when i is the other particle, $NBA\{i\} = \{PBA\{i-1\}, PBA\{i\}, PBA\{i+1\}\}$, add the offspring particles to the NBA archive, keep the top particles and delete the bottom particles by non-dominated special crowding distance sorting.

Algorithm 1 General Framework of MGP_MMPSO

Input: population P, population size N, maximum number of iterations $MaxGen$, personal history optimal archive PBA, neighborhood optimal archive NBA.
Output: All non-dominated solutions in the neighborhood optimal archive NBA.
1: Initialize the population P, $PBA = NBA$,iteration number $t = 1$;
2: **while** $t < MaxGen$ **do**
3: Non-dominated special crowding distance sorting for archived PBA, NBA
4: Select $pbest_i$, $nbest_i$ by the selection strategy in Algorithm 2;
5: Update the velocity and position of each particle in the population according to equation (4),(5)
6: Update PBA, NBA;
7: $t = t + 1$;
8: **end while**

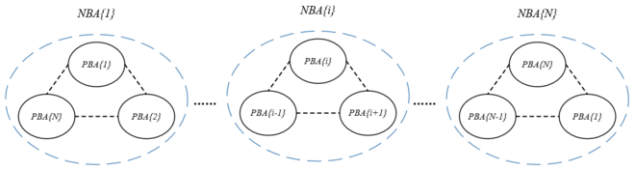

Figure 2. Schematic Diagram of NBA Formation Method

3.2. Selection Strategy

In order to improve the diversity in the objective space, this paper proposes a selection strategy based on multivariate gray prediction, using the non-dominated special crowding distance[13] as the density measure for $pbest_i$ and $nbest_i$, and keeping the two individuals that are closer in the objective space but farther away in the decision space, maintaining the diversity in the decision space. The selection strategy proposed in this paper is shown in Algorithm 2. First, the non-dominated special crowded distance ranking is performed for PBA and NBA ; in the first four generations, the first-ranked archive is directly selected as $pbest_i$ and the first-ranked NBA archive is selected as $nbest_i$. From the fifth iteration onwards, the particle position with better diversity $pre\_pbest_i(t)$ ($pre\_nbest_i(t)$) is predicted based on the $pbest$($nbest$) selected in the first four generations. The specific process is as follows, (in Equation (3)) when $L^{'}L$ is invertible, the more convergent particle position is found according to the multivariate gray prediction method proposed in Section 1.3:

$$pre\_pbest_i(t) = e^{-(i-1)*A}\left(X^{(0)}(1) - A^{-1}B\right) - e^{-(i-2)*A}\left(X^{(0)}(1) - A^{-1}B\right) \quad (6)$$

If L is irreversible, the maximum distance between the two particles of the first three generations of pbest is calculated:

$$Mad_r = max\{d_{pbest_i(t-1),pbest_i(t-2)}, d_{pbest_i(t-1),pbest_i(t-3)}, d_{pbest_i(t-2),pbest_i(t-3)}\} \quad (7)$$

where $d_{pbest_i(t-1),pbest_i(t-2)}$denotes the distance between $pbest_i(t-1)$ and $pbest_i(t-2)$.When Mad_r must be large, that is, when the first three generations of particles are far away, linear prediction is performed according to Equation (8), and $pre\_pbest_i(t)$ and $pre\_nbest_i(t)$ are predicted:

$$pre\_pbest_i(t) = \frac{4pbest_i(t-1) + pbest_i(t-2) - 2pbest_i(t-3)}{3} \quad (8)$$

Otherwise, when the maximum distance is less than a certain threshold, it means that the position diversity and convergence of $pbest_i(t-1)$ selected in the previous iteration are already better, then the perturbation is performed around it to find the particle with better diversity according to Eqs.(9), (10).

$$pre\_pbest_i(t) = pbest_i(t-1) + w * rand(0,1) \tag{9}$$

$$pre\_pbest_i(t) = pbest_i(t-1) + w * Maxd_r \tag{10}$$

Finally, the $pre\_pbest_i(t)$ is ranked with the first ranked particle in the $PBA\{i\}$ archive for non-dominated special congestion distance ranking, and the top ranked particle is $nbpest_i$ and $nbest_i$ is selected by the same process as above.

Algorithm 2 Selection strategy based on multivariate gray prediction

Input: current iteration t, maximum iteration $MaxGen$, personal history optimal archive PBA, neighborhood optimal archive NBA. Distance parameters $\mu_n = 0.5$
Output: Individual optimal particle $pbest_i$. Neighborhood optimal particle $nbest_i$.
1: Non-dominated special crowding distance sorting for archived PBA, NBA;
2: **if** $t \leq 4$ **then**
3: $pbest_i = PBAi(1)$, $nbest_i = NBAi(1)$
4: **else** $\{L'L$ is reversible then$\}$
5: Predictions a and b according to (6);
6: **else** $\{Maxd_r > \mu_n\}$
7: Predictions a and b according to (8);
8: **else** $\{Maxd_r = 0\}$
9: Predictions a and b according to (9);
10: **else**
11: Predictions a and b according to (10);
12: **end if**
13: The predicted particles $pre\_pbest_i(t)(pre\_nbest_i(t))$ are put into $PBA(NBA)$ to compare the non-dominated special congestion distance ranking;
14: Select the particle with the highest ranking $pbest_i = PBA\{i\}(1)$, $nbest_i = NBA\{i\}(1)$.

4. Experiments and Analysis of Results

4.1. Experimental settings

In this study, the performance of the improved algorithm was tested using 11 multimodal test functions with at least two PSs, MMF1-MMF8[14], SYM-PART simple[15], SYM-PART rotated [15], and Omni-test[16]. All these test functions contain two objectives and two or three decision variables.

The proposed algorithm is compared with four classical algorithms, namely, differential evolution based on reinforcement learning (DERLFR)[17], omnidirectional optimization method (Omnioptimizer)[16], evolution based on decision space (DNNSGAII)[18], small habitat particle swarm optimization based on ring topology (MO_Ring_PSO_SCD)[14], evolution using dual archiving and restructuring strategies (TriMOEA-TA&R)[2], new grey prediction evolution(MMGPE)[20].

In this paper, three evaluation metrics, Pareto set proximity (PSP)[14] hypervolume (HV)[19], and inverted generational distance in objective space(IGDF), are used to evaluate the performance of MGP-MMPSO.PSP is used to assess the similarity of the obtained PSs in the decision space to the real PSs, and HV and IGDF is used to evaluate the convergence and diversity of the obtained PFs in the objective space.

4.2. Experimental results and analysis

In the comparison experiments, the population size was set to 800 and the maximum number of evaluations was set to 80,000. Table 1 shows the mean and variance of the PSP obtained from 20 independent runs. The last column of the table, "+", indicates the number of test problems with better performance than MGP_MMPSO, "-", indicates the number of test problems with worse performance than MGP_MMPSO, "= " denotes the number of test problems with little difference from MGP_MMPSO.

From Table 1, we can see that MGP_MMPSO has the best performance among the eight test problems, especially for MMF2 and MMF3, the PSP values are much higher than the other four classical algorithms, and for the irregular PSs in MMF7 and MMF4, it can also obtain high PSP values, only lower than the PSP values of MO_Ring_PSO_SCD and MMGPE. For the test problem SYM_PART_simple, the performance of GP_MMPSO is also higher than the other three compared algorithms, and only lower than the PSP value of DERLFR and TriMOEA-TA&R. The performance of Omni-optimizer and DN-NSGAII is poor in all 11 test problems. In summary, the algorithm performs remarkably well on the MMF test problem and 11 test functions such as SYM_PART_simple, SYM_PART_rotated, and Omni_test, and is able to find all PSs and maintain good convergence and diversity in the decision space.

Table 1. PSP results for each algorithm on 11 test functions

	MGP_MMPSO	DE-RLFR	MO_Ring_PSO_SCD	Omni-optimizer	DN-NSGAII	TriMOEA-TA&R	MMGPE
MMF1	**73.31(2.56)**	59.67(2.99)	66.80(2.89)	47.33(6.95)	45.14(5.45)	31.46(3.28)	72.14(2.85)
MMF2	**312.84(16.21)**	68.70(25.35)	98.13(12.91)	79.83(49.16)	62.79(21.75)	72.77(18.56)	136.69(17.52)
MMF3	**323.62(21.86)**	86.67(35.67)	132.71(23.13)	91.15(47.02)	74.55(30.40)	36.42(24.65)	171.52(15.82)
MMF4	119.16(7.25)	112.66(6.08)	115.30(4.33)	41.63(10.15)	46.78(11.12)	85.51(8.24)	**121.52(5.21)**
MMF5	**36.62(1.52)**	32.53(1.68)	32.91(1.27)	15.43(1.39)	14.17(1.27)	18.97(1.56)	33.61(1.56)
MMF6	**39.06(1.46)**	34.74(1.67)	36.01(1.26)	17.98(1.57)	17.38(2.00)	25.48(1.65)	36.82(1.89)
MMF7	106.66(8.12)	81.29(11.60)	108.01(5.88)	100.48(20.53)	100.09 (4.32)	59.19(7.56)	**118.49(7.25)**
MMF8	**59.81(3.89)**	42.74(5.83)	47.21(1.42)	14.91(5.78)	17.47(6.08)	11.78(4.21)	47.36(4.85)
SYM_PART_simple	42.06(3.24)	58.39(4.87)	21.46(1.01)	0.39(0.18)	0.37(0.13)	**78.46(1.21)**	15.65(3.52)
SYM_PART_rotated	**42.91(2.78)**	28.12(2.59)	18.27(1.52)	2.28 (3.06)	2.93(3.67)	15.65(3.21)	27.52(2.98)
Omni_test	**17.79(0.32)**	15.78(1.05)	11.45(0.58)	0.93(0.17)	1.11(0.17)	11.78(0.69)	7.63(0.59)
+/-/=	8/3/0	0/11/0	0/11/0	0/11/0	0/11/0	1/10/0	2/9/0

Table 2 shows the mean and variance of the HV obtained from 20 independent runs. Observe that in the table MO_Ring_PSO_SCD has the highest HV value on MMF8 and shows the best performance. Omnioptimizer shows the best HV performance on eight test problems including MMF1,MMF3, MMF5MMF7, SYM_PART_rotated, and Omni_test. MMGPE exhibits good performance on MMF5 and MMF7, TriMOEA-TA&R only has higher HV values on MMF3, MGP_MMPSO has the highest HV value and the best performance on MMF4 test problem, and the difference with the best comparative algorithm on the other 11 test problems is less than 0.01. From Table 3, it can be seen that MGP_MMPSO has the highest IGDF on 7 test functions, MO_Ring_PSO_SCD and TriMOEA-TA&R have the highest IGDF values on one test function, and DN-NSGAII has better IGDF values on both test functions. The results of HV and IGDF indicate that this algorithm has good diversity in the target space and can effectively balance the diversity of the target space and decision space.

The test function MMF2 is used to prove the effectiveness of this selection strategy, and the number of populations is taken as 800, and the maximum number of iterations is 100. Figure 3 shows the particle position distribution in the *PBA* archive, and Figure 4 shows the particle position distribution in the *NBA* archive. Figure 4 shows the distribu-

Table 2. HV results for each algorithm on 11 test functions

	MGP_MMPSO	DE-RLFR	MO_Ring_PSO_SCD	Omni-optimizer	DN-NSGAII	TriMOEA-TA&R	MMGPE
MMF1	3.66(3.75e-04)	3.66(7.75e04)	3.66(4.54e04)	**3.67(2.43e05)**	3.66(1.12e03)	3.66(2.43e-05)	3.66(2.89e-05)
MMF2	3.66(4.27e03)	3.64(1.83e02)	3.65(7.61e03)	**3.67(4.69e05)**	3.66(9.08e03)	3.66(5.63e-05)	3.66(3.18e-05)
MMF3	3.66(4.39e03)	3.64(1.23e02)	3.65(6.63e03)	3.67(2.52e05)	3.67(5.25e04)	**3.67(1.33e-05)**	3.66(4.25e-05)
MMF4	**3.33(2.12e03)**	3.33(3.52e03)	3.30(9.54e04)	3.32(3.84e05)	3.18(3.31e04)	3.32(1.86e-05)	3.32(3.56e-05)
MMF5	3.66(5.48e04)	3.66(7.91e04)	3.66(3.89e04)	3.67(1.81e05)	3.67(3.22e04)	3.66(2.45e-05)	**3.37(3.18e-05)**
MMF6	3.66(5.53e03)	3.66(7.42e04)	3.66(3.33e04)	**3.67(2.19e05)**	3.66(1.41e03)	3.66(4.52e-05)	3.37(2.36e-05)
MMF7	3.66(5.42e03)	3.66(1.25e03)	3.67(2.10e04)	3.67(4.44e05)	3.66(1.24e03)	3.66(6.88e-05)	**3.37(2.25e-05)**
MMF8	3.21(2.94e03)	3.21(2.04e03)	**3.21(1.09e04)**	3.21(1.20e04)	3.21(1.22e03)	3.31(2.98e-05)	3.21(3.98e-05)
SYM_PART_simple	1.31(6.76e04)	1.32(8.75e04)	1.30(1.65e03)	1.32 (3.21e04)	**1.32(1.94e04)**	1.31(5.86e-05)	3.31(1.12e-05)
SYM_PART_rotated	1.31(6.23e03)	1.32(1.33e03)	1.29(3.55e03)	**1.32(2.55e04)**	1.32(4.49e04)	1.32(5.15e-05)	3.32(5.32e-05)
Omni_test	62.03(8.62e02)	62.02(1.28e02)	61.93(2.14e01)	**62.06(2.46e04)**	62.06(3.95e04)	62.06(1.85e-05)	62.05(5.69e-05)
+/-/=	1/10/0	0/11/0	1/10/0	5/6/0	1/10/0	1/10/0	2/10/0

Table 3. IGDF results for each algorithm on 11 test functions

	MGP_MMPSO	DE-RLFR	MO_Ring_PSO_SCD	Omni-optimizer	DN-NSGAII	TriMOEA-TA&R	MMGPE
MMF1	**8.03e-04**	8.97e-04	9.94e-04	8.52e-04	9.12e-04	2.37e-03	9.72e-04
MMF2	**1.84e-03**	5.64e-03	5.25e-03	3.73e-03	3.96e-03	4.47e-03	4.44e-03
MMF3	**1.39e-03**	2.91e-03	3.81e-03	3.21e-03	3.21e-03	4.04E-03	3.91E-03
MMF4	8.11e-04	9.37e-04	8.80e-04	8.21e-04	**8.01e-04**	3.21e-02	9.80e-04
MMF5	8.15e-04	7.95e-04	9.45e-04	**7.82e-04**	8.15e-04	4.02e-03	8.75e-04
MMF6	**7.30e-04**	8.28e-04	9.07e-04	7.98e-04	8.08e-04	2.41e-03	8.48e-04
MMF7	**8.31e-04**	8.39e-04	9.17e-04	8.36e-04	8.64e-04	3.13e-03	7.84e-04
MMF8	9.51e-04	9.15e-04	1.41e-03	8.45e-04	**8.33e-04**	2.47e-03	8.95e-04
SYM_PART_simple	**3.66e-03**	5.83e-03	9.60e-03	4.79e-03	4.89e-03	4.05e-02	6.19e-03
SYM_PART_rotated	**4.37e-03**	7.22e-03	1.28e-02	5.12e-03	5.82e-03	1.41e-02	7.12e-03
Omni_test	8.50e-03	9.04e-03	1.70e-02	8.37e-03	8.49e-03	**8.31e-03**	9.22e-03
+/-/=	7/4/0	0/11/0	0/11/0	1/10/0	2/9/0	1/10/0	0/11/0

tion of particles in decision space, and Figure (b) shows the distribution of particles in objective space, the "+" particles indicate the distribution of each particle in the $PBA(NBA)$ archive of the ith particle, the solid particles are the particles $pre\_pbest_i(t)(pre\_nbest_i(t))$ selected by multivariate gray prediction. The convergence and diversity of $pbest_i$ and $nbest_i$ selected by the selection strategy based on multivariate gray prediction are better than the particles in the archive, both in decision space and objective space, indicating the effectiveness of the selection strategy.

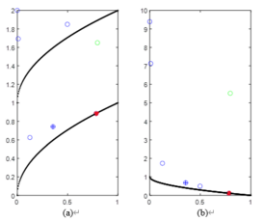

Figure 3. Image of the location of particles in *PBAi* and $pre\_pbest_i(t)$

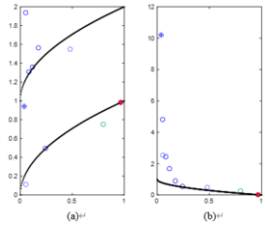

Figure 4. Image of the location of particles in *NBAi* and $pre\_nbest_i(t)$

5. Conclusion

In this paper, we use a selection strategy based on multivariate gray prediction for historical optimal individuals and neighborhood optimal individuals to improve the convergence and diversity of leader particles; we adopt a particle swarm algorithm with fewer parameters to update individual optimal archives with special crowding distance as a

density metric, generate neighborhood optimal archives according to an indicator-based ring topology, induce stable ecological sites, and thus locate multiple equivalent PSs. In the experimental tests, the proposed algorithm is experimentally compared with four classical multimodal multi-objective optimization algorithms on 11 multimodal multi-objective optimization test functions, and the results show that the proposed algorithm has better superiority.

References

[1] Yue Cai-Tong, Liang Jing, Qu Bo-Yang, Yu Kun-Jie, Wang Yan-Li,Hu Yi. A survey on multimodal multiobjective optimization. Control and Decision, 2021, 36(11): 25772588

[2] Y. Liu, G.G. Yen, D. Gong, A multi-modal multi-objective evolutionary algorithm using two-archive and recombination strategies, IEEE Trans. Evol. Comput. 23 (4) (2019) 660674.

[3] Y. Liu, H. Ishibuchi, G.G. Yen, Y. Nojima, N. Masuyama, Handling imbalance between convergence and diversity in the decision space in evolutionary multimodal multiobjective optimization, IEEE Trans. Evol. Comput. 24 (3) (2020) 551565.

[4] Q. Fan, X. Yan, Solving multimodal multiobjective problems through zoning search, IEEE Trans. Syst. Man. Cybern. 51 (8) (2019) 48364847.

[5] W.H. Li, T. Zhang, R. Wang, H. Ishibuchi, Weighted indicatorbased evolutionary algorithm for multimodal multi-objective optimization, IEEE Trans.Evol. Comput. (2021).

[6] Y. Liu, H. Ishibuchi, G.G. Yen, Y. Nojima, N. Masuyama, Handling imbalance between convergence and diversity in the decision space in evolutionary multimodal multiobjective optimization, IEEE Trans. Evol. Comput. 24 (3) (2020) 551565.

[7] Wang Y, Liu Z, Wang G G. Improved differential evolution using two-stage mutation strategy for multimodal multi-objective optimization[J]. Swarm and Evolutionary Computation, 2023, 78: 101232.

[8] Li G, Zhou T. A multi-objective particle swarm optimizer based on reference point for multimodal multi-objective optimization[J]. Engineering Applications of Artificial Intelligence, 2022, 107: 104523.

[9] Luo N, Ye Y, Lin W, et al. A novel multimodal multiobjective memetic algorithm with a local detection mechanism and a clustering-based selection strategy[J]. Memetic Computing, 2023, 15(1): 31-43.

[10] Hu Z , Li Z , Dai C , et al. Multiobjective Grey Prediction Evolution Algorithm for Environmental/Economic Dispatch Problem[J]. IEEE Access, 2020, PP(99):1-1.

[11] Agarwal P , Agrawal R K , Kaur B . Multi-objective particle swarm optimization with guided exploration for multimodal problems[J]. Applied Soft Computing, 2022(120-):120.

[12] Shir O M,Preuss M,Naujoks B,et al.Enhancing Decision Space Diversity in Evolutionary Multiobjective Algorithms[C]//International Conference on Evolutionary Multi-criterion Optimization. Springer-Verlag, 2009.

[13] Handur E . Particle Swarm Optimization for Load Balancing in Distributed Computing Systems A Survey[J]. Turkish Journal of Computer and Mathematics Education (TURCOMAT), 2021, 12(1S):257-265.

[14] C. Yue, B. Qu, J. Liang, A multi-objective particle swarm optimizer using ring topology for solving multimodal multi-objective problems, IEEE Trans. Evol. Comput. 22 (5) (2018) 805817.

[15] Gnter Rudolph, Naujoks B , Preuss M . Capabilities of EMOA to Detect and Preserve Equivalent Pareto Subsets[J]. Springer, Berlin, Heidelberg, 2007.

[16] Deb K , Tiwari S . Omni-optimizer: a procedure for single and multi-objective optimization[J]. Springer Berlin Heidelberg, 2005.

[17] Li Z. Differential evolution based on reinforcement learning with fitness ranking for solving multimodal multiobjective problems[J]. Swarm and Evolutionary Computation, 2019, 49.

[18] Liang J J , Yue C T , Qu B Y .Multimodal multi-objective optimization: A preliminary study[C]//Evolutionary Computation.IEEE, 2016.DOI:10.1109/CEC.2016.7744093.

[19] A R L , A K K , B C M F .A box decomposition algorithm to compute the hypervolume indicator[J].Computers & Operations Research, 2017, 79:347-360.DOI:10.1016/j.cor.2016.06.021.

[20] Zhou T , Hu Z , Zhou Q ,et al.A novel grey prediction evolution algorithm for multimodal multiobjective optimization[J].Engineering Applications of Artificial Intelligence, 2021, 100(1):104173.DOI:10.1016/j.engappai.2021.104173

Fuzzy Systems and Data Mining IX
A.J. Tallón-Ballesteros and R. Beltrán-Barba (Eds.)

doi:10.3233/FAIA231033

A Multi-Modal Multi-Objective Differential Algorithm Based on Hybrid Strategy

Renyun Liu [a], Yunhan Yang [a,1], Yifei Yao [b] and Fanhua Yu [c]
[a] *Department of Mathematics,Changchun Normal University,Jilin 130000,China*
[b] *Department of Computer Science,Changchun Normal University,Jilin 130032,China*
[c] *Department of Computer Science,Beihua University,Jilin 132013,China*

Abstract. In MMOP there are some algorithms that are difficult to find more equivalent Pareto optimal solutions,and unable to balance the performance of solutions in decision space and objective space. In addition, the solution is too densely distributed on the boundary. A multimodal multi-objective differential evolution algorithm based on hybrid strategy (MMODE_HS) is proposed to solve above these problems. First, an effective binary tournament selection mechanism based on special crowding distance is designed to select individuals which performance better diversity in decision space and objective space and balance the performance of the solution in two spaces; Second, The reverse vector mutation strategy is introduced to reduce the quantity of boundary point, which can help the algorithm improve the distribution of Pareto subsets. MMODE_HS is compared with other multimodal multi-objective evolutionary algorithms, the results demonstrate that the proposed algorithm can search for more complete Pareto subsets on nine test problems, and effectively balance convergence and diversity.

Keywords. Multi-objective optimization; Multimodal optimization; Differential evolution algorithm

1. Introduction

MMOPs aims to find multiple Pareto solution sets. When one optimal solution is unavailable due to practical factors, other optimal solutions can also be equally substituted. Finding all the solutions of the problem to be optimized can help decision-makers make better choices. In recent years, many scholars have proposed different multimodal multi-objective optimization algorithms.

Han[1] proposed a method to improve the convergence of particles to multiple solution sets (MMOPSOSS). This method has the advantages of multi-group search method and local search method.Compared with other algorithmsit can converge more accurately into multiple solution sets and has extremely high optimization efficiency.Under the combined effect of this mechanism.In order to overcome the shortcomings of the differential algorithm, Gao[2] proposes Multi-population-based chaotic DE (MPC-DE), which uses chaos mapping in the initialization stage to enhance the uniformity of the random distribution of the population, and then divides the population into two subpopulations, and

[1]Corresponding Author. E-mail: 15284969426@163.com.

the distribution uses different mutation strategies for it, so that the algorithm can continue to explore promising areas.On the basis of the fireworks algorithm,Chen[3] proposes two-stage dual-archive fireworks algorithm (TSDA_MMOFWA),the entire evolutionary process is divided into two stages, the first stage combines binary archiving and genetic operators, so that each fireworks can search independently to find a large number of Pareto optimal solutions, and the second stage adopts an adaptive fire explosion strategy to evenly distribute the solutions.

Liang[4] proposed a differential evolution based on clustering technology and elite selection mechanism (MMODE_CSCD). the calculation of special crowding distance based on clustering (CSCD)is more accurate. In order to improve the diversity of the population, a new distance mechanism based elite selection was introduced. Tanabe[5] proposed a decomposition based evolutionary algorithm framework.The decomposition strategy is beneficial for reducing the difficulty of multi-modal multi-objective problems. Although Liu[6] et al. found more Pareto optimal solutions, the diversity and convergence of the objective space deteriorated.

However, multi-modal multi-objective problems are more complex than multi-objective problems,although some of the algorithms proposed above can solve multi-modal multi-objective problems, they still have the following drawbacks: firstly, the exploration ability of the algorithms is not strong,it's difficult to find as many optimal solutions as possible in the search space. Secondly, the relationship between the diversity of solutions in the decision space and the convergence of solutions in the objective space cannot be balanced. Finally, these algorithms perform simple processing on points beyond the boundary, resulting in overly dense distribution of points on the boundary. Motivated by these observations, an algorithm called multi-modal multi-objective difference algorithm based on hybrid strategy(MMODE_HS) is proposed.The proposed MMODE_HS contains two major contributions:a binary tournament selection based on special crowding distance is presented, which can find Pareto optimal solutions with good diversity in both spaces. The reverse vector mutation strategy is introduced to mutate boundary point again to reduce the density of boundary point and help the algorithm improve the distribution of Pareto solution sets.

The remaining sections are assigned as follows. Section 2 illustrates the basics knowledge of MMOP and DE. The details of MMODE_HS are provided in Section 3, consisting of the binary tournament selection based on special crowding distance method, reverse vector mutation strategy strategy. Simulations including benchmark experiments in Section 4 strive to demonstrate the effectiveness of MMODE_HS.

2. Preliminaries

2.1. Multi-modal multi-objective optimization problems

The multimodal multiobjective optimization problem is defined as follows[7]:In a multi-objective optimization problem, multiple optimal solution sets of the decision space have the same value in the target space. As shown in Fig. 1, there are two equivalent global PS (PS_1 and PS_2) and one local PS in the decision space, and one global PF and one local PF in the objective space. Point A and point C are mapped to the same point E, and point B is mapped to point F. when $\delta > 0$, two solutions A and C were considered equivalent,

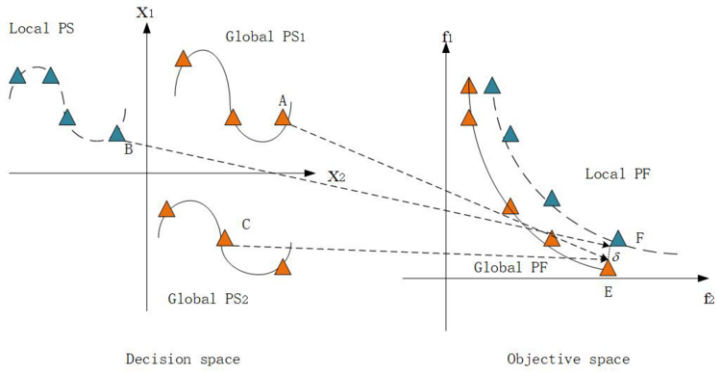

Figure 1. Multimodal multi-objective optimization problem

and when the threshold was within an acceptable range, A and B were also considered equivalent.

2.2. Differential evolution optimization

Differential evolution algorithm (DE)[8] is a simple but powerful stochastic optimization algorithm that retains a global search strategy based on population, simple mutation operations and competitive survival strategies based on difference, reducing the complexity of operations.
The individuals in the population are represented as follows:

$$X_{i,G} = (X^1_{i,G}, X^2_{i,G}, ..., X^D_{i,G}) \tag{1}$$

D represents the dimension of the optimization problem being solved and $X_{i,G}$ is the i-th individual in the G-th generation population with NP individuals.
Only one mutation variation strategy $DE/rand/2$ is described below:

$$V_{i,G} = X_{r_1,G} + F \cdot (X_{r_2,G} - X_{r_3,G}) + F \cdot (X_{r_4,G} - X_{r_5,G}) \tag{2}$$

r_1,r_2,r_3,r_4 and r_5 are random integers from 1 to NP, which are different from i, F is the scaling factor, which controls the magnitude of the difference vector.
The binomial crossover operator is mainly used to obtain trial vector, which is defined as:

$$u_{i,G} = \begin{cases} v^j_{i,G} & if \quad rand \leq CR \quad or \quad j = j_{rand}, \\ x^j_{i,G} & otherwise. \end{cases} \tag{3}$$

i=1,2,...NP, j=1,2,...,D. $CR \in [0,1]$ is the crossover rate parameter. *rand* is a random value evenly distributed between 0 and 1. j_{rand} is a random integer from 1 to D.
The select operator does the following:

$$X_{i,G+1} = \begin{cases} X_{i,G} & if \quad f(X_{i,G}) \leq f(U_{i,G}), \\ U_{i,G} & otherwise. \end{cases} \tag{4}$$

3. Differential evolution algorithm based on hybrid strategy

3.1. Framework of MMODE_HS

The framework of MMODE_HS is as follows. Firstly, the initialization phase is performed by randomly generating a parent population P of size NP within the given range. Each individual in P is evaluated the special crowding distance. Then, the mating pool individuals are selected using a binary tournament based on the special crowding distance, where five individuals are chosen from P. The parent population P undergoes mutation, where each individual is subjected to a variant of the DE/rand/2 mutation strategy. Additionally, a boundary reverse mutation strategy is applied to handle individuals that exceed the boundaries. By using the binomial crossover strategy, crossover points are selected randomly, and offspring population O is generated. Finally, the best individuals are selected for the next generation using the non-dominated sorting and the special crowding distance selection mechanism.

3.2. Binary tournament strategy based on special crowding distance

Based on the idea of binary tournament selection,We combine special crowding distances, as shown in Algorithm 1. After calculating the special crowding distance for individual of parent population, in the first generation iteration, five individuals are randomly selected from the parent population(P) as mutation individuals. From the second generation onwards, two individuals are randomly selected from P, and their special crowding distance values are compared. The better individual is preserved, and this process is repeated until the specified number of individuals is selected. These selected individuals have both randomness and good diversity . Using them as individuals for crossover and mutation can lead the offspring population to explore sparse areas and potentially discover more high-quality solutions.

Algorithm 1 Binary tournament selection mechanism

Input: rep (parent population), n_var (decision variable dimension), n_obj (objective space)

Output: $newpop2$ (The selected five individuals)

1.Calculate the special congestion distance of all individuals in the parent population rep;

2.When $gcount = 1$, five individuals were randomly selected from the parent population rep;

3.Calculate the special crowding distance of all individuals in the parent population rep;

4.Select any serial number $Pointer$, choose the individual of the special crowding distance represented by $Pointer$ and $Pointer + 1$ from rep, and select the individual with better value to keep;

5.Repeat step 4 until five individuals are selected.

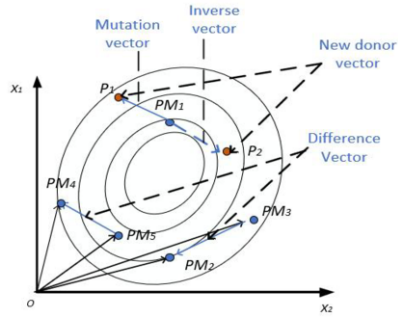

Figure 2. Algorithm flow chart

3.3. Boundary reversal mutation strategy

$pm1$,$pm2$,$pm3$,$pm4$ and $pm5$ are five vectors selected from the current population. $pm1$ serves as the parent vector, and a new offspring $P1$ is generated through the $DE/rand/2$ mutation strategy variant equation (5) with the scaling factor λ. At some point, the newly generated $p1$ may exceed the boundary. The most common operation is to reset the donor vector to the boundary value. However, using this method to reset the values to the boundary may lead to a high population density near the boundary if there are multiple values exceeding the boundary. To address the above issue, a reverse vector mutation strategy is proposed. As shown in Fig 2, $pm1$ is given a reverse vector, and a new donor vector (p_2) is generated within the boundary using equation (6). The reverse vector mutation provides a second opportunity to generate vectors within the boundary for those that have exceeded the boundary. This helps to avoid excessive concentration of solutions on the boundary. The basic idea of this strategy is outlined in Algorithm 2.

$$p = pm_1 + F \cdot (pm_2 - pm_3 + pm_4 - pm_5) \tag{5}$$

$$p = pm_1 - F \cdot (pm_2 - pm_3 + pm_4 - pm_5) \tag{6}$$

Algorithm 2 Boundary reversal mutation strategy

Input:pm (the collection of five individuals selected by the binary tournament), u (decision variable upper bound), l (decision variable lower bound)
Output:p_2(donor vector)
1.Using the individuals in pm, the donor vector p is generated by equation (5);
2.Determine if the vector p exceeds u or l;
3.If p exceeded, the inverse vector is generated using equation (6); otherwise, the generated vector is taken as p_2;
4.If the inverse vector still exceeds u or l, an individual is randomly selected from pm as p_2; Otherwise the inverse vector acts as p_2;

Table 1. Comparison of 1/PSP values obtained by nine algorithms

	MMODE_HS	MMODE_ICD	MMODE	MO_Ring_PSO_SCD	DN-NSGAII	Omni-Opt
MMF1	**0.0403 ± 0.0028**	0.0493 ± 0.0030	0.0492 ± 0.0028	0.0488 ± 0.0019	0.0969 ± 0.0145	0.0975 ± 0.0130
MMF5	**0.0705 ± 0.0033**	0.0853 ± 0.0039	0.0867 ± 0.0075	0.0869 ± 0.0060	0.1773 ± 0.0217	0.1789 ± 0.0245
MMF7	**0.0222 ± 0.0035**	0.0263 ± 0.0046	0.0314 ± 0.0037	0.0267 ± 0.0015	0.0553 ± 0.0151	0.0511 ± 0.0127
MMF8	**0.0540 ± 0.0244**	0.1303 ± 0.0352	0.0754 ± 0.016	0.0678 ± 0.0042	0.2799 ± 0.0911	0.3149 ± 0.1326
MMF9	0.0060 ± 0.0006	**0.0047 ± 0.0003**	0.0066 ± 0.0005	0.0082 ± 0.0008	0.0219 ± 0.0078	0.0316 ± 0.0269
MMF12	0.2444 ± 0.0001	0.2474 ± 0.0003	2.0756 ± 0.1402	0.4847 ± 0.3989	1.9959 ± 0.7573	2.0419 ± 0.5808
SYM_PART_simple	0.0542 ± 0.0067	**0.0427 ± 0.0055**	0.0660 ± 0.0064	0.1776 ± 0.0226	5.4511 ± 2.5760	6.4608 ± 3.0139
SYM_PART_rotated	**0.0563 ± 0.5271**	0.0892 ± 0.0153	0.0759 ± 0.0078	0.2784 ± 0.2500	5.2742 ± 2.7404	6.3357 ± 3.7485
Omni_test	0.1288 ± 0.0061	**0.0512 ± 0.0036**	0.0880 ± 0.0243	0.4279 ± 0.0954	1.5563 ± 0.2878	1.7939 ± 0.6207
+/=/-	5/0/4	3/0/4	0/0/9	0/0/9	0/0/9	0/0/9

4. Simulation

4.1. Testing functions and parameter configuration

This study uses nine test functions from CEC2019[9] to evaluate the performance of MMODE_HS. These functions include MMF test functions, SYM-PART test functions, and Omni-test test function. the competing algorithms compared to MMODE_ HS are MMODE_ ICD[10], MMODE[11], MO_ Ring_ PSO_ SCD[12], DN-NSGAII [13], and Omni-Opt.

4.2. Performance Comparison

4.2.1. Evaluation Metric Results

According to the proposed parameter settings, experiments were conducted by independently running the six algorithms 30 times each under the same maximum evaluation count. The average values were then taken. Table 1 and Table 2 present the results of these algorithms in terms of Indicator 1/PSP and Indicator 1/HV, respectively. The best results are highlighted in bold.

Based on the results shown in Table 1, it can be observed that MMODE_HS and MMODE_ICD have similar values in terms of Indicator 1/PSP for the MMF7 and MMF12 test functions. This indicates that both algorithms exhibit similar performance in the decision space. However, MMODE_HS outperforms MMODE_ICD in the MMF9, MMF12, and SYM_PART_simple test functions. In these three test functions, MMF12 and SYM_PART_simple have multiple sets of solutions distributed in the decision space, with the Pareto solution sets being more scattered. These test functions require high optimization capabilities from the algorithms. Hence, the proposed algorithm performs better than other algorithms on these two test functions.

As shown in Table 2, MMODE_HS achieves the best 1/HV values among the six test functions. MMODE_ICD and Omni-Opt obtain the best values on the MMF7 and Omni_test test functions, respectively. MMODE, MO_ Ring_ PSO_SCD, and DN-NSGAII do not achieve the best values on all the proposed test functions. However, it can be observed that in most test functions, the 1/HV values obtained by all the algorithms are close. This is because these comparative algorithms employ techniques for locating Pareto-optimal solutions in the objective space and perform environmental preservation operations. The individuals retained exhibit similar performance in the objective space.

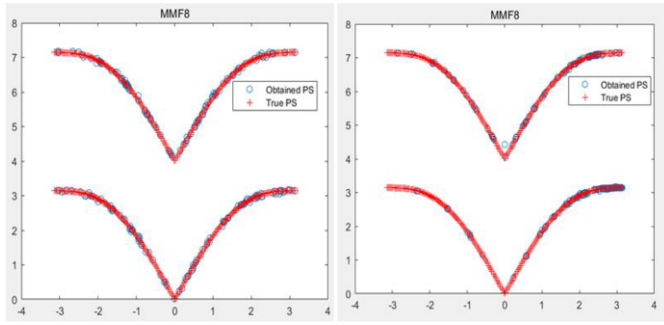

Figure 3. PSs obtained by two algorithms on MMF8

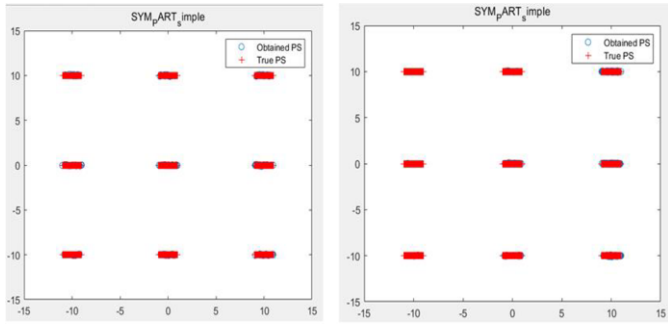

Figure 4. PSs obtained by two algorithms on SYM-PART_simple

Table 2. Comparison of 1/HV values obtained by nine algorithms

	MMODE_HS	MMODE_ICD	MMODE	MO_Ring_PSO_SCD	DN-NSGAII	Omni-Opt
MMF1	**1.14±5e-04**	1.14±3e-04	1.14±4e-04	1.1±5e-04	1.14±1.7e-04	1.14±1.1e-03
MMF5	**1.14±1e-03**	1.14±2.3e-03	1.14±6e-04	1.14±4e-04	1.14±1.1e-03	1.14±8e-04
MMF7	**1.14±4e-04**	**1.14±2e-04**	1.14±3e-04	1.14±8e-04	1.14±1.4e-03	1.14±6e-04
MMF8	**2.38±5.4e-03**	**2.37±3.8e-03**	2.39±1.76e-02	2.4±1.5e-02	2.38±5.3e-03	2.37±1e-03
MMF9	**0.1±1.1e-05**	**0.1±1.1e-05**	0.1± 7.9e-05	0.1±2.6e-05	0.1±2.7e-05	0.1±3.1e-05
MMF12	**0.63±2e-04**	0.63 ±1.1e-03	0.63±2e-04	0.64±2.5e-03	0.65±5.9e-02	0.65±4.9e-02
SYM_PART_simple	**0.06±6.3e-06**	**0.06±6.5e-06**	0.06± 4.1e-06	0.0605±5.6e-05	0.06±1.1e-05	0.06±6.5e-06
SYM_PART_rotated	**0.06±4.4272e-06**	0.06±5.6271e-06	0.06±7.1e-06	0.06±8.8e-05	0.06±1.2e-05	0.06±5.3e-06
Omni_test	0.018±2.8e-06	**0.018±2.9e-06**	0.018±3.7e-06	0.019±1.7e-05	0.018±4.1e-07	**0.018±4.7e-07**
+/=/-	8/1/0	5/4/0	0/9/0	0/9/0	0/9/0	1/8/0

4.2.2. Comparison of PS and PF distribution images obtained by algorithms

To verify the proposed MMODE_ICD performance in two spaces,we selecteed MMF8 and SYM-PART_Simple to analyse. Fig 3 shows that the number of Pareto optimal solutions obtained by MMODE_HS is greater and the distribution is more uniform. Therefore,MMODE_HS performs better than MMODE in decision space.Fig 4 shows MMODE_ HS and MMODE_ICD The Pareto solution set obtained , both algorithms found nine Pareto optimal subsets, but MMODE_ HS locates more optimal individuals on the subset, with more uniform distribution and good diversity.

References

[1] Han, Honggui, et al. Multi-modal multi-objective particle swarm optimization with self-adjusting strategy.Inform Sciences. 2023;629:580-598.

[2] Rauf, Hafiz Tayyab, et al. Multi population-based chaotic differential evolution for multi-modal and multi-objective optimization problems.Appl Soft Comput. 2023;132: 109909.

[3] Chen Y, Zhang K, Shen C. Two-stage dual-archive fireworks algorithm for multimodal multi-objective optimization. Proceedings of the 2022 6th International Conference on Machine Learning and Soft Computing.2022 Jan; 48-55.

[4] Liang J, Qiao K, Yue C, et al. A clustering-based differential evolution algorithm for solving multimodal multi-objective optimization problems. Swarm Evol Comput. 2021;60: 100788.

[5] Tanabe R, Ishibuchi H. A framework to handle multimodal multiobjective optimization in decomposition-based evolutionary algorithms. IEEE Trans Evol Comput. 2019; 24(4): 720-734.

[6] Y. Liu, G. G. Yen, and D. Gong. A multimodal multiobjective evolutionary algorithm using two-archive and recombination strategies. IEEE Trans Evol Comput. 2019; 23:660-674.

[7] Yue Cai-Tong, Liang Jing, Qu Bo-Yang, Yu Kun-Jie, Wang Yan-Li, Hu Yi. A survey on multimodal multiobjective optimization. Control and Decision.vol. 2021; 36(11): 2577-2588.

[8] Storn R, Price K .Differential evolution-a simple and efficient heuristic for global optimization over continuous spaces. J Glob Optim. 1997; 11(4):341-359.

[9] Tanabe R, Ishibuchi H. A review of evolutionary multimodal multiobjective optimization[J]. IEEE Trans Evol Comput. 2019; 24(1): 193-200.

[10] Yue C, Suganthan P N, Liang J, et al. Differential evolution using improved crowding distance for multimodal multiobjective optimization. Swarm Evol Comput. 2021; 62: 100849.

[11] Liang J, Xu W, Yue C, et al. Multimodal multiobjective optimization with differential evolution[J]. Swarm Evol Comput. 2019; 44: 1028-1059.

[12] C. Yue, B. Qu, J. Liang, A multiobjective particle swarm optimizer using ring topology for solving multimodal multiobjective problems,IEEE Trans Evol Comput.2017; 22(5): 805-817.

[13] Liu Y P, Ishibuchi H, Nojima Y, Masuyama N, Shang K. A double-niched evolutionary algorithm and its behavior on polygon-based problems. In: Proceedings of the 15th International Conference on Parallel Problem Solving from Nature. Coimbra, Portugal: Springer. 2018; 262-273.

Fuzzy Systems and Data Mining IX
A.J. Tallón-Ballesteros and R. Beltrán-Barba (Eds.)

doi:10.3233/FAIA231034

Link Prediction Method Combining Node Labels with Common Neighbors

Xinyang Li[a], Yayun LIU[a], Zhijian ZHANG[a,1], Lin JIANG[a], and Hui ZHONG[a]
[a]*Faculty of Science, Kunming University of Science and Technology, China*

Abstract. The link prediction method that only considers topology information without considering node labels does not achieve a good prediction result for label networks. The paper proposes a link prediction method combining Node Labels with Common Neighbors (NL-CN) to solve this problem. First, a similarity index based on node labels (NL) is defined. The similarity of two nodes is measured by the cosine of the angle between the label feature vectors of the two nodes. Secondly, the NL index and the common neighbor index are combined to obtain the binding index and link prediction for social networks using the binding index. Finally, experiments are conducted in six label networks, and the experimental results show that the method can effectively improve prediction accuracy. In the Gene, Citeseer and Cora networks, the AUC values of the NL-CN index were improved by 10.84, 4.76, and 0.22 percentage points, respectively, compared to the traditional Cos+ index with better performance.

Keywords. label networks, link prediction, similarity index, NL(Node Labels) index

1. Introduction

Improving the accuracy of link prediction in different networks is one of the core issues in this field. Link prediction can predict the likelihood that pairs of nodes that are not currently linked will produce connected edges in the future by using known topology and node information, and this prediction includes the prediction of unknown connected edges between two nodes in the network and the prediction of future connected edges[1].

The existing link prediction methods are broadly classified into three categories: based on node attributes, based on network topology, and based on maximum likelihood. However, in some special networks, not only the topology information of the network itself but also the node attribute information is available, and in this class of networks, only considering the topology information of the network does not effectively predict the similarity of connecting edges between two nodes. Therefore, this paper proposes a link prediction method for label networks that combines Node Labels and Common Neighbor (NL-CN).

The NL-CN method first defines an NL index based on the nodes' and neighbors' nodes, which uses the labels to calculate the similarity between nodes. Second, the NL

[1] Corresponding Author: Zhijian ZHANG, E-mail: zhijian@kust.edu.cn. This work is supported by the National Natural Science Foundation of China (11461037), the Scientific Research Foundation of Yunnan Provincial Department of Education (2017ZZX133), and the Introduction of talent scientific research start-up Foundation Kunming University of Science (KKZ3202207025).

index is combined with the CN index to obtain the NL-CN index. In this paper, a new similarity index is defined using node labels. Nodes in real networks have labels or attributes, so the NL-CN method is more applicable to realistic scenarios. Compared with the traditional link prediction methods, the NL-CN method makes more use of the information in the network to have relatively good prediction performance.

2. Related Work

In recent years, many advances have been made in research on link prediction, and in its early studies, most researchers have used link prediction methods based on node attributes. If two nodes share the same attributes, such as the more similar the interests of two people, then the more likely there is a link between these two people. Bu Xinyi et al.[2] used Sina Weibo social network for empirical analysis, defined a new similarity index using the fusion of network structure and node attribute labels, and performed link prediction for nodes.

The most basic link prediction method based on local information is the common neighbor (CN)[3], which describes the similarity between two nodes by defining the number of common neighbor nodes. In addition, many indexes evaluate the similarity between nodes based on local information: Jaccard coefficient[4], Sorensen index, and LHN-I index[5] based on common neighbors, concatenation of neighbors, and degree of nodes, respectively. Adamic and Adar[6] proposed the AA index, which mainly considers the importance of nodes to common neighbors through the degree of common neighbors. Zhou et al.[7] proposed the resource allocation (RA) index with higher prediction accuracy based on the previous index based on local information. The path-based method has three main indexes: the LP index[8], the LHN-II index, and the Katz index[9]. The main methods based on random wandering are the Cos+ index[10], the randomized wandering index (RWR), the restarted randomized wandering index (RWR)[11], and the SimRank index[12], Clauset, Moore, and Newman[13] proposed a link prediction method based on the maximum likelihood value, which is based on the hierarchical model, the stochastic chunking model, and the closed circuit model. Guimera and Sales-Pardo[14] used a stochastic chunking model to divide the nodes in the network into sets. The probability of connecting an edge between two nodes is only related to the corresponding settings in which the node is located.

3. Link prediction method combining node labels with common neighbors

3.1. Link prediction problem description

In link prediction methods for social networks, the social networks are usually regarded as topological graphs. In this paper, we can represent the social network as an undirected graph $G=(V,E)$, which V denotes the set of nodes and E denotes the set of edges. If the node set V contains N nodes, then the graph G contains most $N(N-1)/2$ edges. The link prediction method is mainly given a similarity index S_{xy} of any two nodes x, y.

In performing link prediction, the known edge set E is usually divided into a training set E^R and a test set E^T. In this paper, the ratio of splitting the edge set E is 9:1.

3.2. NL index based on node labels

Consider that in a label network, if two nodes have the same label, the probability of adjacent edges between these two nodes will be higher. In addition, this paper also considers that the labels of node neighbors can also provide information about the similarity between nodes.

In this paper, we use One-Hot Encoding to process the label information of nodes, and then we can obtain a label embedding matrix B, which contains the label embedding vector of each node. B_i denotes the label embedding vector of the node i, which is the first i row of the matrix B. Since both the node's label embedding vector and its neighbor's label embedding vector have an impact on the similarity between nodes, this paper defines the label feature vector as

$$\mathrm{A}_i = \lambda \mathrm{B}_i \oplus (1-\lambda) \sum_{j \in \Gamma(i)} \mathrm{B}_j \tag{1}$$

Where A is the label feature matrix; A_i denotes a row i of the matrix A denotes the label feature vector of node i; $\Gamma(i)$ denotes the set of neighboring nodes of the node i; and the prescribed symbol $\oplus$ is a first and last splicing rule between vectors. Parameter λ is set to assign the effect of the node label embedding vector and its neighbor node label embedding vector on the similarity between nodes.

The matrix of the number of products between the label eigenvectors is

$$\mathrm{Z} = \mathrm{A}\mathrm{A}^T \tag{2}$$

Each node in the network has a corresponding label feature vector, and this paper considers that the similarity between two sets of vectors is related to the angle between the vectors θ, if the angle between two sets of vectors θ is smaller, then they are more similar. Therefore, for any nodes x and y in the network, the similarity index based on the node labels is defined as

$$S_{xy}^{NL} = \cos\theta = \frac{|\mathrm{Z}_{xy}|}{|\mathrm{A}_x||\mathrm{A}_y|} \tag{3}$$

3.3. NL-CN method

In label networks, the label information of nodes is essential for link prediction of the network. However, from a global perspective, topology information in the network should be preserved. Therefore, this section combines the NL index with the most widely used common neighbor (CN) index in network topology-based link prediction methods to form the NL-CN index. The NL-CN index will be defined as

$$S_{xy}^{NL-CN} = \omega |\Gamma(x) \cap \Gamma(y)| + (1-\omega) \frac{|\mathrm{Z}_{xy}|}{|\mathrm{A}_x||\mathrm{A}_y|} \tag{4}$$

Therefore, the proposed algorithm NL-CN is described as follows.

Algorithm 1 NL-CN algorithm

Input:

network diagram G ; node embedding matrix B

Output:

AUC、Precision、RS value

1: **for** each node i **do**

2: Calculate the label feature vector A_i using Equation 1

3: **end for**

4: Calculate Z between label feature matrices using Equation 2

5: **for** $\omega = 0$ to $\omega = 1$ **do**

6: Calculate the similarity between two nodes according to

$$S_{xy} = \omega \left| \Gamma(x) \cap \Gamma(y) \right| + (1-\omega) \frac{\left| \mathrm{Z}_{xy} \right|}{\left| \mathrm{A}_x \right| \left| \mathrm{A}_y \right|}$$

7: Calculate the AUC、Precision、RS value using Equation 5,6,7

8: **end for**

9: Return the optimal AUC、Precision、RS value from Step 7

Suppose the number of nodes in the network is N , and the average degree of nodes is k . For the CN algorithm, its time complexity is $O(N^2 k)$. The proposed link prediction method combining node labels and common neighbors in this paper first embeds node labels into node label feature vectors using unique thermal coding and then makes the number product of label feature vectors of two nodes. Assuming the number of labels in the network is m , then the time complexity of this step is $O(2N^2 m)$, so the time complexity of the NL-CN algorithm is $O(N^2(2m+k))$. Since we consider the label information in the network based on the traditional algorithm, the time complexity of our algorithm increases. However, our algorithm is more applicable to real networks and has better prediction results.

4. Experiment

4.1. Evaluation indexes

AUC index[15] is done by randomly drawing an edge from the test set and then randomly drawing an edge from the unconnected edge set and comparing the size of the connected edge scores between them. Compare independently n times, if there are n' times when the score of the edge in the test set is greater than the score of the edge in the unconnected edge set, and there are n'' times when both scores are equal, then the AUC is calculated as

$$AUC = \frac{n' + 0.5n''}{n} \tag{5}$$

The AUC index should range from [0.5,1]. When the AUC is 0.5, it means that the scores of the edges are randomly assigned. When the AUC indicator is 1, it means that the full prediction is accurate.

Precision index[16] considers edges with scores ranked in the top L. It defines the link prediction accuracy as the proportion of edges in the test set among the top L edges. If m of the top L edges are in the test set, then Precision is computed as

$$\Pr ecision = \frac{m}{L} \tag{6}$$

In this paper, 10% of the edge set of the dataset is chosen as the value of L.

Ranking Score index[17] considers the position of the edges in the test set in the final ranking. Let the set $H = M \cup E^T$, where M is the set of unconnected edges. Let γ_i be the position of the edges $i(i \in E^T)$ in the final ranking, then the Ranking Score of an edge i is $RS_i = \gamma_i / |H|$. By traversing all the edges in the test set, the Ranking Score can be calculated as

$$RS = \frac{1}{\left|E^T\right|} \sum_{i \in E^T} RS_i = \frac{1}{\left|E^T\right|} \sum_{i \in E^T} \frac{\gamma_i}{|H|} \tag{7}$$

Where $|E^T|, |H|$ denotes the number of elements in the set, and smaller RS values indicate higher predictive accuracy.

4.2. Experimental data set

In this paper, we selected six label networks in the network repository[2], which are internet-industry-partnerships (IIP), webkb-wisc (WEB), ENZYMES8 (ENZ), Citeseer, Cora, and Gene. IIP is a dataset based on internet industry partnerships. WEB is a dataset based on world wide knowledge base project. ENZ is a graph data collection built on the structure of biomolecular proteins. Citeseer is a multi-disciplinary dataset consisting of papers from 10 research fields. Cora is a dataset based on citations between scientific papers. Gene is a database of genetic information for all species. The details of the dataset are shown in Table 1.

Table 1. Data set information

Dataset	Number of nodes	Number of consecutive sides	Average degree	Average clustering coefficient	Number of labels
ENZ	88	133	3	0.02	2
Gene	1103	1672	3	0.21	2
IIP	219	631	5	0.18	3
WEB	262	510	3	0.18	5
Citeseer	3264	4536	2	0.14	6
Cora	2708	5429	4	0.25	7

4.3. Experimental Results and Analysis

The link prediction of the network is first performed by the NL index defined in this paper to derive the optimal λ value in each data set. The optimal λ value and the

[2] https://networkrepository.com/

AUC、Precision、RS are different in different datasets, as shown in Table 2. Data in parentheses are the corresponding λ values.

Table 2. AUC, Precision, RS and corresponding λ values for the NL index in the six data sets

Dataset	ENZ	Gene	IIP	WEB	Citeseer	Cora
AUC	0.7106(0.65)	0.7783(0.55)	0.7425(0.53)	0.6293(0.26)	0.8997(0.49)	0.8945(0.39)
Precision	0.71(1)	0.69(0.67)	0.83(1)	0.55(0.27)	0.91(1)	0.89(1)
RS	0.5857(0.47)	0.3691(0.54)	0.3527(0.43)	0.4763(0)	0.3098(0.5)	0.3205(0.33)

Parameter λ in Equation 1 should be chosen for different data sets as its optimal value. It combines the NL index with the most widely used CN index based on network topology. The prediction accuracy and the corresponding ω values for the six networks using the NL-CN index for link prediction are shown in Table 3. Data in parentheses are the corresponding ω values.

Table 3. AUC, Precision, RS and corresponding ω values for the NL-CN index in the six datasets

Dataset	ENZ	Gene	IIP	WEB	Citeseer	Cora
AUC	0.7554(0.17)	0.8875(0.8)	0.8121(0.37)	0.7001(0.6)	0.9338(0.92)	0.9332(0.55)
Precision	0.84(1)	0.69(0.06)	0.83(0)	0.67(0.72)	0.91(0.5)	0.89(0.5)
RS	0.5769(0.5)	0.304(0.64)	0.3309(0.08)	0.4297(0.46)	0.2913(0.74)	0.2982(0.72)

As seen in Table 3, the prediction accuracy of the combined index improves on both the original index compared to the index considering only the network topology or the node labels. Therefore, it is necessary to consider node labels in the link prediction of label networks. After that, the prediction accuracy of the NL-CN index, NL index, and index based on network topology are compared in different networks.

Table 4. Prediction accuracy of different indexes in different data sets

index	ENZ			Gene			IIP			WEB			Citeseer			Cora		
	AUC	P	RS	AUC	P	RS	AUC	P	RS	AUC	P	RS	AUC	P	RS	AUC	P	RS
NL-CN	0.7554	**0.84**	0.5769	**0.8875**	**0.69**	**0.304**	**0.8121**	**0.83**	**0.3309**	**0.7001**	**0.67**	**0.4297**	**0.9338**	**0.91**	0.2913	**0.9332**	**0.89**	0.2982
NL	0.7106	0.71	0.5857	0.7783	0.69	0.3691	0.7425	0.83	0.3527	0.6293	0.55	0.4763	0.8997	0.91	0.3098	0.8945	0.89	0.3205
CN	0.5472	0.65	0.9822	0.8215	0.67	0.4614	0.7434	0.81	0.6077	0.6706	0.45	0.6826	0.7564	0.78	0.5154	0.7704	0.75	0.5521
RA	0.5483	0.63	0.9822	0.8212	0.65	0.4614	0.7522	0.81	0.5671	0.6829	0.65	0.6494	0.7570	0.76	0.5154	0.7714	0.79	0.5518
AA	0.5478	0.63	0.9822	0.8220	0.65	0.4614	0.7529	0.75	0.5744	0.6839	0.65	0.6494	0.7564	0.76	0.5154	0.7718	0.82	0.5517
LHN-I	0.5444	0.58	0.9822	0.8198	0.63	0.4614	0.6858	0.72	0.5923	0.6331	0.63	0.7122	0.7560	0.82	0.5154	0.7701	0.85	0.5528
Sorenson	0.5438	0.54	0.9822	0.8208	0.64	0.4614	0.6971	0.68	0.5858	0.6441	0.62	0.7137	0.7557	0.83	0.5154	0.7701	0.74	0.5524
Jaccard	0.5441	0.61	0.9822	0.8210	0.67	0.4614	0.6986	0.75	0.5858	0.6430	0.64	0.7137	0.7561	0.73	0.5154	0.7703	0.69	0.5524
Cos+	**0.7991**	0.75	**0.4408**	0.8007	0.66	0.3551	0.6466	0.81	0.3861	0.6745	0.59	0.4977	0.8913	0.89	**0.2869**	0.9311	0.88	**0.287**

From Table 4, it can be seen that the prediction accuracy of the NL-CN index is higher than most indexes. It is slightly lower than the Cos+ index in the ENZ data set. Otherwise, the NL-CN index outperformed all other indexes. Also, the AUC of the NL-CN index is higher in the Citeseer and Cora datasets where the data are more extensive, and the number of labels is more elevated, reaching about 0.93.

Precision for the NL-CN index outperforms the other indexes in all six datasets. Meanwhile, the RS of the NL-CN index is second only to the Cos+ index in the ENZ, Citeseer, and Cora datasets. In addition to this, the RS of the NL-CN indicator outperforms most of the indicators.

5. Conclusion

In this paper, we propose a node labels-based similarity index, which uses the label information of nodes to calculate the similarity of node pairs. Then the NL index is combined with the common neighbors index to obtain the NL-CN index. This method makes up for the deficiency that the traditional index only considers the network topology and ignores the node attribute information. Among the six label networks selected, the prediction accuracy of the NL-CN index is improved to varying degrees compared to the index based on the network topology.

In future work, we will consider how to reduce the time complexity of the method to reduce the time to run in large networks, where the framework also works better. In addition, we will consider the case where a node has multiple labels, extending the current one-dimensional to multi-dimensional, to improve the usability of the framework in link prediction studies.

References

[1] Daud N N, Ab Hamid S H, Saadoon M, et al. Applications of link prediction in social networks: A review. Journal of Network and Computer Applications, 2020, 166: 102716.
[2] Bu X Y, Chen M L. A study of link prediction in social networks. Research on Library Science, 2016(17): 17-21.
[3] Liben-nowell D, Kleinberg J. The link prediction problem for social networks//Proceedings of the twelfth international conference on Information and knowledge management. 2003: 556-559.
[4] Qin X, Han X, Chu J, et al. Density peaks clustering based on Jaccard similarity and label propagation. Cognitive Computation, 2021, 13: 1609-1626.
[5] Yue Z H, Xu H Y, Wang Q F. Dynamic Link Prediction of Knowledge Diffusion in Disciplinary Citation Networks Based on Local Information. Information studies: Theory & Application, 2020, 43(2): 84.
[6] Kumar A, Singh S S, Singh K, et al. Link prediction techniques, applications, and performance: A survey. Physica A: Statistical Mechanics and its Applications, 2020, 553: 124289.
[7] Zhou T, Lü L, Zhang Y C. Predicting missing links via local information. The European Physical Journal B, 2009, 71: 623-630.
[8] Lü L, Jin C H, Zhou T. Similarity index based on local paths for link prediction of complex networks. Physical Review E, 2009, 80(4): 046122.
[9] Bai M, Hu K, Tang Y. Link prediction based on a semi-local similarity index. Chinese Physics B, 2011, 20(12): 128902.
[10] Zhang Y X, Feng Y X. A review of methods and developments in link prediction. Measurement & Control Technology, 2019, 38(2): 8-12.
[11] Shao H, Wang LW, Deng J. A link prediction algorithm based on density peak clustering. Small Microcomputer Systems, 2020, 41(5): 1007-1012.
[12] Jiang W C, Lu M M. A link prediction algorithm with superimposed random wandering gravity model. Journal of Chongqing University of Technology (Natural Sciences), 2022, 36(5): 137-146.
[13] Clauset A, Moore C, Newman M E J. Hierarchical structure and the prediction of missing links in networks. Nature, 2008, 453(7191): 98-101.
[14] Guimerà R, Sales-pardo M. Missing and spurious interactions and the reconstruction of complex networks. Proceedings of the National Academy of Sciences, 2009, 106(52): 22073-22078.
[15] Zeng G, Zeng E. On the three-way equivalence of AUC in credit scoring with tied scores. Communications in Statistics-Theory and Methods, 2019, 48(7): 1635-1650.
[16] Wu Z, Lin Y, Zhao Y, et al. Improving local clustering based top-L link prediction methods via asymmetric link clustering information. Physica A: Statistical Mechanics and Its Applications, 2018, 492: 1859-1874.
[17] Zhou T, Ren J, Medo M, et al. Bipartite network pro-jection and personal recommendation. Physical review E, 2007, 76(4): 046115.

Fuzzy Systems and Data Mining IX
A.J. Tallón-Ballesteros and R. Beltrán-Barba (Eds.)

doi:10.3233/FAIA231035

Research on Optimization of Urban Logistics Delivery Path Under Fuzzy Demand

Xuerui QIN and Hao CHEN[1]
School of Economics and Business Administration, Yibin University, Yibin City, Sichuan, China

Abstract. Optimization of delivery routes is a key method to reduce delivery costs. If scientific and reasonable methods are adopted to arrange delivery routes, it can reduce delivery costs, increase enterprise profits, and increase vehicle loading, achieving the goal of stable growth for enterprises. In this paper, the logistics distribution in the same city under the condition of fuzzy demand is taken as the research object, and the vehicle load, customer demand, customer service time and other constraints are taken as the constraints. The Simulated annealing algorithm is used to solve the model, and a reasonable and satisfactory optimization scheme is obtained. By comparing the solutions before and after optimization, it is confirmed that the optimization model can effectively solve the logistics distribution problem under fuzzy demand.

Keywords. Fuzzy, Demand, Path optimization, Simulated annealing algorithm, Optimization

1. Introduction

The logistics industry is a dynamic service industry that not only includes basic functions such as transportation, storage, loading and unloading, handling, and packaging, but also covers many fields such as circulation processing, distribution, and information processing. At the same time, with the continuous development of e-commerce, takeout, errands and other industries, local logistics and distribution have become a key carrier of urban services, facilitating customers' shopping and daily activities. With the continuous expansion of demand in the local logistics market, many internet companies have joined the competition of local logistics, bringing opportunities and challenges to local logistics enterprises. On the one hand, people's consumption concepts are gradually "personalized" and "diversified", and their awareness of time and service is becoming more sensitive. The ambiguity of local logistics needs is increasing, requiring logistics to be more efficient and convenient. On the other hand, at present, local logistics is still in a rough development stage, with low

[1] Corresponding Author, Hao CHEN, Yibin University, Yibin City, Sichuan, China; Email: 1312587451@qq.com
Funding Support: Water Transport Economic Research Center (SYJJ2022B07).

levels of informatization, low resource utilization, and inconsistent technical standards and distribution processes, resulting in low transportation efficiency and high transportation costs of local logistics. It is crucial for local logistics enterprises to effectively meet diverse customer needs, develop reasonable distribution path strategies, reduce distribution costs of local logistics, and improve customer satisfaction.

Optimization of distribution routes is an important way to reduce logistics transportation costs and improve logistics transportation efficiency. On this basis, it is also necessary to consider that fuzzy demands may often be encountered in actual situations. In such cases, conducting distribution routes for local logistics effectively reduces the operating costs of local logistics enterprises, which has important practical significance. Ouyang jingcan proposed the vehicle path optimization model uses heuristic algorithms to obtain solutions with low delivery costs, high vehicle loading rates, high service efficiency, and high profits, which has important theoretical significance[1].

The optimization of distribution paths is a hot research topic in the field of logistics. Carlsson et al. proposed the concept of upper and lower limits for time windows, where the upper limit refers to the time when customers can provide service as early as the delivery vehicle is specified, the lower limit refers to the latest service time, and the intermediate time is the service time[2]. Tao introduces soft time window constraints on the basis of time windows and solves related problems considering time factors by establishing penalty functions[3]. Eslamipoor Reza believes the pollutant of environment is considered an influential factor in the evaluation and selection of the supplier. The suggested model's objectives include lowering the cost of suppliers, minimizing low-quality goods from suppliers, minimizing delivery time, and minimizing the amount of environmental pollutants emitted by vehicles [4]. MA aims to minimize distribution cost and maximize customer satisfaction, he design an improved ant colony algorithm to solve the initial distribution path and use the insertion method to solve the immediate customer demand. [5]. Lisa et al. mainly studied the construction of cold chain distribution models, combined with the distribution data of cold chain companies, and used Matlab programming tools and commonly used hybrid mutation probabilities to obtain optimization results[6].In recent years, research on path planning and algorithms in China has also been greatly strengthened. Wei Junhua divided it into soft time window path problems based on customer needs and established a model, which was solved and optimized using genetic algorithm[7]. Ma Cunrui et al. constructed a path optimization model suitable for express delivery, implemented the solution using genetic algorithm, and conducted sensitivity analysis through actual cases[8]. Scholars like Deng Xueping have turned their attention to express delivery recycling, designing an objective function of distribution cost plus recycling processing cost, constructing relevant recycling models and solving them. Using genetic algorithms to solve, while considering other factors, the optimal solution for the delivery path is obtained[9]. Researchers such as Zhang Duo used an improved genetic algorithm and a multi criteria decision-making method to solve the capacity constrained vehicle delivery problem, taking into account various goals such as carbon emissions and road risks[10].

Current research indicates that foreign scholars are more focused on considering the impact of different time window constraints on path optimization and conducting research on them. However, domestic scholars focus on how to obtain the optimal solution for path optimization under different constraint conditions. Overall, there is still a lack of research on the optimization of logistics delivery paths with fuzzy

demands. There are few research results on fuzzy requirements, especially those that consider both dynamic and stochastic demand changes with strong randomness, such as the location and range of changes.

On the basis of summarizing existing literature, this article proposes to establish an optimization model for urban logistics distribution path under fuzzy demand, build an optimization model for urban logistics distribution path with the minimum total operating cost. The vehicle path optimization model for the constructed fuzzy demand is transformed into a fuzzy demand response problem and a delivery path update strategy problem, and Simulated annealing algorithm is designed to solve the vehicle routing. Finally, take Anji logistics distribution enterprises in Yibin City as an example, select data from 12 distribution points in 1 distribution center to verify the effectiveness of the construction model and solution. By comparing the optimal path for demand determination and different $\left(\mu,\sigma^2\right)$ values, it has been confirmed that the model and algorithm have good application value.

2. Construction of an Optimization Model for Urban Logistics Distribution Path Based on Fuzzy Demand

2.1. Problem Description

The fuzzy demand based distribution path optimization problem is a vehicle path optimization problem that considers fuzzy demand. Compared to the conventional VRPTW problem, it expands the determined cargo demand and time window demand into a dynamic vehicle path optimization problem that considers changes in cargo demand and new demands. The vehicle routing optimization problem with fuzzy demands can be specifically described as: in a distribution system, there is a fixed distribution center and several distribution vehicles, where some customers' demands are accurate, while the demands of other demand points may change, known as fuzzy demand points.

As the demand for new fuzzy points arises, the delivery system must respond with delivery. Under certain constraints, arrange the delivery path of vehicles reasonably to achieve the minimum cost during the delivery process and meet the delivery requirements of fuzzy demand points to the greatest extent[11-13].

2.2. Model Assumptions

The following assumptions are made for the optimization of vehicle routing in urban logistics distribution under fuzzy demand:

(1) In the distribution system, there is a distribution center and multiple distribution points. Each delivery vehicle departs from the distribution center, completes the task of the distribution point, and returns to the distribution center.

(2) All delivery vehicles are subject to load limitations, which can result in varying transportation costs.

(3) In the distribution point, factors such as the location and quantity of demand points are clearly defined; The demand for fuzzy demand points is uncertain.

(4) The demand for goods at any demand point, whether vague or explicit, shall not exceed the maximum carrying capacity of a single vehicle.

(5) The mileage between the distribution center and demand points, as well as between demand points, is fixed.
(6) Once the demand for fuzzy requirements appears, there will be no change.

2.3. Construction of Fuzzy Demand Delivery Path Optimization Model

2.3.1 Parameter Description

The parameter assumptions are shown in Table 1.

Table 1 Parameter Definition

Symbol	Define	Symbol	Define
N	The number of customers that the enterprise needs to serve, when 0 is taken as the distribution center point	FC	Penalty costs
K	Number of vehicles required for delivery	M_a , M_b	Time penalty coefficient
Q	Vehicle load capacity	S_{ik}	The time when vehicle k starts serving customer i
GC	Vehicle Fixed cost	a_i	The time when the vehicle can access customer i
f_k	Fixed cost of the kth vehicle operation	b_i	The time when the vehicle can leave customer j
TC	Vehicle Variable Cost	q_i	The freight demand Customer i
d_{ij}	The shortest distance between delivery point i and delivery point j	X_{ijk}	Decision variable, vehicle k is 1 when transporting from delivery point i to delivery point j, otherwise it is 0
α_k	Unit distance cost of vehicle k	Y_{ik}	Decision variable, using vehicle k to serve customer i

2.3.2 Objective function

(1) Vehicle Fixed cost

Fixed cost of vehicles refer to fixed expenses such as staff salaries and maintenance costs incurred during the normal operation of vehicles, which are recorded as:

$$GC = \sum_{k=1}^{k} f_k \tag{2-1}$$

(2) Variable cost of transportation

During the transportation process of vehicles, variable costs refer to the costs that vary with the distribution mileage and load capacity, including labor, fuel consumption, electricity consumption, etc. For ease of calculation, the variable cost in this article is simply expressed as an equation related only to the delivery mileage, which is:

$$TC = \sum_{k=1}^{k} \sum_{i,j=1}^{n} X_{ijk} \cdot d_{ij} \cdot \alpha_k \tag{2-2}$$

2.3.3 Constraint condition

Visiting the customer's vehicle is the same as leaving the customer's vehicle.

$$\sum_{n=1, n \neq i \neq j} X_{ink} = \sum_{n=1, n \neq i \neq j} X_{njk}, k \in K \tag{2-3}$$

Ensure that all customers receive only one service.

$$\sum_{i \in N} Y_{ik} = 1 \tag{2-4}$$

The starting and ending points of each delivery vehicle are the distribution centers.

$$\sum_{j\in N} X_{0jk} = \sum_{j\in N} X_{i0k} = 1, k \in K \tag{2-5}$$

The total customer demand on each delivery route must be less than the capacity limit of the vehicle.

$$\sum_{i\in N}\sum_{k\in K} q_i Y_{ik} \le Q \tag{2-6}$$

2.3.4 Construction of optimization model
Optimize the model with the goal of minimizing costs:

$$\begin{aligned} &\min C = \sum_{k=1}^{k} f_k + \sum_{k=1}^{k}\sum_{i,j=1}^{n} X_{ijk}\cdot d_{ij}\cdot \alpha_k \\ &s.t. \\ &\sum_{n=1,n\neq i\neq j} X_{ink} = \sum_{n=1,n\neq i\neq j} X_{njk}, k \in K \\ &\sum_{i\in N} Y_{ik} = 1 \\ &\sum_{j\in N} X_{0jk} = \sum_{j\in N} X_{i0k} = 1, k \in K \\ &\sum_{i\in N}\sum_{k\in K} q_i Y_{ik} \le Q \end{aligned} \tag{2-7}$$

3. Algorithm Solution for Fuzzy Demand Intracity Logistics Delivery Path

Simulated annealing algorithm is a stochastic optimization algorithm based on Monte Carlo iterative solution strategy. Its starting point is based on the similarity between the annealing process of solid materials in physics and general Combinatorial optimization problems. The goal is to provide effective approximate solution algorithms for problems with NP complexity. Overcoming the defects of easily falling into local minima and dependence on initial values in other optimization processes. Theoretically, it is a global optimization algorithm. Based on the similarity between the solution of the optimization problem and the annealing process of the Physical system, it uses the Metropolis algorithm and properly controls the temperature decline process to achieve Simulated annealing, so as to achieve the purpose of solving the global optimization problem. The specific steps include:
(1) Set the initial scheme with the objective function T as sufficiently large and use it as the initial solution, with a design termination iteration count of N;
(2) For n=1, Do steps (3) to (5) for N;
(3) Generate a new solution X and calculate the difference between the new solution X and the previous solution, denoted as $\Delta E(X)$;
(4) If $\Delta E(X)$, then accept X as the new current solution, otherwise accept X as the new current solution with probability exp($-\Delta E(X) \big/ T$);
(5) If sufficient search or termination conditions are met, output the current solution as the optimal solution and end the program;
(6) Gradually decrease T until it approaches 0, then proceed to step (2).

Simulated annealing algorithm flow is shown in Figure 1.

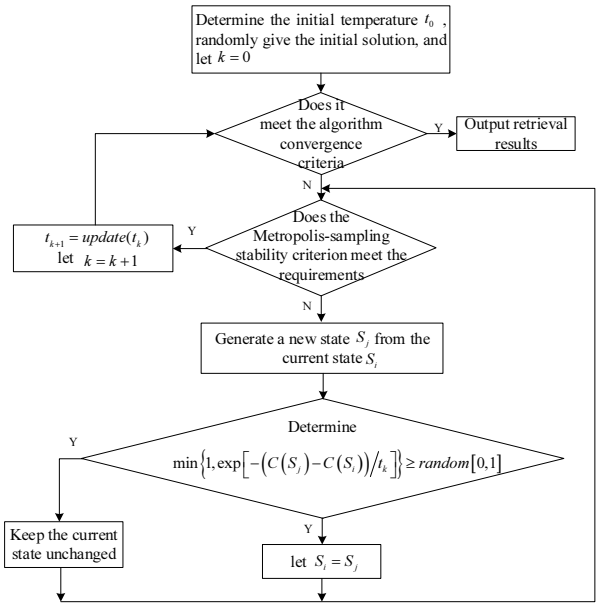

Figure 1 Flow chart of Simulated annealing algorithm

4. Example

This paper takes Yibin Anji Logistics Company as an example. The company has its own logistics distribution center, warehouse and its own distribution team, whose main job is to deliver products to supermarkets and stores. Anji logistics company currently has 12 customer points for delivery services, with 12 delivery vehicles. The distribution center provides services to customers between 4 and 6 a.m. every day to ensure customers' demand on that day and avoid urban traffic peak. The coordinates of the customer point and distribution center are known; The expected demand is known, but the actual demand follows an independent Normal distribution; The maximum load capacity of a single vehicle is 2 tons. The specific parameters are shown in Table 2.

Table 2 Demand Point Information Parameter Table

Point	X	Y	Demand	Point	X	Y	Demand
0	14.07	30.67	/				
1	13.45	30.31	0.43	7	13.77	29.57	0.52
2	13.83	30.04	0.47	8	15.04	29.59	0.72
3	14.21	29.15	0.75	9	16.02	30.45	0.49
4	13.45	30.42	0.51	10	14.56	29.77	0.49
5	11.56	28.51	0.90	11	15.27	28.54	0.86
6	15.57	30.51	0.83	12	16.55	29.57	0.89

According to the basic data in Table 1 and the relevant assumptions in the model, this paper uses Matlab to write code, set the values of relevant parameters in the Simulated annealing algorithm, set the initial temperature T_0=999 , termination temperature T_f=0.001 , temperature attenuation parameters $\alpha = 0.93$, Markov chain length $M_k = 20$, and Fixed cost of 120 yuan/vehicle, Variable cost 2 yuan/km.

(1) When the requirements are clear

The relevant parameters and initial values are imported into Matlab for solution, and the optimal results are obtained after 50 random tests. The convergence and scheme of Simulated annealing algorithm after iteration are shown in Figure 2, and the distribution scheme is shown in Table 3. It can be seen that after iteration, the algorithm begins to converge after 120 iterations, and the total delivery cost in the optimal state is 648.08 yuan.

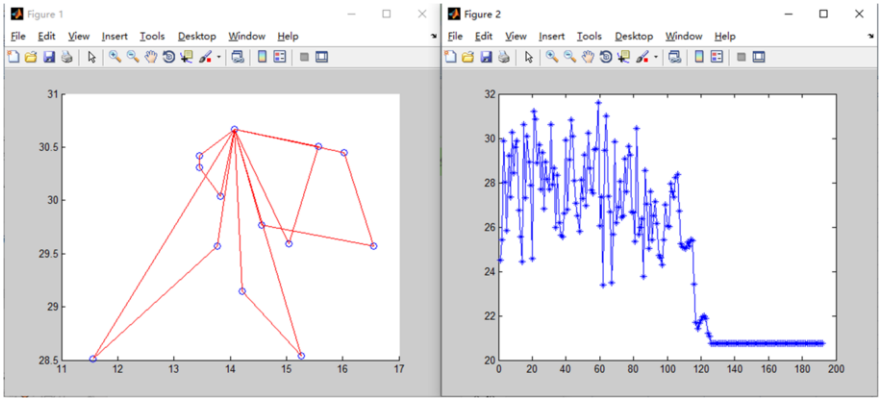

Figure 2 Distribution Plan and Convergence Curve

Table 3 Delivery Plan

Number	Delivery Plan	Distance(km)	Cost(yuan)	Actual Capacity(㎡)	Load factor(%)
1	0-2-1-4-0	1.92	123.84	1.41	70.50%
2	0-3-11-0	5.19	130.38	1.61	80.50%
3	0-6-8-0	4.02	128.04	1.55	77.50%
4	0-10-12-9-0	6.01	132.02	1.87	93.50%
5	0-7-5-0	6.90	133.80	1.42	71.00%
Total		24.04	648.08		

(2) When demand is ambiguous

When the demand is fuzzy, it is calculated by 90% of the demand satisfaction rate, and the customer demand meets the Normal distribution $X \sim N\left(\mu,\sigma^2\right)$. To simplify the solution of the Normal distribution, according to the relevant knowledge learned, z is 1.3 at that time $x = \mu + z\sigma$, and the change of demand of each customer point under the condition of obeying the Normal distribution is shown in Table 4.

Table 4 Normal distribution Change of Customer Point Demand

Demand point	Expected demand	σ =0.1	σ =0.2	σ =0.3	Demand point	Expected demand	σ =0.1	σ =0.2	σ =0.3
1	0.43	0.56	0.69	0.82	7	0.52	0.65	0.78	0.91
2	0.47	0.6	0.73	0.86	8	0.72	0.85	0.98	1.11
3	0.75	0.88	1.01	1.14	9	0.49	0.62	0.75	0.88
4	0.51	0.64	0.77	0.9	10	0.49	0.62	0.75	0.88
5	0.9	1.03	1.16	1.29	11	0.86	0.99	1.12	1.25
6	0.83	0.96	1.09	1.22	12	0.89	1.02	1.15	1.28

Through Matlab software calculation, convergence occurs approximately 130 times when the demand is fuzzy. The summary of path optimization under fuzzy requirements is shown in Table 5.

Table 5 Path optimization based on random requirements

Delivery vehicle	σ =0.1	σ =0.2	σ =0.3
1	0-4-1-2-0	0-10-11-0	0-6-0
2	0-9-10-7-0	0-2-6-0	0-11-0
3	0-12-6-0	0-12-9-0	0-12-0
4	0-11-8-0	0-8-3-0	0-2-3-0
5	0-3-5-0	0-4-1-0	0-8-9-0
6		0-7-5-0	0-1-4-0
7			0-10-7-0
8			0-5-0
Total mileage	24.77	26.10	31.53
total cost	649.53	772.19	1023.05

5. Conclusion

This paper mainly conducts relevant analysis based on the actual situation of Anji Logistics Company in Yibin City. After collecting relevant data, it conducts research and analysis. Assuming that the demand of customer points follows a certain Normal distribution, it then uses Matlab software to write programs to solve the model built by Simulated annealing algorithm according to its location distribution, demand and other conditions, and conducts quantitative analysis on the basis of the model, Finally, the path optimization results for minimizing delivery costs under deterministic and fuzzy demands are obtained. The various costs under deterministic and fuzzy demands are compared, and the results are compared and analyzed to verify the effectiveness of this study.

References

[1] Ouyang jingcan. Research on Optimization of Intra-City LogisticsDistribution Routing Under Uncertain Demand. Beijing Jiaotong University. 2019 . Dec: 1-7.

[2] Desrochers,M. Carlsson,J. Worst-case demand distributions in vehicle routing. European Journal of Operational Research. 2017 Feb ;256(2):462-272.

[3] Tao Y,Weixin W,Qiqi W. Fuzzy Demand Vehicle Routing Problem with Soft Time Windows. Sustainability May;,2022,14(9):1-14.

[4] Eslamipoor Reza. A fuzzy multi-objective model for supplier selection to mitigate the impact of vehicle transportation gases and delivery time. Journal of Data, Information and Management. 2022 Apr;3(4):231-241.

[5] Ma Z,Zhang J,Wang H, et al. Optimization of Sustainable Bi-Objective Cold-Chain Logistics Route Considering Carbon Emissions and Customers' Immediate Demands in China. Sustainability, 2023 Mar;15(7):1-23.

[6] Lisa Z. Establishment of Cold Chain Distribution Route Optimization Model in Big Data Environment. International Journal of Computational and Engineering. 2020 Mar;5(3):101-114.

[7] Wei Junhua, Wang Anling, Tong Yi. The Optimal Approach of Vehicle Route with Time Window Based on Genetic Algorithm: Dynamic Partition of Demand. Highway Transportation Technology.2005 Oct;22(10):165-170.

[8] WANG Jianze, LIAO Yjja, GUO Tingting. Research on Path Optimization of Express Delivery Vehicles of Company A. Modern Information Technology. 2023 Jan;1(01):182-187.

[9] DENG Xueping, XUE Ying, TIAN Shuaihui. Research on vehicle routing optimization of express package recycling with time window. Journal of Chongqing University of Posts and Telecommunications (Natural Science Edition). 2018 Jun;30(06):861-869.

[10] ZHANG Duo, LI Meiyan, LI Haoran, FU Yingjun. Research on Optimal Distribution Route Based on Multi-criteria Decision and Genetic Algorithm. Information and Computers. 2021 Dec;33(24):43-45.

[11] K Pandey, S Jain. A Fuzzy based Sustainable Solution for Smart Farming, Fuzzy Expert Systems and Applications. 2020 Jan;(1):109-129.
[12] Rule Based Trust Evaluation using Fuzzy Logic in Cloud Computing, 6th International Conference on Reliability, Infocom Technologies and Optimization, 2017 Sep: 620-626,
[13] Keystroke Dynamics Authentication using Fuzzy Logic, 10th International conference on Contemporary Computing. 2017 Aug: 319 – 324.

Fuzzy Systems and Data Mining IX
A.J. Tallón-Ballesteros and R. Beltrán-Barba (Eds.)

doi:10.3233/FAIA231036

An Empirical Study on Impact of Guidance Experience on Supervisor Identification Based on Structural Equation Modeling

Wen Luo[a,b], Yuan-Sheng Zhong[b,1], Jun Xu[b]
[a] *Suzhou Centennial College, Suzhou, China*
[b] *Key Laboratory of Data Science in Finance and Economics, Jiangxi University of Finance and Economics, Nanchang, China*

Abstract. The identification of postgraduates to their supervisor will affect their experience of instruction and the relationship of instruction. Analyzing the guidance experience(GE) by postgraduates and its influence on supervisor identification(SI) is helpful to establish a better supervisor-postgraduate relationship(SPR). Based on the definition of informal organization and the theory of organizational identification, this study uses the structural equation model method in data mining to explore the influence of GE on the recognition of postgraduates' supervisors from three dimensions: academic and research guidance(ARG), moral cultivation(MC), employment assistance and management(EAM). The results of 399 valid questionnaires of postgraduates show that: the MC of supervisor has a significant impact on the SI, the GE significantly positively correlated with SPR, and influences on SI via partial mediation of SPR. The students who highly agree with their supervisor have the highest evaluation on their supervisor's research guidance. The factors resulting in the maximum difference in the SI are concentrated on the personality and attitude, followed by the task, the academic plan, and research direction assigned by the supervisor. Supervisors should pay more attention to moral education, improve SPR and manage postgraduates appropriately rather than solely focusing on academic research. These research results provide a theoretical basis for the optimization of GE and provide ideas for the build positive SPR.

Keywords. Guidance Experience; Supervisor Identification; Supervisor-postgraduate Relationship; Structural Equation Model; Supervisor; Postgraduate

1. Introduction

Postgraduates' education under the supervisor responsible system tends to form an informal organization with the supervisor as the core, and a series of organizational activities such as academics, research, and employment are carried out with the participation of the supervisor [1]. In this process, postgraduate gradually arises a sense

[1]Corresponding Author: Yuan-Sheng Zhong, Professor and doctoral supervisor of Jiangxi University of Finance and Economics, Nanchang, China; E-mail: zhong_ys@jxufe.edu.cn.
This research was supported by the Jiangxi Province Degree and Graduate Teaching Reform Project(JXYJG-2021-086), and the Open Project Fund of Key Laboratory of Financial Data Science, Jiangxi University of Finance and Economics.

of belonging to and trust through the long-term and detailed learning of the guidance behaviors by their supervisors. Citing organizational identification theory, this concept, which covers both cognitive and affective characteristics, is summarized as the SI. The sense of acquisition is a manifestation of positive psychological feelings caused by "acquisition", and the "sense of acquisition" can often generate new "acquisition"[2]. The SI is the manifestation of the high quality of GE and SPR obtained by postgraduates. To carry out the research on SI of postgraduates and investigate the factors that postgraduates emphasize more in the content of GE can further reflect on and revise the SPR.

2. Development of research hypotheses and models

2.1 Method

Use Douglas' idea of understanding and analyzing the model, setup constructs from literature review, setup the mathematical relationships among constructs and put forward assumptions [3]. Choosing the structural equation model method in data mining to analyzes SPR from multiple perspectives, and summarizes the impact of GE on SI.

2.2 Hypotheses

In social psychology, identification is a process by which affections, attitudes and even perceptions are moved into the self. The concept of organizational identification was proposed by March and Simon [4]. Subsequently, scholars such as Patchen[5], Ashforth and Mael[6] respectively defined this theory from multiple perspectives such as membership, affective characteristics and individual behavioral cognitive attributes. Although scholars have different understandings of organizational identification, the research content focuses on two levels: cognitive concept and affective experience. Individuals define themselves by organizational identification, and have affective identification with the organization, which is manifested by sense of responsibility and belonging. Measurement of organizational identification can be performed as a holistic concept or divided by dimensions. van Dick et al. proposed a scale that includes not only the identification of individuals with the organization's identification and evaluation, but also the four dimensions of maintaining organizational interests, cognitive, affective, evaluative, and behavioral [7].

Socrates believed that the primary task of education was to cultivate morality, and Spencer proposed that education was to prepare for a perfect life. With the change of educational concept, postgraduates' dependence on supervisor not only stays at the educational level, but also tends to develop the pathway to workplace. The supervisor's guidance is significantly related to the subjective well-being of the trainees [8]. Supervisor influences the employability of their students can help them fulfill personal values [9]. Therefore, we hypothesized that:

Hypothesis 1: The supervisor's ARG, EAM, MC can provide a positive GE for postgraduates.

The harmonious SPR is established on the supervisor's teaching and scientific research activities as the carrier, with supervisor's MC as the driving force [10]. Differentiated guidance behaviors will form different SPR. When postgraduates receive sufficient, efficient, and satisfactory GE, they will form positive feedback on the SPR

due to their abundant sense of achievement in academic, scientific research, and employment aspects, and the rich GE will compensate for the shortcomings of single supervisor guidance. Therefore, we hypothesized that:

Hypothesis 2: There is a positive influence between GE and SPR.

The ideal state of the SPR is not only the conventional interactive relationship between the supervisor and postgraduates, but its core is that through the guidance of constitutive values, both sides have a sense of understanding and identification, and to make choices and reflections on the relationship, so as to complete their own shaping. Postgraduates naturally have a high sense of identification with their supervisors. The professional level, guiding behavior and values of the supervisors will imperceptibly influence them in their daily interactions with postgraduates, and postgraduates will spontaneously learn, accept and internalize them [11]. Therefore, we hypothesized that:

Hypothesis 3: The SPR plays a mediating role between supervisor experience and SI.

2.3 The conceptual framework

According to the relevant literature and empirical research results, this study proposed the theoretical model with GE as the antecedent variable, SI as the outcome variable, and different SPR generated by GE as the intermediate variable (as shown in Figure 1).

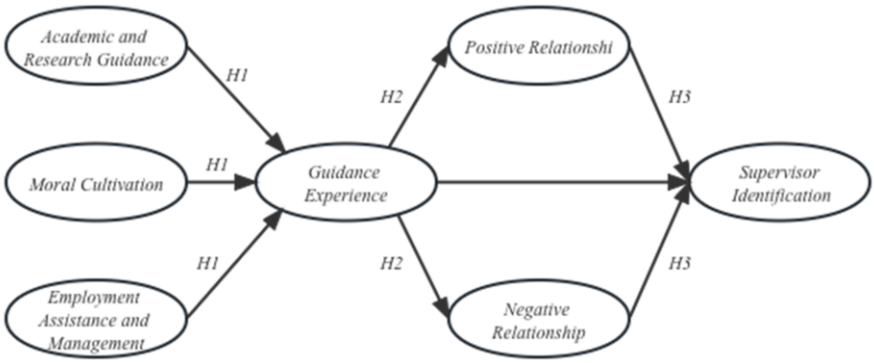

Figure 1. The proposed conceptual framework

3. Results

3.1 Sample information of respondents

The formal survey mainly relies on the online platform, with postgraduates as the survey object, and a total of 424 online questionnaires are distributed. After screening, 399 valid questionnaires were obtained, resulting in a 94% response rate. Among them, academic postgraduates accounts for 38.6%, with 154 valid questionnaires. Professional postgraduates accounts for 61.4%, with 245 valid questionnaires. The distribution is uniform in terms of gender, grade, and major type, with certain representativeness.

3.2 Questionnaire reliability and validity testing

In order to analyze the outcomes in terms of internal reliability and validity, the questionnaire testing with IBM SPSS technology. The Cronbach's alpha rates for GE scale was 0.922, positive relationship(PR) scale was 0.869, negative relationship(NR) scale was 0.863, SI scale was 0.851. The KMO coefficient was within the range of 0.818 to 0.955. Consequently, survey data was helpful for further analysis and suitable conclusion were drawn for measurement items.

3.3 Model fit

This study used AMOS24 software to validate the proposed hypothesis, using the generalized least squares (GLS) method to obtain the fitting model path. According to the internal modification suggestions, make appropriate adjustments to the fitting path diagram without changing the logical relationship of the model. The path estimation results of this model in Table 1 show that 4 paths are significant and the critical ratios of each path meet the requirements and parameter standards. Therefore, the measurement model has high structural reliability and was suitable for testing research hypotheses.

Table 1. Corrected model path coefficients

Path	Standard valuation	S.E.	CR	p-values
GE→PR	0.302	0.052	5.844	0.000***
GE→NR	-0.292	0.052	5.844	0.000***
PR→SI	0.913	0.111	8.222	0.000***
NR→SI	-0.235	0.098	-2.393	0.017*

Note: ***p<0.01, *p<0.05

3.4 SEM results

Using the GLS-SEM procedure analysis variables and verification the three hypothesis which mentioned above.

The path load coefficients of H1 and H2 meet the requirements. Using ZL Wen et al.'s test of the mediating effect [12] and using Bootstrap to analyze the upper and lower bound coefficients, it was found that both direct and indirect effects show significant differences and there is some mediating effect. H3 hypothesis holds.

3.5 Variable score situation

The statistical results showed that the average score of GE scale was 3.76 points. PR scale was 3.79 points, NR scale was 2.15 points, SI scale was 3.77 points. The SI scale that the overall score is optimistic, with over 83% choosing a score more than 3 points. To further explore the causal relationship between the SI score and the observed variables, the observation variable with the lowest score and those with the highest score are shown in Table 2. From this, it can be determined that the biggest difference in SI is mainly due to the MC.

Table 2. Score of groups observed variables

Dimension	Low identification data				High identification data			
Index	MC5	MC2	EAM5	ARG1	ARG3	MC5	MC3	MC2
Score	2.12	2.17	2.24	2.28	4.45	4.38	4.36	4.31

4. Conclusions and suggestions

4.1 Research conclusions

The overall SI of postgraduates is optimistic. The GE of postgraduates has a influence on the SPR, which in turn affects SI. The GE will also influence the SI through the mediating effect of different relationships, which is specifically manifested as partial mediating effect. In the group of high identification scores, postgraduates generally said that their supervisors' scientific research ability and professional level were strong. Under the GE, the supervisor's MC are the factors that have the greatest influential on the GE. The key reasons for the formation of different degrees of identification are the supervisor's attitude towards problems and their own personality, as well as the differences in tasks and planning.

4.2 Suggestions

At the supervisor level. Tago at al. provides insight into the supervisor ethical conduct is a key resource [13]. The scope of responsibilities expected of the supervisor goes way beyond educating and developing pathways. Supervisors should improve their own quality, strengthen the cultivation of ethics and morality, cultivate the comprehensive quality of postgraduates.

At the university level. Give full play to the main role of university education, and improve the quality of school supervisor team and further ensure the maintenance of the relationship. Set up a model of teacher ethics and widely publicize it, so as to strengthen the cultivation of postgraduates' high identification of their alma mater and supervisor.

At the postgraduate level. Actively establish a positive SPR. Postgraduates should make personal planning and select appropriate supervisor based on research direction, research interest, guidance style and other factors. Give timely feedback on the GE, and effectively communicate with the supervisor with questions and thoughts.

4.3 Research prospects

In order to increase the universality and applicability of the model, future research can strengthen the work in four aspects: (a) Add age as the influencing factor. (b) Consider the differences in the identification of the postgraduates-supervisor relationship under different schools of thought. (c) Verify whether the office politics and competitive employment pressure affects the supervisors' identification. (d) Consider adding the supervisor self-assessment part.

References

[1] LIN Jie, CHAO Ya-qun. Impact of 'Supervisor-Postgraduate Fellowship' on the Development of Postgraduates: Qualitative Research Based on Informal Organization Theory(in Chinese) [J]. Journal of Graduate Education, 2019(05):1-8.
[2] ZHOU Hai-tao, ZHANG Mo-han, LUO Wei. Analysis on Students' Sense of Achievement in Private Higher Education Institution(in Chinese) [J]. Journal of Higher Education, 2016, 37(09):54-59.
[3] Hannah D P , Tidhar R , Eisenhardt K M .Analytic models in strategy, organizations, and management research: A guide for consumers[J]. Strategic Management Journal, 2020. DOI:10.1002/smj.3223.
[4] J.G. March, H.A. Simon, Organizations [M]. New York, NY: Wiley, 1958.

[5] M. Patchen. The Locus and Basis of Influence on Organizational Decisions[J]. Organizational Behavior & Human Performance, 1972, 11 (2): 195 - 221.
[6] Ashforth B E , Mael F .Social Identity Theory and the Organization[J]. Academy of Management Review, 1989, 14(1):20-39.DOI:doi:10.5465/AMR.1989.4278999.
[7] Dick R V , Wagner U , Stellmacher J ,et al.The utility of a broader conceptualization of organizational identification: Which aspects really matter?[J].Journal of Occupational and Organizational Psychology, 2004.DOI:10.1348/096317904774202135.
[8] Wen P, Chen C, Dong L, et al. The Role of Mentoring in Protégés' Subjective Well-Being[J]. Journal of Career Development, 2017, 44 (5): 1 - 13.
[9] Caballero G , Vazquez X H , Quintas M A .Improving Employability Through Stakeholders in European Higher Education: The Case of Spain[J]. Long Range Planning, 2015, 48(6):398-411. DOI:10.1016/j.lrp.2015.09.005.
[10] Zhi Liu, TJ Liu. How to build a harmonious relationship between tutors and students—— Analysis based on in-depth interviews(in Chinese) [J]. Degree and Graduate Education, 2021(10):43-50.
[11] CAO Qing-yan, PENG Jiao-jiao. Analysis of the 'Values Guiding' Role Consciousness of Postgraduate Supervisors in Moral Education(in Chinese) [J]. Journal of Graduate Education, 2020(02):40-44.
[12] Wen Zhong-lin, Chang Lei,Hau Kit-Tai, Liu Hong-yun. Testing and application of the mediating effects[J]. Acta Psychological Sinica, 2004, (5):614–620.
[13] Mharapara T L , Cooper-Thomas H D , Hutchison A ,et al. Assessing constructive supervisor behavior: Development and evaluation of a brief follower-rated scale[J].Human Resource Development Quarterly, 2019. DOI:10.1002/hrdq.21339.

Fuzzy Systems and Data Mining IX
A.J. Tallón-Ballesteros and R. Beltrán-Barba (Eds.)

doi:10.3233/FAIA231037

Algorithm Model of People's Value Identification Strategy in Intelligent Media

Jianghui Liu[a, 1], Yingxuan Liu[b], Runlong Wu[c] and Mohan Liu[d]
[a] *Modern Education Technology Center, Experimental Teaching Center, Guangdong University of Foreign Studies, Guangzhou, China.*
[b] *School of Journalism & Communication, Guangdong University of Foreign Studies, Guangzhou, China.*
[c] *School of Finance, Guangdong University of Foreign Studies, Guangzhou, China.*
[d] *School of English Education, Guangdong University of Foreign Studies, Guangzhou, China.*

Abstract. In the age of smart media, information technology is highly developed. This has profoundly changed the way people acquire and disseminate information. In the smart media era, technology has a greater impact on people's value identity. People are the backbone of the future society, and their ideology and values are directly related to the future direction and trend of society. Based on the general environment of the smart media era, this study will analyze the people's value expressions of a social event on media platforms through the actual testing and verification of PCA algorithm and TF-IDF algorithm. It will classify the main component values, and calculate the TF-IDF values of the people's value expressions. So, it can target the people with different mainstream values to conduct guided intelligent story narratives and ultimately improve the people's values identity.

Keywords. Intelligent media; People's value identification; Algorithm model

1. Introduction

In the context of media convergence in the smart media era, artificial intelligence as well as big data and Internet information technology are powerful application. They have largely enhanced the speed and scope of news and stories and other content dissemination. This has given rise to more emerging and diverse media formats and forms, as well as more diverse and independent popular values [1]. People's value information is extracted through the dialogue distribution of documents, so as to classify different people's value orientation and implement targeted value identification and layout [2]. Fu et al. designed a user recommendation model of academic social network platform. It can recommend corresponding users with needs to different aspects of academic social interaction [3]. In such a context, we need to analyze the communication orientation of general popular stories with the help of machine learning algorithms, match the ideas of people with

[1] Corresponding Author: Jianghui Liu, Modern Education Technology Center, Experimental Teaching Center, Guangdong University of Foreign Studies, China; This study is financially supported by the Undergraduate Innovation Training Project of Guangdong University of Foreign Studies in 2023. Email: 247031690@qq.com.

different kinds of values. For a social event, we will use algorithms to mine and analyze comments from the media and give different weights to different comments, so as to efficiently identify and classify the value recognition of the public and create different types of stories for the public. By rewriting the transmission process and all aspects of popular stories. It can spread new ways and new contents for the correct guidance of popular value identity and better shape Chinese popular values.

2. Analysis of the Needs of Constructing People's Value Identity in the Age of Smart Media

The values recognized by the public represent the current general mentality and expectations of young people. It has a driving role in guiding the direction of public opinion and changing the direction of social development. At the same time, the public, having received systematic education on campus, has a relatively high ability to analyze and judge public events. It is more likely to think rationally about various rumors on the Internet and express their voices through various channels. This leads more people to form a correct and positive public opinion orientation [4].

2.1. People's values are personalized in the age of smart media

Compared with the past, in the age of smart media, people attach more importance to their individual identity. They are concerned about self-expression and ways to realize their personal values, and tend to see themselves as thinkers and individualists. They resent traditional thinking that overemphasizes collective values and group actions.

2.2. People's values are diversified in the age of smart media

With the abundance of information and the spread of globalization in the age of smart media, people have a wide range of cultural differences and values among themselves. They are more and more easily exposed to various forms of culture and cultural ways, showing strong characteristics of enlightenment, tolerate and pluralism. A certain amount of cultural collision and integration has occurred in this process [5].

2.3. People's values in the age of smart media have socialization

People not only accept more sources and forms of information in the smart media era, but also make use of new technologies such as social media for emotional resonance and cultural interaction. Various new media platforms not only provide a wide space for people to communicate, but also allow them to learn more about different ideas and cultures [6].

3. The construction of people's value identity

Media content communication plays an important role in the construction of people's value identity. We should apply new technologies such as artificial intelligence to media

communication and then to the construction of people's values to promote people's value identity.

3.1. Adopting media fusion to promote media intelligence and effectively promote people's value identity

The development of media fusion provides a new way for the construction of people's values. This can help people's value recognition. By integrating different media forms and platforms, it can create new communication contents to achieve a win-win situation of technological innovation and content dissemination [7].

3.2. Building a model of intelligent narrative creation and dissemination of excellent people stories to guide correct popular value recognition

AI technology is gradually applied to all aspects of human life. It brings convenience to people. AI technology also affects the development of various industries, and brings new development opportunities to the declining traditional media. The use of intelligent narrative creation and communication is the future development direction of the media industry. Intelligent narratives are gradually transforming from closed creation to open creation. The creation process and the data collection, distribution and effect feedback environment view each other and evolve dynamically. Intelligent narrative is moving from closed creation to open creation process.

The intelligent new narrative under human-computer interaction is the way from closed to open creation. The subjective imagination of human is combined with the data analysis and algorithmic construction of machine to provide users with various types of stories [8]. From data access to data analysis, it requires the analytical and processing capabilities of information technology such as artificial intelligence. Algorithm construction can provide technical support for exploring story themes and generating, embellishing stories. And ultimately, it innovatively creates various types of stories, such as scenario-based stories, customized stories, and interactive stories. These stories are accessed by users and have emotional resonance to realize the core value of the stories. The quality content is embellished and disseminated according to the mainstream values of the people. The different mainstream values of the people also represent their respective user portraits. So, by building user portraits, we can better improve the identification and homogeneity of the mainstream values of various people. The following Figure 1 shows the design process of the portrait model of the people.

The construction of user profile is mainly divided into three processes: basic data collection, behavior modeling, and profile construction. It is mainly through analyzing and mining a large of logs stored on the server and the massive data contained in the database to form a "tagging system" So, different tags represent the identification of different users in a certain dimension of characteristics. Through the user profiling model, we analyze different characteristics of people. This helps to understand the way people understand values and promote their value recognition.

4. The construction of people's value identity

In the era of rapid development and dissemination of information, there are numerous factors affecting values. In order to correctly and well guide people's values and enhance

their sense of identity, it is necessary to understand the different mainstream values of various people.

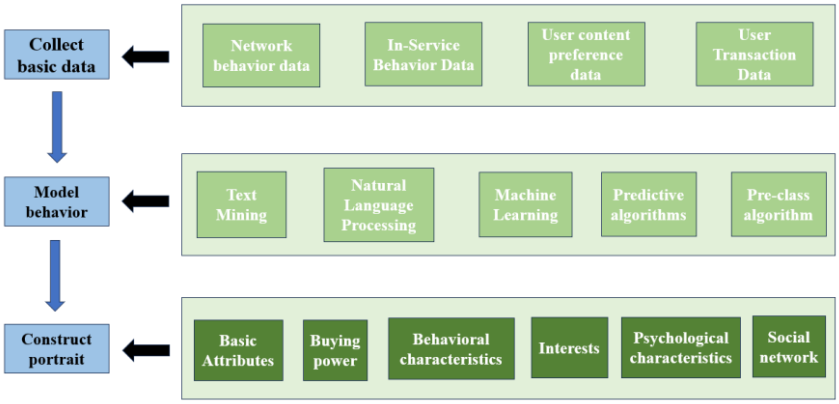

Figure 1. The construction of user portrait model

4.1. PCA Algorithm

4.1.1. About the Principal Component Analysis algorithm

The basic idea of PCA (Principal Component Analysis) is to reduce the dimensionality of the data. It transforms the repetitive data of multiple variables or multiple influences in the original data set into a small number of representativeness, relatively independent and comprehensive indicators (principal components) that can synthesize the multiple variables transformed in the original data set. The PCA algorithm reduces the projection vector of the data to achieve simple and efficient use of complex data sets. And it can remove redundant information and noise from the data set. For example, in the algorithm experiments of this study, considering that the collected data will have a large of duplicated and unimportant parts, we use the PCA algorithm. It can eliminate the duplicated data and retain the important principal components. This is equivalent to retaining several mainstream specific values of the public about the causes and consequences of a particular event when it occurs. At the same time, the PCA algorithm can reduce the computational load of the computer and improve the computational efficiency of the TF-IDF algorithm mentioned below.

4.1.2. The basic formula of PCA algorithm is as follows:

Firstly, we must consider the differences brought about by the different tempering, so we must conduct standardized data processing:

$$S_{ij} = \frac{V_{ij} - \bar{V}_j}{\sigma_j}, i = 1,2,\cdots,n; j = 1,2\cdots,m \tag{1}$$

where there is $\sigma_j^{'} = \frac{\sum_{i=1}^{n}(V_{i,j} - \bar{V}_j)^{'}}{n-1}$ denotes the variance of the jth feature, while $\bar{V}_j = \frac{\sum_{i=1}^{n} V_{ij}}{n}$ gives the normalized matrix S by the above expression.

The correlation coefficient matrix of S is then derived from the following expression:

$$H = \left[h_{ij}\right]_m, V_m = \frac{S^T S}{n-1} \tag{2}$$

In this formula, $h_{ij} = \frac{\sum S_{kj} \cdot S_{kj}}{n-1}$, $i,\ j = 1,2 \cdots, m$

At this point, based on the existing matrix, we can obtain α_i and β_i by calculating $|H - \alpha I| = 0$. Here α_i denotes the eigenroot of the matrix and β_i denotes the eigenvector of the matrix. Finally, in general we consider a feature variable with a cumulative contribution of more than 80%. Then we select that feature variable as the principal component of this class of feature variables.

In the comment section under the wise media communication of different mainstream self-publishing users of a specific platform, there can be different values representing different groups of people. Based on the several mainstream values retained, we analyze what are the main aspects of people's identity differences under different kinds of values. We determine the user profile tendency of people corresponding to either kind of values, and what kind of story elaboration of social events can be more effectively accepted by the people. So, it can realize the improvement of people's value identity.

4.2. TF-IDF algorithm

4.2.1. About the Term Frequency-inverse Document Frequency algorithm

TF-IDF (Term Frequency-inverse Document Frequency) algorithm is a statistical-based mathematical method for information retrieval and data mining analysis. TF refers to the lexical frequency, that is, the occurrence of the target term in the content. IDF is used to solve something that is indistinguishable due to the simplicity of TF. The IDF is used to penalize the words that are present for most of the content, thus reducing the number of filters for invalid information.

4.2.2. The basic formula of the algorithm is as follows:

The formula of TF is:

$$R_{ab} = \frac{X_{ab}}{\sum_p X_{pb}} \tag{3}$$

Where X_{ab} represents the number of times the target term R appears in a selected document D, and $\sum_p X_{pb}$ denotes the number of all target terms in this selected document. In other words, the expression of TF can emphasize the influence of the target vocabulary in the selected document. In addition, the mainstream values are first screened by PCA algorithm, and some irrelevant and invalid vocabulary is eliminated, so as to improve the accuracy of the existence probability of the target vocabulary.

The formula of the IDF is:

$$LDC_{ab} = log \frac{|D|}{1+\left|D_{R_j}\right|} \tag{4}$$

We use LDC to represent the prevalence of target words in the text content. Where the total number of text contents contained in the set of selected documents D is

expressed as $|D|$. And the number of target words contained in any text content is expressed as $\left|D_{R_j}\right|$. To make the formula exist objectively all times, we add a value of 1 to the denominator to ensure that the formula remains valid in the case that too few or almost no target words exist in the selected documents D. Then, after classifying mainstream values through PCA algorithm, a large number of invalid words will be screened out. Then, IDF punishment will screen out some words belonging to mainstream values that are still invalid for classification, and eliminate excessive unnecessary words, and finally improve the accuracy of vocabulary mining.

The final TF-IDF formula is:

$$O_{ab} = R_{ab} \cdot LDC_{ab} = \frac{R_{ab} \cdot log_2 \frac{N}{n_a}}{\sqrt{\sum_{b=1}^{n} \left(R_{ab} \cdot log_2 \frac{N}{n_a}\right)^2}} \tag{5}$$

The purpose of using the TF-IDF algorithm is to mine and analyze people's feelings and attitudes towards the occurrence of a social event. This includes mining and analyzing the comments left by people on different platforms and different self-published media with different ways of elaborating the same event. By calculating the TF-IDF value of some specific words (including synonyms), the TF-IDF algorithm can accurately and efficiently measure and rate the relevance of the values of social events to the values of the public.

4.3. Application based on PCA and TF-IDF algorithms

The PCA algorithm is able to reduce the dimensionality by analyzing the eigenvalues of the data to retain the key principal component data and remove other component data. In the research object of this study, we can use the PCA algorithm to divide the already selected data set into principal components. We can divide numbers of principal components according to the needs of each type of sample. At the same time, we assign weights to the principal components. The several principal components sorted in order obtained after weight assignment can be further analyzed by the TF-IDF algorithm. We calculate the values of TF-IDF for different variables in the principal components and discern the people's value tendencies in detail.

We selected the Titan submarine disappearance that happened in the Atlantic Ocean on June 18, 2023 as a social event. We selected a short video community platform with many different media commentaries on the event, including professional official news media such as "CCTV News", as well as self-published media with high attention level. We intentionally filtered and pre-processed the comments to eliminate the meaningless comments, leave those that can constitute the significance of the study.

According to the application process of the algorithm, we firstly use the PCA algorithm to calculate the selected comment section data. The four principal component values were extracted, namely "humanistic care", "flirtation and hatred of rich", "Seeking knowledge and wondering" and "fear of nature ". According to the calculation of the algorithm for the 4 principal components of the cumulative contribution analysis, the analysis obtained the weights $\omega_1 > \omega_2 > \omega_3 > \omega_4$. Then, based on the existing 4 principal component values, classify 4 kinds of comment data that fit the values, and calculate the TF-IDF values of the target vocabulary of the comment data. As the following table, we selected part of the content of the target vocabulary during the experiment to demonstrate its TF-IDF values.

No matter which aspect of which type of value identification structure, if we can grasp the general values of the people, we can guide them according to their inclinations. Creative storytelling can be used to construct different types of stories that are more relevant to the values of the people. It can guide the people more effectively toward the correct core values of the mainstream and enhance their sense of value identity.

5. Conclusion

Based on the PCA algorithm and TF-IDF algorithm, this study analyzes the expressions of the people's values in the era of smart media. We propose that different story narrative expressions can be constructed through the analyzed results to create different story types in a targeted manner. This will lead people's values to develop in a good direction as a whole and thus improve their value identity. The experimental research in this study has some limitations in data pre-screening. Data mining is not very deep, and the selected data is subjective. However, the algorithm model used is still useful in data pre-processing and natural language processing analysis. Future research will focus more on the application of this kind of algorithm model to the value communication of we-media, the identification and classification of mainstream values, and the value communication and integration. At the same time, a more detailed study will be conducted on the connection and influence of public emotions and value recognition in the context of the era of intelligent media.

References

[1] Francisco Jáñez-Martino, Rocío Alaiz-Rodríguez, Víctor González-Castro, Eduardo Fidalgo, Enrique Alegre, Classifying spam emails using agglomerative hierarchical clustering and a topic-based approach, Applied Soft Computing.2023;139:110-226.

[2] Zhenyu Z, Bowen Y, Haiyang Y, Tingwen L, Cheng F, Jingyang L, Chengguang T, Jian S, and Yongbin L. Layout-Aware Information Extraction for Document-Grounded Dialogue: Dataset, Method and Demonstration. In Proceedings of the 30th ACM International Conference on Multimedia (MM '22). Association for Computing Machinery, New York, NY, USA, 2022.7252–7260.

[3] Fu, C, Yong Tang, Zeng W, and Li, J. SPDNA: A User Recommendation Model for Academic Social Network. In Proceedings of the 12th Chinese Conference on Computer Supported Cooperative Work and Social Computing (ChineseCSCW '17). Association for Computing Machinery, New York, NY, USA; c2017. P. 56–63.

[4] Mounir M. Bendouch, Flavius Frasincar, Tarmo Robal, A visual-semantic approach for building content-based recommender systems, Information Systems.2023;117:102-243.

[5] Hei Tong Lau, Richard Lee, Ethnic media advertising effectiveness, influences and implications,Australasian Marketing Journal (AMJ).2018;26(3):216-220

[6] Anton Voronov, Shen, Y, Pritom Kumar Mondal. Forecasting popularity of news article by title analyzing with BN-LSTM network. In Proceedings of the 2019 International Conference on Data Mining and Machine Learning (ICDMML 2019). Association for Computing Machinery, New York, NY, USA. c2019. p. 19-27.

[7] Andrews, A, "An application of PCA-DEA with the double-bootstrap approach to estimate the technical efficiency of New Zealand District Health Boards", Health Economics, Policy and Law.2022;17(2):175–199.

[8] Zhao, W. Guo, J. Wang, and T. Wang, "Exploring the association of dietary patterns with the risk of hypertension using principal balances analysis and principal component analysis", Public Health Nutrition2023;26(1):160–170.

Fuzzy Systems and Data Mining IX
A.J. Tallón-Ballesteros and R. Beltrán-Barba (Eds.)

doi:10.3233/FAIA231038

Application of a Hybrid Model of HPO and LSTM Neural Network Based on ICEEMDAN for Wind Speed Forecasting

Qi Bi, Yu-long Bai[1], Yu-ting Huang, Jun-tao Hong, Zhi-ru Chen and Zai-hong Hou
College of Physics and Electrical Engineering, Northwest Normal University, Lanzhou, China

Abstract. Wind power has the benefits of low cost, low emission, abundant resources, and renewability. The inherent randomness, intermittency, and fluctuation of wind power bring about the volatility of wind power generation. Ameliorating the precision of wind speed prediction has great significance. This study aimed to put forward a hybrid model of the hunter–prey optimization (HPO) and the long short-term memory (LSTM) neural network based on improved complementary ensemble empirical mode decomposition with adaptive noise (ICEEMDAN) to acquire the exact wind speed forecast. First, the ICEEMDAN–HPO–LSTM model used ICEEMDAN to preprocess the raw wind speed sequence and then used the HPO–LSTM model to forecast each decomposed subsequence. Ultimately, the last predicted outcomes of the original wind speed sequence were attained by synthesizing all prediction subseries. Five comparison models were established based on three sets of data with different sequence lengths in Inner Mongolia, China, to test the dependability and utility of the model, and the advantages of the model were proved. The findings displayed that (1) the constitution of ICEEMDAN decomposition and HPO–LSTM could ameliorate the behavior of wind velocity forecast; and (2) the average values of the mean absolute error, mean absolute percentage error, root mean square error, and determination coefficient (R^2) of the three datasets were 0.22411, 4.60277%, 0.27590, and 0.99719, respectively. The proposed prediction model can be used for wind speed forecasts.

Keywords. Hunter–prey optimization, hybrid models, improved complementary ensemble empirical mode decomposition with adaptive noise, long short-term memory neural network, wind speed prediction

1. Introduction

In the wake of the worsening of the environment, sustainable energy, such as solar energy, water energy, and wind energy, accounts for an increasing proportion of energy generation [1]. Among the numerous nonfossil fuels, wind energy is unpolluted, resourceful, economic, and essential. Wind power generation shows a great development trend in the domain of renewable energy sources. The inherent randomness, intermittency, and fluctuation of wind power generation bring about the nondeterminacy of wind power generation [2], of which wind speed is the principal consideration. Previous studies have

[1] Corresponding Author: Yu-long Bai, Northwest Normal University, Lanzhou, China; E-mail: baiyulong@nwnu.edu.cn.

proposed a large number of wind speed forecast models to exactly forecast the wind speed, which can be roughly divided into four classes: physical models, statistical models, artificial intelligence models, and hybrid models [3].

Physical methods use weather data from a meteorological observatory or remote sensing data to model and forecast. This process requires many resources, and the modeling is complex. The statistical model predicts the wind speed through past records, which reflect the relevance between the input and the output [4]. Artificial intelligence methods emerged quickly in the domain of wind speed forecast in the past to seize these nonlinear characteristics of wind speed changes, greatly improving the prediction accuracy. Recently, hybrid models have been increasingly favorably received and valued by researchers. Many basic models are combined to generate a composite model with strong forecast capacity by taking advantage of the goodness of each model to restrain the poor efficiency of a single model. As the main current forecasting model, the structure of hybrid models has become increasingly complicated and varied. The composition of recent hybrid methods mainly includes data preprocessing, optimization algorithms, determining the weight of the hybrid model, and error postprocessing [5].

2. Methodologies

This section introduces the basic concepts of ICEEMDAN and long short-term memory (LSTM), as well as the detailed theory of the hunter–prey optimization (HPO) algorithm.

2.1. Improved complementary ensemble empirical mode decomposition with adaptive noise

Improved complementary ensemble empirical mode decomposition with adaptive noise (ICEEMDAN) is an improved signal handling method besides Empirical Mode Decomposition (EMD), Ensemble Empirical Mode Decomposition (EEMD), Complementary Ensemble Empirical Mode Decomposition (CEEMD), and Complete Ensemble Empirical Mode Decomposition with Adaptive Noise (CEEMDAN). The improved CEEMDAN method effectively solved problems such as mode duplication, residual noise, and pseudo-Intrinsic Mode Function (IMF)components. Currently, ICEEMDAN decomposition is widely applied in the territory of metal price prediction [6], stock price prediction [7], and wind speed prediction [8]. The ICEEMDAN decomposition algorithm is as follows:

Step 1: Equation (1) indicates that white noise is added to the raw signal:

$$x^{(i)} = x + \beta_0 E_i[\omega^{(i)}] \tag{1}$$

where $\omega^{(i)}$ means the added white noise, and x is the signal used for disassembling.

Step 2: Equation (2) computes the numerical number of the IMF_1 modality component:

$$\tilde{d}_1 = x - r_1 = x - \frac{1}{I}\sum_{i=1}^{I} M[X^i] \tag{2}$$

Step 3: Equation (3) computes the numerical number of the IMF_2 modality component:

$$\tilde{d}_1 = r_1 - r_2 = r_1 - \frac{1}{I}\sum_{i=1}^{I} M[r_1 + \beta_1 E_2[\omega^{(i)}]] \tag{3}$$

Step 4: Equation (4) computes the numerical number of the kth modality weight IMF_k:

$$\tilde{d}_k = r_{k-1} - r_k = r_{k-1} - \frac{1}{I}\sum_{i=1}^{I} M[r_{k-1} + \beta_{k-1} E_k[\omega^{(i)}]] \tag{4}$$

2.2. Long short-term memory

Hochreiter et al. [9] proposed the LSTM neural networks to settle the prolonged dependence problem of conventional recurrent neural networks. LSTM can be better represented in a long sequence than the normal RNN. LSTM is widely used in practical applications and is suitable for tasks related to sequence learning, for example, voice recognition, time series analysis, and part of speech tagging. The unit structure and extension diagrams of LSTM are illustrated in Figure 1.

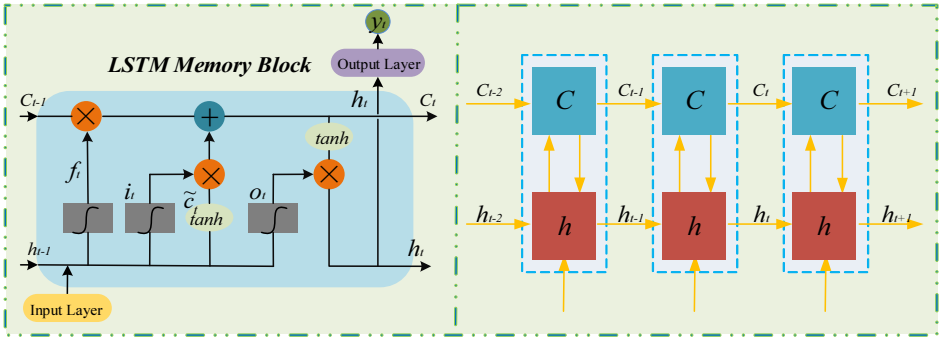

Figure 1. LSTM unit structure diagram and extension diagram.

$$i_t = \sigma(W_i \cdot [h_{t-1}, x_t] + b_i) \tag{5}$$

$$f_t = \sigma(W_f \cdot [\hbar_{t-1}, x_t] + b_f) \tag{6}$$

$$\tilde{C}_t = tan\hbar(W_C \cdot [\hbar_{t-1}, x_t] + b_C)$$
$$C_t = f_t \times C_{t-1} + i_t \times \tilde{C}_t \tag{7}$$

$$tan\hbar(x) = \frac{e^x - e^{-x}}{e^x + e^{-x}} \tag{8}$$

$$o_t = \sigma(W_O \cdot [\hbar_{t-1}, x_t] + b_O) \tag{9}$$

$$\hbar_t = o_t \times tan\hbar(C_t) \tag{10}$$

where i_t, f_t, and o_t are the input, forget, and output gate, respectively; C_t is the cell unit; W_* is the weight; b_* is the threshold value of each function; and σ represents the function of the sigmoid.

2.3. Hunter–prey optimization

Iraj Naruei et al. [10] proposed a new population-based optimization algorithm in 2022: the HPO. The algorithm simulates the conduct of predators such as panthers and lions that feed on bucks and antelope.

2.3.1. Initialization

The predator population is randomly initialized using Equation (11):

$$x_i = rand(1, d) * (u - l) + l \tag{11}$$

where x_i is the hunting position, l is the minimum (lower limit), u is the maximum (upper limit), and d is the amount of problem variables (dimension).

2.3.2. Predator search

Equation (12) is the search mechanism of predators:

$$x_{i,j}(t+1) = x_{i,j}(t) + {}^{1}/_{2}\,[(2BZP_{pos(j)} - x_{i,j}(t)) + (2(1-B)Z\gamma(j) - x_{i,j}(t))] \tag{12}$$

where $x_{i,j}(t)$ is the present location of the predator, $x_{i,j(t+1)}$ is the next location of the predator, P_{pos} is the location of the game, γ is the mean numerical number of the whole locations, and Z is an adaptive parameter. B is the equilibrium parameter between exploration and development. The numerical number is reduced from 1 to 0.02 in the iterations, which is displayed by Equation (14):

$$P = Q_1 < B; IDX = (P == 0) \tag{13}$$

$$Z = Q_2 \otimes IDX + Q_3 \otimes (\sim IDX) \tag{14}$$

where Q_1 and Q_3 are stochastic vectors in the range [0, 1], P is the repertory figure of $Q_1 < B$, Q_2 is a random digit in [0, 1], IDX is the repertory figure of vector Q_1 satisfying the circumstance ($P == 0$), and B is the equilibrium parameter between exploration and development. The numerical number is reduced from 1 to 0.02 in the iterations. As displayed in Equation (15):

$$B = 1 - i\left(\frac{0.98}{M}\right) \tag{15}$$

where i is the numerical digit of current iterations and M is the maximum numerical digit of iterations.

In Equation (16), the expression of γ is as follows:

$$\gamma = \frac{1}{m}\sum_{i=1}^{m} x_i \tag{16}$$

The Euclidean length is displayed as:

$$H_{euc(i)} = \left(\sum_{j=1}^{d}(x_{i,j} - \gamma_j)^2\right)^{\frac{1}{2}} \tag{17}$$

On the basis of the shooting scenario, when the predator seizes the game, the game is about to be killed and the predator moves to the position of the new game. To settle the problem, consider the mechanism of reduction or decrease as displayed in Equation (18):

$$k = round(B \times N) \tag{18}$$

where N is the number of search groups. At first, the value of k equals N of the algorithm. The last search target far away from the mean position a of the search thing is chosen as the quarry and seized by the hunter. The safest place is assumed to be a global optimal location because it gives a better survival opportunity for the prey, and the predator may pick another game. Equation (19) is used for interchanging the location of the game:

$$x_{i,j}(t+1) = T_{pos(j)} + BZ\,cos(2\pi Q_4) \times [T_{pos(j)} - x_{i,j}(t)] \tag{19}$$

where $x_{i,j}(t)$ is the immediate location of the captured food, $x_{i,j}(t+1)$ is the next iteration location of the pillage, $T_{pos}(j)$ is the best location of the overall situation, Z is the adaptive parameter according to Equation (14), and Q_4 is a random digit within the range [0, 1]. The function of *cos* and its input arguments permit the next game location to become the global optimal position of different radii and angles. To select predators and prey, Equations (12) and (19) are combined to obtain the following equations:

$$x_i(t+1) = x_i(t) + {}^1\!/_2\,[(2BZP_{pos(j)} - x_i(t)) + (2(1-B)Z\gamma(j) - x_i(t))] \quad (20)$$

$$x_i(t+1) = T_{pos} + BZ\cos(2\pi Q_4) \times [T_{pos} - x_i(t)] \quad (21)$$

where Q_4 is a random digit within [0,1] and β is a balance parameter, which is set to 0.1 in this study. If $Q_5 < \beta$, the hunt group is considered hunters, and the next location is updated with Equation (20); or else, the search group is considered as prey, and the next location is updated with Equation (21).

3. Framework of the proposed hybrid model

The hybrid model frame is displayed in Figure 2. The main process is as follows:

(1) ICEEMDAN is used for decomposing the primitive wind velocity data, and the decomposition result is to generate n intrinsic mode functions (IMF_1~IMF_n) and a residual R.

(2) HPO is used for optimizing LSTM model parameters.

(3) The ultimate forecast result is the combination of the IMF and the residual error forecast results.

4. Case study

4.1. Data description

The study data came from wind power plants in Inner Mongolia, China. The time span per step of the primitive wind speed data was 15 min, with three groups of diverse datasets. The statistical data of three wind speed datasets are displayed in Table 1. The sizes of these three datasets were diverse: 5 days, 7 days, and 7 days. In Table 1, T, T_a, and T_b, respectively, represent the size of total samples, training set samples, and test set samples. Min, mean, max, std, var, skewness, and kurtosis are the abbreviations of the minimum, mean, maximum, standard deviation, variance, skewness, and kurtosis of the total sample, respectively.

The top 80% of each wind speed series was a training set, and the remaining was a test set. According to skewness, the first and the third datasets were biased to the left, and the value was less than zero. This indicated more abnormal values on the left side of the data. The skewness values of the second dataset were all greater than zero, indicating abnormal digits on the right side of the distribution. Kurtosis is usually used for identifying abnormal values in a preset dataset. The higher the kurtosis, the higher the peak in the data sequence.

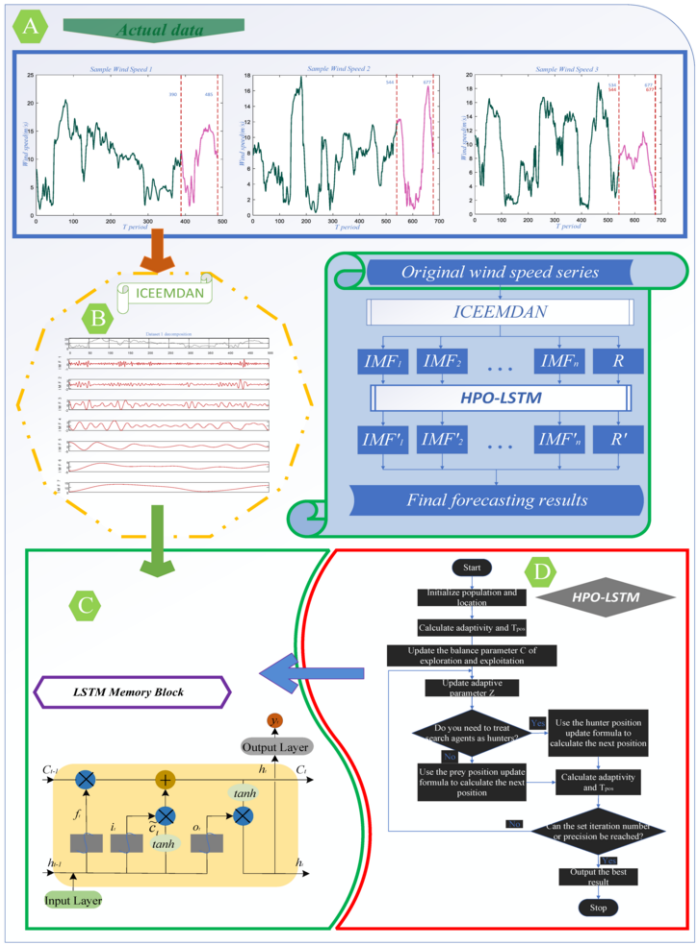

Figure 2. Framework of the hybrid forecasting model.

Table 1. Statistics of the three datasets

Dataset	*T*/period	T_a	T_b	Min (m/s)	Mean (m/s)	Max (m/s)	Std	Var	Skewness	Kurtosis
Dataset 1	485	390	95	1.09	9.9225	20.6	4.7064	22.1498	-0.0468	-1.0239
Dataset 2	677	544	133	0.33	7.1295	17.85	4.0561	16.4521	0.4233	-0.3569
Dataset 3	677	544	133	0.74	9.0723	18.83	4.7239	22.3151	-0.0542	-1.1370

4.2. Model parameter setting

In this study, the hyperparameters of the LSTM neural network were optimized.

All simulations were conducted using the MATLAB R2021a and Python 3.9 platform operating on a Windows 10, with a 3.40-GHz Intel Core i5-11300H CPU and a 64-bit 16-GB RAM.

The hyperparameters in this study are shown in Table 2.

Table 2. LSTM Parameters

Model	Symbol	Meaning	Value
LSTM	n_i	Number of input layer nodes	10
	n_h	Number of hidden layer nodes	Interval optimization with lower and upper limits of [10, 300]
	n	Number of hidden layers	2
	n_o	Number of output layer nodes	1
	η	Fixed learning rate	Interval optimization with lower and upper limits of [0. 005, 0. 05]
	T	Size of batch	One tenth of the training set
	E_p	Epochs of training	Interval optimization with lower and upper limits of [100, 800]

4.3. Experiment: comparison with other models

In this study, the wind speed series in the prediction dataset was delimited into a training set and a test set in the ratio of 8:2. Then, single models, such as Autoregressive integrated moving average (ARIMA), Back propagation neural network (BPNN), Long short-term memory (LSTM), VMD (Variational Mode Decomposition)–LSTM, EMD (Empirical Mode Decomposition)–HPO–LSTM, and ICEEMDAN–HPO–LSTM, were used to forecast the dataset. The test results displayed that the ICEEMDAN–HPO–LSTM model had the optimum forecast effect and could efficaciously increase the forecast precision. Table 3 shows the test results, and the bold values signify that the prediction results are better.

We compared four performance indicators, MAE (Mean Absolute Error), MAPE (Mean Absolute Percentage Error), RMSE (Root Mean Square Error), and R^2, to display the forecast endings of various kinds of models more distinctly, as displayed in Table 3.

Figure 3 displays the forecast results of six diverse models for three groups of wind speed record. The single model forecast results were unstable and needed further improvement. Each single model was run 10 times to test the dependability of the experimentation.

5. Discussions and Outlook

Increasing the precision of wind speed forecasting is important for wind energy transformation. In this study, we proposed and analyzed an ICEEMDAN–HPO–LSTM hybrid dynamic prediction model based on ICEEMDAN decomposition and HPO. The model was validated using three wind speed datasets and contrasted with the outcomes of five other models. The undermentioned conclusions were based on the point prediction evaluation index, line chart, scatter chart, and histogram of the model.

Table 3. Data of Model Comparison Experiment (MATLAB R2021a, Python 3.9, Windows 10, 3.40-GHz Intel 11300H, 16-GB RAM)

Dataset	Models	MAE	MAPE	RMSE	R^2
Dataset 1	ARIMA	1.0876	17.2565	1.3031	0.91976
	BPNN	0.34717	0.05104	0.51003	0.98818
	LSTM	0.65687	11.2856%	0.91751	0.95905
	VMD-LSTM	0.36054	5.7927%	0.50174	0.98931
	EMD-HPO-LSTM	0.5753	8.5384%	0.70799	0.98423
	ICEEMDAN-HPO-LSTM	**0.33749**	**4.9487%**	**0.39986**	**0.9962**
Dataset 2	ARIMA	1.7561	75.0865	2.0755	0.96636
	BPNN	0.24501	0.082264	0.31824	0.99616
	LSTM	0.55392	18.9988%	0.67019	0.98545
	VMD-LSTM	0.44384	16.5308%	0.51864	0.99332
	EMD-HPO-LSTM	0.26948	9.5948%	0.34023	0.99644
	ICEEMDAN-HPO-LSTM	**0.22282**	**6.6486%**	**0.27119**	**0.99847**
Dataset 3	ARIMA	0.5686	9.6747	0.70735	0.92882
	BPNN	0.12992	0.017991	0.16005	0.99431
	LSTM	0.24185	3.9137%	0.3078	0.97938
	VMD-LSTM	0.16646	2.4528%	0.21519	0.98919
	EMD-HPO-LSTM	0.16104	2.5178%	0.20979	0.99069
	ICEEMDAN-HPO-LSTM	**0.11203**	**2.211%**	**0.15666**	**0.99685**

(1) The ICEEMDAN mean decomposed into a few subsequences without transforming the original data, thus improving the overall accuracy.

(2) Verifying the proposed model using three datasets and five comparison models showed that the proposed hybrid model had great forecast precision and robustness.

In conclusion, the model offered a more trustworthy and exact wind speed forecasting method using wind power generation systems. The proposed model can solve not only the wind speed prediction issue but also other time sequence forecasting problems. For instance, the model can be used to forecast metal prices, carbon prices, and solar radiation intensity of solar power generation. In the future, a metaheuristic algorithm should be used to optimize model parameters, correct the predict errors, and adopt double decomposition or quadratic decomposition to improve prediction accuracy and stability.

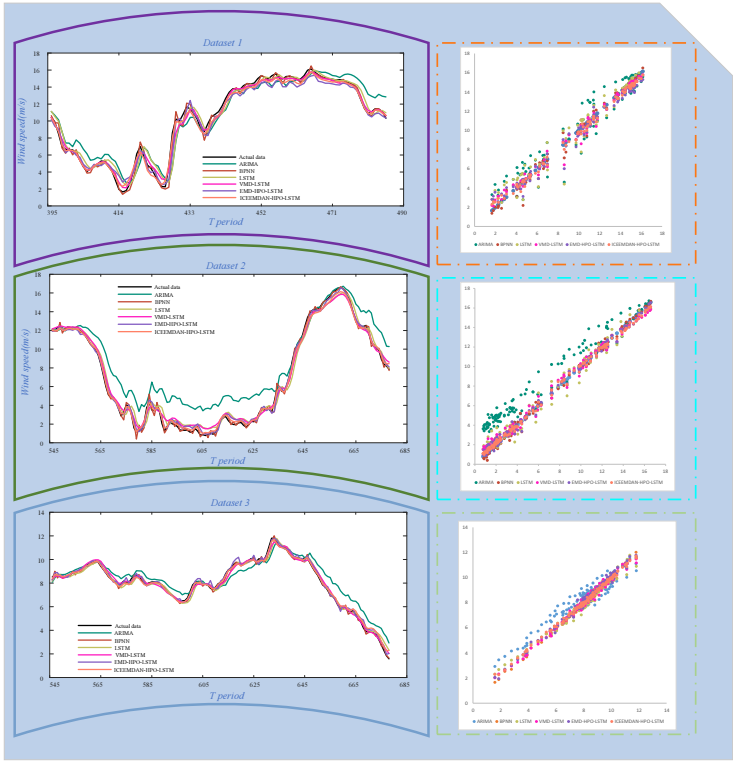

Figure 3. Comparison diagram of single model forecast experiments.

References

1. Wang, L., X. Li, and Y. Bai, Short-term wind speed prediction using an extreme learning machine model with error correction. Energy Conversion and Management, 2018. 162: p. 239-250.
2. Bai, Y., et al., Double-layer staged training echo-state networks for wind speed prediction using variational mode decomposition. Applied Energy, 2021. 301(OCT.15): p. 117461.
3. Ding, L., et al., Predicting short wind speed with a hybrid model based on a piecewise error correction method and Elman neural network. Energy, 2022. 244: p. 122630.
4. Ma, Z., et al., Application of hybrid model based on double decomposition, error correction and deep learning in short-term wind speed prediction. Energy Conversion and Management, 2020. 205: p. 112345.
5. Ding, L., et al., Serial-parallel dynamic echo state network: A hybrid dynamic model based on a chaotic coyote optimization algorithm for wind speed prediction. Expert Systems with Applications, 2023. 212: p. 118789.
6. Huang, Y.-t., et al., Application of a hybrid model based on the Prophet model, ICEEMDAN and multi-model optimization error correction in metal price prediction. Resources Policy, 2022. 79: p. 102969.
7. Wang, J., et al., Asian stock markets closing index forecast based on secondary decomposition, multi-factor analysis and attention-based LSTM model. Engineering Applications of Artificial Intelligence, 2022. 113: p. 104908.
8. Emeksiz, C. and M. Tan, Wind speed estimation using novelty hybrid adaptive estimation model based on decomposition and deep learning methods (ICEEMDAN-CNN). Energy, 2022. 249: p. 123785.
9. Alessandrini, S., et al., An analog ensemble for short-term probabilistic solar power forecast. Applied Energy, 2015. 157: p. 95-110.
10. Naruei, I., F. Keynia, and A.S. Molahosseini, Hunter-prey optimization: algorithm and applications. SOFT COMPUTING, 2022. 26(3): p. 1279-1314.

Fuzzy Systems and Data Mining IX
A.J. Tallón-Ballesteros and R. Beltrán-Barba (Eds.)

doi:10.3233/FAIA231039

Bearing Fault Diagnosis Based on Auto-Encoder Combined with CNN

Fei YUAN [a,1] Panpan XUN [a] Wei WANG [a] and Shibin SU [a]
[a] *Northwest Institute of Mechanical and Electrical Engineering, Xianyang, 712099, China*

Abstract. To address the problem that traditional bearing fault diagnosis methods rely on professional knowledge and are tedious, this paper proposes an end-to-end CNN-based bearing fault diagnosis model to achieve automatic fault recognition. In addition, considering the problem that noise exists in the actual working conditions, a bearing fault diagnosis model based on Auto-encoder(AE) combined with CNN is proposed(AE-CNN). The noisy signal is coded and decoded by the designed AE, and the de-noised result is used as the input of the designed CNN to achieve the bearing fault diagnosis under noisy conditions. Experiments on CWRU have proved the effectiveness of the designed CNN and AE-CNN. The designed CNN achieves 99.83% fault diagnosis accuracy under noise-free condition. The AE-CNN achieves 97.14% fault diagnosis accuracy under - 4db signal-to-noise ratio(SNR) noise condition, which is 2.31% higher than the CNN with the same noise, and compared with the results of other advanced methods, it has achieved competitive results.

Keywords. bearing, auto-encoder, noise, fault diagnosis, signal processing

1. Introduction

During the service of a certain naval gun, it relies on various mechanical equipment. Conducting research on mechanical equipment fault diagnosis can help maintain the safe operation of mechanical equipment, improve its reliability and stability. As an essential component, bearings account for a large proportion of mechanical equipment failures[1]. This paper focuses on the key components of mechanical equipment, bearings, and conducts research on bearing fault diagnosis methods based on vibration signal analysis.

Traditional methods heavily rely on professional knowledge to process raw signals and extract features. The bearing fault diagnosis method based on deep learning can automatically obtain the bearing vibration features of the original vibration signal to achieve end-to-end bearing fault diagnosis, without the need for professional domain knowledge to manually design and extract features. In [2-6], CNN, Long Short Term Memory, attention mechanism and a series of deep learning methods were applied to bearing fault diagnosis and achieved good results.

These methods have made some progress, but have not taken into account the noise issues in actual working conditions. Some researchers have shifted their focus to the

[1]Corresponding Author: Fei Yuan; E-mail: bohelion@hrbeu.edu.cn.

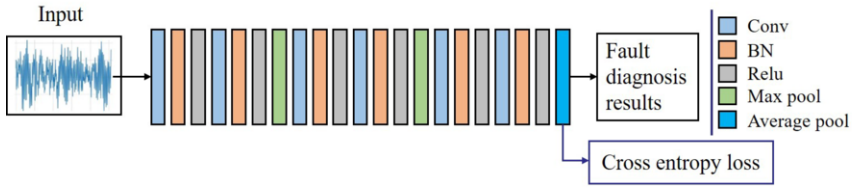

Figure 1. Structure of CNN-based bearing fault diagnosis model.

problem of bearing fault diagnosis under noisy conditions. Li et al. [7] proposed a new Transfer learning method based on domain confrontation training to achieve bearing fault diagnosis under -4dB 8dB SNR. The multi-scale noise-modulated SR method based on wavelet packet transform is studied in [8] and in the data reconstruction stage of [9], noise is reduced and the useful information hidden in the raw data is extracted. Although there have been studies focusing on bearing fault diagnosis in noisy environments, there is relatively little research available, and there is still significant room for improvement in diagnostic accuracy.

In response to the problem of traditional bearing fault diagnosis methods relying on professional knowledge and being cumbersome, this paper first takes the vibration signals of rolling bearings as the object, establishes an end-to-end fault diagnosis model based on CNN, and considers the problem of noise in actual working conditions, a bearing fault diagnosis model based on AE-CNN is proposed. The original vibration signals with added noise are encoded and decoded through AE, and the obtained denoised signal is used as the input of the designed CNN for feature extraction to achieve end-to-end bearing fault recognition and achieve bearing fault diagnosis under noisy conditions.

2. Methodology

This paper first establishes a bearing diagnosis model based on CNN, and the details are introduced in section 2.1. Afterwards, considering the actual working conditions of noise, a bearing diagnosis model based on AE-CNN is established, and the details are introduced in section 2.2.

2.1. CNN based bearing fault diagnosis model

This paper takes the vibration signal of rolling bearings as the object and establishes a bearing fault diagnosis model based on CNN, as shown in figure 1. Utilizing the powerful feature extraction ability of CNN, useful information is automatically extracted from the original bearing vibration signal, thereby achieving end-to-end bearing fault diagnosis.

The specific parameters of the CNN network model are shown in Table 1. The CNN model constructed in this paper has a total of three convolution modules, each of which uses the form of splitting the 3×3 convolution into 1×3 and 3×1 for convolution operations. There are two convolution layers, and each convolution layer passes through a batch normalization layer(BN) and a Relu layer, which can reduce the number of parameters and increase the nonlinear layer. And the first two convolutional modules end up using max pool, while the last convolutional module ends up using average pool, as can be seen in some classic networks [10].

Table 1. Parameter values of CNN-based bearing fault diagnosis model

Network layer	Kernel size	Padding	Stride	Output size
Conv	(3,1,16)	(1,0)	1	(32,32,16)
BN	(-,-,16)	-	-	(32,32,16)
Relu	-	-	-	(32,32,16)
Conv	(1,3,16)	(0,1)	1	(32,32,16)
BN	(-,-,16)	-	-	(32,32,16)
Relu	-	-	-	(32,32,16)
Maxpool	(2,2)	-	2	(16,16,16)
Conv	(3,1,32)	(1,0)	1	(16,16,32)
BN	(-,-,32)	-	-	(16,16,32)
Relu	-	-	-	(16,16,32)
Conv	(1,3,32)	(0,1)	1	(16,16,32)
BN	(-,-,32)	-	-	(16,16,32)
Relu	-	-	-	(16,16,32)
Maxpool	(2,2)	-	2	(8,8,32)
Conv	(3,1,64)	(1,0)	1	(8,8,64)
BN	(-,-,64)	-	-	(8,8,64)
Relu	-	-	-	(8,8,64)
Conv	(1,3,64)	(0,1)	1	(8,8,64)
BN	(-,-,64)	-	-	(8,8,64)
Relu	-	-	-	(8,8,64)
Averagepool	-	-	-	(1,1,64)

2.2. Bearing Fault Diagnosis Model Based on AE-CNN

Under real working conditions, noise is inevitable, and its source and size are uncertain, which will affect the model's extraction of bearing vibration signal features and ultimately affect the diagnostic results. To address this problem, this paper proposes a bearing fault diagnosis model based on AE-CNN. The original vibration signal with added noise is encoded and decoded by AE. The denoised signal is used as the input of the designed CNN for feature extraction to realize bearing fault identification. The network structure is shown in figure 2.

AE is an unsupervised neural network that first extracts data into higher dimensions through feature extraction, and then reconstructs the input. Based on the encoding and decoding structure, the encoder encodes low dimensional data into high dimensional data. The decoder receives high dimensional data and attempts to reconstruct the original low dimensional data, learning by changing the original input data from one representation to another. Some researchers applied AE to bearing fault diagnosis[11-13], but there is still room for improvement. In the fault diagnosis model based on AE-CNN constructed in this paper, AE is used to encode and decode the original vibration signal with added noise, and the denoised signal obtained is used as the input of the designed CNN for feature extraction.

For the details of the encoding and decoding process of the original vibration signal with added noise through AE: firstly, signal x is input into the encoder for feature extraction, and the signal undergoes downsampling, reducing spatial features; afterwards, the feature $y = f(x)$ after passing through the encoder is input into the decoder, and up-

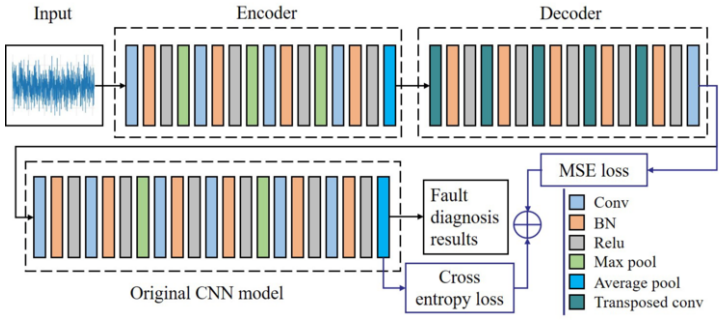

Figure 2. Structure of AE-CNN-based bearing fault diagnosis model.

sampling is carried out through transposed convolution to increase the width and height of the input, in order to achieve the purpose of noise reduction and signal recovery. The signal is restored to the original signal data $\widetilde{x} = g(y) = g(f(x))$ that is close to no noise, allowing $\widetilde{x}$ to replicate the input x as much as possible. During the signal recovery process, the number of channels decreases and the spatial scale increases. The encoding of the middle layer here is the most important mapping from the input signal to the encoder, which is to achieve automatic feature extraction of the signal. It can be expressed as follows:

$$\begin{aligned} y &= f(x) = A(wx+b) \\ \widetilde{x} &= g(y) = A(w^{'}x+b^{'}) \\ L_{AE}(x,\widetilde{x}) &= L_{AE}(x, g(f(x))) \end{aligned} \tag{1}$$

Where, A represents the activation function Relu, L_{AE} represents the loss function mean squared error(MSE).

The whole model is trained end-to-end, and the total loss L is the sum of the MSE after AE and the cross entropy loss after the original model.

$$L = -\frac{1}{N}\sum_{i=1}^{N} log\frac{e^{W_{y_i}^T x_i + b_{y_i}}}{\sum_{j=1}^{n} e^{W_j^T x_i + b_j}} + \frac{1}{2}\sum_{k}(y_k^{'} - y_k)^2 \tag{2}$$

Among them, n represents the number of fault categories; N represents the size of the batch size; $x_i \in \mathbf{R}^d$, which represents the feature vector of the $i-th$ sample, with an d -dimension; y_i represents the category label of the $i-th$ sample; $W \in \mathbf{R}^{d\times n}$ is the weight matrix, and W_j represents the $j-th$ column of W; $b_j \in \mathbf{R}^n$ is offset; $y_k^{'}$ represents data prediction output, i.e. decoder output; y_k represents the true label of the fault data; k represents the dimensionality of the data.

As the parameters of the original CNN model are already described in the previous section, the specific parameters of the encoder and decoder parts in the model are listed here, as shown in Table 2 and Table 3, respectively. The formula for calculating the size of the feature map after transposed convolution operation is:

$$\begin{aligned} H_{out} =& (H_{in}-1)\times stride[0]-2\times padding[0]+ \\ & dialation[0]\times(kernel_size[0]-1)+ \\ & out_padding[0]+1 \\ W_{out} =& (W_{in}-1)\times stride[1]-2\times padding[1]+ \\ & dialation[1]\times(kernel_size[1]-1) \\ & +out_padding[1]+1 \end{aligned} \tag{3}$$

Among them, index [0] represents the data in the height direction, index [1] represents the data in the width direction, and *dialation* is a parameter that uses empty convolution. In this paper, the default is 1.

Table 2. Encoder parameter values of AE-CNN-based bearing fault diagnosis model

Network layer	Kernel size	Padding	Stride	Output size
Conv	(3,3,64)	1	1	(32,32,64)
BN	(-,-,64)	-	-	(32,32,64)
Relu	-	-	-	(32,32,64)
Maxpool	(2,2)	-	2	(16,16,64)
Conv	(3,3,128)	1	1	(16,16,128)
BN	(-,-,128)	-	-	(16,16,128)
Relu	-	-	-	(16,16,128)
Maxpool	(2,2)	-	2	(8,8,128)
Conv	(3,3,128)	1	1	(8,8,128)
BN	(-,-,128)	-	-	(8,8,128)
Relu	-	-	-	(8,8,128)
Maxpool	(2,2)	-	2	(4,4,128)
Conv	(3,3,128)	1	1	(4,4,128)
BN	(-,-,128)	-	-	(4,4,128)
Relu	-	-	-	(4,4,128)
Averagepool	-	-	-	(1,1,128)

3. Experiment

3.1. Dataset

The experiment uses the open dataset CWRU bearing vibration database of Case Western Reserve University in the United States to verify the proposed algorithm [14]. There are three types of bearing faults in this database, and a total of 10 different bearing health status data, corresponding to labels 0-9.

Table 3. Decoder parameter values of AE-CNN-based bearing fault diagnosis model

Network layer	Kernel size	Padding	Out padding	Stride	Output size
Transposed conv	(3,3,128)	1	1	2	(2,2,128)
BN	(-,-,128)	-	-	-	(2,2,128)
Relu	-	-	-	-	(2,2,128)
Transposed conv	(3,3,64)	1	1	2	(4,4,64)
BN	(-,-,64)	-	-	-	(4,4,64)
Relu	-	-	-	-	(4,4,64)
Transposed conv	(3,3,64)	1	1	2	(8,8,64)
BN	(-,-,64)	-	-	-	(8,8,64)
Relu	-	-	-	-	(8,8,64)
Transposed conv	(3,3,64)	1	1	2	(16,16,64)
BN	(-,-,64)	-	-	-	(16,16,64)
Relu	-	-	-	-	(16,16,64)
Transposed conv	(3,3,64)	1	1	2	(32,32,64)
BN	(-,-,64)	-	-	-	(32,32,64)
Relu	-	-	-	-	(32,32,64)
Conv	(1,1,1)	0	-	1	(32,32,1)

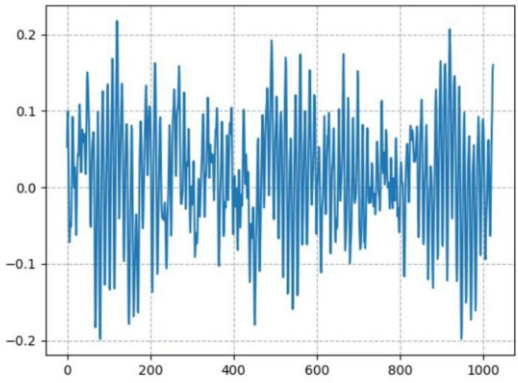

Figure 3. Image of original signal.

3.2. Data preprocessing

Adding noise to the original signal. Noise is widely present in various environments, among which additive white Gaussian noise (AWGN) is one of the most representative and easily quantifiable noises. This paper uses AWGN as additional noise to study the impact of noise on bearing fault signal classification. Five types of SNR are added, from strong to weak: -4dB, -2dB, 0dB, 2dB, and 4dB. Figure 3 and figure 4 shows the normal time-domain signal without noise added and the signal with noise added when the load state is 0. The SNR added is -4db. It is evident in figure 4 that the noise signal will seriously interfere with the original signal feature extraction.

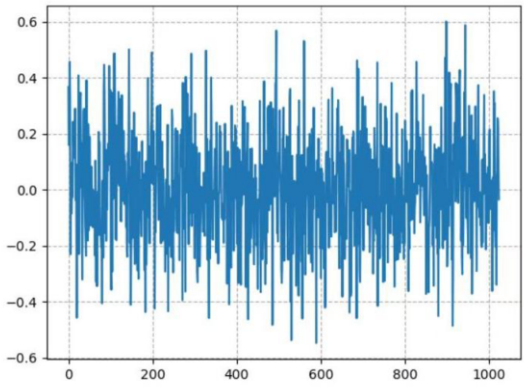

Figure 4. Image of signal after adding noise.

Data segmentation. This paper uses the data processing method where each segment has partial overlap to expand the effective data, and sets the length of a single data sample for overlapping sampling to 1024. During the experimental process of this paper, 70% of the sample data is randomly selected from each type of health status data as training data, 10% of the sample data is selected as validation data, and the remaining 20% of the sample data is selected as testing data.

Data rearrangement. This paper performs a rearrangement operation on one-dimensional time-domain signal, elevating it to a two-dimensional image. To obtain an image of N^2 size, the original vibration signal is randomly truncated with a length of $N \times N$ signal. Let $Q(i), i = 1,2,3...,N$ represent the numerical value of the original one-dimensional vibration signal, and $P(j,k), j,k = 1,2,3...,N$ represent the pixel intensity of the image. This paper rearranges the shape of 1024 one-dimensional data to a two-dimensional 32×32 image as the input.

3.3. Implementation detail

The adam optimizer is used for training. The initial learning rate and weight factor are set to 10^{-3} and 10^{-4} respectively, and the batch size used is 16. There are 25 periods in the training phase, and the learning rate of the 15th and 20th dropped by 90%. The graphics card used in this experiment is GTX1660Ti, with a dedicated GPU memory size of 6GB.

3.4. Experimental results and analysis

3.4.1. Experimental results of bearing fault diagnosis model based on CNN

This paper first conducted experiments on CRWU using the constructed CNN based bearing fault diagnosis model to verify the effectiveness of it. The accuracy of the validation and testing sets at each epoch is shown in the figure 5. It can be seen that at the 25th epoch, the accuracy rates are 100% and 99.83% respectively. Starting from the 15th epoch, the curves obtained on the three datasets tended to be stable and close to 1, proving the stability and accuracy of the model.

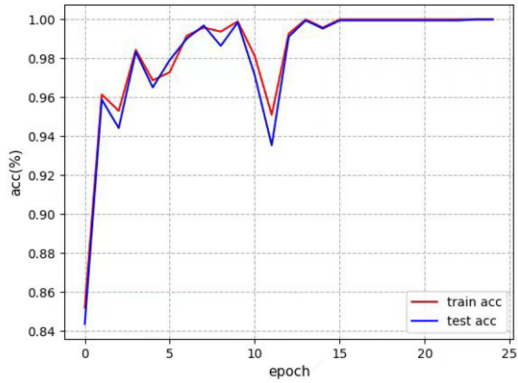

Figure 5. Accuracy of CNN-based bearing fault diagnosis model in the absence of noise.

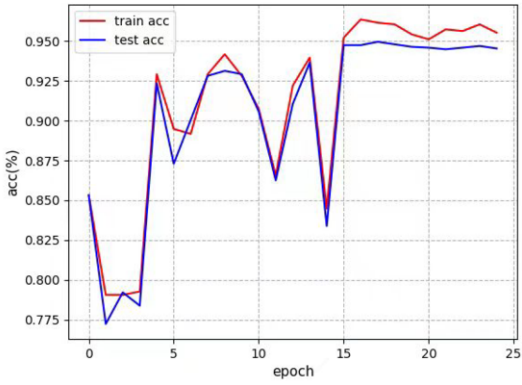

Figure 6. Accuracy of CNN-based bearing fault diagnosis model in the presence of noise.

Considering the noise under actual working conditions, this paper conduct experiments on the CNN based bearing fault diagnosis model with added noise. The experimental results are shown in figure 6. When adding noise of -4db, at the 25th epoch, the accuracy obtained by the validation and test sets are 96.35% and 94.95% respectively, which are 3.65% and 5.04% lower than those without noise. It can be seen that noise interferes with the model's extraction of signal features, which affects the fault diagnosis results.

3.4.2. Experimental results of bearing fault diagnosis model based on AE-CNN

According to the above experimental results, it can be seen that noise will reduce the accuracy of the model. Therefore, this paper proposes a bearing fault diagnosis model based on AE-CNN. The constructed model is tested on CRWU with added noise, and the accuracy obtained on the validation and test sets under different SNR noise conditions

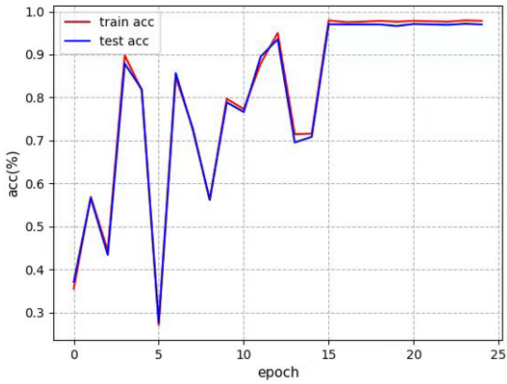

Figure 7. Accuracy of AE-CNN-based bearing fault diagnosis model in the presence of noise.

is shown in Table 4. The curves of the validation and test sets with SNR of -4db noise added are shown in figure 7. Figure 8 shows the confusion matrix, showing the details of AE-CNN fault diagnosis results. Compare the accuracy obtained with some advanced methods, and the experimental results are shown in Table 5.

Table 4. Comparison of fault diagnosis accuracy of AE-CNN model with different SNR

SNR(dB)	-4	-2	0	2	4
Validation set accuracy(%)	97.92	99.14	99.58	99.90	1.00
Test set accuracy(%)	97.14	98.49	99.32	99.64	99.79

From Table 4, it can be seen that the fault diagnosis accuracy of the AE-CNN is at a high level under various SNR conditions, indicating that the method proposed has strong noise suppression ability.

From figure 7, it can be seen that at the 25th epoch, the accuracy rates obtained by the validation and test set of AE-CNN are 97.92% and 97.14% respectively, which are 1.63% and 2.31% higher than the original CNN model, demonstrating the robustness of AE-CNN under noise conditions.

From the Confusion matrix in figure 8, we can see that AE-CNN has a high diagnostic accuracy rate for various bearing fault types. Except for rolling element fault B14 with fault size of 14mil, the diagnostic accuracy rate is 89.30%, the recognition rate for other fault types is higher than 90%, and the recognition rate for eight fault types is higher than 95%, and the recognition rate for three fault types is 100%. The rolling element fault B14 with a fault size of 14mil is easily confused with the rolling element fault B7 with a fault size of 7mil and the outer ring fault OR14 with a fault size of 14mil because their fault features are similar under noise conditions, leading to severe misjudgment by the model.

From Table 5, it can be seen that the AE-CNN has obtained competitive results compared with the experimental results of advanced methods. Compared to the siamese network [9], the AANN[15] and MCNN[16], it has increased by 0.91%, 4.03%, and 8.90% respectively, proving the effectiveness of the proposed AE-CNN model. The model presented in paper [17] [18] is relatively complex and achieves slightly higher accuracy than

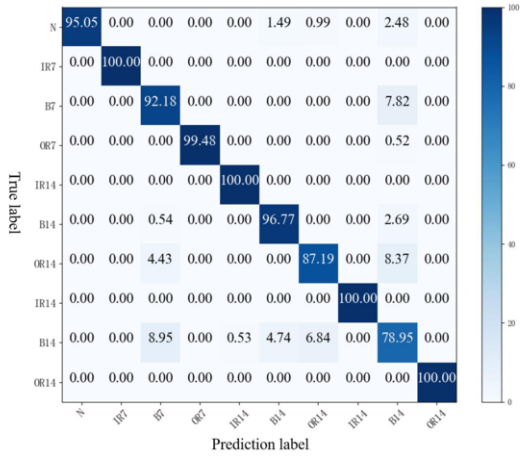

Figure 8. Accuracy of AE-CNN-based bearing fault diagnosis model in the presence of noise.

Table 5. Comparison of fault diagnosis accuracy of different methods under noise situation

Methods	Fault diagnosis accuracy(%)
The designed CNN	94.95
Siamese network[9]	96.26
AANN[15]	93.38
MCNN[16]	89.2
DLSTM[17]	97.21
CORAL[18]	97.85
AE-CNN[This paper]	97.14

our method. Our model is simple and easy to implement, capable of achieving good fault diagnosis accuracy, and has practical engineering significance.

4. Conclusion

This paper is based on deep learning methods for bearing fault diagnosis. Firstly, a CNN model is designed for end-to-end bearing fault diagnosis. Then, considering the presence of strong noise in actual working conditions, a bearing fault diagnosis model based on AE-CNN is proposed to achieve bearing fault diagnosis under noisy conditions. The experiment results on the CWRU demonstrate the effectiveness of the proposed model. The method proposed in this paper can be used for fault diagnosis of bearings under noise conditions, and has engineering practical value. However, due to the simplicity of the model, it still has a certain degree of scalability. On the one hand, the latest methods such as attention mechanism can be added to improve feature extraction capabilities, thereby improving the accuracy of fault diagnosis. On the other hand, the method proposed in this paper is to denoise the data before feature extraction and classification. In future research, we can improve the progressiveness of the model, which can directly extract and classify the data under noise conditions.

Acknowledgment

Young Talent Fund of Association for Science and Technology in Shaanxi, China.

References

[1] Wang R, Jiang H, Zhu K, et al. A deep feature enhanced reinforcement learning method for rolling bearing fault diagnosis[J]. Advanced Engineering Informatics, 2022, 54: 101750.
[2] Guo Z, Yang M, Huang X. Bearing fault diagnosis based on speed signal and CNN model[J]. Energy Reports, 2022, 8: 904-913.
[3] Luo J, Zhang X. Convolutional neural network based on attention mechanism and Bi-LSTM for bearing remaining life prediction[J]. Applied Intelligence, 2022: 1-16.
[4] Yang Z, Zhang J, Zhao Z, et al. Interpreting network knowledge with attention mechanism for bearing fault diagnosis[J]. Applied Soft Computing, 2020, 97: 106829.
[5] Jiang L, Li X, Wu L, et al. Bearing fault diagnosis method based on a multi-head graph attention network[J]. Measurement Science and Technology, 2022, 33(7): 075012.
[6] Yin J, Cen G. Intelligent Motor Bearing Fault Diagnosis Using Channel Attention-Based CNN[J]. World Electric Vehicle Journal, 2022, 13(11): 208.
[7] Li X, Zhang W, Ding Q, et al. Diagnosing rotating machines with weakly supervised data using deep transfer learning[J]. IEEE transactions on industrial informatics, 2019, 16(3): 1688-1697.
[8] He L F, Liu Q L, Jiang Z J. Combined Underdamped Bistatic Stochastic Resonance for Weak Signal Detection and Fault Diagnosis under Wavelet Transform[J]. Fluctuation and Noise Letters, 2023, 22(01): 2350007.
[9] Su H, Xiang L, Hu A, et al. A novel method based on meta-learning for bearing fault diagnosis with small sample learning under different working conditions[J]. Mechanical Systems and Signal Processing, 2022, 169: 108765.
[10] He K, Zhang X, Ren S, et al. Deep residual learning for image recognition[C]. Proceedings of the IEEE conference on computer vision and pattern recognition, 2016: 770-778.
[11] Liu S, Jiang H, Wang Y, et al. A deep feature alignment adaptation network for rolling bearing intelligent fault diagnosis[J]. Advanced Engineering Informatics, 2022, 52: 101598.
[12] Yan X, She D, Xu Y, et al. Deep regularized variational autoencoder for intelligent fault diagnosis of rotor–bearing system within entire life-cycle process[J]. Knowledge-Based Systems, 2021, 226: 107142.
[13] Liu C, He J, Wang P, et al. Characteristic extraction of soliton dynamics based on convolutional autoencoder neural network[J]. Chinese Optics Letters, 2023, 21(3): 031901.
[14] Smith W A, Randall R B. Rolling element bearing diagnostics using the Case Western Reserve University data: A benchmark study[J]. Mechanical systems and signal processing, 2015, 64: 100-131.
[15] Jin G, Zhu T, Akram M W, et al. An adaptive anti-noise neural network for bearing fault diagnosis under noise and varying load conditions[J]. Ieee Access, 2020, 8: 74793-74807.
[16] Zhang J, Yi S, Liang G U O, et al. A new bearing fault diagnosis method based on modified convolutional neural networks[J]. Chinese Journal of Aeronautics, 2020, 33(2): 439-447.
[17] Wang Z, Liu Q, Chen H, et al. A deformable CNN-DLSTM based transfer learning method for fault diagnosis of rolling bearing under multiple working conditions[J]. International Journal of Production Research, 2021, 59(16): 4811-4825.
[18] He J, Li X, Chen Y, et al. Deep transfer learning method based on 1D-CNN for bearing fault diagnosis[J]. Shock and Vibration, 2021, 2021: 1-16.

Fuzzy Systems and Data Mining IX
A.J. Tallón-Ballesteros and R. Beltrán-Barba (Eds.)

doi:10.3233/FAIA231040

Design and Implementation of an Intelligent Mattress for Elderly Night Care Based on ZigBee Technology

Yiqin BAO[a1], Wenbin XU[b], Lei WANG[c]
[a] *College of Information Engineering, Nanjing XiaoZhuang University, China*
[b] *Jiangsu United Vocational and Technical College Suzhou Branch, China*
[c] *Nanjing Yilaichuang Electronic Technology Co., Ltd, China*

Abstract. A smart mattress for night care for the elderly based on ZigBee technology is designed. The smart mattress uses flexible membrane pressure sensor and temperature sensor to realize the care of the sleep of the elderly at night. When only the flexible membrane pressure sensor of the mattress has a pressure value and the detected temperature is within the human body temperature range, it is determined that the elderly are sleeping in bed, so as to achieve the goal of nursing; And through wireless networking, real-time transmission of data is realized. The system uses the CC2630 wireless radio frequency chip as the core, and designs the hardware and software of the node and sensor interface in the ZigBee wireless sensor network. The whole system has good performance and high precision, which can better meet the requirements of intelligent care of the elderly at night.

Keywords: ZigBee, CC2630, flexible thin film pressure sensor, temperature sensor

1. Introduction

Since the 1990s, the aging process in China has accelerated. Whether in hospitals or nursing homes, the number of elderly people is on the rise, so more night care is also needed. Traditional night care for elderly people is done manually. In the environment of hospitals or nursing homes, night care is basically carried out by patrolling the room. In the case of more elderly people and fewer night nurses, this is not only inefficient, but also unable to respond in time when encountering problems. The existing intelligent mattresses mainly have intelligent sensing technology, which can determine whether someone is lying in bed by sensing the pressure at multiple locations and collecting temperature from the mattress; Pressure sensing technology can determine a person's bedridden state by collecting pressure signal values from multiple pressure sensing points; Wireless sensor network technology collects and uploads information through wireless sensor networks to obtain the bedridden status of elderly people at night. At present, many hospitals and nursing homes have also installed mattresses with detection

[1] Corresponding author: Yiqin BAO, Nanjing XiaoZhuang University, China; email: 392335241@qq.com

effects, using sensor technology to detect the status of elderly people in bed for night care purposes. However, due to the large number of selected sensors and the high power consumption of irregular real-time data uploading, external power supply is required, which has certain limitations.

This article is based on the CC2630 microcontroller, using the Iar For Arm program development platform and the C language development environment, to solve the problem of night care personnel in nursing homes not being able to timely know the bedridden status of the elderly, which is proposed in the background technology, achieving true intelligence and energy-saving.

The contributions and innovations of this article are summarized as follows:

1) Design a circuit for an intelligent mattress for elderly night care.

2) Design a program flowchart and complete the program code for related functions.

3) The intelligent mattress for elderly night care was tested. Tested through pressure analog-to-digital conversion and CC2630 power consumption.

The remaining parts of the paper are organized as follows: The second section studies relevant technologies, the third section designs the system architecture and program flowchart of the elderly's night smart mattress, the forth section implements the testing of the smart mattress, and the fifth section summarizes the full text and prospects.

2. Related technology

2.1 CC2630 microprocessor

Cc2630 is a 32-bit arm cotex-m3 core MCU produced by Texas Instruments (TI), running simultaneously with the IEEE802.15.4 MAC system with ARM Cortex-M0 core management. The dual core architecture improves overall system performance and power consumption, and releases flash memory for use. Its main frequency is up to 48MHz, rich in peripherals, up to 128KB Flash and 20KB SRAM, which can effectively solve ZigBee and 6Low WPAN application solutions [1].

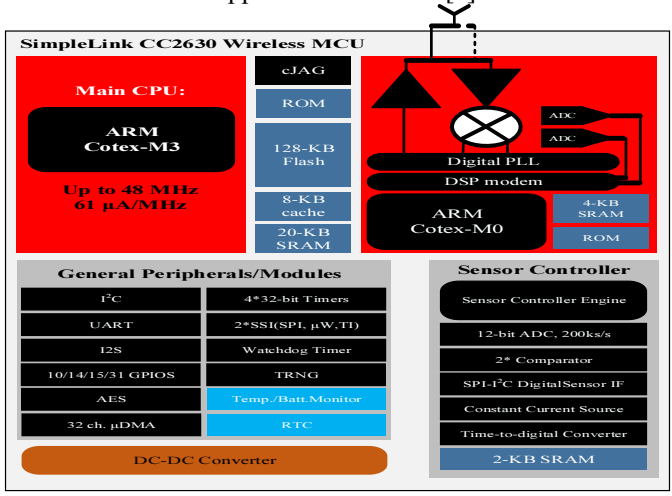

Figure 1. CC2630 Device Block Diagram

Compared with CC2530, which is also a ZigBee scheme, CC2630 has been upgraded from an 8-bit Soc scheme to an ARM Cortex-M3 kernel, which has more peripheral functions and can handle more complex logic to complete more functions; In addition to the main controller, CC2630 integrates a coprocessor with an ARM Cortex-M0 kernel. The coprocessor can collect sensing data in low-power mode of CC2630, thereby reducing overall power consumption. The CC2630 device block diagram is shown in Figure 1.

2.2 Flexible membrane pressure sensor

The principle of a flexible thin film pressure sensor is to represent the magnitude of the pressure signal applied to the thin film by outputting an electrical signal. When a flexible thin film pressure sensor is subjected to pressure and undergoes deformation, a nanofiber undergoes deformation under the applied pressure, resulting in its own polarization phenomenon. Positive and negative ions swim at both ends of the nanofiber, gathering positive ions at one end and negative ions at the other end, forming a potential difference [2]. The principle of a flexible thin film pressure sensor is shown in Figure 2.

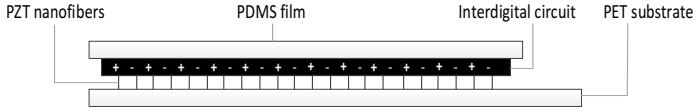

Figure 2. Schematic diagram of flexible film pressure sensor

The physical image of the SF15 long flexible film pressure sensor used in the intelligent mattress is shown in Figure 3. The sensor has two pins that can be connected to the digital conversion module of the flexible film pressure sensor. Connect one end to GND and the other end to the module voltage signal input terminal. When applying pressure to the flexible film pressure sensor, the pressure signal is sent to the conversion module through this pin to obtain the pressure value.

Figure 3. Physical image of flexible film pressure sensor

2.3 Temperature sensors

A temperature sensor is a sensing device that measures the degree of cooling and heating of an object. Its principle is to convert the analog temperature that can be felt into a usable digital output signal. There are various types of temperature sensors, which can be divided into two categories based on measurement methods: contact type and non-contact type; According to the characteristics of sensor materials and electronic components, it can be divided into two categories: thermal resistors and thermocouples [3][4].

The hardware connection method of MAX6675 is shown in Figure 4. MAX6675 is a digital K-type thermocouple sensor integrated circuit used for the Serial Peripheral

Interface (SPI)[5], so there are three different pins used to connect to CC2630 and connect to the SPI peripheral port of CC2630.

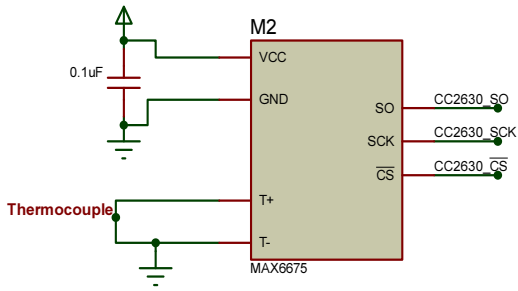

Figure 4. MAX6675 Hardware Connection Diagram

3. Design and Implementation of an Intelligent Mattress for Elderly Night Care Based on ZigBee Technology

3.1 Overall System Architecture

The intelligent mattress for elderly night care based on ZigBee technology is mainly composed of CC2630 chip, flexible film pressure sensor, temperature sensor, battery pack, etc. The device is integrated on the mattress. After integration, the pressure signal and temperature signal of the flexible film are input through the I/O input terminal of CC2630. When powered on, the sensing node begins to detect the elderly's bedridden state. The K-type thermocouple temperature sensor is used to detect the elderly's body temperature, and the flexible film pressure sensor is used to detect the elderly's bedridden state on the mattress. The collected sensing data is transmitted to the main control node through the ZigBee protocol. The main control node receives data from the sensor terminal node and uploads it to the server for monitoring.

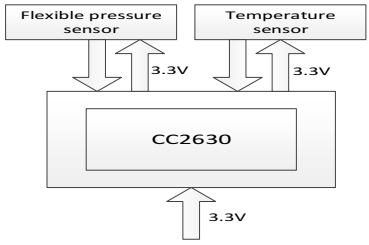

Figure 5. Schematic diagram of system principle

3.2 System Design

The thin film pressure sensor and K-type thermocouple sensor are respectively connected to CC2630, and a total of 5 I/O ports are connected for sensing information exchange. The peripheral functions of their access ports are set in the program. ZigBee uses the TI-MAC protocol for data transmission. Make a preliminary assumption scenario: the

design mattress has been laid in the nursing home. The remote server controls whether the mattress enters nursing mode. When the mattress enters nursing mode, the coprocessor collects pressure film data every 30 seconds; If the pressure values collected are within the weight standard of an adult elderly person, continue to collect temperature data to determine whether the mattress is human. If the mattress does not detect a pressure value in nursing mode or detects a normal pressure value but does not detect human body temperature[6], and one of these two conditions remains in place for more than the set time, it is determined that the elderly person is not in bed and an unknown situation has occurred. At this point, the CC2630 coprocessor wakes up the main processor to send ZigBee data. For the data of the sensor terminal node, the main control node forwards the data, which enables the server to receive the data in a timely manner, allowing evening caregivers to check the situation of the elderly in the corresponding bed. The program design uses C language, and the program flowchart is shown in Figure 6.

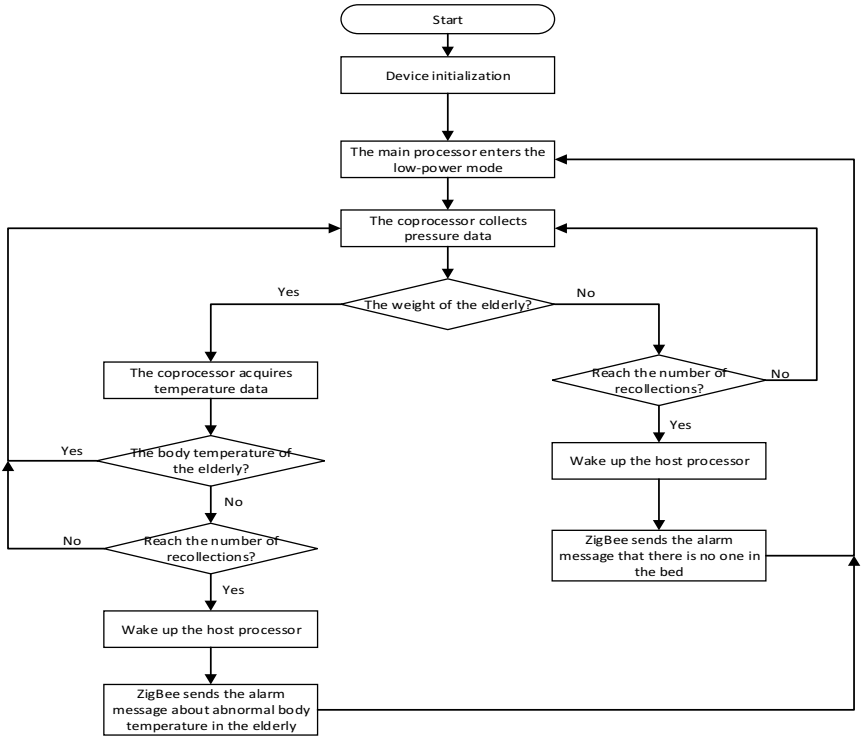

Figure 6. Program flowchart

The collection and processing process of the coprocessor is carried out in low-power mode[7]. The coprocessor periodically collects the sensing data in this design. When the coprocessor collects four channel pressure film sensing data, it performs a simple logical process on the data itself: when only at most two channels of the collected four channel pressure film sensing data have values or when the four channel values are almost zero, it determines that the current bed is empty. According to the process, the coprocessor will no longer collect temperature sensing values and wait for the next cycle of thin film pressure sensing data collection. When at least three channels of the collected four

channel pressure film sensor have values and the values are in the presence of people, the coprocessor will first determine whether the corresponding bed is in a bed state and collect temperature data based on this. The collected values will be saved in a simple database of the design equipment. After completing the above steps, the coprocessor waits for the next collection of sensing data.

4. System test

4.1 Testing of flexible film pressure sensors

In this design, a flexible film pressure sensor is used to measure the weight status of the elderly. For the convenience of measurement, a self-made electronic scale weighing platform is used to contact the weight with a fixed contact area and a fixed thin film.[8] Under the premise of fixed contact area, apply corresponding pressure, record the resistance value and the returned A/D value. The data obtained from the test is shown in Table 1.

Table 1. Relationship between Pressure Value and Resistance Value, AD

Pressure/Kgf	0.5	1	2	3	4	5	6	7	8	9
Resistance/kΩ	11.88	6.92	5.2	4.15	3.56	3.44	3.07	2.71	2.55	2.5
AD	826	525	408	332	288	279	251	223	210	206
0xFFF-AD	3269	3570	3687	3763	3807	3816	3844	3872	3885	3889

From Table 1, it can be seen that with the application of pressure, the resistance value and AD value of the pressure film show a decreasing trend. It is worth noting that the pressure value exhibits a non-linear relationship with the resistance value and AD value. In this design, the pressure value is only used as a basis to determine whether the elderly are bedridden, and there is no need to collect it too accurately.

4.2 ZigBee Power Consumption Test

For this design that uses battery power, it is necessary to monitor the power consumption of the mattress sensing terminal. The power consumption points of the sensing terminal include ZigBee data transmission, standby, and sensing data detection. The measured power consumption for one day is shown in Table 2.

The sensor terminal uses a battery capacity of 14000mAh, and based on power consumption calculations, it can ideally provide normal power for 475.82 days. However, the actual situation generally accounts for 70% of the ideal state, so it is calculated that the actual power supply can be normal for 370.62 days, so there is no need for frequent maintenance.

Table 2. Daily Power Consumption/mAh

Heartbeat green light	Configuration light always on	Sent by ZigBee	Exit sleep and start receiving	Standby	Sensing data collection
0	0	10.944	5.8464	9.6	0.05184

5. Conclusions

The use of this intelligent mattress provides intelligent care for elderly people who sleep at night in nursing homes. When nursing staff in nursing homes take care of the elderly at night, they only need to check their sleep information based on their server, and check the situation of the mattress corresponding to the reported alarm information, without the need for frequent night patrols. Mattresses can save caregiver resources to a certain extent while being intelligent. Due to the special structure of CC2630 dual processing, sensing data is collected through a coprocessor. In addition to receiving control setting commands and sending alarm data, the main processor is in a low-power mode, greatly ensuring the service life of the mattress; At the same time, as a mature ZigBee chip, CC2630 has been tested over time, running smoothly, not easily damaged, and ensuring safety; The program runs stably and reliably, with good selection. Compared to other implementation methods such as microcontrollers, it has the advantages of low power consumption, self-organization, strong stability, and high reliability. The intelligent mattress for elderly night care based on ZigBee technology has high application and promotion value.

Acknowledgement

This work is supported by Natural Science Foundation Project of China (61976118), Key topics of the '13th five-year plan' for Education Science in Jiangsu Province (B-b /2020/01/18).

References

[1] Hu Yu Research on Street Lighting Control System Based on Wireless Sensor Networks [D] Jiangsu: Nanjing University of Technology, 2020.
[2] Liu Shengqiang, Tan Xiaolan, Lv Bo, et al Development of flexible pressure sensors [J] Mechanical Engineer, 2020 (10): 9-12.
[3] Xu Feng, Li Haojie, Cui Feidie Research on Improvement and Enhancement of Refrigeration Faults in Commercial Vehicle Air Conditioning Systems [J] Automotive Electrical Appliances, 2022 (9): 84-87,91.
[4] Julie, Xing Xin, Meng Zhaoxin, et al. Sensors and Microsystems,2021,40(11):143-145+149.DOI:10.13873/J.1000-9787(2021)11-0143-03.
[5] Chen Yuyan, Lao Shenglin, Zhong Guomou Research on a K-type thermocouple temperature control system [J] Volkswagen Technology, 2022-24 (4): 22-26.
[6] Liu Keqin, Pan Xuetao, Jin Qing Digital real-time compensation for thermocouples based on LabVIEW [J] Modern Measurement and Laboratory Management, 2008,16 (6): 18-21.
[7] China Aviation Development Commercial Aviation Engine Co., Ltd Engine temperature measurement device and its insulation sleeve: CN202010350201. X [P]. 2021-10-29.
[8] JIANG Shaojun. Design and simulation of thermocouple temperature measurement circuit[J].Electronic Testing,2019(15):36-37+73.DOI:10.16520/j.cnki.1000-8519.2019.15.011.

Fuzzy Systems and Data Mining IX
A.J. Tallón-Ballesteros and R. Beltrán-Barba (Eds.)

doi:10.3233/FAIA231041

Research on Dynamic Multi-Layer Block Network Evolution Based on Bayesian Inference

Yuping Tang[a] , Yingzi Fu[b, 1] and Yeqing Ding[b]
[a] *College of Science, Kunming University of Science and Technology, China*
[b] *Applied Statistics Research Center, Kunming University of Science and Technology, China*

Abstract. Dynamic multi-layer network analysis is the frontier direction of network science and a prominent challenge in the field of complex network systems. In this paper, a covariate-assisted dynamic multi-layer network community detection method is proposed, which effectively combines the dependence within each network, across time and between different layers. The latent Gaussian process is used to model the edge probability between participants, and a flexible time series analysis is obtained. An extended model based on community is proposed to reduce the computational burden. In terms of parameter estimation, this paper uses the Bayesian method to conduct posterior inference on model parameters. Finally, a set of real business relationship network data is used for experiments, and the results show that the dynamic multilayer block network model has lower estimation time cost and better prediction performance, and the chunking structure of its model is more capable of revealing meaningful community structures, which makes it suitable for dealing with more complex dynamic networks.

Keywords. Dynamic multi-layer blocks; edge covariates; gaussian process; latent space

1. Introduction

Social network research focuses on the analysis of the dependencies between people or other social units, that is, the dependencies caused by the ties that bind them together [1-2]. Nowadays, there is a growing interest in the dynamic interdependencies of networks with other structures. However, these dynamic interactions[3] across time usually occur in multilayer connections, and thus multilayer networks are jointly modeled to fully understand the evolution of the complex network structure under study over time.

Data on social interaction processes are rapidly becoming highly multidimensional, and the availability of multidimensional networks in World Wide Web architectures[4], telecommunication infrastructures[5], and so on continues to increase. A growing number of research directions indicate the need for appropriate approaches to address the

[1] Corresponding Author, Yingzi Fu, Applied Statistics Research Center, Kunming University of Science and Technology, Kunming Yunnan 650500, China; E-mail: 2213971143@qq.com.

complexity associated with network problems, and network modularity analysis[6], network resilience analysis[7], etc. are examples of these new directions.

In recent years, statistical models for multi-layer networks have increased. The latent space model first proposed by Hoff et al.[8] is a classic model because it can flexibly capture common network features, such as node degree heterogeneity, transitivity, homogeneity, etc. Gollini and Murphy[9] and DAngelo et al.[10] proposed a latent space model for multi-layer networks. It is assumed that the latent representation of each node is the same on all layers, and the changes between networks are captured by layer-specific parameters that control the overall network characteristics. Durante and Dunson[11-12] introduced continuous-time dynamics by considering the Gaussian process of potential coordinate evolution over time, and then they extended the model in 2016[13]. Durante et al.[14] proposed a dynamic multi-layer network model, which considers a shared latent space to capture the global structure and a K-layer specific latent space that characterizes the special structure of each layer. On this basis, Carmona et al.[15] proposed a general network model for longitudinal data of multi-layer networks with directed and weighted edges in 2019 to analyze the dynamic multi-layer network structure changes over time more comprehensively. Dealing with large networks is often computationally difficult, however; Yildirimoglu and Kim[16] used modularity-based community monitoring to find demand patterns in a multilayered urban environment for demand analysis at different spatial resolutions. Yap et al.[17] used graph-based community detection to determine which wiring harnesses within the selected hubs to synchronize in order to be applicable to the context of the current public transportation. and Tian et al.[18] significantly reduced the computational cost of the large-scale rebalancing problem by partitioning the shared bicycle network. In 2022, Hector et al.[19] proposed a new probabilistic latent network model to predict multi-layer dynamic graphs that are increasingly common in transportation.

Inspired by the above work, the contributions of this paper's work are as follows. First, this paper proposes a covariate-assisted community monitoring approach for dynamic multilayer networks that effectively combines dependencies within each network, across time, and between different layers, while maintaining flexibility. Second, the computational burden is reduced by jointly considering both the temporal and spatial dimensions of the network to provide an in-depth demonstration of the evolution of the dynamic multilayer network structure over time. Finally, a set of real business relationship network data is used as an example to validate the method, and the experimental results prove that it has lower estimation time cost and better prediction performance, and is suitable for dealing with more complex dynamic networks.

2. Dynamic multi-layer block network model

The dynamic multilayer graph has each layer of graph that evolves over time, and can be represented by $V \times V$ adjacency matrix $Y^k(t)$, each matrix has a binary element $Y_{ij}^k(t) = Y_{ji}^k(t) \in \{0,1\}$, which measures whether there is a connection between nodes i and j. If there is a connection between participants i and j at time $t = t_1,...,t_n$ on the $k = 1,...,K$ -th layer, then $Y_{ij}^k(t) = 1$.

To strengthen the community structure, each node in the network is assumed to belong to a random block[20] or cluster such that the probability of the existence of an edge between any two nodes in the network depends on which block or cluster $b \in \{1,...,B\}$ they belong to. Thus the estimation will be performed on $B(B+1)/2$ blocks rather than on $N(N-1)/2$ nodes, where $B \ll N$, significantly reduces the computational cost. The prior probability is set to $p(z_i = b) = \eta_b$, where z is the vector assigned to the block, indicating that each participant i belongs to which block, and $\eta \sim Dirichlet(\alpha_1,...,\alpha_B)$. The model is extended by considering the inclusion of covariates, specifically the joint modeling of inter-block and intra-block connection probabilities as follows.

$$z_i \sim Categorical(\eta_1,...,\eta_B) \tag{1}$$

$$Y_{ij}^k(t) \Big| (z_i = p, z_j = q) \sim Bernoulli\left(\pi_{pq}^k(t)\right) \tag{2}$$

$$\psi_{pq}^k(t) = Logit\left(\pi_{pq}^k(t)\right) = \begin{cases} \mu(t) + \sum_{r=1}^{R} \bar{x}_{pr}(t)\bar{x}_{qr}(t) + \sum_{h=1}^{H} x_{ph}^k(t)x_{qh}^k(t) + \beta_m(t)' g_{ij}^k(t), & p \neq q \\ \mu_p^k(t) + \sum_{r=1}^{R} \bar{x}_{pr}(t) & , \text{ p=q} \end{cases} \tag{3}$$

3. Bayesian posterior inference

The full data likelihood of the model presented in this paper is:

$$p\left(Y_{ij}^k(t) \middle| \psi_{pq}^k(t)\right) = \prod_{t=1}^{T}\prod_{k=1}^{K}\prod_{i=2}^{V}\prod_{j=1}^{i-1} \frac{\exp\left(\psi_{z_i z_j}^k(t)\right)^{Y_{ij}^k(t)}}{1+\exp\left(\psi_{z_i z_j}^k(t)\right)} = \prod_{t=1}^{T}\prod_{k=1}^{K}\prod_{p=1}^{B}\prod_{q=1}^{p} \frac{\exp\left(\psi_{pq}^k(t)\right)^{y_{pq}^k(t)}}{\left[1+\exp\left(\psi_{pq}^k(t)\right)\right]^{n_{pq}^k(t)}} \tag{4}$$

Where $\psi_{pq}^k(t) = Logit\left(\pi_{pq}^k(t)\right)$, $n_{pq}^k(t)$ and $y_{pq}^k(t)$ denote the number of possible edges and actual edges in $Y_{ij}^k(t)$ between blocks p and q, respectively.

3.1. Gaussian Process Prior for Time - Varying Latent Coordinates

Inspired by the dynamic modeling of a single network, the Gaussian process prior considering the potential coordinates of participants is defined as follows :

$$\mu(t) \sim GP(0, c_\mu), \quad c_\mu(t_i, t_j) = \exp\left\{-k_\mu(t_i - t_j)^2\right\}, \quad k_\mu > 0 \tag{5}$$

$$\bar{x}_{ir}(t) \sim GP\left(0, \tau_r^{-1} c_{\bar{x}}\right), \quad c_{\bar{x}}(t_i, t_j) = \exp\left\{-k_{\bar{x}}(t_i - t_j)^2\right\}, \quad k_{\bar{x}} > 0 \tag{6}$$

$$x_{ih}^{k}(t) \sim GP\left(0, \tau_h^{k-1} c_x\right), \quad c_x(t_i, t_j) = \exp\left\{-k_x\left(t_i - t_j\right)^2\right\}, \quad k_x > 0 \tag{7}$$

independently for $i = 1,...,V$, r=1,...,R, $h = 1,...,H$, $k = 1,...,K$, $c_{\bar{x}}(t_i, t_j)$ and $c_x(t_i, t_j)$ in Equations (6) and (7) represent the square exponential correlation function of the Gaussian process with shared and layer-specific potential coordinates, respectively. $\tau_1^{-1},...,\tau_R^{-1}$ and $\tau_1^{k-1},...,\tau_H^{k-1}$ are the positive shrinkage parameters of the control potential coordinate set of $k = 1,...,K$ for each layer. The multiplicative inverse gamma prior[21] of shrinkage parameters is $\tau_r^{-1} = \prod_{u=1}^{r} \delta_u^{-1}$, r=1,...,R, $\delta_1 \sim Gamma(a_1, 1)$, $\delta_{u>1} \sim Gamma(a_2, 1)$, $\left(\tau_h^k\right)^{-1} = \prod_{v=1}^{h} \left(\delta_v^k\right)^{-1}$, h=1,...,H, k=1,...,K, $\delta_1^k \sim Gamma(a_1, 1)$, $\delta_{v>1}^k \sim Gamma(a_2, 1)$.

And consider that the prior of dynamic coefficient is: $\beta_m(t) \sim GP(0, c_m)$, $m = 1,...,M$, where, c_m is the square exponential correlation function $c_m(t_i, t_j) = \exp\left\{-k_m\left(t_i - t_j\right)^2\right\}$, $k_m > 0$.

Consider the a priori of shared and layer-specific potential coordinates on a finite-time grid $t_1,...,t_n$ as follows.

$$\left\{\bar{x}_{ir}(t_1),...,\bar{x}_{ir}(t_n)\right\}^{\mathrm{T}} \sim N_n\left(0, \tau_r^{-1}\Sigma_{\bar{x}}\right) \tag{8}$$

$$\left\{x_{ih}^{k}(t_1),...,x_{ih}^{k}(t_n)\right\}^{\mathrm{T}} \sim N_n\left(0, \tau_h^{k-1}\Sigma_x\right) \tag{9}$$

independently for $i = 1,...,V$, r=1,...,R, $h = 1,...,H$, $k = 1,...,K$. In equations (8) and (9), the $n \times n$ variance and covariance matrices $\Sigma_{\bar{x}[ij]}$ and $\Sigma_{x[ij]}$ have elements $\Sigma_{\bar{x}[ij]} = \exp\left\{-k_{\bar{x}}\left(t_i - t_j\right)^2\right\}$ and $\Sigma_{x[ij]} = \exp\left\{-k_x\left(t_i - t_j\right)^2\right\}$, which also apply to the baseline process of $\left\{\mu(t_1),...,\mu(t_n)\right\}^{\mathrm{T}} \sim N_n\left(0, \Sigma_\mu\right)$.

3.2. Posterior distribution

Based on the above a priori settings, the posterior distribution of the model parameters is represented as follows.

parameter to be estimated	posterior
η	$Dirichlet\left(\alpha_1 + n_1,..., \alpha_B + n_B\right)$
$\omega_{pq}^{k}(t)$	$PG(b, c), \quad b < 100$ $N\left(\frac{b}{2c}\alpha, \frac{b\left(\alpha^2 - 1\right)}{4c^2} + \frac{b\alpha}{2c^3}\right), \quad b \geq 100$
μ	$N_n\left(\mu_\mu, \Sigma_\mu\right)$
$\bar{x}_p$	$N_{n\times R}\left(\mu_{\bar{x}_p}, \Sigma_{\bar{x}_p}\right)$
x_p^k	$N_{T\times H}\left(\mu_{x_p^k}, \Sigma_{x_p^k}\right)$
δ_1	$Gamma\left(a_1 + \frac{B\times T\times R}{2}, 1 + 0.5\sum_{l=1}^{R}\theta_l^{(-1)}\sum_{p=1}^{B}\bar{x}_{pm}^{\mathrm{T}}K_{\bar{x}}^{-1}\bar{x}_{pm}\right)$

$$\delta_{r\geq 2} \quad Gamma\left(a_2+\frac{B\times T\times (R-r+1)}{2},1+0.5\sum_{l=r}^{R}\theta_l^{(-r)}\sum_{p=1}^{B}\bar{x}_{pm}^{\mathrm{T}}K_x^{-1}\bar{x}_{pm}\right)$$

$$\delta_1^k \quad Gamma\left(a_1+\frac{B\times T\times H}{2},1+0.5\sum_{s=1}^{H}\theta_s^{(-1)}\sum_{p=1}^{B}x_{ps}^{k\mathrm{T}}K_x^{-1}x_{ps}\right)$$

$$\delta_{h\geq 2}^k \quad Gamma\left(a_2+\frac{B\times T\times (H-h+1)}{2},1+0.5\sum_{s=r}^{H}\theta_s^{(-h)}\sum_{p=1}^{B}x_{ps}^{k\mathrm{T}}K_x^{-1}x_{ps}^k\right)$$

$$\mu_p^k \quad N_n\left(\mu_{\mu_p},\Sigma_{\mu_p}\right)$$

$$\beta_m \quad N_n\left(\Sigma_{\beta_m}\begin{bmatrix}\sum_{i=2}^{V}\sum_{j=1}^{i-1}g_{ijm,t_1}\left(y_{ij,t_1}-1/2-\omega_{ij,t_1}v_{ijm,t_1}\right)\\ \vdots \\ \sum_{i=2}^{V}\sum_{j=1}^{i-1}g_{ijm,t_n}\left(y_{ij,t_n}-1/2-\omega_{ij,t_n}v_{ijm,t_n}\right)\end{bmatrix},\Sigma_{\beta_m}\right)$$

$$\gamma_{ip} \quad \eta_p\prod_{t=t_1}^{t_n}\prod_{k=1}^{K}\prod_{q=1}^{B}\left[\pi_{pq}^k(t)\right]^{\sum_{j\neq i,z_j=q}y_{ij}^k(t)}\left[1-\pi_{pq}^k(t)\right]^{\sum_{j\neq i,z_j=q}1-y_{ij}^k(t)}$$

$$z_i \quad Categorical\left(\gamma_i\right)$$

The posterior computation utilizes P´olya-gamma data augmentation for Bayesian logistic regression, which allows for simple and easy-to-handle Gibbs samplers of the conjugate full conditionals. In this paper, the Gibbs sampler algorithm is utilized to sample the joint posterior of all model parameters with the following main steps.

- Calculate the number of clusters given the current assignment z.
- Sample the corresponding P´ olya-gamma enhanced data $\omega_{pq}^k(t)$.
- Update inter-block dynamic averages. Update $\mu(t)=\left[\mu(t_1),...,\mu(t_n)\right]^{\mathrm{T}}$ from its fully conditional multivariate Gaussian distribution process.
- Update cross-layer block coordinates. Sample the coordinate vector $\bar{x}_p(t_1),...,\bar{x}_p(t_n)$ for each block and layer.
- Update the intra-layer coordinates. Sample the coordinate vector $x_p^k(t_1),...,x_p^k(t_n)$ for each block and layer.
- Update the covariate coefficients β_m according to the posterior distribution.
- The update of the gamma parameter characterizing the prior in equations $\tau_r^{-1}=\prod_{u=1}^{r}\delta_u^{-1}$ and $\left(\tau_h^k\right)^{-1}=\prod_{v=1}^{h}\left(\delta_v^k\right)^{-1}$ follows conjugate analysis, proving the gamma full conditions.
- Updates the dynamic average within the block. Sample the vector $\mu_p^k(t)=\left[\mu_p^k(t_1),...,\mu_p^k(t_n)\right]^{\mathrm{T}}$ for each block and layer.
- Dynamic multilayer block probabilities are updated by applying equation (3) to samples of the baseline process, cross-layer coordinates, and intra-layer coordinates.
- Update the block allocation. Sample potential block allocations z in order and indicate z_i^* if the allocation of node i has been updated and z_i otherwise.

Repeat the above steps until the algorithm converges.

4. Experimental data and result analysis

4.1. Data sets and network description

In order to evaluate the effectiveness and adaptability of this method, this paper selects a set of real business relationship data sets (https://data.world/datasyndrome/relatobusiness-graph-database) collected by Relato. Based on these data, a large business relationship network structure diagram is created as shown in Figure 1. The pairs of relationships include 'partners', 'customers', 'competitors', and 'investments'. The dataset is processed into a K=4-layer network. Finally, 151 companies were selected as nodes, and retained the 5 largest industries, such as 'health care' and 'finance', as node covariates, resulting in a multi-layer network of 151*151*4, and considered a time step of T = 6. This paper aims to combine the node covariates to examine the dynamic evolution of the business relationship network structure, the pairwise relationship between companies over time, and the detection of corporate communities.

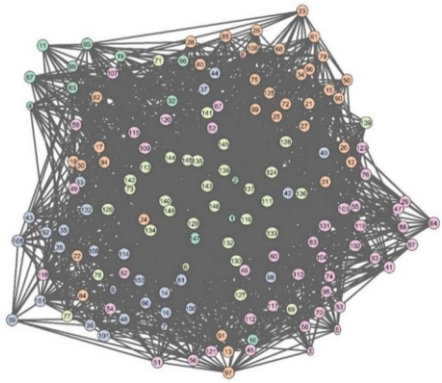

Figure 1. Business relationship network structure diagram.

The above diagram shows the business relationship network structure of 151 companies. The 5 colors in the diagram represent the 5 different industries to which the company belongs. And the more connections exist the larger the node of the company is, and vice versa the smaller it is.

4.2 Experimental results and analysis

4.2.1 Construction of dynamic multi-layer block network

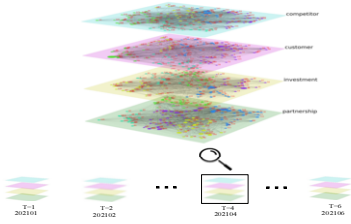

Figure 2. Multi-layer block business relationship network at time t=1,..., 6.

In the constructed dynamic multi-layer block network, the node covariate industry will be regarded as its community label. Figure 2 shows the multi-layer network structure diagram in June 2021. In the first layer of competitor network layer, if there is a competitor relationship between the two companies, there is a connection between them, and it is clear that companies in the same industry often have a competitor relationship, because companies of the same color are mostly close to each other, and only a very small number of companies are in an abnormal position. And with the evolution of time, the multi-layer network structure is also constantly changing, indicating that the pairwise relationship between companies will change within a certain period of time. The relevant network statistics are shown in Table 1.

Table 1. Statistical characteristics of business relationship network

layer	node	edge	network density	average shortest path length	average degree	diameter connection	efficiency	connectivity
1- competitor	312	1519	0.134	1.951	20.119	1	0.433	0.877
2- customer	312	1508	0.133	1.963	19.987	1	0.312	0.878
3- investment	312	1501	0.133	1.986	19.881	1	0.416	0.879
4- partnership	312	1911	0.151	1.801	45.311	1	0.447	0.853

The dynamic multi-layer block network model is further fitted to a selected subset of the complete multi-layer graph shown in Figure 2, including 151 companies in the competitor layer and the investment layer (K=2) network. At the same time, the time step is still considered as T=6 to estimate its potential coordinates.

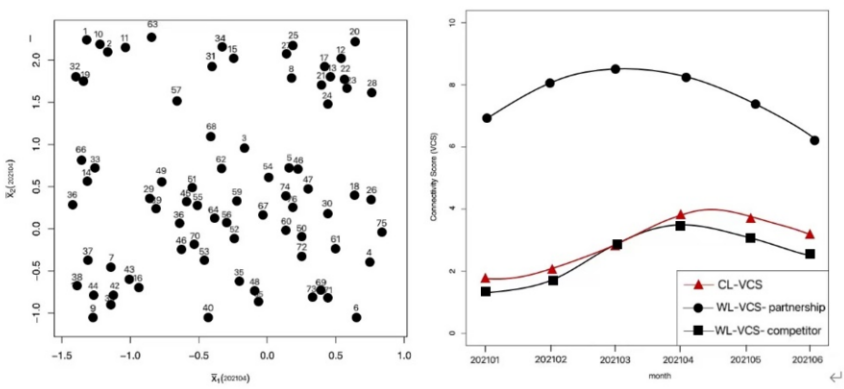

Figure 3. Estimated cross-layer coordinates for all companies for April 2021.

Figure 3 (left) shows the cross-layer coordinates of all companies in April 2021. It can be seen from the diagram that there is a clear cluster structure, indicating that the analysis of adding block structure can better explain its network structure. From Figure 3 (right), we can see the dynamic evolution of the cross-layer and intra-layer vertex connectivity scores of all companies. It can be clearly seen that the intra-layer scores of competitors are growing steadily, while the scores of the partner layer are still high, but the downward trend is obvious.

4.2.2 Dynamic multi-layer prediction of business relationship network

This paper uses available industry company data to verify the proposed extended model

by fitting and predicting a large dynamic multi-layer graph. From the aspects of classification accuracy and estimation time, the dynamic multi-layer network model and the dynamic multi-layer block network model are compared, and whether the block structure of the dynamic multi-layer block network model can implement meaningful corporate community detection is studied.

Firstly, the performance of the dynamic multi-layer network model and the dynamic multi-layer block network model is compared. The first 5 months of the sample are used to train the model, that is $t = \{t_1, ..., t_5\}$, and the data of the last 1 month are used for out-of-sample prediction. Figure 4 (left) shows the ROC curve of the two-model test data with $B = \{3, 4, 5\}$ blocks.

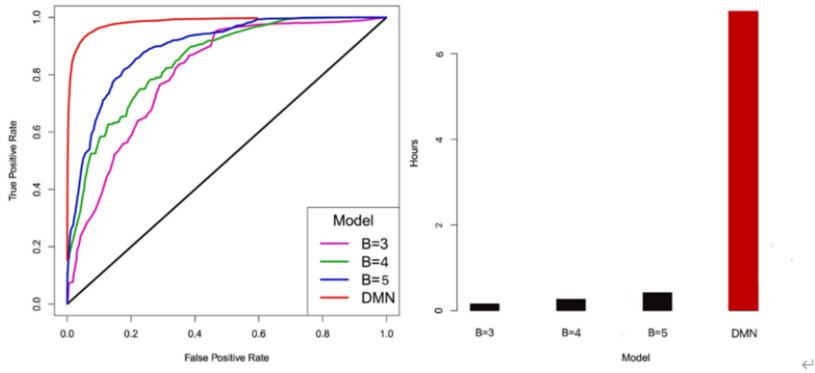

Figure 4. ROC curves for different block numbers (left) and the model estimation time (right).

It can be seen from the above diagram that the dynamic multi-layer network model is a very accurate classifier, but because it is estimated to be N(N-1)/2KT, the dynamic multi-layer block network model is estimated to be B(B+1)/2KT, so the latter calculation cost is much lower than the former. It can be clearly seen from the right of Figure 4 that the performance of the dynamic multi-layer block network model increases with the increase of the number of blocks, and the time spent on estimation is significantly reduced. At the same time, Figure 5 shows the dynamic multi-layer block network model of B = 5 block and the ROC curve of the dynamic multi-layer model. It can be seen from the figure that the worst-structured partner network is the most difficult to predict.

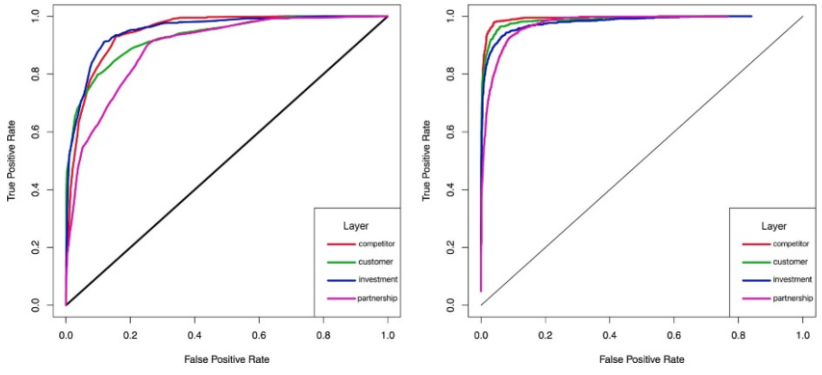

Figure 5. Layer-wise ROC curves from the proposed model with B = 5 (left) and the DMN (right).

The five firm industry clusters tested by the dynamic multilayer block model are also given. The fourth cluster is the largest, including 43 companies, such as Clearswift, Symantec, Imperva, etc., among which there are several abnormal node companies : Trace3 (1), Riverbed, Nokia, Trend Micro (2), VMWare (3), Assessment Systems (5) ; the first cluster is the smallest, including only 13 companies, including Safend, Institute of Asset Management (4) ; the node companies included in clusters 2,3, and 5 are shown in the above table. These three clusters also have several abnormal nodes, such as Software, FireMon, Dell, AT&T, and Hewlett Packard.

Finally, this paper compares the prediction performance of the proposed method with several popular non-probabilistic algorithms such as Katz Index (Katz), Restarted Random Walk (RWR) based on PageRank algorithm.

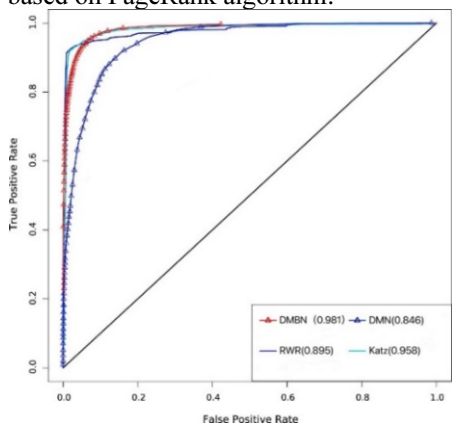

Figure 6. ROC curves for probabilistic and similarity-based prediction methods.

Figure 6 illustrates the ROC curves as well as the area under the curve (AUC) for DMN, DMBN, etc. with 5 blocks, from which it can be seen that DMBN and Katz index are the best probabilistic and similarity-based classifiers, respectively.

5. Conclusion

In this paper, we propose a covariate-assisted dynamic multilayer block network model that models the edge probabilities between nodes by means of a latent Gaussian process to obtain a flexible time series analysis. It not only demonstrates the dynamic evolution process of the multilayer network, i.e., the pairwise relationship between the firms changes in a certain period of time, but also allows time-series clustering of the connection dynamics of the network nodes and related community detection. It also has a relatively low estimation time cost and is better able to capture the dynamic, multilayer, and other properties of large networks than other models. Secondly, the node covariates are incorporated into the multi-layer dynamic network to obtain better community detection accuracy. Experiments show that the model has wide applicability and is more suitable for large-scale social network analysis. In addition, in terms of model comparison, the out-of-sample prediction performance of the dynamic multi-layer block network model is much better than that of the dynamic multi-layer network model, and the computational cost of the former is much lower than that of the latter. The estimation time for the dynamic multilayer block network model ranged from 25 minutes (B=3) to 1.2 hours (B=5), while the dynamic multilayer network model took more than 6 hours.

References

[1] Brandes U, Robins G, McCranie A, et al. What is network science?. Network science, 2013, 1(1): 1-15.
[2] Frantz T L. Garry Robins: Doing social network research: network-based research design for social scientists. SAGE Publications. 2017: 587-589.
[3] Yasami Y. A new knowledge-based link recommendation approach using a non-parametric multilayer model of dynamic complex networks. Knowledge-Based Systems. 2018, 143: 81-92.
[4] Leetaru K, Schrodt P A. Gdelt: Global data on events, location, and tone, 1979–2012. ISA annual convention; 2013 April 3-6; San Francisco, California: 2013, 2(4): 1-49.
[5] Blondel V D, Decuyper A, Krings G. A survey of results on mobile phone datasets analysis. EPJ data science. 2015, 4: 1-55.
[6] Shang Y. Characterization of expansion-related properties of modular graphs. Discrete Applied Mathematics. 2023, 338: 135-144.
[7] Shang Y. Resilient consensus for robust multiplex networks with asymmetric confidence intervals. IEEE Transactions on Network Science and Engineering. 2020, 8(1): 65-74.
[8] Hoff P D, Raftery A E, Handcock M S. Latent space approaches to social network analysis. Journal of the american Statistical association, 2002, 97(460): 1090-1098.
[9] Gollini I, Murphy T B. Joint modeling of multiple network views. Journal of Computational and Graphical Statistics, 2016, 25(1): 246-265.
[10] DAngelo, S., Murphy, T. B., Alf o, M., et al. Latent space modelling of multidimensional networks with application to the exchange of votes in eurovision song contest. The Annals of Applied Statistics, 2019, 13(2): 900‑930.
[11] Durante D, Dunson D B. Bayesian dynamic financial networks with time-varying predictors. Statistics & Probability Letters, 2014, 93: 19-26.
[12] Durante D, Dunson D B. Nonparametric Bayes dynamic modelling of relational data. Biometrika, 2014, 101(4): 883-898.
[13] Durante, Daniele, and David B. Dunson. "Locally adaptive dynamic networks." 2016: 2203-2232.
[14] Durante D, Mukherjee N, Steorts R C. Bayesian learning of dynamic multilayer networks. Journal of Machine Learning Research, 2017, 18(43): 1-29.
[15] Carmona C U, Martinez-Jaramillo S. Learning of weighted multi-layer networks via dynamic social spaces, with application to financial interbank transactions, Complex Networks and Their Applications VIII: Volume 2 Proceedings of the Eighth International Conference on Complex Networks and Their Applications COMPLEX NETWORKS 2019 8. Springer International Publishing, 2020: 722-735.
[16] Yildirimoglu M, Kim J. Identification of communities in urban mobility networks using multi-layer graphs of network traffic. Transportation Research Part C: Emerging Technologies. 2018, 89: 254-267.
[17] Yap M, Luo D, Cats O, et al. Where shall we sync? Clustering passenger flows to identify urban public transport hubs and their key synchronization priorities. Transportation Research Part C: Emerging Technologies. 2019, 98: 433-448.
[18] Tian Z, Zhou J, Szeto W Y, et al. The rebalancing of bike-sharing system under flow-type task window. Transportation research part C: emerging technologies. 2020, 112: 1-27.
[19] Rodriguez-Deniz H, Villani M, Voltes-Dorta A. A multilayered block network model to forecast large dynamic transportation graphs: An application to US air transport. Transportation Research Part C: Emerging Technologies, 2022, 137: 103556.
[20] Snijders T A B, Lomi A, Torló V J. A model for the multiplex dynamics of two-mode and one-mode networks, with an application to employment preference, friendship, and advice. Social networks, 2013, 35(2): 265-276.
[21] Bhattacharya A, Dunson D B. Sparse Bayesian infinite factor models. Biometrika, 2011, 98(2): 291-306.

Fuzzy Systems and Data Mining IX
A.J. Tallón-Ballesteros and R. Beltrán-Barba (Eds.)

doi:10.3233/FAIA231042

Concentration Diagnosis in Soft Sensing Based on Bayesian T-Distribution Mixture Regression

Changhai Xia [a,1], Zhiping Peng [b] , Delong Cui [c] , Qirui Li[c], and Lihui Sun[a]
[a] *School of Information and Control Engineering, Jilin Institute of Chemical Technology, Jilin 132022, China*
[b] *Jiangmen Polytechnic College, Jiangmen City 529090, China*
[c] *School of Computer Science, Guangdong University of Petrochemical Technology, Maoming City 525000, China*

Abstract. This study presents a cutting-edge soft sensing approach for coke-making diagnostics, aimed at tackling the challenges posed by multifaceted, nonlinear, non-Gaussian, and noisy operational data prevalent in coke-making ovens. Our proposed method leverages a Bayesian t-distributed mixed regression model, effectively capturing the intricate nature of multivariate, nonlinear, and non-Gaussian data. The utilization of the t-distribution ensures the model's resilience to interference, with model parameter estimation achieved within a Bayesian framework. Conducting simulation experiments and real industrial experiments, as well as comparative analysis with PLSR, GMR, and GPR models, we demonstrate the model's good robustness, excellent prediction accuracy, and robustness, further confirming its potential application in coking diagnosis.

Keywords. Steam Cracking; t-distribution; t-distribution mixture regression model; Variational Bayesian; Robustness

1. Introduction

An ethylene cracking furnace plays a pivotal role in steam cracking production[1]. The production capacity and technology of the cracking furnace directly influence the production scale, yield, and product quality of the entire ethylene plant[2]. Due to the unique characteristics of hydrocarbon cracking feedstock, the cracking reaction at high temperatures inevitably leads to the formation of coke particles, which adhere to the inner wall of the furnace tube, a phenomenon known as furnace tube coking[3]. Furnace tube

[1] Corresponding Author, Changhai Xia, Jilin Institute of Chemical Technology, Jilin 132022, China; E-mail: xch1195940@163.com.

The work presented in this paper was supported by: National Natural Science Foundation of China (62273109, 61772145, 61672174), the Guangdong Basic and Applied Basic Research Foundation (2021A1515012252, 2020A1515010727, 2022A1515012022, 2019A1515010830, 2023A1515011913), the Key Field Special Project of the Department of Education of Guangdong Province (2020ZDZX3053), the Key Realm R&D Program of Guangdong Province (2021B0707010003), and the Maoming Science and Technology Project (210429094551175, 2022DZXHT028, and mmkj2020033), 2022 Guangdong Province Science and Technology Innovation Strategy Special Project (pdjh2022b0349), Projects of PhDs' Start-up Research of GDUPT (2023bsqd1002).

coking poses a significant threat to ethylene production and can even result in catastrophic accidents in severe cases[4-5]. Consequently, accurately predicting the extent of cracker tube coking holds the utmost importance.

Currently, two main methods are used for tube coking diagnosis in ethylene cracking furnaces: coking diagnosis based on mechanistic models[6-7] and data-driven coking diagnosis through soft sensing[8]. Although mechanistic model-based approaches have been employed early on, their accuracy in coking inference is limited due to challenges in accurately obtaining parameters for crucial mechanistic models[9-11]. On the other hand, data-driven coking diagnosis offers a promising solution by utilizing available cracking process parameters as input variables for artificial intelligence algorithms, establishing relationships with coking thickness through feature extraction and modeling[12]. Among these techniques, artificial neural networks have been widely adopted for identifying operating conditions and developing a system model for the stochastic distribution of outlet temperatures, laying the foundation for advanced coke on temperature (COT) control during the ethylene cracking furnace coking process[13-14]. Given the multi-modality, nonlinearity, and non-Gaussian characteristics of cracking furnace data, modeling methods based on mixture models have proven advantageous, with the Gaussian mixture model (GMM) being commonly employed[15]. Building upon GMM, the Gaussian mixture regression model (GMR) enables predictions of output variables[16-17]. However, in practical scenarios, operating data are susceptible to noise, and the use of Gaussian distribution, with its short tails, may lead to reduced model accuracy[18]. In contrast, the t-distribution mixture model, characterized by wider tails, exhibits better robustness to outliers[19].

To overcome the challenges posed by multi-modality, nonlinearity, non-Gaussian, and strong noise in cracking furnace operating data, this paper introduces a soft sensing method for tube coking diagnosis called the Bayesian t-distribution mixture regression model (STMR). The proposed approach effectively captures the complex features of the multi-modal, nonlinear, and non-Gaussian data by employing the mixture model. By utilizing the t-distribution, the model ensures robustness and accuracy, even in the presence of noise. Parameter estimation for the model is achieved through the variational Bayesian method, enhancing the reliability of the results. Finally, the predictive accuracy of the model is validated through experiments using real-world industrial data, demonstrating its practical utility and effectiveness.

2. Bayesian t-distribution mixture regression model

2.1. Bayesian t-distribution mixture regression

Given the auxiliary variable $\mathrm{X} = \{x_n\}_{n=1}^{N}$, and the dominant variable $\mathrm{Y} = \{y_n\}_{n=1}^{N}$, where N is the number of samples in the dataset, and the data dimensions for the auxiliary variables denoted by *d*, assuming that auxiliary variable X within the input space is a mixture of M t-distributions

$$p(x_n \mid \mu, \Lambda, v, \pi) = \sum_{m=1}^{M} \pi_m \mathcal{St}(x_n \mid \mu_m, \Lambda_m, v_m) \tag{1}$$

where μ is the mean, Λ is the precision, v is the degree of freedom, M is the number of mixed membership components, $\pi = \{\pi_m\}_{m=1}^{M}$ is the mixing coefficients also known as weighting coefficients, where the element π_m represents the a priori probability value of the mth membership component. The constraints are $0 \le \pi_m \le 1$, $\sum_{m=1}^{M} \pi_m = 1$.

It is assumed that the auxiliary variable X and the dominant variable Y under each mixed t-distribution component in the output space obey a linear relationship, i.e.

$$y_n = x_n^T \omega_m + \varepsilon_m \tag{2}$$

where ω_m is the regression coefficient between y_n and x_n, ε_m is the measurement noise, and $\varepsilon_m \sim \mathcal{N}(0, \sigma_m)$.

We can be obtained

$$p(y_n \mid x_n, \omega, \sigma) = \prod_{m=1}^{M} \mathcal{N}(y_n \mid x_n^T \omega_m, \sigma_m) \tag{3}$$

where $\omega = \{\omega_1, \omega_2, \ldots, \omega_m\}$ and $\sigma = \{\sigma_1, \sigma_2, \ldots, \sigma_m\}$.

To facilitate variational processing, discrete binary indicator hidden variables $Z = \{z_n\}_{n=1}^{N}$ and robust hidden variables $U = \{u_n\}_{n=1}^{N}$ are introduced for x_n. where $z_{nm} \in \{0,1\}$, $\sum_{m=1}^{M} z_{nm} = 1$, and z_{nm} denotes the indicator that x_n comes from the mth mixing component, which is indicated when $z_{nm} = 1$, and which is assigned to this x_n, and vice versa when $z_{nm} = 0$. In particular, note that each sample can be for only one mixing component, and the mixing coefficient π is given to characterize the weight that each t-distribution component carries in the mixing model, and thus the conditional probability density function of the indicator hidden variable Z and the robust hidden variable U can be expressed as

$$p(z|\pi) = \prod_{n=1}^{N} \prod_{m=1}^{M} \pi_m^{z_{nm}} \tag{4}$$

$$p(z|\pi) = \prod_{n=1}^{N} \prod_{m=1}^{M} \mathcal{G}\left(u_{nm} \middle| \frac{v_m}{2}, \frac{v_m}{2}\right)^{z_{nm}} \tag{5}$$

Using the conjugate prior property of the exponential family of distributions, the prior distributions of the model variables are chosen in the following manner:

The prior distributions for the mixture coefficients π follow a Dirichlet distribution $\mathcal{D}ir(\pi|k_0)$, with k_0 being the hyperparameter of the Dirichlet prior. The precisions Λ_m of each mixture component follow the Wishart prior distribution $\mathcal{W}(\Lambda_m|r_0, s_0)$, where r_0 and s_0 are the degrees of freedom and scale matrix of the Wishart prior, respectively. The means μ_m of each mixture component follow the Gaussian distribution $\mathcal{N}(\mu_m|m_0, \rho_0)$, with m_0 and ρ_0 being the mean and precision parameters of the Gaussian prior, respectively. The coefficients ω_m in the linear relationship between the auxiliary variables X and dominant variables Y are drawn from the Gaussian distribution $\mathcal{N}(\omega_m|0, \lambda_m^{-1}.I)$, where $\lambda = \{\lambda_1, \lambda_2, \ldots, \lambda_m\}$, and λ_m represents the precision

parameter of the Gaussian prior for ω_m. As both λ and σ are represented as the precisions of Gaussian distributions in the model, the conjugate prior distributions for λ_m and σ_m are specified as Gamma distributions, with a_0, b_0, c_0 and d_0 as the hyperparameters.

The degrees of freedom parameters $v = \{v_m\}_{m=1}^{M}$ have no prior distributions and can be estimated by maximizing the lower bound on v_m.

The joint distribution hierarchy between the data and the variables is expressed as

$$\begin{aligned} p(Y, X, Z, U, \pi, \mu, \Lambda, \omega, \lambda, \sigma) = p(Y \mid X, Z, \omega, \sigma) p(X \mid Z, U, \mu, \Lambda) \\ \times p(U \mid Z) p(Z \mid \pi) p(\pi) p(\Lambda) p(\mu) p(\omega \mid \lambda) p(\lambda) p(\sigma) \end{aligned} \tag{6}$$

2.2. Variational inference for Bayesian t-distributed mixed regression

In the Bayesian framework, variational inference is adopted to estimate the model parameters. The variable $\Theta = \{\Theta^l, \Theta^{vb}\}$ is set to be the ensemble of the latent variable $\Theta^l = \{Z, U\}$ and the variational Bayesian variable $\Theta^{vb} = \{\pi, \mu, \Lambda, \omega, \lambda, \sigma\}$. Considering the approximate posterior $q(\Theta)$, the logarithm of the likelihood can be expressed as

$$ln\, p(X, Y) = \mathcal{L}(q) + KL[q(\Theta)||p(\Theta|X, Y)]\, ln\, p(X, Y)] \tag{7}$$

where $KL[q(\Theta)||p(\Theta|X, Y)]$ is the relative entropy in information theory and satisfies $KL[q(\Theta)||p(\Theta|X, Y)] \geq 0$. It is called KL scatter, which denotes the distance between the true posterior distribution $p(\Theta|X, Y)$ and the approximate posterior $q(\Theta)$. $KL[q(\Theta)||p(\Theta|X, Y)] = 0$ if and only if $p(\Theta|X, Y) = q(\Theta)$. so there is $\mathcal{L}(q) \leq ln\, p(X, Y)$, and $\mathcal{L}(q)$ is an evidential lower bound for $ln\, p(X, Y)$. The variational a posteriori for the variable Θ can be obtained by taking the variational components of $\mathcal{L}(q)$ for each variable in turn.

The hidden variables of the variable Θ are independent of each other and of the individual hyperparameters, factorizing the posterior distribution of the variates, i.e:

$$q(\Theta) = q(Z, U, \pi, \mu, \Lambda, \omega, \lambda, \sigma) = q(Z)q(U)q(\pi)q(\mu)q(\Lambda)q(\omega)q(\lambda)q(\sigma) \tag{8}$$

2.3. Parameter estimates

The approximate posterior distribution of the latent variable Θ^l is computed below

$$q(Z) \propto exp \sum_{n=1}^{N} \sum_{m=1}^{M} {z_{nm}}^{r_{nm}} \tag{9}$$

Consider the uncertainty on the robust variables. After normalization, the expectation of the indicator variable Z is

$$\langle z_{nm} \rangle = \frac{r_{nm}}{\sum_{m=1}^{M} r_{nm}} \tag{10}$$

The posterior distribution $q(U) = \mathcal{G}(u_{nm}|\alpha_{nm}, \beta_{nm})$ of the robust variable U, where

$$\alpha_{nm} = \frac{v_m + \langle z_{nm} \rangle d}{2} \tag{11}$$

$$\beta_{nm} = \frac{v_m + \langle z_{nm} \rangle \langle (x_n - \mu_m)^T \Lambda_m (x_n - \mu_n) \rangle}{2} \tag{12}$$

In addition, we have $\langle u_{nm} \rangle = \alpha_{nm}/\beta_{nm}$, $\langle Ln\, u_{nm} \rangle = \psi(\alpha_{nm}) - ln\, \beta_{nm}$, where $\psi(\cdot)$ is the digamma function.

Similarly, derive the posterior distributions of the other model parameters. In addition, the degree of freedom parameter v_m can be optimized by maximizing the log-likelihood function for v_m, since there is no information about the prior distribution.

In order to simplify the numerical computation, in this paper, the nonlinear equations are not solved, and using Stirling's formula $ln\ \Gamma(z) \approx (z - 1/2) ln\ z - z + 1/2 ln\ 2\pi + O(1/z)$, the updating formula for v_m can be obtained

$$v_m = -\left(1 + \frac{\sum_{n=1}^{N} \langle z_{nm} \rangle \left(\langle ln\, u_{nm} \rangle - \langle u_{nm} \rangle \right)}{\sum_{n=1}^{N} \langle z_{nm} \rangle}\right)^{-1} \tag{13}$$

The purpose of the parameter update is to maximize the evidence lower bound $\mathcal{L}(\mathrm{q})$, which is computed below based on the variational posterior of the parameter

$$\mathcal{L}(q) = \langle ln\, p(X, Y, Z, U, \pi, \mu, \Lambda, \omega, \lambda, \sigma) \rangle - \langle ln\, q(Z, U, \pi, \mu, \Lambda, \omega, \lambda, \sigma) \rangle \tag{14}$$

The difference of the evidence lower bound $\mathcal{L}(q)$ is computed after each iteration, and the algorithm is recognized to have converged when this difference is below a predetermined queer value ξ. i.e:

$$|\mathcal{L}(q)_t - \mathcal{L}(q)_{t-1}| < \xi \tag{15}$$

3. Soft measurements based on STMR

The data of the ethylene cracker consists of two parts: input data x includes the entrance and exit temperatures of the furnace tube, the outer surface temperature of the furnace tube, the adiabatic pressure ratio, the pressure across the section, and the venturi pressure, and the output data y is the coking degree of the furnace tube. Assuming that the new input variable is x_{new} and the corresponding output variable is y_{new}, in order to predict the output, it is necessary to construct a soft-measurement model based on Bayesian t-distribution mixture regression. For the mth mixture component, the posterior probability about x_{new} and the conditional probability about y_{new} are estimated as

$$p(z_{new} = 1 | x_{new}) = \frac{\langle \pi_m \rangle \mathcal{St}(x_{new} | \langle \mu_m \rangle, \langle \Lambda_m \rangle, v_m)}{\sum_{m=1}^{M} \langle \pi_m \rangle \mathcal{St}(x_{new} | \langle \mu_m \rangle, \langle \Lambda_m \rangle, v_m)} = S_{nm} \tag{16}$$

$$p(y_{new} | x_{new}) = \sum_{m=1}^{M} S_{nm} \mathcal{N}\left(y_{new} | x_{new}^T \langle \omega_m \rangle, \langle \sigma_m^{-1} \rangle + x_{new}^T \varphi_m^{-1} x_{new} \right) \tag{17}$$

Finally, the predicted output $\hat{y}_{new}$ is

$$\hat{y}_{new} = \sum_{m=1}^{M} S_{nm} x_{new}^{T} \tau_m \tag{18}$$

4. Experiments and analysis of results

Within this section, a numerical simulation and an application to an actual industrial process are employed to authenticate the viability and efficacy of the soft measurement algorithm based on STMR. In parallel, the Gaussian mixture regression model (GMR), Gaussian process regression model (GPR), and partial least squares regression (PLSR) are chosen for comparative analysis. For GMR, the optimal number of components is determined using the Bayesian Information Criterion (BIC). In tandem, the root mean square error (RMSE) is employed in this study to assess the performance of various models. The configurations of the used computer are given as follows: CPU: Core i7-1165G7@2.80GHz, RAM: 16 GB, OS: Windows 10, and Software: MATLAB (R2016a).

4.1. Numerical simulation

A system is set up with a 2-dimensional input variable $X = (x_1, x_2)^{\mathrm{T}}$ and an output variable Y. The input variable x obeys a mixed Gaussian distribution, and the relationship between X and Y is shown in Eq. (2). The specific parameter settings of the model are shown in Table 1.

Table 1 Parameters of three Gaussian components for numerical simulation

	m=1	m=2	m=3
π_m	0.2	0.2	0.6
μ_m	$(-3,1)^{\mathrm{T}}$	$(2,4)^{\mathrm{T}}$	$(3,-3)^{\mathrm{T}}$
Λ_m	$\begin{pmatrix} 2 & 1 \\ 1 & 1 \end{pmatrix}$	$\begin{pmatrix} 1 & 1 \\ 1 & 2 \end{pmatrix}$	$\begin{pmatrix} 3 & -1 \\ -1 & 1 \end{pmatrix}$
ω_m	$(1,1,-2)^{\mathrm{T}}$	$(1,-1,0)^{\mathrm{T}}$	$(-1,1,1)^{\mathrm{T}}$
σ_m	0.25	0.25	0.25

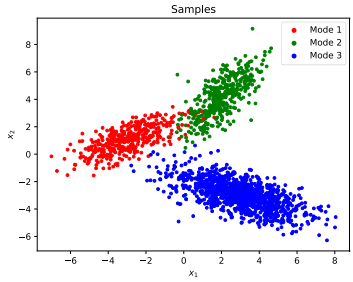

Figure 1 Spatial distribution of pure data

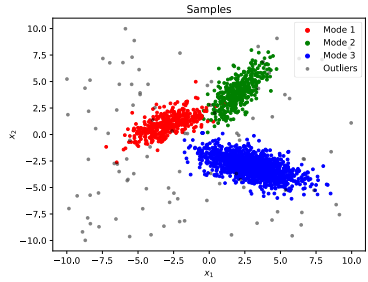

Figure 2 Spatial distribution of data under 7% noise pollution

The overall dataset comprises 5000 samples, with 2000 samples allocated to the training set and 3000 samples assigned to the prediction set. To assess the model's robustness, the training set is intentionally subjected to noise pollution by randomly introducing 1%, 5%, and 7% outliers. These outliers simulate adverse conditions and contribute to the dataset's noise-contaminated variant. Figure 1 visually portrays the spatial distribution of pristine data untarnished by noise, while Figure 2 illustrates the spatial distribution of data exposed to 7% noise pollution. This comparative visualization effectively underscores the impact of noise on the data distribution.

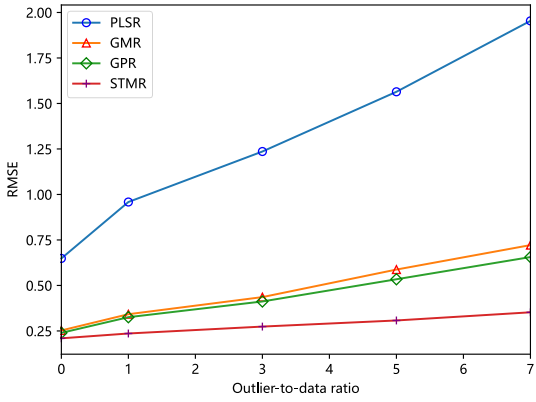

Figure 3 RMSE values of the model at different proportions of outliers

Figure 3 offers a comprehensive evaluation, employing the Root Mean Square Error (RMSE) metrics, to compare the performance of the four models in the presence of varying proportions of outliers. A conspicuous trend unfolds within the visual representation: the STMR model consistently exhibits superior performance as outliers are progressively introduced. As the dataset incrementally incorporates outliers, a discernible yet moderate increase in the RMSE curves of all four models is observed. However, in this context, the performance of the remaining three models experiences a swift degradation. Specifically, both the Gaussian Process Regression (GPR) model and the Gaussian Mixture Regression (GMR) model suffer diminishing accuracy, with the RMSE values of the Gaussian Mixture Regression (GMR) model escalating by 185%, and those of the Gaussian Process Regression (GPR) model increasing by 173% as outlier instances grow to 7% of the dataset. This escalation directly correlates with the

proliferation of outlier instances. Conspicuously, the Partial Least Squares Regression (PLSR) model emerges as particularly vulnerable to the disruptive influence of outliers, evidenced by a substantial 201% elevation in RMSE values. In stark contrast, the STMR model exhibits remarkable resilience, registering a mere 68% increase in RMSE values. This striking contrast underscores the STMR model's exceptional robustness, rendering it minimally susceptible to the adverse influence of outliers. In this regard, the STMR model attains a commendable status, epitomizing both superior predictive accuracy and unparalleled resilience in the face of outlier-influenced datasets.

4.2. Actual industrial data

In this study, the actual data from the #1 ethylene cracker of a large petrochemical company, which has 11 crackers, numbered H-110 to H-120, are used, and each cracker has 8 observation windows, each of which can observe 12 or 13 furnace tubes. The ethylene crackers H-114 and H-115 were selected as the experimental subjects, and the corresponding operating data and the labeled values of the degree of intersection of all the furnace tubes in one operating cycle of the crackers were used as the experimental data to validate the feasibility and validity of the soft measurement algorithm for coking diagnosis with Bayesian t-distributed mixed regression model (STMR). It was also analyzed in comparison with the Gaussian mixture regression model (GMR), Gaussian process regression model (GPR), and partial least squares regression (PLSR). Performance is evaluated using root mean square error (RMSE). A total of six auxiliary variables were screened by the steam cracking process mechanism and the experience of the field experts, which were the outlet temperature of the furnace tube, the inlet temperature of the furnace tube, the outer surface temperature of the furnace tube, the adiabatic pressure ratio, the pressure across the section, and the venturi pressure. The coking degree of the stovepipe was also categorized into four classes. Technicians usually categorize the degree of coking of the furnace tube into four classes: normal, mild coking, moderate coking, and severe coking.

In order to make the output results of the model more accurately express the coking degree of the furnace tube, the output results of the model are processed as follows

$$\hat{y}_{new} = \begin{cases} j_n, & |\hat{y}_{old} - j_n| < 0.5 \\ j_{n+1}, & \hat{y}_{old} - j_n = 0.5 \end{cases} \tag{19}$$

where j_n is the coking degree level of the furnace tube, $\hat{y}_{old}$ is the unprocessed model output, and $\hat{y}_{new}$ is the predicted coking degree level of the furnace tube.

The total number of experimental data samples in this paper is 5000. The number of samples in the training set is 2000 and the number of samples in the prediction set is 3000. the root mean square error RMSE is used as an index to measure the prediction accuracy of the STMR model and other models.

Table 2. Model prediction results

model	RMSE
PLSR	1.1795
GPR	0.3428
GMR	0.2986
STMR	0.1112

The graph of prediction results of the PLSR model, GPR model, GMR model, and STMR model for industrial data is given in Table 2, STMR model has the best model

performance with the smallest RMSE value compared to the other three models. The error distribution of the STMR model is reduced by 90.6%, 67.5%, and 62.8% compared to the PLSR model, GPR model, and GTMR model. The main reason for this analysis is that the STMR model has better robust performance as the model is less affected when dealing with experimental data containing noise.

5. Conclusion

Focusing on the operational data from cracker furnaces, known for their distinctive attributes of multimodality, nonlinearity, non-Gaussianity, and pronounced noise, this study presents a novel approach for coking diagnosis through a Bayesian t-distribution mixed regression (STMR) model. The model's parameter estimation is meticulously conducted within the Bayesian framework, accounting for these intricate characteristics. By means of simulation experiments and real-world industrial data validation, the study establishes that the proposed model not only exhibits remarkable predictive accuracy but also displays robustness in the presence of noise. As a prospect for future investigations, the research aims to explore the amalgamation of deep learning techniques with STMR models. This amalgamation aspires to augment the soft measurement model across dimensions such as characterization, adaptability, and predictive performance. Consequently, this initiative seeks to fortify the model's capability to adeptly address the intricate intricacies inherent in industrial processes linked to cracking and coking.

References

[1] Chen WQ. Research on quantitative evaluation of carburization damage and magnetic detection technology of ethylene cracker furnace tube [D]. Beijing University of Chemical Technology [2023-07-26].
[2] Xiong SH. Simulation and control of coke clearing in tubular ethylene cracker [D]. Beijing: Beijing University of Chemical Technology, 2016.
[3] Wang DW. Causes of coking and prevention and control technology of ethylene cracking furnace[J]. Chemical Management, 2018 (2): 99-99.
[4] Jin PB. Analysis of the impact of high temperature and complex environment on the performance of ethylene cracker tube [D]. China University of Mining and Technology, 2017.
[5] Li M. Effect of chemical cleaning on the operating condition of cracking furnace[J]. Refining and Chemical Industry, 2020, 31(3): 27-29.
[6] Valus M G, Fontoura D V R, Serfaty R, et al. Computational fluid dynamic model for the estimation of coke formation and gas generation inside petrochemical furnace pipes with the use of a kinetic net[J]. The Canadian Journal of Chemical Engineering, 2017, 95(12): 2286-2292.
[7] Symoens S H, Olahova N, Muñoz Gandarillas A E, et al. State-of-the-art of coke formation during steam cracking: Anti-coking surface technologies[J]. Industrial & Engineering Chemistry Research, 2018, 57(48): 16117-16136.
[8] Xin S, et al. Prediction of coke yield of FCC unit using different artificial neural network models[J]. China Pet. Process. Petrochem. Technol, 2016, 18: 102-109.
[9] Karimi H, Olayiwola B, Farag H, et al. Modelling coke formation in an industrial ethane‐cracking furnace for ethylene production[J]. The Canadian Journal of Chemical Engineering, 2020, 98(1): 158-171.
[10] Barza A, Mehri B, Pirouzfar V. Mathematical modeling of ethane cracking furnace of olefin plant with coke formation approach[J]. International Journal of Chemical Reactor Engineering, 2018, 16(9): 20170243.
[11] Abbasali S M Z, Farsi M, Rahimpour M R. Simulation and dynamic optimization of an industrial naphtha thermal cracking furnace based on time variant feeding policy[J]. Chemical Product and Process Modeling, 2017, 13(2): 20170032.

[12] Zhao T, Li P, Cao J. Soft sensor modeling of chemical process based on self-organizing recurrent interval type-2 fuzzy neural network[J]. ISA transactions, 2019, 84: 237-246.
[13] Xin S, Yingya W, Huajian P, et al. Prediction of coke yield of FCC unit using different artificial neural network models[J]. China Pet. Process. Petrochem. Technol, 2016, 18: 102-109.
[14] Chen DK, Wan X, Zhao Z. COT stochastic distribution system modeling of coking process in ethylene cracker based on working condition identification[J]. Chemical Automation and Instrumentation, 2022.
[15] Davis J W. Statistical pattern recognition[J]. 2003.
[16] WEI Meng, LI Jiabo, YE Min, et al. SOC estimation of lithium-ion battery based on Gaussian hybrid regression[J]. Energy Storage Science and Technology, 2020, 9(3): 958.
[17] Yang F, Qiao TZ, Pang YS, et al. Soft measurement of ball mill material level based on improved Gaussian mixture regression[J]. Modern Electronic Technology, 2018, 41(5): 153-158.
[18] Biernacki C, Celeux G, Govaert G. Choosing starting values for the EM algorithm for getting the highest likelihood in multivariate Gaussian mixture models[J]. Computational Statistics & Data Analysis, 2003, 41(3-4): 561-575.
[19] Wei X, Li C. The infinite Student's t-mixture for robust modeling[J]. Signal Processing, 2012, 92(1): 224-234.

Fuzzy Systems and Data Mining IX
A.J. Tallón-Ballesteros and R. Beltrán-Barba (Eds.)

doi:10.3233/FAIA231043

Low-Rank Exponential Integrators for Differential Riccati Equation

Jingyi Li [a] and Dongping Li [a,b,1]

[a] *Department of Mathematics, Changchun Normal University, Changchun 130032, PR China*

[b] *Department of Mathematics, Jilin University, Changchun 130012, PR China*

Abstract. Differential Riccati equation (DRE) is especially important in several fields such as optimal control, filtering, and model reduction. In this paper we present matrix-based exponential integrators for the solution of DRE. The methods are suitable for stiff DRE. In particular, we develop low-rank versions of these methods to solve large-scale DRE. The performance of the proposed methods is compared to existing typical integrators.

Keywords. Differential Riccati equation, Matrix-valued exponential integrators, Low-rank approximation, φ-functions.

1. Introduction

In this paper, we consider the solution of matrix differential Riccati equation (DRE) on the time interval $[t_0, T]$ of the form

$$X'(t) = AX(t) + X(t)A^T + Q - X(t)GX(t), \quad X(t_0) = X_0, \tag{1}$$

where $X(t) \in \mathbb{R}^{N\times N}$ is the unknown matrix-valued function and $A, Q, G \in \mathbb{R}^{N\times N}$ are given coefficient matrices and $X_0 \in \mathbb{R}^{N\times N}$ denotes the initial value with N being the dimension of the equation. The DRE plays a fundamental role in optimal control theory, filter design theory, H_∞-control of linear time-varying systems, model reduction problems, robust control problems and many more (see, e.g., [1,2,3,4,5]). In many practical applications, the coefficient matrix A of Eq. (1) results from the spatial discretization of the differential operator, and the fast and slow modes exist, which means that the associated DRE will be large and stiff.

For stiff DRE, although the most naive approach is to expand the DRE into a vector-valued ordinary differential equation and solve it using implicit time integrators, the method is not suitable for large stiff DRE due to the disadvantages of computationally expensive and considerable storage requirements. Over the past few years some other numerical methods have been proposed for solving the

[1] Corresponding Author: E-mail: lidp@ccsfu.edu.cn.

DRE, see, e.g. [6,7,8,9,10,11,12]). In particular, several low-rank approximations based on matrix versions of classical time integration schemes, such as the BDF method, the Rosenbrock method and the splitting method have been developed, see, e.g., [13,14,15,16]. More recently, a low-rank approximation based on matrix version of the exponential Rosenbrock-type integrator has been introduced in [17].

In this paper we present the matrix-valued versions of two types of exponential integrators: integrating factor method (IF) [18] and generalized integrating factor method (GIF) [19]. Both types of methods have shown good stability and computational efficiency in solving semi-linear problems. We also exploit their low-rank approximations for large DRE. Numerical experiments have shown that the methods proposed are suitable for solving large stiff DRE.

A brief overview of the paper follows. Section 2 focuses on the matrix-based integrating factor (MIF) method. In Section 3, we present the generalized matrix-based integrating factor method. In Section 4, we develop low-rank algorithms for all proposed exponential integrators based on LDL^T-type decompositions, which is the main objective of this paper. In Section 5, we provide some numerical experiments, a comparison of different methods to illustrate the accuracy and effectiveness of the proposed methods. Finally, we summarize some conclusions in Section 6.

2. Matrix-valued Integrating Factor Method

In this section, we describe the IF method for DRE in the matrix-valued form similar to [18] and discuss how to apply this to large-scale problems. For this purpose, we rewrite Eq. (1) as

$$X'(t) = F(X(t)) = \mathcal{L}[X] + \mathcal{N}(X), \tag{2}$$

where $\mathcal{L}$ and $\mathcal{N}$ are Lyapunov and nonlinear operators, respectively:

$$\mathcal{L}[X] = AX + XA^T, \quad \mathcal{N}(X) = Q - XGX. \tag{3}$$

Since the large stiff property of the original Eq. (1), a transformation of variables is considered to ameliorate the stiff part of the equation. For $X(t)$ around $t = t_0$, find a $V : \mathbb{R} \to \mathbb{R}^n$ such that:

$$V(\tau) = e^{-\tau\mathcal{L}}[X(t_0 + \tau)]. \tag{4}$$

Differentiating (4) and then insert it into (2), we have

$$V'(\tau) = g(V(\tau)) = e^{-\tau\mathcal{L}}[\mathcal{N}(e^{\tau\mathcal{L}}[V])], \quad V(\tau_0) = X_0. \tag{5}$$

The aim of this transformation of the differential equation is to remove the explicit dependence of the equation on the operator $\mathcal{L}$, except within the exponential. The exponential function will dampen the behavior of $\mathcal{L}$ removing the stiffness or highly oscillatory nature of the problem. Then, an s-stage explicit Runge-

Kutta method with coefficients b_i, c_i, a_{ij} satisfying the simplifying assumptions $c_1 = 0$ and

$$\sum_{j=1}^{s} b_j = 1, \quad \sum_{j=1}^{s} a_{ij} = c_i, \quad 1 \le i \le s, \tag{6}$$

is used to solve (5), and the process for its numerical solution defines a sequence V_{n+1} approximating $V(\tau_{n+1})$ by:

$$\begin{aligned} k_i &= g(V_n + \tau \sum_{j=1}^{s} a_{ij} k_j), \quad 1 \le i \le s, \\ V_{n+1} &= V_n + \tau \sum_{i=1}^{s} b_i k_i. \end{aligned} \tag{7}$$

By the right of (5) for $g(V(\tau))$, we have

$$\begin{aligned} k_i &= e^{-(\tau_n + c_i\tau)\mathcal{L}}[\mathcal{N}(e^{(\tau_n + c_i\tau)\mathcal{L}}[V_n + \tau \sum_{j=1}^{s} a_{ij} k_j])], \quad 1 \le i \le s, \\ V_{n+1} &= V_n + \tau \sum_{i=1}^{s} b_i k_i. \end{aligned} \tag{8}$$

Then use (4) to transform back to the original variables to obtain the general format for the IF method

$$\begin{aligned} k_i^* &= \mathcal{N}(e^{c_i h\mathcal{L}}[X_n] + h \sum_{j=1}^{s} a_{ij} e^{(c_i - c_j)h\mathcal{L}}[k_j^*]), \quad 1 \le i \le s, \\ X_{n+1} &= e^{h\mathcal{L}}[X_n] + h \sum_{i=1}^{s} b_i e^{(1-c_i)h\mathcal{L}}[k_i^*], \end{aligned} \tag{9}$$

where X_n is the numerical approximation to the exact solution $X(t)$ at time $t = t_n = nh$, and h is the step size. Let us apply the MIF method to Eq. (1), which leads to

$$\begin{aligned} k_i^* &= Q - (e^{c_i h\mathcal{L}}[X_n] + h \sum_{j=1}^{s} a_{ij} e^{(c_i - c_j)h\mathcal{L}}[k_j^*]) \\ &\quad \cdot G \cdot (e^{c_i h\mathcal{L}}[X_n] + h \sum_{j=1}^{s} a_{ij} e^{(c_i - c_j)h\mathcal{L}}[k_j^*]), \quad 1 \le i \le s, \\ X_{n+1} &= e^{h\mathcal{L}}[X_n] + h \sum_{i=1}^{s} b_i e^{(1-c_i)h\mathcal{L}}[k_i^*]. \end{aligned} \tag{10}$$

In order to derive the MIF method, a very careful local error analysis must be performed to determine the coefficients a_{ij} and b_i. Now, the specific form of the MIF method is listed as follows: First, we consider a second-order MIF method and its parameters are given as

$$RK21: \quad \begin{array}{c|cc} 0 & & \\ 1 & 1 & \\ \hline & \frac{1}{2} & \frac{1}{2} \end{array} \tag{11}$$

This yields the following method:

$$\begin{aligned} k_1^* &= \mathcal{N}(X_n), \\ k_2^* &= \mathcal{N}(e^{h\mathcal{L}}[X_n] + he^{h\mathcal{L}}[k_1^*]), \\ X_{n+1} &= e^{h\mathcal{L}}[X_n] + \frac{h}{2}e^{h\mathcal{L}}[k_1^*] + \frac{h}{2}k_2^*. \end{aligned} \tag{12}$$

Second, we consider a third-order MIF method and its parameters are given as

$$RK31: \quad \begin{array}{c|ccc} 0 & & & \\ \frac{2}{3} & \frac{2}{3} & & \\ \frac{2}{3} & \frac{1}{3} & \frac{1}{3} & \\ \hline & \frac{1}{4} & 0 & \frac{3}{4} \end{array} \tag{13}$$

This yields the following method:

$$\begin{aligned} k_1^* &= \mathcal{N}(X_n), \\ k_2^* &= \mathcal{N}(e^{\frac{2h}{3}\mathcal{L}}[X_n] + \frac{2h}{3}e^{\frac{2h}{3}\mathcal{L}}[k_1^*]), \\ k_3^* &= \mathcal{N}(e^{\frac{2h}{3}\mathcal{L}}[X_n] + \frac{h}{3}e^{\frac{2h}{3}\mathcal{L}}[k_1^*] + \frac{h}{3}k_2^*), \\ X_{n+1} &= e^{h\mathcal{L}}[X_n] + \frac{h}{4}e^{h\mathcal{L}}[k_1^*] + \frac{3h}{4}e^{\frac{h}{3}\mathcal{L}}[k_3^*]. \end{aligned} \tag{14}$$

Third, we consider a fourth-order MIF method and its parameters are given as

$$RK41: \quad \begin{array}{c|cccc} 0 & & & & \\ \frac{1}{2} & \frac{1}{2} & & & \\ \frac{1}{2} & 0 & \frac{1}{2} & & \\ 1 & 0 & 0 & 1 & \\ \hline & \frac{1}{6} & \frac{1}{3} & \frac{1}{3} & \frac{1}{6} \end{array} \tag{15}$$

This yields the following method:

$$
\begin{aligned}
k_1^* &= \mathcal{N}(X_n),\\
k_2^* &= \mathcal{N}(e^{\frac{h}{2}\mathcal{L}}[X_n] + \frac{h}{2}e^{\frac{h}{2}\mathcal{L}}[k_1^*]),\\
k_3^* &= \mathcal{N}(e^{\frac{h}{2}\mathcal{L}}[X_n] + \frac{h}{2}k_2^*),\\
k_4^* &= \mathcal{N}(e^{h\mathcal{L}}[X_n] + he^{\frac{h}{2}\mathcal{L}}[k_3^*]),\\
X_{n+1} &= e^{h\mathcal{L}}[X_n] + \frac{h}{6}e^{h\mathcal{L}}[k_1^*] + \frac{h}{3}e^{\frac{h}{2}\mathcal{L}}[k_2^*] + \frac{h}{3}e^{\frac{h}{2}\mathcal{L}}[k_3^*] + \frac{h}{6}k_4^*. \qquad (16)
\end{aligned}
$$

The disadvantage of the MIF method for numerically solving DRE is that there is large error coefficients for $\|\mathcal{L}| \gg 1$. To solve this problem, we will continue to generalize the MIF method.

3. Generalized Matrix-valued Integrating Factor Method (GMIF)

We found that the generalized MIF method in [19] is computationally superior to the standard MIF method, so the matrix-valued version of the generalized MIF method will be further presented in this section. The idea of the method is to approximate the solution of the original equation by solving a simpler ODE exactly. To find an ODE with the same key features as (1)

$$\tilde{X}'(\tau) = \tilde{F}(\tilde{X}(\tau)) = \mathcal{L}[X] + C(\tau), \quad \tilde{X}(\tau_0) = \tilde{X}_0, \qquad (17)$$

using the following approximation for the nonlinear remainder $\mathcal{N}(X)$:

$$C(\tau) = \sum_{j=0}^{s-1} \frac{\tau^j}{j!} c_j, \qquad (18)$$

where

$$c_j = \frac{1}{h^j} \sum_{i=0}^{s-1} \gamma_{ij} \mathcal{N}_{n-i}. \qquad (19)$$

Similar to the construction of the IF method, define the operator $\varphi_{\tau,\tilde{F}} : \mathbb{R}^n \to \mathbb{R}^n$ to represent the solution of (2) by $V(\tau)$ with $V(\tau_0) = X_0$ such that

$$X(t_0 + \tau) = \varphi_{\tau,\tilde{F}}(V(\tau)) = e^{\tau\mathcal{L}}[V] + \sum_{j=1}^{s} \tau^j \varphi_j(\tau\mathcal{L})[c_{j-1}], \qquad (20)$$

and then differentiate this relation with respect to τ leads to the ODE of the form

$$V'(\tau) = (D\varphi_{\tau,\tilde{F}}(V))^{-1}(F(\varphi_{\tau,\tilde{F}}(V)) - \tilde{F}(\varphi_{\tau,\tilde{F}}(V))), \quad V(\tau_0) = X_0. \qquad (21)$$

One can also easily find that by defining the modified vector field $\tilde{F}$ such that $\tilde{F}(X) = \mathcal{L}[X]$ we get the standard IF method. By observing that $D\varphi_{\tau,\tilde{F}}(V) = e^{\tau\mathcal{L}}$, (21) can be simplified

$$V'(\tau) = e^{-\tau\mathcal{L}}[\mathcal{N}(X(t_0+\tau)) - C(\tau)], \quad V(\tau_0) = X_0. \tag{22}$$

Applying the classical fourth-order Runge-Kutta method to the transformed Eq. (22), we obtain

$$\begin{aligned}
k_1 &= e^{-\tau_n\mathcal{L}}[\mathcal{N}[\varphi_{\tau_n,\tilde{F}}(V_n)] - C(\tau_n+\tau)],\\
k_2 &= e^{-(\tau_n+\frac{\tau}{2})\mathcal{L}}[\mathcal{N}(\varphi_{\tau_n+\frac{\tau}{2},\tilde{F}}(V_n+\frac{\tau}{2}k_1)) - C(\tau_n+\frac{\tau}{2})],\\
k_3 &= e^{-(\tau_n+\frac{\tau}{2})\mathcal{L}}[\mathcal{N}(\varphi_{\tau_n+\frac{\tau}{2},\tilde{F}}(V_n+\frac{\tau}{2}k_2)) - C(\tau_n+\frac{\tau}{2})],\\
k_4 &= e^{-(\tau_n+\tau)\mathcal{L}}[\mathcal{N}[\varphi_{\tau_n+\tau,\tilde{F}}(V_n+\tau k_3)] - C(\tau_n+\tau)],\\
V_{n+1} &= V_n + \frac{\tau}{6}k_1 + \frac{\tau}{3}k_2 + \frac{\tau}{3}k_3 + \frac{\tau}{6}k_4.
\end{aligned} \tag{23}$$

Using (21) to calculate the numerical solution in the original variable, that is

$$\begin{aligned}
a &= \varphi_{\frac{h}{2},\tilde{F}}(X_n),\\
b &= \varphi_{h,\tilde{F}}(X_n),\\
c &= a + \frac{h}{2}(\mathcal{N}_a - C(\frac{h}{2})),\\
d &= b + he^{\frac{h}{2}\mathcal{L}}[\mathcal{N}_c - C(\frac{h}{2})],\\
X_{n+1} &= b + \frac{h}{3}e^{\frac{h}{2}\mathcal{L}}[\mathcal{N}_a + \mathcal{N}_c - 2C(\frac{h}{2})] + \frac{h}{6}(\mathcal{N}_d - C(h)),
\end{aligned} \tag{24}$$

where $\mathcal{N}_n = \mathcal{N}(n), n = a, b, c, d$. The corresponding s-1st order interpolation polynomial $C_{s-1}(\tau)$, we call this method ETDs/RK4. In our context, we only consider the following three representative schemes and use them in our numerical experiments.

- **ETD1/RK4** A zeroth-order approximation $C_0(\tau) = \mathcal{N}_n$ to the nonlinear terms $\mathcal{N}(X)$, leads to the ETD1/RK4 method

$$\begin{aligned}
a &= \varphi_{\frac{h}{2},\tilde{F}}(X_n),\\
b &= \varphi_{h,\tilde{F}}(X_n),\\
c &= a + \frac{h}{2}(\mathcal{N}_a - \mathcal{N}_n),\\
d &= b + he^{\frac{h}{2}\mathcal{L}}[\mathcal{N}_c - \mathcal{N}_n],\\
X_{n+1} &= b + \frac{h}{3}e^{\frac{h}{2}\mathcal{L}}[\mathcal{N}_a + \mathcal{N}_c - 2\mathcal{N}_n] + \frac{h}{6}(\mathcal{N}_d - \mathcal{N}_n).
\end{aligned} \tag{25}$$

An interesting property to observe about the ETD1/RK4 method is that when $\mathcal{L} = 0$, the method reduces to the classical fourth-order Runge-Kutta method.

- **ETD2/RK4** A first-order approximation to the nonlinear terms $\mathcal{N}(X)$ of the form

$$C_1(\tau) = \mathcal{N}_n + \tau(\frac{\mathcal{N}_n - \mathcal{N}_{n-1}}{h}), \tag{26}$$

leads to the ETD2/RK4 method

$$\begin{aligned}
a &= \varphi_{\frac{h}{2},\tilde{F}}(X_n),\\
b &= \varphi_{h,\tilde{F}}(X_n),\\
c &= a + \frac{h}{2}(\mathcal{N}_a - \frac{3}{2}\mathcal{N}_n + \frac{1}{2}\mathcal{N}_{n-1}),\\
d &= b + he^{\frac{h}{2}\mathcal{L}}[\mathcal{N}_c - \frac{3}{2}\mathcal{N}_n + \frac{1}{2}\mathcal{N}_{n-1}],\\
X_{n+1} &= b + \frac{h}{3}e^{\frac{h}{2}\mathcal{L}}[\mathcal{N}_a + \mathcal{N}_c - 3\mathcal{N}_n + \mathcal{N}_{n-1}]\\
&\quad + \frac{h}{6}(\mathcal{N}_d - 2\mathcal{N}_n + \mathcal{N}_{n-1}).
\end{aligned} \tag{27}$$

- **ETD3/RK4** A second-order approximation to the nonlinear terms $\mathcal{N}(X)$ of the form

$$\begin{aligned}
C_2(\tau) = \mathcal{N}_n &+ \tau(\frac{\frac{1}{2}\mathcal{N}_{n-2} - 2\mathcal{N}_{n-1} + \frac{3}{2}\mathcal{N}_n}{h})\\
&+ \frac{\tau^2}{2}(\frac{N_{n-2} - 2\mathcal{N}_{n-1} + \mathcal{N}_n}{h^2}),
\end{aligned} \tag{28}$$

leads to the ETD3/RK4 method

$$\begin{aligned}
a &= \varphi_{\frac{h}{2},\tilde{F}}(X_n),\\
b &= \varphi_{h,\tilde{F}}(X_n),\\
c &= a + \frac{h}{2}(\mathcal{N}_a - \frac{15}{8}\mathcal{N}_n + \frac{5}{4}\mathcal{N}_{n-1} - \frac{3}{8}\mathcal{N}_{n-2}),\\
d &= b + he^{\frac{h}{2}\mathcal{L}}[\mathcal{N}_c - \frac{15}{8}\mathcal{N}_n + \frac{5}{4}\mathcal{N}_{n-1} - \frac{3}{8}\mathcal{N}_{n-2}],\\
X_{n+1} &= b + \frac{h}{3}e^{\frac{h}{2}\mathcal{L}}[\mathcal{N}_a + \mathcal{N}_c - \frac{15}{4}\mathcal{N}_n + \frac{5}{2}\mathcal{N}_{n-1} - \frac{3}{4}\mathcal{N}_{n-2}]\\
&\quad + \frac{h}{6}(\mathcal{N}_d - 3\mathcal{N}_n + 3\mathcal{N}_{n-1} - \mathcal{N}_{n-2}).
\end{aligned} \tag{29}$$

This method has two interesting properties. First, it is an exponential general linear method that requires the transfer of two quantities X_n and $\mathcal{N}_{n-k}$ from one

step to another. Second, the coefficient matrices corresponding to the four stages are different from those of the standard integrating factor methods. This property applies to all generalized integrating factor methods, which use the Rung-Kutta methods to approximate the modified initial conditions.

4. Low-rank Methods

4.1. Low-rank Matrix-valued Integrating Factor Method

In order to efficiently implement the MIF method, we consider solving the low-rank formulation of the solution $X(t)$. First, focusing on that Q, G and X_0 in (1) are low-rank positive definite cases, where

$$Q = C^T C, \quad G = BB^T, \quad X_0 = L_0 \Gamma_0 L_0^T, \tag{30}$$

for some $C \in \mathbb{R}^{l\times N}$, $B \in \mathbb{R}^{N\times q}$, $L_0 \in \mathbb{R}^{N\times r}$, and $\Gamma_0 \in \mathbb{R}^{r\times r}$, l, q, $r \ll N$. Let X_n be the desired approximate solution to (1) given as

$$X_n = L_n \Gamma_n L_n^T, \tag{31}$$

where $L_n \in \mathbb{R}^{N\times r}$, $\Gamma_n \in \mathbb{R}^{r\times r}$. Then, k_i^* in (9) can be written as

$$k_i^* = \mathcal{N}(e^{c_i h\mathcal{L}}[L_n \Gamma_n L_n^T] + h\sum_{j=1}^{s} a_{ij} e^{(c_i-c_j)h\mathcal{L}}[L_j \Gamma_j L_j^T]), \quad 1 \le i \le s. \tag{32}$$

In the above formula, k_j^* has the same splitting factor as k_i^*, and its splitting process is described subsequently. The decompositions $L_a \Gamma_n L_a^T$ to $e^{c_i h\mathcal{L}}[X_n]$ and $\hat{L}_a \hat{\Gamma}_a \hat{L}_a^T$ to $h\sum_{j=1}^{s} a_{ij} e^{(c_i-c_j)h\mathcal{L}}[k_j^*]$ are given by the factors

$$\begin{aligned} L_a &= e^{c_i hA} L_n, \\ \hat{L}_a &= [e^{(c_i-c_0)hA} L_0, e^{(c_i-c_1)hA} L_1, \cdots, e^{(c_i-c_{s-1})hA} L_{s-1}], \\ \hat{\Gamma}_a &= \mathrm{blkdiag}(\gamma_0 \Gamma_0, \gamma_1 \Gamma_1, \cdots, \gamma_{s-1} \Gamma_{s-1}), \quad \gamma_{i-1} = h a_{i,i-1}, \quad 1 \le i \le s. \end{aligned} \tag{33}$$

Note that the new matrix L_i has more columns than L_j and more than the rank. This means that the size of the blocks of the new matrix will increase dramatically over time during the decomposition process and the computational cost becomes expensive. It is necessary to find more suitable low-rank factors by column compression strategies. Then, inserting (33) into $e^{c_i h\mathcal{L}}[X_n] + h\sum_{j=1}^{s} a_{ij} e^{(c_i-c_j)h\mathcal{L}}[k_j^*]$ yields a decomposition of form $\tilde{L}_a \tilde{\Gamma}_a \tilde{L}_a^T$ with

$$\tilde{L}_a = [L_a, \hat{L}_a], \quad \tilde{\Gamma}_a = \mathrm{blkdiag}(\Gamma_n, \hat{\Gamma}_a). \tag{34}$$

Again, inserting the splitting factors $\tilde{L}_a$ and $\tilde{\Gamma}_a$ into (32) and direct calculation shows that

Algorithm 1 Low-rank approximation of the MIF method for DRE.

Input: $A \in \mathbb{R}^{N\times N}, C \in \mathbb{R}^{l\times N}$ such that $Q = C^TC, B \in \mathbb{R}^{N\times q}$ such that $G = BB^T, L_0 \in \mathbb{R}^{N\times r}, \Gamma_0 \in \mathbb{R}^{r\times r}$ such that $X_0 = L_0\Gamma_0L_0^T, t \in [a, b]$, and the stepsize h.

1: **for** $n = 0$ to $[\frac{b-a}{h}]$ **do**
2: **for** $i = 1$ to s **do**
3: $L_a = e^{c_ihA}L_n$;
4: $\hat{L}_a = [e^{(c_i-c_0)hA}L_0, e^{(c_i-c_1)hA}L_1, \cdots, e^{(c_i-c_{s-1})hA}L_{s-1}]$;
5: $\hat{\Gamma}_a = \begin{pmatrix} \gamma_0\Gamma_0 & & & \\ & \gamma_1\Gamma_1 & & \\ & & \ddots & \\ & & & \gamma_{s-1}\Gamma_{s-1} \end{pmatrix}, \gamma_j = ha_{i,j}, 1 \le i \le s.$
6: Column-compress L_a, $\hat{L}_a$ and $\hat{\Gamma}_a$.
7: Form $\tilde{L}_a = [L_a, \hat{L}_a]$ and $\tilde{\Gamma}_a = \text{blkdiag}(\Gamma_n, \hat{\Gamma}_a)$.
8: Column-compress $\tilde{L}_a$ and $\tilde{\Gamma}_a$.
9: Form $L_i = [C^T, \tilde{L}_a]$ and $\Gamma_i = \text{blkdiag}(I, -(\tilde{\Gamma}_a\tilde{L}_a^TB)(\tilde{\Gamma}_a\tilde{L}_a^TB)^T)$.
10: Column-compress L_i and Γ_i.
11: $L_b = e^{hA}L_n$;
12: $\tilde{L}_b = [e^{(1-c_1)hA}L_1, e^{(1-c_2)hA}L_2, \cdots, e^{(1-c_s)hA}L_s]$;
13: $\tilde{\Gamma}_b = \text{blkdiag}(\beta_1\Gamma_1, \beta_2\Gamma_2, \cdots, \beta_s\Gamma_s), \beta_i = hb_i, 1 \le i \le s.$
14: Column-compress L_b, $\tilde{L}_b$ and $\tilde{\Gamma}_b$.
15: **end for**
16: Form $L_{n+1} = [L_b, \tilde{L}_b]$ and $\Gamma_{n+1} = \text{blkdiag}(\Gamma_n, \tilde{\Gamma}_b)$.
17: Column-compress L_{n+1} and Γ_{n+1}.
18: **end for**

Output: L_n and Γ_n.

$$\begin{aligned} k_i^* &= \mathcal{N}(\tilde{L}_a\tilde{\Gamma}_a\tilde{L}_a^T) \\ &= C^TC - \tilde{L}_a\tilde{\Gamma}_a\tilde{L}_a^TBB^T\tilde{L}_a\tilde{\Gamma}_a\tilde{L}_a^T \\ &= L_i\Gamma_iL_i^T, \end{aligned} \tag{35}$$

with

$$L_i = [C^T, \tilde{L}_a], \quad \Gamma_i = \text{blkdiag}(I, -(\tilde{\Gamma}_a\tilde{L}_a^TB)(\tilde{\Gamma}_a\tilde{L}_a^TB)^T). \tag{36}$$

Under the LDL^T-type splitting with $k_i^* = L_i\Gamma_iL_i^T$, it can be proved that

$$\begin{aligned} X_{n+1} &= e^{h\mathcal{L}}[L_n\Gamma_nL_n^T] + h\sum_{i=1}^{s} b_ie^{(1-c_i)h\mathcal{L}}[L_i\Gamma_iL_i^T] \\ &= L_b\Gamma_nL_b^T + \tilde{L}_b\tilde{\Gamma}_b\tilde{L}_b^T, \end{aligned} \tag{37}$$

with

$$
\begin{aligned}
&L_b = e^{hA}L_n,\\
&\tilde{L}_b = [e^{(1-c_1)hA}L_1, e^{(1-c_2)hA}L_2, \cdots, e^{(1-c_s)hA}L_s],\\
&\tilde{\Gamma}_b = \mathrm{blkdiag}(\beta_1\Gamma_1, \beta_2\Gamma_2, \cdots, \beta_s\Gamma_s), \quad \beta_i = hb_i, \quad 1 \le i \le s.
\end{aligned} \tag{38}
$$

Now, we obtain the LDL^T-type splitting with $X_{n+1} \approx L_{n+1}\Gamma_{n+1}L_{n+1}$, and then use a column compression strategy to obtain low-rank splitting factors:

$$
L_{n+1} = [L_b, \tilde{L}_b], \quad \Gamma_{n+1} = \mathrm{blkdiag}(\Gamma_n, \tilde{\Gamma}_b). \tag{39}
$$

For completeness, we summarize the above solution process in **Algorithm 1**.

4.2. Low-rank Generalized Matrix-valued Integrating Factor Method

For the ETDs/RK4 method, we similarly assume that the previous solution approximation $X_n = L_n\Gamma_n L_n^T$ with $L_n \in \mathbb{R}^{N\times r}$, $\Gamma_n \in \mathbb{R}^{r\times r}$. We assume that the $\varphi_j(\frac{h}{2}\mathcal{L})[c_{j-1}]$ term can be decomposed into the form $L_C\Gamma_C L_C^T$, $1 \le C \le s$, and then the first stage value a can be written as the form of LDL^T-type:

$$
\begin{aligned}
a &= \varphi_{\frac{h}{2},\tilde{F}}(X_n)\\
&= e^{\frac{h}{2}\mathcal{L}}[X_n] + \sum_{j=1}^{s}(\frac{h}{2})^j\varphi_j(\frac{h}{2}\mathcal{L})[c_{j-1}]\\
&= [e^{\frac{h}{2}A}L_n, L_1, L_2, \cdots, L_s]
\begin{pmatrix}
\Gamma_n & & & & \\
& \frac{h}{2}\Gamma_1 & & & \\
& & \frac{h^2}{4}\Gamma_2 & & \\
& & & \ddots & \\
& & & & \frac{h^s}{2^s}\Gamma_s
\end{pmatrix}
[e^{\frac{h}{2}A}L_n, L_1, L_2, \cdots, L_s]^T\\
&= L_a\Gamma_a L_a^T.
\end{aligned} \tag{40}
$$

Then N_a has the LDL^T-type splitting $\tilde{L}_a\tilde{\Gamma}_a\tilde{L}_a^T$ with

$$
\tilde{L}_a = [C^T, L_a], \quad \tilde{\Gamma}_a = \mathrm{blkdiag}(I, -(\Gamma_a L_a B)(\Gamma_a L_a B)^T). \tag{41}
$$

A similar assumption on $\varphi_j(h\mathcal{L})[c_{j-1}]$ yields that it has the decomposition $\tilde{L}_C\tilde{\Gamma}_C\tilde{L}_C^T$ and the approximation $L_b\Gamma_b L_b^T$ to b is given by

$$
L_b = [e^{hA}L_n, \tilde{L}_1, \tilde{L}_2, \cdots, \tilde{L}_s], \quad \Gamma_b = \mathrm{blkdiag}(\Gamma_n, h\tilde{\Gamma}_1, h^2\tilde{\Gamma}_2, \cdots, h^s\tilde{\Gamma}_s). \tag{42}
$$

Obviously, the process of finding the splitting factor of c involves the polynomial $C(\frac{h}{2})$, so the splitting of the stage value c is achieved by first splitting the polynomial c_j in LDL^T-type format, then performing an LDL^T factorization of the interpolated polynomial $C(\frac{h}{2})$, and finally forming a low-order factor of c by collecting the three terms on the right-hand side. The polynomials c_j cor-

responding to the value of $C(\frac{h}{2})$ in (24) has a low-rank splitting form $\tilde{C}_j\tilde{D}_j\tilde{C}_j^T$ with

$$\begin{aligned}\tilde{C}_j &= [\tilde{L}_0, \tilde{L}_1, \cdots, \tilde{L}_{n-s+1}],\\ \tilde{D}_j &= \text{blkdiag}(\frac{\gamma_{0j}}{h^j}\tilde{\Gamma}_0, \frac{\gamma_{1j}}{h^j}\tilde{\Gamma}_1, \cdots, \frac{\gamma_{(s-1)j}}{h^j}\tilde{\Gamma}_{n-s+1}), \quad 0 \le j \le s-1. \end{aligned} \tag{43}$$

Substitute c_j by the above splitting, we obtain the splitting factors $\bar{C}_j$, $\bar{D}_j$ of $C(\frac{h}{2})$

$$\begin{aligned}\bar{C}_j &= [\tilde{C}_0, \tilde{C}_1, \tilde{C}_2, \cdots, \tilde{C}_{s-1}],\\ \bar{D}_j &= \text{blkdiag}(\tilde{D}_0, \frac{\tau}{2}\tilde{D}_1, \frac{(\frac{\tau}{2})^2}{2!}\tilde{D}_2, \cdots, \frac{(\frac{\tau}{2})^{s-1}}{(s-1)!}\tilde{D}_{s-1}). \end{aligned} \tag{44}$$

And then c can be written as the low-rank form $L_c\Gamma_c L_c^T$ with

$$L_c = [L_a, \tilde{L}_a, \bar{C}_j], \quad \Gamma_c = \text{blkdiag}(\Gamma_a, \frac{h}{2}\tilde{\Gamma}_a, -\frac{h}{2}\bar{D}_j). \tag{45}$$

A proeduce similar to (41) can be applied to N_c yields the splitting factors

$$\tilde{L}_c = [C^T, L_c], \quad \tilde{\Gamma}_c = \text{blkdiag}(I, -(\Gamma_c L_c B)(\Gamma_c L_c B)^T). \tag{46}$$

Using the spliting $C(\frac{h}{2}) = \bar{C}_j\bar{D}_j\bar{C}_j^T$, it follows that d has the following splitting factors

$$L_d = [L_b, e^{\frac{h}{2}A}\tilde{L}_c, e^{\frac{h}{2}A}\bar{C}_j], \quad \Gamma_d = \text{blkdiag}(\Gamma_b, h\tilde{\Gamma}_c, -h\bar{D}_j). \tag{47}$$

In the same way, the splitting factors of N_d can be written as

$$\tilde{L}_d = [C^T, L_d], \quad \tilde{\Gamma}_d = \text{blkdiag}(I, -(\Gamma_d L_d B)(\Gamma_d L_d B)^T). \tag{48}$$

Finally, we obtain the LDL^T-type splitting $C(h) = \hat{C}_j\hat{D}_j\hat{C}_j^T$ with

$$\begin{aligned}\hat{C}_j &= [\tilde{C}_0, \tilde{C}_1, \tilde{C}_2, \cdots, \tilde{C}_{s-1}],\\ \hat{D}_j &= \text{blkdiag}(\tilde{D}_0, \tau\tilde{D}_1, \frac{\tau^2}{2!}\tilde{D}_2 \cdots, \frac{\tau^{s-1}}{(s-1)!}\tilde{D}_{s-1}). \end{aligned} \tag{49}$$

Now, the low-ranking approximation $L_{n+1}\Gamma_{n+1}L_{n+1}^T$ to X_{n+1} is given by forming

$$\begin{aligned}L_{n+1} &= [L_b, e^{\frac{h}{2}A}\tilde{L}_a, e^{\frac{h}{2}A}\tilde{L}_c, e^{\frac{h}{2}A}\bar{C}_j, \tilde{L}_d, \hat{C}_j],\\ \Gamma_{n+1} &= \text{blkdiag}(\Gamma_b, \frac{h}{3}\tilde{\Gamma}_a, \frac{h}{3}\tilde{\Gamma}_c, -\frac{2h}{3}\bar{D}_j, \frac{h}{6}\tilde{\Gamma}_d, -\frac{h}{6}\hat{D}_j). \end{aligned} \tag{50}$$

The details on procedure are summarized in **Algorithm 2**.

Algorithm 2 Low-rank approximation of the ETDs/RK4 method for DREs.

Input: $A \in \mathbb{R}^{N\times N}, C \in \mathbb{R}^{l\times N}$ such that $Q = C^TC, B \in \mathbb{R}^{N\times q}$ such that $G = BB^T, L_0 \in \mathbb{R}^{N\times r}, \Gamma_0 \in \mathbb{R}^{r\times r}$ such that $X_0 = L_0\Gamma_0L_0^T$, $t \in [a, b]$ and the stepsize h.

for $n = 0$ to $\left[\frac{b-a}{h}\right]$ **do**
  for $j = 1$ to s **do**
    Compute the low-rank approximation $L_C\Gamma_CL_C^T$ to $\varphi_j(\frac{h}{2}\mathcal{L})C_{j-1}$ based on a numerical quadrature formula.
    Compute the low-rank approximation $\tilde{L}_C\tilde{\Gamma}_C\tilde{L}_C^T$ to $\varphi_j(h\mathcal{L})C_{j-1}$ based on a numerical quadrature formula.
  end for
  Compute the LDL^T splitting $L_a\Gamma_aL_a^T$ of a with
  $L_a = [e^{\frac{h}{2}A}L_n, L_1, L_2, \cdots, L_s]$, $\Gamma_a = \text{blkdiag}(\Gamma_n, \frac{h}{2}\Gamma_1, \frac{h^2}{4}\Gamma_2, \cdots, \frac{h^s}{2^s}\Gamma_s)$.
  Column-compress L_a and Γ_a.
  Form $\tilde{L}_a = [C^T, L_a]$ and $\tilde{\Gamma}_a = \text{blkdiag}(I, -(\Gamma_aL_aB)(\Gamma_aL_aB)^T)$.
  Column-compress $\tilde{L}_a$ and $\tilde{\Gamma}_a$.
  Compute the LDL^T splitting $L_b\Gamma_bL_b^T$ of b with
  $L_b = [e^{hA}L_n, \tilde{L}_1, \tilde{L}_2, \cdots, \tilde{L}_s]$ and $\Gamma_b = \text{blkdiag}(\Gamma_n, h\tilde{\Gamma}_1, h^2\tilde{\Gamma}_2, \cdots, h^s\tilde{\Gamma}_s)$.
  Column-compress L_b and Γ_b.
  for $j = 0$ to s-1 **do**
    Compute the LDL^T splitting $\tilde{C}_j\tilde{D}_j\tilde{C}_j^T$ of C_j with
    $\tilde{C}_j = [\tilde{L}_0, \tilde{L}_1, \cdots, \tilde{L}_{n-s+1}]$,
    $\tilde{D}_j = \text{blkdiag}(\frac{\gamma_{0j}}{h^j}\tilde{\Gamma}_0, \frac{\gamma_{1j}}{h^j}\tilde{\Gamma}_1, \cdots, \frac{\gamma_{(s-1)j}}{h^j}\tilde{\Gamma}_{n-s+1})$.
    Column-compress $\tilde{C}_j$ and $\tilde{D}_j$.
  end for
  Form $\bar{C}_j = [\tilde{C}_0, \tilde{C}_1, \tilde{C}_2, ..., \tilde{C}_{s-1}]$ and
  $\bar{D}_j = \text{blkdiag}(\tilde{D}_0, \frac{\tau}{2}\tilde{D}_1, \frac{(\frac{\tau}{2})^2}{2!}\tilde{D}_2, \cdots, \frac{(\frac{\tau}{2})^{s-1}}{(s-1)!}\tilde{D}_{s-1})$.
  Column-compress $\bar{C}_j$ and $\bar{D}_j$.
  Compute the LDL^T splitting $L_c\Gamma_cL_c^T$ of c with
  $L_c = [L_a, \tilde{L}_a, \bar{C}_j]$ and $\Gamma_c = \text{blkdiag}(\Gamma_a, \frac{h}{2}\tilde{\Gamma}_a, -\frac{h}{2}\bar{D}_j)$.
  Column-compress L_c and Γ_c.
  Form $\tilde{L}_c = [C^T, L_c]$ and $\tilde{\Gamma}_c = \text{blkdiag}(I, -(\Gamma_cL_cB)(\Gamma_cL_cB)^T)$.
  Column-compress $\tilde{L}_c$ and $\tilde{\Gamma}_c$.
  Compute the LDL^T splitting $L_d\ \Gamma_dL_d^T$ of d with
  $L_d = [L_b, e^{\frac{h}{2}A}\tilde{L}_c, e^{\frac{h}{2}A}\bar{C}_j]$ and $\Gamma_d = \text{blkdiag}(\Gamma_b, h\tilde{\Gamma}_c, -h\bar{D}_j)$.
  Column-compress L_d and Γ_d.
  Form $\tilde{L}_d = [C^T, L_d]$ and $\tilde{\Gamma}_d = \text{blkdiag}(I, -(\Gamma_dL_dB)(\Gamma_dL_dB)^T)$.
  Column-compress $\tilde{L}_b$ and $\tilde{\Gamma}_d$.
  Form $\hat{C}_j = [\tilde{C}_0, \tilde{C}_1, \tilde{C}_2, ..., \tilde{C}_{s-1}]$ and
  $\hat{D}_j = \text{blkdiag}(\tilde{D}_0, \tau\tilde{D}_1, \frac{\tau^2}{2!}\tilde{D}_2 \cdots, \frac{\tau^{s-1}}{(s-1)!}\tilde{D}_{s-1})$.
  Column-compress $\hat{C}_j$ and $\hat{D}_j$.
  Form $L_{n+1} = [L_b, e^{\frac{h}{2}A}\tilde{L}_a, e^{\frac{h}{2}A}\tilde{L}_c, e^{\frac{h}{2}A}\bar{C}_j, \tilde{L}_d, \hat{C}_j]$ and
  $\Gamma_{n+1} = \text{blkdiag}(\Gamma_b, \frac{h}{3}\tilde{\Gamma}_a, \frac{h}{3}\tilde{\Gamma}_c, -\frac{2h}{3}\bar{D}_j, \frac{h}{6}\tilde{\Gamma}_d, -\frac{h}{6}\hat{D}_j)$.
  Column-compress L_{n+1} and Γ_{n+1}.
end for

Output: L_n and Γ_n.

5. Numerical experiments

In the following subsections, we test the performance of the method presented through a number of numerical experiments. All tests were performed under Windows 10 and MATLAB R2021b, running on a computer equipped with an Intel Core i5 processor (1.6 GHz) and 8 GB of RAM. The relative error is measured in the F-norm, i.e.,

$$Error = \frac{||Y - \hat{Y}||_F}{||Y||_F}, \tag{51}$$

where $\hat{Y}$ is the computed solution and Y is the reference solution, respectively.

In the experiment, we use the MATLAB functions recurLrlyap [20] and expmv in [21] to evaluate φ-functions of the form $\varphi(\mathcal{L})[Q]$ and matrix functions of the form $e^A L$, respectively. The MATLAB function recurLrlyap employs the scaling and recursion method, while the MATLAB function expmv employs the scaling and squaring method based on the Taylor series. For the low-rank implementation, the column compression strategy terminates at a tolerance of $N \cdot \epsilon$. Here, N is the system dimension and ϵ denotes the machine accuracy.

Experiment 1. The matrix A was obtained from the 5-point discretization of the following advection-diffusion operator

$$L[u] = \triangle u - f_1(x,y)\frac{\partial u}{\partial x} - f_2(x,y)\frac{\partial u}{\partial y}, \tag{52}$$

on the unit square $[0,1] \times [0,1]$ with homogeneous Dirichlet boundary conditions. The system matrices A, B and C can be generated directly by the MATLAB functions fdm_2d_matrix and fdm_2d_vector in the LYAPACK toolbox [22], respectively. In this test, we set two different function values $f_1(x,y) = 10x$ and $f_2(x,y) = 100y$. The domains of B and C are restricted to the input region of $x, y \in (0.1, 0.3)$ and the output region of $x, y \in (0.7, 0.9)$. The low-rank factor L_0 of the initial value X_0 was randomly generated by the MATLAB function rand. Further, there are $n_0 = 40$ equidistant grid points in each spatial dimension, and that the dimension of the matrix A is n_0^2. The reference solution of equation (1) at time t can be expressed exactly in terms of the fourth-order symmetric splitting scheme for the scheme with time step size $h = 10^{-4}$.

To test the performance of the GMIF method, we compared it with two classes of low-rank integrators developed in [23], including the second-order Rosenbrock method and fourth-order symmetric additive splitting method. We abbreviate them as Ros2 and Split4, respectively.

Figure 1 shows the accuracy and efficiency plots for ETD1/RK4, ETD2/RK4, ETD3/RK4, Ros2 and Split4 for each system on the integration interval $[0, 0.1]$ with time step sizes $h \in \{\frac{1}{500}, \frac{1}{600}, \frac{1}{700}, \frac{1}{800}, \frac{1}{900}, \frac{1}{1000}\}$. We can see that ETD1/RK4, ETD2/RK4 and ETD3/RK4 are more accurate than Ros2 and Split4 for the same time step, on the other hand they are more expensive. To get a better view as well as to compare the three methods, they are again plotted in Figure 2 with the same integration interval and number of steps.

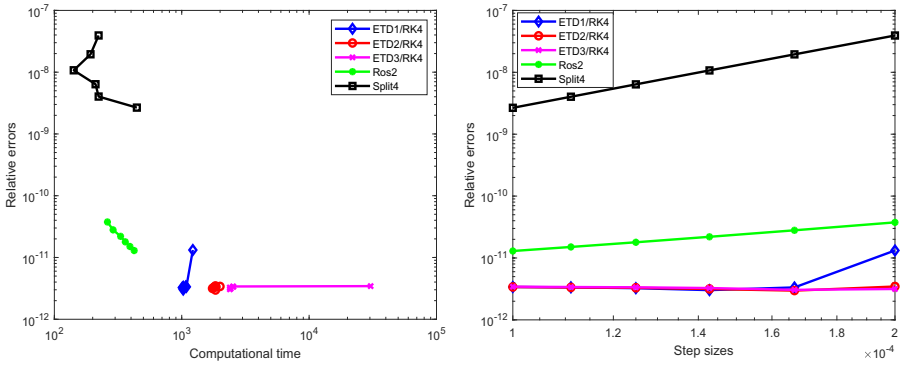

a.Efficiency plot b.Order plot

Figure 1. Experimental results of DRE for Experiment 1. Left: The relative errors versus computational time at t = 0.1. Right: The relative errors versus time step sizes $h \in \{\frac{1}{500}, \frac{1}{600}, \frac{1}{700}, \frac{1}{800}, \frac{1}{900}, \frac{1}{1000}\}$ for the same problem.

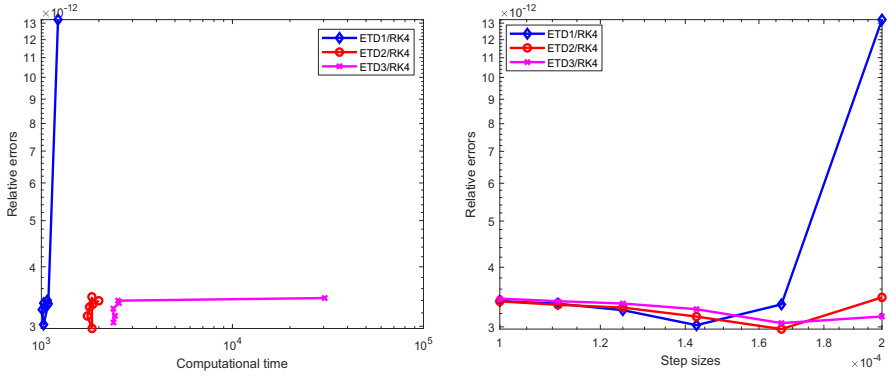

a.Efficiency plot b.Order plot

Figure 2. Same experimental setup as in Fig 1, but now for comparison purposes only the three methods ETD1/RK4, ETD2/RK4, ETD3/RK4 are shown.

Experiment 2. As a second numerical experiment, We consider an artificial symmetric model problem acting on the unit square $\omega = (0, 1)^2$ with $N = n_0^2 = 1600$ degrees of freedom. The matrix $A \in R^{n_0^2 \times n_0^2}$ can be viewed as a finite difference discretization of the two-dimensional Laplace operator in a unitary square matrix with uniform boundary conditions. The matrices $B \in R^{n_0^2 \times 1}$, $C \in R^{1 \times n_0^2}$ and $L_0 \in R^{n_0^2 \times 1}$ are randomly generated using the MATLAB function randn with normally distributed terms. In order to determine the exact reference solution, we use a fourth-order symmetric splitting approach with time step size $h = 10^{-3}$. To test the relative errors and computation times of the GMIF method, we compared it with Ros2 and split4 developed in M.E.S.S. Toolbox [23]. We have carried out

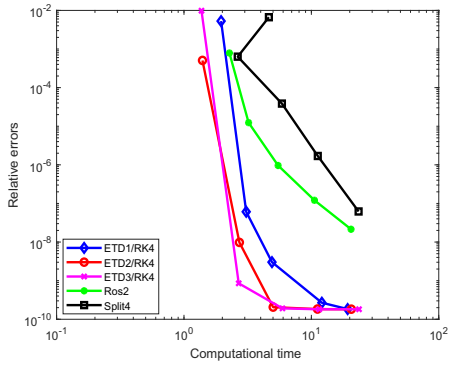

a.Efficiency plot for $\alpha = 2 \cdot 10^{-2}$

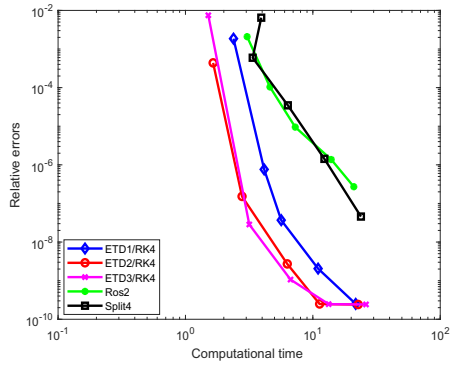

b.Efficiency plot for $\alpha = 2 \cdot 10^{-1}$

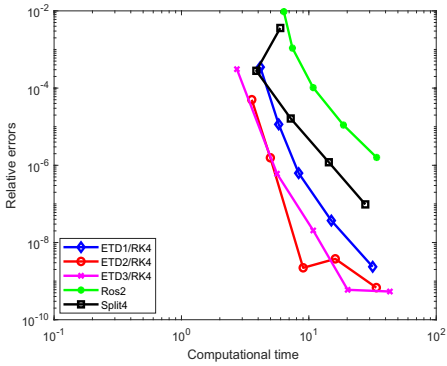

a.Efficiency plot for $\alpha = 2$

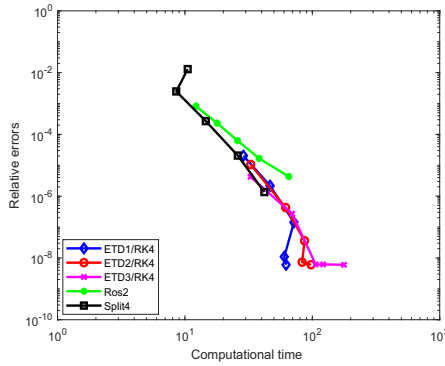

b.Efficiency plot for $\alpha = 2 \cdot 10$

Figure 3. The relative errors of ETD1/RK4, ETD2/RK4, ETD3/RK4, Ros2 and Split4 versus the computation time when integrating each of the equations for Example 2 for t = 1.

numerical experiments with four different values of the coefficient $\alpha = 2 \cdot 10^{-2}$, $2 \cdot 10^{-1}$, 2, $2 \cdot 10$. The stiffness of the problem increases with increasing values of α.

Figure 3 and Figure 4 examine the efficiency plots and accuracy plots of the methods with different coefficients for time steps of $h = 2^{-k}, k = 4, 5, \cdots, 8$ under the integration interval $[0, 1]$, respectively. In Figure 3, we can see that ETD1/RK4, ETD2/RK4 and ETD3/RK4 are more effective than Ros2 and Split4 for the same time step corresponding to a smaller stiffness. As the problem becomes more rigid, our relative errors are always significantly smaller than those of Ros2 and spilt4 , although our method performs slightly worse in terms of validity. Observe in Figure 4 that ETD1/RK4, ETD2/RK4 and ETD3/RK4 have higher accuracy when using the same step size. In particular, they remain more accurate than Ros2 and Split4 in the case of strongly rigid problems.

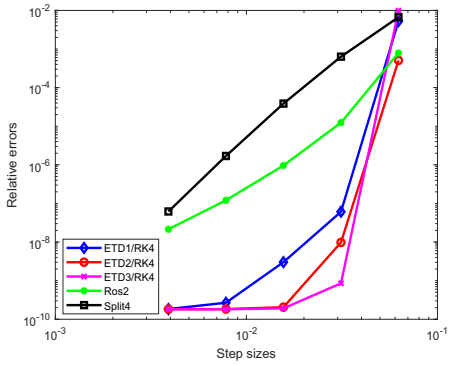

a.order plot for $\alpha = 2 \cdot 10^{-2}$

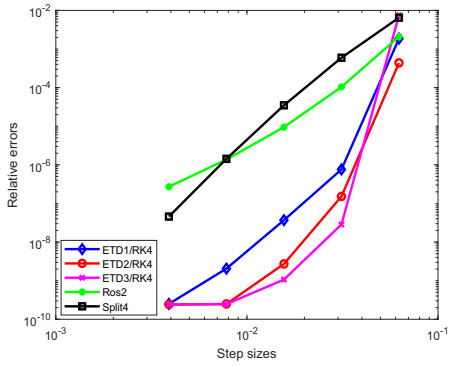

b.order plot for $\alpha = 2 \cdot 10^{-1}$

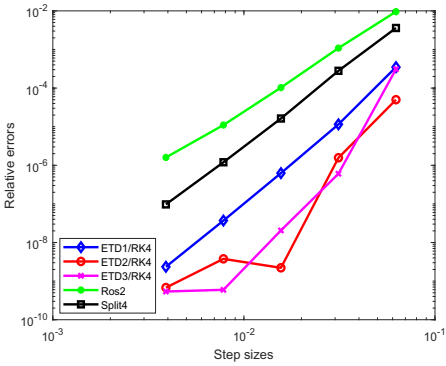

a.order plot for $\alpha = 2$

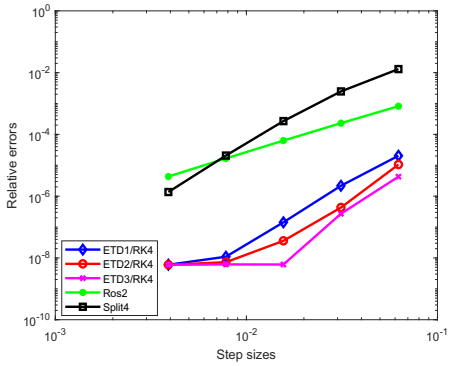

b.order plot for $\alpha = 2 \cdot 10$

Figure 4. The relative errors of ETD1/RK4, ETD2/RK4, ETD3/RK4, Ros2 and Split4 versus the variable number of time step sizes $h = 2^{-k}, k = 4, 5, \cdots, 8$ when integrating each of equations for Experiment 2 on [0, 1].

6. Conclusion

In this paper, we show how two types of exponential integrators can be applied to matrix-valued DRE, one of which is the integrating factor method and the other is the generalized integrating factor method. Based on this, we further construct two efficient algorithms based on low-rank decomposition. The performance is tested in numerical experiments with two different examples, and the results show that the proposed methods are more effective for large-scale rigid problems. In addition, the core of the computation of the generalized integral factor method is the computation of the function. Therefore, we hope that more accurate function computation methods can be proposed in the future to improve the performance.

Acknowledgements

This work was supported in part by the National Nature Science Foundation of China (Grant No. 12371455) and Jilin Scientific and Technological Development Program (Grant No. 20200201276JC) and the Natural Science Foundation of Changchun Normal University (Grant No. 2021001).

References

[1] Abou-Kandil H, Freiling G, Ionescu V, Jank G. Matrix Riccati Equations in Control and Systems Theory. Switzerland: Birkhäuser, Basel; 2003.
[2] Ichikawa A, Katayama H. Remarks on the time-varying H_∞ Riccati equations. Systems Control Lett. 1999;37:335-345.
[3] Jacobs OLR. Introduction to Control Theory. UK: Oxford Science Publications; 1993.
[4] Lancaster P, Rodman L. Algebraic Riccati equations. New York: Oxford Science Publications/The Clarendon Press Oxford University Press; 1995.
[5] Mehrmann V. The Autonomous Linear Quadratic Control Problem: Theory and Numerical Solution. 1991.
[6] Choi CH, Laub AJ. Efficient matrix-valued algorithms for solving stiff Riccati differential equations. IEEE Trans. Automat. Control. 1990;35:770-776.
[7] Lang N, Mena H, Saak J. On the benefits of the LDL^T factorization for large-scale differential matrix equation solvers. Linear Algebra and its Applications. 2015;480:44-71.
[8] Davison EJ, Maki M. The numerical solution of the matrix Riccati differential equation. IEEE Trans. Automat. Control. 1973;18:71-73.
[9] Dieci L. Numerical integration of the differential Riccati equation and some related issues. SIAM J. Numer. Anal. 1992;29:781-815.
[10] Kenne C, Leipnik R. Numerical integration of the differential matrix Riccati equation. IEEE Trans. Automat. Control. 1985;30:962-970.
[11] Kirsten G, Simoncini V. Order reduction methods for solving large-scale differential matrix Riccati equations. SIAM J. Sci. Comput. 2020;42:2182-2205.
[12] Laub AJ. A schur method for solving algebraic Riccati equations. IEEE Trans. Autom. Control. 1979;24:913-921.
[13] Benner P, Mena H. BDF methods for large-scale differential Riccati equations. proc of mathematical theory of network & systems mtns. 2009.
[14] Benner P, Mena H. Rosenbrock Methods for Solving Riccati Differential Equations. IEEE Trans, Automat. Control. 2013;58:2950-2956.
[15] Stillfjord T. Adaptive high-order splitting schemes for large-scale differential Riccati equations. Numer. Algor. 2018;78:1129-1151.
[16] Stillfjord T. Low-rank second-order splitting of large-scale differential Riccati equations. IEEE Trans. Automat. Control. 2015;60:2791-2796.
[17] Li DP, Zhang XY, Liu RY. Exponential integrators for large-scale stiff Riccati differential equation. J. Comput. Appl. Math. 2021;389:113360.
[18] Lawson D. Generalized RungeKutta processes for stable systems with large lipschitz constants. SIAM J. Numer. Anal. 1967;4:372-380.
[19] Krogstad S. Generalized integrating factor methods for stiff PDEs. Journal of Computational Physics. 2005;203:72-88.
[20] Li DP, Zhang XY. A low-rank algorithm for solving Lyapunov operator φ-functions within the matrix-valued exponential integrators. 2022. arXiv: 2212.02408.
[21] Al-Mohy A, Higham N. A new scaling and modified squaring algorithm for matrix functions. SIAM J. Matrix Anal. Appl. 2009;31:970-989.
[22] Penzl T. LYAPACK A MATLAB Toolbox for Large Lyapunov and Riccati Equations, Model Reduction Problems, and Linear-Quadratic Optimal Control Problems Users. 2000.
[23] Saak J, Koehler M, Benner P. M-M.E.S.S.-1.0.1-The Matrix Equations Sparse Solvers Library. 2016.

Fuzzy Systems and Data Mining IX
A.J. Tallón-Ballesteros and R. Beltrán-Barba (Eds.)

doi:10.3233/FAIA231044

Three-Party Evolutionary Game Analysis of the Government Reward and Punishment in Takeaway Food Safety Quality Regulation Under the Platform Economy

Huimin Ma[1] and Yibing Tang
School of Economics and Management, China Jiliang University, Hangzhou, China

Abstract: Food safety is an important guarantee for national stability and development. In recent years, with the popularization of mobile networks, the online food delivery industry has flourished. However, due to issues such as the improper management of food delivery businesses and weak regulation, the problem of food safety in the online food delivery industry has become increasingly prominent. This article addresses the situation where both the government and third-party ordering platforms are involved in regulation. It constructs a tripartite evolutionary game model among the food delivery producers, third-party ordering platforms, and government regulatory departments, and analyzes the evolutionary stability of the strategic choices made by each participant. The research findings are as follows: 1) Increasing the incentives and penalties by the government contributes to the production of safe food by the food delivery businesses and encourages the active participation of third-party food delivery platforms in regulation. However, a larger incentive may hinder the government's own regulatory responsibilities. 2) The government must establish reasonable incentive and penalty mechanisms that ensure the sum of incentives and penalties is greater than the speculative gains of all parties in order to guarantee food safety in the evolving and stable market environment of food delivery. Finally, Matlab 2021a is used for simulation analysis, in order to provide some suggestions for solving the safety problems of takeaway food in our country.

Keywords: Platform economy; takeaway food safety; quality regulation; three-party evolution game; simulation analysis

1. Introduction

In the "14th Five-Year Plan" and the "Long Range Objectives Through the Year 2035," the country clearly proposes to "comprehensively promote the construction of a Healthy China" and emphasizes the need to "prioritize the strategic position of safeguarding people's health." Ensuring food safety is an extremely important aspect in achieving the goals outlined in the plan[1].

Corresponding Author, Huimin Ma, China Jiliang University, Hangzhou, China; Email: 2499110402@qq.com

The reason is that food safety is a major livelihood issue, affecting people's lives and the future development of the country[2]. In recent years, with the development of modern information technology such as the Internet and big data, third-party ordering platforms have expanded rapidly under the impetus of platform economy. However, due to the characteristics of the Internet platform economy, food safety problems are increasingly serious. Insufficient government regulation of such emerging industries has led to a series of frequent food safety incidents, seriously affecting consumer health and the normal operation of the food market[3]. Traditional economics believes that government regulation is a necessary means to compensate for market failure[4], but now puts forward the concept of "social governance", emphasizing the full play of the role of multi-party supervision, and promote the governance model from the government-led to the "government-led, social synergy, public participation "government-led, social collaboration, public participation" synergistic governance change[5].

Around the "social governance", scholars at home and abroad have studied the impact of government rewards and punishments on food safety of takeaways; Caduff believes that the government needs to introduce public policies to maintain food safety, Losasso points out that consumers play an important role in food safety regulation, and Mensah believes that the government and enterprises should be linked to regulate and solve problems[6]. Zhou Guangliang, on the other hand, studied the path of national food safety regulation and emphasized that the synergistic governance of government, market and society is the key to solving food safety problems[7].

The above studies, while confirming that social co-governance significantly contributes to takeaway food safety, have rarely addressed the dynamic game between takeaway merchants, third-party ordering platforms, and the government, as well as the impact of the government's different regulatory strategies on takeaway merchants and third-party ordering platforms on takeaway food safety. Although Hu Chunhua[8] and others, by adopting an evolutionary game approach, considered that the government's penalty for safety regulation of online food ordering platforms would be conducive to increasing the platform's motivation to participate in the regulation as well as the merchants' motivation to operate in a self-disciplined manner. However, takeaway food safety is not a static issue at a point in time, and dynamic evolutionary thinking should be used to analyze its characteristics at different stages and focus on the regulatory coordination between the government and third-party takeaway platforms. In addition, for the subjects involved in regulatory coordination, most scholars generally agree that food safety as a public good should be provided by the government[9], and the government plays a very important role in the regulation of food safety system. For example, the government can effectively alleviate food safety problems by increasing the probability of inspection of enterprises and increasing the penalty for non-self-regulation[10].

Regarding the research on takeaway food safety, Wang Yong and Liu Hang et al. argue that the relationship between the government and the platform is not a simple substitution or complementary relationship, and that the government should strengthen the regulation of the market when the platform has a weak monitoring ability[11]. In order to describe the evolutionary process of takeaway food safety more precisely, an evolutionary game is introduced to consider the strategy selection at the stability point of mixed strategies. Zhu Lilong et al. further investigated the rent-seeking phenomenon in drug testing and proposed various regulatory measures and the role of third-party

participation in regulation, which provided the government with countermeasures and suggestions for efficient regulation[12]. However, regarding takeaway food safety, further research is needed to investigate the impact of takeaway merchants' strategic choices on takeaway food safety when both government and third-party platform regulation exist.

2. Model Hypothesis and Construction

2.1 Model Hypothesis

In order to construct the game model and analyze the stability of each party's strategy and equilibrium point, the following hypotheses are made:

Hypothesis 1: The three parties involved in the game: the takeaway producer, the third-party ordering platform and the government are all finite rational subjects and evolve into optimal strategies over time.

Hypothesis 2: Assume that the takeaway producer has two strategies: safe production and unsafe production, noting that the probability of these two strategies is x, 1-x in turn; the third-party ordering platform, which chooses how to regulate the takeaway producer. The strategy space of its behavior is noted as {positive regulation, negative regulation}, and the probabilities of the corresponding strategies are y, 1-y in order; there are two strategies for the government {strict regulation, ignore regulation}, and the probabilities of the corresponding strategies are z, 1-z in order, where x,y,z are in the range 0 to 1.

Hypothesis 3: The takeout producer's revenue from selling takeout through the platform is R. The cost of providing quality-safe food is C_{ph}. The cost of providing quality-unsafe food is C_{pl}. When the takeaway producer provides quality-safe food, the ordering platform and the governmental pass the inspection; when the takeaway producer provides quality-safe unqualified food, it will rent-seeking from the third-party ordering platform in order to qualify for the shelves through the inspection. The rent-seeking cost is B, $B<(C_{ph}-C_{pl})$, and speculation in undisciplined production will generate speculative cost, which is set at C_1 for takeaway producer.

Hypothesis 4: The detection benefit of the third-party ordering platform is V. When the takeaway producer does not self-regulate production, if the ordering platform refuses to rent-seeking, the detection fails. If the ordering platform intends to rent-seek, it will engage in rent-seeking behavior with the takeaway producer. The speculative cost of the third-party ordering platform's intention to rent-seeking is C_2, which mainly includes the costs of falsifying testing records and issuing false reports.

Hypothesis 5: When the government pays attention to regulation, takeaway producers are fined for providing unsafe food F_p and negatively regulated third-party ordering platforms are fined F_t. Takeaway producers who provide safe food are rewarded M_p and reward actively regulated ordering platforms M_t. When the government neglects to regulate, there is no access to information on strategy choice. It is assumed that strict government regulation would cost C_3.

Hypothesis 6: If the government, platforms and takeaway producers all fulfill their responsibilities, it will benefit consumer health, economic development and social stability. At the same time, it will bring social benefits of value A to the government. Consumers' health is at risk when both takeaways and platforms fail to act in their own interests, and it costs the government C_4 to rectify this phenomenon. When the

government adopts a strategy of neglecting to regulate, resulting in a lack of regulation , will be penalized by higher authorities for their own inaction, denoted by u ($u>C_4$).

2.2 Model Construction

Based on the above hypotheses, the mixed strategy game matrix of takeaway producers, third-party ordering platforms and government, as shown in Table 1.

Table 1 Three parties mixed-strategy game matrix

Strategy combination	Takeaway producers	Third-party ordering platforms	Government
(safe, active, strict)	$R-C_{ph}+M_p$	$V+M_t$	$A-C_3-M_p-M_t$
(safe, active, ignore)	$R-C_{ph}$	V	A
(safe, negative, strict)	$R-C_{ph}+M_p$	$V-C_2-F_t$	$A-C_3-M_p+F_t$
(safe, negative, ignore)	$R-C_{ph}$	$V-C_2$	A
(unsafe, active, strict)	$-C_{pl}-F_p-C_1$	$V+M_t$	$-C_3-M_t+F_p$
(unsafe, active, ignore)	$-C_{pl}-C_1$	V	0
(unsafe,negative,strict)	$R-C_{pl}-F_p-B-C_1$	$V-C_2-F_t+B$	$-C_3+F_t+F_p-C_4$
(unsafe,negative,ignore)	$R-C_{pl}-C_1-B$	$V-C_2+B$	$-C_4-u$

3. Model solution

3.1 Replicated dynamic equations

The replication dynamic equation can describe how individuals with different strategies compete with each other in a group to evolve the final group strategy.

The expected returns and average expected returns (U_1, U_2, U) of takeaway producers providing quality safe or quality unsafe food are as follows:

$U_1=yz[R-C_{ph}+M_p]+y(1-z)[R-C_{ph}]+(1-y)z[R-C_{ph}+M_p]+(1-y)(1-z)[R-C_{ph}]$

$U_2=yz[-C_{pl}-F_p-C_1]+y(1-z)[-C_{pl}-C_1]+(1-y)z[R-C_{pl}-F_p-C_1-B]+(1-y)(1-z)[R-C_{pl}-C_1-B]$

$U=xU_1+(1-x)U_2$

Similarly, the expected returns W_1 and W_2 for positive and negative regulation of third-party ordering platforms, and the average expected return W are:

$W_1=x[z(V+M_t)+(1-z)V]+(1-x)[z(V+M_t)+(1-z)V]$

$W_2=x[z(V-C_2-F_t)+(1-z)(V-C_2)]+(1-x)[z(V-C_2-F_t+B)+(1-z)(V-C_2+B)]$

$W=yW_1+(1-y)W_2$

Similarly, the expected returns E_1 and E_2, and the average expected return E for strict and negligent regulation by government are respectively:

$E_1=xy(A-C_3-M_p-M_t)+x(1-y)(A-C_3-M_p+F_t)+(1-x)y(-C_3-M_t+F_p)+(1-x)(1-y)(-C_3+F_t+F_p-C_4)$

$E_2=xyA+x(1-y)A+(1-x)(1-y)(-C_4-u)$

$E=zE_1+(1-z)E_2$

Then a system of equations is formed from the above three replicated dynamic equations as shown below:

$$F(x)=\frac{dx}{dt}=x(x-1)[C_{ph}-C_{pl}-C_1-B-y(R-B)-z(F_p+M_p)]$$

$$F(y)=\frac{dy}{dt}=y(y-1)[(1-x)B-z(F_t+M_t)-C_2]$$

$$F(z)=\frac{dz}{dt}=z(z-1)[C_3-u-F_t-F_p+x(M_p+F_p+u)+y(M_t+F_t+u)-xyu]$$

3.2 Equilibrium point and stability analysis

The equilibrium points of the system can be obtained from F(x)=0, F(y)=0, F(z)=0: $E_1(0,0,0)$, $E_2(1,0,0)$, $E_3(0,1,0)$, $E_4(0,0,1)$, $E_5(1,1,0)$, $E_6(1,0,1)$, $E_7(0,1,1)$, $E_8(1,1,1)$, $E_9(0,(u+F_t+F_p-C_3)/(M_t+F_t+u),(B-C_2)/(M_t+F_t)$, $E_{10}((F_t+F_p+u-C_3)/(M_p+F_p),0,(C_{ph}-C_{pl}-C_1-B)/(M_p+F_p))$, $E_{11}((F_p-C_3-M_t)/(M_p+F_p),1,(C_{ph}-C_{pl}-C_1-R)/(M_p+F_p))$, $E_{12}((B-C_2)/B,(C_{ph}-C_{pl}-C_1-B)/(R-B),0)$, $E_{13}((B-F_t-M_t-C_2)/B,(C_{ph}-C_{pl}-C_1-B-F_p-M_p)/(R-B),1)$. Since x, y, $z\in[0,1]$, then E9 to E13 are meaningful under certain conditions, and since $(C_{ph}-C_{pl}-C_1-R)<0$, then E_{11} is meaningless.

The Jacobian matrix of the three-party evolutionary game system is

$$J=\begin{bmatrix}J_1 & J_2 & J_3\\ J_4 & J_5 & J_6\\ J_7 & J_8 & J_9\end{bmatrix}=\begin{bmatrix}\partial F(x)/\partial x & \partial F(x)/\partial y & \partial F(x)/\partial z\\ \partial F(y)/\partial x & \partial F(y)/\partial y & \partial F(y)/\partial z\\ \partial F(z)/\partial x & \partial F(z)/\partial y & \partial F(z)/\partial z\end{bmatrix}=\begin{bmatrix}(2x-1)[C_{ph}-C_{pl}-C_1-B-y(R-B)-z(F_p+M_p)] & x(x-1)[B-R] & x(x-1)[-F_p-M_p]\\ y(y-1)[-B] & (2y-1)[(1-x)B-z(F_t+M_t)-C_1] & y(y-1)[-F_t-M_t]\\ z(z-1)[M_p+F_p+u-yu] & z(z-1)[M_t+F_t+u-xu] & (2z-1)[C_3-u-F_t-F_p+x(M_p+F_p+u)+y(M_t+F_t+u)-xyu]\end{bmatrix}$$

According to Lyapunov's first method, when all the eigenvalues of the Jacobian matrix are less than 0, the point is an evolution-stable strategy. When the Jacobian matrix has positive eigenvalues, the equilibrium point is unstable. The stability of each equilibrium point is analyzed, as shown in Table 2.

Table 2 Stability analysis of equilibrium points

Balance points	Jacobian matrix eigenvalues λ_1, λ_2, λ_3	Real symbol	Stability conclusions	conditions
$E_1(0,0,0)$	$C_{pl}-C_{ph}+C_1+B, -B+C_2, F_p+F_t+u-C_3$	(−,−,+)	unstable point	\
$E_2(1,0,0)$	$C_{ph}-C_{pl}-C_1-B, C_2, F_t-C_3-M_p$	(+,+,×)	unstable point	\
$E_3(0,1,0)$	$C_{pl}-C_{ph}+C_1+R, B-C_2, F_t-C_3-M_t$	(+,+,×)	unstable point	\
$E_4(0,0,1)$	$C_{pl}-C_{ph}+C_1+B+F_p+M_p, F_t+C_2+M_t-B, C_3-u-F_t-F_p$	(−,−,−)	ESS	①
$E_5(1,1,0)$	$C_{ph}-C_{pl}-C_1-R, -C_2, -C_3-M_p-M_t$	(−,−,−)	ESS	\
$E_6(1,0,1)$	$C_{ph}-C_{pl}-C_1-B-F_p-M_p, F_t+C_2+M_t, C_3+M_p-F_t$	(×,+,×)	unstable point	\
$E_7(0,1,1)$	$C_{pl}-C_{ph}+C_1+R+F_p+M_p, B-M_t-F_t-C_2, C_3+M_t-F_p$	(+,×,×)	unstable point	\
$E_8(1,1,1)$	$C_{ph}-C_{pl}-C_1-R-F_p-M_p, -F_t-C_2-M_t, C_3+M_p+M_t$	(−,−,+)	unstable point	\
$E_9(0,y_1,z_1)$	$\alpha_1, \lambda_2=\lambda_3=\sqrt{y_1(1-y_1)(F_t+M_t)z_1(1-z_1)(M_t+F_t+u)}\cdot i$	(−,0,0)	uncertainty	②
$E_{10}(x_1,0,z_2)$	$\alpha_2, \lambda_2=\lambda_3=\sqrt{x_1(1-x_1)(F_p+M_p)z_2(1-z_2)(M_p+F_p+u)}\cdot i$	(−,0,0)	uncertainty	③
$E_{12}(x_2,y_2,0)$	$\alpha_3, \lambda_2=-\lambda_3=\sqrt{x_2(1-x_2)(R-B)y_2(1-y_2)B}$	(×,+,−)	unstable point	④
$E_{13}(x_3,y_3,1)$	$\alpha_4, \lambda_2=-\lambda_3=\sqrt{x_3(1-x_3)(R-B)y_3(1-y_3)B}$	(×,+,−)	unstable point	⑤

Note: x denotes that the sign is uncertain, $x_1, x_2, x_3, y_1, y_2, y_3, z_1, z_2$ are the coordinates of the corresponding equilibrium point, which is unstable or meaningless if the equilibrium point corresponding to the hair condition is not satisfied. ① $C_{pl}-C_{ph}+C_1+B+F_p+M_p<0$, $F_t+C_2+M_t-B<0$; ② $\alpha_1<0$, $F_p-C_3<M_t$, $B-C_2-M_t-F_t<0$; ③ $\alpha_2<0$, $F_t-C_3<M_p$, $C_{ph}-C_{pl}-C_1-B-F_p-M_p<0$; ④ $B-C_2>0$, $C_{ph}-C_{pl}-C_1-B>0$; ⑤ $B-M_t-F_t-C_2>0$, $C_{ph}-C_{pl}-C_1-B>0$.

Corollary 1: When C_{pl}-C_{ph}+C_1+B+F_p+M_p<0 and F_t+C_2+M_t-B<0, according to Table 2, E_4(0,0,1) and E_5(1,1,0) are the two stabilization points of the replicated dynamic system. Equilibrium points $E_9(0,y_1,z_1)$ and $E_{10}(x_1,0,z_2)$ are meaningless, while $E_{12}(x_2,y_2,0)$ and $E_{13}(x_3,y_3,1)$ are unstable.

This suggests that when the government sets smaller rewards and penalties or when the takeaway producer tries to avoid the regulatory gains of the third-party ordering platform, depending on the initial point, the system's strategy combinations will stabilize at two stable points (providing unsafe food, negative supervision and strict supervision) and (providing safe food, active supervision and ignoring supervision). At this point, the government's regulation fails to constrain the violation behaviors of takeout producers and third-party ordering platforms. In order to avoid the emergence of the stable strategy combination E4(0,0,1), the government regulator must set a sufficiently large amount of fines or rewards and penalties to play the role of active regulation.

Corollary 2: When F_p+M_p>C_{ph}-C_{pl}-C_1-B>0 and F_t+M_t>B-C_2>0, there exists at least one stabilization point E_5(1,1,0) of the system, and at the same time, when F_p-M_t>C_3 and F_t-M_p>C_3 are satisfied, there is only one stabilization point E_5(1,1,0).

According to table 2, at this time, conditions ① and ⑤ are not satisfied, then E_4(0,0,1) is an unstable point, and $E_{13}(x_3,y_3,1)$ is meaningless; at this time, condition ④ is satisfied, then $E_{12}(x_2,y_2,0)$ is an unstable point; conditions ② and ③ need to be judged by more elements of the conditions, so that the stability of $E_9(0,y_1,z_1)$, $E_{10}(x_1,0,z_2)$ cannot be be judged. For the replicated dynamic system, when the conditions F_p-M_t>C_3 and F_t-M_p>C_3 are increased, conditions ② and ③ are not satisfied, and $E_9(0,y_1,z_1)$, $E_{10}(x_1,0,z_2)$ are meaningless, so there exists only one stabilization point E_5(1,1,0). This suggests that the sum of government fines and incentives for takeout producers and third-party ordering platforms should be at least higher than the revenue generated by their respective regulatory evasions in order to effectively prevent the system from having a combination of strategies (providing unsafe food, negative regulation, strict regulation).

4. Model simulation

In order to verify the validity of the evolutionary stability analysis, the model was assigned numerical values in conjunction with the real situation and numerical simulation was carried out using Matlab2021a. Array 1 is assigned values R=50, C_{ph}-C_{pl}=25, C_1=5, B=15, F_p=10, M_p=10, C_2=5, F_t=10, M_t=5, C_3=5, u=15, which satisfies the conditions in Corollary 2. On the basis of Array 1, the influence of the changes of F_t, M_t and M_p on the evolution process and results are discussed respectively.

First, the simulation results are shown in Fig. 1 for F_t = 0, 10, 20, and. in Fig. 2 for M_t = 0, 5, 10.

Figure 1 shows that the probability of self-regulated production by takeaway producers is gradually stabilized at 1 as F_t increases during the evolutionary process. In this process, the probability that the government chooses to strictly regulate gradually increases to a certain peak and then starts to decline to 0, while the probability that the third-party ordering platform chooses to regulate actively is gradually increasing. Figure 2 shows that M_t increases will make the government tend to choose to ignore regulation. Therefore, the government should formulate a reasonable reward and punishment system according to the actual situation, so that the third-party food ordering platforms can also actively participate in the regulation, and jointly protect the takeaway food safety.

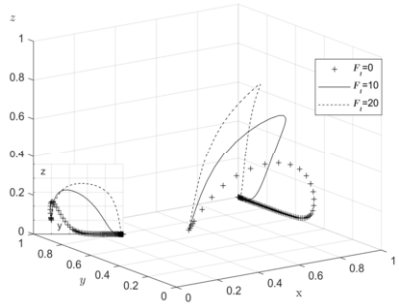

Figure 1 Impact of government fines for third-party ordering platforms

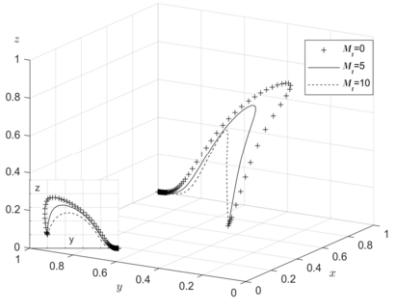

Figure 2 Impact of government incentives for third-party ordering platform

Next, the simulation results of replicating the system of dynamic equations evolving over time 50 times are shown in Fig. 3 by assigning M_p = 0, 10, 20 respectively.

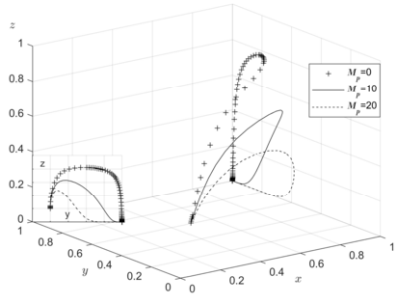

Figure 3 Impact of government incentives for takeaway producers

Figure 3 shows that during evolutionary stabilization, as M_p increases the government will gradually tend to choose to ignore regulation, and the third-party food ordering platform is more likely to choose negative regulation.

Since array 1 satisfies the conditions in Corollary 2, Corollary 2 can be verified. To verify Corollary 1, given array 2: R=50, C_{ph}-C_{pl}=35, C_1=5, B=16, F_p=8, M_p=5, C_2=5, F_t=6, M_t=4, C_3=5, u=15 satisfy its conditions, and letting each of the two sets of values evolve over time 50 times yields the results shown in Figures 4-5.

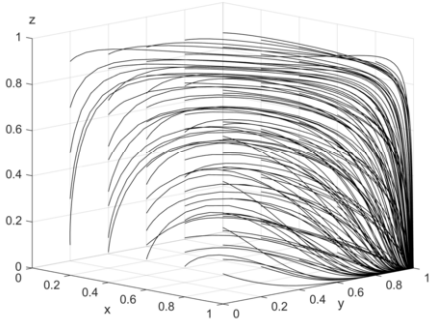

Figure 4 Array 1 evolves 50 times as a result

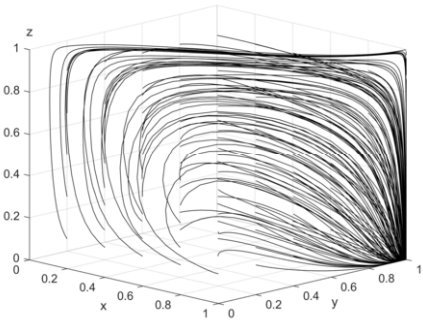

Figure 5 Array 2 evolves 50 times as a result

As can be seen in Figure 4, $E_{10}(x_1,0,z_2)$ is an unstable equilibrium point, and there is only one evolutionarily stable strategy combination (providing safe food, active supervision, and ignore supervision) that satisfies the conclusion of Corollary 2. Figure

5 shows that there are two evolutionary stable points (0,0,1), and (1,1,0) in the system under condition ①. Therefore, the regulator should examine the interests of takeaway producers and third-party ordering platforms from various aspects to ensure that the sum of rewards and penalties for each party is higher than the benefits generated by their circumvention of regulation, so as to avoid the phenomenon that takeaway producers do not exercise self-discipline to make low-quality takeaway food jeopardize consumers. It can be seen that the simulation analysis can more intuitively reflect the strategic stability analysis of the evolutionary game, which is of practical guidance significance for the regulation of takeaway food quality.

5. Conclusion

Taking takeaway food safety supervision as the research object, this paper constructs a tripartite evolutionary game based on the evolutionary game theory of takeaway producers—third-party ordering platforms—government, and discusses the influence of different influencing factors on the behaviors of all parties through simulation analysis. Finally, the following conclusions and suggestions are drawn. The government's incentives and penalties are conducive to the normative behavior of takeaway producers to provide high-quality food in a self-disciplined manner and third parties to actively regulate them; the incentives and penalties set by the government must comply with the condition that the sum of the incentives and penalties for each party is greater than the gains from their circumvention of the regulation in order to safeguard the safety of the takeaway food market.

This paper does not consider the participation of consumers in regulation, and future research can take consumers as a separate participant and consider the four-party evolutionary game among takeaway producers, the government, the third-party ordering platforms and consumers. In addition, in the numerical simulation, the given data are only set according to the constraints based on the real situation, and no corresponding research has been carried out, so future research can be carried out according to the model to obtain the actual data for simulation.

References

[1] DengYan. Study on the problems and Countermeasures of food safety supervision in Sichuan s University[D]. Sichuan Normal University, 2022.

[2] Liu Zimei. Research on optimization of Internet food safety supervision mechanism——Take City M as an example[D]. Nanchang University, 2022.

[3] Liu Peng, Li Wentao. Food Safety Regulation of Online Meal Ordering: A Study from the Perspective of Smart Regulation[J]. Journal of Huazhong Normal University (Humanities and Social Sciences), 2018, 57(01):1-9.

[4] Arrow K J, Cropper M L, Eads G C et al.Is There a Role for Benefit-Cost Analysis in Environmental, Health, and Safety Regulation?[J].Science,1996,272(5259):221-222. Al-Bus.

[5] Zhu Zheyi, Lu Mengting, Liu Zengjin et al.. Internet Meals, Food Safety and Co-governance. Journal of Finance and Economics, 2023:124-138.

[6] Ladina Caduff, Thomas Bernauer. Managing Risk and Regulation in European Food Safety Governance[J]. Reviewof Policy Research, 2006, 23(1):153-168.

[7] Zhou Guangliang. Research on the way of National Food Safety Supervision[J]. Academic Journal of Zhongzhou, 2019(02):73-79.

[8] Hu Chunhua, Sun Siyuan, Zhou Xinmin et al.. Research on Food Security in Online Ordering Based on Evolutionary Game. Consumption economy. 2021:80-87.

[9] Zhang Weiying. Reputational Foundation of the Legal System[J]. Economic Research Journal, 2002,(1):3-13,92-93.

[10] Cao Yu, Yu Chuanyan, Wan Guangyu.Food Company Regulation Game Research under Government Participation[J]. System Engineering Theory and Practice, 2017,(1):140-150.

[11] Wang Yong, Liu Hang, Feng Hua. Public Regulation, Private Regulation and Coordinated Regulation in Platform Markets: A Comparetive Study[J]. Economic Research Journal, 2020,(3):148-162.

[12] Zhu Lilong, Rong Jun mei,Zhang Siyi. Three—party Evolutionary Game and Simulation Analysis of Drug Quality Supervision under the Government Reward and Punishment Mechanism[J]. Chinese Journal of Management Science, 2021,(11):55-67.

Fuzzy Systems and Data Mining IX
A.J. Tallón-Ballesteros and R. Beltrán-Barba (Eds.)

doi:10.3233/FAIA231045

Classification of Odor Drift Data Based on Several Machine Learning Algorithms

Yuhan WU and Yiqin BAO[1]
College of Information Engineering, Nanjing Xiao Zhuang University, China

Abstract. Based on the classification and recognition algorithm of machine learning, this paper analyzes and researches the odor drift data set. First of all, data visualization is used to effectively master the data distribution law, coherence, outlier noise points and other information of the data set. According to the situation, the data is normalized and dimensionality reduction preprocessing, and the training set and test set are divided. KNN model, decision tree model, random forest classifier model and MLP multi-layer perceptron model were used to test and compare the data sets. The test results show that the performance of random forest model for odor drift data classification is relatively good, up to 95%, which can be used in practice.

Keywords. Machine learning, Classification recognition, Odor drift data, Classification prediction algorithms

1. Introduction

With the continuous development of science and technology and data, artificial intelligence has made very significant and excellent progress in the past few decades, and has a wide range of applications in many fields. Among them, classification recognition is a very important technology in artificial intelligence, and it is one of the basic tasks of machine learning. Through classification recognition, machines can learn patterns and rules from a large number of data. And classify the new data[1].

Odor drift is a phenomenon in which odors from a source are transmitted through the air and spread to other locations or the surrounding environment. Odor drift has important applications in many fields, such as environmental monitoring, indoor air quality control and odor control. If it is not well controlled, it may have a negative impact on the surrounding environment and pose a threat to people's life and health. At present, there are few relevant studies on odor drift, because the scope and dimension of odor drift are large, and the discrimination of odor and the accuracy of measurement are very complicated.

Machine learning algorithm has the ability to process large-scale data and complex models[2], and can classify and identify multidimensional data features of odor drift, so as to judge the feature significance and recognizability of odor, so as to better explore and manage odor drift data later. Through experiments on odor drift, we can better

[1] Corresponding Author, Yiqin BAO, Nanjing Xiao Zhuang University, China; Email: 392335241@qq.com.
This work is supported by Natural Science Foundation Project of China (61976118), Key topics of the '13th five-year plan' for Education Science in Jiangsu Province (B-b /2020/01/18).

distinguish the accuracy of machine learning algorithms supported by more superior algorithms and understand the relevant principles.

Based on some classic and powerful machine learning classification algorithms, this paper analyzes the odor drift data set, preprocesses the data, evaluates the classification models respectively, selects appropriate models for data classification and result analysis, and clearly demonstrates the superiority and principle of some classification models while obtaining the degree of recognition of different gases.

The contributions and innovations of this paper are summarized as follows:

1) The data distribution characteristics and pre-processing of odor drift data set are studied.

2) Use models to model and predict data.

3) Compare and analyze the predicted results.

The rest of the paper is organized as follows: the second section analyzes and preprocesses the odor drift data set, the third section conducts data modeling and prediction, the fourth section analyzes the test results, and the fifth section summarizes the full text.

2. Analysis and preprocessing of odor drift data sets

2.1 Data preparation

This article uses the Pycharm platform, Python code for related analysis and modeling tests. For the analysis and implementation of odor Drift dataset, the Gas Sensor Array Drift dataset is a data set related to the gas sensor array and its drift phenomenon over time. This dataset is commonly used to study drift compensation techniques for gas sensors [3] and machine learning algorithms for gas classification.

The dataset contains 13,910 measurements from 16 chemical sensors used to simulate drift compensation in six gases at different concentration levels, 128 dimensional properties (8 features *16 sensors)[4], and six gas types as shown in Table 1.

Table 1. Six gas types

Gas	Introduction
Ethanol	A colorless, odorless liquid, also known as alcohol.
Ethylene	A colorless, flammable gas commonly used as a raw material in industrial production.
Ammonia	A colorless gas with a pungent odor. It is widely used as a fertilizer in chemical manufacturing and agriculture.
Acetaldehyde	An organic compound having a colorless liquid or gaseous state, a strong pungent odor, and a metabolite of alcohol.
Acetone	A colorless liquid that is sweet and volatile. It is a commonly used organic solvent and is widely used in industry and laboratories.
Toluene	A colorless liquid with a strong chemical odor; a component of many solvents, paints, and coatings; also commonly found in industrial processes.

For processing purposes, the dataset is organized into ten batches, each class and the number of measurements per month. This reorganization of the data is to ensure that there is an adequate and as evenly distributed number of experiments in each batch as possible. The data batches and corresponding months are shown in Table 2:

Table 2. Data batches and corresponding months

Batch ID	Month IDs
Batch 1	Months 1 and 2
Batch 2	Months 3, 4, 8, 9 and 10
Batch 3	Months 11, 12, and 13
Batch 4	Months 14 and 15
Batch 5	Month 16
Batch 6	Months 17, 18, 19, and 20

The data format uses the same encoding style as the libsvm format x:v, where x represents the feature number and v represents the actual value of the feature. For example:
1; 10.000000 1:15596.162100 2:1.868245 3:2.371604 4:2.803678 5:7.512213.....
The number 1 indicates the class number (in this case, ethanol), the gas concentration level is 10 PPMV, and the remaining 128 columns list the actual characteristic values for each measurement record organized as described above.

2.2 Data analysis

Read 10 data sets in turn, then convert the data features from sparse matrix to dense matrix and store them as Data Frame, convert the data labels into Series objects, access the feature list and label list in turn, and then combine the data of the feature list and label list together. The first column of the first row, 15596.1621, represents the first gas concentration data measured by the first feature, which is 15596.1621. The relevant information of the data set is shown in Figure 1.

	0	1	2	...	125	126	127
0	15596.1621	1.868245	2.371604	...	-0.545079	-0.902241	-2.654529
1	26402.0704	2.532401	5.411209	...	-0.889333	-1.323505	-1.749225
2	42103.5820	3.454189	8.198175	...	-1.334558	-1.993659	-2.348370
3	42825.9883	3.451192	12.113940	...	-1.432205	-2.146158	-2.488957
4	58151.1757	4.194839	11.455096	...	-1.930107	-2.931265	-4.088756

Figure 1. Data set related infographic

The gas classification label is added to the back of the feature data set, and the average value of each feature of the data is calculated. The histogram shows the distribution of the data, which is divided into 30 boxes. It can be seen that the average value of the data set is more concentrated in the first box. Data set indicators are unbalanced. The histogram of feature mean value is shown in Figure 2.

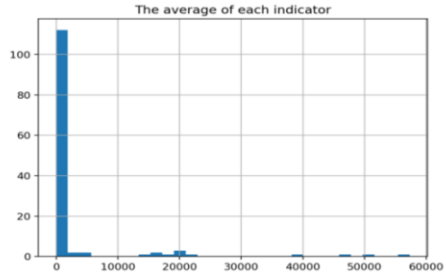

Figure 2. Feature mean histogram

Then let's analyze the average value of features of different indicators. As shown in the bar chart, it can be seen that some feature values are divided into large, and some feature values are very small and unbalanced, requiring normalization and dimensionality reduction. The bar chart of average values of different indicators is shown in Figure 3.

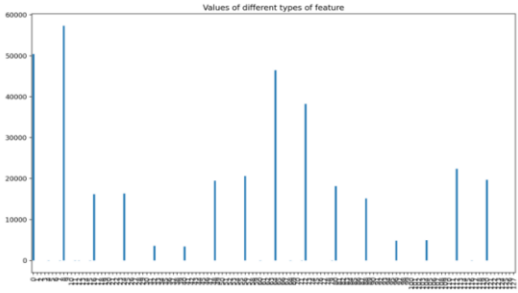

Figure 3. Bar chart of average values of different indicators

Analyze the sample number of 6 kinds of gases, add the digital label, and display it with the bar chart, you can see that the first gas has 3009 samples, the second gas has 2926 samples, and so on, each gas has a certain number of samples, relatively average, but not completely average. The column diagram for sample quantity analysis of 6 kinds of gases is shown in Figure 4.

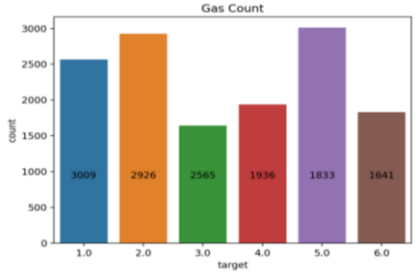

Figure 4. Gas sample number analysis column chart

The amount of data of different gases in each month is calculated, and then analyzed with a bar chart. It can be seen that around 21 months, there are more data, and the fourth gas, acetaldehyde, has the most data, and the monthly gas distribution has a large difference. The bar chart of the variation of different gas quantities over months is shown in Figure 5.

Figure 5. Bar chart of the variation of different gas quantities over months

2.3 Data preprocessing

Normalization: To preprocess the data set and normalize the feature data, we first create a MinMaxScaler object, then use the fit_transform method to scale the data to between 0 and 1, and convert the original value X to the scaled value X_scaled by the following formula:

X_scaled = (X - X.min(axis=0)) / (X.max(axis=0) - X.min(axis=0))

Where, X is the data set to be processed, and axis=0 indicates that operations are performed on each column, so the minimum and maximum values of each column are used in calculation. In this way, not only the distribution form of data can be preserved, but also outliers can be processed and differences between different features can be eliminated.[5].

Dimensionality reduction: Using PCA algorithm to reduce the dimensionality of data to 3 principal components, PCA can map the original high-dimensional data to a new low-dimensional space through linear transformation, and try to retain most of the variance in the original data. Since odor drift data has many features, PCA can effectively reduce the dimensions and remove redundant information, thus reducing the complexity of storage and calculation[6].

PCA(n_components=3).fit(X) library function is used to reduce the dimensionality of the data. PCA measures the correlation between features by calculating the covariance matrix of the original data. The eigenvalues of covariance matrix are decomposed to obtain the eigenvalues and corresponding eigenvectors. The feature vectors are sorted according to the size of the feature values to find the most informative feature, and the number of principal components to retain (here, 3 principal components are retained) or the percentage of the population variance is selected according to the requirements. A transformation matrix of selected principal components is used to map the original data set to the new space after dimensionality reduction[7].

Label: Add labels according to the classification, and finally store the pre-processed data into the table dataset_pca.csv, which is convenient for classification prediction through machine learning.

3. Data modeling and prediction

3.1 Correlation index

To avoid affecting the data observation, set the random seed value to 10 to ensure that the results can be reproduced. Read the data from the table dataset_pca.csv that you just stored, remove the classification labels, extract the labels, and then divide the training set and the test set. Finally, the evaluation index is set as accuracy, the fold number of cross-validation is set to 10, and the data is initialized based on stratified sampling cross-validation.

3.2 KNN model

The KNN(K-nearest neighbor) model is established. Specifying the number of KNN neighbors to be 1, which is sensitive and can more accurately adapt to small or irregular features in the data set. In the KNN algorithm, for a given new sample, it will

find the nearest K neighbors and make prediction or classification based on the labels of these neighbors [8]. KNN model makes classification prediction, calculates accuracy and generates classification report. You can see that the accuracy of the prediction is 94.16%.The relevant Precision, Recall, F1 value and Support are shown in Table 3.

Table 3. KNN model performance

No.	Precision	Recall	F1-score	Support
1	0.94	0.96	0.95	653
2	0.98	0.98	0.98	733
3	0.98	0.98	0.98	401
4	0.89	0.87	0.88	504
5	0.97	0.95	0.96	741
6	0.86	0.89	0.87	446

3.3 Decision tree model

A decision tree model (DecisionTreeClassifier) was established. To prevent overfitting, specify a depth of 3 for the tree. In the decision tree algorithm, a tree-like structure composed of nodes and directed edges was constructed, in which each internal node represented the judgment condition of a feature or attribute, and each leaf node represented a category label or predicted value [9]. The decision tree model makes classification prediction, calculates accuracy and generates classification report. You can see that the accuracy of the prediction is 91.15%.The relevant Precision, Recall, F1 value and Support are shown in Table 4.

Table 4. Decision tree model performance

No.	Precision	Recall	F1-score	Support
1	0.91	0.94	0.92	653
2	0.96	0.95	0.96	733
3	0.97	0.97	0.97	401
4	0.85	0.82	0.84	504
5	0.95	0.94	0.94	741
6	0.82	0.83	0.83	446

3.4 Random forest model

The Random Forest Classifier model is established. Set the number of decision trees to 100 to ease overfitting and improve the accuracy of the model. In the random forest classifier, the classification performance and generalization ability are improved by constructing multiple decision trees at the same time and synthesizing their prediction results [10]. The random forest classifier model is used to predict the classification, calculate the accuracy and generate the classification report. You can see that the accuracy of the prediction is 94.77%. The relevant Precision, Recall, F1 value and Support are shown in Table 5.

Table 5. Random forest performance

No.	Precision	Recall	F1-score	Support
1	0.95	0.95	0.95	653
2	0.98	0.97	0.98	733
3	0.98	0.98	0.98	401
4	0.91	0.91	0.91	504

5	0.96	0.96	0.96	741
6	0.88	0.89	0.89	446

3.5 Multi-layer perceptron model

In the multi-layer perceptron (MLP) model, the number of hidden layer neurons is set to 100, the activation function is set to ReLU, and the optimization algorithm is set to Adam. In the multi-layer perceptron, the classification problem is solved by constructing a forward propagation neural network with multiple hidden layers. Each hidden layer is composed of multiple neurons, each of which uses weighting and activation operations to make a nonlinear transformation of the input data. Through forward propagation, the input data is passed layer by layer to the output layer, and finally the prediction result or classification label is obtained. The multi-layer perceptron model makes classification prediction, calculates accuracy and generates classification report. You can see that the accuracy of the prediction is 80.04%.The relevant Precision, Recall, F1 value and Support are shown in Table 6:

Table 6. Multi-layer perceptron performance

No.	Precision	Recall	F1-score	Support
1	0.81	0.75	0.78	653
2	0.87	0.89	0.88	733
3	0.98	0.96	0.97	401
4	0.65	0.68	0.66	504
5	0.88	0.87	0.87	741
6	058	0.61	0.60	446

4. Test and analysis

Through testing, the odor drift data set was analyzed to master the 6 gas categories of the data set and the distribution of sample number. It is found that the number of data sets is large, the sample distribution is relatively average, there is a certain correlation between some features, the quantity changes of each gas are similar, and the monthly distribution of characteristic data is relatively regular. However, the numerical difference between different data features is too large, and there are some outliers in the data set, so normalization and dimensionality reduction are needed.

The data is normalized, the value range is mapped to between 0 and 1, and then the principal components are reduced to 3 by PCA dimensionality reduction, eliminating the differences between different features and preprocessing for better classification prediction.

Through KNN model, decision tree model, random forest classifier model and MLP multi-layer perceptron model, the model performance was evaluated by cross-validation of data sets, and the model was trained by training sets. The accuracy of prediction was shown in Table 7.

Table 7. Comparison of accuracy of several models

No.	Model name	Accuracy rate (%)
1	KNN	94.16
2	Decision tree	91.15
3	Random forest	94.77
4	MLP multi-layer perceptron	80.04

Through the analysis of test results in Table 7, it is found that the prediction accuracy of random forest model is the highest, reaching about 95%, which also indicates that the preprocessing process of odor drift data has the best effect. The advantage of random forest is to make predictions by integrating multiple decision trees, each of which is trained on different random subsamples and takes into account different features, which enables the model to make full use of the information of the data, reduce overfitting problems, handle large-scale and high-dimensional data, and be insensitive to missing values and outliers[11]. In the future, the parameters and algorithms of random forest will be further studied to make it more suitable for gas drift data sets.

5. Conclusions

In this paper, relevant machine learning classification algorithms for odor drift data are studied. First, the relevant contents of the data set are understood, such as sample quantity, type, characteristic indicators, etc., and the data distribution rule, coherence, outlier noise points and other information of the data set are mastered. The normalization and dimensionality reduction of the data are preprocessed, the training set and the test set are divided, and the KNN model, decision tree model, random forest classifier model and MLP multi-layer perceptron model are used to conduct relevant classification tests on the data set. The results show that the random forest model has a relatively good performance for odor drift data classification. This paper can further study and compare more reasonable algorithms to achieve more accurate classification prediction.

References

[1] R. Zhuo, Y. Guo and B. Guo, A Hyperspectral Image Classification Method Based on 2-D Compact Variational Mode Decomposition. *IEEE Geoscience and Remote Sensing Letters*, 2023, 20(19):1-5.
[2] Shah, S.-C. Design of a Machine Learning-Based Intelligent Middleware Platform for a Heterogeneous Private Edge Cloud System. *Sensors*, 2021, 21(20):7701.
[3] Luo Yu Gas sensor drift compensation based on deep belief networks [D]. *Chongqing University*, 2017.
[4] Ziyatdinov A, Marco S, Chaudry A, et al. Drift compensation of gas sensor array data by common principal component analysis[J]. *Sensors & Actuators: B. Chemical*, 2011,146(2):460-465.
[5] Yang Hanyu, Zhao Xiaoyong, Wang Lei Overview of Data Normalization Methods [J]. *Computer Engineering and Applications*, 2023,59 (03): 13-22.
[6] Guo Husheng, LIU Yanjie, WANG Wenjian. Concept drift processing of streaming Data based on Mixed Feature Extraction [J]. *Computer Research and Development,2023,8(7)*:12-19.
[7] Luo Jun Research on Image Recognition Algorithms Based on PCA and LDA [D]. *Huazhong University of Science and Technology*, 2020.
[8] Chemicals and Chemistry - Chemical Sensors; Research from University of Brescia Has Provided New Data on Chemical Sensors (k-NN and k-NN-ANN Combined Classifier to Assess MOX Gas Sensors Performances Affected by Drift Caused by Early Life Aging)[J]. *Chemicals & Chemistry*, 2020, 12(11):1-7.
[9] Ge Peng, Peng Mengjing Application and Optimization of Decision Tree Algorithm in Classification Prediction [J]. *Journal of Shandong Agricultural University* (*Natural Science Edition*), 2016,47 (06): 936-939.
[10] Research on Cost-sensitive random forest classification algorithm for High dimensional unbalanced data [D]. *Xidian University*, 2020.
[11] Xu Shaocheng. Research on High-dimensional unbalanced data classification based on Random forest [D]. *Taiyuan University of Technology*, 2018.

Fuzzy Systems and Data Mining IX
A.J. Tallón-Ballesteros and R. Beltrán-Barba (Eds.)

doi:10.3233/FAIA231046

The Impact of Sarcasm Contained in Online Media Disinformation Headlines on Enterprise Value: A Study of a Leading Internet Company

Ting WU[a], Guang YU[a, 1], Qiushi WANG[b], Chang LIU[b] and Qiuping CHEN[c]
[a] *School of Management, Harbin Institute of Technology, P.R.China*
[b] *School of Mathematics, Harbin Institute of Technology, P.R.China*
[c] *Zhiwei Research Institute, Beijing, P.R.China*

Abstract. Disinformation in online media has the profound impact on enterprise value. And faced with massive online information, online readers usually only browse through headlines. Therefore, even few negative words including sarcasm within headlines can still impact companies. Given the increasing importance of headlines in online media, it is crucial to examine sarcasm contained in disinformation headlines impact on enterprise value. However, that has received comparatively less attention in the existing literature. Therefore, the primary aim of this article is to address this gap by examining the impact of sarcasm contained in online media disinformation headlines on enterprise value. This article takes a leading Internet company as an example, and combines enterprise value related theory, machine learning, deep learning, pre-training model to mine sarcasm contained in disinformation headlines. Moreover, it uses regression analysis methods to study whether sarcasm contained in online media disinformation headlines will have an impact on the closing price, and further study whether it will exert enterprise value. The results indicate that sarcasm contained in disinformation headlines has a significant impact on enterprise value. This study enriches the relevant research on the impact of sarcasm contained in disinformation headlines on enterprise value, and provides support for companies to reduce enterprise value losses caused by online disinformation.

Keywords. Disinformation, Enterprise value, Sarcasm, Pre-training model

1. Introduction

As an important type of information pollution, fake news in online media has had serious impacts on national security, social stability, business management and other aspects [1-5]. Bodies of research mainly focus on the fake news influence on political system and democratic order [4, 6-11], and some studies pay attention to the field of health care [12]. It's also important to recognize the impact of fake news in online media on companies' overall well-being. In recent years, researchers have gradually focused on the impact of

[1] Corresponding author, Guang YU, School of Management, Harbin Institute of Technology, 92 Xidazhi Street, Nangang District, Harbin, P.R.China; E-mail: yug@hit.edu.cn
This research was funded by the National Natural Science Foundation of China, Grant No. 72074060.

fake news on companies. Some researchers are interesting in the impact of fake news on companies' brand image and employees, and pay attention to companies' solutions to fake news[13-15]. But there are few studies which paid attention to its impact on enterprise value. Wu YAN et al. take the clarification reports of Listed Companies in Shanghai and Shenzhen stock markets in 2000-2009 as samples. They find that the release and dissemination of fraudulent information affects the stock volatility, and there is an obvious information manipulation phenomenon [16]. Chih-chien WANG et al. conduct a study on a Taiwanese company and find that its uses false news to affect its stock price and trade volume [17]. In these above enterprise value studies, information is released by companies themselves.

It should be noted that people usually get useful or interesting information through headlines and tweets (we collectively call them headlines) efficiently. Benjamin D. Horne et al. show that the use of specific nouns in headlines is of great significance for the public to distinguish true information from fake news [18]. Sarcasm also attracts people's attention and affects people's judgment. Maynard D et al. study the effect that sarcasm has on sentiment in tweets, and carry out a number of rules to improve the accuracy of sentiment analysis [19]. Therefore, even few negative words including sarcasm within headlines can still impact companies. Given the increasing importance of headlines in online media, it is crucial to examine their impact on enterprise value.

However, as highlighted by previous studies, it is noteworthy that the impact of sarcasm within fake news headlines in online media on enterprise value has received comparatively less attention in the existing literature. In addition, although there is a wealth of research on fake news, it cannot fully describe the complex and changeable phenomenon of information pollution. A concept of information disorder is proposed to describe information pollution, and three different types of information disorder are defined, namely mis-, dis-, and mal-information. Claire Wardle et al. describe the differences between three types by using dimensions of harm and falseness [20]. The details are shown in Table 1. This study is interesting in disinformation which is false and intended to be harmful to the target.

Table 1. Three types of information disorder

	Falseness?	Harm?
Dis-information	Yes	Yes
Mis-information	Yes	No
Mal-information	No	Yes

Therefore, the primary aim of this study is to address this gap by examining the impact of sarcasm contained in online media disinformation headlines on enterprise value. This study takes a leading Internet company in China as an example. The data comes from Zhiwei Research Institute [21] and China Stock Market & Accounting Research Database [22], respectively. We collect data from January 2018 to October 2021. And we classify sarcasm contained in disinformation headlines by machine learning, deep learning and pre-training algorithms. Further, we use statistical methods, to study the impact of sarcasm contained in disinformation headlines on enterprise value.

Firstly, we use python data processing module and natural language processing technology for disinformation headlines preprocessing and word vectorization.

Secondly, we classify sarcasm contained in disinformation headlines. Sarcasm is considered as an implicit form of sentiment, and conveys the opposite of the intended meaning [23]. We label headlines as sarcasm when they do not express attitudes and

sentiments directly. We select a training dataset of disinformation headlines, and label headlines that do not directly express attitudes and emotions as sarcasm. Then machine learning, deep learning and pre-training algorithms are used to train model. The best performing algorithm is selected for classification model. And it is used to classify unlabeled headlines.

Finally, this paper adopts regression model to analyze the impact of sarcasm contained in disinformation headlines on enterprise value. This paper defines dependent variable as company stock closing price. According to the study of YAN Wu et al. [16], and volume-price relationship, control variables are defined as Hong Kong base interest rate, Hong Kong's Hang Seng Index, and trading volume. Independent variable is defined as whether sarcasm contained in disinformation headlines. Then we establish regression models of the impact of sarcasm contained in disinformation headlines on company stock closing price.

The structure of this paper is as follows: the second part describes the study methods and analyzes the experimental results, including data collection and preprocessing, classification of sarcasm in disinformation headlines, as well as sarcasm impact analysis. The third part analyzes the result. Finally, we conclude and discuss this study.

2. Methodology

Enterprise value consists of two parts: equity capital value and debt value. When the capital structure of a company remains unchanged, the greater overall enterprise value, the greater equity capital value, and the higher stock value. Stock value determines stock price, so enterprise value determines stock price, namely market value. While for debt value, when risk is small, the fluctuation of market price is very small. Stock price of a company reflects enterprise value to a certain extent[24-26]. In this study, closing price is used to replace stock value, and is taken as dependent variable to measure enterprise value.

On the other hand, sarcasm is defined as a more aggressive type of irony. It usually expresses dissatisfaction, criticism, or opposition through mock and ridicule. Aggressive tone, expression, and intention make it a suitable irony type to conceal negative information. [27] So we take sarcasm contained in disinformation headlines as independent variable. In addition, according to volume-price relationship, local base interest rate, Hong Kong's Hang Seng Index and trading volume are taken as control variables because they all affect stock closing price [16].

2.1. Data collection and preprocessing

2.1.1. Data collection

This paper collects the leading Internet company disinformation headlines in online media from Zhiwei Research Institute [21]. Zhiwei Research Institute is an intelligence big data company, and provides leading companies with multi-level services including intelligence perception, intelligence analysis and intelligence think tank. There are two elements in judging whether it is disinformation [20]. One is whether the author intends to cause harm to a company, and the other is whether the information is false. We collect disinformation headlines in five most representative online media platforms (including Network Media, Headline, Weibo, WeChat and Self-media) from January 2018 to

October 2021. And data dimension includes disinformation headlines, release time, release platform, full-text link, relevant information of posters, etc. Firstly, all the company relevant reports headlines on five online media platforms are obtained through keyword search. Secondly, we preliminarily screen company negative reports dataset based on account background check, account historical posting pattern, and expert judgment. This dataset contains all information intended to cause harm to the company. Finally, we judge the information as falseness by two standards. One is that the company issues a response and provides corresponding evidence to prove that the information is wrong. The second is that the company doesn't respond, but in the public information, there is no factual basis to support the information.

Then we get dependent variable and control variables from CSMAR database [22]. CSMAR Database is an economic and financial database combining with the actual situation of China. It comes from the needs of academic research, drawing on the professional standards of CRSP and databases of the University of Chicago. The database covers the fields of economy, listed companies, stocks, Hong Kong stocks and so on, which provides a great help for the research of colleges and universities. The heading Internet company is listed on the Hong Kong Stock Exchange. We collect dependent variable and control variables from CSMAR database from CSMAR Database. Data dimensions include closing price, opening price, trade volume, stock yield, closing price and opening price of Hang Seng Index, etc. Finally, the Hong Kong local interest rate from 2018 to 2021 is obtained from Hong Kong Monetary Authority[28].

2.1.2. Data preprocessing

Natural language processing technology is used for disinformation headlines extraction, preprocessing and word segmentation. First of all, we use pandas tool set (https://pandas.pydata.org/) to extract the company disinformation headlines and release time, and extract the company stock closing price, trade volume and closing price of Hang Seng Index, and store them together with the Hong Kong local interest rate.

Secondly, there are missing, abnormal and noise data in the disinformation headlines. This paper uses pandas tool set to clean them. Specifically, we fill in missing data, replace abnormal data with average value, and delete the noise data. There are 8713 disinformation headlines available after cleaning.

Finally, Jieba Word Segmentation Library (https://pypi.org/project/jieba/) of GitHub opensource community is used for disinformation headlines word segmentation. Jieba Word Segmentation Library is a third-party library of Chinese word segmentation with outstanding performance. It uses Chinese word segmentation to determine the probability of association between Chinese characters to generate the word segmentation results. This article uses Jieba Word Segmentation Library to generate headlines word segmentation results, and after removing stop words, the disinformation headlines dictionary is formed.

2.2. Sarcasm classification models

2.2.1. Dictionary construction based on word2vec

Before classification, we need to vectorize disinformation headlines. This study uses Word2vec word vector model released by Google in 2013. Word2Vec learns semantic knowledge in an unsupervised manner from a large number of text corpora. Because it

has achieved good results [29-31], it is widely used in natural language processing (NLP). Among them, CBOW model uses the context word to predict the head word to obtain word vector, which can accurately obtain the semantic relationship between words and words [29, 30]. This study uses CBOW model to vectorize disinformation headlines.

2.2.2. Sarcasm classification algorithms

In this paper, disinformation headlines attitudes are divided into three categories: sarcasm, direct smear, and others. According to the definition of sarcasm, we label disinformation headlines as sarcasm which contain mock, ridicule and strong emotions. And we label disinformation headlines as direct smear which contain straightforward blackening and strong emotions. And the remaining headlines are labeled as others. This paper uses machine learning, deep learning and pre-training model, namely Decision tree [32], Random forest [33], K-Nearest Neighbor (KNN) [34], Long Short-Term Memory (LSTM) [35], and Chinese-roberta-wwm-ext [36] to conduct disinformation headlines attitude analysis. This paper compares these five algorithms and selects the best for classification prediction.

Decision tree is a tree structure, in which an internal node represents a judgment on attribute, a branch represents a judgment result, and a leaf node represents a classification result. It is established according to minimizing loss function, and usually includes three steps, namely feature selection, decision tree generation and pruning [32]. Decision tree is easy to interpret and can achieve intuitive visualization, but is prone to overfitting.

Random forest can be seen as a set of decision trees, and it largely solves the overfitting problem. It uses a decision tree as a learner and introduces random attribute selection during the training of a decision tree. Each decision tree in the Random forest is judged separately, and then final classification result is selected by voting [33]. Random forest has good generalization performance and high accuracy, and is less prone to overfitting due to the introduction of randomness.

KNN is a special machine learning algorithm with supervised learning. It achieves classification by measuring the distance between different eigenvalues. The core idea of this method is that if most of the k nearest samples in the feature space belong to a certain category, then the sample also belongs to this category [34]. KNN is easy to understand, and is simpler than other algorithms because of not requiring parameter estimation and training. But its time complexity and spatial complexity are higher than others.

LSTM is a popular deep learning algorithm. It is a structural variant of Recurrent Neural Network (RNN), which can well solve the long-term dependence problem. Similar to RNN, LSTM is also a chain recurrent network structure. The difference is that there is only one network layer in the standard RNN network unit, and the LSTM has four network layers. The core of LSTM is the cell state which is controlled by input gate, forget gate and output gate. Among them, the most important is forget gate, which determines which previous memories will be retained or removed, so the LSTM has the function of long-term memory [35].

Due to the presence of forget gate in LSTM, it still cannot effectively handle the matter of long-distance semantic dependence. Transformer based on self-attention structure [37] can effectively solve the above problem. It is one of the best performing structures in natural language processing (NLP). In recent years, pre-training models based on transformer, such as Bidirectional Encoder Representations from Transformers (BERT) [38], a robustly optimized BERT pretraining approach (RoBERTa) [39], have achieved the best performance in NLP. Meanwhile, Chinese pre-training model performs

better in Chinese NLP tasks than Chinese model of BERT, as it can better reflect the semantic connections of Chinese. This study chooses a representative Chinese pre-training model, namely the whole-word mask RoBERTa-wwm-ext, which proposed by the Joint Laboratory of HIT and iFLYTEK Research (HFL) in 2019 [36]. Its performance is significantly better than that of Chinese model of BERT. This model is based on Google's WWM technology, Facebook's RoBERTa pre-training model, and uses HIT Language Technology Platform (LTP) as a word segmentation tool.

2.2.3. Sarcasm classification performance

Firstly, in order to ensure data balance, a hierarchical sampling method is used to construct the training dataset. Among them, sarcasm, direct smear and other types is 1: 1: 1. There are 1274 data after sampling. Secondly, we use 10-folds cross validation to evaluate Decision tree, Random forest and KNN classification accuracy. For LSTM and pre-training model, training set and development set are divided according to the ratio of 7:3. This section evaluates the classification performance four classification algorithms except pre-training model in four words vector length (namely, 50, 100, 150 and 200 dimensions). For pre-training model, we use its built-in word vectorization function to generate word vectors. The classification accuracies are shown in Table 2.

As we can see, the classification accuracy of Chinese-roberta-wwm-ext is the highest, which is 75.64%. Therefore, this article will use Chinese-roberta-wwm-ext to classify unlabeled sarcasm in disinformation headlines.

Table 2. Classification accuracies of sarcasm in disinformation headlines

word vector length	50	100	150	200
Decision tree	62.06%	65.67%	64.18%	66.22%
Random forest	69.05%	70.15%	69.91%	68.50%
KNN	71.78%	71.09%	71.88%	70.22%
LSTM	72.61%	73.64%	72.09%	74.16%
sentence vector length	768			
Chinese-roberta-wwm-ext	75.64%			

2.3. Sarcasm impact analysis

Next, a linear regression model is used to analyze the impact of sarcasm contained in disinformation headlines on company stock closing price. As mentioned above, dependent variable is company stock closing price, control variables are Hong Kong base interest rate, Hong Kong's Hang Seng Index, and trading volume, and independent variable is that whether sarcasm contained in disinformation headlines. We establish a regression model as Eqs. (1):

$$CP = \alpha_1 HIS + \alpha_2 BIR + \alpha_3 Vol + \alpha_4 Sar \quad (1)$$

Among them, CP is company stock closing price, HIS is Hang Seng Index, BIR is base interest rate, Vol is trading volume, and Sar is that whether sarcasm contained in disinformation headlines.

3. Results

In this study, Model 1 investigates the impact of Hong Kong base interest rate and Hang Seng Index on the company stock closing price. On this basis, Model 2 and Model 3 respectively add trading volume and that whether sarcasm contained in disinformation headlines to Model 1. Finally, Model 4 considers the impact of all variables. The linear regression results are shown in Table 3.

It can be seen from Table 3 that the R^2 of four models are about 0.8, indicating that four models have a good fitting on the sample data, and the models have a good interpretation ability. Secondly, the coefficient of Hang Seng Index and Hong Kong base interest rate are significant at the level of 0.01. The coefficient of trading volume is also significant at the level of 0.01. But that whether sarcasm contained in disinformation headlines (Sar) is significant at the level of 0.1. In addition, the coefficient of Sar is positive, indicating that the more sarcasm, the greater the negative impact it will have on stock closing prices. That is, sarcasm has a greater impact on stock closing prices than direct smear.

Table 3. Linear regression results

	Model 1	Model 2	Model 3	Model 4
HSI	0.020863*** (26.45)	0.0210923*** (27.07)	0.0209015*** (26.51)	0.0211376*** (27.17)
BIR	-135.139*** (-60.72)	-136.5661*** (-61.75)	-135.3533*** (-60.77)	-136.8203*** (-61.82)
Vol	-	-5.03*** (-5.24)	-	-5.09*** (-5,31)
Sar	-	-	0.227413* (1.64)	0.2519367* (1.84)
R-squared	0.7998	0.8055	0.8004	0.8062
Adjusted R-squared	0.7994	0.8049	0.7997	0.8054
F-statistic	1873.81	1293.60	1252.33	973.50

Note: * indicates that the 0.1 level is significant; ** indicates that the 0.05 level is significant; *** indicates that the 0.01 level is significant; the value in parentheses is the estimated T statistic; '-' indicates that the corresponding explanatory variable is not included in the model.

4. Conclusion

This paper takes a leading Internet company in China as example. And examines the impact of sarcasm contained in online media disinformation headlines on enterprise value by adopting computer algorithms and using statistical methods. Firstly, we select the best performing algorithm from machine learning, deep learning, and pre-training models to classify sarcasm contained in disinformation headlines. Secondly, we use linear regression analysis to explore the impact of sarcasm on the company stock closing price.

After analysis, we find that compared to machine learning and deep learning algorithms, pre-training model performs better in sarcasm classification. At the same time, we also verify that compared to direct smear, sarcasm contained in disinformation headlines has a more significant negative impact on the company stock closing price.

Further analysis shows that sarcasm contained in online media disinformation headlines has a certain negative impact on enterprise value.

This study emphasizes the importance of negative words such as sarcasm in online media disinformation headlines in influencing factors of enterprise value and managing corporate public opinion, and enriches the theory of enterprise value. Practically, on the basis of paying attention to the impact of disinformation, companies should pay more attention to the significant impact of negative words such as sarcasm, and take timely and effective public relations measures minimize the impact of disinformation on enterprise value. Also, this study provides new methods such as pre-training model to mine potential influencing factors of enterprise value. And the data comes from specific company application scenarios, which enriches the experience of combining research with corporate practice.

Although the current research results are positive, this study still has limitations. This paper only considers a specific company. Future research can compare multiple companies in different industries, and carry out comparative analysis of the impact of sarcasm contained in disinformation on enterprise value. And this paper only focuses on disinformation headlines, follow-up research can take the full text of disinformation into consideration. In addition, sarcasm is a type of emotion, and it may remind us to pay attention to the potential impact of online readers other negative psychological changes on companies.

References

[1] Meel P, Vishwakarma DK. Fake news, rumor, information pollution in social media and web: A contemporary survey of state-of-the-arts, challenges and opportunities. Expert Systems with Applications 2020;153:112986.

[2] Lazer D, Baum MA, Benkler Y, Berinsky AJ, Greenhill KM, Menczer F, et al. The science of fake news. Science 2018;359(6380):1094-6.

[3] Kapantai E, Christopoulou A, Berberidis C, Peristeras V. A systematic literature review on disinformation: Toward a unified taxonomical framework. New Media & Society 2021;23(5):1301-26.

[4] Aimeur E, Amri S, Brassard G. Fake news, disinformation and misinformation in social media: a review. Social Network Analysis and Mining 2023;13(1).

[5] White A. Review essay: fake news, and online misinformation and disinformation Lie machines, by Philip N. Howard, New Haven and Oxford, Yale University Press, 2020, xviii+221 pp., 20 pound (hardback), ISBN 978-0-300-25020-6. Information Communication & Society 2022;25(11):1669-75.

[6] Bennett WL, Livingston S. The disinformation order: Disruptive communication and the decline of democratic institutions. Eur J Commun 2018;33(2):122-39.

[7] Bovet A, Makse HA. Influence of fake news in Twitter during the 2016 US presidential election. Nat Commun 2019;10:14.

[8] Murphy G, Loftus EF, Grady RH, Levine LJ, Greene CM. False Memories for Fake News During Ireland's Abortion Referendum. Psychol Sci 2019;30(10):1449-59.

[9] Vosoughi S, Roy D, Aral S. The spread of true and false news online. Science 2018;359(6380):1146.

[10] Samaras G. The Capitol Riots. Digital Media, Disinformation, and Democracy Under Attack. International Journal of Press-Politics 2023.

[11] Wang Y. Politics of Disinformation: The Influence of Fake News on the Public Sphere. Mass Communication and Society 2023.

[12] Iacobucci G. Vaccination: "fake news" on social media may be harming UK uptake, report warns. BMJ-British Medical Journal 2019;364:1.

[13] Lee LW, Hannah D, McCarthy IP. Do your employees think your slogan is "fake news?" A framework for understanding the impact of fake company slogans on employees. Journal of Product and Brand Management 2020;29(2):199-208.

[14] Martin-Herrera I, Micaletto Belda JP. Effects of disinformation on the brand image and the reaction

of three companies in the food sector to a communication crisis: Starbucks, Mercadona and Burger King. Obra Digital-Revista De Comunicacion 2021(20):49-66.
[15] Obada D-R, Dabija D-C. The Mediation Effects of Social Media Usage and Sharing Fake News about Companies. Behavioral Sciences 2022;12(10).
[16] Wu Y, Dong CY. Study of Stock Volatility Affected by Fraudulent Information:Evidence from Shanghai and Shenzhen Stock Exchanges. Contemporary Finance & Economics 2010.
[17] Wang CC, Chiang CY. Analyzing Online Fake Business News Communication and the Influence on Stock Price: A Real Case in Taiwan. Journal of Information Technology Applications & Management 2019;26.
[18] Horne BD, Adali S. This Just In: Fake News Packs a Lot in Title, Uses Simpler, Repetitive Content in Text Body, More Similar to Satire than Real News. 2017.
[19] Maynard DG, Greenwood MA. Who cares about sarcastic tweets? Investigating the impact of sarcasm on sentiment analysis. *Language Resources and Evaluation Conference (LREC).* 2014.
[20] Wardle C, Derakhshan H. Information disorder: Toward an interdisciplinary framework for research and policymaking. Council of Europe Strasbourg; 2017.
[21] ZhiweiData. Zhiwei Data Research Institute. 2012:www.research.zhiweidata.com.
[22] CSMAR. China Stock Market & Accounting Research Database. 2020:www.cn.gtadata.com.
[23] Sundararajan K, Palanisamy A. Multi-rule based ensemble feature selection model for sarcasm type detection in twitter. Computational intelligence and neuroscience 2020;2020.
[24] Feng Y, Lai K-h, Zhu Q. Legitimacy in operations: How sustainability certification announcements by Chinese listed enterprises influence their market value? International Journal of Production Economics 2020;224.
[25] Jonek-Kowalska I. How do turbulent sectoral conditions sector influence the value of coal mining enterprises? Perspectives from the Central-Eastern Europe coal mining industry. Resources Policy 2018;55:103-12.
[26] Zhang F, Fang H, Wang X. Impact of Carbon Prices on Corporate Value: The Case of China's Thermal Listed Enterprises. Sustainability 2018;10(9).
[27] Frenda S, Teresa Cignarella A, Basile V, Bosco C, Patti V, Rosso P. The unbearable hurtfulness of sarcasm. Expert Systems with Applications 2022;193.
[28] Hong Kong Monetary Authority. 2023:www.hkma.gov.hk.
[29] Mikolov T, Chen K, Corrado G, Dean J. Efficient Estimation of Word Representations in Vector Space. Computer Science 2013.
[30] Mikolov T, Sutskever I, Kai C, Corrado G, Dean J. Distributed Representations of Words and Phrases and their Compositionality. *arXiv.* 2013.
[31] Baroni M, Dinu G, Kruszewski G. Don't count, predict! A systematic comparison of context-counting vs. context-predicting semantic vectors. *52nd Annual Meeting of the Association-for-Computational-Linguistics (ACL).* Baltimore, MD; 2014:238-47.
[32] Safavian SR, Landgrebe D. A SURVEY OF DECISION TREE CLASSIFIER METHODOLOGY. Ieee Transactions on Systems Man and Cybernetics 1991;21(3):660-74.
[33] Breiman L. Random forests. Machine Learning 2001;45(1):5-32.
[34] Denoeux T. A K-NEAREST NEIGHBOR CLASSIFICATION RULE-BASED ON DEMPSTER-SHAFER THEORY. Ieee Transactions on Systems Man and Cybernetics 1995;25(5):804-13.
[35] Hochreiter S, Schmidhuber J. Long short-term memory. Neural Computation 1997;9(8):1735-80.
[36] Cui Y, Che W, Liu T, Qin B, Yang Z. Pre-Training With Whole Word Masking for Chinese BERT. Ieee-Acm Transactions on Audio Speech and Language Processing 2021;29:3504-14.
[37] Vaswani A, Shazeer N, Parmar N, Uszkoreit J, Jones L, Gomez AN, et al. Attention Is All You Need. *31st Annual Conference on Neural Information Processing Systems (NIPS).* 30. Long Beach, CA; 2017.
[38] Devlin J, Chang M-W, Lee K, Toutanova K, Assoc Computat L. BERT: Pre-training of Deep Bidirectional Transformers for Language Understanding. *Conference of the North-American-Chapter of the Association-for-Computational-Linguistics - Human Language Technologies (NAACL-HLT).* Minneapolis, MN; 2019:4171-86.
[39] Liu Y, Ott M, Goyal N, Du J, Joshi M, Chen D, et al. RoBERTa: A Robustly Optimized BERT Pretraining Approach. Information Systems Research 2019.

Fuzzy Systems and Data Mining IX
A.J. Tallón-Ballesteros and R. Beltrán-Barba (Eds.)

doi:10.3233/FAIA231047

RSFnet: A Relation Semantic Fusion-Based Entity Relation Extraction Method

Ruiran Ding [a], Ling Lu [a,1], Qiuyang Yan [a], Yuyan Wu [a] and Dezhi Zeng [a]
[a] *School of Computer Science and Engineering, Chongqing University of Technology, Chongging, China*

Abstract. In existing methods for entity-relation extraction, both entity-driven and relation-driven approaches commonly suffer from insufficient interaction between entities and relationships. Specifically, there is a lack of utilization of the semantic information inherent in relationships. This paper proposed a relation semantic fusion-based entity relation extraction method (RSFnet). Firstly, all possible subjects are extracted from the sentence, and a mapping mechanism is used to obtain corresponding potential relations. At the same time, we treated relations as prior knowledge and used attention mechanisms to obtain sentence representations with relation semantics. The subject information is used as prior features, and the subject features are obtained through a bi-directional long-short term memory (BiLSTM) network. The updated sentence representations and enhanced subject features are further utilized for object and relation extraction, ultimately outputting triplets. The performance of the proposed model was validated through experimental results on three datasets. Additionally, this paper adopts convolutional encoding, resulting in better inference performance than methods based on Bidirectional Encoder Representations from Transformers (BERT), indicating that our model can improve triplet extraction performance while maintaining inference speed.

Keywords. relation semantic, mapping mechanism, prior knowledge, convolutional encoding

1. Introduction

The task of entity relation extraction aims to extract entity and relation facts from given text, forming relation triplets in the form of (subject(s), relation (r), object(o)). The extracted triplets can serve as the fundamental units of a knowledge graph, providing an external knowledge base for downstream tasks such as automatic summarization generation and dialogue generation.

Early approaches to entity relation triplet extraction often employed a pipeline method [1], which consisted of two stages: first, identifying all entities in the sentence, and then performing relation classification for each entity pair. Due to the error propagation issue, where errors in the first stage cannot be corrected in the second stage, this method had limitations. As a result, subsequent research proposed joint learning meth-

[1] Corresponding Author: Ling Lu, Chongqing University of Technology, E-mail:ll@cqut.edu.cn

ods for entities and relations, including feature-based models [2] and neural network-based models [3]. Among them, neural network-based models achieved excellent results in joint learning by using learned representations instead of manually constructed feature representations, gradually becoming the mainstream approach. For example, Wei et al. [4] proposed a cascaded joint extraction model that first extracts subjects and then jointly extracts relations and objects. The method incorporates subject information into the object and relation extraction stage, improving the performance of triplet extraction through the interaction of two tasks and effectively addressing the issue of entity overlap. Joint extraction methods that guide entity extraction with relations have also received significant attention. For example, Wang et al. [5] proposed a multi-hop attention-based entity-relation joint extraction method. It first labels the head entity and outputs multiple related tail entities. Then, it takes the tail entity as the next hop's head entity for input and iteratively performs relation extraction until the final entity relations are outputted. This method fully utilizes the latent relations between entities and enhances the performance of complex multi-hop relation extraction. Dai et al. [6] added a relation label embedding mechanism to the entity extraction layer, integrating text with relation labels. They utilized the subject's position information to selectively match suitable entity relation using attention, thereby improving precision. Although joint extraction methods are widely used due to their better interpretability and good experimental performance, existing methods still have shortcomings in utilizing and interacting with information within triplets, especially in terms of semantic representation of relations and utilization of subject information.

In response to the issues of insufficient information utilization and semantic information loss in existing joint extraction models, this paper proposes an entity-relation extraction method that integrates relation semantics. The main points of this paper's approach are twofold.

Firstly, we believe that by guiding entity extraction with subjects and relations, we can effectively control the redundancy of object extraction. This is because relations in the text generally depend on entities, and the number of relations is usually not much greater than the number of entities. For example, in the sentence "Arhus Airport is located in Tirstrup, Denmark.", the entities include "Arhus Airport", "Tirstrup" and "Denmark" but there is only one relation "located in". Given the known subject "Arhus Airport", we can extract the object "Tirstrup" through the relation "located in" while the unrelated entity "Denmark" will not be extracted.

Secondly, we believe that relations in triplets also contain rich contextual semantics. Integrating the semantic information of relations is beneficial for accurately extracting entities, which has not been widely addressed in existing research. For example, in the sentence "Peter is eating apples while watching TV.", we heuristically assume that since the conditional probability $P(eating \mid apples)$ is much larger than $P(eating \mid TV)$, the posterior probability $P(apples \mid eating)$ is greater than $P(TV \mid eating)$. In other words, perceiving the relation "eating" is helpful for extracting the object "apples". This viewpoint is even more useful in the case of implicit relations. For example, in Figure 1, the triplet in Sentence 2 is (Biden, president_of, United States),where the subject "Biden" has two candidate objects, "China" and "United States". We believe that without the semantic understanding of the implicit relation "president_of", it would be nearly impossible to correctly extract the object "United States".

Figure 1. Example of triplets extracted in implicit relation extraction.

In conclusion, this paper proposes a entity-relation extraction method called RSFnet (Relation Semantic Fusion-based Network) that integrates relationship semantics. Firstly, a convolutional encoder is used to identify the subject, and a mapping mechanism is used to obtain a possible set of relationships. Then, semantic fusion of relationships and entity information enhancement are carried out to further identify the corresponding objects and obtain the final triplet. The main work of this article is as follows:

1.Proposed a triplet extraction framework that integrates relation semantics. By calculating the attention of each word and the global representation under different relations, the relation information is integrated into the sentence, enriching the relations between entities and enhancing the interaction between relations and entities, thereby improving entity extraction performance.

2.Proposed a method for enhancing subject information representation. By integrating subject information with relative positional information and leveraging a BiLSTM network for deeper feature extraction, the subject representation is updated to further identify the corresponding object.

3.Experiments conducted on two datasets, NYT10 and NYT11, achieved performance superior to the baseline. Experiments involving the swapping of subject and object extraction order demonstrate the robustness of the proposed method. Additionally, the use of convolutional encoding in this paper allows RSFnet to outperform the baseline method in terms of inference performance and results.

2. Related Work

2.1. Joint extraction framework

Early methods for entity relation extraction often employed a pipeline approach, which separated entity recognition and relation extraction into two independent tasks. This method ignored the mutual relation between entities and relations, becoming a bottleneck in performance improvement. Subsequently, feature-engineering-based joint extraction methods addressed the interaction issue, but heavily relied on NLP tools for feature acquisition, requiring significant human effort and domain knowledge while also having error propagation issues. Later, with the excellent feature learning capability of neural networks, neural network-based methods gradually found applications in joint extraction.

Miwa et al. [7] proposed a parameter-sharing-based joint extraction method, decomposing joint extraction into different subtasks, where BILSTM and feed-forward neural networks were used for each subtask, reducing the complexity of feature learning. However, entities and relations were still extracted separately. A cascaded binary tagging framework was proposed in reference [6], which effectively resolved the issue of entity overlap while incorporating subject information into the object and relation extraction stages, improving triplet extraction performance. However, this method simply added the

subject to the original text information, resulting in a single form of interaction between the two sub-tasks and the problem of relation redundancy. To address the issue of relation redundancy, Li et al. [8] introduced a mapping mechanism from entity types to predefined relations. This mechanism avoided the need to iterate through all relations when predicting overlapping relations, reducing a significant amount of meaningless computations. Zheng et al.[9] proposed a joint triplet extraction framework based on latent relations and global correspondence, which greatly alleviated the problems of redundant relation judgments, poor generalization of span-based extraction, and low efficiency of subject-object alignment. However, this framework still had limitations in terms of utilizing relation information and interaction between sub-tasks. Zhe et al. [10] proposed an end-to-end relation-first blank filling network. The model encoded prior knowledge of relations in templates and transformed relations into specific relation templates using the semantic information of relations. Finally, it extracted entity pairs through blank filling, effectively improving triplet performance. This approach provides inspiration for subsequent research.

Overall, neural network-based joint extraction methods have gained attention for effectively addressing issues such as error propagation, subtask interaction, and information redundancy. The approach presented in reference [10] used relations as prior knowledge to guide entity extraction, providing insights into subtask interaction. This inspired the method proposed in this paper to enhance text representation by leveraging relational semantic information and establish interaction between entities and relations, further improving triplet extraction performance.

2.2. Method of interaction between triplet relations and entity information

The interaction between entity pairs and between entities and relations is crucial in joint extraction methods. Zhang et al. [11] applied a local focusing mechanism to entity pairs and their corresponding contexts to obtain richer feature representations from local contexts, thereby completing the Relation Extraction (RE) task. Zheng et al. [12] used a weighted relative position attention mechanism to modify the vanilla Transformer encoder, which flexibly captured the semantic features between entities. Sun et al. [13] proposed a recurrent interaction network that allows explicit dynamic interaction between entity recognition and relation extraction tasks, capturing the mutual correlation between them.Yuan et al. [14] utilized an attention gate mechanism to obtain fine-grained semantic representations for specific relations, greatly improving the impact of relevant relation types on entity recognition. These studies demonstrate that better interaction between entity and relation information can be achieved through various approaches.

Inspired by these findings, the present study enhances the interaction between entity and relation information by utilizing attention mechanisms. By integrating subject information with relative positional information and applying further deep-level feature extraction through a BiLSTM network, the representation of the subject is updated. This updated representation is then fused with the sentence representation containing relation information and the subject feature representation. This fusion is used to guide entity extraction, thereby improving the performance of triplet extraction.

2.3. Convolutional Encoder

Currently, many models adopt Transformer-based pre-trained language model encoders, which has a powerful ability to capture long-distance dependencies and contextual semantic features. However, it also increases memory consumption, limiting model training and inference time. Convolutional neural networks have been found to effectively extract text features and explore associations between words. Yu et al. [15] proposed a method using dilated gated convolutional neural networks, which increased the mutual correlation between distant words. Compared to the BERT model, this model achieved optimal results while being lightweight and fast. Therefore, in reference [8], a convolutional encoding structure combining dilated convolution, gating units, and residual connections was designed to improve the computational efficiency of the encoder. Hence, this paper utilizes this convolutional structure as the encoder, not only reducing training and inference time but also ensuring performance requirements.

3. Methodology

The overall framework of RSFnet, as proposed in this paper, is depicted in Figure 2. It is a cascaded binary tagging framework that integrates relationship information. The framework consists of four components: an encoding layer, entity extractor A, information fusion layer, and entity extractor B.Entity extractors A and B are responsible for extracting two entities. For example, entity extractor A can be used to extract the subject, while entity extractor B can be used to extract the object. The reverse is also possible.The information fusion layer comprises two parts: the fusion of relationship semantics and the enhancement of entity features.The encoding layer encodes the input sentence and obtains sentence-level feature vectors using self-attention. Then, entity extractor A is employed to extract one entity, referred to as entity A, from the sentence.The relationship semantic fusion layer incorporates a mapping mechanism [8] to extract the relevant relationship set for entity A and calculates the semantic representation of all relationships. This representation is then fused into the sentence representation to update it. Finally, the updated sentence representation is combined with the enhanced entity features. Entity extractor B is utilized to further extract entity B, resulting in the output of a triple.

3.1. The Encoder Layer

The model takes a sentence $X = [x_1, x_2, ..., x_n]$ as input, where $x_i \in \mathbb{R}^d$ represents the word embedding of the i-th word. The embedding dimension is denoted as d, and n represents the number of words in the sentence. The word embeddings x_i are composed of GloVe word embeddings X_g and trainable position embeddings X_p. The encoder adopts a convolutional encoder proposed in reference [8]. The encoder consists of L stacked blocks $Block(\cdot)$, and each block contains two dilated convolutions with a dilation rate of d_i, a gating unit, and a residual connection. The dilated convolution is represented as $DilatedConv(\cdot)$. By passing the sentence through the encoding layer, the representation of the sentence $H = [w_1, w_2, ..., w_n]$ is obtained as follows:

$$\mathbf{H} = \text{Block}(\cdots(\text{Block}(\mathbf{X}))) \tag{1}$$

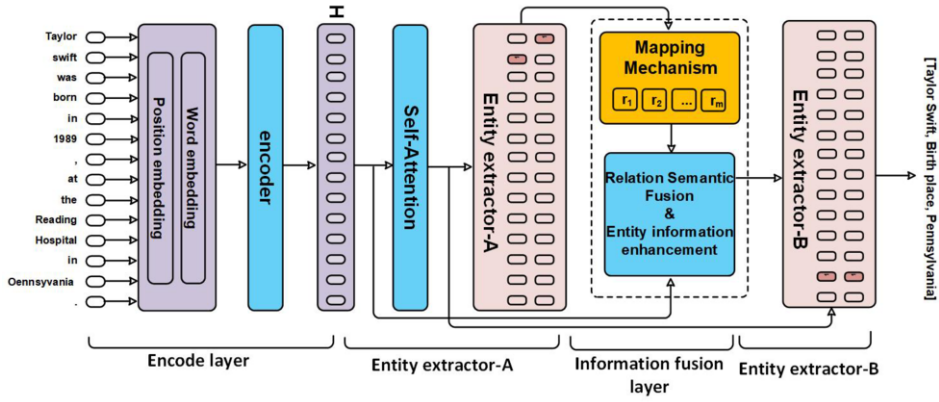

Figure 2. The overall structure of RSFnet.

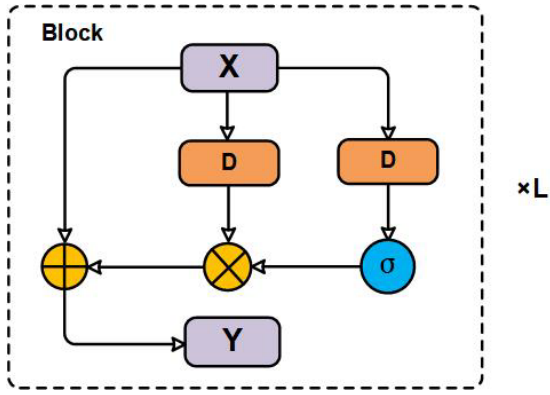

Figure 3. Structure of the Convolutional Encoder.

$$Y_a = DilatedConv_a(X) \tag{2}$$

$$Y_b = DilatedConv_b(X) \tag{3}$$

$$Y_i = Y_a \otimes sigmoid(Y_b) + X \tag{4}$$

Where $H \in \mathbb{R}^{n \times d}$, $w_i \in \mathbb{R}^d$ represent the encoded contextual representation of the i-th word, $\otimes$ denoted as element-wise multiplication. The output of the i-th stacked block and the input of the (i+1)-th stacked block are represented by Y_i, and the final representation of the sentence is denoted as Y_L, which is the output of the last stacked block. The overall structure of the convolutional encoder is depicted in Figure 3.

Since the convolutional encoder shares a significant number of parameters and treats each word x_i in the sentence equally, we introduce multi-head self-attention [16] to generate auxiliary entity features. The entity A feature representation H_h is given as follows:

$$\mathbf{H}_h = \text{softmax}(\frac{\mathbf{Q}\mathbf{K}^{\mathrm{T}}}{\sqrt{d_k}})\mathbf{V} \tag{5}$$

$$\mathbf{Q} = \mathbf{W}_q \cdot \mathbf{H} + b_q \tag{6}$$

$$\mathbf{K} = \mathbf{W}_k \cdot \mathbf{H} + \mathrm{b}_k \tag{7}$$

$$\mathbf{V} = \mathbf{W}_v \cdot \mathbf{H} + b_v \tag{8}$$

Where $d_k = d$ represents the dimension of the attention key vector. The weights and biases for the query, key, and value, denoted as $W_q, W_k, W_v \in \mathbb{R}^{d\times d}$ respectively, are used to obtain the values of $b_q, b_k, b_v \in \mathbb{R}^d$.

3.2. Entity Extractor A

To extract entity A using the entity extractor A, we concatenate the sentence representation H with the entity A feature, resulting in $[[w_1, w_1^h], ..., [w_n, w_n^h]]$. We have a set of relation types $T = \{t_1, t_2, ..., t_m\}$. We calculate the score of the i-th word being the start and end positions of an entity of type t_j as follows:

$$o_{ij}^{hs} = \mathbf{W}_{ij}^{hs} \cdot [\mathbf{w}_i, \mathbf{w}_i^h] + b_{ij}^{hs} \tag{9}$$

$$o_{ij}^{he} = \mathbf{W}_{ij}^{he} \cdot [\mathbf{w}_i, \mathbf{w}_i^h] + b_{ij}^{he} \tag{10}$$

Where o_{ij}^{hs} represents the score of the i-th word belonging to the entity A with respect to the starting position for type t_j. .

The threshold for entity boundaries can be different from the thresholds used for other words. An adaptive threshold strategy [17] is employed to improve the accuracy of entity labeling and enhance the model's generalization capability. Only when the score of an extractor exceeds its position-related threshold, the corresponding position is marked as 1. For all starting positions p_{ij}^s of entity A at position $i \in [1, n]$, we denote positive instances (positions expected to be marked as 1) as P_i and negative instances as N_i. An AT class is introduced to store all starting positions related to the AT type, where $P_{i;AT}$ represents the threshold at position i. During training, the loss for starting position labeling is defined as follows:

$$L_h^s = -\sum_{i=1}^{n} \sum_{p_{ij}^s \in N_i} \log(\frac{\exp(o_{ij})}{\sum_{p_{ik}^s \in P_i \cup \{p_{i;TH}\}} \exp(o_{ik})}) - \sum_{i=1}^{n} \log(\frac{\exp(o_{i;TH})}{\sum_{p_{ik}^s \in N_i \cup \{p_{i;TH}\}} \exp(o_{ik})}) \tag{11}$$

Where $o_{i;AT}$ represents the threshold for position i. Similarly, L_h^e denotes the threshold for marking the end position of the entity, and it follows the same loss function as L_h^s. The label loss for entity A, denoted as L_h, is the sum of the loss for the start position and the loss for the end position:

$$L_h = L_h^s + L_h^e \tag{12}$$

3.3. Information Fusion Layer

The information fusion layer is responsible for re-encoding the sentence representation and the subject information, aiming to further extract relationships and objects. It consists of two parts: relationship semantic fusion and entity feature enhancement.

Relation Semantic Fusion After identifying all possible entities A, in order to capture all entities B under the relationship $R = \{r_1, r_2, ..., r_j\}$, the relationship information is integrated into the sentence to enrich its information representation. The relationship information is obtained by leveraging GloVe embeddings [18] for the relationship R. Since each word in the sentence plays a different role in relation to different entities B, an attention mechanism is used to measure the attention scores for each relationship r_j with respect to the global representation h_g of the sentence and the representation of each word x_i. By taking the weighted sum of the sentence words based on the attention scores, a sentence representation under the relationship type j is generated as follows:

$$h_g = avg\{x_1, x_2, ..., x_n\} \tag{13}$$

$$e_{ij} = \mathbf{v^T} \tanh(\mathbf{W_r r}_j + \mathbf{W}_g \mathbf{h}_g + \mathbf{W}_x \mathbf{x}_i) \tag{14}$$

$$a_{ij} = \text{softmax}(e_{ij}) \tag{15}$$

$$c_j = \sum_{i=1}^{l} a_{ij} \mathrm{x}_i \tag{16}$$

Where n is the length of the sentence, h_g is the global representation of the sentence, e_{ij} represents the attention scores obtained using a multi-layer perceptron (MLP). It denotes the importance of each word and the global sentence representation for different relations. The MLP includes a hidden layer with a tanh activation function. r_j represents the relation embedding. a_{ij} is the weight coefficient calculated through softmax, and the specific sentence representation c_j is obtained through weighted averaging.

Entity Feature Enhancement In addition to incorporating relation embeddings,we further determine a potential set of relations R' based on the current entity type using a type-relation mapping mechanism. Finally, the sentence representation is updated by fusing the weighted connection of the sentence representation c_j with the original sentence representation w_i. The final representation of the i-th word is obtained by setting the entity embedding layer $V_t \in \mathbb{R}^{K \times d_t}$ and the relative position embedding layer $V_p \in \mathbb{R}^{n \times d}$. The start and end features W_a, W_b of entity A are obtained from H,the type features w^t of entity A are derived from V_t, and the relative position features w_a^p and w_b^p are derived from V_p, and then $(w_a + w_a^p), (w_b + w_b^p)$ and w^t are connected. BILSTM model is used to further extract features to form entity A features w^h:

$$w_i' = c_j + w_i \tag{17}$$

$$w^h = BILSTM(w^t; W_a + w_a^p; W_b + w_b^p) \tag{18}$$

Where w_i' represents the new sentence representation after weighted connection, and w^h represents the enhanced feature representation of the entity.

3.4. Entity Extractor B

Finally, to further extract entity B, the merging of entity A's feature information and the updated sentence information is performed to assist in more accurate identification of entity B.We concatenate the sentence representation H, the auxiliary feature H_t for entity B, and the entity A feature w^h to form $[[w_1', w_1^t, w^h, ..., [w_n', w_n^t, w^h]]$. Therefore, we compute scores for the i-th word as the starting and ending positions of entity B with potential relation $r_j \in R' \subset R$.

$$o_{ij}^{t_s} = W_{ij}^{t_s} \cdot [w_i', w_i^t, w^h] + b_{ij}^{t_s} \tag{19}$$

$$o_{ij}^{t_e} = W_{ij}^{t_e} \cdot [w_i', w_i^t, w^h] + b_{ij}^{t_e} \tag{20}$$

Where $o_{ij}^{t_s}$ represents the score of the i-th word as the starting position of entity B with relation r_j. Similar to the loss for entity A labeling, we directly calculate the loss value L_t for entity B labeling using Eq. (12). The final loss value is given by Eq.(21)

$$L = \frac{1}{|D|}\left(\sum_{S_i \in D} \sum_{h_j \in Z_i} L_{h_j} + \sum_{S_i \in D} \sum_{t_j \in Z_i} L_{t_j|h}\right) \tag{21}$$

Where D represents all the sentences, and Z_i represents all the relation triplets in sentence S_i.

4. Experiments

4.1. Datasets

The experiments in this paper were conducted on three datasets: NYT10[19], NYT11[19], and NYT24[20].The entity types [PER], [LOC], [ORG] and [OTH] were used to indicate four entity types and the relation mapping mechanism. We utilize the mapping mechanism to identify potential relations. NYT10 and NYT11 are versions generated by aligning the original data from the New York Times corpus with Freebase (a knowledge graph database). NYT10 is a smaller version, and its test set is manually annotated. NYT24 is created by filtering out sentences with more than 100 words and sentences containing non-positive class triples from the NYT dataset. Then, 5000 sentences were randomly selected as the test set, 5000 sentences as the validation set, and the remaining 56195 sentences as the training set. The composition is shown in Table 1.

Table 1. Statistics of NYT10, NYT11 and NYT24 datasets.

Dataset	#Relation	Train	Valid	Test
NYT10	29	70339	-	4006
NYT11	12	62648	-	369
NYT24	24	56196	5000	5000

Table 2. Experimental results of different methods on the NYT10, NYT11 and NYT24 datasets. † denotes results generated using the source code provided in the original paper, while other results are retrieved from the original paper.

Models	**NYT10**			**NYT11**			**NYT24**		
	Pre.	Rec.	F1	Pre.	Rec.	F1	Pre.	Rec.	F1
CasRel†[4]	78.0	69.0	73.2	50.3	58.1	53.9	89.9	89.1	89.5
TPLinker†[21]	80.1	66.4	72.6	**56.2**	55.1	55.7	91.0	91.8	91.4
PRGC†[9]	80.2	66.5	72.7	54.4	56.3	55.3	89.9	90.9	90.4
CopyRE[3]	45.2	56.9	50.4	34.7	53.4	42.1	61.0	56.6	58.7
WDec[22]	**84.6**	62.1	71.6	-	-	-	**94.5**	76.2	84.4
SPN†[23]	79.5	67.1	72.8	52.7	55.4	54.0	93.3	91.8	92.5
HRL[19]	71.4	58.6	64.4	53.8	53.8	53.8	-	-	-
GRTE†[24]	79.8	67.6	73.2	53.6	58.2	55.8	92.5	**92.7**	**92.6**
FastRE[8]	78.0	**70.1**	73.8	54.1	**58.7**	56.3	89.6	86.3	87.9
RSFnet(ours)	80.3	68.7	**74.1**	56.0	58.1	**57.0**	88.2	87.5	87.9

4.2. Settings

For the parameters used in the experiments of this paper, the convolutional encoder consists of 6 stacked blocks with convolution rates of 1, 2, 4, 1, 1 and 1. The training process utilizes the Adam optimizer with a learning rate of 1e-3 and a batch size of 32. All hyperparameters were adjusted on the validation set. The experiments were conducted on an NVIDIA GeForce RTX 3060 GPU. The effectiveness of the model is validated by calculating the precision (P), recall (R), and F1 score for extracting entity-relation triplets during the experiments.

In experiments 5.1, 5.2, and 5.3, we used extraction mechanism A to extract the subject and extraction mechanism B to extract the object. However, in experiment 5.4, we used extraction mechanism A and B to extract the object and subject, respectively, to validate the robustness of RSFnet.

5. Experimental Results and Analysis

5.1. Comparison with Existing Methods

We compared our model with state-of-the-art relation extraction models: (1) Using labeling methods to accomplish the triplet extraction task, such as CasRel[4], TPLinker[21], PRGC[9], FastRE[8]. (2) Transforming the relationship extraction task into a generation task based on generative models, such as CopyRE[3], WDec[22], SPN[23]. (3) Extracting triplets using reinforcement learning methods, such as HRL[19], GRTE[24].

Table 3. Statistics of NYT10, NYT11 and NYT24 datasets.

Models	P	R	F1
RSFnet	56.0	**58.1**	**57.0**
w/o Relational semantic fusion	55.4	58.1	56.7
w/o Entity feature enhancement	**56.2**	56.5	56.3

The comparative experimental results are presented in Table 2. It can be observed that RSFnet, proposed in this paper, achieves superior results compared to the baselines on the NTY10 and NYT11 datasets. For the NYT10 dataset, our method achieves an F1 score of 74.1%, which is a 0.3% improvement in F1 score over FastRE. On the NYT11 dataset, the F1 score for entity-relation triplet extraction is 57.0%, which is a 0.7% improvement compared to FastRE.On the NYT24 dataset, the proposed method achieves a comparable performance level to FastRE. The experiments demonstrate that the method presented in this paper has a positive impact on improving the overall performance of relation extraction.

5.2. Ablation Study

To evaluate the impact of the relation embedding and entity feature enhancement modules on performance, this paper conducted ablation experiments on the NYT11 dataset, and the results are shown in Table 3. “w/o Relational semantic fusion” indicates the removal of the relational semantic fusion module, while “w/o Entity feature enhancement” indicates the removal of the entity feature enhancement module.

From Table 3, it can be observed that both ablation experiments result in a performance decline on the NYT11 dataset. We believe that relation information contains rich semantic information, and when fused with the sentence, it can capture fine-grained semantic representations that are beneficial for subsequent object extraction. The absence of relational semantic fusion leads to a decrease in overall performance. When the entity feature module is removed, there is a decrease of 0.7 percentage points, indicating that enhancing the subject representation through the fusion of entity features and relative positional information using the BiLSTM network can effectively utilize the subject features to assist in object extraction, resulting in more accurate triplet extraction.

5.3. Performance Analysis

To evaluate the inference efficiency of RSFnet, a comparison was made with a model using the BERT encoder, and the results are shown in Table 4. In the table, ”Param” represents the number of model parameters obtained through the official implementation with default configurations. ”Train” and ”Infer” respectively indicate the total training time (in minutes) and the total inference time (in seconds).

As can be seen, RSFnet utilizes fewer parameters in the GloVe word embeddings. Its use of a convolutional encoder significantly reduces the computational pathways, resulting in shorter training and inference times compared to other models.

5.4. Study on Robustness

To further validate the stability of the RSFnet method, entity extractors A and B were used to extract subjects and objects (s→o), as well as objects and subjects (o→s). A

Table 4. Speed comparison experiments with other encoder models on the NYT10, NYT11 and NYT24 datasets.

Models	NYT10			NYT11			NYT24		
	Param	Train	Infer	Param	Train	Infer	Param	Train	Infer
CasRel	107,729K	251m	266s	107,698K	448m	24s	107,720K	420m	327s
TPLinker	109,606K	984m	191s	109,548K	973m	16s	109,603K	885m	235s
SPN	141,754K	516m	202s	104,648K	380m	19s	141,429K	473m	254s
PRGC	108,931K	290m	134s	108,891K	267m	12s	108,919K	272m	161s
GRTE	119,450K	890m	176s	119,450K	843m	17s	119,387K	795m	221s
Ours	8361K	203m	66s	8356K	178m	5.5s	8359K	164m	83s

Table 5. Robustness experiments to verify subject-first extraction and subject-first extraction on NYT10, NYT11 and NYT24 datasets.

Models	NYT10			NYT11			NYT24		
	P	R	F1	P	R	F1	P	R	F1
FastRE	78.0	70.1	73.8	54.1	58.7	56.3	89.6	86.3	87.9
(s→o)	80.3	68.7	**74.1**	56.0	58.1	**57.0**	88.2	**87.5**	87.9
(o→s)	**80.4**	68.6	74.0	**56.9**	57.0	56.6	88.6	87.1	87.9

comparative experiment was conducted against FastRE, and the results are shown in Table 5. It can be observed that RSFnet consistently maintains stable performance in both the (s→o) and (o→s) processes.

6. Conclusion

This paper addresses the limitations of existing methods for joint extraction of entity and relationship triplets, including insufficient interaction between entity extraction and relationship extraction stages and underutilization of semantic information about relationships. To tackle these issues, a novel joint extraction method called RSFnet is proposed. RSFnet first extracts all possible subjects and then employs a mapping mechanism to obtain a set of potential relationships. It utilizes an attention mechanism to capture the semantic information of relationships and combines it with enhanced subject features for the joint extraction of objects and relationships. This process yields the final triplets. Experimental results demonstrate that RSFnet achieves higher F1 scores compared to baseline methods on the NYT10 and NYT11 datasets. Furthermore, RSFnet exhibits superior inference time efficiency compared to BERT models.

References

[1] Dmitry Zelenko, Chinatsu Aone, and Anthony Richardella. 2003. Kernel methods for relation extraction. Journal of machine learning research,3(Feb):1083–1106.

[2] Xiang Ren, Zeqiu Wu, Wenqi He, Meng Qu, Clare R V oss, Heng Ji, Tarek F Abdelzaher, and Jiawei Han.2017. Cotype: Joint extraction of typed entities and relations with knowledge bases. In Proceedings of the 26th International Conference on World Wide Web, pages 1015–1024.

[3] Xiangrong Zeng, Daojian Zeng, Shizhu He, Kang Liu, and Jun Zhao. 2018. Extracting relational facts by an end-to-end neural model with copy mechanism.In Proceedings of the 56th Annual Meeting of the Association for Computational Linguistics (V olume 1: Long Papers), volume 1, pages 506–514.

[4] Zhe pei Wei, Jianlin Su, Yue Wang, and et al. A novel cascade binary tagging framework for relational triple extraction. In ACL, 2020.
[5] Wang H, Wu Y T. Joint extraction of entity relationships based on multi-hop attention and its application [J]. Proceedings of the Journal of Taiyuan University of Technology, 2022, 53(1):63-70.
[6] Dai Jianfeng, Chen Xingyu, Dong Ligang, et al. Joint Extraction Method of Triplets Combining Hybrid Embedding and Relation Label Embedding [J]. Telecommunications Science, 2023, 39(2): 132-144.
[7] Miwa M, Bansal M. End-to-end relation extraction using LSTMs on sequences and tree structures[C]//Proceedings of the 54th Annual Meeting of the Association for Computational Linguistics, Berlin, Aug 7-12, 2016. Stroudsburg: ACL, 2016: 1105-1116.
[8] Li, G., Chen, X., Wang, P., Xie, J., & Luo, Q. 2022. FastRE: Towards Fast Relation Extraction with Convolutional Encoder and Improved Cascade Binary Tagging Framework. ArXiv, abs/2205.02490.
[9] Hengyi Zheng, Rui Wen, Xi Chen, and et al. PRGC: Potential relation and global correspondence based joint relational triple extraction. In ACL, 2021.
[10] Zhe Li, Luoyi Fu, Xinbing Wang, Haisong Zhang, and Chenghu Zhou. 2022. RFBFN: A Relation-First Blank Filling Network for Joint Relational Triple Extraction. In Proceedings of the 60th Annual Meeting of the Association for Computational Linguistics: Student Research Workshop, pages 10–20, Dublin, Ireland. Association for Computational Linguistics.
[11] Zhang, H., Zhang, G. & Ma, R. Syntax-informed self-attention network for span-based joint entity and relation extraction. Appl.Sci. 11(4), 1480 (2021).
[12] Zheng, W., Wang, Z., Y ao, Q.&Li, X.Wrtre: Weighted relative position transformer for joint entity and relation extraction. Neurocomputing 459, 315–326 (2021).
[13] Sun K, Zhang R, Mensan S, et al. Recurrent interaction network for jointly extracting entities and classifying relations[C]//Proceedings of the 2020 Conference on Empirical Methods in Natural Language Processing, Nov 16-20, 2020. Stroudsburg: ACL, 2020: 3722-3732.
[14] Y . Yuan, X. Zhou, S. Pan, Q. Zhu, Z. Song, and L. Guo, "A relation-specific attention network for joint entity and relation extraction," in International Joint Conference on Artificial Intelligence 2020, pp. 4054–4060, Association for the Advancement of Artificial Intelligence (AAAI), 2020.
[15] Yu, Fisher , and V. Koltun . "Multi-Scale Context Aggregation by Dilated Convolutions." ICLR 2016.
[16] Ashish V aswani, Noam Shazeer, Niki Parmar, and et al. Attention is all you need. In NIPS, 2017.
[17] Zhou, W., Huang, K., Ma, T., & Huang, J. (2020). Document-Level Relation Extraction with Adaptive Thresholding and Localized Context Pooling. ArXiv, abs/2010.11304.
[18] Jeffrey Pennington, Richard Socher, and Christopher D Manning. Glove: Global vectors for word representation. In EMNLP, 2014.
[19] Ryuichi Takanobu, Tianyang Zhang, Jiexi Liu, and Minlie Huang. A hierarchical framework for relation extraction with reinforcement learning. In AAAI,2019.
[20] Xiangrong Zeng, Daojian Zeng, Shizhu He, and et al. Extracting relational facts by an end-to-end neural model with copy mechanism. In ACL, 2018.
[21] Yucheng Wang, Bowen Yu, Yueyang Zhang, Tingwen Liu, Hongsong Zhu, and Limin Sun. 2020. Tplinker:Single-stage joint extraction of entities and relations through token pair linking. In Proceedings of the 28th International Conference on Computational Linguistics, pages 1572–1582.
[22] Tapas Nayak and Hwee Tou Ng. Effective modeling of encoder-decoder architecture for joint entity and relation extraction. In AAAI, 2020.
[23] Dianbo Sui, Y ubo Chen, Kang Liu, and et al. Joint entity and relation extraction with set prediction networks. In CoRR, 2021.
[24] Feiliang Ren, Longhui Zhang, Shujuan Yin, and et al. A novel global feature-oriented relational triple extraction model based on table filling. In EMNLP,2021.

Fuzzy Systems and Data Mining IX
A.J. Tallón-Ballesteros and R. Beltrán-Barba (Eds.)

doi:10.3233/FAIA231048

Fast-Growing Field: Bibliometrics of Cryptocurrency and Blockchain Research

Wei Zhou[a], Hongchang Li[a], Danxue Luo[a*] and Zhe Li[b]
[a.] *School of Finance, Yunnan University of Finance and Economics, Kunming, 650221, P.R. China*
[b.] *School of Mathematics and Statistics, Central South University, Changsha, 410083, P.R. China*

Abstract. Cryptocurrency and blockchain technology have experienced rapid advancement in recent years. Bitcoin, as a representative cryptocurrency, has been acknowledged as a legitimate payment method by numerous countries and institutions, while blockchain technology has significantly matured, particularly in the realm of distributed algorithms and decentralized systems. In this paper, we conduct a bibliometric analysis of relevant studies by using CiteSpace and Pajek, where literature data sourced from the Web of Science (WoS). Through our examination of this literature, we identify that the focal points of research in this technology are the innovation within blockchain platforms and the protection of user privacy. Moreover, in the field of application, we concentrate our analysis on the legal compliance associated with Bitcoin mining.

Keywords. Blockchain, Cryptocurrency, Bibliometrics

1. Introduction

Cryptocurrency has emerged as a novel asset class globally in recent years. As a form of digital currency, it leverages encryption tools and distributed databases derived from computer technology, with its fundamental premise being a decentralized consensus mechanism. Bitcoin, created in 2009, was the pioneer of cryptocurrency. This paper aims to conduct a bibliometric study on the development of cryptocurrency and blockchain technology. The results derived from bibliometric analysis are intended to illuminate the historical progression and the current state of this specific research domain. Utilizing data from authoritative databases, these results will enable us to scrutinize the evolution of thematic trends. By elaborate on evolution, we can predict potential shifts in the research direction of this topic, thereby anticipating its future trajectory.

We used Citespace software designed by Chen Meichao for co citation analysis[1], and selected 1556 articles with the themes of "blockchain" and "cryptocurrency" as the analysis source in WOS. We conducted cluster analysis and burst detection analysis on

* Corresponding Author, Danxue Luo, Yunnan University of Finance and Economics, China; Email: 15123668128@163.com. This work was supported by the Natural Science Foundation of China (No. 72071176), the Social Science Innovation Team Project of Yunnan Province (No. 2022CX01), the Applied Basic Research of Science and Technology Commission of Yunnan Province (No. 202301AV070010), Education Department Scientific Research Fund Project of Yunnan Province (No.2022Y484).

the number of articles published by countries and authors. Secondly, use Pajek software designed by Batagelj and Mrvar for path analysis,

2. Synergy analysis of knowledge network

The objective of conducting synergy analysis is to produce network analysis charts for countries, institutions, and authors using the CiteSpace software. These charts facilitate a comprehensive understanding of the contributions made by various countries within the context of "cryptocurrency and blockchain", as well as revealing the collaboration relationships among key authors. Such insights substantially aid in our study of the developmental trajectory of this specific research topic.

2.1 Analysis of the number of national documents

The following Table 1 shows the names, count, and percentage of the top 10 countries in the number of articles published under the theme of "cryptocurrency and blockchain technology". Among them, the United States has the largest number of articles published with 376 articles, accounting for 24.14%, followed by China with 268 articles published, and the first two countries account for more than one-third of the 1,557 articles published. As a developing country, China occupies an important position in such a relatively new field in the world. The UK, India, and Australia ranked third to fifth, respectively, with a similar number of posts, while the last five posted a similar number. As can be seen from the table, under the research topic of "cryptocurrency and blockchain technology", developed countries still publish a large number of documents, and only two developing countries, China and India, occupy an important position.

Table 1. Top 10 productive countries of cryptocurrency and blockchain.

Countries	Count	Percentage	Countries	Count	Percentage
USA	376	24.14%	Canada	85	5.45%
People R China	268	17.21%	Germany	80	5.13%
England	123	7.89%	South Korea	75	4.81%
India	106	6.80%	Italy	62	3.98%
Australia	100	6.42%	Russia	60	3.85%

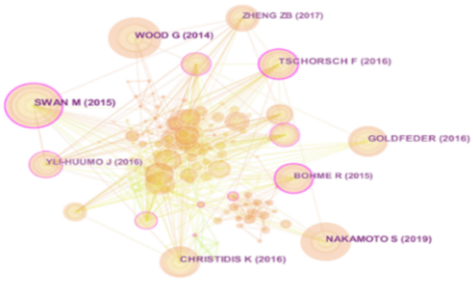

Figure 1. The author's collaboration.

Figure 2. The institution's collaboration.

2.2 Analysis of authors co-citations

Using Citespace as a visual tool enables us to identify key authors and collaborations in the field of cryptocurrencies and blockchain. In the figure below, the larger the node, the more important the author's article is, and the more connected the nodes, the more frequent the collaboration. As illustrated in Figure 1, Tschorsch F[2], Wood G[3], and Swan M[4] are not only the key authors but also the most frequently cited and collaborated authors. It is noteworthy that the most-cited authors published their pertinent papers mainly between 2015 and 2017. During this period, the topics of cryptocurrency decentralization and user privacy protection improvements in the blockchain platform emerged as central themes. Bhome R's high citations[5] are attributed to his contributions to the practical application of decentralization. Other authors in the diagram also made significant contributions. Zheng ZB[6], for instance, contributed a high-quality literature review on blockchain. Antonopoulos who first proposed Ethereum in 2014. By 2023, his article has been cited 7,158 times. Among the remaining authors, Christidis K[7] proposed the application of blockchain decentralization in the realm of the Internet of Things.

2.3 Keywords Timeline Atlas analysis

The first timeline chart introduced here is an analytical function of the CiteSpace software. Fundamentally, it presents the chronological appearance of keywords post-clustering, highlighting some of the most significant moments online for these clustered keywords. The red tags to the right of each cluster in the figure represent the corresponding keywords; the size of each circle indicates the keyword's importance. As visible in Figure 3, articles related to cryptocurrency, Bitcoin, and blockchain were published earlier and carry more importance. This is followed by articles concerning traceability and economic liquidity, while other keywords are dispersed evenly across the timeline. Recent research has pivoted towards information security and permissioned blockchain.

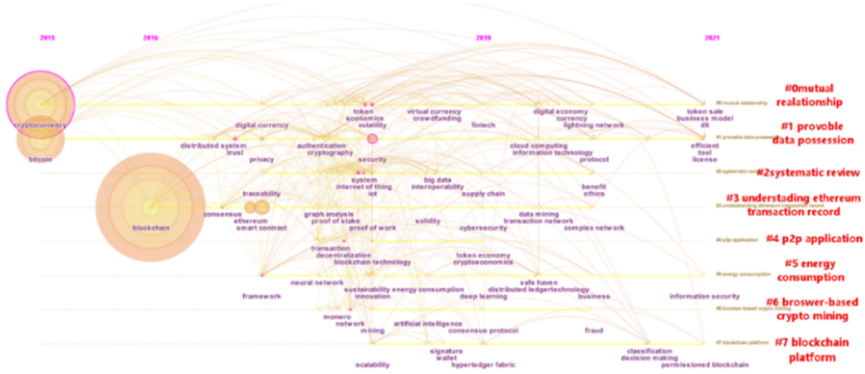

Figure 3. Timeline analysis of cryptocurrency and blockchain.

In this sequence diagram, notable developments include the challenges related to smart contract interaction in the Web 3.0 era, posed after the introduction of Ethereum, followed by the Proof of Data Possession (PDP) protocol issues, which constitute a critical part of the blockchain consensus protocol. Thirdly, a systematic review of articles

since 2014 is highlighted. It is noteworthy that these literature reviews are not merely overviews of prior research but provide a summary and future outlook on existing issues, including comprehensive reviews like Zheng ZB[7], which have garnered a substantial number of citations. The most recent topics are primarily centered on the specific application of blockchain and cryptocurrency, encompassing cryptocurrency mining, energy consumption of applications (a globally prevalent issue), the application of Peer-to-Peer (P2P) technology, and the innovation of blockchain platforms.

3. Keywords statistic and burst detection

Burst detection, a feature offered by CiteSpace, is utilized to identify the emergence and shifts in research hotspots. It facilitates the analysis of references to pinpoint new trends within the research domain.

Table 2. Keywords with the strongest citation bursts

Keywords	Strength	End	2001-2022
Bitcoin	8.498	2016	
Digital currency	3.8519	2017	
Bit blockchain	3.4175	2018	
Anonimity	1.3478	2018	
Peer-to-peer	2.4399	2018	
Hyperledger	2.9286	2018	
Access control	2.0289	2018	
Consensus	2.9899	2019	
Proof of work	2.0519	2020	
Cryptography	2.6941	2022	

As observed from the Table 2, the 10 principal keywords within the theme of "cryptocurrency and blockchain" have brief burst durations, reflecting the swift updates in this fast-paced field. From a strength perspective, Bitcoin, being the first research keyword, wields substantial influence, while other keywords that emerged in 2020, such as peer-to-peer computing, supply chain, and protocol, also hold considerable sway. This pattern indicates that even pioneering contributions in this field, such as hyperledger, only sustain prominence for a year or so, while issues related to peer-to-peer computing and network construction endure a little longer. The commencement year of these bursts also reveals a shift starting from 2020, where encryption technology began extending beyond blockchain to more practical areas like supply chains and peer-to-peer computing. The research focus is no longer solely confined to blockchain itself, the research topic is beginning to extend towards blockchain applications.

4. Evolutionary Analysis

Within Hiscite, LCS is employed to identify the most cited articles amongst the 1557 articles, notably Eyal's (2016) research[8] on Bitcoin mining security. Pajek's main path analysis reveals that the origins of the three pathways are Eyal(2016), Donet (2016)[9], and Feld et al. (2014)[10]. According to Pajek's analysis, this suggests that the series of nodes marked by backward arrows might have been inspired by these articles. Eyal I's

article signifies a concept - the then-emerging technology of Bitcoin mining, with Donet (2014) [9]being the first to consider its system security. In his 2014 article, Donet gathered data, identified hundreds of thousands of distinct Bitcoin nodes, and provided network stability and transmission time analysis in terms of the Bitcoin P2P network's scale, nodes' geographical distribution, and node terminal availability. Feld[10], on the other hand, centered on the then prevailing condition where Bitcoin's exchange rate exceeded $900, examining its distribution across different autonomous networks. He collected data such as network size and client, and analyzed the Bitcoin ecosystem's elasticity, transparency in the blockchain, as well as the propagation and verification of transaction blocks.

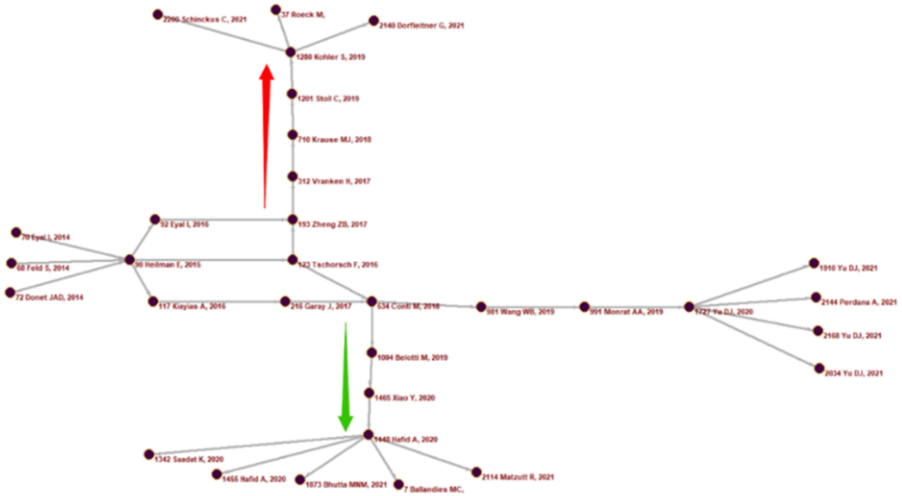

Figure 4. The local standard main path of cryptocurrency and blockchain[11]-[15]

5. Conclusion

Through the comprehensive analysis enabled by CiteSpace, it's evident that articles published by the United States, China, and European countries remain central to the domain of blockchain and Cryptocurrency, guiding the research development within this field. The aforementioned statistics delineate the basic progression of research themes around "cryptocurrency and blockchain". The main trajectory begins with the security and algorithmic enhancement of Bitcoin and blockchain technology, extending to privacy protection and the emergence of new currencies. Novel blockchain platforms and key new algorithms have become critical nodes in the development process. Meanwhile, a secondary thread focuses on the social impact of blockchain and Bitcoin mining, specifically the economic impact (mainly practical issues of decentralized currency), legal compliance, and the increasingly discussed environmental impact of Bitcoin mining.

References

[1] Chen C. CiteSpace II: Detecting and visualizing emerging trends and transient patterns in scientific literature. Journal of the American Society for Information Science and Technology, 2006,57(3), 359-377.

[2] Tschorsch F, Scheuermann B. Bitcoin and beyond: A technical survey on decentralized digital currencies. IEEE Communications Surveys & Tutorials, 2016, 18(3): 2084-2123.

[3] Wood G. Ethereum: A secure decentralised generalised transaction ledger. Ethereum project yellow paper, 2014, 151: 1-32.

[4] Swan M. Blockchain: Blueprint for a new economy. " O'Reilly Media, Inc.", 2015.

[5] Böhme R, Christin N, Edelman B, et al. Bitcoin: Economics, technology, and governance. Journal of economic Perspectives, 2015, 29(2): 213-238.

[6] Christidis K, Devetsikiotis M. Blockchains and smart contracts for the internet of things. IEEE Access, 2016,4, 2292-2303.

[7] Zheng ZB, Xie SA, Dai HN, Chen XP, Wang HM. An Overview of Blockchain Technology: Architecture, Consensus, and Future Trends. IEEE 6th International Congress on Big Data (BigData Congress), 2017,557-564.

[8] Eyal I, Gencer AE, Sirer EG, et al. {Bitcoin-NG}: A scalable blockchain protocol//13th USENIX symposium on networked systems design and implementation (NSDI 16). 2016: 45-59.

[9] Donet JAD, Perez-Sola C, Herrera-Joancomarti J. The Bitcoin P2P Network. 18th International Conference on Financial Cryptography and Data Security (FC),2014, 87-102.

[10] Feld S, Schonfeld M,Werner M. Analyzing the deployment of Bitcoin's P2P network under an AS-level perspective. 5th International Conference on Ambient Systems, Networks and Technologies (ANT) / 4th International Conference on Sustainable Energy Information Technology (SEIT), 2014,1121-1126.

[11] Asl MG, Rashidi MM, Abad, S. Emerging digital economy companies and leading cryptocurrencies: insights from blockchain-based technology companies. Journal of Enterprise Information Management, 2021,34(5): 1506-1550.

[12] Ballandies MC, Dapp MM, Pournaras, E. Decrypting distributed ledger design—taxonomy, classification and blockchain community evaluation. Cluster Computing, 2021,25(3), 1817-1838.

[13] Belotti M, Bozic N, Pujolle G, Secci S. A Vademecum on Blockchain Technologies: When, Which, and How. IEEE Communications Surveys and Tutorials, 2019,21(4) 3796-3838.

[14] Bhutta, MNM, Khwaja AA, Nadeem A, Ahmad HF, Khan MK, Hanif MA, Song HB, Alshamari M, Cao Y. A Survey on Blockchain Technology: Evolution, Architecture and Security. IEEE Access, 2019,9,61048-61073.

[15] Christidis K, Devetsikiotis M. Blockchains and smart contracts for the internet of things. IEEE Access, 2016,4, 2292-2303.

Fuzzy Systems and Data Mining IX
A.J. Tallón-Ballesteros and R. Beltrán-Barba (Eds.)

doi:10.3233/FAIA231049

N-Compactness of Intuitionistic L-Fuzzy Topological Space

Jiaxin GAO, Xiaoxia WANG[1] and Qiaoqiao LI
College of Mathematics and Computer Science, Yan'an University, Yan'an 716000, China

Abstract. In this paper, we extend the N-compactness in L-Fuzzy Topological space to intuitionistic L-Fuzzy Topological space. Firstly, intuitionistic fuzzy N-compactness is defined by α-quasi-coincident family in an intuitionistic L-Fuzzy Topological space, and its equivalent characterization is given by using intuitionistic fuzzy α-net and intuitionistic fuzzy filter. Secondly, it is proved that intuitionistic fuzzy N-compactness has closed heritability; The union of a finite number of intuitionistic fuzzy N-compact sets is still intuitionistic fuzzy N-compact set and intuitionistic fuzzy N-compactness is topological invariance. This research enriches the theoretical system of intuitionistic L-fuzzy Topological space, and provides a certain reference value for the related theoretical research of intuitionistic L-fuzzy Topological space.

Keywords. Intuitionistic L-fuzzy Topological space; N-compactness; Closed heritability; Topological invariance

1. Introduction

In 1983, Atanassov [1] extended the fuzzy set firstly proposed by Zadeh [2] in 1965 and introducing non membership degrees in fuzzy set theory proposed the concept of intuitionistic fuzzy sets. Subsequently, Coker [3] was influenced by the concept of fuzzy topology in the sense of Chang [4], and used intuitionistic fuzzy sets to propose the concept of intuitionistic fuzzy topological spaces and studied their connectivity and separability. The membership function value of traditional fuzzy sets is only a single value, and in practical applications, it cannot simultaneously describe affirmation, negation, and uncertainty. On the basis of fuzzy sets, intuitionistic fuzzy sets add non membership functions and hesitancy, describing fuzzy concepts that are neither definite nor negative, and better characterization of fuzziness and uncertainty. Later, Atanassov and Stoeva[5] further extended the concept of intuitionistic fuzzy sets to residual lattices and proposed intuitionistic *L*-fuzzy sets (i.e. it is based on intuitionistic fuzzy sets on residual lattices). It has more flexibility and applicability than intuitionistic fuzzy sets when dealing with fuzziness problems than intuitionistic fuzzy sets.

Fuzzy sets, intuitionistic fuzzy sets, and their extended forms play a crucial role in decision-making, data analysis, and healthcare in recent years. For example, Xu and Fang [6]mapped medical images into intuitionistic fuzzy sets and applied them to subsequent image segmentation processes, converting images into fuzzy numbers and performing

[1]Corresponding Author, Xiaoxia WANG, Department of Mathematics and Computer Science, Yan'an University, China; E-mail: yd-wxx@163.com.

segmentation; Yager [7] proposed Generalized orthopair fuzzy sets, which is a more general form of intuitionistic fuzzy sets, allowing decision-making analysis to have a larger decision-making space and stronger decision-making information processing capabilities[8]; Peng[9]proposed Pythagorean fuzzy soft set, which combines Pythagorean fuzzy sets with soft set theory, expanding the application scope of intuitionistic fuzzy soft sets, making evaluation results more objective and authentic, and its application in stock investment. Topological spaces composed of different fuzzy sets, their properties have important applications in different disciplinary fields. For example, Gong[10] used the properties in topological space to determine the existence of defects in C language, which is beneficial for developing C language software more effectively and safely. Wang [11] analyzed the topological forms of Chinese classical gardens, identified various topological phenomena in modern urban landscape design, and analyzed the application of topological principles in landscape design. Qian [12] applied topological properties to trajectory planning of intelligent driving vehicles in complex traffic scenarios.

On this basis, in the third section of this paper provides the concept and related knowledge of intuitionistic *L*-fuzzy topological spaces. In the fourth section of this paper extends the *N*-*c*ompactness in *L*-Fuzzy topological spaces to intuitionistic *L*-fuzzy topological spaces. Firstly, in intuitionistic *L*-fuzzy topological spaces, intuitionistic fuzzy *N*-compactness is defined be α -quasi-coincident family, and its equivalent characterization is given using intuitionistic fuzzy α -net and intuitionistic fuzzy filter; Secondly, it was proved that its intuitionistic fuzzy *N*-compactness has closed heritability, topological invariance, and a finite number of intuitionistic fuzzy *N*-compactness sets, which are still intuitionistic fuzzy *N*-compactness sets, and so on. This study enriches the theoretical system of intuitionistic *L*-fuzzy topological spaces and provides certain reference value for related theoretical research on intuitionistic *L*-fuzzy topological spaces. Symbols and concepts not explained in this article can be found in reference [13].

2. Preliminary Knowledge

In this section, we will review some basic concepts of complete regular residual lattices and intuitionistic *L*-fuzzy sets.

Definition 2.1 [14] The algebraic structure $\mathcal{L}=(L,\wedge,\vee,*,\rightarrow,0,1)$ is called a residual lattice if $\mathcal{L}$ satisfies the following conditions:

(1) $(L,\wedge,\vee)$ is a bounded lattice with a partial order relationship, and 0,1 are its minimum and maximum elements, respectively;

(2) $(L,*,1)$ is a commutative monoid, and $*$ preserves order for each argument;

(3) $x*y\le z$ if and only if $x\le y\rightarrow z$, for any $x,y,z\in L$.

If $(L,\wedge,\vee)$ is complete, then the remaining lattice $\mathcal{L}=(L,\wedge,\vee,*,\rightarrow,0,1)$ is called complete.

Definition2.2[15] Defines the negation operator on a residue lattice $\neg: L\rightarrow L:\neg a=a\rightarrow 0$, for any $a\in L$ .if $\neg\neg a=a$,for any $a\in L$,then $\mathcal{L}=(L,\wedge,\vee,*,\rightarrow,0,1)$ is called a regular residue lattice. In fact, the negation operator on a regular residue lattice is an order-reversing-involution.

Definition 2.3[16] $\mathcal{L}=(L,\wedge,\vee,*,\rightarrow,0,1)$ is complete regular residue lattice, set $\overline{\mathcal{L}}=\{(x_1, x_2)\in\mathcal{L}\times\mathcal{L}; x_1\le\neg x_2\}$, define the binary relationship $\le_{\overline{\mathcal{L}}}$ on the set $\overline{\mathcal{L}}$: $\forall x=(x_1,x_2),\ y=$

$(y_1, y_2) \in \overline{\mathcal{L}}$, $x \leq_{\overline{\mathcal{L}}} y \Leftrightarrow x_1 \leq y_1$ and $x_2 \geq y_2$. Then it can be verified that $\leq_{\overline{\mathcal{L}}}$ is a partial order relationship on $\overline{\mathcal{L}}$, and $(\overline{\mathcal{L}}, \leq_{\overline{\mathcal{L}}})$ is a complete lattice with minimum and maximum elements of $0_{\overline{\mathcal{L}}} = (0,1)$、$1_{\overline{\mathcal{L}}} = (1,0)$. The intersection operation on the lattice $\overline{\mathcal{L}}$ about the partial order relationship $\leq_{\overline{\mathcal{L}}}$ is as follows: $x \wedge_{\overline{\mathcal{L}}} y = (x_1 \wedge y_2, x_2 \vee y_2)$. Since the lattice $\overline{\mathcal{L}}$ is a complete lattice, for $\{x^i = (x_1^i, x_2^i) \in \overline{\mathcal{L}}; i \in \Gamma\}$, any intersection and union operations on the lattice $\mathcal{L}$ are as follows: $(\underset{i\in\Gamma}{\wedge})_{\overline{\mathcal{L}}} x^i = (\underset{i\in\Gamma}{\wedge} x_1^i, \underset{i\in\Gamma}{\vee} x_2^i)$.

Definition 2.4 [16] If X be a nonempty set, then $A = \{< x, \mu_A(x), \gamma_A(x) >; x \in X\}$ is an intuitionistic L-fuzzy set on X, where $\mu_A : X \to \mathcal{L}$, $\gamma_A : X \to \mathcal{L}$ satisfies the condition $\mu_A(x) \leq \neg\gamma_A(x)$, for each $x \in X$. Where $\mu_A(x)$ represents the L-membership of x to A, and $\gamma_A(x)$ represents the L-non membership of x to A. All intuitionistic L-fuzzy sets on X are denoted as ζ^X. Note $A(x) = (\mu_A(x), \gamma_A(x))$, $A \in \zeta^X$ if and only if $A(x) \in \overline{\mathcal{L}}$, for each $x \in X$. Note that the maximum element of the intuitionistic L-fuzzy set is $(\tilde{1}, \tilde{0}) = \{< x, 1, 0 >, x \in X\}$, and the minimum element is $(\tilde{0}, \tilde{1}) = \{< x, 0, 1 >, x \in X\}$.

3. Intuitionistic L-fuzzy Topological Space Related Knowledge

Below, we provide the definition of intuitionistic L-fuzzy topological spaces and some basic definitions and conclusions related to intuitionistic L-fuzzy topological spaces.

Definition 3.1 Let X be a nonempty set, and ζ^X be all intuitionistic L-fuzzy sets on X, δ: $\zeta^X \to \overline{\mathcal{L}}$ satisfies the following conditions:(1) $\delta((\tilde{1},\tilde{0})) = \delta((\tilde{0},\tilde{1})) = 1_{\overline{\mathcal{L}}}$;(2) $\forall A, B \in \zeta^X$, $\delta(A \wedge B) \geq \delta(A) \wedge \delta(B)$; (3) $\forall A_t \in \zeta^X, t \in T, \delta(\underset{t\in T}{\vee} A_t) \geq \underset{t\in T}{\wedge} \delta(A_t)$.

Then δ is called an intuitionistic L-fuzzy topology on X, and the pair (X, δ) is an intuitionistic L-fuzzy topological space ($IL-fts$ for short).

Definition 3.2 Let X be a nonempty set, $A = \{< y, \mu_A(y), \gamma_A(y) >, y \in X\} \in \zeta^X$, $\alpha, \beta \in L$, $\alpha \leq \neg\beta$, satisfying $A(y) = \begin{cases} (\alpha, \beta) & if \quad y = x, \\ (0,1) & if \quad y \neq x. \end{cases}$, then A is called an intuitionistic L fuzzy point.

Meanwhile, A is denoted as $x_{(\alpha,\beta)}$. Record $M(L)$ as the set of molecules in L; When $\alpha, \beta \in M(L)$, $x_{(\alpha,\beta)}$ is called an intuitionistic LF molecule. $\{x \in X, \mu_A(x) > 0,\ \gamma_A(x) < 1\}$ is called the support of A, denoted as $SuppA$. x is the support point of $x_{(\alpha,\beta)}$ and α is its height. The set of all intuitionistic L fuzzy points $x_{(\alpha,\beta)}$ is denoted as $Pt(\zeta^X)$.

Definition 3.3 Let $A \in \zeta^X$, $x_{(\alpha,\beta)} \in Pt(\zeta^X)$. If $x_{(\alpha,\beta)} \notin A'$ (i.e. $\alpha > \gamma_A(x)$ or $\beta < \mu_A(x)$),we say that $x_{(\alpha,\beta)}$ quasi-coincides with A, denoted as $Aqx_{(\alpha,\beta)}$.

Definition 3.4 Let (X, δ) be $IL-fts$, $A \in \zeta^X$, $x_{(\alpha,\beta)} \in Pt(\zeta^X)$, and if there is $B \in \delta$ such that $x_{(\alpha,\beta)} qB \subset A$, then A is called the intuitionistic quasi-coincident neighborhood of $x_{(\alpha,\beta)}$. The family of all the intuitionistic quasi-coincident neighborhood of $x_{(\alpha,\beta)}$ is called the system of intuitionistic quasi-coincident neighborhood of $x_{(\alpha,\beta)}$, denoted by $\mathcal{N}(x_{(\alpha,\beta)})$.

Definition 3.5 Let (X,δ) be $IL-fts$, $A\in\zeta^X$, $x_{(\alpha,\beta)}\in Pt(\zeta^X)$. If there is PqA for each $P\in\mathcal{N}(x_{(\alpha,\beta)})$, then $x_{(\alpha,\beta)}$ is the intuitionistic L fuzzy adherence point of A. If $x_{(\alpha,\beta)}$ is the intuitionistic L fuzzy adherence point of A, and $x_{(\alpha,\beta)}\in A$, $P\in\mathcal{N}(x_{(\alpha,\beta)})$, if P quasi-coincident with the intuitionistic L fuzzy points in A that are different from $x_{(\alpha,\beta)}$, then $x_{(\alpha,\beta)}$ is called intuitionistic L fuzzy accumulation point.

Definition 3.6 Let (X,δ) be $IL-fts$ and X be a nonempty set, $\mathcal{F}$ is a family of intuitionistic L-fuzzy sets, if it satisfies the following conditions: (1) If $A_1,A_2\in\mathcal{F}$,then $A_1\wedge A_2\in\mathcal{F}$; (2) If $A\in\mathcal{F}$, for each intuitionistic L-fuzzy set B such that $A\subseteq B$, we have $B\in\mathcal{F}$; We call $\mathcal{F}$ an intuitionistic L fuzzy filter on X. Let $\alpha\in M(L)$, if Min $\{ht(A), A\in F\}=\alpha$,for each $F\in\mathcal{F}$, where $ht(A)=\bigvee\{\mu_A(x),x\in X\}$, then $\mathcal{F}$ is called an intuitionistic L fuzzy α -filter on X.

Definition 3.7 Let (X,δ) be $IL-fts$, $\mathcal{F}$ an intuitionistic L fuzzy filter on X. If for each $F\in\mathcal{F}$,we have $F\not\subset P$,then $x_{(\alpha,\beta)}$ is called an intuitionistic L fuzzy adherence point of $\mathcal{F}$.

Definition 3.8 Let (X,δ) be $IL-fts$, D be an directed set, and X be a nonempty set, $P\in\mathcal{N}(x_{(\alpha,\beta)})$ and the mapping $S:D\to Pt(\zeta^X)$ be an intuitionistic L fuzzy net on X and is denoted as $S=(S(n),n\in D)$ .If $S(n)=\{x^n_{(\alpha_n,\beta_n)},x\in X\}\in A$, for any $n\in D$,then S is called intuitionistic L fuzzy net of A.

Definition 3.9 Let (X,δ) be $IL-fts$, $x_{(\alpha,\beta)}\in Pt(\zeta^X)$, $S=(S(n),n\in D)$ .If for each $P\in\mathcal{N}(x_{(\alpha,\beta)})$, the eventually SqP (i.e. eventually $S(n)\not\in P$), then the intuitionistic L fuzzy net S converges to $x_{(\alpha,\beta)}$ .If for each $P\in\mathcal{N}(x_{(\alpha,\beta)})$,the frequently SqP (i.e. frequently $S(n)\not\in P$),intuitionistic L fuzzy net S with $x_{(\alpha,\beta)}$ as the accumulation point .

Definition 3.10 Let (X,δ) and (Y,τ) be $IL-fts$, $f:X\to Y$ is a mapping. If for each $B\in\tau$,has $f^{-1}(B)\in\delta$, then f is called a continuous mapping.

4. Intuitionistic Fuzzy N-compactness and Equivalent Characterization

In this section, we discussed and explored N-compactness in intuitionistic L-fuzzy topological spaces, and obtained some related results.

Definition 4.1 Let (X,δ) be $IL-fts$, $A\in\zeta^X$, $\Phi\in\delta'$, $\alpha\in M(L)$. If there is $P\in\Phi$, such that $P\in\mathcal{N}(x_{(\alpha,\beta)})$, for each intuitionistic LF molecule $x_{(\alpha,\beta)}$ with a height of α in A, then Φ is called the α -quasi-coincident neighborhood family of A. If there is $r\in\beta^*(\alpha)$, such that Φ is the r -quasi-coincident neighborhood family of A, then Φ is called the α^- -quasi-coincident neighborhood family of A.

Definition 4.2 Let (X,δ) be $IL-fts$, $A\in\zeta^X$,If there is a finite subfamily ψ for any α -quasi-coincident neighborhood family Φ of A, such that ψ constitutes α^- -quasi-coincident neighborhood family of A, then A is called intuitionistic fuzzy N-compact set .If the maximum intuitionistic L-fuzzy set $(\tilde{1},\tilde{0})$ is a N-compact set, then (X,δ) is called an intuitionistic fuzzy N- compact space.

Theorem 4.3 Let (X,δ) be $IL-fts$, $A\in\zeta^X$, $\forall\alpha\in M(L)$. If A is an intuitionistic fuzzy N-compact set, if and only if it satisfies the following conditions: (1) For every α -quasi-coincident neighborhood Φ of A there is finite α -quasi-coincident neighborhood subfamilies; (2) The α -quasi-coincident neighborhood family $\Phi=\{P\}$ of A composed by a closed set is also α^- -quasi-coincident neighborhood family of A.

Proof: $\Leftarrow$ The hypothesis is that holds, Φ is α -quasi-coincident neighborhood family of A. From (1), it can be inferred that Φ all have finite subfamilies ψ to form α -quasi-coincident neighborhood family of A, let $\{P\}$ is also α -quasi-coincident neighborhood family of A. From (2), it can be inferred that $\{P\}$ is also α^- -quasi-coincident neighborhood family of A. i.e. there is a molecule $r\in\beta^*(\alpha)$ in $M(L)$, so that $r\not\le P(x)=\wedge\{Q(x),Q\in\psi\}$,for any intuitionistic LF molecule $x_{(r,\beta)}$ in A. Exist $Q\in\psi$,so that $r\not\le Q(x)$ i.e. $Q\in\mathcal{N}(x_{(r,\beta)})$, so ψ is α^- -quasi-coincident neighborhood family of A. Therefore, A is an intuitionistic fuzzy N- compact set.

$\Rightarrow$ Let A is an intuitionistic fuzzy N-compact set, Φ is α -quasi-coincident neighbor-hood family, then Φ both have finite subfamilies ψ to form α^- -quasi-coincident neighborhood family of A. Obviously, ψ is also α -quasi-coincident neighborhood subfamily of Φ .Therefore, condition (1) holds. If $\Phi=\{P\}$ is α^- -quasi-coincident neighborhood family of A, then there are finite subfamilies ψ of Φ to form α^- -quasi-coincident neighborhood family of A. And at this point, there can only be $\psi=\Phi$, so $\Phi=\{P\}$ is also α^- -quasi-coincident neighborhood family of A, thus condition (2) holds.

Definition 4.4 Let (X,δ) be $IL-fts$, D be the directed set, $S=(S(n),n\in D)$ be the intuitionistic L fuzzy net in X. Use $V(S(n))$ to represent the height of $S(n)$. Let $V(S)=\{V(S(n)),n\in D\}$ be the value net of S. Let $\alpha\in M(L)$, if for any $r\in\beta^*(\alpha)$, $V(S(n))$ is eventually greater than or equal to r (i.e. exists $n_0\in D$,when $n\ge n_0$, $V(S(n))\ge r$),then net S is called an intuitionistic L fuzzy α -net.

Theorem 4.5 Let (X,δ) be $IL-fts$,if A is an intuitionistic fuzzy N-compact set iff for each $\alpha\in M(L)$, intuitionistic L fuzzy α -net in A has accumulation point in A with height α.

Proof: $\Rightarrow$ If A is an intuitionistic fuzzy N-compact set, $S=\{S(n),n\in D\}$ be an intuitionistic L fuzzy α -net in A, and S has no accumulation point in A with height α , then $P(x)\in\mathcal{N}(x_{(\alpha,\beta)})$,for any intuitionistic LF molecule $x_{(\alpha,\beta)}$ in A, exists $n(x)\in D$,when $n\ge n(x)$, $S(n)\le P(x)$ .Let $\Phi=\{P(x),x_{(\alpha,\beta)}\le A\}$ be α -quasi-coincident neighbor-hood family of A. Since A is an intuitionistic fuzzy N-compact set, So Φ has finite subfamilies $\psi=\{P(x_i),\ i=1,2,\cdots,k\}$,so that ψ forms α^- -quasi-coincident neighbor-hood family of A,(i.e. there exists $r\in\beta^*(\alpha)$ such that for any intuitionistic LF molecule $y_{(\gamma,\mu)}$ in A has $i\le k$ such that $y_{(\gamma,\mu)}\not\le P(x_i)$).Let $P=\wedge_{i=1}^n P(x_i)$,for any intuitionistic LF molecule $y_{(\gamma,\mu)}$ in A, which has $y_{(\gamma,\mu)}\not\le P$ (i.e. $\forall y_{(\gamma,\mu)}\in A, r\not\le P(y)$).Also, because D is an directed set, then there is $n_0\in D$,such that $n_0\ge n(x_i)(i=1,2,\cdots,k)$ .Then when $n\ge n_0$, $S(n)\le P(x_i)(i=1,2,\cdots,k)$,so $S(n)\le P$ when $n\ge n_0$ .Also, because $S(n)\le A$,when $n\ge n_0$, $r\not\le V(S(n))$ .This contradicts $S=\{S(n),n\in D\}$ is an intuitionistic L fuzzy a-net in A .Therefore, S has at least one accumulation point with a height of α in A.

$\Leftarrow$ Let each intuitionistic L-fuzzy α -net in A have accumulation point with height α , and Φ be α -quasi-coincident neighborhood family in A. Let any finite subfamily of Φ be not α^- -quasi-coincident neighborhood family in A(i.e. for each $r \in \beta^*(\alpha)$, $\Phi_0 \in 2^{(\Phi)}$,so that $\wedge\Phi_0 < A(r)$ is not hold). For each pair of r and Φ_0 , there is a point $S(r,\Phi_0) \in \wedge\Phi$ in A with a height of r . Let $D = \beta^*(\alpha) \times 2^{(\Phi)}$, it is specified that $(r_1,\Phi_1) \geq (r_2,\Phi_2)$ if and only if $r_1 \geq r_2$, $\Phi_1 \supset \Phi_2$. Since $\beta^*(\alpha)$ and $2^{(\Phi)}$ are both directional sets, then D is also a directional set. Let $S = \{S(r,\Phi_0),(r,\Phi_0) \in D\}$ be an intuitionistic L-fuzzy net in A. Because S has accumulation point in A with height α .In fact, for a point $x_{(\alpha,\beta)} \in A$, there are $P \in \Phi$, $P(x) \in \mathcal{N}(x_{(\alpha,\beta)})$ (i.e. $x_{(\alpha,\beta)} \notin P$), which indicates that S is eventually in P. Therefore, $x_{(\alpha,\beta)}$ is not the accumulation point of S. This contradicts the hypothesis. Therefore, any finite subfamily of Φ is α^- -quasi-coincident neighborhood family of A, that is, A is an intuitionistic fuzzy N-compact set.

Theorem 4.6 Let (X,δ) be $IL-fts$,if A is an intuitionistic fuzzy N-compact set iff every intuitionistic L fuzzy α -filter containing A has an adherence point in A with height α .

Proof: $\Leftarrow$ Assuming that the condition is satisfied and $S = \{S(n), n \in D\}$ be an intuitionistic L fuzzy α -net in A. Let $F_m = V\{S(n), n \geq m\}(m \in D)$, because D is an directed set, we can obtain that the set family $\{F_m, m \in D\}$ can generate an intuitionistic L fuzzy filter $\mathcal{F}$,and $A \in \mathcal{F}$ .Because S is an intuitionistic L fuzzy α -net, for each $r \in \beta^*(\alpha)$, $V(S)$ is eventually greater than r .Therefore, for each $r \in \beta^*(\alpha)$, $\vee_{x\in X} F_m(x) = \vee\{\vee(S(n)),\ n \geq m\} \geq r$, that is $\vee_{x\in X} F_m(x) \geq \alpha$ .Since $\mathcal{F}$ is generated by $\{F_m, m \in D\}$, then each $F \in \mathcal{F}$ contains some F_m , so $\vee_{x\in X} F_m(x) \geq \alpha$. Therefore, $\mathcal{F}$ is an intuitionistic L fuzzy α -filter. Because $\mathcal{F}$ has adherence points with height α , $x_{(\alpha,\beta)} \in A \in \mathcal{F}$ .From Definition3.7, it can be concluded that for $P(x) \in \mathcal{N}(x_{(\alpha,\beta)})$, $F \in \mathcal{F}$,there is $F_m \subset F \not\subset P$, which indicates that the intuitionistic L-fuzzy net S is frequently not in P. Therefore, $x_{(\alpha,\beta)}$ is the adherence point of the intuitionistic L fuzzy net S. From Theorem 4.5, it can be concluded that the intuitionistic L-fuzzy set A is intuitionistic fuzzy N-compact.

$\Rightarrow$ Assuming that A is intuitionistic fuzzy N-compact set, $\mathcal{F}$ is an intuitionistic L fuzzy α -filter containing A $(\alpha \in M(L))$,then for each $F \in \mathcal{F}$, $F \wedge A \in \mathcal{F}$ .Since $r \in \beta^*(\alpha) \subset \beta(\alpha)$ satisfies the condition that for each $\varphi \in L$, $\vee\varphi \geq \alpha$, there is $b \in \varphi$,such that $b \geq r$ .For each $F \in \mathcal{F}$,there is $\vee_{x\in X}(F \wedge A)(x) \geq \alpha$ .Therefore, for each $r \in \beta^*(\alpha)$,there is $s(F,r)$ contained in $F \wedge A$, $s(F,r)$ with height r .Assuming $S = \{s(F,r),\ (F,r) \in \mathcal{F} \times \beta^*(\alpha)\}$,then S is an intuitionistic L fuzzy α -net in A. Because A is intuitionistic fuzzy N-compact set, we can obtain that S adherence point in A with height α .Below, we will prove that $x_{(\alpha,\beta)}$ is also adherence point of $\mathcal{F}$. In fact, for each $P(x) \in \mathcal{N}(x_{(\alpha,\beta)})$,S is frequently not in P, for each $F \in \mathcal{F}$, there is $F_1 \subset F$, for certain $r \in \beta^*(\alpha)$, $s(F_1,r) \notin P$ .Therefore, based on $s(F_1,r) \in F_1$, $F_1 \subset F$, can be obtained. Therefore, $x_{(\alpha,\beta)}$ is also an adherence point of $\mathcal{F}$.

Theorem 4.7 Let (X,δ) be $IL-fts$, $A \in \zeta^X$ .If the support of A is finite, i.e. $\sigma_0(A) = \{x \in X,\ < x, \mu_A(x) \neq 0, \gamma_A(x) \neq 1 >\}$ is a finite set, then A is an intuitionistic fuzzy N- compact set.

Proof: Let $\tau_\alpha(A)=\{x_1,x_2,\cdots,x_n\}$, Φ be any α-quasi-coincident neighborhood family of A. $\forall i\le n$, take $P_i\in\Phi$, so that $\alpha\not\le P_i(x_i)$. Because $\alpha=\sup\beta^*(\alpha)$, there is $r_i\not\le P_i(x_i)$, for $r_i\in\beta^*(\alpha)$. Also, since α is a molecule in L, it can be concluded that $\beta^*(\alpha)$ is an upper directed set, so there is $r_i\in\beta^*(\alpha)$ such that $r\ge r_i(i\le n)$. Meanwhile, there is $r_i\not\le P_i(x_i)$, for $\forall i\le n$. The finite subfamily $\Psi=\{P_1,P_2,\cdots,P_n\}$ of Φ is α^--quasi-coincident neighborhood family of A. Therefore, A is an intuitionistic fuzzy N-compact set.

Theorem 4.8 The union of a finite number of intuitionistic fuzzy N-compact sets remains an intuitionistic fuzzy N-compact set.

Proof : If A is the union of a finite number of intuitionistic fuzzy N-compact sets A_1, $A_2,\cdots,A_n$ in $IL-fts$, i.e. $A=\bigcup_{i=1}^n A_i$. If Φ is any α-quasi-coincident neighborhood family of A, then Φ is also α-quasi-coincident neighborhood family of $A_i(i=1,2,\cdots,n)$. And because $A_i(i=1,2,\cdots,n)$ is an intuitionistic fuzzy N-compact set, then Φ has a finite subfamily ψ_i to form a family of α^--quasi-coincident neighborhood family related to A_i. Therefore, $\psi=\vee_{i=1}^n\psi_i$ is a finite subfamily of Φ and forms α^--quasi-coincident neighborhood family of A. Therefore, A is an intuitionistic fuzzy N- compact set.

Theorem 4.9 Let (X,δ) be $IL-fts$, A is an intuitionistic fuzzy N-compact subset, B is an intuitionistic L-fuzzy closed set, then $C=A\wedge B$ is also intuitionistic fuzzy N-compact set.

Proof : Let S be an intuitionistic fuzzy α-net in C, then S is also an intuitionistic fuzzy α-net in A. Because A is an intuitionistic fuzzy N-compact subset, then S has accumulation point $x_{(\alpha,\beta)}$ in A with height α. S is also an intuitionistic fuzzy net in B, where $x_{(\alpha,\beta)}$ is the accumulation point of S. It can be concluded that $x_{(\alpha,\beta)}\le B$, thus $x_{(\alpha,\beta)}\le A\wedge B$, i.e. $x_{(\alpha,\beta)}$ is the accumulation point of S in C. Therefore, C is an intuitionistic fuzzy N-compact set.

Inference 4.10 If (X,δ) be $IL-fts$ and A is an intuitionistic fuzzy N- compact set, then each intuitionistic fuzzy closed subset contained in A is also an intuitionistic fuzzy N-compact set.

Lemma 4.11 Let (X,δ) and (Y,τ) be $IL-fts$, $P\in\delta$, $Q\in\tau$, $f:(X,\delta)\to(Y,\tau)$ be a continuous mapping, with $P=f^{-1}(Q)$. For any the intuitionistic L fuzzy point $x_{(\alpha,\beta)}$ in X satisfies $x_{(\alpha,\beta)}\not\in P$ then $f(x_{(\alpha,\beta)})$ is an intuitionistic L fuzzy point in Y, satisfies $f(x_{(\alpha,\beta)})\not\in Q$.

Theorem 4.12 Let (X,δ) and (Y,τ) be $IL-fts$, A be an intuitionistic fuzzy N- compact set in X, $f:(X,\delta)\to(Y,\tau)$ is a continuous mapping, then $f(A)$ is an intuitionistic fuzzy N-compact set in Y.

Proof : Let $S=\{S(n),n\in D\}$ be an intuitionistic L fuzzy α-net contained in $B=f(A)$. For each $n\in D$, there is $S(n)=y^n_{(\gamma_n,\mu_n)}$, and y^n is a support point of $S(n)$, then $f^{-1}(y^n)$ is a crisp set in X. For each $k\in N$, there is a crisp point $x^n\in f^{-1}(y^n)$, such that $\mu_A(x^n)>\mu_B(y^n)-1/k$. From $S(n)\in B$, we can obtain $V(S(n))\in\mu_B(y^n)$, therefore $\mu_A(x^n)>V(S(n))-1/k$. For each $n\in D$, $k\in N$, we can choose an intuitionistic L fuzzy point $T((n,k))\in A$, such that $V(S(n))-1/k\le V(S(n,k))\le V(S(n))$, $f(T((n,k)))\in S(n)$. Assuming $D_1=\{(n,k);n\in D,k\in N\}$, and if $n_1\ge n_2$, $k_1\ge k_2$, whenever $(n_1,k_1)\ge(n_2,k_2)$, then D_1 is an directed set, so

$T=\{T((n,k)),(n,k)\in D_1\}$ is an intuitionistic L fuzzy α -net contained in A. Because A is an intuitionistic fuzzy N-compact set, so T has accumulation point $x_{(\alpha,\beta)}\in A$. Let $y_{(\gamma,\mu)}=f(x_{(\alpha,\beta)})$,then $y_{(\gamma,\mu)}$ is the intuitionistic L-fuzzy point in Y, and $y_{(\gamma,\mu)}\in f(A)$ .Now we will verify that $y_{(\gamma,\mu)}$ is the accumulation point of S. Since $x_{(\alpha,\beta)}$ is the accumulation point of T, for each $P\in\mathcal{N}(x_{(\alpha,\beta)})$, $(n,k)\in D$,for certain $(n_0,k_0)\in D$,then $(n,k)\geq(n_0,k_0)$ frequently $T(n,k)\notin P$ .From the lemma, it can be inferred that $f(T(n,k))$ is an intuitionistic L-fuzzy point in Y ,when $Q=f(P)\subset Y$,there is frequently $f(T(n,k))\notin Q$ .Because $f(T((n,k)))\in S(n)$,So $y_{(\gamma,\mu)}$ is accumulation point of S. Therefore, $f(A)$ is an intuitionistic fuzzy N- compact set in Y.

Reference

[1] Atanassov K. Intuitionistic Fuzzy Sets[J]. Interval and Fuzzy Mathematics, 1983(8): 23-26.
[2] Zadeh LA. Fuzzy sets[J]. Inform and Control,1965,8:338-353.
[3] Coker D.An introduction to intuitionistic fuzzy topological spaces[J].Fuzzy Sets and Systems, 1997(88):81-89.
[4] Chang CL. Fuzzy topological spaces[J]. Mathematical Analysis and Applications, 1968, 24 (1):182-190.
[5] Atanassov K. Intuitionistic *L*-fuzzy sets[J]. Cybernetics and Systems Research, 1984, 2:539-540.
[6] Xu XL, Fang XL. Image Segmentation Based on Intuitionistic Fuzzy Kernel C-Means Clustering Algorithms [J]. Computer Engineering and Applications, 2019, 55(17): 227-231.
[7] Yager R. Generalized orthopair fuzzy sets [J]. IEEE Transactions on Fuzzy Systems, 2017, 25 (5).
[8] Wang HL, Zhang FM. A Multi-Criteria Decision-Making Method Based on q-Rung Orthopair Fuzzy Set and Reference Ideal Method[J]. Chinese Journal of Management Science,2022.
[9] Peng XD.Pythagorean Fuzzy Soft Set and Its Application[J].Computer Engineering,2015,41(7):224-229.
[10] Gong MX, Xie HY.Weakness analysis of Cstring functions based on topological space[J].Journal of HEFEI University of Technology, 2020,43(01):52-56.
[11] Wang JC, Yan XY. Classical Gardens in Topological Space and Modern Landscape Design [J]. Modern Landscape Architecture, 2019 (08): 84-85.
[12] Qian LL.The Research of Topological Space Based Behaviour Decision and Trajectory Planning Methods for Intelligent Vehicles[D]. Hunan: National University of Defense Technology,2020.
[13] Wang GJ. L-Fuzzy Topological Space Theory [M] Xi'an: Shaanxi Normal University Press, 1988.
[14] Blount K. The structure of residue lattice[J]. Algebra and Computation,2003 (13):437-461.
[15] Pei DW. The characterization of residue lattices and regular residue lattices[J]. Acta Mathematica Science, 2002(45):271-278.
[16] Zhong Yu. Intuitionistic *L*-fuzzy rough sets, Intuitionistic *L*-fuzzy pre ordered sets, and Intuitionistic *L*-fuzzy topological sets [D]. Nanjing Normal University, 2014.

Fuzzy Systems and Data Mining IX
A.J. Tallón-Ballesteros and R. Beltrán-Barba (Eds.)

doi:10.3233/FAIA231050

Dynamics of a Stochastic SIRI Epidemic Model

Xiaoju Sun, Jing Fu[1] and Jing Guo
Department of Mathematics, Changchun Normal University, Jilin 130000,China

Abstract. Curz Vargas et al studied the dynamics of a deterministic SIRI epidemic model, but it did not take into account the influence of environmental noise on system parameters, in the paper, we consider that the important parameters are disturbed by Ornstein-Uhlenbeck process and we can get a stochastic SIRI epidemic model. First of all, we study the existence and uniqueness of positive solution of system. The second, we also get the stationary distribution of the model . In the end, we get expression of the density function of the stochastic model. Compared with this deterministic model, the dynamical analysis of the system is more reasonable.

Keywords. Stochastic SIRI epidemic model; Stationary distribution; Ornstein-Uhlenbeck process; Probability density function

1. Introduction

Curz Vargas et al[1]studied an infectious diseases models with relapse about global stability, the follow model is studied,

$$\begin{cases} \dfrac{dS}{dt} = \Lambda - \beta^0 SI - \mu S, \\ \dfrac{dI}{dt} = \beta^0 SI - (\alpha + \kappa + \mu)I + \gamma R, \\ \dfrac{dR}{dt} = \kappa I - (\mu + \gamma)R. \end{cases} \tag{1}$$

Above the parameters are positive constants. S is susceptible population, I is infected people , R is the recovered population. The constant Λ is the recruitment rate of S ,μ is the natural death rate of population . β^0 is the disease transmission coefficient. α is the disease related death rate . κ is infectious individuals becomes normal individuals and γ is the normal individuals are reverted to the infectious state. For system (1), the disease-free equilibrium $E_0 = (\frac{\Lambda}{\mu}, 0, 0)$,

$E^* = (S^*, I^*, R^*)$ with$S^* = \frac{\Lambda}{\mu R_0}, I^* = \frac{\mu}{\beta}(R_0 - 1), R^* = \frac{\kappa\mu}{\beta(\gamma+\mu)}(R_0 - 1)$,Where R_0 , the basic reproduction number, is [1]

$$R_0 = \frac{(\mu + \gamma)\beta\Lambda}{\mu(\kappa\mu + (\mu + \gamma)(\alpha + \mu))}. \tag{2}$$

[1]Corresponding Author:Jing Fu, Changchun Normal University, E-mail:fujing@ccsfu.edu.cn

And

$$\Gamma_0 = \left\{(S,I,R) \in \mathbb{R}^3_+ : S \geq 0, I \geq 0, R \geq 0, S+I+R \leq \Lambda/\mu\right\}. \tag{3}$$

However, the above model still falls short in studying infectious disease dynamics because it does not take into account the influence of environmental noise on system parameters[2][3]. In the paper $\beta^0(t)$ is affected by the mean-reverting OrnsteinCUhlenbeck process and its representation is as follows, and δ, σ are positive constants ,where δ^0 means the speed of reversion and $\sigma^2 > 0$ is the intensity of fluctuation:

$$d\beta = -\delta[\beta^0(t) - \bar{\beta}]dt + \sigma dB(t), \tag{4}$$

For(2), we consider $p(t) = \beta^0(t) - \bar{\beta}$, we get

$$\begin{cases} dp = -\delta m dt + \sigma dB(t), \\ dS = [\Lambda - (p+\bar{\beta})SI - \mu S]dt, \\ dI = [(p+\bar{\beta})SI - (\alpha+\kappa+\mu)I + \gamma R]dt, \\ dR = [\kappa I - (\mu+\gamma)R]dt. \end{cases} \tag{5}$$

and we can get a region:

$$\Gamma = \left\{(p,S,I,R) \in \mathbb{R} \times \mathbb{R}^3_+ : S+I+R \leq \frac{\Lambda}{\mu}\right\} \tag{6}$$

In Section 2 we give the conditions for existence and uniqueness of a global solution of system (3). and in Section 3, give the conditions for existence of an ergodic stationary distribution of system (3). Section 4 we will study the density function of the model . Section 5 we give the conclusion for the paper.

2. Existence and uniqueness of a global solution

To prove that there is a unique positive solution to system(3), we will give the following theorem:

Theorem 2.1. *For system (3), it exists a unique solution* $(p(t),S(t),I(t),R(t))$ *on* $t \geq 0$ *for any initial value and the initial value* $(p(0),S(0),I(0),R(0)) \in \Gamma$ *a.s..*

Proof. The system (3) , it is satisfy the local Lipschitz condition, and there is a unique local solution. we will define a C^2 Lyapunov function V: $\mathbb{R} \times \mathbb{R}^3_+ \to \mathbb{R}_+$as follows:

$$V = S - 1 - \ln S + I - 1 - \ln I + R - 1 - \ln R + \frac{p^2}{2}. \tag{7}$$

The remaining evidence is similar to the literature[4], we will omit it.

3. stationary distribution

Define

$$\mathscr{R}_0^S = \mathscr{R}_1 - \frac{\Lambda^2}{\mu^3}\frac{\sigma}{2\sqrt{\pi\delta}}. \tag{8}$$

while$\mathscr{R}_1 = \frac{(\mu+\gamma)\bar{\beta}\Lambda}{\mu(\kappa\mu+(\mu+\gamma)(\alpha+\mu))}$

Theorem 3.1. *Assume that $R_0^s > 1$, then the stochastic system (3)admits at least one ergodic stationary distribution $\rho(\cdot)$on Γ.*

Proof. we proof it need three steps: the first we need construct stochastic Lyapunov functions; the second a compact set is constructed; in the end five the existence and ergodicity of the solution of system (3).

Step 1. (Construct stochastic Lyapunov functions): A C^2 function $H(p,S(t),I(t),R(t))$: $\Gamma \to \mathbb{R} = V - V_{min}$ is defined by

$$\begin{aligned} V(p(t),S(t),I(t),R(t)) &= M[-\ln I - \frac{\Lambda}{\mu^2}\ln S - \frac{\gamma k}{(\mu+\gamma)^2}\ln R] - \ln S - \ln R - \ln(\frac{A}{\mu} - S - I - R) + \frac{p^2}{2} \\ &:= MV_1 + V_2 \end{aligned}$$

where $V_1 = -\ln I - \frac{\Lambda}{\mu^2}\ln S - \frac{\gamma k}{(\mu+\gamma)^2}\ln R$ and $V_2 = -\ln S - \ln R - \ln(\frac{A}{\mu} - S - I - R) + \frac{p^2}{2}$, M is a sufficiently large number and satisfies the expression :

$$-M(\mathscr{R}_0^S - 1) + \mu + (\mu+\gamma) + \frac{\sigma^2}{2} + \sup\left\{-\frac{1}{2}\delta p^2 + p\frac{\Lambda}{\mu} + Mp\frac{\Lambda}{\mu}\right\} \le -2 \tag{9}$$

Employing the $It\hat{o}$'s formula to V_1,V_2 and combining the ergodic theorem[5]and (9), we obtain

$$\int_{-\infty}^{\infty}(p\vee 0)\,\kappa(x)dx = \int_0^{\infty}\frac{\sqrt{\delta}x}{\sqrt{\pi}\sigma}e^{-\frac{\delta x^2}{\sigma^2}}dx = \frac{\sigma}{2\sqrt{\pi\delta}}\int_0^{\infty}e^{-\left(\frac{\sqrt{\delta}x}{\sigma}\right)^2}d\left(\frac{\sqrt{\delta}x}{\sigma}\right)^2 = \frac{\sigma}{2\sqrt{\pi\delta}}, \quad \text{a.s.} \tag{10}$$

$$\begin{aligned} LH &= M[-(p+\bar{\beta})S + (\alpha+\kappa+\mu) - \gamma\frac{R}{I} - \frac{\Lambda^2}{S\mu^2} + (p+\bar{\beta})\frac{\Lambda}{\mu^2}I + \mu I] \\ &\quad - \frac{\Lambda}{S} + (p+\bar{\beta})I + \mu - \kappa\frac{I}{R} + (\mu+\gamma) - \frac{\Lambda - \mu(S+I+R) - \alpha I}{\frac{\Lambda}{\mu} - S - I - R} - \delta p^2 + \frac{\sigma^2}{2} \\ &\le -2 + (M + \frac{\Lambda}{\mu^2})\bar{\beta}I - \frac{\Lambda}{S} - k\frac{I}{R} - \frac{\alpha I}{\frac{A}{\mu} - S - I - R} \\ &\quad - \frac{1}{2}\delta p^2 + M\frac{\Lambda^2}{\mu^3}[(p\vee 0) - \int_{-\infty}^{\infty}(p\vee 0)\kappa(x)dx] \\ &:= F(p,S,I,R) + + M\frac{\Lambda^2}{\mu^3}[(p\vee 0) - \int_{-\infty}^{\infty}(p\vee 0)\kappa(x)dx] \end{aligned} \tag{11}$$

Step 2. (Construct a compact set): Then, we construct a compact set$\mathbb{D} \in \Gamma$as follows

$$\mathbb{D}_\varepsilon = \left\{ (p,S,I,R) \in \Gamma_1 | S \geq \varepsilon, I \geq \varepsilon, R \geq \varepsilon^2, S+I+R \leq \frac{A}{d} - \varepsilon^3, |p| \leq \frac{1}{\varepsilon} \right\}, \tag{12}$$

then,

$$F(m,S,I,R) \begin{cases} -2 + (M + \dfrac{\Lambda}{\mu^2})\bar{\beta}\dfrac{\Lambda}{\mu} - \dfrac{\Lambda}{S} \to -\infty, \text{as} S \to 0^+, \\ -2 + (M + \dfrac{\Lambda}{\mu^2})\bar{\beta} I \to -2, \text{as} I \to 0^+, \\ -2 + (M + \dfrac{\Lambda}{\mu^2})\bar{\beta}\dfrac{\Lambda}{\mu} - k\dfrac{I}{R} \to -\infty, \text{as} R \to 0^+, \\ -2 + (M + \dfrac{\Lambda}{\mu^2})\bar{\beta}\dfrac{\Lambda}{\mu} - \dfrac{\alpha I}{\frac{\Lambda}{\mu} - S - I - R} \to -\infty, \text{as}(S,I,R) \to +\infty, \\ -2 + (M + \dfrac{\Lambda}{\mu^2})\bar{\beta}\dfrac{\Lambda}{\mu} - \dfrac{1}{2}\delta p^2 \to -\infty, \text{as} p \to 0^+ \text{or} +\infty. \end{cases} \tag{13}$$

Clearly, we obtain that for a sufficient smallε ,$F(p,S,I,R) \leq -1$ and$F(p,S,I,R) \leq A$ for any $(m,S,I,R) \in \mathbb{D}$.

Step 3. (Existence and ergodicity): Making the use of Fatou's lemma [7][8][9]and the new method [3], it is easy to get

$$\liminf_{t \to +\infty} \frac{1}{t} \int_0^t \mathbb{P}(\tau, (p(\tau), S(\tau), I(\tau), R(\tau)) \mathbb{D}_\varepsilon) \, d\tau \geq \frac{1}{A+1} > 0 \quad \text{a.s.} \tag{14}$$

This completes the proof.

4. Density function of the stochastic model

In the section let $X_1 = p - p^*, X_2 = S - S^*, X_3 = I - I^*, X_4 = R - R^*$.The linearized system is as follows:

$$\begin{cases} dX_1 = -\delta X_1 dt + \sigma dB(t), \\ dX_2 = (-a_{21}X_1 - a_{22}X_2 - a_{23}X_3)\, dt, \\ dX_3 = (a_{21}X_1 + a_{32}X_2 - a_{33}X_3 + a_{34}X_3)\, dt, \\ dX_4 = (a_{43}X_3 - a_{44}X_4)\, dt. \end{cases} \tag{15}$$

While $a_{21} = S^*I^*, a_{22} = \beta^*I^* + \mu, a_{23} = \beta^*S^*, a_{32} = \beta^*I^*, a_{33} = (\alpha + k + \mu) - \beta^*S^*, a_{34} = \gamma, a_{43} = k, a_{44} = \mu + \gamma$.

Theorem 4.1. *Let (X_1, X_2, X_3, X_4) be the solution of the system (3) with any initial value $(X_1(0), X_2(0), X_3(0), X_4(0)) \in \mathbb{R} \times \mathbb{R}_+^4$. If $R_0^s > 1$,then there is a local normal density function $\Phi(X_1, X_2, X_3, X_4)$ and Σ is satisfy the following function:*

$$\Phi(X_1, X_2, X_3, X_4) = (2\pi)^{-\frac{3}{2}} |\Sigma|^{-\frac{1}{2}} e^{-\frac{1}{2}(X_1, X_2, X_3, X_4)\Sigma^{-1}(X_1, X_2, X_3, X_4)^T}. \tag{16}$$

While

$$\Sigma = (a_{21}a_{43}C_2)^2 J_1^{-1}J_2^{-1}J_3^{-1}J_4^{-1}\Sigma_1\left(J_1^{-1}J_2^{-1}J_3^{-1}J_4^{-1}\right)^T, \tag{17}$$

$$\begin{aligned}
&C_0 = a_{32}+a_{23}+a_{33}-a_{22}, C_1 = C_0-(a_{23}+a_{33}), C_2 = -(\tfrac{C_0C_1+a_{44}C_0}{a_{43}}) \neq 0,\\
&C_3 = -C_0C_2a_{23}+C_2(C_0+a_{44})^2-C_1C_2(C_0+a_{44})+C_2(C_2a_{43}+C_1^2),\\
&C_4 = C_2a_{43}a_{23}+[C_1C_2-C_2(C_0+a_{44})]a_{43}+C_1(C_2a_{43}+C_1^2),
\end{aligned}$$

and

$$J_1 = \begin{pmatrix} 1&0&0&0\\ 0&1&0&0\\ 0&1&1&0\\ 0&0&0&1 \end{pmatrix}, J_2 = \begin{pmatrix} 1&0&0&0\\ 0&1&0&0\\ 0&0&0&1\\ 0&0&1&0 \end{pmatrix}, J_3 = \begin{pmatrix} 1&0&0&0\\ 0&1&0&0\\ 0&0&1&0\\ 0&0&\frac{C_1}{a_{43}}&1 \end{pmatrix},$$

$$J_4 = \begin{pmatrix} C_2a_{21}a_{43} & a_{43}[C_1C_2-C_2(C_0+a_{44})]-C_2a_{43}(a_{23}-a_{22}) & C_3 & C_4\\ 0 & C_2a_{43} & C_1C_2-C_2(C_0+a_{44}) & C_2a_{43}+C_1^2\\ 0 & 0 & C_2 & C_1\\ 0 & 0 & 0 & 1 \end{pmatrix},$$

$$\Sigma_1 = \begin{pmatrix} \frac{d_2d_3-d_1d_4}{2\left(d_1d_2d_3-d_3^2-d_1^2d_4\right)} & 0 & -\frac{d_3}{2\left(d_1d_2d_3-d_3^2-d_1^2d_4\right)} & 0\\ 0 & \frac{d_3}{2\left(d_1d_2d_3-d_3^2-d_1^2d_4\right)} & 0 & -\frac{d_1}{2\left(d_1d_2d_3-d_3^2-d_1^2d_4\right)}\\ -\frac{d_3}{2\left(d_1d_2d_3-d_3^2-d_1^2d_4\right)} & 0 & \frac{d_1}{2\left(d_1d_2d_3-d_3^2-d_1^2d_4\right)} & 0\\ 0 & -\frac{d_1}{2\left(d_1d_2d_3-d_3^2-d_1^2d_4\right)} & 0 & \frac{d_1d_2-d_3}{2d_4\left(d_1d_2d_3-d_3^2-d_1^2d_4\right)} \end{pmatrix}.$$

The parameters in Σ_1 are as follows:

$$\begin{aligned}
&d_1 = \delta+a_{22}+a_{33}+a_{44},\\
&d_2 = a_{23}a_{32}+a_{22}a_{44}+a_{22}a_{33}+a_{33}a_{44}+(a_{22}+a_{33}+a_{44})\delta-a_{34}a_{43},\\
&d_3 = \delta(a_{23}a_{32}+a_{22}a_{44}+a_{22}a_{33}+a_{33}a_{44}-a_{34}a_{43})+a_{23}a_{32}a_{44}-a_{34}a_{43}a_{22},\\
&d_4 = \delta(a_{23}a_{32}a_{44}-a_{34}a_{43}a_{22}).
\end{aligned}$$

Proof. For system (15), it also has the from:

$$dX = AXdt+ZdB(t), \tag{18}$$

while $X = (X_1,X_2,X_3,X_4)^T$, $Z = diag(\sigma,0,0,0)$,

$$A = \begin{pmatrix} -\delta & 0 & 0 & 0\\ -a_{21} & -a_{22} & -a_{23} & a_{24}\\ a_{21} & a_{32} & -a_{33} & 0\\ 0 & 0 & -a_{43} & -a_{44} \end{pmatrix}. \tag{19}$$

and we consider the following equation:

$$\varphi(\lambda) = \lambda^4+d_1\lambda^3+d_2\lambda^2+d_3\lambda+d_4, \tag{20}$$

where

$$
\begin{aligned}
d_1 &= \delta + a_{22} + a_{33} + a_{44},\\
d_2 &= a_{23}a_{32} + a_{22}a_{44} + a_{22}a_{33} + a_{33}a_{44} + (a_{22} + a_{33} + a_{44})\delta - a_{34}a_{43},\\
d_3 &= \delta(a_{23}a_{32} + a_{22}a_{44} + a_{22}a_{33} + a_{33}a_{44} - a_{34}a_{43}) + a_{23}a_{32}a_{44} - a_{34}a_{43}a_{22},\\
d_4 &= \delta(a_{23}a_{32}a_{44} - a_{34}a_{43}a_{22}).
\end{aligned}
$$

According to the RouthCHurwitz criterion, we obtain that $d_1d_2 - d_3 > 0, d_1d_2d_3 - d_3^2 - d_1^2d_4 > 0$. And system (3) has a unique probability density function, according to literature[10][11] and it satisfies the following FokkerCPlanck equation:

$$
\begin{aligned}
&-\frac{\sigma^2}{2}\frac{\partial^2}{\partial X_1^2}\Phi + \frac{\partial}{\partial X_1}(-\delta X_1\Phi) + \frac{\partial}{\partial X_2}\left[(-a_{21}X_1 - a_{22}X_2 - a_{23}X_3)\Phi\right]\\
&+\frac{\partial}{\partial X_3}\left[(a_{21}X_1 + a_{32}X_2 - a_{33}X_3 - a_{34}X_4)\Phi\right] + \frac{\partial}{\partial X_4}\left[(a_{43}X_3 - a_{44}X_4)\Phi\right] = 0,
\end{aligned}
\tag{21}
$$

and

$$
\Phi(x) = l_0 e^{-\frac{1}{2}XQX^T}. \tag{22}
$$

And l_0 is a positive constant and $\int_{\mathbb{R}^3_+}\Phi(x)dX = 1$. And B need accord with the following equation:

$$
BZ^2B + A^TB + BA = 0. \tag{23}
$$

here B is positive definite, let $\Sigma = B^{-1}$, then

$$
Z^2 + A\Sigma + \Sigma A^T = 0. \tag{24}
$$

by calculation, $A_1 = J_4J_3J_2J_1AJ_1^{-1}J_2^{-1}J_3^{-1}J_4^{-1}$, Thus Eq. (24) can be expressed as follows:

$$
J_4J_3J_2J_1Z^2J_1^TJ_2^TJ_3^TJ_4^T + A_1J_4J_3J_2J_1\Sigma J_1^TJ_2^TJ_3^TJ_4^T + J_4J_3J_2J_1\Sigma J_1^TJ_2^TJ_3^TJ_4^TA_1^T = 0. \tag{25}
$$

Through calculating,

$$
J_4J_3J_2J_1Z^2J_1^TJ_2^TJ_3^TJ_4^T = (C_2a_{21}a_{43})^2Z^2 \text{ and } J_4J_3J_2J_1\Sigma J_1^TJ_2^TJ_3^TJ_4^T = (C_2a_{21}a_{43})^2\Sigma_1, \tag{26}
$$

where

$$
\Sigma_1 = \begin{pmatrix}
\frac{d_2d_3 - d_1d_4}{2\left(d_1d_2d_3 - d_3^2 - d_1^2d_4\right)} & 0 & -\frac{d_3}{2\left(d_1d_2d_3 - d_3^2 - d_1^2d_4\right)} & 0\\
0 & \frac{d_3}{2\left(d_1d_2d_3 - d_3^2 - d_1^2d_4\right)} & 0 & -\frac{d_1}{2\left(d_1d_2d_3 - d_3^2 - d_1^2d_4\right)}\\
-\frac{d_3}{2\left(d_1d_2d_3 - d_3^2 - d_1^2d_4\right)} & 0 & \frac{d_1}{2\left(d_1d_2d_3 - d_3^2 - d_1^2d_4\right)} & 0\\
0 & -\frac{d_1}{2\left(d_1d_2d_3 - d_3^2 - d_1^2d_4\right)} & 0 & \frac{d_1d_2 - d_3}{2d_4\left(d_1d_2d_3 - d_3^2 - d_1^2d_4\right)}
\end{pmatrix}.
$$

In the end, we use the Lemma 4.2 of [12], and Σ_1 is a positive definite matrix, thus this completes the proof.

5. Conclusion

Curz Vargas et al studied a deterministic model,but it does not take into account the influence of environmental noise on system parameters, in the paper, we consider that the important parameters are disturbed by Ornstein-Uhlenbeck process, which is more reasonable. We study a stochastic model and consider the disease transmission coefficient is affect by Ornstein-Uhlenbeck process. We prove some dynamic behaviors like solution of the global, and we get the condition of stationary distribution. Compared with this deterministic model, the dynamical analysis of the system is more reasonable.

Acknowledgments: This work was supported by the Natural Science Foundation of Changchun Normal University (No. 2021-005).

References

[1] Vargas-De-Len C. On the global stability of infectious diseases models with relapse[J]. Abstraction and Application Magazine, 2014, 9.

[2] Zhou Y, Jiang D. Dynamical behavior of a stochastic SIQR epidemic model with OrnsteinCUhlenbeck process and standard incidence rate after dimensionality reduction[J]. Communications in Nonlinear Science and Numerical Simulation, 2023, 116: 106878.

[3] Shi Z, Jiang D. Dynamical behaviors of a stochastic HTLV-I infection model with general infection form and OrnsteinCUhlenbeck process[J]. Chaos, Solitons Fractals, 2022, 165: 112789.

[4] Zhou B, Jiang D, Han B, et al. Threshold dynamics and density function of a stochastic epidemic model with media coverage and mean-reverting OrnsteinCUhlenbeck process[J]. Mathematics and Computers in Simulation, 2022, 196: 15-44.

[5] Zhou B, Jiang D, Dai Y, Hayat T. Stationary distribution and density function expression for a stochastic SIQRS epidemic model with temporary immunity. Nonlinear Dynam 2021;105(1):931C55.

[6] Y. Lin, D. Jiang, P. Xia, Long-time behavior of a stochastic SIR model, Appl. Math. Comput. 236 (2014) 1C9.

[7] N.H. Du, G. Yin, Conditions for permanence and ergodicity of certain stochastic predatorCprey models, J. Appl. Pro. 53 (2016) 187C202.

[8] Y. Cai, J. Jiao, Z. Gui, Y. Liu, W. Wang, Environmental variability in a stochastic epidemic model, Appl. Math. Comput. 329 (2018) 210C226.

[9] X. Zhang, R. Yuan, A stochastic chemostat model with mean-reverting OrnsteinCUhlenbeck process and Monod-Haldane response function, Appl. Math. Comput. 394 (2021) 125833.

[10] Gardiner CW. Handbook of stochastic methods for physics. Berlin: Springer; 1983.

[11] Roozen H. An asymptotic solution to a two-dimensional exit problem arising in population dynamics. SIAM J Appl Math 1989;49:1793C810.

[12] Han BT, Zhou BQ, Jiang DQ, Hayat T, Alsaedi A. Stationary solution, extinction and density function for a high-dimensional stochastic SEI epidemic model with general distributed delay. Appl Math Comput 2021;405:126236.

Fuzzy Systems and Data Mining IX
A.J. Tallón-Ballesteros and R. Beltrán-Barba (Eds.)

doi:10.3233/FAIA231051

Single-Channel Maternal ECG Removal with Block Residual Network

Wei Zhong [1] and Jiahui Luo
Guangdong Police College, Guangzhou, China

Abstract. Abdominal ECG (AECG) taken from a pregnant woman's abdomen provides a non-invasive method to monitor the health of the fetus in the pregnant women. However, maternal ECG interference in abdominal ECG leads to a challenging fetal ECG (FECG) extraction problem, and therefore, this work attempts to propose an effective maternal ECG elimination strategy. Specifically, the single channel AECG signal is input into a block residual network (Block-ResNet), which outputs an estimation of the MECG signal. Then, the estimated MECG is eliminated to obtain the FECG signal. Analysis is performed using real AECG signals from two databases. The experimental results show that the Block-ResNet model obtains the best results during the testing process with SE of 93.43%, PPV of 91.51 % and F1 of 92.45%. It sheds light to the topic of MECG elimination in the field.

Keywords. residual network, maternal ECG removal, fetal ECG extraction, fetal monitoring

1. Introduction

Abdominal ECG (AECG) can be used not only to calculate the fetal heart rate, but also to obtain fetal heart waveforms related to health [1]. However, the maternal ECG (MECG) mixed in the AECG leads to a challenging problem of fetal ECG (FECG) extraction. Therefore, useful algorithms are needed to eliminate MECG interference in AECG.

To date, several algorithms have been previously applied for the task of FECG extraction with varying degrees of success. These algorithms include: blind source separation methods (BSS), template subtraction methods (TS) and adaptive filtering methods[1]. The objective of BSS algorithms is to separate the underlying statistically independent sources of the AECG recording into three categories: MECG, FECG and other noise interference. In order to exert the efficiency of the BSS algorithm, it requires to record many AECG channels at the same time. The adaptive filtering algorithm is a classical algorithm for removing noise from corrupted signals[2]. As the maternal ECG collected from the chest does not have the FECG component, it is often used as a reference signal of noise in the ANC algorithm for noise canceling. The goal of adaptive filtering algorithms is to learn a a filter to remove the abdominal noise adaptively. The TS algorithm aims to build a MECG template centered on the mother R-peak. By eliminating the generated MECG template, the fetal ECG component can be obtained.

[1]Corresponding Author: Wei Zhong, Guangdong Police College, Guangzhou, China; E-mail: zhongwdavid@foxmail.com.

Residual network (ResNet) is a kind of neural network capable of non-linear modeling of dynamical systems. In this work, a Block-ResNet model is implemented for MECG cancelation. The proposed methodology has three contributions:

- To address the challenge of cancelling out the maternal component from the AECG to obtain the desired fetal ECG, we build the MECG cancelation model by using a block residual network. This is a useful experiment in the field.
- Unlike the BSS techniques which use multiple abdominal ECG signals, focusing on single-channel MECG cancelation techniques provides new ideas for producing easy-to-use fetal heart monitoring devices.
- By comparing the Block-ResNet model with seven other state-of-the-art maternal ECG interference removal algorithms, it is found that the proposed technique achieves good results in maternal ECG elimination.

2. Methods

2.1. Task Formulation

Neural networks are models with strong generative power. Neural network model with convolution and deconvolution operations has not only achieved success in image processing, but also achieved good results in one-dimensional signal processing, such as arrhythmia detection and fetal ECG compression [3]. Therefore, the Block-ResNet model is used for maternal ECG removal tasks in this work. Abdominal ECG (AECG) taken from a pregnant woman's abdomen is a mixed signal of multiple components

$$Z = X + Y + n \tag{1}$$

where $Z = [z_1, z_2, ..., z_n] \in \mathbf{R}^{1\times n}$ is the mixed abdominal signal AECG. $X = [x_1, x_2, ..., x_n] \in \mathbf{R}^{1\times n}$ is the signal of interest (MECG component), where n is the noise interference. And $Y = [y_1, y_2, ..., y_n] \in \mathbf{R}^{1\times n}$ is the FECG component in the mixed abdominal signal AECG.

The goal of this study is to implement a mapping function $F(\cdot)$ whose inputs are AECG signal Z and whose outputs are estimated MECG component $\hat{X}$.

$$\hat{X} = F(Z) \tag{2}$$

where $\hat{X} = [\hat{x}_1, \hat{x}_2, ..., \hat{x}_n] \in \mathbf{R}^{1\times n}$ is the estimated MECG signal. Then the FECG signal can be extracted by cancelling the maternal component ($\hat{X}$) in the AECG signal,

$$\hat{Y} = Z - \hat{X} \tag{3}$$

where $\hat{Y} = [\hat{y}_1, \hat{y}_2, ..., \hat{y}_n] \in \mathbf{R}^{1\times n}$ is the estimated FECG signal after removing the maternal ECG component, which consists of the FECG component Y and some noise. Noise in the abdominal ECG may still remain in the estimated FECG signal after the maternal ECG removal operation, such as the power-line interference and electromyography.

In this work, we do so by using a Block-ResNet for the task of MECG cancelation. The input in this case is the AECG signal recorded at the maternal abdomen. And the MECG component in the AECG is the target to the Block-ResNet. The Block-ResNet model is first trained with simulated abdominal ECG data during training, and then the performance of the model is evaluated with real abdominal ECG signals during testing.

2.2. Dataset

In the training stage, the ECG data from four different public databases are collected to form the training set. These databases include the FECG synthetic database (FECGSYNDB), the MIT-BIH ST change database (STDB), the MIT-BIH normal sinus rhythm database (NSRDB) and the Fantasia database (Fantasia). In the testing stage, the real abdominal recordings from two datasets are used to assess the performance of the Block-ResNet model. These datasets are the DaISy database (DaISy) and the abdominal and direct foetal electrocardiogram database (ADFECGDB) [4]. The data used in the experiment can be downloaded from the website: https://physionet.org/physiobank/database/adfecgdb/, http://homes.esat.kuleuven.be/ smc/daisy/.

Simulated ECG signals from the FECGSYNDB database are used for model training. To simulate more realistic maternal ECG characteristics, the adult ECG signals from the NSRDB, STDB and Fantasia are collected for further analysis. Specifically, the adult ECG signals are used to simulate the MECG component in the AECG, which is the target MECG to the Block-ResNet. Finally, after adding the FECG and MECG components, the simulated AECG is obtained and used as the input to the Block-ResNet.

To form the test set in this work, the abdominal recordings from DaISy and ADFECGDB datasets are used to test the maternal ECG elimination effect of the proposed methodology in the testing stage. All the data are resampled to 250 Hz and normalized to $[-1,1]$ for further analysis. In this study, we find that the proposed method is not sensitive to the frame size, and the L is set to 4s (1,000 sample points). After the dataset preparation stage, the training set includes $70,000$ training sample pairs. And the test set includes $1,504$ test samples. Note that the samples in the training and test sets do not contain each other. The neural network takes as input a time-series of abdominal features and outputs the generated maternal ECG, which is eliminated to obtain fetal ECG.

2.3. Model Architecture

In the field of medical signal processing, exemplified by arrhythmia detection, deep learning models have demonstrated strong decision-making and generative capabilities. In this study, we use a block residual network (Block-ResNet), which is a trainable nonlinear model, to implement a maternal ECG interference cancellation task.

Maternal ECG cancelation in this work can be seen as a sequence-to-sequence task. The proposed Block-ResNet model takes as input a sequence of abdominal ECG signals (Z), and outputs the generated maternal ECG $(\hat{X})$. The Block-ResNet model aims to form a mapping function $F(\cdot)$ to generate the latent maternal component in the abdominal ECG. During the training of the network model, the averaged mean squared error is used to measure the distance between the target MECG and generated MECG signals.

$$\ell(\Theta) = \frac{1}{M}\sum_{i=1}^{M} \|F(Z_i;\Theta) - X_i\|_F^2 \tag{4}$$

Here Θ is the parameters of the model to be trained, and $\{(Z_i, X_i)\}_{i=1}^{M}$ is a collection of M AECG-MECG training sample pairs, which are used to train the Block-ResNet model.

As shown in the Fig 1, the Block-ResNet model has one Dense block and three Conv-Deconv blocks, which are connected with shortcut connections between neighboring blocks. Therefore, the feature map of a Conv-Deconv block is passed to and summed

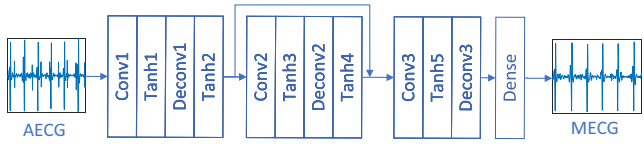

Figure 1. The structure of the Block-ResNet model. The Block-ResNet model contains three Conv-Deconv blocks and one Dense block, and each Conv-Deconv block contains one convolutional layer, one deconvolutional layer and one or two Tanh activation function layers. Dense block contains one fully connected layer.

with the feature map of adjacent Conv-Deconv block. The shortcut connections in the model pass the signal details to bottom layers directly. This operation makes models with deep structure easier to train, as demonstrated by subsequent experimental results.

There are two types of Conv-Deconv blocks in the Block-ResNet model. (*i*) Conv + Tanh + Deconv + Tanh, for the first two Conv-Deconv blocks, each Conv-Deconv block contains one convolutional layer, one deconvolutional layer and two Tanh activation function layers. (*ii*) Conv + Tanh + Deconv, for the last Conv-Deconv block, the last Conv-Deconv block contains one convolutional layer, one deconvolutional layer and only one Tanh activation function layer. Dense block contains one fully connected layer.

Convolutional and deconvolutional layers can be viewed as a feature extractor, which can be used to extract features of the abdominal ECG, and a feature generator, which can be used to generate the maternal ECG component of the abdominal ECG, respectively. And the Tanh activation function is utilized for nonlinearity. In some tasks, using multiple dense layers can improve the model's feature expression ability. However, increasing the number of dense layers did not show significant performance improvement in this study, so only one dense layer is used in the model.

During the experiment, good results can already be obtained by using three Conv-Deconv blocks, although the deeper structure leads to slightly better performance. We use 64 filters with size 1×3 for all the convolutional layers (e.g., Conv-Filter 1) and the first two deconvolutional layers (e.g., Deonv-Filter 1) . The last deconvolution operation consists of only one filter which generates a feature map. It is noted that using Adam to train the network in this study with learning rate 10^{-4} converges faster than using other optimizers. As shown in the Fig 2, the training loss rapidly decreases in the first 10 epochs, then slowly decreases, and gradually converges after 50 epochs.

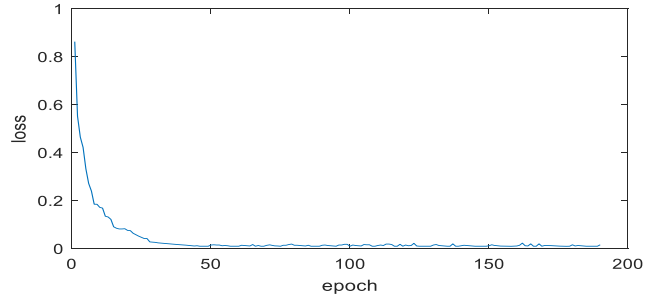

Figure 2. Training loss of the model.

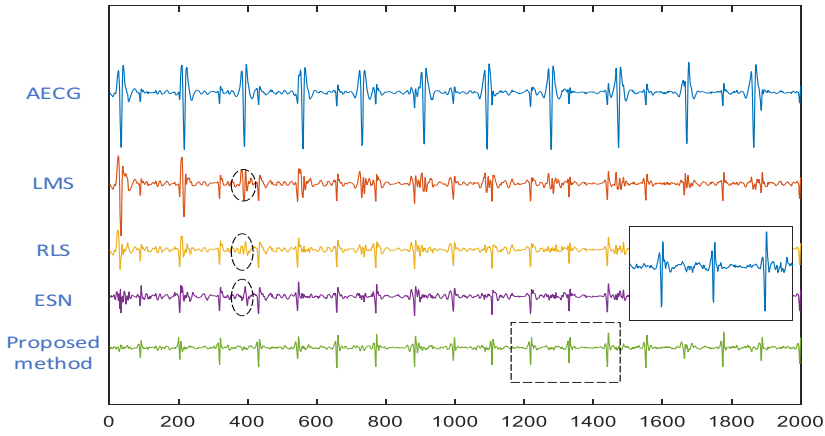

Figure 3. The experiment results on the DaISy.

3. Results

The recordings from the DaISy are collected for qualitative evaluation. Due to the lack of annotation on the fetal R-peak position in the DaISy dataset, R-peak comparison cannot be performed, and the effect of maternal ECG removal can only be analyzed graphically. For comparisons, three other ANC techniques are implemented to extract the FECG components from the same AECG recordings as baselines. These techniques include the the least mean square (LMS), recursive least square (RLS), and the Echo State neural Network (ESN) [5]. The experiment results are shown in Fig 3.

As shown in Fig 3, the superiority of the proposed method is obvious on the maternal ECG elimination task. It is noted that the MECG components are effectively removed, resulting in higher quality fetal ECG signals. More details of the results are discussed in Section 4. In this study, each of the methods is used to cancel out the MECG to get the residual signal, which comprise of the FECG and some noise.

The paper also provides a quantitative assessment of the model's performance using ECG signals from the ADFECGDB. Due to the lack of fetal ECG from abdominal ECG for comparison, the effect of maternal ECG removal is often tested by fetal R-peak detection. That is, the maternal ECG removal is measured here according to the degree of agreement of the detected fetal R-peak with the labeled R-peak. Three indicators are involved: sensitivity (SE), positive predictive value (PPV) and F_1 measure [1].

The proposed technique was compared with four other maternal ECG interference cancellation algorithms. These methods include the Cerutti method (Cerutti), the Suzanna method (Suzanna), the Vullings method (Vullings), and the Kanjial method (Kanjial) [6–8]. The experiment results are shown in TABLE 1. To highlight the robustness of the proposed method, the performance on the mean values of the three metrics are evaluated.

4. Discussions

In this study, a Block-ResNet based method is proposed for MECG elimination that requires only a single-channel abdominal ECG signal. This is a considerable advantage

Table 1. Evaluation results on the ADFECGDB

Methods	*SE* (%)	*PPV* (%)	F_1 (%)
Cerutti	82.47	82.58	82.37
Suzanna	82.26	82.51	82.21
Vullings	78.12	78.55	78.28
Kanjilal	86.71	85.21	85.95
Proposed method	**93.43**	**91.51**	**92.45**

over the techniques which require high number of channels such as the blind source separation techniques. It should be noted that focusing on single-channel FECG extraction techniques provides new ideas for producing easy-to-use fetal heart monitoring devices. And the results show that a reliable performance can also be achieved.

Fig 3 shows the maternal ECG elimination effects on DaISy database of different methods. One of the theoretical limitations of the ANC techniques is that the adaptive filter requires a reference signal that is morphologically similar to the abdominal MECG waveform for MECG cancelling and FECG extraction. Using thoracic MECG as a reference signal to completely remove the MECG component from abdominal ECG is not always feasible because abdominal ECG and thoracic ECG are not always completely similar. It can be noted that the remnants of the MECG component (marked in the ellipses) can still be seen in the extracted FECG by using the three ANC techniques in the Fig 3 . The proposed method can successfully remove the MECG component and extract the FECG component. We believe that this is due to the excellent capability of the proposed Block-ResNet in capturing the features of the maternal component in the AECG. By analyzing the feature outputs of the different layers of the model, it is found that the first two blocks look like a feature extractor whose outputs are more similar to the input abdominal ECG, while the last block looks like a feature generator whose outputs are more consistent with the target maternal ECG.

TABLE 1 shows the performance of the four template subtraction techniques and the proposed method on the abdominal ECG signals obtained from the ADFECGDB database. The template subtraction techniques based on removing maternal templates make the FECG extraction possible. However, to get a satisfactory estimate of maternal component, some priori information such as the exact position of the maternal R peaks is needed. It is important to note that the exact location of the maternal R peak is not readily accessible when the FECG component has a high signal-to-noise ratio (SNR). Then the performance of these MECG elimination methods is reduced in such a situation. The proposed algorithm in this study does not require these priori information and is able to effectively avoid the problems associated with MQRS alignment in the MECG elimination process, resulting in high performance. Considering the mean values on the *SE*, *PPV* and F_1 measure, the Block-ResNet model outperforms the four other techniques, demonstrating that the proposed deep learning approach has higher robustness to effectively cancel out the maternal component and extract the FECG component in the AECG.

During the construction of the simulated abdominal ECG signal, in order to more closely approximate real-world scenarios, real adult ECG signals are used to simulate the maternal ECG component of abdominal ECG, and experimental results demonstrate the effectiveness of the methodology. However, it is difficult to say that it can completely fit the real world situation, because the noise environment in the real scene is more complex, and the model will be less effective on data that has not been seen before.

5. Conclusion

In this work, a Block-ResNet based method is proposed for single-channel MECG elimination. The method utilizes a Block-ResNet that takes as input a single channel of AECG recordings and outputs an estimate of the maternal ECG component. Thus, the FECG component is extracted from the AECG by subtracting the output maternal component. The proposed method could avoid the limitation related to MQRS slicing and alignment in MECG-elimination. The Block-ResNet model is compared with seven recent works on real abdominal ECG recordings from publicly available datasets. And results show that the Block-ResNet achieves the best performance. The key to the surpassing effect is that Block-ResNet is able to estimate the latent MECG component in the AECG very well. This study provides a useful reference for fetal ECG extraction studies in the field.

Acknowledgements

This work was supported by the Basic and Applied Basic Research Project of Guangzhou Basic Research Program (202201011295), Young Innovative Talents Projects in Ordinary Colleges and Universities in Guangdong Province (No. 2021KQNCX059).

References

[1] J. Behar, F. Andreotti, S. Zaunseder, J. Oster, and G. D Clifford, "A practical guide to non-invasive foetal electrocardiogram extraction and analysis," *Physiol. Meas.*, vol. 37, pp. 1–35, 04 2016.

[2] W. Zhong, L. Mao, and W. Du, "A signal quality assessment method for fetal qrs complexes detection," *Mathematical biosciences and engineering*, vol. 20, pp. 7943–7956, 2023.

[3] P. R. Muduli, R. R. Gunukula, and A. Mukherjee, "A deep learning approach to fetal-ecg signal reconstruction," in *2016 Twenty Second National Conference on Communication (NCC)*, pp. 1–6, March 2016.

[4] A. Goldberger, L. Amaral, L. Glass, JMHausdorff, P. Ivanov, R. Mark, J. Mietus, G. Moody, C.-K. Peng, and H. Stanley, "Physiobank, physiotoolkit, and physionet: Components of a new research resource for complex physiologic signals. circulation," *Circulation*, vol. 101, no. 23, pp. 215–220, 2000.

[5] J. Behar, A. Johnson, G. D. Clifford, and J. Oster, "A comparison of single channel fetal ecg extraction methods," *Ann. Biomed. Eng.*, vol. 42, no. 6, pp. 1340–1353, 2014.

[6] S. Cerutti, G. Baselli, S. Civardi, E. Ferrazzi, A. Marconi, M. Pagani, and G. Pardi, "Variability analysis of fetal heart rate signals as obtained from abdominal electrocardiographic recordings.," *J. Perinatal Med. Off. J. WAPM*, vol. 14, no. 6, pp. 445–452, 2009.

[7] R. Vullings, C. H. L. Peters, R. J. Sluijter, M. Mischi, S. G. Oei, and J. W. M. Bergmans, "Dynamic segmentation and linear prediction for maternal ecg removal in antenatal abdominal recordings," *Physiol. Meas.*, vol. 30, no. 3, p. 291, 2009.

[8] P. P. Kanjilal, S. Palit, and G. Saha, "Fetal ecg extraction from single-channel maternal ecg using singular value decomposition," *IEEE Trans. Biomed. Eng.*, vol. 44, pp. 51–59, Jan 1997.

Fuzzy Systems and Data Mining IX
A.J. Tallón-Ballesteros and R. Beltrán-Barba (Eds.)

doi:10.3233/FAIA231052

E-Yolov7: A Life Jacket Detection Algorithm Based on Yolov7

Jiajia XU[a,1] and Changming ZHU[a]
[a]*School of Information Engineering, Shanghai Maritime University, China*

Abstract. As the core equipment of water safety, life jackets play an indispensable role in the safety field and rescue applications. Although existing deep learning techniques and object detection methods have achieved remarkable success in various fields, there are still many challenges in applying them to life jacket detection. Complex environmental changes, occlusion problems caused by water surface fluctuations, etc. will affect the detection effect. In addition, there are relatively few datasets suitable for life jacket detection, which makes many existing detection models lack stability and generalization ability in practical application scenarios. In order to address these challenges, this paper aims to propose an efficient and accurate detection method for life jacket object detection. Specifically, we first review the relevant work of sea rescue, then collect and label a life jacket-related dataset, and then introduce EVC block based on the Yolov7 network to aggregate the local corner area information of the image, and propose an improved life jacket target detection method E-Yolov7. In the experimental and evaluation section, the proposed method was tested, comparing it with Yolov5s, Yolov7-Tiny, Yolov7x, and Yolov7. Experiments show that the improved model E-Yolov7 has better performance in the life jacket detection task, and compared with Yolov7, the precision is increased by 3.7 %, the mAP is increased by 2.5% and the F1 score is increased by 2 %.

Keywords. Yolov7, life jacket detection, deep learning, EVC

1. Introduction

Detecting life jackets is an important application of object detection technology in the field of water safety. To ensure the safety of water activities and improve the efficiency of emergency rescue operations, researchers have conducted extensive work in the detection of life jackets.

In the early stages of life jacket detection research, traditional computer vision methods such as feature-based detection and classifiers were predominantly employed. Researchers used techniques like edge detection and color segmentation to identify the features of life jackets. However, these approaches exhibited limited robustness in complex scenes and under varying lighting conditions, making them inadequate to meet practical requirements.

With the emergence of deep learning, especially the development of Convolutional Neural Networks (CNNs), researchers began to explore the application of deep learning

[1] Corresponding Autho: Jiajia Xu, School of Information Engineering, Shanghai Maritime University, Shanghai, China. E-mail: 1353171026@qq.com.

to life jacket detection. Some studies utilized classic CNN architectures like AlexNet and VGG to train detection models for life jackets.

Ye et al. [1] proposed an automated detection model based on semantic segmentation. To achieve better results, improvements and optimizations were made to the classic U-net network in semantic segmentation. Special convolutional layers were used instead of max-pooling layers, an additional dropout layer was added to prevent overfitting, and reflective padding was applied to enable the extraction of more features by convolutional kernels. Liu et al. [2] introduced a method to simultaneously identify multiple ship targets based on ship color, size, and kinematic features. They established a transformation calculation model between image coordinates and real-world environment coordinates. Zhang et al. [3] applied Adaboost and Haar-like feature algorithms to image recognition. However, most of these approaches were mainly targeted at single-background image libraries. The actual images captured often presented complex backgrounds and significant shape variations due to shooting angles, which made traditional methods less effective in identifying water-based images. Fan et al. [4] used AlexNet as a basic network and employed a deep belief network (DBN) to classify images based on spectral and texture features. Yang et al. [5] designed an algorithm to detect life jackets in complex ferry terminal environments. This algorithm utilized statistical HSV color range information and boundary tracking methods to locate life jacket regions in images. Liu et al. [6] proposed a single-camera vision-based approach for unmanned boats involved in water search and rescue operations. An algorithm based on RGB color features was used for target localization, segmenting the target regions in the images. The VGG-F model was then used to extract and identify the water surface images.

In recent years, the Yolo (You Only Look Once) series has also found application in life jacket detection. Weng et al. [7] utilized Yolov5 to propose a detection algorithm capable of identifying life jackets in backlit environments on rivers, aiming to enhance law enforcement efficiency in water-based units.

Despite the significant successes achieved by existing deep learning techniques and object detection methods in various fields, challenges still exist in applying them to life jacket detection. Challenges include complex maritime environments, varying sea conditions, water turbulence, and occlusions, all of which can impact the accuracy and real-time performance of detection algorithms. To this end, many scholars have also made efforts in this regard [9][11].

Additionally, there is a relative scarcity of specialized datasets suitable for life jacket detection, which limits the stability and generalization capabilities of many existing detection models in real-world application scenarios. In order to address these challenges, this paper aims to propose an efficient and accurate detection method for life jacket object detection. The main contributions of this paper are as follows:

- A detection framework based on Yolov7 to determine whether people are wearing life jackets is proposed.
- The dataset of object detection for whether people are wearing life jackets is collected and annotated, and the situation under different lighting and fogging at sea is simulated by using image enhancement to improve the robustness of the model.
- Through a series of experimental evaluations and comparisons, it is proved that the method proposed in this paper is effective and meaningful.

2. Materials and Methods

2.1. Dataset

Since there are relatively few specialized datasets suitable for life jacket testing, in this research paper, we obtained relevant images on the web through keyword searches, and manually removed images that did not meet our requirements (such as the case of too much obscuration and the person being too small for the human eyes to distinguish whether the person is wearing the life jacket), and then processed the images, unified the size, and enriched the dataset with image enhancement and data enhancement methods. Use color dithering to adjust the saturation, brightness, contrast, etc. of the picture, which is used to simulate the situation under different lighting and climate. The labeling work uses the lableimg, which is used for the annotation. Considering that life jackets are the main detection object, so we pay more attention to life jackets when labeling.

Our proposed dataset contains a total of 4138 images, of which 3100 are in the training set, 534 in the validation set and 504 in the test set. The height and width of the images are 640 pixels. Some of the images in the dataset are shown in Figure 1. The quantitative distribution of labels is shown in Table 1. It contains a total of 7101 'nowear' and 7657 'wear' labels, of which there are 5390 'nowear' labels and 5648 'wear' labels in the training set, 895 'nowear' 993 'wear' labels in the validation set and 816 'nowear' labels and 1016 ' wear' tags in the validation set, 816 'nowear' tags and 1016 ' wear' tags in the test set.

Figure 1. Some examples of dataset.

Table 1. The labels distribution of the dataset

	Train	Val	Test	Total
Nowear	5390	895	816	7101
Wear	5648	993	1016	7657
Total	11038	1888	1832	14758

2.2. Method

So far, Yolo has appeared in several versions [12][20], each with certain improvements over the previous version. The method proposed in this paper is based on Yolov7 [20]. In this article, we used Yolov7 [20] as infrastructure and improved it. The improved network structure in this paper is shown in Figure 2, which consists of a backbone and a head network.

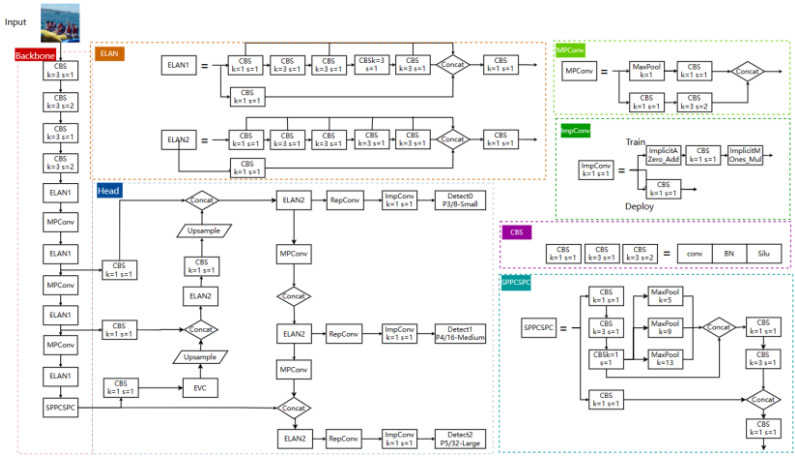

Figure 2. The network structure of E-Yolov7.

The backbone network is used to extract image features. This part follows the backbone network of Yolov7, which is mainly composed of four modules: CBS (Conv-BN-SiLU), ELAN1, MPConv, and SPPCSPC. Besides, There are some changes in the head network. We added ECV block to the top-level feature map.

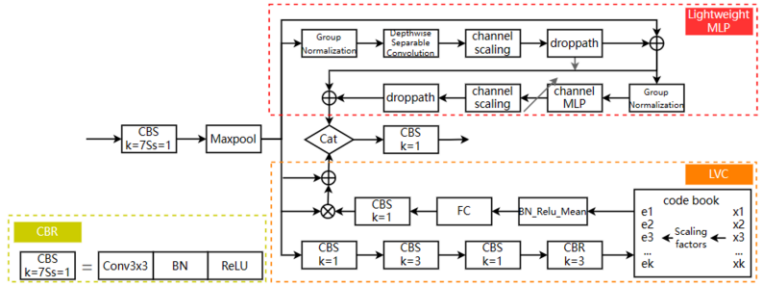

Figure 3. The structure of EVC block.

The new EVC block originated from the CFP network [11], and is mainly composed of lightweight MLP module and LVC (learnable Visual Center) module. The structure of it is shown in Figure 3. Firstly, the obtained feature map is smoothed by a CBS module, and then the obtained feature X_{in} is used as input to the lightweight MLP module and the LVC module through the maxpool. lightweight MLP mainly consists of two residual blocks, one is a residual block based on DWConv and the other is a residual block based on Channel MLP. Specifically, X_{in} is solved by Group Normalization for group normalization, and then the channel number is changed after Depthwise Separable Convolution, and then DropPath randomly drops some branches to improve the generalization ability and robustness of the network.

The obtained result is concated with X_{in} on the channel to get the output $LMLP\_DW_{out}$ of the first residual block, and it is used as the input of the second residual block. In the second residual block, $LMLP\_DW_{out}$ undergoes Group Normalization, then fuses the channel information through the Channel MLP module, then changes the number of channels and performs DropPath to randomly discard some of the branches, and then concat the result with $LMLP\_DW_{out}$ on the channel to obtain the output $LMLP_{out}$ of the lightweight MLP. The output of lightweight MLP is $LMLP_{out}$. The LVC module is an encoder with a fixed codebook. It consists of a fixed codebook and a set of

learnable Scaling Factors. Specifically, X_{in} is first encoded by a convolutional group containing 1x1, 3x3, 1x1, and then grouped by the CBR module, the result obtained. After that, the result is fed into the codebook and a set of scaling factors is used to obtain the encoding result, the k-th codeword can be calculated by Eq. (1).

$$e_k = \sum_{i=1}^{N} \frac{e^{-s_k \|x_i - b_k\|^2}}{\sum_{j=1}^{K} e^{-s_k \|x_i - b_k\|^2}} (x_i - b_k) \tag{1}$$

$$e = \sum_{k=1}^{K} \phi(e_k) \tag{2}$$

Where N is the total spatial number of input features, s_k is the k-th scaling factor, x_i is the k-th pixel point, and b_k is the k-th learnable visual codeword, then x_i-b_k is the relative position information of both, and K is the total number of visual centers. Then use Eq. (2) to get the whole image about k codewords all the information e, where contains BN layer with ReLU and mean layer, and then put the e input to the fully connected layer, after connecting a 1x1 convolution, and then multiply the obtained result with X_{in} on the channel, and then add to get the output LVC_{out} , and finally splice $LMLP_{out}$ and LVC_{out} on the channel and then pass through a 1x1 CBS to get the output EVC_{out} of the EVC module.

3. Experiment

3.1. Experimental Environment and Evaluation Indicators

The training task is implemented on Python 3.8 and Pytorch 2.0.1. The device information for training includes NVIDIA RTX A4000, and 15.73GB of memory.

The experiments are conducted using end-to-end training, for the fairness of the experiments, all the experiments in this case do not use pre-trained weights. The experiments are conducted using data augmentation such as mosaic, mixup, and so on. To assess the performance of the improved model, we use four evaluation metrics, including precision, recall, mAP and F1 score.

3.2. Comparison with Other Object Detection Models

In order to prove that the improved model in our work is effective, we compare the method proposed in this paper with the current mainstream Yolo series of object detection algorithms, such as Yolov5s, Yolov7-tiny, Yolov7x, Yolov7. The experimental results are shown in the Table 2, from which we can see that the precision of the improved model in this paper has 3.7% improvement compared with the results of the original model, 0.3% improvement in recall, 2.5% improvement in mAP, and 2% improvement in F1 score. And compared with other models in the experiment, the improved model in this paper is higher than other models except that Recall is lower than Yolov7x. Besides, The pr-curves of the proposed method and other target detection models are shown in Figure 4, from which we can see that E-Yolov7 is superior to several others.

It can be seen that the introduction of EVC module enables the model to better learn corner area information and long-range dependencies, which can improve the model's ability to extract features, and also proves that the text improvement is effective.

Table 2. The results of proposed method compared with other object detection models

method	p	R	mAP	F1
Yolov5s[16]	0.806	0.775	0.832	0.790
Yolov7-tiny[20]	0.790	0.776	0.818	0.780
Yolov7x[20]	0.832	**0.836**	0.873	0.830
Yolov7[20]	0.856	0.831	0.877	0.840
E-Yolov7	**0.893**	0.834	**0.902**	**0.860**

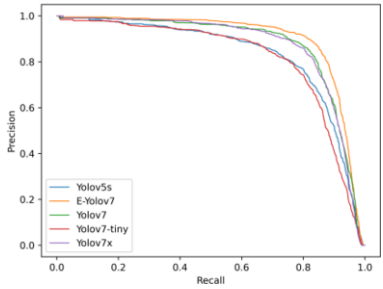

Figure 4. The pr-curves of the proposed method and other target detection models

3.3. Prediction Results of Yolov7 and E-Yolov7

Figure 5. The results of using Yolov7 and E-Yolov7 to predict the dataset presented in this paper.

On the dataset made in this study, Yolov7 and E-Yolov7 were used for prediction, the results are shown in the figure 5. Where (a) is the result of Yolov7 prediction, (b) is the result of E-Yolov7 prediction, through comparison, the improved method in this paper can reduce the false detection and missed detection, which proves that this study is effective for the detection of life jackets.

4. Conclusion

This study proposes a detection framework based on deep learning algorithm to determine whether people are wearing life jackets. In view of the problem of insufficient sea rescue datasets, we collected and annotated life jacket datasets. Using the current mature Yolov7 as the benchmark network, and the feature extraction capability of the model is improved by adding an EVC block at the top level of the feature pyramid. The improved model in this paper can obtain information on whether people are wearing life jackets and people's location information, through which it is convenient for administrators to manage marine or water projects, facilitate supervision of whether people wear life jackets as required, and timely determine their location information and remind tourists who are not wearing life jackets. The life jacket detection model proposed in this paper proves that the method proposed in this paper is effective and meaningful through a series of experimental evaluations and comparisons.

In addition, life jacket inspection faces many challenges, firstly, the time requirements for detection, which require our model to be lightweight enough to achieve

real-time results. Secondly, models need to be universal to adapt to different environments and data sets. The performance of the model presented in this article may degrade when applied to scenarios that are significantly different from the training dataset. Despite these challenges, our findings suggest that the improved model proposed in this paper has great potential to solve real-world problems. In the future, we plan to improve the detection accuracy and speed of life jacket inspection.

References

[1] Cheng Ye, Ji Li. Life Jacket Wearing Recognition Based on Semantic Segmentation. In: 2022 9th International Conference on Digital Home (ICDH). 2022; p. 141–146.
[2] Chenguang Liu, Xiumin Chu, Shuo Xie, et al. Multi-target Locating Method of Surface Ship Based on Monocular Vision. Journal of Traffic and Transportation Engineering. 2015;15(05):91-100.
[3] Junjie Zhang, Shuyan Ding, Lunbo Li. NAO Robot Player Recognition Based on Haar-like Features and Color Features. Computer And Modernization. 2017;(2):30-35.
[4] Hongwei Fan, Deshun Hu, Shuoqi Gao, et al. Intelligent Recognition Method and Experimental Verification of Ferrography Image Based on Deep Belief Network. Lubrication Engineering. 2021; 46(7):15-22.
[5] Xuesong Yang, Biye Cai, Jianming Zhang, et al. Life Jacket Detection Algorithm Based on HSV Color Feature and Contour Area. Computer Engineering and Applications. 2016;52(03):184-188+210.
[6] Mengjia Liu, Hui Feng, Haixiang Xu, et al. CNN-based Multi-object Detection Experiment for Search and Rescue Unmanned Boat on Water Surface. Journal of Wuhan University of Technology (Transportation Science & Engineering).2019;43(05):910-913+919.
[7] Qinglong Weng, Xiaoxiao Du, Kun Zhang. Deep Learning-based Law Enforcement Algorithm For Crew Life Jacket Detection with Color Features and Contour Areas. Chana Water Transport. 2023;(04 vo 23):42-43+46.
[8] Guang Han, Wang Zhou, Ning Sun, Jixin Liu and Xiaofei Li. Feature Fusion and Adversary Occlusion Networks for Object Detection. IEEE Access. 2019;7:124854-124865.
[9] Chunluan Zhou, Junsong Yuan. Occlusion Pattern Discovery for Object Detection and Occlusion Reasoning. IEEE Trans Circuits Syst Video Technol. 2020;2067-2080.
[10] Xuexue Li, Wenhui Diao, Yongqiang Mao, Peng Gao, et al. OGMN: Occlusion-guided Multi-task Network for Object Detection in UAV Images. ISPRS Journal of Photogrammetry and Remote Sensing. 2023;199:242–257.
[11] Yu Quan, Dong Zhang, Liyan Zhang, Jinhui Tang. Centralized Feature Pyramid for Object Detection. IEEE Trans on Image Process. 2023;32:4341–4354.
[12] Joseph Redmon, Santosh Divvala, Ross Girshick, and Ali Farhadi. You Only Look Once: Unified, Real-time Object Detection. Computer vision and pattern recognition. 2016;779-788.
[13] Joseph Redmon, and Ali Farhadi. YOLO9000: Better, Faster, Stronger. arXiv; arXiv preprint arXiv:1612. 08242,2016.
[14] Joseph Redmon and Ali Farhadi. Yolov3: An Incremental Improvement. arXiv preprint arXiv:1804. 02767, 2018. 1, 2, 3.
[15] Alexey Bochkovskiy, Chien-Yao Wang, and Hong-Yuan Mark Liao. Yolov4: Optimal Speed and Accuracy of Object Detection. arXiv preprint arXiv:2004. 10934, 2020. 1, 2, 3, 6.
[16] Glenn Jocher, et al. Yolov5. https://github. com/ ultralytics/yolov5, 2021. 1, 2, 3, 5, 6.
[17] Zheng Ge, Songtao Liu, Feng Wang, Zeming Li, and Jian Sun. YOLOX: Exceeding YOLO series in 2021. arXiv preprint arXiv:2107. 08430, 2021. 1, 2, 7, 10.
[18] Xin Huang, Xinxin Wang, Wenyu Lv, Xiaying Bai, et al. Pp-yolov2: A Practical Object Detector. arXiv preprint arXiv:2104. 10419, 2021. 3, 6.
[19] Chuyi Li, Lulu Li, Hongliang Jiang, Kaiheng Weng, et al. YOLOv6: A Single-Stage Object Detection Framework for Industrial Applications. arXiv preprint arXiv: 2209. 02976,2022.
[20] Chien-Yao Wang, Alexey Bochkovskiy, and Hong-Yuan Mark Liao. YOLOv7: Trainable Bag-of-freebies Sets New State-of-the-art For Real-time Object Detectors. In Proceedings of the IEEE/CVF Conference on Computer Vision and Pattern Recognition, Vancouver, CB, Canada, 18–22 June 2023; pp. 7464–7475.

Fuzzy Systems and Data Mining IX
A.J. Tallón-Ballesteros and R. Beltrán-Barba (Eds.)

doi:10.3233/FAIA231053

Time-Varying Formation Control for Multiagent Systems with Different Time Delays

Fenglan SUN [a,b,1], Qinbo LIANG [a], Wei ZHU [a] and Qiuying LI [a]
[a] *Key Lab of Intelligent Analysis and Decision on Complex Systems, School of Science, Chongqing University of Posts and Telecommunications, Chongqing, 400065, China*
[b] *Key Laboratory of Intelligent Air-Ground Cooperative Control for Universities in Chongqing, College of Automation, Chongqing University of Posts and Telecommunications, Chongqing, 400065, China*

Abstract. This article studies the time-varying formation (TVF) problem of multiagent systems (MASs) with different time delays. By designing the control protocol, the followers could achieve the desired TVF. Considering different communication delays, based on graph theory and stability theory, sufficient conditions for the system to realize TVF are obtained. Finally, the numerical example is employed to validate the effectiveness of theoretical results.

Keywords. TVF, MASs, different time delays.

1. Introduction

Recently, with the development of Internet technology and artificial intelligence technology, it has brought opportunities and challenges to the cooperative control of MASs. MASs cooperative control refers to a system composed of multiple agents, which completes the complex task through the communication, cooperation and control between agents. The collective behavior of MASs such as consensus [1,2,3], enclosure [4,5], formation [6,7] and so on has been widely studied. Particularly, the sthdy on formation control problem of MASs has become one of the research hot spots, such as the formation of wheeled robots [8], satellite detection [9] and UAV reconnaissance [10]. In the formation control problem of MASs, all agents must not only keep a certain distance, but also maintain a predetermined formation. Therefore, it's important to study the for-

[1]Corresponding author: Key Lab of Intelligent Analysis and Decision on Complex Systems, School of Science, Chongqing University of Posts and Telecommunications, Chongqing, 400065, China; Email addresses: sunfl@cqupt.edu.cn

This work is supported by the National Natural Science Foundation of China (No. 62373071), the Science and Technology Research Program of Chongqing Municipal Education Commission (No. KJZD-K202000601), the Natural Science Funds of Chongqing CSTC (No. cstc2019jcyj-msxmX0102), and the Research and Training Program for College Students of Chongqing University of Posts and Telecommunications (No. A2022-256).

mation problem by using the consensus theory [11,12]. In the actual environment, the cooperation between agents need to complete special tasks, such as terrain detection, formation flight [13], etc., which may require the formation of MASs to change with time. Therefore, TVF tracking should be considered. That is, followers track the leader's trajectory and form an expected TVF. TVF tracking problem is studied for single leader [14] and multiple leaders [15], respectively. Due to the time delays in the process of information transmission between agents, TVF problem with time delays is considered. Compared with the above work, this article mainly contributes from the following three aspects. Firstly, the leader's expected trajectory could be designed. In [16], only the final formation is investigated, and the movement of the leader is not considered. Secondly, the influence of time delay in TVF is considered. Thirdly, this paper considers different communication delays, which is more general than a single delay problem.

In the following of this article, concepts and assumption are given in Section 2. Sections 3 gives the main results. In Section 4 a simulation is concluded. Section 5 concludes article.

2. Preliminaries

Consider MAS with $N+1$ agents. Denote graph $G=\{\gamma,\partial,\varpi\}$ the communication between agents, $\gamma=\{\gamma_1,\gamma_2,\ldots,\gamma_{1+N}\}$ represents the vertex set, $\partial\subset\gamma\times\gamma$ means the edge set, $\varpi=[w_{ij}]\subset R^{(1+N)\times(1+N)}$ is the adjacency matrix. $F_1=\{1\}$, $F_2=\{2,3,\ldots,1+N\}$, and $F=F_1\cup F_2$. If $(\gamma_i,\gamma_j)\in\partial$, $w_{ij}>0$, that is, node i can directly get information from node j; otherwise, $w_{ij}=0$. Suppose that for all $i\in F$, $w_{ii}=0$. Denote D as a degree matrix of G, that is $D=diag\left\{\sum_{j=1}^{1+N}w_{ij},i=1,2,\ldots,1+N\right\}$. The Laplacian matrix $L=D-W$.

This article, the n-dimensional Euclidean space is denoted as R^n. The set of $m\times n$ matrices is represented as $R^{m\times n}$. A n-dimensional column vector is indicated as $\mathbf{1}_n$ with each entry being 1, I_n is the $n\times n$ identity matrix. For the matrix Υ, $\Upsilon>0$ means the positive definite matrix, and $diag\{\Upsilon_1,\Upsilon_2,\ldots,\Upsilon_{1+N}\}$ indicates the block diagonal matrix. Moreover, $\otimes$ is the Kronecker product. A^T represents the transpose of matrix A.

Assumption 2.1 *Assuming that the leader cann't accept the follower's information, while the follower accepts the leader's information, and there is information exchange between the followers.*

3. Main Results

Consider MAS consisting of N followers and 1 leader. The dynamic model can be described as

$$\begin{cases}\dot{x}_i(t)=Ax_i(t), & i\in F_1,\\ \dot{x}_g(t)=Ax_g(t)+Bu_g(t), & g\in F_2,\end{cases}\tag{3.1}$$

where $x_i(t)\in R^n$ and $x_g(t)\in R^n$ denote the states of leader i and follower g, and $u_g(t)\in R^m$ means the control input of the follower g. $A\in R^{n\times n}$ and $B\in R^{n\times m}$ indicate the system matrix. According to Assumption 2.1, one can get the Laplacian ma-

trix $L=\begin{bmatrix} 0 & 0 \\ L_2 & L_1 \end{bmatrix}$, where L_1 denotes the topological relationship between followers, L_2 represents the topological relationship between followers and leader.

Remark 3.1 *The system matrix rank(B)=m, and there exits the nonsingular matrix* $C=(\tilde{B}^T,\bar{B}^T)^T$, *where* $\tilde{B}\in R^{m\times n}$ *and* $\bar{B}\in R^{(n-m)\times n}$ *satisfy* $\tilde{B}B=I_m$ *and* $\bar{B}B=0$.

TVF of followers are designated as the vector $h_{F_2}(t)=(h_2^T(t),h_3^T(t),\ldots,h_{(N+1)}^T(t))^T\in R^N$, where $h_g(t)$ is a continuously differentiable vector function .

Definition 3.1 *MAS* (3.1) *with leader achieves TVF tracking, if for any bounded initial state, there is* $\lim_{t\to\infty}(x_g(t)-h_g(t)-x_i(t))=0$.

Design the follow's TVF tracking protocol

$$\begin{aligned} u_g(t)=&K\sum_{j\in F_2} w_{gj}(x_g(t-\iota_1)-h_g(t-\iota_1)-(x_j(t-\iota_1)-h_j(t-\iota_1))) \\ &+Kw_{gi}(x_g(t-\iota_2)-h_g(t-\iota_2)-x_i(t-\tau_2))+v_g(t), \end{aligned} \tag{3.2}$$

where $j\in F_2$, K is the gain matrix, $v_g(t)$ is the TVF compensation and provide by $v_g(t)=-\tilde{B}(Ah_g(t)-\dot{h}_g(t))$.

Remark 3.2 *This paper considers TVF problem with different delays.* ι_1 *represents the communication delay between followers,* ι_2 *denotes the communication delay between followers and leaders.*

Denote $\rho(t)=x(t)-h(t)-x_i(t)$, $\rho(t)=[\rho_2^T(t),\rho_3^T(t),\ldots,\rho_{N+1}^T(t)]^T$, $h(t)=[h_2^T(t),h_3^T(t),\ldots,h_{N+1}^T(t)]^T$, $x(t)=[x_2^T(t),x_3^T(t),\ldots,x_{N+1}^T(t)]^T$.

Derivation of $\rho(t)$, bring (3.2) into (3.1) one can get

$$\dot{\rho}(t)=(\mathrm{I}_n\otimes A)\zeta(t)-(L_1\otimes BK)\rho(t-\iota_1)(diag(L_2)\otimes BK)\rho(t-\iota_2), \tag{3.3}$$

Lemma 3.1 *[17] For any vector* $a,b\in R^m$, *there exists the matrix* $U>0$, *there is*

$$2a^Tb\le a^TUa+b^TU^{-1}b.$$

Lemma 3.2 *[18] If there exists a diagonal matrix* $W=W^T$ *and one of the block descriptions* $H=\begin{bmatrix} H_{11} & H_{12} \\ H_{21} & H_{22} \end{bmatrix}$, *where* $H_{11}\in R^{r\times r}$, *is nonsingular matrix, then* $H_{22}-H_{21}H_{11}^{-1}H_{12}$ *is called Schur complement of* H_{11} *in* W. *At the same time, the following conditions are equivalent:*

$$(i)H<0;(ii)H_{11}<0,H_{22}-H_{21}H_{11}^{-1}H_{12}<0;(iii)H_{22}<0,H_{11}-H_{12}H_{22}^{-1}H_{21}<0.$$

Theorem 3.1 *Under the control protocol* (3.2), *for MAS* (3.1) *with communication delay* τ_1 *and* τ_2, , *if there are matrices* Q_1, Q_2, Q_3, Q_4 *and* $Q_5>0$ *such that*

$$\psi = \begin{bmatrix} \psi_{11} & \psi_{12} & \psi_{13} & \psi_{14} & \psi_{15} & 0 \\ \psi_{12}^T & \psi_{22} & 0 & 0 & 0 & \psi_{26} \\ \psi_{13}^T & 0 & \psi_{33} & 0 & 0 & 0 \\ \psi_{14}^T & 0 & 0 & \psi_{44} & 0 & 0 \\ \psi_{15}^T & 0 & 0 & 0 & \psi_{55} & 0 \\ 0 & \psi_{26}^T & 0 & 0 & 0 & 0 \end{bmatrix} < 0 \tag{3.4}$$

holds, then MAS (3.1) *achieves the expected TVF and follows the tracking trajectory of the leaders, where* ψ *satisfies:*

$$\begin{aligned}
\psi_{11} &= Q_1 [I_n \otimes A - (L_1 + diag(L_2)) \otimes BK] - [I_n \otimes A - (L_1 + diag(L_2)) \otimes BK]^T Q_1 \\
&\quad + Q_2 + Q_3 + \iota_1 (I_n \otimes A)^T Q_4 (I_n \otimes A) + \iota_2 (I_n \otimes A)^T Q_5 (I_n \otimes A), \\
\psi_{12} &= -\iota_1 (I_n \otimes A)^T Q_4 (L_1 \otimes BK) - \iota_2 (I_n \otimes A)^T Q_5 (L_1 \otimes BK), \\
\psi_{22} &= -Q_2 + \iota_1 (L_1 \otimes B)^T Q_4 (L_1 \otimes BK) + \tau_2 (L_1 \otimes B)^T Q_5 (L_1 \otimes B), \\
\psi_{13} &= -\iota_1 (I_n \otimes A)^T Q_4 (diag(L_2) \otimes BK) - \iota_2 (I_n \otimes A)^T Q_5 (diag(L_2) \otimes BK), \\
\psi_{33} &= -Q_3 + \iota_1 (diag(L_2) \otimes BK)^T Q_4 (diag(L_2) \otimes BK) \\
&\quad + \iota_2 (diag(L_2) \otimes BK)^T Q_5 (diag(L_2) \otimes BK), \\
\psi_{14} &= Q_1 (L_1 \otimes BK), \psi_{44} = -\frac{Q_4}{\iota_1}, \psi_{15} = Q_1 (diag(L_2) \otimes BK), \psi_{55} = -\frac{Q_5}{\iota_2}, \\
\psi_{26} &= \iota_1 (L_1 \otimes BK)^T Q_2 (diag(L_2) \otimes BK) + \iota_2 (L_1 \otimes BK)^T Q_5 (diag(L_2) \otimes BK).
\end{aligned}$$

Proof: Choose the Lyapunov function as

$$\begin{aligned}
V(t) =& \rho^T(t) Q_1 \rho(t) + \int_{t-\iota_1}^{t} \rho^T(s) Q_2 \rho(s) \mathrm{d}s + \int_{t-\iota_2}^{t} \rho^T(s) Q_3 \rho(s) \mathrm{d}s \\
&+ \int_{-\iota_1}^{0} \int_{t+\eta}^{t} \dot{\rho}^T(s) Q_4 \dot{\rho}(s) \mathrm{d}s d\eta + \int_{-\iota_2}^{0} \int_{t+\eta}^{t} \dot{\rho}^T(s) Q_5 \dot{\rho}(s) \mathrm{d}s d\eta.
\end{aligned} \tag{3.5}$$

Along the trajectory of (3.3), the derivative of $V(t)$ in (3.5) is

$$\begin{aligned}
\dot{V}(t) =& 2\rho^T(t) Q_1 \dot{\rho}(t) + \rho^T(t) Q_2 \rho(t) - \rho^T(t-\iota_1) Q_2 \rho(t-\iota_1) \\
&+ \rho^T(t) Q_3 \rho(t) - \rho^T(t-\iota_2) Q_3 \rho(t-\iota_2) + \iota_1 \dot{\rho}^T(t) Q_4 \dot{\rho}(t) \\
&- \int_{t-\iota_1}^{t} \dot{\rho}^T(s) Q_4 \dot{\rho}(s) \mathrm{d}s + \iota_2 \dot{\rho}^T(t) Q_5 \dot{\rho}(t) - \int_{t-\iota_2}^{t} \dot{\rho}^T(s) Q_5 \dot{\rho}(s) \mathrm{d}s
\end{aligned} \tag{3.6}$$

By $\rho(t-\iota) = \rho(t) - \int_{t-\iota}^{t} \rho(s) ds$ and Lemma 3.1, one can get

$$\begin{aligned}\lambda_1 =& -2\rho^T(t)Q_1(L_1\otimes BK)\rho(t)+\int_{t-\iota_1}^{t}2\rho^T(t)Q_1(L_1\otimes BK)\dot{\rho}(s)ds\\ &\le -2\rho^T(t)Q_1(L_1\otimes BK)\rho(t)+\int_{t-\tau_1}^{t}\dot{\rho}^T(s)Q_4\dot{\rho}(s)\mathrm{d}s\\ &\quad+\iota_1\rho^T(t)Q_1(L_1\otimes BK)Q_4^{-1}(L_1\otimes BK)^TQ\rho(t),\end{aligned}\tag{3.7}$$

where $\lambda_1 = -2\rho^T(t)Q_1(L_1\otimes BK)\rho(t-\iota_1)$. And

$$\begin{aligned}\lambda_2 =& -2\rho^T(t)Q_1(diag(L_2)\otimes B)\rho(t)+\int_{t-\iota_2}^{t}2\rho^T(t)Q_1(diag(L_2)\otimes BK)\dot{\rho}(s)ds\\ &\le -2\rho^T(t)Q_1(diag(L_2)\otimes BK)\rho(t)+\int_{t-\iota_2}^{t}\dot{\rho}^T(s)Q_5\dot{\rho}(s)\mathrm{d}s\\ &+\iota_2\rho^T(t)Q_1(diag(L_2)\otimes BK)Q_5^{-1}(diag(L_2)\otimes BK)^TQ_1\rho(t),\end{aligned}\tag{3.8}$$

where $\lambda_2 = -2\rho^T(t)Q_1(diag(L_2)\otimes BK)\rho(t-\iota_2)$. Then

$$\dot{V}(t)\le\begin{bmatrix}\rho(t)\\ \rho(t-\iota_1)\\ \rho(t-\iota_2)\end{bmatrix}^T\begin{bmatrix}\tilde{\Psi}_{11} & \tilde{\Psi}_{12} & \tilde{\Psi}_{13}\\ \tilde{\Psi}_{12}^T & \tilde{\Psi}_{22} & \tilde{\Psi}_{23}\\ \tilde{\Psi}_{13}^T & \tilde{\Psi}_{23}^T & \tilde{\Psi}_{33}\end{bmatrix}\begin{bmatrix}\rho(t)\\ \rho(t-\iota_1)\\ \rho(t-\iota_2)\end{bmatrix}.\tag{3.9}$$

Since $\dot{V}(t)\le 0$, the necessary and sufficient condition is $\tilde{\Psi}=\begin{bmatrix}\tilde{\Psi}_{11} & \tilde{\Psi}_{12} & \tilde{\Psi}_{13}\\ \tilde{\Psi}^T{}_{12} & \tilde{\Psi}_{22} & \tilde{\Psi}_{23}\\ \tilde{\Psi}^T{}_{13} & \tilde{\Psi}_{23}^T & \tilde{\Psi}_{33}\end{bmatrix}<0$. The parameter $\tilde{\Psi}$ corresponds to (3.4), so the necessary and sufficient condition of $\tilde{\Psi}<0$ is $\Psi<0$ by Lemma 3.2. If (3.4) holds, there is $\lim_{t\to\infty}\rho(t)=0$. Theorem 3.1 is proved.

4. Examples

This section gives a numerical simulation to illustrate the main results in this paper.

Considering a third-order MAS (3.1) with 6 agents. The leader is marked as 1 and the followers are marked as $2,3,...,6$. Select $A=\begin{bmatrix}0 & 1 & 1\\ 1 & 2 & 1\\ -1 & -3 & -2\end{bmatrix}$, $B=\begin{bmatrix}0 & 1\\ -1 & 0\\ 0 & 0\end{bmatrix}$. The communication topology G_1 is given in Figure 1. The initial state of agents are randomly selected in $(-10,10)$. The expected TVF of the system (3.1) is designed as

$$h_g(t)=[15\sin(t+0.2(g-1)\pi),-15\cos(t+0.2(g-1)\pi),30\cos(t+0.2(g-1)\pi)]^T,$$

where $(g=2,3,\ldots,6)$. Under the control protocol (3.2), choose $K=\begin{bmatrix}1 & 4 & 0.5\\ -1 & -1 & -0.3\end{bmatrix}$. $\tilde{B}=\begin{bmatrix}0 & -1 & 0\\ 1 & 0 & 0\end{bmatrix}$, $\bar{B}=\begin{bmatrix}0 & 0 & 1\end{bmatrix}$. The maximum allowable delays of the system are ι_1=0.493 and ι_1=0.583. Choose ι_1= 0.3s, ι_2= 0.25s. The position state trajectories of the agents

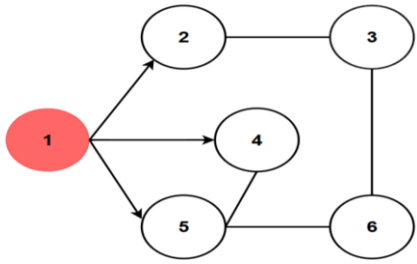

Figure 1. Communication topology G_1.

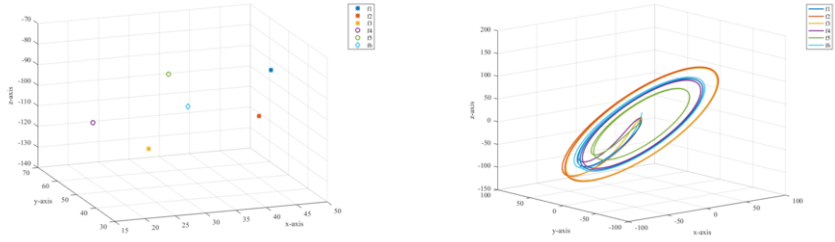

(a) (b)

Figure 2. (a) The position state of the agents at t =20s; (b) The motion trajectory of the agents in 0-20s.

at t =20s are given in (a), and the motion trajectorirs of the agents in 0-20s are given in (b) of Figure 2, respectively.

From (a) in Figure 2, one can be seen that the leader is the center and the followers form a regular pentagon shape. From (b) in Figure 2, one can find that the agent moves from the initial state to the desired trajectory, which means that all agents achieve the desired TVF tracking.

5. Conclusions

This article, TVF control problem of MASs with different time delays is investigated. By designing the control protocol, sufficient conditions for MASs reach TVF tracking is given. The presented simulation example verifies the correctness of the main results. However, the TVF problem of nonlinear MASs with different delays has not been studied. This is the next work to be done.

References

[1] F. Sun, X. Wu, J. Kurths and W. Zhu, Group consensus of heterogeneous multi-agent systems with packet loss and unknown speed of second-order agents in cooperative-competitive networks, Nonlinear Dynamics, 2022, 110(4):3447-3461.

[2] F. Sun, C. Lu, W. Zhu and J. Kurths, Data-sampled mean-square consensus of hybrid multi-agent systems with time-varying delay and multiplicative noises, Information Sciences, 2023, 624:674-685.
[3] S. Chen, L. Li and M. Liu, Fault-tolerant consensus of multi-agent system with distributed adaptive protocol, IEEE Transactions on Cybernetics, 2015, 45(10):2142-2155.
[4] X. Wang, J. Zhu and Z. Cheng, Synchronization reachable topology and synchronization of discrete-time linear multi-Agent systems, IEEE Transactions on Automatic Control, 2015, 60(7):1927-1932.
[5] J. Chen, B. Chen and Z. Zeng, Synchronization and consensus in networks of linear fractional-order multi-agent systems via sampled-data control, IEEE Transactions on Neural Networks and Learning Systems, 2020, 31(8):2955-2964.
[6] W. Zhu, W. Cao and Z. Jiang, Distributed Event-Triggered Formation Control of Multiagent Systems via Complex-Valued Laplacian, IEEE Transactions on Cybernetics, 2021, 51(4):2178-2187.
[7] W. Zhu, W. Cao, M. Yan and Q, Li, Event-Triggered Formation Control of Multiagent Systems with Linear Continuous-Time Dynamic Models, IEEE Transactions on Systems, Man, and Cybernetics: Systems, 2022, 52(10:6235-6245.
[8] F. Sun, H. Li, W. Zhu and J. Kurths, Fixed-time formation tracking for multiple nonholonomic wheeled mobile robots based on distributed observer, Nonlinear Dynamics, 2021, 106(4):3331-3349.
[9] C. Dai, M. Zhang, C. Li and J. Zhao, QoE-aware intelligent satellite constellation design in satellite internet of things, IEEE Internet of Things Journal, 2021, 8(6):4855-4867.
[10] N. Gao, X. Li, S. Jin and M. Matthaiou, 3-D deployment of UAV swarm for massive MIMO communications, IEEE Journal on Selected Areas in Communications, 2021, 39(10):3022-3034.
[11] C. Wang, C. Liu, Y. Chen and Y. Zhang, Fixed-time consensus tracking for second-order leader-follower multi-agent systems with onlinear dynamics under directed topology, International Journal of Control Automation and Systems, 2021, 19(8):2697-2705.
[12] F. Sun, X. Wu, J. Kurths and W. Zhu, Group consensus for heterogeneous multiagent systems with time delays based on frequency domain approach, IEEE Transactions on Systems, Man, and Cybernetics: Systems, 2022, 53(5):2572-2582.
[13] J. Cheng, G. Xu, G. Yuan and L. Yang, A side chain consensus-based decentralized autonomous vehicle group formation and maintenance method in a highway scene, IEEE Transactions on Industrial Informatics, 2022, 18(12):9250-9258.
[14] Y. Zhao, Q. Duan, G. Wen, D. Zhang and B. Wang, Time-varying formation for general linear multiagent systems over directed topologies: a fully distributed adaptive technique, IEEE Transactions on Systems Man Cybernetics-Systems, 2021, 51(1):532-541.
[15] X. Dong and G. Hu, Time-varying formation tracking for linear multiagent systems with multiple leaders, IEEE Transactions on Automatic Control, 2017, 62(7):3658-3664.
[16] Z. Peng, C. Zhen, C. Li and G. Liu, Cloud-based time-varying formation predictive control of multiagent systems with random communication constraints and quantized signals, IEEE Transactions on Circuits and Systems Ii-Express Briefs, 2022, 69(3):1282-1286.
[17] Y. Moon and P. Park, Delay dependent robust stabilization of uncertain state-delayed systems, International Journal of Control, 2010, 74(14):1447-1455.
[18] C. Liu, X. Wu and M. Bing, Formation tracking of second-order multi-agent systems with multiple leaders based on sampled data, IEEE Transactions on Circuits and Systems Ii-Express Briefs, 2021, 68(1):331-335.

Fuzzy Systems and Data Mining IX
A.J. Tallón-Ballesteros and R. Beltrán-Barba (Eds.)

doi:10.3233/FAIA231054

Research on Influencing Factors of Non-Performing Loan Ratio of China Construction Bank Based on LASSO Algorithm

Aijuan LIU and Jibo WU[1]
School of Mathematics and Statistics, Chongqing Jiaotong University, Chongqing, 400074, China

Abstract. Systematic and effective analysis and control of the non-performing loan ratio can promote the steady development of the Bank, improve the non-performing loan prevention mechanism, enhance the Bank's risk prevention and control capabilities, and maintain the order of the financial market. This paper takes China Construction Bank as the research object, collects the relevant data such as the annual reports from 2004 to 2022, selects variables based on the LASSO algorithm, and constructs a multiple regression model. According to the research results, the provision coverage rate and the degree of government economic intervention have a negative correlation with the non-performing loan ratio of CCB, the loan-to-deposit ratio has a positive correlation with the non-performing loan ratio, and the capital adequacy ratio, GDP growth rate and business climate index have no significant impact on the non-performing loan ratio.

Keywords. China Construction Bank, Non-performing loan ratio, LASSO algorithm

1. The Introduction

1.1 Research background and significance

Commercial banks provide financial services in terms of realizing the financing of funds and increasing the deposit currency, however, the total amount of non-performing credit increases the bad debts of banks, making it difficult for banks to recover funds. As the foundation of China's financial market, commercial banks need to control the non-performing loan ratio. Non-performing loans refer to the borrower's repayment difficulties, unable to repay the loan principal and interest within the prescribed time limit, the bank can not recover the loan interest on time. The

[1] Corresponding Author, Jibo WU, Chongqing Jiaotong University, Chongqing, 400074, China; Email: 2628287050@qq.com. The authors wish to thank the referees and the editor for several suggestions which helped improve the presentation's quality. This work is supported by the Scientific Technological Research Program of Chongqing Municipal Education Commission [grant numbers KJZD-K202201302, KJQN202001321]

non-performing credit ratio is the ratio of the bank's non-performing loans to the total loan balance, and the credit risk increases when the bank cannot collect the loans. Comprehensive and effective analysis of the formation factors of non-performing loans can control the stock of non-performing loan ratio, resolve the increment, improve efficiency, promote the supply-side reform of banks, prevent the amount risk, help the development of real economy and the upgrading and transformation of industrial structure, and build a new economic system. China's financial supervision mechanism and non-performing loan prevention mechanism of banks need to be improved, and the low risk prevention and control ability of banks is not conducive to the prevention and control of financial systemic risks and the operation of the real economy.

The main source of profit for commercial banks is loan issuance. Loans are less liquid than other assets because they cannot be converted into cash before maturity, and they have higher default rates than other assets.[1] The increase in the profitability of commercial banks can be achieved by raising loan interest rates and expanding the number of loans. Profitability is the goal of the bank, security is a prerequisite requirement, and liquidity is the operational or instrumental requirement of the bank. The general policy of bank operation is to improve profitability by flexibly adjusting liquidity on the premise of ensuring safety[2]. Banks will inevitably lower their lending and investment standards in order to make profits, leading to a rise in non-performing loan ratios. If banks reduce the size of loans in order to reduce non-performing loans, the capital needs of many small and medium-sized enterprises will not be guaranteed, the profitability of commercial banks will therefore decline, the market vitality will be reduced, and the national economy will also be affected.

1.2 Research status

When the macro economy is in the stage of prosperity and recovery, GDP grows, corporate profit income and national income increase, and corporate development status is good, the probability of credit default is small, and the non-performing loan ratio decreases; When the economy is in recession and depression, the GDP growth rate decreases, the systemic risk increases, the operating efficiency of enterprises decreases, the capital chain breaks, and even the situation of bankruptcy and acquisition occurs, the loans cannot be repaid on time, and the non-performing loan ratio rises.[2] When there is inflation, enterprises need sufficient funds, and the bank loan threshold is lowered, the loan scale is expanded, and the non-performing loan ratio will also increase. The broad money supply M2 is composed of M1, household savings deposits and corporate time deposits, which can reflect the debtor's ability to repay bank loans. The higher the loan interest rate is, the higher the financing cost of corporate loans will be, and enterprises with poor operating ability or projects with low expected returns will not get loans, while enterprises with excellent credit and operating ability and projects with high expected returns will get more loans, and the non-performing loan ratio will decrease. In the foreign exchange market, the change of exchange rate will have different degrees of impact on investment, consumption, import and export. The appreciation of the RMB is detrimental to exports and foreign exchange reserves expressed in dollars and foreign claims. When the RMB appreciates, the expected earnings of domestic enterprises increase, and the non-performing loan ratio decreases. The operating characteristics of the bank, credit asset structure, risk control ability and so on will also affect the non-performing loan ratio. Various factors can increase the non-performing loan ratio, such as when the enterprise has operational

problems, the bank cannot identify potential risks in a timely manner; blind expansion on loan scale without strict examination and negligence of quality control would reducing credit quality; banks not monitoring the flow of funds, implementing risk early warning mechanisms.

In the study of the factors affecting the non-performing credit of banks, Tu Yuhang[3] argued that non-performing loans are affected by macroeconomic factors such as China's gross domestic product growth rate (GDP), broad money growth rate (M2) and inflation rate (IR), as well as micro-economic factors such as net interest margin, asset-liability ratio, capital adequacy ratio, cost-income ratio and provision coverage ratio. Wang Jiawei and Zhu Jiamin[4]believed that the non-performing loan ratio has a negative relationship with the provision coverage ratio, and a positive relationship with the bank loan-to-deposit ratio. Chen Ming [5] held an opinion that the GDP growth rate has the greatest impact on the non-performing loan ratio of joint-stock commercial banks, monetary policy has the greatest impact on the non-performing loan ratio of urban commercial banks, loan-to-deposit ratio and provision coverage ratio have the greatest impact on the non-performing loan ratio of rural commercial banks, and capital adequacy ratio has the greatest impact on the non-performing loan ratio of state-owned commercial banks. Xu Mengdi[6] found that that there was a negative correlation between the non-performing loan ratio of CCB and the GDP growth rate, and a negative correlation between the non-performing loan ratio and the money supply. Government administrative intervention and the lack of pre-loan examination of enterprises, the authenticity of collateral and pledges can not be guaranteed, and there is no responsible person to bear the risk of loans are the important factors affecting the non-performing loans of banks. Jia Mingjun[7] discussed that the level of economic development, the quality of industrial structure, the degree of government intervention and the operating conditions of commercial banks have a significant impact on the non-performing loan ratio of banks. Zhang Heng[8] studied that the profit margin on capital of commercial banks was negatively correlated with the non-performing loan ratio in the initial stage, and the inhibitory effect weakened over time until a long-term equilibrium was reached.

In terms of preventing non-performing loans, correct corporate governance practices and Chinese government regulation of the finance sector are required. With strong government intervention, the risk of NPL market failure will be contained in the short term, while more innovation is needed to make the market more dynamic[9]. When approving the loan, we should pay attention to the source and structure of the customer's loan repayment funds, comprehensively investigate the repayment ability of the lender and the loan team, and comprehensively examine the overall credit level and loan repayment expectation. The current macroeconomic situation should be closely monitored at all times. When the economy is down, lending should be more cautious[10]. Carry out supply chain finance business and maintain the close relationship between banks and core enterprises. Carry out big data risk control, financial technology innovation and intelligent development. Using big data, cloud computing and other technologies to verify the authenticity of transaction background, enterprise production and operation information, and the overall credit level of the industry.[11].

Through the literature study, it is concluded that the macroeconomic situation and government intervention have an important impact on non-performing credit. Non-performing credit is also affected by the bank's own size, capital adequacy ratio, loan-to-deposit ratio, provision coverage ratio, management level, experience

efficiency and other factors. Reducing the non-performing loan ratio requires the smooth operation of the macro economy and the strengthening of financial supervision by the government. Perfect the financial supply chain, play to the role of the financial science and technology, to establish perfect information technology systems, for enterprises to carry out accurate positioning and monitoring data, evaluate the credit risks of the enterprise. Laws and regulations need to be improved, banks need to strengthen risk prevention and control capabilities, and enterprises need to improve their operation and management capabilities.

1.3 Research hypothesis and methodology

This paper takes China Construction Bank as the research object, collects relevant data from 2004 to 2022 through the annual reports of the National Bureau of Statistics and China Construction Bank, selects characteristic variables based on the lasso algorithm, and establishes a multiple regression model to explore the impact of various factors on the non-performing loan ratio of China Construction Bank.

The main factors are the growth rate of China's GDP, the degree of government economic intervention, enterprise climate index and the provision coverage ratio, capital adequacy ratio and loan-to-deposit ratio of China Construction Bank. Based on the research results, provide suggestions for our country to reduce the non-performing loan ratio of China Construction Bank.

2. Analysis on the influencing factors of non-performing loan ratio of China's construction banks

2.1 Key factors

Provision coverage rate, that is, the use ratio of bank loan reserve for bad debts, reflects the degree of commercial banks' loss to non-performing loans, and to a certain extent, reflects the asset quality, credit risk and defense ability of commercial banks. When the provision coverage ratio of banks is high, the more bad debt reserves, the stronger ability to cover losses and deal with bad debts, the less risk of bank operation, and the possibility of non-performing assets and non-performing loans will be low.

Capital adequacy ratio, or capital risk, refers to the ratio of a bank's total capital to its risk-weighted assets. Capital adequacy ratio is the capital ratio necessary to ensure the normal operation and development of banks and other financial institutions. Under normal circumstances, the higher the capital adequacy ratio of a bank is, the less the number of risky assets of the bank is. High capital adequacy ratio reflects a bank's strong ability to resist risks, high-quality bank assets, strict internal management control level and strict loan approval and issuance standards will reduce the possibility of non-performing loans.

The loan-to-deposit ratio, that is, total bank loans divided by total bank deposits, has important implications not only for risk control in the banking system, but also for policy interest rate transmission.

GDP growth rate: GDP refers to the market value of all final products and labor services produced by all resident units in a country or region in a certain period, which is an important indicator to measure the overall economic situation of a country or region. For enterprises, the better the enterprise benefits, the smaller the default risk.

For commercial banks, the most important function is to create credit through non-cash settlement system and deposit reserve system. Commercial banks provide financial support to borrowers, and only normal credit services can boost GDP growth. The improvement and growth of consumption level also determine the repayment of loans, so the greater the growth rate of GDP, the smaller the non-performing loan ratio.

The degree of government economic intervention is the ratio of government fiscal expenditure to GDP. Generally speaking, the market will spontaneously regulate the allocation of social resources, but there will be failures or slow adjustment of the market mechanism. The government will intervene appropriately in the failed market economy.

Enterprise climate index is an index compiled according to the judgment and expectation of the person in charge of the enterprise on the comprehensive production and operation of the enterprise, which can comprehensively reflect the production and operation of the enterprise. The greater the business climate index is, the better the business development is, and the more likely the business will repay the loan in the future. The operating ability, market sensitivity and forward-looking of the lending enterprise are also important factors affecting the ability to repay loans. The repayment ability of enterprises with good capital and financial status and prudent and stable operation is relatively strong. On the contrary, the repayment ability of enterprises is weaker.

2.2 Other factors

Banks' own factors: lending preferences and asset structure will also affect the non-performing loan ratio. A risk-preference lending policy will increase the NPL ratio, while a conservative lending policy will lower the NPL ratio if the bank carefully examines the repayment ability of the borrower. The non-performing loan ratio of a lending bank will be higher than that of an investment bank.

Macroeconomic factors: during the period of rapid economic development, enterprises' operating conditions are good, and banks are more likely to recover loans. During the economic recession, the profitability of enterprises decreases, the market demand decreases, some enterprises go bankrupt, workers lose their jobs, the repayment ability decreases, and the non-performing loan ratio of banks rises.

In this paper, banks' own factors and macroeconomic factors are represented by random disturbance term v.

3. Empirical analysis

3.1 Research methods

Lasso was first proposed by Robert Tibshirani in 1996, and its full name is least absolute shrinkage and selection operator. This method is reductive estimation, and in the reduction process of regression coefficients, insignificant regression coefficients are reduced to 0, that is, variables can be screened. It retains the advantage of subset shrinkage and is a way to deal with biased estimators with multicollinearity data.

The minimization formula of lasso regression model is as Eqs. (1) and (2).

$$J(\beta)=\Sigma(y-X\beta)^2+\lambda\|\beta\|_1=\Sigma(y-X\beta)^2+\Sigma\lambda|\beta|=ESS(\beta)+\lambda l_1\beta$$

$$\Sigma_{i=1}^{n}(y_i-\beta_0-\Sigma_{j=1}^{p}x_{ij}\beta_j)^2+\lambda\Sigma_{j=1}^{p}|\beta_j|=RSS+\lambda\Sigma_{j=1}^{p}|\beta_j| \quad (1)$$

Objective function:

$$\hat{\beta}=\text{argmin}_\beta\Sigma_{i=1}^{N}(y_i-\beta_0-\Sigma_{j=1}^{p}x_{ij}\beta_j)^2$$

$$\text{subject to }\Sigma_{j=1}^{p}|\beta_j|\leq t \quad (2)$$

Where $\lambda\|\beta\|_1$ is the penalty term of the objective function, and the adjustment parameter λ, which refers to the hyper parameter, is the penalty term coefficient, and an optimal value needs to be estimated iteratively. $\|\beta\|_1$ is the $\ell 1$ regular of the regression coefficient β, representing the sum of the absolute values of all regression coefficients. $\Sigma_{j=1}^{p}|\beta_j|$ is the compression penalty, and p represents the number of independent variables.

3.2 Data processing

This paper takes the non-performing loan ratio of China Construction Bank from 2004 to 2022 as the explained variable, and studies the effects of provision coverage, capital adequacy ratio, GDP growth rate, business climate index, government economic intervention degree, and loan-to-deposit ratio on the non-performing loan ratio. Python software was used for analysis and multiple linear regression model Eq. (3) was established:

$$Y=\beta_0+\beta_1X_1+\beta_2X_2+\beta_3X_3+\beta_4X_4+\beta_5X_5+\beta_6X_6+V \quad (3)$$

In the above formula, Y is the non-performing loan ratio, X_1 is the provision coverage ratio, $X_2$is the capital adequacy ratio, X_3 is the loan-to-deposit ratio, $X_4$is the GDP growth rate, X_5 is the business climate index, and X_6 is the degree of government economic intervention.

Table 1 Research data

Year	Non-performing loan ratio	Provision coverage ratio	Capital adequacy ratio	Loan-to-deposit ratio	GDP growth rate	Business climate index	Degree of government intervention in the economy
2004	3.92%	61.64%	11.29%	63.78%	10.10%	134.91	17.61%
2005	3.84%	66.78%	13.57%	61.37%	11.40%	131.98	18.01%
2006	3.29%	82.24%	12.11%	60.87%	12.70%	135.88	18.41%
2007	2.60%	104.41%	12.58%	61.40%	14.20%	143.50	18.44%
2008	2.21%	131.58%	12.16%	59.50%	9.70%	127.30	19.61%
2009	1.50%	175.77%	11.70%	60.24%	9.40%	119.13	21.89%
2010	1.14%	221.14%	12.68%	62.47%	10.60%	136.18	21.82%
2011	1.09%	241.44%	13.68%	65.05%	9.60%	132.75	22.38%
2012	0.99%	271.29%	14.32%	66.23%	7.90%	125.37	23.39%
2013	0.99%	268.22%	13.34%	63.69%	7.80%	121.80	23.64%
2014	1.19%	222.33%	14.86%	67.53%	7.40%	121.83	23.59%

2015	1.58%	150.99%	15.39%	69.80%	7.00%	117.63	25.53%
2016	1.52%	150.36%	14.94%	68.17%	6.80%	109.93	25.16%
2017	1.49%	171.08%	15.50%	70.73%	6.90%	123.35	24.41%
2018	1.46%	208.37%	17.19%	73.71%	6.70%	123.50	24.03%
2019	1.42%	227.69%	17.52%	77.68%	6.00%	124.00	24.22%
2020	1.56%	213.59%	17.06%	78.49%	2.20%	110.10	24.24%
2021	1.42%	239.96%	17.85%	82.28%	8.40%	121.85	21.38%
2022	1.38%	241.53%	18.42%	83.62%	3.00%	103.50	21.53%

According to the statistical data of 2004-2022, the non-performing loan ratio of China Construction Bank decreased year by year from 2008 to 2012, was in the stage of low non-performing loan ratio from 2010 to 2014, and controlled at about 1.5% from 2015 to 2022. The provision coverage ratio increased year by year from 2008 to 2012, and increased after gradually decreasing from 2013 to 2019. The capital adequacy ratio generally increased gradually from 2008 to 2022. The GDP growth rate gradually slowed from 2008 to 2020, the GDP growth rate in 2021 increased by 8.1 percent from 2020, and the GDP growth rate decreased to 3 percent in 2022. The level of government intervention in the economy generally increased gradually from 2008 to 2015. The loan-to-deposit ratio generally increased gradually from 2008 to 2022.

It can be seen that the practice rules of the early construction bank are not perfect, and the awareness of risk prevention and control is insufficient. At the same time of rapid economic development, relevant laws still need to be improved, entrepreneurs have high confidence in the development of enterprises, and the non-performing loan rate is too high. When the awareness of risk prevention and control of banks increased, the provision coverage ratio, capital adequacy ratio and loan-to-deposit ratio all increased. The growth rate of GDP has slowed down, the development of enterprises has slowed down, and the non-performing loan ratio has gradually declined and become stable.

Table 2 Values of variance inflation factor VIF

variable	VIF
X1	2.015320
X2	15.444076
X3	16.908621
X4	9.070282
X5	5.038010
X6	3.588956

Independent variable capital adequacy ratio X_2, loan-to-deposit ratio X_3, GDP growth rate X_4, business climate index X_5 variance inflation factor VIF is greater than 5, indicating that there is multicollinearity between variables.

Table 3 collinear diagnosis

	Y	X1	X2	X3	X4	X5	X6
Y	1.000000	-0.913327	-0.470386	-0.396978	0.544960	0.488449	-0.811771
X1	-0.913327	1.000000	0.537631	0.502395	-0.571292	-0.440674	0.654959
X2	-0.470386	0.537631	1.000000	0.953011	-0.771894	-0.656298	0.567656
X3	-0.396978	0.502395	0.953011	1.000000	-0.777929	-0.655082	0.453924
X4	0.544960	-0.571292	-0.771894	-0.777929	1.000000	0.889231	-0.705167
X5	0.488449	-0.440674	-0.656298	-0.655082	0.889231	1.000000	-0.635405
X6	-0.811771	0.654959	0.567656	0.453924	-0.705167	-0.635405	1.000000

As can be seen from Table 3, the correlation coefficient between capital adequacy ratio X_2 and loan-to-deposit ratio X_3 is 0.953011, and the correlation coefficient between GDP growth rate X_4 and business climate index X_5 is 0.889231, indicating that there is a serious multicollinearity between the variables, and lasso model is used to improve it.

The coefficients after each λ parameter regression and the ratio between the coefficients after each λ parameter regression and the coefficients of the unregularized model ℓ1 norm are recorded.

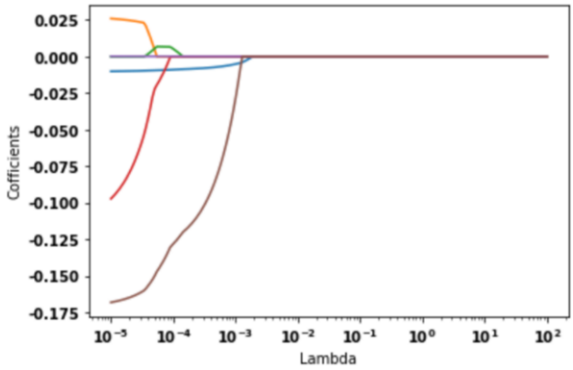

Figure 1. Regularized path diagram of the noose

As can be seen from Figure 1, the λ of the initial iteration falls between 10^{-5} and 10^{-2}. As λ decreases, the compression parameter decreases and the absolute value of the partial regression coefficient increases. When λ increases, the compression parameter increases. Meanwhile, the absolute value of the partial regression coefficient decreases, which may decrease to 0 and be eliminated.

When λ is larger, the corresponding estimated parameters will be compressed smaller, and when λ reaches 10^{-2}, some unimportant variables will be compressed to 0, which means that the variables have been removed from the model.

Firstly, the data set is divided into training set and test set according to 4:1, then different λ values are constructed, and the parameter of cross-validation is set to 3, and iterated 1000 times, and the root-mean-square error is used for evaluation. Finally, lasso is modeled by fitting the optimal λ value and evaluated by the root-mean-square error on the test set. Finally, the optimal λ value is 0.00013354515629298989, and the root-mean-square error of the model on the test set is 0.0026770430302632915, indicating that the model has good prediction effect. The coefficient of determination R^2 is 0.9107204699072416, indicating that the optimal model can explain 91.07% of the change in the response value of the training data. The regression coefficients obtained are shown in Table 4.

Table 4 Lasso regression coefficient table

variable	coefficient
Intercept	0.060107
X1	-0.008664
X2	0.000000
X3	0.001015
X4	-0.000000
X5	0.000000
X6	-0.121716

Based on the optimal λ value modeling, the multiple regression equation is Eq. (4).

$$Y = 0.060107 - 0.008664X_1 + 0.001015X_3 - 0.121716X_6 + \varepsilon \quad (4)$$

The coefficients of independent variable capital adequacy ratio X_2, GDP growth rate X_4 and business climate index X_5 are compressed to zero in the regression model obtained by optimal λ, which reduces the complexity of the model and improves the fitting effect of the model. According to the regression coefficient results, for every 1% increase in provision coverage, the non-performing loan ratio decreases by 0.008664%. For every 1% increase in the loan-to-deposit ratio, the non-performing loan ratio will increase by 0.001015.For every 1% increase in government economic intervention, the non-performing loan ratio decreases by 0.121716%.Capital adequacy ratio, GDP growth rate and business climate index have no significant impact on the non-performing loan ratio.

4. Conclusions and implications

4.1 Conclusion

In the analysis of the non-performing loan ratio of China Construction Bank, the provision coverage ratio and the degree of government economic intervention have a negative correlation with the non-performing loan ratio. From the results of provision coverage, this is similar to the results of Tu Yuhang and Wang Jiawei's studies in the references. From the results of the research on the degree of government economic intervention, it has a significant impact on the non-performing loan ratio of banks, which is consistent with the opinion of Xmundi and Jia Mingjun.

It can be seen that the provision coverage rate is an important indicator to measure whether the financial stability and risk are controllable. The provision coverage rate should be in line with the degree of risk. If it is too low, it will lead to insufficient provision, while if it is too high, it will lead to false profit decline. If the provision coverage rate is kept within the normal range, the bank can maintain the liquidity of funds while resisting risks, ensure expected returns, and help the bank to deal with non-performing loans, reduce capital occupation and improve credit issuance capacity. We will release more funds to support the development of the real economy. Higher capital adequacy ratios and provision coverage ratios reduce banks' credit risk while increasing banks' costs rather than improving efficiency.

Supervision of the provision coverage ratio can help to improve the ability of banks to withstand expected losses, and regulators can moderately increase the loan loss reserve requirements in the economic uptrend and moderately reduce the loan write-off in the economic downtrend. According to the bank's loan quality and profitability, moderate adjustment of loan loss reserve requirements. The dynamic provision adjustment system is conducive to reducing the cyclical fluctuations of bank operations and promoting the steady operation of banks.

Proper economic intervention by the government is conducive to the healthy development of the economy, and macro-control and macro-prudential management are adopted to limit the number of loans and maintain macroeconomic stability. Governments should set sound and sustainable macroeconomic policies, improve public financial infrastructure, and develop a clear framework for crisis management,

recovery, and resolution. In addition, the appropriate system protection mechanism and effective market constraints also play a positive role in the sound operation of banks.

The loan-to-deposit ratio is positively correlated with the non-performing loan ratio, which is consistent with the research conclusions of Wang Jiawei and Zhu Jiaming.

The safety of commercial banks is determined by both liquidity and profitability. The goal of liquidity refers to the ability of commercial banks to obtain available funds at an appropriate price at any time, so as to meet the needs of customers and other bank payments at any time. Profitability is the ultimate goal of commercial banks' business activities, that is, to maximize profits when possible. Non-performing loans reduce available funds and liquidity, and loan principal and interest losses also reduce bank profits. If banks improve liquidity and profitability and increase safety, non-performing loans will decrease.

The index of loan-to-deposit ratio is conducive to strengthening liquidity risk management of banking financial institutions, improving the degree of refinement and specialization of liquidity risk management, prompting commercial banks to reasonably match the maturity structure of assets and liabilities, and enhancing banks' ability to cope with liquidity. Supervision of loan-to-deposit ratio can restrain excessive expansion of credit scale and reduce bank credit risk and operational risk.

4.2 Enlightenment

China should optimize the economic structure, promote the reform of capital and financial market, improve the risk prevention and control mechanism, build a diversified financing structure, and promote the steady development of economy under the background of the new normal of economy. Banking supervision can be divided into four dimensions: business control, capital control, government supervision power and market supervision. Banks need to strengthen the credit risk identification, assessment, the formation of credit risk monitoring report. When controlling credit risks, credit limit management is implemented, customer characteristics are used to select customers, credit scoring tools are used to select customers, key processes of loan business are controlled, effective guarantee and release measures are taken, collection and disposal of defaulted loans, loan verification and securitization of non-performing loans are formulated.

The development of macro economy is an important factor affecting the non-performing loans of commercial banks. In addition, the government provides policy assistance for non-performing loans to reduce the stock of non-performing loans.

We will improve the construction of the credit management system and the risk early warning mechanism of commercial banks, enhance the ability to identify potential risks when approving corporate loans, and incorporate economic entities into the credit management system on a wider scale to ensure the standardization and legitimacy of their operation and management. According to their own business conditions, commercial banks build risk measurement models, predict risk incidence, build risk management systems, improve credit management systems, and earnestly implement risk prevention and control plans in the process of loan application approval, risk assessment and loan tracking.

Accelerating the non-performing loan securitization of commercial banks, the non-performing asset securitization is an effective measure to realize the circulation of

non-performing loans, reduce the non-performing loan ratio of commercial banks, and reduce economic losses. Establish and improve the perfect legal guarantee system to resolve non-performing credit, improve the current implementation of the security law, commercial banking law, scientific management of commercial bank operation, to ensure the steady development of banks.

Commercial banks implement the credit management system, improve the professional skills of credit clerks, expand new businesses, improve profitability, develop Internet finance, and create wealth management business products. Strengthen the awareness of non-performing loans, avoid blindly expanding the scale of loans, neglect the loan approval process, and conduct comprehensive qualification examination of borrowing enterprises or individuals.

5. Summary

Commercial banks should control the non-performing credit ratio within a reasonable value. Commercial banks should strengthen the contact and cooperation with regulatory authorities, so that the risk within a reasonable and controllable range, secondly, commercial banks need to pay attention to the national macroeconomic policies, so that the bank has a good business development.

Banks need to conduct scientific examination of borrowers and improve the credit investigation system. The credit investigation system needs to include the credit situation of customers, monitor the borrowing situation, capital flow and capital use of customers in real time, reduce fraud caused by omission of credit examination and reduce credit risks. Improve the comprehensive quality and professional ability of bank employees, ensure their operational compliance and risk control awareness, and avoid errors, omissions and omissions in the audit of customers. Banks also need sound financial innovations, such as non-performing loan securitization and debt-to-equity swaps. The state improves relevant laws and regulations and clearly stipulates relevant rights and responsibilities of bank loans.

In order to reduce the non-performing loan ratio of commercial banks, it is necessary to establish a good credit environment, strengthen supervision, and at the same time the state intervenes through macroeconomic regulation and control.

References

[1] [US] Frederic S. Mishkin. Monetary finance [M]. Renmin university of China publishing house, 2021.

[2] Hu Qingkang. Modern monetary banking [M]. Fudan university press, 2019.

[3] Tu Yuhang. Research on the influencing factors of non-performing loan ratio of commercial banks in China [J]. Productivity Research,2018,No.317(12):40-44+126.

[4] Wang, J. & Zhu, J. Ming. Analysis on the influencing factors of non-performing loan ratio of Agricultural Bank of China in the new era [J]. Journal of Natural Science of Harbin Normal University,2018,34(02):7-11.

[5] Chen M. A Study on non-performing loans of commercial banks and its influencing factors [D]. Central China Normal University, (2017).

[6] Xu Mengdi. Analysis of China Construction Bank's non-performing loans under the new economic situation [D]. Nanjing University,2018.

[7] Jia Mingjun. Research on the influencing factors of non-performing loan ratio of China's Commercial Banks [D]. Dongbei University of Finance and Economics,2021.

[8] Zhang H. Empirical analysis on the impact of non-performing loan ratio on profit rate of capital of China's commercial banks [D]. Beijing Foreign Studies University, (2019).

[9] Zhong Y. A Study on the Non-performing Loans Market in China[C]// Science and Culture Center for International Academic Contact. Proceedings of The first International Symposium on innovation management and Economics (ISIME 2021).ATLANTIS PRESS, 2021:7. DOI: 10.26914 / Arthur c. nkihy. 2021.040699.

[10] Jiang M ,Zhang X . Research on the Influencing Factors and Paths of Non-performing Loan Ratio of Rural Commercial Banks in China Qualitative Research and Investigation Based on Grounded Theory[C]//International Science and Culture Center for Academic Contacts(Russia),Russian State Specialized Academy of Arts(Russia),Henan University Minsheng College（China）,Zhengzhou Yingchun Conference planning Co., Ltd.(China).Proceedings of 4th International Conference on Economics, Management, Law and Education(EMLE 2018)(Advances in Economics, Business and Management Research,VOL.71).Atlantis Press,2018:8.

[11] Wang L ,Liu X . Research on the Current Situation of Bank Financing Business under Supply Chain Finance[C]//Institute of Management Science and Industrial Engineering. Proceedings of 2019 International Conference on Global Economy and Business Management(GEBM 2019).Clausius Scientific Press,2019:6.DOI:10.26914/c.cnkihy.2019.038027.

Fuzzy Systems and Data Mining IX
A.J. Tallón-Ballesteros and R. Beltrán-Barba (Eds.)

doi:10.3233/FAIA231055

Influence of Step-Feed Ratio on the Nitrogen Removal Efficiency of Two-Stage AO Process in the Treatment of Municipal Sewage with a Low C/N Ratio

Baohua Li, Huijun Fan and You Liu[1]
Hebei Baisha Tobacco Co., Ltd., Baoding Cigarette Factory, Baoding, Hebei, China

Abstract: The present study was envisaged to develop a step-feed two-stage AO process for the removal of nitrogen via biological methods in conformity with regulations for the discharge of low-C/N-ratio municipal wastewater. The carbon source was preserved by setting a preliminary anoxic tank and reducing the content of dissolved oxygen in the effluent of oxic tank 1. The effect of step-feed ratio on the removal rate of nitrogen was investigated. The results showed that the COD removal rate was not significantly affected by the step-feed ratio, and COD concentrations in the effluent were reduced to lower than 30 mg/L in all the samples. The removal rate of the ammonia nitrogen and total nitrogen were obviously affected by the step-feed ratio. When the step-feed ratio of anoxic tank 1 was set to 70, 80, and 90%, the concentration of the ammonia nitrogen and total nitrogen in the effluent was 1.49, 17.57, 0.52, 13.24, 0.31, and 10.28 mg/L, respectively, and the removal rates reached 96.60, 63.58, 98.77, 72.17, 99.27, and 78.74%, respectively. The removal rate of ammonia nitrogen and total nitrogen exhibited an increase with an increase in the step-feed ratio of anoxic tank 1. The removal rate of total phosphorus in the step-feed two-stage AO process was as low as 34.72%. When polyaluminium chloride (PAC) was added to the pipeline connecting oxic tank 2 and secondary sedimentation tank, the concentration of total phosphorus in the effluent was reduced to lower than 0.5 mg/L. The quality of the municipal wastewater with a low C/N ratio could attain the 1A-level discharge standards after the treatment with a combination of step-feed two-stage AO process and chemical phosphorus-eliminating process.

Keywords: Two-stage AO process; Low C/N ratio; Municipal wastewater; Step-feed; Nitrogen-eliminating efficiency

1. Introduction

With the increase in consciousness of the water environment, sewage treatment plants have been established in more and more villages and towns. However, the quality of sewage varies greatly in different regions. Especially, the carbon-nitrogen ratio (C/N, COD/total nitrogen) of sewage influent in some regions of North China is relatively low [1, 2]. For example, the C/N ratio of sewage in a certain town in Hebei is only about 3.5. Anaerobic-Anoxic-Oxic (A^2O) and modified A^2O processes as well as various oxidation

[1] Corresponding author, You Liu, Hebei Baisha Tobacco Co., Ltd., Baoding Cigarette Factory, Baoding, Hebei, 071000, China; E-mail: 156026590@qq.com

ditches and modified oxidation ditches are adopted in most of the urban sewage treatment plants in China [3, 4], but the issue of insufficient carbon source in the removal of nitrogen and phosphorus has been encountered [5-7]. The C/N ratio of the influent in this study was relatively low, so the conventional nitrogen- and phosphorus-eliminating processes were inefficient.

The C/N ratio of the influent in the present study was relatively low, so the carbon source for the removal of nitrogen and phosphorus was insufficient. In the light of the current chemical phosphorus-eliminating technology, a combination of step-feed two-stage AO process and chemical phosphorus-eliminating process was adopted in the experiment. A certain amount of dissolved oxygen was entrained in the recycled sludge and recycled nitrified slurry in biological denitrification processes, and consumed organic matter to waste carbon source. Therefore, in this experiment, the recycled sludge and nitrified slurry were returned to the preliminary anoxic tank to consume the entrained dissolved oxygen through endogenous metabolism [8, 9]. Meanwhile, the dissolved oxygen in the first stage of oxic tank was reduced to decrease the amount of dissolved oxygen entrained in the recycled nitrified slurry [10]. As a result, the carbon source was wasted minimally, and the removal rate of total nitrogen was improved. The urban sewage with a low C/N ratio was treated with a step-feed two-stage AO process coupled with chemical phosphorus-eliminating process in this experiment, and the effect of step-feed ratio on the removal rate of nitrogen was studied. This study can be theoretically and technically beneficial in the design and reconstruction of urban sewage treatment plants dealing with sewage with low C/N ratios.

2. Materials and methods

2.1Influent quality

The influent quality in this experiment and water quality of the 1A-level standard in the "Pollutant Discharge Standard for Urban Sewage Treatment Plants" (GB 18918-2002) is shown in Table 1. The actual urban sewage, with a low influent C/N ratio (COD/total nitrogen) of merely 3.36, acquired from a town in Hebei Province was taken as the research object in this experiment. This C/N ratio was slightly higher than the amount of carbon source (2.86 mg) consumed for the denitrification of 1 mg of nitrate nitrogen. Therefore, this urban sewage was treated with the combination of step-feed two-stage AO process and chemical phosphorus-eliminating process in this experiment. Nitrogen was removed via the two-stage AO process, while phosphorus was removed by the chemical method.

Table 1. Quality parameters of the influent and discharge

Index		Concentration of COD (mg/L)	Concentration of ammonia nitrogen (mg/L)	Concentration of total nitrogen (mg/L)	Concentration of total phosphorus (mg/L)	pH
Influent	Range	132–198	38.7–47.9	42.2–52.8	3.17–4.82	7.18–8.09
	Mean	161.72	43.01	48.13	4.08	7.72
1A-level discharge standard		50	5 (8)	15	0.5	6–9

2.2 The step-feed two-stage AO process

The schematic illustration of the process is shown in Figure 1. The step-feed two-stage AO process was composed of a preliminary anoxic tank, anoxic tank 1, oxic tank 1, anoxic tank 2, oxic tank 2, and secondary sedimentation tank. 70–90% of the influent was pumped into the anoxic tank 1 with a peristaltic pump, and 10–30% of the influent was pumped into the anoxic tank 2. The recycled sludge and recycled nitrified slurry were pumped into the preliminary anoxic tank with a peristaltic pump, and the entrained dissolved oxygen was consumed through an endogenous metabolism. The internal carbon source was consumed for denitrification, thereby saving carbon sources. The effective volumes of preliminary anoxic tank, anoxic tank 1, oxic tank 1, anoxic tank 2, oxic tank 2, and secondary sedimentation tank were 10, 40, 50, 10, 10, and 20 L, respectively. The processing capacity of this setup reached 10 L/h, and the hydraulic residence time of these tanks was 1, 4, 5, 1, 1, and 2 h, respectively. The influent tank was 200 L in volume.

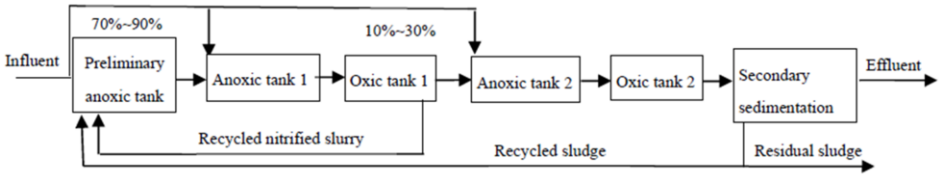

Fig. 1 Schematic representation of the step-feed two-stage AO process

2.3 Experimental procedure

A stable two-stage AO process was selected to treat the actual urban sewage in this experiment. In order to preserve the carbon sources and improve the denitrification efficiency, the concentration of dissolved oxygen (DO) in the oxic tank 1 was controlled in the range of 0.8–1.0 mg/L, and the reflux ratio of nitrified slurry was around 250%. The concentration of dissolved oxygen in the oxic tank 2 was in the range of 1.5–1.8 mg/L, and the reflux ratio of sludge was 65%. The step-feed ratio of anoxic tank 1 and anoxic tank 2 was 70 and 30%, respectively (stage I), and the COD, ammonia nitrogen, and total nitrogen in the effluent were stable for about 25 days. The step-feed ratio of anoxic tank 1 and anoxic tank 2 was adjusted to 80 and 20% (stage II). After stable operation for 25 days, the step-feed ratio was adjusted to 90 and 10% (stage III) to investigate the effect of step-feed ratio in the two-stage AO process on denitrification efficiency. During the experiment, the mixed liquor suspended solids (MLSS), mud age, and water temperature were in the ranges of 2400–2600 mg/L, 10-12 days, and 20–25 °C, respectively. The concentrations of COD, ammonia nitrogen, nitrite nitrogen, nitrate nitrogen, total nitrogen, and total phosphorus in the influent and effluent from oxic tank 1, oxic tank 2, and secondary sedimentation tank were measured each day. After the optimal step-feed ratio was quantified, a common coagulant polyaluminum chloride (PAC) was added to the pipeline connecting oxic tank 2 and secondary sedimentation tank, and the optimal dosage was explored.

2.4 Determination methods

COD was determined by the potassium-dichromate method. Ammonia nitrogen was determined by spectrophotometry with the Nessler's reagent, and total nitrogen was quantified by ultraviolet spectrophotometry (UV-2550, Shimadzu) after oxidation with alkaline potassium persulfate. The nitrite nitrogen was measured by spectrophotometry with N-(1-naphthyl)-ethylenediamine, and nitrate nitrogen was determined by spectrophotometry with thymol. Total phosphorus was determined by Mo-Sb-Vc spectrophotometry after oxidation with potassium persulfate. DO and pH were determined with a portable dissolved oxygen analyzer (HQ30d-HACH) and pH meter (Oxi 315i-WTW), respectively.

3. Results and Discussion

3.1 COD removal performance

The COD removal performance of the step-feed two-stage AO process is presented in Figure 2. The COD value of influent fluctuated, with an average concentration of 161.72 mg/L. The COD concentration in the effluent of oxic tank 1 of stage I was relatively low, with an average concentration of 21.96 mg/L, which was significantly lower than that (27.04 mg/L) in the effluent of oxic tank 2. This is because 70% of the influent accessed the anoxic tank 1, and was mixed with the effluent from the preliminary anoxic tank for denitrification to consume organic matter. Subsequently, it accessed oxic tank 1, and the remaining organic matter was further oxidized and decomposed by heterotrophic bacteria. The hydraulic residence time in the anoxic tank 1 and oxic tank 1 was 4 and 5 h, respectively, resulting in the complete denitrification and oxidation of organic matter. However, the hydraulic residence time of anoxic tank 2 and oxic tank 2 was 1 h, which was very less. As a result, 30% of the organic matter in the influent was not completely consumed by denitrification process and decomposed via aerobic reactions. In the secondary sedimentation tank, the organic matter was further consumed by denitrification process or oxidized by the heterotrophic bacteria. Hence, the COD concentration in the effluent of the secondary sedimentation tank was further reduced to 25.22 mg/L, and the average COD removal rate reached 84.13%. The step-feed ratio of anoxic tank 1 and anoxic tank 2 in stage II was 80% and 20%, and that in stage III was 90% and 10%, respectively. After adjusting the step-feed ratio, the COD removal rates at each stage in the two-stage AO process did not change significantly, indicating that the step-feed two-stage AO process had strong adaptability to the fluctuation of influent COD. The average COD concentration in the effluent of oxic tanks 1 in stage II and III was 23.71 and 23.97 mg/L, respectively, which was slightly higher than that in stage I. With an increase in the organic load of anoxic tank 1 and oxic tank 1, the COD in the effluent slightly increased. The COD concentration in the effluent from oxic tanks 2 in stage II and III was 25.00 and 23.59 mg/L, respectively, which was lower than that of stage I, and the COD decreased with a decrease in the step-feed ratio. The average COD concentration in the effluent of the secondary sedimentation tanks at stage II and III was 22.55 and 20.06 mg/L, respectively, and the average removal rate reached 86.03% and 87.30%, respectively. As the step-feed ratio of the anoxic tank 2 decreased, the organic load of anoxic tank 2 and oxic tank 2 gradually decreased, and the COD removal rate gradually increased. The COD of the effluent in secondary sedimentation tanks after the

stage I, II, and III was lower than 30 mg/L, which was significantly lower than the standard value (50 mg/L) required by the national 1A-level standard in China.

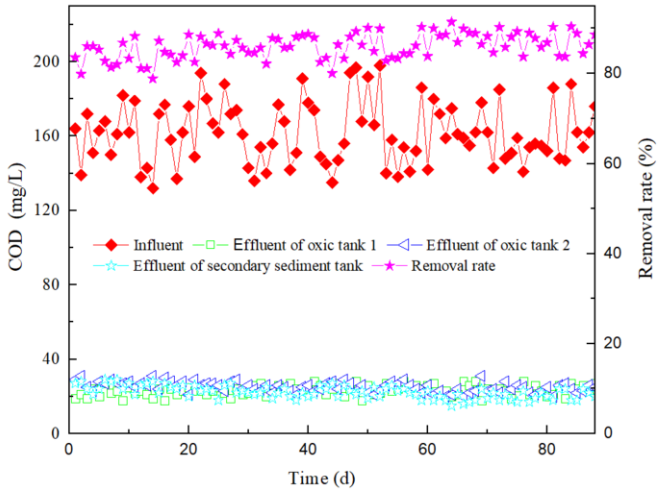

Fig. 2 COD removal performance of the step-feed two-stage AO process

3.2 Nitrogen removal performance

The ammonia-nitrogen removal effect of the step-feed two-stage AO process is shown in Figure 3. The concentration of ammonia nitrogen in the influent fluctuated between 38 and 48 mg/L, with an average concentration of 43.01 mg/L. The oxic tank 1 of stage I exhibited a good removal of the ammonia nitrogen, and the ammonia-nitrogen content in the effluent was below 0.5 mg/L, with an average concentration of 0.29 mg/L. This is because the C/N content in the influent was relatively low, and the organic matter accessing anoxic tank 1 was consumed as carbon source by the denitrifying bacteria for denitrification [11, 12]. Only a small amount of carbon source accessed the oxic tank 1, and the nitrification of ammonia nitrogen was completed during the long hydraulic residence time in oxic tank 1. The average concentration of ammonia nitrogen in the effluent of oxic tank 2 was 1.86 mg/L, significantly higher than that of oxic tank 1. This is because 30% of the influent accessed anoxic tank 2, and the oxidation of ammonia nitrogen was not complete during the short hydraulic residence time (1 h) in the anoxic tank 2 and oxic tank 2. Nevertheless, the concentrations of ammonia nitrogen in the effluent of oxic tank 2 were lower than 3 mg/L, in accordance with the regulation of the national 1A-level standard. The concentration of ammonia nitrogen in the effluent of the secondary sedimentation tanks was slightly decreased, with an average concentration of 1.49 mg/L. This is because the ammonia nitrogen was oxidized by the nitrifying bacteria in the secondary sedimentation tank using the dissolved oxygen entrained in the effluent of oxic tank 2. The removal rate of ammonia nitrogen in the step-feed two-stage AO process at stage I reached 96.60%, and the removal rate of oxic tank 1 at stage II and III was also high. The average concentration of ammonia nitrogen at stage II and III in the effluent of 0.34 and 0.37 mg/L, respectively. The ammonia nitrogen concentration in the effluent was slightly increased with an increase in the step-feed ratio of anoxic tank 1, indicating that oxic tank 1 was resistant to the fluctuations in the concentration of ammonia nitrogen. The average concentration of ammonia nitrogen at stage II and III in

the effluent of oxic tank 2 was 0.78 and 0.41 mg/L, respectively. The concentrations of ammonia nitrogen in the effluent significantly decreased with the decrease of the step-feed ratio of anoxic tank 2. When the step-feed ratio of anoxic tank 2 was decreased from 30% to 10%, the load of ammonia nitrogen in oxic tank 2 was significantly reduced, thereby leading to the complete nitrification of ammonia nitrogen in oxic tank 2. The ammonia nitrogen was further nitrified in the secondary sedimentation tank, and the concentration of the ammonia nitrogen in the effluent of secondary sedimentation tanks in stage II and III was reduced to 0.52 and 0.31 mg/L, respectively, with an average removal rate of 98.77% and 99.27%, respectively.

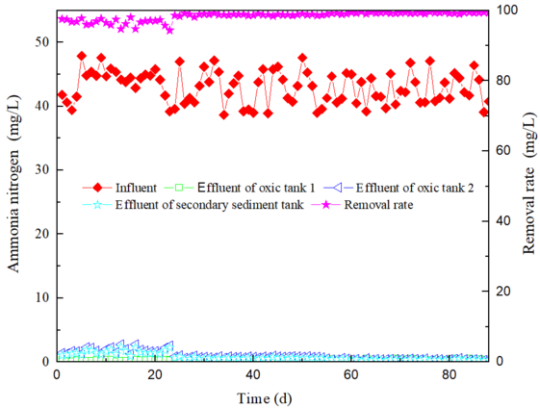

Fig. 3 Ammonia nitrogen removal performance of the step-feed two-stage AO process

The concentration of nitrite nitrogen in the influent was very low and was below 0.15 mg/L (Figure 4) in all the samples. The nitrite nitrogen in the effluent of stage I oxic tank 1 was significantly increased, with an average concentration of 0.54 mg/L. This is because the dissolved oxygen concentration in oxic tanks 1 was as low as 0.8–1.0 mg/L, which was beneficial for the accumulation of nitrite nitrogen [13, 14]. The concentration of nitrite nitrogen in the effluent of oxic tank 2 was significantly decreased to 0.12 mg/L, because the concentration of the dissolved oxygen in oxic tank 2 was as high as 1.5 to 1.8 mg/L, inhibiting the accumulation of nitrite nitrogen. In the secondary sedimentation tanks, the concentration of nitrite nitrogen was further decreased, with an average concentration of 0.077 mg/L. The average concentration of nitrite nitrogen in the effluent of oxic tanks 1 in stage II and III was 0.48 and 0.50 m/L, respectively, which was similar to the values in stage 1. The average concentration of nitrite nitrogen in the effluent of oxic tanks 2 in stage II and III was 0.077 and 0.064 m/L, respectively, which was significantly lower than in stage 1. This is because the hydraulic residence time of oxic tank 2 was only 1 h, and the step-feed ratio of anoxic tank 2 at stage 1 was 30%. This resulted in the incomplete oxidation of COD and ammonia nitrogen in oxic tank 2 and accumulation of nitrite nitrogen. In contrast, the step-feed ratio of anoxic tanks 2 in stage II and III was 20% and 10%, respectively, and thereby the COD and ammonia nitrogen was thoroughly oxidized. Only a small amount of nitrite nitrogen remained. The average concentration of nitrite nitrogen in the effluent of secondary sedimentation tanks in stage II and III was 0.039 and 0.018 mg/L, respectively.

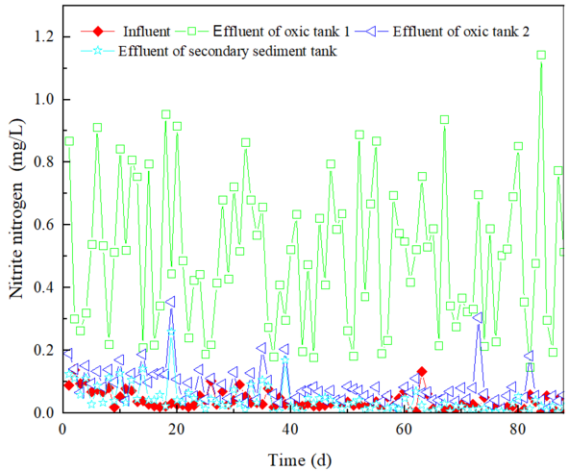

Fig. 4 Nitrite nitrogen removal performance of the step-feed two-stage AO process

The concentration of the nitrate nitrogen in the influent was relatively low, with an average concentration of 1.49 mg/L (Figure 5). After the reflux of nitrified slurry and recycled sludge in stage I to the preliminary anoxic tank, the heterotrophic bacteria entrained in the recycled sludge consumed the dissolved oxygen entrained in the nitrified slurry and recycled sludge in the first place [15]. Subsequently, the denitrification process occurred due to the denitrification bacteria by using the internal carbon resource to remove a certain amount of nitrate nitrogen. The concentration of dissolved oxygen in oxic tank 1 in this experiment was as low as 0.8–1.0 mg/L, beneficial for the nitrogen removal and denitrification in the preliminary anoxic tank. After the access of effluent of preliminary anoxic tank and 70% of the influent to anoxic tank 1, denitrification occurred in the presence of denitrifying bacteria by using the organic matter in the influent as the carbon source. As a result, the nitrate nitrogen entrained in the nitrifying slurry and recycled sludge was removed [16]. Meanwhile, the long hydraulic residence time of anoxic tank 1 was conducive to the hydrolysis and acidification of recalcitrant organic matter in the influent, and the large recalcitrant organic-matter molecules in the influent were converted into easily degradable small organic-matter molecules, thus providing a carbon source for denitrification. After the access of effluent from anoxic tank 1 to oxic tank 1, the ammonia nitrogen in the influent was oxidized by the nitrifying bacteria into nitrite and nitrate nitrogen. Due to low concentration of the dissolved oxygen in oxic tank 1 and hypoxic microenvironment or local hypoxic environment, the nitrite and nitrate nitrogen could be transformed into nitrogen by denitrifying bacteria via denitrification, thereby leading to removal of the nitrogen through simultaneous nitrification and denitrification [17, 18]. The concentration of nitrate nitrogen in the effluent of oxic tank 1 was decreased to 13.18 mg/L. After the access of effluent from oxic tank 1 and 30% of the influent to anoxic tank 2, the organic matter in the influent was utilized as a carbon source by the denitrifying bacteria for denitrification to remove the nitrate nitrogen. The relatively low concentration of dissolved oxygen in the effluent of oxic tank 1 reduced the consumption of carbon source, which was beneficial for the nitrogen removal and denitrification in anoxic tank 2. Later, in the oxic tank 2, the ammonia nitrogen in the influent was oxidized by the nitrifying bacteria into nitrite and nitrate nitrogen. The high concentration of dissolved oxygen in anoxic tank 2 was adverse to the simultaneous nitrification and denitrification process. The average

concentration of nitrate nitrogen in the effluent of oxic tank 2 was 15.63 mg/L. In the secondary sedimentation tank, deep denitrification occurred in the presence of denitrifying bacteria by using the internal carbon sources, resulting in a reduced concentration of nitrate nitrogen of 15.40 mg/L.

With an increase in the feed-ratio of anoxic tank 1 at stage II and III to 80% and 90%, the concentration of nitrate nitrogen in the effluent of oxic tank 1 was slightly increased. This is because after the increase of feed-ratio of anoxic tank 1, the amount of ammonia nitrogen accessing the oxic tank increased, and a large quantity of nitrate nitrogen was produced after the oxidation of the ammonia nitrogen. With the improvement of denitrification effect, the concentration of the nitrate nitrogen in the effluent of oxic tank 1 gradually decreased. In the stable stage, the average concentration of the nitrate nitrogen in the effluent of oxic tank 1 in stage II and III was 10.95 and 9.85 mg/L, respectively. The concentration of the nitrate nitrogen in the effluent of oxic tank 2 gradually decreased with a decrease in the feed-ratio of anoxic tank 2. The reason is that the nitrified slurry in the oxic tank 2 was discharged without reflux, resulting in the nitrification of solely ammonia nitrogen in the influent of anoxic tank 2, and the denitrification process did not occur in the absence of reflux of nitrified slurry. Meanwhile, the high dissolved oxygen in oxic tank 2 impeded the removal of nitrogen due to the simultaneous nitrification and denitrification process. The average concentration of the nitrate nitrogen in the effluent of oxic tank 2 in stage II and III was reduced to 12.48 and 9.76 mg/L, respectively. In the secondary sedimentation tank, with prolonged denitrification, the concentration of nitrate nitrogen further decreased to 12.11 and 9.46 mg/L.

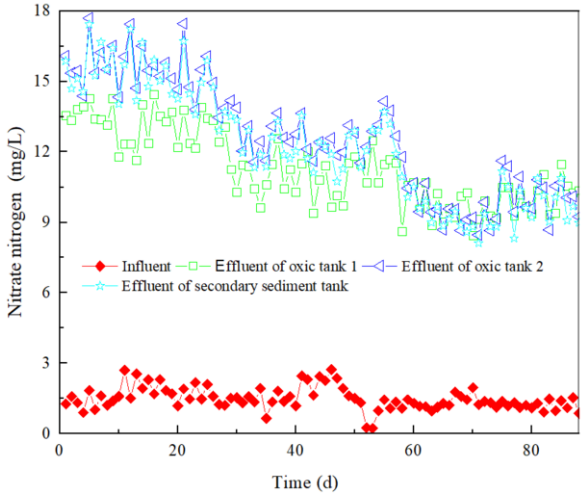

Fig. 5 Nitrate nitrogen removal performance of the step-feed two-stage AO process

The total-nitrogen removal performance of the step-feed two-stage AO process is shown in Figure 6. The average concentration of total nitrogen in the influent was 48.13 mg/L, and the majority of total nitrogen was ammonia nitrogen, which accounted for 89.36%. The average concentration of total nitrogen in the effluent of oxic tank 1 was 14.44 mg/L. The removal of total nitrogen depended on the denitrification effect after the reflex of nitrified slurry to anoxic tank 1, as well as, the simultaneous nitrification and denitrification process in oxic tank 1. The majority of total nitrogen in the effluent of oxic tank 1 was nitrate nitrogen, which accounted for 91.27%. The average

concentration of total nitrogen in the effluent of oxic tank 2 was 18.07 mg/L, which was significantly higher than that in the effluent of oxic tank 1. After the access of 30% of the influent to anoxic tank 2, the nitrification effect was merely completed in oxic tank 2. In the secondary sedimentation tank, the ammonia nitrogen was further oxidized in the presence of nitrifying bacteria and dissolved oxygen in the effluent of the oxic tank, and denitrification occurred in the presence of denitrifying bacteria by using the internal carbon sources. Therefore, the concentration of total nitrogen in the effluent of the secondary sedimentation tank was 17.57 mg/L and the removal rate of 63.58%, which was slightly lower than that of the oxic tank 2. In stage II and III, with an increase in the step-feed ratio in anoxic tank 1, the C/N ratio (the ratio of amount of the organic matter in the influent to the amount of nitrate nitrogen in the recycled sludge and nitrified slurry) in anoxic tank 1 increased, and this was beneficial for the denitrification effect in anoxic tank 1. In the stable stage, the average concentration of the total nitrogen in the effluent of oxic tank 1 in stage II and III was 12.34 and 11.45 mg/L, respectively. After the access of effluent of oxic tank 1 and 20% and 10% of the influent to anoxic tank 2, a proportion of the nitrate nitrogen in the effluent of oxic tank 1 was removed through denitrification, while the ammonia nitrogen in the influent was converted into nitrate nitrogen through the nitrification effect in oxic tank 2. In the stable stage, the average concentration of the total nitrogen in the effluent of oxic tank 2 in stage II and III was 13.71 and 10.67 mg/L, respectively. The concentration of total nitrogen in the effluent of the secondary sedimentation tank was lower than 15 mg/L, meeting the requirement of 1-A level standard. The average concentration was 13.24 and 10.28 mg/L, respectively, with the removal rate of 72.17% and 78.74%. The removal effect of total nitrogen was enhanced with an increase in the step-feed ratio of anoxic tank 1.

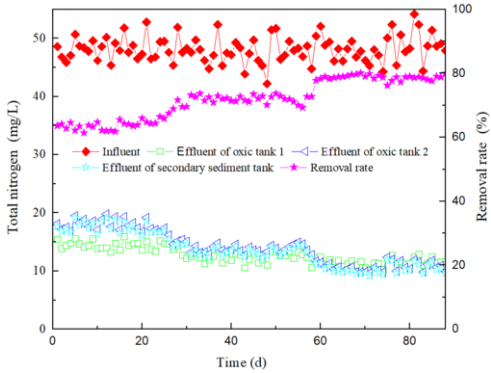

Fig. 6 Total nitrogen removal performance of the step-feed two-stage AO process

3.3 Phosphorus removal performance

The concentration of total phosphorus in the influent during this experiment fluctuated between 3.17 and 4.82 mg/L, with an average concentration of 4.08 mg/L. The step-feed two-stage AO process showed a poor total-phosphorus removal performance, and the average concentration of total phosphorus in the effluent was up to 2.66 mg/L, with a removal rate of only 34.72%. Since no anoxic tank was set in the step-feed two-stage AO process, the growth of phosphorus-accumulating bacteria was impeded due to the lack of an alternating anaerobic/aerobic environment. Therefore, the removal of phosphorus was only dependent on the reproduction of microorganisms. To meet the 1A-level

discharge standard, the concentration of total phosphorus in the effluent was reduced by adding PAC (10–35 mg/L) to the pipeline connecting oxic tank 2 and secondary sedimentation tank. When the dosage of PAC reached 35 mg/L, the concentration of total phosphorus in the effluent was found to be below 0.5 mg/L after 10 consecutive days of operation. The average concentration of total phosphorus in the effluent was 0.37 mg/L, and the removal rate reached 90.93%. After the addition of PAC, the removal effect of total phosphorus was significantly intensified due to following reasons: 1) The phosphate in the effluent of oxic tank 2 reacted with aluminum ions in PAC to yield a precipitate, which was removed readily. 2) The activated sludge in the effluent of oxic tank 2 exhibited a high adsorption capacity for the precipitate in the secondary sedimentation tank, thereby improving the removal effect of total phosphorus.

Table 2 Removal performance of total phosphorus in the step-feed two-stage AO process before and after the addition of PAC

Concentration of total phosphorus in the influent (mg/L)		Before addition of PAC				After addition of PAC			
		Concentration of total phosphorus in the effluent (mg/L)		Removal rate (%)		Concentration of total phosphorus in the effluent (mg/L)		Removal rate (%)	
Range	Mean	Range	Mean	Range	Mean	Range	Mean	Range	Mean
3.17–4.82	4.08	2.01–3.23	2.66	27.56–41.26	34.72	0.43–0.26	0.37	87.61–94.18	90.93

4. Conclusion

In the present study, the urban sewage with a low C/N ratio was treated with a step-feed two-stage AO process coupled with chemical phosphorus-eliminating process, and the effect of step-feed ratio on the removal rate of nitrogen was studied. The major conclusions of the study can be summarized as:

1) The step-feed two-stage AO process exhibited a good removal effect on COD, while the step-feed ratio had a negligible impact on this removal effect. The COD values of effluent met the requirements of the 1A-level discharge standard.

2) The step-feed ratio had a significant impact on the removal rates of ammonia nitrogen and total nitrogen. With an increase in the step-feed ratio of anoxic tank 2, the removal rates of ammonia nitrogen and total nitrogen decreased significantly. When the step-feed ratio of anoxic pool 2 was set at 10%, the removal rates of ammonia nitrogen and total nitrogen were found to be highest, and the requirements of the 1A-level discharge standard were met. The high step-feed ratio of preliminary anoxic tank and reduction of the content of dissolved oxygen in the effluent of oxic tank 1 effectively preserved the carbon sources and improved the removal performance of total nitrogen.

3) The step-feed two-stage AO process exhibited a poor removal performance for total phosphorus. However, after the addition of PAC to the pipeline connecting oxic tank 2 and secondary sedimentation tank, the concentration of total phosphorus in the effluent was decreased below 0.5 mg/L, thereby meeting the requirements of the 1A-level discharge standard.

References

[1] Pang Weihai, Li Huiping, Zhang Kun, et al. Cyclic activated sludge system-based process optimization to improve denitrification efficiency of low C/N municipal wastewater [J]. Journal of Tongji University: Natural Science, 2021, 49 (09): 1257-1264.

[2] Liu Leibin, Gao Shouyou. Technology practice and analysis on the seven-stage Bardenpho process in WWTP [J]. Water & Wastewater Engineering, 2021, 57 (09): 21-25.
[3] Li Libin. Efficiency and mechanism of a process combining A2O-reinforced nitrogen and phosphorus removal with the reduction of sludge [D]. Harbin Institute of Technology, 2019.
[4] Li Haibo. Pilot study on a modified A2O biological nitrogen and phosphorus removal technique based on upgraded AO [D]. Beijing University of Science and Technology, 2017.
[5] Xiao Haike, PengYongzhen, Zhang Qiong, et al. Pre-anaerobic treatment enhanced partial nitrification start-up coupled with anammox for advanced nitrogen removal from low C/N domestic wastewater [J]. Bioresource technology, 2021, 337: 125434.
[6] Lu Wenkang, Zhang Yanli, Wang Qingqing, et al. Achieving advanced nitrogen removal in a novel partial denitrification/anammox-nitrifying (PDA-N) biofilter process treating low C/N ratio municipal wastewater [J]. Bioresource technology, 2021, 340: 125661.
[7] Zheng Juntian, Zheng Jun, Cheng Luowen, et al. Influence of mixed liquid reflux ratio on a new multiple-inflow A/O/A/A/O sludge-biofilm coupling process for denitrification and phosphorus removal [J]. Chinese Journal of Environmental Engineering, 2021, 15 (05): 1744-1752.
[8] Bao Linlin, Cheng Qingfeng, Li Dong, et al. Optimization of energy saving and nutrient removal in modified carrousel oxidation ditch process [J]. China Water & Wastewater, 2011, 27 (13): 8-11.
[9] Li Donghui, Li Weiguang, Zhang Kailei, et al. Effect of denitrifying liquor recycle ratio on nitrogen and phosphorus removal efficiency of BBSNP [J]. Water & Wastewater Engineering, 2020, 56 (10): 37-41.
[10] Li Pengfeng, Zheng Xingcan, Sun Yongli, et al. Construction and Application of Systematic and Accurate Diagnosis Technology for Urban WWTP [J]. China Water & Wastewater, 2021, 37 (12): 1-6+13.
[11] Li Yafeng, Yang Sijing, Yu Yaofu. Optimization measures for denitrification and phosphorus removal based on inverted A2/O process [J]. Industrial Water Treatment, 2019, 39 (08): 15-18.
[12] XuPeng, Xiao Enrong, He Feng, et al. High performance of integrated vertical-flow constructed wetland for polishing low C/N ratio river based on a pilot-scale study in Hangzhou, China [J]. Environmental science and pollution research international, 2019, 26 (22): 22431-22449.
[13] Zhang Xiaojing, Li Dong, Liang Yuhai, et al. Performance and microbial characteristic of SNAD process for treating domestic sewage in a membrane bioreactor [J]. Journal of Harbin Institute of Technology, 2015, 47 (08): 87-91.
[14] Gao Ruitao, PengYongzhen, Li Jianwei, et al. Nutrients removal from low C/N actual municipal wastewater by partial nitritation/anammox (PN/A) coupling with a step-feed anaerobic-anoxic-oxic (A/A/O) system [J]. The Science of the total environment, 2021, 799: 149293.
[15] Zhu Zelong. Research on the application of combination of modified Bardenpho and MBBR processes in urban sewage treatment plants [D]. Hebei University, 2017.
[16] Bao Linlin, Cheng Qingfeng, Li Dong, et al. Experimental study on the enhancement of nitrogen and phosphorus removal with a modified oxidation ditch process [J]. Water & Wastewater Engineering, 2011, 47 (09): 125-128.
[17] Li Ning, Zeng Wei, Miao Zhijia, et al. Enhanced nitrogen removal and in situ microbial community in a two-step feed oxic/anoxic/oxic-membrane bioreactor (O/A/O-MBR) process [J]. Journal of Chemical Technology & Biotechnology, 2019, 94 (4): 1315-1322.
[18] Charlie L. Martin Jr., Clayton J. Clark II. Traditional Nitrogen Removal Coupled with SND to Meet Advanced WWTP Standards at a Full Scale SBR Wastewater Treatment Facility [J]. Journal of Water Resource and Protection, 2017, 9 (10): 1169-1183.

Fuzzy Systems and Data Mining IX
A.J. Tallón-Ballesteros and R. Beltrán-Barba (Eds.)

doi:10.3233/FAIA231056

Dynamic Analysis of a Discrete Predator-Prey Model with Increased Density of Both Predator and Prey

Yong-Xin CEN [a], Ming-Shan LI [b], Zhen-Kun JIANG [a], Wan-Ying LI [a], Song-Bo WANG [c,1] and Xiao-Liang ZHOU [a]

[a] *Department of Mathematics, Lingnan Normal University,Zhanjiang 524048, China*
[b] *College of Economic and Management, Nanjing University of Aeronautics and Astronautics, Nanjing 210016, China*
[c] *School of Business, Lingnan Normal University, Zhanjiang 524048, China*

Abstract. We study the dynamical property of a discrete predator-prey model with increased density of both predator and prey. We survey the existence conditions and stability of the equilibrium points by using the bifurcation theory. We investigate N-S bifurcations at the positive equilibrium point. Finally, We provide a biological explanation for our results.

Keywords. discrete predator-prey model, functional response, Allee effect, stability, Neimark-Sacker bifurcation

1. Introduction

In 2018, Ryu, Ko and Haque [1] discussed the following predation systems

$$\begin{cases} \frac{du}{dt} = Ru\left(1-\frac{u}{U}\right) - vG(u,v), \\ \frac{dv}{dt} = \varepsilon vG(u,v) - \mu v, \end{cases} \tag{1}$$

where u and v represent the prey population density and predator population density at time t, respectively. R is the increasing rate of prey and U is the maximum environmental capacity for the prey, ε represents the rate at which captured prey is converted into predators, μ indicates natural attrition of predators. They introduced function $G(u,v)$ (also see [2]) as follows

$$G(u,v) = \frac{Ce_0uv}{1+hCe_0uv}, \tag{2}$$

where C represents the amount of prey caught by a predator, h is the time to process each prey and e_0 is the encounter probability. The functional response (2) shows the mechanisms by which predators, such as tuna, capture their prey. Obviously, from $G(u,v)$ we

[1]Corresponding Author: Song-Bo Wang, School of Business, Lingnan Normal University, Zhanjiang 524048, China; E-mail: zxlmath@163.com.

see that when the population scale of predators is too large and the foraging line of predators is too long, which leads to the poor foraging signal transmission between predators and reduces the feeding efficiency [2]. This cooperation mechanism in predator-prey interaction may produce strong Allee effects (see [3]) in predator species. This phenomenon is therefore different from that produced by traditional functional functions such as the Lotka-Volterra type, Holling types, Monod-Haldane type ($G(u,v)=\frac{mx}{a+u^2}$, see [4]), Ratio-dependent type ($G(u,v)=\frac{mx}{u+av}$, see [5]) and B-D type ($G(u,v)=\frac{mu}{a+bu+cv}$, see [6,7]).

For simplicity in studying model (1) with functional response (2), the authors of [1] defined the following variable substitutions

$$Rt=\bar{t},\quad \frac{u}{U}=\bar{u},\quad hCe_0Kv=\bar{v},\quad \frac{1}{Ce_0(hK)^2R}=a,\quad \frac{\varepsilon}{Rh}=b,\quad \frac{\mu}{R}=d,$$

still used t, u and v to represent $\bar{t}$, $\bar{u}$ and $\bar{v}$ respectively and rewrote the system in the simplified form

$$\begin{cases}\frac{\mathrm{d}u}{\mathrm{d}t}=(1-uu)-\frac{auv^2}{1+uv},\\ \frac{\mathrm{d}v}{\mathrm{d}t}=\frac{buv^2}{1+uv}-dv,\end{cases}\tag{3}$$

where a, b and d are all positive numbers. They showed that (3) exhibited bifurcation phenomenon.

Due to the system (3) has a new different functional response function exhibiting Allee effects, we want to study what kind of dynamic behavior does the corresponding discrete-time system have. In fact, the discrete system is not a simple analogs of continuous one, and sometimes, even simple models can display complex dynamics (see [8,9]). Therefore, we will expect the corresponding discrete-time system to provide much richer dynamics.

By applying the discretization technique, we get the discrete system

$$\begin{cases}u_{n+1}=u_n+u_n(1-u_n)-\frac{au_n{v_n}^2}{1+u_nv_n},\\ v_{n+1}=v_n+\frac{bu_n{v_n}^2}{1+u_nv_n}-dv_n.\end{cases}\tag{4}$$

Obviously, system (4) has the following functional function

$$f(u_n,v_n):=\frac{u_nv_n}{1+u_nv_n}.\tag{5}$$

After careful examination of the existing literature, we know that many types of functional functions have been proposed and studied by researchers. For example, (i) Lotka-Volterra type: $f(u_n,v_n)=mu_n$ (see [10-12]); (ii) Holling-II type: $f(u_n,v_n)=\frac{mu_n}{a+u_n}$ (see [13-16]); (iii) Holling-III type: $f(u_n,v_n)=\frac{mu_n^2}{a+u_n^2}$ (see [17,18]); (iv) Holling-IV type: $f(u_n,v_n)=\frac{mu_n}{a+bu_n+u_n^2}$ (see [19-21]); (v) other types can refer to [22-28]. Almost all functional responses treated in the above literature are either monotonic or non-monotonic depending on prey. It is therefore novel to consider the simultaneous monotonic functional response (5) of predators and prey.

2. Existence and stability analysis

The corresponding mapping $F : R^2 \mapsto R^2$ of (4) is

$$F : \begin{pmatrix} u \\ v \end{pmatrix} \mapsto \begin{pmatrix} (2-u)u - \frac{auv^2}{1+uv} \\ (1-d)v + \frac{buv^2}{1+uv} \end{pmatrix}. \tag{6}$$

To find the equilibrium points of the mapping (6), we let

$$(2-u)u - \frac{auv^2}{1+uv} = u, \quad (1-d)v + \frac{buv^2}{1+uv} = v.$$

For positive equilibrium point $P(u,v)$ $(u>0, v>0)$, u and v satisfy

$$u^3 - u^2 + \frac{ad^2}{b(b-d)} = 0, \quad v = \frac{d}{(b-d)u}. \tag{7}$$

By simple discussion (omitted), we easy get the following conclusion.

Lemma 1 *Suppose $b > d$ and let $a_c := \frac{4}{27}\frac{b(b-d)}{d^2}$. When $a > a_c$, there is no positive equilibrium point; When $a = a_c$, there is unique positive equilibrium point $P_0 = (\frac{2}{3}, \frac{3d}{2(b-d)})$; When $a < a_c$, there are two different positive equilibrium points $P_1 = (u_1, v_1), P_2 = (u_2, v_2)$ satisfying (7) and $u_1 < \frac{2}{3} < u_2$.*

The Jacobian matrix of mapping (6) at any point $P = (u,v)$ is

$$J(P) = \begin{pmatrix} 2(1-u) - \frac{av^2}{1+uv} + \frac{auv^3}{(1+uv)^2} & -\frac{auv(2+uv)}{(1+uv)^2} \\ \frac{bv^2}{(1+uv)^2} & 1-\gamma + \frac{buv(2+uv)}{(1+uv)^2} \end{pmatrix}.$$

Corresponding to positive equilibrium points P_i $(i = 0,1,2)$, we have

$$J(P_i) = \begin{pmatrix} (2-d_0)s_i & -a(1-d_0^2) \\ \frac{dd_0}{a(1-d_0)}s_i & 1+dd_0 \end{pmatrix}, \ \ i = 0,1,2$$

where $d_0 := 1 - \frac{d}{b}$, and $s_i := 1 - u_i$ $(i = 0,1,2)$, and their characteristic polynomials

$$p(\lambda) = \lambda^2 - ((2-d_0)s_i + dd_0 + 1)\lambda + ((2-d_0)s_i + 3dd_0 s_i),$$

for $i = 0,1,2$.

In the following, we consider positive equilibrium point P_1 only. The discussions of positive equilibrium points P_0 and P_2 are left for another article.

Let

$$d_1 := \frac{1 + s_1(d_0 - 2)}{3s_1 d_0}.$$

lemma 2 *If $a < a_c$, we have*

(i) *when $d < d_1$, P_1 is a sink;*
(ii) *when $d > d_1$, P_1 is a source; or*
(iii) *when $d = d_1$, P_1 is non-hyperbolic.*

Proof. By the conclusion of Lemma 1, we have $u_1 < \frac{2}{3}$ and $s_1 > \frac{1}{3}$. Then, we have $p(1) = dd_0(3s_1 - 1) > 0$, $p(-1) = 2 + 2(2 - d_0)s_1 + dd_0(1 + 3s_1) > 0$ and $p(0) = (2 - d_0)s_1 + 3dd_0s_1$. If characteristic equation $p(\lambda) = 0$ has two real roots λ_1 and λ_2, then, from $p(1) > 0$ and $p(-1) > 0$, we know that one of three cases is true:

(a) $\lambda_1 > 1$ and $\lambda_2 > 1$;
(b) $\lambda_1 < -1$ and $\lambda_2 < -1$; or
(c) $-1 < \lambda_1 < 1$ and $-1 < \lambda_2 < 1$.

If λ_+ and λ_- are a pair of conjugate complex roots of $p(\lambda) = 0$, then $\|\lambda_+\|^2 = \|\lambda_-\|^2 = p(0)$.

(i) When $d < d_1$, we get $p(0) < 1$. If characteristic equation $p(\lambda) = 0$ has two real roots λ_1 and λ_2, then, $\lambda_1\lambda_2 = P(0) < 1$, i.e., the case (c) is true. If λ_+ and λ_- are a pair of conjugate complex roots of $p(\lambda) = 0$, then $\|\lambda_+\|^2 = \|\lambda_-\|^2 = P(0) < 1$. This shows that E_1 is a sink.

(ii) When $d > d_1$, we get $p(0) > 1$. Similar to the proof in (i), If λ_1 and λ_2 are both real roots, then the case (a) or (b) is true. If λ_+ and λ_- are both complex roots, then $\|\lambda_+\|^2 = \|\lambda_-\|^2 = p(0) > 1$. This shows that P_1 is a source.

(iii) When $d = d_1$, we get $P(0) = 1$. Therefore, $p(\lambda) = 0$ can not has real roots. Otherwise, two real roots λ_1, λ_2 satisfy $\lambda_1\lambda_2 = p(0) = 1$, this contradicts with any case of (a), (b) and (c). Hence, $p(\lambda) = 0$ has complex roots, this shows that P_1 is non-hyperbolic.

3. Bifurcations analysis

By Lemma 2, if $d = d_1$ $p(\lambda) = 0$ has complex roots λ_+ and λ_- at equilibrium point P_1 and $\|\lambda_+\| = \|\lambda_-\| = 1$. By using variable substitution

$$\mu = u - u_1, \quad \nu = v - v_1, \quad d^* = d - d_1,$$

We have the following Taylor expansion form at $(\mu, \nu, d^*) = (0, 0, 0)$

$$\tilde{F} : \begin{pmatrix} \mu \\ \nu \end{pmatrix} \mapsto \begin{pmatrix} c_{11} & c_{12} \\ c_{21} & c_{22} \end{pmatrix} \begin{pmatrix} \mu \\ \nu \end{pmatrix} + \begin{pmatrix} f_1(\mu, \nu) \\ f_2(\mu, \nu) \end{pmatrix} \tag{8}$$

where

$$c_{11} = \left(1 + \frac{d_1}{b}\right)(1 - x_1), \quad c_{12} = -a\left(1 + \left(1 - \frac{d_1}{b}\right)^2\right), \quad c_{21} = b_1y_1\left(1 - \frac{d_1}{b}\right)^2,$$

$$c_{22} = (1 - d_1 - d^*) + bx_1\left(1 - \frac{d_1}{b}\right)^2,$$

$$f_1(\mu, \nu) = c_{13}\mu^2 + c_{14}\mu\nu + c_{15}\nu^2 + e_1\mu^3 + e_2\mu^2\nu + e_3\mu\nu^2 + e_4\nu^3 + O(\|(\mu, \nu)\|^4),$$

$$f_2(\mu, \nu) = c_{23}\mu^2 + c_{24}\mu\nu + c_{25}\nu^2 + q_1\mu^3 + q_2\mu^2\nu + q_3\mu\nu^2 + q_4\nu^3 + O(\|(\mu, \nu)\|^4),$$

$$c_{13} = -1 + \left(1 - \frac{d_1}{b}\right)^2(1 - x_1), \quad c_{14} = -2ay_1\left(1 - \frac{d_1}{b}\right)^2(1 - x_1),$$

$$c_{15} = -ax_1\left(1-\tfrac{d_1}{b}\right)^3,$$

$$e_1 = -\left(1-\tfrac{d_1}{b}\right)^2(1-x_1)^2,\ \ e_2 = 3\left(1-\tfrac{d_1}{b}\right)^3(1-x_1),\ \ e_3 = a(2x_1y_1-1)\left(1-\tfrac{d_1}{b}\right)^4,$$

$$e_4 = ax_1{}^2\left(1-\tfrac{d_1}{b}\right)^4,$$

$$c_{23} = -\tfrac{b}{a}\left(1-\tfrac{d_1}{b}\right)^2(1-x_1),\ \ c_{24} = b(1-x_1y_1)\left(1-\tfrac{d_1}{b}\right)^3,\ \ c_{25} = -bx_1{}^2\left(1-\tfrac{d_1}{b}\right)^3,$$

$$q_1 = \tfrac{b}{a}y_1\left(1-\tfrac{d_1}{b}\right)^2(1-x_1),\ \ q_2 = by_1(x_1y_1-2)\left(1-\tfrac{d_1}{b}\right)^4,$$

$$q_3 = bx_1(x_1y_1-2)\left(1-\tfrac{d_1}{b}\right)^4,\ \ q_4 = bx_1{}^3\left(1-\tfrac{d_1}{b}\right)^4.$$

The characteristic equation associated with mapping (8) at $(0,0)$ is

$$\lambda^2 - q_1(d^*)\lambda + q_0(d^*) = 0,$$

where

$$q_1(d^*) = 1+s_1(2-d_0)+(d_1+d^*)d_0,\quad q_0(d^*) = s_1(2+3d_0(d_1+d^*)-d_0).$$

When d^* is near 0, we have

$$\lambda_\pm = \frac{1+s_1(2-d_0)+(d_1+d^*)d_0}{2} \pm i\frac{\sqrt{4s_1(2+3d_0(d_1+d^*)-d_0)-(1+s_1(2-d_0)+(d_1+d^*)d_0)^2}}{2}$$

and

$$\|\lambda_\pm\| = \sqrt{s_1(2+3d_0(d_1+d^*)-d_0)},\qquad \frac{\mathrm{d}\|\lambda_\pm\|}{\mathrm{d}d^*}\Big|_{d^*=0} = \frac{3s_1d_0}{2} \neq 0.$$

In addition, when $d^*=0$, that the non-degenerate condition are

$$d_1 \neq \frac{k+s_1(d_0-2)}{s_1d_0},\quad k=-3,-2,-1,1. \tag{9}$$

It's easy to see from the previous definition of d_1 that the condition (9) is obviously true.

By constructing an invertible linear transformation

$$\begin{pmatrix}\mu\\ \nu\end{pmatrix} = \begin{pmatrix}-c_{12} & 0\\ c_{11}-\rho & -\varphi\end{pmatrix}\begin{pmatrix}\xi\\ \eta\end{pmatrix} \tag{10}$$

where

$$\rho = -\frac{q_1(0)}{2},\quad \varphi = \frac{\sqrt{4q_0(0)-q_1^2(0)}}{2},$$

we transform the mapping (8) into the form

$$\begin{pmatrix}\xi\\ \eta\end{pmatrix}=\begin{pmatrix}\rho & -\varphi\\ \varphi & \rho\end{pmatrix}\begin{pmatrix}\xi\\ \eta\end{pmatrix}+\begin{pmatrix}g(\xi,\eta)\\ h(\xi,\eta)\end{pmatrix}, \tag{11}$$

where

$$\begin{aligned}
g(\xi,\eta)&=-\tfrac{1}{c_{12}}\left(c_{13}\mu^2+c_{14}\mu\nu+c_{15}\nu^2+e_1\mu^3+e_2\mu^2\nu+e_3\mu\nu^2+e_4\nu^3\right)\\
&\quad+O(\|(\xi,\eta)\|^4),\\
h(\xi,\eta)&=\tfrac{1}{c_{12}\varphi}\Big([(\rho-c_{11})c_{13}-c_{12}c_{23}]\mu^2+[(\rho-c_{11})c_{14}-c_{12}c_{24}]\mu\nu\\
&\quad+[(\rho-c_{11})c_{15}-c_{12}c_{25}]\nu^2+[(\rho-c_{11})e_1-c_{12}q_1]\mu^3\\
&\quad+[(\rho-c_{11})e_2-c_{12}q_2]\mu^2\nu+[(\rho-c_{11})e_3-c_{12}q_3]\mu\nu^2\\
&\quad+[(\rho-c_{11})e_4-c_{12}q_4]\nu^3\Big)+O(\|(\xi,\eta)\|^4),
\end{aligned}$$

$$\mu^2=c_{12}^2\xi^2,$$

$$\mu\nu=-c_{12}(c_{11}-\rho)\xi^2+c_{12}\varphi\xi\eta,$$

$$\nu^2=(c_{11}-\rho)^2\xi^2+\varphi^2\eta^2-2(c_{11}-\rho)\varphi\xi\eta,$$

$$\mu^3=-c_{12}^3\xi^3,$$

$$\mu^2\nu=c_{12}^2(c_{11}-\rho)\xi^3-c_{12}^2\varphi\xi^2\eta,\mu\nu^2=-c_{12}(c_{11}-\rho)^2\xi^3-c_{12}^2\varphi^2\xi\eta^2+2c_{12}(c_{11}-\rho)\varphi\xi^2\eta,$$

$$\nu^3=(c_{11}-\rho)^3+\varphi^3\eta^3+3(c_{11}-\rho)\varphi\xi\eta^2-3(c_{11}-\rho)^2\varphi\xi^2\eta.$$

By simple calculation, we get the partial derivatives with respect to g and h at $(\xi,\eta)=(0,0)$

$$\begin{aligned}
g_{\xi\xi}&=-\tfrac{1}{c_{12}}\Big(2c_{12}^2c_{13}-2c_{12}c_{14}(c_{11}-\rho)+2c_{15}(c_{11}-\rho)^2\Big),\\
g_{\xi\eta}&=-\varphi c_{14}+\tfrac{1}{c_{12}}\Big(2\varphi c_{15}(c_{11}-\rho)\Big),\\
h_{\eta\eta}&=-\tfrac{2}{c_{12}}\Big((c_{15}(c_{11}-\rho)+c_{12}c_{25})\Big)\varphi,\\
g_{\xi\xi\xi}&=6e_1c_{12}^2-6e_2c_{12}(c_{11}-\rho)+6e_3(c_{11}-\rho)^2-\tfrac{1}{c_{12}}6e_4(c_{11}-\rho)^3,\\
g_{\eta\eta\eta}&=-\tfrac{1}{c_{12}}6e_4\varphi^3,\\
g_{\xi\xi\eta}&=2\varphi c_{12}e_2-4e_3\varphi(c_{11}-\rho)-\tfrac{1}{c_{12}}6e_4\varphi(c_{11}-\rho)^2,\\
g_{\xi\eta\eta}&=2\varphi^2e_3-\tfrac{1}{c_{12}}6e_4\varphi(c_{11}-\rho),
\end{aligned}$$

$$
\begin{aligned}
h_{\xi\xi} &= -\tfrac{2}{c_{12}\varphi}\Big(c_{12}^2(c_{13}(c_{11}-\rho)+c_{12}c_{23})+c_{12}(c_{14}(c_{11}-\rho)+c_{12}c_{24})(c_{11}-\rho)\\
&\quad +c_{12}(c_{15}(c_{11}-\rho)+c_{12}c_{25})(c_{11}-\rho)^2\Big),\\
h_{\xi\eta} &= -\tfrac{1}{c_{12}\varphi}\Big(\varphi c_{12}(c_{14}(c_{11}-\rho)+c_{12}c_{24})+2((c_{11}-\rho)c_{15}+c_{12}c_{25})(c_{11}-\rho)\varphi\Big),\\
h_{\eta\eta} &= -\tfrac{2}{c_{12}}\Big((c_{15}(c_{11}-\rho)+c_{12}c_{25})\Big)\varphi,\\
h_{\xi\xi\xi} &= \tfrac{1}{c_{12}\varphi}\Big((6e_1(c_{11}-\rho)-c_{12}q_1)c_{12}^3-(6e_2(c_{11}-\rho)+c_{12}q_2)c_{12}^2(c_{11}-\rho)\Big),\\
h_{\xi\xi\eta} &= -\tfrac{2}{c_{12}\varphi}\Big((e_2(c_{11}-\rho)-3(e_4(c_{11}-\rho)+c_{12}q_4)(c_{11}-\rho)^2\varphi-3(e_3(c_{11}-\rho)\\
&\quad +c_{12}q_3)c_{12}^2(c_{11}-\rho)^2-3(e_4(c_{11}-\rho)+c_{12}q_4)c_{12}^2(c_{11}-\rho)^3\\
&\quad +2c_{12}(e_3(c_{11}-\rho)+c_{12}q_3)(c_{11}-\rho)\varphi\Big),\\
h_{\xi\eta\eta} &= \tfrac{1}{c_{12}\varphi}\Big((2e_3(c_{11}-\rho)-c_{12}q_3)c_{12}\varphi^2-6(e_4(c_{11}-\rho)+c_{12}q_4)(c_{11}-\rho)\varphi\Big),\\
h_{\eta\eta\eta} &= -\tfrac{6}{c_{12}}\Big((e_4(c_{11}-\rho)-c_{12}q_4)\Big)\varphi^2.
\end{aligned}
$$

To ensure that N-S bifurcation occurs in mapping (6), we need to make sure that

$$
c(0)=\left(-\mathrm{Re}\Big(\frac{(1-2\lambda_+)\,\bar{\lambda}_-^{\,2}}{1-\lambda_+}A_1A_2\Big)-\frac{1}{2}\|A_2\|^2-\|A_3\|^2+\mathrm{Re}(\bar{\lambda}_-A_4)\right)\Bigg|_{\gamma^*=0}\neq 0
$$

where

$$
\begin{aligned}
A_1 &= \tfrac{1}{8}\left(g_{\xi\xi}-g_{\eta\eta}+2h_{\xi\eta}+i(h_{\xi\xi}-h_{\eta\eta}-2g_{\xi\eta})\right),\\
A_2 &= \tfrac{1}{4}\left(g_{\xi\xi}+g_{\eta\eta}+i(h_{\xi\xi}+h_{\eta\eta})\right),\\
A_3 &= \tfrac{1}{8}\left(g_{\xi\xi}-g_{\eta\eta}-2h_{\xi\eta}+i(h_{\xi\xi}-h_{\eta\eta}+2g_{\xi\eta})\right),\\
A_4 &= \tfrac{1}{16}\left(g_{\xi\xi\xi}+g_{\xi\eta\eta}+h_{\xi\xi\eta}+h_{\eta\eta\eta}+i(h_{\xi\xi\xi}+h_{\xi\eta\eta}-g_{\xi\xi\eta}-g_{\eta\eta\eta})\right).
\end{aligned}
$$

By simple calculation, we get

$$
\begin{aligned}
c(0) = {} & B_1\left((g_{\xi\xi}-g_{\eta\eta}+2h_{\xi\eta})(h_{\xi\xi}+h_{\eta\eta})+(h_{\xi\xi}-h_{\eta\eta}-2g_{\xi\eta})(g_{\xi\xi}+g_{\eta\eta})\right)\\
& -B_2\left((g_{\xi\xi}+g_{\eta\eta}-2h_{\xi\eta})(g_{\xi\xi}+g_{\eta\eta})+(h_{\xi\xi}-h_{\eta\eta}+2g_{\xi\eta})(h_{\xi\xi}+h_{\eta\eta})\right)\\
& -\tfrac{1}{32}\left((g_{\xi\xi}+g_{\eta\eta})^2+(h_{\xi\xi}+h_{\eta\eta})^2\right)\\
& -\tfrac{1}{64}\left((g_{\xi\xi}-g_{\eta\eta}-2h_{\xi\eta})^2+(h_{\xi\xi}-h_{\eta\eta}+2g_{\xi\eta})^2\right)\\
& +\tfrac{1}{16}\left(\rho(g_{\xi\xi\xi}+g_{\xi\eta\eta}+h_{\xi\xi\eta}+h_{\eta\eta\eta})-\varphi(h_{\xi\xi\xi}+h_{\xi\eta\eta}-g_{\xi\xi\eta}-g_{\eta\eta\eta})\right)
\end{aligned}
$$

where $B_1=5\rho^2\varphi-4\rho\varphi^3-4\rho^3\varphi-2\rho\varphi+\varphi^3$, $B_2=2\rho^4-3\rho^3+\rho^2+\rho\varphi^2-\varphi^2-2\varphi^4$.

By Theorem 4.5 in [29], we get the following theorem.

Theorem 1 *If $a < a_c$, condition (9) and $c(0) \neq 0$ hold, then the mapping (6) has a N-S bifurcation at P_1 when d varies in a small neighborhood of d_1. That is, when $d(0) < 0$ and $d > d_1$ (or $d(0) > 0$ and $d < d_1$), then a stable (or unstable) invariant closed curve bifurcates from p_1.*

4. Biological significance of the conclusion

From above theorem, it can be seen that the mapping (6) occurs a N-S bifurcation at P_1 when $c(0) < 0$ and $d > d_1$. The presence of a stable and invariable closed curve indicates that prey and predator populations oscillate periodically and can maintain coexistence. Thus, the strong Allee effect manifested by the functional function determines the fluctuation stability of predator and prey populations. In practical applications, we can obtain the natural factors that affect the evolution of prey and predator populations by studying the bifurcation characteristics of predator-prey model, and regulate the development trend of population by controlling the bifurcation parameters.

Competing interests

The authors promise that there is no competing interest between them.

Fund

This work has been supported by the NSF of China (Grant No. 11961021), the NSF of Guangdong Province (Grant No. 2022A1515010964, 2022A1515010193), the Innovation and Developing School Project (Grant No. 2019KZDXM032) and the Key Project of Science and Technology Innovation of Guangdong College Students (Grant No. pdjh2022b0320, pdjh2023b0325).

References

[1] Ryu K, Ko W, Haque M. Bifurcation analysis in a predator-prey system with a functional response increasing in both predator and prey densities. Nonlinear Dyn. 2018; 94: 1639-56.
[2] Cosner C, Deangelis DL, Ault JS, Olson DB. Effects of spatial grouping on the functional response of predators. Theor Popul Biol. 1999; 56: 65-75.
[3] Allee WC. Animal Aggregations, a Study in General Sociology. Chicago: University of Chicago Press; 1931.
[4] Freedman HI, Wolkowicz GSK. Predator-prey systemswith group defence: the paradox of enrichment revisited. Bull Math Biol. 1986; 48: 493-508.
[5] Arditi R, Ginzburg LR, Akcakaya HR. Variation in plankton densities among lakes: a case for ratio-dependent models. Am Nat. 1991; 138: 1287-1296.
[6] Beddington JR. Mutual interference between parasites or predators and its effect on searching efficiency. J Anim Ecol. 1975; 44: 331-340.
[7] DeAngelis DL, Goldstein RA, ONeill RV. A model for trophic interaction. Ecology. 1975; 56: 881-892.
[8] May RM. Simple mathematical models with very complicated dynamics. Nature. 1976; 261: 459-467.
[9] Rasband SN. Chaotic Dynamics of Nonlinear Systems. New York: Wiley-Interscience; 1990.
[10] Maynard Smith J. Mathematical Ideas in Biology. Cambridge: Cambridge University Press; 1968.

[11] Levine SH. Discrete time modeling of ecosystems with applications in environmental enrichment. Math Biosci. 1975; 24: 307-317.
[12] Liu X, Xiao D. Bifurcations in a discrete time Lotka-Volterra predator-prey system. Discrete Contin Dyn Syst Ser B. 2006; 6: 559-572.
[13] Hadeler KP, Gerstmann I. The discrete Rosenzweig model. Math Biosci. 1990; 98: 49-72.
[14] Neubert MG, Kot M. The subcritical collapse of predator populations in discrete-time predator-prey models. Math Biosci. 1992; 110: 45-66.
[15] Li S, Zhang W. Bifurcations of a discrete prey-predator model with Holling type II functional response. Discrete Contin Dyn Syst Ser B. 2010; 14: 159-176.
[16] Arias CF, Blá G, Falconi M. Dynamics of a Discrete-Time Predator-Prey System with Holling II Functional Response. Qual Theory Dyn Syst. 2022; 31: 21-48.
[17] He ZM, Lai X. Bifurcation and chaotic behavior of a discrete-time predator-prey system. Nonlinear Anal RWA. 2011; 12: 403-417.
[18] Banerjee R, Das P, Mukherjee D. Stability and permanence of a discrete-time two-prey one-predator system with Holling Type-III functional response. Chaos Soliton Fract. 2018; 117: 240-248.
[19] Huang JC, Liu SH, Ruan SG, Xiao DM. Bifurcations in a discrete predator-prey model with nonmonotonic functional response. J Math Anal Appl. 2018; 464: 201-230.
[20] Arsie A, Kottegoda C, Shan C. A predator-prey system with generalized Holling type IV functional response and Allee effects in prey. J Differ Equations. 2022; 309: 704-740.
[21] Shang Z, Qiao Y. Bifurcation analysis of a Leslie-type predator-prey system with simplified Holling type IV functional response and strong Allee effect on prey. Nonlinear Anal-Real. 2022; 64: 103453.
[22] Apreutesei NC. An optimal control problem for a prey-predator system with a general functional response. Appl Math Lett. 2009; 22: 1062-1065.
[23] Saito Y, Sugie J, Lee YH. Global asymptotic stability for predator-prey models with environmental time-variations. Appl Math Lett. 2011; 24: 1973-1980.
[24] Tarfulea N, Minut A. Qualitative analysis of a diffusive prey-predator model. Appl Math Lett. 2012; 25: 803-807.
[25] Montano MC, Lisena B. Diffusive HollingCTanner predator-prey models in periodic environments. Appl Math Lett. 2019; 87: 42-49.
[26] Singh A, Malik P. Bifurcations in a modified Leslie-Gower predator-prey discrete model with Michaelis-Menten prey harvesting. J Appl Math Comput. 2021; 67: 143-174.
[27] Wang ZH, Wang YS. Bifurcations in diffusive predator-prey systems with Beddington-DeAngelis functional response. Nonlinear Dyn. 2021; 105: 1045-1061.
[28] Hamada MY, El-Azab T, El-Metwally H. Bifurcations and dynamics of a discrete predator-prey model of ricker type. J Appl Math Comput. 2023; 69: 113-135.
[29] Kuznetsov YA. Elements of Applied Bifurcation Theory. New York: Springer-Verlag; 1998.

Fuzzy Systems and Data Mining IX
A.J. Tallón-Ballesteros and R. Beltrán-Barba (Eds.)

doi:10.3233/FAIA231057

Derivation Algebras of Restricted Hom-Lie Triple Systems

Hanqi Zhou [a], Yanqin Dong [a,1] Xinyang Li [a], Xin Cong [a] and Bing Liu [a]
[a] *Department of Mathematics, Changchun Normal University, Jilin 130000, China*

Abstract. In this paper, we investigate the properties of derivations of restricted Hom-Lie triple systems. By giving the concepts of derivations, generalized derivations, centroids and Hom-p-subsystems, we obtain some good results on generalized derivation algebras and their subalgebras, which including the subspace $\mho$ satisfying some conditions in the linear transformation $\mathrm{End}(L)$ is a restricted Hom-Lie triple system, the generalized derivation is a Hom-p-subsystem of $\mho$ and the central derivation is the intersection of the centroid and the derivation. The novelty of this paper is to discuss the derivation properties of Hom-Lie triple systems on the field $\mathbb{F}$ of characteristic p, which makes the derivation structure of restricted Hom-Lie triple systems more complete.

Keywords. derivations, restricted Hom-Lie triple systems, Hom-p-subsystems

1. Introduction

Lie triple system first appeared in Cartan's study of Riemannian geometry. As the object of algebraic research, it was introduced by Jacobson in 1949, which is mainly used to study the subspace of closed associative algebras under the triple commutator $[[a,b],c]$. Through Lie triple system, the theory of symmetric space and algebraic theory can be closely linked, so as to establish a bridge between algebraic problems and geometric problems. Therefore, as a new algebraic system, Lie triple system has attracted the attention and extensive research of scholars.

This paper is based on two aspects. On the one hand, Terrell.L Hodge [1] gave the concept of restricted Lie triple systems in 2001. Dong [2] studied some properties and relations of restricted Lie triple systems and restrictable Lie triple systems. In [3], Liu and Chen developed the Frattini theory of groups to restricted Lie triple systems, and obtained the properties of Frattini-subsystems and Frattini p-subsystems of restricted Lie triple systems. On this basis, Chen et al. [4] gave some conditions for the commutative property of restricted Lie triple systems, and characterized some features of p-mappings and semi-elements of restricted Lie triple systems. In 2023, Liu [5] studied the relationship among derivation structures of restricted Lie triple systems.

On the other hand, in the 1990s, Hom-type algebras emerged in physics so as to find quantum deformations of some algebras on vector fields. Hom-type algebras are closely related to theoretical physics, Yang-Baxter equations, braid groups and quantum groups,

[1]Corresponding Author. E-mail:1207915490@qq.com

and many important results have been obtained. In 2012, Yau [6] first discussed Hom-Lie triple systems. In [7], Zhou et al. studied the properties of generalized derivation algebras and centroids of Hom-Lie triple systems and the relationship between them. Then, Chen et al. [8] studied the product structure and complex structure of Hom-Lie triple systems from the algebraic point of view, and gave the corresponding decomposition. In 2022, Bhutia et al. [9] studied equivariant cohomolgy theory, one-parameter formal deformation and central extensions of Hom-Lie triple systems in the case of equivariant.

At present, the discussion on the restricted Hom-structure has attracted more attention from scholars at home and abroad. In 2015, Guan [10] studied the structure of restricted Hom-Lie algebras. In [11], Shaqaqha introduced the restricted Hom-Lie Superalgebras. Although many achievements have been made in such research, the study on the problem of derivation structure is not complete, and there are still many problems that need to be further discussed. In [12], Yara gave the definition of restricted Hom-Lie triple system. Inspired by the above literatures, this paper mainly studies the derivation problem under the premise of restricted Hom-Lie triple system. In particular, it is proved that the subspace $\mho$ satisfying certain conditions in the linear transformation $\mathrm{End}(M)$ is restricted Hom-Lie triple system.

This paper is structured as follows. Firstly, Section 2 mainly contains some related work. Secondly, in Section 3, we mainly present some fundamental definitions about restricted Hom-Lie triple systems, derivations and linear transformations satisfying certain conditions. Then, in Section 4, we prove some properties between them. Finally, we summarize the article and further prospects. In this paper, we always assume that the characteristic of $\mathbb{F}$ is p, p is prime and $p \geq 2$.

2. Related Work

In [7], Zhou et al. studied the properties of generalized derivation algebras and centroids of Hom-Lie triple systems and the relationship between them. In 2023, Liu [5] studied the structural relationship between derivations of restricted Lie triple systems. Recently, the definition of restricted Hom-Lie triple systems is given. However, the properties of the derivation structure in this context have not been studied as far as I know.

3. Preliminaries

Definition 3.1. *[7] Let $(M,[\cdot,\cdot,\cdot],\alpha=(\alpha_1,\alpha_2))$ is a triple, where M is a vector space over a field $\mathbb{F}$, $[\cdot,\cdot,\cdot]: M\times M\times M\to M$ is a trilinear map, and twisted maps $\alpha_i: M\to M(i=1,2)$, such that for all $a,b,c,u,v\in M$,*

$$[a,a,c]=0;$$

$$[a,b,c]+[b,c,a]+[c,a,b]=0;$$

$$[\alpha_1(u),\alpha_2(v),[a,b,c]]=[[u,v,a],\alpha_1(b),\alpha_2(c)]+[\alpha_1(a),[u,v,b],\alpha_2(c)]+[\alpha_1(a),\alpha_2(b),[u,v,c]],$$

then $(M,[\cdot,\cdot,\cdot],\alpha=(\alpha_1,\alpha_2))$ is a Hom-Lie triple system.

Definition 3.2. *[12] Let $(M,[\cdot,\cdot,\cdot],\alpha=(\alpha_1,\alpha_2))$ is a Hom-Lie triple system,*

(1)if $\alpha=\alpha_1=\alpha_2$ and $\alpha([a,b,c])=[\alpha(a),\alpha(b),\alpha(c)]$, for all $a,b,c\in M$, then we call M is a multiplicative Hom-Lie triple system;

(2)if M is a multiplicative Hom-Lie triple system and α is invertible, then M is called regular.

Definition 3.3. *Let $(M,[\cdot,\cdot,\cdot],\alpha)$ be a regular Hom-Lie triple system, H is the subspace of M, if $\alpha(H)\subseteq H$, for all $a,b,c\in H$, $[a,b,c]_M\in H$, then H is a Hom-subsystem of M.*

From Definition 3.3, it is easy to prove that if $M_1=\{a\in M\mid \alpha(a)=a\}$, then M_1 is a Hom-subsystem of M.

Let M is a regular Hom-Lie triple system, we use $L(M,M)$ to represent the space linearly spanned by $L(a,b)$ and define $L_s(M)=L(M,M)\oplus M$.

Definition 3.4. *[12] Let $(M,[\cdot,\cdot,\cdot],\alpha)$ be a regular Hom-Lie triple system, if there is a map $[p]:M_1\to M_1, x\mapsto x^{[p]}$, satisfying the following conditions:*

$$(ka)^{[p]}=k^p a^{[p]},\forall a\in M_1,k\in\mathbb{F},$$

$$(a+b)^{[p]}=a^{[p]}+b^{[p]}+\sum_{i=1}^{p-1}s_i(a,b),\forall a,b\in M_1,$$

$$[\alpha^{-1}(a),\alpha^{-1}(b),c^{[p]}]=(a,b,c,\cdots,c)(p\ copies\ of\ c),\forall a,b\in M,c\in M_1,$$

$$[\alpha^{-1}(a),b^{[p]},\alpha^{-1}(c)]=(a,b,\cdots,b,c)(p\ copies\ of\ b),\forall a,c\in M,b\in M_1,$$

where $is_i(a,b)$ is the coefficient of λ^{i-1} in $(\mathrm{ad}(\lambda a+b))^{p-1}(a)\in L_s(M)$, $(a,b,\cdots,b,c)=[[[[a,b,b],b,b],\cdots],b,c]$ and $(a,b,c,\cdots,c)=[[[[a,b,c],c,c],\cdots],c,c]$, then $(M,[\cdot,\cdot,\cdot],\alpha,[p])$ is a restricted Hom-Lie triple system.

When $\alpha=id_M$, we call restricted Hom-Lie triple system is the restricted Lie triple system. From Definition 3.4, for all $a\in M_1$, we have $a^{[p]}\in M_1$. Then $\alpha(a^{[p]})=a^{[p]}=(\alpha(a))^{[p]}$, that is $\alpha\circ[p]=[p]\circ\alpha$.

Definition 3.5. *Let $(M,[\cdot,\cdot,\cdot],\alpha,[p])$ be a restricted Hom-Lie triple system over $\mathbb{F}$, define the subspace Ω of $\mathrm{End}(M)$ and linear transformation $\widetilde{\alpha}$ on Ω which satisfy*

$$\Omega=\{K\in\mathrm{End}(M)\mid K\alpha=\alpha K\}$$

and

$$\widetilde{\alpha}:\Omega\to\Omega;\widetilde{\alpha}(K)=\alpha K,$$

where $\widetilde{\alpha}$ is multiplicative and $\mathrm{End}(M)$ is composed of linear maps K on M.

By Definition 3.5, Ω is a restricted Hom-Lie triple system with respect to the bracket operation $[K_1,K_2]=K_1K_2-K_2K_1,\forall K_1,K_2\in\Omega$ (see Theorem 4.1).

Definition 3.6. *Let M be a restricted Hom-Lie triple system. H is the subspace of M. If $\alpha(H)\subseteq H,[H,H,H]_M\subseteq H$, for all $a\in H_1$, there is $a^{[p]}\in H_1$, in which $H_1=\{a\in H\mid \alpha(a)=a\}$, then H is the Hom-p-subsystem of M.*

Definition 3.7. *Let M be a restricted Hom-Lie triple system. $K \in \mathrm{End}(M)$ is called to be an α^k-derivation of M (where $(k \geq 0, k \in N)$), if it satisfies for all $a,b,c \in M$,*

$$K\alpha = \alpha K,$$

$$K([a,b,c]) = [K(a), \alpha^k(b), \alpha^k(c)] + [\alpha^k(a), K(b), \alpha^k(c)] + [\alpha^k(a), \alpha^k(b), K(c)].$$

We use $\mathrm{Der}_{\alpha^k}(M)$ to represent all α^k-derivations and define $\mathrm{Der}(M) = \bigoplus_{k\geq 0} \mathrm{Der}_{\alpha^k}(M)$, then $\mathrm{Der}(M)$ about the bracket operation and linear transformation

$$\widetilde{\alpha} : \mathrm{Der}(M) \to \mathrm{Der}(M); \widetilde{\alpha}(K) = K\alpha$$

is the Hom-p-subsystem of Ω, which is called the derivation algebra of M.

Definition 3.8. *Let M be a restricted Hom-Lie triple system. A linear map $K : M \to M$ is called to be a generalized α^k-derivation of M, if there exist $K', K'', K''' \in \mathrm{End}(M)$, such that for all $a,b,c \in M$,*

$$K\alpha = \alpha K, K'\alpha = \alpha K', K''\alpha = \alpha K'', K'''\alpha = \alpha K''',$$

$$K'''([a,b,c]) = [K(a), \alpha^k(b), \alpha^k(c)] + [\alpha^k(a), K'(b), \alpha^k(c)] + [\alpha^k(a), \alpha^k(b), K''(c)].$$

Let $\mathrm{GDer}_{\alpha^k}(M)$ represent the set of generalized α^k-derivation and define $\mathrm{GDer}(M) = \bigoplus_{k\geq 0} \mathrm{GDer}_{\alpha^k}(M)$.

Definition 3.9. *Let M be a restricted Hom-Lie triple system. $K \in \mathrm{End}(M)$ is called to be an α^k-centroid of M, if it satisfies for all $a,b,c \in M$,*

$$K\alpha = \alpha K,$$

$$K([a,b,c]) = [K(a), \alpha^k(b), \alpha^k(c)] = [\alpha^k(a), K(b), \alpha^k(c)] = [\alpha^k(a), \alpha^k(b), K(c)].$$

Let $\mathrm{C}_{\alpha^k}(M)$ be the set of α^k-centroid. Define $\mathrm{C}(M) = \bigoplus_{k\geq 0} \mathrm{C}_{\alpha^k}(M)$.

Definition 3.10. *Let M be a restricted Hom-Lie triple system. A linear map $K : M \to M$ is said to be an α^k-central derivation of M, if it satisfies for all $a,b,c \in M$,*

$$K\alpha = \alpha K,$$

$$K([a,b,c]) = [K(a), \alpha^k(b), \alpha^k(c)] = 0.$$

Let $\mathrm{ZDer}_{\alpha^k}(M)$ be the set of α^k-central derivation, then $\mathrm{ZDer}(M) = \bigoplus_{k\geq 0} \mathrm{ZDer}_{\alpha^k}(M)$.

4. Main Results

Theorem 4.1. *Let M be a restricted Hom-Lie triple system and Ω defined as above, then Ω is a restricted Hom-Lie triple system.*

Proof. Since Lie triple system is the natural ternary extension of Lie algebra, we only need to prove that Ω is a Hom-Lie algebra. For $K_1, K_2, K_3 \in \Omega$, by direct calculation, we can get that

$$[K_1, K_2] = -[K_2, K_1],$$
$$[\widetilde{\alpha}(K_1), [K_2, K_3]] + [\widetilde{\alpha}(K_2), [K_3, K_1]] + [\widetilde{\alpha}(K_3), [K_1, K_2]] = 0.$$

Therefore, Ω is a regular Hom-Lie triple system.

Next, let Ω_1 satisfy $\Omega_1 = \{K_1' \in \Omega \mid \widetilde{\alpha}(K_1') = K_1'\}$, it is obvious that Ω_1 is the Hom-subsystem of Ω. Define a map $[p] : \Omega_1 \to \Omega_1; K_1' \mapsto (K_1')^p$. For $K_1, K_2 \in \Omega, K_1', K_2' \in \Omega_1, k \in \mathbb{F}$, in view of Definition 3.4, we have

$$(kK_1')^{[p]} = (kK_1')(kK_1')\cdots(kK_1') = k^p(K_1')^p = k^p(K_1')^{[p]},$$
$$(K_1'+K_2')^{[p]} = (K_1')^{[p]} + (K_2')^{[p]} + \sum_{i=1}^{p-1} s_i(K_1', K_2').$$

To verify $[\widetilde{\alpha}^{-1}(K_1), (K_1')^{[p]}, \widetilde{\alpha}^{-1}(K_2)] = (K_1, K_1', \cdots, K_1', K_2)$, it is necessary to prove that

$$[K_1, \widetilde{\alpha}((K_1')^{[p]}), K_2] = [K_1, (K_1')^{[p]}, K_2] = [[[\widetilde{\alpha}(K_1), K_1', K_1'], \cdots], K_1', \widetilde{\alpha}(K_2)].$$

The following mathematical induction proves that when $n \geq 3$, we have

$$[[[\widetilde{\alpha}(K_1), K_1', K_1'], \cdots], K_1', \widetilde{\alpha}(K_2)] = [\sum_{i=0}^{n}(-1)^i C_n^i (K_1')^i K_1 (K_1')^{n-i}, K_2].$$

In fact, for $n = 3$,

$$[[\widetilde{\alpha}(K_1), K_1', K_1', K_1', \widetilde{\alpha}(K_2)] = [\sum_{i=0}^{3}(-1)^i C_3^i (K_1')^i K_1 (K_1')^{3-i}, K_2].$$

Assume that the conclusion holds when $n = m$, that is

$$[[[\widetilde{\alpha}(K_1), K_1', K_1'], \cdots], K_1', \widetilde{\alpha}(K_2)] = [\sum_{i=0}^{m}(-1)^i C_m^i (K_1')^i K_1 (K_1')^{m-i}, K_2].$$

When $n = m+1$,

$$\begin{aligned}[[[\widetilde{\alpha}(K_1), K_1', K_1'], \cdots], K_1', \widetilde{\alpha}(K_2)] &= [\sum_{i=0}^{m}(-1)^i C_m^i (K_1')^i K_1 (K_1')^{m-i}, K_1', \widetilde{\alpha}(K_2)] \\ &= [\sum_{i=0}^{m+1}(-1)^i C_{m+1}^i (K_1')^i K_1 (K_1')^{m+1-i}, K_2].\end{aligned}$$

In particular, when $n = p$,

$$[[[\widetilde{\alpha}(K_1),K_1',K_1'],\cdots],K_1',\widetilde{\alpha}(K_2)] = [\sum_{i=0}^{p}(-1)^i C_p^i (K_1')^i K_1 (K_1')^{p-i},K_2]$$

$$= [K_1(K_1')^p - (K_1')^p K_1,K_2] = [K_1,(K_1')^p,K_2] = [K_1,(K_1')^{[p]},K_2].$$

From the proof, we can obtain $[\widetilde{\alpha}^{-1}(K_1),(K_1')^{[p]},\widetilde{\alpha}^{-1}(K_2)] = (K_1,K_1',\cdots,K_1',K_2)$. Repeating the above arguments, we can get that $[\widetilde{\alpha}^{-1}(K_1),\widetilde{\alpha}^{-1}(K_2),(K_1')^{[p]}] = (K_1,K_2,K_1',\cdots,K_1')$, so we will omit its proof.

Therefore, Ω is a restricted Hom-Lie triple system. □

Theorem 4.2. *Let M be a restricted Hom-Lie triple system, then* $\mathrm{GDer}(M)$ *is a Hom-p-subsystem of* Ω.

Proof. For $K_1 \in \mathrm{GDer}_{\alpha^k}(M), K_2 \in \mathrm{GDer}_{\alpha^s}(M), K_3 \in \mathrm{GDer}_{\alpha^m}(M), a,b,c \in M$, we get $\widetilde{\alpha}(K_1) \in \mathrm{GDer}_{\alpha^{k+1}}(M)$, that is $\widetilde{\alpha}(\mathrm{GDer}(M)) \subseteq \mathrm{GDer}(M)$.

Next, by calculation, we have

$$\begin{aligned}&[[K_1,K_2,K_3](a),\alpha^{k+s+m}(b),\alpha^{k+s+m}(c)]\\ &= [K_1''',K_2''',K_3''']([a,b,c]) - [\alpha^{k+s+m}(a),[K_1',K_2',K_3'](b),\alpha^{k+s+m}(c)]\\ &\quad - [\alpha^{k+s+m}(a),\alpha^{k+s+m}(b),[K_1'',K_2'',K_3''](c)].\end{aligned}$$

Therefore, $\mathrm{GDer}(M)$ is a Hom-subsystem of Ω.

For any $K \in \mathrm{GDer}(M)'$, $\mathrm{GDer}(M)' = \{K \in \mathrm{GDer}(M) \mid \widetilde{\alpha}(K) = K\}$, we have $\widetilde{\alpha}(K^{[p]}) = \widetilde{\alpha}(K^p) = \alpha K \cdots K = \widetilde{\alpha}(K)K^{p-1} = K^p = K^{[p]}$. Hence, $\mathrm{GDer}(M)$ is the Hom-p-subsystem of Ω. □

Theorem 4.3. *Let M be a restricted Hom-Lie triple system over $\mathbb{F}$. And the characteristic of field $\mathbb{F}$ is not equal to 2. The following holds that* $\mathrm{ZDer}(M) = \mathrm{C}(M) \cap \mathrm{Der}(M)$.

Proof. On the one hand, for $K \in \mathrm{C}(M) \cap \mathrm{Der}(M)$, $a,b,c \in M$, by $K \in \mathrm{C}_{\alpha^k}(M)$ and $K \in \mathrm{Der}_{\alpha^k}(M)$, we have $3K([a,b,c]) = K([a,b,c])$. As the characteristic is p and $p > 2$, $K([a,b,c]) = 0 = [K(a),\alpha^k(b),\alpha^k(c)]$. Hence $K \in \mathrm{ZDer}_{\alpha^k}(M)$.

On the other hand, for any $K \in \mathrm{ZDer}_{\alpha^k}(M)$, we can get $K \in \mathrm{Der}_{\alpha^k}(M)$. From $K([a,b,c]) = [K(a),\alpha^k(b),\alpha^k(c)] = 0$, we have $[K(a),\alpha^k(b),\alpha^k(c)] = -[\alpha^k(b),K(a),\alpha^k(c)] = 0$. As the arbitrariness of a,b,c, we have $[\alpha^k(a),K(b),\alpha^k(c)] = [\alpha^k(a),\alpha^k(b),K(c)] = 0$. Then $K \in \mathrm{C}_{\alpha^k}(M)$, that is $K \in \mathrm{C}_{\alpha^k}(M) \cap \mathrm{Der}_{\alpha^k}(M)$. Hence, $\mathrm{ZDer}(M) \subseteq \mathrm{C}(M) \cap \mathrm{Der}(M)$.

Consequently the conclusion holds. □

5. Conclusion and Future Direction

In this paper, we give the concepts of derivations, generalized derivations, centroids and Hom-p-subsystems, we prove the subspace Ω satisfying some conditions in the linear transformation $\mathrm{End}(M)$ is a restricted Hom-Lie triple system, the generalized derivation is a Hom-p-subsystem of Ω and the central derivation is the intersection of the centroid and the derivation. About the further research, we can consider the properties of quasi-derivations and quasi-centroids, and try to construct a special restricted Hom-Lie triple system to improve the content.

References

[1] Terrell L.Hodge. Lie triple system,restricted Lie triple system and algebraic groups. Algebra. 2001;244:533-580.
[2] Dong YQ. Restricted Lie triple systems. Northeast Normal University. 2006.
[3] Liu XJ, Chen LY. Frattini *p*-subsystem of restricted Lie triple systems. Mathematics in Practice and Theory. 2009;39(14):145-149.
[4] Chen LY, Xu XN, Lin J. The commutativity of restricted Lie triple systems. Chinese Annals of Mathematics. 2010;31A(03):275-282.
[5] Liu YP, Dong YQ, Zhou HQ. Generalized derivations of restricted Lie triple systems. Journal of Changchun Normal University. 2023;42(02):16-20.
[6] Yau D. On n-ary Hom-Nambu and Hom-Nambu-Lie algebras. Journal of Geometry and Physics. 2012 Feb;62(2):506-522.
[7] Zhou J, Chen LY, Ma Y. Generalized derivations of Hom-Lie triple systems. Bulletin of the Malaysian Mathematical Sciences Society. 2018 Apr;41:637-656.
[8] Chen LY, Hou Y, Ma Y. Product and complex structures on Hom-Lie triple systems. Journal of Shandong University(Natural Science). 2021.56(10):48-60.
[9] Bhutia R, Yadav RB, Behera N. Equivariant cohomology, deformations and central extension of Hom Lie triple systems. arXiv:2203.07409. 2022.
[10] Guan BL, Chen LY. Restricted Hom-Lie algebras. arXiv: Rings and Algebras. 2015.
[11] Shaqaqha S. Restricted Hom-Lie Superalgebras. arXiv:Rings and Algebras. 2018.
[12] Hamdiatou Yara, Patricia L.Zoungrana, On restricted Hom-Lie triple systems. Universal Journal of Mathematics and Mathematical Sciences. 2023;18(1):35-52.

Fuzzy Systems and Data Mining IX
A.J. Tallón-Ballesteros and R. Beltrán-Barba (Eds.)

doi:10.3233/FAIA231058

Restricted δ Lie Triple Systems

Xin Cong [a,1], Yanqin Dong [a], Hanqi Zhou [a] and Bing Liu [a]
[a] *College of Mathematics, Changchun Normal University, Changchun, 130032, China*

Abstract. This article mainly introduces some structural properties of confined δ Lie triple systems are studied by means of the relation among the restricted Lie three systems, modular Lie algebras and δ Lie triple systems. Firstly, we verify by induction that the set of all linear transformations that restricted δ Lie triple systems satisfies the condition of restricted δ Lie triple systems. Next,the first mathematical induction method is used to verify that the generalized derivations and the quasiderivations are p-subsystems of the set of all linear transformations that restricted δ Lie three systems. Finally, it is proved that if the restricted δ Lie system has a trivial center, then the center is the commutator system of the generalized derivations.

Keywords. restricted δ Lie triple systems; δ Lie triple systems; generalized derivations; centroids

1. Introduction

The Lie triple systems first appeared in Cardan's research on riemannian geometry. As a generalization of the Lie triple systems, the concept of a δ Lie triple system is introduced in reference [1]. With the development of the Lie triple systems, the restricted Lie triple systems has also had a certain development [2],[3],[4]. In [5], they present some basic properties of a Lie triple system T, with the relationship $\mathrm{Der}(\mathrm{T}) \subseteq \mathrm{QDer}(\mathrm{T}) \subseteq \mathrm{GDer}(\mathrm{T}) \subseteq \mathrm{End}(\mathrm{T})$. They show that the quasiderivations of T can be embedded as derivations in a larger Lie triple system. [6] mainly studies that T is a necessary condition for decomposability. Then, they study the structure theory of the center of form of Lie super triple system, and give some important properties of tensor products of Lie super triple system and associative algebras with identity elements. [7] gives some basic properties of the generalized derivation derivations, quasi-derivation derivations, core, quasi-core and central derivation derivations of the Jordan-Lie algebra. Peng Jianrong gives the generalized derivation of δ Lie three systems [8]. Cohomological characterizations of δ -Jordan Lie triple systems are established, then deformations, Nijenhuis operators, Abelian extensions and T^*-extensions of δ -Jordan Lie triple systems are studied using cohomology [9]. Liu Yanpei gives the structural properties limiting the Lie three systems [10].

In this paper, we extend the results of Peng Jianrong to restricted δ Lie triple systems, and mainly study some important properties of derivation algebras, quasiderivation algebras, generalized derivation algebras, type centers and central derivations. Assuming that the characteristic of the base field $\mathbb{F}$ is p, where p is a prime number greater than 2.

[1]Corresponding Author: College of Mathematics, Changchun Normal University, Changchun, 130032, China; 15044361668@163.com.

2. Related works

Okubo S first proposed the concept of δ-lie triple systems. On the basis of [1], Peng Jianrong got the concept of δ-lie triple systems and the properties of their derivates [8]. Liu Yanpei got the related properties of limiting the derivations of Lie triple systems [9]. By referring to references [8], [9] and [10], I came to the conclusion that the focus of this paper is the concept of limiting δ-Lie triple systems and the properties of their derivations, which is also my innovation point.

3. Basic Conceptions

Definition 3.1. *[1] Supposing T is a vector space with ternary linear operations on the field $\mathbb{F}$ and satisfies:*
(1) $[z,h,r] = -\delta[h,z,r]; \delta = \pm 1$
(2) $[z,h,r]+[h,r,z]+[r,z,h] = 0;$
(3) $[z,h,[r,u,v]] = [[z,h,r],u,v]+[r,[z,h,u],v]+\delta[r,u,[z,h,v]],$
then T is called δ Lie three systems and T still known as Jordan Lie three systems. Note that δ is a Lie three system when $\delta = 1$.

Definition 3.2. *Supposing T is the δ Lie three system on the field $\mathbb{F}$, if exists a mapping $[p]: T \to T, \forall d,k,c \in T, \alpha \in F$, the next conditions are satisfies:*
(1) $(\alpha d)^{[p]} = \alpha^p d^{[p]};$
(2) $(d+k)^{[p]} = d^{[p]} + k^{[p]} + \sum_{i=1}^{p-1} s_i(d,k);$
(3) $[d,k^{[p]},c] = (d,k,\cdots,k,c).$
where $is_i(d,k)$ is the coefficient of λ^{i-1} in $(\mathrm{ad}(\lambda d+k))^{p-1}(d) \in L_s(T)$, then $(T,[p])$ is called the Restricted δ Lie triple system, here $(d,k,\cdots,k,c) = [[[[d,k,k],k,k],\cdots],k,c]$.

A subspace ψ of a Restricted δ Lie triple systems T, if satisfied $[\psi,\psi,\psi] \subseteq \psi$ and for $\forall x \in \psi, x^{[p]} \in \psi$, then ψ is called a $p-$subsystem of T .

A subspace ω of a restricted δ lie triple systems T, if satisfied $[\omega,T,T] \subseteq \omega$,and for $\forall x \in \omega, x^{[p]} \in \omega$, then ω is called a $p-$ideal of T.

Definition 3.3. *Supposing T is the restricted δ lie triple system on the field $\mathbb{F}$. If exists a linear map $D: T \to T$ satisfies: $\delta^k([D(s),u,n]) + \delta^k([s,D(u),n]) + \delta^k([s,u,D(n)]) = D([s,u,n]), \forall s,u,n \in T, \forall k \in Z$, thus $D: T \to T$ is called a $k-$step derivation of T, so we denote a set of the whole $k-$step derivations by* $\mathrm{Der_k(T)}$.

Definition 3.4. *Let T be the Restricted δ Lie triple system on the field $\mathbb{F}$. If exists* $\mathrm{D}', \mathrm{D}'', \mathrm{D}''' \in \mathrm{End(T)}$ *satisfies* $\delta^k[D(a),b,c] + \delta^k[a,D'(b),c] + \delta^k[a,b,D''(c)] = D'''([a,b,c]), \forall a,b,c \in T$, *thus* $D \in \mathrm{End(T)}$ *is called a $k-$step generalized derivation of T, then we denote the gather of overall $k-$step generalized derivations by* $\mathrm{GDer(T)} = \bigoplus_{k\geq 0} \mathrm{GDer(T)}$.

Definition 3.5. *Supposing T be the restricted δ lie triple system on the field $\mathbb{F}$. If exists* $\mathrm{D}' \in \mathrm{End(T)}$ *satisfies* $\delta^k[D(f),k,o] + \delta^k[f,D(k),o] + \delta^k[f,k,D(o)] = D'([f,k,o]),$
$\forall f,k,o \in T$, *then* $D \in \mathrm{End(T)}$ *is called the $k-$step quasiderivation of T, we denote a gather of all $k-$step quasiderivations by* $\mathrm{QDer(T)} = \bigoplus_{k\geq 0} \mathrm{QDer(T)}$.

Definition 3.6. *Establish T be a Restricted δ Lie triple system on the field $\mathbb{F}$. If* $\mathrm{C_k(T)} = \{D \in \mathrm{End(T)} | \delta^k[D(f),k,o] = \delta^k[f,D(k),o] = \delta^k[f,k,D(o)] = D([f,k,o])\}, \forall f,k,o \in T$, *so* $\mathrm{C_k(T)}$ *is called the k−step centroid of T. Then we can denote the set of all k−step centroids by* $\mathrm{C(T)} = \bigoplus_{k\geq 0} \mathrm{C(T)}$.

Definition 3.7. *Establish a T be the restricted δ lie triple system on the field $\mathbb{F}$. If* $\mathrm{ZDer(T)} = \{D \in \mathrm{End(T)} | [D(e),g,p] = D([e,g,p]) = 0\}, \forall e,g,p \in T$, *so* ZDer(T) *can be called a central derivation of T.*

4. Main Results

Theorem 4.1. *Supposing T be a restricted δ Lie triple system, if* End(T) *is the set of all linear transformations of T, then* End(T) *with respect to the ternary linear operation* $[\cdot,\cdot,\cdot]$ *is a δ lie triple system.*

Proof. End(T) satisfies the three conditions of the δ lie triple system.
$\forall \mathrm{D_1, D_2, D_3, D_4, D_5} \in \mathrm{End(T)}$,
$(1)[D_1,D_2,D_3] = [[D_1,D_2],D_3] = -\delta[[D_2,D_1],D_3] = -\delta[D_2,D_1,D_3]$.

$$\begin{aligned}(2)&[D_1,D_2,D_3]+[D_2,D_3,D_1]+[D_3,D_1,D_2]\\ &= D_1D_2D_3 - D_2D_1D_3 - D_3D_1D_2 + D_3D_2D_1 + D_2D_3D_1 - D_3D_2D_1 - D_1D_2D_3\\ &\quad + D_1D_3D_2 + D_3D_1D_2 - D_1D_3D_2 - D_2D_3D_1 + D_2D_1D_3 = 0\end{aligned}$$

$$\begin{aligned}(3)&[D_1,D_2,[D_3,D_4,D_5]]+[D_4,D_3,[D_1,D_2,D_5]]\\ &= D_1D_2D_3D_4D_5 - D_1D_2D_4D_3D_5 - D_2D_1D_3D_4D_5 + D_2D_1D_4D_3D_5 + D_5D_3D_4D_1D_2\\ &- D_5D_3D_4D_2D_1 - D_5D_4D_3D_1D_2 + D_5D_4D_3D_2D_1 + D_4D_3D_1D_2D_5 - D_4D_3D_2D_1D_5\\ &- D_3D_4D_1D_2D_5 + D_3D_4D_2D_1D_5 + D_5D_1D_2D_4D_3 - D_5D_1D_2D_3D_4 - D_5D_2D_1D_4D_3\\ &+ D_5D_2D_1D_3D_4\\ &= [[D_1,D_2,D_3],D_4,D_5] + [D_3,[D_1,D_2,D_4],D_5]\end{aligned}$$

In summary, End(T) is a δ Lie triple system composed of a ternary linear operation$[\cdot,\cdot,\cdot]$. □

Theorem 4.2. *Supposing T be the restricted δ Lie triple system on the field $\mathbb{F}$, if* End(T) *is the set of total linear transformations of T. We assume* $[p]{:}D \to D^p, \forall D \in \mathrm{End(T)}$, *then* End(T) *is the restricted δ lie triple system.*

Proof. From theorem 3.1 we know that End(T) is a δ Lie triple system. $\forall D, D_1, D_2 \in \mathrm{End(T)}, \alpha \in \mathbb{F}$ $(\alpha D)^p = (\alpha D)(\alpha D)\cdots(\alpha D) = \alpha^p D^p$. Because the characteristic of $\mathbb{F}$ is p, $(D_1+D_2)^p = \sum_{k=0}^{p} C_p^k D_1^{p-k} D_2^k = (D_1)^p + (D_2)^p$. Next we use first induction to prove that $(D_1,D,\cdots,D,D_2) = [\sum_{i=0}^{n}(-1)^i C_n^i D^i D_1 D^{n-i}, D_2]$ is valid when $n \geq 3$ is true. When $n=3$, conclusion $(D_1,D,D,D,D_2) = [D_1D^3 - 3DD_1D^2 + 3D^2D_1D - D^3D, D_2] = [\sum_{i=0}^{3}(-1)^i C_3^i D^i D_1 D^{3-i}, D_2]$ is valid. Assuming when $n=m$ the conclu-

sion is valid, that is $(D_1,D,\cdots,D,D_2)=[\sum_{i=0}^{m}(-1)^iC_m^iD^iD_1D^{m-i},D_2]$.When $n=m+1$, $(D_1,D,\cdots,D,D_2)=[\sum_{i=0}^{m}(-1)^iC_m^iD^iD_1D^{m-i},D,D_2]=[\sum_{i=1}^{m}(-1)^iC_{m+1}^iD^iD_1D^{m+1-i}+D_1D^{m+1}+(-1)^{m+1}D^{m+1}D_1,D_2]=[\sum_{i=0}^{m+1}(-1)^iC_{m+1}^iD^iD_1D^{m+1-i},D_2]$, the conclusion is valid. In particular, let $n=p$, $(D_1,D,\cdots,D,D_2)=[[[[D_1,D,D],D,D],\cdots],D,D_2]=[\sum_{k=0}^{p}(-1)^kC_p^kD^kD_1D^{p-k},D_2]=[D_1D^p-D^pD_1,D_2]=[D_1,D^{[p]},D_2]$. So End(T) is the Restricted δ lie triple system. □

Theorem 4.3. *Let T be the Restricted δ lie triple system on the field $\mathbb{F}$, then:*
*(1)*GDer(T) *is a p−subsystem of* End(T).
*(2)*QDer(T) *is a p−subsystem of* End(T).

Proof. (1)From theorem 3.2 we know that End(T) is a Restricted δ Lie triple system.
$\forall D\in GDer_k(T),D_4\in GDer_k(T),D_5\in GDer_s(T),D_6\in GDer_q(T),t,v,w\in T$.
By reason of

$$
\begin{aligned}
&[D_4D_5D_6(t),v,w]\\
&=\delta^{k+s+q}D_4^{'''}D_5^{'''}D_6^{'''}[t,v,w]-\delta^{k+s}D_4^{'''}D_5^{'''}[t,D_6^{'}(v),w]-\delta^{k+s}D_4^{'''}D_5^{'''}[t,v,D_6^{''}(w)]\\
&-\delta^{k+s}D_4^{'''}D_6^{'''}[t,D_5^{'}(v),w]+\delta^{k}D_4^{'''}[t,D_6^{'}D_5^{'}(v),w]+\delta^{k}D_4^{'''}[t,D_5^{'}(v),D_6^{''}(w)]\\
&-\delta^{k+s}D_4^{'''}D_6^{'''}[t,v,D_5^{''}(w)]+\delta^{k}D_4^{'''}[t,D_6^{'}(v),D_5^{''}(w)]+\delta^{k}D_4^{'''}[t,v,D_6^{''}D_5^{''}(w)]\\
&-\delta^{s+q}D_5^{'''}D_6^{'''}[t,D_4^{'}(v),w]+\delta^{s}D_5^{'''}[t,D_6^{'}D_4^{'}(v),w]+\delta^{s}D_5^{'''}[t,D_4^{'}(v),D_6^{''}(w)]\\
&+\delta^{q}D_6^{'''}[t,D_5^{'}D_4^{'}(v),w]-[t,D_6^{'}D_5^{'}D_4^{'}(v),w]-[t,D_5^{'}D_4^{'}(v),D_6^{''}(w)]\\
&+\delta^{q}D_6^{'''}[t,D_4^{'}(v),D_5^{''}(w)]-[t,D_6^{'}D_4^{'}(v),D_5^{''}(w)]-[t,D_4^{'}(v),D_6^{''}D_5^{''}(w)]\\
&-\delta^{s+q}D_5^{'''}D_6^{'''}[t,v,D_4^{''}(w)]+\delta^{s}D_5^{'''}[t,D_6^{'}(v),D_4^{''}(w)]+\delta^{s}D_5^{'''}[t,v,D_6^{''}D_4^{''}(w)]\\
&+\delta^{q}D_6^{'''}[t,D_5^{'}(v),D_4^{''}(w)]-[t,D_6^{'}D_5^{'}(v),D_4^{''}(w)]-[t,D_5^{'}(v),D_6^{''}D_4^{''}(w)]\\
&+\delta^{q}D_6^{'''}[t,v,D_5^{''}D_4^{''}(w)]-[t,D_6^{'}(v),D_5^{''}D_4^{''}(w)]-[t,v,D_6^{''}D_5^{''}D_4^{''}(w)].
\end{aligned}
$$

The same can be obtained that $[D_5D_4D_6(t),v,w]$,$[D_6D_4D_5(t),v,w]$ and $[D_6D_5D_4(t),v,w]$. So can get$[[D_4,D_5,D_6](t),v,w]=\delta^{k+s+q}[D_4^{'''},D_5^{'''},D_6^{'''}]([t,v,w])-[t,[D_4^{'},D_5^{'},D_6^{'}](v),w]-[t,v,[D_4^{''}D_5^{''}D_6^{''}](w)]$. Hence GDer(T) is a subsystem of End(T). The following is to prove that GDer(T) is a $p-$subsystem of End(T).

Above all we use the first mathematical induction to prove that $[D^n(t),v,w]=\sum_{0\le l,b,r\le n,l+b+r=n}(\frac{n!}{l!b!r!})(-1)^{n-l}\delta^{lk}(D^{'''})^l[t,(D^{'})^b(v),(D^{''})^r(w)]$ is true when $n\ge 3$. If $n=3$, $[D^3(t),v,w]=\sum_{0\le l,b,r\le 3,l+b+r=3}(\frac{3!}{l!b!r!})(-1)^{3-l}\delta^{lk}(D^{'''})^l[t,(D^{'})^b(v),(D^{''})^r(w)]$ conclusion is valid. Supposing when $n=m$ the conclusion is valid, that is $[D^m(t),v,w]=\sum_{0\le l,b,r\le m,l+b+r=m}(\frac{m!}{l!b!r!})(-1)^{m-l}\delta^{lk}(D^{'''})^l[t,(D^{'})^b(v),(D^{''})^r(w)]$. While $n=m+1$,

$$[D^{m+1}(t),v,w] = \sum_{0\le l,b,r\le m, l+b+r=m} (\frac{m!}{l!b!r!})(-1)^{m-l}\delta^{(l+1)k}(D^{'''})^{l+1}[t,(D^{'})^{b}(v),(D^{''})^{r}(w)]$$
$$+ \sum_{0\le l,b,r\le m, l+b+r=m} (\frac{m!}{l!b!r!})(-1)^{m-l}\delta^{lk}(D^{'''})^{l}[t,(D^{'})^{b+1}(v),(D^{''})^{r}(w)]$$
$$+ \sum_{0\le l,b,r\le m, l+b+r=m} (\frac{m!}{l!b!r!})(-1)^{m-l}\delta^{lk}(D^{'''})^{l}[t,(D^{'})^{b}(v),(D^{''})^{r+1}(w)].$$

Define the case where there have a negative number in l,b,r, then $(\frac{m!}{l!b!r!}) = 0$. So in the above equation, the coefficient of $(D^{'''})^{e}[t,(D^{'})^{f}(v),(D^{''})^{g}(w)]$ is $(-1)^{m+1-l}(\frac{m!}{e-1!f!g!}) + (\frac{m!}{e!f-1!g!}) + (\frac{m!}{e!f!g-1!}) = (-1)^{m+1-l}(\frac{m+1!}{e!f!g!})$, that is

$$[D^{m+1}(t),v,w] = \sum_{0\le l,j,r\le m+1, l+b+r=m+1} (\frac{m+1!}{l!b!r!})(-1)^{m+1-l}\delta^{lk}(D^{'''})l[t,(D^{'})b(v),(D^{''})^{r}(w)],$$

then the conclusion is valid when $n = m+1$. In particular, when $n = p$,

$$[D^{p}(t),v,w] = \sum_{0\le l,b,r\le p, l+b+r=p} (\frac{p!}{l!b!r!})(-1)^{p-l}\delta^{lk}(D^{'''})^{l}[t,(D^{'})^{b}(v),(D^{''})^{r}(w)].$$

Because the characteristic of $\mathbb{F}$ is p, so $[D^{p}(t),v,w] = \delta^{pk}(D^{'''})^{p}[t,v,w] - [t,(D^{'})^{p}(v),w] - [t,v,(D^{''})^{p}(w)]$. That is, GDer(T) is a $p-$subsystem of End(T). □

(2) Similarly, it can be proved that QDer(T) is the $p-$subsystem of End(T).

Theorem 4.4. *Let T be the restricted δ lie triple system on the field* $\mathbb{F}$*, then:*
(1) ZDer(T) *is the* $p-$*ideal of* Der(T).
(2) C(T) *is the* $p-$*subsystem of* End(T).
(3) ZDer(T) *is the* $p-$*subsystem of* GDer(T).

Proof. (1) $\forall D_1 \in \mathrm{ZDer(T)}, \forall D_2 \in \mathrm{Der_k(T)}, D_3 \in \mathrm{Der_s(T)}, \forall d,g,o \in T$.
$[[D_1,D_2,D_3](d),g,o] = \delta^{k+s}D_3D_2D_1[d,g,o] - D_1[d,D_2(g),o] - D_1[d,g,D_2(o)]$
$-\delta^{k}D_2D_1[d,D_3(g),o] + D_1[d,D_2D_3(g),o] + D_1[d,D_3(g),D_2(o)] - \delta^{k}D_2D_1[d,g,D_3(o)] +$
$D_1[d,D_2g,D_3(o)] + D_1[d,g,D_2D_3(o)] = 0$.

The same can be obtained that $[D_1,D_2,D_3]([d,g,o])$. Due to the definition of the central derivation $[D_1,D_2,D_3] \in \mathrm{ZDer(T)}$, so ZDer(T) is the ideal of Der(T). $\forall D \in \mathrm{ZDer(T)}, c,z,f \in T.D^{[p]}([c,z,f]) = D^{p}([c,z,f]) = D^{p-1}(D([c,z,f])) = 0$, $[D^{[p]}(c),z,f] = [D^{p}(c),z,f] = D([D^{p-1}(c),z,f]) = \cdots = D^{p-1}[D(c),z,f] = 0$, consequently, $D^{[p]} \in \mathrm{ZDer(T)}$, so by the definition of $p-$ideal, ZDer(T) is the $p-$ideal of Der(T). □

The proof methods of (2) and (3) are similar to those of (1).

Proposition 4.1. *Supposing T be a restricted δ Lie triple system on field* $\mathbb{F}$*, if T has a trivial center, then* C(T) *is a commutative subsystem of* GDer(T).

Proof. From previous studies we know that C(T) is a subspace of GDer(T).

$\forall D_4 \in C_k(T)$, $\forall D_5 \in C_s(T)$,$\forall D_6 \in C_q(T)$, $\forall z,e,r \in T$. $[D_4,D_5,D_6]([z,e,r]) = \delta^q D_4D_5([D_6(z),e,r]) - \delta^q D_5D_4([D_6(z),e,r]) - \delta^s D_6D_4([D_5(z),e,r]) + \delta^k D_6D_5([D_4(z),e,r]) = \delta^{k+s+q}[[D_4,D_5,D_6](z),e,r]$. In a similar way, $[D_4,D_5,D_6]([z,e,r]) = \delta^{k+s+q}[z,[D_4,D_5,D_6](e),r]) = \delta^{k+s+q}[z,e,[D_4,D_5,D_6](r)])$. Hence $[C(T),C(T),C(T)] \subseteq C(T)$. Next we prove the exchange. $[[D_4,D_5,D_6](z),e,r] = [D_6(z),D_5(e),D_4(r)] - [D_6(z),D_5(e),D_4(r)] - [D_5(z),D_4(e),D_6(r)] + [D_5(z),D_4(e),D_6(r)] = 0$. Because e,r is arbitrary and the center of T is 0,so we get $[D_4,D_5,D_6](z) = 0$. And since w is arbitrary, so$[D_4,D_5,D_6] = 0$.

So C(T) is a commutative subsystem of GDer(T) . □

5. Conclusion

This article mainly introduces some structural properties of restricted δ Lie triple systems. First, the basic concepts of restricted δ Lie triple system derivation, generalized derivation and quasi-derivation are given. Then we verify that End(T) is a restricted δ Lie triple system. On this basis, it is proved that GDer(T) and QDer(T) are P-subsystems of End(T). And then proved that ZDer(T) is the $p-$ideal of Der(T),C(T) is the $p-$subsystem of End(T),ZDer(T) is the $p-$subsystem of GDer(T). Finally, it is proved that if the restricted δ Lie system has a trivial center, then the center is the commutator system of the generalized derivations.

6. Future Direction

I will continue to study whether Ker(D) and Im(D) are P-ideals limiting δ Lie triple systems under certain conditions and construct a new restriction δ Lie triple systems τ, and whether the derivations of τ have direct sum decomposition when Z(T) is zero.

References

[1] Okubo S. Triple products and Yang-Baxter equation II, orthogonal and symplectic ternary systems. J Math.phys. 1993;34:3292-3315.

[2] Dong YQ. Restricted Lie Triple Systems. Northeast Normal University. 2006.

[3] Hodge TL. Lie Triple Systems, Restricted Lie Triple Systems, and Algebraic Groups. Journal of Algebra. 2001;244(2):533-580.

[4] Hodge TL, Parshall BJ. On the Representation Theory of Lie Triple Systems. Trans.Amer.Math.Soc. 2002.

[5] Zhou J, Chen LY, Ma Y. Generalized Derivations of Lie triple systems. Open Mathematics. 2014;14(1):260-271.

[6] Peng JR. δ-Lie superalgebra triple supersystems and Generalized derivations of δ-Lie superalgebras. Northeast Normal University. 2016.

[7] Zhou J, Wang ZH. Jordan Generalized derivation of a Lie algebra. Journal of Jilin University(Science Edition). 2017;55(04):765-770.

[8] Peng JR, Chen LY. Generalized Derivations of δ-Lie Triple Systems. Journal of Qiongzhou University. 2016.

[9] Ma LL, Chen LY. On δ-Jordan Lie triple System. Linear and Multilinear Algebra. 2017;65(4):731-751.

[10] Liu YP, Dong YQ, Zhou HQ, Cong X. Generalized derivation of a constrained Lie triple system. Journal of Changchun Normal University. 2023;42(02):16-20.

Fuzzy Systems and Data Mining IX
A.J. Tallón-Ballesteros and R. Beltrán-Barba (Eds.)

doi:10.3233/FAIA231059

FundRecLLM: Fund Recommendation Based on Financial News and Research Analyst Report

Guang YANG [a,1], Peiyang HE [a] and Xuefeng LIU [a]
[a] *Amazon*

Abstract. Adopting AI in financial advisory is a challenging task as there exists multiple sources of information to digest and interpret. Such information consumption process are very lengthy for financial advisors, reducing the efficiency and timeliness for their advice and recommendation given to their clients. In this work, we introduce a multi-step framework that consumes and combines news and industry-focused fund research analyst report to assist in fund recommendation process using Large Language Models (LLMs). To quantitatively evaluate the efficacy of the approach, we track the weekly and monthly market performance of representative industry-focused fund after news and report released date, and compute a Normalized Discounted Cumulative Gain (NDCG) score between the rankings of the fund performance and recommendation rating scores. We find that utilizing analyst report and self consistency in the framework increase the NDCG score from 0.72 to 0.93 comparing to consuming news only without self consistency, based on the time frame of our experimental evaluation.

Keywords. large language model, generative AI, financial advisory, information extraction, text summarization

1. Introduction

Since its introduction, Large Language Models (LLMs) have demonstrated its power in handling complex tasks in various areas [1]. Its capability is continuously evolving and advancing to handle various challenges in different domains [2]. Although LLMs have been explored in finance area for various use cases, their strength exploitation remains on the topics of information extraction, summarization and synthesis. For the purpose of investment advisories, use cases are still constrained to certain types of classification such as sentiment analysis for specific stocks using headlines related to that stock or social media tweets or posts. In [3], ChatGPT is used to determine a sentiment score for a given news headlines. ChatGPT outperforms other basic models based on a numerical score that calculates correlation between "ChatGPT scores" and subsequent daily stock market returns. In [4], PaLM is used to generate financial sentiment labels (i.e. whether the stock price should go up, down or not sure.) for Reddit posts. In [5], FinBERT, a cus-

[1]Corresponding Author: Guang Yang, Amazon, Beijing Aerospace Building Tower 2, Shenzhen, China; E-mail: yaguan@amazon.com.

tomized LLM for financial domain, is used to generate sentiment measures for analyst report sentences, earnings conference call script, and also labels for ESG discussions. LLMs' capability in understanding and reasoning impact on broader financial markets (e.g. industries like travel and agricultural) has not been studied. In this work, we investigate LLMs' such competency over general news headlines and raw analyst report. On top of sentiment classification, we ask LLMs to provide specific recommendation on selected industry-focused funds and also give out specific reasons backed by the facts presented in the news and analyst report.

As making such financial advisories requires consolidated consumption of data from various sources, an intelligent agent needs to take multiple steps to reach to a conclusion. A number of studies have been conducted to examine the capability of LLMs to reason and execute complex tasks that involve multiple steps. CoT [6] is introduced to improve the multi-step reasoning ability of LLMs by explicitly instructing the model to generate intermediate reasoning steps. The reasoning path mimics the reasoning process a person might employ in solving a task. It has been observed that chain-of-thought prompting significantly improves model performance across a variety of multi-step reasoning tasks. As task gets more complicated, each reasoning step can rely on external tools to support computation beyond the core LLM capabilities. ToolLLM [7] is introduced to facilitate tool-use capabilities within open-source LLMs. To interleave the reasoning and acting (i.e. tool usage), ReAct framework [8] is introduced that uses LLMs to generate both reasoning traces and task-specific actions. On the other hand, instead of solving an overarching task in a single run, the concept of *Chaining LLM* [9] is introduced to divide a complex task into sub-tasks and use LLMs to solve sub-tasks sequentially. Each subtask can be completed by an independent run of an LLM, and the output of one or more sub-tasks is used as input for the next.

In this work, we proposed a framework named *FundRecLLM* that combines financial news and fund research report to recommend industry focused fund assets using LLMs. Our contributions include: (1) a chained tool that employs LLMs to generate automated answers that recommend industry focused funds based on news and analyst research report interpretations; (2) a general method to consume raw analyst research report, a typical finance material often released in pdf formats, from the perspective of financial advisories, and (3) a quantitative evaluation method of recommendation using fund market performance.

2. Methodology

Figure 1 shows the overall solution architecture and major components for *FundRecLLM*. A news interpreter is built to interpret the news through CoT prompting. And then important entities (such as industry, sentiment and reason) are extracted from the answers for aggregation and target search. Summaries are stored in a docstore for later usage. A report analyzer is implemented to consume the analyst research report starting from the raw pdf format. Texts blocks are extracted and ordered using a document layout parser and an OCR agent. Since most analyst reports are over 10 pages, the text blocks are normally over the context window size of most LLMs (especially for the open sourced ones), these blocks are processed and interpreted through a Map & Reduce fashion. Similarly to the news interpreter, important entities are extracted from the answers and summaries

are stored in a docstore. Finally, a moderator which is a sequential chain to link entities, consume the docstores from the news and report, and give final answers for the recommended funds with market insights summarization. Entities are linked through the same mapped industries from the news and reports. The sentiments are converted to scores and the scores are summed for news and report separately and then averaged across news and report for the same industry. The summary insights are also concatenated for the same industry.

Let $n_i \in N$ represents a piece of news, $r_j \in R$ represents an analyst report, $d_k \in D$ stands for the collection of target industries in the financial market. $NI_{l,t_{NI}}$, $RA_{l,t_{RA_m},t_{RA_r}}$ stands for the news interpreter and the report analyzer respectively while l denotes the chosen LLM and t denotes the prompt template. A step-by-step breakdown of the methodology is as follows, note that the report analyzer has a map prompt t_{RA_m} and a reduce prompt t_{RA_r}:

(1) Iterate through news data n_i and pass each raw news content to the input variable of the LLM prompt template t_{NI}. Apply LLM to interpret multiple times (M) for self-consistency. The sentiments (s_i^{NI}) and reasoning summaries (u_i^{NI}) on target industries are obtained $s_i^{NI}, u_i^{NI} = \cap_M NI_{l,t_{NI}}(n_i)$. Then the sentiments ($S_{d_k}^{NI}$) and summaries ($U_{d_k}^{NI}$) are aggregated for each target industry $S_{d_k}^{NI} = \sum_N (s_i^{NI}|d_k)$, $U_{d_k}^{NI} = \cup_N (u_i^{NI}|d_k)$.

(2) Iterate through analyst reports r_j. Send each report to a layout parser lp to get the text regions $tr_{j,p} \in TR_{j,p}$ for each page ($p_j \in P_j$). Crop the text regions ($TR_{j,p}$) for each page and pass them through an OCR engine o to get the text strings ($ts_{j,p}$) for each page. The whole process can be described as $ts_j = \cup_{P_j} \cup_{TR_{j,p}} o(lp(r_j))$.

(3) Apply LLM to summarize the texts for each page of the analyst report $U_{m,j} = RA_{l,t_{RA_m}}(ts_j)$. And then pass the summaries of all pages to the report analyzer to get the sentiments (s_j^{RA}) and reasoning summaries (u_j^{RA}) on target industries. This is also repeated multiple times (M) for self consistency $s_j^{RA}, u_j^{RA} = \cap_M RA_{l,t_{RA_r}}(\cup U_{m,j})$. And similarly to the news interpreter, the sentiments and summaries are aggregated $S_{d_k}^{RA} = \sum_R (s_j^{RA}|d_k)$, $U_{d_k}^{RA} = \cup_R (u_j^{RA}|d_k)$.

(4) Aggregate the sentiments and the reasoning summaries across the news source and analyst reports $S_{d_k} = avg(S_{d_k}^{NI}, S_{d_k}^{RA})$, $U_{d_k} = U_{d_k}^{NI} \oplus U_{d_k}^{RA}$.

More details of the key components are discussed in the following sections.

2.1. Sequential chain and docstore

We use a sequential chain to find relevant insights for the target industry from the docstores that are artifacts of the news interpreter and the report analyzer. The sequential chain is implemented with LangChain Sequential Chain and the docstores contain aggregated summaries for target industries. The relevant summaries for the recommended industries are retrieved through embedding space similarity search.

2.2. Layout detection and text OCR for industry research report

Layout Parser library [10] is used to parse the tables, texts and figures out from the pdf file. We use `mask-rcnn-X-101-32x8d-FPN-3x` as the layout detection model which is trained on PubLayNet dataset.

For the OCR engine, we use Tesseract engine which is natively supported within *Layout Parser*. Tesseract supports multiple languages, including simplified Chinese in our experiments.

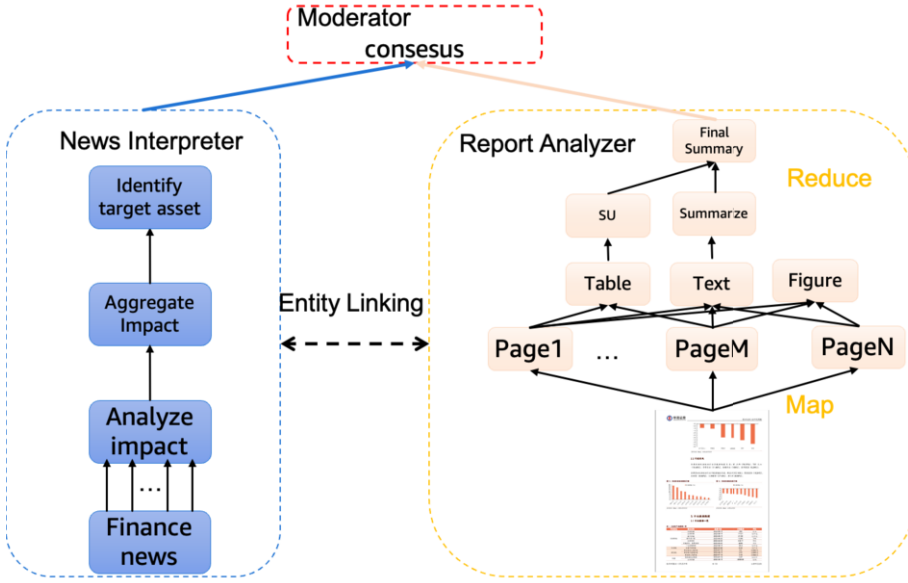

Figure 1. Components of *FundRecLLM*. The model includes a news interpreter to interpret the news, a report analyzer to consume the financial research report, and a moderator to extract, link and aggregate structured and unstructured information from the news interpreter and the report analyzer to reach to a consensus.

2.3. CoT prompting and entity extraction

We adopt CoT to make the LLM answer sub questions, thus implicitly forcing it to think in steps before drawing a conclusion. We instruct the LLM to give concrete answers based on the facts outlined in the source texts and output in json format for easier parsing.

2.4. Mitigation of LLM output stochasticity

One typical challenge of LLMs is model output stochasticity. Self-consistency marginalization [11] is proposed to mitigating the stochasticity of a single sampled generation while avoiding the repetitiveness and local-optimality that plague greedy decoding produces. It first samples a diverse set of reasoning paths instead of only taking the greedy one, and then selects the most consistent answer by marginalizing out the sampled reasoning paths. In this work, we generate multiple interpretations over the news and research report and marginalize the answers through majority voting.

3. Experiment

3.1. Datasets

To examine the proposed solution, we scrape and manually filter out a small dataset containing 251 financial news that are not specific to individual stocks and 141 industry research analyst reports from various brokers from Chinese public websites (e.g. eastmoney). We filter information related to individual stocks as we are interested in

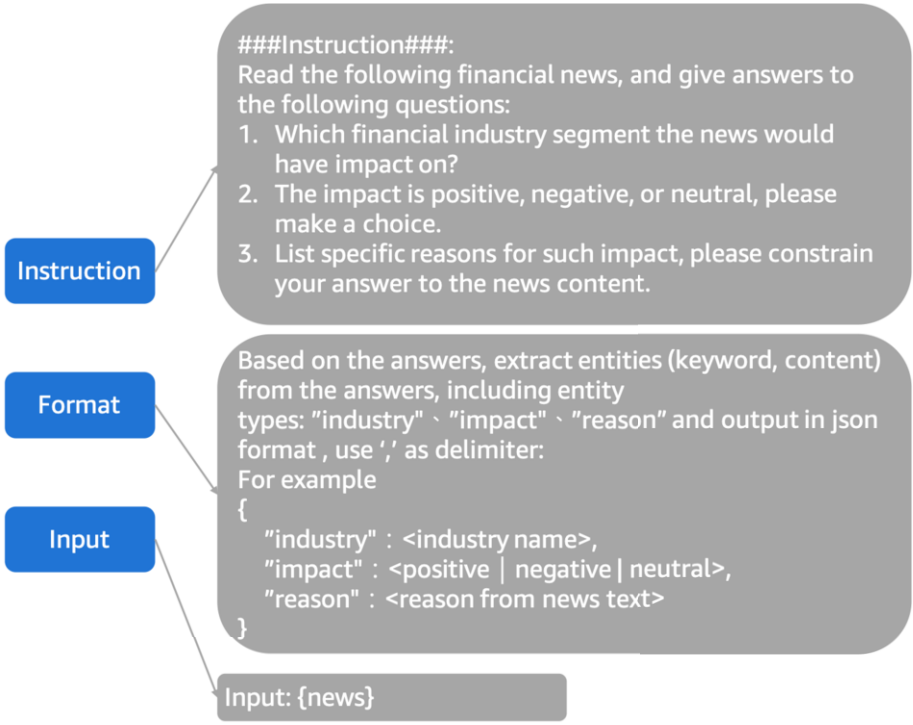

Figure 2. Prompt for News Interpreter.

industry-focused funds for this study. The news and the analyst reports are released on 07/17/2023. We follow the Shenwan(SW) standard for the industry categorization hierarchy standards (three levels) and identify 5 themed-funds for each level I industry on average. The daily price for each fund after 07/17/2023 is obtained using *xalpha*, and the weekly and monthly fund performance is averaged for each level I industry.

3.2. Large language model and prompts

Because the public dataset we obtain are in Chinese, we choose ChatGLM as the LLM for our experiment as ChatGLM is optimized for Chinese QA and dialogue [12]. To enable self consistency, we set the temperature to be 0.8 and generate 5 samples for each same prompt for both news interpreter and report analyzer. The detailed news interpretation prompt is shown in Figure 2. The Map & Reduce instruction prompting for analyst report is not included because of space limit.

4. Experimental results

Based on the experimental results, we find that ChatGLM can logically reason the impacts on financial markets through implicit factors that is not specifically disclosed in the raw news content. Through Map and Reduce operation for analyst reports, the proposed approach can well cover multiple aspects included in the report while overcoming the

limit of the context window size of ChatGLM. However, the target industry and overall recommendation/rating are diverged from the analyst at times upon close examination, since the conclusion from the analyst are often summarized in one page (usually between page 1 to 3).

An example of the extracted structured information from LLM's interpretation on news and analyst report table is shown in Table 1. An interesting observation is made on the real estate sector, for the LLM's interpretation difference between news and analyst report. The sentiment on the news for the housing market is pretty negative and therefore the score rating for real estate is pretty low. On the other hand, for the analyst report, analysts acknowledge that recent downward trend of the real estate market. However, analysts recognize there are great values to the valuable assets that good companies with a long history hold. In addition, central bureaus have provided incentives for housing markets to rebound. Note that the original content is in Chinese, here content is translated into English for readers.

Table 1. Examples of output from the news interpreter and the report analyzer.

Source	Industry	Sentiment	Reason
News	Real estate	Neutral	The National Bureau of Statistics said that in the next stage, it is necessary to adhere to the positioning that "houses are for living in, not for speculation", accelerate the establishment of a housing system with multi-subject supply, multi-channel security, and rent-purchase parallel...
News	Real estate	Negative	The real estate market is shifting from high-speed development in the past to stable development. This is determined by the change in the development stage of the real estate market and the adjustment of market supply and demand relations.
News	Real estate	Negative	Nationwide real estate development investment decreased by 7.9% year-on-year, of which residential investment decreased by 7.3%.
News	Chemical	Neutral	The company is committed to creating a second growth curve for high value-added additives, but did not mention the specific impact on the chemical industry.
News	Leisure services	Positive	The Asian Games is conducive to the development of the industry. Many companies are actively participating in tourism-related work. Hotel booking has reached to the level pre-pandemic.
Report	Real estate	Positive	The report's assessment of real estate investment is positive. Although the real estate market shows a downward trend, overall, the real estate industry still has strong investment value. In addition, the adjustment of credit policies, such as the RRR cut by the People's Bank of China, has a positive impact on the real estate industry.
Report	Chemical	Positive	- Market demand: With the recovery of the global economy, market demand in the chemical industry has gradually recovered. Especially after the COVID-19 epidemic, domestic and foreign market demand has gradually recovered, driving up prices. - Fundamental turning point: The profitability of some chemical companies has turned upward from the profit turning point in Q1 to Q2, which means that the market may continue to rebound.- Technical turning point: Chemical product prices have stopped falling and rebounded recently, suggesting that the market may strengthen.

As there is no ground truth for the textual answers given by *FundRecLLM*, to quantitatively evaluate the recommendation answers rendered by the solution, we design an evaluation schema based on the ratings for the target industry converted from the sentiments and the corresponding industry-focused fund performance. Steps of the calculation are as followings:

(1) Firstly, we parse the sentiment part of the answer for the recommended fund and convert it to a score. The conversion from sentiment to a score rating is shown in Table 2. The conversion for report is different as we find analysts usually write reports to recommend to buy. A neutral sentiment is just a weaker statement to buy in.

Table 2. Conversion from sentiment to recommendation score rating.

Source of information	Sentiment	Score
News	Positive	1
News	Neutral	0
News	Negative	-1
Report	Positive	2
Report	Neutral	1
Report	Negative	-1

(2) Secondly, we aggregate the scores for each industry and rank the scores. While aggregating the industry rating scores, we observe that LLM's interpretation on the industry can be on different levels according to SW standard, and the industry concept from the output are not exact match with the standards. To facilitate the analysis, we use *Sentence Transformer* to find the closet industry concept within SW standards at all levels based on word similarity and map all level III and level II industry to level I industry.

(3) We then calculate market performances for the following week and month of all the related level I industry sectors after 07/17/2023, using representative funds for each industry. Their market performance is calculated as the relative week-on-week and month-on-month ending price change. Then their performances are averaged for each level I industry sector and ranked accordingly. Market performances and the scores for selected industries are shown in Table 3. The rankings for different industry market performance and the sentiment ratings aggregated from both news and analyst report are shown in Figure 3.

(4) Lastly we calculate the Normalized Discounted Cumulative Gain (NDCG) between the ranks. NDCG is a common evaluation metric for comparing rankings.

Table 4 lists the NDCG score under different scenarios. To combine news and report ratings, a simple average is taken before ranking. It is observed that applying self consistency improves the NDCG score for news ratings but does not do so for report. Taking a closer look, by majority voting through more samples, news interpretations converges to a more frequent and reasonable interpretation. On the other hand, report content are much longer and covers multiple aspects. After map and reduce operation, model's interpretation are more diverse. Only strong sector signals such as public sector, financial services and real estate are dominating the rankings for report. In the previous discussion, we mention that the model's interpretation on analyst report towards real estate sector is much more positive compared to that of news. And indeed, market price for real estate sector has rebounded from its bottom since 07/17/2023. This helps to explain that why

Table 3. Fund market performances (shown as fund price change percentages) and sentiment scores with rankings for selected industries.

Industry	Weekly change(rank)	Monthly change(rank)	News score(rank)	Report score(rank)
Real estate	2.86%(1)	11.70%(1)	-1(23)	9(4)
Building materials	1.75%(2)	6.67%(2)	2(7)	5(13)
Leisure services	-0.21%(7)	1.40%(8)	4(3)	1(22)
Chemical	-0.79%(11)	-1.10%(10)	1(17)	12(3)
Auto manufacturing	-2.81%(19)	-3.34%(18)	1(12)	3(16)
Electrical equipment	-4.37%(23)	-9.04%(24)	-1(23)	2(19)

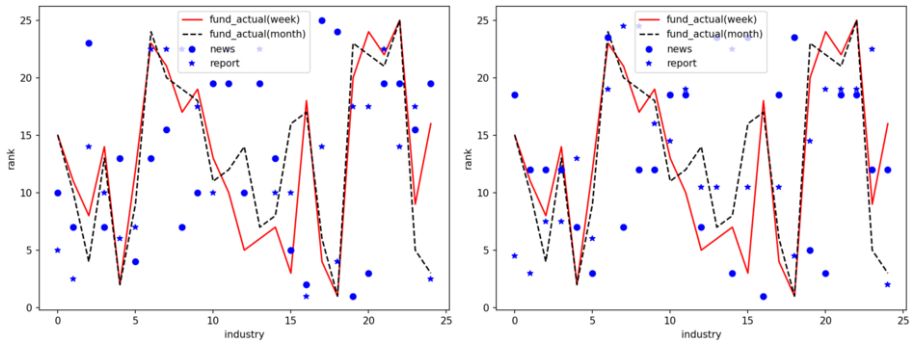

(a) (b)

Figure 3. Fund performance rank against news and report sentiment scoring rank: (a) w/o self consistency (b) w/ self consistency.

the ranking from the report ratings has a higher NDCG score compared with that from the news ratings.

Table 4. NDCG score between fund recommendation rating and fund performance ranking under different experiment setting.

Source of information	w/ self consistency	NDCG@weekly	NDCG@monthly
News Only	No	0.73	0.72
News Only	Yes	0.77	0.82
Report Only	No	0.89	0.90
Report Only	Yes	0.89	0.90
News & Report	No	0.78	0.79
News & Report	Yes	**0.91**	**0.93**

5. Conclusion

In this study, we investigate utilizing LLMs in financial advisories setting. We model our problem as a recommendation and Q&A problem and then design a solution framework of LLMs using a sequential chain of LLMs for interpreting news and analyst reports

respectively. The main challenge we face in our solution design method is on integrating multi-modal data sources and overcoming the context window size limit of the chosen LLM. We develop two parallel pipelines to consume and interpret news and raw analyst reports, and an intelligent agent as a moderator to synthesize the information and make the final conclusion.

The proposed solution and evaluation framework has certain limitations which direct us for future investigation. Firstly, the NDCG score is a noisy evaluation of recommendation efficacy as such measure captures both the accuracy of sentiment classification and how the market reacts to the sentiments. Given the time constraint, we are only able to process limited amount of information released at a single date that is quite near-term. Therefore, only short-term market performance is tracked for the evaluation. More backtests and more evaluation methods are needed to corroborate the effectiveness of the proposed solution. Secondly, we use all pages of the analyst report for the report analyzer. However, since most key contents are in earlier pages (i.e. page 1-2), an ablation study is needed to examine the effect of specifying page range for analysis. Lastly, we only use ChatGLM as the chosen LLM for our experiments. As there are multiple instruction LLMs and customized LLMs specifically for finance domain, it will be interesting study to compare with other alternatives.

References

[1] Kaddour, J, Harris, J, Mozes, M, Bradley, H, Raileanu, R, and McHardy, R. Challenges and Applications of Large Language Models. ArXiv abs/2307.10169 (2023).

[2] Naveed, H, Khan, AU, Qiu, S, Saqib, M, Anwar, S, Usman, M, Barnes, N, and Mian, AS. A Comprehensive Overview of Large Language Models. ArXiv abs/2307.06435 (2023).

[3] Lopez-Lira, A, and Tang, Y. Can ChatGPT Forecast Stock Price Movements? Return Predictability and Large Language Models. ArXiv abs/2304.07619 (2023).

[4] Deng, X, Bashlovkina, V, Han, F, Baumgartner, S, and Bendersky, M. What do LLMs Know about Financial Markets? A Case Study on Reddit Market Sentiment Analysis. Companion Proceedings of the ACM Web Conference 2023; 2023 30 April - 4 May; Austin, TX. Association for Computing Machinery; c2023. p. 107–110.

[5] Huang, AH, Wang, H and Yang, Y. FinBERT: A Large Language Model for Extracting Information from Financial Text. Contemp Account Res, 2023; 40: 806-841. https://doi.org/10.1111/1911-3846.12832

[6] Wei, J, Wang, X, Schuurmans, D, Bosma, M, Chi, EH, Xia, F, Le, Q, and Zhou, D. Chain of Thought Prompting Elicits Reasoning in Large Language Models. ArXiv abs/2201.11903 (2022).

[7] Qin, Y, Liang, S, Ye, Y, Zhu, K, Yan, L, Lu, Y, Lin, Y, Cong, X, Tang, X, Qian, B, Zhao, S, Tian, R, Xie, R, Zhou, J, Gerstein, MH, Li, D, Liu, Z, and Sun, M. ToolLLM: Facilitating Large Language Models to Master 16000+ Real-world APIs. ArXiv abs/2307.16789 (2023).

[8] Wu, TS, Terry, M, and Cai, CJ. AI Chains: Transparent and Controllable Human-AI Interaction by Chaining Large Language Model Prompts. Proceedings of the 2022 CHI Conference on Human Factors in Computing Systems; 2022 29 April - 5 May; New Orleans, LA. Association for Computing Machinery; c2022. p. 1–22.

[9] Shen, Z, Zhang, R, Dell, M, Lee, B, Carlson, J, and Li, W. LayoutParser: A Unified Toolkit for Deep Learning Based Document Image Analysis. In: Lladós, J, Lopresti, D, Uchida, S, editors. Document Analysis and Recognition – ICDAR 2021. 2021 September 5–10; Lausanne, Switzerland. p. 131–146.

[10] Wang, X, Wei, J, Schuurmans, D, Le, Q, Chi, EH, and Zhou, D. Self-Consistency Improves Chain of Thought Reasoning in Language Models. ArXiv, abs/2203.11171 (2022).

[11] Du, Z, Qian, Y, Liu, X, Ding, M, Qiu, J, Yang, Z, and Tang, J. GLM: General Language Model Pretraining with Autoregressive Blank Infilling. In Proceedings of the 60th Annual Meeting of the Association for Computational Linguistics (Volume 1: Long Papers); 2022 May 22-27; Dublin, Ireland. Association for Computational Linguistics. p. 320–335.

Fuzzy Systems and Data Mining IX
A.J. Tallón-Ballesteros and R. Beltrán-Barba (Eds.)

doi:10.3233/FAIA231060

Numerical Comparison of the Three Poisson Arrival Queuing System Models

Lisha Piao[a, 1], Yingli Zheng[a] and Lizhen Wang[a]
[a] *Dianchi College of Yunnan University, Department of Mathematics, Kunming, Yunnan, China*

Abstract. The optimization of service systems is inseparable from the study of queuing models, involving the establishment of models and the comparative analysis between them. First, the general models of the queuing system are introduced. The queuing system is assumed to be *M/M/1* model and *M/M/c* model, in which the customer arrival is Poisson flow and the service time is negative exponential distribution. As any complex queuing model is derived from these two models, they are widely applied in service systems such as production and daily life. Second, in order to enhance the contrast between the two models, the two kinds of models are refined into three comparable cases, and average queuing time models are established separately. Finally, through theoretical derivation, software simulation, and theoretical testing methods, the comparison results of these three queuing models under the Poisson arrival process are obtained, which is of paramount importance for the practical application of queuing models.

Keywords. queuing theory, *M/M/1* model, *M/M/c* model, average queuing time

1. Introduction

Queuing is a common phenomenon in our daily life. For example, customers go to the store to buy things, patients go to the hospital to see a doctor, and when the sales staff and doctors cannot meet the needs of customers or patients in time, there will be queuing. With the rapid advancement in economic and social development, queuing theory has found extensive applications in fields like transportation systems, storage systems, communication systems, and production management systems [1]. As in the berth design scene, through the queuing system can be a reasonable number of parking spaces in the parking lot design, improve the utilization rate of the parking lot. Lam et al. [2] estimated the queuing time of vehicles and the probability of full parking lot by using the queuing theory. Gan et al. [3] used the single-server queuing system with Poisson distribution of customer arrival, namely *M/M/1* model, simplifies the exit lane of the parking lot, and estimates the queuing time of vehicles in the parking lot and the driving time of the evacuated vehicles. With the rapid development of new energy vehicles, the queuing theory has been widely used in charging station location and facility optimization scenarios, Han et al. [4], Yang et al. [5], Min et al. [6] analyzed the various factors affecting the planning of electric vehicle charging stations and proposed optimization

[1] Corresponding Author, Lisha Piao, Dianchi College of Yunnan University, Kunming 650228, Yunnan, China; E-mail: 22378551@qq.com. This work is supported by the scientific research project of Yunnan University Dianchi College (2022XZD03, 2022XZC12).

principles for station location and capacity allocation. Xie et al. [7] and Wang et al. [8] proposed the use of queuing theory models to optimize the planning of charging facilities under specific constraints, with the goal of minimizing overall costs. In the medical planning scene, Liu et al. [9] and Wu et al. [10] used *M/M/c* model to optimize the outpatient schedule and medical equipment configuration, providing a reference for improving the quality of medical service and work efficiency. In the inventory control scene, Zhang [11] uses *M/M/1* model to study the optimal inventory strategy of perishable goods. In the performance analysis scene, Wang et al. [12] used single and multiple queues to analyze the performance of customers with Poisson arrival and to derive the optimal scheduling method. Therefore, the study of queuing theory is of great significance to the optimal design of service system.

The study of queuing theory primarily involves the establishment of queuing models and the comparative analysis of quantitative indicators across models. The most critical step in model establishment is to derive the steady-state probability formula for the birth and death process [13], and then calculate quantitative indicators for model comparison. To achieve this, the *M/M/1* and *M/M/c* queuing models under the Poisson arrival process are studied, using queuing theory to establish the steady-state probabilities and average queuing times under different arrival rates and service rates. These two models serve as the foundation for theoretical analysis, with any complex queuing models being derived from them. Therefore, the modeling and comparison methods employed in these models can be applied to various application scenarios. To enhance the comparability of the models, the two types of models are divided into three cases. The first case is c standard *M/M/1* queuing systems with arrival and service rates that are $\frac{1}{c}$ of the arrival rate of a standard *M/M/c* queuing system, the second case is a single standard *M/M/1* queuing system, and the third case is a single standard *M/M/c* queuing system. Thus, Case 2 is a reference, Case 1 is a simple duplicate of Case 2, Case 3 is Case 2 when multiple service counters are involved. The quality of the model is primarily assessed by the average queuing time, with the comparison method mainly utilizing a combination of theoretical analysis and software calculation. Specifically, the average queuing time for each model is first derived by queuing theory, leading to the conclusion that the model in Case 2 outperforms that in Case 1. Subsequent to this, the average queuing time for the three cases is simulated using software, leading to the suspicion that the model in Case 3 may be superior. Finally, this hypothesis is verified through theoretical analysis. This method enables efficient comparison of queuing models, providing a reliable reference for the optimization design of service systems.

2. Queuing System Model

2.1. General model of queuing theory

The basic idea of queuing theory is to infer some parameters through the distribution of customer arrival time and service time, including average queuing time, average queue length, the number of service objects in the system, and the probability of system vacant. The distribution of customer arrival time and service time is generally assumed in advance. The common distributions in queuing systems include Poisson distribution, negative exponential distribution, Erlang distribution and so on. When using the Kendall notation *X/Y/Z* to represent a queuing system, *X* represents the time interval of customer

arriving one after another, *Y* represents the distribution of service time, and *Z* represents the number of service counters. These three elements are the most important and influential characteristic elements of the queuing system. A complete queuing system model includes input process, queuing rules, service counters, and service rules. As shown in Figure 1, the part in the dotted line is the queuing system [13].

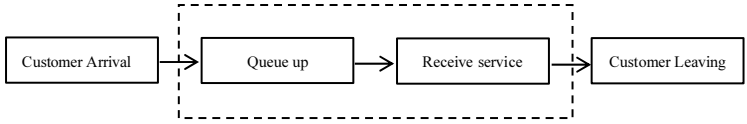

Figure 1. Main components of the queuing system model.

The input process describes how customers arrive at the queuing system according to certain rules. Generally, it can be described from three aspects: the customer population, the customer arrival pattern, and the probability distribution of customer flow. The customer population can be either people or items, and can be a finite or infinite set. The customer arrival pattern describes how customers arrive at the system, either individually or batch arrival. For example, patients visiting a hospital may arrive individually, while materials or products entering the warehouse may arrive in batches.

Customer queuing is divided into unlimited queuing and limited queuing. Unlimited queuing refers to a situation where the number of customers is unlimited and the queue can be of infinite length, also known as waiting-based queuing systems. When customers arrive, if the service counter is currently busy, they will join the waiting queue to wait for service. Limited queuing refers to situations where the number of customers in the system is limited, and is further divided into loss-based queuing systems, waiting-based queuing systems, and hybrid queuing systems.

Service counters can be divided into single service counter and multiple service counters. There are five forms in terms of their composition: a team and a counter, a team and multiple counters, multiple teams and multiple counters, multiple serial formations, and multiple mixed formations. In a waiting-based queuing system, the service counters often use four service models: first-in-first-out (FIFO), last-in-first-out (LIFO), random, and priority services.

2.2. Common models of queuing theory

In queuing theory, *M/M/1* and *M/M/c* are the most common queue systems, and are widely adopted in practical applications. Among them, *M/M/1* is the simplest and most basic standard queuing system model, with the following assumption conditions [13]:

- Input process: (1) The population of customers is infinite; (2) The number of customers entering the system is one at a time; (3) The time interval between customers follows Poisson distribution, with a parameter λ representing the number of customers arriving per unit time.
- Queuing rules: Waiting-based system with unlimited queue length
- Service counters and service rules: (1) single service counter; (2) Customers follow the principle of FIFO; (3) The service time follows a negative exponential distribution with parameter μ, representing the number of customers served per unit time.

The main difference between the standard *M/M/c* queuing system and the *M/M/1* system is that the former has multiple service counters that are independent of each other, with equal service rates. If customers arrive when all service counters are occupied, they will form a queue to wait. The remaining assumptions for the *M/M/c* system are the same as those for the *M/M/1* system.

Next, we will focus our discussion on the standard *M/M/1* and standard *M/M/c* queuing models under the above agreement. Model 1, Model 2, and Model 3 are defined by the juxtaposition of *c M/M/1* queuing systems, one *M/M/1* queuing system, and one *M/M/c* queuing system, respectively. According to the queuing theory, it is assumed that in Model 1, the number of customers arriving in unit time is λ, and the number of customers served in unit time is μ. In Model 2, the parameters are the number of customers arriving in unit time $c\lambda$ and the number of customers served in unit time $c\mu$. And in Model 3, the number of customers arriving in unit time is $c\lambda$, and the number of customers served in unit time is μ. This paper discusses the average queuing time of customers for three models, and compares which queuing model is superior based on this, to provides an important theoretical insights for the queuing systems in practical applications, thereby to better design the queuing system models.

3. Average Queuing Time for Three Queuing Models

3.1. Model 1: c M/M/1 queuing system

Let *c M/M/1* queuing systems be juxtaposed, with $\lambda_1 = \lambda,\ \mu_1 = \mu$ in each system, the queuing system model is shown in Figure 2.

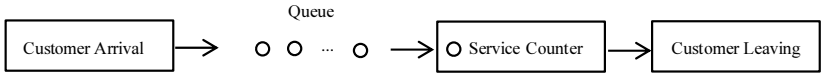

Figure 2. *M/M/1* queuing system of one team and one counter.

According to this queuing system, the state transition process in the infinite state is obtained, as shown in Figure 3.

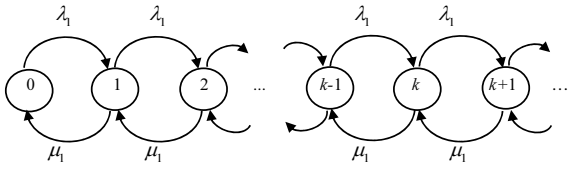

Where *k* represents the number of customers in the queuing system. Based on the state transfer diagram, the equations of state balance is listed under steady state probability.

$$\begin{cases} -\lambda_1 p_0 + \mu_1 p_1 = 0 \\ \lambda_1 p_0 - (\lambda_1 + \mu_1) p_1 + \mu_1 p_2 = 0 \\ \cdots \\ \lambda_1 p_{k-1} - (\lambda_1 + \mu_1) p_k + \mu_1 p_{k+1} = 0 \\ \cdots \end{cases} \tag{1}$$

Solve p_1 from the first equation in Eq. (1), substitute it into the second equation to obtain p_2, and so on to obtain p_k. According to [13], $\rho = \frac{\lambda}{\mu}$ is used to represent service intensity, which refers to the ratio of the average service time to the average interval time between customers. It is a measure of system intensity, with a closer ratio indicating a higher service intensity of the system and a busier service organization. According to the finiteness of the flow [13], the steady-state probability of the system represented by $p_k = \rho^k (1-\rho)$. Additionally, the average queuing time of customers can be calculated by dividing the average length of the queue by the rate of customer arrivals per unit time. Therefore, the average queuing time in Model 1 is expressed as

$$W_1 = \frac{\sum_{k=1}^{+\infty}(k-1)\cdot p_k}{\lambda_1} = \frac{1}{\lambda}\left(\sum_{k=1}^{+\infty} k p_k - \sum_{k=1}^{+\infty} p_k\right) = \frac{1}{\lambda}\cdot\frac{\rho^2}{1-\rho} = \frac{\lambda}{\mu(\mu-\lambda)} \tag{2}$$

3.2. Model 2: 1 M/M/1 queuing system

The establishment process of Model 2 is similar to that of Model 1, but assumes that the arrival and departure speeds of customers are $\lambda_2 = c\lambda$ and $\mu_2 = c\mu$, respectively. This leads to a state transfor process that has the same structure as Figure 3, using a derivation method similar to Model 1, the average queuing time for Model 2 is calculated as

$$W_2 = \frac{\lambda}{c\mu(\mu-\lambda)} \tag{3}$$

3.3. Model 3: 1 M/M/c queuing system

The previous two models fall under the single-server scenario. Here, we establish a multi-server queuing model that more closely represents the real-world scenario, and derive the mathematical expression for the average queuing time. First, we make model assumptions, setting the number of servers in the system to *c* and assuming $\lambda_3 = c\lambda$ and $\mu_3 = \mu$. The queuing model is shown in Figure 4.

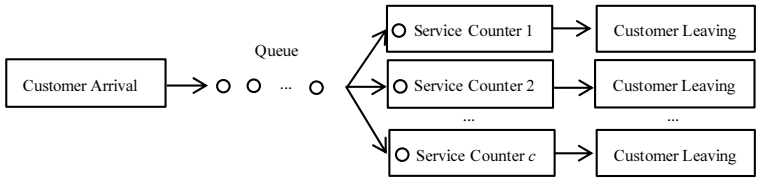

Figure 4. *M/M/c* queuing system of one team and multiple counters.

At this point, the state in the system is also infinite, and the state transition process is as illustrated in Figure 5.

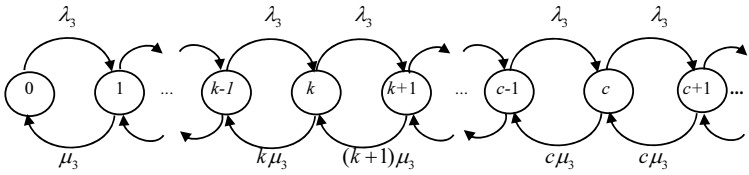

Under the assumption of steady state probability, two situations are considered: when the state is $k = 0,1,...,c-1$, the steady-state probability of the system represented by

$$\begin{cases} -\lambda_3 p_0 + \mu_3 p_1 = 0 \\ \lambda_3 p_0 - (\lambda_3 + \mu_3) p_1 + 2\mu_3 p_2 = 0 \\ \quad ... \\ \lambda_3 p_{k-1} - (\lambda_3 + k\mu_3) p_k + (k+1)\mu_3 p_{k+1} = 0 \end{cases} \tag{4}$$

and when the state is $k = c, c+1,...$, the steady-state probability represented by

$$\lambda_3 p_{k-1} - (\lambda_3 + c\mu_3) p_k + c\mu_3 p_{k+1} = 0 \tag{5}$$

By substituting Eqs. (4) from top to bottom, if $k = 0,1,...,c-1$, then we have $p_k = \frac{1}{k!}\left(\frac{\lambda_3}{\mu_3}\right)^k p_0$. Similarly, if $k = c, c+1,...$, we can also have $p_k = \frac{1}{c^{k-c}c!}\left(\frac{\lambda_3}{\mu_3}\right)^k p_0$.

Then, the average queuing time for Model 3 represented by

$$W_3 = \frac{\sum_{k=c+1}^{+\infty}(k-c)\cdot p_k}{\lambda_3} = \frac{c^{c-1}}{\lambda c!}\frac{\left(\frac{\lambda}{\mu}\right)^{c+1}}{\left(1-\frac{\lambda}{\mu}\right)^2}\left[\sum_{k=0}^{c-1}\frac{1}{k!}\left(\frac{c\lambda}{\mu}\right)^k + \frac{1}{c!}\frac{1}{1-\frac{\lambda}{\mu}}\left(\frac{c\lambda}{\mu}\right)^c\right]^{-1} \tag{6}$$

So far, the mathematical models of the average queuing time in three kinds of queuing models are derived. The developed average queuing time model can functionalize and quantify the performance metrics of the queuing system, laying a foundation for the comparative analysis of models in the next step. The form of the average queuing time in Model 3 is very complicated, and the numerical method is used for comparative analysis with the help of computer.

4. Numerical Comparisons and Further Proofs

The estimates of the average queuing time of the above three queuing models are compared under different parameters. Assuming that the arrival process of customers is

a Poisson flow, the service time follows a negative exponential distribution, and if there are multiple service counters, they are juxtaposed, and a single FIFO queuing model, the customer inflow rate and the service rate are taken as λ and μ respectively in Model 1, $c\lambda$ and $c\mu$ in Model 2, and $c\lambda$ and μ in Model 3. For each model, given the number of service counters, the system service intensity ρ is changed by adjusting the arrival rate of the customers, where $0.1 \leq \rho \leq 0.9$. For each service intensity, the average queuing time of the three queuing models is simulated by *MATLAB*, and Table 1 shows the average queuing time of the three models with different service intensities when the number of service counters is 2, 5, and 10 respectively.

Table 1. Comparison of the average queuing times for the three models, where ρ is the system service intensity, c is the number of service counters, and W_1, W_2 and W_3 is the average queuing time for Model 1, Model 2 and Model 3 respectively.

ρ	c=2			c=5			c=10		
	W_1	W_2	W_3	W_1	W_2	W_3	W_1	W_2	W_3
0.1	0.0111	0.0056	0.0010	0.0111	0.0022	3.9e-06	0.0111	0.0011	1.3e-09
0.2	0.0250	0.0125	0.0042	0.0250	0.0050	9.6e-05	0.0250	0.0025	6.0e-07
0.3	0.0429	0.0214	0.0099	0.0429	0.0086	0.0006	0.0429	0.0043	1.7e-05
0.4	0.0667	0.0333	0.0190	0.0667	0.0133	0.0020	0.0667	0.0667	1.5e-04
0.5	0.1000	0.0500	0.0333	0.1000	0.0200	0.0052	0.1000	0.0100	0.0007
0.6	0.1500	0.0750	0.0563	0.1500	0.0300	0.0118	0.1500	0.0150	0.0025
0.7	0.2333	0.1167	0.0961	0.2333	0.0467	0.0252	0.2333	0.0233	0.0074
0.8	0.4000	0.2000	0.1778	0.4000	0.0800	0.0554	0.4000	0.0400	0.0205
0.9	0.9000	0.4500	0.4263	0.9000	0.1800	0.1525	0.9000	0.0900	0.0669

By analyzing Table 1, the relationship of the average queuing time of the three kinds of queuing models satisfies the inequality:

$$W_3 < W_2 < W_1 \tag{7}$$

Where W_i represents the average queuing time of model i (i=1, 2, 3) .

Figure 6 shows the trend of the average queuing time of the three models with the service intensity when the number of servers is 2, 5 and 10. From the graph, the advantage of Model 3 over Model 1 is more significant when the service intensity increases, regardless of the number of service counters, and Model 3 is better than Model 2. The graph conclusion obtained from the experiment has some reference value, but it cannot be used as the final conclusion and needs more rigorous theoretical proof. So far, a comparative framework has been proposed for analyzing and comparing multiple queuing models, which involves theoretical derivation, software simulation, and theoretical verification. This method is rigorous and intuitive, and can effectively provide a reference for the optimal design of service systems.

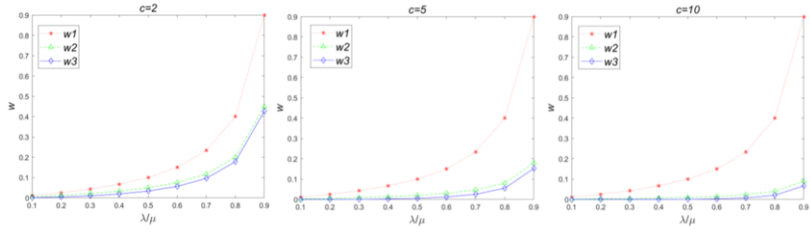

(a) 2 service counters (b) 5 service counters (c) 10 service counters

Figure 6. The change trend of the average queuing time of the three models.

With the previous numerical experimental analysis, we can boldly guess the conclusion that Model 3 is superior to Model 1 and Model 2. Further theoretical proof is given below. Based on the previous discussion, it can be concluded that Model 2 is superior to Model 1, so the following proofs are mainly focused on the comparison of the average queuing time between Model 2 and Model 3. W_3 in Eq. (6) can be expressed in terms of W_2 as follows:

$$W_3 = \frac{c^{c-1}\rho^{c+1}}{\lambda c!(1-\rho)^2} p_0 = W_2 \cdot \frac{c^{c-1}\rho^{c-1}}{(c-1)!(1-\rho)} p_0 \tag{8}$$

Therefore, it is sufficient to show that $\frac{c^{c-1}\rho^{c-1}}{(c-1)!(1-\rho)} p_0 < 1$ must hold for $W_3 < W_2$.

Prove the inequality $\frac{c^{c-1}\rho^{c-1}}{(c-1)!(1-\rho)} p_0 < 1$ below.

$$\begin{aligned}
\frac{c^{c-1}\rho^{c-1}}{(c-1)!(1-\rho)} p_0 &= \frac{c^{c-1}\rho^{c-1}}{(c-1)!(1-\rho)\left[\sum_{k=0}^{c-1}\frac{1}{k!}(c\rho)^k + \frac{1}{c!}\frac{1}{1-\rho}(c\rho)^c\right]} \\
&= \frac{c^{c-1}\rho^{c-1}}{(c-1)!(1-\rho)\left[\sum_{k=0}^{c-2}\frac{1}{k!}(c\rho)^k + \frac{1}{(c-1)!}(c\rho)^{c-1} + \frac{1}{c!}\frac{1}{1-\rho}(c\rho)^c\right]} \\
&= \frac{(c\rho)^{c-1}}{(c-1)!(1-\rho)\sum_{k=0}^{c-2}\frac{1}{k!}(c\rho)^k + (c\rho)^{c-1}}
\end{aligned}$$

The denominator is always larger than the numerator, that is, $\frac{c^{c-1}\rho^{c-1}}{(c-1)!(1-\rho)} p_0 < 1$, since the number of service counters $c \geq 2$ and the system service intensity $\rho < 1$, the conclusion is proved.

5. Conclusions

Based on the Poisson arrival process, analyze system performance metrics, choose to construct three different queuing systems using the *M/M/1* and *M/M/c* models, and calculate the average queuing time respectively with the steady-state probabilities. For the three types of queuing systems, the parameter values of customer inflow rate and service acceptance rate are preset. A model comparison method is proposed, which involves theoretical derivation, software simulation, and ultimately, theoretical verification. It is found that under a Poisson arrival process, the average queuing time relationship among the three queuing models leads to the conclusion of Eq. (7). The comparison results suggest that “one team and multiple counters” structure is the optimal

model of service systems, while a simple copy of "one team and single counter" structure is the most inefficient. The application of this method not only offers a unified framework for analyzing and comparing various queuing models, but also turns system performance indicators into functional and quantitative terms, making the optimal model more precise and intuitive. This facilitates efficient comparison of queuing models and provides a reliable reference for the optimization design of service systems.

References

[1] K. Zhang, Z. Tu, D. Chu, et al. A review of research related to service resource availability based on queuing theory[J]. Computer Science, 2021, 48(01): 26-33.
[2] W. Lam , Z. Li, H. Huang, et al. Modeling time-dependent travel choice problems in road networks with multiple user classes and multiple parking facilities[J]. Transportation Research Part B, 2006, 40(5): 368-395.
[3] J. Gan, X. Mao, J. Zhao. Optimal evacuation model for parking lot vehicles considering dynamic traffic flow[J]. Journal of Southwest Jiaotong University, 2012, 56(01): 123-130.
[4] Y. Han, R. Ren, M. Xu. Optimal allocation of electric vehicle charging facilities at destination charging stations[J]. Operations Research and Management, 2017, 26(08): 76-84.
[5] Y. Yang, P. Gao, C. Zhao. Modeling of temporary charging station siting and capacity setting for electric vehicles in cities[J]. Journal of Chongqing Normal University (Natural Science Edition), 2020, 37(06): 1-6.
[6] D. Min, K. Jiang, R. Liu, et al. A two-stage site selection and capacity determination model for pure electric truck charging station[J]. Journal of Chongqing Polytechnic University (Natural Science Edition), 2023, 37(01): 186-195.
[7] Y. Xie, L. Zhang, S. Deng, et al. Research on Optimizing Network Layout of Electric Vehicle Charging Facilities[J]. Mathematics in Practice and Theory, 2020, 50(10): 168-176.
[8] X. Wang, M. Shahidehpour, C. Jiang, et al. Coordinated planning strategy for electric vehicle charging stations and coupled traffic-electric networks[J]. IEEE Transactions on Power Systems, 2019, 34(1): 268-279.
[9] X. Guo, J. Zhang, W. Yang, et al. Optimization of vaccination clinic resource allocation based on queuing theory model[J]. Modern Preventive Medicine, 2021, 48(17): 3172-3175+3181.
[10] L. Wu, Q. Tan, S. Luo. Assessment and improvement of outpatient pharmacy service quality and efficiency based on queuing theory mathematical model[J]. Anhui Medicine, 2020, 24(08): 1666-1669.
[11] H. Zhang. Perishable M/M/1/N queuing Inventory control system based on (r,Q) strategy[J]. Modern Business Industry, 2019, 40(33): 205-208.
[12] S. Wang, X. Li, L. Chen. A review of random request performance analysis in cloud environments[J]. Journal of Computing, 2022, 45(06): 1241-1260.
[13] Y. Hu. A course in operations research[M]. 4th edition. Beijing: Tsinghua University Press, 2012.

Fuzzy Systems and Data Mining IX
A.J. Tallón-Ballesteros and R. Beltrán-Barba (Eds.)

doi:10.3233/FAIA231061

Three-Way Decision-Making Based on Incomplete Information System and Its Application

Changlin Xu [a,b,1] and Songqian Mao [a]
[a] *School of Mathematics and Information Science, North Minzu University, Yinchuan 750021, China*
[b] *The Key Laboratory of Intelligent Information and Big Data Processing of Ningxia Province, North Minzu University, Yinchuan, Ningxia 750021, China*

Abstract. In order to avoid decision makers from making wrong decisions as much as possible and reduce the losses caused by wrong decisions, a new aggregation method of interval loss function is proposed based on incomplete information system. Firstly, the missing values are filled according to their characteristics and combined with probability, and on this basis, the measurement method of similarity is given, and the horizontal similarity class of each object is obtained according to the similarity between objects. Secondly, according to the number of times each object in the similar class appears in its corresponding horizontal similar class, the corresponding weight is obtained; Then the interval loss function of similar class is defined as the aggregation of interval loss functions of all objects in similar class, and each interval is weighted according to the weight, so that multiple intervals in similar class are aggregated into an interval, and then the aggregated interval is converted into a single value by using the conversion function. Finally, according to the aggregation method, three decision rules are given to make decisions, and the effectiveness of the method is verified by a case.

Keywords. incomplete information system, interval loss function, aggregation, missing value, three-way decision making

1. Introduction

As a further optimization of traditional two-branch decision-making, three-branch decision-making is a decision-making theory with the idea of "rule by three points" proposed by Yao[1]. Its core idea is to divide the universe into three different parts with the help of granular computing[2], adopt different decision-making behaviors or strategies, and then evaluate the corresponding behaviors or strategies. Three-branch decision theory is widely used in many decision-making problems in real life, which simplifies complex problems, not only reduces decision-making time, but also reduces decision-making cost and improves decision-making efficiency[3][4]. Compared with the traditional two-branch decision-making, the three-branch decision-making increases the steps of decision-making, but it reduces the difficulty of decision-making to a certain extent, and lays a solid foundation for making accurate decisions in the future. In a word, the theory of three branches of decision-making provides new ideas for the expansion of many fields and new research directions for countless scholars[5][6].

[1] Corresponding Author: Changlin Xu, School of Mathematics and Information Science, North Minzu University, Yinchuan 750021, China; E-mail: xuchlin@163.com.

In the process of three decision-making, the only step that can't be ignored is to determine the loss function[7]. The loss function is generally given by experts in various fields through investigation and analysis of data, but in the process of its determination, due to many subjective factors, the uncertainty brought by various influencing factors increases the difficulty of the decision-making process[8]. Therefore, granular computing, as a powerful tool to deal with uncertain information, is closely related to the three decisions[9][10]. Through granulation[11][12], granular computing can simulate the structure of the real world, human thinking mode and behavior mode, decompose complex information or problems into several small parts, and better understand them from multiple angles and levels[13]. However, the development direction of a lot of information and things in real life is uncertain. Therefore, how to correctly deal with the interference caused by uncertainty and reduce its losses has become a research focus of the current society[14]. In this process, countless scholars have made unremitting efforts to study all aspects of it [15][16]. Considering the uncertainty of the loss function, Wang and others extended the single-valued loss function to the interval form, and combined with the concept of similar classes to effectively aggregate the intervals, which provided a new idea for the determination of the three decision rules by reducing the errors brought by the determination of the loss function[17].

Considering that most loss values are given by experts, their values may not be accurate enough, so this paper decides to replace single values with interval numbers with "multi-valued" characteristics, and defines the interval loss function of similar classes as the aggregation of interval loss functions of all objects in similar classes, and then makes decisions on incomplete information systems under *L-level* similarity relations after effectively combining the two.

2. Theoretical basis

2.1. Incomplete information system

Definition 1[18] Assumes that $S=(U,A,V,f)$ is an information system, where $U=\{x_1,x_2,\mathrm{L},x_n\}$ is a non-empty finite set of objects, which is called universe; A represents a non-empty finite set of attributes, and $A=C\cup D$, where C is a conditional attribute, D is a decision attribute, and $C\cap D=\varnothing$; V represents the set of attribute domains, V_a represents the range of attribute a, and $f:U\times A\to V$ represents an information function, which makes each object have an information value corresponding to each attribute, that is, $V_a\in A,x\in U,f(x,a)\in V_a$.

Definition 2[19] calls $IIS=(U,A,V,f)$ is an incomplete information system, in which some values in V_a are unknown and unavailable, then $V=V_a\cup\{*\}$, and $*$ represent unknown values. If the information in the information table is complete and there is no missing, the table is called a complete information table; Conversely, if an attribute value in an information table is empty, the table is called an incomplete information table.

2.2. Similarity

In the process of solving the similarity, the similarity formula defined by most scholars does not take into account the missing values in the data, and its formula is generally applicable to complete data, so how to solve the similarity of missing data is hereby defined as follows.

Definition 3[20] Given an incomplete information system $IIS=(U,A,V,f)$, it contains *m* object sets and *n* attribute sets, where $U=\{x_1,x_2,\mathrm{L}\ ,x_m\}$ and $A=\{a_1,a_2,\mathrm{L}\ ,a_n\}$. For $\forall x,y\in U,\forall a_i\in A$, the relationship between $a_i(x)$ and $a_j(x)$, there may be the following four situations:

- IF $a_i(x)\neq *$, $a_j(y)\neq *$, $a_i(x)$ and $a_j(x)$ are equal if and only if $a_i(x)=a_i(y)$;
- IF $a_i(x)\neq *$, $a_j(y)\neq *$, $a_i(x)$ and $a_j(x)$ are unequal if and only if $a_i(x)\neq a_i(y)$;
- IF $a_i(x)=*$ or $a_i(y)=*$, Since $*$ can take any value in the range, the probability of $a_i(x)=a_i(y)$ is $1/|V_{a_i}|$;
- IF $a_i(x)=*$ or $a_i(y)=*$, Since $*$ can take any value in the range, the probability of $a_i(x)=a_i(y)$ is $1/|V_{a_i}|^2$.

To sum up, the similarity between objects x and y in attributes is:

$$Sim_{(a_i)}(x,y)=\begin{cases}1, & a_i(x)=a_i(y)\neq *,\\ 0, & a_i(x)\neq a_i(y)\ \mathrm{I}\ a_i(x)\neq *\ \mathrm{I}\ a_i(y)\neq *,\\ \dfrac{1}{|V_{a_i}|}, & a_i(x)=*\ \mathrm{U}\ a_i(y)=*,\\ \dfrac{1}{|V_{a_i}|^2}, & a_i(x)=*\ \mathrm{I}\ a_i(y)=*.\end{cases} \tag{1}$$

Therefore, the overall similarity between objects x and y is:

$$Sim(x,y)=\sum_{i=1}^{n}\frac{Sim_{(a_i)}(x,y)}{n}. \tag{2}$$

2.3. L level similarity class

Definition 4[21] For incomplete information system $IIS=(U,A,V,f)$, *L-level* similarity relation $SR_A^{\ L}(0\le L\le 1)$ is defined as follows:

$$\forall x,y,SR_A^{\ L}(x,y)\Leftrightarrow\forall a\in A:Sim(x,y)=\sum_{a\in A}\frac{Sim_{(a)}(x,y)}{n}\ge L. \tag{3}$$

2.4. Decision Rough Set

Definition 6[22][23] Given information tables $S=(U,A,V,f)$, $\Omega=\{\omega_1,\omega_2,\mathrm{L}\ ,\omega_m\}$ are *m* finite state sets and $A=\{a_1,a_2,\mathrm{L}\ ,a_n\}$ is *n* finite action sets. $\Pr(\omega_i\mid x)$ represents the conditional probability of *x* in state ω_i, and $\lambda(a_i,\omega_i)$ represents the loss or cost of taking action a_i in state ω_i. If object *x* takes action a_j, its expected loss is:

$$R(a_j\mid x)=\sum_{i=1}^{m}\lambda(a_i,\omega_i)\Pr(\omega_i\mid x). \tag{4}$$

Therefore, the expected losses of and can be expressed as:

$$\begin{cases}R(a_P\mid[x])=\lambda_{PP}\Pr(X\mid[x])+\lambda_{PN}\Pr(\neg X\mid[x]),\\ R(a_B\mid[x])=\lambda_{BP}\Pr(X\mid[x])+\lambda_{BN}\Pr(\neg X\mid[x]),\\ R(a_N\mid[x])=\lambda_{NP}\Pr(X\mid[x])+\lambda_{NN}\Pr(\neg X\mid[x]).\end{cases} \tag{5}$$

According to Bayesian decision theory, the action with the least expected loss should be chosen as the best scheme, from which the following three rules can be obtained:

P) IF $R(a_p|[x]) \le R(a_B|[x])$ and $R(a_p|[x]) \le R(a_N|[x])$, then $x \in POS(X)$;

B) IF $R(a_B|[x]) \le R(a_P|[x])$ and $R(a_B|[x]) \le R(a_N|[x])$, then $x \in BND(X)$;

N) IF $R(a_N|[x]) \le R(a_P|[x])$ and $R(a_N|[x]) \le R(a_B|[x])$, then $x \in NEG(X)$.

Because of $\Pr(X|[x]) + \Pr(\neg X|[x]) = 1$, rule $P) \sim N)$ is only related to the classification condition probability $\Pr(X|[x])$ and the loss function $\lambda_{pg}(g = P, B, N)$, and the relationship between the loss functions should be satisfied $0 \le \lambda_{PP} \le \lambda_{BP} < \lambda_{NP}$ and $0 \le \lambda_{NN} \le \lambda_{BN} < \lambda_{PN}$. So, rule $P) \sim N)$ can be rewritten as:

P1) IF $\Pr(X|[x]) \ge \alpha$, then $x \in POS(X)$;

B1) IF $\beta < \Pr(X|[x]) < \alpha$, then $x \in BND(X)$;

N1) IF $\Pr(X|[x]) \le \beta$, then $x \in NEG(X)$.

In which,

$$\begin{cases} \alpha = \dfrac{\lambda_{PN} - \lambda_{BN}}{(\lambda_{PN} - \lambda_{BN}) + (\lambda_{BP} - \lambda_{PP})}, \\ \beta = \dfrac{\lambda_{BN} - \lambda_{NN}}{(\lambda_{BN} - \lambda_{NN}) + (\lambda_{NP} - \lambda_{BP})} \quad (0 \le \beta < \gamma < \alpha \le 1), \\ \gamma = \dfrac{\lambda_{PN} - \lambda_{NN}}{(\lambda_{PN} - \lambda_{NN}) + (\lambda_{NP} - \lambda_{PP})}. \end{cases} \tag{6}$$

2.5. Conversion function

Definition 7[24] Given the interval number $\hat{\lambda} = [\lambda^-, \lambda^+], \theta \in [0,1]$, the conversion function of $\hat{\lambda}$ is $f_\theta(\hat{\lambda}) = (1-\theta)\lambda^- + \theta\lambda^+$, and the value of θ depends on the risk preference of decision makers.

3. Three-way decision based on incomplete information system

In simple decision-making problems, people usually express the loss function by explicit indicators such as time, money and consumption, but in the actual decision-making process, the loss function is often influenced by various invisible factors, such as the variability of the decision-making environment, the incompleteness of information and the limitation of the decision-maker's own ability. The comprehensive effect of many factors makes it difficult for the decision-maker to give the specific value of the loss function under normal circumstances. Therefore, it is an effective method to reduce decision risk and improve decision efficiency by replacing the single-valued form of loss function with interval number.

3.1. Interval aggregation based on incomplete information system

In the classical decision-making rough set, because the loss function often appears in the form of single value, and most of them are directly given by experts, it is influenced by subjective factors. However, considering its nature and characteristics, the risk should be random, and its value should fluctuate within a certain range, so it can not be accurately expressed only by single value. Therefore, the interval number with multi-valued characteristics can be used as a substitute to make the decision-making result more realistic. Based on this idea, the concept of loss function and interval number is fused, and the interval loss function table under incomplete information system is constructed as shown in Table 1:

Table 1. Interval loss function

	$X(P)$	$\neg X(N)$
a_P	$\hat{\lambda}_{PP}=\left[\lambda_{PP}^{-},\lambda_{PP}^{+}\right]$	$\hat{\lambda}_{PN}=\left[\lambda_{PN}^{-},\lambda_{PN}^{+}\right]$
a_B	$\hat{\lambda}_{BP}=\left[\lambda_{BP}^{-},\lambda_{BP}^{+}\right]$	$\hat{\lambda}_{BN}=\left[\lambda_{BN}^{-},\lambda_{BN}^{+}\right]$
a_N	$\hat{\lambda}_{NP}=\left[\lambda_{NP}^{-},\lambda_{NP}^{+}\right]$	$\hat{\lambda}_{NN}=\left[\lambda_{NN}^{-},\lambda_{NN}^{+}\right]$

According to definition 3, the similarity between different objects is calculated, and after setting specific values, the similarity class of each object is obtained. The interval loss function is defined as the aggregation of interval loss functions of all objects in the similar class, and a new aggregation method is proposed based on the principle of reasonable granularity.

Let $[x_1]_{SR}^{L}=\{x_1,x_2,\mathrm{L}\ ,x_t\}$, taking $\hat{\lambda}_{PP}(x)$ as an example, put forward a new aggregation method according to the principle of reasonable granularity, and do the same for other loss functions. The specific operation is as follows:

- Calculate the similarity between any two objects according to definition 3.
- Set the specific value of *L*, usually order $L=0.5$ (different values can be set according to the specific situation), and according to the similarity between different objects, the *L-level* similarity classes of all objects in $[x_1]_{SR}^{L}$ can be obtained: $[x_1]_{SR}^{L},[x_2]_{SR}^{L},\mathrm{L}\ ,[x_t]_{SR}^{L}$.
- Calculate the number of times that all objects in $[x_1]_{SR}^{L}$ appear in their corresponding *L-level* similar classes, and record them as $a,b,\mathrm{L}\ ,s$ respectively.
- Calculate the weight of each object in $[x_1]_{SR}^{L}$ according to the number of times that each object in $[x_1]_{SR}^{L}$ appears in its corresponding *L-level* similar class:

$$\frac{a}{a+b+\mathrm{L}\ +s},\frac{b}{a+b+\mathrm{L}\ +s},\mathrm{L}\ ,\frac{s}{a+b+\mathrm{L}\ +s}. \tag{7}$$

- Aggregating the intervals of all objects in $[x_1]_{SR}^{L}$ according to the calculated weights to obtain the aggregated intervals:

$$\hat{\lambda}_{PP}\left([x_1]_{SR}^{L}\right)=\left[\frac{a}{a+b+\mathrm{L}\ +s}\lambda_{PP}^{-}(x_1)+\mathrm{L}\ +\frac{s}{a+b+\mathrm{L}\ +s}\lambda_{PP}^{-}(x_s),\frac{a}{a+b+\mathrm{L}\ +s}\lambda_{PP}^{+}(x_1)+\mathrm{L}\ +\frac{s}{a+b+\mathrm{L}\ +s}\lambda_{PP}^{+}(x_s)\right]. \tag{8}$$

- According to the conversion function, the aggregated interval is converted into a single value. In the conversion process, considering the attitude of decision makers and the influence of many factors, it can be divided into three kinds of decisions: optimistic, neutral and pessimistic, and the corresponding value ranges are: $[0,0.5)$、0.5、$(0.5,1]$.

3.2. Three Decision Rules after Aggregation

After the interval is aggregated, the aggregated interval is converted into a single value according to definition 7, and then a new three-way decision rule is obtained as follows:

P2) IF $\Pr\left(X\mid[x]_{SR}^{L}\right)\geq\hat{\alpha}$, then $x\in POS(X)$;

B2) IF $\hat{\beta}<\Pr\left(X\mid[x]_{SR}^{L}\right)<\hat{\alpha}$, then $x\in BND(X)$;

N2) IF $\Pr\left(X\mid[x]_{SR}^{L}\right)\leq\hat{\beta}$, then $x\in NEG(X)$.

$$\begin{cases} \hat{\alpha} = \dfrac{f_\theta(\hat{\lambda}_{PN}([x]_{SR}^L)) - f_\theta(\hat{\lambda}_{BN}([x]_{SR}^L))}{f_\theta(\hat{\lambda}_{PN}([x]_{SR}^L)) - f_\theta(\hat{\lambda}_{BN}([x]_{SR}^L)) + f_\theta(\hat{\lambda}_{BP}([x]_{SR}^L)) - f_\theta(\hat{\lambda}_{PP}([x]_{SR}^L))}; \\ \hat{\beta} = \dfrac{f_\theta(\hat{\lambda}_{BN}([x]_{SR}^L)) - f_\theta(\hat{\lambda}_{NN}([x]_{SR}^L))}{f_\theta(\hat{\lambda}_{BN}([x]_{SR}^L)) - f_\theta(\hat{\lambda}_{NN}([x]_{SR}^L)) + f_\theta(\hat{\lambda}_{NP}([x]_{SR}^L)) - f_\theta(\hat{\lambda}_{BP}([x]_{SR}^L))}; \left(0 \le \hat{\beta} < \hat{\gamma} < \hat{\alpha} \le 1\right) \\ \hat{\gamma} = \dfrac{f_\theta(\hat{\lambda}_{PN}([x]_{SR}^L)) - f_\theta(\hat{\lambda}_{NN}([x]_{SR}^L))}{f_\theta(\hat{\lambda}_{PN}([x]_{SR}^L)) - f_\theta(\hat{\lambda}_{NN}([x]_{SR}^L)) + f_\theta(\hat{\lambda}_{NP}([x]_{SR}^L)) - f_\theta(\hat{\lambda}_{PP}([x]_{SR}^L))}. \end{cases} \tag{9}$$

Based on the above theory, we can get the steps of three decision-making algorithms under the new aggregation method as shown in Table 2:

Table 2. Steps of Three-way Decision Algorithm under the New Aggregation Method

Algorithm Three-way decision algorithm under incomplete information system
Input： $IIS=(U,A,V,f),\lambda_{gg}$, parameter： L、$\theta, X \in U$.
Output：Three decision rules for each $x \in U$.
Step 1: begin
Step 2: entering a given L value.
Step 3: for $x \in U$ do
Step 4: calculate $[x]_{SR}^L = \mathrm{U}_{y \in U}\{y \mid Sim(x,y) \ge L\}$, $f_\theta\left(\hat{\lambda}_{gg}[x]_{SR}^L\right)$.
Step 5: end
Step 6: entering a given θ value.
Step 7: for $x \in U$ do
Step 8: calculate the value of $f_\theta\left(\hat{\lambda}_{gg}[x]_{SR}^L\right)$.
Step 9: for each object $x \in U$, the threshold value $\hat{\alpha}$、$\hat{\beta}$ and $\hat{\gamma}$ is calculated by Equation (9).
Step 10: end
Step 11: for $x \in U$ do
Step 12: if $\Pr\left(X \mid [x]_{SR}^L\right) \ge \hat{\alpha}$, then： $x \in POS(X)$
Step 13: if $\hat{\beta} < \Pr\left(X \mid [x]_{SR}^L\right) < \hat{\alpha}$, then： $x \in BND(X)$
Step 14: else： $x \in NEG(X)$
Step 15: end
Step 16: end

Table 3. Status table

Influencing factor	**meaning**
Gross regional product (a_1)	1-highest, 2- medium, 3- low, *-missing
Permanent population (a_2)	1- many, 2- medium, 3- little, *-missing
Employed persons (a_3)	1- many, 2- medium, 3- little, *-missing
Fixed Assets Investment Construction Project (a_4)	1- many, 2- medium, 3- little, *-missing
Number of primary schools (a_5)	1- many, 2- medium, 3- little, *-missing
Number of secondary schools (a_6)	1- many, 2- medium, 3- little, *-missing

4. Case analysis

In order to verify the effectiveness of the algorithm, the data of the average price of second-hand houses in 2022 and its influencing factors were obtained through the Statistical Yearbook of Shanxi Province. Now, $A=(a_1,a_2,\mathrm{L}\ ,a_6)$ represents six influencing factors (as shown in Table 3), $TWIIS=(U,A,V,f,\lambda_{gg})$ is given to describe the situation of various influencing factors in Shanxi Province (as shown in Table 4), where $U=(x_1,x_2,\mathrm{L}\ ,x_{11})$ is eleven regions and λ_{gg} is the corresponding loss function. State set

$\Omega=\{X,\neg X\}$ represents two different states of sufficient funds and insufficient funds, and action set $A=\{a_P,a_B,a_N\}$ represents three different actions: buying a house, waiting and seeing further, and not buying a house.

Table 4. Table of influencing factors of house price

U	a_1	a_2	a_3	a_4	a_5	a_6	λ_{PP}	λ_{BP}	λ_{NP}	λ_{NN}	λ_{BN}	λ_{PN}
x_1	1	1	1	2	2	1	$[1.0,1.5u]$	$[2.5,3.5u]$	$[4.0,5.5u]$	$[1.0,2.0u]$	$[2.5,4.0u]$	$[4.5,7.0u]$
x_2	3	2	*	2	2	2	$[0.5,1.5u]$	$[2.0,3.0u]$	$[3.5,6.0u]$	$[1.0,2.0u]$	$[3.5,5.5u]$	$[6.0,7.5u]$
x_3	3	3	3	3	*	3	$[1.5,2.5u]$	$[3.5,4.5u]$	$[4.5,6.5u]$	$[0.5,2.0u]$	$[2.5,4.0u]$	$[4.5,7.5u]$
x_4	2	2	2	*	2	2	$[1.0,2.5u]$	$[2.5,3.5u]$	$[4.0,6.5u]$	$[1.0,2.0u]$	$[3.0,5.0u]$	$[5.5,7.0u]$
x_5	3	2	2	2	2	*	$[0.5,2.0u]$	$[2.0,3.5u]$	$[4.5,6.5u]$	$[1.5,2.5u]$	$[3.0,4.0u]$	$[4.5,7.0u]$
x_6	3	*	3	3	3	3	$[1.0,3.0u]$	$[3.5,5.0u]$	$[5.0,7.5u]$	$[0.5,2.0u]$	$[2.5,4.0u]$	$[4.5,6.5u]$
x_7	3	2	2	*	2	1	$[1.0,2.0u]$	$[3.0,3.5u]$	$[4.5,7.0u]$	$[0.5,1.5u]$	$[1.5,3.0u]$	$[4.5,7.5u]$
x_8	2	1	1	1	1	*	$[1.5,3.5u]$	$[3.5,5.0u]$	$[5.0,7.0u]$	$[1.5,3.0u]$	$[3.5,5.0u]$	$[6.0,7.5u]$
x_9	*	2	2	2	2	1	$[2.5,3.5u]$	$[4.0,5.0u]$	$[5.5,6.5u]$	$[1.5,2.5u]$	$[3.0,4.5u]$	$[5.0,5.5u]$
x_{10}	3	2	*	2	1	1	$[0.0,1.5u]$	$[2.0,3.5u]$	$[5.0,7.0u]$	$[0.5,2.0u]$	$[2.5,3.5u]$	$[4.5,6.5u]$
x_{11}	2	2	2	3	2	*	$[1.5,3.0u]$	$[4.0,5.5u]$	$[6.0,7.5u]$	$[0.5,2.5u]$	$[2.5,3.5u]$	$[4.0,6.0u]$

Further, according to definition 3, the similarity between any two is obtained. Let $L=0.5+\varepsilon$ (positive infinitesimal), then there are:

$$[x_1]_{SR}^L=\{x_1,x_9\},\quad [x_2]_{SR}^L=\{x_2,x_4,x_5,x_7,x_9,x_{10}\},\quad [x_4]_{SR}^L=\{x_2,x_4,x_5,x_7,x_9,x_{11}\},\quad [x_8]_{SR}^L=\{x_8\},$$
$$[x_3]_{SR}^L=[x_6]_{SR}^L=\{x_3,x_6\},\quad [x_5]_{SR}^L=\{x_2,x_4,x_5,x_7,x_9,x_{10},x_{11}\},\quad [x_7]_{SR}^L=\{x_2,x_4,x_5,x_7,x_9,x_{10},x_{11}\},$$
$$[x_9]_{SR}^L=\{x_1,x_2,x_4,x_5,x_7,x_9,x_{10},x_{11}\},\quad [x_{10}]_{SR}^L=\{x_2,x_5,x_7,x_9,x_{10}\},\quad [x_{11}]_{SR}^L=\{x_4,x_5,x_7,x_9,x_{11}\}.$$

The data we obtained for the x_3 and x_6 were similar, so they were both belong to state 3 in the table 3. Then calculate them according the definition 3, the calculation results of x_3 and x_6 are the same.

By comparing the average price of second-hand houses in 2021 and 2022, it can be concluded that the areas with rising house prices should make the strategy of buying houses, so it can be assumed that: $X=\{x_3,x_4,x_6,x_9,x_{11}\}$, for $\forall x\in U$, the respective conditional probabilities can be calculated as follows:

$$\Pr\left(X\mid[x_1]_{SR}^L\right)=0.5,\quad \Pr\left(X\mid[x_2]_{SR}^L\right)=0.4,\quad \Pr\left(X\mid[x_3]_{SR}^L\right)=1,\quad \Pr\left(X\mid[x_4]_{SR}^L\right)=0.6,$$
$$\Pr\left(X\mid[x_5]_{SR}^L\right)=0.429,\quad \Pr\left(X\mid[x_6]_{SR}^L\right)=1,\quad \Pr\left(X\mid[x_7]_{SR}^L\right)=0.429,\quad \Pr\left(X\mid[x_8]_{SR}^L\right)=0,$$
$$\Pr\left(X\mid[x_9]_{SR}^L\right)=0.375.\quad \Pr\left(X\mid[x_{10}]_{SR}^L\right)=0.2,\quad \Pr\left(X\mid[x_{11}]_{SR}^L\right)=0.6.$$

Then, according to the interval aggregation method proposed in the algorithm, the weights of each object in the similar class are calculated respectively, and the interval loss functions of all objects in the incomplete information system are aggregated according to the obtained weights to obtain the aggregated interval. In the process of converting the aggregated interval loss function into a single value, decision makers can decide to adopt three kinds of decisions: pessimistic, neutral and optimistic according to their own attitude and economic situation. In this paper, we first adopt a neutral decision, let $\theta=0.5$ be defined in the transfer function of 7, and then get the calculation results of

the single-valued loss function and three thresholds after interval conversion as shown in Table 5.

Table 5. Conversion loss function and calculation results of three parameters

U	$f_{0.5}(\hat{\lambda}_{PP})$	$f_{0.5}(\hat{\lambda}_{BP})$	$f_{0.5}(\hat{\lambda}_{NP})$	$f_{0.5}(\hat{\lambda}_{NN})$	$f_{0.5}(\hat{\lambda}_{BN})$	$f_{0.5}(\hat{\lambda}_{PN})$	$\hat{\alpha}$	$\hat{\beta}$	$\hat{\gamma}$
x_1	2.125	3.750	5.375	1.750	3.500	5.500	0.552	0.519	0.536
x_2	1.542	3.120	5.513	1.550	3.530	5.944	0.605	0.453	0.525
x_3	2.000	4.125	5.875	1.250	3.250	5.750	0.541	0.533	0.537
x_4	1.787	3.407	5.627	1.591	3.501	5.858	0.593	0.462	0.526
x_5	1.668	3.347	5.684	1.553	3.432	5.804	0.586	0.446	0.514
x_6	2.000	4.125	5.875	1.250	3.250	5.750	0.541	0.533	0.537
x_7	1.668	3.347	5.684	1.553	3.432	5.804	0.586	0.446	0.514
x_8	2.500	4.250	6.000	2.250	4.250	6.750	0.588	0.533	0.563
x_9	1.681	3.361	5.654	1.560	3.429	5.787	0.584	0.449	0.515
x_{10}	1.500	3.150	5.600	1.550	3.400	5.850	0.598	0.430	0.512
x_{11}	1.950	3.650	5.850	1.600	3.300	5.650	0.580	0.436	0.509

Under the neutral attitude, the following conclusions can be drawn:

$$\begin{cases} \{x_3, x_4, x_6, x_{11}\} \in POS(X), \\ \{x_1, x_2, x_5, x_7, x_8, x_9, x_{10}\} \in NEG(X). \end{cases}$$

Therefore, on the basis of referring to historical data, according to the rise and fall of the average price of second-hand houses in various regions, it can be known that people in $x_3, x_4, x_6, x_9, x_{11}$ regions are more likely to buy houses. Through the above-mentioned further research, it is found that residents in x_3, x_4, x_6, x_{11} regions should buy houses, and the original decision only gives people in areas with high possibility of buying houses, and no other measures are taken for people in other regions. This paper combines the interval loss function with three decision-making theories and draws the conclusion that residents in $x_1, x_2, x_5, x_7, x_8, x_9, x_{10}$ regions do not need to buy houses. Why x_9 is not in *POS(X)*, there are some reasons: Firstly, the rise and fall of house prices are influenced by many factors, and this paper only obtains six of them. Secondly, the assumption given in this paper is only based on the rise of housing prices, which has certain limitations for the decision whether to buy a house or not. Finally, by comparing the results calculated according to the method given in this paper with the assumptions, it is found that the conclusion is in line with the actual social situation. Similarly, setting different values of θ can get the calculation results under pessimistic and optimistic attitude. Take x_1, x_2, x_3 as an example, change the value of θ, and analyze the robustness of the model parameters with the step of 0.1. The specific results are shown in Table 6.

Through the robustness test of the model, it can be known that the model parameter fitting effect is good. To sum up, the value of parameter L reflects the similarity of different regions under various influencing factors, and the range of parameter θ depends on the attitude of decision makers, reflecting their risk preference for the event itself. The results obtained by changing the size of parameter L、θ are also different, which can be determined by decision makers according to the actual situation. The algorithm comprehensively considers the above two aspects, and puts forward a three-

branch decision-making method of multi-angle decision-making, which enables decision-makers to make better decisions according to their own attitudes and actual conditions.

Table 6. Robustness analysis table

	θ								
	0.1	0.2	0.3	0.4	0.5	0.6	0.7	0.8	0.9
x_1	$NEG(X)$	$NEG(X)$	$NEG(X)$	$NEG(X)$	$NEG(X)$	$NEG(X)$	$NEG(X)$	$NEG(X)$	$NEG(X)$
x_2	$NEG(X)$	$NEG(X)$	$NEG(X)$	$NEG(X)$	$NEG(X)$	$NEG(X)$	$NEG(X)$	$NEG(X)$	$NEG(X)$
x_3	$POS(X)$	$POS(X)$	$POS(X)$	$POS(X)$	$POS(X)$	$POS(X)$	$POS(X)$	$POS(X)$	$POS(X)$

5. Conclusion

In real life, the subject's understanding of the object is not achieved overnight, but a gradual process. In this process, the interaction of various types of data makes it more difficult, and the existence of missing data in incomplete information systems aggravates this situation. Therefore, it is of great significance to study the three decision-making problems in incomplete information systems. Based on the incomplete information system, this paper discusses and studies the missing data in the fuzzy information table, and combines the loss function with the three-branch decision-making, so as to propose a three-branch decision-making method based on the incomplete information system. This method mainly solves the problems of missing data in fuzzy information table and subjectivity of loss function. For missing data, it is mainly filled according to its probability and value range, and on this basis, a similarity calculation method is given, which lays the foundation for the determination of similar classes. At the same time, considering the influence of many factors on the loss function, this paper takes the interval form as a substitute, and optimizes the interval number based on the principle of reasonable granularity. The interval loss function of similar classes is defined as the aggregation of the interval loss functions of all objects in similar classes. Finally, the aggregated interval is converted into a single-valued form by a conversion function, and its effectiveness is verified by a case. Overall, this method reduces the decision risk. In the future, we will further study the three-branch decision-making problem of interval loss function under incomplete information system and its application.

Acknowledgments

This work was supported by the Natural Science Foundation of Ningxia Province (No. 2022AAC03238), the National Natural Science Foundation of China (No. 62066001), and the North Minzu University Graduate Innovation Fund Project (NO.YCX22089).

References

[1] Peng JG, Cai Y, Xia G, et al. Three-way decision theory based on interval type-2 fuzzy linguistic term sets[J]. J Intell Fuzzy Syst . 2022, Aug; 43(4): 3911-3932.

[2] Zheng YH, Xu ZS, Tian YH. Granular computing and optimization model-based method for large-scale group decision-making and its application[J]. Economic Research-Ekonomska Istraživanja, 2022, Dec; 35(1):5221-5252.

[3] Li ZW, Xie NG, Huang D, et al. A three-way decision method in a hybrid decision information system and its application in medical diagnosis[J]. Artif Intell Rev, 2020, Feb; 53(7):1-30.

[4] Childers Pamela B, McDaniel Thomas R. Celebrating the 100th Anniversary of The Clearing House: A Journal of Educational Strategies, Issues, and Ideas for Middle & High School Teachers[J]. The Clearing House: A Journal of Educational Strategies, Issues and Ideas, 2020, Jan; 93(1):2-4.

[5] Cui ZH, Li BG, Lan ZX, et al. Many-objective evolutionary algorithm based on three-way decision[J]. Egyptian Informatics Journal, 2023, Jul; 24(3):100388.
[6] Hailong Y, Huanhuan R. A three-way decision model on incomplete single-valued neutrosophic information tables[J]. J Intell Fuzzy Syst, 2023, Mar; 44(3):5179-5193.
[7] Liu DS, Tian Y, Zhang YJ, et al. Heterogeneous data fusion and loss function design for tooth point cloud segmentation[J]. Neural Computing and Applications, 2022, May; 34(20):17371-17380.
[8] Nezhad F S M, Saredorahi Z F. Designing an economically optimal repetitive group-sampling plan based on loss functions[J]. Communications in Statistics - Simulation and Computation, 2018, Mar; 47(3):783-799.
[9] Jing Tu J, Su SH. Method for three-way decisions using similarity in incomplete information systems[J]. Int J Mach Learn Cyb, 2022, Dec; 14(6):2053-2070.
[10] Zhang HT, Ma XL, Zhan JM, et al. 3WC-D: A feature distribution-based adaptive three-way clustering method[J]. Appl Intell, 2022, Nov; 53(12) : 15561-15579.
[11] Jia ZH, Qiao JS. New constructions of decision evaluation functions in three-way decision spaces based on uninorms[J]. Artif Intell Rev, 2022, Nov; 56(7):41-47.
[12] Yue X, Zhou J, Yao Y, et al. Shadowed Neighborhoods Based on Fuzzy Rough Transformation for Three-Way Classification[J]. Ieee T Fuzzy Syst, 2020, May; 28(5):978-991.
[13] Anwar S, Bahar A, Masood H, et al. An ensemble face recognition mechanism based on three-way decisions[J]. Journal of King Saud University - Computer and Information Sciences, 2023, Apr; 35(4): 196-208.
[14] Ren LH, Ye ZF, Zhao YP. Long short-term memory neural network with scoring loss function for aero-engine remaining useful life estimation[J]. Proceedings of the Institution of Mechanical Engineers, Part G: Int J Aerospace Eng, 2023, Feb; 237(3) : 547-560.
[15] Zhao F, Zhang P, Zhang R, et al. UnifiedFace: A Uniform Margin Loss Function for Face Recognition[J]. Applied Sciences, 2023, Feb; 13(4):2350.
[16] Huang JH, Zhou GJ, Yu ZF, et al. Deep parallel MRI reconstruction based on a complex-valued loss function[J]. Journal of Southern Medical University, 2022, Dec; 42(12):1755-1764.
[17] Wang YL, Wei L. Three - way decision based on improved aggregation method of interval loss function[J]. Journal of NanJing University(Natural Science) 2021, May; 57(03):493-501.
[18] Wang WJ, Zhan JM, Zhang C, et al. A regret-theory-based three-way decision method with a priori probability tolerance dominance relation in fuzzy incomplete information systems[J]. Inform Fusion, 2023, Sep; 89:382-396.
[19] Yu QQ, Li XN. Three-way decision on incomplete interval-valued information tables under L level similarity[J]. Journal of Shaanxi Normal University(Natural Science Edition), 2023, Dec; 51(1): 87-100.
[20] Yu QQ, Li XN. Three-way decision on incomplete interval-valued information tables under L level similarity[J]. Journal of Shaanxi Normal University(Natural Science Edition), 2023, Dec; 51(1): 87-100.
[21] Wang YL, Wei L. Three - way decision based on improved aggregation method of interval loss function[J]. Journal of NanJing University(Natural Science) 2021, May; 57(03):493-501.
[22] Maldonado S, Peters G, Weber R. Credit scoring using three-way decisions with probabilistic rough sets[J]. Information Sciences,2020,507.. Credit scoring using three-way decisions with probabilistic rough sets[J]. Inform Sciences, 2020, Jan; 507(C):700-714.
[23] Qiao JS, Hu BQ. On decision evaluation functions in generalized three-way decision spaces[J]. Inform Sciences, 2020, Jan; 507(C):733-754.
[24] Yu QQ, Li XN. Three-way decision on incomplete interval-valued information tables under L level similarity[J]. Journal of Shaanxi Normal University(Natural Science Edition), 2023, Dec; 51(1): 87-100.

Fuzzy Systems and Data Mining IX
A.J. Tallón-Ballesteros and R. Beltrán-Barba (Eds.)

doi:10.3233/FAIA231062

Research on Backward Cloud Transformation Algorithm Based on Adding Cloud Drops

Changlin Xu[a,b,1] and Lingzhuo Kong[a]
[a] *School of Mathematics and Information Science, North Minzu University, Yinchuan 750021, China*
[b] *The Key Laboratory of Intelligent Information and Big Data Processing of Ning Xia Province, Yinchuan 750021, China*

Abstract. As a tool for studying uncertain information, cloud model is of great significance in uncertain artificial intelligence and data mining. Among them, the backward cloud transformation method is one of the important algorithms of cloud model, which can realize the conversion from quantitative data to qualitative concepts. In this paper, a dynamic incremental backward cloud transformation algorithm is proposed to solve the problem that the estimated value of hyper entropy is imaginary when the backward cloud transformation method is used to calculate hyper entropy. First, according to the formation characteristics of cloud drops, the generated samples and the original samples are fused as new samples by dynamically and randomly generating samples, and then the hyper entropy is estimated until the estimated value of hyper entropy is real. Secondly, the stability and convergence of the algorithm proposed in this paper are analyzed through simulation experiments. The experimental results show that the new dynamic incremental backward cloud transformation algorithm solves the problem that the hyper entropy estimation value is imaginary while the estimation error is small and the stability is good. Finally, the algorithm is applied to brain CT segmentation, and the results show that the algorithm is effective and practical.

Keywords. Cloud model, Backward cloud transformation, Cloud drop, Dynamic increment, Hyper entropy

The vast majority of phenomena in the objective world are uncertain. Similarly, written language, as the most prominent manifestation of human intelligence, is also uncertain. Therefore, the study of natural language uncertainty is one of the works of AI researchers in recent years[1]. Randomness, fuzziness, incompleteness, instability and inconsistency are the main aspects of uncertainty, of which the most basic are randomness and fuzziness[2]. At present, there are many researches on uncertainty For example, probability theory[3] quantifies "randomness" with "probability" from the perspective of randomness; Fuzzy set theory[4] and rough set theory[2][5] study uncertainty from the perspective of fuzziness and incompleteness; The cloud model theory proposed by academician Li studies uncertain things from the perspective of randomness, fuzziness and the correlation between them. It realizes the quantitative expression of uncertain linguistic values and the uncertain transformation between qualitative concepts and quantitative data, and further promotes the research on

[1] Corresponding Author: School of Mathematics and Information Science, North Minzu University, Yinchuan 750021, China; E-mail: xuchlin@163.com.

uncertain problems[6]. For example, Liu Changyu and others proposed a backward cloud transformation algorithm based on cloud *X* information[8]; Yu et al. Proposed a backward cloud transformation algorithm based on normal distribution interval number[9]; Gao Pu et al. Proposed a fourth-order origin moment backward cloud transformation algorithm based on cloud distribution[10]; Xu et al. proposed a multi-step backward cloud transformation algorithm to indirectly estimate entropy and hyper entropy [7]; Chen Hao et al. proposed a backward cloud transformation algorithm based on statistical methods[11]. The algorithm expands the variance of samples by gradually deleting a limited number of samples closest to the expectation, thus solving the problem that the hyper entropy estimate does not exist, but deleting samples will cause information loss, which is unfavorable for the application of the algorithm. In this paper, a dynamic incremental backward cloud transform algorithm is proposed to solve the problem that the hyper entropy estimation does not exist. In the cloud model, normal cloud is the most important cloud model, and it has the characteristics of universality[12], so the normal cloud model is mainly studied.

1. Cloud model theory

1.1 Basic concepts

The cloud model uses three numerical characteristics to represent the connotation of a concept as a whole[13], in which the expectation *Ex* is the value that can best reflect the main information of the cloud drop distribution of the concept as a whole. Entropy *En* is the value reflecting the uncertainty of the qualitative concept, that is, the randomness and fuzziness of the concept. The greater the entropy, the greater the uncertainty of the concept, and the greater the dispersion of cloud drops. Hyper entropy *He* reflects the uncertainty of entropy, that is, the entropy of entropy The cloud model is defined as follows.

Definition 1[14] Let C be a qualitative concept on the U which is quantitative universe. If the quantitative value of $\mu(x) \in [0,1]$ is a random realization of the C, and the uncertainty of x for C as $\mu(x) \in [0,1]$ is a random number with a stable tendency, the distribution of x on the U is called a cloud, and each x is called a cloud drop.

Definition 2[15] Let C be a qualitative concept in the U which is field of quantitative theory, and C contains three numerical characteristics which are (Ex, En, He). If the $x \in U$ which is quantitative value is a random realization of the C, that is to say, it meets: $x = R_N(Ex, |y|)$, $y = R_N(En, He)$, and $\mu(x) \in [0,1]$ which is the uncertainty of x for C is a random number with stable tendency

$$\mu(x) = \exp\left\{-\frac{(x-Ex)^2}{2y^2}\right\}.$$

The distribution of all cloud drops in the universe is called normal cloud.

1.2 Existing cloud transformation algorithms

Forward cloud transformation (FCT) and backward cloud transformation (BCT) can realize the conversion between the extension and connotation of concepts. Forward

cloud transform algorithm (FCT) is shown in Algorithm 1.

The numerical characteristics of qualitative concept can be obtained from a given cloud drop by backward cloud transformation method. There are several backward cloud transformation algorithms, including the backward cloud transformation algorithm based on the first-order absolute center moment (SBCT-1stM)) using moment estimation, such as Algorithm 2.

Algorithm 1. FCT[16]

Input: (Ex, En, He) which is overall description of the digital characteristics of qualitative concept C, and the number of cloud drops generated;

Output: quantitative value of N cloud drops and $\mu(x)$ which is its uncertainty;

step1: generate a normal random number with En as the expected value and He as the mean square deviation: $En' = R_N(En, He)$.

step2: generate a normal random number with Ex as the expected value and En' as the mean square deviation: $x_i = R_N(Ex, En')$.

step3: the determination of x_i is $\mu(x_i) = \exp\left\{-\frac{(x-Ex)^2}{2(En')}\right\}$.

step4: x_i becomes a cloud drop in the universe with a degree of certainty of $\mu(x_i)$.

step5: repeat steps 1-4 until the required cloud drops are generated.

Algorithm 2. SBCT-1stM[8]

Input: N samples are $X_i (i = 1, \cdots, N)$.

Output: the estimated value of the three digital features C of the qualitative concept (Ex, En, He) represented by the sample;

step1: calculate $\overline{X} = \frac{1}{N}\sum_{i=1}^{N} X_i$ according to the given N samples X_i.

step2: $\hat{Ex} = \overline{X}$, $\hat{En} = \sqrt{\frac{\pi}{2}} \times \frac{1}{N}\sum_{i=1}^{N}\left|X_i - \hat{Ex}\right|$.

step3: calculate the variance of cloud drop sample as $S^2 = \frac{1}{N-1}\sum_{i=1}^{N}(X_i - \hat{Ex})^2$.

step4: $\hat{He} = \sqrt{S^2 - \hat{En}^2}$.

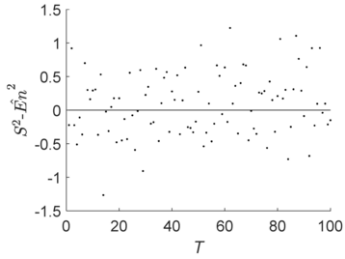

Fig. 1 Calculate $S^2 - E\hat{n}^2$ for 100 times

The calculation process of SBCT-1stM is relatively simple, but there are some limitations. Because if: $S^2 - E\hat{n}^2 < 0$ appears in step4, the value of the hyper entropy estimate $\hat{He}=\sqrt{S^2 - \hat{En}^2}$ will be an imaginary number, which means that $\hat{He}$ cannot be

obtained. For example, given that the three digital features (Ex, En, He) are $(20, 3, 0.1)$, respectively, N=10000 samples are generated by the forward cloud transformation method. In turn, these 10000 samples are used to calculate the estimated $S^2 - E\hat{n}^2$. This process is repeated T=100 times, and the samples are regenerated each time. The results are shown in Fig. 1. From the results shown in Fig. 1, it can be seen that nearly half of the experimental results have $S^2 - E\hat{n}^2 < 0$, which means that nearly half of the SBCT-1stM algorithm has failed in these 100 experiments. However, hyper entropy He is a very important digital feature to describe qualitative concepts, which affects the range and distribution of quantitative data, so it is necessary to improve the backward cloud transformation method to solve the above problems.

Based on the limitations of SBCT-1stM, Chen et al. proposed a stepwise deleted backward cloud transformation algorithm (SDBCT)[11], such as Algorithm 3.

Algorithm 3. SDBCT[11]

Input: N samples are $X_i (i = 1, \cdots, N)$;

Output: the estimated value of the three digital characteristics (Ex, En, He) of the qualitative concept C represented by the sample;

step1: calculate $\overline{X} = \frac{1}{N}\sum_{i=1}^{N} X_i$ according to the given N samples X_i.

step2: $\hat{E}x = \overline{X}$, $\hat{E}n = \sqrt{\frac{\pi}{2}} \times \frac{1}{N}\sum_{i=1}^{N}\left|X_i - \hat{E}x\right|$.

step3: calculate the variance of cloud drop sample as $S^2 = \frac{1}{N-1}\sum_{i=1}^{N}(X_i - \hat{E}x)^2$.

step4: if $S^2 - \hat{E}n^2 \geq 0$, turn to step6; otherwise, turn to step 5.

step5: delete the e = 1% sample points closest to the expected $\hat{E}x$ in the current sample: $\left(delete \sum_{j=1}^{N\times 0.01} sort\left(\left|X_i - \hat{E}x\right|\right)\right)$, $N = 0.99 \times N$, and then turn to step3.

step6: $\hat{H}e = \sqrt{S^2 - \hat{E}n^2}$.

In step5 of Algorithm 3, e is a parameter that can be adjusted according to the actual situation. According to literature[11], when the number of cloud drops meet $N < 100$, one sample point closest to the expectation is deleted each time; When the given cloud drop number meet $N \geq 100$, so $e = 0.01$. Although SDBCT algorithm solves the problem that $\hat{H}e$ in SBCT-1stM algorithm is an imaginary number, when estimating the hyper entropy He, due to the possible deletion of some samples, the estimation error is increased because the sample information cannot be fully utilized.

2. Backward Cloud Transformation Algorithm Based on Adding Cloud Drops

The backward cloud transform algorithm is similar to the process of parameter estimation[17]. If a given sample is used, the more fully the sample information is used, the smaller the estimation error is. Similarly, in the backward cloud transform, the more fully the given sample information is used, the more accurate the eigenvalue estimation will be. The SDBCT algorithm given in reference[11] is to gradually reduce the

samples on the original samples, which will lead to insufficient use of sample information and increase the estimation error. Therefore, this paper proposes a dynamic incremental backward cloud transformation algorithm (DIBCT). According to the formation characteristics of cloud drops, the cloud drops generated by the random realization of normal random variables are used as new samples, in which the normal random variables take the estimated expectation and entropy as the mean and standard deviation respectively. The generated sample and the original sample are fused as the final sample to estimate the hyper entropy until the estimated value of the hyper entropy is calculated DIBCT algorithm is shown in Algorithm 4.

In the algorithm DIBCT, when the condition $S^2 - \hat{E}n < 0$ is true, it means that the estimated value $\hat{H}e$ of the hyper entropy He will be an imaginary number. At this time, the situation will be changed by generating normal random numbers and fusing them into the original sample data until $S^2 - \hat{E}n^2 \geq 0$.

Algorithm 4. DIBCT

Input: N samples are $X_i(i = 1, \cdots, N)$;

Output: the estimated value of the three digital characteristics (Ex, En, He) of the qualitative concept C represented by the sample;

step1: calculate the sample mean $\overline{X} = \frac{1}{N}\sum_{i=1}^{N} X_i$ according to the given N samples X_i.

step2: $\hat{E}x = \overline{X}$, $\hat{E}n = \sqrt{\frac{\pi}{2}} \times \frac{1}{N}\sum_{i=1}^{N}\left|X_i - \hat{E}x\right|$.

step3: calculate the variance of cloud drop sample as $S^2 = \frac{1}{N-1}\sum_{i=1}^{N}(X_i - \hat{E}x)^2$.

step4: if $S^2 - \hat{E}n^2 \geq 0$, turn to step6; otherwise, turn to step5.

step5: generate $e \times N$ normal random numbers with $\hat{E}x$ as the expectation and $\hat{E}x$ as the variance, take them as the new sample, $N = (1+e) \times N$ and then turn to step3.

step6: $\hat{H}e = \sqrt{S^2 - \hat{E}n^2}$.

The estimation methods of expectation Ex and entropy En in DIBCT algorithm and SDBCT algorithm are the same. The difference is that compared with SDBCT algorithm, DIBCT algorithm reduces the loss of effective information, and the estimation method of hyper entropy is improved. In addition, the meaning of e in DIBCT algorithm and SDBCT algorithm is the same, they are adjustable parameters, and the change of parameter e will also change the estimation accuracy. At the same time, DIBCT algorithm is easy to be extended to high-dimensional cases.

3. Experimental comparative analysis

In order to illustrate the effectiveness of DIBCT algorithm for the estimation of hyper entropy He, SDBCT algorithm and DIBCT algorithm are used to compare and analyze the estimation of hyper entropy He, and the following simulation experiments are carried out.

3.1 Algorithm performance analysis

Firstly, given the three numerical characteristics of qualitative concepts as $(20,3,0.1)$, the forward cloud transformation method 1 is used to generate samples with sample size of $N=10000$. Then for these 10000 samples, the SDBCT algorithm and DIBCT algorithm are used to estimate the hyper entropy He, where e is 0.01 The above experiments are repeated $T=20$ times. Finally, the experimental results are shown in Table 1 and Fig. 2 respectively. The estimated mean $\text{Mean}(\hat{He})$ and mean square error $\text{MSE}(\hat{He})$ of these 20 times are calculated. The specific formula is as follows:

$$\text{Mean}(\hat{He})=\sum_{i=1}^{T}\hat{He}_i \Big/ T, \quad \text{MSE}(\hat{He})=\sum_{i=1}^{T}(\hat{He}_i-He)^2 \Big/ T.$$

As shown in Table 1 and Fig. 2, when the hyper entropy is given as $He=0.1$, the mean values of the estimated values of the hyper entropy He repeated 20 times by SDBCT and DIBCT are 0.2008 and 0.1351 respectively, and the mean square errors are 0.0162 and 0.0067 respectively. Because the algorithm SDBCT will delete some valid samples, the estimated value $\hat{He}$ of the hyper entropy He is greater than the true value 0.1 in most cases, while the estimated value $\hat{He}$ of the DIBCT algorithm in this paper fluctuates around the true value 0.1. From the mean $\text{Mean}(\hat{He})$ and mean square error $\text{MSE}(\hat{He})$ of the estimated value $\hat{He}$ of the hyper entropy He, it can also be seen that the mean $\text{Mean}(\hat{He})$ of the DIBCT algorithm in this paper is closer to the true value 0.1 than that of the SDBCT algorithm, and the mean square error $\text{Mean}(\hat{He})$ is much smaller than that of the SDBCT algorithm. This shows that the algorithm DIBCT in this paper is more accurate in estimating the hyper entropy He.

Table 1. $\text{Mean}(\hat{He})$ and $\text{MSE}(\hat{He})$

Mean and Mse	SDBCT	DIBCT
$\text{Mean}(\hat{He})$	0.2008	**0.1351**
$\text{MSE}(\hat{He})$	0.0162	**0.0067**

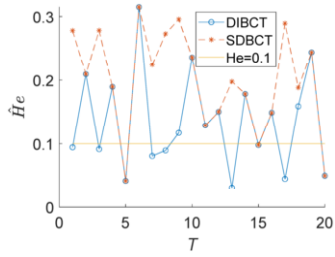

Fig. 2 Hyper entropy estimate

3.2 Stability and convergence analysis of the algorithm

Firstly, the three numerical characteristics of qualitative concepts are given as $(20,3,0.1)$, and then the random samples with sample size of N=1000,2000,$\cdots$, 10000 are obtained by using the forward cloud transformation method 1. Then for different sample sizes N, the hyper entropy He is estimated by SDBCT and DIBCT respectively, where e is 0.01. The above experiment is repeated $T=100$ times, and the estimated mean $\text{Mean}(\hat{He})$ and mean square error $\text{MSE}(\hat{He})$ of the 100 times are calculated respectively by using the two backward cloud transform algorithms. The experimental results are shown in Table 2 and Fig.3 and Fig. 4 respectively.

Table 2. Mean($\hat{He}$) and MSE($\hat{He}$) under different sample sizes

Cloud drop number	SDBCT	DIBCT	SDBCT	DIBCT
	MSE($\hat{He}$)		Mean($\hat{He}$)	
1000	0.0419	**0.0349**	0.2621	**0.2094**
2000	0.0304	**0.0235**	0.2479	**0.1868**
3000	0.0246	**0.0108**	0.2300	**0.1696**
4000	0.0284	**0.0206**	0.2422	**0.1755**
5000	0.0219	**0.0151**	0.2266	**0.1548**
6000	0.0184	**0.0127**	0.2139	**0.1576**
7000	0.0207	**0.0144**	0.2205	**0.1704**
8000	0.0209	**0.0119**	0.2177	**0.1407**
9000	0.0180	**0.0113**	0.2083	**0.1478**
10000	0.0206	**0.0110**	0.2219	**0.1435**

On the one hand, it can be seen from table 2 that under different sample sizes, the mean square error MSE($\hat{He}$) of the DIBCT algorithm for the estimation of hyper entropy He is smaller than that of the SDBCT algorithm, and the mean Mean($\hat{He}$) is closer to the true value of 0.1. This shows that the estimation result of DIBCT algorithm is more accurate and effective. On the other hand, with the increase of sample size, as shown in Table 2 and Fig. 3, the estimated value $\hat{He}$ of hyper entropy He by DIBCT algorithm is accurate from 0.2094 to 0.1435, and the estimated value is getting closer and closer to the real value of 0.1; As shown in Table 2 and Fig. 4, the mean square error MSE($\hat{He}$) of the estimated value $\hat{He}$ of hyper entropy He by DIBCT algorithm converges from 0.0349 to 0.0110, and the mean square error MSE($\hat{He}$) tends to zero faster than SDBCT algorithm. This shows that the estimation of hyper entropy He by DIBCT algorithm is more stable and convergent.

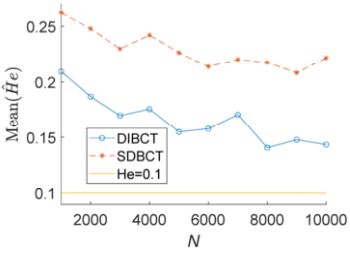

Fig. 3 Mean($\hat{He}$) under different sample sizes

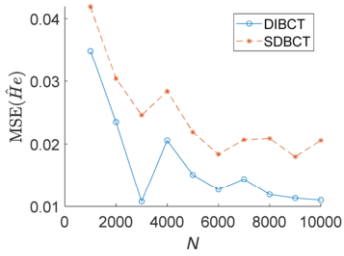

Fig. 4 MSE($\hat{He}$) under different sample sizes

3.3 Analysis of the influence of parameter E on the algorithm

The three numerical characteristics of a given qualitative concept are $Ex = 20, En = 3$, $He = 0.1$、0.3, the sample size is N=1000 . 1000 samples are generated from forward cloud transformation. Then, for these 1000 samples, DBCT algorithm and DIBCT algorithm are used to estimate the hyper entropy He, where the parameter e increases from 0.01 to 0.09 in steps of 0.02. The above experiment is repeated $T = 50$ times, and then the mean square error MSE($\hat{He}$) of the 50 estimated values is calculated respectively for the two backward cloud transform algorithms. The experimental results are shown in Table 3, Fig. 5 and Fig. 6.

Table 3. MSE($\hat{He}$) changes under different e

e	$He = 0.1$		$He = 0.3$	
	SDBCT	**DIBCT**	**SDBCT**	**DIBCT**
0.01	0.0233	**0.0212**	0.0200	**0.0327**
0.03	0.0423	**0.0180**	0.0235	**0.0211**
0.05	0.0798	**0.0257**	0.0426	**0.0297**
0.07	0.1068	**0.0223**	0.0758	**0.0285**
0.09	0.1594	**0.0217**	0.1320	**0.0217**

From the results shown in Fig. 5 and Fig. 6, it can be seen that whether the hyper entropy He is taken as 0.1 or 0.3, with the increase of parameter e, the mean square error MSE($\hat{He}$) of SDBCT algorithm for hyper entropy He estimation is also increasing (when $He = 0.1$, it increases from 0.0233 to 0.1594; when $He = 0.3$, it increases from 0.02 to 0.0217), with poor stability; However, for DIBCT algorithm, the mean square error MSE($\hat{He}$) of hyper entropy estimation is basically stable for He regardless of the change of parameter e (when $He = 0.1$, it is stable at around 0.02; when $He = 0.3$, it is stable at around 0.025). It can be seen that the algorithm SDBCT is sensitive to the change of parameter e. This further shows that the DIBCT algorithm presented in this paper has good adaptability. At the same time, it also shows that the information loss of effective samples caused by the SDBCT algorithm in deleting samples will affect the estimation efficiency, which is well overcome in the DIBCT algorithm in this paper.

3.4 Analysis of the influence of hyper entropy He change on the algorithm

The three numerical characteristics of a given qualitative concept are that $Ex = 20, En = 3$, He increases from 0.05 to 0.1 in steps of 0.02, and the sample size is N=1000 . N samples are generated by using the forward cloud transformation conversion method 1. Then for these 1000 samples, SDBCT and DIBCT are used to estimate the hyper He entropy respectively, including $e = 0.01$、0.03 . The above experiment is repeated $T = 50$ times, and then the mean square error of these 50 estimates is calculated for the two backward cloud transform algorithms. The experimental results are shown in Fig. 7 and Fig. 8 respectively.

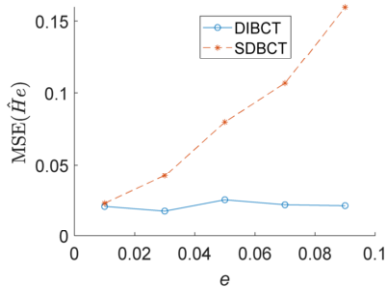

Fig. 5 MSE($\hat{He}$) under different e ($He = 0.1$)

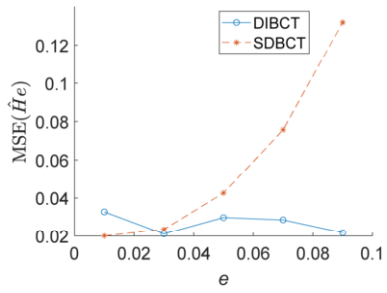

Fig. 6 MSE($\hat{He}$) under different e ($He = 0.3$)

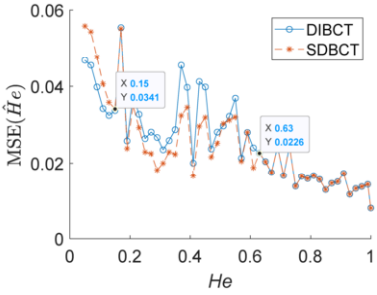

Fig. 7 MSE($\hat{He}$) under different hyper entropy($e = 0.01$)

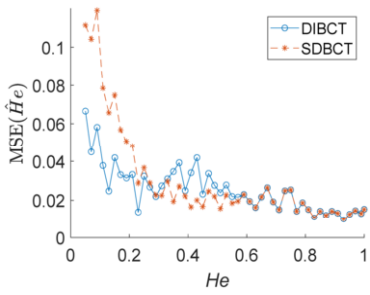

Fig. 8 MSE($\hat{He}$) under different hyper entropy($e = 0.03$)

It can be seen that if $e = 0.01$, as shown in Fig. 7, when $He \le 0.15$, the mean square error MSE($\hat{He}$) of the estimation of hyper entropy He by the algorithm DIBCT is smaller than that by the algorithm SDBCT; If $e = 0.03$, as shown in Fig. 8, when $He \le 0.29$, the mean square error MSE($\hat{He}$) of the estimation of hyper entropy He by the algorithm DIBCT is smaller than that by the algorithm SDBCT. In addition, regardless of the value of e, when the hyper entropy He is large (for example, He is greater than 0.6), the mean square error MSE($\hat{He}$) of the two algorithms for the estimation of hyper entropy He is almost the same. This shows that the estimation of DIBCT is more accurate, especially when the hyper entropy He is small.

4. Application examples

In this section, the cloud model will be used for brain CT image segmentation, which provides a new idea for the development of brain medical image segmentation. First, the Laplace operator is used to convolute the brain CT image as shown in Fig. 9. The convoluted image is shown in Fig. 10, which makes preparations for further segmentation. Then, the gradient histogram of brain CT is transformed into discrete qualitative cloud concept by cloud transformation. The gradient information shows the gray difference between the internal and edge information of the image. The intersection of the expected curve of the cloud model is used as the threshold for the next region growth segmentation. The regional growth method is carried out by using MATLAB. After the regional growth, there will be many small areas due to over segmentation. In order to merge these regions, the dynamic incremental backward cloud generator proposed in this paper is used to qualitatively represent the gray value of each region, then calculate the distance between each region and each field, and re assign the gray value. So far, the segmentation of brain CT is completed, and the segmentation results are shown in Fig. 11 and Fig. 12.

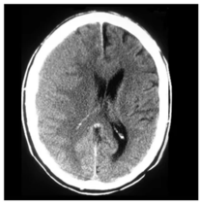

Fig. 9 brain CT to be segmented

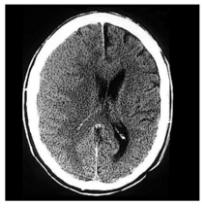

Fig. 10 brain CT after convolution

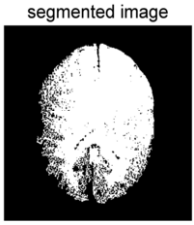

Fig. 11 brain CT before and after segmentation 1

Fig. 12 brain CT before and after segmentation 2

5. Brief summary

Inspired by the algorithm SDBCT, this paper proposes a backward cloud transformation algorithm DIBCT with cloud droplets based on the classical first-order absolute central moment backward cloud transformation algorithm. The algorithm DIBCT corrects the problem that the estimated value of hyper entropy *He* is an imaginary number. The proposed algorithm DIBCT is compared with existing algorithms in four aspects through random simulation experiments. The experimental results show that the error of parameter estimation of the algorithm DIBCT is small, and it has good stability, convergence and adaptability to parameters. Finally, the proposed algorithm is applied to brain CT image segmentation in medicine, and the results show that the algorithm is effective and practical. In addition, the theoretical mechanism of why $S^2 - E\hat{n}^2 < 0$ appears in the backward cloud transformation method SBCT-1stM will be the focus of the next step.

Acknowledgments

This work was supported by the National Natural Science Foundation of China (No. 62066001), the Natural Science Foundation of Ningxia Province (No. 2023AAC05046), and the Ningxia Higher Education First-class Discipline Construction Project (NO. NXYLXK2017B09).

References

[1] Li D Y, Liu C Y, Du Y, Han X. Uncertainty AI [J]. Journal of Software, 2004 (11): 1583-1594.
[2] Wang G Y, Miao D Q, Wu W Z, et al. Rough set representation and processing of uncertain information [J]. Journal of Chongqing University of Posts and Telecommunications (Natural Science Edition), 2010,22 (05): 541-544+550.
[3] Wang Z K, Foundations and Applications of the Probability Theo-ry. 3rd Edition. Beijing, China: Beijing Normal University Press, 1996.
[4] Zadeh L A. Fuzzy Sets. Information and Control, 1965, 8(3): 338-353.
[5] Pawlak Z. Rough Sets. International Journal of Computer and Information Sciences, 1982, 11(5): 341-356.
[6] Chen H, Li B. Uncertainty Reasoning Method Based on Cloud Model [J]. Miniature Microcomputer System, 2011, 32 (12): 2449-2455.
[7] Xu C L, Wang G Y. Backward cloud transformation algorithm for achieving stable two-way cognitive mapping [J]. Pattern recognition and artificial intelligence, 2013, 26(07): 634-642.

[8] Liu C Y, F M, D XJ, Li D Y. A new backward cloud algorithm based on cloud X information [J]. Journal of System Simulation, 2004 (11): 2417-2420.
[9] Yu S W, Shi Z K. A new backward cloud algorithm based on normal distribution interval number [J]. System Engineering Theory and Practice, 2011, 31 (10): 2021-2026.
[10] Gao P, Wang Y J, Li Z G, et al. A new algorithm for uncertainty backward cloud model [J]. Computer Application Research, 2013,30 (08): 2262-2265.
[11] Chen H, Li B, Liu C Y. An uncertain backward cloud algorithm[J]. Miniature Microcomputer System, 2015, 36(03): 544-549.
[12] Li D Y, Liu C Y. On the universality of normal cloud model [J]. China Engineering Science, 2004 (08): 28-34.
[13] Li D Y, Du Y. Artificial Intelligence with Uncertainty. London, UK: Chapman and Hall /CRC, 2007.
[14] Li D Y, Liu C Y, Gan W Y. A new cognitive model: cloud model[J]. Int. J. of Intelligent Systems, 2009, 24(3):357-375.
[15] Yang J, Wang G Y, Liu Q, et al. Review and prospect of normal cloud model research [J]. Journal of Computer Science, 2018,41 (03): 724-744.
[16] Li D Y, Meng H J, Shi X M. Subordinate Cloud and Subordinate Cloud Generator [J]. Computer Research and Development, 1995 (06): 15-20.
[17] Gao Y , Lv W Y, Wang L L, et al. Research on cloud model parameter estimation based on Bayesian theory [J]. Statistics and Decision, 2019, 35 (06): 5-8.

Fuzzy Systems and Data Mining IX
A.J. Tallón-Ballesteros and R. Beltrán-Barba (Eds.)

doi:10.3233/FAIA231063

The Similarity Measurement of Normal Cloud Concept Based on Hellinger Distance and Expectation Curve with Entropy

Changlin XU [a,b,1] , Kuan WANG [a]
[a] *School of Mathematics and Information Science, North Minzu University, Yinchuan 750021,China*
[b] *The Key Laboratory of Intelligent Information and Big Data Processing of Ningxia Province, North Minzu University, Yinchuan, Ningxia 750021,China*

Abstract. Uncertainty exists widely in nature and human society. The handling and analysis of these uncertain phenomena have long been a focal point of research in natural sciences, representing a hot and crucial topic. The cloud model uses three numerical characteristics to realize qualitative and quantitative transformation of uncertain knowledge. Normal cloud is one of the more important and common cloud models. The similarity measurement of cloud model is used to judge the similarity of two cloud concepts, and the purpose is to understand the correlation between different cloud concepts, so as to improve the efficiency of classification and clustering. As a deformation extension of f divergence, Hellinger distance has good properties and is suitable for describing the difference between two probability distributions. HECMk and HCCMk algorithms are proposed by combining Hellinger distance and expectation curve cluster with entropy. Compared with previous algorithms, these two algorithms have higher distinguishing ability. Among them, HCCMk algorithm has better comprehensive performance and is feasible in actual similarity measurement.

Keywords. normal cloud，similarity measure，Hellinger distance，expectation curve cluster with entropy

1. Introduction

Uncertainty exists widely in nature and human society. How to deal with and analyze these uncertain things has been widely concerned by natural science research. To address the existence of fuzziness and randomness, the theory of probability and fuzzy mathematics are often combined. Using three numerical characteristics to quantitatively describe a qualitative concept, Li [1] proposed a mathematical model for qualitative and quantitative transformation of uncertain knowledge using cloud model. Normal cloud is one of the most important and commonly used cloud models, as many real-world phenomena approximate normal distribution, and it has good mathematical properties.

Similarity measurement is used to judge the degree of similarity between two research objects. In practical applications, cloud models often need to compare and

[1] Corresponding Author: School of Mathematics and Information Science, North Minzu University, Yinchuan 750021,China; E-mail: xuchlin@163.com.

classify different cloud concepts in order to understand the correlation between different cloud concepts, so as to improve efficiency in classification and clustering. Therefore, constructing an effective similarity measurement method can not only reduce the computational complexity, but also improve the running efficiency of the cloud model.

There are many methods to measure normal cloud similarity. Zhang [2] proposed to use the included Angle cosine method to obtain the similarity measure of cloud concept, which has a good feature of low computational complexity. However, the differentiation ability of this method becomes weak. Li [3] proposed that the similarity is constructed by the area of the overlapping part of the expected curve of the cloud concept, which has strong differentiation ability, but the calculation complexity is high, and the influence of the cloud model hyper entropy is not considered. Wang [4] proposed a comprehensive similarity calculation framework, which combined the numerical characteristics and shape similarity calculation formulas of the cloud model, but also resulted in high computational complexity. Xu [5] proposed using Hellinger distance to calculate the similarity between cloud concepts, and using expectation curve, Internal and external envelope curves to measure the distance between normal cloud concepts. F-divergence is a function widely used in probability statistics to measure the difference of probability distribution. Hellinger distance is the deformation extension of such divergence, which has good properties and can be used to describe the difference between two probability distributions. However, the expectation curve, Internal and external envelope curves are only a few special cases of the expected curve with entropy, and there is no general study. the influence of hyper entropy is not taken into account when calculating the similarity of expected curve.

2. Normal Cloud Concept and Similarity

2.1. Cloud Model and Normal Cloud

Let U be a quantitative discourse domain represented by an exact number, and A is a qualitative concept on U. If the quantitative value $x \in U$, and x is a one-time random implementation of the qualitative concept A, and the certainty of x to A $\mu_A(x) \in [0,1]$ is a random number with stable tendency, then the distribution of $(x, \mu_A(x))$ on the discourse domain U is called a cloud, and each $(x, \mu_A(x))$ is called a cloud droplet [6].

The numerical characteristics of the cloud are represented by three parameters (Ex, En, He) , called the cloud model (Ex, En, He) . Ex is the expectation of the cloud model, which describes the expected value of the spatial distribution of cloud droplets in the discourse domain, represents the central position of qualitative concepts, and reflects the basic metric value of a certain concept. En is the entropy of the cloud model, which describes the span of the cloud, represents the acceptance range of a qualitative concept, and reflects the fuzziness and randomness of the concept. He is the hyper entropy of the cloud model, which is the entropy of entropy. It describes the thickness of the cloud and reflects the uncertainty of entropy [7,8].

Definition 2.1([1]) If the random variable x satisfies: $x \sim N(Ex, En'^2)$, where $En' \sim N(En, He^2)$ the certainty of the qualitative concept A satisfies:

$$\mu_A(x) = e^{-\frac{(x-Ex)^2}{2En'^2}}, \tag{1}$$

then the distribution of x over the domain U is called a normal cloud, where En' is a normal random number with En as the expectation and He as the standard deviation. Normal cloud mainly realizes the mutual conversion between qualitative concepts and quantitative values through normal cloud transformation, in which the forward normal cloud transformation converts the numerical characteristics $C(Ex, En, He)$, which represents the connotation of concepts, into quantitative values.

2.2. Expectation Curves with Entropy of Normal Cloud

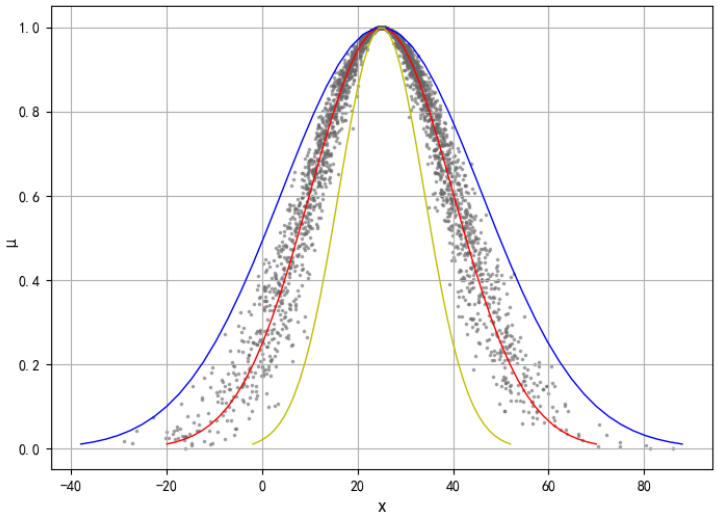

Figure 1. Graph of expectation curve with entropy for the normal cloud model

Definition 2.2([9]) If cloud droplet x is satisfied $x \sim N(Ex, En'^2)$, $En \neq 0$ and $En' \sim N(En, He^2)$, then

$$y_k = \exp[-(x-Ex)^2 / (2(En+kHe)^2)], \tag{2}$$

is a cluster of expected curves with entropy for cloud (Ex, En, He). Where k is an adjustable parameter, and the conventional value range is [-3, 3]. If $k=0$, the curve degenerates into the expected curve of the cloud mode $y = \exp[-(x-Ex)^2 / (2En^2)]$. The inner envelope curve and the outer envelope curve are two cases of $k=-3$ and $k=3$, respectively. According to the 3σ rule, almost all cloud droplets are between the inner envelope curve and the outer envelope curve, and fluctuate around the expected curve. Therefore, the geometric characteristics of the cloud can be directly reflected through the entropy expected curve cluster of the cloud model [10,11].

2.3. Normalization of Expectation Curves with Entropy

According to literature [12], there is no analytic solution to the probability density of second-order normal clouds, so the analytic expression of distance cannot be obtained directly by using the probability density. The normal cloud can also be characterized by the feature curve, and the geometric properties of the original cloud concept will not be changed when the feature curve is scaled according to its uncertainty characteristics (entropy and hyper entropy), so the entropy expected curve cluster of the normal cloud

is used to calculate the distance. First, the characteristic curves are normalized by the corresponding coefficients respectively, and the general formula of the expectation curve cluster with entropy is obtained:

$$p_k(x) = \frac{1}{\sqrt{2\pi}\left|En + kHe\right|} \exp\left\{-\frac{(x-Ex)^2}{2(En + k\cdot He)^2}\right\}, \tag{3}$$

the value range of k is [-3, 3]. The Hellinger distance of the expected curve with entropy under different k values can be obtained easily by this general formula.

2.4. The Hellinger Distance between Two Normal Distributions

Hellinger distance is a measure of the amount of overlap between two statistical samples or populations. In probability statistical theory, Hellinger distance is often used to measure the similarity of two probability distributions [13].

Definition 2.3([5]) For two normal distributions $P \sim N(\mu_1, \sigma_1^2)$ and $Q \sim N(\mu_2, \sigma_2^2)$, their Hellinger distance is :

$$D_H(P,Q) = \sqrt{1 - \sqrt{\frac{2\sigma_1 \cdot \sigma_2}{\sigma_1^2 + \sigma_2^2}} \cdot \exp\left\{-\frac{(\mu_1 - \mu_2)^2}{4(\sigma_1^2 + \sigma_2^2)}\right\}}, \tag{4}$$

it can be seen from the above that for any two normal distributions, the Hellinger distance can be converted into an algebraic operation of expectation and variance without the need for integral operation, which will greatly reduce the computational complexity.

3. Similarity Algorithm Based on Hellinger Distance and Expected Curve Clusters with Entropy

3.1. Similarity of Expected Curves with Entropy at Hellinger Distance

Definition 3.1 Suppose U is a quantitative theoretical domain represented by an exact numerical value, $C_1(Ex_1, En_1, He_1)$ and $C_2(Ex_2, En_2, He_2)$ are two normal cloud concepts on U, then the Hellinger distance based on the expectation curve cluster with entropy is:

$$D_{Hk}(C_1, C_2) = \sqrt{1 - \sqrt{\frac{2\sigma_1 \cdot \sigma_2}{\sigma_1^2 + \sigma_2^2}} \cdot \exp\left\{-\frac{(Ex_1 - Ex_2)^2}{4(\sigma_1^2 + \sigma_2^2)}\right\}}, \tag{5}$$

where $\sigma_1 = \left|En_1 + kHe_1\right|$, $\sigma_2 = \left|En_2 + k\cdot He_2\right|$, $k \in [-3,3]$ further according to the transformation relationship between distance and similarity, the similarity measure of the second order normal cloud concept can be obtained. It can be seen from the above that the value range of Hellinger distance is between [0, 1], and in the calculation, the distance often approaches 1, which makes the similarity basically 0, which makes it difficult to compare the similarity difference between different concepts. Therefore, the similarity measurement based on the expected curve cluster containing entropy is as follows:

$$Sim_{Hk}(C_1, C_2) = 1 - D_{Hk}(C_1, C_2)^2, \tag{6}$$

the similarity measure satisfies the following properties, here, the similarity is simply referred to as $Sim_H(C_1, C_2)$:

(1) $Sim_H(C_1, C_2) = Sim_H(C_2, C_1)$,

(2) $0 < Sim_H(C_1, C_2) < 1$,

(3) when $C_1 = C_2$, $Sim_H(C_1, C_2) = 1$.

Proof :(1) $Sim_H(C_1, C_2) = 1 - D_H(C_1, C_2)^2 = 1 - D_H(C_2, C_1)^2 = Sim_H(C_2, C_1)$.

(2) Since $0 \le 2\sigma_1 \cdot \sigma_2 / (\sigma_1^2 + \sigma_1^2) \le 1$ where $(\sigma_1 > 0, \sigma_2 > 0)$,and when $x \in [0, +\infty)$, exponential function $0 < e^{-x} \le 1$,there is $0 \le D_{Hk}(C_1, C_2) \le 1$. Therefore the similarity is satisfied $0 < Sim_H(C_1, C_2) \le 1$.

(3) $Ex_1 = Ex_2$, $\sigma_1 = \sigma_2$ is satisfied if and only if $C_1 = C_2$,in which case $D_{Hk}(C_1, C_2) = 0$, there is $Sim_H(C_1, C_2) = 1$.

3.2. Similarity Algorithm

Based on the above theory, different values of *k* are set to obtain the similarity of the expected curve clusters containing entropy, and the similarity of the combination is calculated by weighted summation, which reflects the distribution characteristics of the whole cloud concept. Based on this, the following similarity algorithm is designed:

Algorithm 1: HECMk algorithm

Input: numerical characteristics $C_1(Ex_1, En_1, He_1)$, $C_2(Ex_2, En_2, He_2)$ and distance *k* value.

Output: similarity: $Sim_{HECMk}(C_1, C_2)$.

(1) Calculate the expected curve with entropy based on Hellinger distance $D_H(C_1, C_2)$ at corresponding *k* value.

(2) Computational similarity: $Sim_{HECMk}(C_1, C_2) = 1 - D_H(C_1, C_2)^2$.

Algorithm 2: HCCMk algorithm

Input: numerical characteristics $C_1(Ex_1, En_1, He_1)$, $C_2(Ex_2, En_2, He_2)$ and distance *k* value.

Output: similarity $Sim_{HCCMk}(C_1, C_2)$.

(1) For different *k* values, the Hellinger distance $D_{Hk}(C_1, C_2)$ of the expected curve with entropy is calculated respectively, where the value of *k* is between [-*t*, *t*], $t \in [0, 3]$, and:

$$D_{HCCMk}(C_1, C_2) = \frac{1}{2t}\int_{-t}^{t}(C_1, C_2)dk . \tag{7}$$

(2) Computational similarity $Sim_{HCCMk}(C_1, C_2) = 1 - D_{HCCMk}(C_1, C_2)^2$.

These two algorithms retain the good properties of Hellinger distance, and fully consider the numerical characteristics of the cloud model. At the same time, through the derivation of the formula, it can be seen that they have less computational complexity. In addition, on the basis of calculating the Hellinger distance of the expectation curve cluster with entropy, the HCCMk algorithm finally obtains the similarity by weighted average, fully considering the randomness of the cloud concept caused by hyper entropy *He* in the cloud model, and can also measure the similarity between cloud concepts from a geometric point of view, which has a better comprehensiveness.

4. The Similarity Measurement of Normal Cloud Concept Based on Hellinger Distance and Expectation Curve with Entropy

4.1. Discriminative Ability of Cloud Concepts

For cloud concepts, if they belong to the same category, the distance will be smaller and the similarity will be higher. If they do not belong to the same class, then the distance will be greater and the similarity will be smaller [14]. The difference degree is used to measure the effective differentiation ability of different algorithms.

Definition 4.1 The difference degree of cloud concept C_i is defined as:

$$\delta_{C_i} = \sum_{s,t} \left| Sim(C_i, C_s) - Sim(C_i, C_t) \right| , \tag{8}$$

C_s represents a cloud concept of the same class as C_i, and C_t represents a cloud concept of a different class from C_i.

4.2. The Selection of k Value

This method mainly studies the feasibility and differentiation ability of HECMk and HCCMk algorithms. Four classical normal cloud concepts given in literature [2, 3] are used for numerical simulation experiments, and compared with LICM, ECM, MCM and PDCM algorithms. The four normal cloud concepts are: $C_1(1.5, 0.62666, 0.339)$, $C_2(4.6, 0.60159, 0.30862)$, $C_3(4.4, 0.75199, 0.27676)$ and $C_4(1.6, 0.60159, 0.30862)$, the corresponding cloud model diagram is shown in the Figure 2.

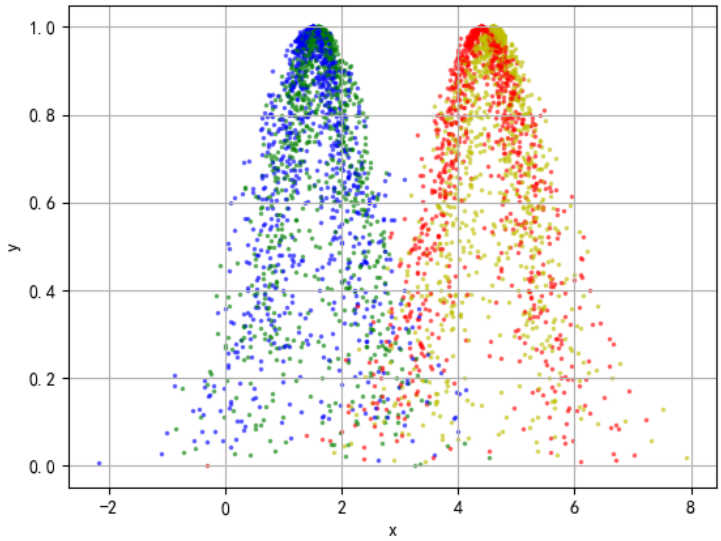

Figure 2. Cloud concept distribution map

The *k* value is [-3, 3], but only part of the value may be more appropriate in practice. Therefore, the experiment first takes a rough value to find out the *k* value with better results, and then takes a fine value to study the similarity measurement capability of expectation curve with entropy of the cloud model under this interval. First of all, in the experiment, the *k* value is [-3, 3], and the step length is 0.25. 25 values are roughly selected and substituted into the algorithm, and the results are shown in the Table 1.

Combined with the results of the comparison algorithm, the results obtained by HECMk algorithm for different k values are all similar to C_1 and C_4, C_2 and C_3, and similarity is $Sim(C_1, C_4) = Sim(C_2, C_3)$. In the experiment, with the change of k value, En and $-k \cdot He$ will be very close to each other, and then the similarity will be close to 0. Such results will be regarded as outliers in the experiment.

Table 1. Cloud concept similarity of HECMk algorithm under different k values

k value	$Sim(C_1, C_2)$	$Sim(C_1, C_3)$	$Sim(C_1, C_4)$	$Sim(C_2, C_3)$	$Sim(C_2, C_4)$	$Sim(C_3, C_4)$
-3	0.0001	0.0000	0.9819	0.6174	0.0000	0.0000
…	…	…	…	…	…	…
-1.75	0.0000	0.0000	0.0000	0.0000	0.0000	0.0000
-1.5	0.0000	0.0000	**0.9215**	**0.7781**	0.0000	0.0000
-1.25	0.0000	0.0000	**0.9710**	**0.8684**	0.0000	0.0001
-1	0.0000	0.0010	**0.9852**	**0.9154**	0.0000	0.0018
-0.75	0.0002	0.0077	**0.9910**	**0.9423**	0.0003	0.0105
-0.5	0.0028	0.0270	**0.9938**	**0.9589**	0.0036	0.0326
-0.25	0.0146	0.0620	**0.9953**	**0.9698**	0.0167	0.0699
0	0.0414	0.1105	**0.9963**	**0.9771**	0.0447	0.1193
0.25	0.0833	0.1676	**0.9969**	**0.9823**	0.0870	0.1763
0.5	0.1361	0.2284	**0.9973**	**0.9861**	0.1396	0.2361
0.75	0.1949	0.2891	**0.9975**	**0.9889**	0.1977	0.2956
1	0.2553	0.3475	**0.9977**	**0.9910**	0.2572	0.3526
1.25	0.3144	0.4021	**0.9978**	**0.9926**	0.3154	0.4059
…	…	…	…	…	…	…
3	0.6197	0.6675	0.9982	0.9976	0.6174	0.6666

As can be seen from Table 1, the similarity distribution may have certain rules. In order to find a more suitable k value, the similarity results were continued to be substituted into formula 7 to calculate the difference degrees of the four cloud concepts under different k values, and the results were drawn into a line chart to obtain the results as shown in Figure 3.

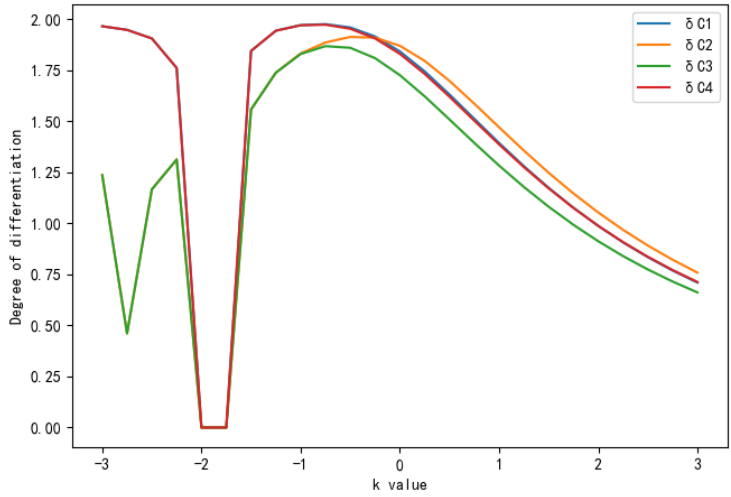

Figure 3. Difference degree curve of HECMk algorithm

The difference degree of HECMk algorithm under different k values is calculated, and the obtained results are drawn into a line chart to get the results as shown in the Figure 3. There are outliers of similarity in the above experiments, so 0 value also appears in the difference degree result Figure 3. It can be seen from the table that the difference degree curve as a whole approximately follows a normal distribution without considering the outliers. Therefore, we strive for the principle of symmetry, take a relatively stable interval, and find that the cluster of entropy-containing expected curves with k value between [-1,1] is better distinguished.

4.3. Distinguishing Ability of HECMk Algorithm and HCCMk Algorithm

In order to further study the expectation curve with entropy, the k value is again selected as [-1,1], and the value is taken as a step of 0.1. 21 values are selected to calculate the similarity of expectation curve with entropy. By changing the k value, a more refined cluster of expected curves containing entropy is obtained, and the corresponding difference degree is calculated according to the obtained similarity results. The results are shown in the Table 2

Table 2. Cloud concept difference degree of HECMk algorithm with different k values

k value	δ_{C_1}	δ_{C_2}	δ_{C_3}	δ_{C_4}
-1	1.9694	1.8307	1.8279	1.9686
-0.9	1.9735	1.8556	1.8491	1.9721
…	…	…	…	…
-0.1	1.8733	1.8886	1.7608	1.8619
0	1.8406	1.8682	1.7244	1.8285
0.1	1.8040	1.8423	1.6847	1.7915
…	…	…	…	…
1	1.4961	1.5724	1.3975	1.4872

Meanwhile, ECM, MCM, PDCM has the same result as HECMk algorithm, while the results of LICM show that the similarity of the four clouds is close, all above 0.95.

Table 3. Cloud concept similarity under different contrast algorithms

Similarity	$Sim(C_1,C_2)$	$Sim(C_1,C_3)$	$Sim(C_1,C_4)$	$Sim(C_2,C_3)$	$Sim(C_2,C_4)$	$Sim(C_3,C_4)$
LICM	0.9561	0.9648	**0.9990**	**0.9992**	0.9679	0.9755
ECM	0.0116	0.0356	**0.9370**	**0.8868**	0.0127	0.0389
MCM	0.3286	0.3688	**0.9714**	**0.9504**	0.3261	0.3680
PDCM	0.0110	0.0306	**0.8858**	**0.8000**	0.0126	0.0319
HCCMk	**0.0698**	**0.1275**	**0.9951**	**0.9714**	**0.0719**	**0.1339**

As can be seen from the Table 2, for the four cloud concepts, HECM has a high concept difference degree under different values, which can better highlight the difference degree among cloud concepts, indicating that the algorithm has a good differentiation ability. In combination with the Table 3, it can be seen that in the cloud concept difference degree results of the comparison algorithm, the concept difference degree of LICM is less than 0.8, which indicates that the method has poor differentiation ability. Both the ECM algorithm and the HECMk algorithm when $k=0$ adopt the expectation curve as the characteristic curve for studying cloud similarity, that is, the expectation curve with entropy if k value is 0, and the uncertainty effect of hyper entropy He on cloud concept is not taken into account. In the case of ignoring the hyper entropy, the HECMk algorithm has higher differentiation ability. In the case of hyper entropy, PDCM has better differentiation ability than MCM algorithm. HECMk algorithm with k

not equal to 0 has stronger differentiation ability and is better than PDCM and MCM algorithm as a whole.

Table 4. Difference degree of cloud concept under different similarity algorithms

Difference degree	δ_{C_1}	δ_{C_2}	δ_{C_3}	δ_{C_4}
LICM	0.0772	0.0744	0.0582	0.0546
ECM	1.8267	1.7492	1.6991	1.8224
MCM	1.2454	1.2462	1.1641	1.2487
PDCM	1.7301	1.5764	1.5376	1.7272
HCCMk	**1.8126**	**1.8174**	**1.7011**	**1.8043**

In contrast algorithm, ECM has the best distinction ability, but it does not take into account the case of hyper entropy, which is equivalent to comparing the similarity of normal distribution. When the hyper entropy is relatively large, that is, when the entropy En is less than three times the hyper entropy He or is close to it, the similarity of the comparison cloud model has its limitations. In addition, HECMk only carries out simple numerical calculation, without using integral operation, and the calculation complexity is far less than that of the comparison algorithm. Therefore, it can be considered that the expectation curve cluster with entropy with k value [-1, 1] has better distinguishing ability and comprehensive ability when a part of the distinguishing ability is abandoned in order to consider the hyper entropy.

After explaining the comprehensive ability of the expectation curve cluster with entropy, the HCCMk algorithm is further used to calculate the similarity. The k value is selected as [-1, 1], and the value is taken as a step of 0.1. 21 values are selected to calculate the Hellinger distance of the expected curve containing entropy. Further, the differentiation ability of HCCMk algorithm was calculated by combining the formula 8, and the results as shown in Table 4 were obtained.

As shown in the Table 4, the difference degree of HCCMk algorithm for the four cloud concepts is greater than that of PDCM algorithm , and is very close to that of ECM algorithm without considering overentropy. It shows that HCCMk has better distinguishing ability and comprehensive performance compared with ECM, MCM and PDCM. By comprehensive comparison, both HECMk algorithm and HCCMk algorithm have better performance, are feasible in measuring cloud concept similarity, and have less computational complexity than other methods.

5. Conclusions

HECMk algorithm and HCCMk algorithm were used to measure the similarity of four classical clouds, and LICM, ECM, MCM and PDCM algorithms were set as comparison experiments. The results show that in the normal cloud expectation curve cluster with entropy, when k is [-1, 1], the similarity measurement results are better and the overall differentiation ability is better. Without considering the influence of hyper entropy, HECMk algorithm ($k = 0$) is superior to ECM algorithm in distinguishing ability, and is suitable for cloud concept similarity measurement with low hyper entropy. Considering the influence of hyper entropy, the HECMk algorithm ($k \neq 0$) The overall differentiation ability is better than the MCM and PDCM algorithms in the comparison experiment, and the computational complexity is smaller than the two algorithms; The HCCMk algorithm synthesizes the expected curve clusters with entropy whose value is [-1, 1]. Compared with the ECM algorithm that does not take cloud concept uncertainty

into account, the HCCMk algorithm has the same differentiation ability and fully considers the influence of overentropy, and the computational complexity is smaller. Therefore, in summary, HECMk algorithm and HCCMk algorithm have good distinguishing ability, feasibility of cloud concept similarity measurement, and low computational complexity.

Acknowledgments

This work was supported by the Natural Science Foundation of Ningxia Province (No. 2022AAC03238), the National Natural Science Foundation of China (No. 62066001), and the North Minzu University Graduate Innovation Fund Project (NO.YCX22089).

References

[1] Li Deyi, Meng Haijun, Shi Xuemei. Affiliated cloud and affiliated Cloud Generator [J]. Journal of Computer Research and Development,1995(06):15-20
[2] Zhang GW, Li DY, Li P, Kang JC, Chen GS. A collaborative filtering recommendation algorithm based on cloud model. Journal of Software, 2007,18(10):2403−2411.
[3] LI Hailin, Guo Chonghui, Qiu Wangren. Similarity Measurement between Normal Cloud Models [J]. Acta Electronica Sinica,2011,39(11):2561-2567.
[4] Wang Jun, Zhu Jianjun, Liu Xiaodi. An integrated similarity measure method for normal cloud model based on shape and distance [J]. Systems Engineering-Theory & Practice,2017,37(03):742-751.
[5] Xu Changlin, Xu Hao. Research on similarity measurement method of normal cloud based on Hellinger distance and its application [J/OL]. CAAI Transactions on Intelligent Systems :1-10[2023-09-19].
[6] Huang Qiongtao, Liu Ruimin. Review on similarity measurement of cloud models [J]. Technology Discussion,2019(06):43-49. (in Chinese)
[7] Di Peng, Ni Zichun, Yin Dongliang. A multi-attribute decision making optimization algorithm based on cloud model and evidence theory [J]. Systems Engineering Theory & Practice, 2019,41(04):1061-1070. (in Chinese)
[8] Lu Yulong, Ye Gaofeng, Yang Xian et al. Study on karst collapse susceptibility in Yonghe Town, Liuyang City based on normal cloud model [J/OL]. Carsologica Sinica :1-11[2023-09-24].
[9] Yan Yan, Tang Zhenmin. Pertinence measurement of cloud model by using expectation-entropy curve[J]. Journal of Huazhong University of Science and Technology(Natural Science Edition),2012,40(10):95-100.
[10] Gong Yan-Bing, XU Xu-Kan, LIU Gaofeng. Research on Linguistic multi-attribute decision making method based on normal cloud expectation and variance distance [J]. Journal of Statistics and Information, 2019,36(10):12-19.
[11] Gong Y B, Chao Y. Research on comprehensive evaluation method based on uncertain normal cloud combination weights [J]. Statistics and Information Forum, 2019,35(05):3-8.
[12] Wang Guoyin, Xu Changlin, Zhang Qinghua et al. p-order Normal cloud model recursive definition and analysis of bidirectional cognitive computing [J]. Journal of Computers,2013,36(11):2316-2329.
[13] ZHENG Yayun, YANG Fang, DUAN Jinqiao, et al. Quantifying model uncertainty for the observed non-Gaussian data by the Hellinger distance[J]. Communications in Nonlinear Science and Numerical Simulation, 2021, 96: 105720.
[14] Xu Hao. Research on Measure and Application of Normal Cloud Similarity [D]. North Minzu University,2023.

Fuzzy Systems and Data Mining IX
A.J. Tallón-Ballesteros and R. Beltrán-Barba (Eds.)

doi:10.3233/FAIA231064

Similarity Measurement and Analysis of Triangular Cloud Models

Changlin XU [a,b,1], Wenyuan WU [a]

[a] *School of Mathematics and Information Science, North Minzu University, Yinchuan 750021, China*

[b] *The Key Laboratory of Intelligent Information and Big Data Processing of Ningxia Province, North Minzu University, Yinchuan, Ningxia 750021, China*

Abstract. The similarity of triangular fuzzy numbers could be served as a measurement of similarity between two triangular cloud models. However, it has been found that existing methods for describing the similarity of triangular cloud models has the drawbacks that can't make full use of utilizing graphic information and assigning inappropriate weights to distances through research and analysis. The method proposed in this literature has adjusted the weight of distance similarity aim to ensure that the characteristic information of the model will not be covered. In addition, the proposed method provides a measurement to describe geometric shape bases on the expected curve included angle of the triangular cloud model. On the foundation of taking abundantly the similarity of distance and shape into account, we provide the measurement to achieve better accuracy. The feasibility and effectiveness of the proposed method have been demonstrated through the time series of KNN algorithm.

Keywords. triangular cloud model, symmetric triangular fuzzy number, exponential closeness, similarity measurement

1. Introduction

The cloud model itself combines fuzziness and randomness, which has great potential in the field of studying uncertainty problems[1]. It is also used as a medium to transforms qualitative concepts into quantitative representations[2]. The concept of membership cloud proposed by Academician Li [3]. The fuzzy concept of cloud model could describe uncertainty, which means that the similarity between two cloud models can be measured[4]. The existing similarity measurement methods for cloud models mainly include the categories of ECM, LICM and DSTCM. ECM, which measures the similarity between two cloud models by integrating and normalizing the overlapping areas of the expected curves and the maximum boundary curves of the two cloud models[5]. LICM method mainly relies on the cosine value of the included angle, which is composed of the characteristic numbers of two cloud models[6]. The DSTCM method regards exponen-

[1]Corresponding Author: School of Mathematics and Information Science, North Minzu University, Yinchuan 750021, China; E-mail: xuchlin@163.com.

tial closeness and ratio of standard deviation as a similarity measure between two cloud models[7]. However, many scholars have found that none of them has an excellent measurement effect[8]. For example, the DSTCM method did not comprehensively consider the similarity of shape. And inappropriate weights has been assigned to distances, which resulting in the loss of useful information and weakened measurement accuracy.

Inspired by Wang, whom used the influence of cloud model distance on similarity[9]. This literature regards the characteristic numbers of the triangular cloud model as triangular fuzzy numbers[10]. Proposed a distance similarity measure through adjusting the weights of existing method. And provided a measuring method of geometric shape, which bases on the expected curve included angle of the triangular cloud model. We finally combine the distance and the shape of similarity to propose a measurement for two cloud models named DCS. Through algorithm analysis, we can draw the conclusion that this method is more feasible and has better discrimination. In addition, we can learn that it has less CPU runtime cost, which makes it a more efficient measurement.

2. Related Concepts

Through research, it is known that the triangular cloud model is a derivative of the normal cloud model, so that the following concepts are related to the triangular cloud model, which means that it will involve the concept of the normal cloud model[11].

Definition 1. *[12] Assuming U is a non empty set, x is a random variable, $u_C(x)$ regarded as uncertainty of x on U. The distribution of x on U is called a triangular cloud model. If $x \sim N(Ex, En')$, $En' \sim N(En, He)$,*

$$u_C(x) = \begin{cases} \frac{x-(Ex-3En')}{3En'}, & x < Ex \\ 1 - \frac{x-Ex}{3En'}, & x \geq Ex \end{cases} \tag{1}$$

Let the triangular cloud model be $\tilde{C} = (Ex, En, He)$. The expected curve of the triangular cloud model $\tilde{C} = (Ex, En, He)$ as y,

$$y = \begin{cases} \frac{x-(Ex-3En)}{3En}, & x < Ex \\ 1 - \frac{x-Ex}{3En}, & x \geq Ex \end{cases} \tag{2}$$

According to the literature [7], $\tilde{D}(x) = En^2 + He^2$ is called the variance of triangular cloud model.

Definition 2. *([7]) Let $y(\tilde{C}) = (Ex, 3En)$ be a symmetric triangular fuzzy number of the triangular cloud model $\tilde{C} = (Ex, En, He)$, while $[Ex-(Ex-3En) = (Ex+3En)-Ex = 3En]$, and $y(\tilde{C})$satisfies:*

$$y(\tilde{C}) = \begin{cases} \frac{x-(Ex-3En)}{3En}, & (Ex-3En) \leq x \leq Ex \\ 1, & x = Ex \\ 1 - \frac{x-Ex}{3En}, & Ex \leq x \leq (Ex+3En) \\ 0, & else. \end{cases} \tag{3}$$

Property 1. *([13]) R is the set of real numbers, and $F^*(R)$ is the set of all fuzzy numbers on R, $\forall \tilde{A}, \tilde{B} \in F^*(R)$, the mapping $d : (F^*(R), F^*(R)) \to [0, +\infty)$ is called a fuzzy distance, if d satisfies the following conditions:*

$$\begin{aligned}&(i)d(\tilde{A},\tilde{B}) \geq 0, \text{ and } \tilde{A}=\tilde{B} \Leftrightarrow d(\tilde{A},\tilde{B})=0,\\ &(ii)d(\tilde{A},\tilde{B})=d(\tilde{B},\tilde{A}),\\ &(iii)\forall \tilde{C} \in F^*(R), d(\tilde{A},\tilde{B}) \leq d(\tilde{A},\tilde{C})+d(\tilde{C},\tilde{B}).\end{aligned} \tag{4}$$

Property 2. *([14]) $F^*(R)$ is the set of all fuzzy numbers on R, $\forall \tilde{A},\tilde{B},\tilde{C} \in F^*(R)$, $\sigma : (F^*(R),F^*(R)) \to [0,1]$ is call a fuzzy exponential closeness, if σ satisfies the following conditions:*

$$\begin{aligned}&(i)\sigma(\tilde{A},\tilde{A})=1,\\ &(ii)\sigma(\tilde{A},\tilde{B})=\sigma(\tilde{B},\tilde{A}),\\ &(iii)\sigma(\tilde{A},\tilde{B})=1 \Leftrightarrow \tilde{A}=\tilde{B},\\ &(iv)\text{while } \tilde{A} \subseteq \tilde{B} \subseteq \tilde{C}, \sigma(\tilde{A},\tilde{C}) \leq \sigma(\tilde{A},\tilde{B}), \text{ and } \sigma(\tilde{A},\tilde{C}) \leq \sigma(\tilde{B},\tilde{C}).\end{aligned} \tag{5}$$

3. Triangular Cloud Model Similarity Measurement

The characteristic numbers of the triangular cloud model are regarded as triangular fuzzy numbers. Therefore, the similarity measurement of distance based on EW-type distance and exponential sticking schedule[15]. In addition, the cosine ratio of half-included angle between the expected curves and standard deviation ratio of triangular cloud models are considered as the shape similarity measure. The proposed method, which has combined the similarity of distance and shape in cloud model contains more adequate information in the model.

3.1. Shape similarity measurement based on half-included angle cosine value of expected curve and cloud droplet variance of triangular clouds

literature[7] uses $\gamma = \frac{\min\left\{\sqrt{\tilde{D}_1(x)},\sqrt{\tilde{D}_2(x)}\right\}}{\max\left\{\sqrt{\tilde{D}_1(x)},\sqrt{\tilde{D}_2(x)}\right\}}$, ($\sqrt{\tilde{D}_i(x)} = \sqrt{{En_i}^2+{He_i}^2}$), as a similarity measurement of shape between two triangular cloud model. However, it has been found that γ can not accurately described the shape distribution. According to the def. (2), the symmetric triangular fuzzy number $y(\tilde{C}) = (Ex, 3En)$ representative a triangular cloud model $\tilde{C}(Ex,En,He)$, which is an isosceles triangle with the base half length of $3En$, and the height of 1[16]. For example, the included angle of the triangular cloud model $\tilde{C}(3.6890, 0.9153, 0.0805)$ is as shown in Figure 1.

Assume the included angle between the two expected curves of the triangular cloud model $\tilde{C}_i(Ex_i,En_i,He_i)$ be α_i, $\varphi_i = \frac{1}{2}\alpha_i$, $\cos\varphi_i = \frac{1}{\sqrt{1+(3En_i)^2}}$. Define the ratio of the minimum to maximum cosine values of two cloud models as $\rho = \frac{\min\{\cos\varphi_1,\cos\varphi_2\}}{\max\{\cos\varphi_1,\cos\varphi_2\}}$, ρ reflects the difference of included angle as well as reveals the vary in shape. Taking inspiration from the literature [9] on distance measurement methods, this literature comprehensively considers the included angle difference-ρ and the shape difference-γ to better measure the similarity of triangular cloud models.

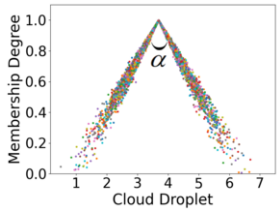

Figure 1. The included angle of the triangular cloud model $\tilde{C}(3.6890, 0.9153, 0.0805)$ is α.

Definition 3. *Let the included angle between two expected curves of the triangular cloud model* $\tilde{C}_i(Ex_i, En_i, He_i)$ *be* α_i, $\varphi_i = \frac{1}{2}\alpha_i$, $\cos\varphi_i = \frac{1}{\sqrt{1+(3En_i)^2}}$. *The ratio of the minimum to maximum cosine values of two triangular cloud models* $\tilde{C}_1(Ex_1, En_1, He_1)$ *and* $\tilde{C}_2(Ex_2, En_2, He_2)$ *is defined as* $\rho(\tilde{C}_1, \tilde{C}_2)$,

$$\rho(\tilde{C}_1, \tilde{C}_2) = \frac{\min\{\cos\varphi_1, \cos\varphi_2\}}{\max\{\cos\varphi_1, \cos\varphi_2\}}, \quad \rho(\tilde{C}_1, \tilde{C}_2) \in (0, 1]. \tag{6}$$

According to the definition, the ratio of the maximum to minimum standard deviation of two triangular cloud models $\tilde{C}_1(Ex_1, En_1, He_1)$ and $\tilde{C}_2(Ex_2, En_2, He_2)$ is defined as $\gamma(\tilde{C}_1, \tilde{C}_2)$,

$$\gamma(\tilde{C}_1, \tilde{C}_2) = \frac{\min\left\{\sqrt{\tilde{D}_1(x)}, \sqrt{\tilde{D}_2(x)}\right\}}{\max\left\{\sqrt{\tilde{D}_1(x)}, \sqrt{\tilde{D}_2(x)}\right\}}, \quad \gamma(\tilde{C}_1, \tilde{C}_2) \in (0, 1]. \tag{7}$$

Definition 4. *Geometric shape similarity measure of two triangular cloud models* $\tilde{C}_1(Ex_1, En_1, He_1)$ *and* $\tilde{C}_2(Ex_2, En_2, He_2)$ *is defined as* $Sim_1(\tilde{C}_1, \tilde{C}_2)$,

$$Sim_1(\tilde{C}_1, \tilde{C}_2) = \rho \cdot \gamma, Sim_1(\tilde{C}_1, \tilde{C}_2) \in (0, 1]. \tag{8}$$

3.2. Distance measurement of triangular cloud model based on improved weights

The literature[7] uses $d[y(\tilde{C}_1), y(\tilde{C}_2)] = \sqrt{(Ex_1 - Ex_2)^2 + \frac{1}{3}(3En_1 - 3En_2)^2}$ as a measurement of distance bases on two triangular symmetric fuzzy numbers $\tilde{C}_1 = (Ex_1, 3En_1)$ and $\tilde{C}_2(Ex_2, 3En_2)$. However, it is unreasonable to give the weight of 1 to $[(Ex_1 - Ex_2)^2]$, while the weight of $[(En_1 - En_2)^2]$ is $\frac{1}{3}$. The reason is that Ex of triangular cloud model is often more larger than En in practical situations. Thus, the value of $\frac{1}{3}[(En_1 - En_2)^2]$ will be masked under such weights by$[(Ex_1 - Ex_2)^2]$, which possible results the consequences of information loss and lower measurement accuracy.

Therefore, this literature has adjusted the weight of such distance similarity and proposed a distance similarity measure named $d_{new}[y(\tilde{C}_1), y(\tilde{C}_2)]$ to improve the accuracy of similarity measurement.

Definition 5. *Let* $d_{new}[y(\tilde{C}_1), y(\tilde{C}_2)]$*be the distance of two triangular cloud models* $\tilde{C}_1(Ex_1, En_1, He_1)$*and* $\tilde{C}_2(Ex_2, En_2, He_2)$,

$$d_{new}[y(\tilde{C}_1), y(\tilde{C}_2)] = \sqrt{\frac{2}{3}(Ex_1 - Ex_2)^2 + \frac{1}{3}(3En_1 - 3En_2)^2}. \tag{9}$$

Based on that, the exponential closeness constructed by two symmetric triangular fuzzy numbers is $Sim_2(\tilde{C}_1,\tilde{C}_2)$, which used to measure the distance similarity of the triangular cloud model,

$$Sim_2(\tilde{C}_1,\tilde{C}_2) = e^{-\left[d_{new}[y(\tilde{C}_1),y(\tilde{C}_2)]\right]^2} \in (0,1]. \tag{10}$$

Theorem 1. *Eq.(9) satisfies all the conditions of fuzzy distance in Property 1.*

Proof 1. *To prove that Eq.(9) is a fuzzy distance, which is equal to prove it satisfies the following conditions:*

(1) *Apparently* $d_{new}[y(\tilde{C}_1),y(\tilde{C}_2)] \geq 0$.

(2)
$$\begin{aligned} d_{new}[y(\tilde{C}_1),y(\tilde{C}_2)] = o, &\Leftrightarrow \sqrt{\frac{2}{3}(Ex_1-Ex_2)^2+\frac{1}{3}(3En_1-3En_2)^2} = 0, \\ &\Leftrightarrow \frac{2}{3}(Ex_1-Ex_2)^2+\frac{1}{3}(3En_1-3En_2)^2 = 0, \\ &\Leftrightarrow (Ex_1-Ex_2) = 0, \text{ and } (3En_1-3En_2)^2 = 0, \\ &\Leftrightarrow Ex_1 = Ex_2, \text{ and } 3En_1 = 3En_2, \Leftrightarrow y(\tilde{C}_1) = y(\tilde{C}_2). \end{aligned}$$

(3)
$$\begin{aligned} d_{new}[y(\tilde{C}_1),y(\tilde{C}_2)] &= \sqrt{\frac{2}{3}(Ex_1-Ex_2)^2+\frac{1}{3}(3En_1-3En_2)^2} \\ &= \sqrt{\frac{2}{3}(Ex_2-Ex_1)^2+\frac{1}{3}(3En_2-3En_1)^2} = d_{new}[y(\tilde{C}_2),y(\tilde{C}_1)]. \end{aligned}$$

(4) *now assume* $y(\tilde{C}_3) = (Ex_3, 3En_3)$,

$$|Ex_1-Ex_2| \leq |Ex_1-Ex_3|+|Ex_3-Ex_2|,$$

$$|3En_1-3En_2| \leq |3En_1-3En_3|+|3En_3-3En_2|,$$

$$d_{new}[y(\tilde{C}_1),y(\tilde{C}_2)] = \sqrt{\frac{2}{3}(Ex_1-Ex_2)^2+\frac{1}{3}(3En_1-3En_2)^2},$$

$$d_{new}[y(\tilde{C}_1),y(\tilde{C}_3)] = \sqrt{\frac{2}{3}(Ex_1-Ex_3)^2+\frac{1}{3}(3En_1-3En_3)^2},$$

$$d_{new}[y(\tilde{C}_2),y(\tilde{C}_3)] = \sqrt{\frac{2}{3}(Ex_2-Ex_3)^2+\frac{1}{3}(3En_2-3En_3)^2},$$

$$d_{new}[y(\tilde{C}_1),y(\tilde{C}_2)] \leq d_{new}[y(\tilde{C}_1),y(\tilde{C}_3)]+d_{new}[y(\tilde{C}_2),y(\tilde{C}_3)].$$

the end .

Theorem 2. *Eq.(10) satisfies all the conditions of fuzzy exponential closeness in Property 2.*

Proof 2. *To prove that Eq.(10) is a fuzzy exponential closeness, which is equal to prove it satisfies the following conditions:*

(1)*Apparently* $Sim_2(\tilde{C}_1,\tilde{C}_1) = e^{[-d_{new}[y(\tilde{C}_1),y(\tilde{C}_1)]]^2} = 1.$

(2)
$$\begin{aligned} &d_{new}[y(\tilde{C}_1),y(\tilde{C}_2)] = d_{new}[y(\tilde{C}_2),y(\tilde{C}_1)], \\ &Sim_2(\tilde{C}_1,\tilde{C}_2) = e^{-\left[d_{new}[y(\tilde{C}_1),y(\tilde{C}_2)]\right]^2} = e^{-\left[d_{new}[y(\tilde{C}_1),y(\tilde{C}_2)]\right]^2} = Sim_2(\tilde{C}_2,\tilde{C}_1). \end{aligned}$$

(3)
$$Sim_2(\tilde{C}_1,\tilde{C}_2)=1 \Leftrightarrow e^{-[d_{new}[y(\tilde{C}_1),y(\tilde{C}_2)]]^2}=1,$$
$$\Leftrightarrow d_{new}[y(\tilde{C}_1),y(\tilde{C}_2)])=0,$$
$$\Leftrightarrow \sqrt{\tfrac{2}{3}(Ex_1-Ex_2)^2+\tfrac{1}{3}(3En_1-3En_2)^2}=0,$$
$$\Leftrightarrow \left\{\begin{array}{c} Ex_1-Ex_2=0 \\ 3En_1-3En_2=0 \end{array}\right\},\Leftrightarrow \left\{\begin{array}{c} Ex_1=Ex_2 \\ En_1=En_2 \end{array}\right\},\Leftrightarrow \tilde{C}_1=\tilde{C}_2,$$
$$Sim_2(\tilde{C}_1,\tilde{C}_2)=1 \Leftrightarrow \tilde{C}_1=\tilde{C}_2.$$

(4) $\tilde{C}_1 \subseteq \tilde{C}_2 \subseteq \tilde{C}_3$, *where* $Ex_1 \le Ex_2 \le Ex_3$, *and* $3En_1 \le 3En_2 \le 3En_3$,
$$\left\{\begin{array}{l} \frac{2}{3}(Ex_1-Ex_3)^2+\frac{1}{3}(3En_1-3En_3)^2 \ge \frac{2}{3}(Ex_1-Ex_2)^2+\frac{1}{3}(3En_1-3En_2)^2 \\ \frac{2}{3}(Ex_1-Ex_3)^2+\frac{1}{3}(3En_1-3En_3)^2 \ge \frac{2}{3}(Ex_2-Ex_3)^2+\frac{1}{3}(3En_2-3En_3)^2 \end{array}\right\},$$
which means $\left\{\begin{array}{l} d_{new}[y(\tilde{C}_1),y(\tilde{C}_3)] \ge d_{new}[(y(\tilde{C}_1),y(\tilde{C}_2)] \\ d_{new}[y(\tilde{C}_1),\tilde{y}(\tilde{C}_3)] \ge d_{new}[(y(\tilde{C}_2),\tilde{y}(\tilde{C}_3)] \end{array}\right\},$
$$\Leftrightarrow \left\{\begin{array}{l} Sim_2(\tilde{C}_1,\tilde{C}_3) \le Sim_2(\tilde{C}_1,\tilde{C}_2) \\ Sim_2(\tilde{C}_1,\tilde{C}_3) \le Sim_2(\tilde{C}_2,\tilde{C}_3) \end{array}\right\},$$
while $Sim_2(\tilde{C}_1,\tilde{C}_2)=e^{-[(d_{new}(\tilde{C}_1,\tilde{C}_2))^2]}$ *is strictly monotone decreasing,*
also, when $d_{new}[(y(\tilde{C}_1),y(\tilde{C}_2)]=0$, $Sim_2(\tilde{C}_1,\tilde{C}_2)=1$.
Therefore, $d_{new}[(y(\tilde{C}_1),y(\tilde{C}_2)] \to \infty$, $\lim\limits_{d_{new}(\tilde{C}_1,\tilde{C}_2)\to\infty} Sim_2(\tilde{C}_1,\tilde{C}_2)=0.$

the end.

3.3. Similarity of two triangular cloud models is composed by adjusted weights of distance and the ratio cosine value with the ratio of standard deviation

The similarity of distance and shape are comprehensively taken into account in order to propose the measurement-DCS to achieve a better similarity measure accuracy.

Definition 6. *Let DCS* $(\tilde{C}_1,\tilde{C}_2)$*, (distance,cosine and shape bases on triangular cloud model) be the similarity measure of two symmetric triangular cloud models* $\tilde{C}_1(Ex_1,En_1,He_1)$ *and* $\tilde{C}_2(Ex_2,En_2,He_2)$.

$$DCS(\tilde{C}_1,\tilde{C}_2)=Sim_1(\tilde{C}_1,\tilde{C}_2)\times Sim_2(\tilde{C}_1,\tilde{C}_2) \tag{11}$$

4. Experimental analysis

The K-nearest neighbor (KNN) algorithm widely be used for supervised learning as well as unsupervised learning to solve the problems of classification and regression[17]. The

principle of this algorithm is to select a few nearest neighbors on the samples according to the value of K [18]. It was used to calculate the classification accuracy in this algorithm analysis base on the proposed method-DCS, which is used as the distance calculation method for selecting the nearest K neighbors.

In this part, the data will be divided into testing data and training data. Further, the training data will be split into six sets, each of them should be tested and calculated the classification accuracy while K ranges from 1 to 10. What's more, in order to better illustrate the feasibility as well as accuracy of the proposed method, we compared DCS with other different methods such as LICM method, Adjust_ LICM, DSTCM method and ECM method in terms of classification accuracy on six training sets. We can learn from the results that the proposed method indeed has a better classification accuracy and less time cost.

4.1. Time series classification algorithm based on DCS method

Time series dataset in the UCI Knowledge Discovery Database (UCI KDD) - Synthetic Control Chart Dataset (SYNDATA) is a data sample set with 600 control charts. It has been divided into 600 rows and 60 columns. Every 100 rows representatives for one category, so that the sample is evenly divided into 6 categories. Each of data type represents a time series trend, which is extremely suitable for analyzing classification accuracy.

The schematic diagrams of six different trends are shown as Figure 2 to Figure 7.

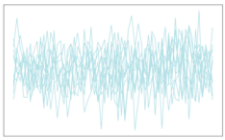

Figure 2. Normal (A)

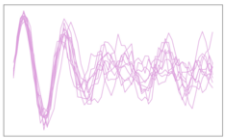

Figure 3. Cyclic (B)

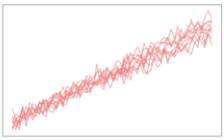

Figure 4. Increasing Trend (C)

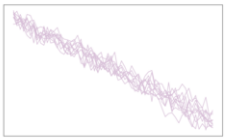

Figure 5. Decreasing Trend (D)

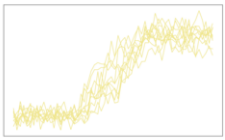

Figure 6. Upward Shift (E)

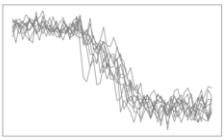

Figure 7. Downward Shift (F)

KNN time series algorithm description:

Input: Time series dataset $Y_{600\times 60}$.

Output: Classification accuracy and CPU runtime cost.

(1) Represent the dataset $Y_{600\times 60}$ as a cloud model.
Represent the 600 rows of data in the dataset as 600 cloud models using the triangular reverse cloud generator, with the $m-th$ cloud model as $\tilde{C}_m(Ex_m, En_m, He_m)$.

(2) Divide training set and testing sets.
Place the last 10 of each type of data as the test set and arrange them in order into 60 test sets, represented by the cloud model as $\tilde{C}_{Testi}(Ex_i, En_i, He_i), (1 \le i \le 60)$. The remaining 540 time series are used as the training set. Furthermore, the first 90 rows of data in each category are evenly divided into 6 parts, forming a total of 6 types of training data with 90 data in each category; then the six training sets are represented by A, B, C, D, E and F. The cloud model of the training set is represented as $\tilde{C}_{Trainj}(Ex_j, En_j, He_j), (1 \le j \le 90)$.

(3) Calculate the similarity matrix $Sim(\tilde{C}_{Testi}, \tilde{C}_{Trainj})$.
Calculate the similarity matrix between the test set and the six types of training set using the DCS method:

$$Sim(\tilde{C}_{Testi}, \tilde{C}_{Trainj}) = \begin{bmatrix} Sim(\tilde{C}_{Test1}, \tilde{C}_{Train1}) & \cdots & Sim(\tilde{C}_{Test1}, \tilde{C}_{Train90}) \\ \vdots & \ddots & \vdots \\ Sim(\tilde{C}_{Test60}, \tilde{C}_{Train1}) & \cdots & Sim(\tilde{C}_{Test60}, \tilde{C}_{Train90}) \end{bmatrix}.$$

$Sim(\tilde{C}_{Testi}, \tilde{C}_{Trainj})$ represents the similarity between time series i and j.

(4) Classify based on the value of K.
Sort the similarity matrix $Sim(\tilde{C}_{Testi}, \tilde{C}_{Trainj})$ from largest to smallest, filter outthe first K values in each row, and then determine which category the test set belongs to based on the number of categories to which K data belong.

(5)Calculate classification accuracy.
Count the number of correctly classified test sets under the training sets A, B, C, D, E and F, and the accuracy of each classification is represented as n_{A}, n_{B}, n_{C}, n_{D}, n_{E} and n_{F}. The accuracy of each classification is expressed as:

$p_{\mathrm{A}} = \frac{n_{\mathrm{A}}}{60}, p_{\mathrm{B}} = \frac{n_{\mathrm{B}}}{60}, p_{\mathrm{C}} = \frac{n_{\mathrm{C}}}{60}, p_{\mathrm{D}} = \frac{n_{\mathrm{D}}}{60}, p_{\mathrm{E}} = \frac{n_{\mathrm{E}}}{60}, p_{\mathrm{F}} = \frac{n_{\mathrm{F}}}{60}$.

4.2. Analysis of accuracy of experimental results

Divide the training data into six sets, namely A, B, C, D, E and F. The training set will be separately used to train the model. Thus, six training models will be obtained. After that, the test set would provide predictions on each model with calculating the classification accuracy of the DCS method while K ranges from 1 to 10. What's more, the classification accuracy of DCS will be compared with other different methods such as LICM method, Adjust_ LICM, DSTCM method and ECM method to show the advantage of classification accuracy. In this algoritm, the proposed method will be used as the measurement to select the nearest neighbors on the training set according to the value of K.

While K=1 $\sim$ 10, the classification accuracy of the proposed method on time series sets is as shown in Figure 8.

Figure 9 to Figure 14 show the comparisons of classification accuracy in five methods on each training set while K=1 $\sim$ 10.

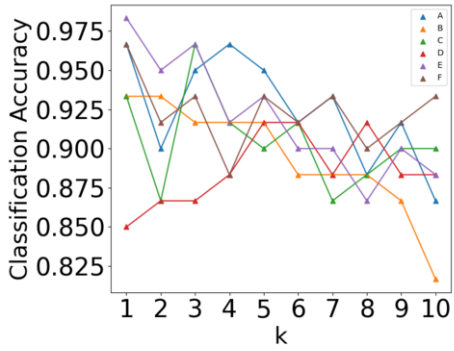

Figure 8. Summary of classification accuracy of DCS method on time series sets.

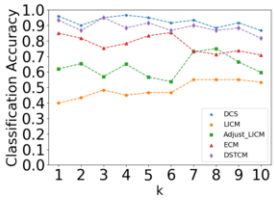

Figure 9. While K= 1 $\sim$ 10, classification accuracy on class A training set.

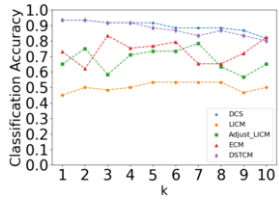

Figure 10. While K= 1 $\sim$ 10, classification accuracy on class B training set.

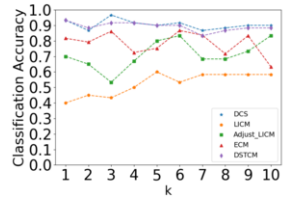

Figure 11. While K= 1 $\sim$ 10, classification accuracy on class C training set.

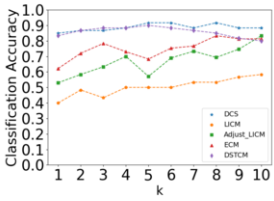

Figure 12. While K= 1 $\sim$ 10, classification accuracy on class D training set.

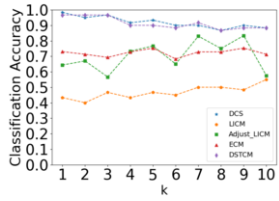

Figure 13. While K= 1 $\sim$ 10, classification accuracy on class E training set.

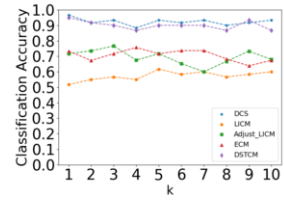

Figure 14. While K= 1 $\sim$ 10, classification accuracy on class F training set.

According to the above charts, it is obvious that in most cases, the classification accuracy of DCS method is better than other methods. It also reveals the similarity measurement that adjusting weights of distance combining the ratio cosine value of included angle and the ratio of standard deviation is practical.

4.3. CPU running cost analysis

It is important to understand and evaluate the CPU running cost when optimizing program performance or conducting system tuning[19]. Suitable algorithms could be selected by evaluating and comparing the CPU running cost. To achieve less running cost,

it is helpful to adjust task parallelism and optimize data access patterns. What's more, it could improve the program efficiency[20].

Figure 15 shows the result of CPU runtime for five methods in same collection.

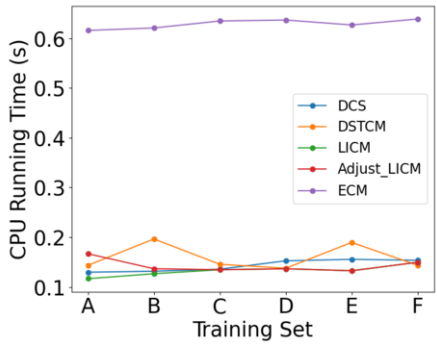

Figure 15. CPU runtime for different methods in the same collection

From the CPU analysis results above, it could be learned that compared with the ECM method that requires calculating the common area, the DCS method significantly reduces its running time and overall superior to the DSTCM method, indicating that the method of DCS is more effective.

5. Conclusion

The proposed method comprehensively considers the distance similarity as well as the shape similarity of triangular cloud models. Since Ex is always more larger than En in practical situations, the solution is to adjust the weight of $[(Ex_1 - Ex_2)^2]$, which intends to make sure the value of $[(En_1 - En_2)^2]$ will not be covered. Additionally, the minimum to maximum ratio of cosine values bases on included angle in triangular cloud model has been regarded as an important part of shape similarity. The advantages of this method with higher classification accuracy and lower runtime cost have been demonstrated through the time series of KNN algorithm.

Investigation indicates that symmetrical triangular cloud model still has great potential for study. According to the relationship between cloud model and fuzzy number, it can be learned that the contents for further study could be included as primarily two aspects. Firstly, it's quite important to figure out how to quantify and evaluate variously uncertain factors by using symmetric triangular fuzzy number. Additionally, the characteristic information of triangular cloud model should be combined with symmetric triangular fuzzy number to better resolute the issue of decision problem.

Acknowledgments

This work was supported by the National Natural Science Foundation of China (No. 62066001), the Natural Science Foundation of Ningxia Province (No. 2023AAC05046), and the Ningxia Higher Education First-class Discipline Construction Project (NO. NXYLXK2017B09).

References

[1] Wang G. Y. Cloud Model and Granular Computing [M] Beijing: Science Press, 2012.

[2] Di Peng, Ni Zichun, Yin Dongliang Multi attribute decision optimization algorithm based on cloud model and evidence theory [J] System Engineering Theory and Practice, 2021, 41 (04): 1061-1070 (08): 28-34.

[3] Li Deyi, Liu Changyu On the Universality of Normal Cloud Models [J] China Engineering Science, 2004, (08): 28-34.

[4] Ma Jiajun. 3D Face shape matching and similarity Analysis based on electrostatic field [D]. University of Chinese Academy of Sciences (Shenzhen Institute of Advanced Technology, Chinese Academy of Sciences),2022.

[5] Li Hailin Research on Feature Representation and Similarity Measurement Methods in Time Series Data Mining [D]. Dalian University of Technology, 2012.

[6] Zhang Guangwei, Li Deyi, Li Peng, Kang Jianchu, Chen Guisheng Collaborative filtering recommendation algorithm based on cloud model [J] Journal of Software Science, 2007, (10): 2403-2411.

[7] Huang qiongtao Research and Application of Cloud Model Similarity Measurement Method [D]. Kunming University of Science and Technology, 2021.

[8] Cha Xiang, Ni Shihong, Xie Chuan, Zhang Peng The Conceptual Jump of Cloud Similarity and Indirect Calculation Method [J] Systems Engineering and Electronic Technology, 2015,37 (07): 1676-1682.

[9] Wang Jun, Zhu Jianjun, Liu Xiaodi Comprehensive Similarity Calculation for Normal Cloud Models Considering Shape Distance [J] System Engineering Theory and Practice, 2017,37 (03): 742-751.

[10] Sun Nini, Chen Zehua, Niu Yuguang, Yan Gaowei Similarity measurement based on cloud model overlap [J] Computer Applications, 2015,35 (07): 1955-1958+1964.

[11] Gong Yanbing, Jiang Yadong, Liang Xuechun Similarity measurement of normal cloud models based on fuzzy closeness [J] Systems Engineering, 2015,33 (09): 133-137.

[12] Wu Simin, Xu Ruoning Comparison of Several Distances in Fuzzy Number Space [J] Coastal Enterprises and Technology, 2010 (2): 34-36.

[13] Li Xia, Zhang Shaolin, Pang Gewei Triangular fuzzy interactive multi-attribute decision-making method based on distance measure [J] Journal of Xihua University (Natural Science Edition), 2022,41 (01): 84-89+110.

[14] Chen Hao, Wang Daiping, Zhang Li Extended Normal Cloud Generator [J] Journal of Hubei University (Natural Science Edition), 2011, 33 (02): 251-255.

[15] Bian wen ,A True Domain Closeness Fuzzy Reasoning Algorithm Based on Triangular Fuzzy Numbers [D]. Northeast Electric Power University, 2022.

[16] Huang Qiongtao, Liu Ruimin A similarity measurement method for cloud models [J] Control Engineering, 2022, 29 (09): 1600-1604

[17] Li Zeyu. Research on Multi-attribute Decision Algorithm based on Evidence Theory and Cloud Model [D]. University of Science and Technology Liaoning,2012.

[18] Gu Xin, Xu Zhengquan, Liu Jin. Cloud Theory based trust research and Prospects [J]. Journal of Communications,2011,32(07):176-181.

[19] Yang Jianjun,Han Jiahao,Wan Qilin,Xing Shanshan,Chen Fei. A novel similarity measurement for triangular cloud models based on dual consideration of shape and distance.[J]. PeerJ. Computer science,2023,9.

[20] Dai Lijin, He Zhenfeng A Method for Measuring Time Series Similarity Based on Cloud Models [A] Uncertain Systems Branch of the China Operations Research Society. Proceedings of the 8th China Annual Conference on Uncertain Systems [C]. Uncertain Systems Branch of the China Operations Research Society: Department of Mathematical Sciences, Tsinghua University, 2010:133-139.

Fuzzy Systems and Data Mining IX
A.J. Tallón-Ballesteros and R. Beltrán-Barba (Eds.)

doi:10.3233/FAIA231065

Periodic Travelling Waves of the Delayed Nicholson's Blowflies Model with Diffusion

Xiaxia Wu [a] and Dong Li [a,1]
[a] *College of Sciences, Chongqing University of Posts and Telecommunications, China*

Abstract. In this paper, we investigate the existence of periodic travelling waves with large wave speed for the diffusion Nicholson's blowflies model with delay effect by applying the perturbation technique. The proof depends on transforming the differential equation with the wave profile into integral equation, combining the implicit function theorem and the Liapunov-Schmidt reduction.

Keywords. Nicholson's blowflies model, Diffusion, Perturbation method, Periodic travelling wave solutions

1. Introduction

The Nicholson's blowflies equation is a classical model, which is widely used to research the population dynamics of some insect pests. Based on the delayed growth of Nicholson's blowflies, in order to overcome the discrepancy in estimating the delay value, Gueney *et al*. [1] proposed the following delay Nicholson's blowflies model

$$\dot{N}(t) = -\delta N(t) + pN(t-\tau)e^{-aN(t-\tau)}. \tag{1}$$

Here $N(t)$ denotes the population density at time $t \geq 0$; δ is the adult mortality rate; τ is a maturation delay; p is the highest average daily egg production rate; $\frac{1}{a}$ is the size at which the population reproduces at its maximum rate; a, δ, p and τ are positive constants. Kulenović and Ladas [2] proved the solution of equation (1) oscillated about its equilibrium state solution. Moreover, Kulenović et al. [3] established sufficient conditions for the global attractivity of the positive equilibrium of equation (1). See [4,5,6,7] for more progress on various types of solutions of system (1).

On account of equation (1), So and Yang [8] proposed the diffusion form of Nicholson's blowflies equation

$$\frac{\partial u(x,t)}{\partial t} = d\Delta u(x,t) - \delta u(x,t) + pu(x,t-\tau)e^{-au(x,t-\tau)}, \tag{2}$$

[1]Corresponding Author: Dong Li, College of Sciences, Chongqing University of Posts and Telecommunications, Chongqing, 400065, P.R. China; E-mail: donglimath@163.com.
This paper is supported by Natural Science Foundation of Chongqing, China (Grant NO.CSTB2022NSCQ-MSX1204) and National Natural Science Foundation of China (Grant No. 12001076).

which described the population growth of Nicholson's blowflies with spatial diffusion. $u(x,t)$ denotes the population density at time $t \geq 0$ and location $x \in \mathbb{R}^N$; Δ is Laplacian operator and $d > 0$ is the diffusion rate. In [8], the stability of the steady-state solutions for equation (2) was investigated. Whereafter, So and Zou [9] researched the existence of travelling wavefront of equation (2) by upper-lower solution method. The existence of nonmonotone travelling waves was investigated [10]. Stability of travelling wavefronts was investigated by weighted energy method in [11,12]. Furthermore, Yang [13] investigated the properties of periodic travelling wave solutions bifurcating from the zero equilibrium by Hopf bifurcation theory.

Inspired by the work in [13], in this paper, we will investigate the existence of periodic travelling waves bifurcating from the non-zero equilibrium for equation (2) by applying the perturbation method. Our approach is different from the method in [13], which depends on transforming the differential equation with the wave profile into integral equation, combining the implicit function theorem and the Liapunov-Schmidt method. Moreover, we associate the existence of periodic travelling wave solutions for equation (2) with the existence of periodic solutions for related delay differential equation. Similar idea also has appeared in the literature (see [14,15]).

Throughout this paper, $C_\rho = \{g \in C(\mathbb{R},\mathbb{R}) : g(t+\rho) = g(t), \rho \in \mathbb{R}\}$ denotes the Banach space of all ρ-periodic functions equipped with the supremum norm $\|g\|_{C_\rho} = \sup\{\|g(t)\|_{\mathbb{R}} : t \in [0,\rho]\}$. For $\Phi \in C(\mathbb{R},\mathbb{R})$ and $s \in \mathbb{R}$, define $\Phi_s \in C([-\tau,0],\mathbb{R})$ by $\Phi_s(r) = \Phi(s+r)$, $r \in [-\tau,0]$. For $\Psi \in C(\mathbb{R},\mathbb{R})$ and $\theta \in \mathbb{R}$, $\Psi^s \in C([0,\tau],\mathbb{R})$ denotes a translation of Ψ defined by $\Psi^s(\theta) = \Psi(s+\theta)$, $\theta \in [0,\tau]$. Furthermore, for $P \in C(\mathbb{R},\mathbb{R})$ and $M \in C_\rho$, define $\langle P, M\rangle = \int_0^\rho P(s)M(s)\mathrm{d}s$.

2. Derivation of the integral equation

The aim of this part is to convert the differential equation with the wave profile into an integral equation. Let $u(t,x) = u^\star(s)$ and $s = \nu \cdot x + ct \in \mathbb{R}$, where ν is a unit vector in $\mathbb{R}^N$. Substituting it into system (2), we have

$$d\ddot{u^\star}(s) - c\dot{u^\star}(s) - \delta u^\star(s) + pu^\star(s-c\tau)e^{-au^\star(s-c\tau)} = 0. \tag{3}$$

Let $\mathcal{U}(s) = u^\star(cs)$ and $\varepsilon = \frac{1}{c^2}$, system (3) can be rewritten as

$$\varepsilon d\ddot{\mathcal{U}}(s) - \dot{\mathcal{U}}(s) - \delta\mathcal{U}(s) + p\mathcal{U}(s-\tau)e^{-a\mathcal{U}(s-\tau)} = 0. \tag{4}$$

Equation (4) is a singular perturbation of system (3). For sufficiently large c, as will be the case later in this work, ε is sufficiently small. When $\varepsilon = 0$, from system (4), we have

$$\dot{u}(s) = -\delta u(s) + pu(s-\tau)e^{-au(s-\tau)}, \tag{5}$$

which has equilibrium $u_* = \frac{1}{a}\ln\frac{p}{\delta} \in \mathbb{R}_+$ as $p > \delta$. For equation (5), the following result can be obtained.

Lemma 2.1 [16] *When $p > \delta e^2$, system (5) admits a periodic solution branch parameterized by τ, bifurcating from positive equilibrium u_*.*

Next, we derive the integral equation on account of Lemma 2.1. Introducing the variable $U(s) = \mathcal{U}((1+\iota)s)$ and $\epsilon = \frac{\varepsilon}{1+\iota}$, where $\iota \in [-\iota^*, \iota^*]$ for a constant $0 < \iota^* < 1$. Moreover, we suppose that $u^*(s)$ is a ρ-periodic hyperbolic solution of equation (5) in Lemma 2.1 (For the proof of hyperbolicity, refer to [15]). Substituting them into system (4), we obtain

$$\epsilon d\ddot{U}(s) - \dot{U}(s) - \delta(1+\iota)U(s) + p(1+\iota)U\Big(s - \frac{\tau}{1+\iota}\Big)e^{-aU\left(s-\frac{\tau}{1+\iota}\right)} = 0. \tag{6}$$

Set $v(s) = U(s) - u^*(s)$, for $s \in \mathbb{R}$, then equation (6) can be rewritten as follows:

$$\epsilon d\ddot{v}(s) - \dot{v}(s) - v(s) + [\mathcal{I}v](s) + \mathcal{M}(\varepsilon, \iota, s, v) = 0, \tag{7}$$

where $\mathcal{I} : C_\rho \to C_\rho$ and $\mathcal{M} : (0,\infty)\times\mathbb{R}\times\mathbb{R}\times C_\rho \to \mathbb{R}$ are defined as

$$[\mathcal{I}v](s) = v(s) - \delta v(s) + \Big[pe^{-au^*(s-\tau)} - apu^*(s-\tau)e^{-au^*(s-\tau)}\Big]v(s-\tau),$$

and

$$\begin{aligned}\mathcal{M}(\varepsilon,\iota,s,v) = {} & d\epsilon\ddot{u}^*(s) - \Big[-\delta u^*(s) + pu^*(s-\tau)e^{-au^*(s-\tau)}\Big] - \delta(1+\iota)[v(s)+u^*(s)] \\ & + p(1+\iota)[v+u^*]\Big(s-\frac{\tau}{1+\iota}\Big)e^{-a[v+u^*]\left(s-\frac{\tau}{1+\iota}\right)} + \delta v(s) \\ & - \Big[pe^{-au^*(s-\tau)} - apu^*(s-\tau)e^{-au^*(s-\tau)}\Big]v(s-\tau).\end{aligned}$$

Since the equation $\epsilon d\lambda^2 - \lambda - 1 = 0$ always has real solutions $\lambda_1(\epsilon) = \frac{1-\sqrt{1+4\epsilon d}}{2\epsilon d} < 0$, $\lambda_2(\epsilon) = \frac{1+\sqrt{1+4\epsilon d}}{2\epsilon d} > 0$. Let $p_i(\epsilon, t) = \frac{e^{\lambda_i(\epsilon)t}}{\sqrt{1+4\epsilon d}}$, for each $i \in \{1,2\}$ and $\epsilon > 0$. Then equation (7) has a ρ-periodic solution $v(s)$ when and only when $v(s)$ is the solution of the integral equation

$$[Lv](s) = \mathcal{P}(\varepsilon, \iota, s, v), \quad s \in \mathbb{R}, \tag{8}$$

where L: $C_\rho \to C_\rho$ and $\mathcal{P}$: $(0,\infty)\times\mathbb{R}\times\mathbb{R}\times C_\rho \to \mathbb{R}$ are defined by

$$[Lv](s) = v(s) - \int_{-\infty}^{s} e^{-(s-t)}[\mathcal{I}v](t)\mathrm{d}t, \tag{9}$$

and

$$\begin{aligned}\mathcal{P}(\varepsilon,\iota,s,v) = {} & \int_{-\infty}^{s}\Big[p_1(\epsilon, s-t) - e^{-(s-t)}\Big][\mathcal{I}v](t) + p_1(\epsilon, s-t)\mathcal{M}(\varepsilon,\iota,t,v)\mathrm{d}t \\ & + \int_{s}^{+\infty} p_2(\epsilon, s-t)[[\mathcal{I}v](t) + \mathcal{M}(\varepsilon,\iota,t,v)]\,\mathrm{d}t.\end{aligned}$$

Our objective of the remaining part is to derive the existence of solution with ρ-periodic for equation (8).

3. The properties of L and $\mathcal{P}$

Before we study the properties of L, let's provide some results of a functional differential equation. Linearizing equation (5) at $u^*(s)$, we yield the following equation

$$\dot{v}(s) = B_1(s)v_s(0) + B_2(s)v_s(-\tau) \triangleq \mathcal{B}(s)v_s, \tag{10}$$

where $B_1(s) = -\delta$, $B_2(s) = pe^{-au^*(s-\tau)} - apu^*(s-\tau)e^{-au^*(s-\tau)}$. For system (10), we have the following results on account of the theory of delay differential equations [17].

Proposition 3.1 *(i) There exists a unique nonzero ρ-periodic solution $\dot{u^*}$ in system (10). (ii) System (10) has the adjoint equation $\dot{\chi}(s) + B_1(s)\chi^s(0) + B_2(s+\tau)\chi^s(\tau) = 0$, which admits a sole nonzero ρ-periodic solution $\chi_*(s) \in C(\mathbb{R}, \mathbb{R})$, satisfying $\langle \chi_*, \dot{u^*} \rangle \equiv 1$. (iii) For any function $F \in C_\rho$, the equation $\dot{v}(s) = \mathcal{B}(s)v_s + F(s)$ exists a solution with periodic ρ when and only when $\langle \chi_*, F \rangle = 0$.*

Moreover, for system (10), we obtain the following consequence.

Lemma 3.1 *Set $W(s) = \dot{u^*}(s) + \tau B_2(s)\dot{u^*_s}(-\tau)$, $s \in \mathbb{R}$. Then the nonhomogeneous system $\dot{v}(s) = \mathcal{B}(s)v_s + W(s)$ has no ρ-periodic solution.*

Proof. Suppose that equation $\dot{v}(s) = \mathcal{B}(s)v_s + W(s)$ has a solution $\varrho(s) \in C_\rho$. Setting $\varpi(s) = \varrho(s) - s\dot{u^*}(s)$, $s \in \mathbb{R}$, we have $\dot{\varpi}(s) = \dot{\varrho}(s) - \dot{u^*}(s) - s\ddot{u^*}(s) = \mathcal{B}(s)\varrho_s + \tau B_2(s)\dot{u^*_s}(-\tau) - s\mathcal{B}(s)\dot{u^*_s}$. Furthermore, let $R_s(0) = R(s) = s\dot{u^*}(s)$, then $\mathcal{B}(s)\varpi_s = \mathcal{B}(s)\varrho_s - \mathcal{B}(s)R_s = \mathcal{B}(s)\varrho_s - s\mathcal{B}(s)\dot{u^*_s} + \tau B_2(s)\dot{u^*_s}(-\tau)$. Hence, we yield $\dot{\varpi}(s) = \mathcal{B}(s)\varpi_s$ for all $s \in \mathbb{R}$. It is a contradiction on account of Proposition 3.1. □

Now we investigate the properties of L. Using $T(L)$ to represent the null space of L, we obtain the following lemma.

Lemma 3.2 *$T(L)$ is spanned by $\dot{u^*}$.*

Proof. Suppose that $v \in C_\rho$ is a solution of $[Lv](s) = 0$. By differentiating $[Lv](s) = 0$, we have $\dot{v}(s) = \mathcal{B}(s)v_s$. It follows Proposition 3.1 that $v = k_1\dot{u^*}$ for $k_1 \in \mathbb{R}$. Moreover, if $v = k\dot{u^*}$, then $v \in C_\rho$, and $\dot{v}(s) = \mathcal{B}(s)v_s = -v(s) + [\mathcal{I}v](s)$. We yield $v(s) = \int_{-\infty}^{s} e^{-(s-t)}[\mathcal{I}v](t)\mathrm{d}t$. Hence, we have $v = k\dot{u^*} \in T(L)$. □

Furthermore, for L, there is the following result.

Lemma 3.3 *For any function $D \in C_\rho$, the nonhomogeneous equation*

$$[Lv](s) = D(s), \tag{11}$$

exists a ρ-period solution when and only when $\langle \chi_* - \dot{\chi}_*, D \rangle = 0$.

Proof. Set $Q(s) = v(s) - D(s)$, substituting it into equation (11), we have

$$Q(s) = \int_{-\infty}^{s} e^{-(s-t)}[\mathcal{I}Q](t)\mathrm{d}t + \int_{-\infty}^{s} e^{-(s-t)}[\mathcal{I}D](t)\mathrm{d}t. \tag{12}$$

Differentiating equation (12), we yield

$$\dot{Q}(s) = \mathcal{B}(s)Q_s + [\mathcal{I}D](s). \tag{13}$$

From Proposition 3.1, we know that there is a ρ-period solution of system (13) when and only when

$$\langle \chi_*, [\mathcal{I}D] \rangle = \int_0^\rho \chi_*(s)\left[D(s) + B_1(s)D(s) + B_2(s)D(s-\tau)\right] \mathrm{d}s = 0. \tag{14}$$

Substituting $\gamma = s - \tau$ into $\int_0^\rho \chi_*(s)B_2(s)D(s-\tau)\mathrm{d}s$, then

$$\int_0^\rho \chi_*(s)B_2(s)D(s-\tau)\mathrm{d}s = \int_0^\rho \chi_*(s+\tau)B_2(s+\tau)D(s)\mathrm{d}s.$$

So, we have

$$\begin{aligned} &\int_0^\rho \chi_*(s)\left[B_1(s)D(s) + B_2(s)D(s-\tau)\right] \mathrm{d}s \\ &= \int_0^\rho \left[\chi_*(s)B_1(s) + \chi_*(s+\tau)B_2(s+\tau)\right] D(s)\mathrm{d}s \\ &= -\int_0^\rho \dot{\chi}_*(s)D(s)\mathrm{d}s. \end{aligned} \tag{15}$$

In view of systems (14) and (15), there is

$$\langle \chi_*, [\mathcal{I}D] \rangle = -\langle \dot{\chi_*}, D\rangle + \langle \chi_*, D\rangle = \langle \chi_* - \dot{\chi}_*, D\rangle = 0. \tag{16}$$

It implies that as equation (16) sets up, there is a solution $v \in C_\rho$ of equation (11). □

From Lemma 3.3, we know that system (8) has a solution v with periodic ρ when and only when $\mathcal{P}(\varepsilon, \iota, s, v) \in \mathcal{R}(L) \triangleq \{D \in C_\rho : \langle \chi_* - \dot{\chi}_*, D\rangle = 0\}$. Noticing that for any function $v \in C_\rho$, we can't ensure that $\mathcal{P}(\varepsilon, \iota, s, v) \in \mathcal{R}(L)$. As a result, the following consequences are needed.

Lemma 3.4 *$C_\rho = T(L) \oplus G_\rho$, where $G_\rho = \left\{H \in C_\rho : \langle \chi_*, H\rangle = 0\right\}$.*

Proof. For any function $v \in C_\rho$, set $v_1 = \langle \chi_*, v\rangle \dot{u^*}$ and $v_2 = v - v_1$. It follows Lemma 3.2 that $v_1 \in T(L)$. From $\langle \chi_*, \dot{u^*}\rangle = 1$, there is

$$\langle \chi_*, v_2\rangle = \langle \chi_*, v - v_1\rangle = \langle \chi_*, v\rangle - \langle \chi_*, v_1\rangle = \langle \chi_*, v\rangle - \langle \chi_*, v\rangle\langle \chi_*, \dot{u^*}\rangle = 0.$$

Furthermore, suppose that $H \in T(L) \cap G_\rho$. It follows $H \in T(L)$ that $H = g_1\dot{u^*}$ for $g_1 \in \mathbb{R}$. Moreover, from $H \in G_\rho$, we have $0 = \langle \chi_*, H\rangle = g_1\langle \chi_*, \dot{u^*}\rangle = g_1$. Then $H = 0$. □

Lemma 3.5 *$L : G_\rho \to \mathcal{R}(L)$ is a bijection.*

Proof. Noticing that $L : G_\rho \to \mathcal{R}(L)$ is onto on account of $L(G_\rho) = L(T(L) \oplus G_\rho) = L(C_\rho) = \mathcal{R}(L)$. Choosing $H_1, H_2 \in G_\rho$ such that $LH_1 = LH_2$, we have $H_1 - H_2 \in T(L)$. From Proposition 3.1, we obtain $H_1 - H_2 = g_2\dot{u^*}$ for $g_2 \in \mathbb{R}$. Furthermore, from Lemma 3.4, we have $\langle \chi_*, H_1\rangle = \langle \chi_*, H_2\rangle = 0$. $0 = \langle \chi_*, H_1 - H_2\rangle = g_2\langle \chi_*, \dot{u^*}\rangle = g_2$. Then $H_1 = H_2$. □

Finally, we give the following result for the nonlinear operator $\mathcal{P}$.

Lemma 3.6 *Extending $\mathcal{P}(\varepsilon,\iota,s,v)$ at $\varepsilon=0$ by $\mathcal{P}(0,\iota,s,v)=\int_{-\infty}^{s}e^{-(s-t)}\mathcal{N}(0,\iota,t,v)\mathrm{d}t$, $s\in\mathbb{R}$, then $\mathcal{P}(\varepsilon,\iota,\cdot,v)$ and $\frac{\partial}{\partial v}(\mathcal{P}(\varepsilon,\iota,\cdot,v))$ are both continuous functions on (ε,ι,v). Moreover, there exist $\mathcal{P}(0,0,\cdot,0)=0$ and $\frac{\partial}{\partial v}(\mathcal{P}(0,0,\cdot,0))=0$.*

Proof. For $s\in\mathbb{R}$, we yield $\int_{-\infty}^{s}\left[p_1(\epsilon,s-t)-e^{-(s-t)}\right]v(t)\mathrm{d}t\le\frac{1-[2+\lambda_1(\epsilon)]\sqrt{1+4\epsilon d}}{\lambda_1(\epsilon)\sqrt{1+4\epsilon d}}\|v\|_{C_\rho}$. Noticing that $\epsilon=\frac{\varepsilon}{1+\iota}\to 0$ and $\lambda_1(\epsilon)\to -1$ as $\varepsilon\to 0^+$, we have $1-[2+\lambda_1(\epsilon)]\sqrt{1+4\epsilon d}\to 0$ as $\varepsilon\to 0^+$. Moreover, we obtain $\int_{s}^{+\infty}p_2(\epsilon,s-t)v(t)\mathrm{d}t\le\frac{1}{\lambda_2(\epsilon)\sqrt{1+4\epsilon d}}\|v\|_{C_\rho}$. It follows from $\lambda_2(\epsilon)\to\infty$ as $\varepsilon\to 0^+$ that $\frac{1}{\lambda_2(\epsilon)\sqrt{1+4\epsilon d}}\to 0$ as $\varepsilon\to 0^+$. So, we yield $\mathcal{P}(0,\iota,s,v)=\int_{-\infty}^{s}e^{-(s-t)}\mathcal{N}(0,\iota,t,v)\mathrm{d}t$. According to the definition of $\mathcal{M}(\varepsilon,\iota,\cdot,v)$, $\mathcal{M}(\varepsilon,\iota,\cdot,v)$ and $\frac{\partial}{\partial v}(\mathcal{M}(\varepsilon,\iota,\cdot,v))$ are continuous. Furthermore, there exist $\mathcal{M}(0,0,\cdot,0)=0$ and $\frac{\partial}{\partial v}(\mathcal{M}(0,0,\cdot,0))=0$. According to the definition of $\mathcal{P}(\varepsilon,\iota,\cdot,v)$, $\mathcal{P}(\varepsilon,\iota,\cdot,v)$ and $\frac{\partial}{\partial v}(\mathcal{P}(\varepsilon,\iota,\cdot,v))$ are continuous and satisfy $\mathcal{P}(0,0,\cdot,0)=0$ and $\frac{\partial}{\partial v}(\mathcal{P}(0,0,\cdot,0))=0$. □

4. Periodic travelling waves

Next, we prove the existence of ρ-periodic solution for system (8). From Lemma 3.4, for any $v\in C_\rho$, we have $v=\varsigma\dot{u}^*+H$, where $\varsigma\in\mathbb{R}$ and $H\in G_\rho$. Substituting it into equation (8), we yield

$$[LH](s)=\mathcal{P}(\varepsilon,\iota,s,\varsigma\dot{u}^*+H). \tag{17}$$

Next, we need to guarantee $\mathcal{P}(\varepsilon,\iota,s,\varsigma\dot{u}^*+H)\in\mathcal{R}(L)$ on account of solve equation (17). Introducing the operator $\mathcal{F}:C_\rho\to C_\rho$ be defined by

$$[\mathcal{F}v](s)=\frac{1}{\langle\chi_*,\chi_*^T\rangle}\langle\chi_*-\dot{\chi}_*,v\rangle\chi_*^T(s),\quad s\in\mathbb{R}.$$

For any function $v\in C_\rho$, we have

$$\langle\chi_*-\dot{\chi}_*,v-\mathcal{F}v\rangle=\frac{1}{\langle\chi_*,\chi_*^T\rangle}\langle\chi_*-\dot{\chi}_*,v\rangle\langle\dot{\chi}_*,\chi_*^T\rangle.$$

Noticing that $\langle\dot{\chi}_*,\chi_*^T\rangle=\int_0^\rho\dot{\chi}_*(s)\chi_*^T(s)\mathrm{d}s=\frac{1}{2}\chi_*(s)\chi_*^T(s)|_0^\rho=0$, we yield $\langle\chi_*-\dot{\chi}_*,v-\mathcal{F}v\rangle=0$ and $(I-\mathcal{F})v\in\mathcal{R}(L)$. Thus system (17) reduces to

$$[LH](s)=(I-\mathcal{F})\mathcal{P}(\varepsilon,\iota,s,\varsigma\dot{u}^*+H),\quad H\in G_\rho, \tag{18}$$

and

$$\mathcal{F}\mathcal{P}(\varepsilon,\iota,s,\varsigma\dot{u}^*+H)=0,\quad H\in G_\rho. \tag{19}$$

It follows Lemma 3.5 that system (18) becomes

$$H=L^{-1}(I-\mathcal{F})\mathcal{H}(\varepsilon,\iota,\cdot,\varsigma\dot{u}^*+H). \tag{20}$$

Define $\Phi : \mathbb{R}\times[-\iota^*,\iota^*]\times\mathbb{R}\times G_\rho$ by $\Phi(\varepsilon,\iota,\varsigma,H) = H - L^{-1}(I-\mathcal{F})\mathcal{P}(\varepsilon,\iota,\cdot,\varsigma\dot{u^*}+H)$. System (20) is equivalent to $\Phi(\varepsilon,\iota,\varsigma,H)=0$. Form Lemma 3.6, we have $\Phi(0,0,0,0)=0$ and $\frac{\partial}{\partial H}(\Phi(0,0,0,0)) = I - L^{-1}(I-\mathcal{F})\frac{\partial}{\partial v}(\mathcal{P}(0,0,\cdot,0)) = I$. Hence, there exist a number $0<a^*\le \iota^*$ and a continuous function $H:[0,a^*]\times[-a^*,a^*]\times[-a^*,a^*]\to G_\rho$ such that $H(0,0,0)=0$, $\Phi(\varepsilon,\iota,\varsigma,H(\varepsilon,\iota,\varsigma))=0$ and $[LH(\varepsilon,\iota,\varsigma)](s) = (I-\mathcal{F})\mathcal{P}(\varepsilon,\iota,s,\varsigma\dot{u^*}+H(\varepsilon,\iota,\varsigma))$. Substituting $H(\varepsilon,\iota,\varsigma)$ into system (19), we obtain

$$\mathcal{F}\mathcal{P}(\varepsilon,\iota,s,\varsigma\dot{u^*}+H(\varepsilon,\iota,\varsigma))=0, \tag{21}$$

which is equivalent to

$$\int_0^\rho \Big[\chi_*(s)-\dot{\chi}_*(s)\Big]\mathcal{P}(\varepsilon,\iota,s,\varsigma\dot{u^*}+H(\varepsilon,\iota,\varsigma))\mathrm{d}s=0. \tag{22}$$

Define $\Psi:[0,a^*]\times[-a^*,a^*]\times[-a^*,a^*]\to\mathbb{R}$ by $\Psi(\varepsilon,\iota,\varsigma)=\int_0^\rho\Big[\chi_*(s)-\dot{\chi}_*(s)\Big]\mathcal{P}(\varepsilon,\iota,s,\varsigma\dot{u^*}+H(\varepsilon,\iota,\varsigma)))\mathrm{d}s$. Then we have

$$\Psi(\varepsilon,\iota,\varsigma)=0. \tag{23}$$

It follows $H(0,0,0)=0$ and $\mathcal{P}(0,0,\cdot,0)=0$ that $\Psi(0,0,0)=0$. Moreover, we need to prove that $\frac{\partial}{\partial\iota}(\Psi(0,0,0))\neq 0$. Suppose that $\frac{\partial}{\partial\iota}(\Psi(0,0,0))=0$, we obtain

$$\frac{\partial}{\partial\iota}\left(\mathcal{F}\mathcal{P}(0,\iota,\cdot,H(0,\iota,0))\right)\Big|_{\iota=0}=0. \tag{24}$$

In view of systems (18) and (24), we yield

$$L\left(\frac{\partial}{\partial\iota}(H(0,\iota,0))\right)=\frac{\partial}{\partial\iota}\left(\mathcal{P}(0,\iota,\cdot,H(0,\iota,0))\right)\Big|_{\iota=0}. \tag{25}$$

From Lemma 3.6 and the expression of $\mathcal{M}$, there are

$$\mathcal{P}(0,\iota,s,v)=\int_{-\infty}^{s}e^{-(s-t)}\mathcal{M}(0,\iota,t,v)\mathrm{d}t, \tag{26}$$

and

$$\frac{\partial}{\partial\iota}\left(\mathcal{M}(0,\iota,t,H(0,\iota,0))\right)\Big|_{\iota=0}=W(t). \tag{27}$$

From equations (25), (26) and (27), we yield

$$\begin{aligned}\left[L\left(\frac{\partial}{\partial\iota}(H(0,\iota,0))\right)\right](s) &= \frac{\partial}{\partial\iota}(H(0,\iota,0))(s)-\int_{-\infty}^{s}e^{-(s-t)}\left[\mathcal{I}\left(\frac{\partial}{\partial\iota}(H(0,\iota,0))\right)\right](t)\mathrm{d}t\\ &=\int_{-\infty}^{s}e^{-(s-t)}W(t)\mathrm{d}t.\end{aligned}$$

Differentiating the above equation, we have $\frac{\partial}{\partial \iota}(\dot{H}(0,\iota,0))(s) = \mathcal{B}(s)\left[\frac{\partial}{\partial \iota}(H(0,\iota,0))\right]_s + W(s)$. Because $\frac{\partial}{\partial \iota}(H(0,\iota,0))(s)$ is not a function with ρ-periodic, it leads to a contradiction. Hence, we have $\frac{\partial}{\partial \iota}(\Psi(0,0,0)) \neq 0$. For system (23), we yield that there exist a number $0 < \varepsilon_* = \frac{1}{c_*{}^2} \leq a^* \leq \iota^*$ and a continuous function $\iota : [0,\varepsilon_*]\times[-\varepsilon_*,\varepsilon_*] \to \mathbb{R}$ such that $\iota(0,0) = 0, \Psi(\varepsilon,\iota(\varepsilon,\varsigma),\varsigma) = 0, (\varepsilon,\varsigma) \in [0,\varepsilon_*]\times[-\varepsilon_*,\varepsilon_*]$. Hence, the following consequence can be obtained.

Theorem 4.1 *When $p > \delta e^2$, there exists a sufficiently large number $c_* > 0$ such that, for each wave speed $c > c_*$, equation (2) has a $[1+\iota(\varepsilon,\varsigma)]\rho$-periodic travelling wave solution*

$$D(x,t) = u^*\left(\frac{\nu\cdot x + ct}{c[1+\iota(\varepsilon,\varsigma)]}\right) + \varsigma\dot{u^*}\left(\frac{\nu\cdot x + ct}{c[1+\iota(\varepsilon,\varsigma)]}\right) + H(\varepsilon,\iota(\varepsilon,\varsigma),\varsigma)\left(\frac{\nu\cdot x + ct}{c[1+\iota(\varepsilon,\varsigma)]}\right).$$

References

[1] Gurney WSC, Blythe SP, Nisbet RM. Nicholson's blowflies revisited. Nature. 1980 Jun;287(5777): 17-21.

[2] Kulenović MRS, Ladas G. Linearized oscillations in population dynamics. Bulletin of Mathematical Biology. 1987 Jan;49(5): 615-27.

[3] Kulenović MRS, Ladas G, Sficas YG. Global attractivity in Nicholson's blowflies. Applicable Analysis. 1992;43(1-2):109-24.

[4] Yi TS, Zou XF. Global attractivity of the diffusive Nicholson blowflies equation with Neumann boundary condition: a non-monotone case. Journal of Differential Equations. 2008 Apr;245(11):3376-88.

[5] Berezansky L, Braverman E, Idels L. Nicholson's blowflies differential equations revisited: main results and open problems. Applied Mathematical Modelling. 2010 Aug;34(6):1405-17.

[6] Ding HS, Nieto JJ. A new approach for positive almost periodic solutions to a class of Nicholson's blowflies model. Journal of Computational and Applied Mathematics. 2013 Mar;253:249-54.

[7] Li JW, Du CX. Existence of positive periodic solutions for a generalized Nicholson's blowflies model. J. Comput. Appl. Math. 2008;221:226-33.

[8] So JWH, Yang YJ. Dirichlet problem for the diffusive Nicholson's blowflies equation. Journal of Differential Equations. 1998 Dec;150(2):317-48.

[9] So JWH, Zou XF. Traveling waves for the diffusive Nicholson's blowflies equation. Applied Mathematics and Computation. 2001 Aug;122(3):385-92.

[10] Faria T, Trofimchuk S. Nonmonotone traveling waves in a single species reaction-diffusion equation with delay. Journal of Differential Equations. 2006 Sep;228(1):357-76.

[11] Lin CK, Mei M. On travelling wavefronts of Nicholson's blowflies equation with diffusion. Proceedings of the Royal Society of Edinburgh Section A: Mathematics. 2010 Feb;140(1):135-52.

[12] Mei M, So JWH, Li MY, Shen SSP. Asymptotic stability of travelling waves for Nicholson's blowflies equation with diffusion. Proceedings of the Royal Society of Edinburgh Section A: Mathematics. 2004 Jun;134(3):579-94.

[13] Yang GX, Zhao LL. Hopf bifurcation of traveling wave of delayed Nicholson's blowflies equation. J. Biomath. 2011;26(1):81-6.

[14] Duehring D, Huang WZ. Periodic traveling waves for diffusion equations with time delayed and nonlocal responding reaction. Journal of Dynamics and Differential Equations. 2007 Jan;19(2):457-77.

[15] Li D, Guo SJ. Periodic traveling waves in a reaction-diffusion model with chemotaxis and nonlocal delay effect. Journal of Mathematical Analysis and Applications. 2018 Jul;467(1):1080-99.

[16] Li D, Wu XX, Yan SL. Periodic traveling wave solutions of the Nicholsons blowflies model with delay and advection. Electronic Research Archive. 2023 Mar;31(5):2568-79.

[17] Hale JK, Verduyn Lunel SM. Introduction to functional differential equations. Springer-Verlag, New York, 2013.

Fuzzy Systems and Data Mining IX
A.J. Tallón-Ballesteros and R. Beltrán-Barba (Eds.)

doi:10.3233/FAIA231066

Crop Pest Image Classification Based on Multi-Scale Convolutional Neural Network

Chi Ma [a], Huikai Li [b,1], Hui Hu [a], Jingyan Li [a] and Jie Wu [b]
[a] *School of Computer Science and Engineering, Huizhou University, 516007, Huizhou, China*
[b] *School of Computer Science and Software Engineering, University of Science and Technology Liaoning, 114051, Anshan, China*

Abstract. Crop diseases and pests are major threats to crop yield and quality, as well as global food security and agricultural livelihoods. Therefore, it is essential to identify crop pests and diseases in a timely, efficient and accurate manner. In this paper, we propose MConvNeXt, a crop pest classification model based on multi-scale feature fusion, which adds a multi-scale module to the original ConvNeXt network model to better capture feature information at different scales. We experimentally analyzed the MConvNeXt model on the IP102 dataset, and the results show that it outperforms the baseline network and other classical image classification models in pest classification.

Keywords. Crop pest classification, Multi-scale feature, Convolutional neural networks

1. Introduction

Pests are one of the most important factors affecting the yield and quality of crops, especially crops susceptible to pests and diseases such as maize, wheat and rice. Failure to deal with crop pests in a timely manner will result in huge economic losses to agricultural practitioners. Therefore, early identification and accurate classification of these pests is essential. For traditional pest classification tasks, selecting and designing appropriate feature extraction methods requires expertise and experience, which is often influenced by human factors and subjectivity, leading to challenges in the accuracy and consistency of results. In addition, traditional methods have low generalization capability and require feature and classifier redesign and adjustment for new pest species or scenarios. These drawbacks limit the accuracy, robustness and usefulness of traditional pest classification methods. With the emergence of deep learning techniques in recent years, overcoming some limitations of traditional methods, it has gained wide attention in the field of pest recognition and achieved good results. Compared with traditional methods, convolutional neural network-based methods can extract pest feature information in complex environments more efficiently and accurately [1][2][3][4]. Cheng et al. [5] proposed a pest recognition method using deep

[1] Corresponding Author: Huikai Li, University of Science and Technology Liaoning, 114051, Anshan, China; E-mail: 372575716@qq.com.
This work is supported by the Foundation of Guangdong Educational Committee (Grant No. 2022ZDZX4052, 2021ZDJS082, 2019KQNCX148).

residual learning, which achieves high recognition accuracy for pest images in complex farmland backgrounds. Li et al. [6] proposed a fine-tuned GoogLeNet model to handle pest recognition in complex farmland backgrounds, and the proposed model classified ten classes of pests with excellent results. Yang et al. [7] proposed a convolutional rebalancing network for classifying rice pests and diseases that outperformed the state-of-the-art methods of the time. Gu et al. [8] used lightweight deep neural network structures and edge computing techniques to achieve efficient crop disease identification. Waheed et al. [9] proposed a DenseNet optimization model for maize leaf identification that uses fewer parameters to improve efficiency. Ayan E et al. [10] proposed an integrated convolutional neural network model GAEnsemble, which achieved 67.13% accuracy on the IP102 dataset. Ung et al. [11] proposed a new convolutional neural network model for pest identification that combines an attention model, a feature pyramid model, and a fine-grained model, achieving an accuracy of 74.13% on the IP102 dataset. In summary, despite the progress made after applying convolutional neural networks in pest recognition, there are still challenges in the field of pest recognition due to the complex environmental background and uneven distribution of pest images usually. In order to reduce the impact of the above problems on the recognition accuracy, we designed a multi-scale deep learning model (MConvNeXt), which is designed to solve the problem of the complex environmental background and the difficulty of capturing the pest region.

The main contributions of this paper are as follows:

- We add a multi-scale feature fusion module to the original ConvNeXt network model, which can better capture feature information at different scales.
- Through experimental analysis on the IP102 dataset, the results show that our proposed MConvNeXt network model outperforms other classical image classification models in terms of classification performance.

2. Material and Model

2.1. Dataset

The experiments used the IP102 [12] dataset proposed by Wu et al. This dataset is a large benchmark dataset for pest recognition, containing more than 75,000 pest images of 102 species, consisting of 45,095 training images, 7,508 validation images and 22,619 test images. Due to the similarity between the color of the pests and their environmental background, and the fact that this dataset contains images of the entire life cycle of the pests from larvae to adults, it makes it more challenging for the deep learning model to extract features from them. In order to increase the generalization ability of the model, we used data enhancement techniques during the training process by randomly flipping, rotating and center cropping the original pest images.

2.2. MConvNeXt

ConvNeXt [13] is a convolutional neural network model proposed by Facebook AI Institute, which is a pure convolutional network model that draws on the idea of Swin Transformer [14] to gradually improve, and it absorbs the advantages of a variety of transformer structures in the network structure setting and parameter selection. As the

pests in the IP102 dataset have different morphologies and complex environmental backgrounds. Therefore, the ConvNeXt network model has some difficulties in the accurate recognition of pests. In order to allow the model to extract feature information at different scales, we proposed the MConvNeXt network model, whose overall structure is shown in Figure 1. The model replaces the ConvNeXt Block in the original network with the MConvNeXt Block that can extract multi-scale feature information. The MConvNeXt Block changes the original 7×7 depthwise separable convolution into a parallel branching structure consisting of 3×3, 5×5 and 7×7 to increase the perceptual field of the model, and then fuses the information from different scales as shown in Eq. (1). The inference time can be reduced while extracting multi-scale information.

$$F_1 = concat\left(F_{11}, F_{12}, F_{13}\right) \tag{1}$$

Where F11, F12, and F13 are three feature maps obtained from the depth convolution of three different sizes, 'concat' is the concatenation operation, and F1 indicates the output feature map.

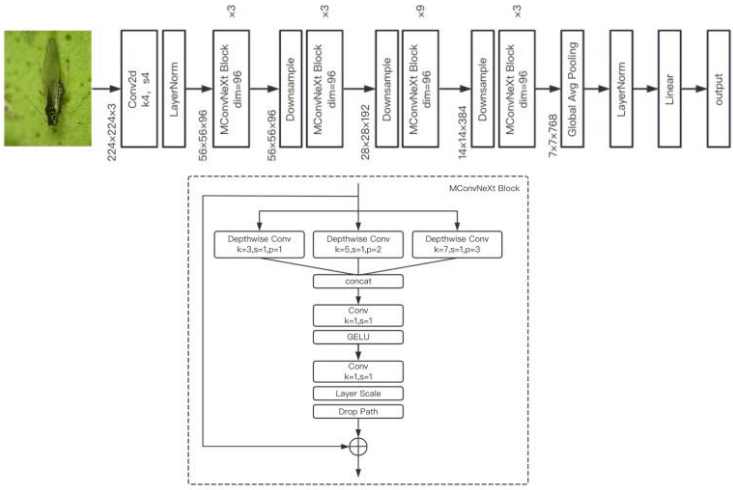

Figure 1. MConvNeXt model structure.

3. Experiments

3.1. Experiment Settings

To ensure the fairness of the experiments, all the experiments were conducted in the same environment. When training the model, the input size of the images was uniformly set to 224 × 224. Cross-entropy was chosen as the loss function, and AdamW was adopted as the training optimizer. The initial learning rate is set to 0.001, the batch size is set to 32, the number of iterations is set to 50. The initialization parameters are loaded with the pre-training weights of ConvNeXt on ImageNet.

3.2. Model Evaluation

In order to measure the classification performance of different models on the IP102 dataset, we choose Accuracy, Precision, Recall and F1-score as the evaluation metrics of the models, as shown in Eqs. (2)-(5).

$$Accuracy = \frac{TP + TN}{TP + TN + FP + FN} \tag{2}$$

$$Precision = \frac{TP}{TP + FP} \tag{3}$$

$$Recall = \frac{TP}{TP + FN} \tag{4}$$

$$F1 - score = \frac{2 \times Precision \times Recall}{Precision + Recall} \tag{5}$$

Where TP, TN, FP and FN are True Positive, True Negative, False Positive and False Negative, respectively. Accuracy denotes the proportion of samples correctly predicted by the model out of the total samples, as shown in Eq. (2). Precision is the proportion of correct predictions in samples where the prediction is a positive example, as shown in Eq. (3). Recall is a judgment based on actual samples, and the proportion of correctly predicted positive cases out of the samples that were actually positive cases out of the total actual positive case samples, as shown in Eq. (4). The F1-score is a weighted harmonic mean of precision and recall, as shown in Eq. (5).

3.3. Comparison experiments with other models

To measure the classification performance of the MConvNeXt model, we compared it with some classical image classification models with comparable number of parameters, such as ResNet-50 [15], ResNeXt-50 [16], Efficientnet-b4 [17], DenseNet-161 [18], and Swin-T. As shown in Figure 2, we compare the classification accuracy curves of each model on the validation set. As can be seen from the figure, after 20 rounds of iterations, the performance of each model on the validation set tends to stabilize. Among them, the ResNet-50 and ResNeXt-50 models perform slightly worse compared to the other models, and the MConvNeXt model has a higher classification accuracy at each iteration than the other image classification models in this experiment. At the same time, we evaluated each model using evaluation metrics, and as shown in Table 1, the MConvNeXt model achieved the best results on all evaluation metrics.

Table 1. Performance Comparison with Other Convolutional Neural Networks.

Model	Parameters	Precision (%)	Recall (%)	F1-Score (%)	Accuracy (%)
ResNet-50	23M	69.89	68.93	69.13	71.01

ResNeXt-50	23M	70.68	69.25	70.25	71.32
EfficientNet-b4	19M	71.30	72.01	71.29	72.07
DenseNet-161	28M	73.66	73.38	73.60	73.91
Swin-T	28M	72.55	72.13	71.62	73.38
MConvNeXt	28M	73.72	73.51	73.67	74.76

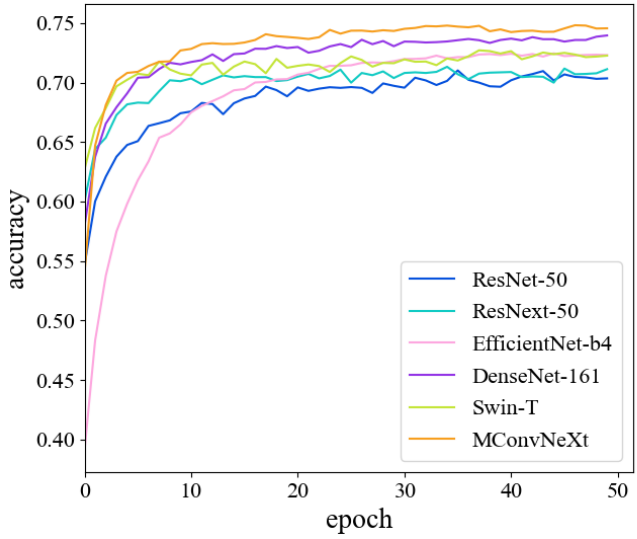

Figure 2. Accuracy of different models on the validation set.

3.4. Ablation Experiment

In order to verify whether the MConvNeXt model has an improvement in performance compared to the benchmark model, we conducted an ablation experiment and the results are shown in Table 2.

Table 2. Ablation Experiment Results.

Model	Parameters	Precision (%)	Recall (%)	F1-Score (%)	Accuracy(%)
ConvNeXt	28M	73.26	73.61	73.29	74.12
MConvNeXt	28M	73.72	73.51	73.67	74.76

The results of the ablation experiments in Table 2 show that our proposed model achieves the best results in terms of Precision, F1-Score and Accuracy, which are improved by 0.46%, 0.38% and 0.64%, respectively. These data indicate that the multi-scale module can improve the network's ability to extract information about pest features at different scales to a certain extent, thus improving the recognition accuracy of the model.

4. Conclusion

Crop pest classification is an important and challenging research area because of the wide variety of crop pests, different morphologies, different colors, and complex field environments. In order to reduce the impact of the above problems on the recognition accuracy, we designed a deep learning model for pest recognition with multi-scale feature fusion and conducted a series of experiments on pest images in complex environmental contexts. The experimental results show that our proposed MConvNeXt model has higher recognition accuracy than other classical image classification models on the IP102 dataset. Therefore, the deep learning model proposed in this paper can be applied to the automatic identification and classification system of crop pests.

References

[1] Xia D, Chen P, Wang B, Zhang J, Xie C. Insect Detection and Classification Based on an Improved Convolutional Neural Network. Sensors. 2018;18(12):4169.
[2] Li W, Wang D, Li M, Gao Y, Wu J, Yang X. Field detection of tiny pests from sticky trap images using deep learning in agricultural greenhouse. Computers and Electronics in Agriculture. 2021;183:106048.
[3] Khanramaki M, Askari Asli-Ardeh E, Kozegar E. Citrus pests classification using an ensemble of deep learning models. Computers and Electronics in Agriculture. 2021;186:106192.
[4] Thenmozhi K, Srinivasulu Reddy U. Crop pest classification based on deep convolutional neural network and transfer learning. Computers and Electronics in Agriculture. 2019;164:104906.
[5] Cheng X, Zhang Y, Chen Y, Wu Y, Yue Y. Pest identification via deep residual learning in complex background. Computers and Electronics in Agriculture. 2017;141:351–356.
[6] Li Y, Wang H, Dang LM, Sadeghi-Niaraki A, Moon H. Crop pest recognition in natural scenes using convolutional neural networks. Computers and Electronics in Agriculture. 2020;169:105174.
[7] Yang G, Chen G, Li C, Fu J, Guo Y, Liang H. Convolutional Rebalancing Network for the Classification of Large Imbalanced Rice Pest and Disease Datasets in the Field. Front Plant Sci. 2021;12:671134.
[8] Gu M, Li K-C, Li Z, Han Q, Fan W. Recognition of Crop Diseases Based on Depthwise Separable Convolution in Edge Computing. Sensors. 2020;20:4091.
[9] Waheed A, Goyal M, Gupta D, Khanna A, Hassanien AE, Pandey HM. An optimized dense convolutional neural network model for disease recognition and classification in corn leaf. Computers and Electronics in Agriculture. 2020;175:105456.
[10] Ayan E, Erbay H, Varçın F. Crop pest classification with a genetic algorithm-based weighted ensemble of deep convolutional neural networks. Computers and Electronics in Agriculture. 2020;179:105809. doi: 10.1016/j.compag.2020.105809.
[11] Ung H T, Ung H Q, Nguyen B T. An efficient insect pest classification using multiple convolutional neural network based models. arXiv preprint arXiv:2107.12189, 2021.
[12] Wu X, Zhan C, Lai Y K, et al. Ip102: A large-scale benchmark dataset for insect pest recognition. Proceedings of the IEEE/CVF conference on computer vision and pattern recognition. 2019: 8787-8796.
[13] Liu Z, Mao H, Wu C Y, et al. A convnet for the 2020s. Proceedings of the IEEE/CVF conference on computer vision and pattern recognition. 2022: 11976-11986.
[14] K Liu Z, Lin Y, Cao Y, et al. Swin transformer: Hierarchical vision transformer using shifted windows. Proceedings of the IEEE/CVF international conference on computer vision. 2021: 10012-10022.
[15] He K, Zhang X, Ren S, et al. Deep residual learning for image recognition. Proceedings of the IEEE conference on computer vision and pattern recognition. 2016: 770-778.
[16] Xie S, Girshick R, Dollár P, et al. Aggregated residual transformations for deep neural networks. Proceedings of the IEEE conference on computer vision and pattern recognition. 2017: 1492-1500.
[17] Tan M, Le Q. Efficientnet: Rethinking model scaling for convolutional neural networks. International conference on machine learning. PMLR, 2019: 6105-6114.
[18] Huang G, Liu Z, Van Der Maaten L, et al. Densely connected convolutional networks. Proceedings of the IEEE conference on computer vision and pattern recognition. 2017: 4700-4708.

Fuzzy Systems and Data Mining IX
A.J. Tallón-Ballesteros and R. Beltrán-Barba (Eds.)

doi:10.3233/FAIA231067

Hyperparameter Adaptive Neural Network Model for E-Commerce Sales Prediction

GuangLu Zhao[a], Ran Tian[a,1] and JingXia Wang[a]
[a] *College of Computer Science & Engineering, Northwest Normal University, China*

Abstract. Sales forecasting plays a vital role in the daily operations of e-commerce companies, impacting market assessment, operational planning, and supply chain management. As the market is constantly changing, accurately predicting sales is a critical challenge that e-commerce companies need to urgently address. However, traditional statistical forecasting methods have disadvantages such as long run times, low accuracy, weak generalization, and strong data periodicity, which lead to unnecessary losses for companies. We propose the QLBiGRU model that utilizes the reinforcement learning Q-Learning algorithm combined with BiGRU to improve forecasting accuracy. Automatic parameter optimization technology is also used to reduce training time and demand for hardware resources, thereby enabling enterprices to accurately analyze the market and make informed decisions.

Keywords. Sales Forecast, Automatic Parameter Optimization, Reinforcement Learning, BiGRU

1. Introduction

With the rapid development of the e-commerce industry, the e-commerce sales system generates a large amount of data. Sales data, as typical time series data, directly reflects the characteristics of commodity circulation and can be collected and utilized to predict sales at a certain point in the future or within a certain period. This is very important for e-commerce companies to formulate reasonable business plans and sales plans based on past experience. However, due to the influence of various factors such as seasons and promotional activities, it is difficult to accurately predict product sales. Inaccurate forecasts can lead to excess inventory and increased costs or lost sales. Therefore, accurate and efficient merchandise sales forecasting is key to reducing uncertainty, minimizing inventory buildup, and reducing opportunity costs.

Traditional statistical methods, such as the Markov model[1], Prophet model[2], autoregressive moving average (ARIMA) [3], etc., have limitations due to the inability to solve problems such as data periodicity and perform poorly. The rise of deep learning has brought better prediction results, but the hyperparameters of the model, such as learning rate, number of iterations, and batch size, can be difficult to determine and require a lot of effort and cost to set. Therefore, optimizing hyperparameters is crucial for predictive models.

[1] Corresponding Author, Ran Tian, College of Computer Science & Engineering, Northwest Normal University, China; E-mail: tianran@nwnu.edu.cn

(1) We propose a prediction model QLBiGRU based on Q-Learning and BiGRU, and optimize the hyperparameters of the BiGRU model, such as the number of neurons, the number of iterations, and the learning rate, to improve the prediction accuracy.

(2) We conducted experiments with different prediction lengths and performance optimization experiments and used multiple data sets to verify the prediction performance and hyperparameter optimization capabilities of the QLBiGRU model. The experimental results validate the effectiveness and superiority of the model.

The rest of the paper is organized as follows, and in section 2, we report a summary of research related to e-commerce sales prediction and hyperparameter optimization. Section 3 presents a detailed description of QLBiGRU. In section 4, we conduct sufficient experiments to verify the validity of the proposed model in section 3. The full paper is summarized in section 5.

2. Background

2.1. E-commerce Sales Prediction

E-commerce sales forecasting is a subfield of time series forecasting that utilizes models to predict future trends, directions, and development processes within a time series. While commonly used classical statistical forecasting methods, including linear regression (LR) and autoregressive moving average model (ARIMA), have limitations such as underfitting, the Prophet-SARIMA model has been proposed by Zhao et al. [4] to solve these problems. The SARIMA model helps improve the limitations of the ARIMA model by accounting for data periodicity, and the Prophet model applies to a wide range of forecasting problems with potential unique features. Combining these models allows for better identification of change points, seasonality, holidays, and emergencies in time series data. However, since training and prediction must be conducted separately, any updates to the model require retraining. Additionally, the Prophet model is not suitable for identifying complex patterns. Markov models are also utilized in time series forecasting; however, these models have limitations in forecasting problems due to the lack of relevance between current and historical data. With the development of deep learning, the use of the recurrent neural network (RNN), long short-term memory (LSTM), and gated recurrent unit (GRU) have shown to improve prediction results. Liu et al. [5] proposed an RNN-based model for vehicle mobility prediction and a rolling subway passenger flow prediction model, while Wang et al. [6] used the LSTM model to solve traffic forecasting problems. While the traditional statistical method has limitations with periodic data, deep learning methods have more accurate predictions but face complexity in training and parameter adjustment.

2.2. Hyperparameter optimization

The selection of hyperparameters for neural network models is a test of researchers' experience and often requires numerous adjustments to achieve better results. As such, automatic optimization of hyperparameters has garnered attention from many researchers in recent years. Shao et al. employed an improved Particle Swarm Optimization (PSO) algorithm to optimize nickel price predictions based on the LSTM

neural network[7]. This method utilized the enhanced PSO algorithm to optimize the number of neurons in the LSTM network. However, the PSO algorithm is prone to falling into local optimal solutions when optimizing neural network parameters. To address this issue, Han et al. proposed an improved Adaptive Particle Swarm Optimization (APSO) algorithm for optimizing rainy road traffic speed prediction model parameters of the GRU network[8]. They used an adaptive nonlinear inertia weight method to strike a balance between the PSO algorithm's local and global search capabilities. Yang et al. suggested an enterprise network marketing prediction model based on a Genetic Algorithm (GA)-optimized BP neural network[9]. However, due to the algorithm's randomness, the local search capability of the GA is poor. Grid search is another common optimization technique; B.D. et al. utilized this method to optimize the hyperparameters of a machine learning model, leading to improved predictions[10]. Traditional grid search algorithms, though, suffer from an excessively large invalid search range and sensitivity to search step size. To overcome these drawbacks, Sun et al. proposed an improved grid search algorithm to optimize the relevant parameter values of the Support Vector Regression (SVR) model, resulting in more accurate predictions[11].

Most traditional optimization algorithms tend to operate slowly and fall into local optimal solutions. In contrast, reinforcement learning has recently gained popularity for its efficient optimization capabilities. Wu et al. introduced an efficient model-based hyperparameter optimization method that models the optimization process as a reinforcement learning model, allowing an agent to sequentially tune hyperparameters and dynamically adjust the usage model[12]. Chen et al. applied deep reinforcement learning with model acceleration to address hyperparameter optimization problems[13]. This method incorporated a predictive reward value module and a guide pool to steer the agent's exploration in the search space, ultimately reducing search time and enhancing search efficiency.

In conclusion, traditional optimization algorithms generally suffer from slow convergence speed, low solution accuracy, and a tendency to fall into local optima. Reinforcement learning-based optimization algorithms, on the other hand, demonstrate high search efficiency and deliver solution strategies from scratch, with superior efficiency, robustness, and generalization.

3. Model Definition

3.1. QLBiGRU

We establish the three parameters to be optimized as a state, generating a set of actions in each state. The agent continuously interacts with the environment to find the optimal strategy. Initially, predictions are made based on the environment's initial state, resulting in a set of actions $A = [a_1, a_2, a_3]$, which serves as the initial strategy. This strategy is then executed within the environment, and the resulting RMSE value is provided as a reward signal. The Q table is updated accordingly. Next, predictions are made based on the updated strategy using the ε-greedy strategy with $\varepsilon = 0.9$ to sample. The output is a new strategy $A' = [a'_1, a'_2, a'_3]$, and the reward value under this updated strategy is calculated. Here, A represents the initial strategy, while A' represents the updated strategy. During the BiGRU prediction phase, standardized data is sent to the three-layer BiGRU network for computation, and the prediction result is generated (see Fig. 1).

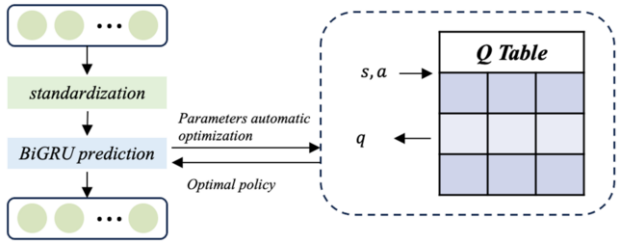

Fig. 1. QLBiGRU framework

First, we define the state. The state in this article is the three hyperparameters that need to be optimized for the BiGRU model, which are the number of neurons, the number of iterations, and the learning rate, as shown below:

$$S = [s1, s2, s3] \tag{1}$$

Among them, s_1 represents the state of the number of neurons, s_2 represents the state of the number of iterations, and s_3 represents the state of the learning rate.

We send the state S into the BiGRU model for prediction and update the model after execution. When updating the Q table (Formula 2), we expect to get the minimum Q value, so the difference between the Q value of the previous state and the subsequent state is calculated to obtain a better Q value and then a better strategy:

$$Q(s,a) = Q(s,a) - \alpha Q(s',a') - Q(s,a) \tag{2}$$

Among them, $Q(s,a)$ represents the Q value of the current state, $Q(s',a')$ represents the Q value of the next state, $Q(s',a')$is calculated as follows:

$$Q(s',a') = \begin{cases} R(s,a) - \gamma max Q(s',a'), \text{NT} \\ R(s,a), T \end{cases} \tag{3}$$

Among them, NT is "not terminate" and T is "Terminated", α is the learning rate, $\gamma \in [0,1]$ is the discount factor, $R(s,a)$ means to take an action a in state s and transfer to s' The reward function value obtained in the prime state, a' is the next action a chosen by the greedy strategy. The calculation of the reward function in this chapter is defined as follows:

$$R(s,a) = RMSE(s,a) \tag{4}$$

Among them, the value of $R(s,a)$ is the RMSE value obtained by executing action a in state s.

3.2. BiGRU

During the experiment, we constructed a three-layer BiGRU network. Each layer of the BiGRU consists of two GRUs connected in series but in opposite directions. The output of each layer is determined collaboratively by these two GRUs, as illustrated in Fig.2.

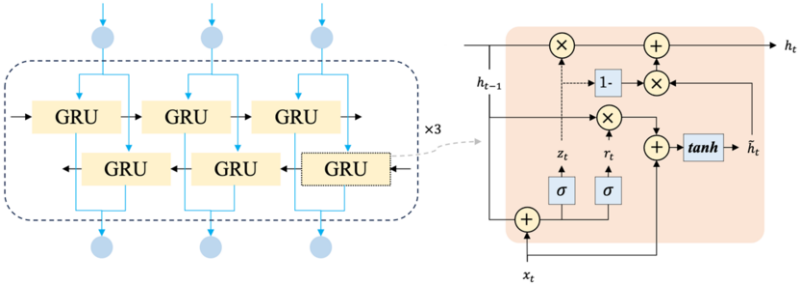

Fig. 2. BiGRU model structure

After the sales data is passed into BiGRU, the forward propagation starts. We regard all the GRUs in the two parts as a BiGRU layer, and the calculation of the first layer is as follows (Formula 5):

$$h_t^l = f\left(W_{\vec{h}_t}^l \vec{h}_t^l + W_{\overleftarrow{h}_t}^l \overleftarrow{h}_t^l + b_t^l\right) \tag{5}$$

Among them, h_t^l represents the hidden layer state at the moment of the l-layer BiGRU network, b_t^l is the bias of the hidden layer state at the l-layer moment, $W_{\vec{h}_t}^l$, $W_{h_t}^l$ represent the l-layer The BiGRU forward hidden state and backward hidden state weight coefficients, $\vec{h}_t^l$ and h_t^l are the states of the forward and backward hidden layers at the l-layer respectively, and their calculations are as follows:

$$\vec{h}_t^l = GRU^l\left(x_t^l, \vec{h}_{t-1}^l\right) \tag{6}$$

$$\overleftarrow{h}_t^l = GRU^l\left(x_t^l, \overleftarrow{h}_{t-1}^l\right) \tag{7}$$

Among them, $\vec{h}_t^l$ and htl represent the state of the forward and backward hidden layers of layer l at time $t-1$. x_t^l is the input at the moment of layer l, and the update gate calculation of layer l of the GRU network is as follows:

$$z_t^l = \sigma(W_z^l x_t^l + U_z^l h_{t-1}^l + b_z^l) \tag{8}$$

Among them, z_t^l is the update gate of the first layer, then W_z^l and U_z^l are the weights of the update gate of the l layer, b_z^l is the bias, and σ is the Sigmoid activation function. The calculation of the layer-l reset gate is as follows:

$$r_t^l = \sigma(W_t^l x_t^l + U_t^l h_{t-1}^l + b_t^l) \tag{9}$$

Among them, represents the l layer reset gate, $W_t^l$and U_t^l are the weights, and b_t^l is the bias. The hidden layer state of layer l is as follows:

$$h_t^l = z_t^l h_{t-1}^l + (1 - z_t^l)\tilde{h}_t^l \tag{10}$$

Among them, h_{t-1}^l and h_t^l respectively represent the hidden layer state at time and time; $\tilde{h}_t^l$ represents the candidate hidden layer state, its calculation is as follows:

$$\tilde{h}_t^l = tanh\left(W_h^l x_t^l + U_h^l (r_t^l h_{t-1}^l) + b_h^l\right) \tag{11}$$

Among them, W_h^l and U_h^l represent the weight of the hidden layer state of layer l, and b_h^l represents the bias of the hidden layer. The specific calculation process is shown in Algorithm 1.

Firstly, the model takes standardized sales time series data as input and predicts the output using the BiGRU model. During the parameter optimization process, the first step involves defining the range for the three optimization parameters. Next, the Q-Learning algorithm's parameters are initialized, and the optimization parameters are established as states. The Q table is also initialized. The process starts from state s_1, where the agent selects and executes action a_1. The agent interacts with the BiGRU environment, calculates the RMSE value, observes the reward function value and s', updates the Q table, and transitions to the next state, s_2. This cycle continues until the termination state, s_3, is reached. At this point, the algorithm updates the state and begins the cycle again from s_1. The algorithm terminates when the maximum number of iterations is reached.

Algorithm1. QLBiGRU
Input: Normalized state data
Output: The optimized parameters enter the BiGRU model, and the prediction results are obtained
1: Set ranges for the number of neurons, number of iterations, and learning rate
2: Initialize the parameters of the Q-Learning algorithm
3: Build state relationships between optimization parameters
4: Initialize $Q(s,a)$
5: **repeat:**
6: initial state s
7: **repeat:**
8: Choose action a from state s in $Q(s,a)$
9: Execute action a, enter the BiGRU model to get the predicted value,
10: To calculate the RMSE value, observe R, s'
11: Calculate the value of $Q(s,a)$by formula 2
12: $s = s'$
13: Calculate the value of $Q(s,a)$by formula 2
13: **until** reaches the terminal state s_3
14: **until** reached the maximum number of iterations
15: **return** Prediction results of BiGRU prediction under the optimal strategy (optimal hyperparameter combination)

4. Result and comparison analysis

4.1. Model parameter setting

During the experiment, we initially defined the parameter ranges for optimization. For instance, the range for the number of neurons was set to $[1, 200]$, the number of iterations was set to $[1, 100]$, and the learning rate was set to $[0.001, 0.005]$. Subsequently, during runtime, we employed the Adam optimizer for gradient descent, and the model was configured with a batch size of 128. Details of other hyperparameters can be found in Table 1:

Table 1. QLBiGRU model parameter settings.

parameters	value
Batch size	128
Loss function	RMSE
Optimizer	Adam

Dropout value	0.5
S_1 (The value range of neuron numbers)	[1, 200]
S_2 (Epoch value range)	[1, 100]
S_3 (Learning rate range)	[1e-3, 5e-3]
α init learning rate	0.01
γ discount factor	0.9
episode iterations	100

4.2. Datasets

Dataset 1: The Cainiao Demand Forecasting and Warehouse Planning Competition Dataset (ETD) from the 2016 Tianchi Competition. This dataset comprises real sales data from Alibaba's e-commerce transactions, encompassing 5,778 products between October 2014 and December 2015.

Dataset 2: The 2021 Alibaba Cloud Infrastructure Supply Chain Competition (SCD) features daily product inventory and demand data spanning June 2018 to March 2021. The product inventory data includes 7 columns: unit, date, product demand, geographical information, geographical aggregation dimension, product information, and product aggregation dimension.

Dataset 3: The Society for Supply Chain and Operations Management-Shanshu Technology Practice-Driven Research Competition Dataset (SSD) contains historical sales data of 72 SKU products across 18 DC warehouses. The dataset includes daily sales information for each DCSKU combination from January 1, 2018, to July 30, 2020. In total, there are 1,080 unique DCSKU combinations and over 830,000 records. The historical sales data encompasses fields such as sales date, warehouse ID, commodity ID, DC*SKU combination ID, and sales volume (box).

4.3. Analysis

To verify the effectiveness of our proposed QLBiGRU model and evaluate its performance in sales forecasting, we conducted experiments of various scales on three datasets: ETD, SCD, and SSD. The prediction lengths considered were 3, 5, 7, and 14. The results of these experiments are presented in Tables 2, 3, and 4.

In addition, we compared our QLBiGRU model with six other baseline methods, namely RNN, LSTM, BiGRU, PSO-LSTM, ACO-LSTM, and IACO-BiGRU. We performed experiments using these methods and analyzed the results. Overall, the QLBiGRU model demonstrated superior performance compared to the other methods. RNN performed the worst due to the issue of gradient disappearance or explosion, which resulted in poor prediction results. LSTM, on the other hand, generally outperformed RNN, but its larger parameter size led to longer running times. GRU, with fewer parameters and slightly faster execution, offered a viable alternative to LSTM. Moreover, BiGRU exhibited the ability to capture contextual information effectively, making it a more reasonable choice for an e-commerce sales forecasting model.

From the experimental data, it is evident that the prediction results obtained after optimizing the model parameters were superior to manually set ones. This highlights the limitations of relying solely on experiential parameter settings, which can affect the

predictive performance of the model. Automatic optimization proves to be more accurate and therefore yields better results. Specifically, in the SSD dataset experiment (Table 4), considering product 4 as an example, when the prediction length is 7, the evaluation indicators of the predicted values obtained by PSO-LSTM were 47.4%, 3.3%, and 27.5% higher than those of LSTM, respectively. Similarly, when the prediction length is 14, the evaluation indicators of IACO-BiGRU improved by 37.5%, 14.4%, and 20.9% compared to BiGRU. These findings affirm the necessity of optimizing the model parameters.

Table 2. Experimental results of the ETD dataset

(Best result in bold, * indicates sub-optimal result)

Commodity	Method	Step=3			Step=5		
		MSE	**MAE**	**RMSE**	**MSE**	**MAE**	**RMSE**
	RNN	0.4440	0.3025	0.6663	0.7726	0.4991	0.8790
	LSTM	0.5061	0.2948	0.7114	0.4265	0.2758	0.6531
	BiGRU	0.2617	0.1986	0.5115	0.2858	0.2181	0.5346
1	PSO-LSTM	0.0739	0.1881	0.2718	0.0744	0.1790	0.2728
	ACO-LSTM	0.0661	0.1723	0.2571	0.0639	**0.1516**	0.2528
	IACO-BiGRU	0.0552*	**0.1502**	0.2350*	0.0601*	0.1520*	0.2453*
	QLBiGRU	**0.0354**	0.1539*	**0.1883**	**0.0391**	0.1611	**0.1978**
	RNN	0.6464	0.4040	0.8040	0.7279	0.3358	0.8531
	LSTM	0.4042	0.2893	0.6358	0.4949	0.2984	0.7034
	BiGRU	0.2836	0.2425	0.2836	0.2797	0.2280	0.2797
2	PSO-LSTM	0.0746	0.2019	0.2732	0.0819	0.2050	0.2862
	ACO-LSTM	0.0694	0.1679	0.2635	0.0638	0.1572*	0.2526
	IACO-BiGRU	0.0541*	0.1377*	0.2326*	0.0532*	0.1626	0.2308*
	QLBiGRU	**0.0269**	**0.1330**	**0.1642**	**0.0273**	**0.1368**	**0.1654**

Table 3. Experimental results of the SCD dataset

(Best result in bold, * indicates sub-optimal result)

Commodity	Method	Step=3			Step=5		
		MSE	**MAE**	**RMSE**	**MSE**	**MAE**	**RMSE**
	RNN	0.8336	0.3293	0.9130	0.8783	0.2976	0.9372
	LSTM	0.8091	0.3092	0.8995	0.7676	0.3102	0.8761
	BiGRU	0.7247	0.3024	0.8512	0.7511	0.3141	0.8666
1	PSO-LSTM	0.1937	0.3123	0.4401	0.2361	0.2780	0.4859
	ACO-LSTM	0.0419	0.1314*	0.2048	0.0455	0.1404*	0.2133
	IACO-BiGRU	0.0313*	0.1361	0.1771*	0.0378*	0.1606	0.1944*
	QLBiGRU	**0.0239**	**0.1295**	**0.1546**	**0.0245**	**0.1278**	**0.1565**
	RNN	0.8046	0.3215	0.8970	0.8942	0.3606	0.9456
	LSTM	0.7438	0.3267	0.8624	0.7306	0.3021	0.8547
	BiGRU	0.6229	0.3482	0.7892	0.6865	0.2959	0.8286
2	PSO-LSTM	0.1861	0.1849	0.4314	0.2195	0.2045	0.4685
	ACO-LSTM	0.0437	0.1433	0.2091	0.0457	0.1302*	0.2139
	IACO-BiGRU	0.0313*	0.1250*	0.1771*	0.0349*	0.1384	0.1869*
	QLBiGRU	**0.0217**	**0.1149**	**0.1474**	**0.0242**	**0.1246**	**0.1558**

Table 4. Experimental results of the SSD dataset

(Best result in bold, * indicates sub-optimal result)

Commodity	**Method**	Step=7			Step=14		
		MSE	**MAE**	**RMSE**	**MSE**	**MAE**	**RMSE**
	RNN	0.2017	0.3863	0.4491	0.2391	0.4045	0.4890
	LSTM	0.1487	0.2040	0.3856	0.1646	0.3008	0.4057
	BiGRU	0.1304	0.2895	0.3611	0.1466	0.1978	0.3829
1	PSO-LSTM	0.1062	0.2249	0.3259	0.1140	0.2267	0.3377
	ACO-LSTM	0.0956	0.2082	0.3092	0.0976	0.1925*	0.3124
	IACO-BiGRU	0.0874*	**0.1682**	0.2956*	0.0965*	0.1932	0.3106*
	QLBiGRU	**0.0653**	0.1885*	**0.2556**	**0.0615**	**0.1728**	**0.2480**
2	RNN	0.2193	0.2166	0.4683	0.2356	0.2238	0.4854

	LSTM	0.1314	0.1786	0.3626	0.1407	0.1854	0.3751
	BiGRU	0.1131	0.1774*	0.3363	0.1367	0.1828*	0.3697
	PSO-LSTM	0.1081	0.2590	0.3288	0.1083	0.2613	0.3292
	ACO-LSTM	0.1035	0.2218	0.3217	0.1174	0.2115	0.3427
	IACO-BiGRU	0.0930*	0.2010	0.3049*	0.0923*	0.1937	0.3039*
	QLBiGRU	**0.0566**	**0.1758**	**0.2380**	**0.0608**	**0.1758**	**0.2465**
	RNN	0.2086	0.2080	0.4567	0.2454	0.2139	0.4954
	LSTM	0.1794	0.2221	0.4235	0.1887	0.2665	0.4344
	BiGRU	0.1322	0.1855	0.3635	0.1388	0.2283	0.3726
3	PSO-LSTM	0.1117	0.2535	0.3343	0.0990	0.2228	0.3146
	ACO-BiGRU	0.0929	0.1805*	0.3048	0.0936	0.2025*	0.3060
	IACO-BiGRU	0.0877*	0.2129	0.2962*	0.0891*	0.2061	0.2985*
	QLBiGRU	**0.0500**	**0.1648**	**0.2237**	**0.0541**	**0.1653**	**0.2327**
	RNN	0.2081	0.2064	0.4562	0.2144	0.1984	0.4630
	LSTM	0.1904	0.1934	0.4363	0.1919	0.2147	0.4380
	BiGRU	0.1186	0.1739	0.3444	0.1397	0.1899	0.3738
4	PSO-LSTM	0.1000	0.1869	0.3163	0.1140	0.2267	0.3377
	ACO-BiGRU	0.0912	0.1806*	0.3021	0.0970	0.1922	0.3114
	IACO-BiGRU	0.0822*	**0.1806**	0.2867*	0.0873*	**0.1625**	0.2954*
	QLBiGRU	**0.0693**	0.1983	**0.2633**	**0.0686**	0.1803*	**0.2620**

Additionally, to further validate the performance of the QLBiGRU algorithm, we compared the super-parameter optimization time among different methods. We conducted five experiments for each method and calculated the average value. The results are presented in Figure 3. As observed, the QLBiGRU model exhibited the shortest running time and high search efficiency.

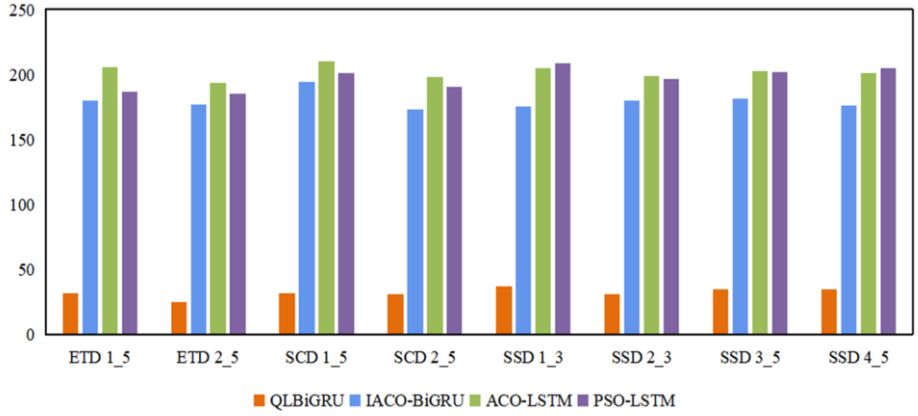

Fig. 3. Comparison of running time

We compared the experimental errors using three different reward functions: RMSE, MAE, and MSE (Fig. 4). Based on the results, it is evident that the use of RMSE as a reward function yields the smallest prediction error. Therefore, it is more reasonable to utilize RMSE as the preferred reward function.

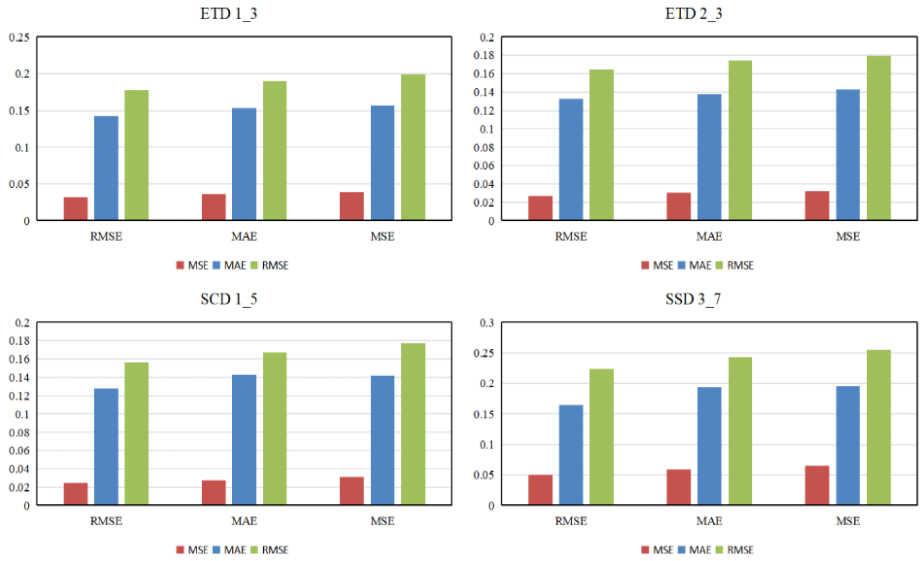

Fig. 4. Error comparison when three evaluation indicators are set as reward functions

To analyze the convergence performance of the model, we compared the convergence curves of its loss function across different datasets (Fig. 5). The results demonstrate that QLBiGRU exhibits faster convergence specifically on the SSD dataset.

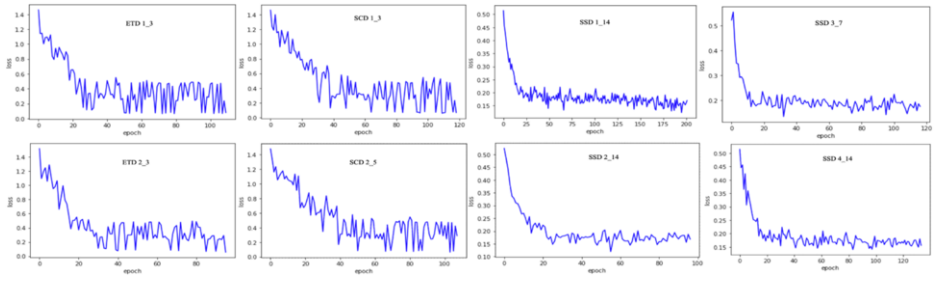

Fig. 5. Loss values of the model on three data sets

Finally, the prediction results obtained using QLBiGRU consistently outperform those of the PSO-LSTM, ACO-LSTM, and IACO-BiGRU models. Analyzing the experimental results from the ETD dataset (Table 2), we observe that for commodity 1, when the prediction length is 3, the QLBiGRU model achieves a 52.0% improvement in the three prediction evaluation indicators compared to the PSO-LSTM model, with a QLBiGRU ratio of 30.7%. Additionally, the ACO-LSTM model experiences a respective increase of 46.4%, 10.6%, and 26.7% in MSE, MAE, and RMSE. When the prediction length is 5, the QLBiGRU model demonstrates a 34.9% increase in MSE and a 19.3% increase in RMSE compared to the IACO-BiGRU model. The advantages of the Q-Learning algorithm in addressing the super-parameter optimization problem compensate for the limitations of the PSO and ACO algorithms, which are prone to local optima, thus leading to improved prediction results.

5. Conclusion

Based on the e-commerce sales forecasting, we employed the Q-Learning algorithm in combination with the BiGRU model to enhance the prediction and optimization of traditional heuristic algorithms. The traditional approaches often face challenges such as getting stuck in local optimal solutions, long execution times, and inadequate performance. The effectiveness of our proposed QLBiGRU model was evaluated across different prediction scales on three distinct datasets: ETD, SCD, and SSD. Following a comprehensive evaluation, we concluded that the QLBiGRU model exhibits superior performance in accurately predicting sales for various commodities at each scale.

Acknowledgment

Project supported by the Key Research and Development Program of Gansu Province, China (No.22YF7GA171), the University Industry Support Program of Gansu Province, China (No.2023QB-115), the Innovation Fund for Science and Technology-based Small and Medium Enterprises of Gansu Province, China (No.23CXGA0136) and the Scientific Research Project of the Lanzhou Science and Technology Program, China (No.2018-01-58).

References

[1] L. E. Baum and J. A. Eagon, "An inequality with applications to statistical estimation for probabilistic functions of Markov processes and to a model for ecology," 1967.
[2] S. J. Taylor and B. Letham, "Forecasting at scale," *The American Statistician,* vol. 72, no. 1, pp. 37-45, 2018.
[3] T. Van Calster, B. Baesens, and W. Lemahieu, "ProfARIMA: A profit-driven order identification algorithm for ARIMA models in sales forecasting," *Applied Soft Computing,* vol. 60, pp. 775-785, 2017.
[4] J. Zhao and C. Zhang, "Research on sales forecast based on prophet-SARIMA combination model," in *Journal of Physics: Conference Series*, 2020, vol. 1616, no. 1: IOP Publishing, p. 012069.
[5] W. Liu and Y. Shoji, "DeepVM: RNN-based vehicle mobility prediction to support intelligent vehicle applications," *IEEE Transactions on Industrial Informatics,* vol. 16, no. 6, pp. 3997-4006, 2019.
[6] J. Q. Wang, Y. Du, and J. Wang, "LSTM based long-term energy consumption prediction with periodicity," *Energy,* vol. 197, p. 117197, 2020.
[7] B. Shao, M. Li, Y. Zhao, and G. Bian, "Nickel price forecast based on the LSTM neural network optimized by the improved PSO algorithm," *Mathematical Problems in Engineering,* vol. 2019, 2019.
[8] D. Han, X. Yang, G. Li, S. Wang, Z. Wang, and J. Zhao, "Highway traffic speed prediction in rainy environment based on APSO-GRU," *Journal of advanced transportation,* vol. 2021, pp. 1-11, 2021.
[9] R. Yang, "Enterprise network marketing prediction using the optimized GA-BP neural network," *Complexity,* vol. 2020, pp. 1-9, 2020.
[10] D. M. Belete and M. D. Huchaiah, "Grid search in hyperparameter optimization of machine learning models for prediction of HIV/AIDS test results," *International Journal of Computers and Applications,* vol. 44, no. 9, pp. 875-886, 2022.
[11] Y. Sun, S. Ding, Z. Zhang, and W. Jia, "An improved grid search algorithm to optimize SVR for prediction," *Soft Computing,* vol. 25, pp. 5633-5644, 2021.
[12] J. Wu, S. Chen, and X. Liu, "Efficient hyperparameter optimization through model-based reinforcement learning," *Neurocomputing,* vol. 409, pp. 381-393, 2020.
[13] S. Chen, J. Wu, and X. Chen, "Deep reinforcement learning with model-based acceleration for hyperparameter optimization," in *2019 IEEE 31st International Conference on Tools with Artificial Intelligence (ICTAI)*, 2019: IEEE, pp. 170-177.

Fuzzy Systems and Data Mining IX
A.J. Tallón-Ballesteros and R. Beltrán-Barba (Eds.)

doi:10.3233/FAIA231068

Interval-Valued Fermatean Fuzzy Multi-Attribute Group Decision-Making Method with a Consensus Mechanism

Huanling Sun[a], Xiuqin Ma[a, 1], Hongwu Qin[a] and Meng Zhao[b]
[a] *College of Computer Science and Engineering, Northwest Normal University, China*
[b] *College of Information Engineering, Xinjiang Institute of Technology, China*

Abstract. Interval-valued Fermatean fuzzy sets are a new powerful tool for dealing with uncertainty problems. However, group decision-making methods under this new model are rarely studied. Therefore, this paper proposes a group decision-making method with a consensus mechanism. First, this paper proposes a new score function. The advantages of the score function are proved through comparative analysis. Secondly, a consensus-reaching method is proposed based on the new score function, and in order to shorten the consensus-reaching time, the preference approval structure is combined with the consensus-reaching process. Finally, this paper proposes a multi-attribute group decision-making framework with a consensus process in interval-valued Fermatean fuzzy environment.

Keywords. Interval-valued Fermatean fuzzy sets, Consensus, Score Function.

1. Introduction

It is a significant challenge to deal with uncertain and fuzzy data in real-world applications [1, 2]. Q-rung orthopair fuzzy sets [3, 4] which can handle uncertainty. The area of the acceptable orthopairs will increase as q rises. There are two examples when q = 1 and q = 2, respectively: intuitionistic fuzzy sets [5] and Pythagorean fuzzy sets [6]. Q-rung orthopair fuzzy sets when q=3 were also referred to as Fermatean fuzzy sets (FFSs) and were suggested by Senapati and Yager [7]. Jeevaraj et al. proposed the notion of interval-valued Fermatean fuzzy sets (IVFFSs) [5] by extending FFSs. When the upper bounds and lower bounds of membership degrees of (IVFFSs) are equal and the upper bounds and lower bounds of non-membership degrees are equal, IVFFSs can be transformed into FFSs. Thus, FFSs are a special case of IVFFSs, which are a crucial type of q-rung orthopair fuzzy sets. The difference between the IVFFSs and FFSs is that the FFSs are a set of membership degrees and non-membership degrees, while IVFFSs are a set of membership degree intervals and non-membership degree intervals. The same is true that FFSs satisfy the sum of the power of membership and the power of non-membership belonging to [0, 1], and the IVFFSs also satisfy the sum of the upper bounds power of membership degrees and the upper bounds power of non-membership degrees belonging to [0, 1]. the IVFFSs involve the advantages of FFSs and have greater flexibility in dealing with fuzzy and imprecise information. As a result, IVFFSs-based multi-

[1] Corresponding Author, Xiuqin Ma, Northwest Normal University, China; Email: maxiuqin@nwnu.edu.cn. Funding was provided by the National Natural Science Foundation of China (62162055), the Gansu Provincial Natural Science Foundation of China (21JR7RA115).

attribute decision-making techniques were developed. The multi-attribute group decision-making (MAGDM) problem has drawn a growing amount of interest due to the decision-making environment's complexity. Consensus building is one of the key research areas of MAGDM challenges because group decision-making has the benefit of being more comprehensive and compelling, but it also presents possible conflicts and inconsistencies among experts. Many consensus models have been put forth in the area of multi-attribute group decision-making lately [8, 9]. The current consensus research process (CRP) focuses on the five aspects listed below.

Models of consensus based on diverse preference structures. For instance, Herrera-Viedma et al.[10] offered a consensus model based on four assessment structures. Models of consensus with minimal adjustment, such as a two-stage consensus-building strategy based on minimal adjustment was presented by Long et al. [11]. Models of consensus that take non-cooperative behavior into account. For instance, a large-scale group decision-making model based on trust consensus was proposed by Xu et al. [12] in 2019. Large-scale group decision-making consensus model. Wu et al. [13] propose a community detection-based clustering method to manage different network setups with dynamic consensus thresholds. Social network consensus models. Wu et al. [14] proposed a distributed linguistic social network group decision-making consensus model based on the minimum adjustment cost.

There are some problems with the existing research: 1) The existing score function does not effectively compare any two IVFFNs. 2) In a multi-attribute group decision-making environment, consensus should measure the level of agreement among experts based on the outcomes of the decision-making process in accordance with the characteristics of the multi-attribute decision-making problem rather than just taking into account the consistency of the assessments made directly by the experts. 3) The decision-makers in the group should comprehend at least some of the solutions. The experts should have faith in the alternatives they are familiar with, allowing the process of consensus feedback to focus solely on adjusting the evaluation of the alternatives they are unfamiliar with.

This essay proposed three crucial contributions: 2) A new consensus-reaching approach based on IVFFSs is proposed. 1) A new scoring function based on IVFFSs is proposed. 3) Based on the consensus method, a multi-attribute group decision-making approach with interval-valued Fermat fuzzy is developed. The remainder is structured as follows: A few concepts are introduced in Section 2, the proposed score function is introduced and proven in Section 3, the suggested consensus framework is introduced in Section 4, this paper is conclusion in Section 5.

2. Preliminaries

Some basic concepts are introduced in this section.

2.1. Interval-valued Fermatean Fuzzy Sets

Definition 2.1.[15] Let S[0,1] be a set of all closed sub-intervals of the interval $[0,1]$. An interval-valued Fermatean fuzzy sets (IVFFSs) on a set $X \neq \emptyset$ is an expression given by $F = \{\langle x, \mu(x), \nu(x)\rangle : x \in X\}$ where $\mu(x): X \to S[0,1]$ and $\mu(x): X \to S[0,1]$ are closed intervals, F can also be expressed as follows: $F = \{\langle x, [\mu_F^L, \mu_F^U], [\nu_F^L, \nu_F^U]\rangle : x \in X\}$, where $[\mu_F^L, \mu_F^U]$denote the lower and upper bounds of the membership respectively,and $[\nu_F^L, \nu_F^U]$ denote the lower and upper bounds of the non-membership $0 \leq {\mu_F^U}^3 + {\nu_F^U}^3 \leq 1$. For each

element $x \in X$, $F1 = [\mu_{F1}^L, \mu_{F1}^U], [\nu_{F1}^L, \nu_{F1}^U]$ is also called an interval-valued Fermatean fuzzy number (IVFFN).

Definition 2.2. Let $F_1 = \left(\left[\mu_{F_1}^L, \mu_{F_1}^U\right], \left[\nu_{F_1}^L, \nu_{F_1}^U\right]\right)$ and $F_2 = \left(\left[\mu_{F_2}^L, \mu_{F_2}^U\right], \left[\nu_{F_2}^L, \nu_{F_2}^U\right]\right)$ be any two IVFFNs, The definition of a subset $S_1 \subset$ IVFFN with relation $\subseteq$ is $F_1 \subseteq F_2$ if $\mu_{F_1}^L \leq \mu_{F_2}^L$, $\mu_{F_1}^U \leq \mu_{F_2}^L$, $\nu_{F_1}^L \geq \nu_{F_2}^L$ and $\nu_{F_1}^U \geq \nu_{F_2}^U$.

Definition 2.3. [16] Assuming $F_i = \left(\left[\mu_{F_i}^L, \mu_{F_i}^U\right], \left[\nu_{F_i}^L, \nu_{F_i}^U\right]\right), (i = 1,2, \dots, n)$ is a set of IVFFNs,w_i is the weight of F_i,and $\sum_{i=1}^n w_i = 1$, then the IVFFWG operator can be given as follow:

$$IVFFWG(F_1, F_2, \dots, F_n) = \oplus_{i=1}^n F_i^{w_i} \tag{1}$$

2.2. The preference-approval structures

The preference-approval structures were initially proposed by Brams and Sanver [17]. Assume that the people give the alternatives in a precise positional order, such as $x_2 > x_1$ or $x_1 > x_2$, for alternativesx_1 and x_2. Each person uses a bar to discern between the approved and non-approved alternatives, depending on the positional ordering of the alternatives.

3. The newly proposed score function

This section proposes a brand-new score function.

3.1. Score Function

Definition 3.1. Let $F_1 = \left(\left[\mu_{F_1}^L, \mu_{F_1}^U\right], \left[\nu_{F_1}^L, \nu_{F_1}^U\right]\right) \in$ IVFFN. Then the score function S for F_1 is defined as follow:

$$S(F_1) = \frac{-1+2{\mu_{F_1}^L}^3+2{\mu_{F_1}^U}^3-{\nu_{F_1}^L}^3-{\nu_{F_1}^U}^3-{\nu_{F_1}^L}^3\times{\nu_{F_1}^U}^3}{3} \tag{2}$$

Theorem 3.1. Let $F_1, F_2 \in$ IVFFN. if $F_1 \subseteq F_2$, then $S(F_1) \leq S(F_2)$.

Proof. If $F_1 \subseteq F_2 \Rightarrow \mu_{F_1}^L \leq \mu_{F_2}^L, \mu_{F_1}^U \leq \mu_{F_2}^U, \nu_{F_1}^L \geq \nu_{F_2}^L, \nu_{F_1}^U \geq \nu_{F_2}^U$, we have

$$S(F_1) - S(F_2) = \frac{2\left({\mu_{F_1}^L}^3 - {\mu_{F_2}^L}^3\right) + 2\left({\mu_{F_1}^U}^3 - {\mu_{F_2}^U}^3\right) + \left({\nu_{F_2}^L}^3 - {\nu_{F_1}^L}^3\right) + \left({\nu_{F_2}^U}^3 - {\nu_{F_1}^U}^3\right) + \left({\nu_{F_2}^L}^3 \times {\nu_{F_2}^U}^3 - {\nu_{F_1}^L}^3 \times {\nu_{F_1}^U}^3\right)}{3} \leq 0$$

Thus $S(F_1) \leq S(F_2)$.

Proposition 3.1. For any $F = \left(\left[\mu_{F_1}^L, \mu_{F_1}^U\right], \left[\nu_{F_1}^L, \nu_{F_1}^U\right]\right) \in$ IVFFN, $S(F) \in \left[-\frac{4}{3}, 1\right]$.

Proof. Because $0 \leq \mu_{F_1}^L \leq \mu_{F_1}^U \leq 1$, $0 \leq \nu_{F_1}^L \leq \nu_{F_1}^U \leq 1$, we have $2{\mu_{F_1}^L}^3 + 2{\mu_{F_1}^U}^3 \in [0,4]$, ${\nu_{F_1}^L}^3 + {\nu_{F_1}^U}^3 + {\nu_{F_1}^L}^3 \times {\nu_{F_1}^U}^3 \in [0,3]$, then it can be seen that $S(F_1) \in \left[-\frac{4}{3}, 1\right]$.

3.2. Comparing existing score functions

This section will compare the proposed score function with the existing scoring function. We compared the three score functions in [15, 18, 19], defined as follows, respectively. The comparison results are shown in Table 1.

$$J_M(F_1) = \frac{1}{2}\left({\mu_{F_1}^L}^3 + {\mu_{F_1}^U}^3 - {\nu_{F_1}^L}^3 - {\nu_{F_1}^U}^3\right) \tag{3}$$

$$R_S(F_1) = \frac{1}{2}\left(\left({\mu_{F_1}^L}^3 - {\nu_{F_1}^L}^3\right)\left(1 + \sqrt[3]{1 - {\mu_{F_1}^L}^3 - {\nu_{F_1}^L}^3}\right) + \left({\mu_{F_1}^U}^3 - {\nu_{F_1}^U}^3\right)\left(1 + \sqrt[3]{1 - {\mu_{F_1}^U}^3 - {\nu_{F_1}^U}^3}\right)\right) \tag{4}$$

$$P_S(F_1) = \frac{1}{2}\left({\mu_{F_1}^L}^3 + {\mu_{F_1}^U}^3 + {\mu_{F_1}^L}^3\sqrt{1 - {\nu_{F_1}^L}^3} + {\mu_{F_1}^U}^3\sqrt{1 - {\nu_{F_1}^U}^3}\right) \tag{5}$$

Table 1. Comparison with existing score functions

	$\mathbf{A_1} = ([\mathbf{0.2}, \mathbf{0.3}], [\mathbf{0.2}, \mathbf{0.3}])$ $\mathbf{A_2} = ([\mathbf{0.3}, \mathbf{0.4}], [\mathbf{0.3}, \mathbf{0.4}])$	$\mathbf{A_1} = ([\mathbf{0}, \mathbf{0}], [\mathbf{0.2}, \mathbf{0.3}])$, $\mathbf{A_2} = ([\mathbf{0}, \mathbf{0}], [\mathbf{0.3}, \mathbf{0.4}])$	**comparability**
[15]	$J_M(A_1) = 0,\ J_M(A_2) = 0$	$J_M(A_1) = -0.017, J_M(A_2) = -0.046$	No
[18]	$R_S(A_1) = 0, R_S(A_2) = 0$	$R_S(A_1) = -0.035, R_S(A_2) - 0.09$	No
[19]	$P_S(\mathrm{A}_1) = 0.2659, P_S(\mathrm{A}_2) = 0.3898$	$P_S(\mathrm{A}_1) = 0, P_S(\mathrm{A}_2) = 0$	No
Proposed	$\mathrm{S}(\mathrm{A}_1) = -0.322, \mathrm{S}(\mathrm{A}_2) = -0.304$	$\mathrm{S}(\mathrm{A}_1) = -0.345, \mathrm{S}(\mathrm{A}_2) = -0.364$	Yes

4. New Consensus Framework

This section proposes a consensus framework to resolve the MAGDM problem.

4.1. Proposed consensus framework

MAGDM problem description: $\mathrm{E} = \{e_1, e_2, e_3, \ldots, e_l\}$ is a set of experts, $\varpi = (\varpi_1, \varpi_2, \varpi_3, \ldots, \varpi_l)$is a weight vector of associated experts, $\mathrm{X} = \{x_1, x_2, x_3, \ldots, x_n\}$ is a set of alternatives, $\mathrm{C} = \{c_1, c_2, c_3, \ldots, c_m\}$ is a set of attributes, $\mathrm{W} = (w_1, w_2, w_3, \ldots, w_m)$ is a weight vector of associated attributes, $D^{t\mathrm{k}} = \left(x_{ij}^{tk}\right)$ is the decision matrix provided by the expert $\mathrm{e^k}$ at state t, and $D^t = \left(x_{ij}^t\right)_{\mathrm{n\times m}}$ is the collective decision matrix of all experts.

The consensus index is defined as follow:

$$\mathrm{GIL}^t = \phi \frac{\sum_{k=1}^{l}\sum_{i=1}^{n}\sum_{j=1}^{m} S_{GE}\left(\mathrm{x}_{ij}^{0k}, \mathrm{x}_{ij}^{0}\right)}{n+m+l} + (1-\phi)\frac{\sum_{k=1}^{l}\sum_{i=1}^{n}\sum_{j=1}^{m} S_{GE}\left(\mathrm{x}_{ij}^{tk}, \mathrm{x}_{ij}^{t}\right)}{n+m+l} \tag{6}$$

The $S_{GE}\left(\mathrm{x}_{ij}^{0k}, \mathrm{x}_{ij}^{0}\right)$ represents the level of consensus among experts in the initial state. $S_{GE}\left(\mathrm{x}_{ij}^{tk}, \mathrm{x}_{ij}^{t}\right)$represents the level of consensus among experts after the t- time adjustment. A higher value GIL^t denotes higher agreement among the expert group. Ideally, when all experts reach absolute agreement, the consensus index GIL^t equals 1, but it is almost impossible for independent experts to reach complete agreement. Therefore, given an acceptable consensus threshold θ, if GIL^t is greater than θ, the expert group reaches an acceptable consensus level, which is also referred to as a "soft consensus".

- The selection process

The selection stage is the first phase of the CRP. The expert who needs to be changed is chosen when the expert group's consensus falls short of an acceptable consensus threshold. The expert who has to be changed should be the one who makes the least overall contribution to the expert group's consensus. According to the ranking results, an expert whose ranking results deviate too much from the expert group's overall rankings has made the least contribution to the expert general consensus, and their evaluation should be revised.

The selection alternatives are similar methods to selecting experts; i.e. the alternatives that deviate the most from the overall ranking contribute the least to the overall consensus and need to be adjusted. The two selection methods differ in that the experts who need to be adjusted are chosen based on the set of all experts, while the alternatives who need to be adjusted are chosen based on a subset of the alternatives set. The reason for this is that each expert chosen to make a decision is more or less competent, and at least some of the assessments given are credible, so only untrustworthy assessments need to be adjusted. For instance, if there are four alternatives, x_1, x_2, x_3, and x_4, and expert e^2 has enough knowledge of alternative x1 and alternative x_2, but little to no knowledge of x_3 and x_4, if expert e^2 is determined to adjust, only alternative x_3 and alternative x_4 evaluation need to be adjusted. This study introduces the concept of the preference approval structure based on that idea. This paper's approval structure denotes that experts provide

unreliable assessments since they lack adequate knowledge of the alternatives; hence, it needs to be further adjusted. In the non-approval structure, the expert's assessment is reliable and doesn't need adjustment. The adoption of the preference approval structure cuts down on CRP time, a benefit that will become more apparent when there are more than enough alternatives.

- The feedback adjustment process

The feedback stage is the second stage of CRP. The second stage of CRP is the feedback stage. The experts who need to be adjusted and the associated alternatives are identified after the first step. To improve the level of consensus, the evaluation of these experts needs to be modified to a certain extent. Therefore, the first issue that needs to be addressed in the feedback stage is how to determine the direction of the adjustment.

4.2. Group Multi-attribute Decision Making Method based on Consensus

The specific consensus process is as follows:

Step1: Calculation of individual ranking and collective ranking results.

Aggregation to obtain a comprehensive decision matrix $D^t = \left(x_{ij}^t\right)_{\mathrm{n\times m}}$. where $\mathrm{x_{ij}^t}$ denotes collective evaluation of alternative $\mathrm{x_i}$ under attribute $\mathrm{c_j}$ at time t.

Calculation of the score matrix. The decision matrix of individual experts and the collective decision matrix of all experts are transformed into score matrices, which are denoted as $\mathrm{P^{tk}} = \left(\mathrm{p_{ij}^{tk}}\right)_{\mathrm{n\times m}}$ and $\mathrm{P^t} = \left(\mathrm{p_{ij}^t}\right)_{\mathrm{n\times m}}$, where $\mathrm{p_{ij}^{tk}} = \mathrm{S}\left(\mathrm{x_{ij}^{tk}}\right)$, $\mathrm{p_{ij}^t} = \mathrm{S}\left(\mathrm{x_{ij}^t}\right)$.

Performing the individual ranking and collective ranking. Separately calculate each expert's score for each alternative.$p_i^{tk} = \sum_{j=1}^{m} w_j S\left(x_{ij}^{tk}\right), (i = 1,2,\ldots,n)$. where p_i^{tk}denotes the expert $\mathrm{e^k}$'s score on alternative x_i.

For each alternative, determine a collective score.$p_i^t = \sum_{j=1}^{m} w_j S\left(x_{ij}^t\right), (i = 1,2,\ldots,n)$. where p_i^t denotes the collective score on alternative x_i.

The ranking results of each expert and the group of experts as a whole are then generated by descending sorting according to score, which is denoted by $\mathrm{PO^{tk}} = \left\{o_1^{tk}, o_2^{tk}, o_3^{tk}, \ldots, o_r^{tk}\right\}, (\mathrm{k} = 1,2,\ldots \mathrm{l})$and $\mathrm{CO^t} = \{o_1^t, o_2^t, o_3^t, \ldots, o_r^t\}$, respectively, where r represents the ranking place.

Step2: Identification of adjustment experts. Comparing $\mathrm{PO^{tk}}$, $\mathrm{CO^t}$ determines the difference matrix $\mathrm{DG^t}$.

$$DG^t = (g_{kr}^t)_{l\times n} = m - r, if\, o_r^{tk} = o_m^{tc}, (k = 1,2,\ldots l, r = 1,2,\ldots n) \tag{7}$$

then chooses the experts who need to be adjusted. g_{kr}^t represents the difference in the position of the alternative in the ranking of experts $\mathrm{e^k}$ and the ranking of the expert group.

According to the difference matrix, experts $\mathrm{NS^t}$ are chosen who provide insufficient contributions to the collective ranking.

$$\mathrm{NS^t} = \left\{e_k \middle| \max \sum_{r=1}^{n} \left|g_{kr}^t\right|\right\} \tag{8}$$

Step3: Selecting the structure for preference approval.

Based on the previously mentioned concepts, the following division method is used to divide the alternatives into two groups: those whose ranking difference between the experts and the expert group exceeds the overall mean value of the difference matrix and those who are divided into a approval structure, indicating that their evaluation does require further adjustment.

$$AP_k^t = \left\{x_i \middle| \left|g_{ki}^t\right| \geq \frac{\sum_{i=1}^{n}\left|g_{ki}^t\right|}{n}\right\}, NAP_k^t = \left\{x_i \middle| \left|g_{ki}^t\right| < \frac{\sum_{i=1}^{n}\left|g_{ki}^t\right|}{n}\right\} \tag{9}$$

Where AP_k^t denotes the approved structure of expert e^k, and NAP_k^t denotes the disapproved structure of expert e^k.

Step4: Feedback adjustment

The selection stage is completed and the feedback adjustment stage is entered. In order to continually close the gap between the adjusted evaluation and the collective evaluation, this study applies the distance measurement approach. Furthermore, as the number of adjustments rises, the adjustment variables gradually close toward 0. We connected adjustment variables with the frequency of the consensus process. Assuming that e^k is the expert who needs to adjust, alternative x_i is separated into a set of approved structures of expert e^k. the feedback regulation is proposed as follows:

$$x_{ij}^{(t+1)k} = \left(\begin{bmatrix} \mu_{x_{ij}^{(t+1)k}}^{L} = \mu_{x_{ij}^{tk}}^{L} \pm \frac{D_{GE}(x_{ij}^{tk}, x_{ij}^{tc})}{t+1} \\ \mu_{x_{ij}^{(t+1)k}}^{U} = \mu_{x_{ij}^{tk}}^{U} \pm \frac{D_{GE}(x_{ij}^{tk}, x_{ij}^{tc})}{t+1} \end{bmatrix}, \begin{bmatrix} \nu_{x_{ij}^{(t+1)k}}^{L} = \nu_{x_{ij}^{tk}}^{L} \pm \frac{D_{GE}(x_{ij}^{tk}, x_{ij}^{tc})}{t+1} \\ \nu_{x_{ij}^{(t+1)k}}^{U} = \nu_{x_{ij}^{tk}}^{U} \pm \frac{D_{GE}(x_{ij}^{tk}, x_{ij}^{tc})}{t+1} \end{bmatrix} \right) \quad (10)$$

It is important to keep in mind that the adjusted evaluation value must satisfied to IVFFN limits during the feedback adjustment procedure. If the consensus level is not satisfied, the consensus process will continue until the acceptable consensus threshold or the Max_circles is reached, whichever occurs first, and then the consensus process is concluded.

5. Conclusion

The consensus method proposed in this paper can save the consensus reaching process time quickly and effectively, and retain the initial information of the expert group to the greatest extent. The method proposed in this paper has certain advantages in small-group decision-making, but it needs to be further expanded if it is to be applied to large-group decision-making. Therefore, the future work direction is to apply the method proposed in this paper to large-group decision-making.

References

[1] Ma, X.Q. and H.W. Qin. A new parameter reduction algorithm for interval-valued fuzzy soft sets based on Pearson's product moment coefficient. Applied Intelligence.2020. 50: p. 3718-3730.

[2] Qin, H., H. Li, X. Ma, Z. Gong, Y. Cheng, and Q. Fei. Data Analysis Approach for Incomplete Interval-Valued Intuitionistic Fuzzy Soft Sets. Symmetry.2020. 12: p. 1061.

[3] Yager, R.R.: Generalized Orthopair Fuzzy Sets. IEEE Transactions on Fuzzy Systems.2017. 25: p. 1222-1230.

[4] Alcantud, J.C.: Complemental Fuzzy Sets: A Semantic Justification of q-Rung Orthopair Fuzzy Sets. IEEE Transactions on Fuzzy Systems.2023.

[5] Atanassov, K.T.: Intuitionistic fuzzy sets. Fuzzy Sets and Systems.1986. 20: p. 87-96.

[6] Yager, R.R.: Pythagorean Membership Grades in Multicriteria Decision Making. Ieee Transactions on Fuzzy Systems.2014. 22: p. 958-965.

[7] Senapati, T. and R.R. Yager. Fermatean fuzzy sets. Journal of Ambient Intelligence and Humanized Computing.2020. 11: p. 663-674.

[8] Dong, Q., X. Zhou, and L. Martínez. A hybrid group decision making framework for achieving agreed solutions based on stable opinions. Information Sciences.2019. 490: p. 227-243.

[9] Cao, M., J. Wu, F. Chiclana, R. Ureña, and E. Herrera-Viedma. A Personalized Consensus Feedback Mechanism Based on Maximum Harmony Degree. IEEE Transactions on Systems, Man, and Cybernetics: Systems.2021. 51: p. 6134-6146.

[10] Herrera-Viedma, E.A.H., F. %A Chiclana, F.: A consensus model for multiperson decision making with different preference structures. IEEE Transactions on Systems, Man, and Cybernetics - Part A: Systems and Humans.2002. 32: p. 394-402.

[11] Long, J., H. Liang, L. Gao, Z. Guo, and Y. Dong. Consensus reaching with two-stage minimum adjustments in multi-attribute group decision making: A method based on preference-approval structure and prospect theory. Computers & Industrial Engineering.2021. 158: p. 107349.
[12] Xu, X.-h., Z.-j. Du, X.-h. Chen, and C. Cai. Confidence consensus-based model for large-scale group decision making: A novel approach to managing non-cooperative behaviors. Inf. Sci.2019. 477: p. 410-427.
[13] Wu, T., X. Liu, J. Qin, and F. Herrera. Balance Dynamic Clustering Analysis and Consensus Reaching Process With Consensus Evolution Networks in Large-Scale Group Decision Making. IEEE Transactions on Fuzzy Systems.2021. 29: p. 357-371.
[14] Wu, J., L. Dai, F. Chiclana, H. Fujita, and E. Herrera-Viedma. A minimum adjustment cost feedback mechanism based consensus model for group decision making under social network with distributed linguistic trust. Information Fusion.2018. 41: p. 232-242.
[15] Jeevaraj, S.: Ordering of interval-valued Fermatean fuzzy sets and its applications. Expert Systems with Applications.2021. 185: p. 115613.
[16] Rani, P. and A.R. Mishra. Interval-valued fermatean fuzzy sets with multi-criteria weighted aggregated sum product assessment-based decision analysis framework. Neural Computing & Applications.2022. 34: p. 8051-8067.
[17] Brams, S.A.S., M.: Voting Systems that Combine Approval and Preference.2009.
[18] Rani, P., A.R. Mishra, M. Deveci, and J. Antucheviciene. New complex proportional assessment approach using Einstein aggregation operators and improved score function for interval-valued Fermatean fuzzy sets. Computers & Industrial Engineering.2022. 169.
[19] Qin, H., Q. Peng, X. Ma, and J. Zhan. A new multi-attribute decision making approach based on new score function and hybrid weighted score measure in interval-valued Fermatean fuzzy environment. Complex & Intelligent Systems.2023.

Fuzzy Systems and Data Mining IX
A.J. Tallón-Ballesteros and R. Beltrán-Barba (Eds.)

doi:10.3233/FAIA231069

A New Interval-Valued Fuzzy Entropy Based on Interval-Valued Q-Rung Orthopair Fuzzy Sets

Yan Zheng[a], Hongwu Qin[a,b, 1], Xiuqin Ma[a,b], and Yibo Wang[a]

[a] *College of Computer Science and Engineering, Northwest Normal University, Lanzhou, 730070, China*
[b] *Institute for Big Data Analytics and Artificial Intelligence (IBDAAI), Universiti Teknologi MARA, 40450, Shah Alam, Selangor, Malaysia.*

Abstract. As an extension of fuzzy sets, the interval-valued q-rung orthopair fuzzy sets (IVq-ROFSs) is a powerful tool for dealing with uncertainty problems. Furthermore, fuzzy entropy is a crucial indicator to measure the fuzzy degree of fuzzy sets. However, the current fuzzy entropy of IVq-ROFSs have some disadvantages. First, for some interval-valued q-rung orthopair fuzzy numbers (IVq-ROFNs), the existing fuzzy entropy cannot accurately measure the fuzzy degree. Second, it is not a reasonable method to utilize exact values as fuzzy entropy in the form of interval values. In this paper, the fuzzy entropy of IVq-ROFSs is characterized by interval values. The axiomatic definitions of IVq-ROFSs fuzzy entropy is given. Strict mathematical proof and a numerical example verify that the proposed axiomatic definition of fuzzy entropy is complete and avoids the loss of interval-valued fuzzy information.

Keywords. Interval-valued q-rung orthopair fuzzy set, Fuzzy entropy, Interval value

1 Introduction

Since Zadeh[1] presented fuzzy sets(FSs), FS has been a hot spot study field for scholars worldwide[2-4]. FS and its extension models had involved multi-attribute decision-making[5], clustering algorithms[6], neural network[7] and so on. Turksen[8] proposed the concept of interval-valued fuzzy sets(IVFS). IVFS takes the interval value as the membership degree (MD) form, which can better reflect the fuzzy concept in fuzzy theory. Furthermore, Takeuti[9] proposed the non-membership degree(NMD) and hesitation degree based on MD. Then the concept of intuitionistic fuzzy set (IFS) was proposed. On the basis of IFS, q-rung orthopair fuzzy set(q-ROFS)[10] and interval-valued q-rung orthopair fuzzy sets(IVq-ROFSs) [11]were presented.

[1] Corresponding Author, Hongwu Qin; Email: qinhongwu@nwnu.edu.cn. This work was supported by the National Natural Science Foundation of China, grant number 62162055 and Gansu Provincial Natural Science Foundation of China, grant number 21JR7RA115.

At the same time, in order to be able to judge the relationship between the degree of fuzziness between different fuzzy numbers, Kosko[12] proposed fuzzy entropy. The proposal of fuzzy entropy can effectively compare the fuzzy degrees of different fuzzy sets or fuzzy elements. Scholars have proposed their axiomatic definitions for different fuzzy sets. Peng[13] proposed q-rung orthopair fuzzy entropy,. For various fuzzy sets whose degrees are exact values, the axiomatic definitions do not change much, but for various fuzzy sets whose data forms are interval values, the axiomatic definitions diverge greatly. Zhang[14] proposed an axiomatic definition based on IVIFSs, using the comparative relations of interval values, and analyzed the judgment of fuzzy entropy under four interval relations step by step. Peng[15] proposed an axiomatic definition based on IVPFSs, which only defined the comparison of fuzzy entropy under the containment relationship.

The current axiomatic definition of fuzzy entropy for various fuzzy sets in the form of interval-valued data is based on the calculation of the endpoint values of MD and NMD to obtain an accurate value of fuzzy entropy to judge the degree of fuzziness. However, in the process of calculating the precise fuzzy entropy from the interval value through the endpoint value, information loss may occur, so we think that the interval value can be directly used as the data form of q-rung orthopair fuzzy entropy. Directly using interval values as the data form of fuzzy entropy, on the one hand, can effectively reduce the information loss in the process of converting interval value data into accurate value data. And on the other hand, it can directly use the size comparison method of interval value data to determine the fuzzy entropy. In this paper, we first propose the axiomatic definitions of interval-valued fuzzy entropy (IVFE) based on the IVq-ROFSs, and explain it through the function graph of fuzzy entropy. And then the IVFE formulas are defined by the axiom, then an example is given to illustrate the effectiveness of the formula.

The structure of the article is as follows: In the Second part, some related concepts based on the fuzzy entropy on IVq-ROFSs are explained. In the Third part the axiomatic definitions of the IVFE on IVq-ROFSs and the related formulas are presented. Its effectiveness is demonstrated by an example compared with existing research. In the Forth part, we summarize the contributions made in this paper.

2 Preliminaries

In this section we introduce the interval-valued size relationship and some related concepts about the fuzzy entropy on IVq-ROFSs.

Definition 1[16] Let$[\varphi_1, \phi_1]$, $[\varphi_2, \phi_2] \in [\mathrm{I}]$, we define

$[\varphi_1, \phi_1] \leq [\varphi_2, \phi_2]$,iff $\varphi_1 \leq \varphi_2, \phi_1 \leq \phi_2$;

$[\varphi_1, \phi_1] \preccurlyeq [\varphi_2, \phi_2]$,iff $\varphi_1 \leq \varphi_2, \phi_1 \geq \phi_2$;

$[\varphi_1, \phi_1] = [\varphi_2, \phi_2]$,iff $\varphi_1 = \varphi_2, \phi_1 = \phi_2$;

$[\varphi_1, \phi_1] \precsim [\varphi_2, \phi_2]$,iff $\begin{cases}[\varphi_1, \phi_1] \leq [\varphi_2, \phi_2] \\ [\varphi_1, \phi_1] \succcurlyeq [\varphi_2, \phi_2]\end{cases}$.

Definition 2[11] Let X be a non-empty set, then the IVq-ROFS A on X can be expressed as:

$$Q = \{< \chi, (\widetilde{\varphi_Q}(x), \widetilde{\phi_Q}(x)) > | \chi \in \mathrm{X}\},$$

where $\widetilde{\varphi_Q}(\chi) = \left[\widetilde{\varphi_Q}^-(\chi), \widetilde{\varphi_Q}^+(\chi)\right] \subset [0,1]$, $\widetilde{\phi_Q}(\chi) = \left[\widetilde{\phi_Q}^-(\chi), \widetilde{\phi_Q}^+(\chi)\right] \subset [0,1]$and the MD and NMD satisfy$0 \leq \left(\widetilde{\varphi_Q}^+(\chi)\right)^q + \left(\widetilde{\phi_Q}^+(\chi)\right)^q \leq 1, q \geq 1$

Definition 3[11] Let $Q_1, Q_2 \in q - ROIVF(\chi)$, some operations can be defined as follow:

$Q_1 \leq Q_2$,iff $[\widetilde{\varphi_{Q_1}}^-(\chi), \widetilde{\varphi_{Q_1}}^+(\chi)] \leq [\widetilde{\varphi_{Q_2}}^-(\chi), \widetilde{\varphi_{Q_2}}^+(\chi)]$,
$[\widetilde{\phi_{Q_1}}^-(\chi), \widetilde{\phi_{Q_1}}^+(\chi)] \geq [\widetilde{\phi_{Q_2}}^-(\chi), \widetilde{\phi_{Q_2}}^+(\chi)], \forall \chi \in X$;
$Q_1 \preccurlyeq Q_2$,iff $[\widetilde{\varphi_{Q_1}}^-(\chi), \widetilde{\varphi_{Q_1}}^+(\chi)] \preccurlyeq [\widetilde{\varphi_{Q_2}}^-(\chi), \widetilde{\varphi_{Q_2}}^+(\chi)]$,
$[\widetilde{\phi_{Q_1}}^-(\chi), \widetilde{\phi_{Q_1}}^+(\chi)] \succcurlyeq [\widetilde{\phi_{Q_2}}^-(\chi), \widetilde{\phi_{Q_2}}^+(\chi)], \forall \chi \in X$;

From definition 2, we can see that IVq-ROFSs degenerates to IVIFS, IVPFS and IVFFS when the values of q are 1, 2 and 3, respectively. So, the axiomatic definition of fuzzy entropy based on IVIFS and IVPFS is given here as an example of the existing research for IVFE.

Definition 4[14] A real function E:$IVIF(X) \to [0,1]$ is named as fuzzy entropy on IVIFS, and E has to satisfy following properties:

(I1)$E(A^*) = 0$ if A^* is a crisp set.
(I2)$E(A^*) = 1$ iff $\mu_{A^*}(\chi_i) = \nu_{A^*}(\chi_i), \forall \chi_i \in X$;
(I3)$E(A^*) = E(B^*)$ if $A^*$is less fuzzy than B^*which is defined as:
$\varphi_{A^*}(\chi_i) \leq \varphi_{B^*}(\chi_i)$, $\phi_{A^*}(\chi_i) \geq \phi_{B^*}(\chi_i)$, for $\varphi_{B^*}(\chi_i) \leq \phi_{B^*}(\chi_i)$
$\varphi_{A^*}(\chi_i) \geq \varphi_{B^*}(\chi_i)$, $\phi_{A^*}(\chi_i) \leq \phi_{B^*}(\chi_i)$, for $\varphi_{B^*}(\chi_i) \geq \phi_{B^*}(\chi_i)$
$\varphi_{A^*}(\chi_i) \preccurlyeq \varphi_{B^*}(\chi_i)$, $\phi_{A^*}(\chi_i) \succcurlyeq \phi_{B^*}(\chi_i)$, for $\varphi_{B^*}(\chi_i) \preccurlyeq \phi_{B^*}(\chi_i)$
$\varphi_{A^*}(\chi_i) \succcurlyeq \varphi_{B^*}(\chi_i)$, $\phi_{A^*}(\chi_i) \preccurlyeq \phi_{B^*}(\chi_i)$, for $\varphi_{B^*}(\chi_i) \succcurlyeq \phi_{B^*}(\chi_i)$
(I4)$E(A^*) = E((A^*)^C)$

Definition 5[15] A real function E:$IVPF(X) \to [0,1]$ is named as fuzzy entropy on IVPFS, and E has to satisfy following properties:

(P1)$E\left(A^{P^*}\right) = 0$ iff $A^{P^*}$is a crisp set;
(P2)$E\left(A^{P^*}\right) = 1$ iff $\varphi_{A^{P^*}}(\chi_i) = \phi_{A^{P^*}}(\chi_i), \forall \chi_i \in X$
(P3)$E\left(A^{P^*}\right) \leq E\left(B^{P^*}\right)$ iff
$A^{P^*} \subseteq B^{P^*}$when $\varphi^-_{B^{P^*}}(\chi_i) \leq \phi^-_{B^{P^*}}(\chi_i)$ and $\varphi^+_{B^{P^*}}(\chi_i) \leq \phi^+_{B^{P^*}}(\chi_i), \forall \chi_i \in X$
$B^{P^*} \subseteq A^{P^*}$when $\varphi^-_{B^{P^*}}(\chi_i) \geq \phi^-_{B^{P^*}}(\chi_i)$ and $\varphi^+_{B^{P^*}}(\chi_i) \geq \phi^+_{B^{P^*}}(\chi_i), \forall \chi_i \in X$
(P4) $E\left(A^{P^*}\right) = E\left((A^{P^*})^C\right)$.

3 Interval-valued fuzzy entropy on IVq-ROFSs

Definition 4 and Definition 5 are the current axiomatic definitions of fuzzy entropy on IVIFS and IVPFS, and they have some defects. First of all the relations between interval values then include four relations of distance, adjacency, intersection and inclusion. In the case of both MD and NMD, defining the interval relationship between the MD and NMD of two IVq-ROFNs is a very complicated process. The (I3) condition of Definition 4 only analyzes the MD and NMD of one of the IVPFS. The (I3) condition of Definition 4 only analyzes the comparison of the fuzzy entropy values of two IVPFSs under the four interval values of MD and NMD of one IVPFS, and does not analyze the interval values of MD and NMD of the other IVPFS under the four interval values of MD and NMD of one IVPFS; the (P3) condition of Definition 5 only takes into account the

existence of both MD and NMD inclusion relationship. In addition, these two fuzzy entropy formulas both transform interval values into specific values to carry out the fuzzy degree of a certain fuzzy set, this transformation process itself will bring some information loss, so in order to solve the above defects, this paper proposes a new IVFE on IVq-ROFSs, which directly expresses the fuzzy degree using IVFE, and judges the size of fuzzy degree by the defined interval-valued dominance relationship, solving the interval relationship problem between MD and NMD from the mathematical point of view, while reducing the information loss.

Consequently, the axiomatic definition of IVFE is proposed.

Definition 6 An interval-valued function E: $IVq - ROF(\mathrm{X}) \to [0,1]$ is named as IVFE on IVq-ROFSs, and E has to satisfy following properties:

(I-Q1)$[0,0] \le E_{\mathrm{IV}}\left(A^{Q^*}\right) \le [1,1]$

(I-Q2) $E_{\mathrm{IV}}\left(A^{Q^*}\right) = [0,0]$ if $A^{Q^*}$is a crisp set.

(I-Q3) $E_{\mathrm{IV}}\left(A^{Q^*}\right) = [1,1]$ if $\widetilde{\varphi_Q}(\chi) = \widetilde{\phi_Q}(\chi)$.

(I-Q4) A^{Q^*}less fuzzy than B^{Q^*}if $E_{\mathrm{IV}}\left(A^{Q^*}\right) \lesssim E_{\mathrm{IV}}\left(B^{Q^*}\right)$

(I-Q5) $E_{\mathrm{IV}}\left(A^{Q^*}\right) = E_{\mathrm{IV}}\left((A^{Q^*})^C\right)$

Also based on the axiomatic definition of the IVFE we can give the graph of the function corresponding to the fuzzy entropy, here for ease of illustration is given when q = 1, i.e., the graph of the fuzzy entropy function of the IVIFS, as shown in Figure 1:

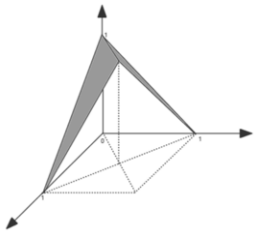

Figure 1. Interval-valued fuzzy entropy function graph on IVq-ROFSs (q=1)

From Figure 1, the x-axis is $\varphi_I(\chi)$, the y-axis is $\phi_I(\chi)$, the z-axis is fuzzy entropy value. Straight line in the plane xOy $\varphi_I(\chi) + \nu_I(\chi) = 1$,where $\varphi_I(\chi)$ and $\phi_I(\chi)$ is the MD and NMD of IFS. When $\varphi_I(\chi) = \phi_I(\chi)$, $E\left(A^{I^*}\right)$=1, according to the axiomatic definition of fuzzy entropy, the image of the function will be symmetrical along $F(\varphi_I(\chi), \phi_I(\chi))$.

The fuzzy elements of IVIFS are $\varphi_I(\chi) + \phi_I(\chi) = 1$ and the subplanes of the plane formed by x-axis, y-axis. So, on the basis of the constant fuzzy entropy function image, the geometric representation of the IVFE is the intercept of the projection of this subplane on the function image on the z-axis. The reasonableness of the (I-Q3) condition can be seen more intuitively through the geometric expression.

Example: Interval-valued fuzzy entropy on IVq-ROFSs:

$$E_{\mathrm{IV}}\left(A^{Q^*}\right) = \left[\frac{1}{n}\sum_{i=1}^{n}\sqrt[q]{\frac{1-\left|\left(\widetilde{\varphi_Q}^{+}(\chi)\right)^q-\left(\widetilde{\phi_Q}^{+}(\chi)\right)^q\right|}{1+\left|\left(\widetilde{\varphi_Q}^{+}(\chi)\right)^q-\left(\widetilde{\phi_Q}^{+}(\chi)\right)^q\right|}}, \frac{1}{n}\sum_{i=1}^{n}\sqrt[q]{\frac{1-\left|\left(\widetilde{\varphi_Q}^{-}(\chi)\right)^q-\left(\widetilde{\phi_Q}^{-}(\chi)\right)^q\right|}{1+\left|\left(\widetilde{\varphi_Q}^{-}(\chi)\right)^q-\left(\widetilde{\phi_Q}^{-}(\chi)\right)^q\right|}}\right]$$

Proof:

(I-Q1) Easy to proof.

(I-Q2) A^{Q^*} is a crisp set means that $\widetilde{\varphi_Q}(\chi) = [0,0]$ and $\widetilde{\phi_Q}(\chi) = [1,1]$ or $\widetilde{\varphi_Q}(\chi) = [1,1]$ and $\widetilde{\phi_Q}(\chi) = [0,0]$.

When $\widetilde{\varphi_Q}(\chi) = [0,0]$ and $\widetilde{\phi_Q}(\chi) = [1,1]$,

$$E_{\mathrm{IV}}(A^{Q^*}) = [\frac{1-1}{1+1}, \frac{1-1}{1+1}] = [0,0]$$

when $\widetilde{\varphi_Q}(\chi) = [1,1]$ and $\widetilde{\phi_Q}(\chi) = [0,0]$,

$$E_{\mathrm{IV}}(A^{Q^*}) = [\frac{1-1}{1+1}, \frac{1-1}{1+1}] = [0,0]$$

(I-Q3) $\widetilde{\varphi_Q}(\chi) = \widetilde{\phi_Q}(\chi)$ means that $\left[\widetilde{\varphi_Q}^{-}(\chi), \widetilde{\varphi_Q}^{+}(\chi)\right] = \left[\widetilde{\phi_Q}^{-}(\chi), \widetilde{\phi_Q}^{+}(\chi)\right]$

$$E_{\mathrm{IV}}(A^{Q^*}) = [\frac{1-0}{1+0}, \frac{1-0}{1+0}] = [1,1]$$

(I-Q4) $E_{\mathrm{IV}}(A^{Q^*}) \lesssim E_{\mathrm{IV}}(B^{Q^*})$ means that $\left[E_{\mathrm{IV}}{}^{-}(A^{Q^*}), E_{\mathrm{IV}}{}^{+}(A^{Q^*})\right] \leq [E_{\mathrm{IV}}{}^{-}(B^{Q^*}), E_{IV}{}^{+}(B^{Q^*})]$

$$\sqrt[q]{\frac{1-\left|\left(\widetilde{\varphi_{A^{Q^*}}}^{-}(\chi)\right)^q - \left(\widetilde{\phi_{A^{Q^*}}}^{-}(\chi)\right)^q\right|}{1+\left|\left(\widetilde{\varphi_{A^{Q^*}}}^{-}(\chi)\right)^q - \left(\widetilde{\phi_{A^{Q^*}}}^{-}(\chi)\right)^q\right|}} \leq \sqrt[q]{\frac{1-\left|\left(\widetilde{\varphi_{B^{Q^*}}}^{-}(\chi)\right)^q - \left(\widetilde{\phi_{B^{Q^*}}}^{-}(\chi)\right)^q\right|}{1+\left|\left(\widetilde{\varphi_{B^{Q^*}}}^{-}(\chi)\right)^q - \left(\widetilde{\phi_{B^{Q^*}}}^{-}(\chi)\right)^q\right|}}$$

and

$$\sqrt[q]{\frac{1-\left|\left(\widetilde{\varphi_{A^{Q^*}}}^{+}(\chi)\right)^q - \left(\widetilde{\phi_{A^{Q^*}}}^{+}(\chi)\right)^q\right|}{1+\left|\left(\widetilde{\varphi_{A^{Q^*}}}^{+}(\chi)\right)^q - \left(\widetilde{\phi_{A^{Q^*}}}^{+}(\chi)\right)^q\right|}} \leq \sqrt[q]{\frac{1-\left|\left(\widetilde{\varphi_{B^{Q^*}}}^{+}(\chi)\right)^q - \left(\widetilde{\phi_{B^{Q^*}}}^{+}(\chi)\right)^q\right|}{1+\left|\left(\widetilde{\varphi_{B^{Q^*}}}^{+}(\chi)\right)^q - \left(\widetilde{\phi_{B^{Q^*}}}^{+}(\chi)\right)^q\right|}}$$

let $\left|\left(\widetilde{\varphi_{A^{Q^*}}}^{+}(\chi)\right)^q - \left(\widetilde{\phi_{A^{Q^*}}}^{+}(\chi)\right)^q\right| = M$, $\left|\left(\widetilde{\varphi_{B^{Q^*}}}^{+}(\chi)\right)^q - \left(\widetilde{\phi_{B^{Q^*}}}^{+}(\chi)\right)^q\right| = N$ then we have

$$\frac{1-M}{1+M} \leq \frac{1-N}{1+N}$$
$$(1-M)(1+N) \leq (1-N)(1+M)$$
$$1-M+N-MN \leq 1-N+M-MN$$
$$-M+N \leq -N+M$$
$$2N \leq 2M$$
$$N \leq M$$

So $\left|\left(\widetilde{\varphi_{A^{Q^*}}}^{-}(\chi)\right)^q - \left(\widetilde{\phi_{A^{Q^*}}}^{-}(\chi)\right)^q\right| \geq \left|\left(\widetilde{\varphi_{B^{Q^*}}}^{-}(\chi)\right)^q - \left(\widetilde{\phi_{B^{Q^*}}}^{-}(\chi)\right)^q\right|$

and $\left|\left(\widetilde{\varphi_{A^{Q^*}}}^{+}(\chi)\right)^q - \left(\widetilde{\phi_{A^{Q^*}}}^{+}(\chi)\right)^q\right| \geq \left|\left(\widetilde{\varphi_{B^{Q^*}}}^{+}(\chi)\right)^q - \left(\widetilde{\phi_{B^{Q^*}}}^{+}(\chi)\right)^q\right|$

So A^{Q^*} is less fuzzy than B^{Q^*}.

or $[E_{\mathrm{IV}}{}^{-}(A^{Q^*}), E_{\mathrm{IV}}{}^{+}(A^{Q^*})] \geqslant [E_{\mathrm{IV}}{}^{-}(B^{Q^*}), E_{\mathrm{IV}}{}^{+}(B^{Q^*})]$

$$\sqrt[q]{\frac{1-\left|\left(\widetilde{\varphi_{A^{Q^*}}}^{-}(\chi)\right)^q - \left(\widetilde{\phi_{A^{Q^*}}}^{-}(\chi)\right)^q\right|}{1+\left|\left(\widetilde{\varphi_{A^{Q^*}}}^{-}(\chi)\right)^q - \left(\widetilde{\phi_{A^{Q^*}}}^{-}(\chi)\right)^q\right|}} \geq \sqrt[q]{\frac{1-\left|\left(\widetilde{\varphi_{B^{Q^*}}}^{-}(\chi)\right)^q - \left(\widetilde{\phi_{B^{Q^*}}}^{-}(\chi)\right)^q\right|}{1+\left|\left(\widetilde{\varphi_{B^{Q^*}}}^{-}(\chi)\right)^q - \left(\widetilde{\phi_{B^{Q^*}}}^{-}(\chi)\right)^q\right|}}$$

and

$$\sqrt[q]{\frac{1-\left|\left(\widetilde{\varphi_{A^{Q^*}}}^{+}(\chi)\right)^q-\left(\widetilde{\phi_{A^{Q^*}}}^{+}(\chi)\right)^q\right|}{1+\left|\left(\widetilde{\varphi_{A^{Q^*}}}^{+}(\chi)\right)^q-\left(\widetilde{\phi_{A^{Q^*}}}^{+}(\chi)\right)^q\right|}} \leq \sqrt[q]{\frac{1-\left|\left(\widetilde{\varphi_{B^{Q^*}}}^{+}(\chi)\right)^q-\left(\widetilde{\phi_{B^{Q^*}}}^{+}(\chi)\right)^q\right|}{1+\left|\left(\widetilde{\varphi_{B^{Q^*}}}^{+}(\chi)\right)^q-\left(\widetilde{\phi_{B^{Q^*}}}^{+}(\chi)\right)^q\right|}}$$

As above, we can obtain

$$\left|\left(\widetilde{\varphi_{A^{Q^*}}}^{-}(\chi)\right)^q-\left(\widetilde{\phi_{A^{Q^*}}}^{-}(\chi)\right)^q\right| \leq \left|\left(\widetilde{\varphi_{B^{Q^*}}}^{-}(\chi)\right)^q-\left(\widetilde{\phi_{B^{Q^*}}}^{-}(\chi)\right)^q\right|$$

and $\left|\left(\widetilde{\varphi_{A^{Q^*}}}^{+}(\chi)\right)^q-\left(\widetilde{\phi_{A^{Q^*}}}^{+}(\chi)\right)^q\right| \geq \left|\left(\widetilde{\varphi_{B^{Q^*}}}^{+}(\chi)\right)^q-\left(\widetilde{\phi_{B^{Q^*}}}^{+}(\chi)\right)^q\right|$

So $A^{Q^*} \subseteq B^{Q^*}$

A^{Q^*} is less fuzzy than B^{Q^*}.

(I-Q5) Easy to proof.

The function valued graph is shown as figure 2.

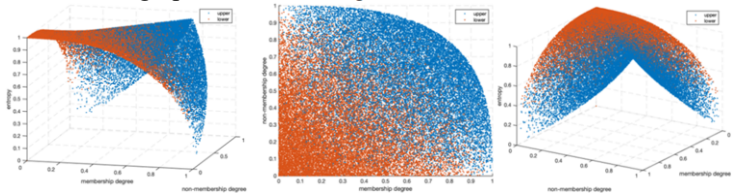

Figure 2. The function valued graph of $E_{\mathrm{IV}}(A^{Q^*})$

4 Examples and Comparation

In this section, the proposed IVFE will be compared with Bu[17]'s IVIFE to verify the rationality of the proposed IVFE in this paper.

The fuzzy entropy formula of Bu[17]'s on IVIFSs as follow:

$$E(A^{I^*}) = \frac{1}{n}\sum_{i=1}^{n} \frac{\min\{\varphi_{I^*}^{-}(\chi_i), \phi_{I^*}^{-}(\chi_i)\} + \min\{\varphi_{I^*}^{+}(\chi_i), \phi_{I^*}^{+}(\chi_i)\} + \pi_{I^*}^{-}(\chi_i) + \pi_{I^*}^{+}(\chi_i)}{\max\{\varphi_{I^*}^{-}(\chi_i), \phi_{I^*}^{-}(\chi_i)\} + \max\{\varphi_{I^*}^{+}(\chi_i), \phi_{I^*}^{+}(\chi_i)\} + \pi_{I^*}^{-}(\chi_i) + \pi_{I^*}^{+}(\chi_i)}$$

To verify the validity as well as the reasonableness of the fuzzy entropy formula proposed in this paper, we set q to 1 for q-RIVOFSs and use the formula to compare with the fuzzy entropy of Bu[17]'s on IVPFS as follows:

Table 1. The comparison of proposed fuzzy entropy with traditional fuzzy entropy

A^{I^*}	(x, [0.3,0.6]) [0.1,0.2])	(x, [0.1,0.2]) [0.3,0.5])	(x, [0.1,0.1]) [0.1,0.1])
$E(A^{I^*})$ [17]	0.65	0.71	1
$E_{IV}(A^{Q^*})$	[0.43,0.67]	[0.54,0.67]	[1, 1]

As can be seen from Table 1, the order of the fuzzy entropy values obtained from the fuzzy entropies is consistent for the three different IVIFNs, which can prove the correctness as well as the validity of the proposed formula. However, the form of the data is different, and for interval values, the information loss that translated to interval values is less than it is converted to exact values.

5 Conclusion

In this paper, according to the disadvantages of existing IVq-ROFSs fuzzy entropy, the IVFE on IVq-ROFSs axiomatic definitions is proposed, and the corresponding fuzzy entropy function image is drawn and the fuzzy entropy values are interpreted accordingly by the graphs, and finally the corresponding formulas are given according to the axiomatic definition, and the rationality, validity and less information loss than traditional fuzzy entropy of the proposed fuzzy entropy are proved by a simple example.

References

[1] Zadeh, L. Fuzzy sets. *Inform Control*, 8 (1965), 338-353.
[2] Qin, H., Fei, Q., Ma, X. and Chen, W. A new parameter reduction algorithm for soft sets based on chi-square test. *Applied Intelligence*, 51 (2021), 7960-7972.
[3] Ma, X., Fei, Q., Qin, H., Zhou, X. and Li, H. New improved normal parameter reduction method for fuzzy soft set. *IEEE Access*, 7 (2019), 154912-154921.
[4] Qin, H., Peng, Q., Ma, X. and Zhan, J. A new multi-attribute decision making approach based on new score function and hybrid weighted score measure in interval-valued Fermatean fuzzy environment. *Complex & Intelligent Systems* (2023), 1-18.
[5] Akram, M., Dudek, W. A. and Ilyas, F. Group decision-making based on pythagorean fuzzy TOPSIS method. *International Journal of Intelligent Systems*, 34, 7 (2019), 1455-1475.
[6] Ananthi, V., Balasubramaniam, P. and Kalaiselvi, T. A new fuzzy clustering algorithm for the segmentation of brain tumor. *Soft Computing*, 20 (2016), 4859-4879.
[7] Dwivedi, A. K., Kaliyaperumal Subramanian, U., Kuruvilla, J., Thomas, A., Shanthi, D. and Haldorai, A. Time-series data prediction problem analysis through multilayered intuitionistic fuzzy sets. *Soft Computing*, 27, 3 (2023), 1663-1671.
[8] Turksen, I. B. Interval valued fuzzy sets based on normal forms. *Fuzzy sets and systems*, 20, 2 (1986), 191-210.
[9] Takeuti, G. and Titani, S. Intuitionistic Fuzzy Logic and Intuitionistic Fuzzy Set Theory. *Journal of Symbolic Logic*, 49, 3 (1984), 851-866.
[10] Ali, M. I. Another view on q-rung orthopair fuzzy sets. *International Journal of Intelligent Systems*, 33, 11 (2018), 2139-2153.
[11] Joshi, B. P., Singh, A., Bhatt, P. K. and Vaisla, K. S. Interval valued q-rung orthopair fuzzy sets and their properties. *Journal of Intelligent & Fuzzy Systems*, 35, 5 (2018), 5225-5230.
[12] Kosko, B. Fuzzy entropy and conditioning. *Information sciences*, 40, 2 (1986), 165-174.
[13] Peng, X. and Liu, L. Information measures for q-rung orthopair fuzzy sets. *International Journal of Intelligent Systems*, 34, 8 (2019), 1795-1834.
[14] Zhang, Q.-s., Jiang, S., Jia, B. and Luo, S. Some information measures for interval-valued intuitionistic fuzzy sets. *Information sciences*, 180, 24 (2010), 5130-5145.
[15] Peng, X. and Li, W. Algorithms for interval-valued pythagorean fuzzy sets in emergency decision making based on multiparametric similarity measures and WDBA. *Ieee Access*, 7 (2019), 7419-7441.
[16] Burillo, P. and Bustince, H. Entropy on intuitionistic fuzzy sets and on interval-valued fuzzy sets. *Fuzzy sets and systems*, 78, 3 (1996), 305-316.
[17] Bu, F., He, J., Li, H. and Fu, Q. Interval-valued intuitionistic fuzzy MADM method based on TOPSIS and grey correlation analysis. *Mathematical Biosciences and Engineering*, 17, 5 (2020), 5584-5603.

Fuzzy Systems and Data Mining IX
A.J. Tallón-Ballesteros and R. Beltrán-Barba (Eds.)

doi:10.3233/FAIA231070

Improvement of User Information Behavior in Online Medical Community Based on Reputation Incentive Game

Jianying Xiong[a,1] and Weilong Hu[b]
[a] *College of Computer Science, Jiangxi University of Chinese Medicine, China*
[b] *Hanlin Hangyu (Tianjin) Industrial Co.,Ltd, Tian Jin, China*

Abstract. Online medical communities can alleviate the imbalance of medical resources. However, the quality of information in the community varies and even contains false information. Online reputation can regulate user behavior and maintain online medical order. The research proposes a reputation reward and punishment model based on user behavior, which is used to guide users to regulate information behavior and improve the quality of medical information. The model rewards and punishes reputation according to the information release, forwarding, self-correction of information behavior and blocking of bad information. It also conducts game analysis on the interaction behavior of nodes in the community towards different quality medical information. By establishing a reputation incentive cooperation mechanism between nodes, information interaction between malicious nodes can be reduced. The experimental results show that the method can establish an incentive cooperation mechanism between nodes, and inhibit the dissemination of low-quality information.

Keywords. Online medical community, Trust, Reputation game, Reputation incentives, User behavior

1. Introduction

With the rapid development of mobile online communities and public health, online medical communities have emerged. Compared to traditional information services, the generation and dissemination of content in online communities are more complex. Medical information is different from other information. If users adopt it without discrimination, it not only threatens the network ecological environment, but also easily misleads users and affects their lives and health. As a result, many online medical websites have established reputation feedback mechanisms to reduce moral hazard issues caused by information asymmetry. For example, Chunyu Doctor and Good Doctor use patient feedback to calculate doctors' scores as service recommendation indicators. There are also some patient social networks that provide feedback on the information shared, such as MyHealthTeams, which is a chronic disease social networking website, and PatientsLikeMe, which is a patient diagnosis and treatment sharing platform.

Every node in the community is a key link in information dissemination, which can be the publisher, supervisor and blocker of content. From the perspective of network

[1] Corresponding Author, Jianying Xiong, Jiangxi UCM, China; E-mail: special8212@sohu.com

node autonomy, we can control the source of security problems and build a good network community ecology. The reputation of nodes in the open community is important network interpersonal relationships [1]. After evaluating the initial reputation, a reward and punishment mechanism is set up based on the node's information behavior to dynamically adjust the reputation. It can create constraints on the behavior of nodes and achieve better self-discipline [2]. In the process of information interaction, nodes need to consider the losses and benefits of themselves and others, so that the whole interaction process can become a game process. Therefore, game theory can be used to handle cooperation process of nodes in medical communities. The incentive strategy will guide nodes to make positive information behavior through the game, inhibit the spread of low-quality, bad and untrue information, and realize the autonomous mechanism of group prevention and control in medical communities [3].

Reputation is a method of establishing trust for strangers in online communities, and research on social network trust has a good foundation. The measurement of trust in online communities is currently mainly divided into global trust and local trust [4]. Global trust is also known as social reputation, and it can be seen as a cumulative social asset. There are many researches on different types of trust evaluation. For example, nodes obtain the global trust through the iteration of mutual satisfaction between adjacent nodes [5]. Some researchers show that the characteristics of users, information and media will affect the information dissemination, the propagation prediction of the trust of the integrated users is better than that of the general model [6]. In terms of improving the user participation of mobile group governance perception network, some researchers show that reputation can stimulate user participation. Reputation not only improves the efficiency of network task processing, but also reduces the processing cost [7]. Some researchers proposed to calculate user attitude through interaction experience, and evaluate the change law of interaction behavior pattern according to interaction time series, forming a comprehensive trust evaluation model for social network users [8]. A punishment mechanism is used to enhance the cooperative behavior of nodes in wireless ad hoc networks [9]. A trust driven model for network architecture software is proposed [10], which enables trust management and online evolution of trust relationship to be realized. Based on the law of trust, it aims to accumulate feedback of different information interactions to calculate the reputation of users, and then dynamically adjust the reputation of users through reputation rewards and punishments for different information behaviors. By simulating reputation gains games in different situations, the model can guide nodes to make reasonable interactions.

2. Construction of Reputation Incentive Model

2.1. Working principle of reputation model

Each user can obtain initial reputation by authentication and personal information in online communities, such as patient communication website. In such a patient social network, each user is also a node. In order to focus on studying the impact of dynamic behavior on reputation, we do not consider the reputation brought by node identity here, but use social reputation (SR) to constrain the information behavior of nodes.

SR is a comprehensive evaluation of historical information behavior. The different feedback on information can affect their evaluation of *SR*. The posting and forwarding behaviors are all medical communities' interactions. The forwarding, liking and stepping

on behaviors given by other nodes are attitude feedback given after receiving information [11]. Three different types of behaviors are quantified as {1,0.5,-1}. The reputation value of the interaction node affects the validity of the score, and the interaction given by the node with high reputation is more valuable to enhance the reputation of the node. SR_j is the node reputation value of the j node's feedback, and fs_j is the quantitative score for the feedback of the j node. Therefore, the interaction degree of node i is weighted and accumulated by the reputation of medical communities. SR_i is calculated as formula (1), where j is the node with the interaction with i node, but except i node itself.

$$SR_i = \sum_{j=1}^{n}\left(\frac{SR_j}{\sum_{j=1}^{n} SR_j} * fs_j\right) \quad (1)$$

Reputation reward and punishment mechanism is used to motivate the information behavior of nodes, guide the nodes to adjust information behavior, and also is a positive expectation of node behavior. The information behavior of nodes will also be limited by reputation. As the figure 1, the system will set up the reputation-based user behavior permission mechanism RC, which can be divided into different levels G, and it can map different behavior permissions C, namely RC: G → C.

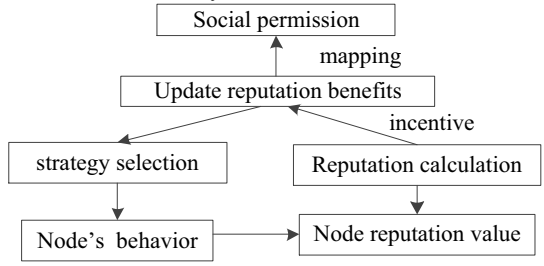

Figure 1. Game process based on reputation incentive

2.2. Reputation reward and punishment

The nodes with high reputation in medical communities will consciously maintain network stability and control negative information transmission in case of crisis, and actively maintain medical communities' security. If the initiative information strategy is guided by reputation reward and punishment, it can promote node autonomy more effectively. There are three dimensions in the mechanism, including content quality, information self-correction, and bad information transmission blocking. The reward and punishment coefficient can also be adjusted according to the platform experience.

The system rewards more punishment scenarios than rewards. Once bad behavior occurs, the reputation will decline faster, and the nodes will be more cautious about their information behavior. The reputation updating mechanism punishes and supervises the reputation behavior by time series, and adjusts the reputation value dynamically. In the process of adjustment, the higher reputation of users, the greater influence of each behavior in the medical communities. The reputation rewards and punishments are proportional to the reputation of nodes. Therefore, after increasing the reward and punishment coefficient, the calculation method of SR_i is shown in expression (2).

$$SR_i = SR_i * (1 + r) \quad (2)$$

2.3. Reputation game evolution of cooperation restrained by bad information

When using game theory to analyze medical communities' communication, the entities in the network are regarded as game participants with bounded rationality. The strategy

of the players is the action taken by the entity nodes. According to this idea, the basic formula of single-stage cooperative game of entity nodes in medical communities is given as follow.

In each game stage, the reputation game between entities can be defined as triple D = (G, S, U). G is the set of entity nodes in the system, and is also the player of the game: $G_i = \{i, N_{-i}\}$. Where N_{-i} is the player of the game except entity node *i*. S is the strategy set of entity nodes participating in the game, $S = \{S_i, S_{-i}\}$. *U* is the income function of the player.

The revenue function *U* is the mapping from the policy set $S = \{S_i, S_{-i}\}$ to the reputation revenue *R*, that is, u: S → R. It is assumed that the benefits of nodes in medical communities are mainly personal reputation and additional benefits related to content promotion.

The game process of entity node cooperation can be described as follows: in the process of cooperation, entity node can be either the initiator of cooperation or the responder of cooperation. In the medical community's environment, the initiator's strategy is {Cooperation (publishing high-quality information), non-cooperation (Publishing bad information)}; The strategy of responders is {Cooperation (forwarding information) and non-cooperation (reporting information)}. It is supposed that there are no incentives in the medical community's environment, the dissemination income of the initiator's high-quality information and bad information is $\{p_1, p_2\}$; and the responder's high-quality information and bad information is $\{0, p_3\}$, such as water army behavior; There is no obvious punishment and incentive for the reported information in medical communities, and the income is 0. If there is no reputation punishment mechanism, the profit matrix of the game can be expressed as table 1.

Table 1. game income matrix under no credit incentive

	Initiator		
Responder		High quality information	Bad information
	Forward	$(0,p_1)$	(p_3,p_2)
	Accuse	(0,0)	(0,0)

It is assumed that all the entities participating in the interaction are rational and selfish. Without reputation punishment mechanism, as long as the $\{p_2, p_2\}$ revenue combination value is large enough, the initiator and responder are more likely to obtain benefits from the dissemination of bad information, so both parties will choose the one with greater benefits to publish and forward bad information. According to the reputation reward and punishment mechanism, for the initiator, the reputation incentive income of publishing information income is set to *q*, then the reputation income of publishing high-quality information and bad information is $\{q_1, -q_2\}$; The reported reputation gain is $\{0, -q_2\}$. For responders, the reputation gain of forwarding high-quality information and bad information is $\{0, -q_3\}$; The reputation gain of reporting behavior is $\{-q_4, q_5\}$. Therefore, after integrating reputation penalty, the income is the combination of reputation and propagation income, and income matrix as table 2.

If the initiator publishes the bad information and the responder forwards it under the condition of reputation rewards and punishments, their respective profits are $(-q_3 + p_3, -q_2 + p_2)$. If bad information is accused, the respective benefits are $(q_5, -q_2)$. As long as $U(q_5) > U(-q_3 + p_3)$, responders will choose to accuse the information. When the originator publishes high-quality information, the responder will not choose malicious report for the revenue relationship $U(-q_4) < U(0)$, so it is easier to choose forwarding. Therefore,

as long as the reward and punishment coefficient are set reasonably, the initiator and responder in medical communities will make the following strategies:

(1) Responders will choose to accuse bad information to gain reputation.

(2) Responders will not lose personal reputation to accuse high-quality information maliciously.

(3) The initiator is not willing to lose his reputation and publish bad information when there is no significant communication benefit.

(4) Sponsors are willing to publish high-quality information to gain Reputation.

Table 2. game income matrix under reputation reward and punishment incentive

	Initiator		
Responder		High quality information	Bad information
	Forward	$(0,q_1+p_1)$	$(-q_3+p_3,-q_2+p_2)$
	Accuse	$(-q_4,0)$	$(q_5,-q_2)$

3. Experiment

3.1. Simulation environment description

Because we hope to focus on observing the impact of behavior on reputation, we do not consider initial trust in the experiment and assume that there are already certain connections and interactions. In the experiment, a medical community with 4000 nodes is simulated, and the reputation value of each node is initialized to 0. Each node is randomly connected to 20% nodes in the community. Assuming that 50% of the connected nodes report the information, the information will be considered as bad information, the information will be verified and tagged, and the person who posts or posts will be punished for reputation, and the informant will be rewarded for reputation.

In order to verify the impact of reputation on the transmission process, SIR model of infectious disease model is used to simulate the process of information transmission [12]. There are three states of user groups in SIR model: uninfected state S(susceptible), infected state I (infected) and immune state R (recovered), which correspond to users who do not receive information, users who transmit information and users who are not interested in information. In traditional SIR model, we add connection state C (connected), which indicates that it is connected with the spreading node of infection. The dynamic process of SIR propagation is improved as shown in (3).

$$\begin{cases} \frac{dC(t)}{dt} = \gamma C(t) \\ \frac{dS(t)}{dt} = -\lambda S(t)I(t) \\ \frac{dI(t)}{dt} = \lambda S(t)I(t) - \mu I(t) \\ \frac{dR(t)}{dt} = \mu I(t) \end{cases} \tag{3}$$

According to the SIR model, iff the number of infected nodes is NI_t and the number of iterations is t, the cumulative total number of infected nodes NI is shown in (4).

$$NI = \sum_{t=1}^{T} NI_t \tag{4}$$

The experimental rules are as follows:

(1) In each time step, the receiving point is the node connected by all infection points.

(2) The infected nodes are infected by probability λ to infect the integrity and connected nodes in the susceptible state, the malicious nodes will be infected directly; After the infection, the node forwards the information for the next iteration.

(3) The susceptible integrity node will accuse bad information with probability p. After the infection, the integrity node will lose interest in spreading with probability μ, and become an immune node, then accuse bad information;

(4) The contact between immune node and infected node will not produce transmission behavior.

(5) When all nodes in the whole network receive bad information or the information is successful be accused, the propagation ends.

In the whole propagation process, the total number of participants n remains unchanged, so S(t) + R (t) + I (t) = n. In SIR model, λ is the probability of infection, μ is immune probability. However, in the model of add the connect nodes, γ Is the connectivity probability.

3.2. Comparison of communication effects under different models

In the simulation experiment, the relevant parameters need to be set after many times of debugging. After 100 times of debugging, the simulation parameters are set as: infection rate λ= 1, recovery rate μ = 5, t = 10 iterations. Under the scenario of any single propagation source, 10% malicious nodes in the community spread bad information. The experimental results in Fig. 2 and Fig. 3 show the number variation curves of four types nodes with time t in NER (No Encourage Reputation) model and ER (Encourage Reputation), including the total number of connected nodes (C), susceptible nodes(S), infected nodes (I) and recovered nodes (R).

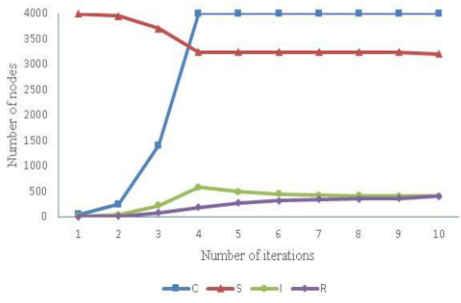

Figure 2. Number of different nodes in of NER

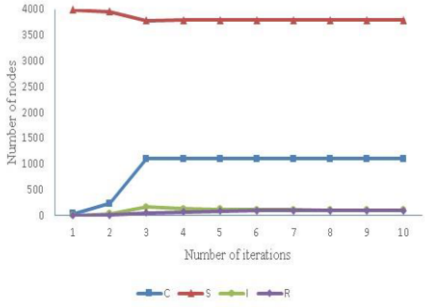

Figure 3. Number of different nodes in ER

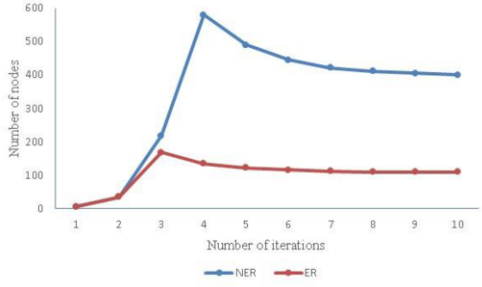

Figure 4. Number of infected nodes in different model

The experimental results show that, compared with the case of no reputation reward and punishment game, the number of nodes receiving bad information in ER model will

be less than that in traditional NER model, and will soon tend to balance. The main reason is that more nodes will accuse bad information after the reputation game in the fast iterative propagation, which blocks the information propagation. And it also prevents other nodes from receiving information in the later propagation network. Under different models, the number of susceptible nodes in ER model will only be infected at the initial stage. With the blocking and disclosure of bad information, the number of infected nodes and recovery nodes will be lower.

Figure 4 is the comparison results of all infected nodes in the community. In NER model, there will be a rapid propagation peak, causing more node infection. In ER model, there will be more blocking behavior of nodes in the community at the propagation peak, resulting in a rapid decline of infected nodes.

4. Summary

Reasonable reputation mechanism in online medical communities can regulate node information behavior. And experiments have shown that the ER model can effectively promote the formation of relationships between nodes, and suppress the dissemination of low-quality information. The study analyzes reputation rewards and punishments from a dynamic game perspective, which helps enrich the research on knowledge sharing and dissemination mechanisms and network trustworthiness. The next step in the research will be to study more intelligent agents and their behavior rules, and analyze the dynamic evolution process of reputation in multiple stages.

References

[1] Popescul, D. , & Georgescu, M. . Social networks security in universities: challenges and solutions. Annals of the Alexandru Ioan Cuza University - Economics, 2015,62(s1):53-63.

[2] Jazaieri H , Logli Allison M , Campos B , et al. Content, structure, and dynamics of personal reputation: The role of trust and status potential within social networks. Group Processes & Intergroup Relations, 2019.22(7):964-983

[3] Jaramillo, Juan Jose , and R. Srikant . "A game theory based reputation mechanism to incentivize cooperation in wireless ad hoc networks." *Ad Hoc Networks*8.4(2010):416-429.

[4] Urena R, Chiclana F, Carrasco R A, et al. Leveraging Users' Trust and Reputation in Social Networks. Procedia Computer Science, 2019: 162, (12):955-962.

[5] Raj, E. D. , & Babu, L. D. D. An enhanced trust prediction strategy for online social networks using probabilistic reputation features. Neurocomputing, 2016, 219(1) :412-421.

[6] Yu, Y. , Jia, Z. , Tao, W. , Xue, B. , & Lee, C. An efficient trust evaluation scheme for node behavior detection in the internet of things. Wireless Personal Communications An International Journal, 2017, 93(2) :571-587.

[7] Srinivasan, A. , & Naseera, S. Trust and location based service in mobile social networks – a survey. Multiagent and Grid Systems,2018,14(3):263-282.

[8] Liu Y.H, Jin X.L, &Shen H.W. Towards early identification of online rumors based on long short-term memory networks. Information Processing & Management, 2019, 56(4):1457-1467.

[9] Kareva, I. , Morin, B. , & Karev, G. Preventing the tragedy of the commons through punishment of over-consumers and encouragement of under-consumers. Bull Math Biol, 2013, 75(4):565-588.

[10] Mughal, B. K. , S. Hameed , and G. M. Shaikh . "A Centralized Reputation Management Scheme for Isolating Malicious Controller(s) in Distributed Software-Defined Networks." International Journal of Advanced Computer science and Applications 7.12(2017):368.

[11] Shen, Y. , et al. "Dynamic socialized Gaussian process models for human behavior prediction in a health social network." *Knowledge and Information Systems*49.2(2016):455-479.

[12] Siqing, S. , Mengni, L. , & Xiaobo, X. Analysis of the key influencing factors of haze information dissemination behavior and motivation in wechat. *Interlending & document supply,* 2017, *45*(1):21-29.

Fuzzy Systems and Data Mining IX
A.J. Tallón-Ballesteros and R. Beltrán-Barba (Eds.)

doi:10.3233/FAIA231071

Two Count Sketch Kaczmarz Algorithms for Linear Systems

Yikang WANG[1], Pingping ZHANG
[a] *School of Science, Chongqing University of Posts and Telecommunications, Chongqing, 400065*

Abstract. In this paper, combining count sketch, we construct a count sketch two greedy subspace Kaczmarz (CS-2GSK) algorithm. In addition, the block count sketch Kaczmarz (BCSK) algorithm is also given, which selects multiple different rows simultaneously at each iteration. We prove that our methods converge to the unique solution of the linear systems. Finally, the numerical experiments show the high efficiency and robustness of our methods.

Keywords. Kaczmarz, count sketch, image reconstruction

1. Introduction

We only consider over-determined linear systems

$$Ax = b, \tag{1}$$

where $A \in \mathbb{R}^{m\times n}$, $b \in \mathbb{R}^m$, m is much bigger than n, and x is what we want to gain. In particular, we also require linear systems (1) to be consistent. The Kaczmarz method [1] is a common projection method for solving (1), which has been studied for many years, and its iterative scheme is

$$x_{k+1} = x_k + \frac{b_i - a_i^T x_k}{\| a_i \|^2} a_i.$$

In 2018, Bai and Wu [2] proposed the greedy randomized Kaczmarz(GRK) algorithm and Gu and Liu [3] extended the GRK algorithm to the 2GSK algorithm in 2020, and the theoretical guarantee the convergence of the 2GSK algorithm.

Numerous random sketching matrices [4–7] have been discovered by researchers over the years. The maximal weighted residual Kaczmarz [8] algorithm was used by Li and Zhang [9] in 2021, and they provided a CS-MWRK method for solving the systems (1). Numerical experiments demonstrated that the CS-MWRK method can effectively reduce computing time, but the number of iterations has significantly increased.

[1]Corresponding Author: Yikang Wang, male, Han, Chongqing, major in numerical algebra.: wyk10071996@163.com.

In this research, we combine the count sketch and 2GSK method, and we present the count sketch two greedy subspace Kaczmarz algorithm (CS-2GSK), which is motivated by the works of Zhang and Gu. Furthermore, in order to decrease the calculation times and iteration times of the CS-2GSK method, we suggest a block count sketch Kaczmarz algorithm (BCSK), which uses a selecting criterion to choose a block.

The main content of our work is structured as follows. Section 2 begins with several lemmas and the definition of count sketch. Sections 3 and 4 detail the proposed approaches as well as the accompanying convergence. Finally, in Section 5, we show the numerical results and followed the conclusion in Section 6.

2. Preliminaries

The following is about the definition and the property of count sketch, respectively. They have been given in detail in [4, 5, 10].

Definition 2.1 A count sketch matrix $\mathbf{S} \in \mathbb{R}^{d\times m}$ is constructed in terms of ΦD. Here, $D \in \mathbb{R}^{m\times m}$ is a random diagonal matrix. Besides, each diagonal entry of D is chosen to be positive unity or minus one, and Φ is an $d \times m$ arbitrary matrix whose entries are either zeros or ones.

Lemma 2.2 If $\mathbf{S}$ is a count sketch matrix defined in **Definition 2.1** with $(n^2 + n)/(\delta\varepsilon^2)$ rows, where δ is a positive constant and ε is a normal number less than 1, then we have

$$(1-\varepsilon)||Ax||_2 \leq ||\mathbf{S}Ax||_2 \leq (1+\varepsilon)||Ax||_2.$$

3. The Count Sketch two greedy subspace Kaczmarz algorithm

Given a sufficiently large positive integer ℓ and initial point x_0, then, the specific process of the CS-2GSK algorithm is in **Algorithm 2**.

Algorithm 1 The CS-2GSK algorithm

1. Input: $A,\ b,\ \ell\ x_0$.
2. Output: x_ℓ.
3. Initialize: Create $\mathbf{S}$, compute $\widetilde{A} = \mathbf{S}A$ and $\widetilde{b} = \mathbf{S}b$.
4. **for** $k = 0, 1, ..., \ell - 1$ **do**

   (a) Compute $r_k = \widetilde{b} - \widetilde{A}x_k$

   (b) Select rows i_k and j_k that satisfy

$$i_k = arg\max_{1\le i\le d}\{\frac{|\widetilde{b}^{(i)} - \widetilde{A}^{(i)}x_k|}{\|\widetilde{A}^{(i)}\|_2^2}\},\ j_k = arg\max_{i\in[m]\setminus i_k}\{\frac{|\widetilde{b}^{(i)} - \widetilde{A}^{(i)}x_k|}{\|\widetilde{A}^{(i)}\|_2^2}\}.$$

   (c) Set

$$x_{k+1} = x_k + \frac{r_k^{(i_k)}(\widetilde{A}^{(i_k)})^T}{\|\widetilde{A}^{(i_k)}\|_2^2} + \frac{r_k^{(j_k)}(\widetilde{A}^{(j_k)})^T}{\|\widetilde{A}^{(j_k)}\|_2^2}.$$

5. **end for**.

Regarding the convergence of the CS-2GSK method, the **Theorem 3.1** is given.

Theorem 3.1 Let each row of $A \in \mathbb{R}^{m\times n}$ not be orthogonal to each other. Solving linear system (1) by CS-2GSK method can produce a series of sequence $\{x_k\}_{k=0}^{\infty}$. Then the sequence $\{x_k\}_{k=0}^{\infty}$ converges to the unique solution of $Ax = b$. Moreover, the solution error obeys

$$\|x_{k+1} - x_\star\|_2^2 \le \prod_{q=0}^{k}(1 - \lambda_{\min}(P_qP_q^T))\ \|x_0 - x_\star\|_2^2,\ k = 0, 1, 2, \ldots,$$

where $P_k = P_{i_k} - P_{j_k}$ with

$$P_{i_k} = \frac{(\widetilde{A}^{(i_k)})^T}{\|\widetilde{A}^{(i_k)}\|_2}\cdot\frac{\widetilde{A}^{(i_k)}}{\|\widetilde{A}^{(i_k)}\|_2}\ and\ P_{j_k} = \frac{(\widetilde{A}^{(j_k)})^T}{\|\widetilde{A}^{(j_k)}\|_2}\cdot\frac{\widetilde{A}^{(j_k)}}{\|\widetilde{A}^{(j_k)}\|_2},$$

where $\lambda_{\min}(P_qP_q^T)$ denotes the minimum eigenvalue of $P_qP_q^T$.

Proof. In fact, we only let

$$P_{i_k} = \frac{(\widetilde{A}^{(i_k)})^T}{\|\widetilde{A}^{(i_k)}\|_2}\cdot\frac{\widetilde{A}^{(i_k)}}{\|\widetilde{A}^{(i_k)}\|_2}\ and\ P_{j_k} = \frac{(\widetilde{A}^{(j_k)})^T}{\|\widetilde{A}^{(j_k)}\|_2}\cdot\frac{\widetilde{A}^{(j_k)}}{\|\widetilde{A}^{(j_k)}\|_2}.$$

The rest of the proof can be completed along the same lines as in [3, Theorem 1], we omit the details. □

4. The block count sketch Kaczmarz algorithm

The basic goal of the block count sketch Kaczmarz (BCSK) algorithm is to gather all of the indices that are closest to the greatest entry as the i_k and j_k in the CS-2GSK

method. Specifically, we select the index set by

$$|r_k^{(j_k)}|^2 \geq \alpha \max_{1\leq j\leq n} |r_k^{(j)}|^2,\ j_k \in \{1,2,...,n\}.\ \alpha \in [0,1)$$

It's clear that BCSK algorithm is retrieving more rows as α increases.

Below, we give the specific process of the BCSK algorithm in **Algorithm 2**.

Algorithm 2 The BCSK algorithm

1. Input: $A,\ b,\ \alpha,\ \ell,\ x_0$.
2. Output: x_ℓ.
3. Initialize: Create $\mathbf{S}$, compute $\widetilde{A} = \mathbf{S}A$ and $\widetilde{b} = \mathbf{S}b$.
4. For $k = 0,1,...,\ell-1$ **do**
   (a) Compute $r_k = \widetilde{b} - \widetilde{A}x_k$
   (b) Compute target block $\tau_k = \{j_k|\ |r_k^{(j_k)}|^2 \geq \alpha \max_{1\leq j\leq n} |r_k^{(j)}|^2\}$
   (c) Set
   $$x_{k+1} = x_k + \widetilde{A}_{\tau_k}^{\dagger} r_k.$$
5. **end for**.

Remark 4.1 In practice, the **CGLS** [11–13] can be used to calculate the approximation of $\widetilde{A}_{\tau_k}^{\dagger}$ in the fourth step of **Algorithm 2**.

Next, we will show the convergence of the BCSK method by **Theorem 4.2**.

Theorem 4.2 Let the condition in **Theorem 3.1** be satisfied. Solving linear system (1) by BCSK method can produce a series of sequence $\{x_k\}_{k=0}^{\infty}$. Then the sequence $\{x_k\}_{k=0}^{\infty}$ will converge to the unique solution of (1). Moreover, the solution error obeys

$$\| x_{k+1} - x_\star \|_2^2 \leq \prod_{q=0}^{k} \left(1 - \frac{\alpha|\tau_q|}{m-|\tau_{q-1}|} \cdot \frac{(1-\varepsilon)^2 \lambda_{\min}(A^TA)}{(1+\varepsilon)^2 \sigma_{\max}^2(A)}\right) \| x_0 - x_\star \|_2^2 . \tag{2}$$

where $|\tau_q|$ represents the cardinality of τ_q and $\alpha \in (0,1]$.

Proof. From **Algorithm 2**, we have

$$\begin{aligned} x_{k+1} - x_\star &= x_k - x_\star + \widetilde{A}_{\tau_k}^{\dagger}(\widetilde{b}_{\tau_k} - \widetilde{A}_{\tau_k} x_k) \\ &= x_k - x_\star - \widetilde{A}_{\tau_k}^{\dagger} \widetilde{A}_{\tau_k}(x_k - x_\star) \\ &= (I - \widetilde{A}_{\tau_k}^{\dagger} \widetilde{A}_{\tau_k})(x_k - x_\star). \end{aligned}$$

Since $\widetilde{A}_{\tau_k}^{\dagger} \widetilde{A}_{\tau_k}$ is an orthogonal projector, we get

$$\begin{aligned} \| x_{k+1} - x_\star \|_2^2 &= \| (I - \widetilde{A}_{\tau_k}^{\dagger} \widetilde{A}_{\tau_k})(x_k - x_\star) \|_2^2 \\ &= \| x_k - x_\star \|_2^2 - \| \widetilde{A}_{\tau_k}^{\dagger} \widetilde{A}_{\tau_k}(x_k - x_\star) \|_2^2 \end{aligned} \tag{3}$$

As explained in [2], we have

$$\| A(x_k - x_\star) \|_2^2 \geq \sigma_r^2(A) \| x_k - x_\star \|_2^2,$$

which leads to

$$\begin{aligned}
\| \widetilde{A}_{\tau_k}^{\dagger} \widetilde{A}_{\tau_k}(x_k - x_\star) \|_2^2 &\geq \frac{1}{\sigma_{\max}^2(\widetilde{A}_{\tau_k})} \| \widetilde{A}_{\tau_k}(x_k - x_\star) \|_2^2 \\
&\geq \frac{1}{(1+\varepsilon)^2 \sigma_{\max}^2(A)} \| \widetilde{A}_{\tau_k}(x_k - x_\star) \|_2^2 \\
&= \frac{1}{(1+\varepsilon)^2 \sigma_{\max}^2(A)} \sum_{i_k \in \tau_k} |\widetilde{A}^{(i_k)}(x_k - x_\star)|^2 \\
&\geq \frac{1}{(1+\varepsilon)^2 \sigma_{\max}^2(A)} \sum_{i_k \in \tau_k} \alpha \max_{1 \leq i \leq m} |\widetilde{A}^{(i)}(x_k - x_\star)|^2 \\
&\geq \frac{|\tau_k|}{(1+\varepsilon)^2 \sigma_{\max}^2(A)} \alpha \max_{1 \leq i \leq m} |\widetilde{A}^{(i)}(x_k - x_\star)|^2.
\end{aligned} \tag{4}$$

From the iteration of the BCSK, we have

$$\begin{aligned}
(\widetilde{b} - \widetilde{A}x_{k+1})_{\tau_k} &= \widetilde{b}_{\tau_k} - \widetilde{A}_{\tau_k} x_k - \widetilde{A}_{\tau_k} \widetilde{A}_{\tau_k}^{\dagger} (\widetilde{b}_{\tau_k} - \widetilde{A}_{\tau_k} x_k) \\
&= \widetilde{b}_{\tau_k} - \widetilde{A}_{\tau_k} x_k - \widetilde{A}_{\tau_k} \widetilde{A}_{\tau_k}^{\dagger} \widetilde{b}_{\tau_k} + \widetilde{A}_{\tau_k} \widetilde{A}_{\tau_k}^{\dagger} \widetilde{A}_{\tau_k} x_k \\
&= \widetilde{b}_{\tau_k} - \widetilde{A}_{\tau_k} x_k - \widetilde{A}_{\tau_k} \widetilde{A}_{\tau_k}^{\dagger} \widetilde{b}_{\tau_k} + \widetilde{A}_{\tau_k} x_k \\
&= \widetilde{b}_{\tau_k} - \widetilde{A}_{\tau_k} \widetilde{A}_{\tau_k}^{\dagger} \widetilde{b}_{\tau_k} \\
&= \widetilde{A}_{\tau_k} x_\star - \widetilde{A}_{\tau_k} \widetilde{A}_{\tau_k}^{\dagger} \widetilde{A}_{\tau_k} x_\star \\
&= \widetilde{A}_{\tau_k} x_\star - \widetilde{A}_{\tau_k} x_\star \\
&= 0,
\end{aligned}$$

which implies the inequality

$$\| \widetilde{b} - \widetilde{A}x_k \|_2^2 = \sum_{i \in [m] \setminus \tau_{k-1}} |\widetilde{b}^{(i)} - \widetilde{A}^{(i)} x_k|^2 \leq (m - |\tau_{k-1}|) \max_{1 \leq i \leq m} |\widetilde{b}^{(i)} - \widetilde{A}^{(i)} x_k|^2.$$

Hence, for any $\alpha \in (0, 1]$, combining **Lemma 2.2**, we have

$$\max_{1 \leq i \leq m} |\widetilde{b}^{(i)} - \widetilde{A}^{(i)} x_k|^2 \geq \frac{\alpha}{m - |\tau_{k-1}|} \| \widetilde{A}(x_k - x_\star) \|_2^2 \geq \frac{(1-\varepsilon)^2 \alpha}{m - |\tau_{k-1}|} \| A(x_k - x_\star) \|_2^2 .$$

As a result, we see that

$$\begin{aligned}
\| \widetilde{A}_{\tau_k}^{\dagger} \widetilde{A}_{\tau_k}(x_k - x_\star) \|_2^2 &\geq \frac{|\tau_k|}{m - |\tau_{k-1}|} \cdot \frac{(1-\varepsilon)^2 \alpha}{(1+\varepsilon)^2 \sigma_{\max}^2(A)} \| A(x_k - x_\star) \|_2^2 \\
&\geq \frac{\alpha |\tau_k|}{m - |\tau_{k-1}|} \cdot \frac{(1-\varepsilon)^2 \lambda_{\min}(A^T A)}{(1+\varepsilon)^2 \sigma_{\max}^2(A)} \| x_k - x_\star \|_2^2 .
\end{aligned} \tag{5}$$

Thus, substituting Eqs.(5) and (4) into Eq.(3), we obtain

$$\| x_{k+1} - x_\star \|_2^2 \leq (1 - \frac{\alpha|\tau_k|}{m-|\tau_{k-1}|} \cdot \frac{(1-\varepsilon)^2\lambda_{\min}(A^TA)}{(1+\varepsilon)^2\sigma_{\max}^2(A)}) \| x_k - x_\star \|_2^2 .$$

Then,

$$\| x_{k+1} - x_\star \|_2^2 \leq \prod_{q=0}^{k} (1 - \frac{\alpha|\tau_q|}{m-|\tau_{q-1}|} \cdot \frac{(1-\varepsilon)^2\lambda_{\min}(A^TA)}{(1+\varepsilon)^2\sigma_{\max}^2(A)}) \| x_0 - x_\star \|_2^2 .$$

Thus, we complete the proof. □

5. Numerical experiments

In this part, we will use BCSK and CS-2GSK methods to solve (1) and compare with the 2GSK [3] and CS-MWRK [9] methods in terms of the number of iteration steps (denoted as IT) and the computing time (denoted as CPU). All experiments were on a personal computer with 2.00 GHz central processing unit (Intel(R) Core(TM) i5-1038NG7 CPU), 16.00GB memory, and Windows 10 operating system. In addition, the version of MATLAB we use is R2018b.

Example 5.1 We consider the case of stochastic systems in this experiment. The matrix $A \in \mathbb{R}^{m\times n}$ and the exact solution $x_\star$ are gained randomly by using the MATLAB function $randn(m,n)$. All the experiments start from zero vector and we repeat the experiment fifty times and average it. Otherwise, the experiment stops if

$$RES = \frac{||x_k - x_\star||_2^2}{||x_\star||_2^2} \leq 10^{-6}$$

or IT exceeds 200,000.

The numerical results are listed in **Table 1** illustrates that the CS-2GSK method has its pros and cons. More particular, CS-2GSK requires fewer IT than CS-MWRK and significantly less CPU time than 2GSK when $m \gg n$. Additionally, CS-2GSK needs more IT than the 2GSK method. This is due to the fact that the CS-2GSK approach converges a little more slowly due to its bigger convergence factor. In addition, we observe that IT of CS-2GSK approach lowers as d increases, suggesting that the CS-2GSK method converges more quickly. The computation of $i_k = arg\max_{1\leq i\leq d}\{\frac{|\widetilde{b}^{(i)} - \widetilde{A}^{(i)}x_k|}{\|\widetilde{A}^{(i)}\|_2^2}\}$ and $j_k = arg\max_{i\in[m]\setminus i_k}\{\frac{|\widetilde{b}^{(i)} - \widetilde{A}^{(i)}x_k|}{\|\widetilde{A}^{(i)}\|_2^2}\}$ in each iteration will take longer as d rises. As a result, the CS-2GSK method's overall processing time grows. Then, we can see that, for all test values of d, BCSK method uses substantially less CPU and has smaller IT than the other three algorithms.

Example 5.2 In this example, we use the function $paralleltomo(N,\theta,p)$ in the *MATLAB* package *AIR TOOLS* [14]. We set $N = 30,\ \theta = 0:2:178^\circ$ *and* $p = 120$, then A is a 10800×1600 matrix. What's more, we run these methods a thousand times and then observe how clear the image recovered.

Table 1. Numerical results for the 2GSK, BCSK (with $\alpha = 0.16$), CS-MWRK and CS-2GSK methods with random matrix.

		IT				*CPU*			
$m \times n$	d	2GSK	CS-MWRK	BCSK	CS-2GSK	2GSK	CS-MWRK	BCSK	CS-2GSK
5000×50	$10n$	34.0000	85.2000	1.1200	56.0000	0.0069	0.0109	0.0013	0.0100
	$20n$	34.0000	67.4800	1.0400	49.4400	0.0075	0.0100	0.0044	0.0091
	$30n$	32.0000	61.5400	1.0600	48.9800	0.0084	0.0128	0.0034	0.0106
	$40n$	35.0000	58.5000	1.0000	47.6000	0.0075	0.0138	0.0028	0.0103
	$50n$	31.0000	56.5600	1.0200	47.2800	0.0075	0.0125	0.0044	0.0134
5000×100	$10n$	60.0000	172.2600	1.3800	119.7000	0.0219	0.0159	0.0075	0.0150
	$20n$	64.0000	137.6000	1.1200	103.1400	0.0222	0.0175	0.0166	0.0166
	$30n$	60.0000	126.6200	1.1000	99.0800	0.0200	0.0297	0.0097	0.0306
	$40n$	60.0000	122.0600	1.0800	97.2200	0.0213	0.0437	0.0091	0.0362
	$50n$	61.0000	118.6600	1.0800	95.5800	0.0213	0.0750	0.0088	0.0316
5000×150	$10n$	92.0000	260.8600	2.1200	189.7400	0.0547	0.0431	0.0128	0.0316
	$20n$	95.0000	213.4600	1.4400	164.1200	0.0603	0.0587	0.0219	0.0547
	$30n$	97.0000	198.6200	1.4000	157.5800	0.0597	0.1744	0.0184	0.0881
	$40n$	90.0000	192.2600	1.3200	154.0800	0.0512	0.2334	0.0244	0.1441
	$50n$	95.0000	191.0000	1.1400	151.1000	0.0591	0.2972	0.0262	0.1844
5000×200	$10n$	131.0000	354.3600	4.1600	267.0400	0.1244	0.0847	0.0338	0.0666
	$20n$	131.0000	295.5000	2.0800	233.1800	0.1247	0.3050	0.0259	0.1672
	$30n$	131.0000	281.5600	1.9000	222.7800	0.1259	0.4469	0.0344	0.2822
	$40n$	135.0000	271.9200	1.6800	212.9000	0.1256	0.5791	0.0384	0.3781
	$50n$	132.0000	265.7800	1.3000	204.1200	0.1278	0.7116	0.0397	0.5525

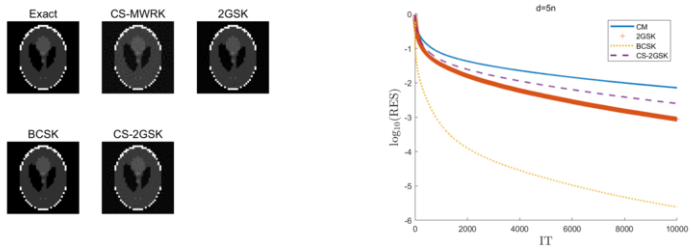

Figure 1. Numerical results for the 2GSK, BCSK (with $\alpha = 0.16$), CS-MWRK and CS-2GSK methods with paralleltomo test problem.

From the left of **Figure 1**, we see again that, under the same IT, BCSK algorithm can achieve better reconstruction results than CS-2GSK, CS-MWRK and 2GSK algorithms with generally smaller working blocks. The right side of **Figure 1** shows that, as IT increases, the RES of the BCSK method decays considerably more fast than those of CS-2GSK, CS-MWRK, and 2GSK algorithms. In fact, we can see that at the thousandth iteration, the RES of BCSK is less than 10^{-6}.

6. Conclusion

In order to solve a sizable consistent linear system (1), we modified the GRK algorithm in this study to the count sketch two greedy subspace Kaczmarz (CS-2GSK) method and the block count sketch Kaczmarz (BCSK) method. We offer theoretical assurances that the two algorithms would converge. We demonstrate certain situations in the experiments section, where the BCSK algorithm performs better than the 2GSK al-

gorithm and the CS-MWRK algorithm in terms of IT and CPU times. In light of this, the BCSK algorithm could be a helpful tool when compared with the CS-2GSK algorithm and the CS-MWRK algorithm.

References

[1] Karczmarz S. Angenäherte auflösung von systemen linearer gleichungen[J]. Bull. Int. Acad. Pol. Sic. Let., Cl. Sci. Math. Nat., 1937: 355-357.
[2] Bai Z Z, Wu W T. On greedy randomized Kaczmarz method for solving large sparse linear systems[J]. SIAM Journal on Scientific Computing, 2018, 40(1): A592-A606.
[3] Liu Y, Gu C. Two Greedy Subspace Kaczmarz Algorithm for Image Reconstruction[J]. IAENG International Journal of Applied Mathematics, 2020, 50(4).
[4] Charikar M, Chen K, Farach-Colton M. Finding frequent items in data streams[C]. Springer Berlin Heidelberg, 2002: 693-703.
[5] Thorup M, Zhang Y. Tabulation-based 5-independent hashing with applications to linear probing and second moment estimation[J]. SIAM Journal on Computing, 2012, 41(2): 293-331.
[6] Woodruff D P. Sketching as a tool for numerical linear algebra[J]. Foundations and Trends in Theoretical Computer Science, 2014, 10(1-2): 1-157.
[7] Sarlos T. Improved approximation algorithms for large matrices via random projections[C]. IEEE, 2006: 143-152.
[8] Du K, Gao H. A new theoretical estimate for the convergence rate of the maximal weighted residual Kaczmarz algorithm[J]. Numer. Math. Theor. Meth. Appl, 2019, 12(2): 627-639.
[9] Zhang Y, Li H. A count sketch maximal weighted residual Kaczmarz method for solving highly overdetermined linear systems[J]. Applied Mathematics and Computation, 2021, 410: 126486.
[10] Meng X, Mahoney M W. Low-distortion subspace embeddings in input-sparsity time and applications to robust linear regression[C]. Proceedings of the forty-fifth annual ACM symposium on Theory of computing. 2013: 91-100.
[11] Björck Å. Numerical methods for least squares problems[M]. Society for Industrial and Applied Mathematics, 1996.
[12] Drineas P, Mahoney M W, Muthukrishnan S, et al. Faster least squares approximation[J]. Numerische mathematik, 2011, 117(2): 219-249.
[13] Clarkson K L, Woodruff D P. Low-rank approximation and regression in input sparsity time[J]. Journal of the ACM (JACM), 2017, 63(6): 1-45.
[14] Hansen P C, Saxild-Hansen M. AIR tools-a MATLAB package of algebraic iterative reconstruction methods[J]. Journal of Computational and Applied Mathematics, 2012, 236(8): 2167-2178.

Fuzzy Systems and Data Mining IX
A.J. Tallón-Ballesteros and R. Beltrán-Barba (Eds.)

doi:10.3233/FAIA231072

Block Multipath Matching Pursuit

Jie ZHOU [a,1], Pingping ZHANG
[a] *School of Science,Chongqing University of Posts and Telecommunications, Chongqing 400065, China*

Abstract. In this paper, we propose a new reconstruction algorithm called Block Multipath Matching pursuit (BMMP), which is an extension of multipath matching pursuit (MMP) in block compressed sensing. Then the reconstruction condition of BMMP based on restricted isometric property (RIP) is established. In addition, we also provides a guarantee of reconstruction in the case of noise measurement. Finally, the effectiveness and advancement of the BMMP algorithm are verified by numerical experiments.

Keywords. Multipath matching pursuit (MMP), Block orthogonal matching pursuit(BOMP), Compressed sensing (CS), Restricted isometry property (RIP),

1. Introduction

Compressed sensing (CS) is widely used to reconstruct the K-sparse signal $\mathbf{x} \in \mathbb{R}^N$ from Eq.(1), and it has received extensive attention in the recent decade [1,2].

$$\mathbf{y} = \Phi\mathbf{x}, \tag{1}$$

where $\Phi \in \mathbb{R}^{M\times N}(N \gg M)$ is the measurement matrix. An original method to reconstruct the sparse signal $\mathbf{x}$ from Eq.(1) is to solve a sparsity promoting optimization problem:

$$\min_{\mathbf{x}\in\mathbb{R}^N} \|\mathbf{x}\|_0 \text{: subject to } \|\mathbf{y} - \Phi\mathbf{x}\|_2 \leq \varepsilon, \tag{2}$$

However, solving Eq.(2) is NP-hard. Recently, greedy algorithm has obtained huge interest due to their high computational efficiency, such as orthogonal matching pursuit (OMP) algorithm [3]. We know that multipath matching pursuit (MMP) [4] based on multipath selection investigates multiple promising candidates by arranging the correlation between the Φ column and the residual, which is is an improved algorithm of OMP in reconstruction performance with computational higher complexity. For the reconstruction of block sparse signal, using the non-zero component distribution of signal to design the algorithm can have better reconstruction performance. For example, block orthogonal matching tracking (BOMP) [5,6] algorithm is more suitable than OMP algorithm because of its better performance for block sparse signals. Our research mainly focus on reconstructing block sparse signals [7,8] in this paper.

[1]Corresponding author. Email addresses: Raison2023@qq.com

In this paper, we introduce MMP algorithm into the block compressed sensing to further improve the reconstruction performance. We propose a algorithm called block multipath matching pursuit (BMMP), which identifies the index of the Φ based on the degree of correlation between the block and residuals, and uses the tree-searching strategy to store these candidates for generating L subpaths on each iteration. BMMP can significantly improve the reconstruction performance, and has obvious advantages over the traditional MMP algorithm in running time.

This paper is structured as follows: Section 2 describes notations. Section 3 introduces the implementation process of the algorithm. In Section 4, we analyze the conditions for accurate sparse signal reconstruction based on RIP. Section 5 compares our work with relevant algorithms for sparse signal reconstruction. In Section 6 we give the conclusions of this paper.

2. Notions

In this section, notations are summarized. Let $D = N/d$ denotes the number of blocks, the initial value of Ω be $\{1,2,\ldots,D\}$. Let $\mathbf{x}$ be a K-sparse signal, $T \in \Omega$ is its true block support set, and $|T| \leq K$. $\Omega \backslash T$ denotes the block index set contained in Ω but not in T, where $|T|$ is the cardinality of T. Φ' denotes the transpose of Φ. Let T^c and S^c be the complementary set of T and S, i.e., $T^c = \Omega \setminus T$ and $S^c = \Omega \setminus S$. $\Phi[S]$ is the submatrix of Φ that contains only the column with block indices by S. $\mathbf{x}[S]$ is a subvector that guarantees only $\mathbf{x}$ with a block index of S, and ϕ_j denotes the j-th column of Φ, x_i is the i-th entry of $\mathbf{x}$. At the k-th iteration, let S^k be the set of all candidate sets, and s_i^k be the i-th candidate. L denotes the number of paths in each iteration. $\mathbf{r}_i^k$ denotes the residual of candidate s_i^k. For any full column rank matrix $\Phi[S]$, $\Phi^{\dagger}[S] = (\Phi'[S]\Phi[S])^{-1}\Phi'[S]$ is the Moore-Penrose pseudoinverse of $\Phi[S]$. Let $\mathbf{P}[S] = \Phi[S]\Phi^{\dagger}[S]$ denote the projection of span$(\Phi[S])$, and $\mathbf{P}^{\perp}[S] = I - \mathbf{P}[S]$ denote the orthogonal complement of $\mathbf{P}[S]$.

3. Proposed Algorithms

In general, the block K-sparse signal $\mathbf{x} \in \mathbb{R}^N$ can be modeled as

$$\mathbf{x} = [\underbrace{x_1,\cdots,x_d}_{\mathbf{x}[1]},\underbrace{x_{d+1},\cdots,x_{2d}}_{\mathbf{x}[2]},\cdots,\underbrace{x_{N-d+1},\cdots,x_N}_{\mathbf{x}[D]}]', \tag{3}$$

where $\|\mathbf{x}\|_{2,0} = \sum_{i=1}^{D} I(\|\mathbf{x}[i]\|_2 > 0) \leq K$, where $\|\mathbf{x}\|_{2,0}$ is a mixed ℓ_2/ℓ_0-norm and $I(\cdot)$ is a indicator function. The mixed ℓ_2/ℓ_p-norm (where $p = 1,2,\infty$) denotes $\|\mathbf{x}\|_{2,p} = \|\mathbf{w}\|_p$, where $\mathbf{w} \in \mathbb{R}^D$ with $\mathbf{w}_\ell = \|\mathbf{x}[\ell]\|_2$ for $1 \leq \ell \leq D$. We found the block-sparsity will reduce to normal sparsity for $d = 1$. Therefore, a signal with block sparsity K can be regarded as a traditional sparse signal which has a special distribution of non-zero components, whose sparsity is dK. Similarly, for $\Phi \in \mathbb{R}^{M \times N}$ we have

$$\Phi = [\underbrace{\phi_1,\cdots,\phi_d}_{\Phi[1]},\underbrace{\phi_{d+1},\cdots,\phi_{2d}}_{\Phi[2]},\cdots,\underbrace{\phi_{N-d+1},\cdots,\phi_N}_{\Phi[D]}], \tag{4}$$

Multipath matching pursuit (MMP) is an algorithm that performs tree search under greedy strategy. Compared with OMP, it has better reconstruct performance but higher computational complexity. We introduce the multipath search idea of MMP algorithm into the block sparse signal reconstruction algorithm. Then we summarize BMMP algorithm in Algorithm 1.

Algorithm 1 THE BMMP ALGORITHM.

Input: $\mathbf{y} \in \mathbb{R}^M$, $\Phi \in \mathbb{R}^{M\times N}$, L, K, D
Output: $\hat{\mathbf{x}}$;
Initialize: $S^0 := \{\emptyset\}$, $k := 0$, $\mathbf{r}_1^0 = \mathbf{y}$;
while $k < K$ **do**
$k := k+1$, $v := 0$, $S^k := \emptyset$
for $j = 1$ **to** $|S^{k-1}|$ **do**
$\tilde{\pi} = \arg \max_{1\le i\le D, |\pi|=L} \left\| \left(\Phi'[i]\mathbf{r}_j^{k-1}\right)_\pi \right\|_2^2$
for $l = 1$ **to** L **do**
$s_{temp} := s_j^{k-1} \cup \tilde{\pi}(l)$
if $s_{temp} \notin S^k$ **then**
$v := v+1$
$s_v^k := s_{temp}$
$S^k := S^k \cup \{s_v^k\}$
$\hat{\mathbf{x}}_v^k = \Phi^\dagger[s_v^k]\mathbf{y}$
$\mathbf{r}_v^k := \mathbf{y} - \Phi[s_v^k]\hat{\mathbf{x}}_v^k$
end if
end for
end for
end while
$i^* = \arg\min \left\|\mathbf{r}_i^K\right\|_2^2$
$\hat{\mathbf{x}} = \begin{cases} \Phi^\dagger[s_{i^*}^k]\mathbf{y}, & \text{on the estimated block-support sets } s_{i^*}^k, \\ \mathbf{0}, & \text{otherwise.} \end{cases}$

4. Perfect reconstruction condition of BMMP

First, we need introduce a natural extension of classic restricted isometry property (RIP), block-RIP [7]. Φ is said to satisfy the block-RIP

$$(1-\delta_B)\|\mathbf{x}\|_2^2 \leqslant \|\Phi\mathbf{x}\|_2^2 \leqslant (1+\delta_B)\|\mathbf{x}\|_2^2 \tag{5}$$

for all block K-sparse signal $\mathbf{x} \in \mathbb{R}^N$, where $\delta_B \in (0,1)$ is a constant. Restricted isometry constant (RIC) δ_K is the minimum of δ_B. Then we list several useful lemmas.

Lemma 1 *[9] Let Φ satisfy the block-RIP with both order K_1 and K_2. If $K_1 \le K_2$, then $\delta_{K_1} \le \delta_{K_1}$.*

Lemma 2 *[9] Let sets S_2, S_1 satisfy $|S_2 \setminus S_1| \ge 1$ and Φ satisfy the block-RIP of order $|S_2 \cup S_1|$. Then for any $x \in \mathbb{R}^{|S_2\setminus S_1|\times d}$*

$$\left(1-\delta_{|S_2\cup S_1|}\right)\|\mathbf{x}\|_2^2 \leqslant \left\|\mathbf{P}^{\perp}[S_1]\Phi[S_2\setminus S_1]\mathbf{x}\right\|_2^2 \leqslant \left(1+\delta_{|S_2\cup S_1|}\right)\|\mathbf{x}\|_2^2. \tag{6}$$

Next we state our main result.

Theorem 1 *Consider the system model in Eq.(1), The BMMP is said to exactly reconstructs any block K-sparse signal* $\mathbf{x}\in\mathbb{R}^N$ *if* Φ *satisfies the Block-RIP of order* $K+L$ *with the RIC*

$$\delta_{K+L} < \sqrt{\frac{L}{K+L}}, \tag{7}$$

Proof: Assume these is a candidate $s_{i_0}^k$ that $|T\cap s_{i_0}^k| = |s_{i_0}^k| = k(0\leq k<K)$ at the k-th iteration. Then we will prove that BMMP can find at least one correct block index at the $(k+1)$-th iteration under Eq.(7). For this purpose, we need to compare the maximum element β_1^{k+1} in $\{\left\|\Phi'[j]\mathbf{r}_{i_0}^k\right\|_2 : j\in T\setminus s_{i_0}^k\}$ with the L-th largest element α_L^{k+1} in $\{\left\|\Phi'[j]\mathbf{r}_{i_0}^k\right\|_2 : j\in T^C\}$. If $\beta_1^{k+1}>\alpha_L^{k+1}$, then the index corresponding to β_1^{k+1} will be chosen.

Noting that $|s_{i_0}^k|=k$, then $|T\setminus s_{i_0}^k| = K-k$ we have

$$\begin{aligned}\beta_1^{k+1} &= \max_{j\in T\setminus s_{i_0}^k}\left\|\Phi[j]'\mathbf{r}_{i_0}^k\right\|_2 = \left\|\Phi'[T\setminus s_{i_0}^k]\mathbf{r}_{i_0}^k\right\|_{2,\infty}\\ &\overset{(a)}{\geq} \frac{\left\|\mathbf{P}^{\perp}[s_{i_0}^k]\Phi[T\setminus s_{i_0}^k]\mathbf{x}[T\setminus s_{i_0}^k]\right\|_2^2}{\sqrt{K-k}\left\|\mathbf{x}[T\setminus s_{i_0}^k]\right\|_2},\end{aligned} \tag{8}$$

where (a) follows $\|\mathbf{x}\|_{2,\infty}\geq\frac{\|\mathbf{x}\|_2}{\sqrt{\|\mathbf{x}\|_{1,0}}}$ and $\left|T\setminus s_{i_0}^k\right| = K-k$. Then we can need to obtain the upper bound of α_L^{k+1}:

$$\begin{aligned}\alpha_L^{k+1} &\leq \frac{1}{L}\sum_{j=1}^{L}\alpha_j^{k+1} = \frac{1}{L}\sum_{j=1}^{L}\left\|\Phi'[t_j]\mathbf{r}_{i_0}^k\right\|_2 = \frac{1}{L}\left\|\Phi'[S]\mathbf{r}_{i_0}^k\right\|_{2,1}\\ &\overset{(a)}{=} \frac{\left\|\Phi'[S]\mathbf{P}^{\perp}[s_{i_0}^k]\Phi[T\setminus s_{i_0}^k]\mathbf{x}[T\setminus s_{i_0}^k]\right\|_{2,1}}{L},\end{aligned} \tag{9}$$

where $S:=\{t_1,t_2,...,t_L\}\subset T^C$. Using Eqs.(8) and (9), we have

$$\beta_1^{k+1}-\alpha_L^{k+1} \geq \frac{\eta}{\sqrt{K-k}\left\|\mathbf{x}[T\setminus s_{i_0}^k]\right\|_2} \tag{10}$$

where

$$\eta = \left\|\mathbf{P}^{\perp}[s_{i_0}^k]\Phi[T\setminus s_{i_0}^k]\mathbf{x}[T\setminus s_{i_0}^k]\right\|_2^2$$

$$- \frac{\sqrt{K-k}\left\|\mathbf{x}[T\setminus s_{i_0}^k]\right\|_2 \left\|\Phi'[S]\mathbf{P}^{\perp}[s_{i_0}^k]\Phi[T\setminus s_{i_0}^k]\mathbf{x}[T\setminus s_{i_0}^k]\right\|_{2,1}}{L} \tag{11}$$

Thus, to show $\beta_1^{k+1} > \alpha_L^{k+1}$, it suffices to show $\eta > 0$. Then we let

$$\theta = \frac{K-k}{L} \text{ and } \sigma = \frac{1-\sqrt{\theta+1}}{\sqrt{\theta}}. \tag{12}$$

and

$$\gamma[j] = \begin{cases} 0 & j \notin S, \\ \frac{\sigma}{\sqrt{L}}\left\|\mathbf{x}[T\setminus s_{i_0}^k]\right\|_2 \operatorname{sgn}\left(\Phi'[j]\mathbf{P}^{\perp}[s_{i_0}^k]\Phi[T\setminus s_{i_0}^k]\mathbf{x}[T\setminus s_{i_0}^k]\right) & j \in S, \end{cases} \tag{13}$$

where $\operatorname{sgn}(\cdot)$ is the signum function. For Eq.(12), we have

$$\frac{1+\sigma^2}{1-\sigma^2} = \sqrt{\theta+1} \text{ and } \frac{2\sigma}{1-\sigma^2} = -\sqrt{\theta}. \tag{14}$$

Now, we consider the right-hand side of Eq.(11),

$$\begin{aligned}\left\|\mathbf{P}^{\perp}[s_{i_0}^k]\Phi\left(\mathbf{x}+\gamma\right)\right\|_2^2 &= \left\|\mathbf{P}^{\perp}[s_{i_0}^k]\Phi[T\setminus s_{i_0}^k]\mathbf{x}[T\setminus s_{i_0}^k]\right\|_2^2 + \left\|\mathbf{P}^{\perp}[s_{i_0}^k]\Phi\gamma\right\|_2^2 \\ &\quad + \frac{2\sigma\left\|\Phi'[S]\mathbf{P}^{\perp}[s_{i_0}^k]\Phi[T\setminus s_{i_0}^k]\mathbf{x}[T\setminus s_{i_0}^k]\right\|_{2,1}\left\|\mathbf{x}[T\setminus s_{i_0}^k]\right\|_2}{\sqrt{L}}, \end{aligned} \tag{15}$$

$$\begin{aligned}\left\|\mathbf{P}^{\perp}[s_{i_0}^k]\Phi\left(\sigma^2\mathbf{x}-\gamma\right)\right\|_2^2 &= \sigma^4\left\|\mathbf{P}^{\perp}[s_{i_0}^k]\Phi[T\setminus s_{i_0}^k]\mathbf{x}[T\setminus s_{i_0}^k]\right\|_2^2 + \left\|\mathbf{P}^{\perp}[s_{i_0}^k]\Phi\gamma\right\|_2^2 \\ &\quad - \frac{2\sigma^3\left\|\mathbf{x}[T\setminus s_{i_0}^k]\right\|_2\left\|\Phi'[S]\mathbf{P}^{\perp}[s_{i_0}^k]\Phi[T\setminus s_{i_0}^k]\mathbf{x}[T\setminus s_{i_0}^k]\right\|_{2,1}}{\sqrt{L}}. \end{aligned} \tag{16}$$

Combining Eqs.(15) and (16) yields

$$\begin{aligned}&\left\|\mathbf{P}^{\perp}[s_{i_0}^k]\Phi\left(\mathbf{x}+\gamma\right)\right\|_2^2 - \left\|\mathbf{P}^{\perp}[s_{i_0}^k]\Phi\left(\sigma^2\mathbf{x}-\gamma\right)\right\|_2^2 \\ &\overset{Eq.(14)}{=} \left(1-\sigma^4\right)\left(\left\|\mathbf{P}^{\perp}[s_{i_0}^k]\Phi[T\setminus s_{i_0}^k]\mathbf{x}[T\setminus s_{i_0}^k]\right\|_2^2 \right. \\ &\quad \left. -\sqrt{\frac{\theta}{L}}\left\|\mathbf{x}[T\setminus s_{i_0}^k]\right\|_2\left\|\Phi'[S]\mathbf{P}^{\perp}[s_{i_0}^k]\Phi[T\setminus s_{i_0}^k]\mathbf{x}[T\setminus s_{i_0}^k]\right\|_{2,1}\right). \end{aligned} \tag{17}$$

Now, recalling Eq.(11) where

$$\eta = \left\|\mathbf{r}_{i_0}^k\right\|_2^2 - \frac{\sqrt{K-k}\left\|\mathbf{x}[T\setminus s_{i_0}^k]\right\|_2\left\|\Phi'[S]\mathbf{r}_{i_0}^k\right\|_{2,1}}{L}$$

and $\mathbf{r}_{i_0}^k = \mathbf{P}^{\perp}[s_{i_0}^k]\Phi[T\setminus s_{i_0}^k]\mathbf{x}[T\setminus s_{i_0}^k]$, along with Eq.(17) and Eq.(12)

$$\eta = \frac{\left\|\mathbf{P}^{\perp}[s_{i_0}^k]\Phi(\mathbf{x}+\gamma)\right\|_2^2 - \left\|\mathbf{P}^{\perp}[s_{i_0}^k]\Phi\left(\sigma^2\mathbf{x}-\gamma\right)\right\|_2^2}{1-\sigma^4}. \tag{18}$$

Applying Eq.(18) to Eq.(10), we further have

$$\begin{aligned}\beta_1^{k+1} - \alpha_L^{k+1} &\geq \frac{\left\|\mathbf{P}^{\perp}[s_{i_0}^k]\Phi(\mathbf{x}+\gamma)\right\|_2^2 - \left\|\mathbf{P}^{\perp}[s_{i_0}^k]\Phi\left(\sigma^2\mathbf{x}-\gamma\right)\right\|_2^2}{(1-\sigma^4)\sqrt{K-k}\left\|\mathbf{x}[T\setminus s_{i_0}^k]\right\|_2} \\ &\overset{Lemma2}{\geq} \frac{(1-\delta_{K+L})\left\|\mathbf{x}[T\setminus s_{i_0}^k]+\gamma\right\|_2^2 - (1+\delta_{K+L})\left\|\sigma^2\mathbf{x}[T\setminus s_{i_0}^k]-\gamma\right\|_2^2}{(1-\sigma^4)\sqrt{K-k}\left\|\mathbf{x}[T\setminus s_{i_0}^k]\right\|_2} \\ &\overset{Eq.(14)}{=} \frac{\left\|\mathbf{x}[T\setminus s_{i_0}^k]\right\|_2}{\sqrt{K-k}}\left(1-\delta_{K+L}\sqrt{\frac{K+L-k}{L}}\right)\end{aligned} \tag{19}$$

Therefore, $\beta_1^{k+1} > \alpha_L^{k+1}$ will be guaranteed when

$$\delta_{K+L} < \sqrt{\frac{L}{K+L-k}}. \tag{20}$$

Eq. 20 holds when Eq.(7) is satisfied for $0 \leq k < K$. □

Remark 1 *When $L = 1$, Theorem 1 becomes an exact reconstruction condition for the BOMP algorithm, which is just [9, Corollary 1].*

Remark 2 *When $d = 1$, Theorem 1 becomes an exact reconstruction condition for the MMP algorithm, which is just [10, Theorem 1].*

Next consider the noisy scenario $\mathbf{y} = \Phi\mathbf{x} + \mathbf{e}$, we present the reconstruction guarantee of BMMP to get true block support set T.

Theorem 2 *For $\mathbf{y} = \Phi\mathbf{x} + \mathbf{e}$, Φ has unit ℓ_2-norm columns and and $\mathbf{e}$ is an ℓ_2-bounded noise. Let the RIC of Φ satisfy $\delta_{K+L} < \frac{\sqrt{L}}{\sqrt{K+L}}$ and*

$$\min_{i\in T}\|x[i]\|_2 \geq \frac{\sqrt{2L(1+\delta_{K+L})}}{\sqrt{L}-\sqrt{K+L}\delta_{K+L}}\|\mathbf{e}\|_2 \tag{21}$$

BMMP algorithm will identify all correct block support of $\mathbf{x}$.

Proof: We assume there is a candidate $s_{i_0}^k$ that $|T \cap s_{i_0}^k| = |s_{i_0}^k| = k (0 \le k < K)$ at the k-th iteration. Then we will prove that BMMP successfully performs the $(k+1)$-th iteration under Eq.(7) and Eq.(21). Therefore, we compare the maximum element β_1^{k+1} in $\{\|\Phi'[j]\mathbf{r}_k\|_2 : j \in T \setminus s_{i_0}^k\}$ with the L-th largest element α_L^{k+1} in $\{\left\|\Phi'[j]\mathbf{r}_{i_0}^k\right\|_2 : j \in T^C\}$. If $\beta_1^{k+1} > \alpha_L^{k+1}$, then the index corresponding to β_1^{k+1} will be chosen.

Noting that $|s_{i_0}^k| = k$, then $|T \setminus s_{i_0}^k| = K - k$ we have

$$\begin{aligned}
\beta_1^{k+1} &= \max_{j \in T \setminus s_{i_0}^k} \left\|\Phi'[j]\mathbf{r}_i^k\right\|_2 = \left\|\Phi'[T \setminus s_{i_0}^k]\mathbf{r}_i^k\right\|_{2,\infty} = \left\|\Phi'[T \setminus s_{i_0}^k]\left(\mathbf{P}^{\perp}[s_{i_0}^k]\mathbf{y} + \mathbf{P}^{\perp}[s_{i_0}^k]\mathbf{e}\right)\right\|_{2,\infty} \\
&\ge \left\|\Phi'[T \setminus s_{i_0}^k]\mathbf{P}^{\perp}[s_{i_0}^k]\mathbf{y}\right\|_{2,\infty} - \left\|\Phi'[T \setminus s_{i_0}^k]\mathbf{P}^{\perp}[s_{i_0}^k]\mathbf{e}\right\|_{2,\infty} \\
&\overset{Eq.(8)}{\ge} \frac{\left\|\mathbf{P}^{\perp}[s_{i_0}^k]\Phi[T \setminus s_{i_0}^k]\mathbf{x}[T \setminus s_{i_0}^k]\right\|_2^2}{\sqrt{K-k}\left\|\mathbf{x}[T \setminus s_{i_0}^k]\right\|_2} - \left\|\Phi'[T \setminus s_{i_0}^k]\mathbf{P}^{\perp}[s_{i_0}^k]\mathbf{e}\right\|_{2,\infty}
\end{aligned} \tag{22}$$

Next, let's analyze α_L^{k+1}

$$\begin{aligned}
\alpha_L^{k+1} &\overset{(a)}{\le} \frac{1}{L}\left\|\Phi'[S]\mathbf{r}_{i_0}^k\right\|_{2,1} = \frac{1}{L}\left\|\Phi'[S]\left(\mathbf{P}^{\perp}[s_{i_0}^k]\mathbf{y} + \mathbf{P}^{\perp}[s_{i_0}^k]\mathbf{e}\right)\right\|_{2,1} \\
&\le \frac{1}{L}\left\|\Phi'[S]\mathbf{P}^{\perp}[s_{i_0}^k]\Phi[T \setminus s_{i_0}^k]\mathbf{x}[T \setminus s_{i_0}^k]\right\|_{2,1} + \frac{1}{L}\left\|\Phi'[S]\mathbf{P}^{\perp}[s_{i_0}^k]\mathbf{e}\right\|_{2,1}
\end{aligned} \tag{23}$$

where $S := \{t_1, t_2, ..., t_L\} \subset T^C$. By relating Eq.(22) and Eq.(23), it is clear that $\beta_1^{k+1} > \alpha_L^{k+1}$ is guaranteed when

$$\begin{aligned}
&\frac{\left\|\mathbf{P}^{\perp}[s_{i_0}^k]\Phi[T \setminus s_{i_0}^k]\mathbf{x}[T \setminus s_{i_0}^k]\right\|_2^2}{\sqrt{K-k}\left\|\mathbf{x}[T \setminus s_{i_0}^k]\right\|_2} - \left\|\Phi'[T \setminus s_{i_0}^k]\mathbf{P}^{\perp}[s_{i_0}^k]\mathbf{e}\right\|_{2,\infty} \\
&\quad \ge \frac{\left\|\Phi'[S]\mathbf{P}^{\perp}[s_{i_0}^k]\Phi[T]\mathbf{x}[T]\right\|_{2,1} + \left\|\Phi'[S]\mathbf{P}^{\perp}[s_{i_0}^k]\mathbf{e}\right\|_{2,1}}{L}.
\end{aligned} \tag{24}$$

For (24), equivalently,

$$\begin{aligned}
&\frac{\left\|\mathbf{P}^{\perp}[s_i^k]\Phi[T \setminus s_i^k]\mathbf{x}[T \setminus s_i^k]\right\|_2^2}{\sqrt{K-k}\left\|\mathbf{x}[T \setminus s_i^k]\right\|_2} - \frac{\left\|\Phi'[S]\mathbf{P}^{\perp}[s_i^k]\Phi[T]\mathbf{x}[T]\right\|_{2,1}}{L} \\
&\quad \ge \frac{\left\|\Phi'[S]\mathbf{P}^{\perp}[s_i^k]\mathbf{e}\right\|_{2,1}}{L} + \left\|\Phi'[T \setminus s_i^k]\mathbf{P}^{\perp}[s_i^k]\mathbf{e}\right\|_{2,\infty}.
\end{aligned} \tag{25}$$

First, we simplify the left-hand side of Eq.(25) with the result of Eq.(19).

$$\frac{\left\|\mathbf{P}^{\perp}[s_{i_0}^k]\Phi[T\setminus s_{i_0}^k]\mathbf{x}[T\setminus s_{i_0}^k]\right\|_2^2}{\sqrt{K-k}\left\|\mathbf{x}[T\setminus s_{i_0}^k]\right\|_2}-\frac{\left\|\Phi'[S]\mathbf{P}^{\perp}[s_{i_0}^k]\Phi[T]\mathbf{x}[T]\right\|_{2,1}}{L}$$
$$\geq\left(1-\delta_{K+L}\sqrt{\frac{K+L-k}{L}}\right)\frac{\left\|\mathbf{x}[T\setminus s_i^k]\right\|_2}{\sqrt{K-k}}$$
$$\geq\left(1-\delta_{K+L}\sqrt{\frac{K-k+L}{L}}\right)\min_{i\in T}\|x[i]\|_2. \tag{26}$$

Let $j_1:=\arg\max_{j\in S}\left\|\mathbf{P}^{\perp}[s_{i_0}^k]\Phi'[T\setminus s_{i_0}^k]\mathbf{e}\right\|_2$ and $j_2:=\arg\max_{j\in T}\left\|\mathbf{P}^{\perp}[s_{i_0}^k]\Phi'[T\setminus s_{i_0}^k]\mathbf{e}\right\|_2$, the right-hand side of Eq.(25) can be simplified as

$$\frac{\left\|\Phi'[S]\mathbf{P}^{\perp}[s_{i_0}^k]\mathbf{e}\right\|_{2,1}}{L}+\left\|\Phi'[T\setminus s_{i_0}^k]\mathbf{P}^{\perp}[s_{i_0}^k]\mathbf{e}\right\|_{2,\infty}$$
$$\leq\left\|\Phi'[j_1]\mathbf{P}^{\perp}[s_{i_0}^k]\mathbf{e}\right\|_{2,1}+\left\|\Phi'[j_2]\mathbf{P}^{\perp}[s_{i_0}^k]\mathbf{e}\right\|_{2,1}$$
$$\overset{(a)}{\leq}\sqrt{2}\left\|\Phi'[j_1\cup j_2]\mathbf{P}^{\perp}[s_{i_0}^k]\mathbf{e}\right\|_2$$
$$\overset{(b)}{\leq}\sqrt{2(1+\delta_{K+L})}\,\|\mathbf{e}\|_2 \tag{27}$$

where (a) because $\Phi'[j_1\cup j_2]\mathbf{P}^{\perp}[s_{i_0}^k]\mathbf{e}\in\mathbb{R}^2$, (b) is due to Lemma 2 and Lemma 1. Combining Eq.(26) and Eq.(27), we have

$$\min_{i\in T}\|x[i]\|_2\geq\frac{\sqrt{2L(1+\delta_{K+L})}}{\sqrt{L}-\sqrt{K+L-k}\delta_{K+L}}\|\mathbf{e}\|_2 \tag{28}$$

which is just Eq.(21). Thus Theorem 2 is proved. □

5. Numerical experiments

In this section, we evaluate the reconstruction performance of BMMP through numerical experiments. In our numerical experiments, we use a random measurement matrix Φ of size 150×300, whose entries are selected independently of the Gaussian distribution $N(0,1/M)$. Then we generate a block K-sparse signal signal $\mathbf{x}$, whose non-zero block indices are randomly selected, and all nonzero elements are taken from $N(0,1)$. We conducted 1000 independent experiments to observe the reconstruction performance of BMMP algorithm.

In Figure.1 (a), we observe the relationship between probability of exact reconstructing block K-sparse signal and the number of measurement M. It can be seen that no matter what value L takes, the reconstruction probability increases with the increase of M. The reconstruction probability becomes better with the increase of L from 1 to 3,

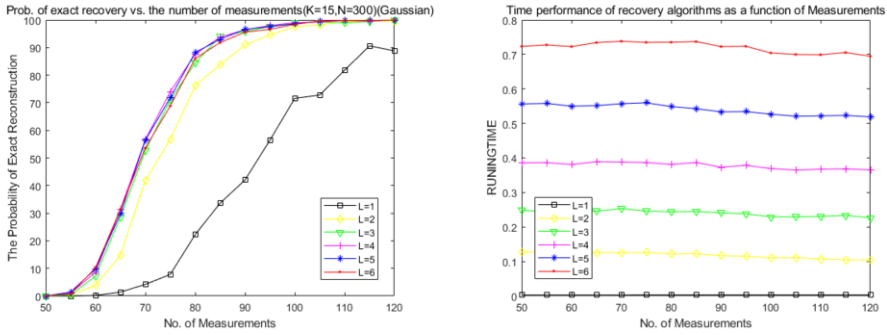

(a) The exact reconstruction probability (b) Average Running time

Figure 1. The performance of BMMP for different L.

while the increase of L hardly improves the reconstruction performance for $L \geq 3$. Then Figure.1 (b) shows that the average running time grows equally as L varies from 1 to 6. Thus, we choose $L = 3$ in the later experiments.

Then the exact reconstruction probability and running time of several reconstruction algorithms are compared, which including (1)OMP algorithm [3], gOMP algorithm [11] with $S = 3$, MMP-BF algorithm [4] with $L = 3$, BOMP algorithm [5], BgOMP algorithm [12] with $S = 3$ and BMMP algorithm with $L = 3$.

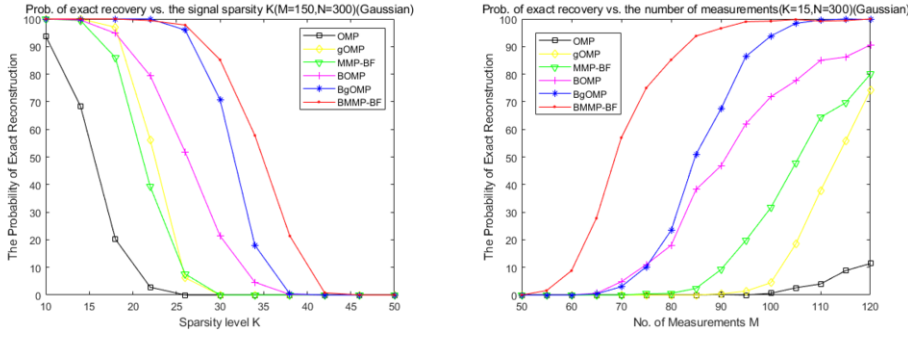

(a) Sparsity K (b) The number of measurement M

Figure 2. The performance of several reconstruction algorithms with different K.

In Figure 2 (a), we show a function of the exact reconstruction probability and block sparsity level K for several reconstruction algorithms. We can see that the reconstruction performance of BMMP algorithm is significantly better than other algorithms, and the critical block sparsity of signals that cannot be exactly reconstructed is larger. Figure.2 (b) describes the effect of measurement M on reconstruction probability, where the block sparsity K is fixed to 15. As can be seen, with the increase of measurement M, the reconstruction probability of all algorithms is significantly improved. The critical number of measurement M that enables BMMP to exactly reconstruct the block sparse signal is significantly smaller than other algorithms.

6. Conclusion

The block sparse signal reconstruction algorithm we describe in this paper, BMMP, can be considered as an extension of the MMP algorithm for block sparse systems. Because there are more than one candidate can be kept each time, the BMMP algorithm has better reconstruction performance. Numerical experiments show that BMMP algorithm has excellent performance in terms of exact reconstruction probability compared with many existing algorithms. In addition, we use block-RIP to study the reconstruction condition of BMMP algorithm. In noise-free case, BMMP algorithm accurately reconstructs K-block sparse signal $\mathbf{x}$ within K iterations under $\delta_{K+L} < \frac{\sqrt{L}}{\sqrt{K+L}}$. Finally, in the noisy scenario $\mathbf{y} = \Phi\mathbf{x} + \mathbf{e}$, if the RIC of Φ satisfy $\delta_{K+L} < \frac{\sqrt{L}}{\sqrt{K+L}}$ and $\min_{i\in T} \|x[i]\|_2 \geq \frac{\sqrt{2L(1+\delta_{K+L})}}{\sqrt{L}-\sqrt{K+L}\delta_{K+L}} \|\mathbf{e}\|_2$, BMMP algorithm can reconstruct true supports T.

References

[1] Candes E J, Tao T. Decoding by linear programming[J]. IEEE transactions on information theory, 2005, 51(12): 4203-4215.

[2] Donoho D L. For most large underdetermined systems of linear equations, the minimal ℓ_1 solution is also the sparsest solution[J]. Communications on pure and applied mathematics, 2006, 59(6): 797-829.

[3] Tropp J A, Gilbert A C. Signal recovery from random measurements via orthogonal matching pursuit[J]. IEEE Transactions on information theory, 2007, 53(12): 4655-4666.

[4] Kwon S, Wang J, Shim B. Multipath matching pursuit[J]. IEEE Transactions on Information Theory, 2014, 60(5): 2986-3001.

[5] Eldar Y C, Kuppinger P, Bolcskei H. Block-sparse signals: Uncertainty relations and efficient recovery[J]. IEEE Transactions on Signal Processing, 2010, 58(6): 3042-3054.

[6] Swirszcz G, Abe N, Lozano A C. Grouped orthogonal matching pursuit for variable selection and prediction[J]. Advances in Neural Information Processing Systems, 2009, 22.

[7] Eldar Y C, Mishali M. Robust recovery of signals from a structured union of subspaces[J]. IEEE Transactions on Information Theory, 2009, 55(11): 5302-5316.

[8] Mishali M, Eldar Y C. Blind multiband signal reconstruction: Compressed sensing for analog signals[J]. IEEE Transactions on signal processing, 2009, 57(3): 993-1009.

[9] Wen J, Zhou Z, Liu Z, et al. Sharp sufficient conditions for stable recovery of block sparse signals by block orthogonal matching pursuit[J]. Applied and Computational Harmonic Analysis, 2019, 47(3): 948-974.

[10] Li H, Wang J, Yuan X. On the fundamental limit of multipath matching pursuit[J]. IEEE Journal of Selected Topics in Signal Processing, 2018, 12(5): 916-927.

[11] Wang J, Kwon S, Shim B. Generalized orthogonal matching pursuit[J]. IEEE Transactions on signal processing, 2012, 60(12): 6202-6216.

[12] Qi R, Yang D, Zhang Y, et al. On recovery of block sparse signals via block generalized orthogonal matching pursuit[J]. Signal Processing, 2018, 153: 34-46.

Fuzzy Systems and Data Mining IX
A.J. Tallón-Ballesteros and R. Beltrán-Barba (Eds.)

doi:10.3233/FAIA231073

Boundedness of Solutions for Indirect Chemotaxis Model with Diffusion-Dependent Signal Concentration

Ya TIAN [a,1] Guoqing XIE [a]
[a] *School of Science, Chongqing University of Posts and Telecommunications, Chongqing 400065, PR China*

Abstract. This work establishes an indirect chemotaxis model with diffusion-dependent signal concentration

$$\begin{cases} u_t = \Delta(u\gamma(v)) \\ v_t = \Delta v - v + w \\ w_t = \Delta w - w + u \end{cases}$$

for all $(x,t) \in \Omega \times (0,\infty)$, in a smooth bounded domain $\Omega \subset \mathbb{R}^2$ under the homogeneous second boundary condition, and the positive function γ fulfills assumptions:

$$\gamma(s) \in C^3([0,\infty)) \text{ and } \gamma'(s) \leq 0 \, (\forall s > 0).$$

By some prior estimation, the boundedness of solutions can be obtained from this model.

Keywords. Boundedness; indirect chemotaxis model; diffusion-dependent signal concentration

1. Introduction

Since the proposal of the Keller-Segel model in the last century, an increasing number of biological phenomena can be described by mathematical models, among which the following models of diffusion-dependent signal concentration are increasingly valued:

$$\begin{cases} u_t = \Delta(\gamma(v)u) \\ v_t = \Delta v + g(u,v) \end{cases} \tag{1.1}$$

(1.1) illustrates stripe pattern formation. Species density and signal are denoted by u and v. Considering that signalling material can be produced by the species, that is, $g(u,v) = -v + u$, Tao and Winkler [1] examined the solution nature in both $n\,(n \geq 2)$-dimensional and γ-bounded cases. In the case $\gamma(v) = \frac{c_0}{v^k}$ with $k > 0$ and c_0 is small enough, considering property of solutions, this is proved by Yoon and Kim in [2]. For other cases, such as $\gamma(v) = v^{-\alpha}$ with $\alpha > 0$ and $\gamma(v) = e^{-v}$, the relevant properties of the solutions can be found [3,4,5,6]. Conversely, considering that the signalling material

[1]Corresponding E-mail: tianya@cqupt.edu.cn

is only consumed and not produced by the species, that is, $g(u,v) = -vu$, many mathematicians have given relevant results. In the case where $\gamma \in C^3([0,+\infty))$ is positive, [7] established global classical solutions and global weak solutions for (1.1). Furthermore, very weak solutions were demonstrated in [8]. Similarly, relevant results of the study when $\gamma(v) = v^{\pm\alpha}$ with $\alpha > 0$ can be found in [9,10,11]. In addition, for the three-component model, different researchers have unique insights into different models, we refer the reader to [12,13,14].

The truth, however, is that reality is far more complex than the above scenario. Signals come from a variety of sources and can be self-generated, externally introduced or indirectly influenced. So far, the results of models with indirect signalling effects have been unsatisfactory. On this basis, we propose the following model:

$$\begin{cases} u_t = \Delta(u\gamma(v)), & (x,t) \in \Omega \times (0,\infty), \\ v_t = \Delta v - v + w, & (x,t) \in \Omega \times (0,\infty), \\ w_t = \Delta w - w + u, & (x,t) \in \Omega \times (0,\infty), \\ \partial_\nu u = \partial_\nu v = \partial_\nu w = 0, & (x,t) \in \partial\Omega \times (0,\infty), \\ (u,v,w)(x,0) = (u_0(x), v_0(x), w_0(x)), & x \in \Omega. \end{cases} \tag{1.2}$$

In this context, species density, direct signal and indirect are denoted by u, v and w. $\gamma(v)$ reflects variations in diffusion rate and chemotactic sensitivity.

To achieve our goal, that is, to obtain the property of the solution, we make $u_0, v_0, w_0 \geq 0$ and

$$\begin{cases} u_0 \in C^0(\overline{\Omega}) \\ v_0, w_0 \in W^{1,\infty}(\overline{\Omega}) \end{cases} \tag{1.3}$$

and the positive function fulfills assumptions:

$$\gamma(s) \in C^3([0,\infty)) \text{ and } \gamma'(s) \leq 0 \, (\forall s > 0). \tag{1.4}$$

Theorem 1.1 *Assuming Ω is a smooth bounded domain in $\mathbb{R}^2$, conditions (1.3) and (1.4) are satisfied and $C > 0$. Then, $\forall t > 0$, (1.2) yields a solution (u,v,w) and has property:*

$$\|u(\cdot,t)\|_{L^\infty(\Omega)} + \|v(\cdot,t)\|_{W^{1,\infty}(\Omega)} + \|w(\cdot,t)\|_{W^{1,\infty}(\Omega)} < C.$$

Main ideas. Based on the duality-based argument, we first obtain the spatio-temporal L^2 estimate of u. Next, we go through the integrals to get the property of $\|w(\cdot,t)\|_{L^2(\Omega)}$, which completes the setup for what follows. Then, owe to the theory related to heat semigroup, we get the result we want.

Remark 1.1 *For brevity, we assume C of each row may vary unless stated otherwise. To avoid repetition, we may omit $\forall t \in (0, T_{\max})$. Besides, This work focuses $n = 2$ based on the spatio-temporal L^2 estimate of u and does not provide an optimal solution for more complex cases. Improved spatio-temporal conditions may allow for a solution.*

2. Proof of theorem

First of all, we establish the solution's local existence over time using Amann's theorem [15].

Lemma 2.1 *Assuming Ω is a smooth bounded domain in $\mathbb{R}^2$ and conditions (1.3) and (1.4) are satisfied. For $T_{\max} \in (0,\infty]$, one can find a function (u,v,w)*

$$\begin{cases} u \in C^0\left(\overline{\Omega}\times[0,T_{\max})\right)\cap C^{2,1}\left(\overline{\Omega}\times(0,T_{\max})\right), \\ v \in \bigcap\limits_{\theta>n} C^0\left([0,T_{\max});W^{1,\theta}(\Omega)\right)\cap C^{2,1}\left(\overline{\Omega}\times(0,T_{\max})\right), \\ w \in C^0\left(\overline{\Omega}\times[0,T_{\max})\right)\cap C^{0,1}\left(\overline{\Omega}\times(0,T_{\max})\right), \end{cases}$$

which establishes (1.2) classically. In the case $T_{\max}<\infty$, we have

$$\limsup_{t\nearrow T_{\max}} \|u(\cdot,t)\|_{L^\infty(\Omega)} = \infty.$$

Lemma 2.2 *Allow conditions (1.3) and (1.4) to occur. Then, for some $C_1, C_2 > 0$ and $\forall t \in (0,T_{\max})$, one can deduce*

$$\int_\Omega u = \int_\Omega u_0 \text{ and } C_1 \le \gamma(v) \le C_2. \tag{2.5}$$

Proof. (2.5) is obtained from (1.4) and integrating the first equation in (1.2). □

Next, based on the duality-based argument [1], we will give the spatio-temporal L^2 estimate of u.

Lemma 2.3 *Allow conditions (1.3) and (1.4) to occur. Then, $\forall t \in (0,T_{\max}-\tau)$ and $\tau := \min\left\{1, \frac{1}{2}T_{\max}\right\}$, for some $C>0$, one can deduce*

$$\int_t^{t+\tau}\int_\Omega u^2 \le C. \tag{2.6}$$

Proof. Let $U := u-\overline{u}$ and suppose $\mathscr{B}$ is a self-adjoint realization of $-\Delta$ and has definition

$$D(\mathscr{B}) := \left\{\zeta \in W^{2,2}(\Omega) \mid \int_\Omega \zeta = 0\ ,\ \partial_\nu \zeta = 0 \text{ on } \partial\Omega\right\}.$$

Hence, according to u_t-equation, by direct calculation, $\forall t \in (0,T_{\max})$, one can infer

$$\begin{aligned} \frac{1}{2}\frac{d}{dt}\int_\Omega \left|\mathscr{B}^{-\frac{1}{2}}U\right|^2 &= -\int_\Omega \mathscr{B}^{-1}U\cdot\mathscr{B}\left(\gamma(v)u-\overline{\gamma(v)u}\right) \\ &= -\bar{u}\int_\Omega \gamma(v)U - \int_\Omega \gamma(v)U^2. \end{aligned} \tag{2.7}$$

Next, using Lemma 2.2 and (2.7), for some $C_1, C_2 > 0$, we indicate

$$\frac{d}{dt}\int_\Omega \left|\mathscr{B}^{-\frac{1}{2}}U\right|^2 + 2C_1\int_\Omega U^2 \le C_2. \tag{2.8}$$

Thanks to the Poincaré inequality and $\int_\Omega \mathscr{B}^{-\frac{1}{2}}U = 0$, for some $C_3, C_4 > 0$ and $\forall t \in (0, T_{\max})$, by simple calculation, we infer

$$\int_\Omega \left|\mathscr{B}^{-\frac{1}{2}}U\right|^2 \le C_3 \int_\Omega U^2,$$

which conjunction with (2.8) infers

$$\frac{d}{dt}\int_\Omega \left|\mathscr{B}^{-\frac{1}{2}}U\right|^2 + C_4 \int_\Omega \left|\mathscr{B}^{-\frac{1}{2}}U\right|^2 + C_1 \int_\Omega U^2 \le C_2. \tag{2.9}$$

Due to Grönwall's inequality, there exists $C_5 > 0$ fulfilling

$$\int_\Omega \left|\mathscr{B}^{-\frac{1}{2}}U\right|^2 \le C_5 \quad \forall t \in (0, T_{\max}). \tag{2.10}$$

Using again Lemma 2.2 and (2.10) and integrating (2.9), for some $C_6 > 0$ and $\forall t \in (0, T_{\max} - \tau)$, we indicate

$$\int_t^{t+\tau}\int_\Omega u^2 = \int_t^{t+\tau}\int_\Omega U^2 + \int_t^{t+\tau}\int_\Omega \bar{u}^2 \le C_6 + \overline{u_0}^2 |\Omega| \tau.$$

Thus, (2.6) is obtained. □

Furthermore, one find the properties of $\|w(\cdot,t)\|_{L^2(\Omega)}$ and $\|u(\cdot,t)\|_{L^2(\Omega)}$ by straightforward computation.

Lemma 2.4 *Allow conditions (1.3) and (1.4) to occur. For some $C_1, C_2, C_3 > 0$, $\forall t \in (0, T_{\max})$, we can establish*

$$\|w(\cdot,t)\|_{L^2(\Omega)} \le C_1 \tag{2.11}$$

and

$$\|v(\cdot,t)\|_{W^{1,4}(\Omega)} \le C_2 \tag{2.12}$$

and

$$\|v(\cdot,t)\|_{L^\infty(\Omega)} \le C_3. \tag{2.13}$$

Proof. Multiplying w_t-equation in (1.2) using w and performing integration, $\forall t \in (0, T_{\max})$, one can infer

$$\frac{1}{2}\frac{d}{dt}\int_\Omega w^2 \le -\int_\Omega |\nabla w|^2 - \frac{1}{2}\int_\Omega w^2 + \frac{1}{2}\int_\Omega u^2,$$

which means

$$\frac{d}{dt}\int_\Omega w^2 + \int_\Omega w^2 + \int_\Omega |\nabla w|^2 \le \int_\Omega u^2. \tag{2.14}$$

Thus, we get (2.11) through (2.14), Lemma 2.3 and the comparison argument [16]. Hence, (2.11) in conjunction with the theory related to heat semigroup implies that (2.12) is the truth. Furthermore, thanks to $W^{1,4}(\Omega) \hookrightarrow L^\infty(\Omega)$, (2.13) is obtained. □

Lemma 2.5 *Allow conditions (1.3) and (1.4) to occur. For some $C>0$ and $\forall t\in(0,T_{\max})$, we can infer*

$$\|u(\cdot,t)\|_{L^2(\Omega)}\le C. \tag{2.15}$$

Proof. Based on the facts that (1.4) and (2.13), similar to Lemma 2.4, $\forall t\in(0,T_{\max})$, by direct calculation, there exists $C_1,C_2>0$ fulfilling

$$\frac{d}{dt}\int_\Omega u^2+2C_1\int_\Omega|\nabla u|^2\le\frac{C_1}{2}\int_\Omega|\nabla u|^2+C_2\int_\Omega u^2|\nabla v|^2. \tag{2.16}$$

Combining (2.12), Lemma 2.2 and the Ehrling type inequality, for some $C_3>0$ and $\forall t\in(0,T_{\max})$, one can find

$$\begin{aligned} C_2\int_\Omega u^2|\nabla v|^2+\int_\Omega u^2&\le C_2\|u\|^2_{L^4(\Omega)}\|\nabla v\|^2_{L^4(\Omega)}+\|u\|^2_{L^2(\Omega)}\\ &\le\frac{C_1}{2}\int_\Omega|\nabla u|^2+C_3. \end{aligned} \tag{2.17}$$

Next, plugging (2.17) into (2.16), $\forall t\in(0,T_{\max})$, we deduce

$$\frac{d}{dt}\int_\Omega u^2+\int_\Omega u^2\le C_3,$$

which means (2.15). □

Last, the boundedness criterion will be given.

Lemma 2.6 *Consider the presence of (1.3) and (1.4). Let $n\ge1$, $\forall t\in(0,T_{\max})$, suppose that there exists $q\ge1$ with $q>\frac{n}{2}$ fulfilling*

$$\|u(\cdot,t)\|_{L^q(\Omega)}\le\infty. \tag{2.18}$$

Then $T_{\max}=\infty$ and

$$\|u(\cdot,t)\|_{L^\infty(\Omega)}+\|v(\cdot,t)\|_{W^{1,\infty}(\Omega)}+\|w(\cdot,t)\|_{W^{1,\infty}(\Omega)}<\infty\quad\forall t>0. \tag{2.19}$$

Proof. Multiplying w_t-equation in (1.2) using w^{q-1} and performing integration, $\forall t\in(0,T_{\max})$, we infer

$$\frac{d}{dt}\int_\Omega w^q+\int_\Omega w^q+(q-1)\int_\Omega w^{q-2}|\nabla w|^2\le\int_\Omega u^q. \tag{2.20}$$

Then, combining (2.18) and (2.20),$\forall t\in(0,T_{\max})$, for some $C_1>0$, we get

$$\int_\Omega w^q\le C_1. \tag{2.21}$$

Next, we can obtain $\frac{nq}{(n-q)_+}>n$ because of $q>\frac{n}{2}$. Thus we choose $\theta>\max\{1,\frac{n}{2}\}$, which fulfills $\frac{nq}{(n-q)_+}>2\theta>n$. Obviously, with the help of (2.21) and the theory related to heat semigroup, for some $C_2>0$, we deduce

$$\|v(\cdot,t)\|_{W^{1,2\theta}(\Omega)} \leq C_2. \tag{2.22}$$

Then, $\forall p > 1$, using u^{p-1}, $\forall t \in (0, T_{\max})$, we infer

$$\frac{d}{dt}\int_\Omega u^p \leq -\frac{p(p-1)}{2}\int_\Omega u^{p-2}\gamma(v)|\nabla u|^2 + \frac{p(p-1)}{2}\int_\Omega \frac{|\gamma'(v)|^2}{\gamma(v)}u^p|\nabla v|^2. \tag{2.23}$$

With the aid of (1.4) and (2.13), for some $C_3, C_4 > 0$ and $\forall t \in (0, T_{\max})$, (2.23) means

$$\frac{d}{dt}\int_\Omega u^p + C_3\int_\Omega \left|\nabla u^{\frac{p}{2}}\right|^2 + \int_\Omega u^p \leq C_4\int_\Omega u^p|\nabla v|^2 + \int_\Omega u^p. \tag{2.24}$$

Furthermore, due to $\theta > \max\left\{1, \frac{n}{2}\right\}$ we have $\frac{2\theta}{\theta-1} < \frac{2n}{(n-2)_+}$, thus by an Ehrling type inequality, Lemma 2.2 and (2.22), for some $C_5 > 0$ and $\forall t \in (0, T_{\max})$, we deduce

$$\begin{aligned} C_4\int_\Omega u^p|\nabla v|^2 + \int_\Omega u^p &\leq C_4\left\|u^{\frac{p}{2}}\right\|^2_{L^{\frac{2\theta}{\theta-1}}(\Omega)}\|\nabla v\|^2_{L^{2\theta}(\Omega)} + \left\|u^{\frac{p}{2}}\right\|^2_{L^2(\Omega)} \\ &\leq C_4C_2^2\left\|u^{\frac{p}{2}}\right\|^2_{L^{\frac{2\theta}{\theta-1}}(\Omega)} + \left\|u^{\frac{p}{2}}\right\|^2_{L^2(\Omega)} \\ &\leq C_3\int_\Omega \left|\nabla u^{\frac{p}{2}}\right|^2 + C_5. \end{aligned} \tag{2.25}$$

Owe to the comparison argument, plugging (2.25) into (2.24), we deduce $\|u(\cdot,t)\|_{L^p(\Omega)} \leq \infty$. Hence, according to [17, Lemma A.1], $\forall t \in (0, T_{\max})$, for some $C_6 > 0$, we indicate

$$\|u(\cdot,t)\|_{L^\infty(\Omega)} \leq C_6. \tag{2.26}$$

Using the theory related to heat semigroup again, $\forall t \in (0, T_{\max})$, we can find some $C_7 > 0$ fulfilling

$$\|v(\cdot,t)\|_{W^{1,\infty}(\Omega)} + \|w(\cdot,t)\|_{W^{1,\infty}(\Omega)} \leq C_7. \tag{2.27}$$

Thus, we obtain (2.19) through (2.26), (2.27) and Lemma 2.1. □

Finally, using lemmas, we can complete Theorem1.1.

short proof. Explicitly, with the aim of establishing Theorem 1.1, we only need to take $n = 2$ and $q = 2$ in Lemma 2.6. □

3. Conclusion

This paper addresses the problem of boundedness of solutions for indirect chemotaxis model with diffusion-dependent signal concentration in the two-dimensional case by means of the duality-based argument. The novelty of this work lies in the absence of a logistic term in u_t-equation and the diffusive behavior of Δw, setting it apart from previous findings. Furthermore, the conventional methodology would necessitate $v_0(x)$ to be sufficiently small, a requirement effectively obviated by the use of the duality-based argument. However, it's important to note that this paper does not provide optimal solutions for more complex scenarios($n \geq 3$). Improved spatio-temporal conditions may offer potential solutions in such cases.

References

[1] Y. Tao, M. Winkler, *Effects of signal-dependent motilities in a Keller-Segel-type reaction-diffusion system*, Math. Models Methods Appl. Sci. **27(09)** (2017) 1645-1683.

[2] C. Yoon, Y. J. Kim, *Global existence and aggregation in a Keller-Segel model with Fokker-Planck diffusion*, Acta App. Math. **149(1)** (2017) 101-123.

[3] J. Ahn, C. Yoon, *Global well-posedness and stability of constant equilibria in parabolic-elliptic chemotaxis systems without gradient sensing*, Nonlinearity **32** (2019) 1327-1351.

[4] K. Fujie, T. Senba, *Global boundedness of solutions to a parabolic-parabolic chemotaxis system with local sensing in higher dimensions*, Nonlinear Anal. **35** (2022) 3777-3811.

[5] K. Fujie, J. Jiang, *Comparison methods for a Keller-Segel-type model of pattern formations with density-suppressed motilities*, Calc. Var. Partial Differential Equations **60** (2021) 92.

[6] H. Y. Jin, Z. A. Wang, *Critical mass on the Keller-Segel system with signal-dependent motility*, Proc. Am. Math. Soc. **148(11)** (2020) 4855-4873.

[7] G. Li, M. Winkler, *Refined regularity analysis for a Keller-Segel-consumption system involving signal-dependent motilities*, Appl. Anal., https://doi.org/10.1080/00036811.2023.2173183.

[8] G. Li, M. Winkler, *Relaxation in a Keller-Segel-consumption system involving signal-dependent motilities*, Commun. Math. Sci. **21(2)** (2023) 299-322.

[9] M. Winkler, *Application of the Moser-Trudinger inequality in the construction of global solutions to a strongly degenerate migration model*, B. Math. Sci. doi: 10.1142/S1664360722500126.

[10] M. Winkler, *Global generalized solvability in a strongly degenerate taxis-type parabolic system modeling migration-consumption interaction*, Z. Angew. Math. Phys. **74** (2023) 32.

[11] Y. Tao, M. Winkler, *Global solutions to a Keller-Segel-consumption system involving singularly signal-dependent motilities in domains of arbitrary dimension*, J. Differential Equations **343** (2023) 390-418.

[12] D. Li, Z. Li, J. Zhao, *Boundedness and large time behavior for a chemotaxis system with signal-dependent motility and indirect signal consumption*, Nonlinear Anal. Real World Appl. **64** (2022) 103447.

[13] M. Zheng, L. Wang, *Global boundedness in a chemotaxis system with signal-dependent motility and indirect signal consumption*, Appl. Math. Lett. **146** (2023) 108838.

[14] W. Lv, Q. Wang, *A chemotaxis system with signal-dependent motility, indirect signal production and generalized logistic source: global existence and asymptotic stabilization*, J. Math. Anal. Appl. **488(2)** (2020) 124108.

[15] H. Amann, *Dynamic theory of quasilinear parabolic systems III. Global existence*, Math. Z. **202** (1989) 219-250.

[16] Y. Tao, M. Winkler, *Blow-up prevention by quadratic degradation in a two-dimensional Keller-Segel-Navier-Stokes system*, Z. Angew. Math. Phys. **67** (2016) 1-23.

[17] Y. Tao, M. Winkler, *Boundedness in a quasilinear parabolic-parabolic Keller-Segel system with subcritical sensitivity*, J. Differential Equations **252(1)** (2012) 692-715.

Fuzzy Systems and Data Mining IX
A.J. Tallón-Ballesteros and R. Beltrán-Barba (Eds.)

doi:10.3233/FAIA231074

Discolored Transformer Breather Recognition for Substation Based on Improved YOLOv8

Qiang HE[a,1], Xin YOU[a], Zhiyuan QIU[a], Wenxin FENG[a], Daoyu LI[a], Xianzhong CHEN[a] and Zhaoye ZHENG[b]
[a]*China Southern Power Grid Co., Ltd. Extra High Voltage Transmission Company Guiyang Bureau*
[b]*North China Electric Power University*

Abstract. Transformer breather is an important equipment to ensure the normal operation of transformer in substations. In order to identify the discoloration defects of breathers accurately and reduce the operation and maintenance costs of substations, this paper proposes a recognition method of discolored transformer breathers based on improved YOLOv8. Firstly, to solve the problem of sample imbalance in original image data, this paper augments the data by cropping and generating, and trained a more robust model with "real + virtual" data. Secondly, considering the various scales of breather, the BiFPN structure is incorporated to achieve more efficient multi-level feature fusion. Finally, since breathers exist in complex substation scenes, this paper introduces CBAM attention mechanism to enhance the feature extraction ability of the model. The experimental results show that the proposed method can improve the mAP of discolored transformer breather detection by 2.1% compared to the baseline and inference in real-time, while hardly increasing the number of parameters and computation cost, which verifies the effectiveness of the proposed method.

Keywords. substation transformer breather, YOLOv8, data augmentation, BiFPN, attention mechanism

1. Introduction

Power transformer is an important equipment in substation, and its normal operation provides the fundamental guarantee for the safe production of substation. The breather is an important part of the transformer used to isolate the moisture in the air, which can avoid the insulation strength of transformer oil decline due to moisture [1]. Therefore, recognizing the discoloration of breathers is one of the key steps of the transformer defect detection. The traditional substation generally adopts the manual inspection mode to find the defect of transformer breathers, which consumes a lot of human resources and has low efficiency. With the popularity of inspection robots in recent years, the operation and maintenance of substations have gradually shifted to an unattended mode [2]. It has gradually become the mainstream method to capture transformer images through

[1] Corresponding Author, Qiang HE, China Southern Power Grid Co., Ltd. Extra High Voltage Transmission Company Guiyang Bureau, Guiyang, China; Email: 15831255315@163.com.

inspection robots equipped with cameras and detect the status of different components by Computer Vision (CV) technology [3].

However, the characteristics of the substation scene and the limitations brought by inspection robots pose new challenges to the design of CV models for substation inspection. Compared with models in the general field, a model used for substation inspection should have following characteristics: 1) Subject to deployment conditions, it needs to have as small a number of parameters and computation cost as possible; 2) The key features should be effectively learned from the limited substation images which often accompanied with the problem of sample imbalance; 3) It can achieve higher detection accuracy as well as real-time detection under the complex scene of substation. Although some achievements have been made in the research of discolored breather recognition, these methods based on detectors with a large number of parameters and a high computation cost, and cannot achieve the optimal speed-precision tradeoff.

To solve the above problems, we propose a discoloration recognition method for transformer breathers based on improved YOLOv8. The main contributions can be summarized in three folds:

- To solve the problem of sample imbalance in original data, we adopt the method of "cropping + generation" to enhance the training data, and uses "real + virtual" data to train the model, so that the model has stronger generalization ability.
- In terms of the breathers photographed with various scales, the structure of Bi-directional Feature Pyramid Network (BiFPN) is integrated into the detector's neck network for more efficient feature fusion.
- In view of the characteristics of breathers existing in complex substation scenes, we introduce Convolutional Block Attention Module (CBAM) to improve the model's ability to extract key features of breathers in complex backgrounds.

2. Related Work

Existing object detection methods based on deep learning can be divided into two types: two-stage methods and one-stage methods. The representative works of the two-stage methods are the Region with CNN features (R-CNN) series [4-5], which firstly obtain the region proposals with the region proposal network then classify these proposals. One-stage methods are represented by the You Only Look Once (YOLO) series [6-7], which treat the object detection task as a whole regression task, using an end-to-end network to directly predict the location and class of the object in the image.

On the other hand, in the scene of power system, the detection of breathers and their defects based on above object detection methods has been concerned by researchers for a long time. Reference [3] proposed an improved RetinaNet and achieve a higher the detection accuracy for components in transformer including breathers. Reference [8] combined a feature matching algorithm with SSD network to realize rapid and stable recognition of the defects in transformer breathers. Reference [9] used a modified YOLOv4 network for the defect detection of breathers and other equipment in substation. Although these methods achieved relatively good results in breather detection, they all rely on earlier object detectors with a large number of parameters and a large amount of calculation, neglecting the deployment condition of inspection robots in which the

computing power and storage space are limited, while cannot achieve the optimal balance between speed and precision as well.

3. Proposed Method

According to the deployment condition of substation inspection robots, we choose YOLOv8n as the baseline model, and improve the training strategy as well as the model structure on the basis of the characteristics of transformer breather images. The improved network structure is shown in Figure 1.

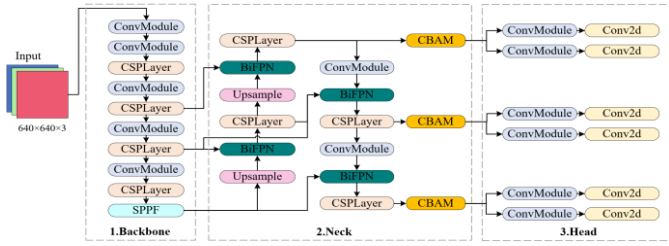

Figure 1. Structure of the improved YOLOv8n model.

3.1. Base Architecture

Since we take YOLOv8n as base architecture, we describe its operating principle, characteristic and the reason for choosing it briefly. YOLOv8 is developed to achieve a better trade-off between speed and precision based on YOLOv5. YOLOv8 includes five models of different sizes, all of them consist of backbone, neck and head, which used to extract image features, fuse multi-scale features and detect object of different scales, respectively. Compared with YOLOv5, it mainly improves in the following aspects: 1) The model works in an anchor-free way; 2) More elaborate image feature extraction modules with more residual connections are used; 3) The head adopts the decoupled design. 4) More advanced loss function and sample assigning strategy are used in training. With these improvements, YOLOv8 can achieve advanced detection accuracy and inference speed performance with lightweight models.

Compare to the existing discolored breather detection methods which based on earlier object detector, YOLOv8 is a more powerful baseline with a better balance between speed and precision. Meanwhile, considering the accessibility of edge deployment in practical applications which is not fully taken into account in previous work, we choose the lightest YOLOv8n model among the five sizes as the baseline, the original structure of it is shown in Figure 2.

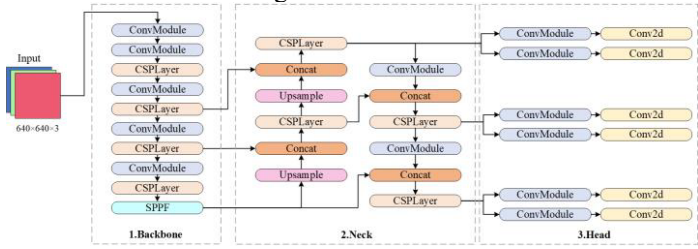

Figure 2. Structure of the original YOLOv8n model.

3.2. Data Augmentation with Cropping and Generating

According to the observation of the original images of transformer breathers, we find that the number of breathers without iron shell is relatively small and the background is relatively single as well. This problem of data imbalance may not be conducive to the model's effective recognition of the breathers without iron shell and their discoloration defects. In this paper, some images of breathers without iron shell are cropped at random scale. Then, a variety of different scale images of breathers without iron shell are generated by using FastGAN [10] network with the original and cropped images in a few-shot way. Finally, the cropped images and generated images are used to enhance the original training data, these "real + virtual" images are used to train a more robust discolored breather detection model, as shown in Figure 3.

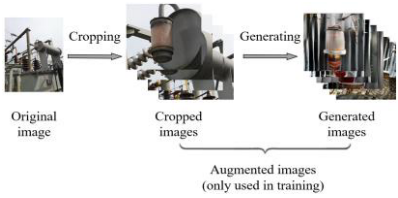

Figure 3. Process of data augmentation.

3.3. Introducing BiFPN Structure

Since the breathers have many different sizes in the image, sufficient multi-scale feature fusion plays an important role in improving the detection accuracy. We introduce BiFPN [11] structure to replace the original Path Aggregation Network (PANet), using its more efficient multi-scale feature fusion design to obtain fused features with stronger representation ability and improve the performance of breather discoloration detection. The comparation between PANet and BiFPN is shown in Figure 4.

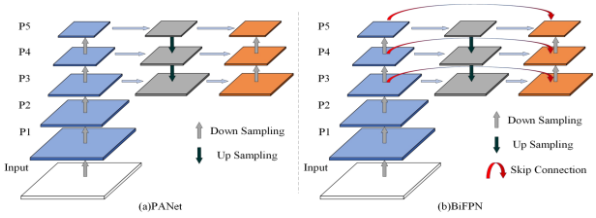

Figure 4. Comparation between PANet and BiFPN.

3.4. Introducing CBAM Attention Mechanism

Transformer breathers are often existing in the complex substation background, so it is of great significance for the model to accurately extract the relevant features of breathers from the complex substation scenes to improve the detection accuracy. We introduce the CBAM [12] attention mechanism at the output end of neck network to enhance the model's ability for extracting effective features from breathers, the structure of CBAM is shown in Figure 5. By calculating the attention scores from both spatial and channel dimensions, and then reweighting the convolutional feature map, the CBAM attention mechanism enables the model to focus more effectively on the key features related to breathers and their discoloration defects.

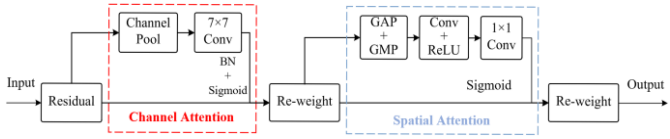

Figure 5. Comparation between PANet and BiFPN.

4. Experimental Evaluation

4.1. Experiment Settings

All of our experiments are implemented with an NVIDIA GeForce GTX 1080 Ti GPU and PyTorch 1.10.1 framework. We train and evaluate models with the discolored breather detection dataset containing 2537 original substation transformer breather images, in which the training set and validation set is divided in a 9:1 ratio. We set the batch size to 8 and the number of iterations to 50 while keep the default settings of the remaining hyperparameters for fair comparison. In order to effectively evaluate the comprehensive performance of different models in the substation scenario, we use Parameters (Params), FLOating Point operations (FLOPs), and Frames Per Second (FPS) to evaluate the size, computational complexity, as well as inference speed of models, respectively. And we use Average Precision (AP) for different categories and mean Average Precision (mAP) to evaluate the detection accuracy of models.

4.2. Comparison Experiment

We select four object detection models widely used in engineering and the baseline model YOLOv8n for comparison with our method. The experimental results are shown in Table 1. Firstly, in terms of deployment, SSD, TOOD and two RCNN series models have a larger number of parameters and a higher computation cost while our method only has 3.1M Params and 8.2G FLOPs, which means our method is more feasible for deployment in the inspection robot. Secondly, in terms of real-time detection, the YOLO models can significantly exceeds the threshold of real-time detection (i.e., higher than 30 FPS), reaching over 100 FPS, while other detectors have much lower inference speed which slightly over or under 30 FPS. In this case, we make a slight sacrifice of speed for higher precision. Finally, in terms of detection accuracy, the proposed method can achieve 97.2% mAP, which is 2.1% higher than the baseline model and significantly higher than other reference models. Therefore, our method has better performance on the task of discolored breather detection while maintaining a high inference speed for real-time detection and a lightweight model for edge deployment.

Table 1. Performance comparison of different models

Methods	Params(M)	FLOPs(G)	FPS(frame/s)	mAP(%)
Faster RCNN [6]	41.1	206.7	14.8	95.2
Sparse RCNN [14]	106.0	149.9	14.3	95.7
SSD [13]	24.3	344.9	51.3	92.6
TOOD [15]	31.8	180.7	14.7	96.1
YOLOv3 [8]	12.2	19.0	78.7	91.8
YOLOv5	3.1	9.0	117.4	94.3
YOLOv8	3.0	8.2	109.1	95.1
Our method	3.0	8.2	102.6	97.2

4.3. Ablation Experiment

In order to verify the effectiveness of each improvement scheme in the proposed method and its contribution to the ultimate model, we implement the ablation experiment, the results are shown in Table 2.

Table 2. Results of ablation experiment

Data Augment	BiFPN	CBAM	Params(M)	FLOPs(G)	FPS(frame/s)	mAP(%)
-	-	-	3.0	8.2	109.1	95.1
√	-	-	3.0	8.2	109.7	95.7
-	√	-	3.0	8.2	108.3	96.0
-	-	√	3.0	8.2	103.4	95.8
√	√	√	3.0	8.2	102.6	97.2

Firstly, with the data augmentation of cropping and generating, we obtain to a new training set with a more balanced sample distribution, the instance number and APs for different categories are shown in Table 3. The APs for all kinds of breather and their discoloration problem have been improved after data augmentation, and the metric of mAP is improved by 0.6% without additional model parameters and computation cost. The result verifies that the model is more robust to different types of breathers.

Secondly, by integrating BiFPN structure into the neck network of the model, it can effectively improve the perception ability of the model to the targets of different scales, and increase the mAP of the model by 0.9%, while having little impact on other metrics of the model.

Table 3. Result of different training sets

Methods	Before augmentation		After augmentation	
	Number	AP(%)	Number	AP(%)
Normal breather with shell	875	95.6	875	95.7
Normal breather without shell	193	93.4	867	94.9
Discolor breather with shell	824	97.1	824	97.3
Discolor breather without shell	391	94.2	830	95.1

Thirdly, by introducing CBAM attention mechanism at the output end of the neck network, the ability of extracting key features related to breathers is effectively enhanced, and the mAP of the model is increased by 0.7% compared with the baseline as well, while the number of parameters and computational complexity of the model are almost unchanged. Although the inference speed is slightly decreased in exchange for higher mAP, the cost is acceptable because the inference speed has already significantly exceeded 30 FPS which is enough for real-time detection.

Finally, when all three improvement schemes are used together, the mAP of the proposed method improved by 2.1% compared to the one of the baseline. The mAP curves of training process are shown in Figure 6. At the beginning of training, the mAP of the original YOLOv8n model is higher, which is caused by the modified structure and introduced new parameters in the improved model. At the later stage of training, the mAP of the improved model gradually exceeds that of the baseline, and the original model begins to overfit while the improved model does not. The above results verify that the improved model is more accurate and robust than the baseline model, while maintaining a relatively high inference speed for detecting in real-time and hardly increasing the parameters and computation cost.

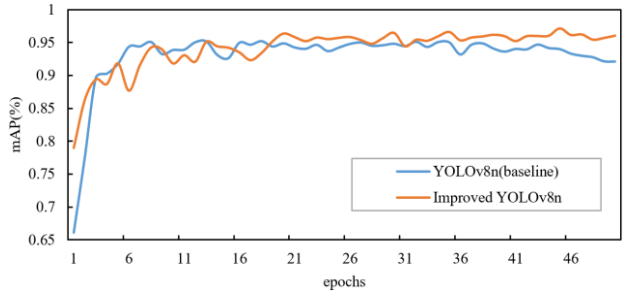

Figure 6. mAP curves of original and improved models.

4.4. Qualitative Experiment

The above experiments have verified the effectiveness of the proposed method and the contribution of each improvement scheme on the discolored breather detection task. In order to observe the effects brought about by above improvements more intuitively, we visualize the detection results, as shown in Figure 7. In all images for comparison, the improved YOLOv8 model can pay more attention to the effective features of breathers to effectively avoid the false detection and improve the confidence score of the detected object. This result further verifies the effectiveness of our proposed method.

Figure 7. detection results of original and improved models.

5. Conclusion

This paper proposes a discolored breather recognition method based on improved YOLOv8 by analyzing the characteristics of application scenarios, deployment conditions and original data. Firstly, the problem of sample imbalance is solved by a novel data augmentation strategy of cropping and generating. Secondly, a more powerful multi-scale feature fusion is enabled by incorporating the structure of BiFPN. Finally, CBAM attention mechanism is used to improve the ability of extracting effective features. The experimental results show that our method can realize the discolored breather detection with a lightweight model and a low computation cost which is suitable for deployment on inspection robots while achieving a better speed-precision tradeoff.

References

[1] Chen L, Zhu Y, Wang K, et al. Study of intelligent vision detection device for transformer respirator. Modern Manufacturing Technology and Equipment, 2023,59(05): 48-50.
[2] Chu G, Zhu W, Zhang G, et al. Design of intelligent unmanned inspection system for transformer substation. Proceedings of the 16th National Conference on Signal and Intelligent Information Processing and Application. 2022: 455-459.
[3] Wan J, Wu G, Guan M, et al. Intelligent recognition method for transformer small components based on RetinaNet. Power System Protection and Control, 2021,49(12): 166-173.
[4] Girshick R, Donahue J, Darrell T, et al. Rich feature hierarchies for accurate object detection and semantic segmentation. Proceedings of the IEEE conference on computer vision and pattern recognition. 2014: 580-587.
[5] Ren S, He K, Girshick R, et al. Faster r-cnn: Towards real-time object detection with region proposal networks. Advances in neural information processing systems, 2015, 28.
[6] Redmon J, Divvala S, Girshick R, et al. You only look once: Unified, real-time object detection. Proceedings of the IEEE conference on computer vision and pattern recognition. 2016: 779-788.
[7] Redmon J, Farhadi A. Yolov3: An incremental improvement. arXiv preprint arXiv:1804.02767, 2018.
[8] Xiang X, Pan L, Wu H. Respirator defect detection method based on feature matching and deep learning. Research and Exploration in laboratory, 2022,41(06): 57-61+97.
[9] Chen T, Zhou M, Han Q, et al. Defect Detection for Substation Based on Improved YOLOv4. Computer Systems & Applications, 2022,31(06):245-251.
[10] Liu B, Zhu Y, Song K, et al. Towards faster and stabilized gan training for high-fidelity few-shot image synthesis. International Conference on Learning Representations. 2020.
[11] Tan M, Pang R, Le Q V. Efficientdet: Scalable and efficient object detection. Proceedings of the IEEE/CVF conference on computer vision and pattern recognition. 2020: 10781-10790.
[12] Woo S, Park J, Lee J Y, et al. Cbam: Convolutional block attention module. Proceedings of the European conference on computer vision. 2018: 3-19.
[13] Liu W, Anguelov D, Erhan D, et al. Ssd: Single shot multibox detector. Computer Vision–ECCV 2016: 14th European Conference, Amsterdam, The Netherlands, October 11–14, 2016, Proceedings, Part I 14. Springer International Publishing, 2016: 21-37.
[14] Sun P, Zhang R, Jiang Y, et al. Sparse r-cnn: End-to-end object detection with learnable proposals. Proceedings of the IEEE/CVF Conference on Computer Vision and Pattern Recognition. 2021: 14454-14463.
[15] Feng C, Zhong Y, Gao Y, et al. Tood: Task-aligned one-stage object detection. 2021 IEEE/CVF International Conference on Computer Vision. IEEE Computer Society, 2021: 3490-3499.

Fuzzy Systems and Data Mining IX
A.J. Tallón-Ballesteros and R. Beltrán-Barba (Eds.)

doi:10.3233/FAIA231075

RM-GAN: Region Attention Mechanism and Multi-Scale Features for Respirator Defect Generation

Qiang HE[a,1], Xuewu LI[a], Yang LIU[a], Xin YOU[a], Bing LI[a], Yufeng WANG[a] and Yangjie XIAO[b]
[a]*China Southern Power Grid Co., Ltd. Extra High Voltage Transmission Company Guiyang Bureau*
[b]*North China Electric Power University*

Abstract. As a key component to ensure the efficient and safe operation of the transformer, the substation respirator's performance and status have a direct impact on the overall safety of the power system. Aiming at the problem that the defect characteristics of respirators are diverse and unbalanced, this paper proposes a respirator defect generation method based on a regional attention mechanism and multi-scale features, called RM-GAN. First, based on the structural characteristics of the respirator, the model adopts a feature-preserving image preprocessing method and introduces a regional attention mechanism to improve the precise positioning and modeling of respirator components. Then, by combining the multi-scale features of the respirator in the discriminator, defect characteristics can be captured on respirators of different scales, thereby enhancing the accuracy and robustness of the generated results. Finally, experiments were conducted on a custom-built dataset of respirator defects to validate the effectiveness of RM-GAN. The results indicate that RM-GAN is capable of generating high-quality images of respirator defects.

Keywords. substation respirator; GAN; regional attention; multi-scale features; defect generation

1. Introduction

Transformers are important equipment in substations. Once a transformer fails, it will have a very serious impact on the normal operation of the power system. The respirator is an important part of the transformer. It can effectively filter the moisture in the air to reduce moisture and oxidation of the transformer oil. If the respirator becomes discolored and fails due to saturation of adsorbed moisture, it will easily cause the transformer oil to become damp, causing the insulation strength of the transformer oil to decrease, and there is a risk of internal failure of the transformer. Therefore, timely detection and replacement of failed respirator silica gel is crucial to ensure the normal operation of the transformer [1-3].

Currently, the detection of respirator discoloration mainly relies on manual inspection, which not only consumes a lot of manpower and time but also the effect is

[1] Corresponding Author, Qiang HE, China Southern Power Grid Co., Ltd. Extra High Voltage Transmission Company Guiyang Bureau, Guiyang, China; Email: 15831255315@163.com.

also affected by subjective factors, resulting in inaccurate detection. With the rapid development of deep learning and computer vision technology, it is more effective to use computer vision methods to detect respirator discoloration [4-7]. However, due to the complex style of respirator equipment in substations, resulting in an imbalance of positive and negative samples, the effectiveness of current respirator discoloration detection methods is mostly limited by the quality of the data set. Current research on respirator defect recognition and detection mainly focuses on traditional image recognition and deep learning methods and lacks discussion of generative models. This is primarily because respirator defects are diverse and, in most cases, real defect samples are scarce. Therefore, generating diverse and credible respirator defect images with limited defect samples to improve the effect of defect detection is a very important but challenging task.

In recent years, generative adversarial networks [8] (GAN) have received extensive attention and research as a powerful data generation tool [9-10]. Although GAN has achieved certain success in various application scenarios, such as image restoration, data enhancement, etc., there is still a lack of research on defect generation of substation respirators, and many problems and challenges still exist. First, because the structure and working environment of respirators are very complex, and the sizes and forms of respirators are also different; second, because the samples of respirators in different environments are different and the types are diverse. How to accurately generate defect images with various characteristics is still an open problem.

To address these problems, this paper proposes a novel respirator defect generation method based on regional attention mechanism and multi-scale features, called RM-GAN. By introducing a regional attention mechanism and multi-scale features, our model is able to capture the regional characteristics of respirator defects more effectively. At the same time, it can handle respirators of different sizes, which effectively enhances the model's feature extraction capabilities for respirators, thereby improving the quality of generated respirator images. It has achieved good generation results on the experimental data set and can help improve detection performance.

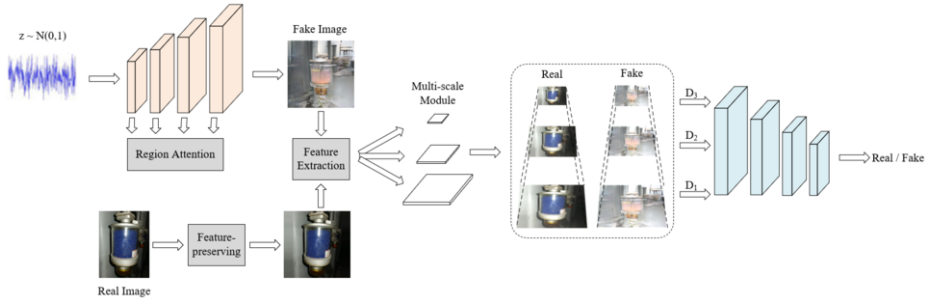

Figure 1. The structure of RM-GAN

2. RM-GAN

The imbalance in the quantity of various respirator types adversely impacts the efficacy of defect detection mechanisms in respirators. This paper proposes a respirator defect generation model RM-GAN based on regional attention mechanism and multi-scale features to solve this problem. Its structure is shown in Figure 1. RM-GAN mainly

includes three core improvements: 1) A feature-preserving preprocessing method is designed to ensure that the input image still has the basic structural characteristics of the original respirator, improving the quality and usability of the data. 2) The model integrates a regional attention mechanism to more accurately extract and focus on the features of the respirator area, thereby greatly improving the model's feature recognition capabilities. 3) A multi-scale shared convolution structure is adopted in the discriminator part to more effectively supervise the training of the generator and thereby improve the overall quality of the generated respirator images.

2.1. Feature-preserving Module

Due to the particularity of the respirator structure, the target image usually presents a rectangular shape with significantly different aspect ratios, as shown in Figure 2(a). Deep learning models generally process square inputs. Conventional resize preprocessing methods will cause distortion to the shape characteristics of the respirator image, as shown in Figure 2(b). This method will affect the accuracy of subsequent generated models. In order to solve this problem, this paper designs a feature-preserving preprocessing method, as shown in Figure 2(c). This method avoids directly stretching the original image but uses an edge expansion strategy to fill in the background information. This method not only meets the size requirements of the model input but also preserves the shape features of key parts of the image. Furthermore, this preprocessing method also plays a role in guiding the model's attention by retaining key areas of the image. It provides higher-quality input data for the subsequent regional attention module, thereby further strengthening the model's ability to identify and analyze specific regions.

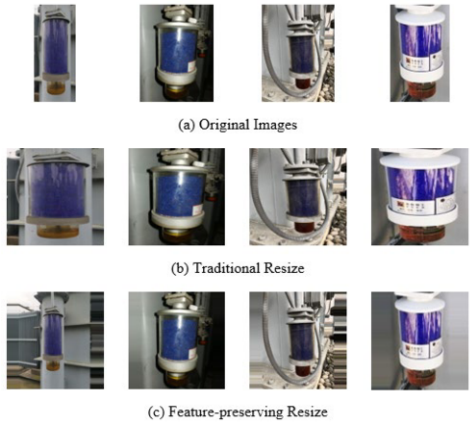

Figure 2. Examples of input images with different preprocessing methods

2.2. Region Attention Mechanism

Breathers usually only occupy a sub-region of the image and have significant regional color features, and traditional attention mechanisms perform poorly in this task. We propose an efficient regional attention module targeting the overall structural characteristics of respirator images. This module performs feature aggregation in the X and Y directions and encodes it into a region-sensitive attention map, thereby more

effectively enhancing the feature representation capabilities of the region of interest, aiming to capture regional information related to the respirator.

The regional attention module is shown in Figure 3, and the inputs are defined as $I \in R^{C\times H\times W}$. The input is encoded through a 1×1 convolutional layer and an average pooling layer in the X and Y directions. The encoded result is concatenated and then passed through a 1×1 convolutional layer followed by an activation layer, resulting in the generation of two independent tensors $t^h \in R^{C\times H\times 1}$ and $t^w \in R^{C\times 1\times W}$. After the matrix product, the regional attention feature map is obtained. The calculation process is as follows:

$$f_r = \frac{1}{N}\sum_{0\le n\le N} Sigmoid(t_c(h)\bullet t_c(w)) \in R^{1\times H\times W} \tag{1}$$

where c denotes the features of the *c-th* channel. To preserve global information, a 1×1 convolution layer with a single output channel and a sigmoid activation function is employed. The calculation formula is as follows:

$$f_g = Sigmoid(Conv_{c=1}(I)) \in R^{1\times H\times W} \tag{2}$$

where I denotes the input features. Finally, the global and regional attention feature maps are accumulated and multiplied with the input to obtain the final output of the regional attention module. The output formula is as follows:

$$O = (f_r \oplus f_g) \otimes I \tag{3}$$

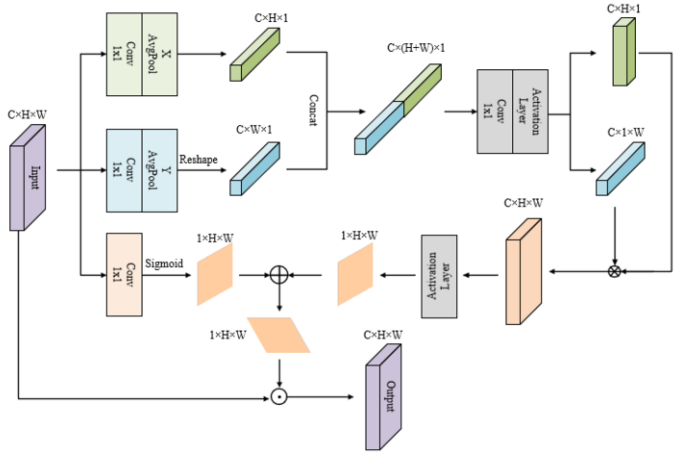

Figure 3. The structure of region attention

2.3. Multi-scale Discriminator

Due to the different locations where the inspection images were taken, the proportion of the respirator in the image is significantly different. In order to accurately identify respirators of different sizes, the discriminator needs to introduce multi-scale feature

inputs. Therefore, we propose a multi-scale discriminator to process images of different scales, represented by D_1, D_2, and D_3 respectively, and adopt a shared convolution architecture. Specifically, the input image is passed through a shared convolution layer to extract the features of the sample and obtain the corresponding feature map. Then, the feature maps of the real samples and the generated samples are downsampled with different sampling factors to obtain images of three different scales. Then D_1, D_2, and D_3 process feature maps of different scales respectively, and learn different discriminator parameters from them. The learning formula of the multi-scale module is as follows:

$$L = \min_{G} \max_{D_{1,2,3}} \sum_{i=1,2,3} E_{x\sim p(x)}[\log D(x)] + E_{x\sim p(z)}[\log(1 - D(G(z)))] \tag{4}$$

3. Experiment

3.1. Dataset

In accordance with the substation equipment labeling specifications, this paper uses the VOC2007 dataset construction method to construct a professional substation inspection respirator defect detection image dataset. The dataset has a total of 1909 images, including 4 types of respirators, of which discoloration of the respirators is the main defect. The details are shown in Table 1:

Table 1. Respirator Image Dataset

Types	Nums	Types	Nums
normal with shell	878	normal without shell	105
discoloration with shell	824	discoloration without shell	102

3.2. Image Generation Results and Analysis

In the generation experiment, to reflect the superiority of this method, comparative experiments were conducted on the same data set between this method and several popular generative models at this stage. The quantitative experimental results are shown in Figure 4. In addition, this paper selects the commonly used evaluation indicators FID (Frechet Inception Distance) and IS (Inception Score) of generative adversarial networks as a basis for fairly measuring the quality of generated images. The definitions of FID and IS are as follows:

$$IS(G) = \exp\left(E_{x\sim Pg} KL(p(y \mid x) \,\|\, p(y))\right) \tag{5}$$

$$FID(x, g) = \| \mu_x - \mu_g \|_2^2 + Tr(\Sigma_x + \Sigma_g - 2(\Sigma_x \Sigma_g)^{0.5}) \tag{6}$$

where *KL* represents the Kullback-Leibler Divergence, *Tr* denotes the trace, μ and Σ represent the mean and covariance matrix of the image feature vectors, respectively.

Specifically, we utilized the generative model to produce 5,000 synthetic samples and computed the distance between them and the real dataset, yielding the FID and IS values. Ideally, we aspire for the generative model to exhibit a high IS and a low FID. The qualitative experimental results are shown in Table 2.

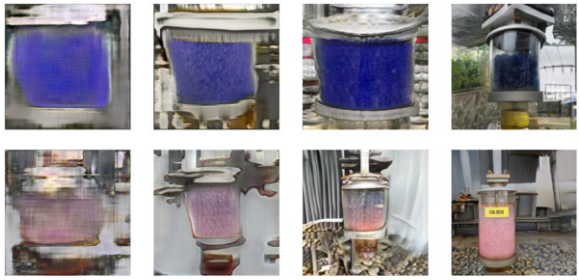

(a) DCGAN (b) ACGAN (c) StyleGAN-ADA (d) RM-GAN

Figure 4. The generation results of different models

Table 2. Experimental comparison of different models

Models	FID	IS
DCGAN[11]	174.83	1.34
ACGAN[12]	148.59	1.58
StyleGAN-ADA[13]	124.03	1.95
RM-GAN(ours)	**112.48**	**2.23**

This method is compared with the classic generative models DCGAN, ACGAN, and StyleGAN-ADA. As can be seen from Figure 4, the respirator image generated by our proposed method is more realistic and the target respirator is generated more accurately. We believe that this is because the regional attention mechanism and multi-scale module of RM-GAN play a role in the color area and different proportions of the respirator respectively, thus improving the quality of the generated respirator. Our generation method RM-GAN not only has the best visual effect but also achieves the best value in evaluation indicators. RM-GAN has the lowest FID, indicating that the respirator defect samples generated by our method are closer to the data distribution of real samples and have better generation quality. RM-GAN has the highest IS, indicating that the generated samples have better diversity. RM-GAN is significantly better than other generation methods in terms of evaluation indicators, which corresponds to the effect in Figure 4.

In order to further verify the effectiveness of each module on the RM-GAN network, ablation experiments were performed as shown in Table 3. As can be seen from Table 3, each module plays a role in improving performance. Among them, the regional attention and multi-scale discriminator have more obvious improvements in performance. We believe this is because they have improved the network architecture based on the characteristics of respirator defect samples, so they can achieve greater improvements. The feature preservation preprocessing is an adjustment to the original image. Although it has been improved, it is not as obvious as other modules. In addition, experiments show that using three improvements simultaneously can achieve the best results.

Table 3. Ablation experiment

Feature-preserving	Region Attention	Multi-scale D	FID	IS
√			126.93	1.91
	√		117.65	2.01
		√	116.72	2.12
√	√	√	**112.48**	**2.23**

3.3. Detection Results and Analysis

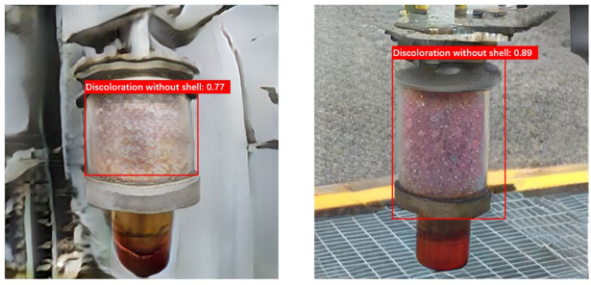

Figure 5. Detection display of images generated by different models.

We perform detection and display on the generated respirator defect images to reflect the advantages of this method. The detection effect is shown in Figure 5. Among them, Figure 5(a) is the detection result of the respirator generated by StyleGAN-ADA, and Figure 5(b) is the detection result of the respirator generated using this method RM-GAN. As can be seen from the detection result diagram, the detection effect on the image generated by RM-GAN is significantly better than the detection effect on the image generated by StyleGAN-ADA. Since the image quality generated by the latter is poor, it can easily lead to false detection; while the image generated by our method is still far from the real image, but it can accurately detect the regional part of the respirator. This shows that the method in this paper can improve the performance of detection and the quality of the generated results is better than other methods.

4. Conclusion

This paper proposes a respirator defect generation method based on regional attention mechanism and multi-scale features, called RM-GAN. By introducing a feature-preserving image preprocessing method and a regional attention mechanism, the precise positioning and modeling of respirator components are improved. At the same time, combining the multi-scale features of respirators in the discriminator can capture defect characteristics on respirators of different scales, thereby enhancing the accuracy and robustness of the generated results. Through experiments, it has been verified that RM-GAN can generate high-quality respirator defect images. This method is of great significance for ensuring the safe and stable operation of transformers.

References

[1] Liu S. Treatment of discoloration of silica gel in transformer respirators [J]. Popular Electricity, 2014, 29(10): 30-31.
[2] Xie W. Analysis on the treatment of silicone discoloration of transformer respirators [J]. China High-tech Enterprises, 2016(25):152-153.
[3] Li C, Zeng Q, Zeng L, et al. Operation risk analysis and operation and maintenance strategy research and application of main transformer breather [J]. Electrical Switch, 2022, 60(05): 84-87.
[4] Xin M, Xiao X, Liu B, et al. Automatic detection of transformer respirators based on image processing [J]. Practice and Understanding of Mathematics, 2018, 48(02): 127-133.

[5] Li R, Xu D, Zhai D, et al. Intelligent identification method of transformer respirator defects based on HSV feature transformation and target detection [J]. High Voltage Technology, 2020, 46(09): 3027-3035.
[6] Shi R. Power transformer respirator discoloration detection method based on adaptive threshold segmentation [J]. Jiangxi Electric Power, 2022, 46(08): 36-41+44.
[7] Xiang X, Pan L, Wu H. Respirator defect detection method based on feature matching and deep learning [J]. Laboratory Research and Exploration, 2022, 41(06): 57-61+97.
[8] Goodfellow I, Pouget-Abadie J, Mirza M, et al. Generative adversarial nets[J]. Advances in neural information processing systems, 2014, 27.
[9] Huang W, Xu A, Ming Z, et al. Method for predicting substation worker behavior based on generative adversarial network [J]. China Southern Power Grid Technology, 2019, 13(02): 45-50.
[10] Yang P, Li J, Hao R. Small sample image data enhancement technology based on generative adversarial network [J]. Network Security and Data Governance, 2023, 42(06):79-84+102.
[11] Radford A, Metz L, Chintala S. Unsupervised representation learning with deep convolutional generative adversarial networks[J]. arXiv preprint arXiv:1511.06434, 2015.
[12] Odena A, Olah C, Shlens J. Conditional image synthesis with auxiliary classifier gans[C]//International conference on machine learning. PMLR, 2017: 2642-2651.
[13] Karras T, Aittala M, Hellsten J, et al. Training generative adversarial networks with limited data[C]. Advances in neural information processing systems, 2020, 33: 12104-12114.

Fuzzy Systems and Data Mining IX
A.J. Tallón-Ballesteros and R. Beltrán-Barba (Eds.)

doi:10.3233/FAIA231076

DC-YOLOv5: Improved YOLOv5 for Transmission Line Fittings Detection Based on Deformable Convolution and Coordinate Attention

Qiang HE[a,1], Biaojun LI[a], Ting LIANG[a], Pei ZHOU[a], Mingquan YANG[a], Jun ZHU[a] and Ruiheng ZHOU[b]
[a]*China Southern Power Grid Co., Ltd. Extra High Voltage Transmission Company Guiyang Bureau*
[b]*North China Electric Power University*

Abstract. Transmission lines are an important component of the power system, and the detection of transmission line fittings is of great significance for ensuring the safe and stable operation of the power grid. In the inspection of transmission lines, drones are mainly used for taking photos and deep learning technology is used to achieve automatic detection. Due to the complex inspection background, high occlusion interference, and the variety of metal object categories and varying shapes and sizes, common detection methods have poor performance. This paper proposes an improved YOLOv5 method based on deformable convolution and coordinate attention, called DC-YOLOv5. Firstly, we construct the YOLOv5 network as the basic framework for the detection model. In order to extract more effective features from images containing complex background interference, we use deformable convolution to improve the original convolution module and enhance the feature extraction ability of the backbone network. Then, we use the coordinate attention module to process the output of the backbone network, improve the model's attention to fitting targets. This article hopes to effectively improve the performance of the model and maintain low complexity of the model for subsequent UAV deployment by using such uncomplicated lightweight modifications. Finally, in order to verify the effectiveness of DC-YOLOv5, a fitting detection dataset was established and experiments were conducted. The results indicate that DC-YOLOv5 has higher detection accuracy compared to other models and can accurately detect various metal object targets in complex environments.

Keywords. fittings detection; deformable convolution; attention mechanism; YOLOv5

1. Introduction

Transmission lines are an important component of emerging energy systems such as the energy internet and smart grids. Ensuring the stable operation of key components in transmission lines is the key to maintaining the stability of the power system, and is also an important part of the construction of the energy internet and smart grids[1]. Key

[1] Corresponding Author, Qiang HE, China Southern Power Grid Co., Ltd. Extra High Voltage Transmission Company Guiyang Bureau, Guiyang, China; Email: 2115049288@qq.com.

components such as fittings are widely used iron or aluminum metal accessories on transmission lines, mainly used for supporting, fixing, connecting bare wires, conductors, etc., including suspension clamps, grading rings, shockproof hammers, weights, etc. There are many types of fittings, and the shapes of different fittings also have certain differences. Due to being outdoors all year round and having complex contact with the environment, such components are likely to experience displacement, tilting, damage, etc. If these defects are not detected in a timely manner, they may lead to widespread power outages[2]. Therefore, automatic detection of fitting and prediction of faults are of great significance for ensuring the safe operation of the power grid[3].

With the maturity of drone technology, drone aerial photography technology has gradually replaced manual inspection. In recent years, with the advancement of deep learning, the use of computer vision technology to process aerial images of unmanned aerial vehicles on transmission lines and construct automated intelligent detection systems has become a current research hotspot. Reference [4] improved Faster R-CNN [5] as a component identification model for transmission lines, adjusted the size of convolutional kernels in convolutional operations, and expanded the dataset through data augmentation, verifying the feasibility of these two methods in improving accuracy. Reference [6] proposed an improved IoU (intersection over union) SSD [7] model for dense detection, which is more sensitive to target scale and adds repulsive loss to dense targets, achieving better dense detection results. There are many similar applications of computer vision technology in the field of transmission line detection.

The above research has to some extent achieved the detection of transmission line fittings, but there are still some problems. The inspection environment for power transmission lines is complex, with many interferences, and the shapes of different types of fitting vary greatly. The angles taken by drones are different, and conventional convolutional networks have weak adaptability to this, making it difficult to effectively extract available features. In order to solve these problems and improve the accuracy of transmission line fitting detection, this paper proposes an improved YOLOv5 transmission line fitting detection method based on deformable convolution [8] and coordinated attention [9] to address the problems in transmission line fitting detection. Our method is named DC-YOLOv5.

2. YOLOv5

2.1. Framework of YOLOv5

YOLOv5, like other algorithms in the series, is a typical one-stage object detection algorithm with a more efficient structure than two-stage algorithms such as Faster R-CNN. The structure of YOLOv5 framework is mainly composed of three parts: ① Backbone; ② Neck; ③ Detection Head The role of the backbone network is to extract features from input images and obtain feature layers for subsequent processing. The neck network is responsible for sampling and fusing feature layers at different scales, thereby enhancing the model's perception of targets at different scales, and effectively combining the shape information of large-scale feature layers with the semantic information of small-scale feature layers. The detection head will process the processed feature layers and predict the type and position information of different targets in the image.

2.2. Specific composition

In YOLOv5, the backbone adopts an improved CSPDarknet network. In the backbone network, feature extraction mainly relies on convolution, and the convolutional blocks in CSP Marknet are composed of convolution, batch normalization, and activation functions. In order to increase the depth of the network while avoiding the problem of gradient vanishing during the training process, CSPDarknet adopted the residual idea of ResNet [10] and constructed a C3 module, which utilizes channel dimensionality reduction and dimensionality increase to increase the receptive field of the model, facilitating the extraction of more detailed features.

The YOLOv5 neck network adopts a PAFPN [11] structure. Compared to traditional feature pyramid networks, PAFPN adds a reverse downsampling path, combining semantic features transmitted from top to bottom and shape features transmitted from bottom to top, enhancing the aggregation ability of the network and ensuring accurate prediction of images of different sizes. Similarly, YOLOv5 has added a C3 module to the neck network PAFPN, allowing the model to learn more features. Finally, the feature layer will be fed into the detection head, predicted by the model, and the loss will be calculated for training. The loss function of YOLOv5 mainly consists of three parts, including basic classification loss and regression loss, as well as confidence loss. The three parts of the loss will be summed after weighting to obtain the total loss, which will be used for backpropagation and model training.

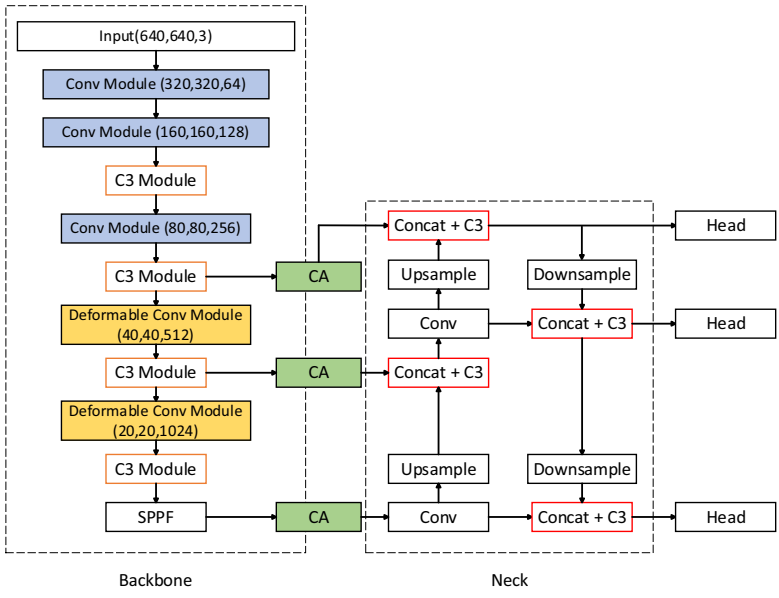

Figure 1. The structure of DC-YOLOv5

3. DC-YOLOv5

The YOLOv5 model can achieve good results in object detection and relies on its lightweight characteristics, making it very friendly for industrial deployment. This paper

proposes an improved YOLOv5 transmission line fitting detection model called DC-YOLOv5. Its structure is shown in Figure 1. DC-YOLOv5 has been mainly improved and expanded in two aspects: (1) using deformable convolution to improve partial convolution operations in the original backbone network. Deformable convolution enhances the model's feature extraction ability for targets of different scales by adding irregular offsets to the convolution. (2) Add coordinate attention mechanism to the network to make the model pay more attention to useful features of images outside the background and improve detection accuracy.

3.1. Deformable convolution

In order to enhance the feature extraction ability of the backbone network for targets of different scales and irregular targets, we use deformable convolution to replace some ordinary convolutions in the YOLOv5 backbone network. Figure 2 shows the difference between standard convolution kernels and deformable convolution kernels.

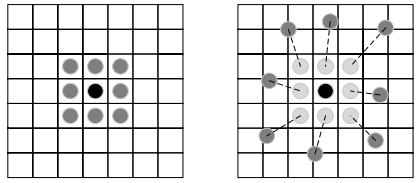

Figure 2. The structure of deformable convolution

The left figure shows the standard convolutional kernel, which slides at a fixed size during operation; The figure on the right shows the deformable convolution kernel with learnable offsets added. Deformable convolution kernel is not constrained by a fixed size near the sampling point position and is trained to learn how to set the optimal offset without additional supervision. Deformable convolution enhances the network's feature extraction ability for targets of different scales through sampling at irregular positions.

3.2. Coordinate attention mechanism

In order to enhance the features extracted by the model in complex backgrounds and focus the model's attention on key features, we use coordinate attention mechanism to improve the backbone output and improve the accuracy of detection. The structure of the coordinate attention mechanism is shown in Figure 3.

The calculation of coordinate attention not only considers the relationship between channels, but also considers the position information in the direction of the feature space, and is lightweight enough to not increase too much computational overhead. Firstly, the input feature map will undergo global average pooling in both the width and height directions to obtain features in both directions, $Z^h \in \mathbf{R}^{\mathrm{C}\times\mathrm{H}\times 1}$ and $Z^w \in \mathbf{R}^{\mathrm{C}\times 1\times\mathrm{W}}$.Then, the two directional feature maps obtained from the global receptive field are concatenated and fed into the shared 1 × 1 convolution module, which reduces the dimensionality of the channel by r times and sends it into the normalization layer and activation function to obtain the feature layer f, $f \in \mathbf{R}^{\mathrm{C/r}\times 1\times(\mathrm{H+W})}$. Then decompose f again along the dimensions of height and width to obtain $f^h \in \mathbf{R}^{\mathrm{C/r}\times\mathrm{H}\times 1}$ and $f^w \in \mathbf{R}^{\mathrm{C/r}\times 1\times\mathrm{W}}$, and separately utilize the other 1 × 1 convolution module to adjust the

convolution to the original number of channels and activate it using the sigmoid activation function to obtain the attention weights g^h in the height direction and g^w in the width direction of the feature map, respectively. After the above calculation, the attention weights of the input feature map in the high and wide directions will be obtained. Finally, by multiplying and weighting the height and width of the original feature map, the final feature map with attention weight will be obtained, which improves the model's attention to effective features.

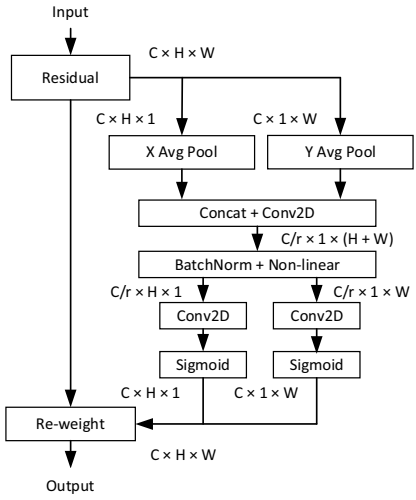

Figure 3. The structure of coordinate attention mechanism

4. Experiments

4.1. Dataset

This paper collects aerial images of unmanned aerial vehicles and constructs a transmission line fitting detection dataset after data screening. The dataset includes 12 types of fittings, including suspension clamps, grading rings, shielded rings, shockproof hammers, and includes 1586 images and 8329 annotation objects. We divided the dataset into a training set and a validation set in a 4:1 ratio for experimental purposes. Some example images of the dataset are shown in Figure 4. The detailed dataset composition is shown in Table 1.

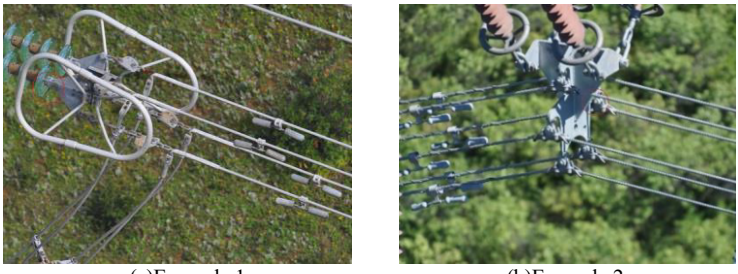

(a)Example 1 (b)Example 2

Figure 4. Dataset examples

Table 1. Transmission Line Fitting Detection Dataset

Fittings	Nums	Fittings	Nums
pre-twisted suspension clamp	160	shielding ring	141
bag-type suspension clamp	986	grading ring	726
shockproof hammer	1213	u-type hanging ring	1325
yoke plate	832	wedge-tpye strain clamp	105
adjusting plate	619	weight	357
hanging board	1524	spacer	341

4.2. Experimental Results and Analysis

In the experiment, we compare our model with several object detection models on the dataset. To demonstrate the superiority of our method, we use the metric mAP in object detection to measure model performance. The AP^{50} indicator is relatively broad while the AP^{50-95} indicator is more stringent. The experimental results are shown in Table 2.

Table 2. Comparison of different models

Method	mAP(%)		FPS
	AP^{50}	AP^{50-95}	
SSD[12]	70.54	49.27	43.7
Faster R-CNN	76.32	52.33	26.8
RetinaNet[13]	74.18	50.41	31.6
YOLOv5	76.25	52.36	82.6
DC-YOLOv5(Ours)	**80.31**	**54.52**	79.2

The experiment compared our proposed method with models such as SSD, RetinaNet, original YOLOv5, Faster R-CNN, etc. Compared with Faster R-CNN, the one-stage detection models SSD and RetinaNet have improved inference speed, but their accuracy is slightly lower. Our DC-YOLOv5 model is a one-stage detection model, but it has improved accuracy and detection speed compared to them, and its indicators exceed the two-stage model Faster R-CNN, demonstrating good detection performance. Overall, our method has a significantly faster inference speed and higher effectiveness than traditional models. Compared with the original YOLOv5 model, DC-YOLOv5 has an increase of 4.06% in AP^{50} and 2.16% in AP^{50-95}, resulting in a certain improvement in detection accuracy. Although deformable convolution and coordinated attention mechanism sacrifice some computational effectiveness and slightly reduces FPS, it is still acceptable. Overall, DC-YOLOv5 performs the best in the detection.

To further validate the effectiveness of the proposed improvement method on the model, we conducted ablation experiments on the model, and the experimental results are shown in Table 3. After introducing deformable convolution into the backbone of the baseline model, the accuracy improved by 1.91%; After using the coordinate attention mechanism in the baseline model, the accuracy improved by 2.38%. After combining these two improved methods, DC-YOLOv5 achieved the optimal detection accuracy, increasing AP^{50} to 80.31%, an increase of 4.06%, proving the effectiveness of the proposed method. Due to the introduction of additional parameters and modules in both of our improved methods, the FPS of the model decreased slightly but it is acceptable.

Table 3. Ablation study

Method		AP^{50}(%)	FPS
Deformable convolution	Coordinate attention		
		76.25	82.6
√		78.16	80.2
	√	78.63	81.4
√	√	**80.31**	**79.2**

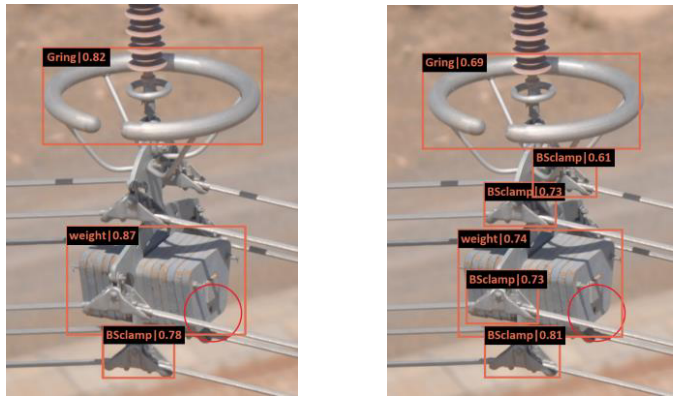

(a)YOLOv5 (b)DC-YOLOv5

Figure 5. Comparison of detection results between YOLOv5 and DC-YOLOv5

Figure 6. Different metrics in the training process

Finally, we conducted visualization experiments. The results are shown in Figure 5. Figure 5 (a) shows the result of original YOLOv5, and Figure 5 (b) shows the result of DC-YOLOv5. From the detection results, it can be seen that in the middle of the image, due to the complex occlusion relationship, the original YOLOv5 missed three suspension clamps, resulting in missed detection. The improved DC-YOLOv5 successfully detected these three easily missed clamps, and the detection effect was better than the baseline YOLOv5, proving the effectiveness of the improved method in this paper. In addition, Figure 6 shows the metrics of our model in training epochs such as AP^{50}, Recall and Loss, demonstrating the stability of the improved model during the training process.

5. Conclusion

Using computer vision technology to process UAV aerial images on transmission lines and constructing automated intelligent detection systems has become a research hotspot

in recent years. This paper proposes DC-YOLOv5, which uses deformable convolution and coordinate attention mechanism to extract more effective features in images with complex background interference and allow the model to focus on key features and improve detection accuracy. Experiments on the transmission line fitting detection dataset show that DC-YOLOv5 can accurately detect multiple fitting targets in complex environments, and has higher detection accuracy compared to other models.

In further work, we plan to deploy our lightweight model on UAVs with edge intelligent devices and achieve real-time detection during UAV inspections. We hope our method can make a contribution to ensuring the stable operation of the power grid.

References

[1] DONG Zhaoyang, ZHAO Junhua, WEN Fushuan, et al. From smart grid to energy internet : basic concept and research framework[J]. Automation of Electric Power Systems, 2014, 38(15) : 1-11.

[2] Li L. The UAV intelligent inspection of transmission lines. In Proceedings of the 2015 International Conference on Advances in Mechanical Engineering and Industrial Informatics. Atlantis Press, 2015; pp.1542-1545.

[3] ZHAO Zhenbing, JIANG Zhigang, LI Yanxu, et al. Overview of visual defect detection of transmission line components[J]. Journal of Image and Graphics, 2021, 26(11) : 2545-2560.

[4] Tang Yong, Han Jun, Wei Wenli, et al Research on part recognition and defect detection of transmission line in deep learning[J]. Electronic Measurement Technology, 2018, 41(6): 60-65.

[5] Ren S, He K, Girshick R, et al Faster r-cnn: Towards real-time object detection with region proposal networks[J]. Advances in neural information processing systems, 2015, 28.

[6] Qi Yincheng, Jiang Aixue, Zhao Zhenbing, et al Detection method of transmission line inspection image fittings based on improved SSD model [J]. Electrical Measurement & Instrumentation, 2019, 56(22): 7-12.

[7] Liu W, Anguelov D, Erhan D, et al Ssd: Single shot multibox detector[C]//Computer Vision–ECCV 2016: 14th European Conference, Amsterdam, The Netherlands, October 11–14, 2016, Proceedings, Part I 14. Springer International Publishing, 2016: 21-37.

[8] Dai J, Qi H, Xiong Y, et al. Deformable convolutional networks[C]//Proceedings of the IEEE international conference on computer vision. 2017: 764-773.

[9] Hou Q, Zhou D, Feng J. Coordinate attention for efficient mobile network design[C]//Proceedings of the IEEE/CVF conference on computer vision and pattern recognition. 2021: 13713-13722.

[10] He K, Zhang X, Ren S, et al Deep residual learning for image recognition[C]//Proceedings of the IEEE conference on computer vision and pattern recognition. 2016: 770-778.

[11] Liu S, Qi L, Qin H, et al. Path aggregation network for instance segmentation[C]//Proceedings of the IEEE conference on computer vision and pattern recognition. 2018: 8759-8768

[12] Liu W, Anguelov D, Erhan D, et al. Ssd: Single shot multibox detector[C]//Computer Vision–ECCV 2016: 14th European Conference, Amsterdam, The Netherlands, October 11–14, 2016, Proceedings, Part I 14. Springer International Publishing, 2016: 21-37.

[13] Lin T Y, Goyal P, Girshick R, et al. Focal loss for dense object detection[C]//Proceedings of the IEEE international conference on computer vision. 2017: 2980-2988.

Fuzzy Systems and Data Mining IX
A.J. Tallón-Ballesteros and R. Beltrán-Barba (Eds.)

doi:10.3233/FAIA231077

Generalized Countable Fuzzy Semi-Compactness in L-Topological Spaces

Qiaoqiao LI, Xiaoxia WANG[1] and Jiaxin GAO
College of Mathematics and Computer Science, Yan'an University , Yan'an 716000, China

Abstract. In this paper, the generalized countable fuzzy semi-compactness is defined in LTS, and its weak topological invariance and topological generation are proved. When L is complete Heyting algebra, the union of two generalized countable fuzzy semi-compactness L-set is generalized countable fuzzy semi-compactness; the intersection of a generalized countable fuzzy semi-compactness L-set and a generalized semi-closed countable L-set is generalized countable fuzzy semi-compactness.

Keywords. L-topological space; generalized countable fuzzy semi-compactness; generalized semi-open countable; generalized semi-closed countable

1. Introduction

In 1976, the concept of fuzzy compactness is introduced in [0,1] –TPS([0,1] –topological Spaces) by reference[1]. In 1988, [2] extended it to LTS, where L is a completely allocated DeMorgan algebra. [3] proposed a new definition of fuzzy compactness in LTS. [4] studies the countably compactness of L-set.[5]gives the Generalized semi-open L-sets and generalized semi-closed L-sets. [6]gives the concept of generalized fuzzy semi-compactness, properties of generalized fuzzy semi-compactness and some equivalent characterizations.[7]-[14]many experts have studied the related properties of compactness and semi-compactness in L-topological Spaces.[15]-[19]experts have studied some properties of compactness by means of operators. This paper gives the definition of generalized countable fuzzy semi-compactness, Some of its properties are studied. The remaining concepts and notations not described in the text can be found in [2]. For convenience, we will hereafter refer to L – topological space as LTS for short.

2. Related works

In this paper, the compactness of LTS is extended on the basis of [6], and some related properties of [6] are studied. On this basis, the weak topological invariance and topological generatability of generalized countable fuzzy semi-compactness are also studied.

[1] Corresponding author, Xiaoxia WANG, Yan'an University , Yan'an 716000, China; E-mail: yd-wxx@163.com.

3. Preliminary Knowledge

In this part, we will review some primary concepts of generalized fuzzy semi-compactness.

Definition 3.1[5]Hypothesis $\left(L^X,\delta\right)$ is an LTS, $B\in L^X$ .Then B is the generalized semi-closed L – set, if the semi-open countable L – set U satisfying $B\le U$ there is $cl\left(B\right)\le U$. B is called generalized semi-open if B' is generalized semi-closed.

$GSO\left(X\right)$ is denoted as the sets of the all generalized semi-open L – sets on X and $GSC\left(X\right)$ is denoted as the sets of the all generalized semi-closed L – sets on X .

Definition 3.2[6]Hypothesis $\left(L^X,\delta\right)$ is an LTS, $M\in L^X$. If for each family $P\subset GSO\left(X\right)$ there is

$$\underset{x\in X}{\cap}\left(M'\left(x\right)\cup\underset{D\in P}{\cup}D\left(x\right)\right)\le\underset{V\in 2^{(P)}}{\cup}\underset{x\in X}{\cap}\left(M'\left(x\right)\cup\underset{D\in V}{\cup}D\left(x\right)\right).$$

Then M is called generalized fuzzy semi-compact.

Definition 3.3[7]Hypothesis $\left(L^X,\alpha\right)$ and $\left(L^Y,\beta\right)$ are LF topological space, $f:\left(L^X,\alpha\right)\to\left(L^Y,\beta\right)$ is L – value Zadeh- type function, if $\forall H\in\beta$ have $f^{-1}\left(H\right)\in\alpha$, f is called continuous.

Lemma3.1[8] Hypothesis $\left(L^X,\omega_L\left(F\right)\right)$ is an LTS induced by the distinct topological space $\left(X,F\right)$. Hypothesis U is the semi-open set in $\left(X,F\right)$, then χ_U is the semi-open set in $\left(L^X,\omega_L\left(F\right)\right)$.If R is the semi-open set in $\left(L^X,\omega_L\left(F\right)\right)$, then for $\mathrm{b}\in L$, $R\left(\mathrm{b}\right)$ is the semi-open set in $\left(X,F\right)$.

For the subset $P\subset L^X$, $2^{(P)}$ is denoted as the set of all finite subfamilies of P .

4. Generalized countable fuzzy semi-compactness

Definition 4.1 Hypothesis $\left(L^X,\delta\right)$ is an LTS, $M\in L^X$. Hypothesis for every countably family $P\subset GSO\left(X\right)$ there is

$$\underset{x\in X}{\cap}\left(M'\left(x\right)\cup\underset{D\in P}{\cup}D\left(x\right)\right)\le\underset{V\in 2^{(P)}}{\cup}\underset{x\in X}{\cap}\left(M'\left(x\right)\cup\underset{D\in V}{\cup}D\left(x\right)\right).$$

Then M is denoted generalized countable fuzzy semi-compact.

Definition 4.2 Hypothesis $\left(L^X,\delta\right)$ is an LTS, $c\in L-\{1\}$, $M\in L^X$ .A countable family $P\subset GSO\left(X\right)$ is called generalized semi-open countable $c-$*shading* of M , hypothesis for every $x\in X$ there is $\left(M'\left(x\right)\cup\underset{D\in P}{\cup}D\left(x\right)\right)\le c$. P is called generalized semi-open

countable strong $c-shading$ of M hypothesis for any $x\in X$ there is $\underset{x\in X}{\cap}\left(M'(x)\cup\underset{D\in P}{\cup}D(x)\right)\le c$.

The generalized semi-open countable strong $c-shading$ of M is the generalized semi-open countable $c-shading$ of M.

Definition 4.3. Hypothesis $\left(L^X,\delta\right)$ is an LTS, $c\in L-\{1\}$, $M\in L^X$.A countable family $Q\in GSC(X)$ is called generalized semi-closed countable $c-remote$ family of M, hypothesis for every $x\in X$ there is $\left(M(x)\cap\underset{B\in Q}{\cap}B(x)\right)\ge c$. Q is called generalized semi-closed countably strong $c-remote$ family of M, if $\underset{x\in X}{\cup}\left(M(x)\cap\underset{B\in Q}{\cap}B(x)\right)\ge c$.

The generalized semi-closed countably strong $c-remote$ family of M is the generalized semi-closed countably $c-remote$ family of M.

By Definition 4.1 and order inversing involution ,we will introduce theorem4.1.

Theorem 4.1. Hypothesis $\left(L^X,\delta\right)$ is an LTS, $M\in L^X$.Then M is generalized countably fuzzy semi-compact if and only if for any countably family $Q\in GSC(X)$, there is $\underset{x\in X}{\cup}\left(M(x)\cap\underset{B\in Q}{\cap}B(x)\right)\ge\underset{F\in 2^{(Q)}}{\cap}\underset{x\in X}{\cup}\left(M(x)\cap\underset{B\in F}{\cap}B(x)\right)$.

Theorem 4.2. Hypothesis M is generalized fuzzy semi-compact, then it is generalized countable fuzzy semi-compact.

Proof. If M is generalized fuzzy semi-compact, by definition 3.2, for every family $P\subset GSO(X)$, there is

$$\underset{x\in X}{\cap}\left(M'(x)\cup\underset{D\in P}{\cup}D(x)\right)\le\underset{V\in 2^{(P)}}{\cup}\underset{x\in X}{\cap}\left(M'(x)\cup\underset{D\in V}{\cup}D(x)\right).$$

There is certainly $P\subset GSO(X)$ countable subset $V\subset GSO(X)$ meet

$$\underset{x\in X}{\cap}\left(M'(x)\cup\underset{D\in V}{\cup}D(x)\right)\le\underset{C\in 2^{(V)}}{\cup}\underset{x\in X}{\cap}\left(M'(x)\cup\underset{D\in C}{\cup}D(x)\right).$$

Prove that M is generalized countably fuzzy semi-compact.

By Definitions 4.1 and 4.2 we will introduce theorem4.3.

Theorem 4.3 Hypothesis $\left(L^X,\alpha\right)$ is an LTS, $M\in L^X$. Then M is generalized countably fuzzy semi-compact if and only if for every $c\in L-\{1\}$,every generalized semi-open countably strong $c-shading$ P of M has finite subfamily D is generalized semi-open countably strong $c-shading$ of M.

By Definitions 4.1 and 4.3 we will introduce theorem4.4.

Theorem 4.4 Hypothesis $\left(L^X,\alpha\right)$ is an LTS, $M\in L^X$.Then M is generalized countably fuzzy semi-compact if and only if for every $c\in L-\{0\}$,every generalized semi-closed countably strong $c-remote$ family K of M has finite subfamilies C is generalized semi-closed countably $a-remote$ family of M.

5. Properties of generalized countable fuzzy semi-compactness

Definition 5.1 Hypothesis $\left(L^X,\delta\right)$ and $\left(L^Y,\mu\right)$ are LTS, $f:\left(L^X,\delta\right)\to\left(L^Y,\mu\right)$ is an homomorphism said to be a continuous order homomorphism if for any countably closed set H in $\left(L^Y,\mu\right)$, $f^{-1}\left(H\right)$ is countably closed set in $\left(L^X,\delta\right)$ .If $L_1=L_2=L$, f is a *Zadeh*- type mapping, f is said to be the $L-$ continuum mapping from $\left(L^X,\delta\right)$ to $\left(L^Y,\mu\right)$.

Definition 5.2 Hypothesis $\left(L^X,\delta\right),\left(L^Y,\mu\right)$ is an LTS, $f:\left(L^X,\delta\right)\to\left(L^Y,\mu\right)$ as the one-to-one mapping, f and f^{-1} are $L-$ continuous , says f is $L-$ homeomorphism mapping. The property that remains invariant under $L-$ homeomorphism mapping is called weak topological invariance.

Definition 5.3 Hypothesis $\left(L^X,\omega_L\left(T\right)\right)$ is an LTS induced by the distinct topological spaces $\left(X,T\right)$. Hypothesis U is the generalized semi-open countable set in, then χ_U is the generalized semi-open countable set of $\left(L^X,\omega_L\left(F\right)\right)$.If A is the generalized semi-open countable set of $\left(L^X,\omega_L\left(F\right)\right)$,then for $a\in L$, $A\left(a\right)$ is the generalized semi-open countable set in $\left(X,T\right)$.

Theorem 5.1 Hypothesis $\left(L^X,\delta\right)$ and $\left(L^Y,\mu\right)$ are LTS, $f:\left(L^X,\delta\right)\to\left(L^Y,\mu\right)$ is continuous $L-$ value *Z*adeh- type function and $M\in L^X$ .Then $f\left(M\right)$ is generalized countably fuzzy semi-compact set in $\left(L^Y,\mu\right)$ when M is the generalized countably fuzzy semi-compact set in $\left(L^X,\delta\right)$.

Proof. Let P be countable family of $f\left(M\right)$, then $f^{-1}\left(P\right)$ is a countable family of M .Is defined by Definition 4.1 has

$$\underset{y\in Y}{\cap}\left(f\left(M\right)'\left(y\right)\cup\underset{D\in P}{\cup}D\left(y\right)\right)=\underset{x\in X}{\cap}\left(M'\left(x\right)\cup\underset{D\in P}{\cup}f^{-1}\left(D\right)\left(x\right)\right)$$

$$\leq\underset{V\in 2^{(P)}}{\cup}\underset{x\in X}{\cap}\left(M'\left(x\right)\cup\underset{A\in V}{\cup}f^{-1}\left(D\right)\left(x\right)\right)=\underset{V\in 2^{(P)}}{\cup}\underset{y\in Y}{\cap}\left(f\left(M\right)'\left(y\right)\cup\underset{D\in V}{\cup}D\left(y\right)\right).$$

That is $f\left(M\right)$ is the generalized countably fuzzy semi-compact set in $\left(L^Y,\mu\right)$.

Corollary 1 Generalized countable fuzzy semi-compact in $L-$ topological spaces is weakly topologically invariant.

Theorem 5.2 Makes L is a complete Heyting algebra.Hypothesis both M and N are generalized countably fuzzy semi-compact, then $M\vee N$ is generalized countably fuzzy semi-compact.

Proof. For every countable family $U\in GSC\left(X\right)$, given by theorem 4.1 have

$$\underset{x\in X}{\cup}\left(\left(M\cup N\right)\left(x\right)\cap\underset{B\in U}{\cap}B\left(x\right)\right)$$

$$= \left\{ \bigcup_{x\in X} M(x) \cap \bigcap_{B\in U} B(x) \right\} \cup \left\{ \bigcup_{x\in X} \left(N(x) \cap \bigcap_{B\in U} B(x) \right) \right\}$$

$$\geq \left\{ \bigcap_{F\in 2^{(U)}} \bigcup_{x\in X} \left(M(x) \cap \bigcap_{B\in F} B(x) \right) \right\} \cup \left\{ \bigcap_{F\in 2^{(U)}} \bigcup_{x\in X} \left(N(x) \cap \bigcap_{B\in F} B(x) \right) \right\}$$

$$= \bigcap_{F\in 2^{(U)}} \bigcup_{x\in X} \left((M\cup N)(x) \cap \bigcap_{B\in F} B(x) \right).$$

Therefore $M \vee N$ is generalized countably fuzzy semi-compact.

Theorem 5.3 Hypothesis M is the generalized countably fuzzy semi-compact L – set, $N \in GSC(X)$,then $M \wedge N$ is the generalized countably fuzzy semi-compact L – set.

Proof. Since M is the generalized countably fuzzy semi-compact L – set,for every countably family $U \in GSC(X)$, given by theorem 4.1 have

$$\bigcup_{x\in X} \left((M\cap N)(x) \cap \bigcap_{B\in U} B(x) \right) = \bigcup_{x\in X} \left(M(x) \cap \bigcap_{B\in U\cup\{N\}} B(x) \right)$$

$$\geq \bigcap_{F\in 2^{(U\cup\{N\})}} \bigcup_{x\in X} \left(M(x) \cap \bigcap_{B\in F} B(x) \right)$$

$$= \left\{ \bigcap_{F\in 2^{(U)}} \bigcup_{x\in X} \left(M(x) \cap \bigcap_{B\in F} B(x) \right) \right\} \cap \left\{ \bigcap_{F\in 2^{(U)}} \bigcup_{x\in X} \left(M(x) \cap \left(N(x) \cap \bigcap_{B\in F} B(x) \right) \right) \right\}$$

$$= \bigcap_{F\in 2^{(U)}} \bigcup_{x\in X} \left((M\cap N)(x) \cap \bigcap_{B\in F} B(x) \right).$$

Therefore $M \wedge N$ is the generalized countably fuzzy semi-compact L – set.

Theorem 5.4 Hypothesis $\left(L^X, \omega_L(F)\right)$ is an LTS induced by the distinct topological spaces (X,F), $T \subset X$, then T is generalized countably fuzzy semi-compact in (X,F) if and only if χ_T is generalized countably fuzzy semi-compact in $\left(L^X, \omega_L(F)\right)$.

Proof. $\Leftarrow$. Hypothesis Γ is generalized semi-open countable family of $\left(L^X, \omega_L(F)\right)$, let $\bigcap_{x\in X} \left((\chi_T)'(x) \cup \bigcup_{B\in\Gamma} B(x) \right) = a$.

When $a = 0$, There is obviously

$$\bigcap_{x\in X} \left((\chi_T)'(x) \cup \bigcup_{B\in\Gamma} B(x) \right) \leq \bigcup_{\Upsilon\in 2^{(\Gamma)}} \bigcap_{x\in X} \left((\chi_T)'(x) \cup \bigcup_{B\in\Upsilon} B(x) \right).$$

Let $a \neq 0$, then for $b < a$ have $b < \bigcap_{x\in X} \left((\chi_T)'(x) \cup \bigcup_{B\in\Gamma} B(x) \right)$.

Thus $\left\{ B_{(b)} \mid B \in \Gamma \right\}$ is generalized semi-open countable covering of T . By T is generalized countable fuzzy semi-compact of (X,F), exist $\Upsilon \in 2^{(\Gamma)}$ make $\left\{ B_{(b)} \mid B \in \Upsilon \right\}$ is generalized half-open countable covering of T .

Then $b \leq \bigcap_{x\in T} \left(\bigcup_{B\in\Upsilon} B \mid T(x) \right)$. Thus

$$b \le \underset{x\in T}{\cap}\left(\underset{B\in\Upsilon}{\cup}(B \mid T)\right)(x) = \underset{x\in X}{\cap}\left(\left(\chi_T\right)'(x)\cup\left(\underset{B\in\Upsilon}{\cup}B(x)\right)\right)$$

$$\le \underset{\Upsilon\in 2^{(\Gamma)}}{\cup}\underset{x\in X}{\cap}\left(\left(\chi_T\right)'(x)\cup\left(\underset{B\in\Upsilon}{\cup}B(x)\right)\right), \text{ Thus have}$$

$$\underset{x\in X}{\cap}\left(\left(\chi_T\right)'(x)\cup\underset{B\in\Gamma}{\cup}B(x)\right) = a = \cup\{b \mid b < a\} \le \underset{T\in 2^{(\Gamma)}}{\cup}\underset{x\in X}{\cap}\left(\left(\chi_T\right)'(x)\cup\left(\underset{B\in\Upsilon}{\cup}B(x)\right)\right)$$

Therefore χ_T generalized countable fuzzy semi-compact of $\left(L^X, \omega_L(F)\right)$.

$\Rightarrow$ .Hypothesis B be any generalized semi-open countable covering of T ,then $\{\chi_J \mid J \in B\}$ is the generalized semi-open countable sets in $\left(L^X, \omega_L(F)\right)$ and

$$\underset{x\in X}{\cap}\left(\left(\chi_T\right)'(x)\cup\underset{J\in B}{\cup}\chi_J(x)\right) = 1.$$

By χ_T is the generalized countably fuzzy semi-compact in $\left(L^X, \omega_L(F)\right)$ known,

$$\underset{\Upsilon\in 2^{(B)}}{\cup}\underset{x\in X}{\cap}\left(\left(\chi_T\right)'(x)\cup\left(\underset{J\in\Upsilon}{\cup}\chi_J(x)\right)\right) = 1.$$

There are $\Upsilon \in 2^{(B)}$ make $\underset{x\in X}{\cap}\left(\left(\chi_T\right)'(x)\cup\underset{J\in\Upsilon}{\cup}\chi_J(x)\right) = 1$.

So $\underset{x\in T}{\cap}\left(\underset{J\in\Upsilon}{\cup}(\chi_J \mid T)(x)\right) = 1$, thus $\{J \mid T \mid J \in \Upsilon\}$ is generalized semi-open countable covering of T , namely Υ is generalized semi-open countable covering of T .

6. Conclusion

In this paper, the generalized countable fuzzy semi-compactness is defined in LTS. This definition does not depend on the structure of L and does not require distributivity. As a generalization of the compactness of L-topological Spaces, some good properties of the generalized countably fuzzy semi-compactness are proved. In the future, can continue to study some properties such as equivalent characterization and good generalization.

Reference

[1] Lowen R. Fuzzy topological spaces and fuzzy compactness. J. Math. Anal. Appl.,56(1976)621-633.

[2] Wang GJ. L-Fuzzy Topological Space Theory [M] Xi'an: Shaanxi Normal University Press, 1988.

[3] Shi FG. Fuzzy compactness in L-topological spaces[J]. Fuzzy Sets and Systems, 2007, 58:1486-1495.

[4] Shi FG. Countable compactness and the Lindelof property of L-fuzzy sets [J].Iranian Journal of Fuzzy Systems, 2004,1:79-88.

[5] Yang GQ, Li HY, Xu ZG. Generalized semi-open L-sets and generalized semi-closed L-sets[J]. Journal of Liaoning Normal University(Natural Science Edition), 2006, 29(4):194-196.

[6] Xu ZG, Liu MG. Generalized fuzzy semi-compactness in L-topological spaces[J]. Journal of Liaoning Normal University(Natural Science Edition), 20 21, 44(4):450-453.

[7] Jiang JP. The countably pairwise ultra-compactness in L-bitopological spaces[J].Fuzzy Systems and

Mathematics, 2015, 29(3):75-78.

[8] Shi FG. Semi-compactness in L-topological spaces[J]. International Journal of Mathematics and Mathematical Sciences, 2005, 12: 1869-1878.

[9] Pan W, Xu ZG, Zhao Y. Countable semi-compactness L-fuzzy topological spaces[J]. Fuzzy Systems and Mathematics, 2015, 29(4):71-75.

[10] Han HX, Meng GW. Local semi-compactness of L-topological spaces[J]. College Mathematics, 2010, 26(4): 76-79.

[11] Shi FG, Li RX. Compactness in L-fuzzy topological spaces[J]. Hacettepe journal of Mathematics and Statistics, 2011,40 (6):767-774.

[12] Shi FG. A new definition of fuzzy compactness[J]. Fuzzy Sets and Systems, 2007,158:1486-1495.

[13] Zhang J, Shi FG, Zheng CY. On L-fuzzy topological spaces[J]. Fuzzy Sets and Systems, 2005,149:473-484.

[14] Shi FG, Li RX. Semi-compactness in L-fuzzy topological spaces[J]. Annals of Fuzzy Mathematics and Informatics, 2011, 2:163-169.

[15] Benkhaled H, Elleuch A, Jeribi A.Demicompactness Properties for Uniformly Continuous Cosine Families[J].Mediterranean Journal of Mathematics, 2022, 156-169.

[16] Slim C, Aref J, Bilel K. Demicompactness perturbation in Banach algebras and some stability results[J].Georgian Math, 2023, 30(1):53-63.

[17] Hedi B,Elleuch A,Jeribi A.Relative Demicompactness Properties for Exponentially Bounded C 0-Semigroups[J].Russian Mathematics, 2023, 1-7.

[18] Krichen B,Trabelsi B.B-Weyl and Drazin invertible operators linked by weak pseudo \(S_0\)-demicompactness [J] Ricerche di Matematica, 2021, 1-18.

[19] Wasi HA,Rajihy Y.On various properties of (;m, n;)-semi-compactness in bitopological spaces [J].Journal of Interdisciplinary Mathematics,2021,1119-1122.

Fuzzy Systems and Data Mining IX
A.J. Tallón-Ballesteros and R. Beltrán-Barba (Eds.)

doi:10.3233/FAIA231078

Research and Application of Power Monitoring System Based on Internet of Things

Lanyong ZHANG [a] and Renbing ZHANG [a,1]
[a] *College of Intelligent Systems Science and Engineering, Harbin Engineering University, Harbin 150001, China*

Abstract. IoT technology is widely used in various fields because of its ability to intelligently process data. The operation of power facilities is closely related to human development. Real-time monitoring of the working conditions of power equipment is conducive to timely handling of faults and greatly reduces unnecessary accidents. This article mainly designs a software monitoring platform based on the Internet of Things framework to realize data collection and processing, wireless transmission, real-time monitoring, fault alarm. In order to improve the accuracy and stability of data processing, this article applies the unscented Kalman filter algorithm to the data processing link. The visualization function of the software monitoring platform can visually present real-time data and historical trends of power equipment in the form of charts and curves providing a user-friendly interface and operating experience. Finally, the functional test was completed on the monitoring platform, which can be used in fields such as power system working status monitoring and power equipment environment monitoring.

Keywords. IoT technology, electric equipment, surveillance system, UKF

1. Introduction

With the development of science and technology, Internet of Things technology has been widely used. The Internet of Things includes a three-layer structure, namely the perception layer, the network layer, and the application layer[1]. The realization of the Internet of Things technology first needs to realize the collection of object information through the terminal collection equipment, and then send the collected data to the upper layer equipment through the wireless network to realize the integration of data. Based on the huge underlying information collection terminal, the Internet of Things can form a Highly intelligent and integrated network. Finally, the status monitoring and intelligent control of the object are completed through the software platform of the host computer[2].

People's work and life are inseparable from the use of electricity. People have put forward higher requirements for the predictability and security of power systems[3]. Since power facilities usually consist of a large number of complex equipment and

[1] Corresponding Author, Renbing ZHANG, College of Intelligent Systems Science and Engineering, Harbin Engineering University, Harbin, China; E-mail: zhangrenbing@hrbeu.edu.cn.

involve dangerous factors such as high voltage, high temperature, and large current, they are hazardous equipment[4]. There are potential failures and safety hazards in power equipment. Monitoring and maintenance personnel need to take special safety measures and equipment to maintain the system. The monitoring and maintenance of power systems have become a major problem that consumes human and financial resources[5]. For this reason, my country's research on integrated monitoring of power systems has never stopped.

In order to solve the above problems, this paper studies a method of applying Internet of Things technology to the power monitoring system to achieve remote monitoring of power equipment, reduce capital investment and accident risks, and integrate the unscented Kalman filter algorithm into the power monitoring system The software platform enables accurate processing and analysis of power data and provides strong support for the monitoring and maintenance of the power system[6]. The monitoring platform studied in this paper can well solve the problems of high power system maintenance costs and untimely fault detection[7].

2. Overall design of power monitoring system

In the power monitoring system based on the Internet of Things technology studied in this paper, the combination of C/S architecture and the three-tier architecture of the Internet of Things is adopted[8]. The system consists of four parts: information collection terminal, database, wireless transmission network, and power monitoring software platform.

The perception layer is responsible for completing the collection and transmission of data and sending the data to the host computer. Wireless transmission of network layer data is the prerequisite for realizing remote monitoring functions. The application layer implements terminal data processing through the monitoring system, such as data integration, filtering, visualization.[9]

The monitoring system platform is built using the Visual Studio 2017 development environment, and the database is built using SQL Server Management Studio 2012. The overall structure block diagram of the power monitoring system is shown in Figure 1.

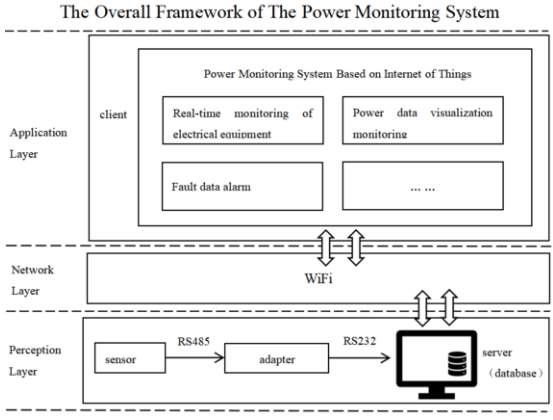

Figure 1. IoT three-tier architecture.

2.1. Power data collection and transmission

The perception layer of the Internet of Things is built based on the information collection terminal equipment of the sensor. The sensor sends the collected data to the server through the serial port. The data is received through the serial port APP based on the ModBus-RTU. The design diagram for hardware device connection is shown in Figure 2.

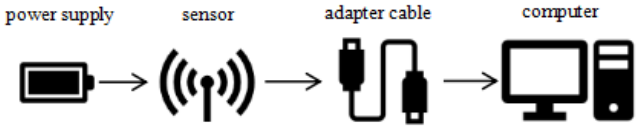

Figure 2. Hardware device connection design diagram.

2.2. Design of wireless transmission based on database

Wireless transmission is implemented using WiFi technology, and the wireless transmission function of data is realized through the database. The data collected by the sensor are classified and stored in the database in the server through the serial port program. The schematic diagram of wireless transmission is shown in Figure 3.

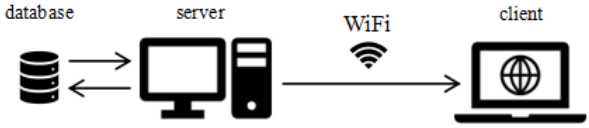

Figure 3. Schematic diagram of wireless transmission.

2.3. Data processing based on unscented Kalman filter algorithm

During the transmission process, data information will be affected by various factors such as sensors. Due to the presence of these interferences, the actual data content sent to the server will be incomplete and inaccurate. Therefore, after the server collects all the data, it needs to filter the data in the data preprocessing stage, monitor bad data and remove it. Considering that the power system is a nonlinear system, we introduced the unscented Kalman filter algorithm as Core methods of data processing[10].

The unscented Kalman filter algorithm uses an approximation method, using probability density to approximate nonlinear functions[11]. Because the power system is nonlinear, its state equation and measurement equation are also nonlinear. Construct a sigma point set $\{\xi_i\}$ through the sampling plan, and calculate the weights W_i^m and W_i^c of the corresponding sigma points, which can be expressed by the following formula:

$$x_k = f\left(x_{k-1}\right) + q_{k-1} \tag{1}$$

$$y_k = h\left(x_k\right) + r_k \tag{2}$$

$$\overline{x} = \sum_{i=1}^{L} W_i^m \xi_i \tag{3}$$

$$P_x = \sum_{i=1}^{L} W_i^c \left(\xi_i - \overline{x}\right)\left(\xi_i - \overline{x}\right)^T \tag{4}$$

In the prediction step, based on the state quantity x_{k-1} and covariance P_{k-1} at time $k-1$, the Sigma point set $\{\xi_{i,k-1}\}$ is constructed according to the selected sampling plan to obtain the statistics at time k.

$$\overline{x}_{k|k-1} = \sum_{i=1}^{L} W_i^m \xi_{i,k|k-1} \tag{5}$$

$$P_{k|k-1} = \sum_{i=1}^{L} W_i^c [\xi_{i,k|k-1} - \tilde{x}_{k|k-1}][\xi_{i,k|k-1} - \tilde{x}_{k|k-1}]^T \tag{6}$$

$$\overline{y}_{k1k-1} = \sum_{i=1}^{L} W_i^m y_{i,k} \tag{7}$$

$$S_k = \sum_{i=0}^{2n} W_i^c (y_{i,k} - \overline{y}_{k|k-1})(y_{i,k} - \overline{y}_{k|k-1})^T \tag{8}$$

$$C_k = \sum_{i=0}^{2n} W_i^c (\xi_{i,k|k-1} - \overline{x}_{k|k-1})(y_{i,k} - \overline{y}_{k|})^T \tag{9}$$

In the update step, sensor measurements and observation models are used to revise the predicted state. By comparing the predicted state with the actual measurements, the Kalman gain K is calculated, which is used to adjust the predicted state estimate x_k and covariance estimate P_k.

$$K_k = C_k S_k^{-1} \tag{10}$$

$$x_k = K_k (y_k - \overline{y}_{k|k-1}) + \overline{x}_{k|k-1} \tag{11}$$

$$P_k = -K_k S_k K_k^T + P_{k|k-1} \tag{12}$$

By applying the above algorithms, combined with specific data from the power monitoring system, preprocessing, noise filtering and state estimation of power data can be achieved, thereby improving data processing capabilities and the accuracy of analysis results.

2.4. Monitoring software platform design

The Internet of Things application layer is the power system monitoring platform mainly designed in this article. The monitoring platform completes data transmission by accessing the database, and can realize functions such as real-time monitoring of electrical equipment, visual display, abnormal situation alarms, and fault data display.

For the sake of software platform security, a user login interface design is also required. The following will conduct specific interface design analysis and functional design analysis based on these functions to form a complete technical route. The schematic diagram of the software function design is shown in Figure 4.

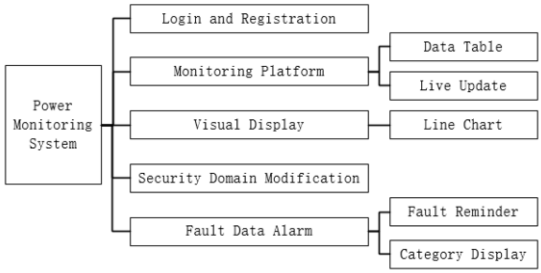

Figure 4. Monitoring software function design.

3. System hardware design

The hardware design of the power monitoring system will be introduced below focusing on the following two aspects. The first is to collect monitoring data from the sensor terminal, and the second is to complete data transmission based on the ModBus-RTU.

3.1. Sensors collect data

The construction of the IoT perception layer is achieved by collecting power and environmental data through sensors. The actual hardware connections are shown in Figure 5.

Figure 5. Sensor hardware connection.

The sensor used in this article uses RS485 communication interface and standard ModBus-RTU communication protocol. The sensor also has a protection function against incorrect operation, such as reverse power connection, to prevent equipment damage caused by reverse power connection.

3.2. Data transmission based on ModBus-RTU

In the standard ModBus-RTU communication using the RS485 communication interface[12], the host computer sends an inquiry frame first, and the slave machine processes and replies to the response frame after receiving the command, during which it is half-duplex communication. Therefore, there is a fixed query command for the sensor, and this query command is applied to the serial port software programming in the data transmission process to realize real-time data collection.

The sensor data transmission software designed in this article consists of three parts: serial port configuration, query command sending, and received data display. Through this software, you can send query frames to the sensor and receive response frames from the sensor. Finally, the received data is displayed on the interface, and the response frame is converted into actual data for display. The data transmission situation is shown in Figure 6.

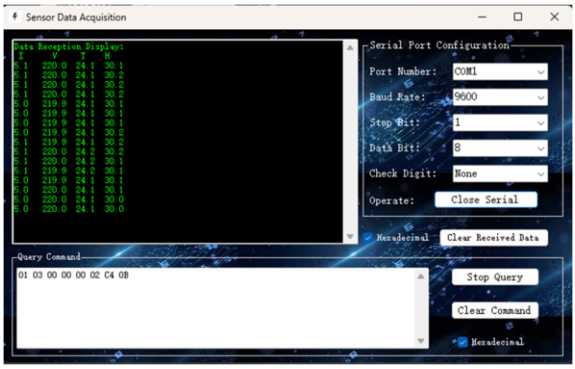

Figure 6. Sensor data transmission software.

In order to meet the needs of long-distance and large-scale data storage, the software will also classify and store the data into the data table of the SQL database while collecting and displaying the data. The data table contains various information involved in the monitoring system, realizes data integration, and forms a data network of the power system. The database serves as an intermediary for data transmission and realizes wireless transmission of data through WiFi.

4. Software monitoring platform design

Monitoring software platform design includes four aspects: function, interface, visualization and fault alarm design of the power monitoring system.

4.1. System function settings

The power monitoring system software platform mainly has four major functions: real-time monitoring, fault monitoring settings, visual display and fault alarm.

First, real-time monitoring is applied to the main interface and visual interface. The monitoring system uses tables and polylines to display data, and the data can be dynamically updated in real time. Real-time data update is the prerequisite for timely detection of power system faults.

Second, the monitoring system also provides users with a modifiable security domain, which can be adjusted independently according to the type of power equipment that the user needs to monitor to meet the application in multiple scenarios.

Third, Visual display is applied to the main interface and secondary monitoring interface. Equipment information is displayed on the interface in the form of charts, which facilitates users to intuitively discover problems and handle them in a timely manner.

Finally, fault alarm is implemented in the form of a pop-up window. When the data exceeds the safety threshold, such as overload, ambient temperature is too high, the software will pop up an alarm pop-up window to remind the user to inspect the electrical equipment to prevent major accidents.

4.2. System interface design

The interface design of the power monitoring system software platform is divided into two aspects, the login interface and the main interface.

In order to improve the security of the platform, login verification and registration functions are set up to satisfy security while enhancing practicality. User information is stored in the database, and user screening is implemented through data processing. The login registration interface is shown in Figure 7.

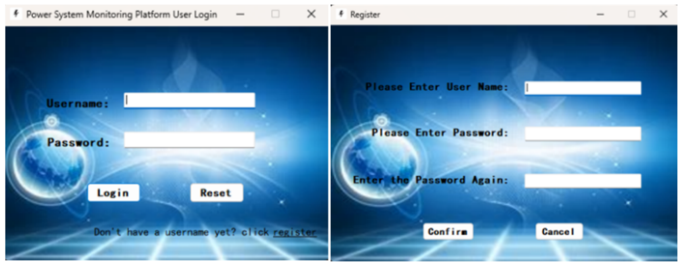

Figure 7. Login and registration interface.

The main interface displays all functions of the software platform. In order to satisfy the aesthetics, a menu bar and secondary interface are provided. The main interface is shown in Figure 8.

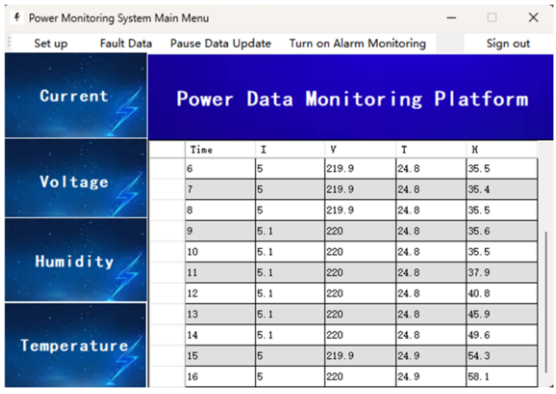

Figure 8. Main interface.

4.3. Visualization design

The secondary visualization interface uses line charts to visually display trends and changes in data. When there are outliers in the data, it helps observers quickly discover anomalies. The visual display interface is shown in Figure 9.

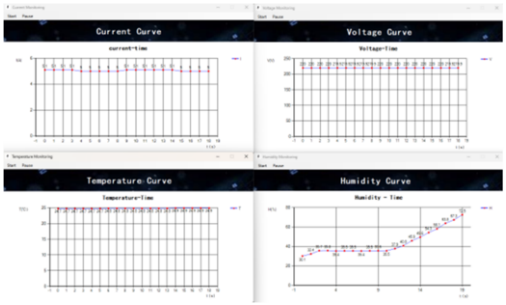

Figure 9. Visual display interface.

4.4. Alarm display design

The monitoring system provides alarm functions for abnormal situations, and sets alarm pop-up windows and fault data display interfaces. In order to meet more use places, fault monitoring settings have been added. The interface design is shown in Figure 10.

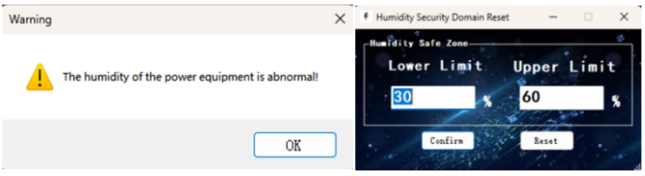

Figure 10. Alarm prompts and fault monitoring settings.

The fault data display interface is convenient for the user to enter this interface to view the fault data after receiving the alarm prompt. The fault data viewing interface design is shown in Figure 11.

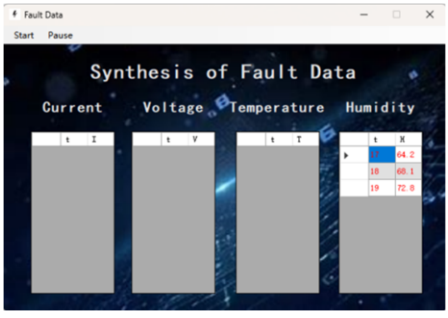

Figure 11. Fault data viewing interface.

5. Monitoring system function test

To verify its reliability and functional. Functional testing includes two aspects. The first is the real-time nature of power data display, which can show dynamic changes. On the other hand, software can filter out abnormal data and issue alerts for faulty data types.

5.1. Monitoring function test

After completing the connection of the hardware device, turn on the power of the sensor, open the software platform of the power monitoring system, and you can see the continuous update of the data on the main interface. The monitoring status of the software platform is shown in Figure 12.

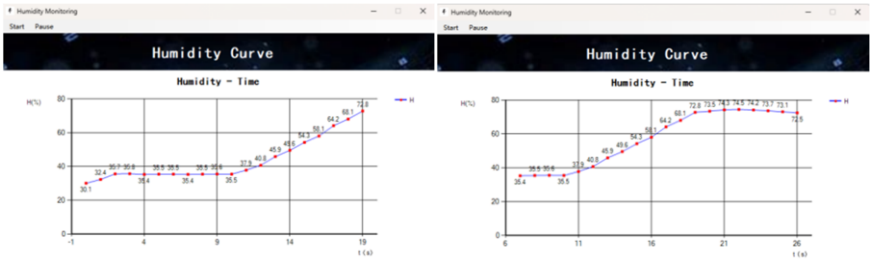

Figure 12. Data dynamic monitoring.

The pictures above are screenshots of the same interface at 19s and 26s respectively. It can be seen from the above pictures that the monitoring system can realize the visual display of real-time data. The specific changes in the data 14s-25s are shown in the table below:

Table 1. Specific changes in humidity data from 14s to 25s

	14	15	16	17	18	19	20	21	22	23	24	25
left	49.6	54.3	58.1	64.2	68.1	72.8	-	-	-	-	-	-
right	49.6	54.3	58.1	64.2	68.1	72.8	73.5	74.3	74.5	74.2	73.7	73.1

5.2. Fault alarm function test

Use changes in sensor data to detect whether the software platform is able to detect data that exceeds normal thresholds. Here we take humidity as an example to conduct alarm testing. By increasing the ambient humidity, the humidity of the sensor increases sharply and exceeds the safety threshold. The fault alarm and fault data display is shown in Figure 13.

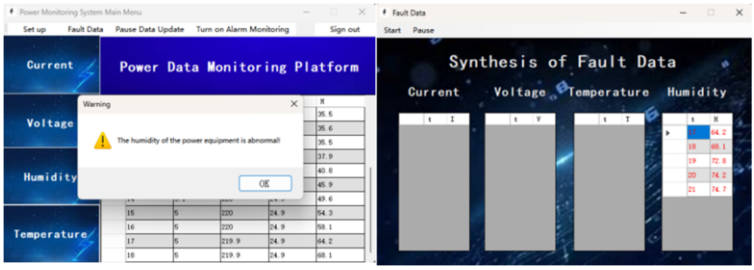

Figure 13. Fault alarm and fault data.

When ambient humidity poses hidden dangers to the operation of power equipment, the monitoring platform will alarm for humidity data and the fault data display interface will display abnormal humidity values. Monitoring this data effectively reduces the possibility of power short circuit due to high humidity and ensures the safe operation of power equipment.

By testing the power monitoring system software platform, real-time monitoring can be achieved, and alarm prompts for dangerous data can be realized, completing the expected goals of the software function.

6. Conclusion

This article designs a complete power monitoring system. Based on the ModBus-RTU communication protocol, the sensor data transmission design is completed, the database construction is completed based on SQL, and the data processing is implemented based on the unscented Kalman filter algorithm. The monitoring platform can realize real-time data monitoring, visual display, fault alarm and other functions to meet users' centralized monitoring of remote equipment. The system includes the interaction between hardware and software. Finally, the monitoring system is tested and verified as a whole. The monitoring platform can complete the expected functions.

The system integrates multiple key technologies into a complete solution. It can realize functions such as real-time data monitoring, visual display and fault alarm to meet users' centralized monitoring needs for remote equipment. It can be applied to power companies, operation and maintenance teams, safety and regulatory agencies and other departments to improve the stability and reliability of the power grid. Reduce the risk of power outages, provide better response and fault handling capabilities, and have a wide range of application scenarios.

References

[1] Yu L, Nazir B, Wang Y. Intelligent power monitoring of building equipment based on Internet of Things technology[J]. Computer Communications,2020,157.
[2] Lee T K, Mun K H. Real-time power monitoring using field-programmable gate array with IoT technology[J]. IET Science, Measurement & Technology,2019,13(6).
[3] Amandeep D, Rehana P. Application of UP IoT based power monitoring system[J]. Materials Today: Proceedings,2022,71(P2).
[4] Liang WW, Ma WL, Zhang LX, et al. Distributed communication power monitoring system based on big data technology[J]. Journal of Physics: Conference Series,2021,2087(1).
[5] Santos D, Ferreira C J. IoT Power Monitoring System for Smart Environments[J]. Sustainability,2019,11(19).
[6] Wu JW, Lin KM, Wu F, et al. Improved unscented Kalman filter based interval dynamic state estimation of active distribution network considering uncertainty of photovoltaic and load[J]. Frontiers in Energy Research,2023.
[7] Yu YJ, Li Q, Chen CC, et al. Improved dynamic state estimation of power system using unscented Kalman filter with more accurate prediction model[J]. Energy Reports,2022,8(S15).
[8] M. V, R. L, A. A. Real Time Vehicle Status Monitoring under Moving Conditions Using a Low Power IoT System[J]. 1 Institute of Communication and Computer Systems, Athens, Greece;2 AIMEN Centre Technologic, Pontevedra, Spain,2023,4(4).
[9] Gopal M, Maisagalla G, T P C, et al. IoT Based Solar Power Monitoring System[J]. IOP Conference Series: Materials Science and Engineering,2020,981(3).
[10] Zhang ZH, Zhang ZJ, Zhao S, et al. Robust adaptive Unscented Kalman Filter with gross error detection and identification for power system forecasting-aided state estimation[J]. Journal of the Franklin Institute,2023,360(13).
[11] Yu YJ, Li Q, Chen CC, et al. Improved dynamic state estimation of power system using unscented Kalman filter with more accurate prediction model[J]. Energy Reports,2022,8(S15).
[12] Peng H, Zheng Y, Lu G, et al. The Realization of Serial Communication Between King view 6.55 and MCU Based on Modbus-RTU Protocol[P]. Proceedings of the 2016 6th International Conference on Machinery, Materials, Environment, Biotechnology and Computer,2016.

Fuzzy Systems and Data Mining IX
A.J. Tallón-Ballesteros and R. Beltrán-Barba (Eds.)

doi:10.3233/FAIA231079

Heterogeneous Multi-Attribute Group Decision-Making Integrating Multi-Granulation Weighting Model and Improved VIKOR in Uncertain Linguistic Environment

Jifang PANG [a,1], Peng SONG [b], Baoli WANG [c], and Chao ZHANG [a]

[a] *Key Laboratory of Computational Intelligence and Chinese Information Processing of Ministry of Education, School of Computer and Information Technology, Shanxi University, Taiyuan 030006, Shanxi, China.*

[b] *School of Economics and Management, Shanxi University, Taiyuan 030006, Shanxi, China*

[c] *School of Mathematics and Information Technology, Yuncheng University, Yuncheng 044000, Shanxi, China*

Abstract. Heterogeneous multi-attribute group decision-making (HMAGDM) is a complex decision-making problem that widely exists in the real world. However, there is relatively little research on the HMAGDM problems when the attribute set and alternative set are both heterogeneous, and the existing studies still have some limitations, such as the weight calculation is too simple, lacking objectivity and comprehensiveness; the ranking methods does not consider the utility of both group and individuals simultaneously, lacking flxibility and practicality. In order to obtain more effective decision results, a HMAGDM method integrating multi-granulation weighting model and improved VIKOR in uncertain linguistic environment is proposed in this paper. Our contributions can be identified as follows: (1) On the basis of the uncertainty and closeness of uncertain linguistic terms (ULTs), a measure indicator for the effectiveness of experts' opinions is proposed, and a finest-granulation weight optimization model for experts is established by maximizing the effectiveness; (2) Based on comprehensive consideration of effectiveness and deviation, a bi-objective optimization model is proposed to obtain the multi-granulation weights of attributes; (3) An improved VIKOR method combining the boundedness of ULTs and the multi-granulation weights of attributes is proposed to obtain more stable and effective ranking results. Finally, the case study and comparative analysis illustrate the feasibility and characteristics of the proposed method.

Keywords. heterogeneous multi-attribute group decision-making, uncertain linguistic term, probabilistic uncertain linguistic term set, multi-granulation weight, improved VIKOR method

[1]Corresponding Author: Jifang Pang, School of Computer and Information Technology, Shanxi University, Taiyuan 030006, Shanxi, China; E-mail: purplepjf@sxu.edu.cn.

1. Introduction

Multi-attribute group decision-making (MAGDM) can be used to deal with many practical decision-making problems such as development of large project [1], urban waste recycling partner selection[2], photovoltaic power station evaluation [3] and so on. In the real decision-making environment, experts prefer to select some attributes they are familiar with and the alternatives belonging to their professional fields for evaluation. In addition, experts may use different types of evaluation information to express their opinions. This type of MAGDM problem with different types and/or structures of evaluation information is collectively referred to as heterogeneous MAGDM (HMAGDM). The existing research on HMAGDM can be classified into two frameworks: heterogeneous type of evaluation information [4,5,6] and heterogeneous sets of attributes and/or alternatives. The second framework can be subdivided into two cases: one is that only the attribute set is heterogeneous[7,8,9,10,11,12]; The other is that the attribute set and alternative set are both heterogeneous[13,14]. At present, research on HMAGDM with heterogeneous sets of attributes and alternatives is relatively insufficient. This is mainly because the decision space structure of such problems has characteristics of diversity and personalization, further increasing the difficulty of information aggregation and decision analysis. How to effectively aggregate such complex heterogeneous information and obtain reasonable and reliable decision results is one of the important challenges faced by current research.

In order to better solve the complex HMAGDM problems in uncertain linguistic environment, a HMAGDM method integrating multi-granulation weighting model and improved VIKOR will be proposed in this paper. The research motivation of this paper is summarized as follows:

(1) ULTs can well reflect the uncertainty in the decision process [15] and the HMAGDM problems in uncertain linguistic environment are widespread in the real world. However, there are relatively few related studies.

(2) In existing HMAGDM research, weights are mostly subjectively given by experts and lack objectivity [7,8,9,10]. Moreover, the objective weighting methods currently used are too simple[11,12,13,14], and the obtained weights lack comprehensiveness, which is not conducive to obtaining reasonable decision results.

(3) Most HMAGDM methods use weighted aggregation [7,10,11,12,13] or TOPSIS (Technique for Order Preference by Similarity to Ideal Solution) methods [8,9] to rank the alternatives. However, both of them do not consider the utility of group and individuals simultaneously and cannot well reflect the decision-maker's subjective preferences. Compared with them, VIKOR (VIsekriterijumska Optimizacija I Kompromisno Resenje) method is more flexible and practical, which can obtain a compromise solution finally accepted by experts [16,17]. However, the classical VIKOR method is prone to encounter reverse ranking situations when adding, deleting, or replacing an alternative [18], so it is necessary to develop an improved VIKOR method.

Our contributions can be mainly summarized in the following three aspects:

(1) On the basis of uncertainty and closeness of ULTs, an effectiveness measure is proposed, which provides theoretical support for further analyzing the effectiveness of decision results.

(2) Two multi-granulation weighting models with the goal of maximizing effectiveness measures are established for experts and attributes respectively, which can obtain more flexible and comprehensive weight and are more suitable for the aggregation of heterogeneous decision matrices.

(3) An improved VIKOR method combined with the boundedness of ULTs and the multi-granulation weights of attributes is proposed to effectively improve the stability and reliability of the ranking results.

The rest of the paper is organized as follows. Section 2 reviews some basic concepts. Section 3 provides an introduction to the HMAGDM method proposed in this paper. Section 4 demonstrates the feasibility of the method through a supplier selection case. Section 5 conducts experimental analysis from three aspects: sensitivity, stability, and effectiveness. Section 6 draws our conclusions and points out future research directions.

2. Preliminaries

Definition 1 *[19] Let $S = \{s_\alpha | \alpha = 0, 1, \cdots, l\}$ be a finite and totally ordered discrete linguistic term set, where l is an even value, s_α represents a linguistic term.*

Xu [20] extended S into the continuous set $\overline{S} = \{s_\alpha | \alpha \in [0, q]\}$, where $q(q \geq l)$ is a sufficiently large natural number. $I(s_\alpha)$ denote the term index of s_α in $\overline{S}$, i.e., $I(s_\alpha) = \alpha$.

Definition 2 *[20] Let $\tilde{s} = [s_L, s_R]$, where $s_L, s_R \in \overline{S}$, s_L and s_R are the lower and upper limits of $\tilde{s}$, respectively. We call $\tilde{s}$ the uncertain linguistic term (ULT).*

For two ULTs $\tilde{s}_1 = [s_{L_1}, s_{R_1}]$, $\tilde{s}_2 = [s_{L_2}, s_{R_2}]$, the operational laws are [20]: (1) $\tilde{s}_1 \oplus \tilde{s}_2 = [s_{L_1}, s_{R_1}] \oplus [s_{L_2}, s_{R_2}] = [s_{L_1+L_2}, s_{R_1+R_2}]$; (2) $\rho \tilde{s}_1 = \rho [s_{L_1}, s_{R_1}] = [s_{\rho L_1}, s_{\rho R_1}]$, $\rho \geq 0$.

Definition 3 *Let $\tilde{s}_1 = [s_{L_1}, s_{R_1}]$ and $\tilde{s}_2 = [s_{L_2}, s_{R_2}]$ be two ULTs, the Euclidean distance between $\tilde{s}_1$ and $\tilde{s}_2$ is given by* $d(\tilde{s}_1, \tilde{s}_2) = \dfrac{1}{l}\sqrt{\dfrac{1}{2}[(I(s_{L_1}) - I(s_{L_2}))^2 + (I(s_{R_1}) - I(s_{R_2}))^2]}$.

Xu [21] also proposed the uncertain linguistic weighted averaging (ULWA) operator.

Definition 4 *[21] The ULWA operator is defined as $ULWA_\lambda(\tilde{s}_1, \tilde{s}_2, \cdots, \tilde{s}_n) = \lambda_1 \tilde{s}_1 \oplus \lambda_2 \tilde{s}_2 \oplus \cdots \oplus \lambda_n \tilde{s}_n$, where $\lambda = (\lambda_1, \lambda_2, \cdots, \lambda_n)$ is the weighting vector of ULTs $\tilde{s}_j (j = 1, 2, \cdots, n)$, and $\lambda_j \in [0, 1]$, $\Sigma_{j=1}^n \lambda_j = 1$.*

Definition 5 *[22] A PULTS is defined as $S(p) = \{\langle \tilde{s}^k, p^k \rangle | p^k \geq 0, k = 1, 2, \cdots, |S(p)|, \sum_{k=1}^{|S(p)|} p^k \leq 1\}$, where $\tilde{s}^k = [s_L^k, s_R^k]$ is an ULT, s_L^k and $s_R^k (s_L^k, s_R^k \in S, s_L^k \leq s_R^k)$ are the lower and upper limits of $\tilde{s}^k$, respectively. $|S(p)|$ is the cardinality of $S(p)$, and p^k is the probability of $\tilde{s}^k$.*

PULTS is an effective tool to depict uncertain linguistic opinions [23], which provides a new means of modeling ULTs by computing their occurrence probabilities.

3. HMAGDM method integrating multi-granulation weighting model and improved VIKOR in uncertain linguistic environment

3.1. Problem description

For a HMAGDM problem in uncertain linguistic environment, let $X = \{x_1, x_2, \cdots, x_m\}$ be an alternative set, $A = \{a_1, a_2, \cdots, a_n\}$ be an attribute set, $E = \{e_1, e_2, \cdots, e_f\}$ be an

expert set, $S=\{s_\alpha|\alpha=0,1,\cdots,l\}$ be a linguistic term set. $X^h=\{x_i^h|x_i^h\in X\}$ represents a subset of the alternatives selected by e_h, $A^h=\{a_j^h|a_j^h\in A\}$ represents a subset of the attributes selected by e_h. The decision matrix of e_h can be expressed as $R^h=[\tilde{s}_{ij}^h]_{|X^h|\cdot|A^h|}$, where $|X^h|$ is the number of alternatives in X^h, $|A^h|$ is the number of attributes in A^h, $\tilde{s}_{ij}^h=[s_{ijL}^h,s_{ijR}^h]$ represents the evaluation value of x_i under a_j given by e_h.

Let $E_{ij}=\{e_h|\tilde{s}_{ij}^h\neq\emptyset,e_h\in E\}$ represent the set of experts who evaluate x_i under a_j. The number of experts in E_{ij} is denoted as $|E_{ij}|$. The set of evaluation value given by the experts in E_{ij} is denoted as $V_{ij}=\{\tilde{s}_{ij}^h|e_h\in E_{ij}\}=\{[s_{ijL}^h,s_{ijR}^h]|e_h\in E_{ij}\}$

In order to ensure the objectivity and comprehensiveness of decision results, a HMAGDM method needs to meet the following conditions:(1) $X^1\cup X^2\cup\cdots\cup X^f=X$; (2) $A^1\cup A^2\cup\cdots\cup A^f=A$; (3) $|E_{ij}|\geq 3(i=1,2,\cdots,m,j=1,2,\cdots,n)$.

3.2. Multi-granulation weighting model for experts

In this subsection, the ULT evaluation values provided by different experts are first aggregated into PULTS. Then, the finest-granulation weights of experts are calculated from the perspectives of uncertainty and closeness. Finally, a bi-objective optimization model is established to fuse the two kinds of weights together.

First, by counting the number of occurrences of each $\tilde{s}_{ij}^h$ in $V_{ij}=\{\tilde{s}_{ij}^h|e_h\in E_{ij}\}$, the set V_{ij} can be transformed into a PULTS $S_{ij}(p)$, that is,

$$S_{ij}(p)=\{\langle\tilde{s}_{ij}^k,p_{ij}^k\rangle|p_{ij}^k=\frac{\#\tilde{s}_{ij}^k}{|V_{ij}|},\tilde{s}_{ij}^k\in V_{ij},k=1,2,\cdots,|S_{ij}(p)|,\sum_{k=1}^{|S_{ij}(p)|}p^k=1\} \quad (1)$$

where $\tilde{s}_{ij}^k=[s_{ijL}^k,s_{ijR}^k]$, $\#\tilde{s}_{ij}^k$ represents the number of occurrences of each $\tilde{s}_{ij}^k$ in V_{ij}, $|V_{ij}|$ represents the cardinality of V_{ij}, $|S_{ij}(p)|$ is the cardinality of $S_{ij}(p)$.

Then, calculate the multi-granulation weights of experts.

(1) The expert weight based on uncertainty degree

Step 1. Calculate he uncertainty degree $UND(\tilde{s}_{ij}^h)$ of expert e_h as follows

$$UND(\tilde{s}_{ij}^h)=\frac{I(s_{ijR}^h)-I(s_{ijL}^h)}{l} \quad (2)$$

Step 2. Calculate the uncertainty degree $UND(S_{ij}(p))$ of subgroup E_{ij} as follows

$$UND(S_{ij}(p))=\sum_{k=1}^{|S_{ij}(p)|}p_{ij}^kUND(\tilde{s}_{ij}^k) \quad (3)$$

Step 3. Calculate the weight ω_{ijh}^u of expert e_h in E_{ij} based on uncertainty degree

$$\omega_{ijh}^u=\frac{1-UND(\tilde{s}_{ij}^h)}{|E_{ij}|\times(1-UND(S_{ij}(p)))} \quad (4)$$

(2) The expert weight based on closeness degree

Step 1. Calculate the closeness degree $CLD(\tilde{s}_{ij}^h,S_{ij}(p))$ between expert e_h and the subgroup E_{ij} as follows

$$CLD(\tilde{s}_{ij}^h, S_{ij}(p)) = \sum_{k=1}^{|S_{ij}(p)|} p_{ij}^k (1 - d(\tilde{s}_{ij}^h, \tilde{s}_{ij}^k)) \tag{5}$$

Step 2. Calculate the weight ω_{ijh}^c of expert e_h in E_{ij} based on closeness degree

$$\omega_{ijh}^c = \frac{CLD(\tilde{s}_{ij}^h, S_{ij}(p))}{\sum_{e_h \in E_{ij}} CLD(\tilde{s}_{ij}^h, S_{ij}(p))} \tag{6}$$

(3) Expert weight optimization model

Let ω_{ijh} be the multi-granulation weight of e_h under a_j w.r.t x_i. Then the weighted overall uncertainty of E_{ij} under a_j w.r.t x_i is $UND_{ij} = \sum_{e_h \in E_{ij}} \omega_{ijh} UND(\tilde{s}_{ij}^h)$. Using ULWA operator and ω_{ijh}, the weighted overall evaluation value of E_{ij} can be obtained and denoted by $\tilde{s}_{ij}$. Then the consensus degree of E_{ij} can be expressed as $COD_{ij} = \sum_{e_h \in E_{ij}} \omega_{ijh}(1 - d(\tilde{s}_{ij}^h, \tilde{s}_{ij}))$. The effectiveness degree of subgroup E_{ij}'s opinions can be expressed as $EFD_{ij} = COD_{ij} - UND_{ij}$. By solving the following model (M-1) with the goal of maximizing EFD_{ij}, the weight ω_{ijh} of expert can be obtained.

$$\max EFD_{ij} = COD_{ij} - UND_{ij} = \sum_{e_h \in E_{ij}} \omega_{ijh}(1 - d(\tilde{s}_{ij}^h, \tilde{s}_{ij})) - \sum_{e_h \in E_{ij}} \omega_{ijh} UND(\tilde{s}_{ij}^h)$$

$$\text{s.t.} \begin{cases} \omega_{ijh} \geq \min\{\omega_{ijh}^u, \omega_{ijh}^c\}, e_h \in E_{ij} \\ \sum_{e_h \in E_{ij}} \omega_{ijh} = 1 \end{cases} \tag{M-1}$$

3.3. Multi-granulation weighting model for attributes

Through the above calculation, the effectiveness under each attribute can be expressed as $EFD_j = \frac{1}{m}\sum_{i=1}^m EFD_{ij}$. Let v_j be the final weight of attribute, the total effectiveness of group opinions can be expressed as $EFD = \sum_{j=1}^n v_j EFD_j$. Next, we will give an objective comprehensive weighting method for attributes.

(1) The attribute weight based on effectiveness degree

The weight v_{ij}^r of a_j based on effectiveness under x_i can be calculated as follows:

$$v_{ij}^r = \frac{EFD_{ij}}{\sum_{j=1}^n EFD_{ij}} \tag{7}$$

(2) The attribute weight based on maximizing deviation

By using the weights of experts and ULWA operator, the individual decision matrices of experts can be aggregated into the group decision matrix $\tilde{R} = [\tilde{s}_{ij}]_{m \times n}$, where $\tilde{s}_{ij} = [s_{ijL}, s_{ijR}]$ represents the overall evaluation value of the subgroup under a_j w.r.t x_i.

The weight v_j^d of a_j based on maximizing deviation can be calculated as follows[24]:

$$v_j^d = \frac{\sum_{i=1}^m \sum_{t=1}^m d(\tilde{s}_{ij}, \tilde{s}_{tj})}{\sum_{j=1}^n \sum_{i=1}^m \sum_{t=1}^m d(\tilde{s}_{ij}, \tilde{s}_{tj})} \tag{8}$$

(3)Attribute weight optimization model

Let v_j denote the synthetic weight of attribute and $DEV_j = \sum_{i=1}^{m}\sum_{t=1}^{m} d(\tilde{s}_{ij}, \tilde{s}_{tj})$ represent the deviation under a_j. Then, the total deviation under all attributes can be expressed as $DEV = \sum_{j=1}^{n} v_j DEV_j$. Combined with the total effectiveness $EFD = \sum_{j=1}^{n} v_j EFD_j$, a bi-objective optimization model (M-2) with the goal of maximizing both EFD and DEV can be established to fuse the above two kinds of attribute weights.

$$\max EFD * DEV = \left(\sum_{j=1}^{n} v_j EFD_j\right) * \left(\sum_{j=1}^{n} v_j DEV_j\right)$$

$$\text{s.t.} \begin{cases} v_{ij} = \dfrac{v_{ij}^r v_j^d}{\sum_{j=1}^{n} v_{ij}^r v_j^d}, i = 1,2,\cdots,m, j = 1,2,\cdots,n \\ \min\{\min\limits_i v_{ij}^r, v_j^d, \min\limits_i v_{ij}\} \le v_j \le \max\{\max\limits_i v_{ij}^r, v_j^d, \max\limits_i v_{ij}\}, j = 1,2,\cdots,n \\ \sum\limits_{j=1}^{n} v_j = 1 \end{cases} \tag{M-2}$$

3.4. The improved VIKOR method

In order to effectively improve the stability of the ranking results, an improved VIKOR method is proposed in this subsection, which replaces the maximum and minimum values in the current alternative set with the upper and lower limits of the linguistic term set as PIS and NIS, and uses the multi-granulation weights of attributes to calculate the group utility and individual regret respectively. The specific ranking method is as follows:

Step 1. Let $\tilde{s}^+ = [s_l, s_l]$ be the PIS and $\tilde{s}^- = [s_0, s_0]$ be the NIS under all attributes.

Step 2. Calculate the group utility value $S_i = \sum_{j=1}^{n} v_j d(\tilde{s}^+, \tilde{s}_{ij})$ and individual regret value $R_i = \max_j\{v_j d(\tilde{s}^+, \tilde{s}_{ij})\}$ of alternative x_i $(i = 1,2,\cdots,m)$.

Step 3. Calculate the overall evaluation value Q_i of alternative $x_i (i = 1,2,\cdots,m)$

$$Q_i = \mu \frac{S_i - S^-}{S^+ - S^-} + (1-\mu)\frac{R_i - R^-}{R^+ - R^-} \tag{9}$$

where $S^+ = \max\limits_i S_i$, $S^- = \min\limits_i S_i$, $R^+ = \max\limits_i R_i$, $R^- = \min\limits_i R_i$. $\mu \in [0,1]$ is the compromise coefficient.

Step 4. Arrange the alternatives in ascending order according to the values of S_i, R_i and Q_i, respectively. Suppose the ranking result obtained from Q_i is $x^{(1)}, x^{(2)}, \cdots, x^{(m)}$, the determination process of the optimal alternative is as follows:

If $x^{(1)}$ satisfies condition 1: $Q(x^{(2)}) - Q(x^{(1)}) \ge \dfrac{1}{m-1}$, and condition 2: $x^{(1)}$ is still the optimal alternative according to the ascending order of S_i or R_i. Then $x^{(1)}$ is a stable optimal alternative in the decision process.

If the above two conditions cannot be met at the same time, the compromise solution can be generated according to the following two situations: if condition 2 is not met, $x^{(1)}$ and $x^{(2)}$ are both compromise solutions; If condition 1 is not met, the compromise solution set is $X = \{x^{(1)}, x^{(2)}, \cdots, x^{(J)}\}$, where J is the maximum positive integer calculated by $Q(x^{(J)}) - Q(x^{(1)}) < \dfrac{1}{m-1}$.

4. An illustrative example

The following takes an e-commerce enterprise as an example to illustrate the feasibility of the method. $X = \{x_1, x_2, \cdots, x_6\}$ are six candidate suppliers, and the corresponding evaluation indices are $A = \{a_1, a_2, \cdots, a_5\}$, where a_1–service quality, a_2–logistics cost, a_3–enterprise capability, a_4–informatization degree, a_5–enterprise development prospect. Five experts are $E = \{e_1, e_2, \cdots, e_5\}$. The linguistic term set adopted by the experts is $S = \{s_0 =$ extremely poor, $s_1 =$ very poor, $s_2 =$ poor, $s_3 =$ slightly poor, $s_4 =$ fair, $s_5 =$ slightly good, $s_6 =$ good, $s_7 =$ very good, $s_8 =$ extrimly good$\}$. The decision matrices $R^h (h = 1, 2, \cdots, 5)$ provided by the experts are shown in Tables 1-3.

Table 1. The decision matrix R^1 provided by e_1

X^1	A^1				
	a_1	a_2	a_3	a_4	a_5
x_1	$[s_7, s_7]$	$[s_6, s_7]$	$[s_6, s_7]$	$[s_4, s_4]$	$[s_6, s_7]$
x_2	$[s_5, s_8]$	$[s_7, s_7]$	$[s_3, s_3]$	$[s_4, s_5]$	$[s_2, s_5]$
x_5	$[s_6, s_8]$	$[s_4, s_5]$	$[s_4, s_6]$	$[s_5, s_5]$	$[s_6, s_7]$
x_6	$[s_0, s_3]$	$[s_5, s_7]$	$[s_5, s_6]$	$[s_4, s_6]$	$[s_6, s_8]$

Table 2. The decision matrices provided by e_2 and e_3

	X^2	A^2					X^3	A^3			
		a_2	a_3	a_4	a_5			a_1	a_2	a_4	a_5
e_2	x_2	$[s_5, s_6]$	$[s_4, s_6]$	$[s_6, s_6]$	$[s_2, s_5]$	e_3	x_1	$[s_5, s_8]$	$[s_7, s_8]$	$[s_3, s_4]$	$[s_5, s_5]$
	x_3	$[s_5, s_6]$	$[s_3, s_5]$	$[s_4, s_5]$	$[s_3, s_5]$		x_2	$[s_5, s_8]$	$[s_7, s_8]$	$[s_6, s_6]$	$[s_2, s_5]$
	x_4	$[s_5, s_6]$	$[s_5, s_7]$	$[s_4, s_4]$	$[s_4, s_5]$		x_3	$[s_1, s_3]$	$[s_6, s_6]$	$[s_5, s_5]$	$[s_4, s_6]$
	x_5	$[s_4, s_5]$	$[s_5, s_5]$	$[s_4, s_4]$	$[s_6, s_6]$		x_4	$[s_1, s_4]$	$[s_5, s_8]$	$[s_4, s_5]$	$[s_5, s_5]$
	x_6	$[s_4, s_5]$	$[s_4, s_6]$	$[s_5, s_5]$	$[s_5, s_7]$		x_5	$[s_4, s_7]$	$[s_5, s_5]$	$[s_4, s_6]$	$[s_3, s_5]$

Table 3. The decision matrices provided by e_4 and e_5

	X^4	A^4				X^5	A^5			
		a_1	a_3	a_4			a_1	a_2	a_3	a_5
e_4	x_1	$[s_3, s_6]$	$[s_6, s_8]$	$[s_4, s_5]$	e_5	x_1	$[s_7, s_7]$	$[s_7, s_8]$	$[s_8, s_8]$	$[s_5, s_8]$
	x_2	$[s_3, s_5]$	$[s_3, s_5]$	$[s_4, s_5]$		x_3	$[s_4, s_7]$	$[s_5, s_7]$	$[s_4, s_5]$	$[s_4, s_5]$
	x_3	$[s_1, s_3]$	$[s_4, s_5]$	$[s_3, s_4]$		x_4	$[s_1, s_4]$	$[s_5, s_6]$	$[s_5, s_7]$	$[s_4, s_7]$
	x_4	$[s_1, s_4]$	$[s_5, s_5]$	$[s_4, s_5]$		x_5	$[s_3, s_3]$	$[s_3, s_6]$	$[s_2, s_5]$	$[s_2, s_5]$
	x_6	$[s_1, s_4]$	$[s_1, s_3]$	$[s_4, s_5]$		x_6	$[s_5, s_7]$	$[s_4, s_5]$	$[s_5, s_5]$	$[s_3, s_6]$

The specific supplier selection process is as follows:

Step 1. By using Eq.(1), the group PULTS matrix are obtained.

Step 2. By using Eqs.(2)-(4), the weights ω^{μ}_{ijh} of $e_h \in E_{ij}$ are obtained; By using Eqs.(5) and (6), the weights ω^{c}_{ijh} of $e_h \in E_{ij}$ are obtained. By solving model (M-1), the weights ω_{ijh} of $e_h \in E_{ij}$ are obtained.

Step 3. By using Eqs.(7), the weights v_{ij}^r of attributes under each alternative based on effectiveness are obtained.

Step 4. By using the weights of experts ω_{ijh} and ULWA operator, the group ULT decision matrix $\tilde{R}$ are obtained and shown in Table 4.

Table 4. Group ULT decision matrix $\tilde{R}$

X	A				
	a_1	a_2	a_3	a_4	a_5
x_1	$[s_{5.848}, s_7]$	$[s_{6.676}, s_{7.676}]$	$[s_6, s_{7.3}]$	$[s_{3.682}, s_{4.318}]$	$[s_{5.342}, s_{6.434}]$
x_2	$[s_{4.388}, s_{7.082}]$	$[s_{6.364}, s_7]$	$[s_{3.3}, s_{4.5}]$	$[s_{5.068}, s_{5.534}]$	$[s_2, s_5]$
x_3	$[s_{1.88}, s_{4.175}]$	$[s_{5.385}, s_{6.286}]$	$[s_{4.898}, s_{5.888}]$	$[s_{4.046}, s_{4.682}]$	$[s_{3.684}, s_{5.316}]$
x_4	$[s_1, s_4]$	$[s_5, s_{6.526}]$	$[s_5, s_{6.2}]$	$[s_4, s_{4.636}]$	$[s_{4.411}, s_{5.5}]$
x_5	$[s_{4.211}, s_{5.632}]$	$[s_{4.116}, s_{5.185}]$	$[s_{3.808}, s_{5.403}]$	$[s_{4.396}, s_{4.942}]$	$[s_{4.539}, s_{5.824}]$
x_6	$[s_{1.872}, s_{4.576}]$	$[s_{4.3}, s_{5.6}]$	$[s_{3.918}, s_{5.051}]$	$[s_{4.381}, s_{5.286}]$	$[s_{4.743}, s_{7.037}]$

Step 5. By using Eq.(8), the weights v_j^d of each attribute based on maximizing deviation in $\tilde{R}$ are obtained, $v_1^d = 0.326$, $v_2^d = 0.196$, $v_3^d = 0.193$, $v_4^d = 0.091$, $v_5^d = 0.195$.

Step 6. By solving model (M-2), the synthetic weights v_j of attributes are obtained, $v_1 = 0.324$, $v_2 = 0.269$, $v_3 = 0.155$, $v_4 = 0.091$, $v_5 = 0.161$.

Step 7. Let $\mu = 0.5$, $\tilde{s}^+ = [s_8, s_8]$ and $\tilde{s}^- = [s_0, s_0]$. By using the improved VIKOR method, the values of S_i, R_i and Q_i are obtained (see Table 5). The ranking result obtained from Q_i is $x_1 \succ x_2 \succ x_5 \succ x_3 \succ x_6 \succ x_4$ and the optimal solution is x_1.

Table 5. The values and rankings of the alternatives

X	Values			Rankings		
	S_i	R_i	Q_i	S_i	R_i	Q_i
x_1	0.219	0.068	0	1	1	1
x_2	0.359	0.107	0.406	2	2	2
x_3	0.446	0.207	0.892	4	5	4
x_4	0.463	0.231	1	6	6	6
x_5	0.406	0.128	0.568	3	3	3
x_6	0.460	0.201	0.902	5	4	5

5. Comparative analysis

5.1. Sensitivity analysis

The overall evaluation values $Q_i (1 \leq i \leq 6)$ and ranking results corresponding to different compromise coefficient μ are shown in Table 6.

It can be seen from Table 6 that different μ will result in different ranking results. However, no matter what value μ takes, the optimal alternative is always x_1 and the order of the first three alternatives has not changed. If weighted aggregation or TOPSIS is used instead of the improved VIKOR method, only one ranking result can be obtained, i.e., $x_1 \succ x_2 \succ x_5 \succ x_3 \succ x_6 \succ x_4$. By contrast, the improved VIKOR method is more flexible and practical.

Table 6. The decision results under different compromise coefficient μ

μ	Q_1	Q_2	Q_3	Q_4	Q_5	Q_6	Ranking results	Optimal alternative
0	0	0.238	0.851	1	0.368	0.817	$x_1 \succ x_2 \succ x_5 \succ x_6 \succ x_3 \succ x_4$	x_1
0.1	0	0.272	0.860	1	0.408	0.834	$x_1 \succ x_2 \succ x_5 \succ x_6 \succ x_3 \succ x_4$	x_1
0.2	0	0.305	0.868	1	0.448	0.851	$x_1 \succ x_2 \succ x_5 \succ x_6 \succ x_3 \succ x_4$	x_1
0.3	0	0.339	0.876	1	0.488	0.868	$x_1 \succ x_2 \succ x_5 \succ x_6 \succ x_3 \succ x_4$	x_1
0.4	0	0.373	0.884	1	0.528	0.885	$x_1 \succ x_2 \succ x_5 \succ x_3 \succ x_6 \succ x_4$	x_1
0.5	0	0.406	0.892	1	0.568	0.902	$x_1 \succ x_2 \succ x_5 \succ x_3 \succ x_6 \succ x_4$	x_1
0.6	0	0.440	0.900	1	0.607	0.919	$x_1 \succ x_2 \succ x_5 \succ x_3 \succ x_6 \succ x_4$	x_1
0.7	0	0.473	0.909	1	0.647	0.936	$x_1 \succ x_2 \succ x_5 \succ x_3 \succ x_6 \succ x_4$	x_1
0.8	0	0.507	0.917	1	0.687	0.954	$x_1 \succ x_2 \succ x_5 \succ x_3 \succ x_6 \succ x_4$	x_1
0.9	0	0.541	0.925	1	0.727	0.971	$x_1 \succ x_2 \succ x_5 \succ x_3 \succ x_6 \succ x_4$	x_1
1.0	0	0.574	0.933	1	0.767	0.988	$x_1 \succ x_2 \succ x_5 \succ x_3 \succ x_6 \succ x_4$	x_1

5.2. Stability analysis

In this subsection, the stability of the proposed method will be verified through ablation experiments. Table 7 lists the differences between the improved VIKOR method (I-VIKOR) and three comparison methods M-VIKOR, D-VIKOR and MD-VIKOR.

Table 7. The improved VIKOR method and three comparison methods

Methods	PIS	NIS	Attribute weights
I-VIKOR (ours)	$[s_l, s_l]$	$[s_0, s_0]$	multi-granulation weight
M-VIKOR	$[\max_i s_{ijL}, \max_i s_{ijR}]$	$[\min_i s_{ijL}, \min_i s_{ijR}]$	multi-granulation weight
D-VIKOR	$[s_l, s_l]$	$[s_0, s_0]$	single-granulation weight based on maximizing deviation
MD-VIKOR	$[\max_i s_{ijL}, \max_i s_{ijR}]$	$[\min_i s_{ijL}, \min_i s_{ijR}]$	single-granulation weight based on maximizing deviation

Tables 8 show the ranking results of the four methods mentioned above. It can be seen that the stability of the proposed I-VIKOR is the best, while the stability of MD-VIKOR is the worst.

Table 8. Ranking results of four methods before and after deleting x_1

Methods	Before deleting x_1	After deleting x_1
I-VIKOR	$x_1 \succ x_2 \succ x_5 \succ x_6 \succ x_3 \succ x_4$ $(0 \le \mu \le 0.3)$ $x_1 \succ x_2 \succ x_5 \succ x_3 \succ x_6 \succ x_4$ $(0.4 \le \mu \le 1)$	$x_2 \succ x_5 \succ x_6 \succ x_3 \succ x_4$ $(0 \le \mu \le 0.4)$ $x_2 \succ x_5 \succ x_3 \succ x_6 \succ x_4$ $(0.5 \le \mu \le 1)$
M-VIKOR	$x_1 \succ x_2 \succ x_6 \succ x_5 \succ x_3 \succ x_4$ $(\mu \le 0.1)$ $x_1 \succ x_2 \succ x_5 \succ x_6 \succ x_3 \succ x_4$ $(0.2 \le \mu \le 0.5)$ $x_1 \succ x_2 \succ x_5 \succ x_3 \succ x_6 \succ x_4$ $(0.6 \le \mu \le 0.9)$ $x_1 \succ x_2 \succ x_5 \succ x_3 \succ x_4 \succ x_6$ $(\mu = 1)$	$x_2 \succ x_5 \succ x_6 \succ x_3 \succ x_4$ $(0 \le \mu \le 0.6)$ $x_2 \succ x_5 \succ x_3 \succ x_6 \succ x_4$ $(0.7 \le \mu \le 1)$
D-VIKOR	$x_1 \succ x_2 \succ x_5 \succ x_6 \succ x_3 \succ x_4$ $(0 \le \mu \le 0.6)$ $x_1 \succ x_2 \succ x_5 \succ x_3 \succ x_6 \succ x_4$ $(0.7 \le \mu \le 1)$	$x_5 \succ x_2 \succ x_6 \succ x_3 \succ x_4$ $(0 \le \mu \le 0.2)$ $x_2 \succ x_5 \succ x_6 \succ x_3 \succ x_4$ $(0.3 \le \mu \le 1)$
MD-VIKOR	$x_1 \succ x_2 \succ x_5 \succ x_6 \succ x_3 \succ x_4$ $(0 \le \mu \le 0.9)$ $x_1 \succ x_2 \succ x_5 \succ x_3 \succ x_6 \succ x_4$ $(\mu = 1)$	$x_5 \succ x_2 \succ x_6 \succ x_3 \succ x_4$ $(0 \le \mu \le 0.4)$ $x_2 \succ x_5 \succ x_6 \succ x_3 \succ x_4$ $(0.5 \le \mu \le 1)$

5.3. Effectiveness analysis

In this subsection, the advantages of the multi-granulation weighting model for expert will be explained through comparative analysis of effectiveness. The proposed HMAGDM method is called M-HMAGDM. The other three comparison methods are U-HMAGDM using the uncertainty based expert weight ω_{ijh}^{u}, C-HMAGDM using the closeness based expert weight ω_{ijh}^{c}, and E-HMAGDM with equal expert weight. The difference between them is only reflected in the calculation method of expert weights. Table 9 lists the effectiveness and ranking results corresponding to the above four methods.

Table 9. Comparison of effectiveness and ranking results of four HMAGDM methods

Mehtods	EFD_1	EFD_2	EFD_3	EFD_4	EFD_5	EFD	Ranking results
M-HMAGDM (ours)	0.576	0.78	0.686	0.822	0.662	0.684	$x_1 \succ x_2 \succ x_5 \succ x_6 \succ x_3 \succ x_4$ $(0 \le \mu \le 0.3)$ $x_1 \succ x_2 \succ x_5 \succ x_3 \succ x_6 \succ x_4$ $(0.4 \le \mu \le 1)$
U-HMAGDM	0.572	0.78	0.686	0.822	0.66	0.683	$x_1 \succ x_2 \succ x_5 \succ x_6 \succ x_3 \succ x_4$ $(0 \le \mu \le 0.7)$ $x_1 \succ x_2 \succ x_5 \succ x_3 \succ x_6 \succ x_4$ $(0.8 \le \mu \le 1)$
C-HMAGDM	0.566	0.764	0.681	0.812	0.637	0.671	$x_1 \succ x_2 \succ x_5 \succ x_6 \succ x_3 \succ x_4$ $(0 \le \mu \le 0.3)$ $x_1 \succ x_2 \succ x_5 \succ x_3 \succ x_6 \succ x_4$ $(0.4 \le \mu \le 1)$
E-HMAGDM	0.559	0.705	0.679	0.811	0.633	0.644	$x_1 \succ x_5 \succ x_2 \succ x_6 \succ x_3 \succ x_4$ $(0 \le \mu \le 0.6)$ $x_1 \succ x_5 \succ x_2 \succ x_3 \succ x_6 \succ x_4$ $(0.7 \le \mu \le 1)$

From Table 9, it can be seen that the proposed method M-HMAGDM has the best performance, while E-HMAGDM has the lowest performance. The other two methods are between M-HMAGDM and E-HMAGDM.

6. Conclusions

The proposed HMAGDM method can effectively overcome the limitations of existing methods in weight setting, information aggregation and alternative ranking, and obtain more reasonable and high-quality decision results. The advantages of the proposed method are demonstrated through comparative analysis of sensitivity, stability, and effectiveness. However, this study is limited to uncertain linguistic environment and cannot be directly used to handle the HMAGDM problems with different forms and granulations of fuzzy linguistic preference information in the open dynamic environment. In the future, we will closely connect with practical decision-making problems and combine factors such as trust relationships, self-confidence, attribute priority, and alternative grade to study consensus analysis models and decision feedback mechanisms for complex HMAGDM problems in different linguistic environments. On this basis, explore more flexible and reliable group decision-making methods to provide decision-makers with more scientific and practical decision support.

Acknowledgements

This work was supported by the National Natural Science Foundation of China [No. 62006148, 72171137, 62272284], the Open Project Foundation of Intelligent Information Processing Key Laboratory of Shanxi Province [No. CICIP2022002] and the 1331 Engineering Project of Shanxi Province, China.

References

[1] Pang K, Martínez L, Li N, Liu J, Zou L, Lu MY. A concept lattice-based expert opinion aggregation method for multi-attribute group decision-making with linguistic information. Expert Systems With Applications. 2024 Mar; 237: 121458.

[2] Haseli G, Torkayesh AE, Hajiaghaei-Keshteli M, Venghaus S. Sustainable resilient recycling partner selection for urban waste management: Consolidating perspectives of decision-makers and experts. Applied Soft Computing. 2023 Apr; 137: 110120.

[3] Zhu JX, Ma XL, Kou G, Herrera-Viedma E, Zhan JM. A three-way consensus model with regret theory under the framework of probabilistic linguistic term sets. Information Fusion. 2023 Jul; 95: 250-274.

[4] Li WW, Yi PT, Li LY. Superiority-comparison-based transformation, consensus, and ranking methods for heterogeneous multi-attribute group decision-making. Expert Systems With Applications. 2023 Mar; 213: 119018.

[5] Zhao CW, Xu XH, Liu RH, He JS. A novel multi-attribute group decision-making method for heterogeneous preferences and attribute interaction contexts. Expert Systems With Applications. 2023 Jul; 221: 119752.

[6] Zheng J, Wang YM, Zhang K, Gao JQ, Yang LH. A heterogeneous multi-attribute case retrieval method for emergency decision making based on bidirctional projection and TODIM. Expert Systems With Application. 2022 Oct; 203: 117382.

[7] Morente-Molinera JA, Wu X, Morfeq A, Al-Hmouz R, Herrera-Viedma E. A novel multi-criteria group decision-making method for heterogeneous and dynamic contexts using multi-granular fuzzy linguistic modelling and consensus measures. Information Fusion. 2020 Jan; 53: 240-250.

[8] Lourenzutti R, Krohling RA. A generalized TOPSIS method for group decision making with heterogeneous information in a dynamic environment. Information Sciences. 2016 Feb; 330: 1-18.

[9] Gao Y, Li DS. A consensus model for heterogeneous multi-attribute group decision making with several attribute sets. Expert Systems With Application. 2019 Jul; 125: 69-80.

[10] Liu X, Xu YJ, Gong ZW, Herrera F. Democratic consensys reaching process for multi-person multi-criteria large scale decision making considering participants' individual attributes and concerns. Information Fusion. 2022 Jan; 77: 220-232.

[11] Ye J, Sun BZ, Chu XL, Zhan JM, Cai JX. Valued outranking relation-based heterogeneous multi-decision multigranulation probabilistic rough set and its use in medical decision-making. Expert Systems With Applications. 2023 Oct; 228: 120296.

[12] Li WW, Yi PT, Zhang DN, Wang L, Dong QK. Stochastic-integration-based decision support methods for heterogeneous multi-attribute group decision making with several attribute sets. Expert Systems With Applications. 2023 Dec; 234: 121100.

[13] Yu SM, Du ZJ, Wang JQ, Luo HY, Lin XD. Trust and behavior analysis-based fusion method for heterogeneous multiple attribute group decision-making. Computers & Industrial Engineering. 2021 Feb; 152: 106992.

[14] Dong YC, Zhang HJ, Herrera-Viedma E. Consensus reaching model in the complex and dynamic MAGDM problem. Knowledge-Based Systems. 2016 Aug; 106: 206-219.

[15] Tan X, Zhu JJ, Palomares I, Liu X. On consensus reaching process based on social network analysis in uncertain linguistic group decision making: Exploring limited trust propagation and preference modification attitudes. Information Fusion. 2022 Feb; 78: 180-198.

[16] Opricovic S, Tzeng GH. Compromise solution by MCDM methods: a comparative analysis of VIKOR and TOPSIS, European Journal of Operational Research. 2004 Jul; 156: 445-455.

[17] Liu GZ, Wang XG. A trapezoidal fuzzy number-based VIKOR method with completely unknown weight information. Symmetry. 2023 Feb; 15: 559.

[18] Yang WG, Wu YJ. A new improvement method to avoid rank reversal in VIKOR. IEEE Access. 2020 Apr; 8: 21261-21270.

[19] Herrera F, Herrera-Viedma E, Verdegay JL. A sequential selection process in group decision making with a linguistic assessment approach. Information Sciences. 1995 Jul; 85(4): 223-239.

[20] Xu ZS. A method based on linguistic aggregation operators for group decision making with linguistic preference relations. Information Sciences. 2004 Oct; 166(1-4): 19-30.

[21] Xu ZS. Uncertain linguistic aggregation operators based approach to multiple attribute group decision making under uncertain linguistic environment. Information Sciences. 2004 Dec; 168(1-4): 171-184.

[22] Lin MW, Xu ZS, Zhai YL, Yao ZQ. Multi-attribute group decision-making under probabilistic uncertain linguistic environment. Journal of the Operational Research Society. 2018 Dec; 69(2): 157-170.

[23] Bashir Z, Ali J, Rashid T. Consensus-based robust decision making methods under a novel study of probabilistic uncertain linguistic information and their application in Forex investment. Artificial Intelligence Review. 2021 Mar; 54: 2091-2132.

[24] Wu ZB, Fang TF. A consensus and maximizing deviation based approach for multi-criteria group decision making under linguistic setting. 2014 IEEE Irenational Conference on Fuzzy Systems. IEEE Press; c2014. p.469-475.

Fuzzy Systems and Data Mining IX
A.J. Tallón-Ballesteros and R. Beltrán-Barba (Eds.)

doi:10.3233/FAIA231080

Data-Driven E-Commerce End-to-End Inventory Optimization Algorithm

Qin Zhang [a] and Yi Tan[a,1]
[a] *School of management, Shanghai University, Shanghai 200444, China*

Abstract. In the field of inventory management, due to the rapid development of artificial intelligence technology, especially data mining and machine learning, new research paradigm has been added to inventory decision-making. Compared with demand forecasting based on sales volume in previous studies, existing research aims to more fully utilize various ancillary information related to products to assist decision-making. In addition, compared with the traditional two-step decision-making (predict first and then optimize), the end-to-end (E2E) proposed in recent years can effectively avoid errors caused by the intermediate process. Based on the idea of E2E, this paper builds an end-to-end integration model E2E-Weighted on how to make optimal ordering decisions for e-commerce companies under the conditions of inventory backlog and service level target constraints. This paper also iteratively developed the model solution method KNN-Weighted based on the KNN algorithm. Results proves that as the number of samples increases, the KNN-Weighted algorithm converges to the theoretical optimal value and is better than other traditional algorithms. Furthermore, the E2E-Weighted model is more suitable for situations with high inventory target service levels.

Keywords. Data-driven, inventory optimization, KNN-weighted algorithm, end-to-end, machine learning

1. Introduction

In the context of big data, with the full penetration of information technology, machine learning and artificial intelligence technologies are being applied in various scenarios. Inventory management is a very important part of modern enterprise operations. How enterprises currently use data to cope with increasing competition and control various uncertainties, such as uncertainty in demand, has become a top priority for the sustainable development of enterprises. Most of the previous analyses assumed that the demand distribution was known [1]. However, with the dramatic changes in the business environment, the uncertainty of demand has greatly increased, therefore inventory control based on random demand emerged. In order to avoid losses caused by stockout, safety stock is added to reduce potential forecast errors [2]. In addition, time series-based demand forecast models are used in inventory management. However, demands are easily affected by various exogenous variables (such as weather conditions, promotional activities) and endogenous variables (such as seasonality). Thus indicates that forecast models based only on time series may cause in large errors, leading to out-of-stocks or inventory accumulation, thereby incurring large costs [3].

[1] Corresponding Author, Yi Tan, School of Management, Shanghai University, Shanghai 200444, China; E-mail: tobby@shu.edu.cn

Previously research mainly provides a two-step procedure for inventory optimization: 1) Assume the demand distribution and obtain the corresponding parameters; 2) solve the optimal order quantity based on the set distribution and parameters, as shown in Figure 1. However, the application results of the distribution hypothesis in practice may not be satisfied. In recent years, data-driven inventory management has become a key research direction. Liyanage and Shanthikumar [4] uses the concept of "Operational Statistics" to make integrated decisions on the estimation of demand parameters and inventory optimization in the newsvendor problem. Bertsimas and Kallus [5,6] applied five common non-parametric machine learning methods to holistic framework of data-driven integrated decision-making, i.e., K-nearest neighbor regression (KNN), kernel optimization (KO), local regression (LOESS), classification regression tree (CART), and random forest (RF). Qin et al. [7] aimed at the data-driven multi-period inventory replenishment problem. They considered the user demand and vendor lead time (VLT) on the premise of factors, thus designing a single-stage end-to-end (E2E) decision-making framework based on the deep learning model [8]. By integrating the demand forecasting and optimization models into one model, optimal inventory decisions are obtained based on historical demand and characteristic data, thus avoiding systematic errors caused by the link between forecasting and optimization in the two-step process [9]. In order to further optimize the classical machine learning algorithms that are difficult to apply to solve the problem of lack of correctly formatted input-output historical data, reinforcement learning methods have been applied to research related to inventory management. Boute et al. [10] detailed the roadmap and future direction of reinforcement learning in inventory management in their study.

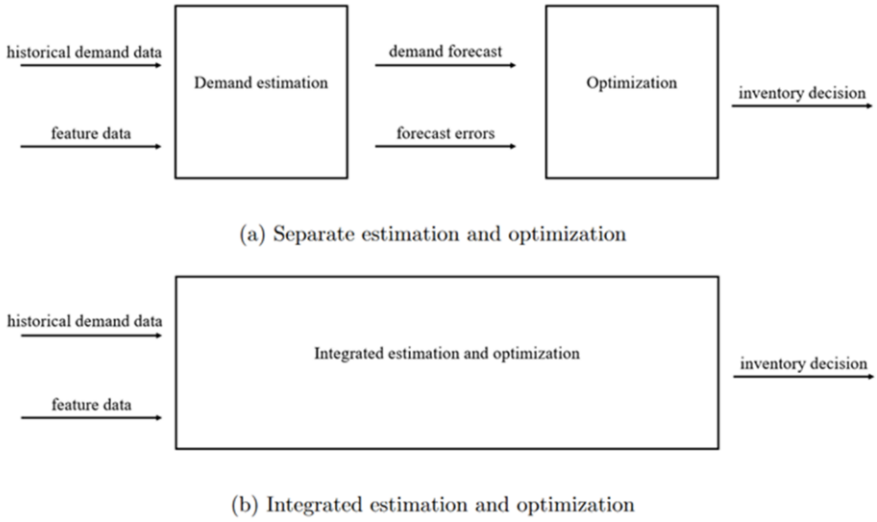

Figure 1.The two modes of data-driven inventory decision

Referring to the study of Bertsimas and Kallus [6], this paper is to propose a new integrated decision-making model. This model integrates data-driven demand forecasting and inventory optimization, and utilizes machine learning methods to design a model solving algorithm. Inventory decisions can be output based solely on characteristic data and historical demand data, thus providing a reference for e-commerce companies' operational decisions. This paper considers the inventory service level constraints faced by e-commerce enterprise warehouses instead of the classic

newsvendor model. Meanwhile, this paper also expands the application of the framework method proposed by Bertsimas and Kallus [6]. The KNN algorithm used is improved by adding service constraints and constructing conditional expectation distributions by assigning weights to historical samples based on their feature data.

2. Methodology

2.1. Problem description

The distribution of consumer demand is constantly changing, decision makers are not aware of the distribution of real consumer demand, and demand is easily affected by external factors, such as promotional activities. Decision makers need to determine the optimal order quantity in the next few days based on the characteristics of the product and historical related data. The relevant assumptions are as follows:

- The data is assumed to be stored and updated after the end of each sales cycle, and the relevant data of each product in the current warehouse will be recorded comprehensively.
- For a certain product j, the sales data and the related feature vector x_i^j of the N day are available, assuming that the sales cycle is 1 day.
- For a product $j \in J = \{1,2,3,\cdots,j\}$, the characteristic data set of T days in the future is $X_N^j = \{X_{N+1}^j, X_{N+2}^j, \cdots, X_{N+T}^j\}$, but the future demand is unknown.
- After the end of each sales period, the remaining inventory cannot be entered into the next period of sales, resulting in remaining inventory costs.
- The ordering strategy is set to q_z^j, assuming that within the next T days, the probability of product shortage will not exceed α^j, then the inventory service level is $1-\alpha^j$.

2.2. List of Symbols

Table 1. List of symbols

Symbol	Description
J	Index of product, $j \in J = \{1,2,3,\cdots,U\}$
I	Index of historical days, $i \in I = \{1,2,3,\cdots,N\}$
Z	Index of days to be decided in the future, $z \in Z = \{N+1, N+2, \cdots, N+T\}$
q_z^j	The order quantity of product j on the z day in the future
γ_i^j	Binary variable, equal to 1 if product j is out of stock on the i day in history, otherwise 0
y_i^j	The remaining inventory of product j on the i day in history,$y_i^j \geq 0$
D_i^j	The demand for product j on the i day in history
x_i^j	p-dimensional feature vector of product j on the i day in history
x_z^j	p-dimensional feature vector of product j on the z day in the future
M	Penalty coefficient
α^j	Out of stock rate, $\alpha^j \in (0,1)$
$1-\alpha^j$	Target inventory service level

2.3. Proposed model

In the theoretical model, when the service level (SL) is $1-\alpha^j$, the random demand is D, and the order quantity is set to q, if the expected inventory is minimized, then:

$$\min_{q\geq 0}\{E(q-D)^{+}: P[q \geq D] \geq 1-\alpha\} \tag{1}$$

The above formula does not consider feature vectors. When the data set $S_N^j = \{(d_1^j, x_1^j), (d_2^j, x_2^j), \cdots, (d_N^j, x_N^j)\}$is available, then the minimum expected remaining inventory is:

$$\min_{q\geq 0}\{E(q-D)^{+}|x: P[q \geq D|x] \geq 1-\alpha\} \tag{2}$$

In reality, when the demand distribution is unknown, characteristic data can be used to link the unsolved product order quantity with historical demand of "similar" situations in the form of a weight function. Historical demand with "similar" scenarios and their weights are then used to approximate the conditional expected remaining inventory. As for the inventory service level constraint, it is required to meet the out-of-stock rate target at a selected confidence level while minimizing the conditional expected remaining inventory level. Then the model can be described as:

$$\min \sum_{i=1}^{N}\left[w\left(x_z^j, x_i^j\right)y_i^j\right] \tag{3}$$

$$s.t. \quad y_i^j \geq q_z^j - D_i^j \tag{4}$$

$$y_i^j \geq 0 \tag{5}$$

$$q_z^j + \gamma_i^j M \geq D_i^j \tag{6}$$

$$\sum_{i=1}^{N}\left[w\left(x_z^j, x_i^j\right)\gamma_i^j\right] \leq \alpha \tag{7}$$

$$\sum_{i=1}^{N} w\left(x_z^j, x_i^j\right) = 1 \tag{8}$$

$$y_i^j \in \{0,1\} \tag{9}$$

$$q_z^j \geq 0 \tag{10}$$

Among them, $w\left(x_z^j, x_i^j\right)$ represents the similarity between future product characteristics and historical characteristics represented by weights. Formulas (4) and (5) together constitute the decision variable remaining inventory $y_i^j = \left(q_z^j - D_i^j\right)^+$, γ_i^j is a Binary variable. When it is 0, formula (6) becomes $q_z^j \geq D_i^j$, indicating that the demand is met, otherwise, a shortage occurs. Formula (8) indicates that the service level constraint is met within the historical N days.

This model makes full use of the information of feature data and apply machine learning methods to establish the relationship between features and sales (including linear and nonlinear relationships), which can be quickly solved by optimization solvers such as Gurobi.

To give a relatively specific example, an e-commerce company wants to determine the A brand of black jumpers to determine the optimal order quantity for the next day. Known jumper price, discount, brand, sales channels, categories and other attribute features, the need to find in the existing database and these features are very similar to the historical features corresponding to the historical sales, and give weight based on the set level of service, to find the jumper's optimal inventory decision. Then it can be seen that the key to solving the model is how to define the similarity between the samples to be decided and the historical samples, i.e. how to determine the weight function in the constructed model.

2.4. Algorithm development

K-Nearest Neighbor (KNN) learning is a commonly used supervised learning method in machine learning. This paper proposes the KNN-Weighted method based on the original KNN method to solve the above integrated inventory problem. The differences and advantages between it and KNN can be stated into two ways. Firstly, KNN uses the square loss formula as the loss function, while KNN-Weighted uses the objective function in the above model as the loss function. Secondly, KNN-Weighted directly outputs the order quantity instead of the demand quantity. The detailed steps are as follows:

Step1: Enter the Kvalue range and select a value;

Step2: Select the characteristic data x of a sample in the verification set;

Step3: Calculate the Euclidean distance between $x_i$and K, sort the values of K by distance. Then select the K with the shortest distance for sales training, thus assigning the sales volume of the training set feature with a weight of $1/K$. According to these K sales, calculate the optimal order quantity that meets the service level by weight and record it;

Step4: Determine whether the verification set has been calculated, if so, proceed to step6, otherwise jump to step2;

Step5: Determine whether the K value has been traversed, if so, proceed to step6, otherwise jump to step1;

Step6: Summarize and select the K value corresponding to the minimum inventory remaining quantity as the optimal K value;

Step7: Select the feature data to be tested in the test set and repeat the same operation as step3;

Step8: Determine whether the test set has been calculated, if so, proceed to step9, otherwise jump to step7;

Step9: Output the optimal K value, optimal ordering decision, actual service level and remaining inventory level.

3. Experiment and Results

3.1. Data sets

This paper applies the sales data of an e-commerce company in June 2019, including 260 SKUs and a total of 4,234 pieces of data. Table 2 shows each product contains 9 attributes, among which Facility, Channel Name, SKU Name, and Discount are used as characteristic attributes. Apply one-hot encoding feature attributes corresponding to the word text for processing before solving.

Table 2. List of characteristic attributes

Attribute	Description
SKU_ID	Product unique identifier
Facility	Sales address
Channel Name	Sales channels
SKU Name	SKU category name
Quality	Sales volume
Total Price	Total sales price
Discount	Discount
Date	Sales date
Vendibility	Binary variable, equal to 1 when the day's sales generate inventory, otherwise 0

The data is divided into training set, validation set and test set, the details are shown in table 3:

Table 3. Data partition

Data set	Data amount	Number of identification codes
Training set	3387(80%)	245
Validation set	212(5%)	253
Test set	635(15%)	260

The verification set is used to tune the weight parameters in the E2E-Weighted model, and the test set is used to calculate the final results after parameter tuning and to evaluate the performance of the integrated decision-making model.

3.2. Comparison of results

Since the service level in practice is generally higher than 50% [11], this experiment assumes that the target service levels are located at 50%, 70%, 90%, and 95% respectively. The solution methods used include: ARIMA, LR (linear regression), KNN, DTR (decision tree regression), and the integrated model KNN-Weighted algorithm proposed in this article.

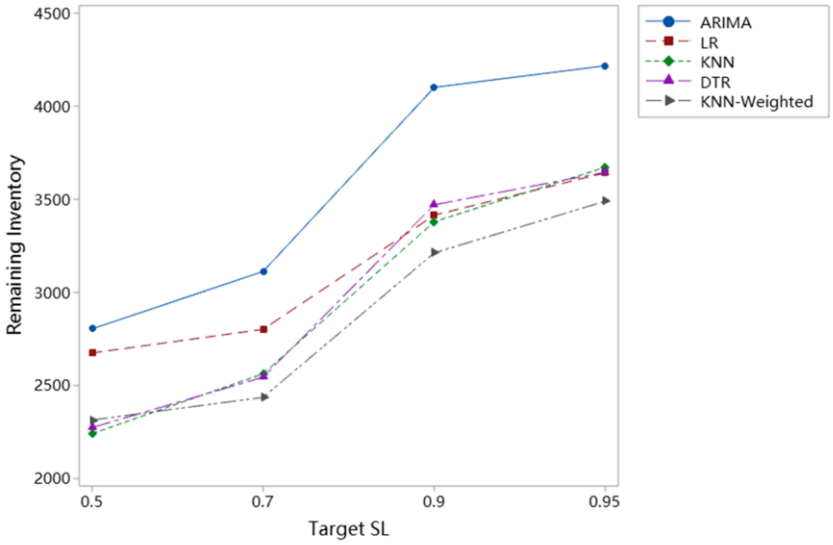

Figure 2 Results of different methods (Remaining inventory)

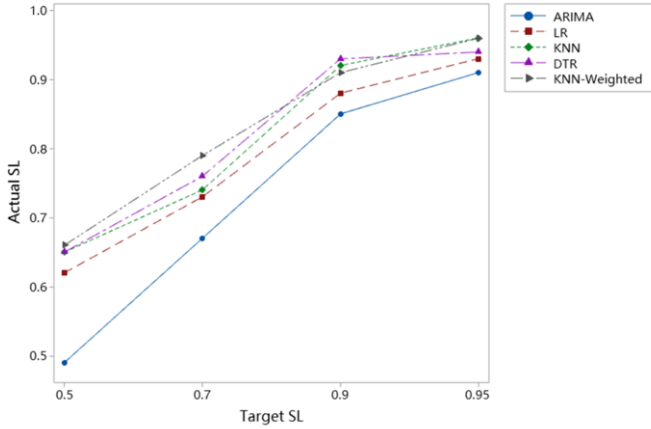

Figure 3 Results of different methods (Remaining inventory)

The results shown in Figure 3 and Figure 4 reveal that KNN-Weighted performs well when the target service level is higher than 70%, and is suitable for situations with high inventory service level requirements. Whether it is the actual inventory service level or the remaining inventory level, the performance of the integrated decision-making method is better than that of other methods.

3.3. Asymptotic optimality

The sample sizes are set to 10, 100, 1000, 5000, and 10000 respectively, and the target inventory service level is 0.5 [9]. This paper compares the running performance of various methods for different sample sizes.

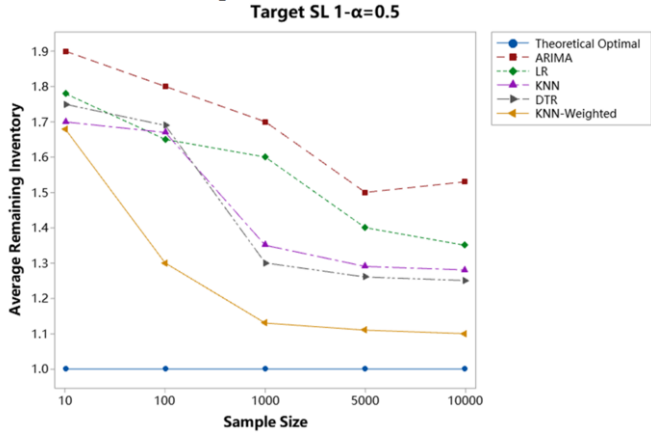

Figure 4 Asymptotic optimality of various methods

Overall, when the sample size is between 100 and 1,000, the performance of each method can be significantly improved. When the sample size exceeds 10,000, as the sample continues to increase, it is hard to improve the performance of the model. It can also be concluded from Figure 4 that the KNN-Weighted method proposed in this article has better performance than the other four methods, followed by the decision tree regression (DTR) method.

4. Conclusion

This article is based on the idea of end-to-end (E2E) and considers how e-commerce companies make optimal ordering decisions under inventory backlog and service level target constraints. Through data mining and machine learning technology, the research uses the minimum amount of remaining inventory as the optimization goal to build an end-to-end integrated model E2E-Weighted with service level constraints. This article iterates the KNN-Weighted solution algorithm suitable for this model based on the KNN algorithm. In using the obtained historical sales data and characteristic data of products on sale in e-commerce, inventory decisions rather than demand forecasts are obtained in one step. In addition, this study proves that as the number of samples increases, the KNN-Weighted algorithm converges to the theoretical optimal value, and compared with other traditional methods, it reflects the advantages of feature data in searching optimal inventory decisions. Actual data experimental results demonstrate that the E2E-Weighted model is more suitable for high target service levels. When the target service level is higher than 70%, the corresponding decision algorithm can reduce more inventory remaining amounts. This article has the following follow-up research directions. Firstly, more complex inventory scenarios can be considered. Secondly, this article mainly concluded inventory level constraints, there are other constraints that can be added in subsequent research. Thirdly, more suitable solution algorithms or comparisons with other more complex algorithms can be considered to provide better decision-making solutions for the enterprise.

References

[1] Silver E A, Pyke D F, & Douglas T J. Inventory and production management in supply chains. New York: Taylor and Francis, 2017.
[2] Beutel A L, Minner S. Safety stock planning under causal demand forecasting. International Journal of Production Economics, 2012, 140(2): 637-645.
[3] Carrizosa E, Olivares-Nadal A V, & Ramírez-Cobo P. Robust newsvendor problem with autoregressive demand. Computers & Operations Research, 2016, 68: 123–133.
[4] Liyanage L H, Shanthikumar J G. A practical inventory control policy using operational statistics. Operations Research Letters, 2005, 33(4): 341-348.
[5] Bertsimas D, Thiele A. A data-driven approach to newsvendor problems. Working Paper, Massachusetts Institute of Technology, 2005.
[6] Bertsimas D, Kallus N. From Predictions to Data-Driven Decisions Using Machine Learning. Management Science, 2020, 66(3): 1025-1044.
[7] Meng Q, Yuanyuan S, Yongzhi Q, et al. A Practical End-to-End Inventory Management Model with Deep Learning. Management Science, 2022, 69(2): 759-773.
[8] Bengio Y, Lodi A, & Prouvost A. Machine learning for combinatorial optimization: a methodological our d'horizon. European Journal of Operational Research, 2021, 290(2): 405-421.
[9] Ban G Y, Rudin C. The Big Data Newsvendor: Practical Insights from Machine Learning. Operations Research, 2019, 67(1): 90–108.
[10] Boute R N, Gijsbrechts J, Jaarsveld W V, et al. Deep reinforcement learning for inventory control: A roadmap. European Journal of Operational Research, 2022, 298(2): 401-412.
[11] Oroojlooyjadid A, Snyder L V, Takáč M. Applying deep learning to the newsvendor problem. IISE Transactions, 2020, 52(4): 444-463.

Fuzzy Systems and Data Mining IX
A.J. Tallón-Ballesteros and R. Beltrán-Barba (Eds.)

doi:10.3233/FAIA231081

Research on Speed Control Strategy of Asynchronous Motor in Marine Electric Propulsion System

Han WANG[a], Fan ZHANG[b,1] and Yuanjie REN[c]
[a] *Marine Design and Research Institute of China, Shanghai 200000, China*
[b] *Wuhan Marine Electric Propulsion Research Institute, Wuhan 430064, China*
[c] *College of Intelligent Systems Science and Engineering, Harbin Engineering University, Harbin 150001, China*

Abstract. With the widespread application of new technologies and new equipment, due to the differences between ship power systems and land power systems, it is necessary to model and digitally simulate the ship electric propulsion system. This paper establishes a mathematical model of the ship's electric propulsion system, and uses Matlab to initially implement digital simulation of the system. The simulation adopts a hierarchical structure and modular design. Based on the slip frequency speed regulation control strategy, the motor speed, electromagnetic torque, three-phase current and dq-axis current of the asynchronous motor starting process and loading process are simulated and analyzed. Under two common working conditions, the speed change curve was simulated and verified using the slip frequency speed regulation control strategy and without using the control strategy. The examples proved the correctness of the simulation model and method.

Keywords. Marine electric propulsion system, Asynchronous motor, Speed control strategy

1. Introduction

Since the 1980s, the application of AC electric drive technology in ship propulsion systems has become a new development direction. Compared with land power systems, ship power systems using electric propulsion have some significant characteristics [1]: The power supply capacity and propulsion load of ship power systems are comparable, and their propulsion power usually accounts for 60% to 70% of the total power supply. [2], the complexity of ship operating conditions will directly affect the operation of ship power supply, and the interaction between the two places more stringent requirements on the coordination between control systems.

In order to study, calculate, and analyze these issues, it is necessary to provide a digital simulation tool that can reflect the static and dynamic performance of the ship's power system. In response to this, a lot of research has been done at home and abroad. Literature [3] proposed the PFM concept for frequency conversion speed regulation devices in ship power systems; Literature [4] used the simulation software EMTP to

[1] Corresponding Author: Fan Zhang, Wuhan Marine Electric Propulsion Research Institute, Wuhan 430064, China; Email: gdlst@163.com.

simulate the ship's electric propulsion system. Simulation research has been carried out; Literature [5-6] focuses on the research of propulsion motors and generators in ship power systems; Literature [7] uses Matlab software to conduct simulation research on ship propulsion devices. These works focus on Separate study of the motor speed control in the electric propulsion device and the separate study of the control effect of the generator set adjustment device lacks digital simulation research on the overall ship power system; although literature [8-9] has established separate power generation systems for diesel engine ship electric propulsion systems, and mathematical model of the load system, and simulated the generator terminal frequency and voltage. However, the load model only considered the static model and did not simulate the dynamic performance of the propulsion system.

The main work of this paper includes simulating ship propulsion performance under different steady-state operating conditions based on ship speed, mainly the rotation speed and torque of the propulsion shaft motor. And it refers to the simulation of ship maneuverability, that is, it can realize the simulation of dynamic processes such as the speed and torque of the propulsion motor when the ship's operating conditions change. An example was simulated using this system, and the results proved the correctness of the simulation model and method.

This paper consists of five parts. The first part is the introduction, which mainly introduces the development status and existing problems in the field of asynchronous motor control. The second part gives the overall architecture of Marine electric propulsion system and the modeling of analytical problems. The third part mainly introduces vector control theory and method and design of asynchronous motor slip frequency closed-loop speed regulation the system. The fourth part is mainly simulation verification analysis. These include simulation and verification of slip frequency closed-loop speed regulation system and comparative simulation analysis of the system typical working conditions. The fifth part summarizes the full text.

2. Ship electric propulsion system

2.1. Structure of ship electric propulsion system

This article uses this simulation system to simulate an example of a ship's power system. The main electrical wiring of this example is shown in the figure 1. The central power station of the system consists of 5 diesel generator sets, 4 of which are main generators with a power of 4400kW, and 1 is an auxiliary generator with a power of 1600kW. The AC propulsion system adopts AC-DC-AC frequency conversion, and the rectifier part adopts 12-pulse rectification. The main propulsion motor uses two 3000kW asynchronous motors, and the side propulsion motor uses three 2200kW asynchronous motors.

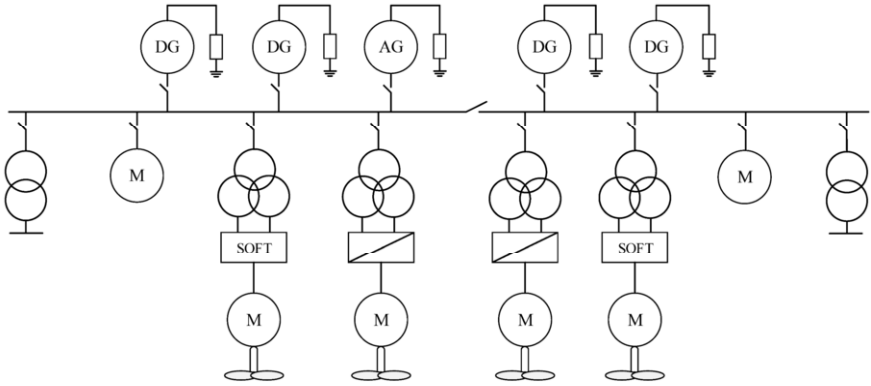

Figure 1. Electrical main wiring diagram of ship electric propulsion system.

2.2. Modeling of asynchronous propulsion motor and its speed control system

The propulsion motor in Marine integrated electric propulsion system is a high order, nonlinear and strongly coupled multivariable complex system. In order to simplify the analysis and calculation of the physical relationship inside the motor, some important simplifying assumptions are adopted in the establishment of the induction motor mathematical model. In this simplified model, we mainly consider the main physical characteristics of the motor, and introduce the following simplified assumptions: the core loss is ignored; The phenomenon of magnetic circuit saturation is ignored. The variation of winding resistance with temperature is ignored. Assume that the three-phase windings are symmetrically distributed. Based on these assumptions, we get a primitive asynchronous motor model, as shown in figure 2.

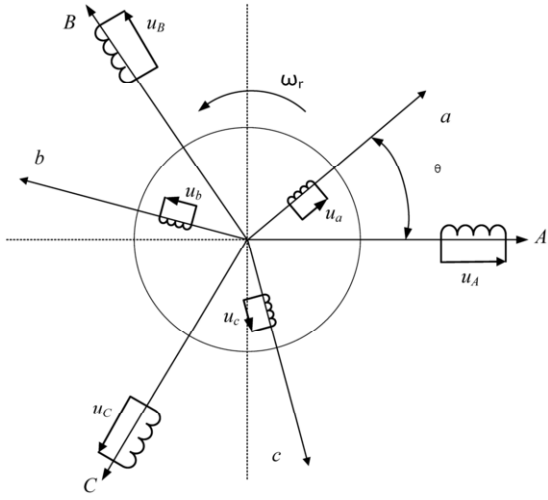

Figure 2. Original motor model of asynchronous motor.

The mutual coupling relationship matrix between the three-phase stator winding and the equivalent three-phase rotor winding of an asynchronous motor is:

$$\begin{bmatrix}\psi_A\\ \psi_B\\ \psi_C\\ \psi_a\\ \psi_b\\ \psi_c\end{bmatrix}=\begin{bmatrix}L_{AA} & L_{AB} & L_{AC} & L_{Aa} & L_{Ab} & L_{Ac}\\ L_{BA} & L_{BB} & L_{BC} & L_{Ba} & L_{Bb} & L_{Bc}\\ L_{CA} & L_{CB} & L_{CC} & L_{Ca} & L_{Cb} & L_{Cc}\\ L_{aA} & L_{aB} & L_{aC} & L_{aa} & L_{ab} & L_{ac}\\ L_{bA} & L_{bB} & L_{bC} & L_{ba} & L_{bb} & L_{bc}\\ L_{cA} & L_{cB} & L_{cC} & L_{ca} & L_{cb} & L_{cc}\end{bmatrix}\begin{bmatrix}i_A\\ i_B\\ i_C\\ i_a\\ i_b\\ i_c\end{bmatrix} \tag{1}$$

where ψ_A, ψ_B and ψ_C are the stator three-phase winding flux, ψ_a, ψ_b and ψ_c are the rotor equivalent three-phase winding flux, i_A, i_B and i_C are the stator three-phase winding current, i_a, i_b and i_c are the rotor equivalent three-phase winding current, and L_{xy} is the three-phase inductance.

Convert the voltage equation of the propulsion motor to the $dq0$ rotation coordinate system:

$$\begin{bmatrix}u_{sd}\\ u_{sq}\\ u_{rd}\\ u_{rq}\end{bmatrix}=\frac{d}{dt}\begin{bmatrix}\psi_{sd}\\ \psi_{sq}\\ \psi_{rd}\\ \psi_{rq}\end{bmatrix}+diag\begin{bmatrix}R_s\\ R_s\\ R_r\\ R_r\end{bmatrix}\begin{bmatrix}i_{sd}\\ i_{sq}\\ i_{rd}\\ i_{rq}\end{bmatrix}+\begin{bmatrix}-\omega\psi_{sq}\\ \omega\psi_{sd}\\ 0\\ 0\end{bmatrix} \tag{2}$$

where u is the voltage, i is the current; ψ is the magnetic linkage; r represents the rotor; s represents the stator. The flux linkage equation of an asynchronous motor is:

$$\begin{bmatrix}\psi_{sd}\\ \psi_{sq}\\ \psi_{rd}\\ \psi_{rq}\end{bmatrix}=\begin{bmatrix}L_s & 0 & L_m & 0\\ 0 & L_s & 0 & L_m\\ L_m & 0 & L_r & 0\\ 0 & L_m & 0 & L_r\end{bmatrix}\begin{bmatrix}i_{sd}\\ i_{sq}\\ i_{rd}\\ i_{rq}\end{bmatrix} \tag{3}$$

where L_r is the three-phase equivalent rotor winding self-inductance; L_s is the motor stator winding self-inductance; L_m is the motor stator and rotor winding mutual inductance. The electromagnetic torque and rotor motion equations are:

$$\begin{aligned}T_e &= n_p L_m(i_{sq}i_{rd}-i_{rq}i_{sd})\\ \frac{d\omega}{dt} &= \frac{n_p}{J_1}(T_e-T_L-B\omega)\end{aligned} \tag{4}$$

where T_L is the load resistance torque; J_1 is the rotor inertia of the asynchronous motor; n_p is the number of pole pairs of the asynchronous motor; B is the friction coefficient.

3. Asynchronous motor control technology for ship electric propulsion system

3.1. Vector control theory and method

Vector control is currently a relatively advanced control method in the field of asynchronous motor control. Usually, AC motor control methods containing vector transformation are called vector control. The principle of vector transformation and the equivalent DC motor model are shown in the figure 3.

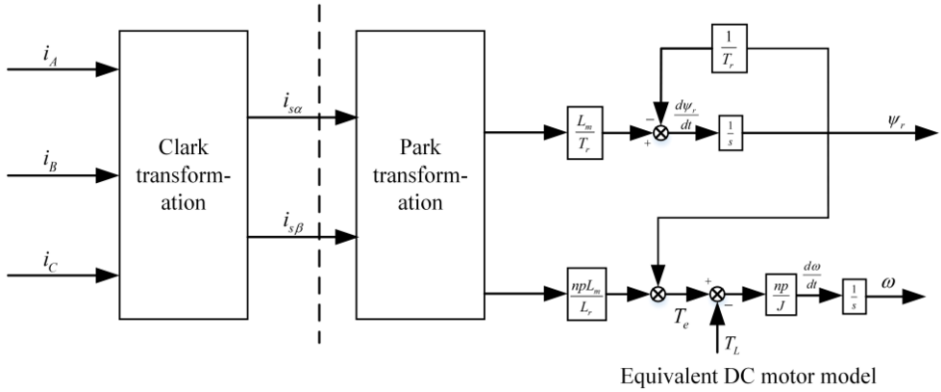

Figure 3. Principle of vector transformation and equivalent DC motor model.

3.2. Design of asynchronous motor slip frequency closed-loop speed regulation system

To solve the torque control problem of AC asynchronous motor, it can be achieved by controlling the slip frequency. The basic idea of the scheme is to realize the torque control problem of the asynchronous motor and improve the stability of the bus voltage by controlling the slip frequency. The figure 4 below is a schematic block diagram of an asynchronous motor vector control speed regulation system with speed closed-loop slip frequency control.

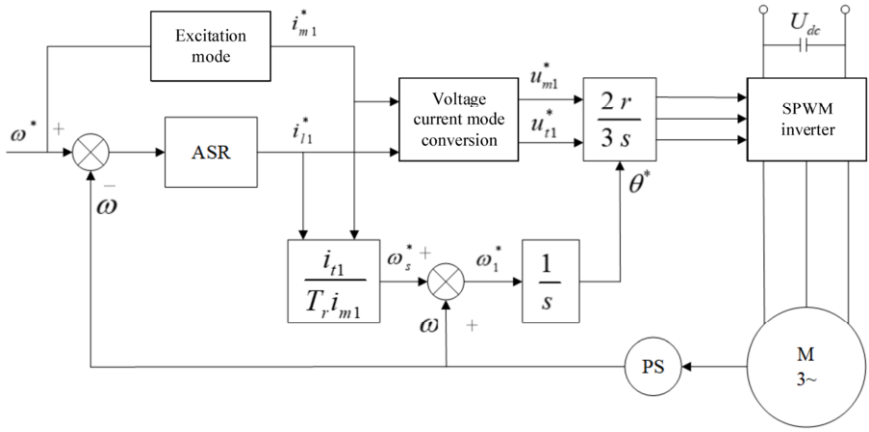

Figure 4. Principle block diagram of the vector control speed system of speed closed-loop slip frequency.

The main circuit of the speed control system is a SPWM voltage-type inverter, which is the circuit topology generally used in general-purpose frequency converters. For asynchronous motor speed control, the slip frequency control method is selected as follows:

$$\omega_1 = \omega + \omega_s \tag{5}$$

Among them: ω_s is the slip angular frequency; ω is the angular frequency of the rotor; ω_1 is the stator angular frequency of the asynchronous motor.

According to this formula, during the adjustment process of the motor speed, the stator current frequency of the AC asynchronous motor and the actual rotor speed can

rise or fall synchronously from beginning to end, so that the speed can be adjusted smoothly.

The vector control equation of an asynchronous motor can be described as:

$$T_e = n_P \frac{L_m}{L_r} i_{st} \Psi_r \tag{6}$$

$$\omega_s = n_P \frac{L_m i_{st}}{T_r \Psi_r} \tag{7}$$

$$\Psi_r = n_P \frac{L_m}{T_r p + 1} i_{sm} \tag{8}$$

where n_P is the number of pole pairs; i_{st} is the torque component of the stator current; i_{sm} is the excitation component of the stator current; Ψ_r is the rotor flux linkage of the motor; T_r is the rotor electromagnetic time constant, $T_r = L_m / R_r$, L_m is the same in the two-phase coordinate system The mutual inductance between the stator and rotor windings, R_r is the resistance value of the rotor one-phase winding.

It can be concluded from the vector control equation of the asynchronous motor that if Ψ_r is kept unchanged, T_e will be directly controlled by i_{st}, and the slip angular frequency ω_s can also be directly obtained from i_{st}, and Ψ_r can be obtained from i_{sm}. In the vector control speed regulation system of AC asynchronous motor with speed closed-loop slip frequency control, the speed regulator (ASR) adopts PI (proportional integral) control mode, and the output signal of PI is the given value of the stator current torque component. From this, the given value of slip frequency ω_{s1}^* can be obtained. During the control and adjustment process, if the magnetic flux is kept at a constant value, then $p\Psi_r = 0$. It can be seen from Eq.8 that,

$$\Psi_r = L_m i_{sm} \tag{9}$$

According to Eq.7, it can be obtained:

$$\omega_s = \frac{i_{st}}{T_r i_{sm}} \tag{10}$$

4. Simulation verification and analysis

4.1. Simulation and verification of slip frequency closed-loop speed regulation system

In order to observe the dynamic adjustment process of the system more directly, the step signal n^* is used to set the given speed value in the simulation model of the slip frequency closed-loop speed regulation system, so that the dynamic operation of the speed regulation system at different given speed values can be observed.

First, verify the simulation analysis of the stability performance of the whole system of the closed-loop speed regulation system with slip frequency. The simulation time is set as 1s, the given speed of the propulsion motor is n=200r/min, the load torque of the motor when starting is TL=25000N·m, and the load torque is abruptly increased to the rated torque of the motor TL=48800N·m when it runs to 0.5s. The simulation results are shown in the figure 5-8 below.

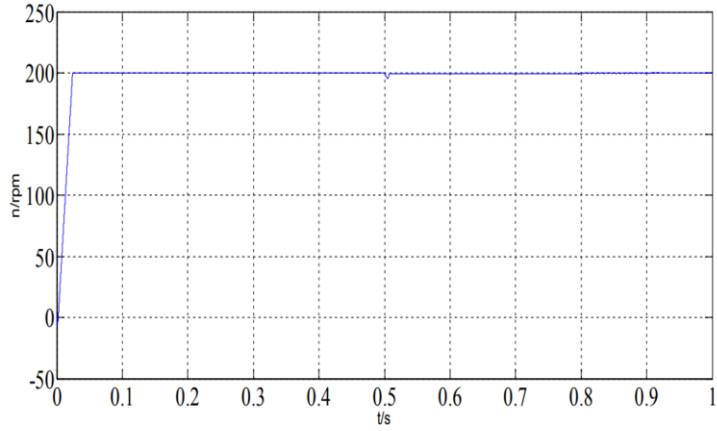

Figure 5. Motor speed simulation waveform.

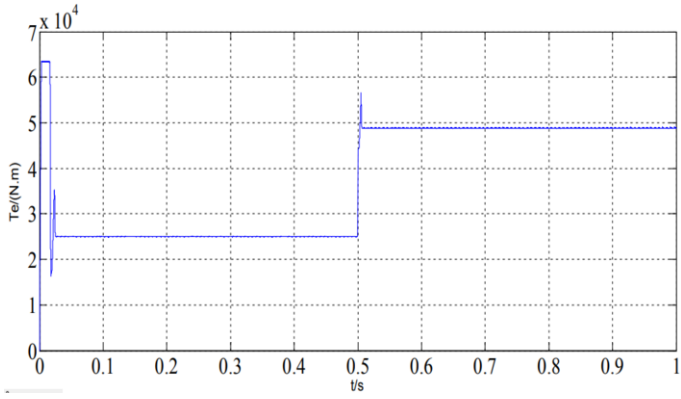

Figure 6. Motor electromagnetic torque simulation waveform.

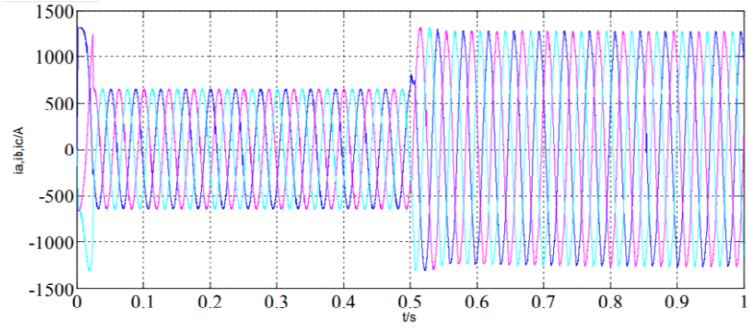

Figure 7. Motor stator three-phase current simulation waveform.

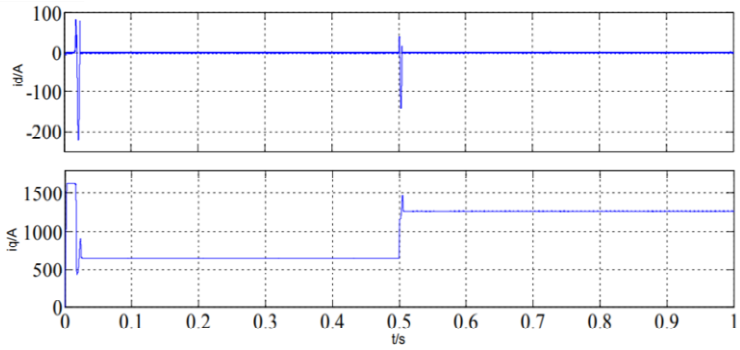

Figure 8. Motor dq axis current simulation waveforms.

Figure 5 shows the speed adjustment waveform. From the figure, we can see the starting, steady speed and loading process of the motor. The speed gradually rises from zero to 200r/min and remains stable. When running to 0.5s, the load torque is suddenly added to the motor. rated torque. Figures 6 to 8 show the motor electromagnetic torque simulation waveforms, three-phase stator current simulation waveforms, and d and q-axis current simulation waveforms respectively. It can be seen from the figure that the current and torque are relatively large during the starting stage. The motor starts with a given maximum current. After 0.5s of loading, the electromagnetic torque and armature current increase, and the torque and current also increase. corresponding fluctuations.

4.2. Comparative simulation analysis of typical working conditions

Compared with traditional control methods, the above-mentioned slip frequency closed-loop speed control system has a more superior speed control effect. The impact of high maneuverability indicators on the system response characteristics under cruising conditions and full-speed sailing conditions is analyzed, and the propulsion force and speed of the ship are controlled by adjusting the motor speed.

Calculate the dynamic adjustment accuracy and action response time of the main propulsion motor before and after using slip frequency control under the two working conditions, as shown in the following table 1.

Table 1. Comparison table of high mobility indicators before and after adopting slip frequency control strategy under different working conditions

	Different working conditions	Before use	After use	Optimization and improvement
Dynamic adjustment accuracy	Cruise condition	1.13%	1.04%	0.09%
	Full speed sailing condition	1.14%	1.11%	0.03%
	Different working conditions	Before use	After use	Optimization and improvement
Action response time	Cruise condition	18.3s	17.6s	0.7s
	Full speed sailing condition	18.8s	17.8s	1s

Based on the above calculation results, in order to further analyze the influence of slip frequency control strategy on asynchronous motor control, we drew three results through simulation: expected speed curve, asynchronous motor speed curve with slip frequency control strategy and asynchronous motor speed curve without slip frequency control strategy, as shown in the figure 9 and 10 below.

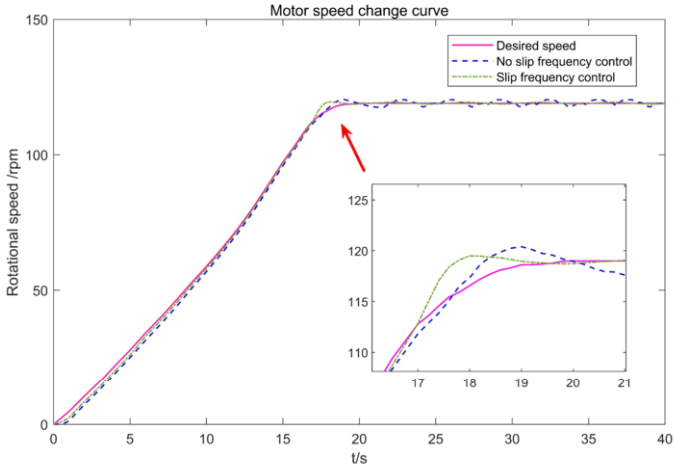

Figure 9. Motor speed variation curve during cruising condition.

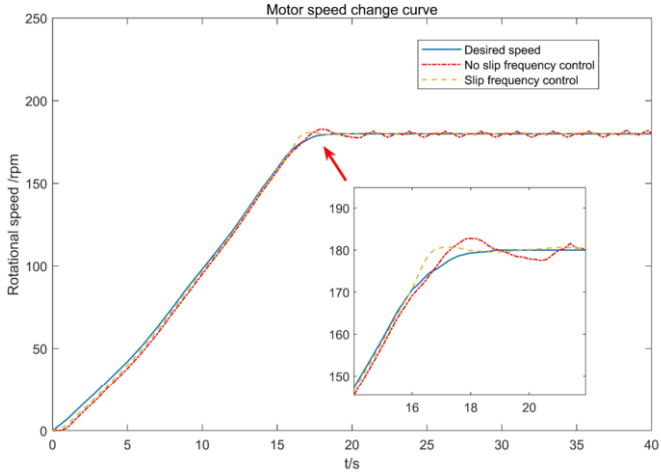

Figure 10. Motor speed change curve under full speed sailing condition.

Therefore, the use of slip frequency control strategy can help improve the flexibility and safety of ship operation, and at the same time, it can achieve smooth control of the main propulsion motor, avoid sudden changes and fluctuations in propulsion force, and reduce vibration and vibration of the hull.

5. Conclusion

In view of the differences between ship electric propulsion systems and land power systems and the rapid development of ship power systems, this article gives a mathematical model of the key parts of the ship electric propulsion system and uses Matlab to realize the digital simulation of the ship electric propulsion system. The simulation research of the example system shows that the mathematical model and digital

simulation system established in this article can effectively simulate the steady-state and dynamic performance of the ship's power system.

References

[1] Dimitrov, L. Kanturska, S. Features in the selection and operation of AC Motors for electric propulsion system in ship. 15th International Conference on Electrical Machines, Drives and Power Systems; 2017 Jun 01-03; Sofia, Bulgaria.

[2] Reusser, C. et al. Power Electronics and Drives Applications to Modern Ship Propulsion Systems. IEEE Industrial Electronics Magazine. 2021 Jan;14(4):106-122.

[3] An, L. Cheng, T. and Lu, D. Single-Stage Boost-Integrated Full-Bridge Converter With Simultaneous MPPT, Wide DC Motor Speed Range, and Current Ripple Reduction. IEEE Transactions on Industrial Electronics. 2019 Sep; 66(9):6968-6978.

[4] Yin, J. et al. Software Optimization of Welding Machine Motion System Based on Switch Control Algorithm. Mobile Information Systems. 2022 Jun;2022: 1271190.

[5] Chasiotis, I. and Karnavas, Y. A Study on Design and Optimization of High Power Density PMSM for Pod Propulsion System. 13th International Conference on Electrical Machines; 2018 Sep 03-06; Alexandroupoli, Greece.

[6] Lim, C. et al. Electric Power Consumption Predictive Modeling of Electric Propulsion Ship Considering the Marine Environment. 4th International Conference on Systems and Informatics; 2018 Nov 11-13; Hangzhou, China.

[7] Lim, C. et al. Electric power consumption predictive modeling of an electric propulsion ship considering the marine environment. International Journal of Naval Architecture and Ocean Engineering. 2020 Jul; 11(2):765-781.

[8] Guo J. Yu E. and Zhang A. Vector control system of permanent magnet synchronous motor for marine electric propulsion. 2014 International Conference on Mechatronics and Control; 2014 Jul 03-05; Jinzhou, China.

[9] Hu, H. and Shi, W. Modeling and simulation of all-electric propulsion system with three-closed loop control. Journal of Computational Methods in Sciences and Engineering. 2021 May; 21(1):109-123.

Fuzzy Systems and Data Mining IX
A.J. Tallón-Ballesteros and R. Beltrán-Barba (Eds.)

doi:10.3233/FAIA231082

Research on Harmonic Suppression Method Based on Control Active Filter in Ship Integrated Power System

Xiang Han[a], Huan Fang[b,1] and Yuanlin Yao[c]
[a] *Marine Design and Research Institute of China, Shanghai, 200000, China*
[b] *Wuhan Marine Electric Propulsion Research Institute, Wuhan 430064, China*
[c] *College of Intelligent Systems Science and Engineering, Harbin Engineering University, Harbin 150001, China*

Abstract. With the continuous development of power transmission technology and automation control technology, the application of high-power inverter devices in modern ship power systems is increasing. Moreover, as the ship operates under different conditions such as cruising and platform lifting, the degree of harmonic pollution in the ship's electrical grid varies. If harmonics in typical operating conditions like cruising and platform lifting are not effectively managed, it can seriously affect the safe operation of the ship. To address this issue, this paper proposes an intelligent harmonic suppression method for active power filters based on fuzzy PID and model predictive control. It combines fuzzy control with conventional PID control to enhance control robustness. The optimization objective in the model predictive current control is shifted from compensation current provided by the active power filter to the inverter output voltage. By adjusting the phase of the inverter output voltage corresponding to the voltage vector reference value, the range of inverter output voltage vectors participating in rolling optimization is narrowed, thereby achieving control of harmonic currents. Finally, by modeling the ship's integrated power system and simulating two operating conditions, cruising and platform lifting, this study analyzes voltage waveforms and harmonic content before and after harmonic suppression using fuzzy PID and model predictive control active power filters. The results demonstrate that the proposed method can significantly improve voltage quality in power systems under power supply voltage distortion and has excellent harmonic suppression effects.

Keywords. Ship power grid; Active power filter; Fuzzy PID control; Model predictive voltage control

1. Introduction

Different from land transportation, ships, as a means of transportation for maritime trade, are an independent control system when sailing at sea. With the rapid development of automation technology and power electronics technology theory and put into practical use, the independent ship power system composed of power supply device, power distribution device, power grid and load is more and more frequently used in ships [1]. In order to maintain the high quality of the ship 's power grid, it is required that the

[1] Corresponding Author, Huan Fang, Wuhan Marine Electric Propulsion Research Institute, Wuhan 430064, China; E-mail: huanf712@163.com

amplitude, frequency and phase of the ship 's power grid voltage can quickly restore stability when encountering large changes such as sudden changes. The capacity and . quantity of ship power electronic devices have increased greatly, which improves the performance advantages of ships, and inevitably leads to the harmonic problem of ship power grid [2]. The harmonics of the ship 's power grid bring more and more safety hazards and ship operating costs. The harmonic pollution of the ship 's power grid will bring many negative effects, including the decline of the power quality of the ship 's power system, the reduction of the power efficiency, the reduction of the transmission capacity of the system, the reduction of the service life of the equipment connected to the system, the safety hazards of the power system and the electrical equipment, and the reduction of the operation efficiency [3]. Therefore, it is an inevitable trend to suppress the harmonics of the ship power grid and improve the power quality of the power grid.

The harmonic suppression methods of ship power system are divided into active [2] and passive [4]. The active harmonic suppression method is to transform the harmonic source device itself, such as the power electronic devices carried by the ship, such as frequency conversion devices. The active harmonic suppression method cuts off the harmonics from the source or greatly reduces the harmonic output. Because electric propulsion technology has more advantages in speed regulation performance, most ship power systems will use electric propulsion technology instead of diesel engine propulsion technology in the future [5]. The passive harmonic suppression method is not aimed at the harmonic source itself. It uses the filter to filter out the harmonics at the initial location of the harmonic source, which can theoretically reduce the harmonic content input to the ship power grid [6]. Passive power filter is divided into passive power filter, active power filter and hybrid power filter [7]. The design of old ships is simple, and it is better to use passive power filter for harmonic control. However, the design of modern ships is complex, and the structural characteristics of passive power filters are limited, which is not suitable for modern ship power systems. Modern ship power system harmonic suppression using more active power filter [8].

In view of this, a lot of research has been done at home and abroad. In Reference [9], the method of integrating neural network and fuzzy control and then applying it to APF compensation current control is adopted. In Reference [10-12], the sliding mode variable structure control is applied to the ship electric propulsion system, which improves the harmonic pollution of the system and proves the practicability of the method. However, the serious problem is the high accuracy of the chattering phenomenon damage control. In Reference [13], the active power filter based on fuzzy sliding mode control is applied to the ship electric propulsion system, which reduces the harmonic input of the inverter to the power grid. References [14-15] used repetitive control APF to repeatedly correct the output current signal, and finally achieved the purpose of completely erasing the steady-state error. However, because it is an inherent controller based on periodic type, it is difficult to avoid a periodic delay in control.

The main work of this paper is to model the ship 's integrated power system, and use the system to carry out an example simulation to realize the detection of harmonics in the ship 's operating conditions. The results prove the correctness of the simulation model and method.

2. electric propulsion system

2.1. Structure of ship electric propulsion system

In this paper, the simulation system is used to simulate a ship power system. The single line diagram of the example is shown in the figure. The power generation unit of the system consists of five diesel generator sets, including four main generators and one auxiliary generator. The power of the main generator is 4400 kW and the power of the auxiliary generator is 1600 kW. The AC propulsion system adopts AC-DC-AC frequency conversion, and the rectification part adopts 12-pulse rectification. In addition to the daily load, the system also includes the main propulsion motor, the side thrust motor and the lifting system, and the running state of each equipment under different working conditions is different.

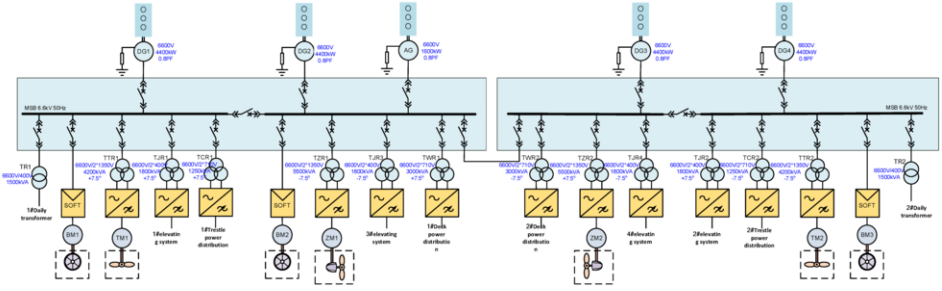

Figure 1. Single-line diagram of ship electric propulsion system.

2.2. Modeling of shunt active power filter

The three-phase three-wire grid topology is usually used in the ship power system, and the parallel active power filter can produce better harmonic control effect, as shown in the figure. The three-phase grid voltage is U_a, U_b and U_c ; the three-phase grid current is i_{1a}, i_{1b} and i_{1c} ; the three-phase load current is i_{2a}, i_{2b} and i_{2c} ; i_a, i_b, i_c provide three-phase compensation current for APF ; u_a, u_b and u_c are the output three-phase voltages of the inverter. C is the DC-side capacitor, and U_{DC} is the DC-side voltage ; L is the AC side inductance ; R is the inductance parasitic resistance ; IGBT is a power switch tube.

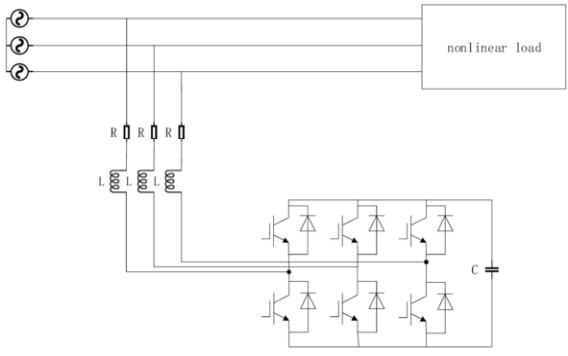

Figure 2. Three-phase three-wire shunt APF topology structure.

According to Kirchhoff 's voltage law, the mathematical model of APF is :

$$\begin{cases} L\, di_a/dt = u_a - \mathrm{U}_a - i_a R \\ L\, di_b/dt = u_b - \mathrm{U}_b - i_b R \\ L\, di_c/dt = u_c - \mathrm{U}_c - i_c R \end{cases} \tag{1}$$

In order to convert the mathematical model from the three-phase coordinate system to the two-phase coordinate system, the Clarke transformation of equation (1) can be obtained :

$$\begin{cases} L\, di_\alpha/dt = u_\alpha - \mathrm{U}_\alpha - i_\alpha R \\ L\, di_\beta/dt = u_\beta - \mathrm{U}_\beta - i_\beta R \end{cases} \tag{2}$$

In the formula : i_α , i_β , u_α , u_β and e_α , e_β are the three-phase compensation current provided by APF, the three-phase voltage output by the inverter and the three-phase grid voltage components in α , β coordinate systems, respectively.

3. Harmonic suppression strategy of ship electric propulsion system

3.1. Active power filter based on fuzzy PID control

In the face of nonlinear load in ship electric propulsion system, it is impossible to achieve high precision control by using fuzzy theory and PID algorithm alone. In order to improve the control effect of power system, according to the combination optimization theory, combined with the advantages of fuzzy theory and PID algorithm, a control method of power system based on fuzzy theory and PID algorithm is designed. The K_p, K_i and K_d values are optimized online by fuzzy theory to track the state of power system, so that the ship electric propulsion system can be suitable for different working conditions. The control principle is shown in the figure.

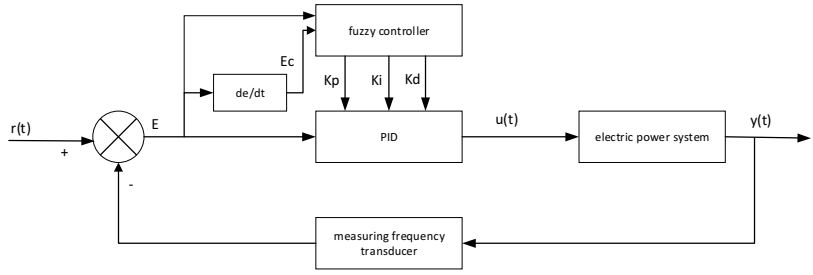

Figure 3. Fuzzy PID Control Block Diagram.

There is a great relationship between K_p, K_i, K_d and e, e_c, the formula is as follows.

$$\begin{aligned} K_p &= K_p^{'} + \Delta K_p = K_p^{'} + \{e, e_c\}_p \\ K_i &= K_i^{'} + \Delta K_i = K_i^{'} + \{e, e_c\}_i \\ K_d &= K_d^{'} + \Delta K_d = K_d^{'} + \{e, e_c\}_d \end{aligned} \tag{3}$$

The pre-setting values of the controller are $K_p^{'}$、$K_i^{'}$、$K_d^{'}$, and the correction values of the parameters are ΔK_p，ΔK_i、ΔK_d. The fuzzy PID controller first detects e and e_c in real time to ensure accurate detection, and corrects ΔK_p，ΔK_i and ΔK_d in real time,

so that e and ec can meet the needs of Kp, Ki and Kd changes when they change. The correction of the parameters is based on the set fuzzy control rule table.

3.2. APF Model Predictive Control (MPC)

Model Predictive Control (MPC) is a predictive control method based on discretized mathematical models. It is a novel digital control technique. The essence of MPC is an online optimization-based control approach, offering advantages such as fast response and adaptability to changing control objectives.

3.2.1 APF Model Predictive Current Control

In the three-phase three-wire parallel active power filter (APF), the switching states of the three-phase inverter are limited, and the optimal switching state is selected from the limited set of switching states within one sampling period. This control method follows the conventional finite-set model predictive control approach. For APF model predictive current control, it typically involves two main steps: prediction model establishment and rolling optimization.

Prediction Model Establishment: To obtain the predicted compensation current for the next inverter output, it is necessary to establish a prediction model. Based on the mathematical model of the APF, the prediction model can be represented as follows:

$$\begin{cases} u_{ca} = e_a + L\frac{di_{ca}}{dt} + i_{ca}R \\ u_{cb} = e_b + L\frac{di_{cb}}{dt} + i_{cb}R \\ u_{cc} = e_c + L\frac{di_{cc}}{dt} + i_{cc}R \end{cases} \tag{4}$$

Performing a Clark transformation on Equation (4) and representing it after the transformation can be translated as

$$\begin{cases} u_{c\alpha} = e_\alpha + L\frac{di_{c\alpha}}{dt} + i_{c\alpha}R \\ u_{c\beta} = e_\beta + L\frac{di_{c\beta}}{dt} + i_{c\beta}R \end{cases} \tag{5}$$

APF Model Predictive Current Control (MPCC) requires the establishment of a discrete mathematical model for APF. Therefore, discretize equation (5), set the system sampling time to T_s, and expand it using Euler forward difference as follows

$$\begin{cases} i_{p\alpha}(k+1) = \frac{T_s}{L}[u_{c\alpha}(k) - e_\alpha(k) - i_{c\alpha}(k)R] + i_{c\alpha}(k) \\ i_{p\beta}(k+1) = \frac{T_s}{L}\left[u_{c\beta}(k) - e_\beta(k) - i_{c\beta}(k)R\right] + i_{c\beta}(k) \end{cases} \tag{6}$$

Among them, $u_{c\alpha}(k)$ $u_{c\beta}(k)$ are the sampling values of the inverter output voltage at time k . $e_\alpha(k)$、$e_\beta(k)$ is the sampling value of the grid voltage at the time k . $i_{c\alpha}(k)$、$i_{c\beta}(k)$ is the sampling value of the compensation current at the moment $k+1$. $i_{p\alpha}(k+1)$、$i_{p\beta}(k+1)$ is the predicted value of compensation current at time $k+1$. After sorting, the relationship between the predicted compensation current at time k and the sampling values of various variables at time $k+1$ can be obtained as follows:

$$\begin{cases} i_{p\alpha}(k+1) = \frac{T_s}{L}[u_{c\alpha}(k) - e_\alpha(k) - i_{c\alpha}(k)R] + i_{c\alpha}(k) \\ i_{p\beta}(k+1) = \frac{T_s}{L}\left[u_{c\beta}(k) - e_\beta(k) - i_{c\beta}(k)R\right] + i_{c\beta}(k) \end{cases} \tag{7}$$

According to equation (7), it can be seen that using the grid voltage sampling value, compensating for the current sampling value and inverter AC side transmission. By obtaining the voltage sampling value, the predicted compensation current at the next sampling time can be obtained.

3.2.2 APF Model Predictive Voltage Control

Substitute the output voltage vectors of inverters with different effects into equation (7) to obtain the predicted compensation current provided by APF at the time $k+1$. Due to the high sampling frequency of MPC, in order to reduce the number of calculations for the compensation current prediction value provided by APF in one sampling cycle, shorten the program running time, and improve the system's response speed in one sampling cycle, APF Model Predictive Voltage Control (MPVC) changes the variables in the value function based on the advantage of variable MPC control objectives, Change the compensation current provided by APF in the value function to the inverter output voltage. According to equation (7), it is assumed that the predicted compensation current provided by APF at time $k+1$ is equal to the reference compensation current provided by APF obtained from equation.

$$\begin{cases} i_{c\alpha}^{*}(k+1) = 3i_{c\alpha}^{*}(k) - 3i_{c\alpha}^{*}(k-1) + i_{c\alpha}^{*}(k-2) = i_{p\alpha}(k+1) \\ i_{c\beta}^{*}(k+1) = 3i_{c\beta}^{*}(k) - 3i_{c\beta}^{*}(k-1) + i_{c\beta}^{*}(k-2) = i_{p\beta}(k+1) \end{cases} \tag{8}$$

The value function that allows the output voltage of the inverter to be used as the control objective is

$$g = \frac{T_S^2}{L^2}\left[u_{c\alpha}^{*}(k) - u_{c\alpha}(k)\right]^2 + \frac{T_S^2}{L^2}\left[u_{c\beta}^{*}(k) - u_{c\beta}(k)\right]^2 \tag{9}$$

At this point, by controlling the output voltage of the inverter, the compensation current provided by the APF can be controlled. This process reduces the process of converting the output voltage of the inverter into the predicted compensation current provided by the APF through equation (7) within one sampling period, simplifies the computational complexity within one sampling period, and improves the system response speed.

In APF MPVC, the tracking control of harmonic current is indirectly achieved by changing the variables in the value function, and the process of calculating the predicted compensation current provided by APF through the inverter output voltage is omitted. Reduced the computation time within the sampling period and improved response speed. The sampling frequency of MPC control is high and the sampling period is short. APF harmonic current control requires high real-time performance, and the control algorithm needs to be further optimized to reduce the computational pressure of the main control chip. Moreover, the problem with high sampling frequency is that the switching frequency increases and the switching loss increases. To address the above issues, the process of rolling optimization is further optimized. Based on the idea of space vector pulse width modulation (SVPWM), the sector in the inverter output reference voltage vector graph where the voltage vector corresponding to the inverter output reference value is located is judged. The effective vector and zero vector adjacent to the voltage vector corresponding to the inverter output voltage reference value are selected as candidate vectors for rolling optimization.

Four alternative inverter output voltage reference vectors were selected, and during the rolling optimization process, the number of calculations to obtain the minimum value of the value function was reduced from 7 to 4, taking into account both zero vectors with

the same effect. Simplified the rolling optimization process. To solve the problem of high switching frequency and high switching loss caused by high sampling frequency, and to achieve multi-objective control of compensating current tracking and switching frequency, a switching frequency control term is added to the value function to add switching frequency constraints when selecting the optimal voltage vector among alternative voltage vectors. The newly established value function :

$$g = \frac{T_s^2}{L^2}[u_{c\alpha}^*(k) - u_{c\alpha}(k)]^2 + \frac{T_s^2}{L^2}\left[u_{c\beta}^*(k) - u_{c\beta}(k)\right]^2 + K_s\{|S_a^*(k) - S_a(k-1)| + |S_b^*(k) - S_b(k-1)| + |S_c^*(k) - S_c(k-1)|\} \quad (10)$$

Among them, S_a^*、$S_b^*(k)$ and $S_c^*(k)$ is the switching state of each bridge arm corresponding to the reference vector inverter at time k,$S_a(k-1)$、$S_b(k-1)$、$S_c(k-1)$ is the switching state of each bridge arm corresponding to the inverter in the previous sampling period, and K_s is the weight coefficient. By adjusting the weight coefficient K_s, the weight occupied by compensating current tracking control and switching frequency control during the online optimization process can be controlled to balance the effectiveness of compensating current tracking control and switching frequency control. The value of K_s is usually determined through multiple simulations and experimental results. The improved APF MPVC principle is shown in Figure 4.

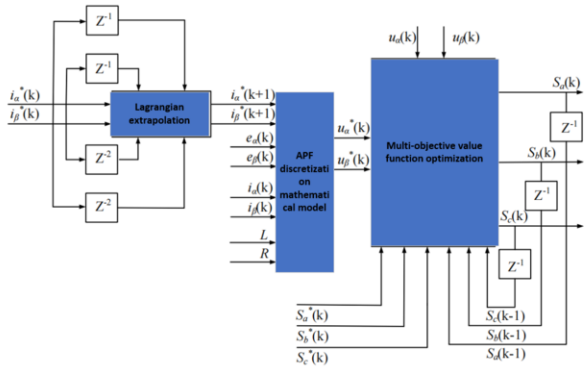

Figure 4 Schematic Diagram of Improved APF MPVC

4. Simulation verification and analysis

4.1. Simulation Results and Analysis of Fuzzy PID Active Power Filter

Harmonics are components of a current or voltage waveform where the frequency is a multiple of the fundamental frequency (usually the grid frequency). These harmonic currents can cause voltage distortion in the power grid, affecting the stability and reliability of the power system. Harmonics may also cause interference to other equipment and users. Therefore, the impact of nonlinear loads on harmonics in the power grid is very important.

Due to the different operating conditions of the equipment in the ship's electric propulsion system, the loads in the circuit will also vary, and the harmonic components are relatively complex. Compared with traditional control methods, for the fuzzy PID

control strategy, the harmonic content of the system under cruise conditions and platform lifting conditions was analyzed separately.

Under cruising conditions, three 4400kw generators and one 1600kw generator operate on the grid, while two main propulsion motors with a power of 2300kw and a low-voltage load of 1500kw operate on the grid. The results of using fuzzy PID active filter before and after harmonic suppression in ship electric propulsion system are shown in Figure 5 and Figure 6.

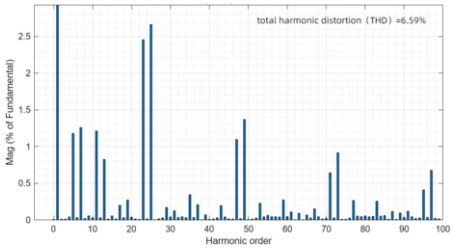

Figure 5. The harmonic content before suppressing the fuzzy PID active filter under cruising conditions.

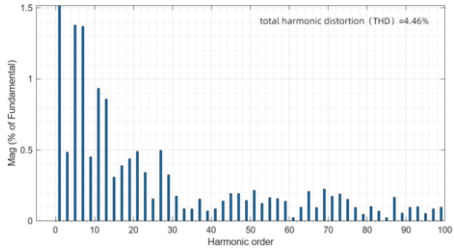

Figure 6. The harmonic content after suppressing the fuzzy PID active filter under cruising conditions.

Two 4400kw generators, one 500kw elevator, and a low voltage load of 1800kw are operating on the grid under the condition of lifting the platform. The results of using fuzzy PID active filter before and after harmonic suppression in ship electric propulsion system are shown in Figure 7 and Figure 8.

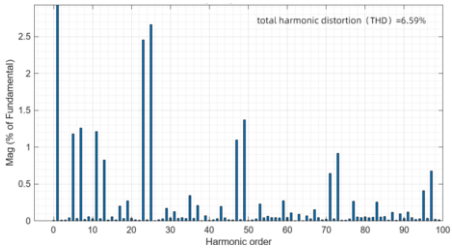

Figure 7. Harmonic content before suppression of fuzzy PID active filter under elevated platform operating conditions.

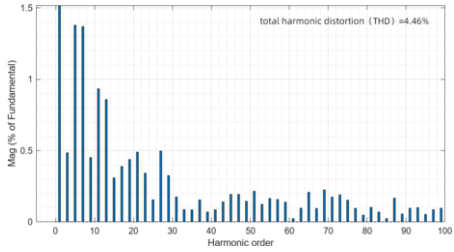

Figure 8. The Harmonic Content of Fuzzy PID Active Filter Suppressed under Elevated Platform Condition.

Figures 5 and 7 show the harmonic content of the ship's electric propulsion system under cruising and platform raising conditions, respectively. Figures 6 and 8 show the harmonic content after suppressing using fuzzy PID active filters under cruising and platform raising conditions, respectively. The voltage distortion rate THD before cruise control is suppressed is 6.59%, and the maximum single harmonic value is 2.75%. After suppression, the voltage distortion rate THD is 4.46%, and the maximum single harmonic value is 1.76%; The voltage distortion rate THD before suppression under elevated platform conditions is 7.36%, and the maximum single harmonic value is 1.97%. After suppression, the voltage distortion rate THD is 4.54%, and the maximum single harmonic value is 1.88%. From the figure, it can be seen that the total voltage distortion rate of both operating conditions after using fuzzy PID active filter suppression does not exceed 5%, and the maximum value of single harmonic does not exceed 3%, meeting the standards of China Classification Society for total harmonic distortion rate.

4.2. Simulation Results and Analysis of Model Predictive Control Active Power Filter

Due to the complexity of harmonic components in equipment such as the main propulsion motor, the frequency converter of the full rotation thruster motor, and the frequency converter of the pile leg lifting device air compressor under the lifting platform working condition during cruising, not only integer multiples of harmonics are included, but also fractional harmonics. These types of devices generally have higher power, and with the increasing use of frequency conversion speed regulation, the harmonics caused to the power grid are also increasing. This article establishes a Matlab simulation model for parallel active power filters based on the topology structure of three-phase three-wire parallel active power filters (Figure 2) and the control system of active power filters (Figure 4). The system parameters of the active power filter are as follows:

Table 1. Active Power Filter System Parameters

Grid line voltage	resistance	inductance	L	R	C	U_{dc}	sampling frequency	K_s
710V	15Ω	3mH	1.5mH	0.15Ω	3300	1050V	15kHz	0.15

The harmonic content after using APF MPVC suppression under cruise and platform up conditions is as follows:

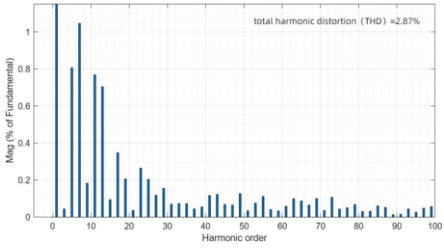

Figure 9. Model predictive control of harmonic content after active filter suppression under cruising conditions.

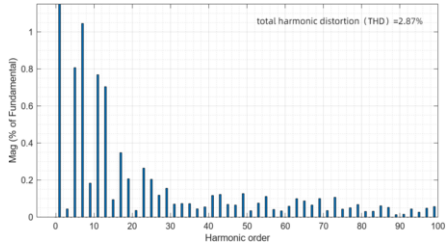

Figure 10. Model predictive control of harmonic content after active filter suppression under elevated platform operating conditions.

Under cruising conditions, the model predictive control active filter is used to suppress the voltage distortion rate THD=2.87%, and the maximum single harmonic value is 1.73%; Under elevated platform conditions, the model predictive control active filter is used to suppress the voltage distortion rate THD=3.39%, and the maximum single harmonic value is 1.40%. From the figure, it can be seen that the total voltage distortion rate of both operating conditions after using model predictive control active filter suppression does not exceed 5%, and the maximum value of single harmonic does not exceed 3%, meeting the standards of China Classification Society for total harmonic distortion rate, and the suppression effect is better than that of fuzzy PID active filter.

Table 2. Parallel Active Power Filter Using Fuzzy PID and Model Predictive Control under Different Operating Conditions Comparison Table for Harmonic Suppression

	Different working conditions	Fuzzy PID use	Model Predictive Control use	Optimization and improvement
Total voltage distortion rate	Cruise condition	4.46%	2.87%	1.59%
	Upgrade platform condition	4.54%	3.39%	1.15%
Maximum single harmonic value	Different working conditions	Fuzzy PID use	Model Predictive Control use	Optimization and improvement
	Cruise condition	1.76s	1.73%	0.03%
	Upgrade platform condition	1.88s	1.40%	0.48%

From the comparison table of harmonic suppression using fuzzy PID and model predictive control in parallel active power filters under different operating conditions, it can be seen that the parallel active power filters using fuzzy PID and model predictive control have significant suppression effects on harmonics under both cruising and platform raising operating conditions. The parallel active power filter with model predictive control has a better suppression effect on harmonics than the fuzzy PID active power filter. The total voltage distortion rate can be improved by 1.15% -1.19%, and the maximum single harmonic can be improved by 0.03% -0.48%. Ensure that the total voltage distortion rate under both cruising and platform lifting conditions is not more than 5%, and the maximum single harmonic does not exceed 3%, meeting the standards of China Classification Society for total harmonic distortion. The suppression effect of model predictive control is good, with lower suppression effects both in terms of total voltage distortion rate and maximum single harmonic.

5. Conclusion

Under the MATLAB/SIMULINK platform, active filter harmonic suppression measures were used to simulate the harmonic suppression of the cruise and platform up conditions of a large capacity AC integrated power system. The modeling methods and parameter design of fuzzy PID control and fuzzy model predictive control were also provided. Simulation verification was conducted on the suppression of power supply voltage distortion. By comparing the harmonic content of the bus after harmonic suppression, it can be seen that using fuzzy PID control and model predictive control for active filters can achieve good harmonic suppression effects in the case of power supply voltage distortion.

Under cruising conditions, fuzzy PID control and model predictive control active filters can suppress the total voltage distortion rate of the ship's power system by 2.13% and 3.72%, respectively, and have a suppression effect of 0.99% and 1.02% on the maximum single harmonic, respectively; Under elevated platform conditions, fuzzy PID control and model predictive control active filters can suppress the total voltage distortion rate of the ship's power system by 2.82% and 3.97%, respectively, and have suppression effects on the maximum single harmonic by 0.09% and 0.57%, respectively; Compared to the fuzzy PID control active power filter, the model predictive control active power filter has a 1.59% and 0.03% improvement in suppressing total voltage distortion rate and maximum single harmonic under cruise conditions, and a 1.15% and 0.48% improvement under elevated platform conditions; Therefore, active power filters

based on model predictive control have more significant suppression effects in terms of total voltage distortion rate and maximum single harmonic.

References

[1] B.Fan,Q.Wang,Burgos R,et al.Adaptive Hysteresis Current Based ZVS Modu lation Voltage Gain Compensation for High-Frequency Three-Phase Converters[J].IEEE Transactions on Power Electronics,2021,36(1):1143-1156.

[2] [1] Bian Qingchao, Hu Ming, Yang Peihao. Research on grid connected inverter system based on PI+adaptive internal model repetitive control [J]. Journal of Power Supply, 2021,19 (01): 97-106. DOI: 10.13234/j.issn.2095-2805.2021.1.97.

[3] C.Tan,Q Chen,K Zhou,et al.A Simple High-Performance Current Control Strategy for V2G Three-Phase Four-Leg Inverter With LCL Filter[J].IEEE Transactions on Transportation Electrification,2019,5(03):695-701.

[4] H.Geng,Z .Zheng,T.Zou,et al.Fast Repetitive Control With Harmonic Correction Loops for Shunt Active Power Filter Applied in Weak Grid[J].IEEE Transactions on Industry Applications,2019,55(3):3198-3206.

[5] Geng Xiaofu.Research on harmonic detection and suppression methods in power system [D].Dalian University of Technology, 2016.

[6] Li Guangbing, Pu Yuxing. Research on a novel harmonic detection method for parallel active power filters [J]. Power Capacitors and Reactive Power Compensation, 2018,39 (4): 7-11.

[7] Liu Changliang. Application of multiphase rectification technology in harmonic suppression of large ships [J].ship science and technology, 2015.1 (37) : 148-151.

[8] Zheng Ying. Research and development of active power filter device for small electric ship propulsion system [D].Xiamen : Jimei University, 2013.

[9] Wang Gechao.Research on harmonic suppression technology of ship power system [D].Jiangsu University of Science and Technology, 2016.

[10] Liu Peizhe, Zhao Hong, Guo Chen. Application of neural fuzzy control APF in electric propulsion ship [J].Journal of Dalian Maritime University, 2013, 1 (39) : 107-110.

[11] Liu Jinkun. Sliding mode variable structure control MATLAB simulation [M].Beijing:Tsinghua University Press, 2012 : 46-52.

[12] Li Chunhua, Dai Yuewei, Chen Jiahong. Simulation study of SAPF based on FSMC applied to harmonic suppression technology of ship power grid [J].Ship Engineering, 2015,56(9):53-57.

[13] Wang Lin.Study on repetitive control strategy of three-phase photovoltaic grid-connected inverter [D].Shandong University, 2016.

[14] SHA Deshang, WU Dan, LIAO Xiaozhong School of Automation, Beijing Institute of Technology, Beijing 100081, P.R.China. Implementation of Three-Phase Grid Connected Inverters with SVPWM-Based Repetitive Control[A]. 2010,51(4):4978-4981.

[15] He Y, Liu J , Wang Z ,et al.An Improved Repetitive Control for Active Power Filters with Three-Level NPC Inverter[C]//IEEE Applied Power Electronics Conference & Exposition.IEEE, 2009.DOI:10.1109/APEC.2009.4802879.

Fuzzy Systems and Data Mining IX
A.J. Tallón-Ballesteros and R. Beltrán-Barba (Eds.)

doi:10.3233/FAIA231083

Research on Simulation Evaluation of Stability of Integrated Power System Network

Tuo WU[a], Yanhe YIN[b,1] and Tong LIU[c]
[a] *Marine Design and Research Institute of China, Shanghai 200000, China*
[b] *Wuhan Marine Electric Propulsion Research Institute, Wuhan 430064, China*
[c] *College of Intelligent Systems Science and Engineering, Harbin Engineering University, Harbin 150001, China*

Abstract. The ship's medium-voltage AC integrated power system, hereinafter referred to as the integrated power system, is the core part of the ship's power system. Its networking method and operational stability are crucial to the ship's power supply and navigation safety. Currently, as the power load of ships increases and the complexity of the power system increases, the integrated power system is facing many problems and challenges, including how to select the topology of the integrated power system while taking into account the requirements of stable economy, and the impact of sudden changes in load on system stability. System voltage stability when impact or short-circuit fault occurs, whether the relay protection system has sufficient selectivity, etc. Therefore, this study aims to study the stable operation of integrated power system networking through simulation evaluation.

Keywords. integrated power system; topological structure; load mutation; short-circuit fault; relay protection

1. Introduction

With the increasing power load of ships and the increasing complexity of electrical equipment, the ship's integrated power system has become the "central nervous system" of the ship 12. Among them, the medium-voltage power supply and distribution network, as an important part of the ship's power system 12, is responsible for supplying power to various ship systems and equipment. Its network stability and reliability are of great significance to the normal operation and safe navigation of ships. Therefore, studying the topology and network operation mode of ship medium-voltage power supply and distribution network 12 is of great significance for optimizing the performance of the power system and improving the reliability and stability of the power system.

As the core part of the ship's power system, the ship's medium-voltage AC integrated power system is crucial to the ship's power supply and navigation safety 12. Currently, with the increase in ship power load and the complexity of the power system,

[1] Corresponding Author: Yanhe YIN is with the Wuhan Marine Electric Propulsion Research Institute, Wuhan 430064, China (e-mail: yinyh712@163.com).

the integrated power system is facing many problems and challenges, such as how to select the topology of the integrated power system while taking into account the requirements of stable economy 12, and the impact of sudden load changes on system stability. impact 12, system voltage stability when a short-circuit fault occurs 12, whether the relay protection system has sufficient selectivity, etc. 12. Therefore, this study aims to study the stable operation of integrated power system networking through simulation evaluation.

In terms of solving the problem of stable operation of integrated power system networking, many domestic and foreign scholars have done a lot of research. Reference 12 proposed sewing training-based optimization (STBO). This algorithm iteratively optimizes control parameters by using a set of candidate solutions. , to find the optimal solution set that minimizes frequency deviation and enhances system stability. Literature 12 introduced Caputo's fractional-order definition into a ship power system with two parallel generators, and constructed a fractional-order ship power system with extreme multi-stability. Literature 12 uses a double closed-loop control method combined with a pulse width modulation algorithm (PWM) to control the energy storage system to smooth the power fluctuations caused by the electric propulsion system. Literature 12 modeled FC-TCR and designed a closed-loop control algorithm to ensure voltage stability to evaluate and compare the performance of PPF and FC-TCR compensators in reducing high-power SPS harmonics and improving voltage stability. Literature 12 implements a dynamic compensation device that can convert the EEN into a flexible network. When the EEN is affected by small or large disturbances, the performance of the power grid on the ship is improved. These improvements are achieved by integrating automatic voltage regulators to ensure temporary This is achieved by stabilizing the state voltage.

This study mainly uses simulation software for simulation, and combines the parameters and conditions of the actual ship power system to establish a simulation model of the integrated power system, conduct simulation experiments and data analysis, and evaluate the stability and reliability of the integrated power system network through simulation. , determine the stability and reliability of the system design scheme and ensure the safe navigation of the ship. Mainly includes integrated power system simulation modeling, integrated power system power flow calculation under different working conditions, focusing on integrated power system network topology selection, integrated power system stability under load mutation conditions, selective evaluation of relay protection schemes, Problems such as voltage stability analysis of integrated power systems under short circuit faults.

2. Network topology research

In the comprehensive power system of the slipway, the medium voltage power supply and distribution network is one of the core components of the ship's power system. The medium-voltage power supply and distribution network is mainly responsible for boosting the electric energy generated by the ship's generator set through the transformer and supplying various ship electrical equipment [5]. At the same time, it also needs to meet the different power requirements of the ship's electrical equipment. Therefore, the medium-voltage power supply and distribution network The topological structure is of extremely high importance.

Choose a tree layout as the layout method. The tree wiring method can improve the reliability of the system by providing multiple backup paths. If one branch fails, other branches can still work normally. Tree routing makes it easier to add new branches and connections. This flexibility can provide convenience when new equipment needs to be added to the slipway or the system architecture needs to be adjusted. Tree wiring can make system management and maintenance more decentralized because each branch can be managed independently. This simplifies troubleshooting and maintenance because different branches can operate independently without affecting the entire system.

The connection method should be series connection.

The cable wiring method should be centralized wiring. The electric energy generated by the ship's generator set is boosted through the transformer and then uniformly supplied to each ship's electrical equipment. By adopting centralized wiring, Slip A can simplify the wiring structure, reduce material and installation costs, and simplify the wiring design and management of the entire system. At the same time, the centralized wiring method can concentrate all connections in one place, saving space and improving the compactness of the layout. In addition, centralized wiring can make the management of the entire system more centralized and simplified. All connections are in one place, making troubleshooting, maintenance and management easier. This centralized management approach helps improve system efficiency and reliability. A centralized cabling approach may be more cost-effective in terms of material and installation costs. Tree cabling may require more cables and connectors, increasing cost and maintenance complexity.

3. Network running stability analysis simulation modeling

Three-phase alternating current is used in most ships, and diesel engines and synchronous generators are generally used as the main power supply equipment of the ship to provide electrical energy for the ship load. The synchronous generator converts the mechanical energy of the diesel engine into electrical energy, and the performance of the power generation equipment determines the performance of the power grid. Therefore, only a suitable mathematical model can correctly reflect the dynamic characteristics and adjustment accuracy of the system. For this reason, the most important thing when studying a system is to establish a suitable model. Mathematical models summarize the changing laws of dynamic systems by using mathematical expressions. The coefficient matrix of the state equation of the synchronous generator is a time-varying matrix, and since the load carried by the ship power grid is generally not completely symmetrical, the stator generally works in an asymmetric state. The rotor of a synchronous motor is symmetrical about the dq axis, so when establishing a mathematical model of the motor, it is usually converted to dq coordinates for analysis.

The synchronous generator is a high-order, nonlinear, strongly coupled multi-variable system. In the process of establishing the mathematical model of the synchronous generator, simplifying assumptions are made: the magnetic saturation phenomenon is ignored; the three-phase windings of the stator are symmetrically distributed; the rotor has a direct axis and The cross-axis structure is symmetrical; the stator magnetic potential changes sinusoidally in space; high-order harmonics are ignored (the role of the groove is ignored). The fifth-order practical model of the generator selected for this study is as follows.

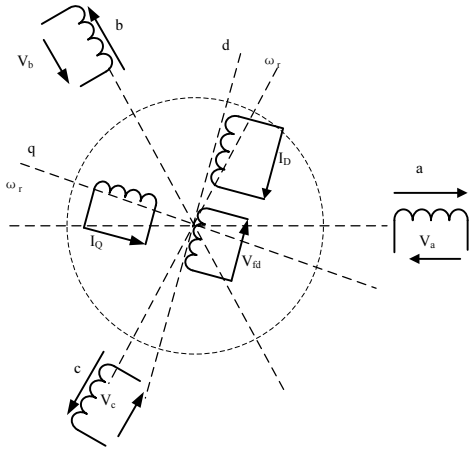

Fig.1 Structure diagram of synchronous generator

The mathematical expression of the direct axis (D-axis) of the synchronous generator is:

$$T_{d0}^{'}\frac{dE_q^{'}}{dt}=E_f-\frac{X_d-X_d^{'}}{X_d^{'}-X_d^{''}}E_q^{'}+\frac{X_d-X_d^{'}}{X_d^{'}-X_d^{''}}E_q^{''} \tag{1}$$

$$T_{d0}^{''}\frac{dE_q^{''}}{dt}=E_q^{'}-E_q^{''}-(X_d-X_d^{'})i_d \tag{2}$$

$$u_q=E_q^{''}-r_a i_d-X_d^{''}i_d \tag{3}$$

The mathematical expression of the quadrature axis (q axis) of a synchronous generator is:

$$T_{q0}^{''}\frac{dE_d^{''}}{dt}=-E_d^{''}+(X_q-X_q^{''})i_q \tag{4}$$

$$u_d=E_d^{''}-r_a i_d+X_q^{''}i_q \tag{5}$$

Rotor motion equation:

$$J\frac{d\omega_m}{dt}=T_m-T_e \tag{6}$$

$$\frac{d\alpha_m}{dt}=\omega_m \tag{7}$$

In the formula: T′d0 and T″d0 represent the transient and sub-transient open circuit time constants on the direct axis, T″q0 represents the sub-transient open circuit time constant on the quadrature axis; Xd, X′d, X″d represents the armature reactance, transient reactance and sub-transient reactance on the direct axis of the synchronous generator, and Xq and X″q represent the armature reactance and sub-transient reactance

on the quadrature axis. E′d represents the direct-axis transient electromotive force, E′q represents the quadrature-axis transient electromotive force, E″q represents the quadrature-axis super-transient electromotive force, Ud is the d-axis output voltage, Uq is the q-axis output voltage, and ra is the stator winding. value.

4. Selective protection analysis

4.1. System description

This chapter analyzes the selective protection of the 6.6kV and 380V power distribution system of the integrated power system of A slipway based on the single-line diagram of the whole ship's power system, the load calculation sheet of the whole ship's power system, and the short-circuit current calculation sheet of this project provided by the overall , forming a selective protection analysis report for the whole ship's power distribution system.

The single-line diagram of the comprehensive electric propulsion system of slipway A is shown in the figure 2 below. The system mainly includes the following contents:

There are 5 sets of diesel generator sets, 4 sets of 6600V, 50Hz, 4400kW units, 1 set of 6600V, 50Hz, 1600kW auxiliary generator sets, all 5 sets are equipped with grounding resistors, 1#, 2# main units and auxiliary units are connected to the port side medium voltage distribution Board busbar, 3# and 4# main unit are connected to the starboard medium voltage distribution board busbar;

2 sets of 6600V marine medium-voltage distribution boards (the port and starboard medium-voltage distribution boards are connected through bus tie breakers). The distribution boards are connected to the following equipment through cables:

2 sets of virtual 24-pulse shaft propeller main propulsion branches: each set has 1 phase-shifting transformer (6600V/2 × 1350V, Dd0Y11 (± 7.5 ° respectively), 4200kVA), 1 12-pulse main propulsion inverter (3000kW), 1 main propulsion motor (3000kW, 130rpm);

2 sets of virtual 24-pulse rudder propeller main propulsion branches: each set has 1 phase-shifting transformer (6600V/2 × 1350V, Dd0Y11 (± 7.5 ° respectively), 5500kVA), 1 12-pulse rudder propeller inverter (4000kW), 1 rudder propeller propulsion motor (4000kW, 1000rpm);

3 sets of 12-pulse side propulsion branches: each set has 1 soft starter and 1 side propulsion motor (2200kW, 1000rpm);

8 sets of 12-pulse lifting systems; each set has 1 phase-shifting transformer (6600V/2×400V, Dd0Y11, 1000kVA) and 1 12-pulse frequency converter;

2 sets of 12-pulse winch systems; each set has 1 phase-shifting transformer (6600V/2×710V, Dd0Y11, 3000kVA) and 1 12-pulse frequency converter;

2 sets of 12-pulse lifting systems; each set has 1 phase-shifting transformer (6600V/2×690V, Dd0Y11, 2000kVA) and 1 12-pulse frequency converter;

2 sets of daily distribution transformers: 6600V/400V, 50Hz, 2500kVA.

The design of the selective protection scheme of this system mainly targets the generator branch, main propulsion transformer branch, rudder propeller transformer branch, side propulsion motor branch, upgrade system power supply branch, winch

system power supply branch, and hoisting system power supply. Branch circuits, daily distribution transformer branch circuits, etc.

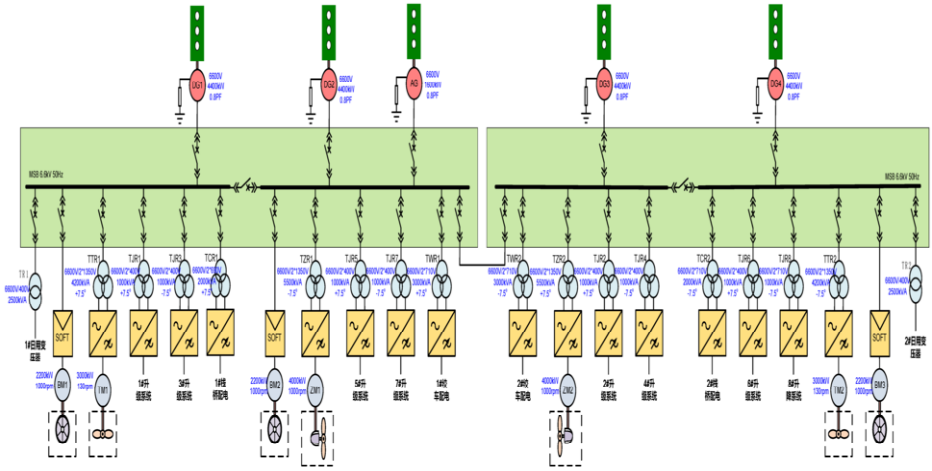

Fig.2 Single line diagram of integrated electric propulsion system

4.2. Circuit breaker and trip selection

According to the short-circuit current calculation sheet and the actual selective protection requirements of the system, the selection of the main comprehensive relay protection devices in the system is as shown in the following table:

Table 1 Main circuit breaker and trip device selection

Protection device name	Circuit breaker type	Comprehensive relay protection device model	remark
No. 1 main generator set	VD4-12/630A	REG630	
No. 2 main generator set	VD4-12/630A	REG630	
No. 3 main generator set	VD4-12/630A	REG630	
No. 4 main generator set	VD4-12/630A	REG630	
Auxiliary generator set	VD4-12/630A	REG630	

Protection device name	Circuit breaker type	Comprehensive relay protection device model	remark
Contact switch breaker	VD4-12/630A	REF615	
Number 1 to 2 main propulsion transformer	VD4-12/630A	RET615	
Number 1 to 2 propeller transformer	VD4-12/630A	RET615	
Soft initiators are pushed on sides 1 to 3	VD4-12/630A	RET615	
1~8 lifting system transformer	VD4-12/630A	RET615	
1~2 hoisting system transformer	VD4-12/630A	RET615	
1~2 winch system transformer	VD4-12/630A	RET615	
1~2 daily distribution transformer	VD4-12/630A	RET615	

4.3. Selective analysis

Take the cooperation between the main generator branch circuit, the contact switch circuit breaker, the primary circuit breaker of the daily distribution transformer, and the secondary circuit breaker of the daily distribution transformer as an example. Selectivity between 6600V equivalent generator branch (2×4400kW=8800kW), tie switch circuit breaker, daily distribution transformer primary circuit breaker, daily distribution transformer secondary circuit breaker (converted to high voltage side) The fit curve is shown in Figure 3. It can be seen from the figure that the protection between the main generator branch, the tie switch circuit breaker, the primary circuit breaker of the daily distribution transformer, and the secondary circuit breaker of the daily distribution transformer is selective.

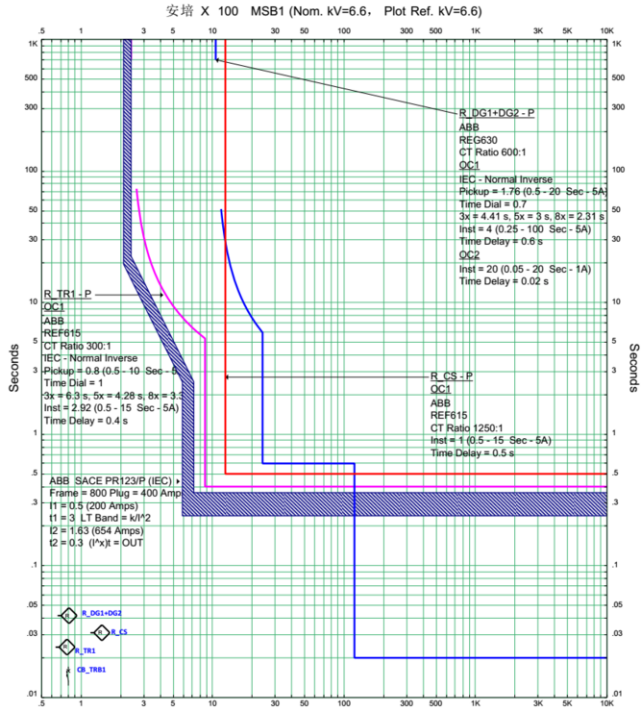

Fig.3 Main generator branch and liaison switch circuit breaker, primary side circuit breaker of daily distribution transformer, secondary side circuit breaker of daily distribution transformer selective protection matching curve

5. Transient performance simulation analysis

5.1. Short-circuit fault and voltage crossing analysis

Under cruising conditions, Shipyard A uses a total of four generators to power the entire medium-voltage system, including three main generators with a rated power of 4400kw and an auxiliary generator with a rated power of 1600kw. Electrical equipment includes two main propulsion motors with a total power of 4666.7kw, two full-rotation thruster motors with a total power of 6222.2kw, and low-voltage load power of 1526.4kw. When a single-phase grounding short-circuit fault occurs, the No. 1 main generator generates a generator-side short-circuit fault and the voltage ride-through simulation is shown in Figure 4. When the short-circuit fault occurs at 0.2s, the three-phase AC bus voltages all drop, but the degree of drop is different due to different types of short-circuit faults. Among them, when the three-phase short-circuit fault occurs, the three-phase bus voltage drops the most seriously, and has almost dropped to For a single-phase grounding short-circuit fault, the bus voltage drops slightly, but the three-phase voltage is seriously unbalanced. This result is consistent with the power system analysis theory. After the 0.7s circuit breaker removes the short-circuit fault after a short operating time, the bus voltage returns to normal.

According to the requirements of IEC62271-1 "High Voltage Switchgear and Control Equipment", the short circuit duration of the ship's integrated power system under the most serious short circuit fault is within 1s, and the recommended time is within 0.5s. According to the above simulation analysis, the ship's integrated power system can restore voltage within 0.5s under the most serious short-circuit fault, which fully meets the requirements of IEC standards and is better than the recommended indicators. Therefore, the slipway meets the stability requirements under short-circuit conditions and has excellent voltage ride-through performance.

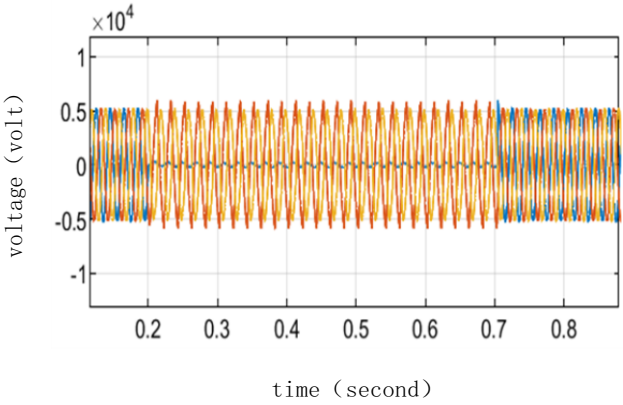

Fig.4 Single-phase grounding short-circuit voltage crossing

5.2. Heavy load starting

Under cruising conditions, Shipyard A uses a total of four generators to power the entire medium-voltage system, including three main generators with a rated power of 4400kw and an auxiliary generator with a rated power of 1600kw. Electrical equipment includes two main propulsion motors with a total power of 4666.7kw, two full-rotation thruster motors with a total power of 6222.2kw, and low-voltage load power of 1526.4kw. Under this load condition, the main propulsion motor starts. At this time, the simulation results of the medium voltage bus voltage are shown in Figure 5. The main thrust motor starts at 0.2s, and the loaded power is 6666.7kw, which causes the voltage of the medium voltage system to drop. After about 0.5s, the voltage rises to a steady state value.

According to IEC61000 "Power Quality Standard", the short-term voltage drop of the integrated power system should be less than 10%, and the recovery time should be less than 10s. Therefore, based on the above analysis, the voltage drop of the shipyard integrated power system due to the startup process of large motor loads fully complies with IEC standards. Stable when starting with large motor loads.

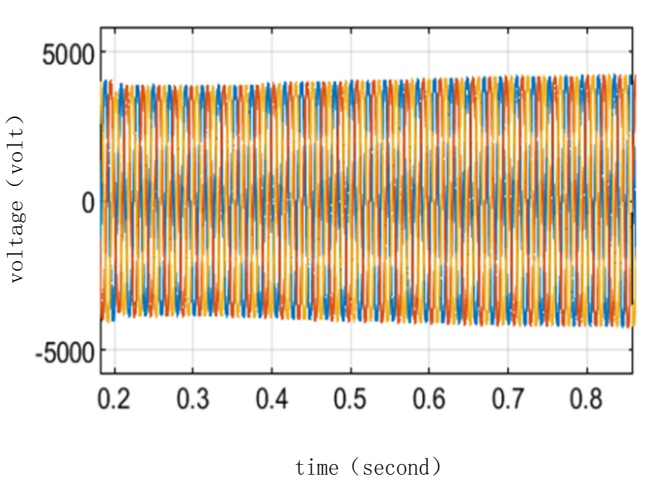

Fig.5 Three-phase voltage of medium voltage system in cruising condition

5.3. Sudden change in propulsion system load

Taking slipway A under full-speed cruising conditions as an example, the propulsion system load suddenly decreases at 1 second, and the bus voltage simulation analysis of the system switching from full-speed cruising conditions to cruising conditions is as follows.

Under full-speed cruising conditions, Shipyard A uses a total of five generators to power the entire medium-voltage system, including four main generators with a rated power of 4400kw and an auxiliary generator with a rated power of 1600kw. Electrical equipment includes two main propulsion motors with a total power of 6666.7kw, two full-rotation thruster motors with a total power of 8888.9kw, and low-voltage load power of 1526.4kw.

Under cruising conditions, Shipyard A uses a total of four generators to power the entire medium-voltage system, including three main generators with a rated power of 4400kw and an auxiliary generator with a rated power of 1600kw. Electrical equipment includes two main propulsion motors with a total power of 4666.7kw, two full-rotation thruster motors with a total power of 6222.2kw, and low-voltage load power of 1526.4kw.

At 1s, the propulsion system load suddenly decreased, the power of the main propulsion motor suddenly decreased to 2000kw, and the power of the full-turn thruster motor suddenly decreased to 2666.7kw. At this time, a 4400kw main generator was unloaded. The simulation curve is shown in Figure 6. The medium-voltage bus voltage rises and then drops to a steady-state value after 0.5s. During this process, the medium-voltage bus voltage will increase compared to the voltage before the propulsion system load suddenly decreases.

According to the CCS ship regulations, the dynamic performance of the marine power system is that the voltage fluctuation range is ±20% and the recovery time is 1.5S; the frequency fluctuation range is ±10% and the recovery time is 5S. Therefore, the slipway integrated power system has very good stability under sudden changes in propulsion load.

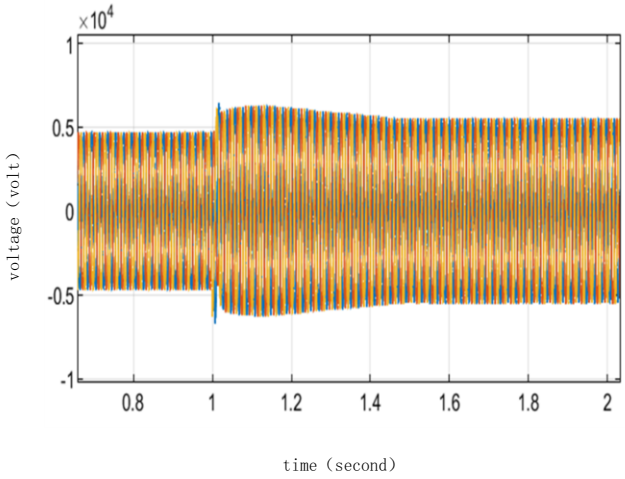

Fig.6 Medium voltage bus bar voltage during sudden load loss of main propulsion system

6. Conclusion

This article first analyzes the topology of the integrated power system of the slipway from the perspective of stability, and obtains the advantages and disadvantages of different topological design methods of the slipway. Integrating economy, the use space of the ship, and maintainability, the analysis concludes that the slipway should adopt a tree layout. method, series connection method, cable layout should adopt centralized layout method.

Based on the above analysis of the topology of the integrated power system of the slipway, and based on the mathematical models of different components of the integrated power system of the slipway, the calculation model of the integrated power system of the slipway is established by using simulation software.

Based on the short circuit calculation results, the setting value calculation and delay curve configuration are performed to obtain the setting table. According to the setting table, the selectivity between different switches under different short-circuit faults is verified. It can be found that the relay protection devices of different lines of the shipyard integrated power system meet the selectivity requirements. When a fault occurs, the fault can be minimized as much as possible. Cut off the range to ensure that the remaining part can operate stably.

By performing short-circuit calculations on the comprehensive power system calculation model of the shipyard under different working conditions and under impact conditions such as large motor load startup, static load startup, propulsion system load mutation, etc., the node voltage can still be maintained to fluctuate within the allowable range and quickly transition to a stable state.

In summary, it can be concluded that the integrated power system of the slipway has good stability.

References

[1] Zhengzhuo L,Wanlu Z,Jian S, et al. Ship Integrated Power System reconfiguration research under partia l observation[J]. Energy Reports,2022,8(S5):444-452.

[2] Sándor A K,Bálint H. Formulation of reference network models for the Hungarian medium voltage distri bution level[J]. Sustainable Energy, Grids and Networks,2022,31:29-33.

[3] Elkadeem M,Alaam M,Azmy M A. Improving performance of underground MV distribution networks u sing distribution automation system: A case study[J]. Ain Shams Engineering Journal,2016,9(4):469-48 1.

[4] Qi Q,Long C,Wu J, et al. Impacts of a medium voltage direct current link on the performance of electric al distribution networks[J]. Applied Energy,2018,230:175-188.

[5] Jiahui J,Yonghui L,Peiyue L, et al. Cooperative Resilience of Cyber–Physical Power Systems Under Hy brid Attacks via Dynamic Topology[J]. Frontiers in Energy Research,2022,10:2296-5986.

[6] Yao N,Zhang Z,Wang Z. A research on closed-loop control strategy for single-phase off-grid inverter un der abrupt load variation[J]. CIRP Annals,2020,20(1)126-132.

[7] Technology; Findings from Nanyang Technological University in the Area of Technology Described (S hort-circuit Fault Management In Dc Electric Ship Propulsion System: Protection Requirements, Revie w of Existing Technologies and Future Research Trends)[J]. Journal of Engineering,2019:1945-8711.

[8] Kalyabin V Y,Gusev E V,Bochkarev N V. Substantiation of requirements to selectivity of relay protecti on of ship power systems[J]. Russian Electrical Engineering,2011,82(7):1934-8010.

[9] Amil D. Optimized cascaded controller for frequency stabilization of marine microgrid system[J]. Appli ed Energy,2023,350:1872-9118.

[10] Zhang,Haoyu,Sun, et al. A fractional-order ship power system with extreme multistability[J]. Nonlinea r Dynamics,2021,106(1):1-14.

[11] Peng B,Wanting W. Stability Improvement of Electric Ship Propulsion System Using Supercapacitor [J]. Journal of Physics: Conference Series,2021,203(1):1742-6596.

[12] Yacine T,Lien C S,Abderezak L, et al. Design of Cost-Effective Compensators to Enhance Voltage Sta bility and Harmonics Contamination of High-Power More Electric Marine Vessels[J]. IEEE TRANSAC TIONS ON INDUSTRY APPLICATIONS,2021,57(4):4130-4142.

[13] Benmahdjoub A M,Mezouar A,Bossche D V A, et al. Dynamic voltage stability for embedded electrica l networks in marine vessels using FACTS devices[J]. International Journal of Dynamics and Control,20 21,9(4)1-17.

Fuzzy Systems and Data Mining IX
A.J. Tallón-Ballesteros and R. Beltrán-Barba (Eds.)

doi:10.3233/FAIA231084

A Complexity Measure for Data Classification Based on KNN with Dynamic Optimal K-Value Finding

Qiangkui Leng[1] , Liang Zhou and Xiangfu Meng
College of Electronics and Information Engineering, Liaoning Technical University, Huludao, Liaoning 125105, China

Abstract. The outcome of data classification is affected not only by the goodness of the classifier, but also by the complexity of the data itself. As a result, quantifying the complexity of the data itself can serve as a reference point for evaluating categorization models. Current approaches to quantifying data complexity overlook the significance of local data complexity in favor of a global viewpoint. In this research, we present a KNN-based data classification complexity measure with dynamic optimisation k-value (C^2M_kNN) that gives greater weight to border sample classification difficulty. First, using dynamic optimization, the best k-value for k-Nearest-Neighbors is determined for each dataset. The samples that have a significant impact on classification complexity are next filtered by the kNN algorithm, and the classification complexity of the data is finally assessed. Based on created and real datasets, C^2M_kNN performs better in experiments than 11 traditional data categorization complexity metrics.

Keywords. Machine learning, data classification, data complexity, k-nearest-neighbors, boundary sample

1. Introduction

Data classification is an important part of machine learning research that aims to build classification models by learning the principles of mapping current data to class labels, which are then used to predict the classes of unknown data. While studying the model is important, performance is also determined by data. Because the learning ability of a given model is fixed, model learning is dependent on the data. This begs the question of whether a model works best when the results of the categorization are ambiguous. Furthermore, the standards now in use for evaluating a model's capacity for generalization are still debatable[1].

In practical activities, we frequently observe that a classifier performs optimally in one task but struggles to get the best results in another. This does not explain the classifier's lack of robustness because the complexity of the data itself limits the classification results in addition to the classifier's capacity to model it. An precise assessment of this intrinsic data complexity might be a valuable point of reference for

[1] Corresponding Author, Qiangkui Leng, College of Electronics and Information Engineering, Liaoning Technical University, Huludao, Liaoning 125105, China. Email: lqk_306@163.com

assessing classification models. This data intrinsic complexity that is involved in the classification process is referred to as data classification complexity in this research. In a narrow sense, data categorization complexity is also known as data separability, which characterizes how sample points from distinct classes mix with one another[2].

At present, there are multiple traditional techniques to measure the intricacy of data classification. The directional-vector maximum fisher's discriminant ratio (F1V) seeks a vector that divides two classes once data is projected onto it[3]. The metric known as maximum individual feature efficiency (F3) evaluates the effectiveness of every feature in district classification by taking into account the highest value among all characteristics. F4 evaluates the rate of data samples that are finally left behind when selecting the most discriminative features based on F3 and de-duplicates the dataset based on feature filtering. One metric used to determine the misclassification rate of SVM classifiers is the error rate of linear classifiers (L2). The non-linearity of a linear classifier (L3) is determined by linearly interpolating the original data to create a new dataset, training the classifier on the original dataset, and then measuring the error using the new dataset[4]. The misclassification rate of a 1NN classifier, as determined by the leave-one-out approach, is represented by the error rate of the nearest neighbor classifier (N3) metric. NN classifiers are used in place of linear classifiers in the non-linearity of the nearest neighbor classifier (N4) metric, which is comparable to L3. The data is used to create a data graph, and each vertex's clustering coefficient is determined by dividing the total number of edges that can possibly connect it with its neighbors by that number. The clustering coefficient (ClsCoef) metric is the sum of the clustering coefficients. The number of connections that each node has with other nodes determines the hub score, which is then weighted according to the number of connections that these neighbors have. A dataset's average number of features per point (T2) indicator is calculated by dividing the total number of samples by its dimensions. Data dimensionality is reduced in relation to the original dimensions when the average number of PCA dimensions per point (T3) is used[5].

All of the methods mentioned above produce good results, but they typically adopt a global perspective and disregard the significance of the complexity of local data classification. This work presents a data classification complexity metric for k-Nearest-Neighbors (kNN) with a dynamically seeking optimal k-value (called C^2M_kNN) in order to address the aforementioned issues. First, the most appropriate k value of kNN for each dataset is determined through dynamic optimization, and then the data contributing to the classification complexity of the data is filtered using k-nearest neighbors, and finally the data contributing to the classification complexity of the filtered data is subjected to the data classification complexity measure. Compared to previous methods, we pay more attention to the importance of boundary samples[6].

2. Methodology of the paper

2.1 k Nearest Neighbours

The k in kNN represents the k closest data samples to itself and is commonly employed in classification and regression applications. Once the labels and data in the training set are known, enter the test data, compare its features to those in the training set, and identify the top k data samples that most closely resemble the test data. The category that most frequently appears in the k data samples is the one that corresponds to the

test data. The selection of the number of k-values of the closest neighbors, the distance metric, and the classification decision rule are the three key elements of the kNN algorithm.

(1) Distance metrics

The distance standard between the samples is calculated using a variety of distance metric functions in the kNN algorithm[7]. Some of the often-used distance metric functions are the Markov distance, the Manhattan distance, and the Euclidean distance. During the modeling process, the Euclidean distance is typically used as the distance calculation index, and the distance metric function is frequently chosen based on the actual sample distribution characteristics and data feature information.

(2) Selection of the number of nearest neighbours k value

The selection of the k value during the modeling process has a significant impact on the model's predicted outcomes[8]. If the number of nearest neighbors k is too small, the number of domain samples for training the model is too small, resulting in low model prediction accuracy; if the k value is too large, the phenomenon of underfitting is easily produced. As a result, in real-world applications, the model's parameters are changed by comparing its output. In most situations, grid search and cross-validation can be used to choose an appropriate k value.

(3) Categorical decision rules

Following the identification of the k nearest neighbors of the samples to be tested, the samples to be tested and the nearest samples with the highest percentage of categories belonging to them are grouped together using the majority voting criterion[9].

2.2 Classification Complexity Measure for KNN with Dynamic Optimisation K-values

C^2M_kNN basic idea is to use the kNN algorithm to first identify the optimal k-value for the dataset through cross-validation. Then, using this k-value, screen out samples that significantly affect the data's classification complexity. Finally, apply the data classification complexity measure to the samples that were screened out.

Step 1: Finding the optimal k value

To train a kNN model on each part, divide the dataset X into k parts, each of which is then divided into a training set and a validation set. Finally, add up and divide the accuracy evaluated for each part by k to find the final accuracy of the kNN model for a given k value. When all of the k values' final accuracy is evaluated, the k value with the highest accuracy is determined to be the most suitable of all of the k values[10].

$$k = SearchK(X) \tag{1}$$

Step 2: Screening out samples that have a significant impact on the complexity of data classification

Step 1 assists us in determining the ideal k, which allows us to identify the k nearest neighbour samples of sample x_i in the training set of samples. These samples are represented as $A(x_i,k)=(x_i^1, x_i^2,...,x_i^j,...,x_i^k)$, where x_i^j represents the jth nearest neighbour sample of sample x_i. The sample stores the point x_i as new data X_new if sample x_i contains samples from a different class than $A(x_i,k)$.

$$A(x_i,k) = SearchkNN(x_i,k) \tag{2}$$

Step 3: Calculate the categorical complexity of the data

Traverse $A(x_i,k)$ for $x_i \in$ X_new and compute the number dnum of $A(x_i,k)$ that are different from x_i's sample category. define dum/k as the divisibility of x_i's sample points, and then find the average of the divisibility of all the sample points average as the first

term. data_ratio =Length(X_ new)/len(X) as the second term, k as the third term, the three terms are multiplied by the function sigmoid () mapping to obtain the dataseparability (DS).

$$DS = Sigmoid(average \times Data\_ratio \times k) \tag{3}$$

Algorithm 1 is as follows.

Algorithm 1: Classification Complexity Measure for KNN Based on Dynamic Optimisation K-values

Input:X={x_1,x_2,…,x_n}
Output: DS
1.k = SearchK(X)
2.For x_i in X do
3. A(x_i,k)=SearchkNN(x_i,k)
4.If the sample x_i has a different class than in A(x_i,k), then the point x_i as new data X_new.
5.For x_i in X_new do
6. Calculate the number dnum of samples in A(x_i,k) that differ from x_i's sample class
7. Define dum/k as the divisibility of x_i sample points, the divisibility mean average of all sample points is obtained, as the first term
8. Data_ratio = Length(X_new)/len(X) as second term, k as third term
9. DS = Sigmoid(average×Data_ratio×k)

3. Experiments

3.1 Evaluation indicators and classifiers

The experiments in this paper were conducted on a PC with Windows 10, AMD 7-5800H@3.20 GHz with 16GB of RAM and the programming language was Python based on the Jupyter Notebook platform.

In this paper, we use is Accuracy[11] to evaluate the experimental results of 12 methods, and the evaluation index is based on the confusion matrix in Table 1.

Table 1. confusion matrix

	Predictive Positive	Predictive Negative
Actual Positive	TP = True Positive	FN = False Negative
Actual Negative	FP = False Positive	TN = True Negative

$$Accuracy = \frac{TN + TP}{TP + TN + FN + FP} \tag{4}$$

This work introduces five classifiers to improve the fairness of the classification evaluation index. The evaluation index Accuracy is derived from the average of the five classifiers. RandomForest, Decision Tree, Gradient Boosting Decision Tree, Adaboost, and k Nearest Neighbour are the 5 classifiers.

3.2 Generating data sets

In this research, we establish six traditional measures of data classification complexity for two classes of datasets, each with 500 data points, and the classification complexity of the six datasets steadily increases from Blobs to Random, as shown in Figure 1.

We introduce 11 additional categorization complexity metrics for comparison with the one established in this paper. Table 2 presents the classification complexity results statistically for the 12 metrics on six classical datasets. The dataset's classification complexity progressively rises from blobs to random. Only the approach presented in this research has a monotonically growing classification complexity from the Blobs dataset to the

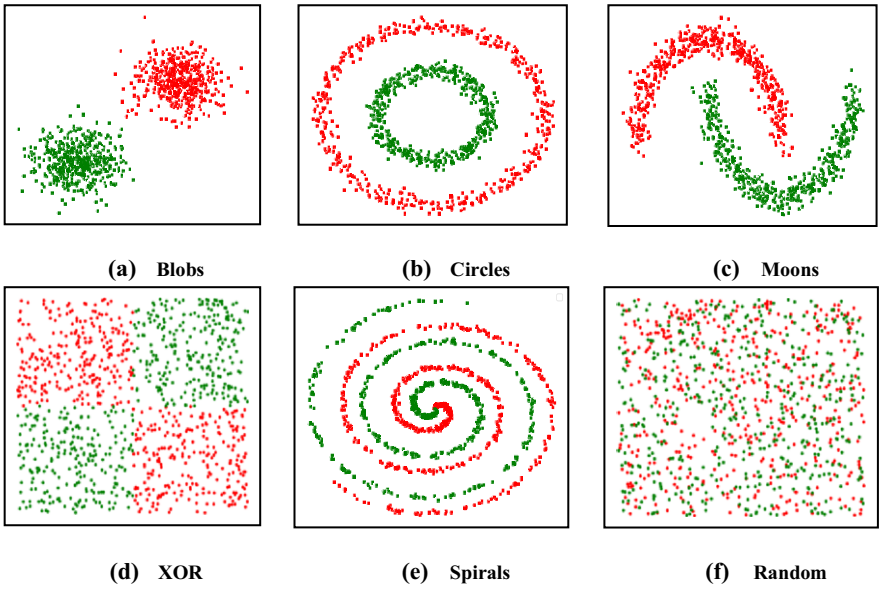

Figure 1. Typical two categories

random dataset out of the 12 classification complexity techniques, demonstrating the efficacy of our suggested approach. Accuracy is provided as a comparison in this study, and the average accuracy values of the five classifiers exhibit a monotonic decrease from Blobs to Random. The higher the classification complexity of the data, the more difficult it is to classify, resulting in poor classification performance, and its accuracy value is lower, indicating an inverse relationship with classification complexity. The accuracy value further demonstrates our method's efficacy.

The classification complexity of the data measured by T2 and T3 methodologies is 0.002, but the classification complexity of these six datasets differs; therefore, the T2 and T3 metrics are ineffective for evaluating classification complexity. Because the probability of correctly classifying binary data is 0.5, the values of the metrics L2, L3, N3, N4, and Clscoef on the six datasets are less than 0.5, so this paper considers metrics of classification complexity less than 0.5 to be meaningless compared to human classification results. In this research, we consider that the classification complexity of the metric is less than 0.5, is no longer meaningful, and is already worse than the result of artificial classification. In classification, the likelihood of the right classification result is 0.5. On the Circles dataset, the F1 method returns a classification complexity

of 1, indicating that F1 feels Circles cannot be categorised, which contradicts the results of our classifiers. The F3 and F4 techniques both consider the Circles dataset to have a higher classification difficulty than the Moons dataset; however, when paired with the accuracy value, we discover that the Moons dataset has a higher classification complexity than the Circles dataset. The random dataset ranks fourth among the six datasets according to the Hubs metric, but when the accuracy value is taken into account, the random dataset has the highest classification complexity.

Table 2. The results of classification complexity measurement in two types of generated datasets

Method	Blobs	Circles	Moons	XOR	Spirals	Random
F1v	0.0360	1.0000	0.1390	0.9920	0.9630	0.9850
F3	0.2300	0.7450	0.6850	0.9970	0.9870	0.9950
F4	0.0220	0.5410	0.3830	0.9940	0.9790	0.9930
L2	0.0080	0.4950	0.1280	0.3930	0.4520	0.4750
L3	0.0000	0.5030	0.0770	0.4150	0.4420	0.4850
N3	0.0110	0.0120	0.0360	0.0280	0.2110	0.5210
N4	0.0040	0.1790	0.1050	0.1430	0.4340	0.4800
Clscoef	0.2100	0.2660	0.2590	0.2840	0.3490	0.3640
Hubs	0.6450	0.6920	0.7560	0.8350	0.8330	0.8030
T2	0.0020	0.0020	0.0020	0.0020	0.0020	0.0020
T3	0.0020	0.0020	0.0020	0.0020	0.0020	0.0020
C^2M_KNN	**0.5259**	**0.5616**	**0.6111**	**0.6348**	**0.6659**	**0.9976**
Accuracy	0.9928	0.9856	0.9648	0.8904	0.6816	0.4680

3.3 Real data sets

In this paper, we use 15 datasets from KEEL[12], which are all binary datasets, and we label these datasets with a serial number, described in detail in Table 3.

Table 4 displays the categorization complexity metrics results for the 12 metrics across the 15 datasets. Only the metrics from the approaches given in this study show a monotonically growing outcome from D1 to D15 and a monotonically lowering value of accuracy, demonstrating the validity of our methods once more.

The F4, L2, L3 and N4 metrics measure a classification complexity of 0 on the D1 dataset, and the results of the metrics of these methods on these datasets have lost their significance. In D3 and D4, the F3 method's classification complexity measurement is 1, meaning that the two data can no longer be distinguished from one another. Nevertheless, we discovered that D3 and D4 are reasonably simple to categorise in these 15 datasets by combining the accuracy scores. The issue with the T2 and T3 approaches is that not a single measured value is more than 0.01—a value too little to accurately represent the 15 datasets' categorization difficulty. The algorithms F1V, N3, Clscoef, and Hubs are also unsuitable for quantifying the data's classification difficulty because their results on the 15 datasets do not show a monotonic increase from D1 to D15.

Table 3. Description of the datasets

Data_name	Sequence	Amount	features
dermatology-6	D1	358	34
poker-8_vs_6	D2	1477	10
poker-8-9_vs_6	D3	1485	10
poker-8-9_vs_5	D4	2075	10
winequality-white-3_vs_7	D5	900	11
winequality-red-8_vs_6-7	D6	855	11
yeast-1-2-8-9_vs_7	D7	947	8
winequality-red-4	D8	1599	11
ecoli-0-1-4-7_vs_5-6	D9	322	6
yeast-0-2-5-6_vs_3-7-8-9	D10	1044	8
vehicle3	D11	846	18
appendicitis	D12	106	7
heart	D13	270	13
yeast1	D14	1484	8
bupa	D15	345	6

Table 4. The results of classification complexity measurement in two types of real datasets

Method	D1	D2	D3	D4	D5	D6	D7	D8	D9	D10	D11	D12	D13	D14	D15
F1V	0.0040	0.8210	0.8330	0.7000	0.1390	0.3130	0.3580	0.3990	0.0920	0.1960	0.3110	0.2090	0.1710	0.4410	0.6120
F3	0.0110	0.8300	1.0000	1.0000	0.6460	0.6050	0.8180	0.9490	0.6690	0.9250	0.9630	0.7080	0.9850	0.9640	0.9680
F4	0.0000	0.6650	1.0000	1.0000	0.3330	0.2000	0.5310	0.7240	0.3860	0.8460	0.7740	0.2740	0.9370	0.9140	0.8930
L2	0.0000	0.0120	0.0170	0.0120	0.0210	0.0210	0.0320	0.0330	0.0510	0.0740	0.2520	0.1320	0.4040	0.2480	0.5590
L3	0.0000	0.0120	0.0170	0.0120	0.0220	0.0210	0.0320	0.0330	0.0450	0.0790	0.2490	0.1420	0.1220	0.2350	0.3770
N3	0.0110	0.0140	0.0160	0.0170	0.0220	0.0410	0.0490	0.0550	0.0330	0.0080	0.2810	0.1980	0.3480	0.2820	0.3800
N4	0.0000	0.0110	0.0130	0.0140	0.0200	0.0220	0.0320	0.0330	0.0150	0.0570	0.2480	0.0940	0.2370	0.2010	0.2320
Clscoef	0.5460	0.7860	0.7860	0.4930	0.4620	0.4860	0.2270	0.4260	0.3760	0.2580	0.4070	0.3260	0.6190	0.2660	0.4360
Hubs	0.8500	0.9730	0.9730	0.8780	0.8280	0.8550	0.3870	0.7600	0.7520	0.4860	0.8400	0.5960	0.9050	0.6220	0.7830
T2	0.0095	0.0070	0.0070	0.0050	0.0120	0.0130	0.0080	0.0070	0.0180	0.0080	0.0210	0.0660	0.0480	0.0050	0.0170
T3	0.0080	0.0050	0.0050	0.0030	0.0020	0.0020	0.0070	0.0010	0.0150	0.0070	0.0010	0.0280	0.0110	0.0050	0.0090
C^3M_KNN	**0.5027**	**0.5033**	**0.5038**	**0.5087**	**0.5119**	**0.5216**	**0.5242**	**0.5293**	**0.5472**	**0.6203**	**0.7987**	**0.8133**	**0.9939**	**0.9974**	**0.9992**
Accuracy	0.9933	0.9897	0.9833	0.9799	0.9777	0.9728	0.9628	0.9605	0.9469	0.9155	0.8150	0.7925	0.7676	0.7320	0.6942

The approach suggested in this paper produces the best results when 12 measures of classification difficulty are put together and applied to both generated and real datasets. This indicates the efficacy of the approach suggested in this paper.

4. Conclusion

This article proposes a new method for measuring the complexity of data classification, C^2M_KNN. C^2M_KNN overcomes the previous classification measurement methods from a global statistical perspective and focuses more on the importance of local data classification complexity. We utilize the clustering characteristics of kNN to propose the classification complexity of a single data point, focusing on the different contributions of each sample to the classification complexity. This article validates the proposed C^2M_KNN The effectiveness of the kNN method is far superior to other methods in both generated and real datasets.

Metrics measuring the difficulty of data classification can offer a foundation for examining, comprehending, and enhancing model performance. It can, in fact, be used to assess clustering outcomes, comprehend each feature's limitations[13], offer theory for building multi-classifier decisions[14], lessen data complexity as a loss function[15], and in other domains. Furthermore, a more thorough measure ought to be applied as a universal standard. When comparing datasets with varying sample sizes and feature dimensions, these values stay similar.

References

[1] Sen P C, Hajra M, Ghosh M. Supervised classification algorithms in machine learning: A survey and review[C]//Emerging Technology in Modelling and Graphics: Proceedings of IEM Graph 2018. Springer Singapore, 2020: 99-111.

[2] Guan S, Loew M, Ko H. Data separability for neural network classifiers and the development of a separability index[J]. arXiv preprint arXiv:2005.13120, 2020.

[3] Orriols-Puig A, Macia N, Ho T K. Documentation for the data complexity library in c++[J]. Universitat Ramon Llull, La Salle, 2010, 196(1-40): 12.

[4] Armano G, Tamponi E. Experimenting multiresolution analysis for identifying regions of different classification complexity[J]. Pattern Analysis and Applications, 2016, 19: 129-137.

[5] Lorena A C, Costa I G, Spolaôr N, et al. Analysis of complexity indices for classification problems: Cancer gene expression data[J]. Neurocomputing, 2012, 75(1): 33-42.

[6] Cousins I T, Johansson J H, Salter M E, et al. Outside the safe operating space of a new planetary boundary for per-and polyfluoroalkyl substances (PFAS)[J]. Environmental Science & Technology, 2022, 56(16): 11172-11179.

[7] Santos M S, Abreu P H, Wilk S, et al. How distance metrics influence missing data imputation with k-nearest neighbours[J]. Pattern Recognition Letters, 2020, 136: 111-119.

[8] Uddin S, Haque I, Lu H, et al. Comparative performance analysis of K-nearest neighbour (KNN) algorithm and its different variants for disease prediction[J]. Scientific Reports, 2022, 12(1): 6256.

[9] Thakur R, Panse P. Classification Performance of Land Use from Multispectral Remote Sensing Images using Decision Tree, K-Nearest Neighbor, Random Forest and Support Vector Machine Using EuroSAT Data[J]. International Journal of Intelligent Systems and Applications in Engineering, 2022, 10(1s): 67-77.

[10] Wazirali R. An improved intrusion detection system based on KNN hyperparameter tuning and cross-validation[J]. Arabian Journal for Science and Engineering, 2020, 45(12): 10859-10873.

[11] Kherif O, Benmahamed Y, Teguar M, et al. Accuracy improvement of power transformer faults diagnostic using KNN classifier with decision tree principle[J]. IEEE Access, 2021, 9: 81693-81701.

[12] Triguero I, González S, Moyano J M, et al. KEEL 3.0: an open source software for multi-stage analysis in data mining[J]. 2017.

[13] Dong N T, Khosla M. Revisiting feature selection with data complexity[C]//2020 IEEE 20th International Conference on Bioinformatics and Bioengineering (BIBE). IEEE, 2020: 211-216.

[14] Sen P C, Hajra M, Ghosh M. Supervised classification algorithms in machine learning: A survey and review[C]//Emerging Technology in Modelling and Graphics: Proceedings of IEM Graph 2018. Springer Singapore, 2020: 99-111.

[15] Charte D, Charte F, Herrera F. Reducing data complexity using autoencoders with class-informed loss functions[J]. IEEE Transactions on Pattern Analysis and Machine Intelligence, 2021, 44(12): 9549-9560.

Fuzzy Systems and Data Mining IX
A.J. Tallón-Ballesteros and R. Beltrán-Barba (Eds.)

doi:10.3233/FAIA231085

Learning of Bounded Treewidth Bayesian Networks via A-kg

Ronghao Su [a] and Yungang Zhu [a,1]
[a] *College of Computer Science and Technology, Jilin University, Changchun, China*

Abstract. Bounded-treewidth Bayesian networks can reduce overfitting and exact inference complexity. Several known methods learn bounded treewidth Bayesian networks by learning from k-trees. However, they adopt an approximate method instead of an accurate method. This work presents an accurate algorithm called A-kg for learning bounded treewidth Bayesian networks. Our approach consists of two parts. The first part is an accurate algorithm that learns Bayesian networks with high BIC scores, which measures the Bayesian network's quality. In the second part, we adopt the greedy strategy to perform parent set selection efficiently. A-kg achieves better performance compared to some approximate solutions in small domains.

Keywords. Bayesian network, Bounded treewidth, A-kg, BIC

1. Introduction

Bayesian networks are directed graphs widely used to represent the joint probability distribution on multivariate domains and achieve excellent performance in fields such as prediction, inference, diagnosis, decision risk, and reliability analysis.

Learning a Bayesian network refers to inferring its structure from data, a work proven to be an NP-hard problem [1]. Bayesian networks are usually used for inference, such as calculating the posterior probability of some variable given some evidence or finding the mode of the posterior joint distribution. Those inferences are NP-hard to compute even approximately [2]. To make efficient inferences, Bayesian networks need to have small treewidth, assuming exponential time hypothesis (ETH).

The learning methods of Bayesian networks can be divided into accurate and approximate. Yuan found an accurate method to learn Bayesian networks. The method formulated the learning Bayesian network as a shortest path-finding problem and used an A* search algorithm to approach the problem [3]. Di proposed a BN structure learning algorithm based on dynamic programming, which integrated improved MMPC and MWST [4]. In the A* search algorithm, Wang improved the simple heuristic and the static k-cycle conflict heuristic to adapt to ancestral constraints [5]. However, the Bayesian networks learned by these methods are not unbounded treewidth.

For the existing accurate algorithm, in the worst case, the time complexity is the exponential level of the treewidth [6]. So it is necessary to limit the treewidth of Bayesian networks.

[1] Corresponding Author,Yungang Zhu, College of Computer Science and Technology, Jilin University, Changchun ,China; E-mail: zhuyungang@jlu.edu.cn

In recent years, many methods have been proposed to limit the treewidth of Bayesian networks. Ramaswamy combined heuristic BN structure learning algorithms with the recently introduced MaxSAT-powered local improvement method [7]. Ramaswamy also proposed an approach whose key was applying an exact method locally, to improve the score of a heuristically computed BN [8]. Xu proposed a Bayesian network structure learning approach based on full permutation and extensible ordering-based search [9]. Scanagatta proposed k-greedy, k-A*, and k-max algorithms [10]. The researchers used the idea of searching directly for high-quality K-trees and proposed a sampling variable order to learn the optimal DAG. They initialized (k+1) cliques iteratively by adding other variables to the k-clique of the current graph K-tree, establishing the DAG greedily. This method is different from the previous one. And there is no need to learn DAG from a given K-tree. It samples a variable order rather than a tree, resulting in a substantial reduction in search space. There is no need to learn DAG from a given K-tree, and it samples a variable order rather than a tree, resulting in a substantial reduction in search space The difference between k-greedy and k-A* is the way of selecting parent sets. K-greedy selects parent sets with the highest score, while k-A* formulates it as the shortest path-finding problem and solves the problem by the A* algorithm. K-max can learn Bayesian networks from incomplete data sets. All of them can get Bayesian networks with bounded treewidth. However, they are an approximate method that gets lower scores than the accurate method.

This paper presents a new accurate algorithm called A-kg for score-based Bayesian network learning with bounded treewidth. A-kg algorithm consists of two parts: parent identification and structure optimization. In the part of structure optimization, we formulate a learning Bayesian network as a shortest path-finding problem and use an A* search algorithm to approach the problem. This is an accurate method. In the part of parent identification, we draw on the idea of the k-greedy algorithm which selects parent sets by greedy strategy. Here, we can get Bayesian networks with limited treewidth. A-kg is proven to learn a Bayesian network with bounded treewidth and achieve higher scores than traditional algorithms. To test our methods, we compare A-kg and some other algorithms. We compare them with the BIC score. Moreover, we compare them on data sets with different treewidth.

2. Treewidth and K-tree

2.1. Treewidth

The treewidth represents the extent to which a graph resembles a tree. Assuming G (V, E) is an undirected simple graph, the tree decomposition H of graph G is composed of a subset $Yt \subseteq V$ associated with each node of tree T. Tree T and subset $\{Yt:t \in T\}$ should satisfy the following three conditions. The first condition is Eq. (1).

$$\cup \left(Y_t:t \in T\right)=V \tag{1}$$

Eqs. (1) means that the nodes contained in subsets Yt. cover all nodes of graph G, or that each node of graph G belongs to at least one subset Y_t. The second condition is that for each edge $e \in E$ of graph G, there is at least one subset Y_t containing two endpoints of e. The third condition is that if n1, n2, and n3 are the three nodes of tree T,

where n2 is on the path from n1 to n2, and node v of G belongs to Y_{n1} and Y_{n3}, then v will belong to Y_{n2}.

The width of a tree decomposition is equal to max ($|Y_t|$: $t \in T$) -1 where $|Y_t|$ is the number of vertices in $|Y_t|$. The treewidth of H is the minimum width among all possible tree decompositions of G.

2.2. K-tree

The k-tree is the largest graph with a treewidth of k, and every graph with a treewidth ≤ k is a subgraph of some k-trees.

The family of k-trees is defined inductively as follows:(1)A (k+1)-clique is a k-tree. (2) If G=(V, E) is a k-tree and $C \subseteq V$ is a k-clique, then the graph obtained by adding a new vertex v and an edge u−v for each $u \in C$ is a k-tree.

3. A-kg

The main framework of A-kg is the A* search algorithm. By combining the idea of the k-greedy algorithm, A-kg can learn the Bayesian network with bounded treewidth. The Bayesian network obtained by this algorithm is treewidth bounded because each node has a parent set which must be a subset of a k-clique. At the same time, A-kg adopts a greedy strategy to select parent sets. The parent sets are chosen to have the highest score. The following is the definition of A* search and k-greedy.

3.1. A search*

The basic idea of this algorithm is to formulate learning optimal Bayesian networks as a shortest path-finding problem. A * search algorithm starts from an empty set and searches until all nodes are found. The shortest path among all possible paths corresponds to the global optimal Bayesian network. The scoring function is MDL. A-kg uses BIC score. Let U be a node in Figure 1 and V be all nodes, then the heuristic value h(U) is represented by Eqs. (2).

$$h(U)=\sum_{x\in V\setminus U} \text{BestScore}(X, V\setminus\{X\}) \quad =\sum_{x\in V\setminus U} \text{BestMDL}(X, V\setminus\{X\}) \tag{2}$$

The arc from U to $U \cap \{X\}$ in the figure represents the generation of subsequent nodes by adding a new variable {X} to the existing variable set U; The cost of an arc is equal to the cost of selecting a parent set for X from U. The cost is represented by Eqs. (3).

$$\text{BestScore}(X, U)=\min_{P_{A_X}\subseteq U}\text{score}\left(X\middle|P_{A_X}\right) =\min_{P_{A_X}\subseteq U}\text{MDL}\left(X\middle|P_{A_X}\right) \tag{3}$$

3.2. K-greedy

K-greedy first samples a variable order and uses the first （k+1） variable to establish a k-tree. *The accurate* learning algorithm is taken to learn the best DAG on the same k+1 variable. Then, the algorithm iteratively add*s* each remaining variable. The parent set*s* of

this variable are constrained to the k-clique (or subset) in *k*-tree. The selected parents set has the highest score. This results in a new DAG. To update the k-tree, the algorithm links variables to the same k-*clique*. Assuming the sampling variable order is<v1, v2, v3 >, Figure 1 illustrates the process of the algorithm.

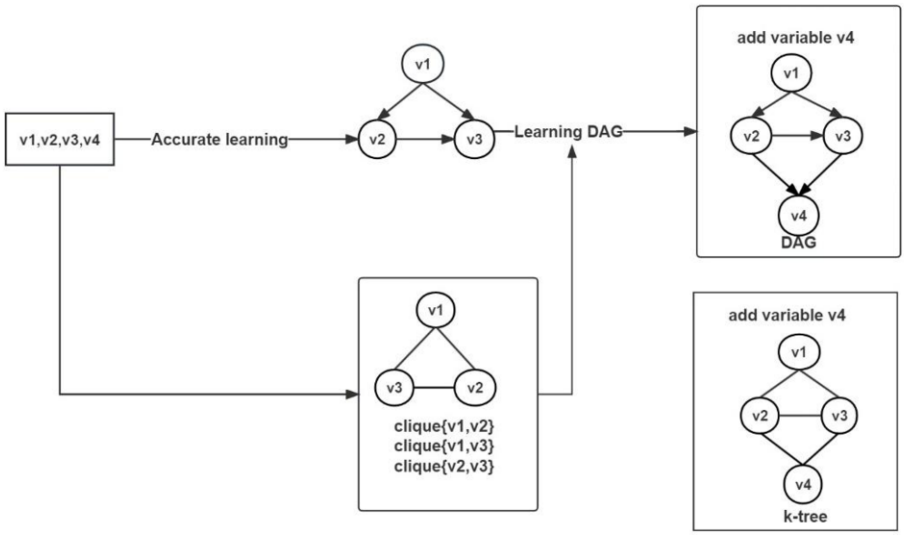

Figure 1. The process of k-greedy.

In the A-kg, we construct a k-clique like the k-greedy algorithm in the process of learning the Bayesian network. The parent set with the highest scoring is chosen for the variable. The parent set of the added node is a subset of k cliques. When connecting this node with the parent set, the maximum clique obtained is also k+1 clique, and the treewidth is still not greater than k. In this way, the learned Bayesian networks are bounded by treewidth. Algorithm 1 shows the process of A-kg.

Algorithm 1 A-kg.

```
1: procedure A-kg
2:     Q1 ← ∅;              // Q1 is open queue
3:     while Q1 is not empty do
4:         S ← H(Q1);   // get the header of Q1
5:         if S contains all variables then
6:             end procedure;
7:         end if
8:         Q2 ← S;       // place S in closed queue(Q2)
9:         for v do       // v is a variable that is not present in S
10:            S1 ← P(v)+S;       // select parent set for  v
11:        end for
12:        if  Q2 contains S1 & the score of S1 is lower  then
13:            discard S1;
14:        else
15:            Q1 ← S1;
16:        end if
17:    end while
18: end procedure
```

In Algorithm 1, the open queue is a priority queue, with BIC as the scoring standard, used to store the states that need to be traversed. The closed queue is a priority queue, with BIC as the scoring standard, used to store the searched status.

4. Experiment

In our experiment, we use an indicator which is the difference between the BIC scores (△BIC) of the DAG [11].

Assuming that there are two graphs G1 and G2, the value of △BIC is the BIC scores of the G1 minus the BIC scores of the G2. A positive △BIC means that G1 is better than G2. Otherwise, it's the opposite. For example, a △BIC that is greater than 2 and less than 6 implies positive evidence in favor of G1. A △BIC that is greater than 10 implies extremely positive evidence in favor of G1. The value of △BIC can be interpreted according to Table 1. We only present the case of positive △BIC. If the value of △BIC is negative, then the evidence is negative.

Table 1. Meaning of different △BIC.

	△BIC<2	**2<△BIC≤6**	**6<△BIC ≤10**	**△BIC >10**
G1vsG2	neutral evidence	positive evidence	strongly positive evidence	extremely positive evidence

4.1. Comparison

We use 4 data sets to compare k-greedy, k-max, k-A* and A-kg. Table 2 shows the details of these data sets. In Table 2,n represents the number of variables and d represents the number of data points.

Table 2. The 4 data sets used in the experiments.

Name	**n**	**d**
Sachs	11	5000
Survey	6	5000
Msnbc	17	58265
Child	20	5000

We start the experiment by calculating the value of △BIC between A-kg and other algorithms. The experiments were run on a computer with 8 cores, a memory limit of 8GB, a time limit of 10 hours, and a maximum number of parents of three**.** The △BIC achieved by different methods is given in Table 3.

Table 3. △BIC between A-kg and other algorithms.

△BIC	**k-greedy**	**k-max**	**k-A***
△BIC >10	0	0	0
6<△BIC ≤10	0	0	0
2<△BIC≤6	2	3	2
0≤△BIC<2	2	1	2
− 6≤△BIC<0	0	0	0
− 10≤△BIC< − 6	0	0	0
△BIC< − 10	0	0	0

The results show that A-kg gets more BIC scores than other algorithms. Take △BIC between A-kg and k-max for example, there are 3 △BICs whose values are greater than

2 and less than 6. According to Table 1, these △BICs mean positive evidence for the Bayesian network learned by A-kg over the Bayesian network learned by k-max. And there is a △BIC between A-kg and k-max whose value is greater than 0 and less than 2. According to Table 1, this △BIC means neutral evidence for the Bayesian network learned by A-kg over the Bayesian network learned by k-max. In the same way, there are 2 △BICs between A-kg and k-greedy which mean positive evidence for the Bayesian network learned by A-kg over the Bayesian network learned by k-greedy, and 2 △BICs between A-kg and k-greedy which mean neutral evidence for the Bayesian network learned by A-kg over the Bayesian network learned by k-greedy. The △BICs between A-kg and k-A* are the same as the △BICs between A-kg and k-greedy.

We further compare A-kg and k-A* under various treewidth. The results are presented in Table 4.

Table 4. Comparison between A-kg and k-max with the treewidth k ∈{3, 5, 7}.

A-kg vs k-max	Treewidth		
	3	*5*	*7*
Extremely positive	0	0	0
Strongly positive evidence	0	0	0
Positive evidence	2	2	2
Neutral evidence	2	2	2
Negative evidence	0	0	0
Strongly negative evidence	0	0	0
Extremely negative evidence	0	0	0

In most cases, there is a piece of positive evidence for the model learned by A-kg over the model learned by k-A*.

5. Conclusions

This paper presents a new algorithm (A-kg) for learning Bayesian networks with bounded treewidth. We compare A-kg and some of the other algorithms. The results show that A-kg gets better scores and finds better structures than its competitors. Furthermore, we compare A-kg and k-max under various treewidth. The results also show that A-kg achieves a better score.

References

[1] Chickering DM. Learning Bayesian Networks is NP-Complete. Learning from Data.1996;112: 121-130.

[2] Roth D. On the hardness of approximate reasoning. Artificial Intelligence.1996;82: 273-302.

[3] Yuan C, Malone B. Learning Optimal Bayesian Networks: A Shortest Path Perspective. Journal of Artificial Intelligence Research. 2013; 48: 23-65.

[4] Di RH, Li Y, Li TP. Dynamic Programming Structure Learning Algorithm of Bayesian Network Integrating MWST and Improved MMPC. Mathematical Problems in Engineering. 2021;2021(53):1-17.

[5] Wang ZD, Gao XG. Learning Bayesian networks using A* search with ancestral constraints. Neurocomputing. 2021; 451: 107- 124.

[6] Kwisthout J, Bodlaender HL, Gaag vr, Linda C. The Necessity of Bounded Treewidth for Efficient Inference in Bayesian Networks. Frontiers in Artificial Intelligence and Applications. 2010; 215: 237-242.

[7] Ramaswamy VP, Szeider S. Learning Fast-Inference Bayesian Networks. In: 35th Conference on Neural Information Processing Systems. 2021. p. 34-46

[8] Ramaswamy VP, Szeider S. Turbocharging Treewidth-Bounded Bayesian Network Structure Learning. In: 35th AAAI Conference on Artificial Intelligence. 2021. p. 3895-3903.

[9] Xu RH, Liu SH. PEWOBS: An efficient Bayesian network learning approach based on permutation and extensible ordering-based search. Future Generation Computer Systems. 2022; 128: 505-520.

[10] Scanagatta M, Corani G, Campos CP, Zaffalon M. Learning Treewidth-Bounded Bayesian networks with thousands of variables. In:30th Annual Conference on Neural Information Processing Systems.2016.p.1470 – 1478.

[11] Lv YL, Miao JZ. BIC-based node order learning for improving Bayesian network structure learning. Frontiers of Computer Science. 2021; 15(6): 2095-2228.

Fuzzy Systems and Data Mining IX
A.J. Tallón-Ballesteros and R. Beltrán-Barba (Eds.)

doi:10.3233/FAIA231086

Research on Value Co-Creation Mechanism in the Digital Transformation of Manufacturing Enterprise Supply Chain

Deqiang Fu[a] and Ruyi Li[a,1]
[a] *Modern Postal College, Chongqing University of Posts and Telecommunications, China*

Abstract. With the advent of the era of big data, the relationship between manufacturing enterprises and consumers is getting closer. Under the value co-creation model, the new value generated by the interaction between manufacturing enterprises and consumers is conducive to improving the competitive advantages of manufacturing enterprises and consumers' satisfaction with products and services. This paper takes the digital transformation of the supply chain of manufacturing enterprises as the research object and is dedicated to studying its value co-creation activities. By sorting out the relevant literature, the paper mainly focuses on two issues: First, the digital transformation process of the supply chain of manufacturing enterprises. Second, combining cases to analyze the various stages of the value co-creation activities of the digital transformation of the supply chain of manufacturing enterprises. This paper selects the "consumer experience-led" type to discuss the case of Haier, a manufacturing enterprise, as the research object. Through research, we concluded that: in the process of joint participation in value creation between manufacturing enterprises and consumers in the digital transformation of the supply chain, both enterprise value and consumer value have increased. This paper provides a reference for research and practice in this area.

Keywords. Manufacturing enterprise supply chain, digital transformation, consumer experience, value co-creation

1. Introduction

In the era of big data, the complexity of the supply chain of our manufacturing companies is increasing rapidly. The speed of product replacement is accelerated, and consumers' needs for product customization and product quality are increasing. To meet customer demands and help companies operate digitally, supply chains need to undergo digital transformation. Hennelly et al. believe that digitization is the use and adoption of external digital technologies by organizations to improve their supply chain and operational performance [1]. According to the research of previous scholars, this paper summarizes the definition of digital transformation of the supply chain as follows: supply chain digital transformation is the process of optimizing and improving supply chain management through the application of digital technologies and information systems to increase efficiency, visibility and responsiveness.

[1] Corresponding Author, Corresponding author, E-mail: 1792393251@qq.com

The main body of value co-creation includes the manufacturing enterprises themselves and the group of consumers. The core content of value co-creation is to change the positioning of consumers and the original supply chain nodes in the value chain, to allow consumers to participate in the entire process of creating value, and to allow customers to participate in the service and production process of the enterprise. Create value for enterprises, and enterprises can gather through the platform to form complementary advantages and share resources. Based on the digital transformation of the supply chain of manufacturing enterprises, the problem of value co-creation is discussed, and the systematic research of the problem is strengthened. Jaakkola and Alexander (2014) [2] analyzed the impact of customer participation in the value creation of manufacturing enterprises, presented four different customer participation models, and discussed the value effects experienced by different stakeholders. Wang Ligai (2020) [3] established a value co-creation model for manufacturing enterprises based on the concept of value co-creation and put forward corresponding countermeasures and suggestions for the development of its service model. Wu Kai (2020) [4] discussed the value created by brands from the perspectives of local value, consumer value perception, consumer value appreciation, and brand local value. Prahalad and Ramaswamy [5] argue that the interaction between the customer and the firm is fundamental to value creation. Firstly, the essence of value co-creation is the co-creation of customer experience between the firm and the customer and the continuous creation of its own experience in products and services. Secondly, the interaction between firms and consumers is the fundamental way to generate value. Value co-creation, on the other hand, is generated by the heterogeneous interactions between customers and firms. Thus, value co-creation is a consumer-business interaction and co-operation that goes beyond the traditional medium of supply and demand.

2. Related Work

This paper provides an in-depth discussion of the current state of supply chain digital transformation in manufacturing companies and the value of the benefits it brings, followed by an examination of the factors that influence value co-creation. Finally, using Haier's COSMOPlat as a case study, based on the 'Consumer Experience Dominant Logic' framework, the paper discusses how this manufacturing company achieves value creation in the process of supply chain digital transformation. This paper adopts a single-case study approach, selecting COSMOPlat, a highly representative and best-practice feature of the Haier Group's intelligent manufacturing platform, to explore how manufacturing enterprises achieve value co-creation in the process of digital transformation.

3. Digital Transformation of Manufacturing Enterprise Supply Chain and Its Benefit Value

3.1. Status Quo of Digital Transformation of Manufacturing Enterprise Supply Chain

Many large domestic manufacturing enterprises are carrying out or preparing to carry out the digital transformation of the supply chain. For example, Haier uses COSMOPlat to open up a communication platform from consumers to suppliers, from

demand terminals to supply terminals. Through the application of the Internet of Things and big data technology, it can create accurate, efficient and low-risk online and offline communication platforms. However, for small and medium-sized manufacturing enterprises, there are still many difficulties to be overcome in the process from the development of the implementation programme to the final implementation of the programme. There is still a lot of room for progress in the digitization of the supply chain.

3.2. Changes in the Digital Transformation Method of the Supply Chain

Traditional supply chains employ a linear and reactive approach, where the functioning of the chain depends on specific predefined workflows. Historical transactions from the system control how the chain works, not real-time conditions. Problems of information isolation and lag may exist.

Supply chain digital transformation uses a network approach to apply digital technologies throughout the supply chain to achieve a more integrated, dynamic and predictive supply chain. These techniques help identify problems earlier and respond proactively to outages based on real-time conditions rather than predefined workflows. Connectivity is critical to eliminating silos and providing visibility across the supply chain. For businesses, the digital transformation of the supply chain is the process of delivering digital products to their customers, leveraging electronic technology in all aspects of the end-to-end supply chain [6].

3.3. Benefit Value After the Digital Transformation of the Supply Chain

3.3.1. Cost Reduction and Efficiency Increase

Manufacturing companies use the real-time sales and demand data provided by the digital transformation of the supply chain to adjust their strategies, focus on selling high-demand products. In addition, most manufacturing companies spend a lot of money and time maintaining problems and products left over from legacy systems, and supply chain digital transformation can save time and money by integrating efficient processing processes and quickly identifying problems [7].

3.3.2. Improve Transparency

The biggest change brought about by the digital transformation of the supply chain is the transparency of the closed-loop process of supply, procurement, processing, and sales. It fundamentally shortens the distance between cost and profit, and between resources and resources [8]. The distance between users makes the entire supply chain active at once, and the efficiency is rapidly improved. This transparency facilitates the detection of previously unseen inefficiencies, improved relationships between different stakeholders, and reduced time-to-market as bottlenecks are eliminated.

3.3.3. Improve the User Experience

An improved user experience means that transformation is valuable. Digital transformation of the supply chain enables systems to view and gain insights into the consumer spending process, better understand customer preferences as well as needs

[9], understand inventory surplus, available services and products, save on sales, shorten lead times, and make the entire buying process more streamlined.

4. Analysis on the Principle of Value Cocreation in the Digital Transformation of the Supply Chain of Manufacturing Enterprises

4.1. The Concept of Value Cocreation in the Digital Transformation of the Supply Chain of Manufacturing Enterprises

The concept of digital transformation of a manufacturing company's supply chain is to realize cooperation and collaboration between all parties in order to co-create added value. This transformation focuses not only on internal improvements within a single enterprise, but also on the optimization of the entire supply chain ecosystem to achieve the goal of co-creation of value. After the digital transformation of the supply chain of manufacturing enterprises, information has become timely and transparent. In order to form a "fan economy" and shorten the distance with consumers, manufacturers have established online communities. In this way, manufacturing enterprises can better understand the real needs of customers, provide customers with better products and services, improve customer stickiness, and enhance competitiveness. For consumers, they can get satisfactory products and services, and a sense of achievement [10]. Thereby, manufacturing enterprises and consumers achieve a win-win situation and achieve a win-win situation. The model diagram is shown in Figure 1.

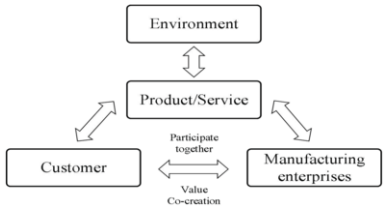

Figure 1. Value co-creation model diagram

4.2. Manufacturing Enterprise Supply Chain Digital Transformation Value Cocreation and Construction Conditions

4.2.1. Participation of Various Stakeholders and Effective Communication

Effective interaction is the source of generating value, and the participation of effective multiple subjects is a prerequisite for generating value. First of all, to ensure the participation of various stakeholders, it is necessary to clarify their value orientation and adopt various incentives to make all stakeholders participate in the value-sharing system. Secondly, the quality of interaction needs to be ensured in the online environment. Due to the existence of virtual communities, the complexity and diversity of interaction have increased. Therefore, for direct and indirect interactions, different methods should be used to stimulate users' ability to interact.

4.2.2. Diversified Communication Channels and Perfect Service System

Through diversified communication channels, participants can better grasp information and use their knowledge, skills, experience and other actionable resources to create value. Through Internet technology and mobile terminals, etc., optimize the service system of the enterprise, establish and enhance the company's brand value, and promote the behavior of value co-creation among all stakeholders.

4.2.3. Resource Sharing and Information Transparency

In the digital transformation and co-creation mechanism of the supply chain of manufacturing enterprises, although the roles and responsibilities of various stakeholders are different, they are all in the same position, which can ensure the sharing of resources, thereby promoting mutual value creation. At the same time, the transparency of information can enable participants to accurately evaluate risks and benefits, reduce the risk of co-creation, and promote co-creation.

5. Haier's Case Study

The value co-creation system in the relevant literature today mainly includes two logic, "service-led logic" and "consumer experience-led logic". Due to space constraints, this part focuses on the analysis of the field of the "consumer experience-led logic model", and takes "Haier Company" as an example to explore the value co-creation in the digital transformation of the supply chain of manufacturing enterprises.

In order to adapt to diverse consumer demands and maximize user value, Haier first launched COSMOPlat, a supply chain digital platform that introduces users to participate in the whole process experience, in 2016. The core of COSMOPlat is mass customization, which transforms consumers from passive buyers to participants and creators. In the past, the concept of "production and consumption between the enterprise and the user" has been changed to "creating lifelong value for the user". COSMOPlat is a platform for the iteration of the user's whole process experience and a multilateral ecological platform for value-added sharing. The process of value co-creation between users and other members on COSMOPlat is as follows. Figure 2 is the schematic of supply chain value co-creation.

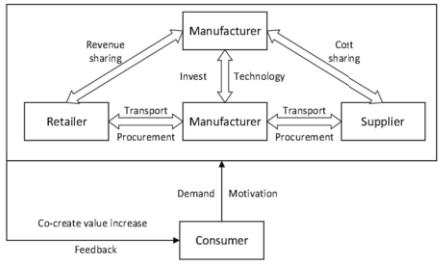

Figure 2. Supply chain value co-creation diagram

5.1. The process of value co-creation

The process of value co-creation among supply chain members consists of three main parts: "connection" - "interaction" - "co-creation".

5.1.1. "Connection Process"

Haier uses COSMOPlat to connect various members in the supply chain, so those manufacturing enterprises, resources and users are directly connected. COSMOPlat allows consumers to participate in all aspects of the entire life cycle, opening up the walls between users and manufacturing companies. On this basis, the connection between suppliers, manufacturers, sellers and consumers is finally realized, which lays the foundation for the next value co-creation through interaction.

5.1.2. "Interaction Process"

In the interactive system, Haier provides resource carriers, and consumers are the main body of value creation. Haier passes its value proposition to consumers through COSMOPlat, and consumers feedback relevant opinions to manufacturers through COSMOPlat. During this interactive process, product design and production begin, and value propositions are generated. Consumers pass COSMOPlat to obtain products and services, share content and interact with other consumers in the community, communicates with manufacturing enterprises, and conducts cooperative production. Figure 3 is the interactive mode diagram:

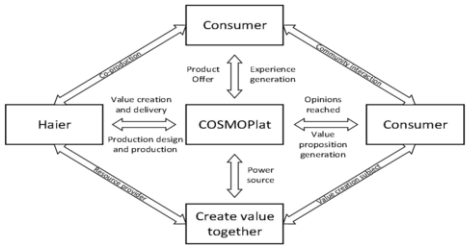

Figure 3. Interaction pattern diagram

5.1.3. "Cocreation Process"

Users can participate in the entire product lifecycle through the COSMOPlat process. Through COSMOPlat, the user experience and feedback of the product are passed to Haier, so that Haier can better understand the user's behavior according to the user's use feedback, and continuously optimize and improve the product to improve the user's satisfaction.

For Haier, COSMOPlat can obtain user experience and feedback in a timely manner, optimize product functions and services, and improve the efficiency of product upgrades. At the same time, Haier timely feeds back the changed plans to suppliers and sellers to help them make corresponding adjustment strategies to maximize the benefits of other members of the supply chain while satisfying users. The timely response of enterprises helps to retain old customers and attract new users. In addition, Haier has gathered hundreds of millions of user information feedback resources on the COSMOPlat platform, and can also apply to the domestic business model to foreign countries through co-creation activities, expand international business, and help enterprises occupy more international markets.

5.2. The results of value co-creation

The essence of COSMOPLAT is to realize the disruption of the three systems of R&D, marketing and production by working together with stakeholders through the platform to achieve a seamless connection of the entire industry chain. After the digital transformation of the supply chain, the collaborative network structure of enterprises is expanded. Manufacturers, equipment vendors, logistics providers and service providers come together, and each subject is able to innovate and cultivate new modes of cooperation on the platform. In addition, system members are no longer constrained by enterprise boundaries, resource utilization is expanded, and asset flexibility and specialization is increased. Digital transformation not only reduces social and procurement costs for network members, but also improves operational forecasting and risk identification [11].

6. Conclusion

With the development of the times, more and more manufacturing enterprises are implementing digital transformation of their supply chains. In the process of transformation, consumers join in to make enterprises gain more value. The article analyses the role of enterprises and consumers in the process of value co-creation and the process of value co-creation, which provides a reference for the implementation of value co-creation in digital transformation of supply chain of manufacturing enterprises in China, and lays a theoretical foundation for further in-depth research.

This study is based on a single case study, which is still limited in terms of the target audience and only examined from the consumer experience-driven logic. Future research should increase the number of samples from specific industries, conduct multiple case studies, and on this basis, further conduct large-sample empirical research on the value co-creation process in the digital transformation process of manufacturing enterprises.

References

[1] Hennelly P, Srai J, Graham G, et al. Rethinking supply chains in the age of digitalization. Production Planning & Control. 2020 Dec; 31(2-3): 93-95.
[2] Jian Zhaoquan, Linghu Kerui, Li Lei. Evolution and Prospect of Value Co-creation Research——From the Perspective of "Customer Experience" to "Service Ecosystem". Foreign Economics and Management. 2016 Sep; 38(09): 3-20.
[3] Wang Ligai. Research on the development strategy of manufacturing servitization based on the theory of value co-creation. Science and Technology Entrepreneurship Monthly. 2020 Nov; 33(11): 45-48.
[4] Gao Zhijun, Liu Wei, Gao Jie. The value co-creation mechanism of logistics service supply chain under the service-dominant logic. China Circulation Economy. 2014 Nov; 28(11): 71-77.
[5] Hua Zhaohong, Zhang Ling. Research on the Value Co-creation Mechanism of Chinese Leisure Agriculture under the Internet Background. Business Economics. 2022 Feb; 1(03): 123-126.
[6] Sun Fengjiao, He Ting, Jin Chuanming, Dong Guangqiao. A symbiotic evolution model of value co-creation units in service ecosystems. Computer Integrated Manufacturing Systems. 2022 Jul; 28(5): 1549-1561.
[7] Liu Jie, Xie Hai, Zhang Yan, Zhang Qianyou. An analysis of the value co-creation evolution path of platform-based enterprises from the perspective of dynamic capabilities—a single case study based on the Integration of Microelectronics. Soft Science. 2021 May; 35(5): 138-144.

[8] Xu Wentao. Raw materials rose sharply, but Haier Zhijia handed over a wonderful answer sheet. State-owned Enterprises. 2021 Oct; 1(19): 68-69.
[9] Wang Mansi, Huo Ning, Zhou Xiang. Research on the Value Co-creation Mechanism of Digital Brand Community——Based on the Perspective of Experience-led Logic. Nankai Management Review. 2021 Jun; 24(3): 92-101.
[10] Wan Xiaole, Hao Tingting, Rong Xiaoxia, Meng Qingchun. Research on value creation of supply chain considering open innovation from the perspective of co-creation. China Management Science. 2017 Jul; 7(25): 1-10.
[11] Wang Shuilian, Yu Chengying, Zhang Jiayue. Research on Value Creation Process of Industrial Internet Platform. Forum on Science and Technology in China. 2022 Apr; 1(4): 78-88.

Fuzzy Systems and Data Mining IX
A.J. Tallón-Ballesteros and R. Beltrán-Barba (Eds.)

doi:10.3233/FAIA231087

Topic Knowledge Based Controlled Generation for Long Documents Using Retrieval-Based Language Models

Xuefei Zhang [a,1], Peiyang He [a], Tomal Deb [a], Guang Yang [a], Xuefeng Liu [a], Ziqing Hu [a], Tianyi Mao [a]
[a] *Amazon, Shenzhen, China*

Abstract. Current LLM summarization systems Produce broad overviews which are disconnected from people specific interests and expectations. Basically, people preferences (topics) can be expressed by a collection of semantic keywords. Previous work exploit these keywords as extra input to generate summary. That requires additional human annotations. To tackle these constraints, we propose a novel framework, Topic Knowledge based Controlled Generation (TKCG), to control generated summaries through a set of topic keywords that are extracted automatically from source documents. First, as large language models (LLMs) are limited by context window length, we need to split the documents into small pieces like chapters acccording to the document format, as one chapter is a semantically complete section. Secondly we extract some topic keywords from source documents with a transformer-based model. These topic keywords are used to retrieve the chapters that are related to the topic. We then input the combination of topic keywords and chapters as prompts into LLM to get conditional summaries. We also demonstrate the effectiveness of TKCG on two standard datasets, MACSum and arXiv.

Keywords. text generation, LLM, word embedding, RAG

1. Introduction

Text summarization systems aim to compress documents into a condensed summary. Now extractive and abstractive summarization are two primary research topics. Extractive summarization identifies and copies key portions of the original text [1]. Abstractive summarization is focused on generating texts to expresss main ideas of documents [2]. This work focuses on abstractive summarization using LLM. While current LLM summarization systems can generate generic summaries, they often fail to align with individual people preferences and expectations. we propose a generic framework, Topic Knowledge based Controlled Generation (TKCG), that moves beyond generic summarization to provide truly people-centric experiences tailored to each user.

Summarization methods typically generate generic summaries from source documents by arbitrarily selecting content to include. However, for automatically generated

[1]Corresponding Author: Xuefei Zhang, Beijing Aerospace Beijing Tower 2, Shenzhen, China; E-mail: xuefegzh@amazon.com

summaries to be useful, they should cover information deemed important by people. For instance, as shown in Figure 1, summaries can be tailored to specific attributes of interest, like "Pope Francis" or "blood moon." This allows for mixed-attribute control so that summaries align with people business-specific interests in various topics.

Motivated by the need for conditional summarization that aligns with people interests, in this work, we propose a novel framework, TKCG, to control summaries through specified keywords. Since people data consists of long documents that exceed language models' limited context window, we split documents into chapters, which typically convey semantically isolated idea. To identify relevant chapters related to people interests, TKCG uses KeyBERT [3] to extract topic keywords from the source document as topic knowledge for retrieving pertinent chapters. The model is instructed to generate summaries based on both the source document and keywords. We then input the combined topic keywords and selected chapters as prompts into LLMs to control the summaries. This allows people to steer summaries to cover information they care about.

We introduce a novel framework for controllable text summarization. This allows people to generate personalized summaries that fully utilize the fact that automatic summaries are created on demand. Our main contributions are: (1) We automatically extract topic keywords from source documents using transformer-based model (KeyBERT). (2) These topic keywords as knowledge guide the summarization process. (3) Our summaries adhere to people-personalized preferences. In comparisons with strong LLM summarization methods on the standard datasets MACSum [4] and arXiv [5], which contain long document summarization examples, our approach demonstrated clear advantages.

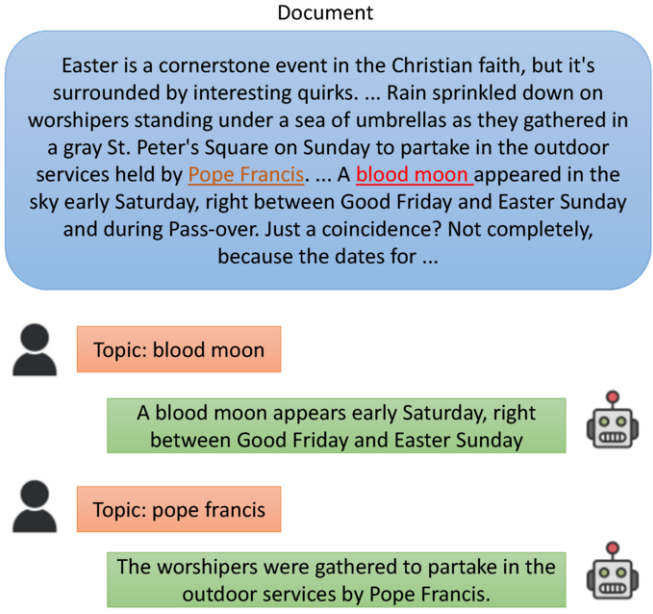

Figure 1. An illustration of topic conditional summary. For the same input source text, the system needs to generate different reference summaries (green boxes) for different topics (orange boxes).

2. Related Work

Large Language Model. OpenAI ChatGPT, Google Bard, Anthropic Claude and other LLMs are certainly having a moment—the next generation of conversational software tools promise to do everything. Pre-trained on general text, LLMs could be fine-tuned for specific tasks such as translation, question answering and text generation. Summarization is one of tasks.

Conditional Summarization. Conditional summarization is a automatic text summarization where the generated summary is controlled based on certain specified conditions or attributes. Prior conditional summarization methods often need labeled control codes for supervision [6]. Fan et al. utilized an entity tagger to extract entities from reference summaries as control codes. He et al. [7] trained a BERT-based model to label keywords for entity control. That requires additional human annotations to train the BERT-based model from entity extraction. Our proposal automatically extracts topic keywords from documents and is unsupervised. Keyword-guided summarization has been used before in various ways. These work are then provided keywords as extra input to enhance unconstrained summarization or decrease hallucinations [7], the goal is to leverage topic knowledge to guide the summarization process. Our approach can automatically extract topic keywords from source document.

3. Method

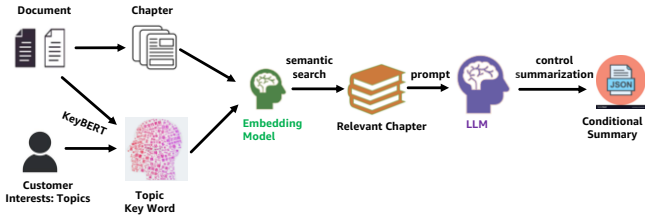

Figure 2. Topic Knowledge based Controlled Generation (TKCG) Framework

3.1. Formulation

Neural summarization models are typically trained on the conditional probability of generating a summary y given a source document x, or $p(y|x)$. This means the model produces summaries solely based on the input document without any other guidance. To better control the summary content, we can provide the model with keywords z representing user preferences. The model would then generate summaries based on the conditional probability distribution $p(y|x,z)$ - generating summary y given document x and keywords z. The keywords allow users to steer the model's summarization towards desired topics. This keyword-conditioned approach enables more controllable and customizable text summarization.

Unlike previous work, we propose the Topic Knowledge based Controlled Generation (TKCG) framework, which automatically extracts topic keywords using KeyBERT. It

incorporates user interests as topic seed words to guide keyword extraction from the document:

$$z = g(x, c) \tag{1}$$

$$y = f(x, z) \tag{2}$$

where g denotes the automatic keyword extraction algorithm, and c represents people preferences (topics), and f is conditional generation algorithm. c can be instantiated as topic seed words list. In this framework, keywords z are extracted from the source document x based on specified topics c. The extracted keywords z then serve as conditional inputs to guide the summarization process. This allows generating summaries tailored to particular user preferences. Figure 2 shows the whole TKCG framework.

3.2. Topic Keywords Extraction

Guided Topic Modeling based on BERT embedding [3] utilizes pre-defined seed topics to guide the topic modeling process. First, embeddings are created for each seed topic by passing the concatenated seed words through BERT. These embeddings are compared to document embeddings using cosine similarity to assign topic labels. Documents most similar to a seed topic receive that topic label, while other documents receive a default label. These labels are fed into Uniform Manifold Approximation and Projection to create a semi-supervised approach that nudges topic creation towards the seeded topics.

Similar to KeyBERT [3], seed words can convey the semantic meaning of a topic. It is a sensible assumption that a document containing the seed words of a topic likely belongs to that topic.

In particular, given a document x, we can determine its topic distribution z_x^c in this manner:

$$f(x, c) = \sum_{s \in c} tf(s, x) \tag{3}$$

$$z_x^c = \frac{\ln(1 + f(x, c) + \gamma)}{\sum_{s \in c}(\ln 1 + f(x, c)) + R\gamma} \tag{4}$$

where $tf(s, x)$ represents the frequency of a seed word s in document x. γ is a Dirichlet smoothing parameter set to 0.01. $R is the total number of seed words per topic$.

Instead of tf, we can use TF-IDF to better capture the importance of a word to a topic. Here, the "document" is the collection of seed words per topic. The inverse document frequency is replaced with inverse class frequency, measuring a term's information content across topics. It is computed as the log of the average seed words per topic divided by the term frequency across all topics, plus one for positivity [8].

This class-based TF-IDF models the significance of words s within a topic c. It allows deriving topic-word distributions for each document. We sum the topic seed words from a single KeyBERT run, which extracts keywords per topic [3].

3.3. Retrieval Augmented Knowledge

LLMs can acquire a substantial amount of knowledge implicitly from data, without needing external memory. However, LLMs have limitations - they struggle to expand or edit their knowledge on their own, explain their predictions, and can generate incorrect "hallucinated" information [9]. To address this, Lewis et al. [9] proposed retrieval-augmented generation (RAG) models. RAG combines the parametric memory of an LLM with a non-parametric dense vector index of Wikipedia, accessed through a retriever. RAG conditions on the same retrieved passages consistently throughout the full generated sequence.

Similarly, we use faiss as the retriever and knowledge store. Since documents are long and LLMs have limited context, we split documents into chapter-sized pieces, like paragraphs or sentences, as defined by the author. Chapters convey content on different topics. We split each document into chapters. We retrieve relevant chapters t using the topic keywords z_x^c as the knowledge. This treats the retrieved document x as a single latent variable, marginalized via a top-K approximation to get the summary probability $p(y|x)$. Specifically, the top-K chapters t are retrieved by faiss using the topic keywords. The generator then produces the output summary probability $p(y|x)$ for each document, and these are marginalized across the retrieved chapters.

$$t = \max_k f(x, z_x^c) \tag{5}$$

$$p(y|x) \approx p(y|t, z_x^c) p(z_x^c|x) \tag{6}$$

3.4. Prompt Engineering

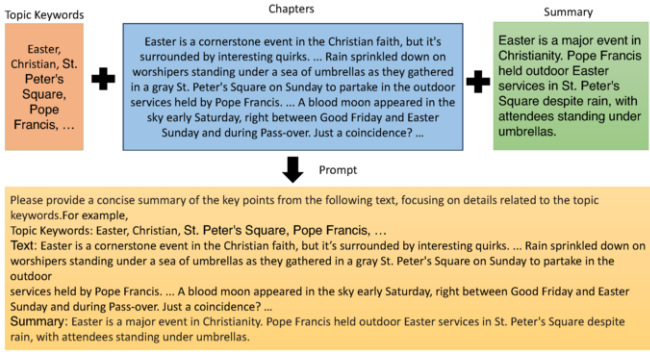

Figure 3. Prompt

Motivated by recent progress in prompting pre-trained models, we explore combining keywords and prompts for summarization. Specifically, we use both topic keywords and top retrieved chapters as prompt. We also leverage in-context learning [10] to provide a few examples as demonstration context. These examples follow natural language

Table 1. Statistic of Datasets. Train, Validation and Test are the number of samples in dataset. Avg. Token is average token length of documents in dataset.

	Train	Validation	Test	Avg. tokens
MACSum	2013	272	266	2754
arXiv	1545	247	240	5946

templates. In-context learning concatenates the instruction and demonstration context to form a prompt, which is then fed into LLMs for prediction.

In summary, our approach utilizes topic keywords, retrieved chapters, and demonstration examples via in-context learning prompts to perform summarization with LLMs. The prompts allow us to provide both content input and format examples to guide the model's summarization predictions. Figure 3 shows the prompt example.

4. Experiments

In this section, we present datasets, test TKCG quantitatively and show experimental results. Our experiment results demonstrate that TKCG significantly outperforms the baselines, highlighting the advantages of topic keywords.

4.1. Dataset and Evaluation

Dataset: We conduct experiments on two long document summarization datasets from different domains: **MACSum** [4] and **arXiv** academic papers [5]. MACSum [2] contains news articles with human-written summaries controlled for various attributes like length, extractiveness, specificity, topic, and speaker perspective. Since customrs are focused on topic-based summarization, we only condition on the topic attribute in our experiments. The arXiv dataset [3] contains lengthy scientific papers with standard structure and abstractive summaries. We use key phrases as topic seed words. Table 1 shows statistic about the two datasets.

Hyper-parameters: The number of topic seed words is 4 for each document. The hyper parameters for Claude generation is temperature as 0.1, top p as 0.9 and top k as 50.

Metric: We evaluate summarization quality using ROUGE metrics and BERTScore [11] when ground truth summaries are available.

* **ROUGE-1** calculates the overlap of individual words (unigrams) between the system and reference summaries.
* **ROUGE-2** calculates the overlap of word pairs (bigrams) between the system and reference summaries.
* **ROUGE-L** measures the length of the longest common subsequence in the reference and hypothesis texts.
* **BERTScore** evaluates language generation using BERT embeddings. BERTScore computes similarity as the sum of cosine similarities between token embeddings in the system and reference.

[2] https://github.com/psunlpgroup/MACSum
[3] https://info.arxiv.org/help/datasets.html

Table 2. F1 scores for ROUGE (1/2/L) on arXiv and MACSum datasets

Model	MACSum			arXiv		
	Rouge-1	Rouge-2	Rough-L	Rouge-1	Rouge-2	Rough-L
Claude	27.8	13.1	26.9	23.2	11.9	21.4
K-means + Claude	28.9	13.6	26.3	**25.4**	14.6	22.3
TKCG + Claude	**31.3**	**14.7**	**29.4**	24.9	**16.7**	**23.7**

Baseline: We evaluate the design choices of our model and the impact of topic keywords. As our method is designed for unlabeled data in an unsupervised fashion, we focus comparisons on unsupervised baselines. For all methods, we use Claude v1 in BedRock Service as LLM.

* **K-means clustering + Claude** This clusters sentences of text semantically into topics itteratively and passes topic information between clustering and then uses Claude to do summarization steps. In experiments, the number of clusters k is 3.
* **Claude** Regular summarization without topic keywords guidance where the LLM summarizes the full input text.

4.2. Results

Table 2 shows the performance of *Claude*, *K-means + Claude* and *TKCG + Claude* on arXiv and MACSum datasets. *K-means + Claude* decently outperforms the strong *Claude* and *K-means + Claude* baselines in terms of Rouge Score. It also performs comparably to *Claude* and *K-means + Claude* on those two datasets in terms of BERTScore as Figure 4 shows. There is a performance gap between *TKCG + Claude* and *K-means + Claude*, possibly due to the effect of topic keywords as TKCG uses KeyBERT [3] to extract key phrases from documents based on BERT Embedding.

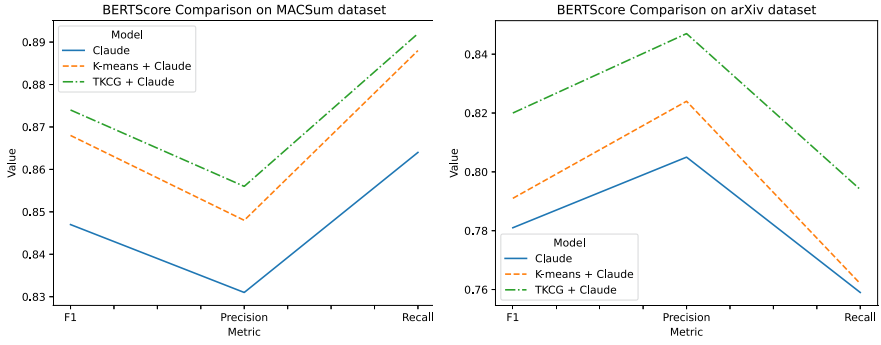

Figure 4. BERTScore for Precision, Recall and F1 on MACSum and arXiv datasets

5. Conclusion and Future Work

Current LLM summarization systems produce generic summaries that do not align with user preferences. To address this, we propose the Topic Knowledge based Controlled Generation (TKCG) framework to control summaries using automatically extracted topic keywords from documents. Experiments on two datasets demonstrate TKCG's efficacy.

TKCG has limitations in handling unrelated input, potentially causing problematic model behaviors. For example, if a user mistakenly inputs "war gun kill" for an NBA article, the model may fabricate content. TKCG does not sufficiently handle such unrelated input, representing an important area for future work. Regarding keyword extraction, TKCG relies on pre-defined seed words per topic being provided. An interesting extension could automatically generate synonyms for topics using a lexical database.

References

[1] Jianpeng Cheng and Mirella Lapata. Neural summarization by extracting sentences and words. In *Proceedings of the 54th Annual Meeting of the Association for Computational Linguistics, ACL 2016, August 7-12, 2016, Berlin, Germany, Volume 1: Long Papers*. The Association for Computer Linguistics, 2016.

[2] Alexander M. Rush, Sumit Chopra, and Jason Weston. A neural attention model for abstractive sentence summarization. In *Proceedings of the 2015 Conference on Empirical Methods in Natural Language Processing*, pages 379–389, Lisbon, Portugal, September 2015. Association for Computational Linguistics.

[3] Maarten Grootendorst. Keybert: Minimal keyword extraction with bert., 2020.

[4] Yusen Zhang, Yang Liu, Ziyi Yang, Yuwei Fang, Yulong Chen, Dragomir Radev, Chenguang Zhu, Michael Zeng, and Rui Zhang. Macsum: Controllable summarization with mixed attributes. *Transactions of the Association for Computational Linguistics*, 11:787–803, 2023.

[5] Arman Cohan, Franck Dernoncourt, Doo Soon Kim, Trung Bui, Seokhwan Kim, Walter Chang, and Nazli Goharian. A discourse-aware attention model for abstractive summarization of long documents. In *Proceedings of the 2018 Conference of the North American Chapter of the Association for Computational Linguistics: Human Language Technologies, Volume 2 (Short Papers)*, pages 615–621, New Orleans, Louisiana, June 2018. Association for Computational Linguistics.

[6] Angela Fan, David Grangier, and Michael Auli. Controllable abstractive summarization. In *Proceedings of the 2nd Workshop on Neural Machine Translation and Generation*, pages 45–54, Melbourne, Australia, July 2018. Association for Computational Linguistics.

[7] Junxian He, Wojciech Kryscinski, Bryan McCann, Nazneen Rajani, and Caiming Xiong. CTRLsum: Towards generic controllable text summarization. In *Proceedings of the 2022 Conference on Empirical Methods in Natural Language Processing*, pages 5879–5915, Abu Dhabi, United Arab Emirates, December 2022. Association for Computational Linguistics.

[8] Maarten Grootendorst. Bertopic: Neural topic modeling with a class-based tf-idf procedure. *arXiv preprint arXiv:2203.05794*, 2022.

[9] Patrick S. H. Lewis, Ethan Perez, Aleksandra Piktus, Fabio Petroni, Vladimir Karpukhin, Naman Goyal, Heinrich Küttler, Mike Lewis, Wen-tau Yih, Tim Rocktäschel, Sebastian Riedel, and Douwe Kiela. Retrieval-augmented generation for knowledge-intensive NLP tasks. In Hugo Larochelle, Marc'Aurelio Ranzato, Raia Hadsell, Maria-Florina Balcan, and Hsuan-Tien Lin, editors, *Advances in Neural Information Processing Systems 33: Annual Conference on Neural Information Processing Systems 2020, NeurIPS 2020, December 6-12, 2020, virtual*, 2020.

[10] Xiaochuang Han, Daniel Simig, Todor Mihaylov, Yulia Tsvetkov, Asli Celikyilmaz, and Tianlu Wang. Understanding in-context learning via supportive pretraining data. *arXiv preprint arXiv:2306.15091*, 2023.

[11] Tianyi Zhang*, Varsha Kishore*, Felix Wu*, Kilian Q. Weinberger, and Yoav Artzi. Bertscore: Evaluating text generation with bert. In *International Conference on Learning Representations*, 2020.

Fuzzy Systems and Data Mining IX
A.J. Tallón-Ballesteros and R. Beltrán-Barba (Eds.)

doi:10.3233/FAIA231088

The Impact of Social Responsibility Disclosure on R&D Investment in Small and Medium Enterprises

Jiani Huang[1]
Lanzhou University of Technology, China

Abstract. Small and medium-sized enterprises (SMEs) are an important cornerstone of the national economy and social development, and a key driving force in promoting innovation and development. This paper selects a sample of China's SME and GEM listed companies from 2012 to 2021 to explore the relationship between social responsibility disclosure, executive compensation incentives and R&D investment. The study found that: whether state-owned or non-state-owned, the disclosure of social responsibility information in small and medium-sized enterprises can promote R&D investment; for SMEs, executive compensation incentives can enhance the driving force of social responsibility disclosure on R&D investment, and this enhancement effect is higher in non-state-owned enterprises than in state-owned enterprises.

Keywords. Small and medium-sized enterprises; social responsibility disclosure; R&D investment; executive compensation incentives

1. Introduction

The report of the 20th Party Congress clearly states that "innovation is the first driving force"[1]. In recent years, the state has paid increasing attention to the innovation of SMEs. 2021 In December 2021, the Ministry of Industry and Information Technology and other departments jointly issued the "14th Five-Year Plan for Promoting the Development of Small and Medium-Sized Enterprises", which puts forward measures to promote the innovation of SMEs. SMEs are a new force for national economy and social development [2], but their capacity for innovation is low [3]. In recent years, CSR accidents have occurred frequently, for example, Sanlu Milk Powder closed down because of the melamine incident, and Shuanghui Group paid a huge amount of compensation due to the illegal use of additives . Such CSR issues have been focused and amplified, which has aroused a strong demand from all sectors of the society for enterprises to disclose their social responsibility information [4]. Social responsibility information disclosure is categorized into mandatory and voluntary disclosure [5]. China's current policies on social responsibility disclosure mainly include the Company Law, Administrative Measures on Information Disclosure of Listed Companies and Guidelines on Corporate Social Responsibility Reporting (for Trial Implementation). With the growing importance of social responsibility, most SMEs with awareness and

[1] Corresponding Author, Jiani Huang, Lanzhou University of Technology, China; Email: a1047139057@126.com

resources have begun to voluntarily disclose social responsibility information to enhance their corporate image and competitiveness. Therefore, this paper will explore the impact of SMEs' social responsibility information disclosure on R&D investment, and provide a theoretical basis for promoting SMEs' R&D investment. Reviewing previous studies, most scholars at home and abroad believe that social responsibility disclosure and R&D investment are positively correlated. Based on the data of A-share listed companies from 2010 to 2019, Zhao Shengmin and Yu Xinghui (2023) showed that social responsibility has a significant positive promotion effect on innovation input, innovation output, and innovation efficiency [6]. However, there are also a few scholars who believe that the two have a negative correlation or an inverted U-shaped relationship.Isabel et al. (2011), based on a sample of global R&D inputs from 2003-2007, found that social responsibility inhibits R&D inputs [7]. The contribution of this paper is mainly reflected in the following three aspects: first, this paper innovatively promotes the sustainable development of small and medium-sized enterprises (SMEs) from the core issues of SMEs' development; second, this paper discusses the impact of social responsibility disclosure on R&D investment and analyzes the moderating role of executive compensation incentives in the relationship between the two, which enriches the research in the related fields of social responsibility disclosure and R&D investment; and third, this paper discusses whether there are differences in the role of social responsibility disclosure on R&D investment and the moderating role of executive compensation incentives among SMEs with different property rights, with a view to providing useful references for the implementation of differentiated innovation incentives for SMEs with different property rights in China.

2. Theoretical analysis and research hypothesis

2.1. Social Responsibility Disclosure and R&D Investment

In recent years, more and more SMEs have begun to recognize the importance of social responsibility for their enterprises and have integrated it into their strategies and operations [8]. Many SMEs take a positive attitude towards social responsibility information disclosure and have begun to take the initiative to prepare and voluntarily disclose CSR reports to publicize the fulfillment of corporate social responsibility to the public and stakeholders. Social responsibility information disclosure has been a long-term strategy for the development of SMEs, which has the effect of alleviating information asymmetry and improving the financing difficulties of enterprises [9]. On the one hand, through information disclosure, SMEs can provide stakeholders (e.g., suppliers, customers, etc.) with information on corporate social responsibility, enhance effective communication with stakeholders, establish a solid relationship with stakeholders [10], enable stakeholders to have an in-depth understanding of enterprise operation and investment, and thus obtain stakeholders' support for SMEs' innovation resources [11], alleviate financing constraints, and increase the amount of financing resources. On the other hand, SMEs can send favorable signals to the society through the disclosure of social responsibility information, so that the enterprise's social image and competitive advantage can be further improved, and the outside world's trust in the enterprise's R & D capabilities and recognition. This not only helps to attract more investors to join, but also enhances their willingness to invest, so that SMEs can get

investors to invest more resources [12], and then increase the enterprise's R & D investment. In addition, social responsibility disclosure can effectively inhibit the opportunistic behavior of executives [13] and reduce the agency problem. When executives know that their behavior will be publicly disclosed and monitored by the public, they are more motivated to take more reliable decisions to ensure the success of the enterprise. This constraint can motivate executives to invest more actively in R&D and provide more resources for SMEs to innovate. Based on the above analysis, this paper proposes the Hypothesis 1: There is a significant positive effect of social responsibility disclosure of SMEs on R&D investment.

2.2. The moderating effect of executive compensation incentives

There are two channels through which CSR disclosure affects R&D investment, one is to satisfy the needs of stakeholders; the other is to obtain various resources. Executive compensation incentives have an important moderating role in both processes [14]. First, executives tend to pursue personal interests at the expense of long-term company development, and are reluctant to invest resources in R&D activities that have a long payback period [15]. The optimal contract theory points out that executive compensation incentives, as a mechanism to alleviate agency conflicts [16], can link the interests of executives with the interests of the company [17] and effectively reduce the agency problem. Therefore, the higher the executive compensation, the more they understand the stakeholders' expectations of their own firms' disclosure of social responsibility information, and they are able to satisfy them better than executives with lower compensation when communicating with stakeholders and take the initiative to conduct research and development activities. Secondly, resource dependence theory states that enterprises usually cannot be self-sufficient and need to seek resources from the environment in order to grow and develop [18]. The executive compensation incentive mechanism can enhance the motivation of executives [19], thus increasing the executives' motivation to seek external resources and their ability to obtain them, which in turn will bring more financial and non-financial resources to SMEs, so that the enterprises will put more time, energy and resources in R&D activities. In addition, higher compensation incentives can attract more executives with specialized knowledge and experience to join SMEs [20], which in turn can provide new ideas and strategies for the firm in terms of meeting the needs of stakeholders and acquiring resources, which in turn can attract investors to join the firm to a greater extent and promote R&D activities. Based on the above analysis, this paper proposes the Hypothesis 2: Executive compensation incentives play a positive moderating role in the relationship between social responsibility disclosure and R&D investment in SMEs.

3. Study design

3.1. Sample Selection and Data Sources

Since the research object of this paper is small and medium-sized enterprises , the samples of listed companies in China's small and medium-sized enterprises and the Growth Enterprise Market from 2012 to 2021 are selected as samples, and undergo a series of screening. Financial and ST and *ST listed companies are excluded, and samples with missing variables are excluded. This resulted in 13,097 observations, with

the underlying data coming from the Cathay Pacific database. In addition, all continuous variables in this paper were subjected to a two-way shrinkage of the top and bottom 1%, and the data were analyzed using a combination of Excel and Stata 17.0 software.

3.2. Definition of variables

Research and development (R&D) investment: referring to Zhao Shengmin and Yu Xinghui (2023), the natural logarithm of the amount of firms' R&D investment after adding 1 is used as a measure [6].

Social responsibility disclosure (CSR): drawing on Zou Ping (2018), a value of 0 to 1 is assigned to whether or not a certain criterion is disclosed in the social responsibility report, e.g., whether or not to disclose the protection of shareholders' rights and interests, yes is 1 and no is 0.The standardized scores were then summed and divided by 12 to obtain the metrics [21].

Executive Compensation Incentives (EC): with reference to Zhang Guofu and Wang Ran (2021), the natural logarithm of the total compensation of the top three executives is used as a measure [19].

Control variables (Control): with reference to existing studies, variables related to social responsibility disclosure, executive compensation incentives and R&D investment were selected as control variables. Industry and year dummy variables are also introduced. The variables are defined as shown in Table 1.

Table 1. Definition of variables

Variable Type	Variable Name	Variable Symbol	Variable Definition
Explained Variables	R&D investment	R&D	The natural logarithm of the amount of R&D investment made by the enterprise in the year plus one
Explanatory Variable	Disclosure of social Responsibility information	CSR	Summarize and standardize the 12 criteria scores of the social responsibility reports in the Cathay Pacific database
Moderator Variable	Executive compensation incentives	EC	Natural logarithm of total compensation for top three executives
Control Variable	Company size	Size	Natural logarithm of total assets
	Tobin's Q	TobinQ	Enterprise market value/total assets
	Fixed asset ratio	Fixed	Fixed assets/total assets × 100%
	Return on assets	ROA	Net profit/total assets × 100%
	Nature of property rights	State	State-owned firms take 1, otherwise 0
Virtual Variable	Sector	Industry	Industry dummy variables
	Vintages	Year	Year dummy variables

3.3. Model construction

To test the hypotheses of this paper, the following regression model is constructed:

$$R\&D = \beta_0 + \beta_1 CSR_{i,t} + \beta \sum Control_{i,t} + Industry_{i,t} + Year_{i,t} + \varepsilon_{i,t} \quad (1)$$

$$R\&D = \beta_0 + \beta_1 CSR_{i,t} + \beta_2 EC_{i,t} + \beta_3 CSR_{i,t} \times EC_{i,t} + \beta \sum Control_{i,t} + Industry_{i,t} + Year_{i,t} + \varepsilon_{i,t} \quad (2)$$

Among them, model (1) is a multiple regression model to test the impact of SMEs' social responsibility disclosure on R&D investment, and model (2) is to examining the moderating role of executive compensation incentives by adding the moderating

variables and their cross-multiplication terms with the explanatory variables on the basis of model (1).

4. Empirical analysis

4.1. Descriptive statistics

As shown in Table 2, the overall R&D investment of China's SMEs is weak, and there is a large gap between the R&D investment of different enterprises. The degree of social responsibility information disclosure of SMEs varies greatly, and the minimum value of CSR is 0, which indicates that some SMEs disclose information that does not include any of the 12 criteria, and these SMEs have negative disclosure of social responsibility information. There is a large difference in the incentives for executive compensation.

Table 2. Descriptive statistics

VARIABLES	N	mean	sd	min	max
$R\&D_{i,t}$	13,097	17.82	1.156	14.60	20.92
$CSR_{i,t}$	13,097	0.454	0.246	0	0.833
$EC_{i,t}$	13,097	14.42	0.649	12.91	16.20
$Size_{i,t}$	13,097	21.70	0.937	19.98	24.37
$TobinQ_{i,t}$	13,097	2.238	1.270	0.964	8.136
$Fixed_{i,t}$	13,097	18.46	12.39	0.410	54.14
$ROA_{i,t}$	13,097	3.895	7.340	-34.08	20.27
$State_{i,t}$	13,097	0.110	0.312	0	1

4.2. Correlation analysis

As can be seen from Table 3, the correlation coefficients of CSR and R&D are significantly positive at the 1% level, initially verifying hypothesis 1. The values of the coefficients between the variables are all less than 0.7, and the mean value of the VIF does not exceed the critical value of 10, which indicates that there is no problem of multicollinearity.

Table 3. Descriptive statistics

	$R\&D_{i,t}$	$CSR_{i,t}$	$EC_{i,t}$	$Size_{i,t}$	$TobinQ_{i,t}$	$Fixed_{i,t}$	$ROA_{i,t}$	$State_{i,t}$
$R\&D_{i,t}$	1							
$CSR_{i,t}$	0.218***	1						
$EC_{i,t}$	0.473***	0.215***	1					
$Size_{i,t}$	0.662***	0.271***	0.448***	1				
$TobinQ_{i,t}$	-0.033***	-0.052***	0.035***	-0.228***	1			
$Fixed_{i,t}$	-0.080***	0.090***	-0.092***	0.024***	-0.048***	1		
$ROA_{i,t}$	0.070***	0.028***	0.120***	-0.0140	0.162***	-0.057***	1	
$State_{i,t}$	0.086***	0.070***	0.075***	0.145***	-0.004	0.063***	-0.033***	1

Note: *, **, and *** indicate significant at the 10%, 5%, and 1% significance levels, respectively.

4.3. Regression analysis

As shown in Table 4, the regression coefficients for CSR are significantly positive at the 10% level, and Hypothesis 1 is valid. The regression coefficients for both CSR and cross-multiplier terms are significantly positive at the 10% level, and Hypothesis 2 is valid.

Table 4. Regression results

VARIABLES	(1) $R\&D_{i,t}$	(2) $R\&D_{i,t}$
$CSR_{i,t}$	0.042*	0.063*
	(1.78)	(1.75)
$EC_{i,t}$		0.148***
		(6.69)
$CSR_{i,t}\times EC_{i,t}$		0.084*
		(1.68)
$Constant_{i,t}$	-1.890***	-2.564***
	(-6.95)	(-3.37)
$Industry_{i,t}$	YES	YES
$Year_{i,t}$	YES	YES
N	13,097	13,097
R^2	0.612	0.620

4.4. Robustness Tests

In this paper, we perform robustness tests on explanatory variables lagged by one period. As shown in Table 5, hypotheses 1 and 2 are tested and the results are robust.

Table 5. Robustness test results

VARIABLES	(1) $R\&D_{i,t}$	(2) $R\&D_{i,t}$
$CSR_{i,t-1}$	0.052**	0.065***
	(2.14)	(2.64)
$EC_{i,t}$		0.190***
		(14.68)
$CSR_{i,t-1}\times EC_{i,t}$		0.069**
		(2.25)
$Constant_{i,t}$	-1.723***	-3.225***
	(-5.85)	(-10.43)
$Industry_{i,t}$	YES	YES
$Year_{i,t}$	YES	YES
N	10,779	10,779
R^2	0.591	0.596

4.5. Heterogeneity test

This study conducts group tests based on whether they are state-owned or not. As shown in Table 6, the coefficients of CSR are all significantly positive, indicating that social responsibility disclosure of SMEs, whether SOEs or non-SOEs, can promote R&D investment. The cross-multiplier term in column (2) is not significant, while the the cross-multiplier term in column (4) is significantly positive at the 1% level, indicating that the moderating effect of executive compensation incentives is more pronounced in non-state-owned.

Table 6. Robustness test results

VARIABLES	Nationalized Enterprises		Non-State-Owned Enterprises	
	(1) $R\&D_{i,t}$	(2) $R\&D_{i,t}$	(3) $R\&D_{i,t}$	(4) $R\&D_{i,t}$
$CSR_{i,t}$	0.196**	0.174**	0.167***	0.153***
	(2.40)	(2.13)	(6.78)	(6.11)
$EC_{i,t}$		0.181***		0.214***
		(4.04)		(16.20)
$CSR_{i,t}\times EC_{i,t}$		0.062		0.100***
		(0.50)		(3.18)
$Constant_{i,t}$	-5.551***	-6.460***	-2.312***	-3.175***
	(-6.60)	(-7.35)	(-8.89)	(-11.99)

$Industry_{i,t}$	YES	YES	YES	YES
$Year_{i,t}$	YES	YES	YES	YES
N	1,436	1,436	11,661	11,661
R^2	0.538	0.545	0.595	0.606

5. Conclusions and recommendations of the study

5.1. Conclusions of the study

This paper selects China's SME and GEM listed companies from 2012 to 2021 as the research object, discusses the relationship between social responsibility information disclosure, executive compensation incentives and R&D investment, puts forward the research hypotheses based on relevant theories and carries out the empirical analysis. The paper draws the following conclusions: SMEs' social responsibility disclosure has a positive impact on R&D investment, and this impact exists in both state-owned and non-state-owned enterprises; executive compensation incentives positively modulate the positive impact of SMEs' social responsibility disclosure on R&D investment, and this moderating effect is stronger in non-state-owned enterprises than in state-owned enterprises.

5.2. Recommendations for countermeasures

SMEs should take the following measures: first, SMEs should actively disclose social responsibility information to make SMEs sustainable in the long term. Second, SMEs should combine social responsibility with R&D activities, formulate relevant strategies for the enterprise, and alleviate the pressure of financing in order to promote R&D investment. Finally, SMEs with different property rights need to build a comprehensive executive incentive system according to their own different situations. Government departments should strengthen their requirements in the following three areas: first, the government should encourage SMEs to disclose social responsibility information to promote SMEs' active innovation. Second, the government should help SMEs to establish information disclosure channels, in order to facilitate their timely updating of dynamic information. Finally, the government should provide more support and backing measures to promote SMEs to actively engage in innovative activities.

References

[1] Li Zheng,Liao Xiaodong. The theoretical origin, inner essence and contemporary value of Xi Jinping's important exposition on science and technology innovation[J]. Study and Exploration,2023(02):93-100+2.

[2] Zhou Shi. Research on the Trends, Problems and Support Strategies of Small and Medium-sized Enterprises[J]. Macroeconomic Research,2022(07):163-175.

[3] "14th Five-Year Plan" for Promoting the Development of Small and Medium-sized Enterprises[J]. Small and Medium-sized Enterprises Management and Technology,2022(09):1-12.

[4] Yang Jinkun. Corporate Social Responsibility Disclosure and Innovation Performance: An Empirical Study of Chinese Listed Companies in the Era of Mandatory Disclosure[J]. Science and Science and Technology Management,2021,42(01):57-75.

[5] YAO Haixin, WANG Xuanqiao, WANG Peng. A study of social responsibility disclosure to enhance the effectiveness of executive compensation contract - based on the supervisory governance effect of disclosure[J]. Journal of Management,2023,36(02):80-98.

[6] Zhao Shengmin,Yu Xinghui. A study of the impact of corporate social responsibility on corporate innovation--empirical evidence from Chinese listed companies[J]. Research Management,2023,44(04):144-153.

[7] Isabel Gallego-Álvarez and José Manuel Prado-Lorenzo and Isabel-María García-Sánchez. corporate social responsibility and innovation: a resource-based theory[J]. Management Decision,2011,49(10):1709-1727.

[8] JIN Xiaocui, ZHU Lingling. Corporate social responsibility and technological innovation: compatible or repulsive? --An analysis based on the perspective of corporate strategic management[J]. Scientific Decision Making,2021(09):59-72.

[9] Gao F, Dong Y, Ni C, et al. Determinants and Economic Consequences of Non-financial Disclosure Quality[J]. European Accounting Review,2015,25(2).

[10] Hao Ying, Li Xueyi, Ni Juan. Corporate Social Responsibility and Financing Constraints: A Study Based on the "Avoidance-Risk" Effect[J]. Journal of Yantai University (Philosophy and Social Science Edition),2023,36(04):76-86.

[11] Xie Yi,Tong Li,Ran Rong. Industry Heterogeneity, Social Responsibility and Corporate Technological Innovation[J]. Chongqing Social Science,2022(06):59-78.

[12] Han Zichao,Zhang Youtang. Social Responsibility Disclosure, Cost of Capital and Corporate Sustainability - Based on Impression Management Perspective[J]. Accounting Newsletter,2022(03):41-46+56.

[13] Zhang Yingming,Xu Chen. Executive Team Characteristics, Social Responsibility Awareness and Financial Fraud Risk - A Threshold Effect Test Based on A-share Listed Companies[J]. Friends of Accounting,2021(22):58-65.

[14] Kamidi A, Guo JH. Corporate social responsibility and innovation: the moderating role of executive team tenure and its heterogeneity[J]. China Science and Technology Forum,2021(03):133-142+180.

[15] LI Huaijian,GENG Xiaohan. R&D investment, executive incentives and corporate performance--an empirical study based on listed companies in China[J]. Journal of Harbin University of Commerce (Social Science Edition),2021(06):36-48.

[16] Bourke J, Crowley F. THE INFLUENCE OF THE MANAGER ON FIRM INNOVATION IN EMERGING ECONOMIES[J]. International Journal of Innovation Management, 2017:1850028.

[17] WANG Jing, ZHU Ruixue, LI Chang'e. Executive compensation stickiness and corporate innovation--an empirical test based on state-owned listed companies[J]. Dongyue Lecture Series,2022,43(08):109-122+192.

[18] Wan, L.-Q., Deng, K.. Chain shareholders and corporate innovation: promotion or inhibition?[J]. Friends of Accounting,2022(12):135-143.

[19] Guofu Zhang,Ran Wang. Executive trade association tenure, compensation incentives and corporate social responsibility[J]. Finance and Accounting Monthly,2021(22):38-46.

[20] Hu Xiajie. How Pay Gap Affects Firms' Innovation-Based on the Dual Perspectives of Internal and External Perspectives[J]. Friends of Accounting,2022(23):116-122.

[21] Zou Ping. "Practice what you preach" or "Return the favor"? --Corporate Social Responsibility Disclosure and Effective Tax Liability[J]. Economic Management,2018,40(03):159-177.

Fuzzy Systems and Data Mining IX
A.J. Tallón-Ballesteros and R. Beltrán-Barba (Eds.)

doi:10.3233/FAIA231089

Innovative Approach to Children's Desk Lamp Using Stable Diffusion Technology

Tianxin Li[1]
School of the Art Institute of Chicago, USA

Abstract. The emergence of AI intelligent drawing technology has completely revolutionized the traditional model of the design industry. With the help of smart technology, designers can quickly generate a large number of creative images in various styles and content. This greatly enhances design efficiency and has a revolutionary significance in promoting design innovation. This article focuses on the creative process in the design of children's table lamps. It uses the AI drawing software "Stable Diffusion Web UI" based on deep generation technology as a tool to combine the professional skills of designers with AI drawing technology to achieve the creative design goal of personalized children's table lamps. The specific content and methods include: (1) building a lamp image library, quantitatively describing the design style of children's table lamps, extracting composition, and summarizing the different structural-semantic features of lamps. (2) Generating feasible creative lamp product ideas based on the Stable Diffusion Web UI software. Through research and exploration, the style description and structural characteristics of children's table lamps were summarized, and the parameters for generating creative lamp ideas using the Stable Diffusion Web UI software were determined. This has been helpful in furthering the integration of artificial intelligence and product design.

Keywords. Children's desk lamp, creative approach, deep generation technology, stable diffusion.

1. Introduction

The creative process is a critical component of product design. For a long time, the design of the creative process heavily relied on the divergent thinking and manual drawing abilities of designers. However, traditional methods of manually creating creative images are limited by cognitive constraints, as well as the personal drawing styles and skills of the designers. This makes it difficult to achieve stylistic variations and innovations. At the same time, the inefficiency of manual creative drawing cannot meet the demands of rapid design iteration, creating bottlenecks in the development of the design industry.

The emergence of AI intelligent drawing technology has completely revolutionized the traditional model of the design industry. It significantly enhances design efficiency, which is revolutionary in promoting design innovation. However, the question remains: how can intelligent technology be harnessed by designers to better serve design goals? What are the different applications of intelligent drawing technology in various scenarios? Designers often encounter challenges during the application process and need to continually address and resolve them.

[1] Corresponding Author, Tianxin Li, School of the Art Institute of Chicago, USA; Email: litianxin2014@gmail.com

2. Related works

In recent years, the application of Artificial Intelligence (AI) technology across various domains has garnered significant attention. Researchers such as Gao Xuchao [1] and Li qinggang[2] have delved into the application of AI technology in railway construction and operation, while Zhao Tianqi[3]and others have explored the profound impact AI technology will have on the engineering field, particularly in fine-tuned design contributions. Wang Xiaohui[4] and his team have focused on AI's application in personalized cultural design, with an emphasis on the use of deep generation models.

Cheng Sun[5] and colleagues have applied AI technology in architectural design, discussing its practical application in the field from three perspectives: information integration, mapping modeling, and decision support. This provides a new perspective on how to use AI effectively in design. Sun[6] and his team have introduced a human-machine collaborative drawing system based on Generative Adversarial Networks (GAN) in their research, which can be used to generate highly realistic images. Further research by Ma Yongjie[7] and others categorizes and analyzes the improvements in GAN, showcasing its innovations and accomplishments in the field of AI drawing. Lianglei[8], Zhan Shi[9], and their peers explore the potential of SD models in generating general images. Zheng Kai and Wang Di's[10] research examines the application and development of AI image generation from a modular perspective, providing comprehensive insights into the relevant usage scenarios, methods, and instructions.

Dehouche Nassim[11] and others evaluate the potential of AI drawing in teaching art history, aesthetics, and techniques from an art education perspective. The British company Arom has successfully designed and produced candle products using their AromAI, signifying the vast application potential of AI technology in product design[12].

In summary, in the currently published papers, although researchers have made some progress in the area of AI-generated design, their research results and quantity are not sufficient, and most of the research areas remain in the field of architecture and engineering. The research on artificial intelligence technology in the field of product design is still weak.

This paper focuses on exploring the application of SD technology in creative product sketching. Taking specific goals and applications as a starting point, the study compares the problems, causes, and solutions of different SD technology approaches in realizing specific task goals. The study is a tentative exploration of SD technology in the field of product design. The research process and conclusions provide some references for the application of AI applications in the creative design stage of products.

3. Relevant theories and methodologies

3.1 Denoising Diffusion Probabilistic Models (DDPM)

DDPM is the foundation of the Stable Diffusion model, tasked with producing images that accurately reflect the training data's distribution. Its process involves feeding a text description and a random image into the model, which, upon learning, yields an image that aligns with the provided text. Figure 1 provides a visual depiction.

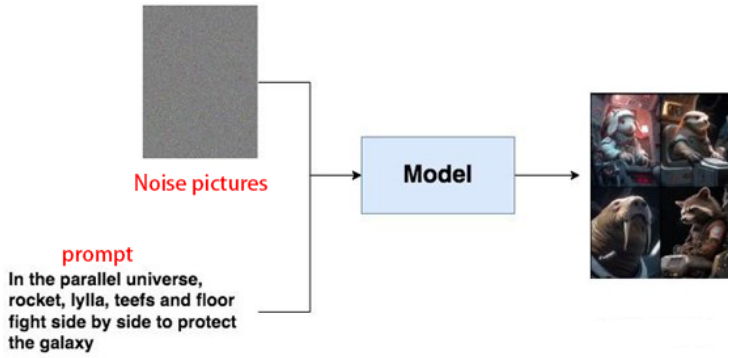

Figure 1 DDPM Image Generation Principle

3.2 Stable diffusion model

The Stable Diffusion Web UI is a drawing software based on the Stable Diffusion (SD) model. The SD model, also known as the Stable Diffusion model, is an advanced version of the DDPM model. When the SD model is used to create or edit an image, it first maps the image to a lower-dimensional space called the latent space. Compared to the original image space, this space has fewer dimensions, which greatly improves computational efficiency. The core of the SD model is the diffusion process, which includes both forward and backward diffusion.

In the forward diffusion process, the model gradually adds noise to the original image, causing the original features of the image to become progressively blurred until it finally appears as an image resembling random noise. The main focus of the diffusion model is on the backward diffusion process. In reverse diffusion, starting from a noise image without any features, the model gradually removes the noise and guides the generation process to eventually recover the original image.

To achieve this goal, the model must compute an "optimal noise" at each step, which indicates the amount of noise to be removed in the current step. This calculation can be effectively performed using a deep learning model, such as the noise predictor UNet. During the training process, the noise predictor continuously adjusts its weights to improve prediction accuracy. In the reverse diffusion process, using the predicted "optimal noise", the noise is gradually removed and the original image is recovered from the noisy image. Through repeated execution, a clear original image can be obtained.

In summary, the SD model utilizes both forward and backward diffusion processes as well as the predictive ability of the noise predictor to effectively recover the original image from a noisy image. In addition, the SD model library allows users to select and customize their training, resulting in the creation of model libraries with specific styles, such as realistic models. This high level of control has opened up new possibilities in the field of AI art and image generation.

3.3 Introduction to Sampling Methods

During the image generation process, users need to select different sampling methods to remove excess noise when generating images. The Stable Diffusion web interface integrates several samplers, most of them created by Katherine Crowson and based on

research by Jiaming Song, Karras, Cheng Lu, and others. This article focuses primarily on the following sampling methods

(1) DPM2 by Karras

The DPM2 method uses ancestral sampling, and the setting of the "eta" parameter can affect the results.

(2) DPM++ 2S by Karras

This sampling method is based on the research of Cheng Lu and others. It uses K-diffusion technology to achieve second-order one-step operations and combines ancestral sampling. The parameter "eta" also affects the results in the DPM++ 2S a sampling method. Cheng Lu has made the implemented code available on GitHub, and users can customize their choices for first-order, second-order, third-order, and single-step or multi-step operations as needed. The web interface uses a version with default parameters.

(3) DPM++ 2M

This is a second-order multi-step sampling method based on the research of Cheng Lu and others, implemented under K-diffusion technology.

(4) LMS of Karras

This method, based on Karras' research, applies Karras' noise schedule method and shows strong advantages in terms of image color and vibrancy.

3.4 ControlNet

ControlNet is a neural network architecture that can control the SD model, allowing the SD model to accommodate a wider range of input conditions. The original SD model could accept input from prompts and source images, while ControlNet provides various input conditions, including canny edges, semantic segmentation maps, key points, and doodles, thus expanding the boundaries of SD's capabilities and greatly enhancing the controllability of AI art creation. The visual structure of ControlNet is shown in Figure 2.

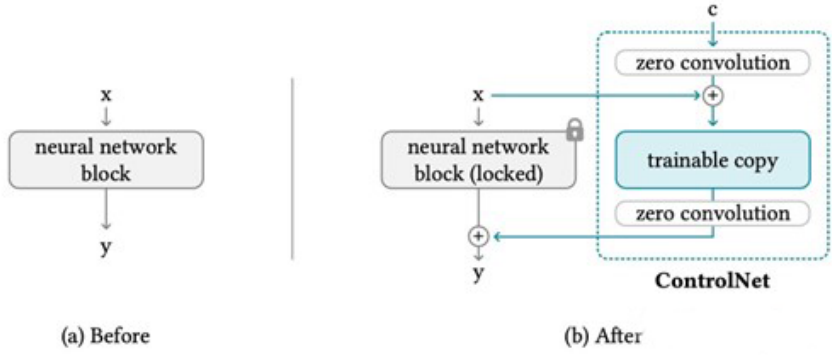

Figure 2 ControlNet's visual structure diagram.

The network structure of ControlNet can be divided into two parts: the "locked copy" and the "trainable copy". The "locked copy" fixes the original weights of the stable diffusion, preserving the image generation capabilities already learned by the stable diffusion.

In Figure 2, the zero convolution is a 1x1 convolutional layer with weight and bias initialized to zero. Since the zero convolution initializes both weight and bias to zero before training begins, the entire ControlNet model remains in its original stable diffusion state. Only after training with your own data will the trainable copy in Figure 2(b) and the learnable parameter values in the zero convolution change, allowing the entire network to learn the specific task you specify. In short, users can influence and control the generated images by uploading their own data, such as product structure images.

4. Experimental Exploration

This section provides a detailed description of the experimental process, the problems and challenges encountered, and how these problems were solved.

4.1 Experimenting with the Standard Stable Diffusion Model

In the initial phase of the research, this thesis chose the default stable diffusion model SD 1.5.safetensors as the starting point for the experiments. The experiments were conducted on a Windows 10 operating system with WebUI version ID 1.60. The goal of the experiment was for the model to generate images that meet the requirements of the experimenter, based on given keyword prompts.

Since the target audience is children, who tend to prefer cute product styles, keywords such as "desk lamp," "animals," and "children" were chosen as input in this paper. Several sampling methods were chosen for the sampling process, including DPM++ 2S a Karras, DPM2 a Karras, LMS Karras, and DPM++ 2M Karras. A step size of 30 was chosen, the CFG scale was set to 8, and the model was used to generate images corresponding to the given scenes (see Figures 3-6).

Figure 3 DPM2 a Karras Sample Generation

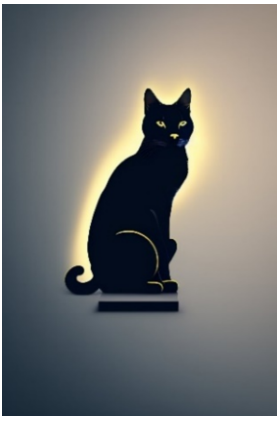

Figure 4 DPM++ 2S a Karras Sample Generation

Figure5 DPM++ 2M Karras Sample Generation

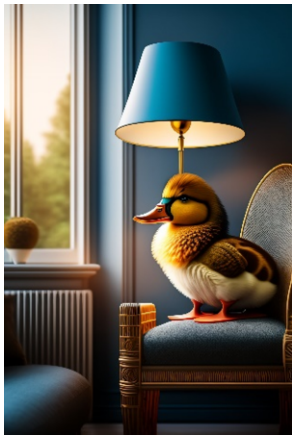

Figure 6 LMS Karras Sample Generation

From the above text, it can be seen that the images generated by the SD 1.5.safetensors model have a certain artistic quality in terms of visual style, but their performance does not meet expectations. For example, the generated image in Figure 3 has a strong artistic quality, but does not correspond to normal human perception. Figure 4 lacks the key element of a desk lamp, and shows only light and an animal. Figure 5 lacks a sense of design and does not meet the author's expectations for the animal-shaped desk lamp, showing only separate elements of an animal and a desk lamp. Figure 6 lacks a logical connection, and the connection between the animal and the desk lamp seems rigid and cannot be used as a creative image.

The research results show that SD 1.5.safetensors can accommodate different styles and are suitable for designers trying to generate images for the first time. However, its disadvantage lies in the lack of control over the style and logical coherence of the generated images, which requires operators to make detailed adjustments.

Regarding the sampling method, based on experiments, LMS Karras produces the best results in generating creative product images among the four sampling methods. Despite a strong artistic quality, the generated products have bright colors, relatively good texture, and logical coherence compared to the other sampling methods. Therefore, LMS Karras is chosen as the sampling method for the following experiments.

In terms of descriptions, the performance of the standard SD 1.5.safetensors model is quite poor. In most cases, it cannot correctly interpret the intended meaning of the text expressed by the author. This is especially obvious when it comes to generating images that combine two nouns, e.g. when the author enters "animal lamp", as the generated image often shows separate entities of an animal and a lamp. According to the analysis, the reason for this is that the standard training dataset of the stable diffusion model consists mainly of images with an artistic style, which results in images that often show pronounced fusion features. In addition, the model clearly lacks the necessary training for more complex product image generation tasks.

4.2 Experimental approach using the realistic model

Given the limitations of the default stable diffusion model, SD 1.5.safetensors, this experiment aims to explore alternative solutions. Specifically, we're attempting creative image generation using the advanced Realistic model, which is based on SD

1.5.safetensors. In addition, we will optimize and modify the input prompts, including reverse prompts, to improve the image generation process. Some examples of reverse prompt keywords are "blur", "low resolution", "text", "crop", "worst quality", "low quality", "normal quality", "jpeg", "artifacts", "signature", "watermark", "username", "blur", "text", "signature", "watermark", "simple background", "cartoon", "date", "low resolution", "line art", "flat color", and so on.

For the sampling method, we use LMS Karras. In addition, we've chosen the "Latent (nearest)" option in the upscaling algorithm to perform high-resolution enhancement of the images. This process involves 10 iterations, a redraw magnitude of 0.7, and a magnification factor of 2. These settings are used for image generation. In this experiment, we also use different product style keywords such as "Chinese style," "antique style," "simple style," and "European style" to guide and diversify the image generation trials (see Figures 7-10).

Figure 7 Chinese style

Figure 8 antique style

Figure 9 simple style

Figure 10 European style

The research results show that by using the realistic model and adjusting the parameters while optimizing the prompts, the generated images show improved logical coherence and visual quality compared to the standard model. However, there are still limitations in terms of structure; the model struggles to produce fine and precise results. For example, there are logical inconsistencies in the position of the light bulb design, structural anomalies in the animals (such as the head appearing in the chest area and strange proportions), and illogical relationships between the desk lamp and the animal (where the lamp is positioned over the animal and the animal is treated as a decorative element).

An analysis of the generated images suggests that the realistic model relies more on random processes for generation, indicating its shortcomings in detail control. As a result, it can be concluded that the Realistic model, compared to the standard Stable Diffusion model, is more inclined to a realistic style in its training dataset. Therefore, it is more suitable for generating everyday objects.

4.3 ControlNet Introduction Experiment

To address the problems of the unreasonable animal structure in the creative image generation of the above product, the irrational relationship between the animal and the table lamp, and the illogical positioning of the bulb design, the ControlNet plugin was introduced in this experiment. This plugin provides more maneuverability for AI drawing, for example, it can clearly show the image structure generated by the model through a simple schematic, as shown in Figure 10. The author used the ControlNet plugin to draw the desired product structure features - the lower body is elliptical, the upper head is smaller relative to the lower part, and their relationship is superimposed. At the same time, the keywords were set as an animal table lamp, children, minimalist style, and the lamp inside the animal. ControlNet used the perfect pixel mode, with the control type set to segmentation, the preprocessor set to reference_only, the control weight set to 1, the guided access set to 0.28, the termination timing set to 1, and the control mode set to balanced. Image generation was then performed. After filtering, the creative image of the product that met the author's expectations was obtained (see Figure 11).

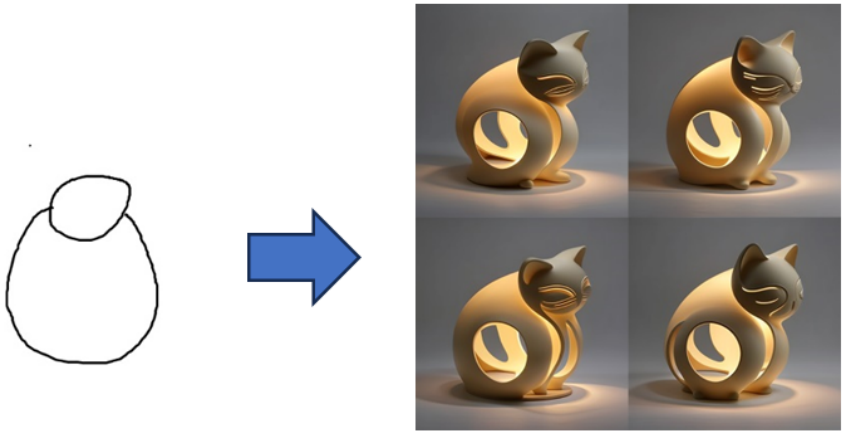

Figure 11 The partial product creative image generated after adjustments through ControlNet

The research has shown that by using the ControlNet plugin, the generated images can be more precisely controlled in terms of content and structure by the author, allowing for more accurate image generation. This is a significant step forward. The ControlNet plugin not only addresses previous issues with model-generated structures but also provides a more flexible and controllable approach to generation. It has proven to be a great help in product design and creative image generation. The author predicts that with further optimization of the ControlNet plugin's options and prompts, the AI will be able to better understand human drawing intentions and thus generate more accurate images that meet specific requirements.

5. Conclusion

The research of this paper is based on AI drawing technology, exploring its potential and limitations in the field of product design and creative image creation. Through experimental research using the Stable Diffusion original model, the Realistic model, and the ControlNet plugin, it explores the possibilities of AI-generated product creative images while discussing their practicality and limitations.

Through the experimental research, it was found that in generating product creative images, designers can use the Realistic model as a basic model. At the same time, they should use simple descriptive vocabulary as positive prompts and terms such as blur, low resolution, text, cropping, worst quality, low quality, normal quality, JPEG artifacts, signatures, and watermarks as negative prompts. Furthermore, when the prompt is clearly defined along with the desired product structure, using the ControlNet plug-in to generate creative images yielded the best results.

The experimental research also revealed the importance of selecting and fine-tuning the appropriate AI models and providing precise inputs (such as the ControlNet plug-in's schematic and fitting parameters) when using AI drawing to generate product creative images.

This study validates to some extent the potential application of AI technology in the field of product design and creative image creation. It also reveals some challenges and problems that may be encountered in practical operation, such as logical problems with the internal structure of products and machine misinterpretation of prompts. Subsequent research will further explore and develop the application of AI in product creative image generation, focusing on improving the accuracy of creative image generation and the feasibility of generating product internal structures.

Reference

[1] Gao Xuchao. Research on Engineering Brain Technology Based on Artificial Intelligence and Federated Learning. Railway Construction Technology, 2023(3), 1-4, 13.
[2] Li Qinggang. Research on the Technology Framework and Development Direction of Intelligent Metro. Railway Construction Technology, 2022(11), 52-56.
[3] Zhao Tianqi, Gou Hongye, Chen Xuanying, et al. Research Progress on Bridge Informatization and Intelligent Bridges in 2020. Journal of Civil and Environmental Engineering (in Chinese and English), 2021, 43(S1), 268-279.
[4] Wang Xiaohui, Qin Jingyan, and Quan Hongchen. "Personalized Cultural Creative Product Design Method Based on AI Artwork Generation." Packaging Engineering, 41.06 (2020): 7-12. doi:10.19554/j.cnki.1001-3563.2020.06.002.
[5] Sun Cheng, Han Yunsong, and Ren Hui. "Research on Architectural Computational Design for Artificial Intelligence." Architectural Journal, 2018(9), 98-104.
[6] SUN Lingyun, CHEN Pei, XIANG Wei, et al. "SmartPaint: A Human-Machine Collaborative Drawing System Based on Generative Adversarial Neural Networks." Frontiers of Information Technology & Electronic Engineering, 2019, 20(12), 1644-1657.
[7] Ma Yongjie, Xu Xiaodong, Zhang Ru, et al. "Research Progress on Generative Adversarial Networks and Their Application in Image Generation." Computer Science and Exploration, 2021, 15(10), 1795-1811.
[8] Liang L. Exploration and Improvement of the Stable Diffusion Model in the Field of Image Generation. Advances in Computer and Communication, 2023, 4(3).
[9] Shi Z. AI Application to Generate an Expected Picture Using Keywords with Stable Diffusion. Journal of Artificial Intelligence Practice, 2023, 6(1).
[10] Zheng Kai, Wang Di. Application of Artificial Intelligence in the Field of Image Generation - Using Stable Diffusion and ERNIE-ViLG as Examples. Technology Vision, 2022, 35, 50-54.

[11] Nassim D, Kullathida D. What's in a text-to-image prompt? The potential of stable diffusion in visual arts education. Heliyon, 2023, 9(6).
[12] AromAI Launches First Candle Designed Entirely by AI: The Future of Fragrance is Here. M2 Presswire, 2023.

Fuzzy Systems and Data Mining IX
A.J. Tallón-Ballesteros and R. Beltrán-Barba (Eds.)

doi:10.3233/FAIA231090

Power of Fuzzing and Machine Learning in Smart Contract Security Validation

Ghazi Mergani Ali[a,1] and Hongsong Chen [a]
[a] *University of Science and Technology Beijing, China*

Abstract. Blockchain technology revolutionized digital payments and transactions by introducing disruptive capabilities. It operates through smart contracts, automated software code facilitating transactions without intermediaries. Smart contracts, written in various languages, have gained popularity but are vulnerable to logic flaws and security threats, potentially leading to financial losses and undermining blockchain integrity. Validating their security is essential, although current tools only detect specific attacks, lacking a comprehensive automated solution. This article presents a two-stage process wherein the initial phase involves the extraction of characteristics from smart contracts through the analysis of abstract syntax trees (ASTs) and control flow graphs (CFGs). In order to improve the precision of our results, we can leverage the distinctive capabilities of the fuzzing technique to label the data prior to its integration into the training model. In the subsequent phase, approach is utilized neural decision tree (NDT) typically combines a decision tree structure with neural network components. The mixed-method approach is utilized, leveraging the distinct advantages offered by neural networks and decision trees. The purpose of this collaborative technique is to enhance the probability of identifying vulnerabilities in smart contracts. The experimental assessment yielded favorable outcomes in the detection of smart contract vulnerabilities, namely those pertaining to Reentrancy, integer overflow, and Block Number Dependency.

Keywords. Blockchain, smart contract, fuzzing tools, machine learning, neural decision trees

1. Introduction

In the age where blockchain technologies are flourishing, smart contracts have become a fundamental element in decentralized applications, bestowing automation, transparency, and security to a range of transactions and engagements. Smart contracts are contracts that execute themselves, with the conditions embedded directly into the code [1]. These contracts serve as the foundational elements of decentralized applications and are crucial for executing intricate business processes on the blockchain. Nevertheless, the attributes that make smart contracts so vital, such as their unchangeable nature and independence, also make them vulnerable to harmful manipulations if they are not meticulously crafted.

[1] Corresponding author: Department of Computer Science and Technology, University of Science and Technology Beijing (USTB), Beijing 100083, China. E-mail: ghazi_en87@yahoo.com.
[2] Second author: a professor in Department of Computer Science, University of Science and Technology Beijing (USTB), Beijing 100083, China. E-mail: chenhs@ustb.edu.cn

The escalating emergence and deployment of smart contracts have concurrently revealed an abundance of security impediments, with vulnerabilities being at the forefront. The sensitivities of these contracts, particularly due to their extensive integration with digital assets, bear the risk of engendering significant financial detriments. These substantial setbacks have spurred significant attention towards the imperative task of safeguarding and ensuring the stability of smart contracts. A scrutiny of existing literature evinces that a multitude of efforts have been initiated to tackle the security conundrums associated with smart contracts [2].

Several studies have delved into the exploration of methods for detecting vulnerabilities in smart contracts. One approach, formal verification, has encountered various challenges. It tends to be susceptible to errors due to its reliance on artificial rules, and it struggles to encompass intricate patterns comprehensively. Additionally, the comparative analysis in this method often necessitates the use of complex symbols and contrast indicators, demanding substantial computational resources and leading to prolonged detection times.

This paper presents a machine learning model for detecting vulnerabilities in smart contracts, utilizing over 1100 verified contracts. The approach involves a two-step process: Preparation and Training. During Preparation, meaningful attributes are extracted from contract code, including static features from abstract syntax trees (ASTs) and control flow graphs (CFGs). Then we used established vulnerability detection tools such as sFuzz [3], CONFUZZIUS [4], and xFuzz [5] to label our training data. In the Training Model step, a mixed-method approach combines decision trees and neural networks, specifically employing the Neural Decision Trees(NDT) model. This model combines decision tree-based partitioning with neural networks to capture complex data relationships, offering both accuracy and interpretability. To summarize, our main contributions are as follows:

1. We propose a model for automated detection of vulnerabilities in Ethereum smart contracts using neural decision trees.
2. It differs from the existing works in that for the first time in our knowledge, labeling data by using the fuzzing tools (xFuzz, sFuzz, CONFUSS) for more accuracy.
3. The efficacy of the model has been demonstrated in terms of its suitability for identifying vulnerabilities in smart contracts. The model was executed on authentic contracts, resulting in a prediction recall and precision of 92%. Furthermore, the model has a detection time of around 5 seconds per contract.

2. Background

We briefly review smart contracts vulnerabilities detection in Section 2.1, and machine learning vulnerability detection in smart contracts in Section 2.2, and Neural Decision Trees in Section 2.3

2.1. Smart Contracts Vulnerability Detection Methods

The ascendancy of Blockchain technology and the concomitant prominence of smart contracts have engendered a burgeoning interest in smart contract security. Consequent to the high stakes often implicated by smart contracts, particularly in financial applications, the detection and amelioration of vulnerabilities have become an area of critical import. In this section, we will introduce three kinds of smart contract

vulnerability detection methods, including Static analysis, Dynamic analysis, Fuzzing Method.

Static analysis is a technique that can be employed to scrutinize Solidity smart contracts without the need for their execution[6]. This methodology involves examining the Solidity source code of the smart contract to identify potential vulnerabilities and verify adherence to coding standards [7]. Several tools have been developed for static analysis, Slither [8], is a tool that requires access to the source code of the smart contract. It's mainly used to identify vulnerabilities and issues at the code level, but it may not be as effective in identifying runtime vulnerabilities that only manifest when the contract is executed. Slither can generate false positives.

Dynamic analysis is a method that examines a program while it is executing or running [9]. It involves analyzing the program's behavior and interactions with its environment, including the inputs and outputs, to identify vulnerabilities and potential issues that may not be apparent from the source code alone. Dynamic analysis can simulate various scenarios, including the injection of malicious inputs, to uncover vulnerabilities that an attacker might exploit.

Fuzzing Method Fuzzing is a software testing approach that is automated, wherein potential data is supplied as inputs to a program[10]. The process of fuzzing generates partially valid inputs that are not immediately rejected by the parser. However, these inputs do expose corner cases that were inadequately handled in earlier stages of the program. ContractFuzzer [11] is the first smart contract fuzzing tool that creates fuzzing inputs by leveraging the Application Binary Interface (ABI) specifications of smart contracts. It further employs test oracles to find potential security vulnerabilities and utilizes the Ethereum Virtual Machine (EVM) to capture runtime behaviors of smart contracts.

2.2. Machine Learning Vulnerability Detection in Smart Contract

The public's interest in smart contract security has been considerable, which has prompted noteworthy developments in machine learning-based contract vulnerability detection methods. The two steps of current software vulnerability detection methods, which are based on machine learning and cutting-edge techniques, are 1) training and 2) detection. When the prediction model is fully trained, satisfactory results can be obtained. Currently, there is a need to address the issue of integrating ML technologies with smart contract detection methods. A few papers provide an overview of the literature[12] [13] [14] [15] [16] have been proposed and they have been using machine learning models to detect vulnerabilities in smart contract All these deep learning methods papers are trying to extract features from opcode and label contracts with types of vulnerabilities of smart contract to prepare data and employ machine learning algorithms to detect vulnerabilities in smart contracts.

Other papers [17][18][19] have been conducted to identify smart contract vulnerabilities through the application of deep learning methodologies. However, these studies have primarily focused on extracting features directly from the source code of smart contracts in order to construct a training dataset based on the Abstract Syntax Tree (AST) representation. This approach is advantageous as it allows for the utilization of high-level programming languages and facilitates the processing of the AST. The utilization of static code analyzers for the purpose of extracting features and assigning labels to the smart contract. After the preparation of a training dataset, deep learning models can be trained on it in order to classify new data and identify vulnerabilities. All

existing machine-learning papers are trying to label dataset by using Symbolic Execution or Static analysis methods to detect potential vulnerabilities in the contracts.

2.3. Neural Decision Trees (NDT)

Neural Decision Trees be used for classification tasks. NDT are hybrid machine learning models that combine the strengths of decision trees and neural networks [20]. The primary concept of Neural Decision Trees (NDT) is employing a neural network to reduce interdependencies among input variables initially, followed by feeding the changed input variables into a decision tree learning process for the purpose of categorization. Therefore, the NDT algorithm commences by accepting training data as input for the neural network model. The subsequent output is subsequently forwarded for decision reconstruction, and the resulting rules will be the final output of the NDT model. The NDT model can be applied to predict by combining decision tree-based partitioning with neural networks for capturing complex relationships in the data. It offers the advantage of interpretability while delivering accurate predictions [21].

3. Overview Our Method

The proposed model for detecting smart contract vulnerabilities in machine learning leverages the utilization of multiple fuzzing analyzers, thereby optimizing the accuracy. To accomplish this, a collection of machine learning classifiers is trained using established vulnerabilities. The objective is to forecast the presence of similar security vulnerabilities in a novel contract. There are two main steps to creating our machine learning model vulnerability detection in smart contracts the first step is machine learning preparation and the second step is the machine learning training model. The Proposed Architecture in Figure 1. A comprehensive elucidation of each individual phase is included in the subsequent sections.

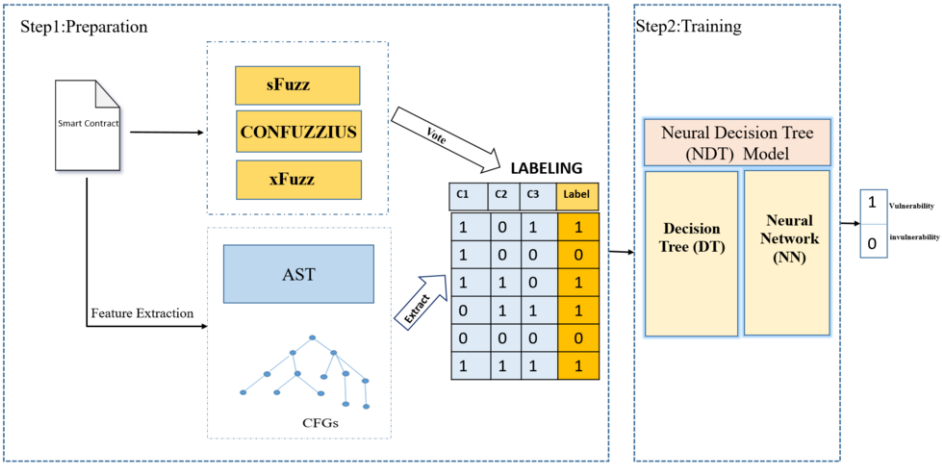

Figure 1. Proposed Architecture

3.1. Step1: Machine Learning Preparation

In this section, we provide a detailed explanation of the preparation process employed for training the machine learning model, which is designed to identify vulnerabilities present in smart contracts. We discuss the data collection in Section 3.1.1 and introduce Feature Extraction in Section 3.1.2, Labeling data in Section 3.1.3

3.1.1. Data Collection and Preprocessing

Supervised learning necessitates a dataset that is adequately large and labeled, while blockchain systems commonly serve as hosts for publicly accessible smart contracts. The decision was made to download and compile contracts via Etherscan, a well-known Ethereum service platform [22]. The data sets at our disposal comprise contracts that exhibit three distinct types of vulnerabilities, namely Reentrancy, Integer Overflow, and Block Number Dependency. In order to ensure representativeness, a comprehensive dataset comprising a total of 1100 contracts was gathered for subsequent analysis. The dataset was partitioned into an 80% training set and a 20% testing set.

3.1.2. Building AST and Feature Extraction

In preparing the training dataset, features are directly extracted from the smart contract's source code by utilizing a Solidity parser [23] to generate an abstract syntax tree (AST). The data structure of AST is chosen because it contains the abstract syntactic structure and content-related details. Solidity parser is an open-source tool that is relatively simple to install and operate. It examines the syntax of Solidity code and constructs an AST, which can be navigated using the parser's built-in functions and dictionary methods. Moreover, The CFG is employed to extract an additional set of features a graph representation of the different paths a program can take during execution [24]. CFGs provide a visual representation of the program's control flow and are instrumental in extracting information regarding the different execution paths within a program. we use a tool specifically designed for analyzing smart contract Slither (8). This tool provides features extracted from CFGs and can help to identify potential issues and opportunities for improvement in smart contract code. features extracted are 20, of which 13 are extracted from ASTs and the other 7 Features from CFGs

3.1.3. Labeling

The benefit of using fuzzing tools instead of a particular static tool is that fuzzing tools can reduce false negatives Thus, it increases the accuracy of vulnerability detection We chose the fuzzing tools sFuzz (3), CONFUZZIUS (4), and xFuzz (5). because they detect smart contract vulnerabilities with greater accuracy than other fuzzing tools. In this process, we chose these tools that could detect a variety of common smart contract vulnerabilities. In the labeling process, vulnerability reports from various detection tools are collected for each contract by taking the common vulnerabilities (Reentrancy, Integer Overflow, Block Number Dependency), and the value of each label is either 0 or 1. When the value is 1, it indicates that the contract does have a vulnerability of that sort. and when the value is 0, it indicates that the contract does not have a vulnerability, a contract is labeled as vulnerable (1) if it secures at least two votes in the analysis of fuzzing tools indicating a vulnerability. otherwise, the labels as non-vulnerable (0). the quality of the

labels and features will directly impact the performance of the machine learning models, so it's important to ensure accuracy in this labeling process.

3.2. Step2: Machine Learning Training Model

We take the features from smart contracts and use a neural decision tree (NDT) model to train three types of vulnerability. a neural diction tree network was trained with the following parameters:

1) Number of Trees: 10
2) Depth: 10
3) Feature Rate: 1.0
4) Number of Classes:3
5) Number of Features: 11

The core of the algorithm involves building and training a Neural Decision Tree (NDT) model, which is a hybrid of neural networks and decision trees. Once the model is trained, it can predict class labels (0 or 1) for each data point in the testing set. The algorithm also evaluates the model's performance using metrics such as accuracy, precision, recall, and F1-score, and it generates a confusion matrix to assess how well the model identifies normal and vulnerable contracts.

4. Experimental Evaluation

In this section, we first present the metrics used for the model evaluation. Then we introduce the evaluation results of the implications of using our (NDT) model compared with the decision tree (DT) on security vulnerability analysis on smart contracts.

4.1. Evaluation Metrics

The proposed work employs a set of metrics including accuracy, precision, recall, F1 score, and the confusion matrix to assess the performance of learning algorithms for classification (NDT), with the choice of metrics playing a pivotal role in model selection. Specifically, the study primarily focuses on accuracy as the predominant metric for evaluating classification models, defined as the ratio of correctly predicted instances to all predictions and calculated through the confusion matrix components (False Negatives, True Negatives, True Positives, and False Positives). In the context of vulnerability detection, the work emphasizes the significance of recall, precision, and F1-score as critical indicators. Additionally, the evaluation includes accuracy and loss values during the training process, with a preference for minimizing false negatives to detect all potential vulnerabilities and minimizing false positives to enhance the effectiveness of the analysis. As a result, the F1-score emerges as a reliable measure, accommodating imbalanced data, while performance evaluation relies on precision, recall, and the F1 measure computed from the confusion matrix metrics.

4.2. Evaluation Results

Obviously, the performance of (NDT) is the best compared with the decision tree (DT) model (see Table 1) in the sense that all of its indicators are the highest. When comparing

the results of the vulnerability detection models, we observe variations in accuracy, recall, F1-score, and precision across different types of vulnerabilities. We report the experimental results in Table 1.

The findings of our study indicate that the traits we retrieved have the capability to identify vulnerabilities with a satisfactory level of accuracy. Hence, it is postulated that both the structural patterns of code and its complexity have an influence on the presence of vulnerabilities. It has been observed that the detection accuracies of the three vulnerabilities exceed 85%. with other evaluation metrics consistently surpassing the 90% threshold. In the context of the Block Number Dependency vulnerability, it is seen that the NDT model exhibits an accuracy rate of 92.73%, whilst the DT model demonstrates an accuracy rate of 85.45%. The NDT model exhibits superior performance in terms of recall (94%), F1-score (95%), and precision (96%) compared to the DT model in relation to this particular vulnerability. It is worth noting that the NDT model exhibits a slightly lower accuracy index in the case of Integer Overflow, potentially stemming from the multifaceted nature of this vulnerability, where the extracted features may not capture all relevant aspects.

Table 1 experimental results of three vulnerabilities in terms of accuracy, recall, precision, F1-score and precision

Vulnerability	Model	Accuracy	Recall	F1-score	Precision
Reentrancy	NDT	86.82%	93%	91%	89%
	DT	84.55%	91%	90 %	88%
Integer Overflow	NDT	84.55%	94%	90%	86%
	DT	80.91%	98%	88%	81%
Block Number Dependency	NDT	92.73%	94%	95%	96%
	DT	85.45%	86%	90%	95%

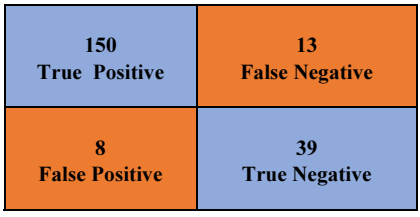

Figure 2: NDT Confusion Matrix

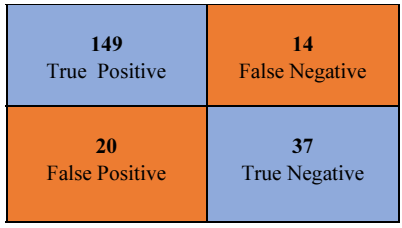

Figure 3: DT Confusion Matrix

The confusion matrix, as depicted in Figure 2 and Figure 3, reveals that the NDT algorithm exhibits a lower number of False Positive instances compared to the NT algorithm. This observation suggests that the prediction methodology employed by NDT is effective. The lower value seen in the Precision index of the two models may be attributed to the higher likelihood of false positives associated with Integer Overflow vulnerabilities. The presence of numerous valid operations can lead to integer overflows.

5. Conclusion & future work

In this article, we introduce an innovative system for automating the detection of vulnerabilities in Ethereum smart contracts, leveraging machine learning algorithms. Our approach stands out as it pioneers the use of the fuzzing method for data labeling, aiming to enhance accuracy. The model's effectiveness is substantiated by its time-saving capabilities and its proficiency in identifying vulnerabilities within smart contracts. We conducted experiments on real contracts, resulting in an impressive prediction recall and precision rate of 92%. Additionally, the model demonstrates a remarkable detection time of approximately 5 seconds per contract. This article also presents a two-step method strategy, with the first step involving feature extraction from smart contracts using abstract syntax trees (AST) and control flow graphs (CFGs), in the second step by a mixed-method approach combining neural networks and decision trees to data set training. The model we developed exhibited a notable enhancement in both accuracy and efficiency when compared to the direct utilization of fuzzing techniques.

References

[1] Kerikmäe T, Rull A. Smart Contracts. Futur Law ETechnologies 2016:1–233. https://doi.org/10.1007/978-3-319-26896-5.

[2] Wohrer M, Zdun U. Smart contracts: Security patterns in the ethereum ecosystem and solidity. 2018 IEEE 1st Int Work Blockchain Oriented Softw Eng IWBOSE 2018 - Proc 2018;2018-Janua:2–8. https://doi.org/10.1109/IWBOSE.2018.8327565.

[3] Nguyen TD, Pham LH, Sun J, Lin Y, Minh QT. Sfuzz: An efficient adaptive fuzzer for solidity smart contracts. Proc - Int Conf Softw Eng 2020:778–88. https://doi.org/10.1145/3377811.3380334.

[4] Torres CF, Iannillo AK, Gervais A, State R. Towards Smart Hybrid Fuzzing for Smart Contracts. Proc - 2021 IEEE Eur Symp Secur Privacy, Euro S P 2021 2021:103–19. https://doi.org/10.1109/EuroSP51992.2021.00018.

[5] Xue Y, Ye J, Zhang W, Sun J, Ma L, Wang H, et al. xFuzz: Machine Learning Guided Cross-Contract Fuzzing. IEEE Trans Dependable Secur Comput 2022:1–14. https://doi.org/10.1109/TDSC.2022.3182373.

[6] Cousot P, Cousot R. Abstract interpretation: "A" unified lattice model for static analysis of programs by construction or approximation of fixpoints. Conf Rec Annu ACM Symp Princ Program Lang 1977;Part F1307:238–52. https://doi.org/10.1145/512950.512973.

[7] Harer JA, Kim LY, Russell RL, Ozdemir O, Kosta LR, Rangamani A, et al. Automated software vulnerability detection with machine learning 2018.

[8] Feist J, Grieco G, Groce A. Slither: A static analysis framework for smart contracts. Proc - 2019 IEEE/ACM 2nd Int Work Emerg Trends Softw Eng Blockchain, WETSEB 2019 2019:8–15. https://doi.org/10.1109/WETSEB.2019.00008.

[9] Praitheeshan P, Pan L, Yu J, Liu J, Doss R. Security Analysis Methods on Ethereum Smart Contract Vulnerabilities: A Survey 2019.

[10] Liu C, Liu H, Cao Z, Chen Z, Chen B, Roscoe B. ReGuard: Finding reentrancy bugs in smart contracts. Proc - Int Conf Softw Eng 2018:65–8. https://doi.org/10.1145/3183440.3183495.

[11] Jiang B, Liu Y, Chan WK. ContractFuzzer: Fuzzing smart contracts for vulnerability detection. ASE 2018 - Proc 33rd ACM/IEEE Int Conf Autom Softw Eng 2018:259–69. https://doi.org/10.1145/3238147.3238177.

[12] Wang W, Song J, Xu G, Li Y, Wang H, Su C. ContractWard: Automated Vulnerability Detection Models for Ethereum Smart Contracts. IEEE Trans Netw Sci Eng 2021;8:1133–44. https://doi.org/10.1109/TNSE.2020.2968505.

[13] Xing C, Chen Z, Chen L, Guo X, Zheng Z, Li J. A new scheme of vulnerability analysis in smart contract with machine learning. Wirel Networks 2020. https://doi.org/10.1007/s11276-020-02379-z.

[14] Gopali S, Khan ZA, Chhetri B, Karki B, Namin AS. Vulnerability Detection in Smart Contracts Using Deep Learning. Proc. - 2022 IEEE 46th Annu. Comput. Software, Appl. Conf. COMPSAC 2022, 2022, p. 1249–55. https://doi.org/10.1109/COMPSAC54236.2022.00197.

[15] Solomon GJ, Zhang P, Liu Y, Brooks R. An Efficient Vulnerability Detection Model for Ethereum

Smart Contracts. Lect Notes Comput Sci (Including Subser Lect Notes Artif Intell Lect Notes Bioinformatics) 2019;11928 LNCS:371–86. https://doi.org/10.1007/978-3-030-36938-5_22.

[16] Wang Z, Wu W, Zeng C, Yao J, Yang Y, Xu H. Graph Neural Networks Enhanced Smart Contract Vulnerability Detection of Educational Blockchain 2023.

[17] Momeni P, Wang Y, Samavi R. Machine Learning Model for Smart Contracts Security Analysis. 2019 17th Int Conf Privacy, Secur Trust PST 2019 - Proc 2019. https://doi.org/10.1109/PST47121.2019.8949045.

[18] Narayana KL, Sathiyamurthy K. Automation and smart materials in detecting smart contracts vulnerabilities in Blockchain using deep learning. Mater Today Proc 2022. https://doi.org/10.1016/j.matpr.2021.04.125.

[19] Zhou Q, Zheng K, Zhang K, Hou L, Wang X. Vulnerability Analysis of Smart Contract for Blockchain-Based IoT Applications: A Machine Learning Approach. IEEE Internet Things J 2022;9:24695–707. https://doi.org/10.1109/JIOT.2022.3196269.

[20] Lee YS, Yen SJ. Neural-based approaches for improving the accuracy of decision trees. Lect Notes Comput Sci (Including Subser Lect Notes Artif Intell Lect Notes Bioinformatics) 2002;2454 LNCS:114–23. https://doi.org/10.1007/3-540-46145-0_12.

[21] Li X, Chan CW, Nguyen HH. Application of the Neural Decision Tree approach for prediction of petroleum production. J Pet Sci Eng 2013;104:11–6. https://doi.org/10.1016/j.petrol.2013.03.018.

[22] Etherscan n.d. https://etherscan.io/ (accessed September 27, 2023).

[23] solidity-parser-antlr n.d. https://github.com/federicobond/solidity-parser-antlr (accessed September 15, 2023).

[24] Huang TH-D. Hunting the Ethereum Smart Contract: Color-inspired Inspection of Potential Attacks 2018.

Fuzzy Systems and Data Mining IX
A.J. Tallón-Ballesteros and R. Beltrán-Barba (Eds.)

doi:10.3233/FAIA231091

The Influence of Semantic and Semiotic Features of Furniture Shape Design on Consumer Preference Based on Fuzzy Computing

Xiaohong Lin[a,c] , Natrina Mariane P. Toyong[b] and Nurul 'Ayn Binti Ahmad Sayuti[a, 1]
[a]*College of Creative Arts, Universiti Teknologi MARA, Kedah, Malaysia*
[b]*Universiti Teknologi MARA, Shah Alam, Malaysia*
[c]*College of Design, Heibei Academy of Fine Arts, China*

Abstract. This study uses fuzzy computing theory to explore the impact of semantic and semiotic features of furniture shape design on Chinese consumers' preferences and provides a possible reference for designers. In the early stage of relevant research on design, an integrated consumer survey is conducted on furniture form design, and the correlation between the semantic and semiotic features of furniture form design and the semantics and symbols preferred by consumers is invested in the early stage of research and development of furniture design. At the same time, linear regression analysis method is used to analyze the correlation of consumer preference based on the semantic and semiotic features of furniture shape design, and the mathematical function relationship is established to predict the variables of consumer preference. This study is helpful to understand consumers' preference for furniture, so as to carry out relevant design, improve consumers' purchase intention, promote the sale of furniture, and thus become a successful design.

Keywords. Fuzzy Computing, Furniture shape design, Semantics, Semiotics, Consumer Preference.

1. Introduction

Fuzzy computing is based on fuzzy set theory, which can simulate the human brain's imprecise and nonlinear information processing ability and is helpful in many application fields.[1] People can generally use "Fuzzy computing" to represent the calculation methods and theories used in Fuzzy application fields such as Fuzzy Inference Systems (FIS), fuzzy Logic, and fuzzy systems. In these systems, fuzzy set theory is widely applied, and other artificial intelligence means are combined. Therefore, in this study, fuzzy computing can effectively deduce consumer preference for furniture shape design, which is also a meaningful combination of mathematics and design at present and has fundamental research significance for future design. It can make the design less ambiguous and more scientific. Then, consumers' preference for furniture shape design is calculated by the fuzzy comprehensive evaluation method, which is a comprehensive

[1] Nurul 'Ayn Binti Ahmad Sayuti, College of Creative Arts, Universiti Teknologi MARA, Merbok, kedah, Malaysia. E-mail: nurulayn@uitm.edu.my

evaluation method based on fuzzy mathematics. According to the membership degree theory of fuzzy mathematics, this comprehensive evaluation method transforms qualitative evaluation into quantitative evaluation, which uses fuzzy mathematics to evaluate things or objects that are restricted by many factors. It has the characteristics of explicit and systematic results, can better solve fuzzy and difficult-to-quantify problems, and is suitable for solving various non-deterministic problems.

In this study, the fuzzy computing theory is used to study the influence of semantic and semiotic features of furniture shape design on Chinese consumers' preference. In the early stage of furniture research and development, consumers' preference is investigated and the results are integrated. In addition, the fuzzy computing theory is applied to the research of furniture shape design to provide the basis for furniture shape design and development,[2] so that the design is no longer fuzzy and more scientific, and at the same time, it can shorten the development time of furniture design in the early stage, thus extending the furniture market circulation cycle and increasing the possibility of design success.

2. Research Background and Theoretical Basis

Due to the current economic expansion, market competition is becoming more and more fierce, and consumers' purchase desire for furniture is also changing, which is directly related to the shape design of furniture. The external shape design of furniture directly affects the desire of consumers to buy, and consumers' preference for the shape design of furniture has also become important. On the other hand, the early stage of product development has become an essential means to enhance the value of products; through the early stage of consumer preference research, one can more accurately grasp the direction of furniture external shape design. Therefore, in today's fierce market competition, in the process of furniture design research and development, consumers should be fully investigated in the early stage of design, fully understand consumer preferences, market research should occupy an important position. On the other hand, designers should learn product development and design under the premise of understanding consumers' preferences and needs for the external shape design of furniture. Enterprises can improve consumers' purchase willingness through consumers' perceived value of products, achieve product purchase goals, and improve their own market competitiveness.

2.1. Fuzzy Computing Theory

Fuzzy computing involves obtaining the final output from the input of several control variables according to fuzzy rules. In life, the output is often determined based on the input of several variables and a set of rules of thumb expressed in natural language. This is a fuzzy calculation process.[3] As in real life, we often decide the air conditioner's temperature in the summer according to the temperature and humidity. The goal of fuzzy computing is to use as few resources as possible to complete the goal under the given accuracy and reliability of computing requirements. The biggest feature of fuzzy computing is that the time required for calculation is limited by both the size of the data set and the required precision. Reducing the accuracy can speed up the calculation, which can be as accurate as possible according to the existing capacity of the machine, and at

the same time, when the data volume rises, it is not necessary to increase the machine, but only need to reduce the calculation accuracy.

Fuzzy computing is generally suitable for two situations: (1) complex nonlinear problems without complete mathematical models, and empirical rules can be used to obtain the final result without knowing the model at all. (2) In addition, fuzzy computing can be combined with other intelligent algorithms, and at the same time, it can realize the complementary advantages, and introduce the way for the machine and its control in the fuzzy aspects of human recognition, decision and understanding, and increase the scientific analysis.

In this study, furniture shape design's semantic and semiotic features impact consumer preference, while the reference and application of semantics and semiotics of design essence are vague. However, according to Einstein's relativity theory, the impact of anything is based on evidence. Similarly, when the design semantics are determined at the beginning of the design, the design semantics are determined when the theme is determined. What kind of symbols can better express design semantics? At the same time, what impact do the semantics and semiotics of furniture shape design have on consumers? The researchers used fuzzy calculations to survey consumers to reach their conclusions.

2.2. Semiotics Theory

Semiotics is a controversial historical semiotics: Since the late 1930s, designers inspired by Morris have applied the field more interactively to design, and although the number of studies on semiotics has now increased, scholarly contributions to the field have been episodic rather than systematic, and only in a few cases have the semiotics of design projects been accurately studied.[4]

Looking back at the history of modern design development, it can be found that the so-called "crisis of meaning" occurred in Western design in the 1950s. The emergency reconstruction after World War II was the background to this historical period, so the global spread of the post-World War II "international style" was inevitable. However, following the emergence of many undifferentiated standardized designs in Western cities.

This phenomenon has given rise to the design thinking circle, which questions the theoretical principles proposed by the first generation of design masters. The new design concept has a fundamental theoretical point: the different reactions of individuals to products. Since individuals observe products from different perspectives and adhere to different viewpoints to evaluate products, the evaluation conclusions need to be consistent.[5] Thus, "meaning" events occur in design. The new thinking trend requires people to pay close attention to this new Angle to explore the design problem, so the design semiotics emerged. From the practical point of view of symbols, the practical study of design semiotics focuses on the relationship between users and audiences generated by design as a symbolic system.

However, most of the above literature deals with the dimensions of hermeneutics and cognitive psychology, and there needs to be a summary or lack of design research with detailed and applied design methods. The design semiotic literature is more limited than the semiotic design literature, and the relationships between the literature need to reveal interdisciplinary research processes. However in previous research, the relationship between time-progressive research and cross-sectional study is mainly focused on case analysis and applying semiotic thought rather than discussing product design methods.(cross-sectional study is a comparative study of groups of different collectives at the same point in time. This method mainly focuses on the similarities and

differences between different individuals, and reveals the differences and similarities between different groups by comparing the same or different variables of different groups, so as to explore the universality and regularity of social phenomena. This research method is good at horizontal comparison and can be used to study the popularity, prejudice and values of certain kinds of problems in different groups.)

2.3. Semantics Theory

Semantics is the study of language; a sentence is composed of different words, and the relationship between the words constitutes the sentence's meaning. The essence of semantics is to study the relationship between its words or contexts, that is, the sentence itself, to reveal what kind of meaning. In the design community, this "relationship" is applied to the design of products, what is the meaning of designing a product, what is the effective communication with consumers, that is, how to "dialogue" with consumers to produce "product semantics." [6]At the same time, its theoretical structure started from the design semiotics of Ulm School of Design in Germany in 950. It can be traced back to the semiotics of Charles and Morris in the new Bauhaus School in Chicago.[7] Semantics is a more specific continuation of semiotics. At the same time, Morris's theory pays more attention to the essence of meaning attributes.

As mentioned before, the essence of product semantics focuses on effective communication between people and things, that is, what does the product convey to the consumer? Function? Culture? In other words, the product's internal structure is revealed or hinted at to the user through the visual language of the product material, shape, structure, color, texture, etc., so that the product's function is evident.[8] The human-machine interface is simple and easy to understand to remove the user's confusion about the operation of the product and to design the shape with a more precise visual image and more symbolic significance. Convey to the user more cultural connotation, but also produce an exciting lifestyle to achieve the harmony and unity of people, machines, and the environment.

On the other hand, the meaning of product semantics includes extensional semantics and intensional semantics. Extensional semantics is the basis of product existence and the most direct semantic transmission, which is more intuitive, more rational, and more logical than the connotation of product modeling. While intensional semantics is premised on extensional semantics, the two are interrelated.

3. Questionnaire data processing and fuzzy calculation statistics

In this study, according to the semiotic and semantic features of furniture shape design, the fuzzy symbols and semantics favored by Chinese consumers belong to the category of human psychological cognition, which is fuzzy, subjective, and uncertain. Therefore, it is difficult for designers to describe and express consumers' preferred semantics and symbols scientifically. However, in the research, Likert scale can be used for declarative expression, while numbers can be used for specific division expression, as follows:

This scale is expressed by the following statements: strongly agree, agree, not necessarily, disagree, strongly disagree five kinds of answers, respectively recorded as 5, 4, 3, 2, 1. The total score of each respondent's attitude is the sum of his answers to each question, and this total score can indicate the strength of his attitude or his different states on this scale.[9]

Therefore, in this study, the method of fuzzy calculation is used to divide the questionnaire into five levels. Firstly, fuzzy computing theory is used to process the preference data generated by Chinese consumers according to the semantic and semiotic characteristics of furniture shape design, and then related research and analysis are carried out.

In the fuzzy rule step, the triangular fuzzy points are attached to these five statements: "strongly agree, agree, not necessarily, disagree, strongly disagree," then these become the expected semantic variables, and B represents the triangular fuzzy number. Define S= (0, 0, 1), (0, 1, 2), (1, 2, 3), (2, 3, 4), and (3, 4, 5) to represent these five statements respectively, then the defuzzification formula for S is as follows:

$S=(m,n,o),\ W_S=(m+2n+o)/4$

Starting from the fuzzy descriptive statistical equation, the following equation can be derived:

Fuzzy Semantic Mean=$[\sum_1^n(m+2n+o)]/4N$ *(N= Number of participants)*

The above calculation formula is used to carry out questionnaire investigation and analysis.

4. Statistics and analysis of research results

According to the survey results on the semantic and semiotic features of furniture shape design, semantics, semiotics, and interaction impact consumers' purchase preferences. Table 1 shows item 17: "Consumers like furniture that has symbolic meaning and conveys semantics." It is the most significant, and the fuzzy semantic value is 4.4205. At the same time, item 11, "Consumer concerns about furniture size." It is the least significant, and the mean value of fuzzy semantics is 3.8562.

Table 1. Questionnaire survey descriptive statistics.

	N	Fuzzy Semantic Mean	Std. Deviation		N	Fuzzy Semantic Mean	Std. Deviation
item11	723	3.8562	.79736	item11	723	3.8562	.79736
item12	723	4.0553	.80836	item12	723	4.0553	.80836
item13	723	4.1245	.83284	item13	723	4.1245	.83284
item14	723	4.0858	.80052	item14	723	4.0858	.80052
item15	723	4.1452	.69997	item15	723	4.1452	.69997
item16	723	4.2254	.72952	item16	723	4.2254	.72952
item17	723	4.4205	.73701	item17	723	4.4205	.73701
item18	723	4.3430	.77614	item18	723	4.3430	.77614
item19	723	4.1411	.73648	item19	723	4.1411	.73648
item110	723	4.2282	.72102	item110	723	4.2282	.72102

The impact of integration and interaction on consumer fuzzy semantics is distinguished according to furniture semantics and semiotic design features, as shown in Table 1. "Consumers like furniture that has symbolic meaning and conveys meaning." If the highest and the mean value of fuzzy semantics is 4.4205, then the fuzzy membership function is u(s):1=(4.42-4.0):(5-4), and the obtained fuzzy membership function is u(s)=0.42. Therefore, the questionnaire value of this study is between "strongly agree" and "more agree," and the ambiguity is 0.42, indicating that consumers prefer furniture that has symbolic meaning while conveying semantic meaning. At the same time, in the experimental research, the quality and comfort of furniture are 4.0553 and 4.0858

respectively, accounting for the middle fuzzy value, so consumers pay less attention to the quality and comfort in the process of buying furniture.

Finally, the linear regression analysis method is used to analyze the correlation of consumer preference for the semantic and semiotic features of furniture shape design, and the mathematical function relationship is established to predict the perceived value variables. (Z_1, Z_2, Z_3) are the features of semantic and semiotic design, that is, semantics, semiotics, and interaction, respectively, and they are independent variables. (C) Fuzzy semantics take consumer preference as the dependent variable to predict the change of consumer perceived value over time. The resulting time series regression model is as follows:

$$C = m + n_1 Z_1 + n_2 Z_2 + n_3 Z_3$$

Where C is the prediction of consumer preference; m is an additional constant; Z_1 (semantics), Z_2 (semiotics), and Z_3 (interactions) are predictors; n_1, n_2, and n_3 are linear slope ratios.

In the linear regression model, the result shows that G2 =.990; Adjusted G2 =.989; F (3,718) =21648.038; p=.000. As shown in Table 2 and Table 3. Figure 1 shows the scatter plot of consumer preference predicted by linear regression analysis of furniture semantics and semiotic design features.

Table 2. Linear regression analysis

G			
Model	**G**	**G^2**	**Adjusted G^2**
1	.995(a)	.990	.989
Independent variables: differentiation, integration, interaction Dependent variable: consumer preference			

Table 3. Linear regression analysis

Mean					
Model		**df**	**Mean Square**	**F**	**Sig.**
1	Regression	3	38.281	21648.038	.000(m)
	Residual	718	.003		
	Total	711			
Independent variables: differentiation, integration, interaction Dependent variable: consumer preference					

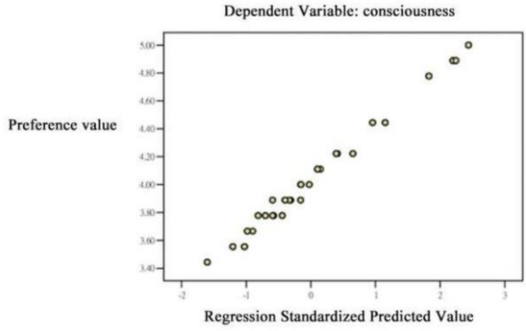

Figure 1. Regression Standardized Predicted Value

5. Conclusions and recommendations

In the current fierce market competition, in the early stage of product development, relevant research for consumers' needs for furniture can significantly shorten the product research and development cycle while being more targeted, and the possibility of product success is significantly increased.[10] By understanding the preferences of consumers, we can choose the semantics and symbols suitable for consumers to carry out relevant designs, increase the sales of furniture, and increase the purchase willingness of consumers, to achieve the final goal of furniture sales. This study provides a reference for designers when designing furniture. According to the study of fuzzy computing, the semantic meaning, symbol, and interaction of furniture are positively related to consumer preference in furniture shape design. At the same time, consumers do not care about the size of furniture but prefer furniture that has symbolic meaning and conveys semantic meaning.

To sum up, it is recommended that designers integrate the semantics and symbols recognized by consumers into the design process during the furniture design development period to improve consumers' purchase intention, shorten the design cycle, and thus improve the circulation cycle of furniture in the market.

References

[1] Bose, Mahua, and Kalyani Mali. "Designing fuzzy time series forecasting models: A survey." International Journal of Approximate Reasoning. 111 (2019): 78-99.
[2] Lee, A. S. "The investigation into the influence of the features of furniture product design on consumers' perceived value by fuzzy semantics." South African Journal of Business Management. 45.1 (2014): 79-93.
[3] Ojha, Varun, Ajith Abraham, and Václav Snášel. "Heuristic design of fuzzy inference systems: A review of three decades of research." Engineering Applications of Artificial Intelligence 85 (2019): 845-864.
[4] Dunleavy, Dennis. "Visual semiotics theory: Introduction to the science of signs." Handbook of visual communication. Routledge. 2020. 155-170.
[5] KOÇ, MIHRIBAN NIHAN. "Distributed senses. Semiotic analysis of recent technological tendencies in product design. Perceptual semiotics: the sensorial interaction between the body and the product." (2021).
[6] Ye, Jialei, et al. "Neo-Chinese Style Furniture Design Based on Semantic Analysis and Connection." KSII Transactions on Internet & Information Systems. 16.8 (2022).
[7] Duan, and Dou. Proceedings of the Seventh Asia International Symposium on Mechatronics. Springer Singapore, 2020.
[8] Xue, Fan, et al. "BIM reconstruction from 3D point clouds: A semantic registration approach based on multimodal optimization and architectural design knowledge." Advanced Engineering Informatics. 42 (2019): 100965.
[9] Taherdoost, Hamed. "What is the best response scale for survey and questionnaire design; review of different lengths of rating scale/attitude scale/Likert scale." Hamed Taherdoost. (2019): 1-10.
[10] Schmidt, Jonas, and Tammo HA Bijmolt. "Accurately measuring willingness to pay for consumer goods: a meta-analysis of the hypothetical bias." Journal of the Academy of Marketing Science. 48 (2020): 499-518.

Fuzzy Systems and Data Mining IX
A.J. Tallón-Ballesteros and R. Beltrán-Barba (Eds.)

doi:10.3233/FAIA231092

Exploration of the Path for School Principals to Promote the Construction of Artificial Intelligence Curriculum——Based on Case Study[1]

Dongying Wang[a] and Yuting Han[b,2]
[a] *Ordos City Dongsheng District Yikezhao Middle School, 017002, China*
[b] *Inner Mongolia Normal University, 010028, China*

Abstract. Popularizing artificial intelligence education in primary and secondary schools is an important measure to cultivate talents in the intelligent era. At present, the AI courses in primary and secondary schools are mainly based on information technology courses, makers, STEAM, programming and other elective courses or school-based courses. This promotion method further strengthens the leading position of principals in the process of AI curriculum construction. However, how primary and secondary school principals can effectively promote the high-quality and sustainable development of school AI curricula has not attracted enough attention. Research selected artificial intelligence education to be carried out more than three years and widely recognized school, using more case study methods, from the "curriculum consciousness, curriculum planning, curriculum management, curriculum evaluation, curriculum efficiency" perspective, following the principle of triangle mutual certificate, concise the primary and secondary school principals to promote the effective path of artificial intelligence curriculum.

Keywords. Primary and secondary schools, principal, artificial intelligence curriculum, case study

1. Introduction

Artificial intelligence is profoundly changing the way people live, study and work. The popularization of artificial intelligence education in primary and secondary schools has become a strategic move for countries all over the world to compete for the fourth industrial revolution. Developed countries such as the United States, The United Kingdom, Japan, Finland and other developed countries have respectively issued relevant policies and plans to promote the popularization of K12 AI education. Although about 90 percent of primary and secondary schools in China have taught AI in various forms, only less than 9 percent have used AI as a regular teaching content [1]. On the whole, the popularization of AI education in primary and secondary schools is in the initial exploration stage in China[2], Domestic scholars have an understanding of AI

1 Fund Project: The 2023 14th Five-Year Plan of Inner Mongolia Autonomous Region "Professional Development Difficulties and Solving Path of Information Technology Teachers in Junior Middle School under the Background of New Curriculum Standards" (No. 2023NGHCZ054)
2.Corresponding Author, Yuting Han, Inner Mongolia Normal University; E-mail: 943443200@qq.com.

education in primary and secondary schools from the theoretical level[3], practice approach[4], Current status and problems of curriculum construction[5], and Foreign experience for reference[6]. Pointed out the existing problems, and put forward the optimization strategies and suggestions. Foreign studies pay more attention to the ability and accomplishment that teachers should have, students' attitudes towards artificial intelligence, curriculum development and other aspects [7]. As a key role in school development, principals of primary and secondary schools in China play an important role in artificial intelligence curriculum planning, resource allocation, cultural construction and other aspects [8]. However, how the primary and secondary school principals can effectively promote the construction of AI curriculum has not yet received effective attention [9]. In view of this, the research selects three primary and secondary schools with good AI curriculum construction from different regions, carries out research through various methods, follows the principle of multiple evidence sources and triangular mutual evidence, and reveals the effective path of principals of primary and secondary schools to promote the high-quality and sustainable development of AI curriculum.

2. Related works

With the development of AI, AI technology has gradually been introduced in education to provide a more efficient and personalized learning experience. Many scholars and researchers in the field of education have also noticed the application prospect of artificial intelligence in education. There have been several studies on AI education. Foreign ai education has some exploration and practice in curriculum setting, teaching methods, teaching material development and other aspects, which provides a useful reference for the development of AI education. According to the White Report on the Development of AI Education in China, published by the Education Management Information Center of the Ministry of Education, only less than 9 percent of schools use AI as a regular teaching content [1]. According to the Artificial Intelligence Curriculum Development Standards for Primary and Secondary Schools published by the Information Technology Education Professional Committee of the Chinese Society of Education, the popularization of AI education in primary and secondary schools is still in the exploratory stage [2]. Lu Yu, Zhang Shanshan, Xie Zhongxin, Fangyuan Yuan and other scholars analyzed the current situation and challenges of primary and secondary school education in the era of artificial intelligence, and put forward the corresponding solution strategies [3], [4], [5], [6].

As the leader of education, principals play a very important role in the development of artificial intelligence education. Chiu T K F Put forward six principles of AI curriculum design in middle schools [7], McNeill K L starts from the practice of the principal, as the "helmsman" of school development, plays a key role in AI curriculum planning, resource allocation, cultural construction and other aspects [8], but this problem has not been effectively paid close attention to [9].Robert K.Yin Detailed interpretation and analysis of the case design and research, including how to choose cases, make research plans, field investigation, collection and analysis of data, writing research report, etc. In addition, the book also discusses the theoretical basis, application field and limitations of case studies, including [10]. In view of this problem, many scholars have conducted the corresponding research. For example, Yu Bing, Lu Lijie et al. studied and analyzed the leadership thinking [11], [12], [13], [14], [15]. Based on the reading and

thinking of the above literature, the author has studied and explored the effective path for principals in primary and secondary schools to promote high-quality artificial intelligence curriculum and sustainable development.

3. Research design

3.1. Research methods

This paper adopts multiple case study methods to analyze the practical behavior of the principal's leadership, so as to answer the questions of "how" to promote artificial intelligence, curriculum construction, and "why" can effectively promote curriculum development, which fits to the applicable situation of case study [10]. In addition, compared with single case studies, multiple case studies follow the replication law and have better external validity, we can explore the leadership activities of principals under different forms of practice, and deduce the conclusions that are more convincing and explanatory [10].

3.2. Case selection / study object

The case study subjects selected by the institute are detailed in Table 1.

School A, A full middle school in Shenzhen, Guangdong Province, is one of the earliest AI education pilot schools in the city. After nearly 5 years of development, it has formed a team of excellent teachers and won the title of "Artificial Intelligence Demonstration School" in the district.

School B is a provincial demonstration ordinary high school in Henan Province. As one of the first pilot schools of education informatization by the Ministry of Education and the top ten modern schools in China, it built an artificial intelligence innovation laboratory in 2017, began to popularize AI education and was awarded the "National Artificial Intelligence Education Experimental School".

School C is a model high school in Xinjiang Uygur Autonomous Region. It is one of the first key middle schools to "run well" in China. The school has set up systematic artificial intelligence education courses, and selects and trains outstanding innovative talents through top-notch talent promotion projects such as subject research.

Table 1. Introduction of the case schools

base situation	A school	B school	C school
School type	In the end	senior middle school	senior middle school
practical form	STEAM	ROBOT	MAKER
School honor	District artificial intelligence education model school, provincial STEM education practice research subject school.	National Smart education model school, national artificial intelligence education Experimental school	National primary and secondary school scientific research and development demonstration base, youth science and technology activities demonstration school
achievements in scientific research	4 provincial projects; 3 district-level projects; 10 papers;	4 provincial projects; 4 district-level projects; 7 papers;	5 provincial projects; 3 district-level projects; 8 papers;

	Participated in the compilation of 3 textbooks	Participate in the compilation of 1 textbook.	Participate in the compilation of 2 textbooks.
Teaching honor	First prize of provincial and district education and teaching achievements	Silver Award of National Youth Computer Robot Competition and champion of VEX China Open	VEX Asian Cup champion, VEX World Championship High School Group Gold Award, Best Design Award and Best Creation Award.

3.3. Data collection

The study followed the principle of using multiple sources of evidence, and the data collection method is detailed in Table 2. The first-hand information is mainly from the one-on-one semi-structured interviews, and the interview outline is given in the final appendix of the article. And the second-hand materials mainly include the teaching materials. The data collection process followed the principle of triangular mutual evidence to ensure comprehensiveness, accuracy, and validity.

Table 2. Methods for case data collection

Data type	**school**	**data source**			**Data acquisition method**
		record length	**Interview number**	**member**	
First-hand data	A school	110 Minutes	Two people	Principal W, Miss L	Semi-structured interviews were conducted independently
	B school	40 Minutes	One person	President L	
	C school	46 Minutes	One person	H teacher	
secondary data	A, B, C school	School, laboratory, school teachers' website introduction and internal publicity materials, teaching planning, teaching plans and other teaching materials			Network search, text data collection

3.4. Case analysis framework

The principal is the leader and responsible person of the school curriculum, and the principal's curriculum leadership behavior is an important fulcrum for the high-quality development of basic education[11].Students comprehensively studied the curriculum leadership of principals at home and abroad, and divided the leadership behavior of principals into five dimensions: curriculum consciousness[12],Course planning, course management, course evaluation, and course leadership[13].

4. Typical case analysis result

Compared with other subjects of education, the artificial intelligence curriculum is still in the initial stage of exploration, with remarkable comprehensive, practical, and developmental characteristics [2]. To this end, the paper analyzes and summarizes the data around the five dimensions of curriculum consciousness, curriculum planning,

curriculum management, curriculum evaluation, and curriculum leadership efficiency, in order to see and condense the effective curriculum leadership behavior of principals in primary and secondary schools.

4.1. Curriculum awareness

The promotion of the AI curriculum in School A has generally experienced the process of "government leading- -copying foreign countries- -independent development". Base on failure, we reflect and summarize, and try to walk out of the evolution of AI curriculum suitable for our school. The original intention of Principal L of School B to popularize artificial intelligence education is to try to build an artificial intelligence curriculum based on the original robot education in the school through the construction of the school's characteristic curriculum. The awakening of the curriculum awareness of Principal L of School C originated from the excellent teaching achievements made by the teaching team in the early stage. As the head of AI education in School C, Teacher H's team tried to shift from robot education to artificial intelligence, hoping to make it a characteristic name card of the school.

4.2. Curriculum planning

School A has set up A special project team for artificial intelligence courses. Drawing on foreign experience, the project team explored the curriculum plan of teaching, scientific research, management, and artificial intelligence evaluation.

School B establishes a teaching team headed by Principal L to learn the development experience of AI education in the school; formulate a three-year action plan for AI education and obtain sufficient funds. The C school has formed an AI teaching team with Teacher H and his team teachers as the backbone, formulated the school artificial intelligence curriculum plan, and sought government financial support, and built a science and technology innovation center with a total area of 1,500 square meters.

4.3. Course management

Teachers' professional quality is the key element to determine whether the AI curriculum can take root, and the three principals reached a consensus on this.

School A invites experts and scholars from universities to give lectures and training, establishes an alliance of four universities, and carries out school-enterprise cooperation to strive for opportunities for overseas study Tours. Both primary and junior high schools have offered AI classes, promoting the development of AI education in combination with extracurricular activities. School B also actively seeks cooperation with universities, inviting university experts and doctors to come into the classroom and bring cutting-edge knowledge and advanced concepts of artificial intelligence to teachers and students, and offers two AI elective courses and two robot club activities every week to encourage the integration of AI elements in other disciplines. C school set up a teaching and research team to improve the AI curriculum teaching and research system and management system. A two-hour weekly AI school-based course is offered at the Science and Technology Innovation Center for all students

4.4. Course evaluation

Artificial intelligence courses pay more attention to the cultivation of intelligent literacy for the future society, and their teaching effect has a certain lag and recessive. In the practice process, the evaluation scheme adopted by the three schools all showed significant consistency. According to the evaluation results, the teacher team revised the curriculum plan and improved the design of curriculum activities.

4.5. Curriculum leadership efficiency

Artificial intelligence curriculum has not only enriched the school's curriculum system, but has become the name card of the school's publicity. School A has won the honor of the AI Education Model School. The AI curriculum of School B has become a catalyst for educational innovation. At present, School C has become the best AI curriculum school in Xinjiang.

5. Study discussion

5.1. The awakening of artificial intelligence curriculum consciousness is the starting point of artificial intelligence curriculum construction

The subject's understanding of artificial intelligence directly affects his/her decision-making behavior of the subject. In the educational practice, the principal considers various factors comprehensively, constantly improves the construction of the curriculum significance in practice, and dynamically generating and constructing the curriculum consciousness [14].

5.2. The construction of a service-oriented leadership team is the basic guarantee of artificial intelligence curriculum construction

Service-oriented leadership team, that is, the leadership team with principals as the core, regards students and teachers as the objects of service, puts the interests of teachers and students above individuals, becomes the "scavenger" of obstacles to the implementation of artificial intelligence curriculum, cultivates the soil of teachers 'teaching innovation and stimulates teachers' drive [15].

5.3. Supporting teachers' professional development is the core of promoting artificial intelligence curriculum

Teachers are an important influencing factor in school education, and the key to the implementation of AI education curriculum. AI education faces major challenges due to its weak faculty strength. AI education is mostly held by information technology teachers, who lack professional knowledge background, as it is difficult for primary and secondary schools to recruit professionals who understand both AI technology and education [16]. Therefore, promoting the professional development of AI teachers has become the optimal choice. Primary and secondary schools and Internet companies such as Tencent

and Huawei will jointly promote the application of AI in education, which can provide students with better educational resources and improve the quality of education.

5.4. Curriculum efficiency perception is the key to the sustainable development of artificial intelligence curriculum

Curriculum efficiency perception is the perception of each interest subject in comparing whether the "input" and the income "benefit" match, and whether there is a gap between the expected effect of the input and the actual situation [17].

6. Conclusion and Future direction

By selecting the AI curriculum construction from three schools in different regions and studying through various methods, this paper reveals the effective path for primary and secondary school principals to promote high-quality AI curriculum and sustainable development. With the continuous advancement of technology and increasingly expanding application scenarios, AI education will play an increasingly important role in the future. However, the implementation of AI education is also faced with many difficulties, such as the issue of educational equity. Some schools may not be able to enjoy the benefits of AI education due to financial and equipment problems. Or privacy issues, where students may involve personal privacy issues when using AI tools. Principals of primary and secondary schools, as the leaders of education, should actively promote the application and development of artificial intelligence education. First, increase investment in AI education and improve the coverage of AI education in rural and poor areas. Secondly, further study the educational algorithm and model of artificial intelligence, improve the precision and personalization of education and teaching, explore the application of artificial intelligence in education management, evaluation, guidance and teaching, and develop the construction and strategy of the school, promote the construction and training of teachers and encourage teachers to learn and master AI knowledge and skills. Finally, strengthen the cooperation with the outside world, share resources and technological achievements, and promote the innovation and development of artificial intelligence education.

References

[1]The Education Management Information Center of the Ministry of Education. The China AI Education Development Report of the White Paper on Internet Learning in China [R]. Beijing: Tsinghua University Press. 2019:17-18.

[2]Information Technology Education Professional Committee of Primary and Secondary schools of Chinese Education Association. Artificial Intelligence Curriculum Development Standards for Primary and Secondary Schools (Trial)[DB/OL].https://xw.qq.com/cmsid/20211216A0DHRX00,2021-10-31.

[3]Lu Yu, Tang Xiaoyu, Song Jiacen, Yu Shengquan. Artificial intelligence education in primary and secondary schools in the era of intelligence: overall positioning and core content field [J]. China distance education,2021(05):22-31+77.

[4]Zhang Shanshan, Du Xiaomin, Zhang Anan. Challenges, priorities, and strategies for developing AI education in primary and secondary schools [J]. Audio-visual education in China,2020(11):67-72+96.

[5]Xie Zhongxin, Cao Yanglu, et al. Research on the content design of artificial intelligence curriculum in primary and secondary schools [J]. Audio-visual education in China,2019,(4):17-22..

[6]Fangyuan Yuan, Huang Xuguang. Artificial intelligence education in primary and secondary schools: What to learn and how to teach —— comes from the "American K-12 Artificial Intelligence Education Action" [J]. Audio-visual education in China,2020(10):32-39.

[7]Chiu T K F. Six Key Principles in Designing Artificial Intelligence (AI) Curriculum for Middle Schools[J]. Association for Educational Communications and Technology (AECT) International Convention.2020(2):383-392.

[8]McNeill K L, Lowenhaupt R J, Katsh-Singer R. Instructional leadership in the era of the NGSS: Principals' understandings of science practices[J]. Science Education, 2018, 102(3): 452-473.

[9]Kong S C, Wang Y Q. Investigating primary school principals programming perception and support from the perspective of reasoned action: A mixed methods approach[J]. Computers & Education, 2021, 172: 104267.

[10]RobertK.Yin.Case Study: Design and Methods (Fifth Edition) [M]. Chongqing: Chongqing University Press.2010:21+71.

[11]Yu Bing, Wu Zhihui. Principal Curriculum Leader: an important fulcrum for the high-quality development of basic education in the new era [J]. The social science front,2020(09):240-246.

[12]Guo Yuanxiang. Teachers' curriculum awareness and its generation [J] Education research,2003(06):33-37.

[13]Lv Lijie, Ding Yiran. Study on the components and action mechanisms of curriculum leadership for primary and secondary school principals —— An empirical study based on PLS-SEM [J]. Journal of East China Normal University (Education Science Edition),2022,40(03):20-29.

[14]Tan Hongjun, Chinese Academy of Sciences, Huo Guoqing, Miao Jianming. And Vision Leadership Research [J]. science of leadership,2009(06):26-29.

[15]Yang Tingfang, Ling Wen. Summary of service-oriented leadership theory [J]. Science and technology management research,2008(03):204-207.

[16]Zhang Dan, Cui Guangzuo. Artificial intelligence education research in primary and secondary schools [J]. Modern educational technology,2020,30(01):39-44.

[17]Courduff, J., & Szapkiw, A. Technology integration in the resource specialist program environment: Research-based strategies for technology integration in complex learning environments. Journal of Research in Innovative Teaching, 2015,8(1), 81–98.

Appendix

1. When did we start teaching related to AI education? What was the consideration at that time? Let's start doing this? How many teachers do we have here? What is your subject background? Is it voluntary or selected by the school? The specific situation of the school science and technology innovation? Or in the form of a community? Is there a systematic teaching plan and curriculum plan?
2. Does our school or our team have a long-term expectation or plan for AI education? How is this oneself expected or the school leaders to give?
3. Do our team or other teachers in the school recognize AI education? Do the parents support this? How did they get to know each other? What do you think is how ai education is reflected in the growth of students?
4. Do we have any partner companies? What are the ways of cooperation?
5. At the school level, what kind of support is there for our team to start AI?(Is there a tilt in hardware and software, capital, professional title evaluation and project evaluation?) What specific measures are taken in teacher professional development?
6. If we want to make AI better, what do you think schools need to do better? Have you communicated anything with the school leaders? How did they reply?
7. There are also two questions. From your teaching experience, what are the biggest characteristics of AI education in the teaching of Chinese, mathematics, physical education and art? If a school wants to promote AI education, which is different from other subject education, assuming that from the perspective of principals, what do you think should be the most important measure? How should it be effectively promoted?

Fuzzy Systems and Data Mining IX
A.J. Tallón-Ballesteros and R. Beltrán-Barba (Eds.)

doi:10.3233/FAIA231093

On a New Kind of Quartic Integro-Spline Over a Uniform Partition

Feng-Gong LANG [a] and De-Bao ZHANG [a,1]
[a] *School of Mathematical Sciences, Ocean University of China, Qingdao, Shandong, 266100, People's Republic of China*

Abstract. In this paper, we construct a new kind of quartic integro-spline by applying two constraints on integral values to the piecewise polynomials on the first and the last subintervals, respectively. This quartic integro-spline does not require any additional given boundary values and is relatively simple to implement. It is theoretically proved that this integro-spline has a satisfactory convergence rate for approximating unknown functions and its derivatives at the knots. Especially for an unknown function y with fifth order derivative values of 0 at the left and right endpoints, its approximation of function values and second-order derivative values may even exhibit superconvergence at the knots. Numerical experiments have verified our theoretical results and compared the differences in approximation performance between our quartic integro-spline and other integro-splines.

Keywords. Spline, Quartic integro-spline, Superconvergence, Integral values, Uniform partition

1. Introduction

For an unknown real-valued function $y = y(x)$ and an interval $[a,b]$ with a uniform partition

$$\Delta := \{a = x_0 < x_1 < \cdots < x_n = b\},$$

it is assumed that we are given

$$I_j := \int_{x_j}^{x_{j+1}} y(x)dx, \quad j = 0,1,\cdots,n-1. \tag{1}$$

If a spline $s = s(x)$ satisfies

$$\int_{x_j}^{x_{j+1}} s(x)dx = I_j, \quad j = 0,1,\cdots,n-1, \tag{2}$$

then we call $s = s(x)$ an integro-spline of $y = y(x)$.

[1]Corresponding Author: School of Mathematical Sciences, Ocean University of China, Qingdao, Shandong, 266100, People's Republic of China; E-mail: zhangdebaoouc@sina.com.

To construct an integro-spline, we generally need n integral values I_j $(j = 0, 1, \cdots, n-1)$ and several boundary conditions. In recent years, there are many studies about integro-spline interpolation ([1,2,3,4,5,6,7,8,9,10,11,12]).

In this paper, our main focus is on studying the quartic integro-spline. There have been many studies on quartic integro splines.

In [7], the authors used the following four exact boundary conditions

$$s(x_0) = y(x_0), \quad s(x_1) = y(x_1), \quad s(x_{n-1}) = y(x_{n-1}), \quad s(x_n) = y(x_n)$$

to construct quartic integro-spline. This kind of quartic integro-spline exhibits superconvergence (sixth-order and fourth-order, respectively) in approximating function values and second-order derivative values at the knots. As for approximating first-order and third-order derivative values at the knots, it exhibits ordinary convergence (fourth-order and second-order, respectively).

The authors also proposed a method for constructing quartic integro-spline without any exact boundary conditions, that was using the following four approximate values

$$\begin{aligned}
\widetilde{y}_0 &= \frac{1}{60h}(147I_0 - 213I_1 + 237I_2 - 163I_3 + 62I_4 - 10I_5),\\
\widetilde{y}_1 &= \frac{1}{60h}(10I_0 + 87I_1 - 63I_2 + 37I_3 - 13I_4 + 2I_5),\\
\widetilde{y}_{n-1} &= \frac{1}{60h}(10I_{n-1} + 87I_{n-2} - 63I_{n-3} + 37I_{n-4} - 13I_{n-5} + 2I_{n-6}),\\
\widetilde{y}_n &= \frac{1}{60h}(147I_{n-1} - 213I_{n-2} + 237I_{n-3} - 163I_{n-4} + 62I_{n-5} - 10I_{n-6}),
\end{aligned}$$

to approximate $y(x_0)$, $y(x_1)$, $y(x_{n-1})$, $y(x_n)$ and then constructing quartic integro-spline. Furthermore, it was demonstrated that this kind of quartic integro-spline still possessed similar approximation properties including superconvergence as discussed above.

In [12], the authors derived the approximation properties of the aforementioned two kinds of quartic integro-splines at the mid-knots. Specifically, the two quartic integro-splines exhibit superconvergence (sixth-order, fourth-order and second-order, respectively) in approximating function values, second-order derivative values and fourth-order derivative values at the mid-knots. As for approximating first-order and third-order derivative values at the mid-knots, they exhibit ordinary convergence (fourth-order and second-order, respectively).

In [4], the authors proposed a new local construction method of quartic integro-spline without using any additional boundary conditions and without solving any equations system. In fact, they provided an excellent algorithm for values of the quartic integro-spline and up to its third-order derivatives values at the knots. This local quartic integro-spline still possesses similar approximation properties including superconvergence to that in [7].

In this paper, we will study a new kind of quartic integro-spline by using a new type of boundary conditions. In fact, we construct the boundary conditions by applying constraints on integral values to the first and the last piecewise polynomial functions, that is

$$\int_{x_1}^{x_2} s_{[x_0,x_1]}(x)dx = I_1, \tag{3}$$

$$\int_{x_2}^{x_3} s_{[x_0,x_1]}(x)dx = I_2, \tag{4}$$

$$\int_{x_{n-3}}^{x_{n-2}} s_{[x_{n-1},x_n]}(x)dx = I_{n-3}, \tag{5}$$

$$\int_{x_{n-2}}^{x_{n-1}} s_{[x_{n-1},x_n]}(x)dx = I_{n-2}, \tag{6}$$

where $s_{[x_j,x_{j+1}]}(x)$ $(j=0,1,\cdots,n-1)$ are the piecewise polynomial functions of $s=s(x)$ on subinterval $[x_j,x_{j+1}]$. Can we construct a quartic integro-spline by using Eqs. (2), (3), (4), (5) and (6) and what are the approximation properties of this kind of quartic integro-spline?

In this paper, we did construct the above new kind of quartic integro-spline $s=s(x)$ by using Eqs. (2), (3), (4), (5) and (6) under the assumption of $y(x)\in C^6[a,b]$ and then we studied the approximation properties of $s=s(x)$ at the knots x_i $(i=0,1,\cdots,n)$.

The rest of this paper is organized as follows. In Section 2, we will provide the construction method for the quartic integro-spline mentioned above. Then we will study the approximation properties of this quartic integro-spline at the knots in Section 3. In Section 4, we will validate our theoretical results and compare the differences in approximation performance between our quartic integro-spline and other integro-splines through numerical tests. Finally, we will conclude the paper in Section 5.

2. The Construction Method of the New Quartic Integro-spline

In this section, we will construct the new kind of quartic integro-spline $s(x)=\sum_{i=-2}^{n+1} c_iB_i(x)$ ([13,14,15]), where

$$B_i(x)=\frac{1}{24h^4}\begin{cases}(x-x_{i-2})^4, & \text{if } x\in[x_{i-2},x_{i-1}]\\ (x-x_{i-2})^4-5(x-x_{i-1})^4, & \text{if } x\in[x_{i-1},x_i]\\ (x-x_{i-2})^4-5(x-x_{i-1})^4+10(x-x_i)^4, & \text{if } x\in[x_i,x_{i+1}]\\ (x-x_{i+3})^4-5(x-x_{i+2})^4, & \text{if } x\in[x_{i+1},x_{i+2}]\\ (x-x_{i+3})^4, & \text{if } x\in[x_{i+2},x_{i+3}]\\ 0, & \text{else}\end{cases} \tag{7}$$

$(i=-2,-1,\cdots,n+1)$ are quartic B-splines, $x_i=a+ih$ $(i=-4,-3,\cdots,n+4)$ are the knots and $h=\frac{b-a}{n}$ is the length of the subintervals.

From Eq. (2), for $j=0,1,\cdots,n-1$, we have

$$I_j=\int_{x_j}^{x_{j+1}}\sum_{i=-2}^{n+1}c_iB_i(x)dx=\frac{h}{120}(c_{j-2}+26c_{j-1}+66c_j+26c_{j+1}+c_{j+2}). \tag{8}$$

From Eq. (3), we have

$$\int_{x_1}^{x_2} s_{[x_0,x_1]}(x)dx=\frac{1}{24h^4}\left(\int_{x_1}^{x_2}c_{-2}(x-x_1)^4dx+\int_{x_1}^{x_2}c_{-1}((x-x_2)^4-5(x-x_1)^4)dx\right.$$

$$
\begin{aligned}
&+\int_{x_1}^{x_2} c_0((x-x_{-2})^4-5(x-x_{-1})^4+10(x-x_0)^4)dx\\
&+\int_{x_1}^{x_2} c_1((x-x_{-1})^4-5(x-x_0)^4)dx+\int_{x_1}^{x_2} c_2(x-x_0)^4dx\Big)\\
&=\frac{h}{120}(c_{-2}-4c_{-1}+36c_0+56c_1+31c_2).
\end{aligned}
$$

From Eq. (3), we have

$$
\frac{h}{120}(c_{-2}-4c_{-1}+36c_0+56c_1+31c_2)=\frac{h}{120}(c_{-1}+26c_0+66c_1+26c_2+c_3),
$$

that is

$$
c_{-2}-5c_{-1}+10c_0-10c_1+5c_2-c_3=0. \tag{9}
$$

Similarly, from Eqs. (4), (5) and (6), we have

$$
c_{-1}-5c_0+10c_1-10c_2+5c_3-c_4=0, \tag{10}
$$

$$
c_{n-5}-5c_{n-4}+10c_{n-3}-10c_{n-2}+5c_{n-1}-c_n=0, \tag{11}
$$

$$
c_{n-4}-5c_{n-3}+10c_{n-2}-10c_{n-1}+5c_n-c_{n+1}=0. \tag{12}
$$

Now we get $n+4$ equations Eqs. (8), (9), (10), (11) and (12), which can be rewritten as the following linear system

$$
\begin{pmatrix}
1 & -5 & 10 & -10 & 5 & -1 & & & \\
 & 1 & -5 & 10 & -10 & 5 & -1 & & \\
1 & 26 & 66 & 26 & 1 & & & & \\
 & 1 & 26 & 66 & 26 & 1 & & & \\
 & & \ddots & \ddots & \ddots & \ddots & \ddots & & \\
 & & & 1 & 26 & 66 & 26 & 1 & \\
 & & & & 1 & 26 & 66 & 26 & 1 \\
 & & 1 & -5 & 10 & -10 & 5 & -1 & \\
 & & & 1 & -5 & 10 & -10 & 5 & -1
\end{pmatrix}
\begin{pmatrix} c_{-2}\\ c_{-1}\\ c_0\\ c_1\\ \vdots\\ c_{n-2}\\ c_{n-1}\\ c_n\\ c_{n+1}\end{pmatrix}
=
\begin{pmatrix} 0\\ 0\\ \frac{120}{h}I_0\\ \frac{120}{h}I_1\\ \vdots\\ \frac{120}{h}I_{n-2}\\ \frac{120}{h}I_{n-1}\\ 0\\ 0\end{pmatrix}. \tag{13}
$$

Theorem 2.1. *The coefficient matrix of the linear system (13) is invertible.*

Proof. Firstly, we transform the coefficient matrix A by the following elementary transformation.

(i) Add row one multiplied by -1 to row three, also add row $n+4$ multiplied by 1 to row $n+2$;

(ii) Add row two multiplied by -31 to row three, also add row $n+3$ multiplied by 31 to row $n+2$;

(iii) Add row two multiplied by -1 to row four, also add row $n+3$ multiplied by 1 to row $n+1$;

(iv) Add row three multiplied by $-\frac{31}{211}$ to row four, also add row $n+2$ multiplied by $-\frac{31}{211}$ to row $n+1$;

(v) Add row three multiplied by $-\frac{1}{211}$ to row five, also add row $n+2$ multiplied by $-\frac{1}{211}$ to row n.

Then A can be transformed to

$$\widetilde{A}=\begin{pmatrix}
1 & -5 & 10 & -10 & 5 & -1 & & & & & & & \\
 & 1 & -5 & 10 & -10 & 5 & -1 & & & & & & \\
 & & 211 & -274 & 306 & -154 & 31 & & & & & & \\
 & & & \frac{20310}{211} & -\frac{1890}{211} & \frac{3930}{211} & -\frac{750}{211} & & & & & & \\
 & & & \frac{5760}{211} & \frac{13620}{211} & \frac{5640}{211} & \frac{180}{211} & & & & & & \\
 & & & 1 & 26 & 66 & 26 & 1 & & & & & \\
 & & & & \ddots & \ddots & \ddots & \ddots & \ddots & & & & \\
 & & & & & 1 & 26 & 66 & 26 & 1 & & & \\
 & & & & & & \frac{180}{211} & \frac{5640}{211} & \frac{13620}{211} & \frac{5760}{211} & & & \\
 & & & & & & -\frac{750}{211} & \frac{3930}{211} & -\frac{1890}{211} & \frac{20310}{211} & & & \\
 & & & & & & & 31 & -154 & 306 & -274 & 211 & \\
 & & & & & & & 1 & -5 & 10 & -10 & 5 & -1 \\
 & & & & & & & & 1 & -5 & 10 & -10 & 5 & -1
\end{pmatrix}.$$

Obviously, the central block matrix of $\widetilde{A}$ is strictly diagonally dominant. Based on the basic theory of linear algebra, A is invertible. □

Theorem 2.1 shows that the linear system Eq. (13) has a unique solution, which means that we can determine a quartic integro-spline $s=s(x)=\sum_{i=-2}^{n+1} c_i B_i(x)$ by using Eqs. (2), (3), (4), (5) and (6).

3. Approximation Properties

In this section, we will study the approximation properties of the new kind of quartic integro-spline constructed in Section 2.

Firstly, we give some relations at the knots on the boundary.

Lemma 3.1. *For the quartic integro-spline $s=s(x)$ determined by Eqs. (2), (3), (4), (5) and (6), we have the following relations.*

$$s(x_0)+6s(x_1)+3s(x_2)=\frac{1}{3h}(10I_0+19I_1+I_2), \tag{14}$$

$$3s(x_1)+6s(x_2)+s(x_3)=\frac{1}{3h}(I_0+19I_1+10I_2), \tag{15}$$

$$s(x_{n-3})+6s(x_{n-2})+3s(x_{n-1})=\frac{1}{3h}(10I_{n-3}+19I_{n-2}+I_{n-1}), \tag{16}$$

$$3s(x_{n-2})+6s(x_{n-1})+s(x_n)=\frac{1}{3h}(I_{n-3}+19I_{n-2}+10I_{n-1}), \tag{17}$$

$$s'(x_0)+10s'(x_1)+s'(x_2)=-\frac{12}{h^2}(I_0-I_1), \tag{18}$$

$$s'(x_1)+10s'(x_2)+s'(x_3)=-\frac{12}{h^2}(I_1-I_2), \tag{19}$$

$$s'(x_{n-3})+10s'(x_{n-2})+s'(x_{n-1})=-\frac{12}{h^2}(I_{n-3}-I_{n-2}), \tag{20}$$

$$s'(x_{n-2})+10s'(x_{n-1})+s'(x_n)=-\frac{12}{h^2}(I_{n-2}-I_{n-1}), \tag{21}$$

$$s''(x_0)+6s''(x_2)-s''(x_3)=\frac{6}{h^3}(I_0-2I_1+I_2), \tag{22}$$

$$s''(x_1)+s''(x_2)=\frac{2}{h^3}(I_0-2I_1+I_2), \tag{23}$$

$$s''(x_{n-2})+s''(x_{n-1})=\frac{2}{h^3}(I_{n-3}-2I_{n-2}+I_{n-1}), \tag{24}$$

$$-s''(x_{n-3})+6s''(x_{n-2})+s''(x_n)=\frac{6}{h^3}(I_{n-3}-2I_{n-2}+I_{n-1}), \tag{25}$$

$$s'''(x_0)-2s'''(x_1)+s'''(x_2)=0, \tag{26}$$

$$s'''(x_1)-2s'''(x_2)+s'''(x_3)=0, \tag{27}$$

$$s'''(x_{n-3})-2s'''(x_{n-2})+s'''(x_{n-1})=0, \tag{28}$$

$$s'''(x_{n-2})-2s'''(x_{n-1})+s'''(x_n)=0. \tag{29}$$

Proof. Considering $s(x)=\sum_{i=-2}^{n+1}c_iB_i(x)$ and Eq. (7), for $j=0,1,\cdots,n$, we have

$$s(x_j)=\frac{1}{24}(c_{j-2}+11c_{j-1}+11c_j+c_{j+1}), \tag{30}$$

$$s'(x_j)=\frac{1}{6h}(-c_{j-2}-3c_{j-1}+3c_j+c_{j+1}), \tag{31}$$

$$s''(x_j)=\frac{1}{2h^2}(c_{j-2}-c_{j-1}-c_j+c_{j+1}), \tag{32}$$

$$s'''(x_j)=\frac{1}{h^3}(-c_{j-2}+3c_{j-1}-3c_j+c_{j+1}). \tag{33}$$

By using the above equations and Eqs. (8), (9), (10), (11) and (12), we can easily get the relations in Lemma 3.1. □

Next we will study the approximation properties of the quartic integro-spline $s=s(x)$ determined by Eqs. (2), (3), (4), (5) and (6) at the knots.

Let $y_j=y(x_j)$ and $e^{(k)}(x_j)=s^{(k)}(x_j)-y_j^{(k)}$ $(k=0,1,2,3;\ j=0,1,\cdots,n)$, we define

$$\|E^{(k)}\|=\max_{0\le j\le n}|e^{(k)}(x_j)|,\quad k=0,1,2,3.$$

Firstly, we study $\|E^{(0)}\|$. Considering Eq. (1), using the Taylor expansion of $y=y(x)$ at x_0, we can get

$$I_j=\sum_{i=1}^{6}\frac{(j+1)^i-j^i}{i!}y_0^{(i-1)}h^i+\mathcal{O}(h^7),\ \ j=0,1,2. \tag{34}$$

Also expand $y = y(x)$ at x_0, we have

$$y_j = \sum_{i=0}^{5} \frac{j^i}{i!} y_0^{(i)} h^i + \mathscr{O}(h^6), \quad j = 1,2,3. \tag{35}$$

From Eqs. (14) and (15), using Eqs. (34) and (35), we get

$$\begin{aligned} e(x_0) + 6e(x_1) + 3e(x_2) &= \frac{1}{3h}(10I_0 + 19I_1 + I_2) - y_0 - 6y_1 - 3y_2 \\ &= \frac{1}{60} y_0^{(5)} h^5 + \mathscr{O}(h^6) = \mathscr{E}_0 = \begin{cases} \mathscr{O}(h^6), \text{ if } y_0^{(5)} = 0, \\ \mathscr{O}(h^5), \text{ if } y_0^{(5)} \neq 0, \end{cases} \end{aligned} \tag{36}$$

$$\begin{aligned} 3e(x_1) + 6e(x_2) + e(x_3) &= \frac{1}{3h}(I_0 + 19I_1 + 10I_2) - 3y_1 - 6y_2 - y_3 \\ &= -\frac{1}{60} y_0^{(5)} h^5 + \mathscr{O}(h^6) = \mathscr{E}_1 = \begin{cases} \mathscr{O}(h^6), \text{ if } y_0^{(5)} = 0, \\ \mathscr{O}(h^5), \text{ if } y_0^{(5)} \neq 0. \end{cases} \end{aligned} \tag{37}$$

Similarly, by using the Taylor expansion of $y = y(x)$ at x_n and Eq. (1), from Eqs. (16) and (17), we can get

$$\begin{aligned} e(x_{n-3}) + 6e(x_{n-2}) + 3e(x_{n-1}) &= \frac{1}{3h}(10I_{n-3} + 19I_{n-2} + I_{n-1}) - y_{n-3} - 6y_{n-2} - 3y_{n-1} \\ &= \frac{1}{60} y_n^{(5)} h^5 + \mathscr{O}(h^6) = \mathscr{E}_{n-1} = \begin{cases} \mathscr{O}(h^6), \text{ if } y_n^{(5)} = 0, \\ \mathscr{O}(h^5), \text{ if } y_n^{(5)} \neq 0, \end{cases} \end{aligned} \tag{38}$$

$$\begin{aligned} 3e(x_{n-2}) + 6e(x_{n-1}) + e(x_n) &= \frac{1}{3h}(I_{n-3} + 19I_{n-2} + 10I_{n-1}) - 3y_{n-2} - 6y_{n-1} - y_n \\ &= -\frac{1}{60} y_n^{(5)} h^5 + \mathscr{O}(h^6) = \mathscr{E}_n = \begin{cases} \mathscr{O}(h^6), \text{ if } y_n^{(5)} = 0, \\ \mathscr{O}(h^5), \text{ if } y_n^{(5)} \neq 0. \end{cases} \end{aligned} \tag{39}$$

From [7], for $j = 2,3,\cdots,n-2$, we have

$$e(x_{j-2}) + 26e(x_{j-1}) + 66e(x_j) + 26e(x_{j+1}) + e(x_{j+2}) = \mathscr{O}(h^6). \tag{40}$$

Integrating Eqs. (36), (37), (38), (39) and (40), we get the following linear system

$$\begin{pmatrix} 1 & 6 & 3 & & & & & \\ & 3 & 6 & 1 & & & & \\ 1 & 26 & 66 & 26 & 1 & & & \\ & 1 & 26 & 66 & 26 & 1 & & \\ & & \ddots & \ddots & \ddots & \ddots & \ddots & \\ & & & 1 & 26 & 66 & 26 & 1 \\ & & & & 1 & 26 & 66 & 26 & 1 \\ & & & & & 1 & 6 & 3 \\ & & & & & & 3 & 6 & 1 \end{pmatrix} \begin{pmatrix} e(x_0) \\ e(x_1) \\ e(x_2) \\ e(x_3) \\ \vdots \\ e(x_{n-3}) \\ e(x_{n-2}) \\ e(x_{n-1}) \\ e(x_n) \end{pmatrix} = \begin{pmatrix} \mathscr{E}_0 \\ \mathscr{E}_1 \\ \mathscr{O}(h^6) \\ \mathscr{O}(h^6) \\ \vdots \\ \mathscr{O}(h^6) \\ \mathscr{O}(h^6) \\ \mathscr{E}_{n-1} \\ \mathscr{E}_n \end{pmatrix}.$$

By doing elementary transformation on the coefficient matrix M of this linear system, we have

$$M=\begin{pmatrix}
1 & 6 & 3 & & & & & & \\
 & 3 & 6 & 1 & & & & & \\
1 & 26 & 66 & 26 & 1 & & & & \\
 & 1 & 26 & 66 & 26 & 1 & & & \\
 & & \ddots & \ddots & \ddots & \ddots & \ddots & & \\
 & & & 1 & 26 & 66 & 26 & 1 & \\
 & & & & 1 & 26 & 66 & 26 & 1 \\
 & & & & & 1 & 6 & 3 & \\
 & & & & & & 3 & 6 & 1
\end{pmatrix}\longrightarrow
\begin{pmatrix}
1 & 6 & 3 & & & & & & \\
 & 3 & 6 & 1 & & & & & \\
 & & 23 & \frac{58}{3} & 1 & & & & \\
 & & 24 & \frac{197}{3} & 26 & 1 & & & \\
 & & & \ddots & \ddots & \ddots & \ddots & & \\
 & & & & 1 & 26 & \frac{197}{3} & 24 & \\
 & & & & & 1 & \frac{58}{3} & 23 & \\
 & & & & & & 1 & 6 & 3 \\
 & & & & & & & 3 & 6 & 1
\end{pmatrix}=\widetilde{M}.$$

The central block be of $\widetilde{M}$ is strictly diagonally dominant. It shows that the infinity norm of the inverse of the coefficient matrix is also bounded. So we get

$$\|E^{(0)}\|=\begin{cases}\mathscr{O}(h^6), \text{ if } y_0^{(5)}=0 \text{ and } y_n^{(5)}=0,\\ \mathscr{O}(h^5), \text{ if } y_0^{(5)}\neq 0 \text{ or } y_n^{(5)}\neq 0.\end{cases}$$

Next, we study $\|E^{(1)}\|$. From Eqs. (18), (19), (20) and (21), using the Taylor expansion of $y=y(x)$ at x_0 and x_n in Eq. (1) and the Taylor expansion of $y'(x)$ at x_0 and x_n, we have

$$e'(x_0)+10e'(x_1)+e'(x_2)=-\frac{1}{20}y_0^{(5)}h^4+\mathscr{O}(h^5)=\mathscr{E}_0'=\begin{cases}\mathscr{O}(h^5), \text{ if } y_0^{(5)}=0,\\ \mathscr{O}(h^4), \text{ if } y_0^{(5)}\neq 0,\end{cases} \tag{41}$$

$$e'(x_1)+10e'(x_2)+e'(x_3)=-\frac{1}{20}y_0^{(5)}h^4+\mathscr{O}(h^5)=\mathscr{E}_1'=\begin{cases}\mathscr{O}(h^5), \text{ if } y_0^{(5)}=0,\\ \mathscr{O}(h^4), \text{ if } y_0^{(5)}\neq 0,\end{cases} \tag{42}$$

$$e'(x_{n-3})+10e'(x_{n-2})+e'(x_{n-1})=-\frac{1}{20}y_n^{(5)}h^4+\mathscr{O}(h^5)=\mathscr{E}_{n-1}'=\begin{cases}\mathscr{O}(h^5), \text{ if } y_n^{(5)}=0,\\ \mathscr{O}(h^4), \text{ if } y_n^{(5)}\neq 0,\end{cases} \tag{43}$$

$$e'(x_{n-2})+10e'(x_{n-1})+e'(x_n)=-\frac{1}{20}y_n^{(5)}h^4+\mathscr{O}(h^5)=\mathscr{E}_n'=\begin{cases}\mathscr{O}(h^5), \text{ if } y_n^{(5)}=0,\\ \mathscr{O}(h^4), \text{ if } y_n^{(5)}\neq 0.\end{cases} \tag{44}$$

From [7], for $j=2,3,\cdots,n-2$, we have

$$e'(x_{j-2})+26e'(x_{j-1})+66e'(x_j)+26e'(x_{j+1})+e'(x_{j+2})=\mathscr{O}(h^4). \tag{45}$$

Similarly, we integrate Eqs. (41), (42), (43), (44) and (45) and get the following linear system

$$\begin{pmatrix}
1 & 10 & 1 & & & & & \\
 & 1 & 10 & 1 & & & & \\
1 & 26 & 66 & 26 & 1 & & & \\
 & 1 & 26 & 66 & 26 & 1 & & \\
 & & \ddots & \ddots & \ddots & \ddots & \ddots & \\
 & & & 1 & 26 & 66 & 26 & 1 \\
 & & & & 1 & 26 & 66 & 26\ 1 \\
 & & & & & 1 & 10 & 1 \\
 & & & & & & 1 & 10\ 1
\end{pmatrix}\begin{pmatrix}e'(x_0)\\ e'(x_1)\\ e'(x_2)\\ e'(x_3)\\ \vdots\\ e'(x_{n-3})\\ e'(x_{n-2})\\ e'(x_{n-1})\\ e'(x_n)\end{pmatrix}=\begin{pmatrix}\mathscr{E}_0'\\ \mathscr{E}_1'\\ \mathscr{O}(h^4)\\ \mathscr{O}(h^4)\\ \vdots\\ \mathscr{O}(h^4)\\ \mathscr{O}(h^4)\\ \mathscr{E}_{n-1}'\\ \mathscr{E}_n'\end{pmatrix}. \tag{46}$$

By doing elementary transformation on the coefficient matrix of the above linear system Eq. (46) and using the same method mentioned above, we can get

$$\|E^{(1)}\| = \mathcal{O}(h^4).$$

We can study $\|E^{(2)}\|$ and $\|E^{(3)}\|$ in the same way. Here we only give the results. For $\|E^{(2)}\|$, we have

$$\|E^{(2)}\| = \begin{cases} \mathcal{O}(h^4), \text{ if } y_0^{(5)} = 0 \text{ and } y_n^{(5)} = 0, \\ \mathcal{O}(h^3), \text{ if } y_0^{(5)} \neq 0 \text{ or } y_n^{(5)} \neq 0. \end{cases}$$

For $\|E^{(3)}\|$, we have $\|E^{(3)}\| = \mathcal{O}(h^2)$.
Summarize the above analysis results, we get the following theorem.

Theorem 3.1. *For the quartic integro-spline $s = s(x)$ determined by Eqs. (2), (3), (4), (5) and (6),*

- *for $k = 0, 2$, we have*

$$\|E^{(k)}\| = \begin{cases} \mathcal{O}(h^{6-k}), \textit{ if } y_0^{(5)} = 0 \textit{ and } y_n^{(5)} = 0, \\ \mathcal{O}(h^{5-k}), \textit{ if } y_0^{(5)} \neq 0 \textit{ or } y_n^{(5)} \neq 0, \end{cases}$$

- *for $k = 1, 3$, we have $\|E^{(k)}\| = \mathcal{O}(h^{5-k})$.*

This theorem demonstrates that, when $y_0^{(5)} = 0$ and $y_n^{(5)} = 0$, this kind of quartic integro-spline exhibits superconvergence in function values approximation (sixth-order convergence) and in second-order derivatives approximation (fourth-order convergence) at the knots, which are similar to that of the quartic integro-spline in [7].

4. Numerical Tests

4.1. Performance of Our Quartic Integro-spline

In this subsection, we choose two functions

$$y_1 = \frac{1}{1+25x^2} \text{ and } y_2 = cos(\pi x), \ x \in [0,1]$$

to test the approximation performance at the knots of the quartic integro-spline $s = s(x)$ determined by Eqs. (2), (3), (4), (5) and (6). We calculated the maximum absolute errors (MAEs) and the average numerical convergence orders (ANCOs) of y_1 and y_2 (see Table 1 and Table 2 respectively) under some uniform partitions.

For $y_1 = \frac{1}{1+25x^2}$, we can see that the ANCOs of $\|E^{(k)}\|$ $(k = 0, 1, 2, 3)$ are around $5-k$. For y_1, we have $y_1^{(5)}(0) = 0$ but $y_1^{(5)}(1) \neq 0$, so the results in Table 1 are consistent with Theorem 3.1.

Table 1. The MAEs and ANCOs of $y_1 = \frac{1}{1+25x^2}$.

	$n=20$	$n=40$	$n=80$	$n=160$	$n=320$	ANCO
$\|E^{(0)}\|$	3.910×10^{-3}	2.939×10^{-4}	6.805×10^{-6}	1.174×10^{-7}	1.881×10^{-9}	5.25
$\|E^{(1)}\|$	4.097×10^{-1}	5.586×10^{-2}	2.552×10^{-3}	8.781×10^{-5}	2.811×10^{-6}	4.29
$\|E^{(2)}\|$	2.452×10^{1}	5.785×10^{0}	5.172×10^{-1}	3.542×10^{-2}	2.265×10^{-3}	3.35
$\|E^{(3)}\|$	9.410×10^{2}	3.628×10^{2}	6.266×10^{1}	8.515×10^{0}	1.087×10^{0}	2.44

Table 2. The MAEs and ANCOs of $y_2 = cos(\pi x)$.

	$n=20$	$n=40$	$n=80$	$n=160$	$n=320$	ANCO
$\|E^{(0)}\|$	2.678×10^{-6}	4.232×10^{-8}	6.631×10^{-10}	1.037×10^{-11}	1.645×10^{-13}	5.99
$\|E^{(1)}\|$	2.502×10^{-4}	7.906×10^{-6}	2.478×10^{-7}	7.748×10^{-9}	2.453×10^{-10}	4.99
$\|E^{(2)}\|$	1.261×10^{-2}	7.962×10^{-4}	4.989×10^{-5}	3.120×10^{-6}	1.971×10^{-7}	3.99
$\|E^{(3)}\|$	3.784×10^{-1}	4.775×10^{-2}	5.983×10^{-3}	9.962×10^{-4}	2.664×10^{-4}	2.62

For $y_2 = cos(\pi x)$, the ANCOs of $\|E^{(k)}\|$ $(k=0,2)$ are around $6-k$, considering $y_2^{(5)}(0) = y_2^{(5)}(1) = 0$, so the results are still accordance with Theorem 3.1. As for $\|E^{(k)}\|$ $(k=1,3)$, the ANCOs seem higher than our theoretical order $5-k$, they are even very close to $6-k$, but as $\mathscr{O}(h^5)$ is also $\mathscr{O}(h^4)$, and $\mathscr{O}(h^3)$ is $\mathscr{O}(h^2)$ too, so the results are still not contradictory to Theorem 3.1. We take $\|E^{(1)}\|$ as an example to explain this phenomenon, from Eq. (46), that is

$$(e'(x_0),\cdots,e'(x_n))^T = N^{-1}(\mathscr{E}_0',\mathscr{E}_1',\mathscr{O}(h^4),\cdots,\mathscr{O}(h^4),\mathscr{E}_{n-1}',\mathscr{E}_n')^T,$$

where $N^{-1} = (u_{i,j})_{(n+1)\times(n+1)}$ is the inverse of the coefficient matrix of linear system Eq. (46) and $\mathscr{E}_0',\mathscr{E}_1',\mathscr{E}_{n-1}',\mathscr{E}_n' = \mathscr{O}(h^5)$. For y_2, we find $\|E^{(1)}\|$ is always taken as $e'(0)$, however,

$$\frac{|u_{1,1}+u_{1,2}+u_{1,n}+u_{1,n+1}|}{|u_{1,3}+\cdots+u_{1,n-1}|} > 10,$$

which means $e'(0)$ is mainly determined by $\mathscr{E}_0',\mathscr{E}_1',\mathscr{E}_{n-1}',\mathscr{E}_n'$, so the ANCO of $\|E^{(1)}\|$ tends to manifest as 5 rather than 4. Consequently, the aforementioned phenomenon has been elucidated. In a similar manner, we can employ analogous techniques to explain other numerical phenomena, including y_1.

Furthermore, based on the numerical results, we can find that this kind of quartic integro-spline indeed exhibits a faster convergence rate even the phenomenon of super-convergence (for function values and second-order derivative values approximation) at the knots for function $y = y(x)$ satisfying $y_0^{(5)} = y_n^{(5)} = 0$.

In summary, the numerical experiments validate our theoretical results and the new kind of quartic integro-spline demonstrates excellent approximation capability.

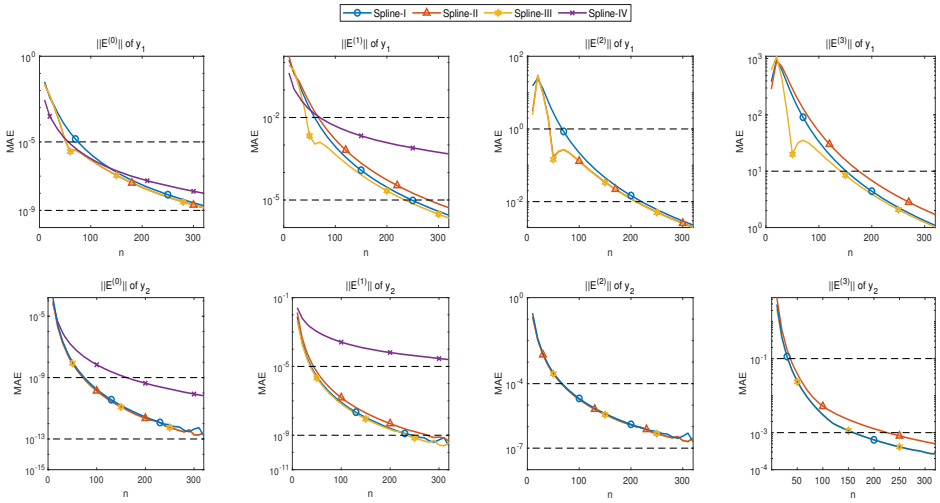

Figure 1. The MAE-n plots for $\|E^{(k)}\|$ $(k=0,1,2,3)$ of Spline-I, Spline-II and Spline-III and that for $\|E^{(k)}\|$ $(k=0,1)$ of Spline-IV approximating functions y_1 and y_2 and up to their third-order derivatives.

4.2. Comparison with Other Integro-splines

In this subsection, we compare the approximation ability at the knots of our quartic integro-spline (Spline-I), the local quartic integro-spline in [4] (Spline-II), the quartic integro-spline with approximate boundary values in [7] (Spline-III) and the quadratic integro-spline with exact boundary values in [11] (Spline-IV).

We still used the two functions y_1 and y_2 mentioned in Subsection 4.1 as test functions and we generated the MAE-n plots for $\|E^{(k)}\|$ $(k=0,1,2,3)$ of Spline-I, Spline-II and Spline-III and that for $\|E^{(k)}\|$ $(k=0,1)$ of Spline-IV approximating functions y_1 and y_2 and up to their third-order derivatives (see Figure 1).

From the four plots on the left-hand side in Figure 1, for Spline-IV, despite using exact boundary values, its approximation capability remains the poorest.

For Spline-I, Spline-II and Spline-III, they do not require any exact boundary values. By comprehensively comparing all eight plots in Figure 1, we find that the approximation performance of these three quartic integro-splines is very similar. Overall, our quartic integro-spline (Spline-I) exhibits intermediate approximation performance between Spline-II and Spline-III. However, the MAE-n curves of our quartic integro-spline is smoother, indicating better stability in its approximation.

In summary, our quartic integro-spline not only has the advantage of simplicity in operation but also exhibits more stable approximation capability while maintaining the approximation effectiveness.

5. Conclusions

In this paper, we construct a new kind of quartic integro-spline by imposing two additional constraints on the integral values of the first and last piecewise polynomials (Eqs.

(3), (4), (5) and (6)), respectively. This quartic integro-spline does not require any boundary conditions and is relatively simple to implement. Theoretical analysis and numerical tests have verified that this integro-spline exhibits a favorable convergence rate in approximating the function $y = y(x)$ and its derivatives, and they have also confirmed the faster convergence rate in function values and second-order derivative values approximation at the knots for function $y = y(x)$ with $y_0^{(5)} = y_n^{(5)} = 0$. Compared to other quartic integro-splines, our quartic integro-spline not only ensures approximation effectiveness but also exhibits more stable performance. We believe that the construction method of this integro-spline will open up new perspectives for other studies of integro-splines. However, likes other integro-splines, this kind of quartic integro-spline has certain limitations, such as the potential issue of overfitting when the partition is too dense. Addressing this concern will be our focus and direction of future efforts and research.

Acknowledgements

We thank the support received from the National Natural Science Foundation of China under Grant No. 11501533. We appreciate the reviewers and editors for their careful reading, valuable suggestions, timely review and reply.

References

[1] Behforooz H. Approximation by integro cubic splines. Appl Math Comput. 2006; 175:8-15.
[2] Behforooz H. Interpolation by integro quintic splines. Appl Math Comput. 2010; 216:364-367.
[3] Zhanlav T, Mijiddorj R. Integro quintic splines and their approximation properties. Appl Math Comput. 2014; 231:536-543.
[4] Zhanlav T, Mijiddorj R. On local integro quartic splines. Appl Math Comput. 2015; 269:301-307.
[5] Wu JM, Zhang XL. Integro sextic spline interpolation and its super convergence. Appl Math Comput. 2013; 219:6431-6436.
[6] Wu JM, Zhang XL. Integro quadratic spline interpolation. Appl Math Model. 2015; 39:2973-2980.
[7] Lang FG, Xu XP. On integro quartic spline interpolation. J Comput Appl Math. 2012; 236:4214-4226.
[8] Lang FG, Xu XP. Quintic B-spline method for integro interpolation. Appl Math Comput. 2015; 263:353-360.
[9] Lang FG. A new quintic spline method for integro interpolation and its error analysis. Algorithms. 2017; 10(1). doi:10.3390/a10010032.
[10] Lang FG, Xu XP. On a new approximation method with four times continuously differentiable quintic integro-differential spline. IAENG International Journal of Applied Mathematics. 2017; 47:371-380.
[11] Lang FG, Xu XP. On the superconvergence of some quadratic integro-splines at the mid-knots of a uniform partition. Appl Math Comput. 2018; 338:507-514.
[12] Lang FG, Xu XP. Some new super convergence of a quartic integro-spline at the mid-knots of a uniform partition. ScienceAsia. 2022; 48:479-487.
[13] Boor CD. A practical guide to splines. New York: Springer-Verlag; 1978.
[14] Schoenberg IJ. Contribution to the problem of approximation of equidistant data by analytic functions. Quart Appl Math. 1946; 4:45-99 and 112-141.
[15] Wang RH. Numerical approximation. Beijing: Higher Education Press; 1999.

Fuzzy Systems and Data Mining IX
A.J. Tallón-Ballesteros and R. Beltrán-Barba (Eds.)

doi:10.3233/FAIA231094

Blockchain Framework for Healthcare Data Management System in Clinical Trials

Nail Adeeb Ali Abdu[a,b,1], Zhaoshun Wang[a] and Mohammed Ahmed Ali Abdualrhman[b,c]
[a] *University of Science and Technology Beijing (USTB), Beijing 10083, China.*
[b] *University of Science and Technology, Aden, Yemen*
[c] *Al-Saeed University, Taiz, Yemen*

Abstract: The concept of information management involves the identification and organization of data into distinct sectors, sometimes referred to as silos, in order to anticipate and address future situations. One of the primary obstacles encountered in the administration of clinical trials pertains to the presence of information silos among the several stakeholders involved in the process. The improvement of cooperation and integration may be achieved by processing information in real-time and implementing a comprehensive system. This manuscript evaluates the viability of implementing the blockchain model for auditing clinical trials. It also proposes a blockchain-based solution that has the potential to enhance the overall quality of the practiced solutions and establish sustainable approaches for conducting clinical trials auditing. The suggested model focuses on the development of a grid-based system for organizing the many stages of a clinical trial. This involves creating distinct blocks for each phase and then constructing a complete network of these blocks to be shared across the consortium responsible for managing the trial data. The suggested architecture has substantial potential for enhancing security and adaptability, hence facilitating systematic improvements to information systems in the context of clinical trials.

Keywords: Healthcare Data Management System, blockchain, clinical trials, Architecture of Grid Blockchain framework.

1. Introduction

Clinical research is pivotal in advancing pharmaceutical accessibility for high-quality healthcare. To uphold research quality, effective clinical training is crucial. Recruiting and retaining subjects in trials significantly impacts study cost and duration. Quality assurance in clinical research is resource-intensive but pivotal for innovative healthcare solutions. Given procedural complexity, optimizing management efficiency is imperative. Ethical and regulatory compliance enhance participant recruitment and trial

[1] Corresponding author: Department of Computer Science and Technology, School of Computer and Communication Engineering, University of Science and Technology Beijing (USTB), Beijing 10083, China; E-mail: b20190665@xs.ustb.edu.cn , n3a_alkershi@yahoo.com.
[2] author: a professor Department of Computer Science and Technology, School of Computer and Communication Engineering, University of Science and Technology Beijing (USTB), Beijing 10083, China; E-mail: zhswang@ustb.edu.cn
[3] author: assistant professor Department of Computer Science, College of Engineering and Information Technology, Al-Saeed University, Taiz, Yemen; E-mail: moh_alherwi@hotmail.com

conduct. Subject retention is vital for progress monitoring and generating informative data [1]. Stakeholder involvement bolsters clinical trial infrastructure. Current practices exhibit a concerning 80% lack of reproducibility, attributed to various factors, including human errors and ethical lapses. Inaccuracies in data collection and transcription greatly affect study data integrity, necessitating stricter supervisory protocols. Evaluating data integrity requires expertise in both the business domain and data modeling. This multifaceted effort ensures satisfactory data quality levels in clinical research [2]. Blockchain technology exhibits significant potential for elevating the quality and reproducibility of clinical studies. It offers secure data transmission within academic contexts, ensuring privacy for patient groups. Recently, there has been a surge in recognition of blockchain as a transformative technology, facilitating secure data exchange through a distributed ledger system. This relies on consensus mechanisms for parties with limited mutual trust. Blockchain's robust security and decentralized structure involve collaborative efforts of multiple participants in storing and recording data from various sources. Interconnected nodes enable seamless data transmission through linked blocks, and its transparency allows swift access without third-party involvement [3]. Smart contracts, situated on the blockchain, represent decentralized programs with functionalities such as autonomous execution of an application's logic, verification of predefined operational regulations, and assignment of obligations upon regulation fulfillment [4][5]. Compliance is integral across various aspects of clinical trials, encompassing reporting of animal trial findings, obtaining informed consent, and securing approvals from competent medical authorities. Adhering to Good Clinical Practice (GCP) and the International Conference on Harmonization (ICH) guidelines is vital for effective informed consent management. Recognizing the vulnerability of certain individuals is fundamental to understanding clinical research dynamics [1]. The intensity of clinical trial procedures is amplified by the multitude of trials conducted in diverse research laboratories. Thus, effective management of clinical trial conditions, emphasizing comprehensive and manipulation-resistant information management techniques, is crucial. This approach fosters holistic growth throughout the entire process. The advent of contemporary technology, particularly blockchain models, has significantly transformed information and communication systems in healthcare research. It provides a means to address deficiencies in information management within clinical trials, offering mitigation against fraudulent or mismanaged information [6].

2. Related Literature

Clinical trials are initiated when there exists a sound and logical rationale for how a novel testing or treatment modality may result in improved quality of care and treatment outcomes for patients. Before the commencement of clinical trials, tests and treatments are subjected to review in pre-clinical research settings. Human clinical trials are considered relevant for the study only after receiving the necessary authorization. Following this, before to the debut of the market, more examinations are carried out.

2.1. Stages of Clinical Trials

According to the criteria set out by the Good Clinical Practice (GCP), it is essential to conduct clinical trials in accordance with the prescribed therapies. Clinical trials are conducted to evaluate the safety of a certain medicine or treatment modality for

individuals. Broadly speaking, the stages involved in clinical trials pertaining to novel medicinal treatments include:

- Phase 0: involves a minimal dosage of a medication administered to a limited cohort of human subjects, aiming to understand pharmacokinetics, metabolism, and effects within the human body.
- Phase 1: centers on identifying a suitable drug-induced composition with minimal adverse effects, establishing safety thresholds. Phase II follows for a more specific patient group evaluation.
- Phase II: involves closely monitoring patients within a broader participant base, lacking comprehensive comparison with existing medications. Efficacious drugs proceed to Phase III.
- Phase III: entails comparing the novel drug with standard-of-care medications on a larger sample size for comprehensive analysis. Randomization ensures unbiased participant distribution. FDA approval precedes widespread usage.
- Phase IV: involves large-scale testing post-FDA approval, providing deeper insights into drug performance, effectiveness, and potential adverse effects, both short-term and long-term.

The phases of clinical trials are of paramount relevance in managing situations related to clinical research. The use of this approach facilitates the thorough evaluation of novel medications and therapies, ensuring their safety and efficacy prior to their approval for use among the general population. However, it is important to take into account the contextual circumstances in which historical records indicate instances of compromised clinical trials or manipulation of results at various stages. Any discrepancies in the approval process could potentially have significant consequences on the efficacy of a drug in meeting the specific needs of patients [7].

2.2. Conditions of Clinical Trials in Silos

The text highlights the extensive ongoing research in therapeutic approvals worldwide, with regulatory bodies like the FDA expediting approval rates. The focus of clinical research is to streamline the clinical development process, ensuring safety and compliance with regulations. While technology integration has enhanced operational efficiency, there remain fundamental gaps. Electronic Data Capture (EDC) software in the 1990s revolutionized data collection. Randomization and Supplies Management (RTSM) systems have since evolved, aiding biostatisticians and clinical supplies managers. A global standard for drug safety reporting was established, a pivotal functional milestone. However, the fragmented nature of existing solutions leads to overlapping and isolated systems, resulting in challenges like data redundancy and consistency issues. Within pharmaceutical research labs and CROs, electronic data capture (EDC) systems and research supply tracking management (RSTM) systems are crucial for data collection and supplies management. Additionally, the pharmaco-vigilance (PV) system monitors adverse events during clinical trials. Despite functional responsibilities in siloed systems, redundancy and inconsistency in generated reports persist. To enhance operational efficiency, there's a call to address integration challenges and implement a unified, cloud-based clinical trial management system. The integration of blockchain technologies is proposed as a significant advancement, emphasizing effective coordination of shared functionalities for all major stakeholders involved [8].

2.3. The Effect of Blockchain in Addressing Silos

The presence of data silos in information technology presents a persistent challenge, hindering seamless data sharing within organizations. Despite technological advancements, implementing an enterprise systems strategy remains a significant obstacle. These robust silos adversely affect organizational efficiency, influencing broader industrial ecosystems. Addressing this issue requires overcoming barriers in data politics, compliance, data architecture foresight, research culture, enterprise solutions, service agreements, standards, and underlying schemas. Distributing data among network participants enhances transparency and establishes a practical framework for collection, shifting data ownership to consumers. While valuable, blockchain technology necessitates careful consideration of stakeholder access amidst silo challenges. Rigorous examination is crucial, as not all information can be entirely public and alternative methods may lack enforceable requirements. Blockchain systems, with their primary focus on transactions, may have limitations in accommodating metadata conditions. The inflexible structure of schemas may impede adaptability. [9].

2.4. The Impact of Fragmented Processes and Silos on Clinical Trials

This study emphasizes the need for a collaborative framework to enhance clinical trial management within companies, supported by empirical evidence. The Veeva 2019 Unified Clinical Operations Survey highlights the industry's urgency to prioritize sharing capabilities among sponsors, contract research organizations (CROs), and stakeholders. Integration across multiple tiers is crucial for sustained, effective collaboration. Manual processes pose a significant risk of incomplete or incongruous information dissemination. Reluctance to share arises from prioritizing core responsibilities, including patient care, precise data collection, and regulatory compliance. Survey results indicate concerns about streamlining information exchange, eliminating manual procedures, enhancing collaboration, ensuring consistency, and bolstering oversight throughout trials. Integration and reporting processes face impediments due to existing gaps and silos in healthcare systems. The incorporation of blockchain technologies alongside a comprehensive system holds potential to mitigate these challenges. Given substantial stakeholder involvement and the extensive processing of numerous clinical trials, establishing a comprehensive system is imperative. This envisioned system aims to provide timely updates, support improved research conditions, streamline communication, and enhance reporting efficiency. Blockchain technology facilitates instantaneous data exchange and reinforces data governance, fostering a unified framework for information dissemination during clinical trials. [10].

3. Methodology Overview

The concept of blockchain may be defined as a digital framework that encompasses a shared and unchangeable ledger. This framework aims to guarantee a high degree of traceability, durability, and general effectiveness in managing data among various parties involved. The use of blockchain technology was first launched inside cryptocurrency systems. However, over time, this solution has been pragmatically adopted across several industrial sectors. In the healthcare industry, research findings consistently demonstrate

the considerable efficacy of using blockchain-based solutions, which can make a holistic difference to the system.

3.1. Blockchain Framework Architecture for the Healthcare Sector

The architecture of blockchain may be described as a decentralized system in contrast to the conventional centralized database. In this distributed system, data is exchanged in real-time across several computers or database systems referred to as "nodes." Each node inside the group has an identical copy of the transactional information [11]. The blocks are interconnected via the use of digital signatures represented by random letters in the form of a hash. This process results in the formation of a chain that represents a comprehensive record of transactions, hence enhancing resistance against tampering. Reference [12] have been provided one of the primary advantages of using blockchain technology is its emphasis on security. This is achieved by the use of sophisticated encryption techniques, which instill confidence, acceptance, and approval among participant nodes while dealing with data blocks [12]. This architectural design leads to increased decentralization of data systems, whereby a single source of information is shared across all nodes. Consequently, this fosters more confidence and unanimity among the participating nodes. In an alternate dimension, the blockchain system may be managed via two distinct approaches: public sharing, which allows for widespread access, and a private system that restricts access to a certain group of stakeholders [13]. The blockchain systems that may be managed inside the system include the use of many computers as an essential component of the network, the implementation of smart contracts among the involved parties, and the integration of a unified system [14]. Figure 1 illustrates the foundational architecture used as the framework for creating the suggested solution. This approach entails the conditional acceptance of blocks and the subsequent recording of transaction links to establish a chain. The primary benefit of implementing such a system is in its ability to provide a comprehensive verification framework, hence reducing discrepancies in reports and enhancing the general efficiency of reporting and communication among members.

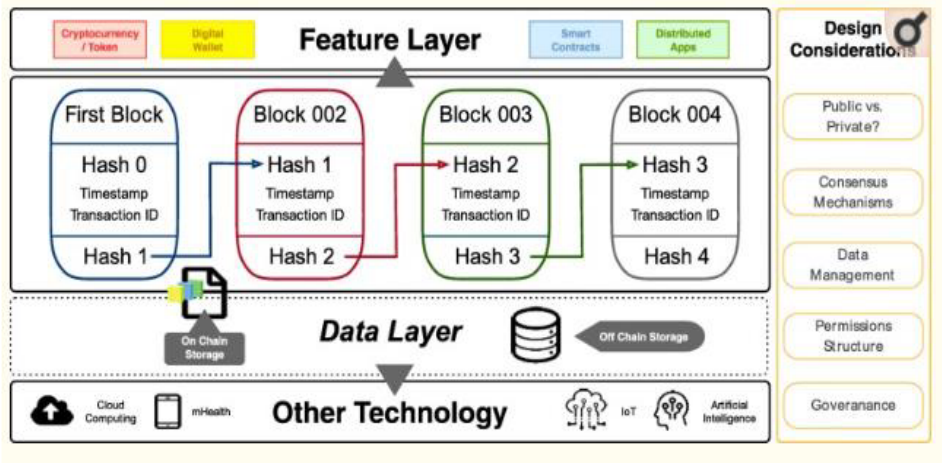

Figure 1: Blockchain Layer

3.2. Fundamentals of the Framework

The process flow governing the integration of blockchain-based systems within the context of clinical trials is delineated by a set of regulatory principles, as illustrated in Figure 2. These regulatory precepts are considered pragmatically advantageous in the context of deploying a blockchain-based solution for overseeing the entirety of clinical trial processes.

- Block chain Design Type: The proposed system incorporates a private blockchain framework, characterized by constrained participation and a clearly defined permission structure governing data dissemination.
- Data sharing and access: The management of data adheres to specific privacy and legal stipulations, including compliance with the Health Insurance Portability and Accountability Act (HIPAA) and the General Data Protection Regulation (GDPR). Determination regarding the scope of data sharing amongst participants and the storage locus of data whether on chain, off chain, or on a side-chain coupled with a prescribed permission model, is contingent upon the nodes.
- Block chain Governance: Central to the operational efficacy of the blockchain is its governance framework, constituting a pivotal facet. This encompasses the decision-making process involving the nodes, users, and peers. The delineation of the validation protocol for blocks and the establishment of a procedural framework for approvals are mandated to be determined by the consortium, in strict adherence to the regulatory guidelines delineated by the Food and Drug Administration (FDA) pertaining to the clinical trial milieu.
- System Enhancement: The administration of clinical trial solutions is advised to be executed through the application of smart contracts, a measure that serves to mitigate the potential for data tampering or manipulation amongst principal stakeholders. These smart contracts are pertinent to the validation of outcomes by duly authorized entities, particularly within the ambit of collaborations between pharmaceutical enterprises and Contract Research Organization (CRO) entities. Additionally, these contracts encompass the procedure for obtaining informed consent from individuals participating in human clinical investigations.

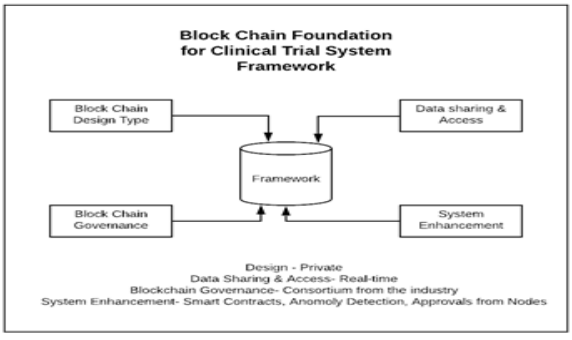

Figure 2: Proposed solution's blockchain framework.

3.3. Adopting the Blockchain Framework Method

Table 1 outlines the operational procedure and proposed architecture for deploying a blockchain framework in enterprises conducting clinical trials. The block architecture, as depicted in Figure 3, is fundamental for validating information within the blockchain system. For instance, the successful completion of the pre-clinical trial block is a prerequisite for forming the phase-1 grid. This grid represents a cohesive entity composed of a series of blocks, referred to as a superblock structure. In a hypothetical scenario, collaboration among stakeholders (CRO, sponsoring company, competent authority, and trial participants) could lead to the establishment of 20 blocks in Phase-1. These interconnected blocks form a comprehensive superblock grid. The creation of the second grid block is contingent upon the production of all requisite blocks in Phase-1, as regulated by the consortium overseeing the framework's structure and data collection.

Table 1: Architectural Framework of Blockchain for Entities Engaged in Clinical Trial Operations.

Details	A description
System Adapted	The integration of a clinical trial system based on blockchain technology.
Objective	To effectively tackle the problem of manipulation and inconsistencies in the given data and its reporting. Improve the reliability of the information architecture and data obtained from the system.
Expected Outcome	Improved and systematic methodology for the comprehensive documentation of clinical research, including pre-clinical trials as well as the five distinct phases of clinical trials. The implementation of real-time information exchange across authorities has the potential to enhance the overall result.
Network	A distributed peer-to-peer (P2P) network. A Peer-to-Peer network is a decentralized system in which data is distributed and shared among all stakeholders involved in the exchange of information.
Stakeholders	The pharmaceutical sector involves various entities like the FDA, CROs, medication manufacturers, and regulatory bodies. This system comprises multiple stakeholders acting as users, with their information systems functioning as nodes.
Approval Structure	The approval of the blocks relies on endorsement from key user networks like the FDA and local competent authorities. The approval framework for specific clinical trials may undergo periodic decision-making by the consortium.
Block	The topics discussed include compliance reports, the filing of research reports, the use of smart contracts, the dissemination of anomaly information, and the acquisition of informed permission from study participants.

The proposed block's grid established by including numerous integral blocks inside each grid unit. The process flow phases that are essential for the process may be seen in Figure 4.

- The transaction is recorded inside the block.
- The provided or compliant standard format of reporting shall include the transaction information as clinical trials information.
- Each block that is successfully added to the blockchain will possess a hash value, which will be included into subsequent blocks, therefore establishing the link chain.
- The signature of each block is predetermined and should not be modified after agreement is reached among the participating nodes.

- Once a clinical trial phase receives approval, each subsequent phase will be structured as a grid consisting of numerous subset blocks.
- In the subsequent grid, the preceding grid block will be transformed into the feed, while the data will be collected as a super grid block.

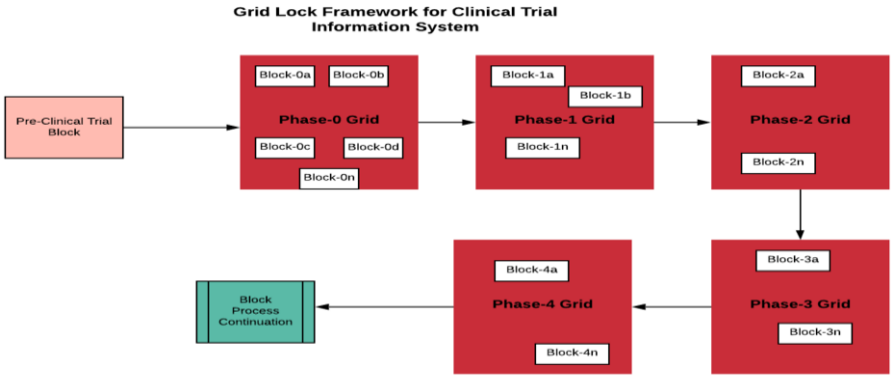

Figure 3: Architecture of Grid Block

- The ongoing use of corresponding sets of blocks in the creation process is expected to result in an enhancement of system development.
- The use of a ranking system will be employed to determine the requisite number of consensuses necessary to get permission for the effective connection of the block.

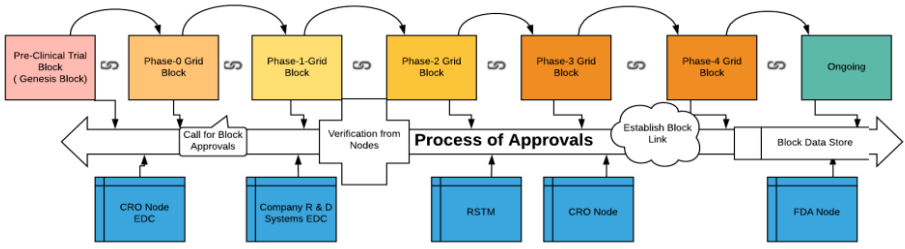

Figure 4: Comprehensive Framework Outlook

If any modifications are made to a single block inside the grid, it would result in a cascade effect on all blocks dispersed throughout the grids. As a result, any endeavor to engage in data tampering is rendered impracticable. Thus, with regard to the security paradigm of the system, it is evident that the model exhibits a heightened degree of resilience, predicated on the specific category of block and the requisite number of consensuses for its approval.

4. Conclusion

In conclusion, the rise in clinical trials and research volume, along with pending approvals across various organizations, emphasizes the need for an improved collaborative information and transaction processing system. These systems are pivotal

for governance and consistency in clinical trial processes. Current corporate models exhibit fragmentation with isolated systems, leading to redundant efforts and data. Operating in isolated compartments further exacerbates inconsistencies. Considering the potential of blockchain solutions, this paper introduces a novel framework for clinical trials in healthcare based on a grid structure and blocks, aimed at enhancing the auditing process. The study suggests future research avenues, including consensus protocols, block size, and interval impacts on blockchain performance, as well as integrating the framework into existing clinical trial systems for practicality assessment in real-world scenarios.

References

[1] McCoy C. Writing Clinical Research Protocols: Ethical Considerations. Clinical Laboratory Science. 2006;19(1):60.
[2] Hang, Lei, BumHwi Kim, KyuHyung Kim, and DoHyeun Kim. "A permissioned blockchain-based clinical trial service platform to improve trial data transparency." BioMed research international 2021 (2021).
[3] Golosova, Julija, and Andrejs Romanovs. "The advantages and disadvantages of the blockchain technology." In 2018 IEEE 6th workshop on advances in information, electronic and electrical engineering (AIEEE), pp. 1-6. IEEE, 2018.
[4] SZABO, Nick. "The Idea of Smart Contracts, 1997, disponível em http://www. fon.hum.uva.nl/rob/Courses/InformationInSpeech/CDROM/Literature." LOTwinterschool2006/szabo. best. vwh. net/smart_contracts_idea. html, acessado em 1º/3 (2019).
[5] Kirli, Desen, Benoit Couraud, Valentin Robu, Marcelo Salgado-Bravo, Sonam Norbu, Merlinda Andoni, Ioannis Antonopoulos, Matias Negrete-Pincetic, David Flynn, and Aristides Kiprakis. "Smart contracts in energy systems: A systematic review of fundamental approaches and implementations." Renewable and Sustainable Energy Reviews 158 (2022): 112013.
[6] Abdu, Nail Adeeb Ali, and Zhaoshun Wang. "Blockchain for Healthcare Sector-Analytical Review." In IOP Conference Series: Materials Science and Engineering, vol. 1110, no. 1, p. 012001. IOP Publishing, 2021.
[7] https://www.nccn.org/patients/resources/clinical_trials/phases.aspx.
[8] http://www.clinicalinformaticsnews.com/2018/03/05/eliminating-silos-dismantling-frankenstein-clinical-rnd.aspx
[9] https://www.dataversity.net/can-blockchain-eliminate-the-data-silo/#
[10] https://www.mddionline.com/survey-says-fragmented-processes-and-system-silos-are-hurting-clinical-trials
[11] Yli-Huumo J, Ko D, Choi S, Park S, Smolander K. Where is current research on blockchain technology?—a systematic review. PloS one. 2016 Oct 3;11(10):e0163477.
[12] Boulos, Maged N. Kamel, James T. Wilson, and Kevin A. Clauson. "Geospatial blockchain: promises, challenges, and scenarios in health and healthcare." (2018): 25.
[13] Kuo TT, Kim HE, Ohno-Machado L. Blockchain distributed ledger technologies for biomedical and health care applications. Journal of the American Medical Informatics Association. 2017 Nov 1;24(6):1211-20.
[14] Park JS, Youn TY, Kim HB, Rhee KH, Shin SU. Smart contract-based review system for an IoT data marketplace. Sensors. 2018 Oct;18(10):3577.

Fuzzy Systems and Data Mining IX
A.J. Tallón-Ballesteros and R. Beltrán-Barba (Eds.)

doi:10.3233/FAIA231095

Portable Brainwave Controlled Robotic Dog for Therapy

Chi-Yat Lau [a] , Man-Ching Yuen [b,1] , Chi-Wai Yung [b] , JiaJie Liang [a], Wing-Chi Mak [a], Ho-Yeung Chan [a], Fong-Yu Ha [a], Zheng-Tan Ng [a] and Hong-San Wong [c]
[a] *Department of Information Technology, Vocational Training Council, China*
[b] *Department of Applied Data Science, Hong Kong Shue Yan University, China*
[c] *R2C2 Limited, China*

Abstract. With the revolution of technology, robots are an inevitable trend as robots can do what humans do more efficiently and at a lower cost. However, humans have retained labor force dominance because robots have suffered from immature software and hardware. To solve the problem of immatureness, we exploit a platform that can integrate the systems of multi-robots and strives to let all the users control their own robots through the platform. Our goal is to develop a ROS (Robot Operating System) package that can incorporate a small robot dog which allows the robot dog to respond to our industrial partner, R2C2, webapp commands and in addition to using brain waves to control the walking path. Our platform provides an intuitive and accessible interface for users to control the robot's movements and behavior, increasing the robot' s versatility and usage for applications such as therapy, entertainment, education, and research. Overall, our project represents an exciting step forward in the field of robotics, and we are excited to continue exploring new ways to improve the interaction between humans and machines.

Keywords. EEG, brain wave control, robot

1. Introduction

1.1. Background

In an era where technology is rapidly advancing, robots have emerged as a powerful tool that can help humans in numerous ways. Robots are used in different applications such as teaching and learning [1]. With this in mind, our research project aims to provide a comprehensive platform that unites the control of robots, making it easier for users to control and interact with these machines. Our project is being developed in collaboration with our industrial partner, R2C2, who has provided us with a website platform that helps us integrate our work with their platform. R2C2 is a Hong Kong-based robotic startup that focuses on construction and agriculture automation.

To explore new possibilities for robot control, we use brainwave control, which will enable us to control the robot using our thoughts. To achieve this, we use an EEG (Electroencephalography) [2] sensor, which will pick up signals from our brain and translate them into commands that the robot dog can understand. We believe that this

[1] Corresponding Author, Man-Ching YUEN, Department of Applied Data Science. Hong Kong Shue Yan University, Hong Kong, China; E-mail: mcyuen@hksyu.edu.

new level of control will not only make it easier for users to operate the robot dog but also opens new possibilities for how we interact with machines. By tapping into our brain's natural abilities, we can create a more intuitive and seamless way of controlling robots, making them more accessible to a wider range of users.

1.2. Our Contribution

The project aims to develop a comprehensive and functional ROS (Robot Operating System) package for a small robot dog which can be controlled by human brain waves. Our contribution includes:

- This package enables the robot dog to respond to commands from the R2C2 web application and control its walking path using brain waves. The package is designed with a clear and detailed software architecture that includes communication protocols and control mechanisms to ensure the robot operates effectively to provide users with a versatile and easy-to-use platform to control their robot.
- We conduct extensive testing and validation to ensure that the ROS package functions correctly, meets all the required specifications, and is robust and reliable.
- We provide clear documentation and user guides to enable users to easily install, configure, and use the ROS package, reducing the complexity of the startup process for the robot.

The organization of this paper is as follows. Section 2 describes the background and related work. Section 3 presents the methodology used in our proposed system. Section 4 shows the solution design. Section 5 presents the system testing and performance analysis. Section 6 draws out the conclusion.

2. Background and Related Works

2.1. Robot Operating System (ROS)

The original aim of creating the Robot Operating System (ROS) was to develop a stable and versatile robotics software platform. ROS is an open-source meta-operating system that provides core operating system services such as message-passing between processes and package management. It already includes a wide range of drivers, state-of-the-art algorithms, and robust developer tools. ROS simplifies the process of building stable and complex robot behaviors on various robotic platforms by providing a set of tools, libraries, and conventions. The ROS Filesystem can streamline the project's build process while allowing for flexibility in managing dependencies [3]. Our robotics project can benefit from ROS's comprehensive features and capabilities.

Figure 1 shows the ROS conversation. In ROS, topics serve as named communication channels that enable nodes to exchange messages. They employ anonymous publish/subscribe semantics, which decouples the generation of information from its consumption. Topics are designed for unidirectional, streaming communication, and are not suitable for nodes that require bidirectional communication, such as remote procedure calls - in such cases, services should be used instead. Our project utilizes topics

to facilitate communication between the robot and the platform, allowing the robot to make calls and receive responses that inform its actions.

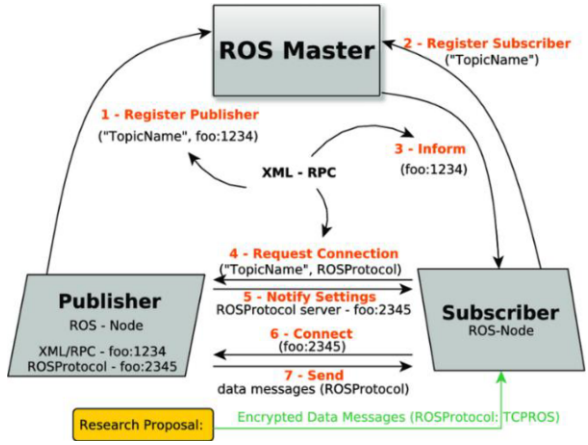

Figure 1. ROS Conversation

2.2. Electroencephalography (EEG)

Electroencephalography (EEG) [2] is a technique used to map the spontaneous electrical activity of the brain by measuring the electrical signals generated by pyramidal neurons in the neocortex and allocortex. Figure 2 shows the EEG concept [2]. This method typically involves placing noninvasive EEG electrodes along the scalp, often using the International 10-20 system or similar variations.

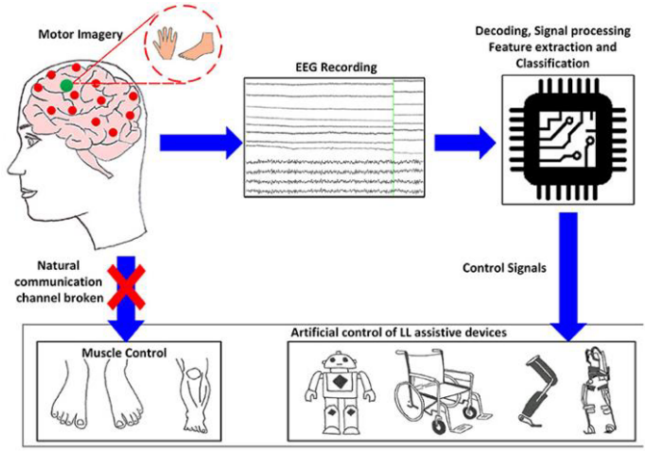

Figure 2. the EEG concept [2]

EEG recordings are commonly interpreted either visually by examining the traces or through quantitative EEG analysis. This technique is widely used in clinical settings for diagnosing and monitoring neurological conditions. EEG is a noninvasive procedure that provides valuable insight into the electrical activity of the brain, making it a valuable

tool for understanding brain function and for diagnosing and treating neurological disorders.

EEG data analysis is a unique approach to studying cognitive processes that has diverse applications. Medical practitioners can use EEG data analysis to make accurate diagnoses, while researchers can explore how brain processes shape human behavior.

2.3. Related Work

There are some existing works on studying EEG and robot interaction, such as [4]. However, these systems did not have an easy-to-use interface, so it can only be used for demonstration in the laboratory. In this project, we develop an easy-to-use interface and our system is a portable solution, so it is can be used anywhere.

3. Methodologies used in our Proposed System

In the project, we develop a comprehensive and functional ROS (Robot Operating System) package for a small robot dog which can be controlled by human brain waves. In our Robot Operating System (ROS) package, we add Web ROS Proxy and Minipupper Control to receive and process information from the Web App.

3.1. Web ROS Proxy

We use Web ROS Proxy in Minipupper to receive and parse the data from the Web App via socketio. After receiving the data from socketio, trigger_event will split the data. This is to make it easier to distinguish between different message types, because the msg type must be the same between two topics to communicate with each other. This allows Minipupper control to send the data to the corresponding topics smoothly.

3.2. Minipupper Control

The Minipupper control is mainly responsible for how these messages should be handled in the catkin workshop after receiving the Web ROS Proxy message. As the request is received, the topic handler will call out the functions that are related and send data to make movement.

3.3. Minipupper Bringup

Based on the open source project CHAMP, the Bringup package is mainly responsible for the operation of the basic functions of Minipupper. It allows Python programs to connect to Minipupper's hardware for deployment. This is the main package that controls the four motors and twelve joints of Minipupper, and it handles the operation of the four motors by subscribing to the relevant topic message and calling the callback.

3.4. Systemd Module

We use the *Systemd* module to create different services for the robot dog. It enables the robot dog to automatically listen to multiple topics at the same time when it is booted,

and to handle multiple programs at the same time. Eventually, Minipupper will be able to initialize the base package and control it directly from the Web App when booting Ubuntu.

3.5. Camera

To remotely control a robot dog, you typically need to have access to information about the robot's current environment, such as its location, orientation, and any obstacles that may be present. This information can be obtained through various sensors and systems that are built into the robot. In order to remote control the robot dog, we also need to know the current environment of the robot dog. In this case, we are equipped with cameras. Cameras are a valuable tool for remote control of robotic dogs because they provide a visual representation of the robot's environment. Moreover, cameras can provide real-time video feedback.

3.6. EEG: Convert data into digital data for data analysis by using machine learning methods

To convert EEG data into digital data for data analysis, we use several libraries, including ssqueezepy, timm, pytorch-lightning, mne and pylsl.

In the following, we describe the steps of EEG data signal processing.

Step 1: Read CSV Data.

- Figure 3 shows the international 10-20 system [5]. Extract the natural, forward and turn left EEG data from the emotiv. Read three CSV files into three separate data frames named ‘df0’, ‘df1’, and ‘df2’. After a series of data concatenation operations, a new data frame is generated.

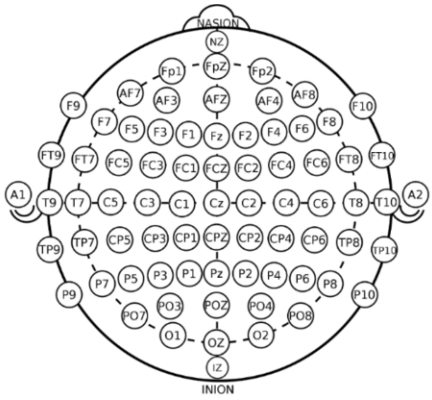

Figure 3. International 10-20 system [5]

Step 2: Convert each data from CSV file to mne format.

- We segregate the subject based on the ‘group_id’ and ‘subject_id’ so we create a group by object which creates a group on each ‘group_id’ and ‘subject_id’. We pass the ‘grp1’ variable to the ‘convertDF2MNE’ function, convert the data

frame to mne and check the shape. There are 97 epochs, 5 channels and each epoch has a length of 384.

Step 3: Convert signal to image.

- We pass 5 channels and 384 sequence length data to the continuous wavelet transform function. We use a function called 'imshow' from 'ssqueezepy' to plot the scale gram image. We can see our scalogram image in Figure 4.

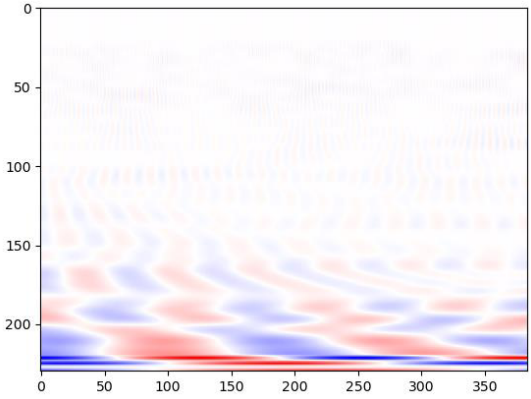

Figure 4. Convert signal to image

Step 4: Iterate all groups one by one.

- After computing the wavelet transform, the next step is to save the resulting images for each trial in a separate directory. We use a loop that iterates through each group of MNE data and each trial within that group. For each trial, the wavelet transform is computed, converted to an absolute value, and saved as a numpy array in a directory specific to the corresponding subject and trial.

Step 5: Train a pre-trained ResNet model.

- We define a PyTorch Dataset class called 'DataReader' for efficiently loading and processing the data during training and validation. Since we can't pass all of the images at once. We preprocessed the images and randomly selected images for the flip operation.
- First, we split the dataset into training and validation sets using the 'random_split' function from the torch.utils.data module. Then, we initialize the 'OurModel' class to create the neural network model. Next, we initialize the 'Trainer' class with various parameters that determine how the model will be trained, such as the maximum number of epochs, the learning rate, and the precision of the computations. The 'Trainer' class also specifies that the training will be done on a GPU if one is available. Finally, the fit method is called on the 'Trainer' object to train the model.

4. Solution Design

In this section, we present the design of our solution – a ROS (Robot Operating System) package that can incorporate a small robot dog which allows the robot dog to respond to

our industrial partner, R2C2, webapp commands and in addition to using brain waves to control the walking path.

4.1. System Architecture

In Figure 5, our system is mainly divided into three layers by using socket.io and the ROS publisher passing through the request and response. By using the webapp or the EEG EMOTIV data and signal will be sent to the Web ROS Proxy inside the Minipupper ROS through the socket.io and the data and signal will be processed by the Web ROS Proxy and publish to the Minipupper file system catkin and execute by the Minipupper control package and the Minipupper control package call out and send data to the champ_controller and achieve the movement. Table 1 shows the hardware requirements of our system. Table 2 shows the software requirements of our system.

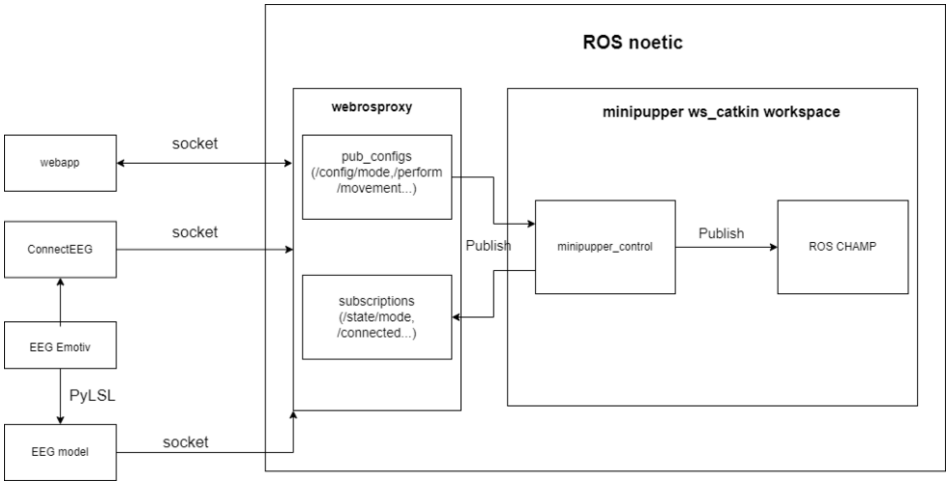

Figure 5. Architecture of our system (3-layer design)

Table 1. Hardware Requirements

	Required Hardware	Requirement
1	Robot Dog	A ROS based system robot
2	Raspberry Pi	SD card with Ubuntu 20.04 and ROS installed
3	EEG Sensor	A sensor to detect our brainwaves
4	Computer	A computer that can run MacOS/Windows.

Table 2. Software Requirements

Component	Required Software
Computer	Ubuntu 20.04
	Ros noetic
	Python 3.6
Raspberry Pi	Ubuntu 20.04
	Ros noetic
	R2C2 Web App
	Web Ros Proxy
	Cortex API

4.2. Testing Module

Our testing is based on the below module:

Minipupper

- Minipupper is a dog-shaped robot sidekick for learning and experimenting with robotics, exploring advanced functions of a dynamic robot. Figure 6 shows Mangdang Minipupper.

EEG sensor

- To implement the EEG control a EEG controller installed with the API is essential. Additionally, the laptop equipped with Bluetooth is used to control EEG API to record EEG samples.
- The chosen EEG sensor is shown in Figure 7.
    - Product: Emotiv Insight
    - Channel: 5 channels
    - Shape: wireless headset

Figure 6. Minipupper

Figure 7. Emotiv Insight

4.3. Target Users

The EEG robot dog is a relatively new technology, and its target user can vary depending on the specific application and intended use case. However, in general, the EEG robot dog is often designed and marketed as a therapeutic tool for individuals with autism, ADHD, or other neurodevelopmental disorders. The robot dog is equipped with an EEG sensor that can detect brain waves. When a patient interacts with the robot dog, the doctor will go to observe the patient's brain waves, and then process them through machine learning algorithms to interpret the user's emotional and cognitive state. This feedback can be used to provide personalized therapeutic interventions, such as calming exercises or social skills training, to help improve the user's overall well-being and quality of life. Additionally, the robot dog can also be used as a research tool in neuroscience and psychology to better understand the brain's response to different stimuli.

4.4. Limitations

There are a number of limitations in this project which are shown as follows:

- *Battery Life*: We find that if we add all the plugins to the robot the default battery of the Minipupper is not enough to keep moving the robot for 30 minutes, the motor will not have enough power to push up the Minipupper. It is hard to test Minipupper

movements. We are going to try to link to another battery to increase the battery life. We also need to decide on all the plugins we need for our project.

- *Sample data*: We cannot find any sample data from the internet, so we need to enter the 70% training and 30% testing split to train our machine learning.
- *Low Sensitivity*: The EEG boasts only produce 5 channels of EEG sensor which is not enough for observing the changes of the brain waves, so the sensitivity of the boasts is lower than ideal. Due to the low sensitivity, 3 directions can only be made and detected successfully.

5. System Testing and Performance Evaluation

We successfully establish a connection between the Minipupper and the R2C2 webapp. Next, we collect data on the movements and behaviors of the Minipupper and use the collected data for model training. Finally, we integrate an EEG sensor with the Mini Pupper and R2C2 webapp, develop software to interpret the signals from the EEG sensor and use the interpreted signals to control the movements of the Mini Pupper through the R2C2 webapp.

Figure 8 and Figure 9 show the system testing result. The test set accuracy was **86%**, which is a decent performance. The classification report shows precision, recall, f1-score, and support for each class. The macro-average F1-score is **0.79**, indicating that the model has a fair ability to classify three classes.

	precision	recall	f1-score	support
0	0.78	0.44	0.56	16
1	1.00	0.93	0.96	42
2	0.76	1.00	0.86	31
accuracy			0.87	89
macro avg	0.84	0.79	0.79	89
weighted avg	0.88	0.87	0.86	89

sklearn 0.8651685393258427

Figure 8. Test accuracy

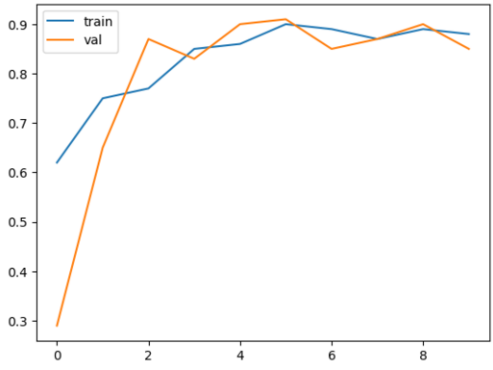

Figure 9. Test model image

6. Conclusion

Our project provides a significant insight to the future of robotic design in commercial products and research topics. The outcome of this project is the successful development and implementation of a ROS package that enables a small robot dog to respond to commands from the R2C2 web application and control its walking path using brain waves. This will provide users with a versatile and easy-to-use platform to control their robot, reducing the complexity of the startup process and increasing the robot's usage and versatility. Specifically, the expected outcomes are: (1) The ROS package undergoes a robust and reliable implementation process, including extensive testing and validation to ensure it meets all necessary specifications and functions effectively under various conditions and scenarios. The implementation process ensures that the package is user-friendly and easily accessible. (2) Clear and comprehensive documentation and user guides will be provided to assist users in the installation, configuration, and use of the ROS package. This documentation will reduce the complexity of the startup process for the robot and enable users to easily operate the robot according to their needs.

Overall, successful completion of this project results in a versatile and user-friendly platform for controlling a small robot dog. This platform provides an intuitive and accessible interface for users to control the robot's movements and behavior, increasing the robot' s versatility and usage for applications such as entertainment, education, and research. We use Minipupper for testing the connection, in the future we will be transporting our coding to other robots to achieve robot mission collaboration. Moreover, we will conduct more experiments for comparison with state-of-the-art fusion techniques.

Acknowledgements

This research was in part supported by grants from the Research Grants Council of the Hong Kong Special Administrative Region, China (Project No. UGC/FDS15/E02/20 and UGC/FDS15/E01/21).

References

[1] Yuen M. C., Chan K. K., Li K. S. (2021). Mobile App Controlled Modular Combat Robot for STEM Education. Proceedings of 2021 13th International Conference on Communication Systems & Networks (COMSNETS), Workshop on Machine Intelligence in Networked Data and Systems (MINDS), IEEE CS Press, Webinar, January 2021.

[2] Tariq Madiha, Trivailo Pavel M., Simic Milan (2018). EEG-Based BCI Control Schemes for Lower-Limb Assistive-Robots. Frontiers in Human Neuroscience 12.

[3] Anggraeni, Pipit. (2019). Decentralized leader-follower consensus for multiple cooperative robots under temporal constraints.

[4] Mao, X., Li, M., Li, W., Niu, L., Xian, B., Zeng, M., & Chen, G. (2017). Progress in EEG-based brain robot interaction systems. Computational intelligence and neuroscience, 2017.

[5] The International 10-20 system. https://zh-yue.wikipedia.org/wiki/10-20_%E7%B3%BB%E7%B5%B1

Fuzzy Systems and Data Mining IX
A.J. Tallón-Ballesteros and R. Beltrán-Barba (Eds.)

doi:10.3233/FAIA231096

Game Recommendation System

Man-Ching Yuen [a,1], Chi-Wai Yung [a], Wing-Fat Cheng [a],
Hon-Pong Tsang [b], Chi-Ho Kwan [b], Chun-Lok Chan [b], Po-Yi Li [b]
[a] *Department of Information Technology, Vocational Training Council, China*
[b] *Department of Applied Data Science, Hong Kong Shue Yan University, China*

Abstract. Recommendation systems are widely adopted in many areas to provide better services to customers. As there are many games stored in online games platforms, people may be confused when choosing or buying the game that is suitable for them. Many game platforms would like to have a game recommendation system, so that it can automatically recommend the right games to their customers. However, there are a lot of difficulties in developing game recommendation systems. First, it is difficult to collect and organize data on customers' behavior. Second, the user interface needs to be easier to use for customers, such as the charts displayed that customers are interested in. In this paper, we have developed a games recommender system with complete functional recommending features. By using machine learning techniques and applying data visualization on our system, we build a recommendation system that can showcase flexible outcomes with the same element as the user input, which can give the user more choice when finding the games they want.

Keywords. Recommendation system, game, machine learning, web scraping and data visualization.

1. Introduction

Nowadays, there are loads of games platforms such as PS4 store, Steam, Xbox etc. However, not all the games platforms have a built-in recommender system to help users to find games they desire [1, 2, 3, 4, 5]. It is because some games platforms do not have enough data visualization to show the current trend of games clearly. Furthermore, some people think that most of the existing recommender systems can not satisfy the users. They may face difficulties when trying to find a suitable game to play using the existing recommender systems.

Based on these reasons, we want to build a recommendation system to users who want to play games which suit their taste. We will investigate the relationship between each of the categories and the analytics of the trend of the selected game platform. So, we can find out the most popular games for each type of genre. By entering different elements of the game that the user is interested in, the recommender system can list out the game that the user may prefer.

Our goal of this project is trying to build a recommender system that is uniquely different from other recommender systems. We hope to improve the accuracy, efficiency to about 10% better than the existing recommender system. And to make our system

[1] Corresponding Author, Man-Ching YUEN, Department of Applied Data Science. Hong Kong Shue Yan University, Hong Kong, China; E-mail: mcyuen@hksyu.edu.

uniquely different from the other existing work, we are trying to develop a system to have unique features like showing trends by using data visualization and can showcase flexible outcomes with the same element as the user input rather than the other system to have the same output every time. We may consider choosing one of the online game platforms for datasets. We will scrap the data including the basic information, categories and system requirements to develop our game recommendation system.

The organization of this paper is as follows. Section 2 presents the related work. Section 3 describes our game recommendation system with the data analytical framework. Section 4 shows the experimental result analysis. Section 5 draws out the conclusion.

2. Related Work

There are a number of existing works. Content-based filtering and collaborative filtering are usually used for recommendation systems [6, 7, 8]. In the following, we describe some existing works and highlight the improvement in our game recommendation system.

1) *Games Finder* - The website is one of the databases of online games (Games Finder) [9]. You can click the game icon. Then, it will display other similar games. However, it does not have any data visualization. You can input your favorite game on the website. Our model also has the function to get recommendations which use content-based filtering. Moreover, we have designed a dashboard to show distribution of reviews in different genres.
2) *Quantic Foundry* - By entering 3 game titles, this website will show a list of games that are similar with those you enter, and the platform you can buy the game from [10]. However, the input items are quite simple and without data visualization. Our system adopts data visualization techniques to enhance customer experiences.
3) *Deep Visual Semantic Multimedia Recommendation Systems (D_VSMR)* –The proposed approach employs content-based techniques to expand users' profiles based on the visual content of games [11]. However, the features extracted by the system might not be equally representative for all users.
4) *Social-aware Contextualized Graph Neural Recommender System (SCGRec)* – It proposed using user personalized data (such as social connections) to improve the game recommendation [12]. However, due to the high complexity, frequent update on social media data in the system is not possible.

3. Our System

3.1. Overview

Our first step is to apply web scraping on STEAM (A video game digital distribution platform), the scraped data will be stored in a .JSON file. Then, the data will be cleaned and used for data visualization. After that, content-based filtering and collaborative filtering may be used for designing the recommendation system. Finally, the Flask application will be used for demonstration of our final prototype.

3.2. System Architecture

Figure 1 shows the system architecture of our game recommendation system.

1. Build a model with data
   - *MongoDB Database* - MongoDB is a source-available cross-platform document-oriented database program. Classified as a NoSQL database program, MongoDB uses JSON-like documents with optional schemas. MongoDB is developed by MongoDB Inc. and licensed under the Server-Side Public License (SSPL).
   - *Machine Learning Algorithms (Content-based filtering)* – We use both TF-IDF and Cosine similarity in our system. We use Python to implement our system.
2. UI Client
   - *Web Application (Flask)* - We use Flask API to run our recommendation system, Data Visualization and the basic function of a client.
   - *Server*

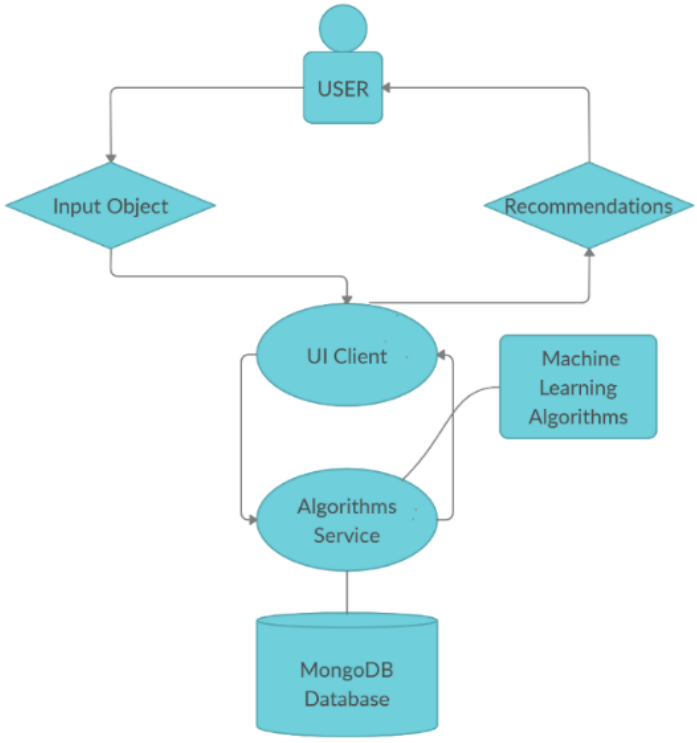

Figure 1. The system architecture of our game recommendation system.

3.3. Data Collection and Preparation

To acquiring data, we have created 3 programs to apply web scraping on the STEAM platform to acquire data into datasets. Three of them are URLs of the game, game information and comments from some games.

1. *Scraping all the URLs of the video games*. The input and the output are as shown in Figures 2 and 3. Figure 2 shows the list of games on the webpage we want to scrap. We need to scroll the page with "Page Down" button many times if we want to see all the games. The code in Figure 3 shows we used the web driver from selenium to scroll the page. Selenium is used mostly in this program. After that, we need to find the URLs of all the games by XPath and store them into a list.

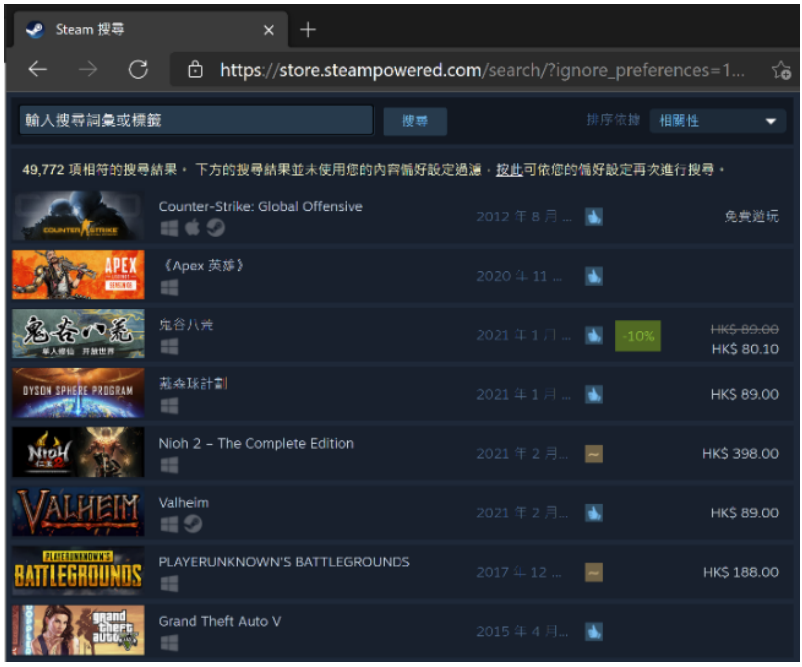

Figure 2. The input of scraping all the URLs of the video games.

```
    for x in tqdm(range(20000)):    # for loop is created to scroll to the bottom of the page
        driver.execute_script("window.scrollBy(0,document.body.scrollHeight)")    # Scrolling the page by 20000 times

  0%|          | 61/20000 [00:08<01:10, 283.65it/s]
The Webdriver is scrolling ...
100%|          | 20000/20000 [46:54<00:00,  7.11it/s]
```

Figure 3. The output of scraping all the URLs of the video games.

2. *Scraping the information of the games*. By reading the .pkl file, which have been mentioned above, we have to scrap the information of the game that we need. Figure 4 shows a website of one of the games. Useful data for content-based filtering have been scraped such as Game Title, Genre, User Tags, Overview and so on. A single game data will be stored in a dictionary and all the data we acquire will be stored into

"game_data" which is a list. All of the data is exported into a .JSON file (output_2F.JSON). To speed up the process of scraping the game information, we found that we can scrap the information by running eight programs at the same time. This has benefits to update our datasets more frequently.

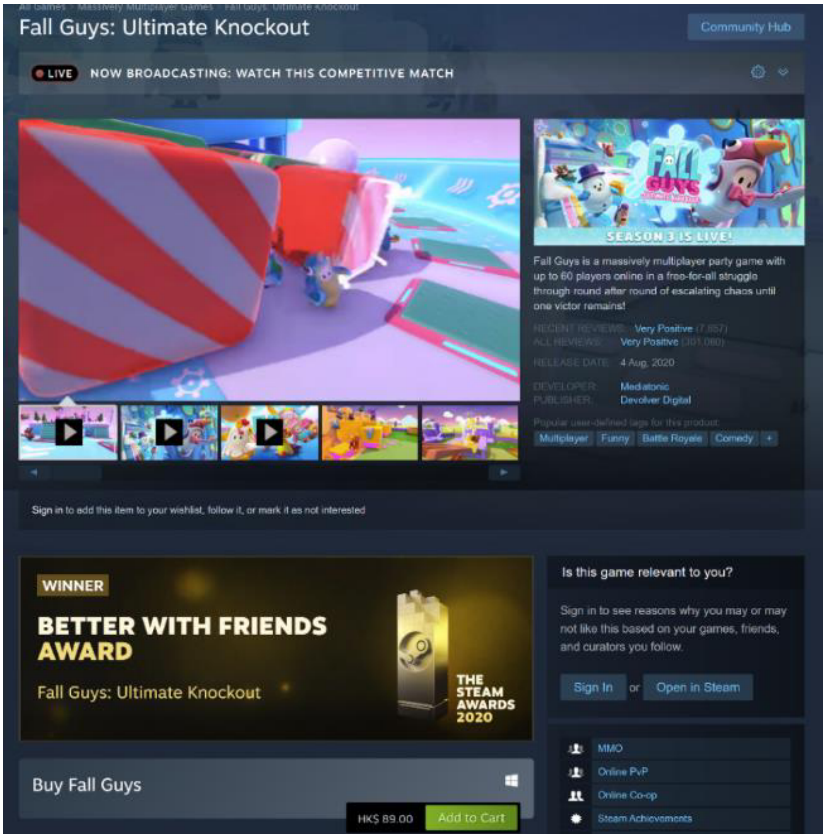

Figure 4: A website of one of the games with useful data for content-based filtering.

3. *Scraping the comments of the games*. The scraped data in this part is for building the recommendation system using content-based filtering. We are not using collaborative filtering because we found out that the scrapping time will increase sharply when scraping loads the comments in each game. If we scrap less comments in each game, it is hard to find the games which have positive comments from the same player. It is because the STEAM platform has many players. Figure 5 shows one of the websites about the game's comments. Three types of data are scraped, the id of the game, users' id which is highlighted in yellow color and the comments which are highlighted in green color. By getting the game id from output_1F.pkl, we have to change all the URLs to the comments page. Like scraping the URLs of the game, we need to scroll down the page to try to scrap the greatest number of comments. A JSON file will be created which stores the scraped comments.

4. *Data Preparation*. Some of the values will be modified during web scraping. For example, to make the analysis process easier, '()' and ',' are replaced by empty space so that the data type of this information is integer.

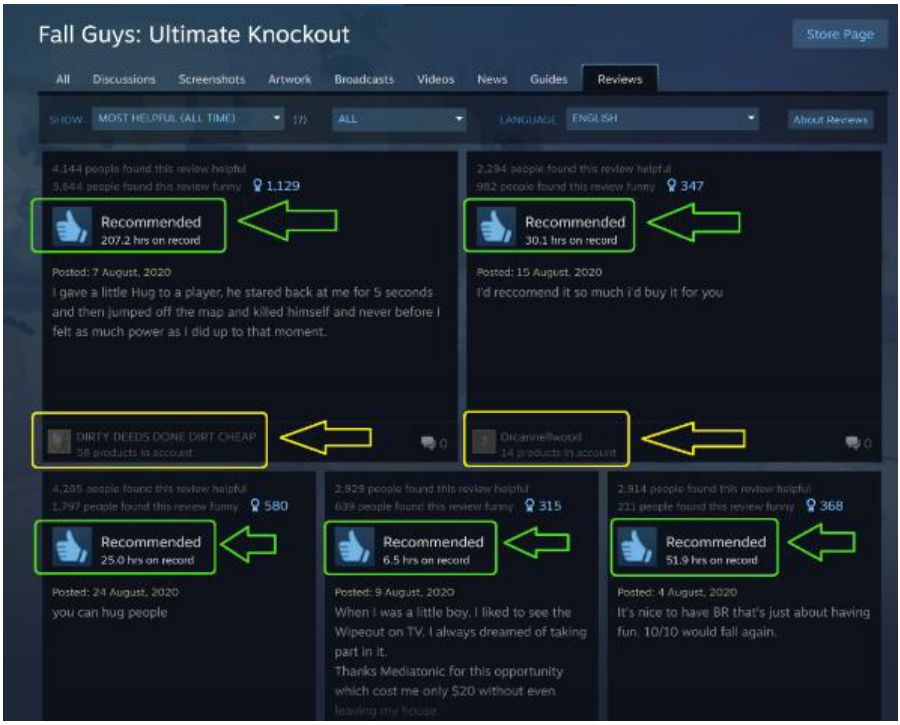

Figure 5. One of the websites about the game's comments.

3.4. Data Modelling / Algorithm

In this model, we decided not to split data into training parts and testing. As the content-based filtering is calculating their similar value by using matrix. We use **cosine similarity** as a model to build the game recommender system with Python. **cosine similarity** measures the similarity between two vectors of an inner product space. It is measured by the cosine of the angle between two vectors and determines whether two vectors are pointing in roughly the same direction.

```
from sklearn.metrics.pairwise import cosine_similarity
cosine_sim = cosine_similarity(tfidf_matrix, tfidf_matrix)
```

Compute **Term Frequency-Inverse Document Frequency** (TF-IDF) vectors for each document. TF-IDF is the frequency of a word occurring in a document, down-weighted by the number of documents in which it occurs. This is done to reduce the

importance of words that frequently occur in plot overviews and, therefore, their significance in computing the final similarity score.

```
from sklearn.feature_extraction.text import TfidfVectorizer
```

```
tfidf_matrix = tfidf.fit_transform(df['ABOUT THE GAME'])
# Construct the required TF-IDF matrix by fitting and transforming the data
```

3.5. Data Presentation

Figure 6 shows the sunburst chart with no selection input. Figure 7 shows the sunburst chart with the 'Very Positive' cell in 'Recent Reviews' path selected. Figure 8 shows the sunburst chart with the 'Action' cell in 'Genre' path selected AFTER 'Very Positive' cell in 'Recent Reviews' path was selected.

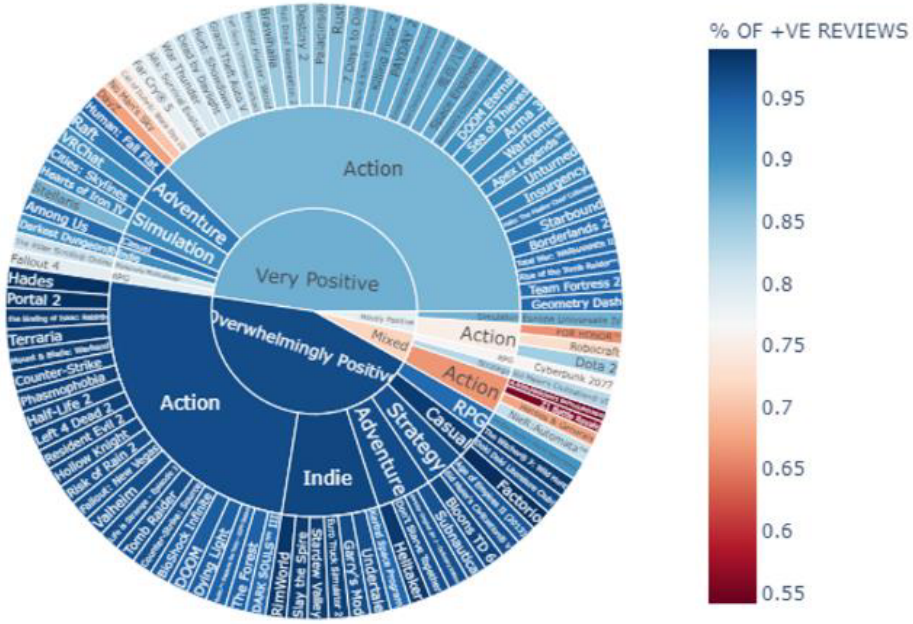

Figure 6. The sunburst chart with no selection inputted.

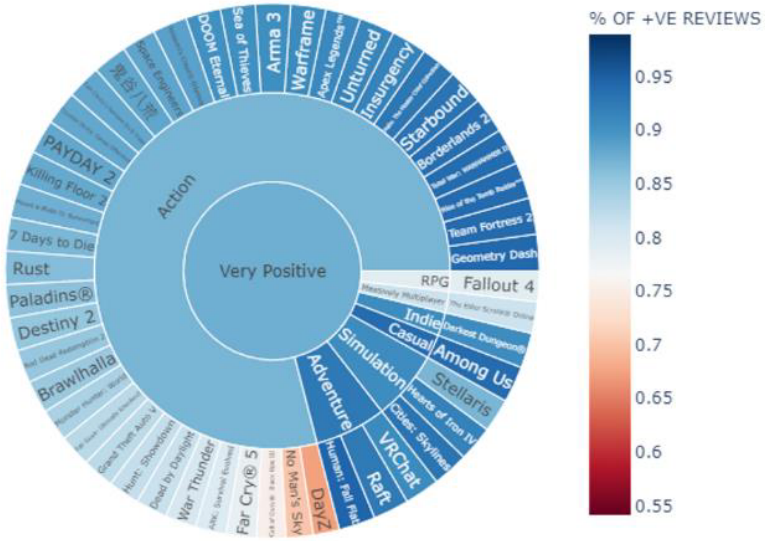

Figure 7. The sunburst chart with the 'Very Positive' cell in 'Recent Reviews' path selected.

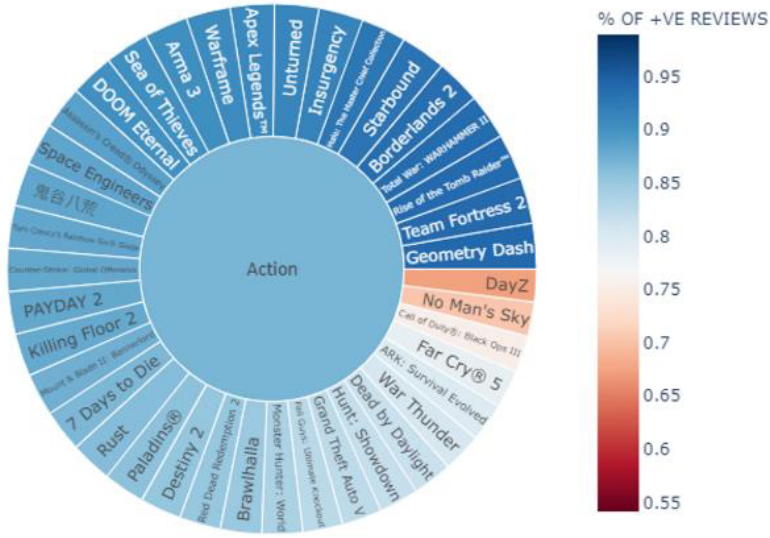

Figure 8. The sunburst chart with the 'Action' cell in 'Genre' path selected AFTER 'Very Positive' cell in 'Recent Reviews' path was selected.

We design and develop interactive dashboards by using Python and Tableau. Figure 9 shows the dashboard that is built with four basic graphs with the data we obtained. Figure 10 shows the dashboard with one cell selected. Bottom left shows the top-rated game which matches the element selected in that graph. Figure 11 shows the dashboard with two cells selected. Bottom left shows the top-rated game which matches the elements selected in those graphs. Figure 12 shows the dashboard with only the game's cell selected.

In this project, we used the Flask framework to run our recommendation system. It includes the basic UI for user input and out and some data visualization charts. Our business value is how much profit can be earned in the game selling. If the company wants to launch a first-person shooting (FPS) game in the STEAM, we can help this game evaluate whether it can make money. We can use the dashboard to check whether the FPS game is one of the most popular games which is played by many people. The company can analyze the dashboard and have a better consideration on launching the games.

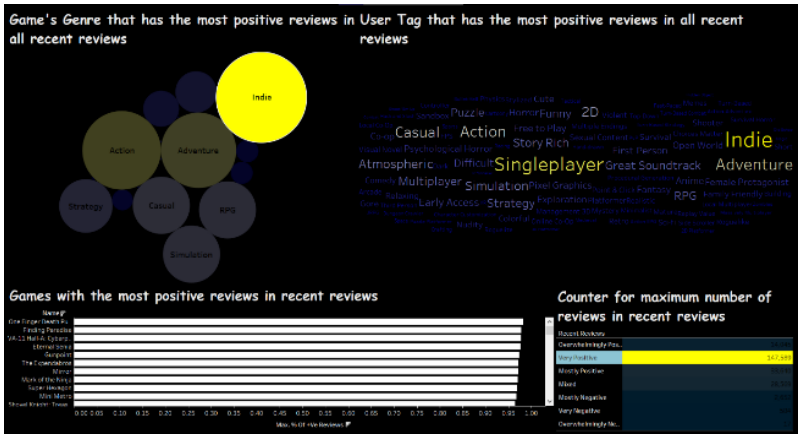

Figure 9. The dashboard.

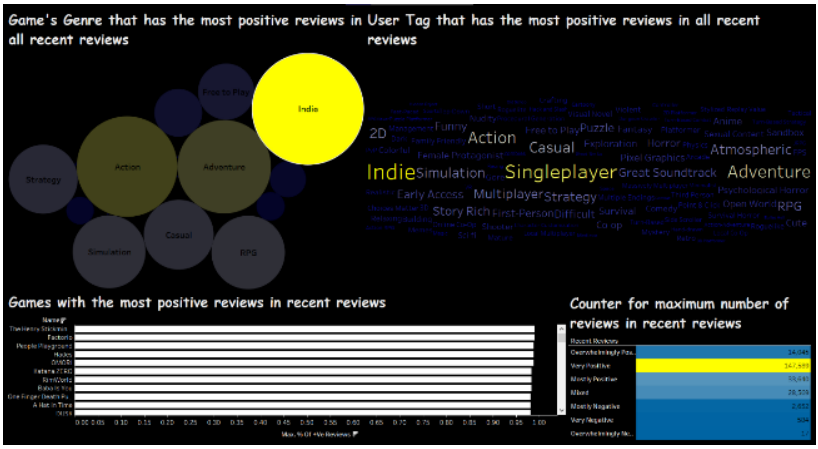

Figure 10. The dashboard with one cell selected.

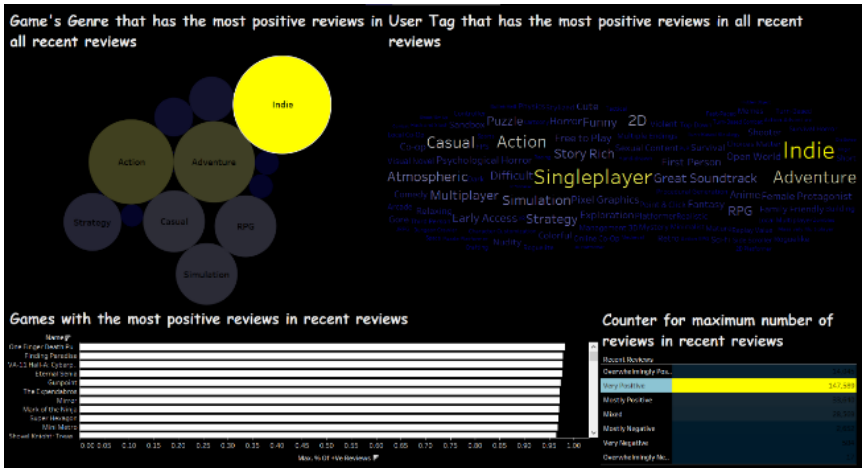

Figure 11. The dashboard with two cells selected.

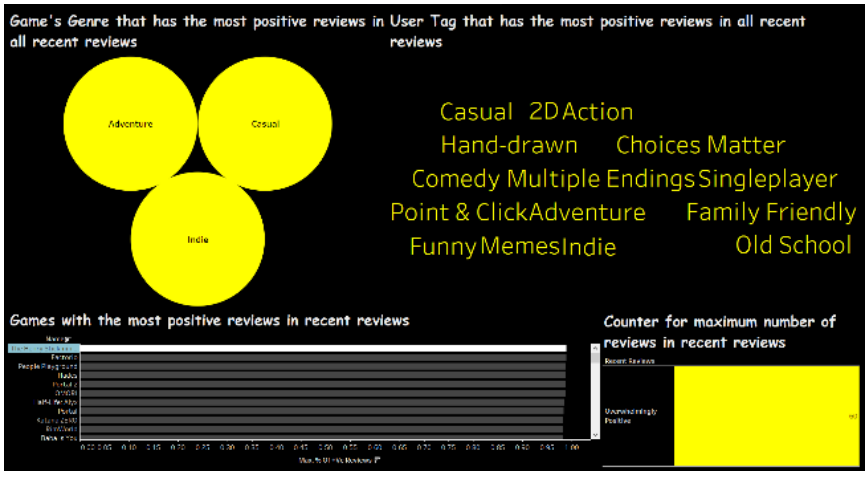

Figure 12. The dashboard with only game's cell selected.

3.6. Website

3.6.1 System Design

A website is created on localhost server. By running the program of the Flask framework, the browser will be opened and go to the home page which is mentioned in the following part. HTML, CSS are used to create the content and layout.

3.6.2 *Interface Design*

In our website, three interfaces are designed as shown in Figure 13. Figure 14 shows the home page of our game recommendation system. The home page provides a simple background and mainly in blue color. A search box is created for the users to input the full name of games. By clicking the submission button, the users page shows the recommended results or the page which shows the results are not found. A bottom left container shows our summary of the website. Figures 15 and 16 show the sunburst chart by scrolling down the home page. By scrolling down the page, you can see the sunburst chart which shows the percentage of positive reviews by recent reviews as shown in Figure 15. The chart is interactive to users by clicking the genre of the game and the recent review like the figure shown in Figure 16. Figure 16 shows the sunburst chart after a user selected the 'Very Positive' in the 'Genre' path. By selecting this path, it shows all the games and its genre which has a 'Very Positive' recent review in overall review.

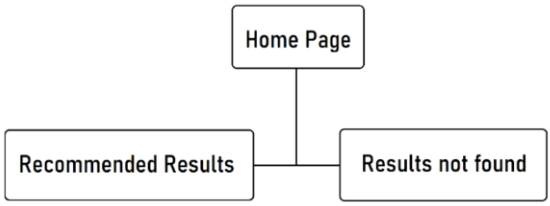

Figure 13. Three interfaces in our website.

Figure 14. Home page of our game recommendation system.

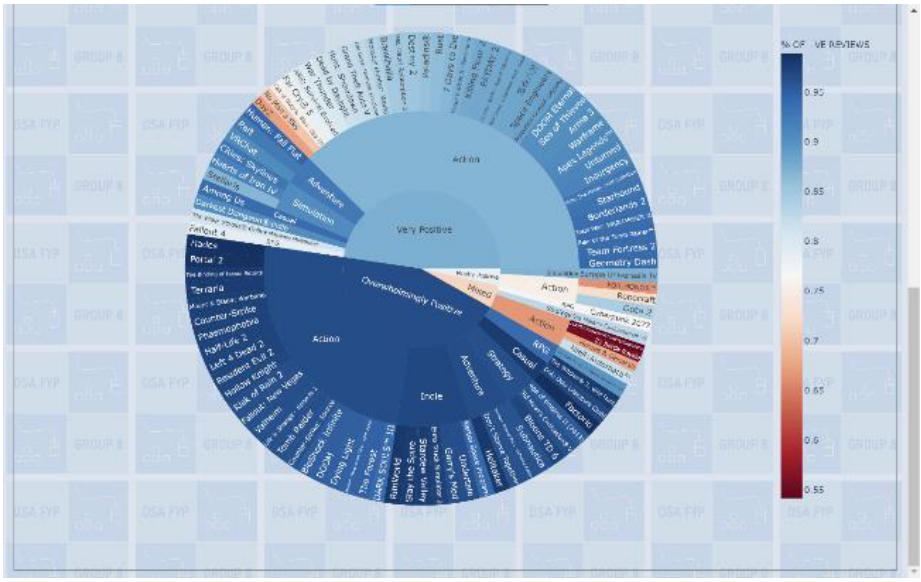

Figure 15. The sunburst chart which shows the percentage of positive reviews by recent reviews.

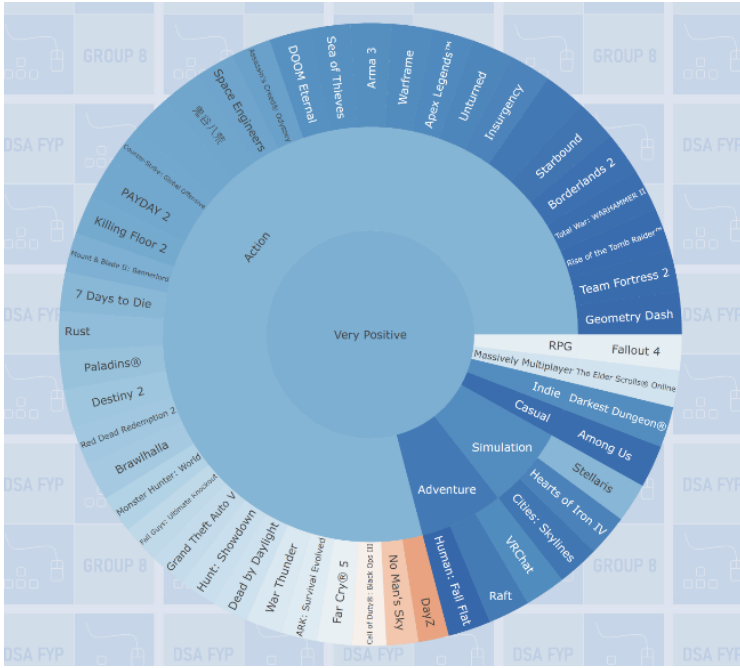

Figure 16. The chart is interactive to users by clicking the genre of the game and the recent review.

4. Preliminary Result on Performance Evaluation

4.1. Performance Metrics

The model can recommend games with the same taste as the user based on the game's attribute information. For example, the user chooses “Counter-Strike: Global Offensive” (objective-based, multiplayer first-person shooter) as input data of the model.

There is a similarity score to compare similarities between different games and “Counter-Strike: Global Offensive”. If the similarity of two games is high, the score is closer to 1. We expect our model to accurately recommend a similar game according to the similarity score (1).

$$similarity(A,B) = \frac{A \cdot B}{\|A\| \times \|B\|} = \frac{\sum_{i=1}^{n} A_i \times B_i}{\sqrt{\sum_{i=1}^{n} A_i^2} \times \sqrt{\sum_{i=1}^{n} B_i^2}} \tag{1}$$

Figure 17 shows the similarity score to compare similarities between different games and “Counter-Strike: Global Offensive”. If the score is closer to 1, it is more similar between two games.

```
[42]  M↓
      (cosine_sim[0][0:50])

array([1.        , 0.00679463, 0.03896105, 0.05112952, 0.00361326,
       0.01131284, 0.01945855, 0.02359504, 0.03278151, 0.03405163,
       0.        , 0.01451812, 0.01490077, 0.03607917, 0.00974434,
       0.00592617, 0.01711934, 0.00895149, 0.03843671, 0.01322813,
       0.01807475, 0.02489037, 0.0531111 , 0.00765787, 0.02170089,
       0.01307389, 0.02633358, 0.02759137, 0.02715629, 0.00195284,
       0.01198886, 0.        , 0.01534731, 0.01985157, 0.01305624,
       0.07699277, 0.00820874, 0.00926968, 0.01431223, 0.00740711,
       0.08873251, 0.01054007, 0.01402753, 0.01373282, 0.01457977,
       0.02343282, 0.02971694, 0.04464596, 0.0332134 , 0.03495005])
```

Figure 17. The similarity score.

4.2. Preliminary Results

In Figure 18, the page of recommendation results provides a simple background and mainly in purple color. ‘Cities: Skylines’ is chosen as an example; it will show the top five results related to ‘Cities: Skylines’ with their genres. And display like a food menu. The link of the title of the game can be clicked to go to the website from STEAM to check further details. The page displays the error message if the recommended results are not found.

Figure 18. The page of recommendation results.

5. Conclusion

In this project, we have developed a games recommender system with complete functional recommending features. We applied data visualization to our solution and can successfully make the recommending system more appealing to the user, which completes our goal of making a recommending system that feels more refreshing to the existing one. Also, we achieve our goal of making a system that can showcase flexible outcomes with the same element as the user input, which can give the user more choice when finding the game they want.

We successfully apply machine learning, data science skills such as web scraping, data preparation, machine learning algorithms, data visualization and Flask application and build a working recommendation system, these skills will surely help us furthermore in the future with our data science work. And we hope that our recommender system can successfully help those people who want to find their favorite games.

References

[1] Cheuque, G., Guzmán, J., & Parra, D. (2019, May). Recommender systems for Online video game platforms: The case of STEAM. In Companion Proceedings of The 2019 World Wide Web Conference (pp. 763-771).

[2] Hannula, R., Nikkilä, A., & Stefanidis, K. (2019, September). GameRecs: Video Games Group Recommendations. In European Conference on Advances in Databases and Information Systems (pp. 513-524). Springer, Cham.

[3] Pathak, A., Gupta, K., & McAuley, J. (2017, August). Generating and personalizing bundle recommendations on steam. In Proceedings of the 40th International ACM SIGIR Conference on Research and Development in Information Retrieval (pp. 1073-1076).

[4] Yuen M. C., Chan S. L., Leung H. T., Wu P. L., Yip P. Y. (2019). "A System for Collecting and Analyzing Data from Existing Game Selling Platforms", Proceedings of The 2019 15th International Conference on Natural Computation, Fuzzy Systems and Knowledge Discovery (ICNC-FSKD 2019), July 2019, Kunming, China.
[5] Dokoupil, P., & Peska, L. (2023, June). The Effect of Similarity Metric and Group Size on Outlier Selection & Satisfaction in Group Recommender Systems. In Adjunct Proceedings of the 31st ACM Conference on User Modeling, Adaptation and Personalization (pp. 296-301).
[6] Yang S., Korayem M., AlJadda K., Grainger T., Natarajan S. (2017). Combining content-based and collaborative filtering for job recommendation system: A cost-sensitive statistical relational learning approach, Knowl.-Based Syst. 136 (2017) 37–45.
[7] Yuen M. C., King I., Leung K. S. (2015) "TaskRec: A Task Recommendation Framework in Crowdsourcing Systems", Neural Processing Letters Volume 41 Number 2, 2015.
[8] Yuen M. C., King I., Leung K. S. (2021) "Temporal Context-Aware Task Recommendation in Crowdsourcing Systems", Knowledge-Based Systems, Elsevier.
[9] Games Finder. https://gameslikefinder.com/
[10] Quantic Foundry. https://apps.quanticfoundry.com/recommendations/gamerprofile/videogame/
[11] Ikram F., Farooq H., and Nawaz W.. (2022). Multimedia Recommendation System for Video Game Based on High-Level Visual Semantic Features. Sci. Program. 2022 (2022). https://doi.org/10.1155/2022/6084363
[12] Yang L., Liu Z., Wang Y., Wang C., Fan Z., and Yu P. S. (2022). Large-scale Personalized Video Game Recommendation via Social-aware Contextualized Graph Neural Network. In Proceedings of the ACM Web Conference 2022 (WWW '22). Association for Computing Machinery, New York, NY, USA, 3376–3386. https://doi.org/10.1145/3485447.3512273

Fuzzy Systems and Data Mining IX
A.J. Tallón-Ballesteros and R. Beltrán-Barba (Eds.)

doi:10.3233/FAIA231097

Intelligent Driver Behavior and Emotion Detection System

Chi-Yat Lau [a] , Man-Ching Yuen [b,1] , Chi-Wai Yung [b] , Ka-Ho Yeung [a], Ho-Yin Chung [a], Ho-Wang Ngai [a], Chau-Wai Wong [a], Ching-Yee Wong [a], Alan Li [c]
[a] *Department of Information Technology, Vocational Training Council, China*
[b] *Department of Applied Data Science, Hong Kong Shue Yan University, China*
[c] *Sampras (HK) Limited, China*

Abstract. According to the road traffic injuries fact sheet from the World Health Organization, approximately 1.3 million people die each year because of road traffic crashes. There are many risk factors and one of the most important is distracted driving, especially caused by using a mobile phone. The fact sheet shows that drivers using mobile phones are approximately 4 times more likely to be involved in a crash than drivers not using a mobile phone. Apart from this, dangerous driving behaviors and driver emotions are growing concerns for road safety. This project aims to develop a model for detecting dangerous driving behaviors and analyzing drivers' emotions in order to avoid and minimize traffic accidents. We focus on detecting several distractive behaviors, bad driving practices, and abnormal emotions. We carry out experiments to evaluate the system performance through the integration of our system with existing infrastructure. To the best of our knowledge, we design and develop the first small and portable device to collect data from drivers, then the collected data is transferred to the cloud for further analysis. The trial service is already available for drivers for a few months in Hong Kong.

Keywords. Driver behavior, emotion detection, driving, traffic accidents

1. Introduction

Since traffic accidents, casualties and vehicle licenses are keep increasing, the main reason of accidents is distracted driving. In the literature, there are many traffic monitoring systems [1], but the number of traffic accidents is still high. Moreover, the highest accident vehicle involvements are private cars. Therefore, we design an Intelligent Driver Behavior and Emotion Detection system for monitoring driver behavior which is for private car usage.

"CAOME", our project is proposed on faith to protect road users' safety by reducing risky driving practices. Other than some uncontrollable and unexpected situations caused by passengers and pedestrians, drivers are inevitably to take responsibility for any accidents. Hence, our project's target users are drivers.

This research project is composed of four parts, which include model development, cloud service building, IoT deployment, and user platform development. We have

[1] Corresponding Author, Man-Ching YUEN, Department of Applied Data Science. Hong Kong Shue Yan University, Hong Kong, China; E-mail: mcyuen@hksyu.edu.

applied several emerging technologies in the whole project, which include Artificial Intelligence (AI), Machine Learning, Deep Learning, and 5G.

First, our project developed an intelligent driving system with a customized detective model for detecting drivers' dangerous behaviors including hands-off driving, smoking, using the mobile phone, and physical reactions of tiredness. Moreover, we have built an analysis model to capture the driver's facial expressions and then identify the driver's emotions of anger, fear, happiness, sadness, and neutrality. We design and develop the sensors that we used in the project.

Second, we build and develop our service on Alibaba Cloud. The system operation and maintenance are performed on the cloud server. We build connections and communication between the cloud and IoT devices.

Third, we make our custom device to ensure the best quality for I/O. We choose the most suitable parts for handling nighttime driving and offline operation.

Finally, we provide user-friendly platforms on the website and smartphone app. Users can obtain our service through easy operations.

The organization of this paper is as follows. Section 2 describes motivation. Section 3 presents our data analytical framework. Section 4 shows the object detection model and performance evaluation. Section 5 presents the system function. Section 6 shows the solution implementation. Section 7 draws out the conclusion.

2. Motivation

2.1. Comparison of major driver contributory factors of traffic accident

Refer to Figure 1. Corresponding to comparison of major driver contributory factors of traffic accidents from Hong Kong Police Traffic Report [2], traffic accidents caused by inattentive driving are in first place in the past 3 years and 2021 have proliferated obviously.

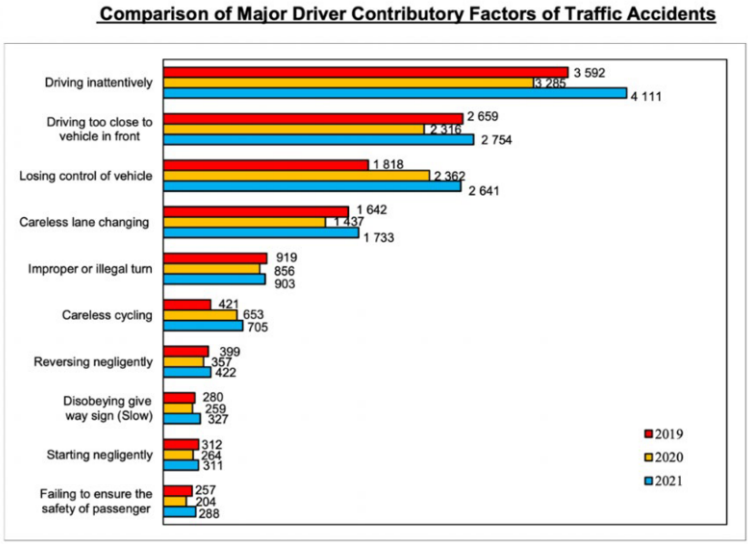

Figure 1. Comparison of major driver contributory factors of traffic accident from Hong Kong Police [2]

2.2. Our Contribution

Concerning the problem issued above, we developed a customized system, CAOME, for monitoring drivers' driving behaviors. Our project's ultimate goal is to minimize traffic accidents caused by drivers. The contributions of our system are:

1. Achieve stable performance in daytime and nighttime driving.
2. Develop automated and fully connected operations between clients and servers.
3. Build a self-learning and improvement model for future optimization.

3. Data Analytical Framework

3.1. Data acquisition and understanding

Since we have two models for driver behavior detection and emotion analysis, we have created two corresponding datasets.

3.1.1 Dataset for driver behavior detection

We have some of the functions performed through this model, which include hands-off from steering wheels, smoking, and using the mobile phone. Thus, we have collected images of cigarettes, mobile phones, steering wheels with hands, and steering wheels without hands. We looked for images that are under driving conditions. These images are collected from different channels, such as Kaggle, Google search engine, and YouTube videos. There were around 18,000 images collected.

3.1.2 Dataset for driver emotion analysis

In the emotion analysis model, we classify the driver's emotions into 5 categories, **angry, fear, happy, sad, and neutral**. We have collected 54,796 images from different open-source datasets, such as Kaggle, RAF-ML dataset, Basel Face dataset, Chicago Face dataset, and Color FERET dataset. We classify into five emotion categories which are neutral, happy, angry, sad, and fear. There are criteria regarding data acquisition;

1. Clear detection object.
2. High resolution.
3. Light distributed evenly as much as possible.

We found that there exist problematic data due to blurred objects, too dark for object detection, not related objects, low resolution, images generated from video recorded at low light environments. All problematic data in these datasets is removed.

3.2. Data Preprocessing

Data collected from various channels which are Kaggle, Search engine, and YouTube. Around 23,00 pictures collected for the driver behavior model, 54,796 pictures collected for the emotion model.

All image data is checked manually if there is any irregularity which is mentioned before. After data validation, data was labeled according to the image features. Data is labeled by labelstudio which exports TXT format, and YOLOv5 accepts TXT format. Therefore, no data format converters are needed.

4. Object Detection Model and Performance Evaluation

Object detection is a popular computer vision task that involves identifying and localizing objects of interest within an image or video frame. It has numerous applications in fields such as surveillance, autonomous driving, robotics, and augmented reality. Object detection models are designed to automatically identify and locate objects within an image or video. There are several types of object detection models [3, 4, 5, 6]. Object detection models are poised to play an increasingly important role in many real-world applications [7].

4.1. Algorithm of YOLO

In this project, we use an object detection model to detect if the driver is in safety status, smoking, hands-off or using a phone. YOLO algorithm [5] performs real-time object detection using CNN [3, 4]. YOLO is well-fit for real-time applications like video surveillance and autonomous driving due to its effective architecture and capacity to recognize objects at various scales [8].

The commonality among all object detection architectures is that, as shown in Figure 2 [9], the input picture characteristics are first compressed by the feature extractor (Backbone) before being sent to the object detector (which includes the Detection Neck and Detection Head). In order to prepare for the detection stage in Detection Head (or Head), Detection Neck (or Neck) functions as a feature aggregation that is tasked with mixing and combining the features created in the Backbone.

Here, the distinction is that the head is in charge of each bounding box's detection, localization, and classification. As shown in Figure 2, the one-stage detector implements the two jobs simultaneously (Dense Detection), whereas the two tasks are implemented separately by the two-stage detector and combined subsequently [9].

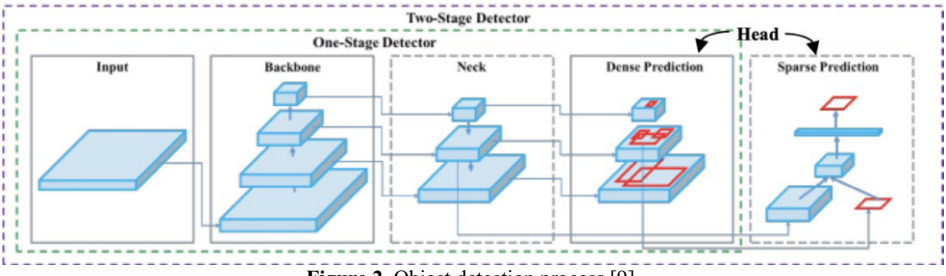

Figure 2. Object detection process [9].

4.2. Performance Evaluation Measures

To evaluate the speed of recognition and accuracy of our model, we use the following performance measures: IoU, precision, recall and mAP.

Precision is the ratio of positive prediction value over all predictions. The formula of precision is (Eq. 1). Recall is the ratio of positive prediction value over ground truth. The formula of recall is (Eq. 2). Eq. 3 shows the calculation of F1 score. Intersection Over Union (IoU) is the measure used to calculate the overlap of the area where the predicted bounding box and the actual bounding box intersect. The formula of IoU is described at (Eq. 4). Mean average precision (mAP) refers to the mean average of the Average Precision (AP) values for all classes. Average Precision is the average precision of all predictions.

$$Precision = \frac{TP}{TP+FP} \quad \text{(Eq. 1).}$$

$$Recall = \frac{TP}{TP+FN} \quad \text{(Eq. 2).}$$

$$F1\ Score = 2 \times \frac{recall \times precision}{recall + precision} \quad \text{(Eq. 3).}$$

$$IoU = \frac{R_A \cap R_P}{R_A \cup R_P} \quad \text{(Eq. 4).}$$

4.3. Performance Evaluation on Object Detection Model

All of the models' results are presented in Table 1. As can be seen, both YOLOv5 models achieved the best mAP value, which is 99.5. Other models' mAP levels are higher. The performance of the YOLOv4 small model outperformed the competition in terms of training speed. These findings show that while the YOLOv4 small model's training duration is the best, its mAP value is the worst.

There are fewer convolutional network layers in little models than in larger ones. Although YOLOv5s requires twice as much training time as the competition in tiny models, it has surpassed YOLOv4 and YOLOv3 tiny.

Table 1. Performance results of different models

Result	mAP@0.5 IoU	loss	Precision	Recall	Training Time (mins)
Yolov3 tiny	90.3	0.74	0.93	0.83	55
Yolov3	92.9	0.18	0.96	0.93	297
Yolov4 tiny	86.2	0.09	0.96	0.79	**48**
Yolov4	96.6	1.35	0.95	0.97	379
Yolov5 s	**99.5**	0.01	0.997	**0.99853**	108
Yolov5 xl	**99.5**	**0.007**	**1.00**	0.99783	279

In summary, we find out that YOLOv5 has the most consistent and superior performance among all these models. Therefore, YOLOv5 was selected even though its training period was longer than that of other models since we wanted a model that would be very accurate given the situation.

4.4. Performance Evaluation on Emotion Detection Model

For emotion detection, it uses EfficientNetV2s. To determine the model's ideal parameters, we apply the finetune method. The knowledge and representations that a pre-trained model has gained from a big dataset are used in fine-tuning. In comparison to training from scratch, the fine-tuning procedure requires fewer iterations and less training time when the model is started using these pre-trained weights. And EffcientNetV2s provides faster training times and highest accuracy compared to the previous version.

We thoroughly explored model scaling and discovered that performance may be enhanced by adjusting network depth, width, and resolution. A neural convolutional network that is more accurate and efficient than previously, so it makes a lot of progress. EfficientNetV2 obtained the best top-1 accuracy of 84.3% on ImageNet while downscaling by a factor of 8.4 and performing 6.1x faster inference than the best Convolutional neural network [10].

5. System Function

The model contains two separate models which are driver behavior detection and emotion classification.

5.1. Driver behavior detection

In this model, face, hand and eyes landmarks are used for analysis to detect driver behavior. Therefore, Face Mesh and Hand Mesh from Mediapipe packages and Dlib package are used for extracting user face, hand and eyes landmarks respectively. All functions are performed in "model.py". The system will issue a warning once the following driver's behavior is detected:

- Holding phone
- Looking around
- Eye closed
- Yawning
- Camera covered
- Smoking

5.2. Driver emotion classification

"Emotion" function is to perform a driver's emotion classification. There are a total five classes of the classification, which are neutral, happy, sad, fear, and angry. It predicts emotions from a given image using face detection and emotion recognition models.

6. Solution Implementation

6.1. System architecture

Figure 3 shows the system architecture. Our system adopts a three-tiered system architecture, which divides the application into physical and logical layers. This architecture allows for better scalability, maintainability, and reliability. Each layer has different responsibilities and functions.

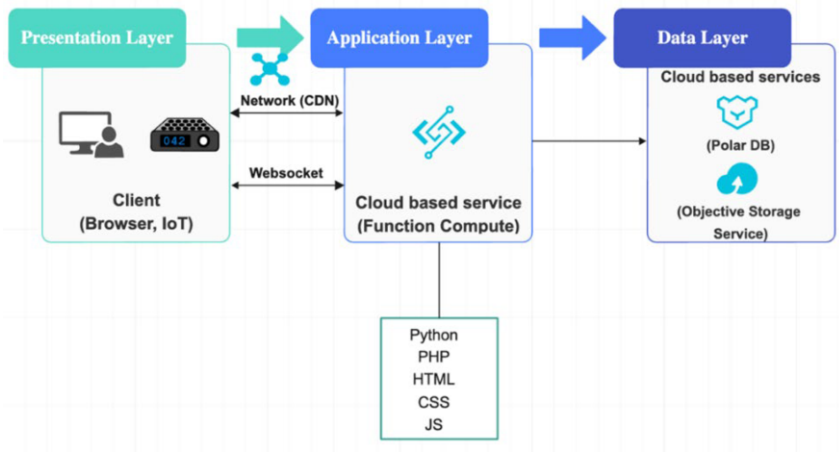

Figure 3. System architecture

6.2. System Flow

Figure 4 shows the system flow. The end user can start the operation through either the IoT device or our website. As soon as the camera starts streaming, the images are captured and collected. These images are then uploaded to the cloud-based server via web-socket. The processed image and alert sounds are retrieved through web-socket and sent back to the device. Figure 5 shows our system website.

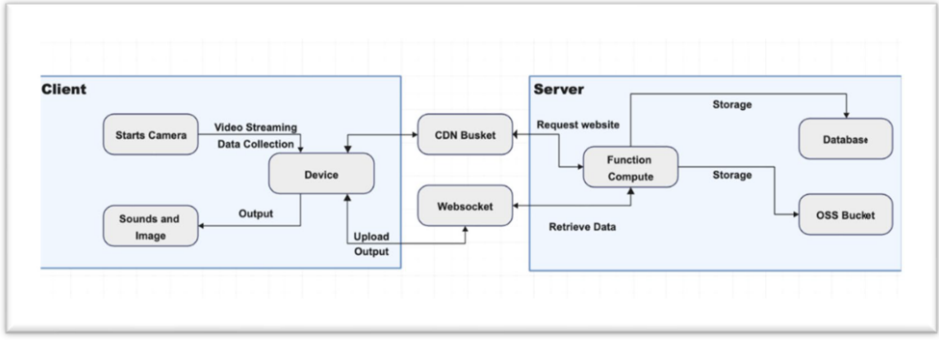

Figure 4. System flow

6.3. Website

Figure 5 shows our system website. Our one-page website features a user-friendly interface that provides a simple way to view the system's performance. Users can start and stop the streaming by clicking buttons, and the real-time streaming is displayed in the center of the page. The images are processed and retrieved with model performance results and alert sounds.

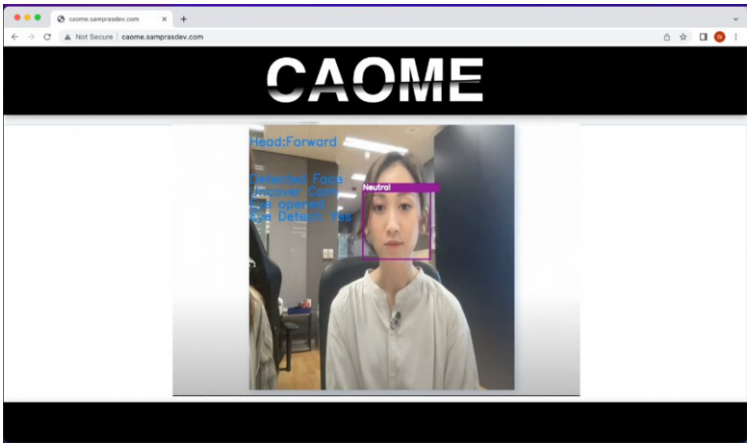

Figure 5. Our System Website

7. Conclusion

In this project, we have successfully developed a comprehensive driver behavior and emotion detection model. Our model ensures accurate detection and analysis of various driver-related factors, including phone usage, smoking, and instances of eyes-closed scenarios. We have applied data preparation techniques, machine learning algorithms, cloud services, and Vehicle-to-Everything (V2X) technology to build a robust driver behavior and emotion detection system.

By capturing real-time frames and uploading them to the cloud for computation and analysis, our system can promptly alert drivers when it detects inappropriate driving behavior. The primary objective of our model is to minimize traffic accidents caused by such behaviors. By effectively identifying and monitoring driver actions, our system helps to enhance the overall road safety and prevent the potential risks associated with distracted driving.

Our system aims to raise safety awareness among drivers by providing real-time alerts and feedback on their behaviors. By actively monitoring and analyzing driver actions, we not only strive to prevent traffic accidents but also protect other drivers and pedestrians on the road. Through the integration of our system with existing infrastructure, we can call for the smart city and reduce the burden on police forces in handling traffic accidents, allowing them to allocate resources more efficiently.

Acknowledgements

This research was in part supported by grants from the Research Grants Council of the Hong Kong Special Administrative Region, China (Project No. UGC/FDS15/E02/20 and UGC/FDS15/E01/21).

References

[1] Lau C. Y., Yuen M. C., Yeung K. H., Fan C. P., Ko O. Y., Ngan L. W., Tam W. C., Yeung W. N., "PC-based Intelligent Traffic Monitoring System with Real-time Analysis for Smart Cities", Proceedings of 2022 14th International Conference on Communication Systems & Networks (COMSNETS), IEEE, January 2022.
[2] Hong Kong Police Traffic Report https://www.police.gov.hk/ppp_en/09_statistics/ts.html
[3] Ren, S., He, K., Girshick, R., & Sun, J. (2016). Faster R-CNN: Towards Real-Time Object Detection with Region Proposal Networks. Advances in neural information processing systems, 91-99.
[4] He, K., Gkioxari, G., Dollar, P., & Girshick, R. (2017). Mask R-CNN. Proceedings of the IEEE international conference on computer vision, 2961-2969.
[5] Redmon, J., Divvala, S., Girshick, R., & Farhadi, A. (2016). You Only Look Once: Unified, Real-Time Object Detection. Proceedings of the IEEE conference on computer vision and pattern recognition, 779-788.
[6] Liu, W., Anguelov, D., Erhan, D., Szegedy, C., & Reed, S. (2016). SSD: Single Shot MultiBox Detector. European conference on computer vision, 21-37.
[7] Han, C., Ye, Y., & Zhong, G. (2021). Object Detection in 20 Years: A Survey. arXiv preprint arXiv:2105.01988.
[8] Jiang, P. et al. (2022) A review of Yolo algorithm developments, Procedia Computer Science. Available at: https://www.sciencedirect.com/science/article/pii/S1877050922001363 [Accessed: 10 May 2023].
[9] Solawetz, J. (2020). YOLOv5 New Version - Improvements And Evaluation. Roboflow. Search date 04.2020. https://blog.roboflow.com/yolov5-improvements-and-evaluation/
[10] Koonce, B. (2021). EfficientNet. In: Convolutional Neural Networks with Swift for Tensorflow. Apress, Berkeley, CA. https://doi.org/10.1007/978-1-4842-6168-2_10

Fuzzy Systems and Data Mining IX
A.J. Tallón-Ballesteros and R. Beltrán-Barba (Eds.)

doi:10.3233/FAIA231098

Under the Digital Background Marzano's New Taxonomy of Educational Objectives: Conception of Deep Learning Analysis

Mei Yang[a] and Jiatao Li[b,1]
[a]*Wuhan City Vocational College, China*
[b.]*Central China Normal University, Wuhan, Hubei Province, 430064, China*

Abstract. Under the digital background, Marzano's New Taxonomy of Educational Objectives proposes a new taxonomy for classifying educational objectives, which emphasizes teaching higher levels of thinking and deals with three knowledge domains, namely, the domain of information, the domain of mental procedures, and the domain of psychomotor procedures. This study compares and analyzes the classification of different educational goals, the New Taxonomy is underlain by the conception of deep learning, which discloses the mechanism of how knowledge, thinking and emotions interact with each other and develop through learning in the information flow process. The core of deep learning in the New Taxonomy is to advocate coordinated development of cognition, meta-cognition, and self-system. The ultimate goal of deep learning is to improve the self-system by teaching high levels of thinking and developing students' metacognition.

Keywords. Under the digital background, Taxonomy of educational objectives, depth of learning, high levels of thinking

1. Introduction

Educational objectives lie somewhere between the ultimate goals of education and instructional objectives and are more specific and concrete than the ultimate goals. It is also true that educational objectives convey a more open, richer sense of intended student learning than that conveyed by narrower instructional objectives. [1] Defining educational objectives can assist teachers in understanding curriculum standards, interpreting teaching materials, setting teaching goals, monitoring and assessing students' academic performance, and adjusting and reflecting on the teaching process. An essential step to achieve educational objectives is to translate educational objectives into cultivation goals, which are further broken down into instructional objectives. The translation and decomposition of educational objectives are mediated by a proper

[1] Corresponding Author: Jiatao Li, Central China Normal University, China; Email: 27778676@qq.com
First Author, Mei Yang, associate professor at Wuhan City Vocational College, China.
Fund project: Phased research results from the "Study on building STEM education training curriculum for primary and secondary school teachers in Hubei Province" (2020GB194), an education planning project of Hubei Province in 2020; phased research results from the "Science microlesson design and development of rural primary schools" (20G158), a philosophy and social sciences research project of the Department of Education of the Hubei Province in 2020.

taxonomy of educational objectives. However, the three dimensions of educational objectives are separated from each other in the current educational theories and practice at home and abroad. Besides, there seems to be lack of operability of integrating the three dimensions of educational objectives in teaching[2]. Therefore, defining a new integrative and systematic taxonomy of educational objectives is a key step in moving toward an integration of cultivation goals. As pointed out in the preface of *New Taxonomy of Educational Objectives* [3] Marzano has built a distinct and practical model for learning, which integrates all important elements of each dimension of learning together and represents the relationship between these elements and their development using simple, explicit logics. Marzano's taxonomy is original and enjoys bright prospects of application.

2. Related works

Taxonomy of educational objectives based on deep learning can be traced back to Bloom's taxonomy of educational objectives, which is later revised by Anderson. Biggs proposed the SOLO taxonomy as a measure of the quality of learning. Webb conceptualized the depth of knowledge (DOK). Marzano presented the new taxonomy of educational objectives that integrates three domains of knowledge. See Table 1.

Table 1 Taxonomies of educational objectives based on deep learning

Taxonomy	Bloom (Bloom,1956)	Anderson (Anderson,2001)	Biggs (Biggs,1982)	Webb (Webb, 1997)	Marzano (Marzano, 2007)
Basis of classification	Cognitive level	Cognitive level	Quality of learning	Depth of knowledge	Multi-dimensional integration
Superficial learning	Knowledge Comprehension	Remembering Comprehension	Prestructural Unistructural Multistructural	Recall Skill/concept	Information retrieval Comprehension
Deep learning	Applying Analyzing Synthesizing Evaluating	Applying Analyzing Evaluating Creating	Relational Extended abstract	Strategic thinking Extended thinking	Analysis Knowledge utilization Metacognition Self-system

Bloom's taxonomy covers a wide spectrum of educational objectives, which range from simple to complex, from lower to higher levels, and from the superficial to the deeper level, which is the behavioral level. Knowledge and comprehension are superficial levels of learning, while application, analysis, synthesis and evaluation are four deeper levels of learning. The four deeper levels involve using concepts in abstract contexts, decomposing elements in the context materials, combining or restructuring the elements, and interpreting, transforming, inferring, analyzing or commenting the knowledge. One can form intellectual skills by moving through the hierarchy of cognitive skills[4]. Bloom's taxonomy opens up a new theoretical approach to classifying the objectives of deep learning. Anderson et al. latter revised Bloom's taxonomy to correct the defects in the structure and formulation of Bloom's: Anderson separates the knowledge domain from the cognitive process domain and defines objectives in two dimensions. He divides the cognitive process domain into six types of thinking, namely, remembering, understanding, applying, analyzing, evaluating and creating; he further combines the two dimensions by establishing the interactions and interconnections between them during the actual learning process. Anderson's revision provides a solution to inadequate blending of the knowledge and cognitive process

domains in Bloom's taxonomy and highlights the role of metacognition in the learning process. However, one major problem with Anderson's taxonomy is that achieving higher educational objectives relies heavily upon whether the lower ones are realized or not. The intersection or boundaries between superficial and deep learning are less clearly defined.

Comparatively, the taxonomies proposed by Biggs and Webb more distinctly define the boundary between superficial and deep learning. To measure the quality of learning, Biggs's taxonomy consists of five levels. The first three, namely, pre-structural, unistructural and multi-structural, are aspects of superficial learning, while the last two, namely, relational and extended abstract, are aspects of deep learning. Biggs's taxonomy can be conveniently used to measure the quality of learning by structuring the complexity and quality of students' thinking into distinct levels. But this taxonomy reveals very little about the cognitive and behavioral processes underlying problem solving. Therefore, Bigg's taxonomy is only applicable to assess students' academic achievements in a specific field, but can be hardly used by teachers to define educational objectives in advance or guide procedural behaviors. Webb categorized learning objectives into recall, skill/concept, strategic thinking, and extended thinking. The latter two are the goals of deep learning. Webb's taxonomy defines the boundary of deep learning from the perspective of DOK and well resolves the ambiguity of the SOLO taxonomy regarding the behavioral dimension. But similar to the other three taxonomies described in Table 1, Webb's taxonomy pays little attention to the learning of motor skills and juxtaposes metacognition and conceptual knowledge that occur simultaneously with conceptual cognition or neglect them altogether. There is a lack of understanding about the interaction mechanism between different knowledge types and different levels of cognition in the learning process. Different objectives seem to be hardly related to each other in these taxonomies.

Addressing the above problems, Marzano's New Taxonomy clearly defines the positions of cognition, emotions and psychomotor in learning and separates out metacognition as distinct from the knowledge category. On this basis, the New Taxonomy defines two higher levels of thinking, namely, metacognition and self-system.

3. Methods

This study compares and analyzes the classification of different educational goals, and ultimately summarizes and forms the mechanism, essence, goals, and methods of Mazano's educational goals towards deep learning.

4. Result

The New Taxonomy orders the educational objectives in terms of control. Marzano proposes a two-dimensional framework for classifying educational objectives in light of the mechanism of information processing and how some processes control over the operation of other processes (hereafter referred to as "the New Taxonomy"). One dimension is knowledge as domains, which is further categorized into information, mental procedures, and psychomotor procedures. The other dimension is the thinking domain, which is further categorized into the cognitive system, metacognitive system,

and self-system (Fig. 1). The two dimensions, namely, knowledge and thinking, constitute two sides of the same coin, and interact and influence each other. Each is one integral part of the learning process.

It can be seen from Fig. 1 that the three systems of thought are composed of several subsystems. For example, the metacognitive system consists of four subsystems, namely, specifying goals, monitoring process, monitoring clarity, and monitoring accuracy. On account of the information processing process, Marzano obtains a six-tiered taxonomy by ordering elements of cognitive system within the hierarchy of the three systems of thought. It should be kept in mind that the six levels of the New Taxonomy do not represent levels of complexity. For example, the processes within the self-system are not more complex than the processes within the metacognitive system, and so on. It is important to note that the New Taxonomy makes no claims that the components within the self- and metacognitive systems are themselves hierarchical in nature. For example, there is no necessary ordering of the processes of examining importance, efficacy, and emotional response in terms of levels of consciousness. This is in contrast to Bloom's Taxonomy, which attempt to use processing difficulty as the critical feature separating one level from the next. The New Taxonomy is more applicable to depict the actual processes involved in learning and integrates different dimensions together.

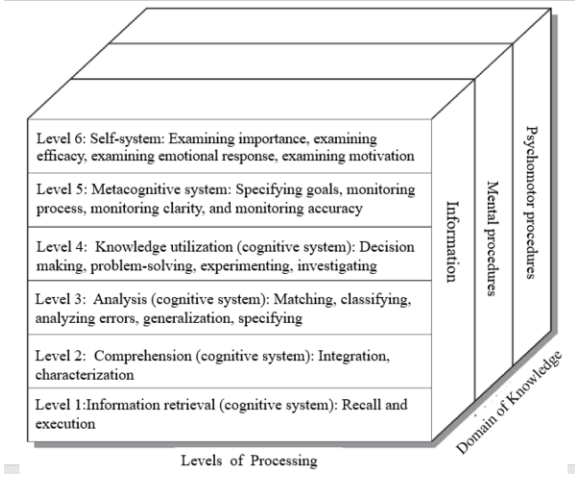

Fig. 1 Marzano's taxonomy of educational objectives[4]

5. Discussion

Based on the latest findings in the psychology of learning and development, the New Taxonomy is a brand new model of learning oriented towards students' all-around and integrative development. As demonstrated by the model, learning is a process where the self-system, metacognitive system, and cognitive system work synergistically. The learners know, understand, create and transform knowledge by evoking different systems of thought. Besides, Marzano's model embodies the pursuit for integrative, coordinated, and holistic education, revealing the mechanism, nature, goals, and methodology of deep learning.

(1) Interaction: The mechanism of deep learning is the deep interaction between knowledge, thinking and emotions in the information flow process

The model of learning proposed by the New Taxonomy deals with the interaction and development of knowledge, thought and emotions during task accomplishment through learning. The model of behavior is shown in Fig. 2, where learning is represented as task-driven. First, the self-system makes the decision, evoking the cognitive system to specify goals and strategies. Finally, the cognitive system is elicited to process relevant information, itself interacting with information as well.

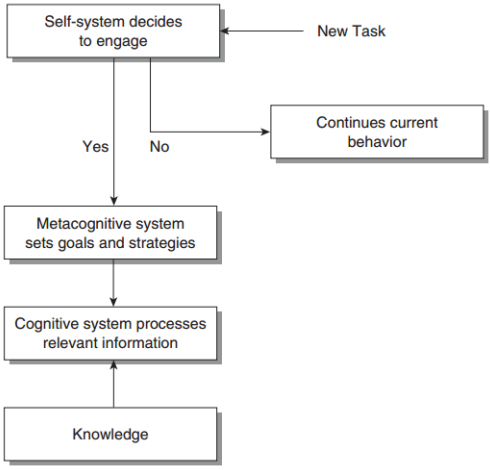

Fig. 2 Model of behavior [4]

The difficulty of task and the degree to which each system of thought is involved jointly determine the depth of learning. When deep learning happens, the learners are driven by higher levels of knowledge utilization tasks, including problem-solving, experimenting, investigating, and decision-making. Self-system, cognitive system, and metacognitive system collaborate with each other and interact with tools, others, society, and self to finally promote the perfection of the self-system and development of higher levels of cognition and metacognition. Obviously, deep learning starts from evoking attitudes, emotions and beliefs as parts of the self-system and happens when the learner interacts with the world, others and self, enabling information adaptation, assimilation and restructuring. Learning is deepened as thought develops through the practical activities of investigating, experimenting, problem solving, and decision making, and sublimates via the introspection and reflection processes as one specifies goals and strategies, monitors the process, and evaluates the result. Deep learning matures as one experiences positive emotions, a good sense of self-efficacy, and lasting motivation for learning.

In a word, the New Taxonomy is centered round information processing by the cognitive system, with the self-system and metacognitive system being evoked to create subject knowledge. During this process, thought and knowledge interact and promote each other. Knowledge is generated and created by thinking practice, and one develops higher levels of thinking through knowledge utilization.

(2) Integration: The nature of deep learning is the coordinated and integrative development of cognition, metacognition, and self-system

Knowledge learning is not only a process whereby one knows about the world through the cognitive achievements by predecessors, but also a process where one reflects upon oneself and listens to one's inner voice. Through learning, we look inside ourselves and build philosophy of life, thinking style, and methodology. [5] Marzano's New Taxonomy is oriented towards developing higher levels of thinking by knowledge comprehension and utilization, by building a self-system, and asserting the controlling role of the metacognitive system. The three systems of thought work together to accomplish challenging knowledge utilization tasks, including problem solving, experimenting, and decision making. The cognitive system, metacognitive system, and self-system are integrated into a whole as they each develop. During the learning process, the subsystems of thought examine the importance of tasks, efficacy of accomplishing the tasks, and one's emotional response, which further governs the degree to which each subsystem of the self-system is evoked. Besides, the specific cognitive level evoked by a task also influences the type and the degree to which each subcategory of the cognitive level is evoked, as shown in Fig. 2. The degree to which the self-system is evoked determines the progress of learning. Furthermore, the degree to which the metacognitive system and the cognitive system are evoked determines the depth and breadth of learning. It is easy to see that in the New Taxonomy, learning is a process where the self-system, metacognitive system, and cognitive system work synergistically and develop in an integrative manner. The learners' cognition, emotions and thought are all evoked and involved, working synergistically and collaboratively to generate knowledge. Knowledge is no longer a permanent truth and an abstract symbol but goes far beyond being a simple instrumental rationality. Knowledge constitutes a multi-value body that is related to one's development, happiness, and self-actualization, is being constantly generated and created, integrates the scientific, social, humanitarian, cultural, and aesthetic properties, shows humanistic concern, and deeply engages the learners. As one acquires knowledge, he or she will orient themselves towards knowledge and wisdom, which can be activating both physically and psychologically. In the meantime, knowledge activities contribute to self-enhancement and growth of personal virtues. Only when knowledge activities fully enlighten a person's body and soul and give true power to one's life will the individual acquire spiritual life and achieve an overall growth through learning. [6] The highest level of development is wholeness, which may be what we have been endeavoring to achieve, either consciously or unconsciously, in terms of human skills. [7] As one accrues multi-structured knowledge, his or her thoughts and emotions interact with knowledge. The deep engagement in learning facilitates the all-around, integrative development of learners. In a word, Marzano's New Taxonomy conceptualizes deep learning that is holistic in nature and points towards self-improvement and self-actualization. It echoes with China's advocacy of cultivating students' core competencies to develop key capacities and essential characters.

(3) Synthesis: The goal of deep learning is to improve the self-system

Marzano considers the self-system as the highest level of humans' conscious activities and the ultimate pursuit of learners. There is no doubt that self-recognition is based on self-recognition systems, which not only process information and monitor other parts of the system, but also serve as the basis for our awareness of our own phenomenological experiences and behavioral tendencies. [8] According to Marzano, self-system lies at the center of human thoughts and stands alone from the metacognitive system, occupying a dominant position among all other systems of thought. The Motivation in the secondary system is considered to be a mixture of the

secondary parts of the other self-system, that is, examining importance, examining efficacy, and examining emotional response (as shown in Fig. 1). Marzano's point of view is supported by several other studies. That is, when a task comes up, the self-system is first evoked, and the individual will decide whether to engage in the task or neglect the task and continue with the current task, depending on motivation (see Fig. 2). Lodewyk & Wine summarize the importance of the self-efficacy dimension in the self-system. Studies have shown that students with stronger self-efficacy tend to have a higher self-regulatory ability. They are more likely to engage in challenging tasks, set higher goals, work harder, and experience less anxiety. Moreover, they will choose more effective strategies, achieve better academic performance, and more effectively process cognitive information. Schoenfeld further emphasized the close connections between students' beliefs and perseverance in problem solving. According to findings in neuroscience, individuals with super cognitive ability but lacking in correct emotional response are hardly able to make major decisions. [9] Obviously, self-system plays a crucial role in the learning process as it determines whether one engages in a specific task and with which level of motivation. The self-system in the New Taxonomy consists of examining importance, examining efficacy, examining emotional response, and examining overall motivation. Examining overall motivation involves three factors: (1) perceptions of its importance, (2) perceptions of efficacy relative to learning or increasing competency in the knowledge component, and (3) one's emotional response to the knowledge component. [3] As Csikszentmihalyi once said, The ego permeates almost all consciousness: all memories, actions, desires, pleasures, pains, and more importantly, self-reflection is a system of goals that people have built up over the years[3]. As the self-system improves, the degree of integration of individuals' cognition and practice will be promoted. The interaction of cognition and practice will in turn facilitate the perfection of the self-system. An individual will finally achieve effective integration and unity of cognition, emotion, motivation, and behavior. In light of the above, the development and improvement of self-system are ultimate goals of deep learning. The self-system determines the motivation, orientation, width, and breath of the cognitive system and defines the object, contents and goals of metacognition. It embodies the synthesis of the metacognitive and cognitive systems in learners striving to achieve multi-dimensional development. It is noteworthy that to improve the self-system, students need to first achieve all-around, high-quality development, without which self-system can never been fully established. To sum up, improving the self-system unifies the goals and pathways of deep learning.

(4) Deep thinking: Developing students' high levels of thinking is a pathway towards deep learning

Marzano et al. point out that The thinking dimension of learning is to stimulate and maintain the thinking of learning content, regardless of the specific process or skills involved, an individual's thinking can be described as more or less critical or creative. [10] In other words, thinking activities associated with learning are in essence manifestations of higher levels of thinking, which are key components of capacities required of talents in the 21th century. Developing higher levels of thinking also offers the pathway and method to realize balanced development of education. First of all, even small children begin to show capacities for higher levels of thinking. A three-year-old child differs little from a scientist in terms of the nature of thinking. Both acquire knowledge by evoking critical thinking and through observation and experimenting. It is only that the differences in the levels of knowledge and practice result in varying complexity of the contents of thinking. Secondly, failure to develop

higher levels of thinking even in primary schools may be the root cause of major learning difficulties. [11] Thirdly, when teaching high levels of thinking in the classroom, students with higher academic achievements score higher in thinking than those with lower academic achievements. However, the latter have a much higher net benefit than the former. Therefore, teachers should encourage and instruct students at various levels to engage in tasks involving higher levels of thinking. [12]

In the New Taxonomy, higher levels of thinking are a bridge between cognition and self-system. Higher levels of thinking are not only the goal of developing a deeper cognition, but also a pathway to improve the self-system. As shown in Fig. 2, an individual's cognitive system, metacognitive system, and self-system are all evolved in the development of higher levels of thinking. When one attains higher levels of thinking, all of the three systems of thinking are more developed. An individual is able to achieve the coordinated development of cognition and self-system thinking, especially when the metacognition is working. In a word, higher levels of thinking connect and govern the setting and attainment of learning goals for each system, offering the method and feasible pathway to improve oneself. Remarkably, while the New Taxonomy emphasizes developing higher levels of thinking, the roles of lower levels of thinking as cornerstones in learning are also described. However, currently studies rarely discuss the boundaries and connotation of higher levels of thinking and their specific roles and values in humans' high-quality, all-around development. Most researchers tend to classify different levels of cognitive learning based on Bloom's taxonomy and its revision. As mentioned above, teaching higher levels of thinking has encountered several difficulties, such as less clear demarcation of pathways and imbalanced development of different levels due to differences in interpretation, overlaps between the levels of learning, and unclear definition of each level. The empirical study by Wang et al. just proves this point of view.[13] It is highly important that we review the connotation and structure of higher levels of thinking and their values in unifying the ontology and methodology of developing core competences in students by drawing inspiration from the New Taxonomy.

(5) Introspection: The key to deep learning is to develop metacognition

Deep learning manifests as an understanding about knowledge and why, who, where and how to use the knowledge learnt, as well as how to connect the problems propping up in new scenarios to knowledge learnt and solve the problems. Deep learning is a pathway to deep awakening. The latter not only consists of awakening to the learning process and result, but more importantly, an introspection about the interactions between oneself, others, tools and society. Deep awakening is considered the key for achieving self-improvement and all-around development. Deep awakening and self-regulatory capacities required for deep learning echo with what is meant by metacognition, the latter lying at the core of skills in the 21st century and serving as a means to acquire knowledge. In ideal situations, learning is the combination of acquiring concepts, skills, and metacognition. [14] Studies in cognitive psychology have shown that metacognition plays a key role in all cognitive tasks, which range from cognitive behavior to problem solving and to developing professional skills in a specific discipline. [15] A large number of researches have indicated that students with stronger learning capacities tend to be also higher in the level of metacognitive development. Such students have mastered abundant metacognitive knowledge and also the proficiency in reaching learning goals by monitoring the learning process and flexibly implementing various strategies. [16] Therefore, metacognition is the theoretical basis and effective pathway to teach students how to learn. Flavell identified

what he believed to be two elements of metacognition: knowledge of cognition and regulation of cognition. Regulation refers to the monitoring and control of one's cognitive processes during learning. Based on John Hurley Flavel's metacognitive regulation, Marzano treats metacognition as an independent system, known as the metacognition system consisting of four subsystems (see Fig. 1). Marzano singles out the beliefs and self-attributes in metacognition to constitute an independent self-system, a level higher above the metacognition. The above positioning of metacognition is supported in McCombs and Marzano's earlier work: the metacognitive subsystem is a group of more clearly defined executive thinking and self-cognitive abilities that are higher in hierarchy and involved in knowledge interaction. The metacognitive subsystem contributes, to a large extent, to the development of the entire system, especially the metacognitive abilities, such as self-awareness and self-regulation. With the cognitive subsystem giving supports, the metacognitive subsystem and self-system are specifically built in the cognitive development system, making plans and guiding the accomplishment of tasks and goals. Finally, the emotional subsystem of the self-system sustains the learning behaviors and triggers one's emotional perception of self, others and society, which further promotes self-development. Metacognitive teaching method can help students control their learning by defining learning goals and monitoring their learning process. (Nunes & Davis) [17] As seen from above, metacognition determines the levels of awareness, management and regulation of learning goals and has a large bearing on the depth of learning.

6. Conclusion and Prospect

The New Taxonomy is a brand new model of learning oriented towards students' all-around and integrative development. As demonstrated by the model, learning is a process where the self-system, metacognitive system, and cognitive system work synergistically. The learners know, understand, create and transform knowledge by evoking different systems of thought. Besides, Marzano's model embodies the pursuit for integrative, coordinated, and holistic education, revealing the mechanism, nature, goals, and methodology of deep learning.

The model of learning proposed by the New Taxonomy deals with the interaction and development of knowledge, thought and emotions during task accomplishment through learning. First, the self-system makes the decision, evoking the cognitive system to specify goals and strategies. Finally, the cognitive system is elicited to process relevant information, itself interacting with information as well.

Marzano's New Taxonomy is oriented towards developing higher levels of thinking by knowledge comprehension and utilization, by building a self-system, and asserting the controlling role of the metacognitive system.

An individual will finally achieve effective integration and unity of cognition, emotion, motivation, and behavior. In light of the above, the development and improvement of self-system are ultimate goals of deep learning. The self-system determines the motivation, orientation, width, and breath of the cognitive system and defines the object, contents and goals of metacognition..

Higher levels of thinking connect and govern the setting and attainment of learning goals for each system, offering the method and feasible pathway to improve oneself.

Metacognition determines the levels of awareness, management and regulation of learning goals and has a large bearing on the depth of learning.

Mazano's educational goal taxonomy provides a good teaching basis for students' deep learning. However, further exploration is needed on how to combine teaching with different disciplines. In addition, further research is needed on how different disciplines can collaborate to cultivate students to form individuals with core competencies.

References

[1]Lorin W·Anderson et al. A Revision of Bloom's Taxonomy of Educational Objectives [M].Translated by Jiang et al. Beijing: Foreign Language Teaching and Research Press: 2009: 16.
[2] He YM. Cultivating students' key competencies requires a revision of the "three-dimensional curriculum objectives" [J]. Journal of Educational Science of Hunan Normal University, 2016(5):28.
[3] Robert J. Marzano. New Taxonomy of Educational Objectives (Second Edition) [M]. Translated by Gao et al. Beijing: Educational Science Publishing House, 2020:12,3,16,49-52,19.
[4]Robert J. Marzano, John S. Kendall. The New Taxonomy of Educational Objectives (2nd ed.)[M]. CA: Corwin Press, 2007:13,11.
[5] Guo YX, Wu H. Intrinsic attributes of curriculum knowledge and teaching expression [J]. Curriculum, Teaching Material and Method, 2018(8):43-44.
[6] Liu TF. Key competencies of whole person and curriculum design [J]. Global Education,2016(9):16.
[7] Kolb, D.A. Experiential Learning: Experience as the Source of Learning and Development [M]. Translated by Wang and Zhu et al. Shanghai: East China Normal University Press, 2008:191-192.
[8] McCombs, B., & Marzano. R.Putting the self in self-regulated learning: The self as agent in integrating will and skill[J].Educational Psychologist,1990:25(1):53.doi:10.1207/s15326985ep2501_5
[9] Rafael A. Calvo, Sidney K. D'Mello. New Perspectives on Affect and Learning Technologies [M]. Translated by Huang Y. Shanghai: East China Normal University Press, 2020: 3.
[10] Marzano, Robert.(1988).Dimensions of thinking: a framework for curriculum and instruction [M]. Virginia : Assoiciation for Supervision and Curriculum Development,1998:9.
[11] LAUREN B. RESNICK.Education and Learning to Think [M]. D. C. Washington: NATIONAL ACADEMY PRESS, 1987:8.
[12] Anat Zohar & Yehudit J. Dori. Higher Order Thinking Skills and Low Achieving Students: Are They Mutually Exclusive? [J].The Journal of the Learning Sciences,2003,12(2):145-181.
[13]Wang MH. A study on the assessment of higher levels of thinking [D].East China Normal University, 2018:130.
[14] [Germany] Dumont H et al. Translated by Yang et al. The nature of learning: Using research to inspire practice [M]. Beijing: Education & Science Press, 2020:58-59.
[15] [The United States] R. Keith Sawyer. Translated by Xu et al. The Cambridge Handbook of Learning Sciences (Second Edition) [M]. Beijing: Education and Science Press, 2021. 64.
[16] Li Y, Li RM. Cultivating metacognition to teach students how to learn [J].Journal of the Chinese Society of Education, 1999(4):33-34.
[17] Nunes, C., Nunes, M., & Davis, C.Assessing the inaccessible: Metacognition and attitudes[J]. Assessment in Education, 2003, 10(3):377.

Fuzzy Systems and Data Mining IX
A.J. Tallón-Ballesteros and R. Beltrán-Barba (Eds.)

doi:10.3233/FAIA231099

A Novel Personalized Incremental Arrhythmias Classification Method for ECG Monitoring

Zhiyuan LI[a], Yuanyuan TIAN[a], Yanrui JIN[a,1], Xiaoyang WEI[a], Mengxiao WANG[a], Chengliang LIU[a,2] Liqun ZHAO[b] and Xiaoxue YANG[c]
[a]*State Key Laboratory of Mechanical System and Vibration, School of Mechanical Engineering, Shanghai Jiao Tong University, Shanghai 200240, China*
[b]*Department of cardiology, Shanghai First People's Hospital Affiliated to Shanghai Jiao Tong University, Shanghai 200080, China*
[c]*Shanghai University of Finance and Economics, Shanghai200433, China*

Abstract. With the development of smart healthcare, ECG monitoring has become an integral part of remote health care and plays a crucial role in diagnosing arrhythmias. However, the current mainstream ECG automatic diagnosis models lack research on incremental learning with accumulated personal data. Therefore, this paper proposes a personalized incremental learning method for diagnosing arrhythmias to facilitate the development of individualized models for personal users. Initially, the individual's ECG signals are encoded through ECG feature extractor composed of ResBlock, and Bi-LSTM. Subsequently, ECG diagnosis is performed using a personalized classifier tailored to the individual. As the personal data accumulates to a sufficient quantity, the personalized classifier is fine-tuned by incorporating the individual sample dataset with an arrhythmias-priority examplars based on herding, thus enabling the model to adapt to the individual domain. The experimental results demonstrate that the proposed model achieves an accuracy of 87.08% on the CPSC2018 dataset. Moreover, upon personalized incremental fine-tuning on the CPSC2020 dataset, the model's performance improves by over 13% compared to the initial model. Hence, the proposed personalized incremental learning method is effective.

Keywords. ECG, arrhythmias classification, incremental learning, deep learning

[1] Corresponding Author, Yanrui JIN, School of Mechanical Engineering, Shanghai Jiao Tong University, Shanghai 200240, China; E-mail: jinyanrui@sjtu.edu.cn.
[2] Corresponding Author, Chengliang LIU, School of Mechanical Engineering, Shanghai Jiao Tong University, Shanghai 200240, China; E-mail: chlliu@sjtu.edu.cn.

1. Introduction

According to statistics from the World Health Organization (WHO) [1], cardiovascular diseases account for 31% of the global total deaths each year, making it the most significant threat to people's health and lives. Arrhythmia is an important disease within the cardiovascular field, and its diagnosis often requires the aid of electrocardiography to observe the cardiac function. However, interpreting an electrocardiogram (ECG) is a time-consuming and highly specialized task, particularly when it comes to interpreting Holter monitors. This process can often take several days, significantly depleting medical resources and delaying the diagnosis of diseases.

In recent years, research focus has shifted towards methods for automated diagnosis of electrocardiograms (ECG), making it a hot topic of study. Ma [2] developed an end-to-end multi-scale convolutional neural network (CNN) with a Seq-to-Seq architecture to achieve beat-level arrhythmia classification. Hong [3] combined diagnostic knowledge of ECG with a fusion of beat-level and rhythm-level features, constructing a multi-level attention network for atrial fibrillation classification. Awni [4] introduced a 34-layer deep neural network-based single-lead ECG diagnostic model, which was trained and validated on a self-constructed clinical dataset consisting of 53,549 patients and the performance of this model demonstrated clinical cardiologists-level performance.

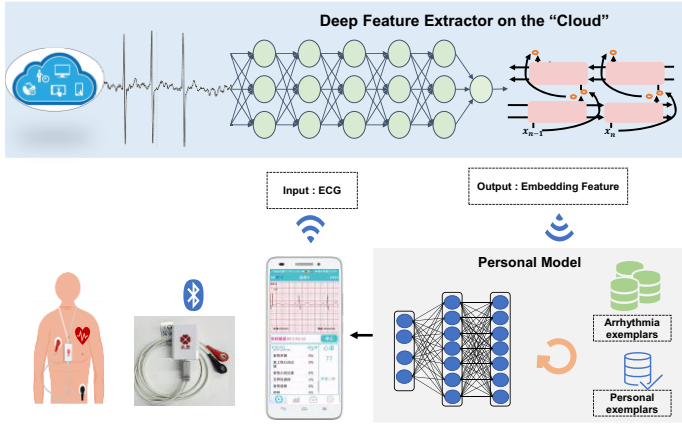

Figure 1. the proposed incremental framework for individual ECG monitoring.

Meanwhile, with the development of smart healthcare and wearable devices, some ECG medical products targeting individual applications have been developed, such as Heart Guardian by LEPU [5] and Apple Watch. These products often adopt a "hardware + cloud" architecture, where ECG data is collected through wearable devices, and automatic diagnosis is performed on the cloud with a diagnostic report returned. Mary [6] designed an IoT system based on ECG classification, deploying adaptive deep neural networks on the cloud for real-time ECG monitoring. S. Karthiga [7] designed an ECG classification framework based on an IoT system and researched the diagnostic performance of SVM, ANN, and CNN in such systems. In this IoT-based system, the models are typically deployed on cloud servers, lacking the adaptive ability to accommodate the varied distribution of ECG signals accumulated from individual users. As a result, personalized updates and accuracy improvement of the models cannot be achieved.

Based on the above issues, this paper proposes a personalized incremental learning approach for the diagnosis of arrhythmias, as shown in Figure 1. The proposed approach consists of three main components: 1) an ECG feature representation module, which provides a reliable representation of ECG based on clinical electrocardiographic data, enabling highly accurate classification of cardiac arrhythmias; 2) a prioritized exemplar selection module, which stores important samples within the model's classification range and personalizes the samples; and 3) a personalized classifier, which is a dedicated classifier for each patient and maps the unified ECG representation to their individual disease domain, achieving adaptive classification.

The main contributions of this paper are as follows:

1) Considering the lack of research on incremental learning in ECG intelligent monitoring systems, we design an ECG monitoring incremental learning approach based on residual convolutional-bidirectional long short-term memory (RCB-LSTM) networks, prioritized exemplars selection and personalized classifiers, which enables proactive optimization and incremental updates of personalized ECG diagnostic models.

2) The prioritized exemplar selection strategy, which combines herding and random strategies, is used to establish both a disease sample set and an individual incremental sample set. This strategy effectively alleviates catastrophic forgetting caused by sample imbalance during the incremental process.

3) The results demonstrate that, for the classification and diagnosis of AF, PAC, and PVC rhythm disorders, this method achieves an accuracy of 87.08% on the CPSC2018 dataset [8], showing significant improvement over existing methods. In terms of incremental learning, with the application of personalized incremental methods, the diagnostic accuracy of the model on the CPSC2020 [9] dataset increases by an average of 13%.

The structure of the paper for the following sections is as follows: the materials and methods are described in Section II. Section III provides a detailed explanation of the experimental setup, results, and analysis. Section IV serves as the conclusion.

2. Material and Method

2.1. Data Preprocessing

Dataset 1 CPSC2018: This dataset was collected from 11 hospitals and consists of 6,877 12-lead ECG records of 10 different diseases (3,178 records from females and 3,699 records from males). Each record has a sampling frequency of 500 Hz and varies in length from 6 to 60 seconds.

Dataset 2 CPSC2020: This dataset includes 10 long-term ECG records from patients with cardiac arrhythmias. Each record has duration of approximately 24 hours and a sampling frequency of 400 Hz. The corresponding PVC and SPB annotation files are provided.

We resample the above dataset to a uniform sampling frequency of 400 Hz and applied a finite impulse response (FIR) bandpass filter to remove noise from the ECG signals. Considering the requirements of wearable monitoring scenarios, we only utilize single-lead (lead II) data [16]. For dataset 1, we align the data length for each record by zero-padding records with fewer than 4,096 points and truncating records with excessive points. For dataset 2, we use a sliding window of length 4,096 with a stride of 5 seconds to extract the data.

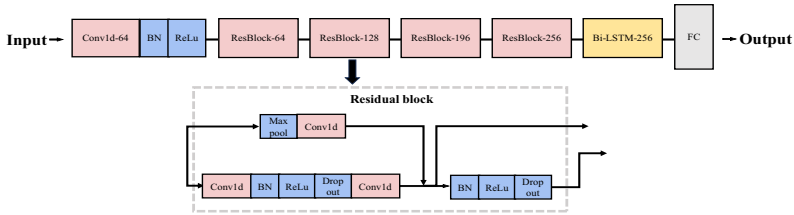

Figure 2. the proposed RCB-LSTM model structure.

2.2. Arrhythmia Classification Model (RCB-LSTM)

The structure of the RCB-LSTM model is shown in Figure 2, which includes a convolutional layer based Res-block [10], as well as a bidirectional LSTM attention layer [11], to achieve feature extraction of the ECG.

2.2.1 Residual Neural Network and Bi-LSTM

Considering the disease characteristics for classification, it is necessary to extract fine-grained semantic features such as P-wave, RR interval, and QRS complex. Therefore, we choose utilize a residual convolutional structure for automatic feature extraction from the cardiac signals. Besides, we employ bidirectional long-short term memory (Bi-LSTM) to model the features extracted by convolutional layers. This approach allows the features to capture both the contextual information and waveform characteristics over time.

2.2.2 Prior Sample Selection Strategy

For the typical disease sample set, we employ a priority sample selection strategy based on herding. For the personal labeled sample set, we use a random sample selection strategy and sample labeling to complete the construction of this sample set.

(a) Herding-based prioritized exemplar selection

Inspired by the work [12], we utilize a priority sample selection strategy based on herding to construct a sample set of typical diseases. This data set will be used to mitigate model catastrophic forgetting when constructing individual incremental models. Firstly, we compute the features of all available samples using a trained model. Then, we calculate the average of each class's data in the sample set. In the third step, m prioritized samples are obtained for each class by traversing according to formula (1).

$$p_k^i \leftarrow \underset{x \in X^i}{\operatorname{argmin}} \left\| \mu^i - \frac{1}{k} \left[F(x) + \sum_{j=1}^{k-1} F\left(p_j^i\right) \right] \right\| \tag{1}$$

(b) Personal Sample Selection and Re-labeling

After accumulating a sufficient amount of personal ECG data, we randomly select a small number of samples from the accumulated personal data. We then query and obtain their corresponding true labels (sample labeling) and store them in the personal priority sample set for personalized model incremental training.

2.3. Personalized Model Training

Once the ECG classification model training is completed, we employ a method of constructing an incremental learning model for personalized ECG monitoring scenarios. In the initial stage t_0, the personalized classifier is initialized with the classifier weights of the initial model. As data is gradually collected, in stage t_1, sample selection and labeling are performed from a large amount of unlabeled ECG records following, resulting in the personal sample set Mp_1. Subsequently, Mp_1 is merged with the disease sample set M, which is used to optimize the classifier. During the training process, we only optimize the classifier using an Adam optimizer with a learning rate of *1e-4* and a batch size of 8 for 5 epochs, allowing the classifier to better adapt to the individual signal distribution.

3. Experimental Results and Discussion

3.1. Experimental Setup

In this section, we conduct two experiments to validate the effectiveness of the proposed arrhythmia classification model and personalized incremental learning method for ECG monitoring. In Experiment 1, we train, validate, and test the RCB-LSTM using a total of 3,244 ECG samples from four categories: Normal, AF, PVC, and PAC, collected from the CPSC2018 dataset. We compare the performance of our model with existing cardiac arrhythmia diagnosis methods. In Experiment 2, we obtain the ECG representation model and initial personalized classifier from the model trained in Experiment 1. We use each record from dataset 2 as individual user data, where the first 50% of each Holter record is selected as the gradually collected personal dataset, while the remaining 50% is used as the individual test set.

Table 1. Comparison classification results on the Test set (CPSC2018).

Model	*Acc*	*Specificity*	*Sensitivity*	*F1 score*	*MCC*
ResNet [14]	72.62%	*90.22%*	*66.41%*	*70.59%*	*0.6327*
VGG [15]	28.62%	*75.00%*	*25.00%*	*12.73%*	*0.000*
ATI-CNN [13]	81.20%	-	-	81.20%	-
Our's	**87.08%**	***95.51%***	***84.08%***	**86.69%**	***0.8256***

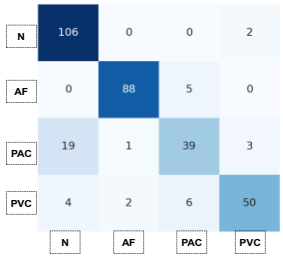

(a) the confusion matrix on the CPSC2018

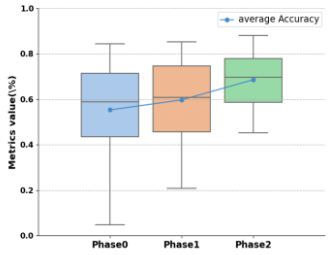

(b) the incremental performance on the CPSC2020.

Figure 3. the experiment results.

3.2. Experiment 1 – RCB-LSTM Classification Results

We divide the dataset into a training set, validation set, and test set in a ratio of 8:1:1. The model is trained for 30 epochs with a batch size of 16 and a learning rate of 0.001. The confusion matrix results on the test set are shown in Figure 3a. Table 1 compares the performance of our model with several existing models, demonstrating that our model achieves better performance. The overall accuracy is 87.08%, with F1 scores of 85.05% for the overall performance. For the four categories, the F1 scores are 89.45%, 95.65%, 69.64%, and 85.47% respectively. Our model outperforms common models by 16.41% Acc and 10.03% F1. Besides, our model outperforms these models in terms of sensitivity, specificity, and Matthews correlation coefficient (MCC).

3.3. Experiment 2 - Personalized Incremental Learning Results

In this experiment, we obtain a well-trained RCB-LSTM based on Experiment 1. We use a herding-based priority sample selection strategy on the CPSC2018 dataset to construct a typical disease sample set for individual incremental updates. For each patient's data in CPSC2020, we perform two-stage incremental learning on the training set. First, we construct the personal dataset using the training set data and conduct the second phase of incremental learning, optimizing the personalized classifier. Then, we test the incremental results on the test set. The specific experimental results are shown in Figure 3b. The "phase0" represents the diagnosis results of the model before personalized incremental learning. After two rounds of incremental learning (“phase 1”, “phase 2”), the average ACC of the model diagnosis increased by 13.3%, demonstrating significant improvement in the incremental learning effect.

4. Conclusion

In this paper, we propose a personalized incremental learning method for automatic arrhythmia diagnosis, which achieves improved model performance in the context of ECG monitoring. This method consists of three main modules: 1) ECG feature extractor based on RCB-LSTM, 2) herding-based typical disease sample selection

strategy and personal sample set, and 3) personalized classifier. The experimental results demonstrate that the proposed classification method achieve an accuracy of 87.07% and an F1 score of 86.69% on the CPSC2018 dataset. Furthermore, using the incremental method on the CPSC2020 dataset results in a 13% improvement in individual ECG monitoring.

Acknowledgements

Funding: This work was supported by China Postdoctoral Science Foundation (Grant No. 2023M732219) and Shanghai Municipal Science and Technology Major Project (No. 2021SHZDZX0102).

References

[1] S. Mendis, P. Puska, B. Norrving, W.H. Organization, et al., Global Atlas on Cardiovascular Disease Prevention and Control, Geneva: World Health Organization, 2011.
[2] Ma C, Lan K, Wang J, et al. Arrhythmia detection based on multi-scale fusion of hybrid deep models from single lead ECG recordings: A multicenter dataset study[J]. Biomedical Signal Processing and Control, 2022, 77: 103753
[3] Hong S, Xiao C, Ma T, et al. MINA: multilevel knowledge-guided attention for modeling electrocardiography signals[J]. arXiv preprint arXiv:1905.11333, 2019.
[4] Hannun A Y, Rajpurkar P, Haghpanahi M, et al. Cardiologist-level arrhythmia detection and classification in ambulatory electrocardiograms using a deep neural network[J]. Nature medicine, 2019, 25(1): 65-69.
[5] Wang B, Liu C, Hu C, et al. Arrhythmia classification with heartbeat-aware transformer[C]//ICASSP 2021-2021 IEEE International Conference on Acoustics, Speech and Signal Processing (ICASSP). IEEE, 2021: 1025-1029.
[6] Mary G A A, Sathyasri B, Murali K, et al. Electrocardiogram signal classification in an IoT environment using an adaptive deep neural networks[J]. Neural Computing and Applications, 2023: 1-10.
[7] Karthiga S, Abirami A M. Deep Learning Convolutional Neural Network for ECG Signal Classification Aggregated Using IoT[J]. Computer Systems Science & Engineering, 2022, 42(3).
[8] Liu F, Liu C, Zhao L, et al. An open access database for evaluating the algorithms of electrocardiogram rhythm and morphology abnormality detection[J]. Journal of Medical Imaging and Health Informatics, 2018, 8(7): 1368-1373.
[9] Wang X, Ma C, Zhang X, et al. Paroxysmal atrial fibrillation events detection from dynamic ECG recordings: The 4th China physiological signal challenge 2021[J]. Proc. PhysioNet, 2021: 1-83.
[10] He K, Zhang X, Ren S, et al. Deep residual learning for image recognition[C]//Proceedings of the IEEE conference on computer vision and pattern recognition. 2016: 770-778.
[11] Hochreiter S, Schmidhuber J. Long short-term memory[J]. Neural computation, 1997, 9(8): 1735-1780.
[12] Rebuffi S A, Kolesnikov A, Sperl G, et al. icarl: Incremental classifier and representation learning[C]//Proceedings of the IEEE conference on Computer Vision and Pattern Recognition. 2017: 2001-2010.
[13] Yao Q, Wang R, Fan X, et al. Multi-class arrhythmia detection from 12-lead varied-length ECG using attention-based time-incremental convolutional neural network[J]. Information Fusion, 2020, 53: 174-182.
[14] Ribeiro AH, Ribeiro MH, Paixão GMM, et al. Automatic diagnosis of the 12-lead ECG using a deep neural network. Nat Commun 2020; 11: 1–9.
[15] K. Simonyan and A. Zisserman, “Very deep convolutional networks for large-scale image recognition,” in ICLR, 2015.
[16] Jin Y., Qin C., Liu J., Liu Y., Li Z., Liu C. A novel deep wavelet convolutional neural network for actual ECG signal denoising. Biomedical Signal Processing and Control, 2024, 87:105480.

Fuzzy Systems and Data Mining IX
A.J. Tallón-Ballesteros and R. Beltrán-Barba (Eds.)

doi:10.3233/FAIA231100

Real-Time Detection for Abnormal Segments of Electrocardiographic Signal During Ewing Test

Xiuwen CHEN[a] and Rongqian YANG[b,1]
[a] *Medical Devices Research & Testing Center, South China University of Technology, Guangzhou, China*
[b] *School of Electronic and Information Engineering, South China University of Technology, Guangzhou, China*

Abstract. Ewing test is often applied to study function of autonomic nerve system. Combining Ewing test and heart rate variability (HRV) is useful for detecting autonomic dysfunction. HRV is an objective physiological signal obtained from electrocardiographic (ECG) signal. However, physical movement, baseline shifting or electrode shedding usually produce abnormal ECG signals. So, it is important to detect abnormal segments of ECG signal. In this study, we proposed an entropy algorithm with a normalized frequency distribution histogram (FDH) to detect abnormal segments of ECG signal during Ewing test in real-time. Experimental results show that this entropy algorithm of normalized FDH is used to test ECG signal of 20 subjects during Ewing test. The detectable rates of abnormal segments of physical movement, baseline shifting, and electrode shedding are 92%, 88%, and 95%, respectively. Due to the high detectable rates and efficiency, this algorithm can widely be used to detect abnormal segments of ECG signal during Ewing test in real time.

Keywords. Electrocardiographic, entropy, Ewing test, frequency distribution histogram

1. Introduction

Ewing test is a standard tool to study the function of autonomic nerve system (ANS) and cardiovascular autonomic reactivity [1]. Ewing test was reported by Ewing in 1982, and it is still being used [2]. It consists of a series of stimulation tests which combined dissimilar occasions. Testing HRV during deep breathing, Valsalva test, and standing up, are probably the most widely used tests [1]. In clinical practice, Ewing test is mainly used for diagnosing diabetic chronic complications such as diabetic cardiovascular autonomic neuropathy [3].

It is useful to combine Ewing test and heart rate variability (HRV) to detecting autonomic dysfunction. HRV is an objective physiological signal obtained from electrocardiographic (ECG) signal [4, 5]. Analyzed from the time domain and frequency domain, HRV parameters can reflect the activity and balance of the

[1] Corresponding Author, Rongqian YANG, School of Electronic and Information Engineering, South China University of Technology, Guangzhou, China; E-mail: rqyang@scut.edu.cn.

sympathetic nervous system (SNS) and parasympathetic nervous system (PNS) [6, 7]. HRV parameters are quantitative assessment indexes of the autonomic nervous system. Therefore, ECG signal collection and analysis during Ewing test have important significance in studying function of the autonomic nerve system or even mental diseases and diabetes [8, 9]. Ewing test is an autonomic multi-states stimulation test, which consists of different body positions and physiological states. Ewing test mainly contains resting state, deep breathing state, Valsalva test state, and standing up state. These four states could reflect different conditions of ANS. PNS and SNS are the two main branches of ANS. The functional balance between PNS and SNS is normal in resting state [10], the activity of PNS increases, and the balance of ANS is broken during deep breathing state and Valsalva state [11, 12]. The activity of SNS increases and activity decreases in PNS during standing up state [13].

Abnormal issues would appear during particular body positions, such as deep breathing and Valsalva test, or even during changing different body positions. Abnormal issues mean physical movement, baseline shifting or electrode shedding usually produce abnormal ECG signals. Abnormal issues are likely to influence ECG signal collecting and then lead to errors in the analysis of ECG signal and calculation of HRV parameters. So, it is important to detect abnormal segments of ECG signal.

There has been research on abnormal ECG signal detection in previous studies. Fook presented a fast critical arrhythmic ECG waveform identification method using cross-correlation and multiple template matching [14]. But this method was only used in arrhythmias detection, which cannot detect abnormal segments of ECG signal result from abnormal issues Ruiz introduced a cross-correlate method for a reference signal and a base signal; the reference signal was the first 0.6 sec segment of the examined ECG signal, and the base signal was the rest of the signal [15]. Patil introduced Fourier transform and wavelet transform to analyze the frequency domain of ECG signal for ECG abnormal conditions detection. The results show that the detection accuracy of this method is about 90% [16]. Frequency domain analysis cannot detect abnormality in real time, as Fourier transform and wavelet transform require longer data to analyze.

However, Ewing test consists of different body positions and physiological states, ECG signal data will change significantly. The previous studies had not focus on detecting real-time abnormal ECG signal segments during Ewing test. In this paper, an algorithm that combines histogram and entropy in real-time and automatically detects abnormal ECG signal segments during Ewing test will be presented. This method could evaluate the efficiency of ECG signal and improve data availability during test conditions.

2. Methods of abnormal ECG signal real-time detection

Physical movement, baseline shifting, or electrode shedding is the main source of abnormal ECG signals during Ewing test. In order to improve effectiveness, abnormal ECG signal is detected when recording ECG signal data. The procedure is divided into three steps: (1) calculates frequency distribution histogram (FDH) of ECG signal per unit length and normalizes FDH; (2) calculate the entropy of the normalized FDH; (3) entropy adaptive and process the next unit ECG signals circularly. The unit ECG signals segment is 1 second of real-time ECG data.

Calculated FDH of unit ECG signal, which is obtained according to the amplitude of unit ECG signal. The FDH concerning the amplitude of ECG signal and frequency of amplitude. And then normalize FDH. The formula of normalization is as follows:

$$p(i)=\frac{r(i)}{\sum_{i=1}^{n} r(i)} \tag{1}$$

where i represents the i class of FDH. The class represents the frequency of FDH. The i range 1 to n, where n is the number of classes in FDH. $r(i)$ represents the cumulative frequency of the i class. $p(i)$ represents the normalized $r(i)$. Discrete probability distribution $\boldsymbol{p}=(p_1, p_2, \ldots, p_n),\ p_i \geq 0,\ i=1 \sim n,\ \sum_{i=1}^{n} p(i)=1$. Abnormal issues of electrode shedding and baseline shifting can be detected by distribution on normalized FDH.

We calculate the entropy of the normalized FDH. The definition of entropy is as follows:

$$H_n(\boldsymbol{p})=-\sum_{i=1}^{n} p(i)\log p(i) \tag{2}$$

$H_n(\boldsymbol{p})$ represents the entropy of the normalized FDH of the unit ECG signal. Entropy is an expression of the disorder or randomness of a system; entropy represents the uncertainty of random variables. The more disordered of the variables, entropy of the variables becomes larger. According to the definition of entropy in Eq. 2, entropy satisfies the inequality as follows:

$$0 \leq H_n \leq \log n \tag{3}$$

The maximum entropy principle implies that the maximum value of $H_n=\log n$ is obtained for the uniform distribution $\tilde{\boldsymbol{p}}=(\frac{1}{n}, \ldots, \frac{1}{n})$. That is to say, the entropy of the noise signal is larger than the normal signal, as the noise signal approaches to the random uniform distribution signal [17, 18]. Compare the entropy of the unit ECG signal to the initial threshold, when entropy is lower than threshold, the unit ECG signal is normal signal. On the contrary, the unit ECG signal is regarded as abnormal segment ECG signal. The first 5 seconds of normal ECG signal of the resting state is used as a template to obtain the initial threshold.

The threshold is adapted, and the next unit ECG signal is processed. Combining the initial threshold and the entropy of the test unit ECG signal, which is calculated in the second step, the threshold is adaptively calculated. The next unit ECG signal is judged as normal or abnormal according to the new adaptive threshold. To verify the detectable rates of this method based on histogram entropy, we used Ewing experiment.

3. Experiment results

3.1. Subjects

Twenty healthy subjects participated in this study. 8 were female and 12 were male, and their mean age was 23.3 ± 2.9 years (age range = 18 to 30 years), their mean height

was 167.4 ± 8.9 cm, their mean weight was 57.5 ± 10.2 kg. All subjects were healthy. None of them reported any history of myocardial infarction, diabetes, arrhythmia, alcohol abuse, epilepsy, and psychiatric illness.

3.2. ECG signal collection

In this study, 10-minute Ewing test is introduced, and ECG signal data is recorded simultaneously. The whole test contains 4-minute resting state, 1-minute deep breathing state, 1.5 minutes Valsalva test state and 2 minutes standing up state. There are 0.5-minute to relax among each state. ECG is recorded in a supine position by using three-limb ECG leads (ECG-B; SAYES, Shenzhen, China) through Red DotTM Ag/AgCl disposable electrodes placed under a sample rate at 500 Hz.

Subjects followed the prompts and did stimulation actions in Ewing test. ECG signals of subjects contained normal segments and abnormal segments. Normal segments of the ECG signal were able to detect R wave through KUBIOS HRV software (version 2.1, released by Biosignal Analytics and Medical Imaging Group) to calculate the HRV signal. Physical movement, baseline shifting or electrode shedding usually produces abnormal ECG signals. For example, in deep breathing state or standing up state, physical movement produced abnormal ECG signal. Abnormal ECG signal could not detect R wave through KUBIOS HRV software. The length of each segment of ECG signal was about 3 to 10 seconds. In the data collection process, ECG signal was detected as a normal or abnormal signal based on the entropy algorithm of normalized FDH in real time.

3.3. Results

20 normal ECG signals and 20 abnormal ECG signals judged by KUBIOS HRV software were detected by the entropy algorithm of normalized FDH in real-time in this experiment. The normal ECG signal waveform during normative Ewing test is shown in Fig. 1. The RR interval extracted from the R wave of ECG signal is shown in Fig. 2. From Fig. 2, we can know that the RR interval changed in different states of Ewing test, the length of RR interval cannot reflect whether ECG signal is normal or not. Therefore, entropy algorithm of the normalized FDH was better than the length of the RR interval to detect abnormal ECG signal.

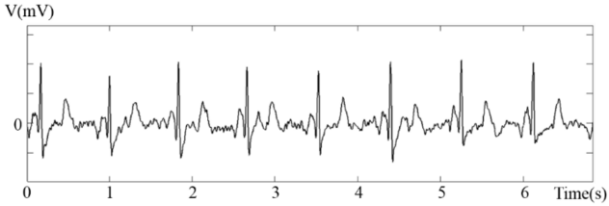

Figure 1. Normal electrocardiographic signal waveform during normative Ewing test

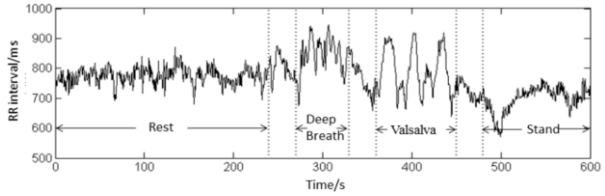

Figure 2. The RR interval of the normal electrocardiographic signal during Ewing test

Fig. 3 shows the effect of abnormal ECG signal detection based on the entropy algorithm of normalized FDH. Fig. 3 (a)-(d) show the detection effect of abnormal segments of ECG signal which were caused by physical movement. Fig. 3 (e)-(f) shows the detection effect of abnormal segments of ECG signal, which were caused by baseline shifting. Fig. 3 (g)-(h) shows the detection effect of abnormal segments of ECG signal, which were caused by electrode shedding. The waveforms marked in red represented abnormal segments of ECG signal. Abnormal ECG signal can be detected by the entropy algorithm of normalized FDH. Fig. 4 shows the abnormal ECG signal was incorrectly marked as normal ECG signal. The reason was the shape of abnormal ECG signal is approximate as the anterior normal ECG signal, the entropy of abnormal ECG signal was slightly less than the threshold.

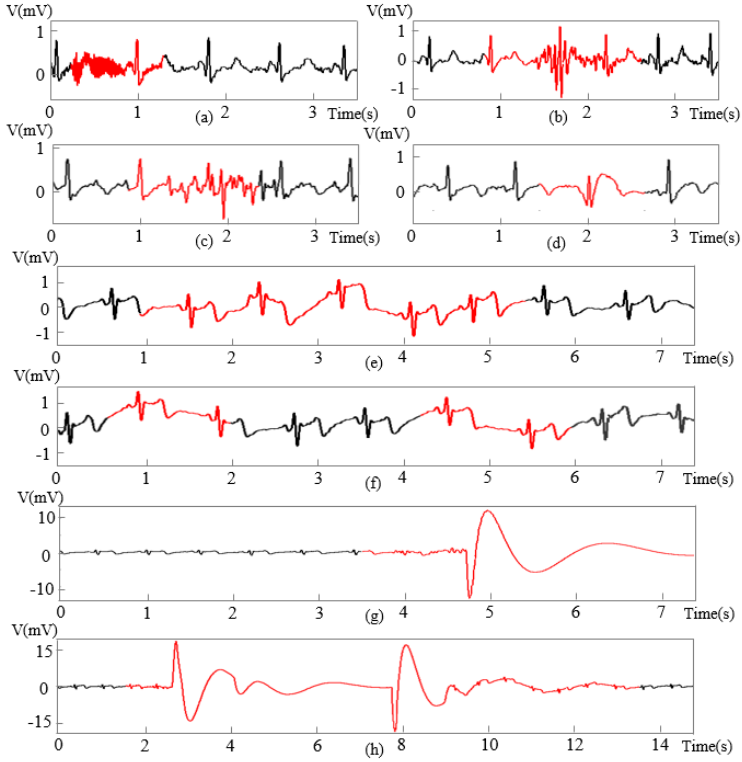

Figure 3. Abnormal segments of electrocardiographic (ECG) signal detection based on entropy algorithm of normalized frequency distribution histogram. (a)- (d) Abnormal segments of ECG signal caused by physical movement detection. (e)- (f) Abnormal segments of ECG signal caused by baseline shifting detection. (g)-(h) Abnormal segments of ECG signal caused by electrode shedding detection.

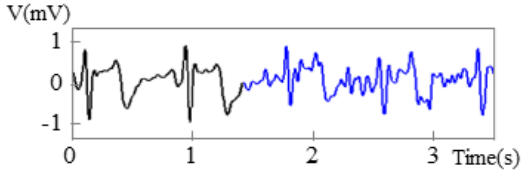

Figure 4. The abnormal ECG signal was incorrectly marked as normal ECG signal

Detectable rates result of abnormal ECG signal segments detection experiment, based on the entropy algorithm of normalized FDH during Ewing test, shown in Table

1. From the 20 subjects, ECG signals were divided into four types by KUBIOS HRV software: ECG signal (n=1200), abnormal segments ECG signal of physical movement (n=320), abnormal segments ECG signal of baseline shifting (n=102), abnormal segments ECG signal of electrode shedding (n=60).

Table 1. Results of abnormal segments of electrocardiographic signal detection experiment

Sample	*n*	Detectable rates
Normal ECG signal	1200	90%
Physical movement	320	92%
Baseline shifting	102	88%
Electrode shedding	60	95%

The results table shows that (1) the detectable rates of normal ECG signal detection algorithm was 90%. (2) 92% of abnormal segments of ECG signal of physical movement were detected. (3) The detectable rate of abnormal segments of ECG signal of baseline shifting detection was 88%. (4) 95% of abnormal segments ECG signal of electrode shedding were detected.

4. Discussion and conclusions

As an effective tool to study autonomic function, Ewing test is widely used in measuring clinical cardiovascular autonomic reactivity. However, physical movement, baseline shifting or electrode shedding usually produces abnormal ECG signals. Therefore, it is important to detect abnormal ECG signal during Ewing test and prompt error when abnormal ECG signal is generated.

In this study, we introduce a method based on the entropy algorithm of normalized FDH to detect abnormal segments of ECG signal during Ewing test. With the principles that the normalized FDH entropy of physical movement ECG signal was higher than normal ECG signal, the FDH of abnormal baseline shifting ECG signal deviated from the baseline, and the FDH of electrode shedding ECG signal was centered on the baseline, abnormal segments of ECG signal can be distinguished from normal ECG signal. This study used the entropy algorithm of normalized FDH to test ECG signal from 20 subjects during Ewing test. The detectable rates of abnormal segments of physical movement, baseline shifting, and electrode shedding are 92%, 88%, and 95%, respectively. In the case of a false positive of the abnormal ECG signal, the entropy was slightly less than the threshold. To increase the detectable rate, threshold improvement is an appropriate way.

In addition, the entropy algorithm of normalized FDH can detect abnormal ECG signal in real-time, this method has high detectable rates and efficiency. When the abnormal ECG signal was detected with this algorithm, subjects were guided to retake the abnormal states after the whole Ewing test, which can improve data availability. With the advantages of simple principles and efficient results, this algorithm was able to be widely used in abnormal segments of ECG signal detection during Ewing test. Further research may improve algorithms to diagnose heart diseases, such as arrhythmia and heart failures.

References

[1] J.G. Dijk, Heart rate variability testing, or listening to a conversation in a foreign language, Clin. Auton. Res. 13(5) (2003) 304-305.
[2] D.J. Ewing, B.F. Clarke, Diagnosis and management of diabetic autonomic neuropathy, Br. Med. J. 285(2) (1982) 916-918.
[3] F.J. Wackers, L.H. Young, S.E. Inzucchi, D.A. Chyun, J.A. Davey, E.J. Barrett, R. Taillefer, S.D. Wittlin, G.V. Heller, Detection of silent myocardial ischemia in asymptomatic diabetic subjects: the DIAD study, Diabetes Care. 27(8) (2004) 1954-1961.
[4] B. Alessandro, D.M. Simpson, N.C. Carvalho, A.R.S. Carvalho, Low-frequency heart rate variability is related to the breath-to-breath variability in the respiratory pattern, Psychophysiology. 51(2) (2014) 197-205.
[5] M. Kikuchi, A. Hanaoka, T. Kidani, G.B. Remijn, Y. Minabe, T. Munesue, Y. Koshino, Heart rate variability in drug-naïve patients with panic disorder and major depressive disorder, Prog. Neuro-psychoph. 33(33) (2009) 1474-1478.
[6] R.E. Kleiger, J.T. Bigger, M.S. Bosner, M.K. Chung, J.R. Cook, L.M. Rolnitzky, R. Steinman, J.L. Fleiss, Stability over time of variables measuring heart rate variability in normal subjects, Am. J. Cardiol. 68(6) (1991) 626-630.
[7] B.L. Henry, A. Minassian, M.P. Paulus, M.A. Geyer, W. Perry, Heart rate variability in bipolar mania and schizophrenia, J. Psychiatr. Res. 44(3) (2010) 168-176.
[8] A.H. Kemp, D.S. Quintana, M.A. Gray, K.L. Felmingham, K. Brown, J.M. Gatt, Impact of depression and antidepressant treatment on heart rate variability: A review and meta-analysis, Bio. Psychiat. 67(11) (2010) 1067-1074.
[9] P. Esposito, R. Mereu, G.D. Barbieri, T. Rampino, A.D. Toro, P.H. Groop, A.D. Canton, L. Bernardi, Trained breathing-induced oxygenation acutely reverses cardiovascular autonomic dysfunction in patients with type 2 diabetes and renal disease, Acta Diabetol. 53(2) (2015) 1-10.
[10] C.V. Russoniello, Y.N. Zhirnov, V.I. Pougatchev, E.N. Gribkov, Heart rate variability and biological age: Implications for health and gaming, Cyberpsychol. Behav. Soc. Netw. 16(4) (2013) 302-308.
[11] P. Chalaye, P. Goffaux, S. Lafrenaye, S. Marchand, Respiratory effects on experimental heat pain and cardiac activity, Pain Med. 10 (2009) 1334-1340.
[12] E.S. Prakash, P.N. Ravindra, Madanmohan, R. Anilkumar, J. Balachander, Effect of deep breathing at six breaths per minute on the frequency of premature ventricular complexes, Int. J. Cardiol. 111(3) (2006) 450-452.
[13] F. Mahananto, T. Igasaki, N. Murayama, Potential force dynamics of heart rate variability reflect cardiac autonomic modulation with respect to posture, age, and breathing pattern, Comput. Biol. Med. 64(1) (2015) 197-207.
[14] F.J. Chin, Q. Fang, T. Zhang, I. Cosic, A fast critical arrhythmic ECG waveform identification method using cross-correlation and multiple template matching, IEEE Engineering in Medicine and Biology Society. (2010) 1922-1925.
[15] J. Ruiz, E. Aramendi, S.R.D. Gauna, A. Lazkano, L.A. Leturiondo, J.J. Gutierrez, Distinction of ventricular fibrillation and ventricular tachycardia using cross correlation, Comput. Cardiol. 30 (2003) 729-732.
[16] R.S. Patil, J.G. Ghodekar, Artificial neural network based system using transform domain methods for ECG abnormality detection, Iete Tech. Rev. 21(6) (2015) 409-416.
[17] S. Guiasu, Information Theory with Applications, first ed., McGraw Hill, New York, 1997.
[18] R. Trandafir, Determination of a discrete distribution with given entropy, Oper. Res. 3(1) (2003) 41-46.

Fuzzy Systems and Data Mining IX
A.J. Tallón-Ballesteros and R. Beltrán-Barba (Eds.)

doi:10.3233/FAIA231101

ECG Quality Assessment Framework by Using Attentional Convolution Neural Network

Yanrui JIN[a], Zhiyuan LI[a], Yuanyuan TIAN[a], Mengxiao WANG[a], Xiaoyang WEI[a], Chengliang LIU[a,1] and Xiaoxue YANG[b,2]
[a] *State Key Laboratory of Mechanical System and Vibration, School of Mechanical Engineering, Shanghai Jiao Tong University, Shanghai 200240, China*
[b] *Shanghai University of Finance and Economics, Shanghai 200433, China*

Abstract. ECG is an important means of diagnosis of arrhythmia. In daily health monitoring, serious noise pollution, reverse leads connection, and so on make cannot meet the requirements of subsequent automatic diagnosis. Thus, it is of great significance to further evaluate the ECG quality and screen out the ECG that meet the requirements of subsequent diagnosis. However, complex interference factors affect the quality of the signal and has brought the huge challenge to quality assessment. Additionally, the current algorithms depend on the wave detection, which also brings additional cumulative error. Meanwhile, the current algorithms cannot intuitively present the attention degree to ECG signals during the assessment process. This paper proposes a novel method (ACNN) for evaluating the ECG quality. ACNN directly targets the whole ECG signal and does not detect the waveform of the ECG signal. Then, ACNN uses convolutional blocks to extract the deep features and designs a novel attention layer to enhance the beneficial features of the results. Finally, the fully connected layer is employed for obtaining the final quality evaluation. Compared with existing methods, ACNN obtains better performance, with 100.0% sensitivity, 83.33% specificity and 98.0% accuracy, which shows ACNN can be applied in clinical scenarios.

Keywords. Attention layer; Convolution block; ECG quality assessment framework

1. Introduction

Arrhythmias are the important type of cardiovascular disease, which leads to about 31% of global deaths [1, 2]. Electrocardiogram (ECG) is utilized as a main noninvasive tool for detecting arrhythmia [3, 4]. However, in the actual signal acquisition process, the ECG signal is prone to be affected by serious noise pollution, lead drop, and incorrect placement of lead electrodes. At this time, the user should be prompted to resample in time, rather than input the signal into the subsequent automatic diagnosis

[1] Corresponding Author, Chengliang LIU, School of Mechanical Engineering, Shanghai Jiao Tong University, Shanghai 200240, China; E-mail: chlliu@sjtu.edu.cn.

[2] Corresponding Author, Xiaoxue YANG, Shanghai University of Finance and Economics, Shanghai 200433, China; E-mail: xxyang@sufe.edu.cn.

system for analysis, which will cause a waste of diagnostic resources. Therefore, accurate ECG quality assessment methods have attracted lots of attention in recent years.

Generally, traditional machine learning (ML) algorithms and deep learning (DL) algorithms are there are two main methods for ECG quality assessment. Traditional ML algorithms need characteristics according to expert knowledge of artificial extraction [5-11], then the evaluation characteristics of input into the subsequent classifier to complete the quality evaluation of ECG signal.

With the development of DL technology, many researchers have shown that DL algorithms can be based on many automatic feature extractions, greatly improve the ECG signal quality evaluation model of performance. Compared with traditional ML methods, DL algorithms can automatically acquire many features to represent signal quality. Nowadays, some researchers have utilized DL algorithms for assessment. Zhao et al. [12] proposed a new noise suppression method by using Convolutional neural network (CNN). Huerta et al. [13] used continuous wavelet transform for converting heart electric signal to measure and utilized the time-frequency representation into CNN to acquire efficient quality evaluation model. Zhang et al. [14] designed a new type of cascade CNN, which contained two parts: the first part is used for distinguishing the interference type and the second part is utilized for determining the interference degree, to complete ECG quality assessment.

The current DL algorithms cannot intuitively display attention during the evaluation process, that is, the current researchers at home and abroad have not tried to study which parts of ECG signal the DL model focuses on to have an impact on the final quality evaluation. Therefore, the current DL-based quality assessment algorithms belong to completely black box model. This paper builds a novel attentional convention neural network (ACNN) for quality assessment, which is devoted to improving the quality assessment performance and studying the model interpretability to a certain extent. ACNN targets the whole ECG signal and does not detect the whole ECG waveform to avoid superposition error caused by waveform detection.

2. Materials

This paper assesses ECG quality from PhysioNet/CINC challenge 2011 (Challenge2011) [15]. Each ECG recording in Challenge2011 are collected by 500 Hz sampling frequency and 16 bits resolution with 10s duration. All recordings are manually annotated by technicians, nurses, and volunteers with varying degrees of training, for more accurate labeling. Similar to literature [16, 17], data set A in Challenge2011 is used to verify the proposed quality assessment mode. In addition, ECG recordings in the dataset are uniformly segmented for obtaining the corresponding ECG, and the sampling length of each ECG signal is 4096 sampling points. The Challenge2011 dataset contains 225 electrocardiographic signals with poor quality and 773 electrocardiographic signals with good quality.

3. Methodology

3.1. Overview of ACNN

Figure 1 represents the flow chart of ACNN in this paper. The acquired ECG signal from wearable device is directly input to the network input layer and then is fed into the construction of a complete quality assessment of ECG signals based on CNN and attention mechanism model, and then complete the quality evaluation of ECG signal.

Figure 1. Overview of ACNN

3.2. Overview of ACNN

CNN was proposed in the article [18] and has been applied in medical applications [19-21], fault diagnosis [22], and other fields in recent years. CNN can learn deep representation from labelled data and acquire deep features for classifying. Therefore, this paper utilizes CNN for extracting features.

Attention mechanisms are commonly used in image analysis and natural language processing. Recently, the attention mechanism has also been widely used in medical diagnosis [23, 24]. However, we find that the use of attention mechanisms in ECG quality assessment have not been investigated by researchers. Therefore, this paper designs a novel attention mechanism combined with CNN to realize the ECG signals quality evaluation. Figure 2 illustrates the flow of the designed attention mechanism.

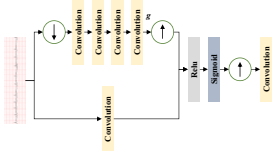

Figure 2. The flow of the designed attention mechanism

For a given input data X, as well as the input data through a series of convolution operation for gating characteristics of g. The gating feature g is to facilitate the co-production of the corresponding attention weight in combination with X in the subsequent structure. Equation (1) and (2) represent that attention weights are obtained through a series of convolution operations using input data and gating features. It is worth noting that convolution operation is introduced here instead of other operations. On this basis, the output of the weight and dimension of the input data consistent attention and input data Elementwise operation, should be to obtain the final phase characteristics.

$$q_{att} = \psi\left(\sigma_1\left(W_x * x + W_g * g\right)\right) \tag{1}$$

$$\alpha_i = \sigma_2\left(q_{att}\left(x_i, g_i\right)\right) \tag{2}$$

3.3. The Architecture of ACNN

Figure 3 depicts the proposed the structure of the network. ACNN consists of four convolutional blocks, an attention layer, and a fully connected classification layer. Convolution block includes convolution layer and pooling layer. The convolution layer is mainly to various nonlinear data processing, and then to extract the ECG signal data contained in the deep hidden features. It is worth noting that since the ECG signal is a one-dimensional discrete signal, a one-dimensional convolutional layer is used here. Additionally, to simplify the model structure and improve training and testing speed, the pooling layer directly adopts the maximum pooling operation. Four convolutional blocks are applied for automatically extracting the deep feature, and many extracted deep features are input into the attention layer. The attention weight is used to multiply the deep features to highlight the significant features and relatively suppress the features that are not related to the final quality assessment task. Then, the weighted features are flattened and input into a fully connected layer for nonlinear processing to enhance the nonlinear characteristics of the features, and finally output to the classifier for classification.

Finally, ACNN is trained by a workstation, which contains two NVIDIA GTX 1080 GPUs. Further, this paper selects Adam optimizer [25] as optimizer and 256 as batch size.

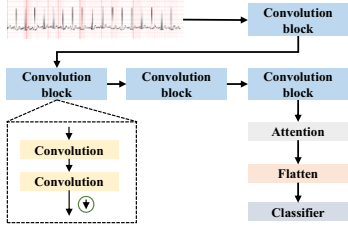

Figure 3. The architecture of the proposed ACNN

4. Results and discussion

In this paper, we randomly select 80%, 10% and 10% of the data in the Challenge2011 dataset as the training set, validation set and test set. To further compare the effectiveness of the proposed ACNN, we compare ACNN with the latest existing methods. The same Challenge2011 dataset is used for comparison to allow for reasonability. In this paper, specificity, sensitivity and accuracy are utilized for evaluating the model assessment performance.

4.1. Model Performance

In comparison experiments, ACNN is compared with existing methods to verify the superiority of ACNN. Figure 4 indicates the comparison results with existing methods based on Challenge2011 dataset. From Figure 4 you can see, compared with the existing methods [16, 17, 26-30], ACNN creatively combines CNN with the attention layer, uses multi-layer convolutional layers to automatically extract many deep features, and enhances effective features and inhibits invalid features through the attention layer. After manual correction of wrong label, ACNN obtained better performance with 100%

sensitivity, 83.33% specificity and 98% accuracy, which indicates that ACNN have potential to practical application.

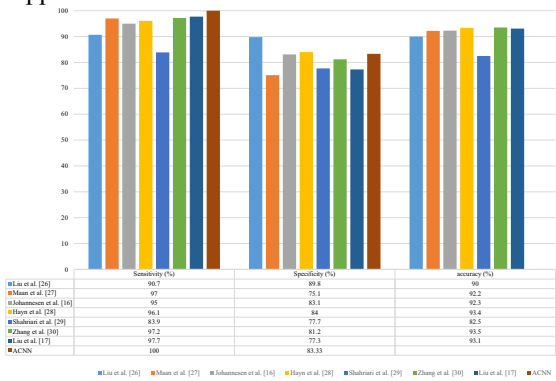

	Sensitivity (%)	Specificity (%)	accuracy (%)
Liu et al. [26]	90.7	89.8	90
Maan et al. [27]	97	75.1	92.2
Johannesen et al. [16]	95	83.1	92.3
Hayn et al. [28]	96.1	84	93.4
Shahriari et al. [29]	83.9	77.7	82.5
Zhang et al. [30]	97.2	81.2	93.5
Liu et al. [17]	97.7	77.3	93.1
ACNN	100	83.33	

Figure 4. Comparison results with the existing methods

4.2. Model Interpretability

The proposed attention layer is used to improve the model quality assessment performance, and to establish the relationship between the classification results and the ECG signals. Figure 5 shows the attention weight of the ECG signal. Compared to the ECG signals in other regions, the middle segment of the input ECG signal is most severely disturbed, and its waveform could not be applied in the subsequent analysis at all. The attention weight provided by the attention layer also shows the greatest degree of attention in this region, that is, enhances the features of this region. On the contrary, although the interference of ECG signals in other regions is not as great as that in the middle region, they are also greatly interfered, and the attention layer also shows a greater degree of attention.

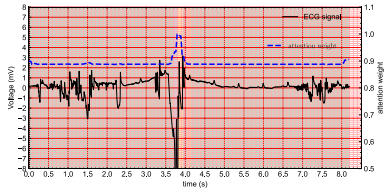

Figure 5. The effect of attention weights of ECG recording

5. Conclusion

This paper designs a relatively interpretable, automated, and accurate method for ECG quality assessment. ACNN uses CNN to extract deep representations from ECG signals. Additionally, this paper proposes attention layer to enhance the useful deep features and suppress the invalid deep features. Further, the attention layer can intuitively show the attention degree of the model to different time periods on the ECG signal. And then, by comparing with the existing methods, ACNN achieves better performance, with 100.0% sensitivity, 83.33% specificity and 98.0% accuracy. Therefore, ACNN has superior quality assessment performance and a certain interpretability ability, which

represents that it has the potential to be used as signal quality assessment system in clinical centers.

Acknowledgements

This work was supported by National Postdoctoral Program for Innovative Talents (No. BX20230215), China Postdoctoral Science Foundation (No. 2023M732219) and Shanghai Municipal Science and Technology Major Project (No. 2021SHZDZX0102).

References

[1] S. Mendis, P. Puska, B. Norrving, W.H. Organization, et al., Global Atlas on Cardiovascular Disease Prevention and Control, Geneva: World Health Organization, 2011.
[2] Mehra, R. 2007. Global public health problem of sudden cardiac death. Journal of Electrocardiology, 40, S118-S122.
[3] B.J. Maron, R.A. Friedman, P. Kligfield, B.D. Levine, S. Viskin, B.R. Chaitman, P.M. Okin, J.P. Saul, L. Salberg, G.F. Van Hare, Assessment of the 12-lead ECG as a screening test for detection of cardiovascular disease in healthy general populations of young people (12–25 years of age) a scientific statement from the American Heart Association and the American College of Cardiology, Circulation 130 (2014) 1303–1334
[4] J. Jin, Screening for cardiovascular disease risk with ECG, JAMA 319 (2018) 2346.
[5] Al-Fahoum AS, Quality assessment of ECG compression techniques using a waveletbased diagnostic measure. IEEE Transactions on Information Technology in Biomedicine. 2006, 10: 182-191.
[6] Li Q, Rajagopalan C, Clifford G D, A machine learning approach to multi-level ECG signal quality classification. Comput. Methods Programs Biomed. 2014, 117: 435–447.
[7] Clifford G D , Behar J , Li Q, et al. Signal quality indices and data fusion for determining clinical acceptability of electrocardiograms. Physiol. Meas. 2012, 33: 1419.
[8] Johannesen L, Galeotti L. Automatic ECG quality scoring methodology: mimicking human annotators. Physiol. Meas. 2012, 33: 1479.
[9] Zhang Y, Wei S, Zhang L, et al. Comparing the performance of random forest, SVM and their variants for ECG quality assessment combined with nonlinear features. J. Med. Biol. Eng. 2019, 39: 381–392.
[10] Andreotti F, Grer F, Malberg H, et al. Non-invasive Fetal ECG Signal Quality Assessment for Multichannel Heart [J]. IEEE Transactions on Biomedical Engineering. 2017, 64: 2793 – 2802.
[11] Kalkstein N, Kinar Y, Na'Aman M, et al. Using Machine Learning to Detect Problems in ECG Data Collection. 2011 Computing in Cardiology, IEEE, 2011.
[12] Zhao Z, Liu C, Li Y, et al. Noise rejection for wearable ECGs using modified frequency slice wavelet transform and convolutional neural networks. IEEE Access. 2019, 7: 34060–34067.
[13] Huerta A, Martínez-Rodrigo A, González V B, et al. Quality assessment of very longterm ECG recordings using a convolutional neural network. Proceedings of the 2019 E-Health and Bioengineering Conference (EHB), IEEE. 2019, pp. 1–4.
[14] Zhang Q, Fu L, Gu L, A cascaded convolutional neural network for assessing signal quality of dynamic ECG [J]. Comput. Math. Methods Med. 2019, 7095137, doi:10.1155/2019/7095137.
[15] Silva I, Moody G B, Celi L. Improving the quality of ECGs collected using mobile phones: the physionet computing in cardiology challenge 2011. Proceedings of the 2011 Computing in Cardiology, IEEE. 2011: 273–276.
[16] Jin Y., Li Z., Qin C., Liu J., Liu Y., Zhao L., Liu C. A novel attentional deep neural network-based assessment method for ECG quality. Biomedical Signal Processing and Control, 2023, 79:104064.
[17] Liu G, Han X, Tian L, et al. ECG quality assessment based on hand-crafted statistics and deep-learned S-transform spectrogram features. Computer Methods and Programs in Biomedicine, 2021, 41.
[18] K. Fukushima, Neocognitron: a self organizing neural network model for a mechanism of pattern recognition unaffected by shift in position. Biological cybernetics, 36 (1980) 193-202.
[19] Y. Jin, J. Liu, Y. Liu, L. Zhao, C. Liu, A Novel Dual-scale Dilated Convolutional Neural Network for Heartbeat Classification, 2021 4th International Conference on Information Communication and Signal Processing (2021).

[20] Jin Y., Qin C., Liu J., Liu Y., Li Z., Liu C. A novel deep wavelet convolutional neural network for actual ECG signal denoising. Biomedical Signal Processing and Control, 2024, 87:105480.
[21] Y. Jin, C. Qin, J. Tao, C. Liu, An accurate and adaptative cutterhead torque prediction method for shield tunneling machines via adaptative residual long-short term memory network. Mechanical Systems and Signal Processing, 165 (2022) 108312. https://doi.org/10.1016/j.ymssp.2021.108312.
[22] Y. Jin, C. Qin, Y. Huang, C. Liu, Actual bearing compound fault diagnosis based on active learning and decoupling attentional residual network. Measurement, 173 (2021).
[23] Hong S, Xiao C, Ma T, et al. MINA: Multilevel Knowledge-Guided Attention for Modeling Electrocardiography Signals. 20th International Joint Conference on Artificial Intelligence (IJCAI-19), 2019.
[24] Liu F, Zhou X, Wang T, et al. An Attention-based Hybrid LSTM-CNN Model for Arrhythmias Classification. 2019 International Joint Conference on Neural Networks, 2019.
[25] D.P. Kingma, J. Ba, Adam: a method for stochastic optimization, arXiv preprint arXiv: 1412.6980, (2014).
[26] Liu C, Li P, Zhao L, et al. Real-time signal quality assessment for ECGs collected using mobile phones. Proceedings of the Computing in Cardiology At: Hangzhou, IEEE. 2011: 357–360.
[27] Maan A C, Zwet E, Man S, et al. Assessment of signal quality and electrode placement in ECGs using a reconstruction matrix. Proceedings of the Computing in Cardiology, IEEE. 2011: 289–292.
[28] Hayn D, Jammerbund B, Schreier G. QRS detection based ECG quality assessment. Physiol. Meas. 2012, 33: 1449.
[29] Shahriari Y, Fidler R, Pelter M M, et al. Electrocardiogram signal quality assessment based on structural image similarity metric. IEEE Trans. Biomed. Eng. 2017, 65: 745–753.
[30] Zhang J, Wang L, Zhang W, et al. A signal quality assessment method for electrocardiography acquired by mobile device. Proceedings of the 2018 IEEE International Conference on Bioinformatics and Biomedicine (BIBM), IEEE. 2018, pp. 1–3.

Fuzzy Systems and Data Mining IX
A.J. Tallón-Ballesteros and R. Beltrán-Barba (Eds.)

doi:10.3233/FAIA231102

Global Warming Analysis Based on Long Short-Term Memory and Extreme Gradient Boosting Feature Engineering Models

Haoxuan LIU[a], Lanhua ZHANG[a] and Yujuan LI[a,1]
[a] *School of Medical Information and Engineering, Shandong First Medical University and Shandong Academy of Medical Sciences, Tai'an, 271016, China*

Abstract. Global warming brings negative impacts to people's lives. In order to explore the factors that contribute to global warming and predict temperature changes, engineering models using Long Short-Term Memory and Extreme Gradient Boosting algorithms were built. With the global year-average temperature data after preprocessing by Python, the mathematical models were computed to discover the factors that influence the global temperature change with temperature parameters and fluctuations of anomalies, including the global average temperature, carbon dioxide concentration, solar activity, etc. With the multi-variable linear differential equation, we conclude that the global climate is determined by a variety of factors. The results implied that a high concentration of greenhouse gases had a very limited impact on climate change, and solar activity had the greatest impact on global temperature.

Keywords. Global warming, XGBoost model, LSTM model, gray correlation analysis, feature engineering

1. Introduction

Global change is the term used to describe worldwide changes in the functioning of the Earth system due to natural and human factors, including changes in atmospheric and ocean circulation, biogeochemical cycles, the water cycle, the carbon cycle, resources, land use, urbanisation and economic development. Global warming is a prominent symbol of global change, and the Greenhouse Effect, resulting from massive emissions of greenhouse gases caused by human activities [1].

The causes of global warming include both natural factors and human activities. Solar activity, volcanic activity and multi-scale vibration within the climate system may affect global or regional temperature changes [2]. The influence of solar activities on climate change also includes ultraviolet radiation and solar magnetic field. One view is that with the solar activity cycle, solar irradiance changes little but ultraviolet radiation changes greatly, and the influence of ultraviolet radiation changes may be amplified through the absorption of the ozone layer in the middle atmosphere. Another

[1] Corresponding Author, Yujuan LI, School of Medical Information and Engineering, Shandong First Medical University and Shandong Academy of Medical Sciences, Tai'an, 271016, China; E-mail: 13605487932@163.com.

view is that cosmic rays contribute to the formation of condensation nuclei, and condensation nuclei can increase cloud cover [3].

Global warming is caused by human activities mainly through changes in the properties of the underlying surface, changes in certain components of the atmosphere [4], and anthropogenic heat release. However, natural factors have also had a great influence on the inter-annual temperature changes in the last hundred years [5].

The essence of machine learning is to simulate human learning through computers to find and learn the hidden laws behind them from a large amount of data, so as to achieve the purpose of simulation and prediction [6]. It has been widely used in commercial fields such as search engines, machine translation, spam filtering, speech recognition and other commercial fields, and also provides new methods for academic research in climate research [7, 8] and other fields. In recent years, with the increasing maturity of machine learning techniques, temperature prediction techniques based on machine learning have also been developed.

Long Short-Term Memory is a neural network that has the ability to remember long and short-term information. LSTM was first proposed by Hochreiter & Schmidhuber [9] in 1997 resulting in a more systematic and complete LSTM framework with the rise of deep learning. Another deep learning algorithm is XGBoost which was proposed by Tianqi Chen in 2016 [10] based on GBDT.

In the field of meteorology, Le [11] et al. achieved spatial and temporal prediction of air pollution at the second level with high accuracy by using LSTM with convolutional neural network to model a wide range of environmental variables. Nidhin [12] et al. constructed the ConvLSTMSR model by combining ConvLSTM with SR module to analyse the most climatically diverse India with better ability to predict extreme events. Seyed Matin Malakouti [13] used LSTM to predict the climate characteristics with a variety of LSTM types. Li [14] et al. combined three algorithms of linear regression, random forest and Extreme Gradient Boosting to establish a model for estimating biomass based on forest types. There are advantages in aboveground estimation, and the XGBoost and RF models significantly improve the estimation accuracy.

In order to further characterise the global warming scenario and to assist non-specialists in understanding global climate change trends, we disucuss the global temperature change and the related factors affecting the temperature using LSTM and XGBoost based on feature engineering analysis and other models for mutual validation to provide some references to ameliorate the global climate change and to achieve the healthy and green sustainable development strategy.

2. Methods

2.1. Model Assumptions

Suppose that the Earth's ecosystem can remain relatively stable in the future, and there will be no major or serious plate movements and geological activities. Assuming that there will be no major breakthroughs in human science and technology, and the main energy used in the future will still be similar to the existing energy sources. Assume that no new anthropogenic and non-anthropogenic factors affecting the Earth's climate will emerge in the short term. Suppose that the data used in this paper are true and reliable and can accurately reflect the rule of global climate change.

2.2. Data sources and Algorithm Models

In order to make a comprehensive and detailed analysis of the global warming problem, we construct LSTM and XGBoost feature engineering analysis model based on temporal features to carry out controlled experiments. Visualisation of the data can lead to a clearer and more explicit conclusion related to global warming.

The datasets are the Berkeley dataset (http://berkeleyearth.lbl.gov/) and the NOAA dataset (https://psl.noaa.gov/data/) from which data on temperature changes in 100 cities from 1833 to 2013. 81 of them are cities in the northern hemisphere and 19 are cities in the southern hemisphere. Some temperature data of some months or years is missing, and the Lagrangian interpolation method was used to interpolate the missing values. It is worth mentioning that there is a unit of measurement of temperature anomalies in meteorology as the distance level. The distance level is the difference between one of a series of values and the mean, divided into positive and negative. The mean temperature distance level is the difference between a series of mean temperatures and the total mean temperature. An increase in the mean temperature level is an indication that this difference has increased and that there is an anomaly in the temperature for the corresponding time period.

2.3. Work flow of our works

For LIST model, we standardize the data, build the model structure, define three LSTM layers, and output a fully connected layer. We adopt the average temperature of each month in the first 5 years as the input parameter of the model with the input dimension of (60, 1).

For XGBoost model, a feature engineering model based on time series and machine learning algorithm is designed. We take the average temperature of each month around the world to reflect the global temperature. Then we calculate the average monthly temperature values. To filter classification problems, machine learning strategies can be used. After filtering the collected data, we use the XGBoost algorithm in machine learning for testing.

About the realization in programming, the data set is read first, and then we use Tensorflow and Keras libraries in deep learning to predict it. The data sets are used for training and regression prediction. After that, the time series analysis is carried out to derive the model parameters and formulas. Finally, we compare the accuracy of the two models by calculating R2_score.

3. Results

With the LSTM model, the forecast results simulating the past temperature to predict the temperature from October 2022 to December 2100 are as follows (Fig. 1, Fig. 2):

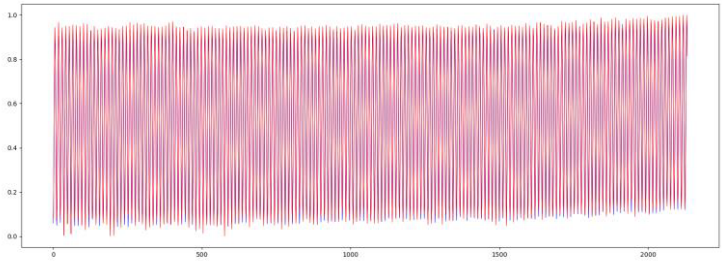

Figure 1. LSTM's past temperature fitting map

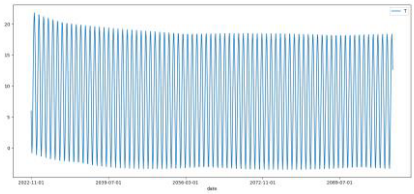

Figure 2. LSTM's temperature forecast image

The LSTM model is a very good fit to reflect the temperature change. According to the forecast results, the average monthly temperature in 2050 and 2100 will be below 20 degrees Celsius. Using Python programming, the temperature around the year 2135 was predicted to reach 20 °C. The visualization results are as follows (Fig. 3):

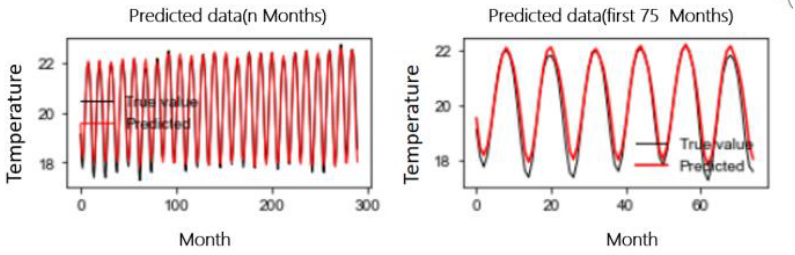

Figure 3. The temperature prediction in 2135 with LSTM model

For XGBoost feature engineering based on ARIMA, the system automatically searched for the optimal parameter based on AIC information criterion with the temperature variable. The model result was the ARIMA model (0,1,1) test table based on 2 different data (Fig. 4).

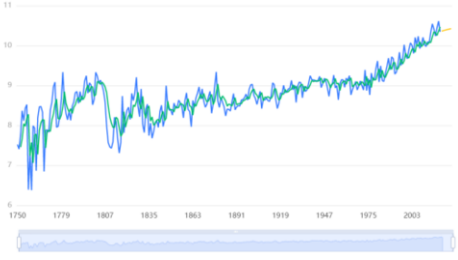

Figure 4. The simulation results of ARIMA model

Based on the time series-feature project, the searched data set is used. The prediction results are as follows (Fig. 5):

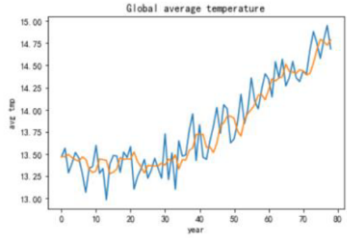

Figure 5. The training effects of XGBoost model

After the training, we can get a more accurate estimate of future global temperature with the XGBoost algorithm. The prediction results are as follows (Tab. 1):

Table 1. The prediction results with XGBoost model

Date	Time series	Feature Engineering
2050	15.205377	15.2560791
2100	15.968084	16.0983494

It is concluded that the average temperature at the global observation point in 2050 or 2100 does not reach 20.00°C.

Combining the running global temperature with future temperature projections, we can conclude that global temperatures have been and will continue to rise.

4. Discussion

According to the future global temperature forecast by LSTM and XGBoost feature engineering models, the global temperature will reach 20 ℃ around 2135. The temperature will not exceed 20℃ before then. Compared with model accuracy, the R2 value of LSTM is 0.97, which is higher than 0.95 of XGBoost feature engineering. Therefore, LSTM has higher accuracy in long-term temperature prediction than XGBoost feature project. At the same time, both models confirm that global temperatures have been and will continue to rise.

Through the quadratic curve fitting of K sequence and E2 sequence, the resulting parameters are shown in Table 2, and the fitting degree is obviously high. It is clear that the last hundred years the CO2 concentration is relatively strict rise. This is very different from the wild fluctuations in temperature changes, that is, the effect of greenhouse gases on the climate will be much smaller than previously estimated. Although the greenhouse gases will contribute to global warming, it is not feasible to describe global temperatures in terms of greenhouse gas concentrations alone.

Table 2. Concentration fitting table of greenhouse gas concentration growth curve

parameters	K	E2
R^2	0.999	0986
p	313.643	282.873
a	0.012	00.083
b	0.796	0.002

In addition to greenhouse gases, solar activity also has an effect on temperature. The influence of solar activity on global temperature is mainly reflected in the change of irradiance. To quantify the total solar energy received at the top of the atmosphere, one of the most commonly used metrics is total solar irradiance (TSI). Therefore, we use TSI as a variable and use TSI sequence to describe solar activity. We choose the T I sequence made by Kopp et al. (hereinafter referred to as T sequence for reference) and

the sequence made by ourselves as J sequence. Pearson coefficient was used to show the correlation between TSI and global temperature. Comparing T series and J series, the Pearson correlation coefficient of the two sequences was 0.540, indicating a certain correlation with global temperature change. Compared with solar activity, the Pearson correlation coefficient of J series and T series is 0.846, indicating a high correlation between TSI and global mean temperature. Since solar activity has a large influence on the global average temperature, it should be limited to about 11 years based on the results. At the same time, according to the solar anomaly sequence data from 1854 to 2004, it can be found that the direction of J-M series and T-M series is the same in most areas, but the variation trend is slightly different in some areas, which may be affected by other factors such as geological activities. Using TSI to examine solar activity and discuss its relationship with global temperature changes, we can learn that solar activity has a high correlation with long-term changes in global temperature, and that solar activity has increased significantly over the past 100 years, which is consistent with global temperature increases. This suggests that solar activity has a significant influence on global temperature change.

The epidemic also has an impact on global warming. Energy-related CO2 emissions rose 6% to 36.3 billion tonnes in 2021, the largest year-on-year increase in energy-related CO2 emissions on record. The 2021 rebound reverses a decline of nearly 1.9 billion tonnes in emissions due to the 2020 pandemic. On top of this, CO2 emissions in 2021 are about 180 million tonnes higher than pre-pandemic levels in 2019. As global warming worsens, massive emissions of greenhouse gases will reduce the benefits of previous carbon cuts. Therefore, we believe that while COVID-19 related shutdowns have mitigated global temperature change to some extent, the impact of subsequent resumption of work on global temperature change has not only made up for the reduced emissions during the pandemic, but the emissions will further exacerbate global warming.

Based on the analysis of the global surface air temperature and the CO2 concentration TSI series in recent years, we draw a conclusion different from the traditional view:

(1) In the periodicity of global temperature, the current global temperature is at the peak of the wave and the change of global temperature in the last hundred years may not be caused by the increase of greenhouse gas concentration.

(2) Global climate is determined by a combination of factors, none of which can fully describe changes in temperature.

(3) Significant increases in greenhouse gas concentrations caused by human activities since the industrial revolution have had a very limited impact on climate change. It can neither determine the trend of global climate change nor fully describe global climate change.

(4) Solar activity has the greatest influence on global climate, and TSI has a strong correlation with the sliding average series of temperature.

5. Conclusions

In this paper, the LSTM and XGBoost feature engineering models were constructed for the prediction and analysis of global temperature from the perspective of global warming. It is concluded that the global temperature will not be more than 20 degrees before 2100, but the temperature will continue to rise. The mathematical methods and models used have undergone several iterations and the processing logic is excellent.

The use of Lagrange interpolation to interpolate the missing values in the data can improve the prediction accuracy of the data.

Based on the analysis results, we have found that emissions of greenhouse gases such as carbon dioxide were only part of the causes of rising global temperatures, and that solar activity has the greatest effect on global temperature. Other natural factors, such as geological and oceanic activity, also have some effect on temperature, but the effect cannot yet be estimated due to uncertainties. At the same time, the research and discussion in this paper is still incomplete. Although solar activity is strongly correlated with global temperature, there are still some periods unclear such as the negative correlation, moreover, the reasons for that are not yet known. Meanwhile, what effect CO2 concentration has on global temperature and how many other natural factors play roles in global temperature change need to be further discussed.

Acknowledgements

This research was supported by the Students' project for innovation and entrepreneurship training program of Shandong First Medical University and Shandong Academy of Medical Sciences (No.2022104391602), the Youth Science Foundation Cultivation Support Program of Shandong First Medical University and Shandong Academy of Medical Sciences (No. 202201-036) and the Tai'an Science and Technology Innovation Development Project (No. 2022GX019).

References

[1] Change IPOC. Climate Change 2014—Impacts, Adaptation and Vulnerability: Regional Aspects. Cambridge University Press, Cam-bridge, 2014.
[2] Ring MJ, Lindner D, Cross EF, e t al. Causes of the Global Warming Observed since the 19th Century. Atmospheric and Climate Sciences, 2012, 02(4). DOI:10.4236/acs.2012.24035.
[3] Stover SK, Mcarthur LB, Mabry ML. Presenting Global Warming and Evolution as Public Health Issues to Encourage Acceptance of Scientific Evidence. Bioscene, 2013, 38(2):3-10.
[4] Change IPOC. Climate Change: The IPCC Scientific Assessment. Press Syndicate of the University of Cambridge, New York, 1990.
[5] Berlie AB. Global Warming: A Review of the Debates on the Causes, Consequences and Politics of Global Response. Journal of Geography, 2018(2018):144-164.
[6] Uche-Anya E, Anyane-Yeboa A, Berzin TM, et al. Artificial intelligence in gastroenterology and hepatology: how to advance clinical practice while ensuring health equity. Gut, 2022, 71(9):1909-1915.
[7] Mi Xiaoxi, Tang Aitao, Zhu Yuchen, et al. Machine learning: A potential powerful tool for materials science research. Materials Reports, 2021, (15): 1-18.
[8] Ma Tinghuai, Mu Qiang, Tian Wei, et al. Research on meteorological data mining. Journal of Wuhan University of Technology, 2010, 32(16): 110-114.
[9] Hochreiter S, Schmidhuber J. Long short-term memory. Neural Computation, 1997, 9(8):1735-1780.
[10] Chen T, Guestrin C. XGBoost: A Scalable Tree Boosting System. ACM, 2016. DOI:10.1145/2939672.2939785.
[11] DUC LE V, CHA SK. Real-time Air Pollution prediction model based on Spatiotemporal Big data. The ternational Conferece on Big data, IoT and Cloud Computing, Guangzhou, 2018.
[12] Harilal N, Singh M, Bhatia U. Augmented Convolutional LSTMs for Generation of High-Resolution Climate Change Projections. IEEE Access, 2021(9):25208-25218.
[13] Malakouti, Seyed. Utilizing time series data from 1961 to 2019 recorded around the world and machine learning to create a Global Temperature Change Prediction Model. Case Studies in Chemical and Environmental Engineering. 2023,7:100312.
[14] Li Y, Li C, Li M, et al. Influence of Variable Selection and Forest Type on Forest Aboveground Biomass Estimation Using Machine Learning Algorithms. Forests, 2019, 10(12). DOI:10.3390/f10121073.

Fuzzy Systems and Data Mining IX
A.J. Tallón-Ballesteros and R. Beltrán-Barba (Eds.)

doi:10.3233/FAIA231103

Evaluate the Correlation Between Electrocardiogram Age and Cardiovascular Disease Using a 12-lead ECG Dataset

Yuanyuan TIAN[a,b], Xiaoyang WEI[a,b], Zhiyuan LI[a,b], Yanrui JIN[a,b,1], Mengxiao WANG[a,b], Liqun ZHAO[c], Xiaoxue YANG[d] and Chenliang LIU[a,b,2]

[a] *State Key Laboratory of Mechanical System and Vibration, School of Mechanical Engineering, Shanghai Jiao Tong University, Shanghai 200240, China*
[b] *MoE Key Lab of Artificial Intelligence, AI Institute, Shanghai Jiao Tong University, Shanghai 200240, China*
[c] *Department of Cardiology, Shanghai First People's Hospital Affiliated to Shanghai Jiao Tong University, Shanghai 200080, China*
[4] *Shanghai University of Finance and Economics, Shanghai 200433, China*

Abstract. Leveraging deep learning and vast clinical datasets can reveal crucial, previously indiscernible patterns in electrocardiogram (ECG) records, enhancing the diagnosis and assessment of cardiovascular diseases. In this study, we first construct a large-scale clinical 12-lead ECG dataset, then exploit the potential of deep learning models to analyze ECG data and identify a significant link between a patient's cardiovascular health and the discrepancy between their chronological (CHR) age and the age as predicted from ECG data. Through analyzing ECG records, the research determines correlations between predicted ECG age and CHR age in different populations. The results demonstrate ECG age is strongly correlated with CHR age only in the normal population, while the correlation is weaker in the cardiovascular disease population. Further analysis showed that when the ECG age is higher than the CHR age, the individual has a higher risk (the average is 1.64 times higher) of developing various types of cardiovascular disease. Conversely, if the ECG age is lower, they tend to have a lower risk (the average is 0.72 times lower). This evidence suggests that the difference between the ECG age and the CHR age can be viewed as a marker for cardiovascular health.

Keywords. Electrocardiogram, Age prediction, Deep learning, Cardiovascular disease

1. Introduction

Electrocardiogram is the most commonly used non-invasive test for assessing cardiovascular disease (CVD). Cardiologists can infer whether a patient has a specific disease by analyzing feature points and waveforms in the ECG[1]. Although this

[1] Corresponding Author, Yanrui JIN, School of Mechanical Engineering, Shanghai Jiao Tong University, Shanghai 200240, China; E-mail: jinyanrui@sjtu.edu.cn.
[2] Corresponding Author, Chengliang LIU, School of Mechanical Engineering, Shanghai Jiao Tong University, Shanghai 200240, China; E-mail: profclliu@163.com.

method is time-consuming and laborious, with the recent development of end-to-end models, efficient diagnosis of electrocardiograms with deep learning models has achieved great success [2-3]. However, ECG signals may often hide subtle signals and patterns that do not conform to traditional knowledge and are not recognizable to the naked eye [4]. Therefore, it is meaningful to use deep learning, along with large-scale clinical datasets, to explore information that is not intuitively reflected on the ECG and to analyze some features or knowledge not yet discovered by humans.

It is known that neural networks can predict a person's age based on an ECG [5-6]. We assessed whether the discrepancy between the ECG age and the CHR age could represent the cardiovascular health status and be related to cardiovascular disease. We collected ECG test records from hospital emergency room visits over four years, retaining only one ECG record per patient to avoid "cross-contamination". We trained a model based on a one-dimensional convolutional neural network with 12-lead ECG signals as input and the patient's actual age as a label. The correlation between ECG age and CHR age in different populations was then evaluated in unseen ECG recordings, and the difference between the two was used as a marker of cardiovascular health. The groups with differences greater than 8 or less than -8 were used as experimental groups, and the group with differences between -8 to 8 as the control group. The relationship between the different types and heart disease was evaluated using relative risk and odds ratio.

The experimental results show that among the normal population, there is a high correlation between the predicted age and actual age, while among the CVD population, the correlation between the predicted age and actual age is low. The risk of developing myocardial infarction, atrial fibrillation, and atrial flutter is 1.18, 1.37, 2.07, 1.64, and 1.92 times higher, respectively, for individuals whose predicted age is 8 years older than their actual age than those with comparable predicted and actual ages. Conversely, individuals whose predicted age is 8 years younger than their actual age have respectively 0.96, 0.67, 0.61, 0.55, and 0.82 times the risk of developing ST-T changes, conduction block, myocardial infarction, atrial fibrillation, and atrial flutter than those with comparable predicted and actual ages. The conclusion is that the risk of developing cardiovascular disease is higher when the ECG age is higher than the CHR age, and lower when the ECG age is lower than the CHR age. There is a significant correlation between the difference in ECG age and CHR age, and cardiovascular disease.

2. Methods

2.1. Data Sources and Study Population

We collected records of 12-lead electrocardiogram tests conducted at Shanghai First People's Hospital, affiliated with Shanghai Jiao Tong University, from January 2018 to March 2021, totaling 162,622 records. The ECG sampling rate was 500 Hz, with lengths ranging from 500 to 133,500. As shown in Fig. 1, we first excluded patients under 16 years old and over 90 years old and retained only one electrocardiogram record for patients with multiple cardiac examination records to avoid "cross-contamination" when dividing datasets. Furthermore, we also discarded records with significant interference and invalid test results. Based on this, we divided the data into training and test sets at a ratio of 7:3. From the training set, we selected 10,000 records

for model verification, and the remaining records were used for model training. In the test set, we filtered out electrocardiogram records diagnosed by doctors as normal(NORM), ST-T change(ST_T), atrial fibrillation(AF), conduction block(CD), myocardial infarction(MI), and atrial flutter(AFL) for further analysis.

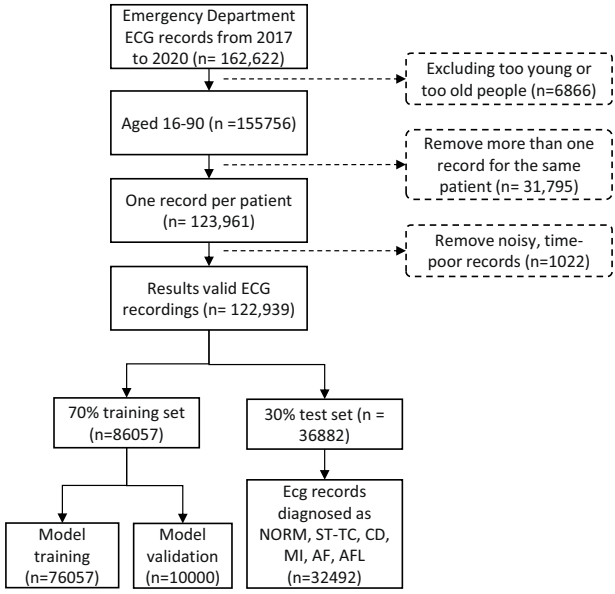

Figure 1. Clinical dataset inclusion and exclusion criteria.

2.2. Overview of Algorithm

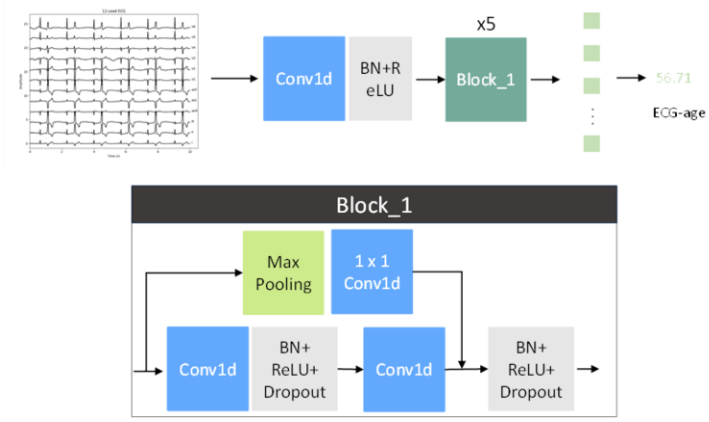

Figure 2. ECG age predicted convolution neural network architecture.

We implemented a one-dimensional Resnet using the Pytorch framework [7]. For electrocardiogram samples in the training set, those shorter than 4096 are padded with zeros on both ends, and those longer than 4096 are truncated to get a fixed-length electrocardiogram signal, which is then fed into the model. The model's output is the predicted age for the record. As shown in Fig. 2, the model c comprises an initial

convolutional layer succeeded by five sets of residual structures, each embodying two convolution layers. After each convolution layer, batch normalization is applied to rescale the output and then goes through the Rectified Linear Unit (ReLU) as an activation mechanism, with Dropout applied after that. The convolution kernel size is 17, with the five residual blocks having 64, 128, 196, 256, and 320 respectively, and the feature numbers are 4096, 1024, 256, 64, and 16 respectively. In the residual connections[7], max pooling and convolution with a kernel size of 1 are added to make the size match the signal in the main branch. Our approach makes use of the Adam [7] optimizer, which is applied with an initial learning rate set to 0.001, aiming at the minimization of the weighted mean squared error. During training, if the loss of the validation set does not improve over seven consecutive epochs, the learning rate is reduced by a factor of 10. With a total span of 50 epochs for the training, we opt for the model that exhibits the most superlative performance on our validation set throughout the optimization. This chosen model is then deployed as our final one.

2.3. Models Evaluation and Statistical Methods

For the ECG records in the test set, we use the model to obtain their ECG age, then evaluate the correlation between ECG age and CHR age in different populations using the mean square error (MSE) and Pearson correlation coefficient(PCC), thereby indirectly assessing the accuracy of the model's predicted ECG age compared to the actual age. We assume that the disparity between the predicted ECG age and the chronologic age may serve as a biomarker for a cardiac condition, we will classify the disparity between the predicted ECG age and chronologic age into three categories: greater than 8, less than -8, and between -8 and 8. We used relative risk (RR) [8] and odds ratio(OR)[9] to assess the relationship between this cardiac status marker and cardio-related diseases. RR refers to the risk of disease occurrence in an exposed group relative to a non-exposed group in an experiment, calculated as RR= (incidence rate of the exposed group/incidence rate of the non-exposed group). OR refers to the chance of disease occurrence in the exposed group relative to the non-exposed group in an experiment, calculated as OR= (exposed number/non-exposed number in case group)/(exposed number/non-exposed number in the control group). In this study, the exposed groups refer to the two groups with age differences greater than 8 and less than -8, and the non-exposed group is the one with an age difference between -8 and 8.

3. Results

3.1. Age Estimation

Since the ECG age predicted convolution neural network's output is a continuous variable, we compute the statistics of the absolute error, as well as the population correlation. Fig. 3 illustrates a scatter plot of the ECG age vs. CHR age in various populations. For the test dataset, the average absolute error in the normal population is 7.99±10.34 years, with a PCC of 0.80; in the population with ST-T changes, the average absolute error is 8.60±11.03 years, with a PCC of 0.76; in the population with conduction blockages, the average absolute error is 8.57±10.85 years, with a PCC of 0.66; in the population with myocardial infarctions, the average absolute error is 9.74±11.16 years, with a PCC of 0.62; in the population with atrial fibrillation, the

average absolute error is 8.76±10.94 years, with a PCC of 0.38; in the population with atrial flutter, the average absolute error is 9.89±11.94 years, with a PCC of 0.38, as shown in Table 1. This suggests that although the model is trained uniformly across all populations when ECG age in different populations, the correlation and error between the predicted age and the CHR age are smaller in the normal population, but the ECG age and the CHR age of the population with CVD have a lower correlation and a larger error.

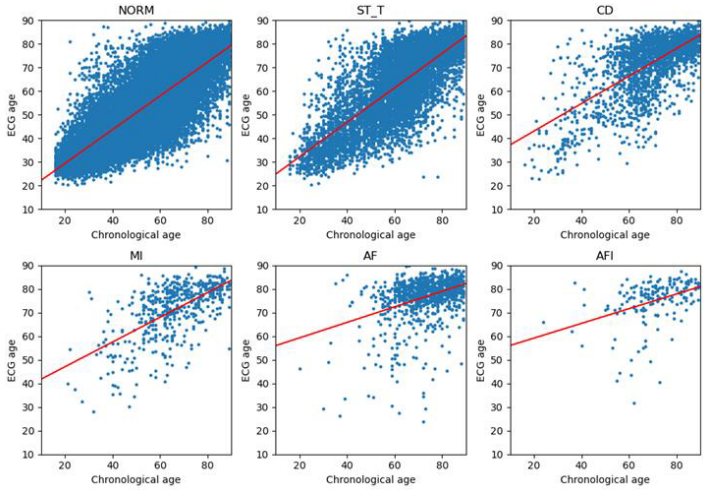

Figure 3. ECG age vs. CHR age in different populations. The red line is the correlation fitting line.

3.2. Diff-age as a Cardiovascular Marker

Table 1. MAE, PCC, RR, OR values of ECG age and CHR age among different populations

Population	MAE	PCC	RR of ECG-Age Exceeds CHR Age by >8	RR of ECG-Age Less Than CHR Age by 8	OR of ECG-Age Exceeds CHR Age by >8	OR of ECG-Age Less Than CHR Age by 8
NORM	7.99±10.34	0.8	0.93	0.99	0.72	0.97
ST_T	8.60±11.03	0.76	1.18	0.96	1.24	0.95
CD	8.57±10.85	0.66	1.37	0.67	1.4	0.66
MI	9.74±11.16	0.62	2.07	0.61	2.1	0.61
AF	8.76±10.94	0.38	1.64	0.55	1.67	0.55
AFL	9.89±11.94	0.38	1.92	0.82	1.92	0.83

Based on the analysis above, we assume that there is a correlation between the difference in ECG age and CHR age, and CVD. As shown in Tab. 1, the risk of diseases such as ST-T changes, conduction block, myocardial infarction, atrial fibrillation, atrial flutter, etc., in those whose predicted age is 8 years older than their actual age, is respectively 1.18, 1.37, 2.07, 1.64, and 1.92 times as high as that of those whose predicted age is equivalent to their actual age. While for those whose predicted age is 8 years less than their actual age, the risk of such diseases is respectively 0.96, 0.67, 0.61, 0.55, and 0.82 times of those of equivalent predicted and actual age group.

In addition, in several groups of people with cardiovascular diseases, the OR values for the group whose predicted age is 8 years greater than their actual age are all greater than 1, indicating a positive correlation, while the OR values are all less than 1 for groups of people whose predicted age is less than their actual age by 8 years, which shows a negative correlation. From this, we can reasonably speculate that the older the ECG age compared to actual age, the greater the risk of cardiovascular disease. Conversely, the younger the ECG age compared to the actual age, the smaller the risk of cardiovascular disease.

4. Conclusion

In summary, we explored the correlation between the difference in electrocardiogram age and actual age with several cardiovascular diseases. First, we built a real clinical dataset with ECG as the input and the actual age as the predicted value to train a deep learning model and then used this model to predict the ECG age on unseen ECGs. There is a strong correlation between the predicted age and the actual age in the normal population, but there is a smaller correlation and larger error in the population with cardiovascular diseases. The risk of cardiovascular diseases is higher in the population where the predicted age is 8 years older than the actual age and lower in the population where the predicted age is 8 years younger than the actual age.

Acknowledgement

This project is supported by China Postdoctoral Science Foundation (Grant No. 2023M732219) and Shanghai Municipal Science and Technology Major Project (No. 2021SHZDZX0102).

References

[1] E. Merdjanovska and A. Rashkovska, “Comprehensive survey of computational ECG analysis: Databases, methods and applications,” Expert Syst. Appl., vol. 203, p. 117206, Oct. 2022, doi: 10.1016/j.eswa.2022.117206

[2] “Automatic diagnosis of the 12-lead ECG using a deep neural network | Nature Communications.” https://www.nature.com/articles/s41467-020-15432-4 (accessed Jul. 28, 2023).

[3] A. Y. Hannun *et al.*, “Cardiologist-level arrhythmia detection and classification in ambulatory electrocardiograms using a deep neural network,” *Nat. Med.*, vol. 25, no. 1, Art. no. 1, Jan. 2019, doi: 10.1038/s41591-018-0268-3.

[4] K. C. Siontis, P. A. Noseworthy, Z. I. Attia, and P. A. Friedman, “Artificial intelligence-enhanced electrocardiography in cardiovascular disease management,” *Nat. Rev. Cardiol.*, vol. 18, no. 7, pp. 465–478, Jul. 2021, doi: 10.1038/s41569-020-00503-2.

[5] Z. I. Attia *et al.*, “Age and Sex Estimation Using Artificial Intelligence From Standard 12-Lead ECGs,” *Circ. Arrhythm. Electrophysiol.*, vol. 12, no. 9, p. e007284, Sep. 2019, doi: 10.1161/CIRCEP.119.007284.

[6] A. O. Ladejobi *et al.*, “The 12-lead electrocardiogram as a biomarker of biological age,” *Eur. Heart J. Digit. Health*, vol. 2, no. 3, pp. 379–389, Sep. 2021, doi: 10.1093/ehjdh/ztab043.

[7] E. M. Lima *et al.*, “Deep neural network-estimated electrocardiographic age as a mortality predictor,” *Nat. Commun.*, vol. 12, no. 1, p. 5117, Aug. 2021, doi: 10.1038/s41467-021-25351-7.

[8] L. Hernandez *et al.*, “Multimodal tensor-based method for integrative and continuous patient monitoring during postoperative cardiac care,” *Artif. Intell. Med.*, vol. 113, p. 102032, Mar. 2021, doi: 10.1016/j.artmed.2021.102032.

[9] W.-Y. Ko *et al.*, "Detection of Hypertrophic Cardiomyopathy Using a Convolutional Neural Network-Enabled Electrocardiogram," *J. Am. Coll. Cardiol.*, vol. 75, no. 7, pp. 722–733, Feb. 2020, doi: 10.1016/j.jacc.2019.12.030.

Fuzzy Systems and Data Mining IX
A.J. Tallón-Ballesteros and R. Beltrán-Barba (Eds.)

doi:10.3233/FAIA231104

Multi-Class Arrhythmia Classification and R-Peak Detection Method of ECG Signal Based on One-Dimensional U-Net with Skip-Connection and Data Augmentation

Yamin LIU[a], Hanshuang XIE[a,1], Jiayi YAN[a], Zhen WANG[a], Mengna ZHENG[a], Fan WU[a] and Yun PAN[b]
[a] *Research and Development Department, Hangzhou Proton Technology Co. Ltd., Hangzhou, China*
[b] *College of Information Science and Electronic Engineering, Zhejiang University, Hangzhou, China*

Abstract. Automatic arrhythmia analysis techniques and QRS detection provide convenience for the prevention and diagnosis of cardiac disease. The existing studies generally study arrhythmia classification and QRS recognition separately, which requires two different models and may result in time and resource wasting. To realize the goal of arrhythmia classification and R-peak detection of electrocardiograms at the same time, we proposed a method for multi-class arrhythmia classification and R-peak detection method based on one-dimensional U-net with skip-connection and data augmentation. First, the ECG signals were preprocessed by filtering and segmentation, and the ECG annotations were also processed into pixel labels of equal length. Then, we applied data augmentation techniques such as changing gain, adding noise, and flipping signals up and down to increase the diversity of the data. Finally, a modified one-dimensional U-net with skip-connection layers was built to adaptively extract deep features and to detect the arrhythmia type and R peaks of ECG at the same time. We set up an 8-category experiment using five publicly available datasets, and the experimental results show that the macro average F1 value is 94.57%, which is over 4.3% and 3% higher than that of original U-net and the skip-connection U-net without data augmentation, respectively. Meanwhile, the F1 of R-peak detection is 99.64%.

Keywords. ECG, arrhythmia classification, R-peak detection, 1-D U-net, data augmentation

1. Introduction

Cardiovascular diseases are one of the major diseases that threaten human life [1]. Therefore, a rapid and accurate diagnosis of arrhythmia is of great importance for the prevention and treatment of heart disease. The electrocardiogram (ECG) has been widely used for cardiovascular disease diagnosis as physiological signals generated by the heart's excitement.

In recent years, with the rapid development of artificial intelligence techniques, researches on arrhythmia classification methods based on machine learning continue to emerge. Compared to the limitations of traditional machine learning [2-4], deep learning always has better performance. Xu et al. [5] first divided ECG signals into single heartbeat and then use deep neural network (DNN) for end-to-end arrhythmia classification. Similarly, Acharya, et al [6] utilized a deep convolutional neural network (CNN) to automatically identify different categories of heartbeats in ECG signals. The division of a single heartbeat is simple, but it may cause the loss of the rhythm

[1] Corresponding Author, Hanshuang XIE, Research and Development Department, Hangzhou Proton Technology Co. Ltd., Hangzhou, China; E-mail: hanshuang.xie@protontek.com.

information of the preceding and following heartbeats. To avoid this problem, L. -H et al. [7] proposed a novel classification method for arrhythmia that uses three-heartbeat ECG signals based on one-dimensional CNN. The rationale for using recurrent neural network (RNN) in ECG analysis lies on its ability to interpret the idea of time. They can hence learn complex temporal dynamics within time-varying data. In this way, Lu et al. [8] proposed a gated recurrent unit (GRU) and decision tree fusion model to explore the problem of arrhythmia recognition and to improve the credibility of deep learning methods. Luo et al. [9] proposed an arrhythmia classification method based on a hybrid convolutional recurrent neural network (CRNN) for the time-series signal of ECG. The above methods are used to identify ECG arrhythmia from a classification point of view. Importantly, the prediction models are based on ECG signal readouts with single arrhythmic conditions. However, there are always contain mixed arrhythmic conditions in real-life. Hence, Oh et al. [10] proposed an improved U-net model, which is usually used in the semantic segmentation domain to perform beat-wise analysis of ECG segments of different lengths. Although the above methods provide some solutions for ECG arrhythmia diagnosis, there are still problems. For example, the input ECG signal of these models is usually one or three heartbeats. Even in [10], the ECG signals segment is only 2.7 seconds, which contains about three to five heartbeats. In the absence of fragmented rhythm information, certain arrhythmia categories may be difficult to classify, such as normal beats and atrial premature contraction.

To solve such problem mentioned above, we propose an ECG arrhythmia multiple classification and R-peak detection method based on data augmentation and U-net with skip-connection, for convenience, we call it SDA U-net. In detail, we split the ECG signal into consecutive 30-second segments, introducing effective information among the segments while retaining the rhythmic information of the heartbeat. We verify the proposed method on five public datasets and the results show that the method has good performance in terms of precision, recall, and F1 score.

2. Proposed Method

2.1. Data Description

The ECG arrhythmia recordings used in this paper are obtained from 5 public databases: St Petersburg INCART 12-lead Arrhythmia Database (INCART12) [11], MIT-BIH Arrhythmia Database (MIT-BIH) [12], Sudden Cardiac Death Holter Database (SCDHD) [13], MIT-BIH Long-Term ECG Database (MIT-BIH LTDB) [12] and European ST-T Database (ESTT) [14].

We use the heartbeats processing methods in [15] as reference, the heartbeats are divided into eight classes and represented by eight labels. Table 1 shows the number of heartbeats of each type in the reconstructed database.

Table 1. Number of heartbeats

Type	Number	Our label	Data label
Baseline	-	BG	-
Normal	905679	N	N
Bundle branch block beat	62861	B	L, R, B
Atrial premature contraction	11273	A	A, a, J, S
Premature ventricular contraction	140508	V	V, r
Fusion of ventricular and normal beat	18433	F	F
Supraventricular escape beat	3518	AE	E, j, n
Ventricular escape beat	1248	VE	E
Question	27322	Q	/, f, q, ?, 0

2.2. Data Preprocessing

First, due to the sampling rate of the 5 datasets is different, we resampled all signals to 200 Hz. The optimal lead of the multi-lead data is selected according to the criterion of minimum abnormal interference and the signal is as smooth as possible. For example, the lead of a raw ECG signal in MIT-BIH is {V5, II} shown in the left two blue signals in Figure 1, after the optimal lead selection algorithm, the sorted lead is {II, V5} shown in the right two red signals in Figure 1, in this case, the lead II is our selected signal. Second, we segment ECG signals into 30 seconds as one data sample. At the same time, ECG labels are also processed into pixel labels of equal length as shown in Figure 2. Specifically, we take the labeled peak R as the base point, then take the time before and after 0.1 seconds of R peak as the label of this beat. BG, N, B, A, V, F, AE, VE, Q are mapped to {0, 1, 2, 3, 4, 5, 6, 7, 8} as shown in Figure 2. During model training, the pixel labels are converted into one-hot labels. Third, we apply a 7-level wavelet transform with db6 to remove the electromyographic noise information and baseline drift of ECG data. Figure 3 shows the ECG signal comparison before and after filtering. Finally, the data set is divided according to the ratio of approximately 8:1:1 for the training set, validation set, and test set.

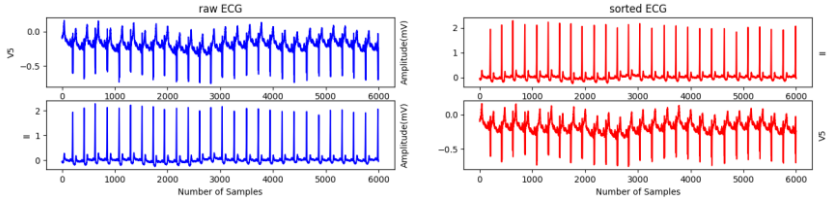

Figure 1. The leads of ECG signal in MIT-BIH are sorted before and after

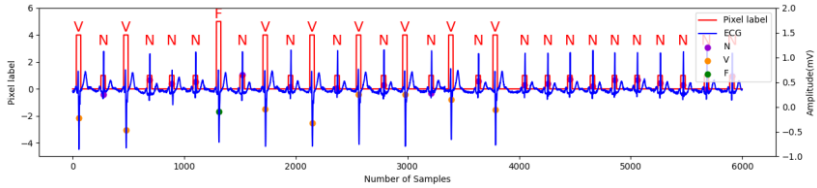

Figure 2. The ECG signal and pixel label

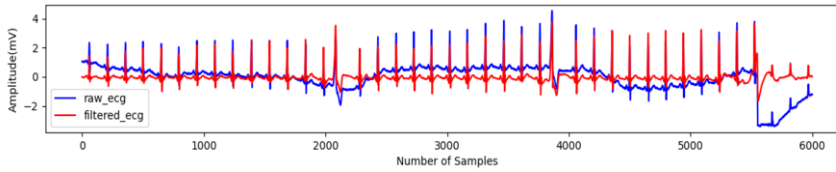

Figure 3. The ECG comparison before and after filtering, blue: before filtering, red: after filtering

2.3. Data Augmentation

To enrich the information of ECG data, we apply data augmentation before model training. Specifically, the data augmentation includes methods such as changing gain, adding noise, and flipping signals up and down as shown in Figure 4. The purpose of changing the gain of ECG signals is to avoid missed R peaks of small amplitude. The reason of adding noise is to enhance the robustness of the model. The signal is flipped up and down to enrich the data distribution of the data set.

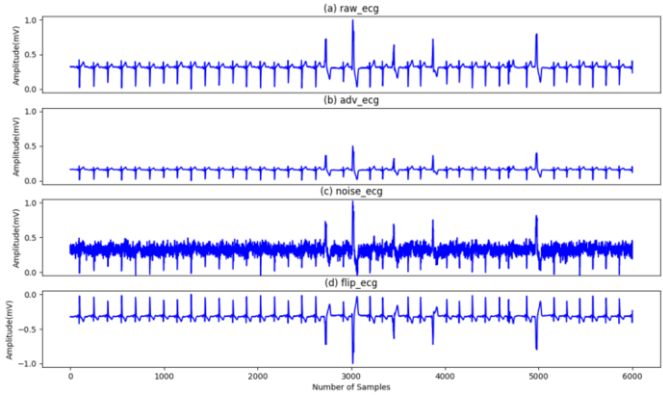

Figure 4. The ECG after data augmentation, (a) raw ECG, (b) change gain, (c) add noise and (d) flip signals

2.4. Model Build and Train

U-net has been proved its superior performance in images segmentation processing [16]. We use U-net as the base network and make some improvements to get better results. Unlike 2-dimensional images, ECG signals are 1-D signals, so we build U-net with a 1-D layer.

The model structure diagram is shown in Figure 5. As we can see, we add eight skip-connections (black dotted lines in Figure 5) from the shallow layer to the deep layer of the model, and the skip-connections are directly added after the corresponding convolution layer. As we all know, spatial domain information is very important for segmentation tasks. However, the pooling layers in the encoder part of the U-net have reduced the feature map resolution to a very small size, which is not conductive to accuracy segmentation mask. Skips-connection can be used to introduce shallow convolution layer features with high resolution to reduce the information loss for a better segmentation mask. The input and output of the build model are both 1*6000. The model with the minimum loss during training is saved as the best-trained model for the next test process.

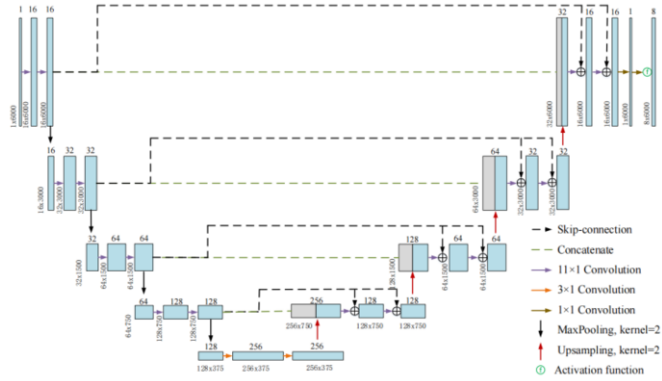

Figure 5. The structure of 1-D SDA U-net

3. Result and Discussion

The test set is put into the trained model to judge model performance. The output of the trained model is the probability corresponding to the input, as is shown in Figure 6, and

we determine the label according to the set threshold, which is set to 0.5. Meanwhile, in order to detect the R-peak, we add the prediction probability of each category of heartbeat as the probability of R-peak and also use the threshold to determine whether it is R-peak. In this way, we can obtain both arrhythmia classification results and R-peak detection results.

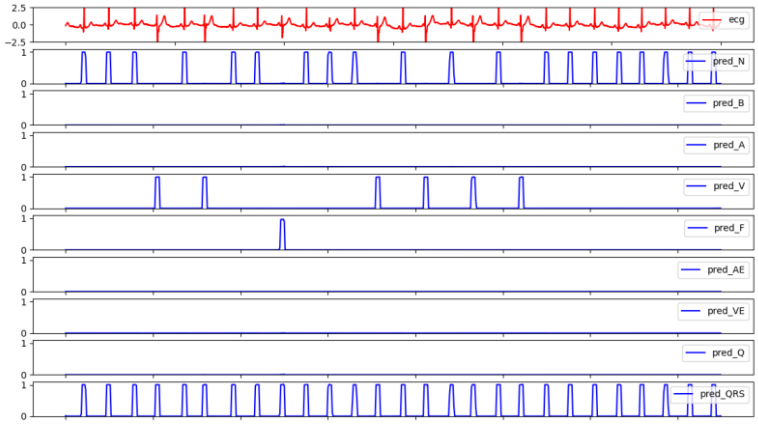

Figure 6. The red line represents the ECG signal, and the blue line represents the one-hot labels of different categories

The metrics of the proposed method on the test set are shown in Table 2. We also provide the comparison metrics of the original U-net and skip-connection U-net without data augmentation. From Table 2, we can see that all categories except Q showed significant improvement, especially the category of AE and VE using SDA U-net (our method). Combined with data volume, we think data augmentation can improve the recognition effect of categories with little data volume by enriching data information. In conclusion, the macro average F1 of SDA U-net is over 4.3% and 3% higher than that of U-net and U-net with skip-connection, respectively. The R-peak detection (QRS) of the SDA U-net also outperforms U-net and skip-connection U-net without data augmentation. Thus, we can draw the conclusion that the skip-connection in U-net could increase the performance of U-net to some extent. In our opinion, this may be because the skip-connection could reduce the loss of feature information extracted from shallow convolution layers. What's more, the data augmentation could enrich the data distribution for better model training.

Table 2. The comparison metrics of different methods (unit: %)

	U-net			U-net with skip-connection			SDA U-net (Our method)		
Type	precision	recall	F1	precision	recall	F1	precision	recall	F1
N	96.38	97.51	96.94	97.71	96.61	97.16	97.01	97.31	97.16
B	92.48	91.02	91.75	98.01	97.24	97.63	98.21	97.97	98.09
A	75.79	70.11	72.84	85.64	77.27	81.24	87.78	80.97	84.24
V	95.66	91.45	93.51	96.54	90.55	93.44	94.09	92.99	93.54
F	88.54	77.21	82.48	92.82	83.79	88.07	92.97	91.36	92.16
AE	89.64	90.51	90.07	95.95	95.29	95.62	96.42	96.46	96.44
VE	90.04	90.11	90.07	93.81	92.69	93.24	96.38	95.92	96.15
Q	94.99	96.29	95.64	94.75	93.02	93.87	94.84	93.12	93.73
QRS	99.13	99.35	99.24	99.78	99.08	99.43	99.91	99.36	99.64
Macro average	91.41	89.28	90.28	95.01	91.72	93.30	95.29	93.94	94.57

4. Conclusion

In this paper, an arrhythmia multiple classification and R-peak detection method based on SDA U-net with semantic segmentation was proposed. The application of semantic segmentation not only introduces effective information among the ECG segments but also retains the rhythmic information of the heartbeat. What's more, data augmentation techniques also make the proposed method more robust and generalization performance, which has been verified on five public datasets.

The validation of the methods presented in this paper is based on inner-patient analysis, and we will try more methods to explore more robust models for different databases in the future.

References

[1] The American Heart Association Statistics Committee and Stroke Statistics Subcommittee. Heart Disease and Stroke Statics 2009 Update: A Report from the American Heart Association Statistics Committee and Stroke Statistics Subcommittee.Circulation, 2009, 119.

[2] Kohli N, Verma N K. SVM based Methods Optimized by Feature Selection for Arrhythmia Classification in ECG. International Conference on Computer and Communication Technology (ICCCT). 2010: 486-490.

[3] Lee G B, Cho B J. EMD based Cardiac Arrhythmia Classification using Multi-class SVM. Journal of the Korea Institute of Information and Communication Engineering. 2010. 14(1).

[4] Marasović T, Papić V. A Comparative Study of FFT, DCT, and DWT for Efficient Arrhytmia Classification in RP-RF Framework. International Journal of E-Health and Medical Communications, 2018; 9(1):15.

[5] Xu SS et al. Towards End-to-End ECG Classification with Raw Signal Extraction and Deep Neural Networks. IEEE Journal of Biomedical & Health Informatics, 2018; 23(4):1574-1584.

[6] Rajendra Acharya U et al. A deep convolutional neural network model to classify heartbeats. Computers in Biology and Medicine, 2017 Oct; 89:389-396.

[7] Wang LH et al. Three-Heartbeat Multilead ECG Recognition Method for Arrhythmia Classification. IEEE Access, 2022, 10:44046-44061.

[8] Lu P, Zhang Y, Zhou B et al. Identification of Arrhythmia by Using a Decision Tree and Gated Network Fusion Model. Computational and Mathematical Methods in Medicine, 2021.

[9] Luo X, Yang L, Cai H, et al. Multi-classification of Arrhythmias Using a HCRNet on Imbalanced ECG Datasets. Computer Methods and Programs in Biomedicine, 2021, 208(9):106258.

[10] Oh, Shu Lih., et al. Automated beat-wise arrhythmia diagnosis using modified U-net on extended electrocardiographic recordings with heterogeneous arrhythmia types. Computers in biology and medicine. 2019: 105:92-101.

[11] Goldberger AL, Amaral LA, Glass L et al. PhysioBank, PhysioToolkit, and PhysioNet: components of a new research resource for complex physiologic signals. Circulation. 2000 Jun 13; 101(23):E215-20.

[12] Moody GB, Mark RG. The impact of the MIT-BIH Arrhythmia Database. IEEE Engineering in Medicine and Biology Magazine. 2001; 20(3):45-50.

[13] Greenwald SD. The development and analysis of a ventricular fibrillation detector. Massachusetts Institute of Technology. 2015.

[14] Taddei A, Distante G, Emdin M et al. The European ST-T Database: Standard for evaluating systems for the analysis of ST-T changes in ambulatory electrocardiography. European Heart Journal, 1992, 13(9):1164-1172.

[15] Hanshuang Xie, Mengna Zheng, Huaiyu Zhu, Fan Wu, Yun Pan. Arrhythmia Detection Based on Semantic Segmentation for Multi-lead ECG. 2022 Computing in Cardiology (CinC). 2022: 1-4.

[16] Ronneberger O, Fischer P, Brox T. U-Net: Convolutional Networks for Biomedical Image Segmentation. International Conference on Medical Image Computing and Computer-Assisted Intervention. Springer, Cham. 2015, 9351.

Fuzzy Systems and Data Mining IX
A.J. Tallón-Ballesteros and R. Beltrán-Barba (Eds.)

doi:10.3233/FAIA231105

Interpretable Deep Learning Model for Identifying the Immediate Risk of Myocardial Infarction Complications

Mengxiao WANG[a,b], Yanrui JIN[a,b,1], Zhiyuan LI[a,b], Xiaoyang WEI[a,b], Chengliang LIU[a,b,2] and Xiaoxue YANG[c]
[a] *State Key Laboratory of Mechanical System and Vibration, School of Mechanical Engineering, Shanghai Jiao Tong University, Shanghai 200240, China*
[b] *MoE Key Lab of Artificial Intelligence, AI Institute, Shanghai Jiao Tong University, Shanghai 200240, China*
[c] *Shanghai University of Finance and Economics, Shanghai200433, China*

Abstract. Electronic health records (EHR) encompass extensive personal information, diagnostic records, and medical history, enabling the prediction of disease occurrence and mortality risk. The objective of this study is to predict myocardial infarction complications and assess the risk of death by comparing the performance of various deep learning models and traditional machine learning approaches. The findings demonstrate similar performance between two kinds of models in predicting complication. The DeepFM model is commonly employed for Click-through rate (CTR) prediction. To the best of our knowledge, this is the first application of the DeepFM model to the EHR domain, and we have demonstrated its exceptional predictive performance, achieving the accuracy of 93.95%. Moreover, we further classify samples into low, intermediate, and high-risk categories with high confidence. To comprehend these results, we conduct an interpretability analysis of the models' predictions employing SHAP values. This analysis involves ranking the significant features, and summarizing ECG-related features, which hold clinical decision-making revelance for clinicians.

Keywords. DeepFM, multi-label classification, lethal risk assessment, SHAP value

1. Introduction

Coronary artery disease (CAD), also referred to coronary heart disease, is currently the leading cause of death among adults worldwide, and this trend is expected to continue over the next decade. However, despite many patients who die from coronary heart disease being previously diagnosed and treated, over 50% of sudden cardiac death cases occur without any clear history of coronary artery disease [1]. Current risk prediction models employed in conventional medicine for coronary heart disease, such as the Framingham Risk Score [1] and the Charlson Comorbidity Index [2] for cancer.

[1] Corresponding Author, Yanrui JIN, School of Mechanical Engineering, Shanghai Jiao Tong University, Shanghai 200240, China; E-mail: jinyanrui@sjtu.edu.cn.
[2] Corresponding Author, Chengliang LIU, School of Mechanical Engineering, Shanghai Jiao Tong University, Shanghai 200240, China; E-mail: chlliu@sjtu.edu.cn.

These indicators primarily address the long-term population-level risk of coronary heart disease. However, when it is not possible to measure biochemical markers such as troponin due to delayed presentation, data collected by wearable detection devices, including demographic information, electronic health records (EHR), and ECG patterns/conclusions, can be used to initially assess the patient's risk level for coronary heart disease.

In this work, we implement two main tasks. Firstly, we construct a multi-label classification model, and determine the ranking of influential features in predicting myocardial complications. Secondly, considering the unique characteristics of tabular data, which consists of highly sparse and heterogeneous (categorical-continuous-mixed) features, small sample sizes, and extreme values [3], we explore a new deep learning method DeepFM to predict the risk of death for patients and compare it with conventional machine learning methods. To the best of our knowledge, the DeepFM model is commonly used for Click-through rate (CTR) prediction, but few researchers have applied it in the disease risk prediction. This study facilitates the assessment of disease risks in cardiac patients and provides insights into the trajectory of disease prognosis.

2. Methodology

2.1. Multi-label Strategy

The objective of multi-label classification is to train a model on the training set $D = \{(X_i, Y_i) \mid 1 \le i \le m\}$ to represent the function mapping $h : \chi \to 2^{\gamma}$ [4]. The multi-label classification problem is transformed into an optimization problem, where we seek to determine the weight values that minimize the average loss function for each label as expressed in Equation (1).

$$\arg\min_{\beta \in \mathbb{R}^n} \frac{1}{qm} \sum_{j=1}^{q} \sum_{i=1}^{m} L(y_{ik}, \hat{y}_{ik}) \tag{1}$$

2.2. DeepFM

Deep learning architectures are specifically designed to incorporate inductive biases that align with the invariances and spatial dependencies present in the data. However, identifying the corresponding invariances in tabular data is challenging, making it difficult to find state-of-the-art deep learning models for prediction.

Linear models assume independence among individual features, disregarding the interrelationships between them. However, in practice, correlations among a large number of features are common. Moreover, medical electronic health records often contain high-dimensional sparse matrices, and directly modeling these matrices can result in heavy computational burdens and slow updates of feature weights. Factorization Machines (FM) have the advantage of addressing both issues, as represented by Equation (2).

$$y_{FM} = \langle w, x \rangle + \sum_{i=1}^{d} \sum_{j=i+1}^{d} \langle V_i, V_j \rangle x_i \cdot x_j \tag{2}$$

DeepFM model combines the FM model with a deep neural network[5]. As shown in **Figure 1**, the Wide & deep architecture of DeepFM includes an embedding stage and a feature interaction stage, allowing for simultaneous extraction of low and high dimensional features.

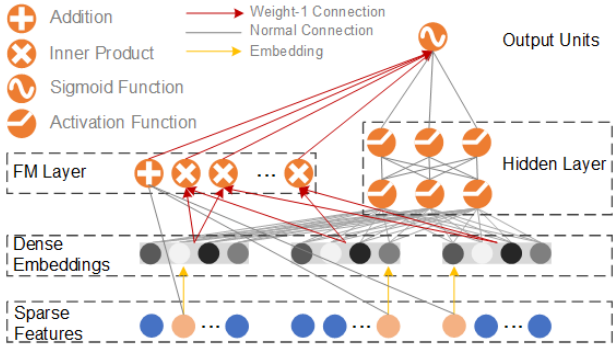

Figure 1. Network architecture of DeepFM.

3. Experiment Setups

3.1. Dataset

The Myocardial infarction complications Database (MIC)[6] was collected from Krasnoyarsk Interdistrict Clinical Hospital №20 named after I. S. Berzon (Russia) in 1992-1995. The dataset comprises records of 1700 patients, including demographic information, medical history records, electrocardiogram measurements et al. The input features are heterogeneous, which contain 99 categorical features and 12 numeric features. The target labels consist of 11 types of complications and 1 lethal (death) outcome.

3.2. Preprocessing

Initially, a primary data cleaning strategy is implemented, which consists of two steps: removing features and samples with a high missing ratio. The present study employed the Predictive Mean Matching (PMM) imputation method to address the issue of missing values. Since tabular data often consists of both binary and numeric values, it is crucial to standardize the numeric features with Z-score normalization method.

3.3. Implementation Details

In the training process, the Matthews Correlation Coefficient (MCC) is utilized to choose the best threshold. Subsequently, a cross-validated grid search strategy is employed to select the optimal parameters for the machine learning model. The AUC ROC is chosen as the indictor to evaluate the performance of the cross-validated model. We use *scikit-learn*, *pytorch* and *deepctr_torch* to implement the models. All neural network architectures are trained by Adagrad optimization with binary cross-entropy loss.

4. Results

Applying different machine learning method to the tabular data, the classification results can be evaluated through different metrics. Results of multi-label classification are revealed in Table 1, which traditional machine learning methods perform better in F1 macro and Jaccard macro. However, for Hamming loss and Accuracy, the NN model stands out.

Table 1. Evaluation results of multi-label classification

Model	Hamming loss	F1 macro	Jaccard macro	Accuracy
BR-MultiNB	0.1386	**0.2583**	**0.1548**	0.2939
CC-MultiNB	0.1427	0.2483	0.1500	0.2909
LP-MultiNB	0.0967	0.1778	0.1092	0.3667
MLKNN	0.0914	0.0649	0.0379	0.3697
MLARAM	0.1265	0.0717	0.0446	0.1364
BRKNNa	0.1258	0.1082	0.0625	0.2394
BRKNNb	0.4687	0.1160	0.0644	0.0303
MLSVM	0.1682	0.2061	0.1200	0.1576
NN(MLP)	**0.0788**	0.0732	0.1024	**0.4061**

The prediction results of whether patients have lethal risk of myocardial infarction is depicted in Figure 2. Each value represents the test score of the best model (on the validation set) obtained after a specific number of iterations in a random search. These values are extracted over 5 shuffles of the random search order. In comparison, DeepFM performs excellent with accuracy of 0.9395.

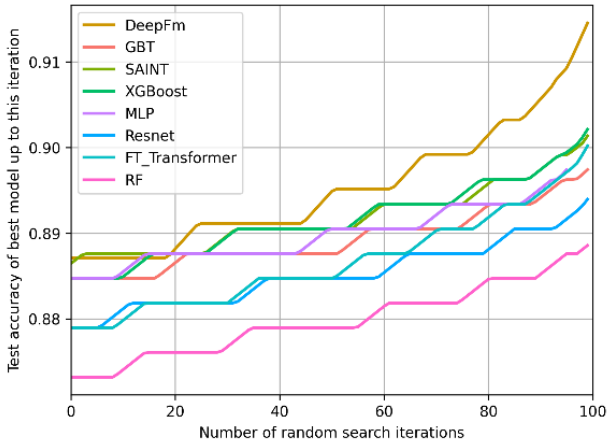

Figure 2. Test accuracy of predicting in lethal outcome

According to the recommendations in guideline [7] , the death risk levels of coronary heart disease are categorized into three levels: low risk, intermediate risk, and high risk. The risk thresholds are set based on the model's probability density plots on the validation set. As shown in **Figure 3**(a), a probability below 0.2 indicates low risk (+), a probability between 0.2 and 0.6 suggests intermediate risk (++), and a probability beyond 0.6 indicates high risk (+++). These findings indicate a positive correlation between increasing risk levels and higher mortality rates, which can be found in **Figure 3**(b).

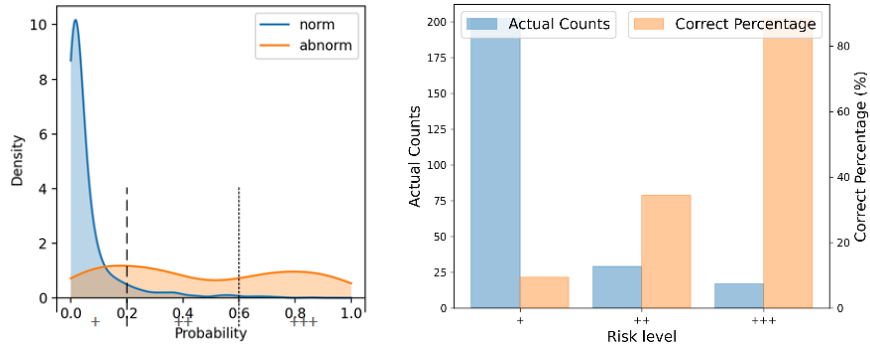

Figure 3. Lethal risk assessment by DeepFM model. (a) Probability density plots of training set. (b) Risk prediction results in test set.

5. Discussion

In addition to analyzing the prediction accuracy of classification models for different labels, it is also possible to further analyze the interpretability of the models. For deep learning methods, it's usually hard to find the balance between accuracy and interpretability. Here, the SHAP (SHapley Additive exPlanations) [8] method is utilized to explain the input features, which is congruent with human intuition. The SHAP method should fulfill the addictive attribute as shown in Equation (3).

$$f(x) = g(x') = \phi_0 + \sum_{i=1}^{M} \phi_i x_i' \tag{3}$$

The $g(x')$ signifies the explanation model that matches the original model $f(x)$ when $x = h_x(x')$, where $\phi_0 = f(h_x(0))$ denotes the base value.

As shown in Figure 4, SHAP values explain the contribution of each feature to the prediction of a given black box model. The bar charts of Figure 4(a) explain the impact of features on multi-label classification. Figure 4(b) depicts a beeswarm plot explaining the key feature influences for the lethal label. After inspection, the SHAP with NN model fulfills better the Equation (3), while the SHAP with RF model has larger error. Furthermore, we use force plots on individual cases to examine local interpretability of feature importance of the NN model, as shown in Figure 4(c). Taking the negative sample as an example, the base value of the model is 0.24, which signifies the average risk indicator and the threshold of MCC. The predictive value of the original model is 0.07, so this sample is documented as benign, and the feature AGE has negative feature contribution in this specific sample.

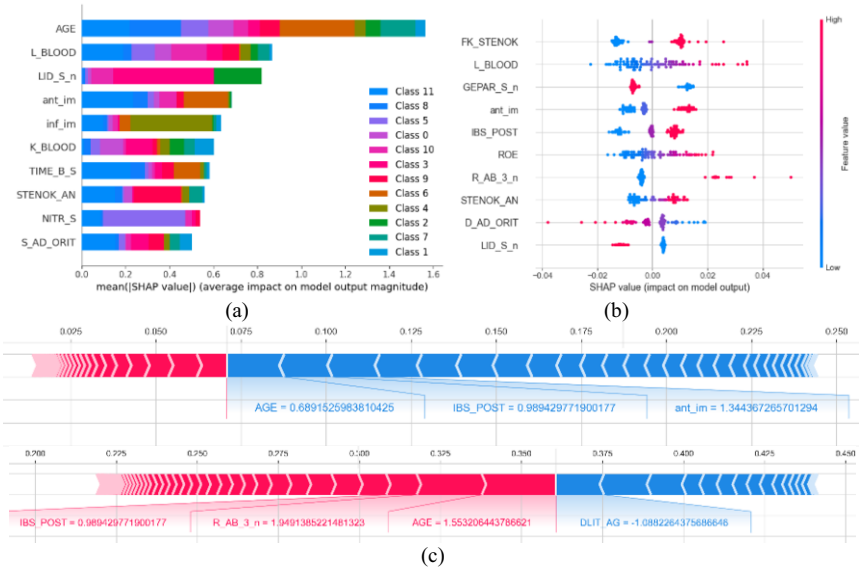

Figure 4. Model interpretability. (a) Top 10 SHAP value for multi-label classification. (b) Top 10 SHAP value for binary classification. (c) Local interpretability (negative sample for upper while positive sample for lower).

6. Conclusion

While traditional machine learning methods are commonly used for tabular data, this study aims to investigate the performance of various deep learning models in predicting the risk of Myocardial infarction complications. In terms of multi-label classification, some evaluation metrics of the NN model are surpassed by traditional machine learning methods, but overall performance is similar. In binary classification, the DeepFM model proposed in this study exhibits higher accuracy in predicting myocardial infarction samples with potentially lethal risks in this dataset. In addition, this study conducts interpretability analysis of the models, thus dispelling the opaque nature of deep learning models, thereby facilitating future research on the deep integration of ECG signals.

Acknowledgements

This work was supported by China Postdoctoral Science Foundation (Grant No. 2023M732219) and Shanghai Municipal Science and Technology Major Project (No. 2021SHZDZX0102).

References

[1] P. W. F. Wilson, R. B. D'Agostino, D. Levy, A. M. Belanger, H. Silbershatz, and W. B. Kannel, 'Prediction of Coronary Heart Disease Using Risk Factor Categories', *Circulation*, vol. 97, no. 18, pp. 1837–1847, May 1998, doi: 10.1161/01.CIR.97.18.1837.

[2] M. E. Charlson, P. Pompei, K. L. Ales, and C. R. MacKenzie, 'A new method of classifying prognostic comorbidity in longitudinal studies: Development and validation', *Journal of Chronic Diseases*, vol. 40, no. 5, pp. 373–383, Jan. 1987, doi: 10.1016/0021-9681(87)90171-8.

[3] L. Grinsztajn, E. Oyallon, and G. Varoquaux, 'Why do tree-based models still outperform deep learning on typical tabular data?', in *36th Conference on Neural Information Processing Systems (NeurIPS 2022) Track on Datasets and Benchmarks*, in Advances in Neural Information Processing. New Orleans, United States, Nov. 2022. Accessed: Aug. 16, 2023. [Online]. Available: https://hal.science/hal-03723551

[4] M.-L. Zhang and Z.-H. Zhou, 'A Review on Multi-Label Learning Algorithms', *IEEE Transactions on Knowledge and Data Engineering*, vol. 26, no. 8, pp. 1819–1837, Aug. 2014, doi: 10.1109/TKDE.2013.39.

[5] H. Guo, R. Tang, Y. Ye, Z. Li, and X. He, 'DeepFM: A Factorization-Machine based Neural Network for CTR Prediction', in *Proceedings of the Twenty-Sixth International Joint Conference on Artificial Intelligence*, Melbourne, Australia: International Joint Conferences on Artificial Intelligence Organization, Aug. 2017, pp. 1725–1731. doi: 10.24963/ijcai.2017/239.

[6] Golovenkin, S.E.; Gorban, Alexander; Mirkes, Evgeny; Shulman, V.A.; Rossiev, D.A.; Shesternya, P.A, 'Myocardial infarction complications Database'. University of Leicester, Jul. 07, 2020.

[7] M. Gulati *et al.*, '2021 AHA/ACC/ASE/CHEST/SAEM/SCCT/SCMR Guideline for the Evaluation and Diagnosis of Chest Pain: A Report of the American College of Cardiology/American Heart Association Joint Committee on Clinical Practice Guidelines', *Journal of the American College of Cardiology*, vol. 78, no. 22, pp. e187–e285, Nov. 2021, doi: 10.1016/j.jacc.2021.07.053.

[8] S. M. Lundberg and S.-I. Lee, 'A Unified Approach to Interpreting Model Predictions', in *Advances in Neural Information Processing Systems*, Curran Associates, Inc., 2017. Accessed: Aug. 09, 2023. [Online]. Available: https://proceedings.neurips.cc/paper_files/paper/2017/hash/8a20a8621978632d76c43dfd28b67767-Abstract.html

Fuzzy Systems and Data Mining IX
A.J. Tallón-Ballesteros and R. Beltrán-Barba (Eds.)

doi:10.3233/FAIA231106

Dual-Function Microfluidic Chip for Identification and Drug Response Testing of Lung Cancer Organoids

Jiyu Xi[a], Zewen Wei[a,1], Xin Wu[a], Kexin Zhang[a], Huiting Zhao[a] and Yu Zhang[a]
[a]*Department of Biomedical Engineering, School of Medical Technology, Beijing Institute of Technology, Beijing 100081, China.*

Abstract. Organoids, as a novel in vitro drug screening platform, have received widespread attention due to their relevance to clinical research as they are derived from patient samples. Lung cancer organoids are categorized into two subtypes: EGFR mutation type and EGFR wild type. EGFR mutation lung cancer organoids exhibit better therapeutic effects with tyrosine kinase inhibitors (TKIs), whereas EGFR wild type lung cancer organoids have better responses to chemotherapy drugs. However, the current lack of a microfluidic chip capable of identifying EGFR mutations in lung cancer organoids and testing their drug response poses a challenge. To address this, we have developed a dual-functional chip that streamlines EGFR mutation identification and drug testing in lung cancer organoids. This method not only reduces time and cost but also enhances drug screening efficiency.

Keywords. microfluidic chip, drug response, organoids

1. Introduction

Organoids, which preserve the specific matrix of pathological patients and retain the cellular structures and molecular characteristics of tumor tissues, are widely recognized as reliable drug platforms. [1,2] They can be maintained long-term, making them useful for effective drug testing and individualized drug development. [3]

However, there are limitations in terms of variability and scalability in organoid culture on traditional platforms such as Petri dishes, including lack of vascularization[4], limited scalability[5], and technical difficulties in handling[6], making high-throughput drug screening for lung cancer organoids challenging. To address these issues, researchers have turned to microfluidic technology, which offers precise control over organoids[7-9], dynamic physical conditions[10,11], and homogeneous culture within microchambers[12-15]. Although some high-throughput microfluidic platforms have been developed for organ-on-a-chip drug response assays, there are still limitations that need to be addressed. These include the lack of identification functional areas resulting in a longer and more labor-intensive drug response testing process, the single drug administration mode on these platforms, and the lack of integration with subtype identification for drug screening.

[1] Corresponding Author: Zewen WEI. Department of Biomedical Engineering, School of Medical Technology, Beijing Institute of Technology, Beijing 100081, China; E-mail: weizewen@bit.edu.cn.

In our study, the identification and drug response testing of lung cancer organoids on a chip were achieved. The organoids' single cells were captured and identified in situ using a single-cell trapping module. Based on the identification results, corresponding drugs were added to the drug injection module to complete the final drug response testing of lung cancer organoids. This study has enhanced the efficiency of drug response testing, reducing the required time and workload.

2. Methods

2.1. Fabrication Process of DF-Chip

The DF-Chip is composed of three tightly bonded layers of PDMS. Through traditional photolithography technology, the mold of the drug injecting layer with a thickness of 200 μm is obtained by photolithography on the SU-2075 negative photoresist mask. The template for the cell loading layer is prepared using ICP technology and two overlay mask lithography techniques, with PDMS molds used for fabrication. Finally, the three layers are tightly bonded together through plasma treatment.

2.2. Establishment of PDOs

The postoperative clinical specimen was cut into 1-3 mm^3 pieces, digested with a digestion solution at 37 ℃ for 1.5 h, and then the digestion was stopped with FBS. The cell suspension was obtained by filtering it through a 70 μm filter, and the red blood cells were lysed using a red blood cell lysis solution. The cells were then suspended in a mixture of PDO medium and an ECM solution with double volume and injected into the cell loading layer, where they solidified for 30 minutes. PDO culture medium was added to the drug injecting layer. After a period of cultivation, the establishment of a PDO is completed.

3. Results and Discussion

To achieve the identification of EGFR mutations in lung cancer organs and drug response testing, a dual-function microfluidic chip (named DF-chip) was invented as shown in Figure 1. Figure 1a shows the three-dimensional image of the DF-chip, which consists of three layers: the drug injecting layer, the cell loading layer and the glass substrate. The drug injecting layer is used for injecting organ culture medium, drugs, and cell dyes; the cell loading layer is used for cell capture and cultivation; and the glass substrate supports the entire chip. The physical photo of the chip is shown in Figure 1b, with the drug injecting layer filled with blue and the cell loading layer filled with red. The DF-chip mainly consists of two functional modules: the single-cell trapping module (Figure 1c) and the drug injecting module (Figure 1d). The single-cell trapping module consists of 6 rows, with 100 trapping sites in each row, totaling 600 trapping sites. It is used to capture single cells from the organ and perform in-situ staining and EGFR mutation identification. The drug injecting module is composed of 7 spiral channels and can be controlled by valves for the addition of drugs in a fixed proportion or without mixing.

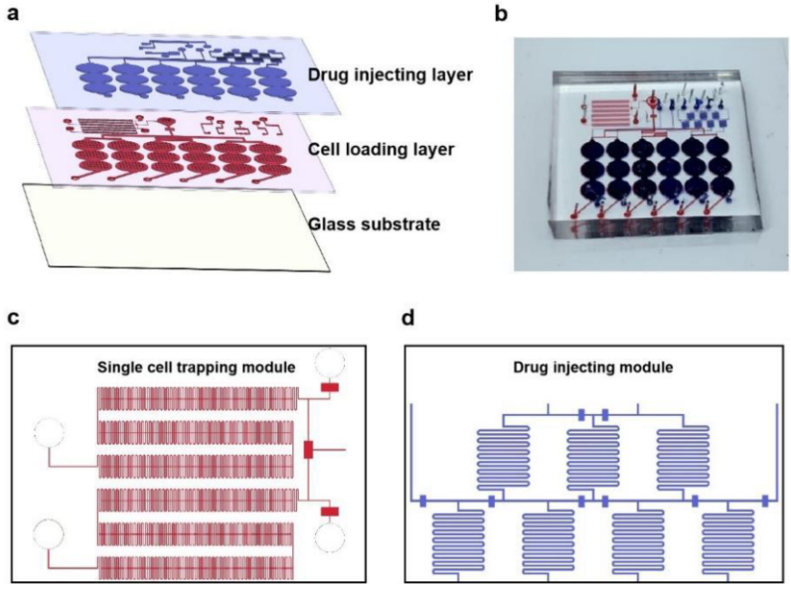

Figure 1. Design of the DF-chip. a 3D display diagram of the chip. b Photograph of the physical chip. c Overall display diagram of single cell trapping module. d Overall display diagram of drug injecting module.

To achieve the true capture of single cells in Organoids, the dimensions of the single-cell trapping module need to be precisely designed, as shown in Figure 2a. The width of the single-cell flow channel and the width of the single-cell trapping sites are both 30 μm, while the length and width of the cell trapping site are both 5 μm. The actual photo

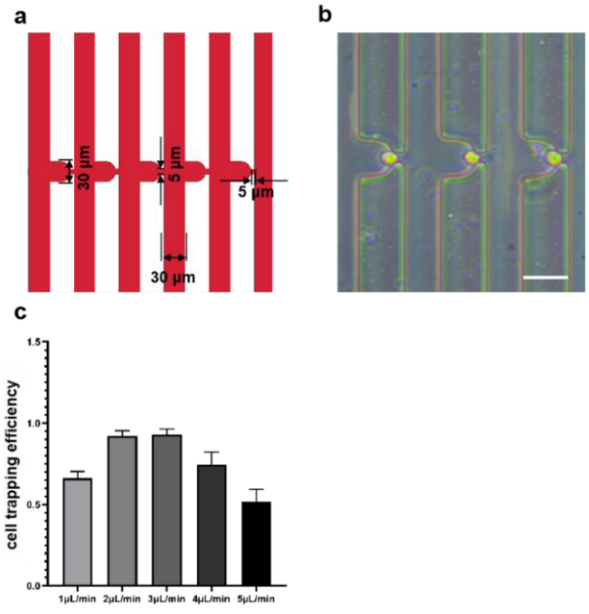

Figure 2. Design of the single cell trapping module. a The photo of single cell trapping. b Detailed dimensions of the single cell trapping module. c The relationship between the cell trapping efficiency and the flow rate. Scale bars: 30 μm.

of cell trapping is shown in Figure 2b, where cells are successfully trapped by the cell. Figure 2c shows the relationship between cell trapping efficiency and flow rate. As the flow rate increases from 1 μl/min to 3 μl/min, the cell trapping efficiency improves. However, when the flow rate exceeds 4 μl/min, the cells deform and pass through the trapping site, resulting in a decrease in cell trapping efficiency.

In order to ensure the stable operation of the DF-chip, the design and arrangement of the valve structure should be reasonable. Figure 3 shows the valve arrangement of the DF-chip, with the valve-controlled channels located in the single cell trapping module on the Drug injecting layer, and the opposite arrangement in the Drug injecting module. The opening and closing of the valves respectively control the flow and interruption of the channels, thereby achieving the programmable operation of the DF-chip.

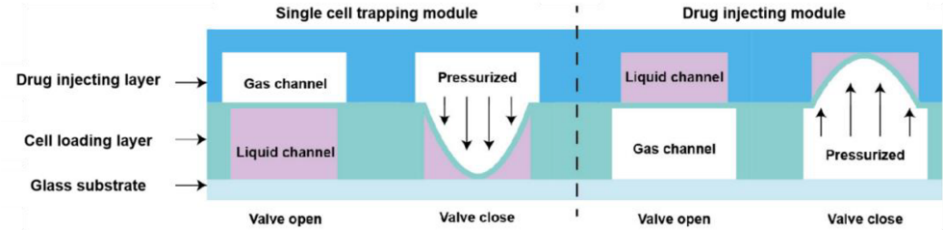

Figure 3. The valve arrangement of the DF-chip.

The functional status of the DF-chip is demonstrated by the patient-derived organoids (PDOs). The PDOs were obtained from clinical samples and cultured in the DF-chip. The molecular characterization of the organoids is shown in Figure 4. Unstained images displayed the growth status of the organoid. Blue fluorescent images showed the cell count of the organoid cluster, and green fluorescent images demonstrated the successful establishment of lung cancer organoids by indicating the staining of Cytokeratin 7.

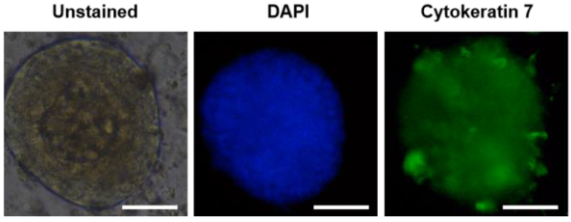

Figure 4. Staining image of PDOs. Scale bars: 100 μm.

Based on current methods, organoids are primarily identified through organoid staining. Although organoid identification results have not been obtained yet, single-cell trapping of organoids has already been achieved from the current experimental results, allowing us to obtain identification results through in situ staining. In the current stage, lung cancer organoids have been cultured on chips to lay the foundation for obtaining drug response test results. In the upcoming experiments, the focus will be on in situ staining identification of organoids and drug response tests, which holds great promise for completing the entire study based on the current experimental results.

4. Conclusions

In our study, the identification and drug response testing of lung cancer organoids on a chip were achieved. The study introduces a dual-function microfluidic chip for the identification and drug response testing of lung cancer organoids, which has the following advantages: 1) It enables the capture and identification of lung cancer organoid single cells within the chip; 2) It includes two drug administration modes for switching and adding different drugs; 3) It integrates the identification and drug response testing of lung cancer organoids, reducing time consumption and enhancing drug screening efficiency.

Acknowledgements

This work was supported by the Quancheng-5150 Talent Supporting Project of Jinan (Laureate, Zewen Wei) and the Industrial Talent Supporting Project of Huaiying (Laureate, Zewen Wei) and the Beijing Institute of Technology Research Fund Program for Young Scholars (No. 3160011181907). We thank the Biological & Medical Engineering Core Facilities of the Beijing Institute of Technology and the Analysis & Testing Center of the Beijing Institute of Technology for characterization services.

References

[1] Clevers H. Modeling Development and Disease with Organoids. Cell. 2016 Jun 16;165(7):1586-1597.
[2] Lancaster MA, Huch M. Disease modelling in human organoids. Dis Model Mech. 2019 Jul 29;12(7):dmm039347.
[3] Drost J, Clevers H. Organoids in cancer research. Nat Rev Cancer. 2018 Jul;18(7):407-418.
[4] Zhao X, Xu Z, Xiao L, Shi T, Xiao H, Wang Y, Li Y, Xue F, Zeng W. Review on the Vascularization of Organoids and Organoids-on-a-Chip. Front Bioeng Biotechnol. 2021 Apr 12;9:637048.
[5] Gjorevski N, Sachs N, Manfrin A, Giger S, Bragina ME, Ordóñez-Morán P, Clevers H, Lutolf MP. Designer matrices for intestinal stem cell and organoid culture. Nature. 2016 Nov 24;539(7630):560-564.
[6] Kim SK, Kim YH, Park S, Cho SW. Organoid engineering with microfluidics and biomaterials for liver, lung disease, and cancer modeling. Acta Biomater. 2021 Sep 15;132:37-51.
[7] Fang G, Lu H, Rodriguez de la Fuente L, Law AMK, Lin G, Jin D, Gallego-Ortega D. Mammary Tumor Organoid Culture in Non-Adhesive Alginate for Luminal Mechanics and High-Throughput Drug Screening. Adv Sci (Weinh). 2021 Nov;8(21):e2102418.
[8] Zhang YS, Aleman J, Shin SR, Kilic T, Kim D, Mousavi Shaegh SA, Massa S, Riahi R, Chae S, Hu N, Avci H, Zhang W, Silvestri A, Sanati Nezhad A, Manbohi A, De Ferrari F, Polini A, Calzone G, Shaikh N, Alerasool P, Budina E, Kang J, Bhise N, Ribas J, Pourmand A, Skardal A, Shupe T, Bishop CE, Dokmeci MR, Atala A, Khademhosseini A. Multisensor-integrated organs-on-chips platform for automated and continual in situ monitoring of organoid behaviors. Proc Natl Acad Sci USA. 2017 Mar 21;114(12): E2293-E2302.
[9] Pinho D, Santos D, Vila A, Carvalho S. Establishment of Colorectal Cancer Organoids in Microfluidic-Based System. Micromachines (Basel). 2021 Apr 28;12(5):497.
[10] Shirure VS, Hughes CCW, George SC. Engineering Vascularized Organoid-on-a-Chip Models. Annu Rev Biomed Eng. 2021 Jul 13;23:141-167.
[11] Schuster B, Junkin M, Kashaf SS, Romero-Calvo I, Kirby K, Matthews J, Weber CR, Rzhetsky A, White KP, Tay S. Automated microfluidic platform for dynamic and combinatorial drug screening of tumor organoids. Nat Commun. 2020 Oct 19;11(1):5271.
[12] Bovard D, Sandoz A, Luettich K, Frentzel S, Iskandar A, Marescotti D, Trivedi K, Guedj E, Dutertre Q, Peitsch MC, Hoeng J. A lung/liver-on-a-chip platform for acute and chronic toxicity studies. Lab Chip. 2018 Dec 4;18(24):3814-3829.

[13] Jung DJ, Shin TH, Kim M, Sung CO, Jang SJ, Jeong GS. A one-stop microfluidic-based lung cancer organoid culture platform for testing drug sensitivity. Lab Chip. 2019 Sep 7;19(17):2854-2865.
[14] Ng S, Tan WJ, Pek MMX, Tan MH, Kurisawa M. Mechanically and chemically defined hydrogel matrices for patient-derived colorectal tumor organoid culture. Biomaterials. 2019 Oct;219:119400.
[15] Szvicsek Z, Oszvald Á, Szabó L, Sándor GO, Kelemen A, Soós AÁ, Pálóczi K, Harsányi L, Tölgyes T, Dede K, Bursics A, Buzás EI, Zeöld A, Wiener Z. Extracellular vesicle release from intestinal organoids is modulated by Apc mutation and other colorectal cancer progression factors. Cell Mol Life Sci. 2019 Jun;76(12):2463-2476.

Fuzzy Systems and Data Mining IX
A.J. Tallón-Ballesteros and R. Beltrán-Barba (Eds.)

doi:10.3233/FAIA231107

Classification for Early Imaging of Alzheimer's Disease Based on Deep Learning

Xiuxu LI[a], Lanhua ZHANG[a], Xiaodong LIU[a] and Jin WANG[b,1]
[a] *School of Medical Information and Engineering, Shandong First Medical University and Shandong Academy of Medical Sciences, Tai'an, 271016, China*
[b] *Cybersecurity Industry Development Center (Information Center) of Ministry of Industry and Information Technology, Beijing, 100846, China*

Abstract. Deep learning is important for early warning of Alzheimer's disease in imaging histology studies. In order to realize the early warning of medical images based on deep learning models, traditional machine learning and deep learning models as well as techniques such as confusion matrix and ROC are combined to complete the model classification situation evaluation function, and finally visualize the results of deep learning VGG outperforming the effect of traditional machine learning models. The conclusion of the deep learning VGG model shows that the deep learning model is feasible or meaningful after certain pre-processing and in early Alzheimer's disease image classification, and has an important role in early medical image recognition of certain diseases.

Keywords. Machine Learning, classification, deep learning, confusion matrix, Alzheimer's disease

1. Introduction

Alzheimer's disease is a common progressive neurodegenerative disease of the central nervous system, with clinical symptoms such as progressive memory loss, cognitive decline, and mental and behavioral abnormalities. Alzheimer's disease is a neurodegenerative disease that is clinically characterized by progressive cognitive and memory impairment. It is a complex progressive neurodegenerative disease affecting approximately 14 million people in Europe and the United States, including almost one-half of the population aged 85 years (43%)[1-3].

It is well known that Alzheimer's disease is currently a neuroglial inflammatory disorder involving association with amyloid plaques. The associated pathomechanism explains that microglia is usually associated with specific plaque types that can be explained by characteristic formation mechanisms [4]. The common machine learning models can be used for classification. Deep learning is the extend function based on

[1] Corresponding Author, Jin WANG, Cybersecurity Industry Development Center (Information Center) of Ministry of Industry and Information Technology, Beijing, 100846, China; E-mail: wangjin@miit.gov.cn.

machine learning. Machine learning allows us to classify types of diseases that are close to each other in terms of a parametric factor [5, 6].

Confusion matrix is a matrix showing the predicted and actual classifications [7]. It is an important evaluation indicators in machine learning, and can be seen quite visually model performance in a certain type of data [8]. The logistic function is originally designed to be used in population growth [9]. Later on, it is gradually used to solve the machine learning approach of correlation binary classification, which is used to estimate the likelihood of a certain thing [10].

Support vector machines are machine learning models which can be applied to continuous, binary, and categorical outcome type problems [11]. Naive Bayes utilizes Bayes' law and a strong assumption that the properties of a given class of data are conditionally independent, and it is widely used in the field of machine learning [12]. The nearest neighbor algorithm uses the K-nearest pattern label in the data space as the local feature of the model [13].

Visual geometry group (VGG) network is one of the commonly used pattern recognition models in computer vision, and it has been verified in the previous years that it has a certain effect on the recognition of objects in static images [14]. The use of a small convolutional filter structure for enhancing the depth of the network shows that improvements to the existing technical configuration can be achieved by adding a depth of 16-19 layers to the weight hierarchy [15].

To address degradation issues, ResNet network introduces a deep residual learning approach to simplify the training of deeper networks [16].

In machine learning, we will classify the classification problem in more than two categories, called multi-classification problem; when we need to compare performance metrics between multiple methods and models, a qualified performance metric is useful, and many metrics can be used when testing the capability of a multi-classification classifier [17].

2. Methods

2.1. Data sources and Algorithm Models

The dataset is from Kaggle group which is consists of MRI images, and all images are resized into 128*128 pixels. The dataset has a total of 6400 images and is divided into four types: Mild Demented, Moderate Demented, Non Demented and Very Mild Demented. Data was collected from several website, hospitals, public repositories. And at last these data are preprocessed in advance to facilitate subsequent processing. The sources of the dataset can be gotten from webs (https://www.kaggle.com/datasets/jboysen/mri-and-alzheimers; https://catalog.data.gov/dataset/alzheimers-disease-and-healthy-aging-data) [18].

In order to test the efficient of the different algorithms for the classification of the imaging, we use a variety of machine learning and deep learning methods to classify early medical images. The algorithms includes support vector machine, random forests, K-nearest neighbors, Naïve Bayes, logistic regression, VGG and ResNet.

Support vector machine can perform nonlinear classification through kernel method [11]. Random forest is the extension of decision tree algorithms. In the feature space, if most of the k nearest samples near a sample belong to a certain category, then the samples also belong to that category, that is K-nearest neighbors [13]. Bayesian

classification algorithm is a statistical classification method that utilizes probability and statistical knowledge for classification, Naïve Bayes is an algorithm formed based on this method [12]. Through logistic regression analysis, the weights of the independent variables can be obtained.

VGG network is a convolutional neural network, and it is often used to extract image features [14, 15]. In order to compare, ResNet50 networks execute the same operation.

AdaDelta, Adam, AdaMax, and Nadam are four adaptive learning rate algorithms [19]. These algorithms are commonly used in neural networks to address the issue of vanishing learning rates and improve training performance. AdaDelta is a modified version of the AdaGrad method. Adam, short for adaptive moment estimation, combines gradient descent with momentum and RMSProp. AdaMax is a variant of Adam that uses the L∞ norm instead of the L2 norm to calculate the gt term. It also includes the same update equations as Adam, with slight modifications. Nadam, or Nesterov accelerated adaptive moment estimation, incorporates Nesterov accelerated gradient into Adam. These algorithms have different hyperparameters, such as learning rate (η), momentum term ($\beta 1$), RMSProp term ($\beta 2$), and ε. The information also provides details on the training time, memory utilization, and accuracy of these algorithms on a test set.

2.2. Work flow of our works

First, we collected fMRI images from open source dataset about early-stage Alzheimer's disease. The data has four classes of images both in training as well as a testing set: Non Demented, Mild Demented, Very Mild Demented, and Moderate Demented. The dataset contains a total of 6400 images. The dataset is listed above, and we adopt some of them as the test samples.

Then, about the computing and programming, we used the Python as surrounding, except the basic libraries, we use the sklearn-kit to normalization the images, and then structured some basic models by logistic, support vector machine, Naïve Bayes, K-nearest neighbor, VGG and ResNet. Both machine learning and deep learning are utilized to ensure that the results are convincing.

Finally, we continuously adjusted and optimized some parameters of the models. By the basic results we conclude that deep learning models work better than machine learning models on early Alzheimer's classification problems, even some machine learning models even make mistakes.

In the final results, we can observe each model through the graphs of confusion matrix and ROC curve, and we can roughly estimate the classification effect of the relevant models.

3. Results

In detailed of the data processing, the image data was first divided into four types according to the early, middle, late and later stages. We resized them into 126*126 sizes, and divided them into test sets and training sets according to the ratio of 3:7 after entering each model method.

About the model building, we used Pytorch architecture [20] to build VGG16, VGG19 networks and used scikit-learn library [21] to build machine learning methods.

All the results can be finally visualized by matplotlib function library. By the programming, the final confusion matrix of every model was normalized. The corresponding python packages contain functions for pre-processing the data and methods for related operations.

Finally we got the confusion matrix for each model and the ROC curve for each model predicting each class. The results of the confusion matrix and the ROC curve were listed below after the normalization process (Fig. 1, Fig. 2). The worst performance of the different models in the test sample is the Naïve Bayes.

The confusion matrices of VGG16 and VGG19 were different (Fig. 3), but they had the similar accuracy and loss (Fig. 4). Meanwhile, ResNet50 was introduced to compare with VGG. We list the score in all the models (Tab. 1).

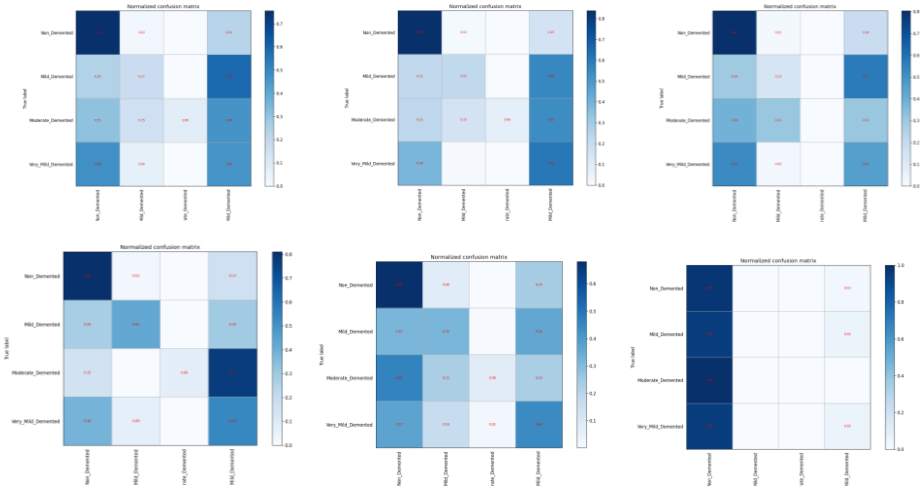

Figure 1. Confusion matrix results in models

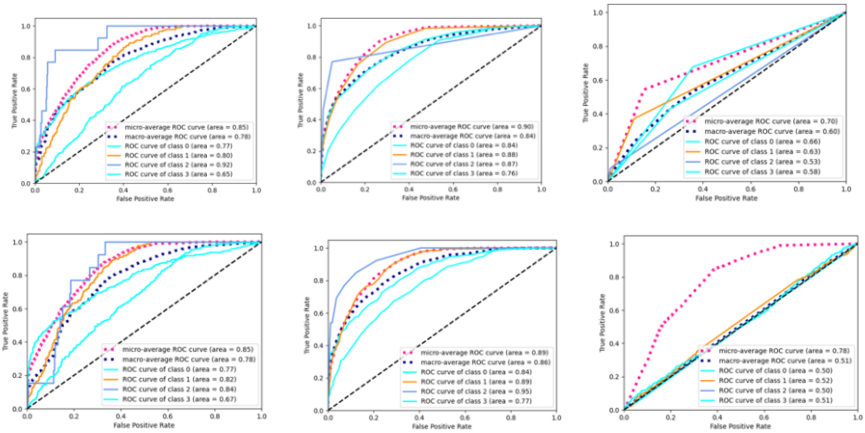

Figure 2. ROC curve results in models

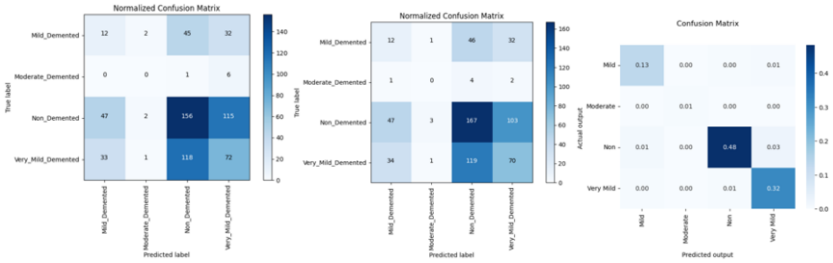

Figure 3. Confusion matrix results of VGG16 and VGG19

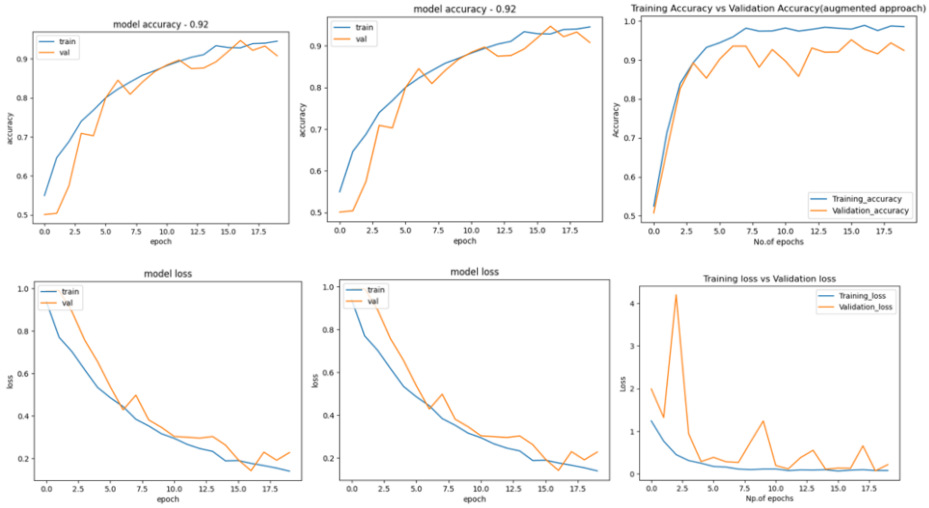

Figure 4. Accuracy and loss results of VGG16, VGG19 and ResNet50

Table 1. Score in Models

	SVM	KNN	RF	Naïve Bayes	Logistic	DT	VGG	ResNet50
Accuracy	0.57	0.65	0.66	0.50	0.59	0.57	0.90	0.92
F1-Score	0.55	0.65	0.64	0.37	0.56	0.57	0.89	0.93
Recall	0.57	0.50	0.66	0.50	0.59	0.57	0.89	0.92
Precision	0.56	0.72	0.67	0.40	0.57	0.57	0.90	0.93

4. Discussion

In the processing of our models, we find that the classification effect of the models is not very good when the data size is small. With the increasing of the size of the data, the classification of our models can achieve better results. Therefore, it can be proposed that machine learning and deep learning are all data-based training methods, and a certain effect can only be seen when a certain amount of data is available. In our models, we didn't do the strengthening of data which can also bring good effect for the models.

From the results of the confusion matrix, the models of support vector machine, logistic, K-nearest neighbors, decision tree and random forest finished the classification of the imaging data although the values of different models are different which implies that the algorithm express the basic functions. But the results of plain Bayes are worse than those of several other methods and models.

From the results of the ROC curves, the models of support vector machine, logistic, K-nearest neighbors and random forest got the efficient results. The decision tree got worse results than others. The Naïve Bayes is the worst same as the confusion matrix which implied that the Naïve Bayes didn't suit for these MRI imaging classification because Naïve Bayes demands individual features to be independent of each other in the calculations. Meanwhile the results implies that too little training data for some categories can also lead to worse classification results in the end.

The reason why such a problem occurs, we suspect that the amount of the model data is the main reason in the process of training in some, which resulted in the results of the training without achieving a satisfactory effect.

And through the final results, it is found that the results of the deep learning model are slightly improved compared to the traditional machine learning methods.

5. Conclusions

In this paper, we try to use traditional machine learning models and deep learning models for early medical image classification of Alzheimer's disease. In order to provide more methods for image classification in the clinical application, we used support vector machine, random forests, K-nearest neighbors, Naïve Bayes, logistic regression, and VGG networks to test the classification function. We computed the confusion matrix and ROC curves for all the models to demonstrate the effects of the models.

By the comparing of different models with confusion matrix and ROC curves, we found that most of the classification algorithm model could achieve the function with different effects. Data factors may lead to these reasons, and in the future, this result can be tested through a larger amount of data.

Acknowledgements

This research was supported by the Students' project for innovation and entrepreneurship training program of Shandong First Medical University and Shandong Academy of Medical Sciences (No. 2022104391174), Youth Science Foundation Cultivation Support Program of Shandong First Medical University and Shandong Academy of Medical Sciences (No. 202201-036) and the Tai'an Science and Technology Innovation Development Project (2022GX025).

References

[1] Alzheimer's Association. 2011 Alzheimer's disease facts and figures. Alzheimer's & Dementia, 2011,7(2):208–244.

[2] Blennow K, Dubois B, Fagan AM, et al. Clinical utility of cerebrospinal fluid biomarkers in the diagnosis of early Alzheimer's disease. Alzheimer's & Dementia, 2015,11(1):58–69.
[3] Hort J, O'Brien JT, Gainotti G, et al. EFNS guidelines for the diagnosis and management of Alzheimer's disease: EFNS guidelines for AD. European Journal of Neurology, 2010,17(10):1236–1248.
[4] D'Andrea MR, Cole GM, Ard MD. The microglial phagocytic role with specific plaque types in the Alzheimer disease brain. Neurobiology Aging, 2004,25(5): 675-683.
[5] Rakhimov M, Akhmadjonov R, Javliev S. Artificial Intelligence in Medicine for Chronic Disease Classification Using Machine Learning. 2022 IEEE 16th International Conference on Application of Information and Communication Technologies, 2022:1–6.
[6] Xie S, Guo R, Li N, et al. Brain fMRI processing and classification based on combination of PCA and SVM. 2009 International Joint Conference on Neural Networks, 2009:3384–3389.
[7] Kohavi R, Provost F. Glossary of terms. Machine Learning, 1998,30(2-3):271-274.
[8] Sammut C, Webb GI. Encyclopedia of machine learning and data mining. Springer, 2017.
[9] Cramer JS. The Origins of Logistic Regression. Tinbergen Institute Working Paper, 2002(119):4.
[10] Landwehr N, Hall M, Frank E. Logistic model trees. Machine Learning, 2005,59(1-2):161-205.
[11] Guenther N, Schonlau M. Support vector machines. Stata Journal, 2016, 16(4):917-937.
[12] Webb GI, Keogh E, Miikkulainen R. Naïve Bayes. Encyclopedia of machine learning, 2010,15(1):713-714.
[13] Kramer O, Kramer O. K-nearest neighbors. Dimensionality reduction with unsupervised nearest neighbors, 2013:13-23.
[14] Wang L, Guo S, Huang W, et al. Places205-VGGNet Models for Scene Recognition, Computer science, 2015. DOI:10.48550/arXiv.1508.01667.
[15] Simonyan K, Zisserman A. Very Deep Convolutional Networks for Large-Scale Image Recognition. Computer Science, 2014. DOI:10.48550/arXiv.1409.1556.
[16] He KM, Zhang XY, Ren SQ, et al. Deep Residual Learning for Image Recognition. Proceedings of the IEEE conference on computer vision and pattern recognition, 2016:770-778.
[17] Grandini M, Bagli E, Visani G. Metrics for Multi-Class Classification: an Overview. Preprint, 2020. DOI:10.48550/arXiv.2008.05756.
[18] Sachin Kumar, Sourabh Shastri. Alzheimer MRI Preprocessed Dataset. Kaggle. 2022. https://www.kaggle.com/datasets/sachinkumar413/alzheimer-mri-dataset.
[19] Iqbal I, Odesanmi GA, Wang J, et al. Comparative Investigation of Learning Algorithms for Image Classification with Small Dataset. Applied Artificial Intelligence, 2021, 35(10):697-716.
[20] 10.34740/kaggle/dsv/3364939Paszke A, Gross S, Massa F, et al. PyTorch: An Imperative Style, High-Performance Deep Learning Library. 2019. DOI:10.48550/arXiv.1912.01703.
[21] Pedregosa F. Scikit-learn: Machine Learning in Python. Journal of Machine Learning Research, 2013, 12(10):2825-2830.

Fuzzy Systems and Data Mining IX
A.J. Tallón-Ballesteros and R. Beltrán-Barba (Eds.)

doi:10.3233/FAIA231108

An Interpretable Residual Neural Network for the Diagnosis of Myocardial Infarction

Xiaoyang WEI[a,b], Mengxiao WANG[a,b], Yanrui JIN[a,b,1], Zhiyuan LI[a,b], Yuanyuan TIAN[a,b] and Chengliang LIU[a,b,2]
[a] *State Key Laboratory of Mechanical System and Vibration, School of Mechanical Engineering, Shanghai Jiao Tong University, Shanghai 200240, China*
[b] *MoE Key Lab of Artificial Intelligence, AI Institute, Shanghai Jiao Tong University, Shanghai 200240, China*

Abstract. Acute myocardial infarction (AMI) is a kind of heart disease with a high mortality rate and easy to ignore the early symptoms. Patients need to obtain timely and accurate diagnosis at the onset of the disease. Automatic ECG diagnosis based on deep learning method is significant for treating such patients because of its timeliness and ease of use. However, the "black box" nature of deep learning methods affects the confidence of doctors and patients and seriously restricts the popularity of its clinical applications. Therefore, it is necessary to study its explainability. This paper uses a residual neural network to realize the end-to-end diagnosis of myocardial infarction disease in a 12-lead electrocardiogram. By designing a specific data processing method, the residual network is used to preserve the characteristics of the feature time order. With the time attention mechanism, we can realize the interpretability of the channel between 12 leads and the time interpretability of the signal segments in each lead. This study reveals the reliability of deep learning methods in clinical Settings.

Keywords. ECG; Residual neural network; Acute myocardial infarction; Interpretability

1. Introduction

Heart disease is one of the most common causes of death worldwide [1], and many specific causes of death are cardiogenic shock after acute myocardial infarction [2]. Acute myocardial infarction is the mass death of cardiomyocytes caused by ischemia. Most of the attack scenes are outside the hospital, and patients easily ignore it in the initial stage. Therefore, there is an urgent need for an automated diagnostic system that is independent of doctors and recognized as reliable to diagnose the occurrence of acute myocardial infarction.

Many researches focus on the automatic diagnosis algorithm of electrocardiogram, among which the traditional machine learning classification algorithm starts early. The principle of this method is to manually screen the representative features of the

[1] Corresponding Author, Yanrui JIN, School of Mechanical Engineering, Shanghai Jiao Tong University, Shanghai 200240, China; E-mail: jinyanrui@sjtu.edu.cn.
[2] Corresponding Author, Chengliang LIU, School of Mechanical Engineering, Shanghai Jiao Tong University, Shanghai 200240, China; E-mail: chlliu@sjtu.edu.cn.

electrocardiogram of various diseases and use it as the basis for automatic diagnosis. For example, Kropf [3] selected 380 different features of ECG signals as the basis for classifier training through research, distinguishing normal ECG, noise signals, atrial fibrillation and other arrhythmias. Limited by the complexity of feature selection, traditional machine learning algorithms can diagnose fewer types of diseases with low accuracy. They can only be used as auxiliary tools in doctors' diagnoses. In recent years, deep learning algorithms have begun to be applied in ECG diagnosis. Network models such as CNN [4] and residual network [5] have excellent performance in diagnosing disease types and accuracy. Many studies have focused on detecting myocardial infarction [6-7], and network models such as CNN, RNN, and ResNet have been used. However, compared to machine learning methods based on fixed features with clear meaning [8-9], doctors and patients often consider deep learning methods "black boxes" [10], and their reliability at the medical level has been widely questioned. Therefore, the interpretability of the ECG deep learning diagnosis methods have begun to be studied [11], which is significant for its clinical application and popularization.

In this study, we designed an interpretable residual neural network that demonstrated excellent performance in experiments using data from patients with prior MI. The network structure's unique design enables the channel's interpretability between 12 leads and the time interpretability of the signal segments in each lead to be realized simultaneously through the attention mechanism.

2. Methodology

2.1. Data Processing and Data Set Partitioning

The ECG data used in this paper are from the PTB Diagnostic ECG Database[12-13]. The database contains 549 15-lead electrocardiograms with a sampling frequency of 1000. This study uses 98 ECG records with former MI, including ordinary ECG without AMI and ECG of six kinds of AMI. Figure 1 (A) shows the data distribution. The number of data in the original database needs to be bigger, and the inconsistent data length is not conducive to batch processing. Therefore, we chose to enhance the original data and split the original data into 2.5 seconds (2500 data points), as shown in Figure 1 (B). The enhanced data set contains 4003 12-lead ECG data of 2500 data points in length, and Figure 1 (C) shows its data distribution. This study aimed to analyze the interpretability of 12-lead myocardial infarction electrocardiograms, and the experiment was designed with the option of conducting an in-patient experiment, i.e. the training set and the test set could be derived from parts of the same raw data. Therefore, we randomly extract 80% of the data set as the training set, 10% as the verification set, and 10% as the test set.

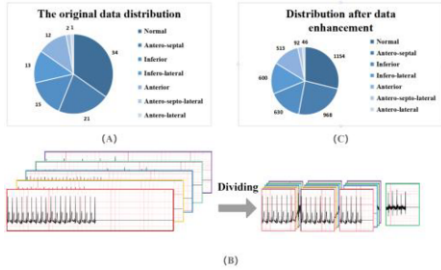

Figure 1. Data distribution.

2.2. Neural Network Architecture

As shown in Figure 2, we designed a neural network consisting of pre-processing, preliminary feature extraction layer, residual network, attention layer, and fully connected layer, as shown in Figure 2 (B).

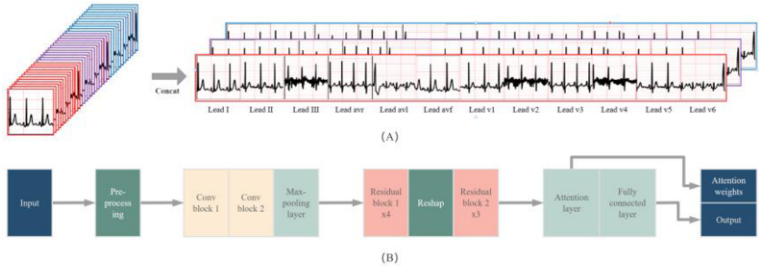

Figure 2. Network architecture.

The input to the network is a 12-lead electrocardiogram fragment. The pre-processing layer splices the 12 channels of ECG fragments into one channel in sequence, as shown in Figure 2 (A) so that the attention layer can calculate the weight within and between leads for interpretability analysis.

The initial feature extraction layer consists of two two-dimensional convolution blocks using large convolution kernels and a maximum pooling layer, where convolution block 1 is a two-dimensional convolution layer, and convolution block 2 is composed of BatchNormalization, ReLU activation layer, maximum pooling layer, and two-dimensional convolution layer.

The residual network consists of a two-dimensional residual block, a flattening layer and a one-dimensional residual block. We use Residual networks to solve the problem of overfitting deep networks [14]. One-dimensional residuals require downsampling due to changes in data size during the process. We use the structure with optimal performance for residual units, as the article [15] proved, which performs batch normalization and Relu activation before the convolutional layer.

The attention layer consists of a fully connected layer, a Tanh nonlinear layer, another fully connected layer, and a Sigmod activation layer whose output is the elements' importance in the input sequence's chronological order. Finally, the final classification result is obtained by calculating the dot product of the input sequence and its weight and using the fully connected layer.

3. Results and Discussion

3.1. Experimental Summary and Results

In the model's training process, we used Focal Loss to select the network loss function [16]. Compared with the traditional cross-entropy Loss function, Focal Loss can solve the problem of unbalanced data distribution by setting weights so that the network model can effectively focus on the categories with a small amount of data. The Adam optimizer is used in backpropagation. The batch size is 128, and the number of training repetitions is 50 epochs. We use Area Under Curve (AUC), Accuracy Rate (ACC) and F1-macro to evaluate network performance. Table 1 shows the performance of the model. The network's performance reaches a very high level because it is set as an in-patient experiment, training set and test set with a high probability of different fragments of ECG data from the same patient.

Table 1. Performance indicators of the network

AUC	ACC	F1-macro	Sensitivity	Specificity	PPV	NPV
99.98%	99.75%	99.86%	99.86%	99.95%	99.86%	99.95%

We use t-Distributed Stochastic Neighbor Embedding (t-SNE) to visualize the network classification results to show the network characteristics before the fully connected connection layer. t-SNE is a dimensionality reduction algorithm that maps high-dimensional feature space to low-dimensional visual space, reflecting the similarity between samples through visual distance. Figure 3 (A) and (B) show the feature space of the network model corresponding to epoch 0 (untrained) and epoch 50 (trained) of the test set, respectively, reflecting the training effect of the network.

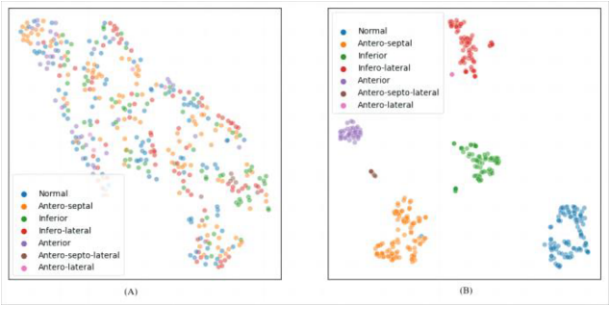

Figure 3. t-SNE for epoch 0 and epoch 50.

3.2. Interpretability

The object of this study is the interpretability analysis of the 12-lead ECG myocardial infarction classification network, that is, the attention mechanism to identify and visualize the network's areas of interest on signals between leads and within leads.

In the previous experiment, we tried to use the channel attention mechanism for interpretability between leads. The signals of 12 leads were respectively input into 12 parallel neural network channels, and the output was fitted using the attention layer. However, the experimental results show that the performance of this idea is not ideal; ACC can only reach close to 60%, and the oscillation is violent. Therefore, we finally

chose to splinter the original signals of the 12 channels into a single channel signal in order so that the timing characteristics of the output features of the residual network can be used to achieve inter-lead interpretability and intra-lead interpretability at the same time by using the time-attention mechanism. After pre-processing, the network input is a one-dimensional signal of length 30000, which can be divided into 12 original signals of length 2500 in order 12 equals. Therefore, since the residual network does not change the temporal relationship on the feature dimension, the feature weights calculated by the attention layer reflect the chronological importance of the original inputs. By dividing the weight sequence 12 equally and calculating the mean of each segment separately, the attention of the network for a particular disease on 12 leads can be determined. Taking FIG. 4 (A) as an example, the network concerns of antero-septal acute myocardial infarction are Lead v1, Lead v2, and Lead v3, consistent with medical judgment.

For interpretability within leads, that is, areas of concern within an ECG fragment, the degree of concern at each point in time can be obtained by resampling the weight value of the corresponding fragment to the same length as the input sequence. As shown in Figure 4 (B), (C), and (D), we reflected the network attention of Lead v1, Lead v2, and Lead v3 fragments of antero-septal acute myocardial infarction by colour, and the regions closer to red received greater network attention.

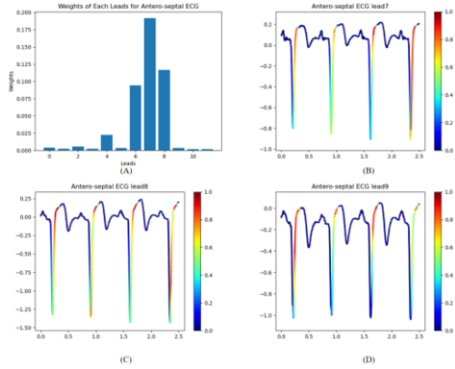

Figure 4. Interpretability of antero-septal myocardial infarction.

4. Conclusion

The deep learning method has excellent application prospects in electrocardiogram automatic diagnosis. However, doctors and patients often view it as a "black box" and question it. In this paper, we propose an explainable residual neural network method and show excellent performance in experiments. In this method, 12-lead ECG signals are spliced into the same channel to convert the information between channels into time information. Then, multi-scale features are extracted through multiple convolution blocks and residual blocks, which still preserve the time order of the original input signal. Through the attention layer, we get the attention weight of the feature sequence. This weight information can be restored to the channel attention between the 12 leads and the time attention of the signal fragments within each lead in chronological order. This study verified the interpretability of the 12-lead ECG deep learning method for

diagnosing myocardial infarction between leads and within leads. It proved the great potential of deep learning in the clinical application of ECG diagnosis. In future work, we plan to improve the applicability and reliability of this work in more complex and realistic experimental environments.

Acknowledgement

This project is supported by China Postdoctoral Science Foundation (Grant No. 2023M732219) and Shanghai Municipal Science and Technology Major Project (No. 2021SHZDZX0102).

References

[1] Roth, G.A. et al. Global, regional, and national age-sex-specific mortality for 282 causes of death in 195 countries and territories, 1980–2017: a systematic analysis for the Global Burden of Disease Study 2017, The Lancet (British edition), 2018; 392(10159), pp. 1736–1788.
[2] Samsky, M.D. et al. "Cardiogenic Shock After Acute Myocardial Infarction: A Review," JAMA: the journal of the American Medical Association, 2021; 326(18), p. 1840.
[3] Kropf, M., Hayn, D. and Schreier, G. "ECG classification based on time and frequency domain features using random forests," 2017 Computing in Cardiology (CinC), 2017; pp. 1–4.
[4] Qi, L. et al. "ECG Arrhythmia Heartbeat Classification Using Deep Learning Networks," in Cloud Computing. Switzerland: Springer International Publishing AG (Lecture Notes of the Institute for Computer Sciences, Social Informatics and Telecommunications Engineering), 2021; pp. 175–189.
[5] Ribeiro, A.H. et al. "Automatic diagnosis of the 12-lead ECG using a deep neural network," Nature Communications, 2020; 11(1).
[6] Chen, Z. et al. "Automatic deep learning-based myocardial infarction segmentation from delayed enhancement MRI," Computerized medical imaging and graphics, 2022; 95, p. 102014.
[7] Xiong, P., Lee, S.M.-Y. and Chan, G. "Deep Learning for Detecting and Locating Myocardial Infarction by Electrocardiogram: A Literature Review," Frontiers in cardiovascular medicine, 2022; 9, p. 860032.
[8] Dong, X. and Si, W. "Heartbeat dynamics: a novel efficient interpretable feature for arrhythmias classification," IEEE access, 2023; 11, p. 1.
[9] Katsushika, S. et al. "An explainable artificial intelligence-enabled electrocardiogram analysis model for the classification of reduced left ventricular function," European heart journal. Digital health, 2023; 4(3), pp. 254–264.
[10] Bodini, M., Rivolta, M.W. and Sassi, R. "Opening the black box: interpretability of machine learning algorithms in electrocardiography," Philosophical transactions of the Royal Society of London. Series A: Mathematical, physical, and engineering sciences, 2021; 379(2212), p. 20200253.
[11] Abdullah, T.A.A. et al. "B-LIME: An Improvement of LIME for Interpretable Deep Learning Classification of Cardiac Arrhythmia from ECG Signals," Processes, 2023; 11(2), p. 595.
[12] Bousseljot, R.; Kreiseler, D.; Schnabel, A. Nutzung der EKG-Signaldatenbank CARDIODAT der PTB über das Internet. Biomedizinische Technik, Band 40, Ergänzungsband 1, 1995; S 317.
[13] Kreiseler, D.; Bousseljot, R. Automatisierte EKG-Auswertung mit Hilfe der EKG-Signaldatenbank CARDIODAT der PTB. Biomedizinische Technik, Band 40, Ergänzungsband 1, 1995; S 319.
[14] He, K. et al. "Deep Residual Learning for Image Recognition," 2016 IEEE Conference on Computer Vision and Pattern Recognition (CVPR), 2016; pp. 770–778.
[15] He, K. et al. "Identity Mappings in Deep Residual Networks," arXiv.org, 2016; pp. arXiv.org.
[16] Lin, T.-Y. et al. "Focal Loss for Dense Object Detection," IEEE transactions on pattern analysis and machine intelligence, 2020; 42(2), pp. 318–327.

Fuzzy Systems and Data Mining IX
A.J. Tallón-Ballesteros and R. Beltrán-Barba (Eds.)

doi:10.3233/FAIA231109

Bayesian Updating Using DBSCAN-Based Hybrid Importance Sampling and Subset Simulation

Yihao LIAO[a,1]
[a]*Department of Statistics, Rice University, Houston, 77251, TX, United States*

Abstract. A novel methodology for Bayesian updating is proposed by seamlessly integrating the power of DBSCAN, an unsupervised learning algorithm renowned for its ability to identify dense clusters in data, with the concept of importance sampling. While traditional Bayesian updating methods heavily rely on supervised learning and labeled data, our approach unleashes the true potential of unsupervised updating. Through the utilization of DBSCAN, we obtain remarkable insights by effectively extracting similarities and patterns within the data, allowing for a comprehensive understanding of the underlying structure. By incorporating importance sampling, we intelligently select representative samples, thus enhancing the accuracy and efficiency of the Bayesian updating process. Empirical validation reinforces the profound impact of our approach, demonstrating its ability to achieve unprecedented levels of accuracy and efficiency in Bayesian updating, all while negating the necessity of labeled data. Consequently, our pioneering method enriches the field of unsupervised learning in the context of Bayesian updating, offering novel avenues for exploratory data analysis and informed decision-making.

Keywords. Bayesian updating, Subset Simulation, Importance Sampling, Bayesian Inference, Uncertainty Quantification

1. Introduction

Bayesian updating is a fundamental statistical concept employed to revise prior beliefs based on new information. Traditional approaches to Bayesian updating predominantly rely on supervised learning techniques, which necessitate labeled data for accurate inference. In this study, we propose an innovative methodology that integrates the algorithm of Density-Based Spatial Clustering of Applications with Noise (i.e., DBSCAN), an unsupervised learning technique, with importance sampling to facilitate Bayesian updating in an unsupervised manner.

The DBSCAN algorithm discerns dense regions within data points, enabling the identification of meaningful clusters. By applying DBSCAN to our dataset, we can identify subsets of data that are likely to exhibit similar characteristics. This clustering insight not only offers valuable comprehension of the underlying data structure but also allows for efficient Bayesian updating. Moreover, Importance sampling, a widely adopted technique in Monte Carlo simulations, enables the effective estimation of desired properties by sampling from a suitable distribution. Our approach incorporates importance sampling to make informed decisions regarding the selection of representative samples for the updating of prior beliefs. This adaptive sampling

[1] Corresponding Author, Yihao LIAO, Department of Statistics, Rice University, United States; E-mail: liaoyihao123@outlook.com.

approach optimizes the allocation of computational resources, subsequently reducing the time and cost associated with the updating process.

Through meticulous experimental validation, we substantiate the effectiveness of our proposed approach in facilitating unsupervised Bayesian updating. Moreover, we emphasize the numerous advantages of combining DBSCAN and importance sampling, including heightened accuracy, reduced dependence on labeled data, and enhanced computational efficiency. By contributing novel insights to the field of unsupervised learning in the context of Bayesian updating, our findings present a valuable alternative for researchers and practitioners working with unlabeled data. The introduction of unsupervised learning techniques within the framework of Bayesian updating enables a broader range of data analysis possibilities. Future research endeavors can focus on further refining our approach, expanding its applicability across diverse domains and datasets.

In summary, this study expands the horizons of unsupervised learning in Bayesian updating, opening new avenues for effective decision-making and insightful data analysis. The proposed methodology empowers researchers and practitioners to embrace unsupervised learning techniques while updating prior beliefs, unlocking a realm of opportunities in various domains.

2. Bayesian Updating with Structural Reliability Methods

The traditional Markov Chain Monte Carlo (MCMC) method has several limitations in terms of stability. One major drawback is its sensitivity to initialization. MCMC's convergence relies on finding a good starting point, and poor initialization can result in slow convergence, or worse, in chains that fail to converge at all. Another stability issue is related to sampling inefficiency. MCMC algorithms often encounter difficulties in traversing high-dimensional probability spaces, leading to slow exploration and inadequate mixing of the Markov chains. This inefficiency can result in long autocorrelation times, further hindering convergence. Moreover, MCMC methods may struggle with multimodal distributions, where multiple distinct maxima or modes exist in the probability distribution. The chains can get stuck in one mode and fail to fully explore other regions, leading to biased estimates and incomplete sampling of the posterior distribution.

In order to overcome this limitation, the method of Bayesian Updating with Structural Reliability Methods (i.e., BUS) are proposed by Straub and Papaioannou [1]. This method can be leveraged to enhance the accuracy and efficiency of the estimate of posterior probability. Hence, several effective techniques can be employed to aid in Bayesian updating. These include optimization-based approximation methods such as the optimization-based First & Second Order Reliability Methods (FORM and SORM) [2], [3], sampling-based methods such as crude Monte Carlo Simulation (i.e., MCS) [4], [5], importance sampling (i.e., IS) [6-9], and subset simulation (i.e., SS) [10]. Within BUS, the Simple Rejection Method (SRM) is implemented, which is briefly explained in this subsection. It's important to note that the accepted domain Ω_a can be defined according to the restructured random variables [x, p], where P is an auxiliary uniform random variable and the corresponding regions can be defined according to the following equations:

$$\Omega_a = [p \leq cL(\mathbf{x})] = [h(\mathbf{x}, p) \leq 0] \#(1)$$

where

$$\mathrm{B}(\mathbf{x},\mathrm{p}) = \mathrm{p} - \mathrm{cL}(\mathbf{x}) \#(2)$$

$\mathrm{B}(\mathbf{x},\mathrm{p})$ is the equivalent limit state function parameterized by the random variables $[\mathbf{x},\mathrm{p}]$ and c is a constant satisfying $\mathrm{cL}(\mathbf{x}) \leq 1$ for all the outcomes of $\mathbf{X}$. c can be defined as,

$$\mathrm{c} = \frac{1}{\max\left(\mathrm{L}(\mathbf{x})\right)} \#(3)$$

Here, one can define the posterior distribution,

$$\mathrm{f}'(\mathbf{x}) = \frac{\int_{\mathrm{p}\in\Omega_\mathrm{a}} \mathrm{f}(\mathbf{x})\mathrm{dp}}{\int_{[\mathbf{x},\mathrm{p}]\in\Omega_\mathrm{a}} \mathrm{f}(\mathbf{x})\mathrm{dpd}\mathbf{x}} \#(4)$$

where $\mathrm{I}^{\mathrm{a}}([\mathbf{x},\mathrm{p}] \in \Omega_{\mathrm{acc}})$ can be treated as an indicator along with the new defined limit state function, $\mathrm{B}(\mathbf{x},\mathrm{p}) = \mathrm{p} - \mathrm{cL}(\mathbf{x})$. Therefore, Eq. (4) can be developed as follows,

$$\int_{\mathrm{p}\in\Omega_\mathrm{a}} \mathrm{f}(\mathbf{x})\mathrm{dp} = \int_0^{\mathrm{cL}(\mathbf{x})} \mathrm{f}(\mathbf{x})\mathrm{dp} = \mathrm{cL}(\mathbf{x})\mathrm{f}(\mathbf{x}) \#(5)$$

and

$$\int_{[\mathbf{x},\mathrm{p}]\in\Omega_\mathrm{a}} \mathrm{f}(\mathbf{x})\mathrm{dpd}\mathbf{x} = \int_{\mathbf{X}} \mathrm{cL}(\mathbf{x})\mathrm{f}(\mathbf{x})\mathrm{d}\mathbf{x} \#(6)$$

Equation (5) and (6) represent the precise formulations given in Equation (4). Within this context, simple rejection sampling method has a drawback in exhibiting a low acceptance rate. As the number of obtained information and observations increases, this rate decreases significantly. In their study, Straub and Papaioannou [1] highlighted that, under the assumption that those information are mutually independent, the average acceptance rate is inversely proportional to m ($1/\sqrt{m}$). This limitation poses computational challenges when performing Bayesian updating since only a small number of target points will be utilized for estimating the posterior distribution, while a large number of redundant points are generated. This problem tends to be particularly pronounced as dealing with complex and time-consuming models.

3. DBSCAN Algorithm

Inspired by the work represented in [11], [12], this paper proposes a new method of Bayesian Updating, called BUUL, (i.e., Bayesian updating with Unsupervised learning) to improve the computational efficiency. The proposed BUUL method integrates the unsupervised learning method and importance sampling within the framework of BUS. In this context, unsupervised learning is a set of machine learning techniques that aim to identify hidden patterns within a dataset without prior labels. In the context of reliability problems, the labels for the response function, which indicate failure or safety, are typically unknown before conducting simulations. The computational performance of our proposed method pertains to accurately identifying target sampling regions, as explained in the previous subsection. To address this, unsupervised learning techniques can be employed to define clusters and enhance the identification of effective sampling regions. However, some of these unsupervised learning techniques, such as parameterized K-means, require the predefined number of clusters, which is not suitable for cases where the number of failure domains is unknown. DBSCAN, on the other hand, overpowers other state-of-the-art methodologies due to its computational

efficiency in automatically determining the number of clusters, aligning with our goal of clustering multiple failure domains. Therefore, we have integrated the DBSCAN algorithm with our proposed BUUL method in this article.

The DBSCAN algorithm focuses on identifying core points, density-reachable points, and outliers within the dataset. A point, is considered a core point if the number of points within a distance ε from it, denoted as $n_{\leq\varepsilon}(x_{seed})$, is greater than or equal to n_{min}, a predefined constant. Additionally, x_{seed} is classified as a border point if it has at least one core point within distance ε, denoted as $C(x_{seed})$, but is not a core point itself. The concept of "directly reachable" is represented by $D(x_{seed}, x_{core})$, indicating whether x_{seed}, can be reached from a core point, x_{core}. Furthermore, x_q can be reachable and rendered from another point, x_p, if there exists a path $\mathbb{p}_1$, ..., $\mathbb{p}_n$, with $\mathbb{p}_1 = x_p$ and $\mathbb{p}_n = x_q$, where each subsequent point, $\mathbb{p}_{i+1}$, is directly reachable from $\mathbb{p}_i$. It is important to note that all the samples need to be transformed into an isoprobabilistic space with a transformed standard normal distribution before applying the proposed BUUL algorithm. In this paper, we will employ DBSCAN to integrate with the BUS algorithm in order to achieve an unbiased estimation of the Bayesian posterior probabilities.

4. Case Study

This section investigates a numeric example to elaborate the overall procedures of the proposed algorithm. Moreover, the parameters $\epsilon = 1.5$ and $n_{min} = 3$ are set for the proposed BUUL algorithm along with DBSCAN. In this example, a numerical case with two degrees of freedom (two-DOF) dynamic system which was documented in [13] and subsequently explored in form of reinterpreted structural reliability problems [1], [14]. Via acquiring the eigen-frequencies of the structure, the posterior distribution of inter-story stiffnesses can be estimated using the Bayesian updating technique such as BUS algorithm (i.e., Bayesian Updating with Structural reliability problem). **Figure 1** illustratively elaborates the scheme of this example. The masses of the two different stories are, respectively, defined as $m_1 = 16.531 \cdot 10^3$ kg and $m_2 = 16.13.1 \cdot 10^3$ kg. The inter-story stiffnesses are modeled as $K_1 = X_1 k_n$ and $K_2 = X_2 k_n$, where K_1 and K_2 are the stiffness values of the first and second stories, respectively, $k_n = 29.7 \cdot 10^6$ N/m is the nominal value, and X_1 and X_2 are correction factors to be updated. Damping is not considered in this case. Observations of the first two eigen-frequencies f_1 and f_2 are used to update the distribution of $\mathbf{X} = [X_1, X_2]$. The corresponding transformed limit state function of the transformed structural reliability problem can be read as,

$$B(\mathbf{x}, p) = p - C \cdot \exp\left[-\frac{J(\mathbf{X})}{2\sigma_\varepsilon^2}\right] \#(7)$$

where p is an auxiliary uniformly distributed random variable, C is the so-called constant and equal to 1, and $J(\mathbf{X})$ is a measure-of-fit function parameterizing the likelihood of observed information, which can be represented as,

$$J(\mathbf{X}) = \sum_{j=1}^{2} \lambda_j^2 \left[\frac{f_j^2(\mathbf{X})}{\tilde{f}_j^2} - 1\right]^2 \#(8)$$

where $f_i(\mathbf{X})$ is the jth eigen-frequency estimated from the structural model with random variables $\mathbf{X}$, and $\tilde{f}_j^2$ is the measurement of the jth eigen-frequency. $\lambda_1 = \lambda_2 = 1$ are the means and $\sigma_\varepsilon = \frac{1}{16}$ is the standard deviation of the prediction error. Two measurements of eigen-frequencies are available: $\tilde{f}_1 = 3.13$ Hz and $\tilde{f}_2 = 9.83$ Hz. The distribution of X_1 and X_2 are uncorrelated lognormal distributions with means 1.87 and 1.43 and standard deviations $\sigma_{X_1} = \sigma_{X_2} = 1$. Moreover, $f_j(\mathbf{X})$ are calculated according to the equation below,

$$f_j(\mathbf{X}) = \frac{-\left((K_1 + K_2)m_2 + m_1K_2\right) \pm \sqrt{\left((K_1 + K_2)m_2 + m_1K_2\right)^2 - 4m_1m_2K_1K_2}}{-4\pi m_1m_2}, \#(9)$$

For this example, methods including brute MCS, IS, FORM, SS and the proposed BUUL methodology are investigated to explore their computational efficiencies.

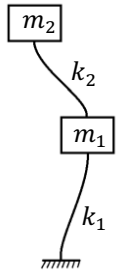

Figure 1. Two-DOF shear building model.

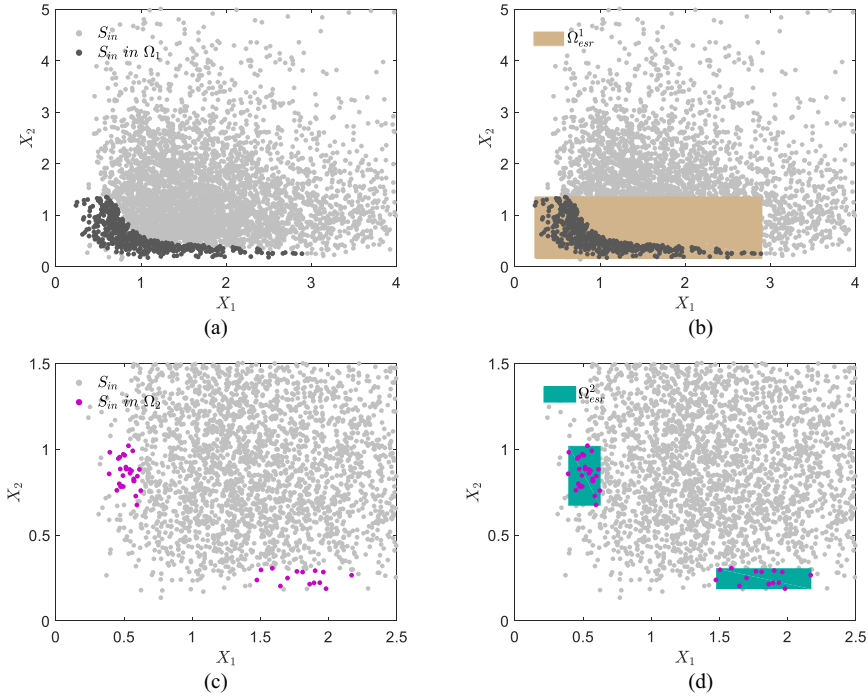

Figure 2. Illustrations of the implementations of the proposed BUUL method

Fig 2 illustrates the identification of effective sampling regions in different layer of subsets. According to **Fig** 2(a), the back samples denote the seeds located in the first subset after the initial subset is drawn through MCS. By taking the advantage of DBSCAN, the BUUL method can automatically identify one cluster, which facilitates the identification of the first ESR as shown in **Fig** 2(b). Moreover, the first intermediate failure threshold is estimated as 36.21. **Fig** 2(c) showcases the seeds located in the first effect sampling regions, which are distributed in different regions. Fortunately, the BUUL can strategically identify these two clusters. According to **Fig** 2(d), the areas of the second effective sampling region is much smaller than that of the first one. The second and third intermediate failure thresholds, $\hat{t}_2$ and $\hat{t}_3$, are estimated as 4.424 and -0.5406, respectively. Moreover, **Fig** 3 illustrates the implementations of Crude MCS, FORM, IS and SS. According to the simulation results, it can be observed that the traditional FORM and IS method can merely provide inaccurate estimate for the Bayesian updating due to the existence of multiple failure regions. As an alternate for Bayesian updating, the proposed BUUL provides the posterior estimate with less uncertainty compared to the traditional SS for the same level of computational cost.

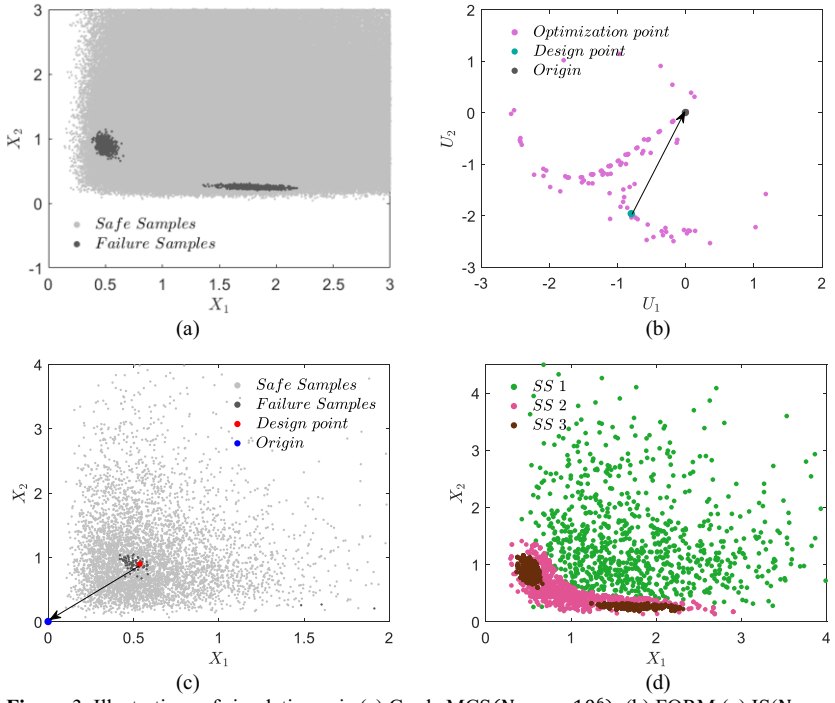

Figure 3. Illustrations of simulations via (a) Crude MCS($N_{mcs} = 10^6$) (b) FORM (v) IS($N_{is} = 1000$) and (d)SS($N_{ss} = 1000$).

5. Conclusion

This study focused on Bayesian updating using a novel approach that combines DBSCAN-based hybrid importance sampling and subset simulation. By integrating the DBSCAN algorithm, we were able to overcome the limitations of traditional methods

and provide unbiased estimations of Bayesian posterior probabilities. The proposed framework demonstrated its effectiveness in accurately updating the posterior distribution, even in scenarios involving high-fidelity Finite Element models. Through the hybrid importance sampling and subset simulation techniques, we achieved an improved acceptance rate and reduced computational burden, overcoming the challenges posed by complex models and large numbers of observations. The integration of DBSCAN added robustness to the method by effectively handling both clustered and sparse data. The results obtained in this study highlight the potential of the DBSCAN-based hybrid approach for Bayesian updating in various fields, including engineering, finance, and risk analysis. Future work could explore further enhancements and applications of this method in complex and multidimensional systems.

References

[1] Straub Daniel and Papaioannou Iason, "Bayesian Updating with Structural Reliability Methods," *Journal of Engineering Mechanics*, vol. 141, no. 3, p. 04014134, Mar. 2015, doi: 10.1061/(ASCE)EM.1943-7889.0000839.

[2] R. Rackwitz and B. Flessler, "Structural reliability under combined random load sequences," *Computers & Structures*, vol. 9, no. 5, pp. 489–494, Nov. 1978, doi: 10.1016/0045-7949(78)90046-9.

[3] Kiureghian Armen Der and Stefano Mario De, "Efficient Algorithm for Second-Order Reliability Analysis," *Journal of Engineering Mechanics*, vol. 117, no. 12, pp. 2904–2923, Dec. 1991, doi: 10.1061/(ASCE)0733-9399(1991)117:12(2904).

[4] R. Y. Rubinstein and D. P. Kroese, *Simulation and the Monte Carlo method*. John Wiley & Sons, 2016. Accessed: May 12, 2017.

[5] G. Fishman, *Monte Carlo: concepts, algorithms, and applications*. Springer Science & Business Media, 2013. Accessed: May 12, 2017.

[6] B. Echard, N. Gayton, M. Lemaire, and N. Relun, "A combined importance sampling and kriging reliability method for small failure probabilities with time-demanding numerical models," *Reliability Engineering & System Safety*, vol. 111, pp. 232–240, 2013.

[7] S. K. Au and J. L. Beck, "A new adaptive importance sampling scheme for reliability calculations," *Structural safety*, vol. 21, no. 2, Art. no. 2, 1999.

[8] R. E. Melchers, "Importance sampling in structural systems," *Structural safety*, vol. 6, no. 1, Art. no. 1, 1989.

[9] N. Pedroni and E. Zio, "An Adaptive Metamodel-Based Subset Importance Sampling approach for the assessment of the functional failure probability of a thermal-hydraulic passive system," *Applied Mathematical Modelling*, vol. 48, pp. 269–288, Aug. 2017, doi: 10.1016/j.apm.2017.04.003.

[10] S.-K. Au and J. L. Beck, "Estimation of small failure probabilities in high dimensions by subset simulation," *Probabilistic Engineering Mechanics*, vol. 16, no. 4, pp. 263–277, 2001.

[11] Y. Zhao and Z. Wang, "Subset simulation with adaptable intermediate failure probability for robust reliability analysis: An unsupervised learning-based approach," *Structural and Multidisciplinary Optimization*, vol. 65, no. 6, p. 172, 2022.

[12] Z. Wang and A. Shafieezadeh, "Bayesian updating with adaptive, uncertainty-informed subset simulations: High-fidelity updating with multiple observations," *Reliability Engineering & System Safety*, vol. 230, p. 108901, Feb. 2023, doi: 10.1016/j.ress.2022.108901.

[13] Beck James L. and Au Siu-Kui, "Bayesian Updating of Structural Models and Reliability using Markov Chain Monte Carlo Simulation," *Journal of Engineering Mechanics*, vol. 128, no. 4, pp. 380–391, Apr. 2002, doi: 10.1061/(ASCE)0733-9399(2002)128:4(380).

[14] D. G. Giovanis, I. Papaioannou, D. Straub, and V. Papadopoulos, "Bayesian updating with subset simulation using artificial neural networks," *Computer Methods in Applied Mechanics and Engineering*, vol. 319, pp. 124–145, Jun. 2017, doi: 10.1016/j.cma.2017.02.025.

Fuzzy Systems and Data Mining IX
A.J. Tallón-Ballesteros and R. Beltrán-Barba (Eds.)

Subject Index

A.J. Tallón-Ballesteros and R. Beltrán-Barba (Eds.)

Author Index

This page intentionally left blank